Vol. 64, No. 2 / 2021

e: ISSN 2068 – 2239
p: ISSN 2068 – 4215

INMATEH -

AGRICULTURAL ENGINEERING

MAY - AUGUST

INMATEH - Agricultural Engineering **journal is indexed in the next international databases:**
ELSEVIER /SciVerse SCOPUS, CLARIVATE - WEB of SCIENCE- Emerging Sources Citation Index (ESCI), ULRICHS Web: Global Serials Directory, CABI, SCIPIO, Index COPERNICUS International, EBSCO Publishing, Elektronische Zeitschriftenbibliothek

INMATEH - Agricultural Engineering
vol. 64, no.2 / 2021
e-ISSN: 2068 – 2239; p: ISSN: 2068 – 4215

https://inmateh.eu/ *E-mail: inmatehjournal@gmail.com*

Edited by: INMA Bucharest

National Institute for Research-Development of Machines and Installations Designed for Agriculture and Food Industry - INMA Bucharest
6, Ion Ionescu de la Brad Bvd., sector 1, Bucharest, ROMANIA

CONTENT

EQUIPMENT TO ADMINISTER IN-DEPTH AMENDMENTS ON LAND AFFECTED BY SALINISATION
/
ECHIPAMENT PENTRU ADMINISTRAT AMENDAMENTE ÎN ADÂNCIME PE TERENURILE AFECTATE DE SĂRĂTURARE

Bularda M. [1], Ungureanu N. [2], Isticioaia S. F. *[3], Ciuperca R.[4], Mitrache P.M.[5]
[1] University Dunărea de Jos Galaţi / Romania; [2] University Politehnica of Bucharest, Faculty of Biotechnical Systems Engineering / Romania; [3] SCDA Secuieni / Romania; [4]National Institute of Research Development for Machines and Installations Designed to Agriculture and Food Industry – INMA Bucharest/ Romania; [5] University of Craiova / Romania
E-mail: simonapochi@yahoo.com
DOI: https://doi.org/10.356.33/inmateh-64-01

Keywords: *salted lands, deep loosening, phosphogypsum, phosphogypsum administration*

ABSTRACT
This paper presents the results obtained regarding the realization of a functional model of equipment for managing in-depth amendments on salted lands and the results regarding the effect of the work performed in three soil conditions. At the same time, the physical properties of the amendment used (phosphogypsum), determined in laboratory conditions, in order to know the problems that may occur during the application work, are presented.

REZUMAT
In lucrare se prezinta rezultatele obținute privind realizarea unui model funcțional de echipament pentru administrat amendamente in adâncime pe terenurile sărăturate si rezultatele privind efectul lucrării efectuate in trei condiții de sol. Totodată, se prezinta proprietățile fizice ale amendamentului folosit (fosfogips), determinate in condiții de laborator, in scopul cunoașterii problemelor ce pot sa apară in timpul efectuării lucrării de aplicare.

INTRODUCTION
At present, agriculture must provide the necessary food for a population of 7.7 billion inhabitants, respectively to an expected 9.0 billion inhabitants in 2040 and 9.8 billion inhabitants in 2050 (*FAO, 2012; Ungureanu et al., 2020*), which means an increase of 16% in 20 years and respectively 27% in 30 years. By 2050, worldwide food production shall increase by 70% (*WRI, 2020*) and this increase will be mainly supplied by agriculture. Due to population increase, climate change, freshwater crisis, deterioration of soil quality by inadequate works (*Biriş et al., 2007; Biriş et al., 2011; Croitoru et al., 2015; Croitoru et al., 2016; Croitoru et al., 2017*), increasing environmental pollution and changing biodiversity (*Cujbescu et al., 2019; Bularda et al., 2020*), the agriculture must quickly find the solutions to overcome these difficulties and achieve the parameters related to food safety and security. In order to ensure the food requirement in 2050, agriculture must find and prepare strategic solutions and measures to allow a significant increase in agricultural production (*Vlăduţ D.I. et al., 2017a; Vlăduţ D.I., et al., 2017b; Vlăduţ D.I., et al., 2018; Vlăduţoiu et al., 2016; Vlăduţoiu et al., 2017*). It is estimated that about 90% of the increase in agricultural production will be made from existing and cultivated land and 10% from new land that will be improved by specific works (embankment, drainage, improvement, etc.) (*Bularda M., 2020*).

Ensuring the necessary food growth for mankind, complementary to population growth, is largely agricultural. This economic branch has two main ways of action, namely, intensifying activity and increasing agricultural production to maintain or increase the amount of food per capita per year, and expanding agriculture by cultivating new areas to maintain or increase the agricultural area, statistically per capita, as a food source. In the context of those presented, it is known that in 1999 the average specific production worldwide was 0.35 t/inhabitant, 18% higher than 30 years ago. The annual growth rate of world agricultural production was 3% between 1960 and 1970 and below 2% after 1980. In many geographical areas, the average cereal production is very low, of only 0.16 t/inhabitant in Africa and 0.29 t/inhabitant respectively in Asia and Oceania.

With this type of data at hand and taking into account both a specific average level of agricultural production per capita and the estimated number of inhabitants at a given time, the food needs can be calculated and the additional burden on agriculture can be assessed. The task of agriculture to provide food becomes even more difficult as the area of cultivated land per capita fell globally from 0.45 ha/inhabitant in 1961 to 0.25 ha/inhabitant now. Romania returned in 2004 to an average 0.4 ha/inhabitant. To cope with population increase, agriculture must produce 4.0 billion tons of grain, which is double the current situation.

Soil degradation processes imply the need to protect, maintain and improve soil quality (*Ungureanu et al., 2019*). Salinisation (salinity) is one of the most widespread processes of soil degradation on Earth (*Phogat et al., 2020*). About 830 million ha of soil area are estimated to be afflicted by salinity and sodicity (*Carmeis-Filho et al., 2017*; *Minhas et al., 2020*). In this context, it can be appreciated that the improvement of saline soils and the prevention of secondary salinisation of soils are activities that need to be given more attention (*Biggs and Jiang, 2009; Endo et al., 2011*).

Annually, the irrigation facilities are degraded by secondary salinisation and wilting (*Muyen et al., 2011; Ungureanu et al., 2020*) and 125 thousand ha exit the agricultural circuit. On saline and alkaline soils, special attention must be paid to amendments, without which fertilizers cannot have the expected effect. Both amendments and fertilizers aim to increase the productivity of saline soils (*Phogat et al., 2020*). Gypsum-based amendments ($CaSO_4$ + $2H_2O$) are used to improve saline and alkaline soils, with the exception of solodized soils (*Ezlit et al., 2010*). The exchange reactions result in Na_2SO_4, a salt with a lower alkaline reaction than Na_2CO_3, and at the same time very soluble, which can be easily removed with washing water. As gypsum is used in large quantities in industry, the most widely used amendment today is phosphogypsum, waste from phosphorus and sulfuric acid fertilizer plants, with the following chemical composition: 75-80% $CaSO_4$ + $2H_2O$; 5-8% P_2O_5.

Phosphogypsum is administered in a dose of 10-20 t/ha, after ploughing with which the manure is incorporated. It is spread on the surface and introduced into the soil by discus. Phosphogypsum contributes to soil desalination and at the same time improves its permeability to water and as a result increases the storage capacity of water accessible to plants (*Wang J., 2020*). The in-depth amendment leads to a decrease in the improvement time and an increase in the depth improvement effect. This work must be carried out mechanically on the occasion of another work such as deep loosening or scarification, so that the additional costs for its execution are minimal.

MATERIALS AND METHODS

The working method consisted in determining the physical-mechanical indices of phosphogypsum, in establishing the agrotechnical requirements for the execution of experimental equipment, in designing and executing a functional model of equipment for managing in-depth amendments on saline lands and in testing it in laboratory-field conditions.

Determination of physical-mechanical indices of phosphogypsum. The purpose of the research regarding the determination of the physical-mechanical indices of the phosphogypsum was to highlight the influence of humidity on these indices and to verify some possibilities for their improvement by mixing the phosphogypsum with other materials. The method for determining the flow properties uses for this purpose a cylinder open at the top (Fig. 1a) and provided with a disc-shaped piston fixed on a threaded rod (*Krasnicenco A.V., 1963*). When the piston is at the bottom, the cylinder is filled with the phosphogypsum passed through a sieve, with the help of a plate the phosphogypsum placed at the top of the cylinder is straightened and the piston will be raised to a certain height h, which will lead to the evacuation of a certain volume of phosphogypsum:

$$V_h = \frac{\pi}{4} \cdot d^2 \cdot h \;\; [cm^3] \tag{1}$$

where: V_h - volume of phosphogypsum discharged [cm^3]; d - cylinder diameter [cm]; h - piston lift height [cm], by weight of:

$$Q_h = V_h \cdot \gamma_f \;\; [g] \tag{2}$$

where:

Q_h - mass of the volume of discharged phosphogypsum [g]; V_h - volume of phosphogypsum discharged [cm^3]; γf - volumetric mass of phosphogypsum [g/cm^3].

Depending on the flow property, some of the phosphogypsum removed from the cylinder will leak and some will remain at the top. If the part of the leaked phosphogypsum (Qs) is weighed, then flow index is:

$$\eta_c = \frac{Q_s}{Q_h} \tag{3}$$

The ability of the phosphogypsum to form vaults uses the apparatus of Figure 1b, which is in the form of a box provided at the bottom with a hole closed by a calliper (*Krasnicenco A.V., 1963*). When the hole is closed, the box is filled with phosphogypsum in a uniform layer having a height of 40 mm and a pressure of 14.71 kPa is applied over the entire surface for 2 sec; pour the second layer of phosphogypsum to a height of 30 mm and press at the same time. By removing the calliper from the bottom of the box it can be seen that in some humid conditions a vault is formed. The pressure that destroys the vault is considered as an index of the resistance of the formed vault, P [kPa]. The stronger the vault formed, the greater the ability of the material to form the vault.

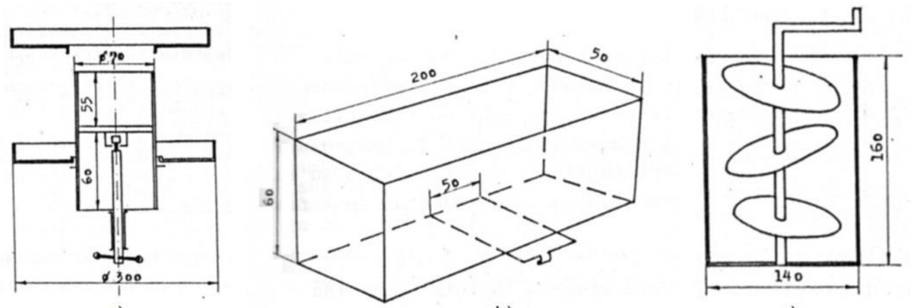

a) b) c)

Fig. 1 - Apparatus for determining the physical and mechanical properties of phosphogypsum

a-apparatus for determining flow properties; b-apparatus for determining the capacity to form a vault; c-Apparatus for determining the ability to form lumps and adhesion

The method for determining the properties of forming land lumps and adhering to bodies is limited to mixing the phosphogypsum poured into a vertical cylinder, using a stirred disk mounted inclined to the horizontal plane (Fig. 1c). Phosphogypsum mixed for 75 sec at a speed of 1 $rot \cdot s^{-1}$ is separated with a 5 mm diameter sieve. The land lumps left on the sieve and the amendment that adhered to the agitator's discs are weighed (*Krasnicenco A.V., 1963*). The ratio between their weight and the weight of the phosphogypsum introduced in the device can serve as an index of the ability to form lumps and its adhesion to bodies, p:

$$p = \frac{G_{lumps} > 5\ mm + adhering\ material}{G_{total}}$$

The mentioned properties are influenced by humidity. Thus, in the case of high humidity, the mechanical distribution of the amendment spreaders works poorly or is not able to perform its function. For this reason, phosphogypsum needs to be used only in humidities that allow good administration. In order to have a more suggestive image of the properties of the phosphogypsum, two other materials were used: sand and the mixture of sand + phosphogypsum in equal parts.

Establishing the agrotechnical requirements imposed for the execution of the experimental equipment. Agrotechnical requirements to be met by the functional model of equipment for managing in-depth amendments refer to the establishment of some technical characteristics, so that the machine can be aggregated with an existing tractor in operation, to work in complex with another agricultural machine, to allow the organization of a workflow regarding the phosphogypsum supply correlated with the dimensions of the agricultural plots and to execute the work at a quality level as good as possible. Several technical types were analysed in writing and that who best met the imposed agrotechnical requirements was chosen.

Establishing the influence of the work to be administered in depth on agricultural production and on biometric indices. These influences were established in a field experience. The experimental variants regarding the application of the depth amendment were performed on three types of soil and considered the application of two values of the phosphogypsum norm at two distances between passes. The plots within the experiment were identical in shape, were placed on three different textural classes (coarse, medium and fine) and received the treatment of the differentiated intensity of the phosphogypsum, created by two values of the amendment norm (2.0 and 4.0 t/ha) and two values of the distance between passages (1.6 and 3.2 m).

The variants were based on the control variants to which the in-depth amendment does not apply and also the variants were compared with each other (*Pintilie et al, 1980*).

The analysis of the experimental data was done according to the method of calculation and capitalization of the experiments with two factors placed in the subdivided plots. The main factor is the agrofund, in this case the soil texture, with three graduations (coarse, medium and fine) resulting from the percentage of clay content. The coarse texture has 16.8% clay; medium texture 28.7% and fine texture 66.6%. The secondary factor is the applied working variant, with the five graduations, obtained by varying the action intensity of the phosphogypsum that is applied. These graduations are the result of combining the two values of the phosphogypsum norm (2.0 and 4.0 t/ha) with the two values of the distance between the amendment application passages (1.6 and 3.2 m). The large experimental plots each placed on a type of texture were sown with winter wheat and all received the same technological cultivation works (land preparation works, quantity of seed per hectare, fertilization and maintenance works, washing norms/irrigation). The influence of the paper to administer in-depth amendments on the production and on the biometric indices of the plants was determined by collecting samples in three repetitions.

RESULTS

Establishing the physical-mechanical indices of phosphogypsum. To obtain a more suggestive picture of these indices, two other materials were also used: sand and the mixture of sand + phosphogypsum in equal parts. The results obtained from establishing the flow coefficient and the vaulting capacity of the studied materials are presented in Table 1.

Table 1

Results obtained when establishing the flow coefficient and the capacity of studied materials to form the vault

No.	Material	Humidity [%]	Material flow			Material's ability to form a vault		
			Qs [g]	Qh [g]	η	S [cm^2]	F [daN]	P [kPa]
1	Phosphogypsum	8.41	120	195	0.61	14.1	0	0
2		12.12	121	225	0.53	14.1	0.030	0.196
3		13.34	74	211	0.35	14.1	0.419	2.942
4		14.64	47	187	0.25	14.1	1.040	7.355
5		16.02	25	156	0.16	14.1	1.258	8.924
6		17.12	5	137	0.03	14.1	1.316	9.316
7		19.45	0	115	0	14.1	1.273	9.022
8	Mixture of sand + phosphogypsum in equal parts	1.15	207.5	329.5	0.63	14.1	0	0
9		3.25	214	336	0.62	14.1	0	0
10		3.70	211	353	0.59	14.1	0	0
11		4.64	100	290	0.34	14.1	0.647	4.511
12		6.31	33	247	0.13	14.1	1.343	9.512
13		7.37	0	233	0	14.1	1.676	11.866
14		8.34	0	203	0	14.1	1.891	13.337
15	Sand	0.39	331	441	0.75	14.1	0	0
16		0.50	306	418	0.73	14.1	0	0
17		0.77	263	403	0.65	14.1	0	0
18		1.40	135	354	0.38	14.1	0.256	1.765
19		1.89	73	329	0.22	14.1	0.430	3.040
20		2.50	55	325	0.16	14.1	0.487	3.432
21		3.44	0	326	0	14.1	0.638	4.511

Variation of humidity index as a function of humidity for phosphogypsum, sand and sand + phosphogypsum mixture, in equal parts is shown in Figure 2. It is observed that in the case of phosphogypsum, the flow index η has high values at humidity of 8%. This humidity value can only be achieved by forced drying. In its natural state, the humidity of the phosphogypsum can be 10-11% and this in optimal storage conditions. For values of 10-12% humidity, the flow of phosphogypsum is good, but with the increase of humidity over 12% there is a more marked decrease in the flow coefficient so that, over the value of 17%, the phosphogypsum no longer flows.

In the case of other materials, the same phenomenon of the decrease of the flow index takes place with the increase of the humidity, but this happens in lower humidity areas. So, the sand flow index is cancelled at a humidity of 3.4%, and in the case of the mixture sand + phosphogypsum in equal parts, at 6.3%. Graph of the variation of the resistance index to the breaking of the vault depending on the humidity (Fig. 3) shows that at humidities higher than 12% the phosphogypsum begins to form a vault. The maximum value of the resistance index of the formed vault, P, is 9.316 kPa and occurs at a humidity of 17.1%. Increasing humidity, the P index decreases. For the other materials the range of humidity values at which the vaults are formed is for sand 0.7-4% and for sand + phosphogypsum in equal parts 3.7-9%. It is observed that mixed with sand, the phosphogypsum achieves high values of the vault breaking strength index, respectively 13.337 kPa.

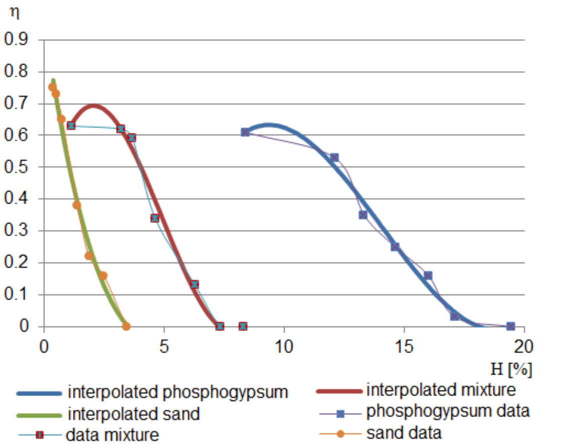

Fig. 2 - Variation of flow coefficient depending on the humidity for different materials

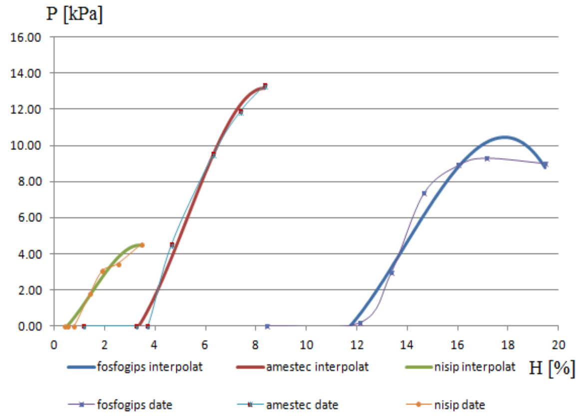

Fig. 3 - Variation of the capacity to form a vault depending on the humidity for different materials

Table 2 presents the results obtained in the experiments performed to establish the variation of the phosphogypsum's capacity to form lumps and to adhere to the bodies, namely p.

Table 2

Results obtained when establishing the phosphogypsum's capacity to form lumps and adhere to bodies

No.	Humidity [%]	$G_b + G_{ad}$ [g]	G_t [g]	p
1	12.25	0	1245	0
2	13.71	0	1241	0
3	14.77	10	1225	0.008
4	15.49	10	1065	0.009
5	16.94	30	800	0.037
6	18.71	60	825	0.072
7	21.43	135	720	0.182
8	23.40	145	740	0.195
9	27.25	275	805	0.341

Graph of the variation of the index of the capacity to form lumps and of the adhesion to bodies (Fig. 4) shows that phosphogypsum begins to form lumps at humidity higher than 13.7% and begins to adhere to bodies at humidity higher than 21.4%.

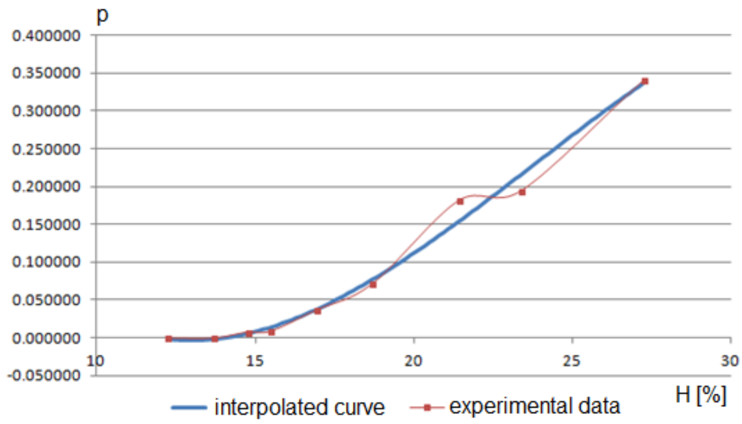

Fig. 4 - Variation of the ability to form lumps and adhesion of phosphogypsum depending on humidity

Agrotechnical requirements for the execution of the functional model of equipment for the administration of in-depth amendments. The following main agro-technical requirements were taken into account when designing the equipment for in-depth amendments: execution of the in-depth amendment simultaneously with the accomplishment of the deep loosening work of the soil; performing in depth by applying phosphorus in strips at a depth of 30-60 cm within the limits of 500-5000 kg/ha; ensuring the uniform introduction of amendments along the entire length of the course and as much as possible without concentrating it in the lower areas; ensuring the possibility of achieving the intensity of the global amelioration process both by adjusting the dose of phosphogypsum applied and by establishing the corresponding distance between the bands. The working process of the aggregate for the administration of phosphogypsum in depth, U-650 + MAS-60 + EAAA-60 (Fig. 5) is: the U-650 tractor moves the machine to loosen the soil depth, MAS-60. It mobilizes and loosens the soil to a depth of 60 cm. The horizon of 30-60 cm is also involved in this mobilization process. Immediately after the active loosening body is inserted, by free fall, phosphogypsum is dosed and carried to the work area by the equipment to administer in-depth amendments EAAA-60. The intensity of the in-depth amendment process varies by adjusting the dose of amendment introduced into the soil and by establishing the distance between adjacent passages.

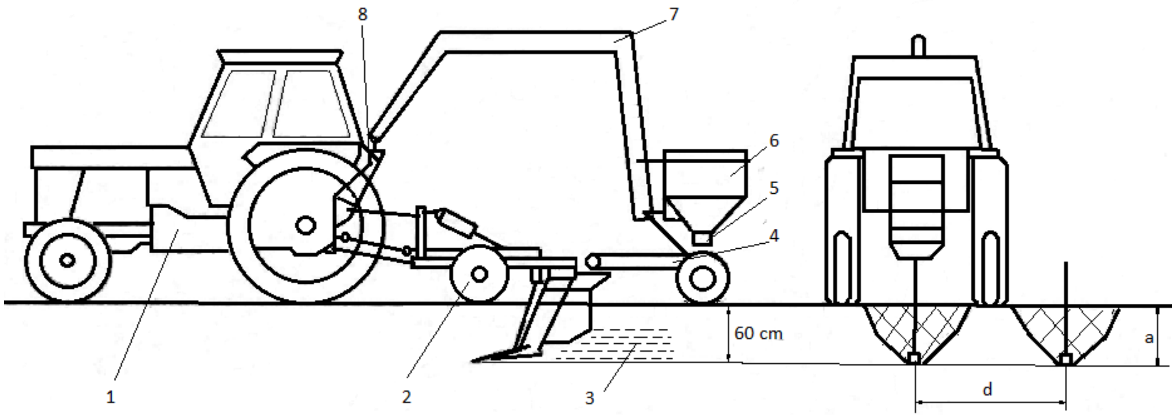

Fig. 5 - Diagram of the U-650 + MAS-60 + EAAA-60 unit in operation

1-tractor U-650; 2-deep soil loosening machine MAS-60; 3-phosphogypsum applied in depth; 4-belt mobile conveyor; 5-ring calliper; 6-hopper; 7-spit; 8-connection coupling; a-working depth; d-distance between crossings

Development of the functional model of equipment for managing amendments in the soil at depth. Some parts or subassemblies of the EAAA-60 machine were taken from other machines to obtain a construction that is easy to do, cheap and functional. The main components of the unit are: U-650 tractor which is the basic part of the unit, part that provides the energy needed to operate the other agricultural machines; MAS-60 deep soil loosening machine, which engages the suspension mechanism of the U-650 tractor, and by moving in work, the soil is mobilized at a depth of 60 cm; equipment for the administration of the in-depth amendment EAAA-60, which engages also, to the U-650 tractor by means of a special coupling. EAAA-60 equipment provides storage, dosing and training of phosphogypsum in the work process. *The special coupling* is attached to the tractor U-650 so as to allow its aggregation with a worn agricultural machine and at the same time through this coupling it is possible to aggregate a towed machine. If EAAA-60 is not used, it is possible to use the U-650 tractor for any work without the need to disassemble the special coupling. *The EAAA-60 dowel* is made with a vault from the pipe. It is a welded construction having as elements the prop itself, the part comprising a movable ball coupling system which is mounted on the bolt of the special coupling, the grip triangle on the body of the machine for administering amendments and reinforcements. The construction is executed in the form of a module that allows reuse for other machines that would require such an aggregation. The execution of the dowel in the construction with vault allows the movement of the U-650 + MAS-60 + EAAA-60 unit without problems of attachment between the machines. *The elements that ensure storage, the dosing and training of the phosphogypsum* are mounted on a frame, connected to the gripping triangle of the arch with the vault. The movement is transmitted to the conveyor belt from the support wheel of the equipment, which in this way ensures the uniformity of the norm that applies regardless of the speed variations that occur during work. *The takeover funnel* has the role to effectively contribute to the introduction of phosphogypsum in depth.

When the conveyor belt reaches above the pick-up funnel, the transmission is coupled and the amendment is driven, which by free fall reaches the actual funnel provided at the top with elastic rubber walls. In the funnel, the amendment is focused on the flow tube which, through the section it has, it limits the maximum value of the flow rate and through the sides prevents the walls from collapsing before the phosphogypsum reaches the depth. The bottom, cut obliquely, allows the superficial mixing of the phosphogypsum with the soil due to the effect of directed collapse of the walls from the bottom up.

Experimental results on the influence of amendments administering works on agricultural production and on biometric indices. The experiment was set up in 1995, in the Corbu-Nou Experimental Field, Brăila County. Amendments were made with two values of the phosphogypsum norm, namely 2.0 and 4.0 t/ha, for two variants of the distance between passages, respectively 1.6 and 3.2 m. The land was then cultivated with wheat, variety Lovrin 41, at a sowing density of 550 plants/m^2. N100 and P80 fertilization was also applied in the culture technology, and herbicidation with Oltisan Extra, 1 l/ha (*Framework technologies for field crop cultivation, 1989*). Five experimental variants resulted on three textures: V0: witness; V1: amendment norm 4.0 t/ha (N) - distance between passages 3.2 m (D); V2: amendment norm 2.0 t/ha (n) - distance between passages 3.2 m (D); V3: amendment norm 2.0 t/ha (n) - distance between passages 1.6 m (d); V4: amendment standard 4.0 t/ha (N) - distance between passages 1.6 m (d). Experimental results on production, plant density, the number of grains in the ear, TKM (mass of a thousand grains) and plant size are shown in Table 3.

Table 3

Influence of administering in-depth amendments on production and on biometric indices in wheat cultivation

Texture (soil type)	Work variant	Production [kg/ha]	Plants density [pl/m^2]	No. of grains in the ear [pieces]	TKM [g]	Plant height [cm]
Coarse (easy)	Witness	2520	454.0	21.0	36.3	77.6
	n, D	2550	468.3	21.3	36.3	10.3
	N, D	2630	458.3	22.0	37.6	72.6
	n, d	3150	458.6	23.3	38.0	76.6
	N, d	3620	462.3	26.6	40. 0	80.3
Texture average:		2894	460.3	22.8	37.6	75.4
Medium (medium)	Witness	3670	446.0	23.3	33.3	78.6
	n, D	3930	448.0	24.6	37.0	81.0
	N, D	4100	452.3	25.0	39.3	81.3
	n, d	4230	462.0	27.0	40.3	84.3
	N, d	4310	458.6	28.3	40.6	85.3
Texture average:		4048	453.3	25.6	39.1	82.1
Fine (heavy)	Witness	2310	442.0	19.0	32.3	73.1
	n, D	2530	456.6	19.6	34.3	76.6
	N, D	2640	442.3	20.3	35.0	76.3
	n, d	2840	440.3	22.0	35.6	73.0
	N, d	3220	438.0	23.6	36.3	74.3
Texture average:		2708	443.8	20.9	34.7	74.7

Note: plants/m^2=pl/m^2 represents the density of plants

Table 4 shows the influence of texture on production and on the biometric indices studied. Considering the coarse control texture, it is observed that wheat production is positively influenced by the average texture where there is an increase of 40%, the influence being very significant, and in the case of fine texture, a decrease in production by 7% resulted, respectively a significant negative influence. These results are explicable considering the better fertility and aerohydric conditions that favour their average texture and respectively the difficult conditions of growth and development of plants on the fine texture where the soil is colder, prone to compaction, with low permeability and lower water recovery capacity. Also in these conditions, plant density decreases on fine texture by 4%, significant negative influence, due to the lower twinning capacity on heavy soils and an insignificant influence of the average texture on plant density. For the same reasons, there was also a very significant influence of the average texture on the number of grains in the ear and a very significant negative influence of the fine texture on the same index.

For TKM, there is a significant negative influence of the fine texture and in the case of plant size a very significant influence of the average texture. It follows that texture is a factor that decisively influences production, the average texture being the most favourable for significant production increases.

Table 4

Influence of soil texture on production and biometric determinations for winter wheat

Texture	Production			Plants density			No. of grains in the ear			TKM			Plant height		
	kg/ha	Differences		pl/m^2	Differences		pcs	Differences		g	Differences		cm	Differences	

		kg/ha	%	Significance		pl/m^2	%	Significance		pcs	%	Significance		g	%	Significance		cm	%	Significance
Coarse (easy)	2890	Wit.	100	Wit.	460.3	Wit.	100	Wit.	22.8	Wit.	100	Wit.	37.6	Wit.	100	Wit.	76.4	Wit.	100	Wit.
Medium (medium)	4050	1106	140.1	xxx	453.3	-0.7	98.5	-	25.6	2.8	112.3	xxx	39.1	1.5	103.9	-	82.1	6.7	109.9	xxx
Fine (heavy)	2710	-180	93.8	0	443.8	-16.5	96.4	0	20.9	-1.9	91.7	000	34.7	-2.9	92.3	0	74.7	-0.7	99.1	-

DL 5% = 1.19 15.48 0.61 1.99 1.08
DL 1% = 1.97 25.62 1.01 3.29 1.77
DL 0.1% = 3.70 41.95 1.88 6.16 3.34

Table 5 shows the influence of the working variant on the production and on the biometric indices for winter wheat in the experiment performed. The control variant is not worked in terms of phosphogypsum in-depth application.

Table 5

Influence of the working variant on phosphogypsum in-depth application on production and biometric determinations for winter wheat

Working variant	Production				Plants density				No. of grains in the ear				TKM				Plant height			
	kg/ha	Differences		Significance	pl/m^2	Differences		Significance	pcs	Differences		Significance	g	Differences		Semnific.	cm	Differences		Significance
		kg/ha	%			pl/sqm.	%			pcs	%			g	%			cm	%	
Witness	2290	Wit.	100	Wit.	447.0	Wit.	100	Wit.	21.1	Wit.	100	Wit.	35.7	Wit.	100	Wit.	76.7	Wit.	100	Wit.
n, D	3010	720	131.4	xxx	457.7	10.7	102.4	x	21.9	0.8	103.8	-	35.9	0.2	100.6	-	76.0	-0.7	99.1	-
N, D	3130	840	136.7	xxx	451.4	4.4	101.0	-	22.7	1.6	107.6	-	37.3	1.6	104.5	-	76.8	0.1	100.1	-
n, d	3140	1120	148.9	xxx	453.7	6.7	101.5	-	24.1	3.0	114.2	xx	38.0	2.3	106.4	-	78.0	1.3	101.7	-
N, d	3720	1430	162.4	xxx	453.0	6.0	101.3	-	26.2	5.1	124.2	xxx	38.9	3.2	108.9	-	80.0	3.3	104.3	-

DL 5% = 1.91 9.17 1.60 3.99 6.56
DL 1% = 2.78 13.33 2.33 5.81 9.54
DL 0.1% = 4.18 20.01 3.49 6.95 14.31

It is observed that all working variants influence production very significantly, reaching production increases of 62%. These increases are due to the cumulative effects of deep loosening of the soil and the action of phosphogypsum. For biometric indices, the effect of deep loosening (d = 1.6 m) is more obvious and is also manifested in the case of the number of grains in the ear, when the influence is distinctly significant and very significant, with increases of 14% (n = 2.0 t/ha) and 24% (N = 4.0 t/ha). For other biometric determinations, the variants of the work exert insignificant influences. Table 6 shows the combined influence of the considered factors, respectively soil texture and working variants on the agricultural production.

Table 6

Influence of soil texture and working variant on phosphogypsum in-depth application to wheat production, Lovrin 41 variety

Working variant	Production											
	Coarse texture				Medium texture				Fine texture			
	kg/ha	Differences		Significance	kg/ha	Differences		Significance	kg/ha	Differences		Significance
		kg/ha	%			kg/ha	%			kg/ha	%	
Witness	2520	Wit.	100	Wit.	2670	Wit.	100	Wit.	2310	Wit.	100	Wit.
n, D	2550	30	101.2	-	3930	1260	147.2	xxx	2530	220	109	-
N, D	2630	110	104.4	-	4100	1430	153.5	xxx	2640	330	114.5	x
n, d	3150	630	125.0	xxx	4230	1560	158.4	xxx	2840	530	122.9	xxx
N, d	3620	1100	143.6	xxx	4310	1640	161.4	xxx	3220	910	139.4	xxx

DL 5% = 2.49; DL 1% = 3.54; DL 0.1% = 5.13

It was found that on the average texture all working variants have a very significant influence (Fig. 6). Production increases of 47-61% are registered. On the coarse texture, very significant crop increases of 25-43% are registered only on the variants that present an accentuated influence from the point of view of loosening the soil in depth (d = 1.6 m). The same happens on the fine texture where the increases are 22-39%.

Also on the heavy texture there is a significant influence of the increased norm of phosphogypsum (N = 4.0 t/ha). It turns out that, in the first year of application, the working variants have a greater influence where the deep loosening is more intense due to the small distance between the passages. Deep loosening regulates the aerohydric regime of the soil, having immediate effect for all types of texture.

It is also reported that, where the phosphogypsum norm is high (N = 4.0 t/ha), the first signs of the positive intake of phosphogypsum appear. Table 7 shows the influence of texture and working variants on phosphogypsum in-depth application on wheat plant density, Lovrin 41 variety.

It was observed that in the context of the cumulative influence of the two factors there are no significant influences on the degree of twinning, parameter that influences plant density. Only on the average texture is signalled a significant influence on the working variant n, D. The tendency of the average texture and the deep loosening to positively influence the density of the plants is highlighted (Fig. 7).

Table 7

Influence of soil texture and working variant on the phosphogypsum in-depth application on plant density in wheat cultivation, Lovrin 41 variety

Working variant	Plants density											
	Coarse texture				Medium texture				Fine texture			
	pl/m²	Differences		Significance	pl/m²	Differences		Significance	pl/m²	Differences		Significance
		pl/m²	%			pl/m²	%			pl/m²	%	
Witness	454.0	Wit.	100	Wit.	446.0	Wit.	100	Wit.	442.0	Wit.	100	Wit.
n, D	468.3	14.3	103.1	-	448.0	2.0	100.4	-	456.6	14.6	103.3	-
N, D	458.3	4.3	109.5	-	452.3	6.3	101.4	-	442.3	0.3	100.1	-
n, d	458.6	4.6	101.0	-	462.0	16.0	103.6	x	440.3	1.7	99.6	-
N, d	462.5	8.5	101.9	-	458.6	12.6	102.8	-	438.0	-4.0	99.1	-

DL 5% = 15.28; DL 1% = 22.04; DL 0.1% = 31.24

Table 8 shows the influence of soil texture and working variants on phosphogypsum in-depth application.

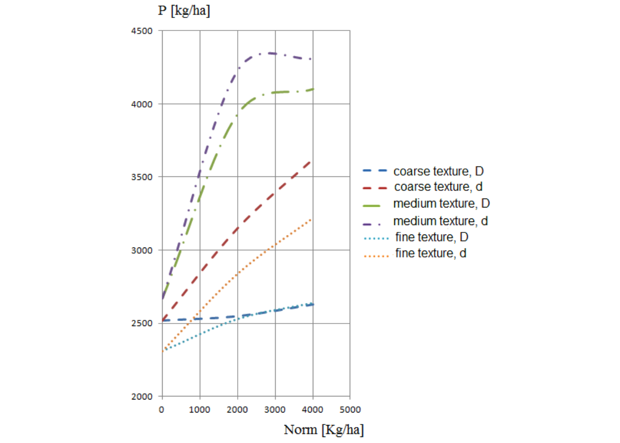

Fig. 6 - Influence of phosphogypsum norm applied in depth on production on coarse, medium and fine texture

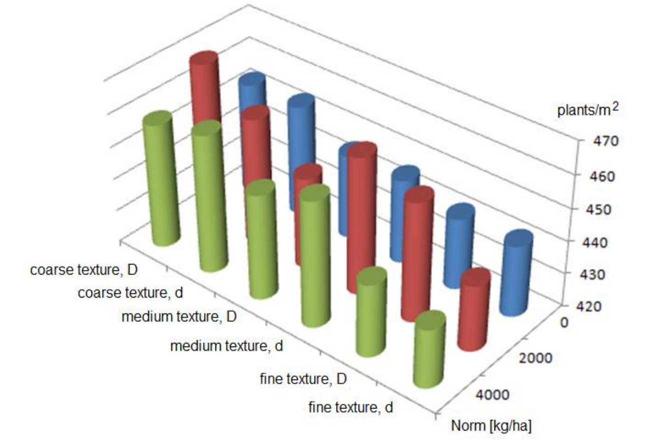

Fig. 7 - Influence of phosphogypsum norm applied in depth on plant density on coarse, medium and fine texture

Table 8

Influence of soil texture and working variant on phosphogypsum in-depth application on the number of grains in the ear, in wheat cultivation, Lovrin 41 variety

Working variant	No. of grains in the ear											
	Coarse texture				Medium texture				Fine texture			
	pcs	Differences		Significance	pcs	Differences		Significance	pcs	Differences		Signifi-cance
		pcs	%			pcs	%			pcs	%	
Witness	21.0	Wit.	100	Wit.	23.3	Wit.	100	Wit.	19.0	Wit.	100	Wit.
n. D	21.3	0.3	101.4	-	24.6	1.3	105.6	-	19.6	0.6	103.2	-
N. D	22.0	1.0	104.8	-	25.0	1.7	107.3	-	20.3	1.3	106.8	-
n. d	23.3	2.3	110.9	-	27.0	3.7	115.9	xx	22.0	3.0	115.8	x
N. d	26.3	5.3	125.2	xxx	28.3	5.0	121.4	xxx	23.6	4.6	124.2	xx

DL 5% = 2.43; DL 1% = 3.43; DL 0.1% = 4.89

There is a more significant influence in the case of medium texture and in the case of works characterized by a higher degree of loosening of the other types of texture (Fig. 8). At the same time, it is observed that the action of phosphogypsum begins to manifest itself, which at the working variants with high amendment norms (N = 4.0 t/ha) leads to increases of the number of grains in the ear of over 20%. For the other working variants the influences are insignificant. Table 9 shows the influence of soil texture and working variants on phosphogypsum in-depth administration on TKM (mass of a thousand grains).

Table 9

Influence of soil texture and working variants on phosphogypsum in-depth application on the TKM for winter wheat, Lovrin 41 variety

Working variant	TKM											
	Coarse texture				Medium texture				Fine texture			
	g	Differences		Significance	g	Differences		Significance	g	Differences		Significance
		g	%			g	%			g	%	
Witness	36.3	Wit.	100	Wit.	38.3	Wit.	100	Wit.	32.3	Wit.	100	Wit.
n, D	36.3	0.0	100.0	-	37.0	-1.3	96.6	-	34.3	2.0	106.2	-
N, D	37.6	1.3	103.6	-	39.3	1.0	102.6	-	35.0	2.7	108.3	-
n, d	38.0	1.7	104.7	-	40.3	2.0	105.2	-	35.6	3.3	110.2	-
N, d	40.0	3.7	110.2	-	40.6	2.3	106.0	-	36.3	4.0	112.4	-

DL 5% = 5.48; DL 1% = 7.77; DL 0.1% = 11.20

It is found that the mentioned factors do not influence the studied parameter significantly (Fig. 9). The greatest influence is presented by the variants with accentuated loosening.

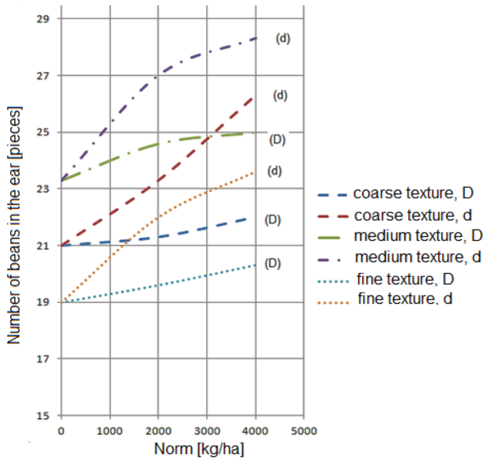

Fig. 8 - Influence of phosphogypsum norm applied in depth on the number of grains in the ear on the coarse, medium and fine texture

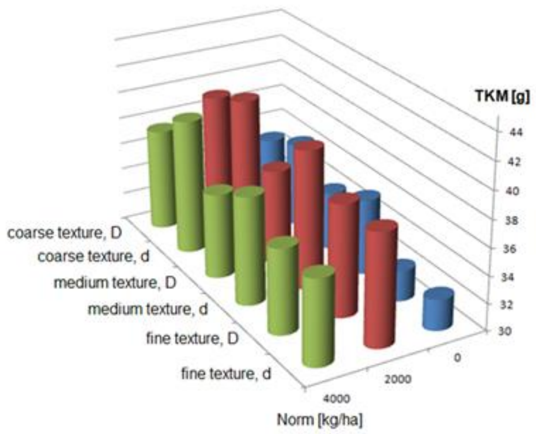

Fig. 9 - Influence of the phosphogypsum norm applied in depth on the TKM on coarse, medium and fine texture

Table 10 shows the combined influence of soil texture and working variants on in-depth administration of phosphogypsum on the size of winter wheat plants, Lovrin 41 variety, in the experimental field Corbu-Nou, Brăila County.

Table 10

Influence of soil texture and working variant on phosphogypsum in-depth application on the height of the plants, to winter wheat, Lovrin 41 variety

Working variant	The height of the plants											
	Coarse texture				Medium texture				Fine texture			
	cm	Differences		Significance	cm	Differences		Significance	cm	Differences		Significance
		cm	%			cm	%			cm	%	
Witness	77.6	Wit.	100	Wit.	78.6	Wit.	100	Wit.	73.6	Wit.	100	Wit.
n, D	70.3	-7.3	90.6	-	81.0	2.4	103.0	-	76.6	3.0	104.1	-
N, D	72.6	-5.0	93.5	-	81.3	2.7	103.4	-	76.3	2.7	103.7	-
n, d	76.6	-1.0	98.7	-	84.3	5.7	107.3	-	73.0	-0.6	99.2	-
N, d	80.3	2.7	103.5	-	85.3	6.7	108.5	-	74.3	-0.7	100.9	-

DL 5% = 10.74; DL 1% = 15.11; DL 0.1% = 21.44

It is observed that size parameter, the height of the plants, is not significantly influenced by the two factors presented above (Fig. 10).

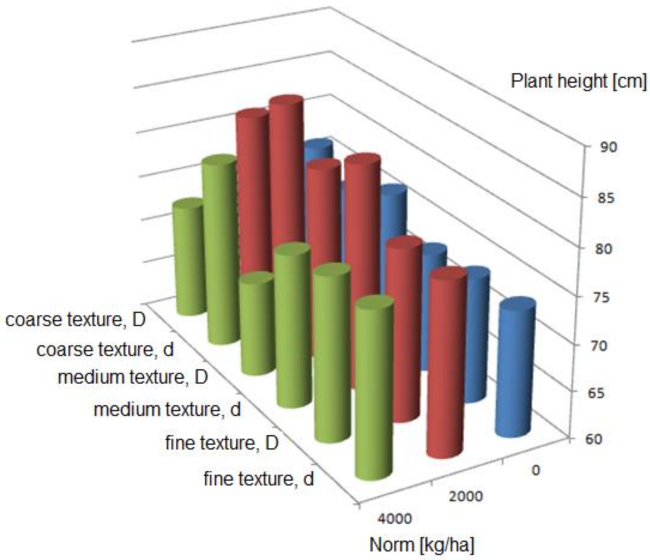

Fig. 10 - Influence of phosphogypsum norm applied in depth on plant height on coarse, medium and fine texture

Analysing the influence of soil texture specified by the clay content and the influence of working variants on phosphogypsum in-depth application, a series of curves have been established that highlight the dependence of agricultural production on the two factors. For a clearer presentation, the curves are presented in two groups in Figure 11 (witness (no amendment in depth) - nD - ND) and Figure 12 (witness (no amendment in depth) - nd - Nd).

It is observed that, in all cases, the decrease or increase of the clay content leads to the decrease of the production. The maximum values of the production are found in the case of applying an energetic loosening of the soil (d = 1.6 m) and at a high norm of phosphogypsum (N = 4.0 t/ha), followed by the variant in which the phosphogypsum norm is low (n = 2.0 t/ha). It turns out that in the first phase the immediate effect of deep loosening is manifested and only in the second phase is the action of phosphogypsum proportional to the administered norm manifested, against the background of a lighter looseness (D = 3.2 m). At all textures, the working variants bring production increases (all the curves with the working variants are above the witness curve).

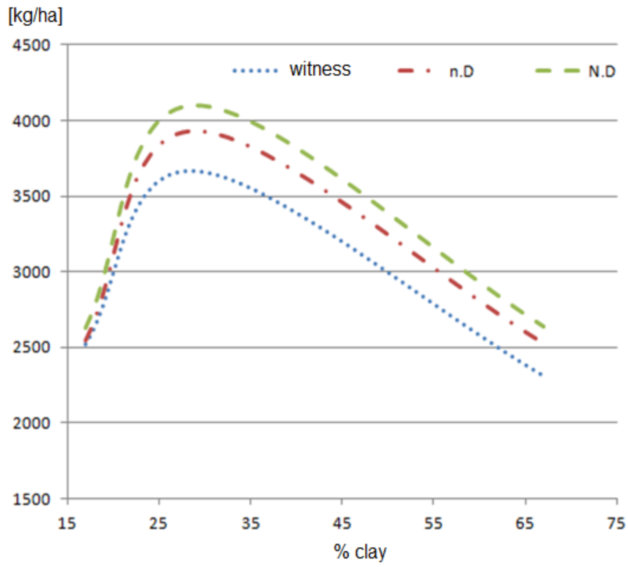

Fig. 11 - Influence of soil texture and working variants on phosphogypsum in-depth application (D = 3.2 m) on production

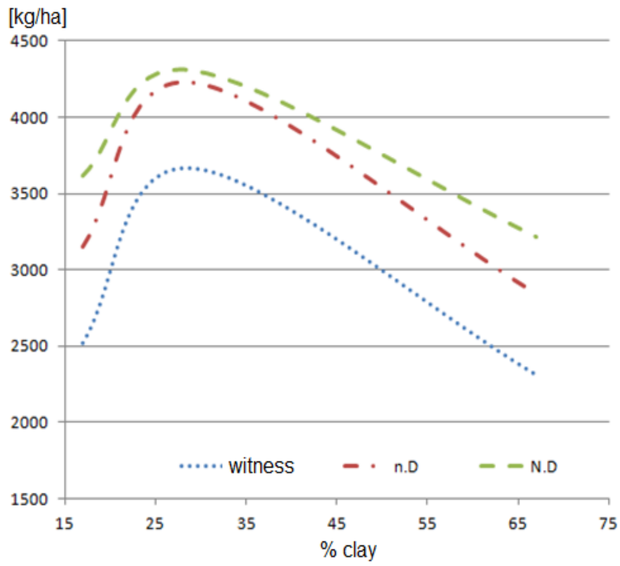

Fig. 12 - Influence of soil texture and working variants on phosphogypsum in-depth application (d = 1.6 m) on production

CONCLUSIONS

Phosphogypsum can be used properly when it has a humidity of 10-12% and application should be made in the warmer and drier periods of the year, and storage must be done in the best possible conditions. The maximum ameliorating effect of phosphogypsum applied in depth is obtained only when the whole complex of pedo-hydro-agro-ameliorative measures is carried out (soil loosening, irrigation / washing, mole drainage, proper performance of the basic works of soil).

The equipment for the administration of in-depth amendments EAAA-60 works in the unit with the U-650 tractor and the MAS-60 soil loosening machine. By applying a norm of 4.0 t/ha, in bands spaced at 1.6 m, production increases of about 40% were obtained. In the first year of application, the effect of deep loosening becomes more obvious and in cumulation with the effect of phosphogypsum applied in depth, leads to increases in agricultural production by over 25%.

Medium-textured soils respond very well to the measures applied through a higher production capacity, to help cover the costs of the improvement works. The EAAA-60 equipment is intended to work on saline terrain, but it can also be used on soils with salinisation potential, in order to prevent this phenomenon. In this case, the efficiency of the works is higher because the expenses are made on an already productive land, so that financial efforts are covered to a greater extent.

Incorporation of phosphogypsum in depth and deep loosening are heavy works that are performed with high energy consumption, hence they should be made on raw land, where possible or on the move, and the condition of the drive wheels is good. This avoids unjustified fuel consumption and additional wear and tear due to skating. On the ground discussed at the mentioned works, skating can reach 30-35%, and on ploughing the execution of works to incorporate phosphogypsum in depth or mole drainage cannot be performed.

Immediately after the execution of the deep loosening lines, the work must be intervened on by ploughing or discing the soil in order to avoid its drying in the mobilized area. It creates the possibility of obtaining a better quality for surface tillage works, a high and uniform degree of crushing over the entire surface, a constant humidity in the superficial horizon and in depth with positive repercussions on the uniformity of emergence and of growth and development of the plants.

The onset of Na ion replacement reactions in the soil adsorbent complex with Ca in the phosphogypsum composition occurs in the presence of water. Also, water dissolves some of the phosphogypsum that it transports into permeable spaces, thus increasing the area of influence of the amendment. In this context, after applying the phosphogypsum to the surface and in depth and after homogenizing it with the soil, respectively the cultivation of the land, it is recommended to apply increased watering rules or to monitor the existence of a natural water supply that contributes to the growth and development of cultivated plants, but which should also lead to the passage of Na into the composition of soluble salts which will later be taken up by other quantities of water and discharged outside the perimeter.

When applying in-depth amendments, the conditions imposed on the work of deep loosening of the soil must be observed. After a period of 6-12 months, during which sodium replacement reactions occur with calcium, it is necessary to carry out the mole drainage work, and then the intensification of the irrigation / washing works in order to take over the resulting salts and eliminate them outside the perimeter.

ACKNOWLEDGEMENT

This work was supported by a grant of the Romanian Ministry of Research and Innovation CCDI - UEFISCDI, Project INNOVATIVE TECHNOLOGIES FOR IRRIGATION OF AGRICULTURAL CROPS IN ARID, SEMIARID AND SUBHUMID-DRY CLIMATE, project number PN-III-P1-1.2-PCCDI-2017-0254, Contract no. 27 PCCDI / 2018, within PNCDI III.

REFERENCES

[1] Biggs T.W., Jiang B.B., (2009), Soil salinity and exchangeable cations in a wastewater irrigated area, India, *Journal of Environmental Quality*, vol. 8, pp. 887-896;

[2] Biriş S.Șt., Maican E., Faur N., Vlăduţ V., Bungescu S., (2007), FEM model for appreciation of soil compaction under the action of tractors and agricultural machines, *Proceedings of the 35th International Symposium on Agricultural Engineering "Actual Tasks on Agricultural Engineering",* pp. 271-280, ISSN 1333-2651, Opatija/Croatia;

[3] Biriş S.Șt., Maican E., Ungureanu N., Vlăduţ V., Murad E., (2011), Analysis of stress and strain distribution in an agricultural vehicle wheel using finite element method*, Proceedings of the 39th*

International Symposium on Agricultural Engineering "Actual Tasks on Agricultural Engineering", pp.107-118, ISSN 1333-2651, Opatija/Croatia, WOS: 000290918800010;

[4] Bularda M., (2020), Contributions to the mechanization of the work to administer in-depth amendments on the lands affected by salinisation (Contribuții privind mecanizarea lucrării de administrat amendamente în adâncime pe terenurile afectate de sărăturare), *Galaţi University Press,* ISBN 978-606-696-184-4*;*

[5] Bularda M., Vişinescu I, Ghiorghe A., Vlăduţ V., Cujbescu D., (2020), The effect of conservative agricultural works on soil and field plants and optimized mechanization technologies, *INMATEH – Agricultural Engineering*, vol. 61 (2), pp. 323-338, DOI: *https://doi.org/10.35633/inmateh-61-35*;

[6] Carmeis-Filho A.C.A., Penn C.J., Crusciol C.A.C., Calonego J.C., (2017), Lime and phosphogypsum impacts on soil organic matter pools in a tropical Oxisol under long-term no-till conditions, *Agriculture, Ecosystems & Environment,* vol. 241, pp. 11-23;

[7] Croitoru Şt., Marin E., Bădescu M., Vlăduţ V., Ungureanu N., Manea D., Boruz S., Matei Gh., (2015), Agrotechnical and energetic characteristics of new designed subsoiler*, Proceedings of the 43th International Symposium on Agricultural Engineering "Actual Tasks on Agricultural Engineering",* pp. 165-176, Opatija, Croatia, WOS: 000373450700014;

[8] Croitoru Şt., Vlăduţ V., Marin E., Matache M., Dumitru I., (2016), Determination of subsoiler's traction force influenced by different working depth and velocity, *Proceedings of the 15th International Scientific Conference "Engineering for Rural Development",* vol. 15, pp. 817-825, Jelgava/Latvia;

[9] Croitoru Şt., Vlăduţ V., Voicea I., Gheorghe Gh., Marin E., Vlăduţoiu L., Moise V., Boruz S., Pruteanu A., Andrei S., Păunescu D., (2017), Structural and kinematic analysis of the mechanism for arable deep soil loosening, *Proceedings of the 45th International Symposium on Agricultural Engineering "Actual Tasks on Agricultural Engineering",* pp. 207-216, Opatija/Croatia;

[10] Cujbescu D*.,* Ungureanu N., Vlăduț V., Persu C., Oprescu M.R., Gheorghiță N.E., (2019), Field testing of compaction characteristics for farm tractor Universal 445, *INMATEH – Agricultural Engineering*, vol. 59(3), pp. 245-252, WOS: 000504038200028;

[11] Endo T., Yamamoot S., Larinnaga J.A., Fujiyama H., Honna T., (2011), Status and causes of soil salinisation of irrigated agricultural land in southern Baja California, Mexico, *Applied and Environmental Soil Science*, vol. 2011, article ID 873625, 12 p.;

[12] Ezlit Y.D., Smith R.J., Raine S.R., (2010), A review of salinity and sodicity in irrigation, *CRC for Irrigation Futures, Irrigation Matters Series*, no. 01/10;

[13] Krasnicenco A.V., (1963), Agricultural Machinery Manufacturer's Manual (Manualul constructorului de maşini agricole), vol. I-II, *Technical Publishing*, Bucharest/Romania;

[14] Minhas P.S., Ramos T.B., Ben-Gal A., Pereira L.S., (2020), Coping with salinity in irrigated agriculture: Crop evapotranspiration and water management issues, *Agricultural Water Management*, vol. 227, 105832;

[15] Muyen Z., Moore G.A., Wrigley R.J., (2011), Soil salinity and sodicity effects of wastewater irrigation in South East Australia, *Agricultural Water Management*, vol. 99, pp. 33-41;

[16] Phogat V., Mallants D., Coxa J.W., Šimůnek J., Oliver D.P., Awad J., (2020), Management of soil salinity associated with irrigation of protected crops, *Agricultural Water Management*, vol. 227,105845;

[17] Pintilie C., Budoi Gh., (1980), Agrotechnics and experimental technique (Agrotehnică şi tehnică experimentală)*, Didactic and Pedagogical Publishing House*, Bucharest/Romania;

[18] Ungureanu N., Vlăduț V., Cujbescu D., (2019), Soil compaction under the wheel of a sprayer, *8th International Conference on Thermal Equipment, Renewable Energy and Rural Development (TE-RE-RD*), *E3S Web-of-Conferences,* vol. 112, 03027, 6-8.06.2019,Târgoviște/Romania;

[19] Ungureanu N., Vlăduț V., Voicu Gh., (2020), Water scarcity and wastewater reuse in crop irrigation, *Sustainability*, vol. 12, no. 21, 9055, WOS: 000589697700001;

[20] Vlăduţ D.I., Vlăduţ V., Grigore I., Biriş S.Șt., (2017a), Experimental research on qualitative indices of work for equipment for seedbed preparation in conservative system, *16th International Scientific Conference "Engineering for Rural Development"*, vol. 16, pp. 1174-1179, Jelgava/Latvia;

[21] Vlăduţ V., Gheorghe G., Marin E., Biriş S.Șt., Paraschiv G., Cujbescu D., Ungureanu N., Găgeanu I., Moise V., Boruz S., (2017b), Kinetostatic analysis of the mechanism of deep loosening system of arable soil, *Proceedings of the 45th International Symposium on Agricultural Engineering "Actual Tasks on Agricultural Engineering",* pp. 217-228, Opatija, Croatia, WOS: 000432420200022;

[22] Vlăduţ D.I., Biriş S., Vlăduţ V., Cujbescu D., Ungureanu N., Găgeanu I., (2018), Experimental researches on the working process of a seedbed preparation equipment for heavy soils, *INMATEH – Agricultural Engineering*, vol. 55 (2), pp. 27-34, WOS: 000445181000004;

[23] Vlăduţoiu L., Andrei T., Marin E., Vlăduţ V., Biriş S.Şt., Matache M., Fechete L., Dumitru I., Kiss I., (2016), Determination of soil resistance related to wear of a chisel share*, Proceedings of the 44th International Symposium on Agricultural Engineering "Actual Tasks on Agricultural Engineering",* pp. 187-194, Opatija/Croatia;

[24] Vlăduţoiu L., Cârdei P., Vlăduţ V., Fechete L., (2017), Modern trends in designing and selecting the machine / equipment for soil deep tillage, *16th International Scientific Conference "Engineering for Rural Development",* vol. 16, pp. 1415-1420, Jelgava/Latvia;

[25] Wang J., (2020), Utilization effects and environmental risks of phosphogypsum in agriculture: a review, *Journal of Cleaner Production*, vol. 276, 123337;

[26] ***FAO, (2012), Coping with water scarcity - an action framework for agriculture and food security, FAO Water Reports 38, *Food and Agriculture Organization of the United Nations* (http://www.fao.org/3/a-i3015e.pdf);

[27] ****Framework technologies for field crop cultivation (Tehnologii cadru pentru cultura plantelor de câmp)* (1989), Academy of Agricultural and Forestry Sciences (Academia de Științe Agricole și Silvice), Bucharest;

[28] ***WRI, (2020), Food. Supporting agriculture, environment, and sustainable development, *World Resources Institute* (https://www.wri.org/our-work/topics/food).

EFFECTS OF DIFFERENT GEOMETRICAL STRUCTURES ON THE SOIL DISTURBANCES AND WORKING RESISTANCES OF VERY NARROW TINES APPLIED ON NATURAL GRASSLAND

/

极窄齿类耕作部件形状结构参数对草地作业阻力和扰动情况的影响

Changbin He [1,2)], Yong You [*2)], Hongjian Wu [2,3)], Bingnan Ye [2)], Decheng Wang [*2,4)] [1]

[1)] Inner Mongolia Agricultural University, College of Mechanical and Electrical Engineering, Hohhot / China;
[2)] China Agricultural University, College of Engineering, Beijing / China;
[3)] Tsinghua University, Department of Mechanical Engineering, State Key Laboratory of Tribology, Beijing / China;
[4)] China Agricultural University, Key Laboratory of Grassland Management and Rational Utilization, the Ministry of Agriculture, P.R. China, Beijing/China;
Tel: +86 10 010-62737977; +86 10 010-62737208; E-mail: youyong@cau.edu.cn; wdc@cau.edu.cn
Corresponding authors: Yong You, Decheng Wang
DOI: https://doi.org/10.356.33/inmateh-64-02

Keywords: *Furrow, draft force, soil translocation, natural grassland, tillage tines*

ABSTRACT

Novel tillage tools with high working performance are desired in improving degraded natural grassland tillage system. This paper aimed to find the influence of various geometry structures of very narrow tines on related soil disturbance characteristics and tillage resistances. Four shank-type tillage tines with different cutting head shapes, and the test bench were designed and manufactured. Field experiments under different working depths were conducted. The working depth uniformity, soil over-turning rate, cross-section area of disturbed soil layer, and related forces were obtained, analysed, and compared. Results showed that, the working depth uniformities were above 70%, and soil overturning rates did not exceed 5%. Furrows with V-shaped cross-section were formed. The tine with an arc-shaped cutting edge (AT) obtained a lower draft force value, and the tine with chamfer structure (TTD) presented big differences on the draft force and soil disturbance compared to the tine with blunt cutting edge (TT). Both the draft force and the area of disturbed soil cross section had a good linear relationship with the working depth, and the specific draft force increased with the working depth increasing. Using a very narrow tine with chamfers to split and break the soil layer on the natural grassland without pulling or dragging the roots could be an appropriate tillage method applied for improving degraded natural grassland, but still need further surveys.

摘要

为设计和优化退化草地开沟部件，对具有不同形状结构参数的极窄齿类耕作部件的作业效果展开研究。设计了 4 种铲尖形状不同的极窄齿类开沟部件，搭建了试验台，进行了草地开沟扰动试验。试验结果表明，在 0~15 cm 作业深度范围，各部件的开沟深度稳定性系数均在 70%以上，造成的地表翻垡率不超过 5%，作业后形成具有“V”形扰动截面沟槽的扰动区域。牵引阻力和土层扰动截面积均与作业深度呈良好的线性正相关关系（R^2≥0.78），且单位面积牵引力随深度的增加而增大。入土角相同的情况下，铲尖形状对开沟部件的牵引阻力和草地扰动情况影响不显著，但有无刃口对二者具有较大影响；采用具有刃口的极窄齿类开沟部件以切断或割裂土层的方式能够有效打破板结性退化草地的土壤-根系复合土层结构，降低地表植被破坏程度，采用凹曲线的铲尖刃线形状可适当降低开沟部件的牵引阻力。

INTRODUCTION

Leymus chinensis (Trin.) Tzvel., referred to as L-C hereafter, is a native perennial rhizomatous grass, widely distributed in the natural grasslands of the Northeast China Plain, the Northern China Plain, and the Inner Mongolia Plateau of China *(Wang et al., 2004)*. It is a popular fodder grass with economic and ecological importance due to its good palatability and high forage value *(MOA, 1996).* However, in recent years, the L-C natural grasslands have been showing degradation trends with the behaviours of soil hardening, reduction of natural vegetation cover, decrease of grassland productivity, and deterioration of ecosystem conditions.

---

[1] *Changbin He, Lecturer Ph.D. Eng.; Yong You, As. Prof. Ph.D. Eng.; Hongjian Wu, Ph.D. Eng.; Bingnan Ye, Ph.D. Eng.; Decheng Wang, Prof. Ph.D. Eng.*

Continuous livestock grazing was verified to be one of the main reasons resulting in soil compaction on the grassland due to trampling by the livestock *(Martınez and Zinck, 2004; Bell et al., 2011)*. In addition, the biological characteristic of long strong rhizomes and vigorous vegetative propagation was regarded as another reason causing soil compaction and pasture degradation, by consolidating the tangled long roots and soil, forming the soil-root composite structure underground on the natural grassland *(He et al., 2016).*

The degraded natural grassland restoration has been a long-term research topic in China. Apart from the measures of grassland management and excluding grazing arrangement, using tillage tools to break the hardened soil layer and the complicated soil-root structure on the degraded natural grasslands by improving the soil physical, chemical, and biological properties, was verified to be one effective practice for the degraded natural grassland restoration *(Chen et al., 2017; Tang et al., 2016; Alvarez and Steinbach, 2009; Diabate et al., 2018; You et al., 2012).* In addition, appropriate conservation tillage practices with low soil over-turning rate and surface disturbance should be taken into account, due to the soil nutrition loss and severe soil erosion problems caused by conventional tillage tools *(Su et al., 2004; Lal, 2007; Ramírez et al., 2019).*

Drilling or reseeding practice is one effective and long-standing recommendation mean for improving degraded grasslands *(Bueno et al., 2007; Liu et al., 2015; Zhou et al., 2017).* The special and complicated soil layer structure of natural grasslands are different from the common crop fields, making it hard to build a good seedbed because of the hardened soil layer and complicated soil-root structure, and the disturbance on the grassland causing by tillage tools varied as well. So, applying appropriate tillage tools is necessary. The drilling or reseeding methods used for degraded grassland restoration still mostly adopted the openers used for the conventional crop field tillage system as the furrow openers for improving degraded natural grasslands, having limitations to achieve good working performances by causing soil nutrition loss and severe soil erosion problems *(Zhao et al., 2006; Su et al., 2004).* However, limited reports about specialized openers used for natural grassland tillage system could be found.

To select an appropriate tillage implement, the soil disturbance type and degree are the prime factors but must be considered together with the working resistances for efficient operation *(Godwin, 2007; Godwin and O'Dogherty, 2007).* This paper aimed to find the influence of different geometrical structures of very narrow tillage tools on the soil disturbances and tillage forces applied on natural L-C grassland, providing basic references and supports for designing novel and specialized furrow openers applicable to natural grasslands. The Shank-type tillage tines were selected as the tillage tools working on natural grassland because of the characteristics of simple structure, easy processing, and causing low disturbance. Three types of tine geometries (i.e. triangle tine, arc tine, and convex tine) were designed, and the influence coming from the cutting edges (i.e. chamfer and blunt) were also considered. The soil disturbances and soil cutting forces were obtained, analysed, and compared between these tillage tines applied on natural grassland.

MATERIALS AND METHODS

- **Experimental site description and soil physical properties survey**

The experiment site was located in a typical natural grassland in Chabei district of Hebei province (41°28'31.649″N, 115°1'28.733″E, Alt.±2 m). L-C was the dominant grass species in this area. No conventional tillage practices were used in this area before and no livestock grazing was allowed in recent three years.

The soil penetration resistance (i.e., soil cone index) was measured using a hand-held cone penetrometer (SC 900, Spectrum Technologies, Inc.) with the small cone described in *ASAE standards S313.3 (2009).* Ten points were randomly selected along the diagonals of the experimental area for each soil layer with the depth interval of 2.5 cm. The maximum reading of the penetrometer at the bottom of each depth range was recorded as the cone index value. Then, the average values were calculated. The soil cone index and depth curves were shown in Fig. 1. It showed that the soil cone index reached a peak value around the depth of 5 cm, then a sharp decline came after that, when the depth of soil layer underground exceeded 10 cm, the curves turned into slightly stable gradually.

Three sites were randomly selected as sample-taken places, and three soil cores (30 cm^2 in bottom area, 4 cm in height) were randomly taken from the soil layer at each place, within the depth range of 0-5 cm, 5-10 cm, and 10-15 cm, respectively. The soil cores were weighed, oven-dried at 105℃ for 24 h, and weighed again to determine the soil moisture content and bulk density. The bulk density was calculated by the ratio of the oven dried soil sample mass to the soil core volume.

The moisture content was calculated on a dry mass basis (d.b.) according to ISO standard *(IOS, 1993),* expressed with the unit by mass, i.e., $g\cdot(100g)^{-1}$. The soil bulk density and moisture content were shown in Table 1.

In addition, the L-C roots' distribution underground was also observed. The L-C root distribution characteristics could be summed up as shown in Fig. 2. The figure showed that the L-C roots in the horizontal direction mainly distributed in the subsoil layer at the depth range of around 5 cm, and almost no roots could be observed clearly beyond the depth of 10 cm underground. The roots and soil formed composite structure underground.

Table 1

Physical properties of the soil in the experimental area

Depth (cm)	Bulk density (g/cm³)	Moisture content (g/(100g), d.b.)
0-5	1.04±0.05	9.99±2.43
5-10	1.26±0.13	13.68±2.42
10-15	1.34±0.12	17.18±2.35

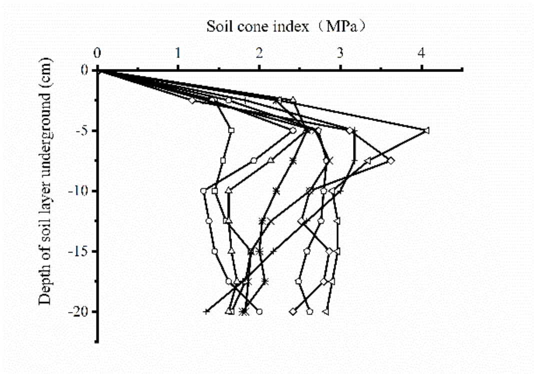

Fig. 1 - Curves of soil cone index and depth

Fig. 2 - Distribution of L-C roots underground

- **Very narrow tines**

Four vertical very narrow shank tines with different geometry structures were designed, i.e. triangle tine (TT), triangle tine with double-side chamfer (TTD), arc tine (AT), and convex tine (CT). Three of these tools (i.e., TT, AT, and CT) were blunt, the other one was designed with a double side chamfer (symmetric) based on TT, i.e. TTD, as shown in Fig. 3. The double side chamfers were sharpened at an angle of 30° to the travel direction.

These shank tines were constructed from 14 mm thick steel. The details of their shapes were shown in Fig. 4. These tines were manufactured to be one body, mainly composed of two portions, one was the cutting head, the other one was the shank. The tines were expected to have different characteristics in terms of soil disturbance and cutting forces. Comparisons between the four tines (all with the same rake angle and working width) would reflect the effects of the geometry structures. The shank bodies had the same width and thickness, and the same fixation point (i.e. three through-holes on the shank body) as well. Among the four shank bodies, only TTD was partially chamfered along the shank edge and the cutting head.

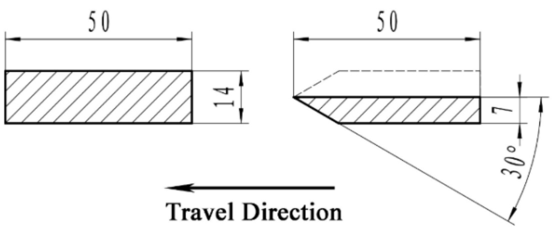

(a) blunt (b) double-side chamfer (half body)

Fig. 3 - Cross-sections of shank tine geometries. Dimensions are in mm

- **Testing facility**

A test bench was designed and manufactured, which was composed of the frame and depth limiting device, making the working depth adjustable with the interval of 5 cm. The maximum working depth limit was designed as 20 cm. The test bench was linked with a tractor by three-point hydraulic suspension frames.

The tillage tine was fixed on the frame in an articulated connection way. Two tension and pressure sensors (BK-2B, China Academy of Aerospace Aerodynamics) were fixed on the frame. The sensors connected the tillage tine and the frame in horizontal and vertical direction, so that the resistances in the two directions could be monitored and collected during the on-the-go movements. The real device was as shown in Fig. 5.

A data collector (SQ 2020, Grant Squirrel) was placed and fixed on the frame, which could gather the data from the two tension and pressure sensors. During the experiments, the collector was used to gather and reserve the data from the sensors, and the data was exported to the laptop when the experiments were finished. The working principle of data collecting was as shown in Fig. 6. Besides, in order to evaluate the soil disturbance of the grassland caused by tillage tines, a profile metering device was designed and manufactured to measure the cross-section profile of disturbed soil-layer, as reported by *He et al. (2020).* By selecting the points of the disturbed area, the cross-section profile could be drawn by the Computer Aided Design (CAD) software through the coordinate values.

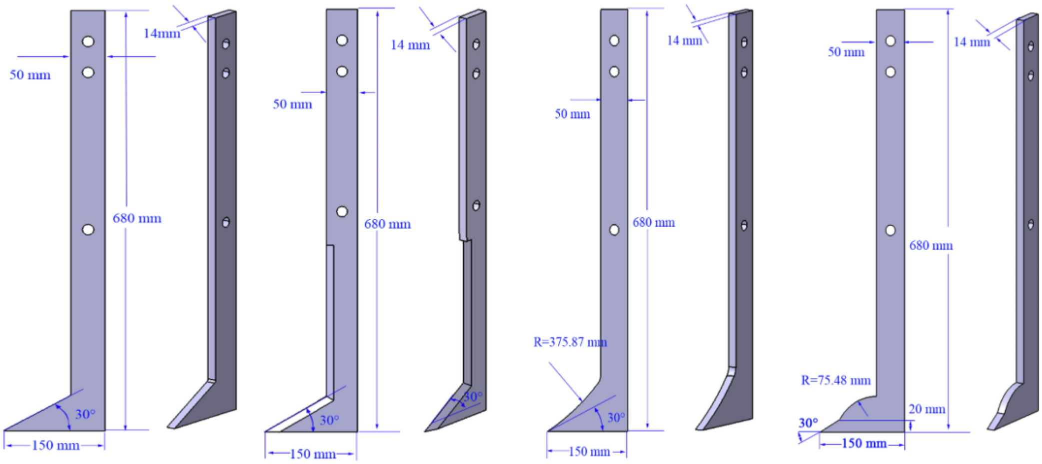

(a) TT (b) TTD (c) AT (d) CT

Fig. 4 - Details of shank tine shapes

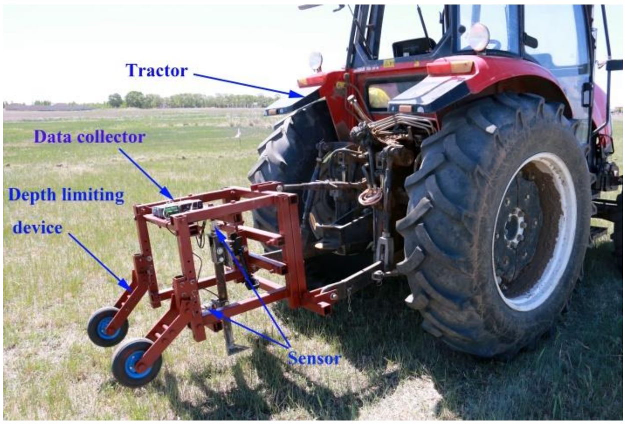

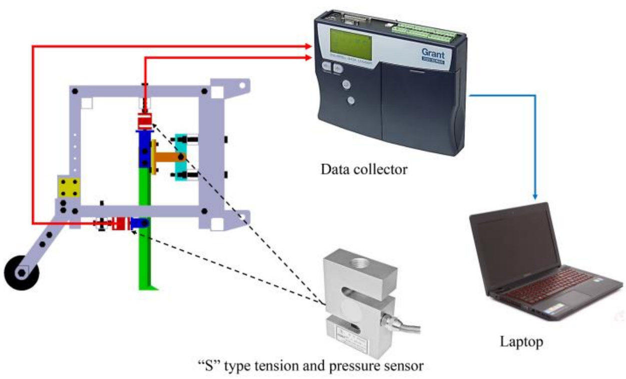

Fig. 5 - The picture of the real device **Fig. 6 - Working principle of data collecting**

- **Experiment procedure and calculation**

Based on the pre-experiments, the tines always went through two phases when they were working, i.e. the phases of penetrating into the soil and moving stably. The tillage tines usually gradually entered the soil layer at the first distance of 1 meter along the moving direction, and then kept on-the-go movements stably. During the stable movement phase, the results were obtained from every 8 meters along the length. There were three repetitions for each tine. The tines were operated at a forward speed of 1.08±0.14 km·h^{-1} along the length direction pulled by the tractor. The operating depth were 5 cm, 10 cm, and 15 cm, respectively.

The depth uniformity was used to describe the stability of the working depth during the tillage movements. The soil disturbance status of the grassland (i.e. the visual analysis of grassland surface disturbance, soil over-turning rate, and cross-section area of disturbed soil layer), and the draft force were chosen as the main indexes to evaluate the working performances of the tillage tines. Besides, specific draft forces were also calculated and compared, which was defined as the force per unit area of soil disturbed.

The depth uniformity, soil overturning rate, and specific draft force were described as reported by *He et al. (2020)*, and calculated by the formulas as shown in Table 2.

Table 2

Formulas for calculating the depth uniformity, soil overturning rate, and specific draft force

Parameters	Formulas	
Depth uniformity (MOMI, 2003)	$U = \left(1 - \frac{V}{100}\right) \times 100\%$	(1)
	$V = \frac{S}{h} \times 100\%$	(2)
	$S = \sqrt{\frac{\sum_1^n (h_i - h)^2}{N-1}}$	(3)
Soil overturning rate (MOMI, 1993)	$F_L = \frac{L_f}{bL} \times 100\%$	(4)
Specific draft force	$S.D = \frac{F}{A}$	(5)

Note: Where U is the uniformity of working depth, V is the coefficient of variation, S is the standard deviation of depth, h is the average value of depth, h_i is the measured depth value at the point i, N and n are the numbers of the measurement points in the operation area. F_L is soil over-turning rate, L_f is the average value of the total length of overturned soil clods, b is the numbers of tillage tines while working, L is the travel distance. S.D is specific draft force, F is draft force of the tillage tine, A is soil loosened area. Average draft force and disturbed soil layer area were used to calculate the specific draft force.

The disturbance range of soil underground causing by tillage tines was described by the value of disturbed cross-section area, which was defined as Askari (2013) reported, calculated as equation (6):

$$\mathrm{A} = \left[\left(2 \sum_{i=1}^{n} d_i\right) - (d_1 + d_n)\right] \times \frac{l}{2} \quad (6)$$

where *A* is soil loosened area; d_i is profile meter reading; d_1 and d_n are the first and the last profile meter readings for every section of the profile, respectively; and *l* is the interval distance of every two adjacent measurement points, which was controlled at 10 mm along horizontal direction in this study.

RESULTS

- **Working depth and its uniformity**

Table 3 showed that the actual working depths of all tines were basically located in the range of 0-5 cm, 5-10 cm, and 10-15 cm as desired. For the same tine, significant differences existed between different working depths. Within the depth of 0-5 cm, there were no significant differences between the tillage tines. In the depth range of 5-10 cm and 10-15 cm, the depth values of AT, TT, and TTD had significant differences at the significance level of 0.05, but no significant differences existed between AT and CT, there were no significant differences between TT, TTD and CT.

The working depth uniformity was obtained based on equations from equation (1) to (3). All the tillage tines had good working depth uniformities with the values of more than 71%, even went over 83% within the depth range of 5-10 cm and 10-15 cm, demonstrating that the tillage tines have stable movements when they were working.

Table 3

The actual working depth of all tillage tines

Tines	Desired depth of 0-5 cm	Desired depth of 5-10 cm	Desired depth of 10-15 cm
	Actual working depth (cm)		
TT	5.5±1.59aC	8.3±1.31bB	11.73±0.50bA
TTD	3.6±0.62aC	8.6±1.13bB	11.67±1.89bA
AT	5.17±1.32aC	10.77±0.5aB	14.5±0.96aA
CT	4.8±0.1aC	9.5±0.95abB	13.3±1.42abA

Note: The letters (i.e. a, and b) in each column, and the letters (i.e. A, B, and C) in each row, represent the significant difference at the significance level of 0.05 by the Duncan Multiple Range Test.

- **Soil disturbance characteristics on the grassland**

The disturbed soil surface profiles were measured via the profile meter device aforementioned. Results showed that the cross-section profiles of the furrows underground were all like a “V” type, as shown in Fig. 7(a). It was also observed that within the zone near to the bottom of the furrow, the width of the disturbed cross-section was closed to the thickness of the tine, especially, when the working depth increased, this characteristic showed more obviously.

There were two kinds of disturbed surface remained after working, one was that small clods were overturned along the furrow, the other one was only narrow slit with no clods overturned left. Only TTD brought about the second disturbance situation described above, and the other three tines caused the small clods overturned along the opening furrow when they were moving. The disturbed surfaces were as shown in Fig. 7(b) and Fig. 7(c).

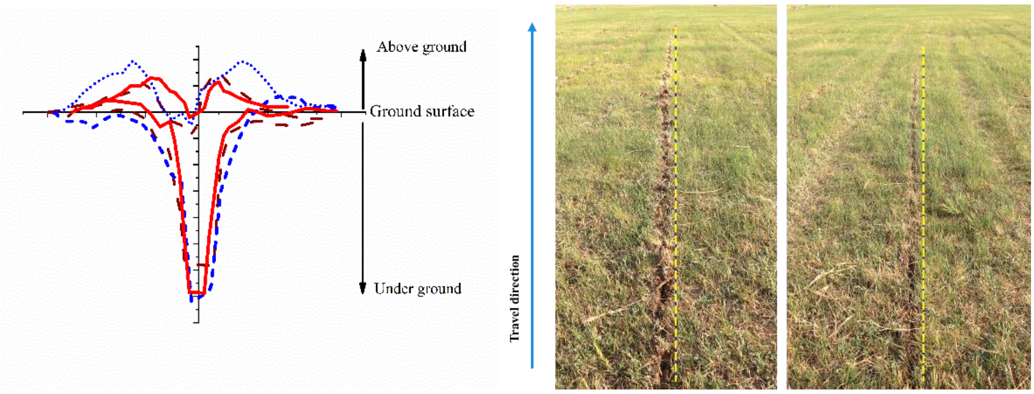

(a) (b) (c)

Fig. 7 -Soil disturbance characteristics on the grassland

(a) typical geometry of disturbed soil layer cross-section area; (b) overturned small clods along the furrow; (c) only narrow slit

In addition, it was found that the TTD tine cut the soil layer like a blade, the roots were cut by the chamfers instead of pulled out, and the tine was mainly wrapped by dry grass aboveground (Fig. 8 (a)). However, for the other three tines, the roots in the soil layer were pulled by the tines, and the aboveground parts of the tines were usually wrapped by the composite structure of soil and roots, clods and dry grass, especially for the tine of CT (Fig. 8 (b)).

(a) (b)

Fig. 8 - Soil layer disturbance situation

(a) soil layer and roots were cut by the tine, dry grass wrapped the tine; (b) soil layer were disturbed, and roots were pulled by the tine, which was wrapped by clods, soil-roots composite, and dry grass aboveground

- **The soil over-turning rate and cross-section area of disturbed soil layer**

The soil over-turning rate was less than 5%, obtained by measuring and calculating through equation (4), as shown in Table 4. TTD had the least values of the soil over-turning rates, which demonstrated that it would cause less surface disturbance on the grassland.

Table 4

Soil over-turning rates of different tillage tines

Depth（cm）	Soil over-turning rate (%)			
	TT	TTD	AT	CT
0-5	3.16	0.00	3.60	-
5-10	3.88	0.00	2.52	3.08
10-15	1.76	0.00	4.08	-

Note: The values of soil over-turning rates were obtained based on measuring the over-turned clods with the diameter of more than 5 cm along the furrows.

The area of disturbed soil layer cross-section underground was calculated by equation (5), listed in Fig. 9. The line graph (Fig. 9(b)) presented that the cross-section area of the disturbed soil layer underground increased with the working depth increasing linearly with the R^2 value of more than 0.78. In Fig. 9(a), it could be seen that all the cross-section areas of tillage tines were larger than that of theoretical cross-sectional areas which were calculated by actual working depths and theoretical shank widths.

It implied that the tillage tine caused disturbances in surrounding areas when it was moving in the soil layer, and the disturbed area was wider than its thickness. TTD had the smallest disturbed cross-section area, with the value range of 18-35 cm^2, was 35.6% less than that of TT on average. The disturbed cross-section areas of the other three tines were located in the range of 26-78 cm^2.

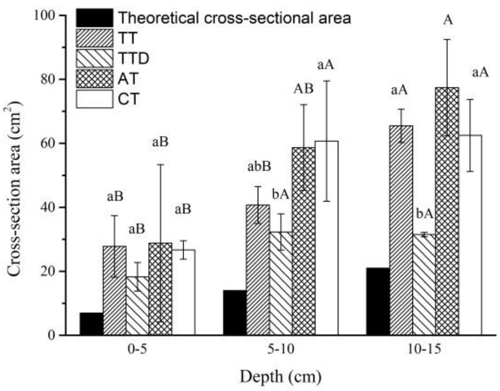

(a)

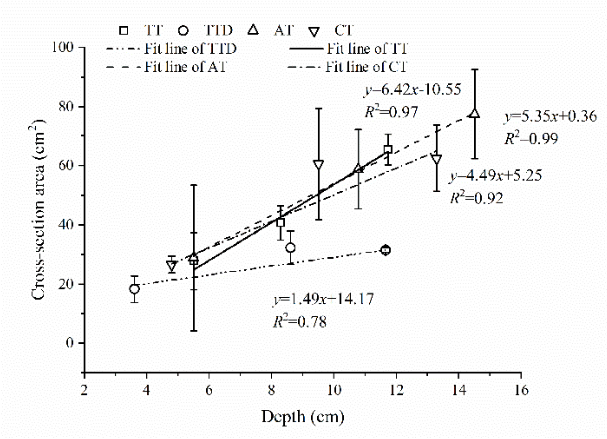

(b)

Fig. 9 - Cross-section area of disturbed soil layer underground

(a) comparison between different tillage tines; (b) relationship between cross-section area and working depth

Note: In Fig.9 (a), the lowercase letters reflect the significant differences between cross-section areas of different tines at the same depth range at the significance level of 0.05 by the Duncan Multiple Range Test. The capital letters represent the significant differences between cross-section areas at different depth ranges of the same tine at the significance level of 0.05 by the Duncan Multiple Range Test.

For TTD and CT, the cross-section area values showed significant differences with the depth ranges changing, respectively. Within the depth range of 0-5 cm, no significant differences could be observed between the areas. For the range of 5-10 cm and 10-15 cm, the cross-section area value of TTD showed significantly different from CT, while TT and CT did not. Combined with Table 3, it could be found that there were no significant differences ($P<0.05$) between the actual working depths of AT and CT within the depth range of 5-10 cm and 10-15 cm, implying significant differences caused by depth changes would not be compared by using multiple comparison method because of the sample numbers less than three, so the method of Independent Samples Test was used at the significance level of 0.05, related results were listed in Table 5. Table 5 showed there were no significant differences between the cross-section areas of AT and CT in the depth range of 5-10 cm and 10-15 cm, respectively.

Table 5

Independent Samples Test of disturbed soil layer cross-section area

Depth (cm)		Levene's Test for Equality of Variances		t-test for Equality of Means		
		F	Sig.	t	df	Sig. (2-tailed)
5-10	Equal variances assumed	.876	.402	-.149	4	.889
	Equal variances not assumed			-.149	3.613	.890
10-15	Equal variances assumed	.297	.615	1.378	4	.240
	Equal variances not assumed			1.378	3.699	.246

- **Soil cutting forces**

The sensor data in the horizontal direction reflected the soil resistance, i.e. the draft force. In Fig.10, the column graphs showed that AT had the smallest draft force among all the tillage tines, TT came after that. TTD owned the largest average draft force value, and no significant differences were observed between the other three tines under the same working depth. Fig. 10(b) also presented that the draft forces increased with the actual working depth increasing, and good linear relationships could be found between draft force and working depth with the R^2 value of exceeding 0.99. As the working depth increasing, the draft force of TT increased sharply by observing a high slope value, AT and CT showed the increasing characteristic more slightly compared to TT, and the slopes had no big differences. The draft force of TTD always stayed in the highest value with the working depth increasing.

It could be found that there were significant differences between the draft forces of the same tillage tine under different working depths at the significance level of 0.05. Combined with Table 3, the actual working depths of AT and CT showed no significant differences ($P<0.05$) at the depth range of 5-10 cm and 10-15 cm, significant differences between draft forces caused by the depth variation could not be compared by using multiple comparison method. Independent Samples Test was used at the significance level of 0.05, related results were listed in Table 6. It showed that there were no significant differences between the draft forces of AT and TT within the depth range of 5-10 cm and 10-15 cm, respectively.

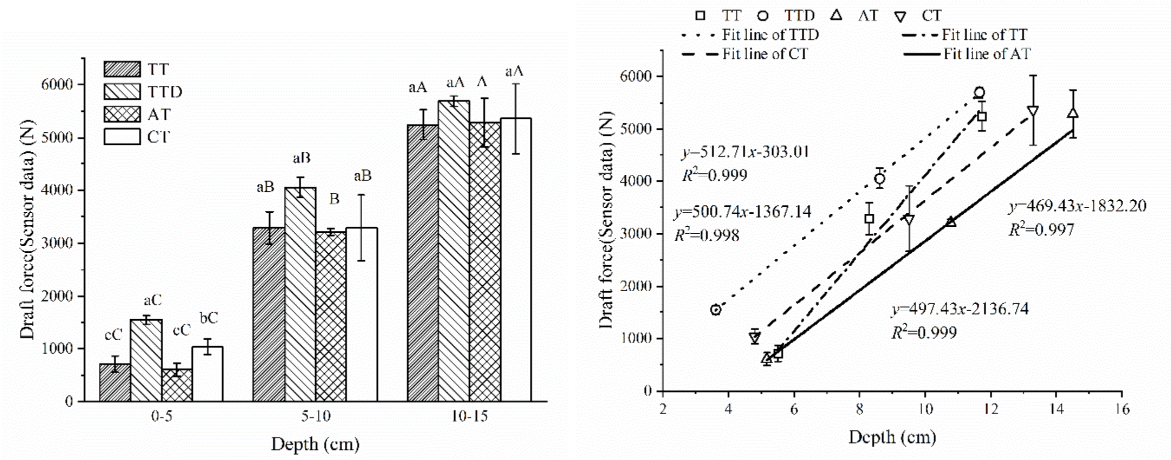

(a) (b)

Fig. 10 - Soil cutting forces

(a) draft force; (b) relationship between draft force and working depth

Note: In Fig. 10 (a), the lowercase letters reflect the significant differences between the forces of different tines at the same depth range at the significance level of 0.05 by the Duncan Multiple Range Test. The capital letters represent the significant differences between the forces at different depth ranges of the same tine at the significance level of 0.05 by the Duncan Multiple Range Test.

Table 6

Independent Samples Test of draft force

Depth (cm)		Levene's Test for Equality of Variances		t-test for Equality of Means		
		F	Sig.	t	df	Sig.(2-tailed)
5-10	Equal variances assumed	12.410	.024	-.202	4	.850
	Equal variances not assumed			-.202	2.040	.858
10-15	Equal variances assumed	1.007	.372	-.151	4	.887
	Equal variances not assumed			-.151	3.554	.888

At the depth of 0-5 cm, the draft force of TTD was significantly different from that of the other tines ($P < 0.05$), which was 2.5 times larger than that of AT. There were no big differences between the draft forces of TT and AT within the depth range of 0-5 cm. At the depth range of 5-10cm and 10-15 cm, the draft forces of TT, TTD, and CT had no significant differences ($P < 0.05$), but the draft force of TTD increased by 24.27% and 7.51% averagely compared to the other three tillage tines. The draft force of TTD was larger than TT with a percentage of 23.44 and 8.62 at the depth of 5-10 cm and 10-15 cm, respectively, but the differences were not significant.

The specific draft forces were calculated through equation (6), and the relationship between specific draft force and working depth was obtained and drawn in Fig. 11.

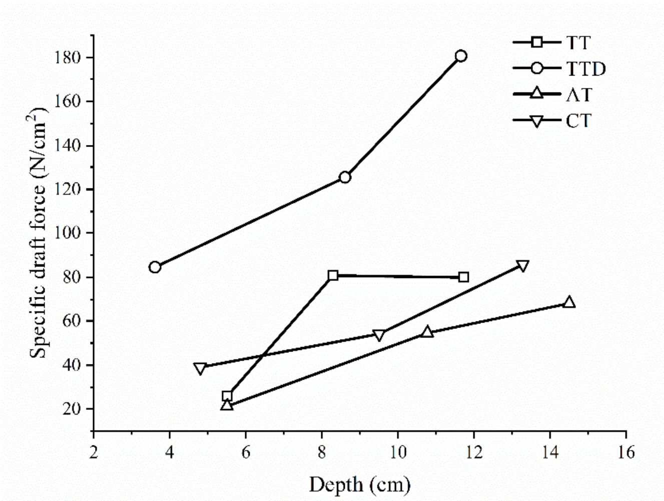

Fig. 11 - Relationship between specific draft force and working depth

The lines showed the specific draft forces of the tillage tines increased with the working depth increasing. TTD had the largest value. The Specific draft force-depth curves of TT, AT, and CT had no big differences, implying the specific draft forces were not affected by various geometry structures significantly, but the tine with a double side chamfer (symmetric) did result in big differences between the specific draft forces.

CONCLUSIONS

(1) The selected shank type tillage tines could break the soil layer underground and create disturbance on natural grassland. Different geometry structures of the tines showed different influences on the working resistance and disturbance characteristics caused by the tines. The cutting heads with different shapes showed no significant effects on the draft force and soil disturbed cross-section area on natural grassland under the same rake angle, but had influences on the translocations of soil clods and soil-root composites.

(2) Chamfers presented large influences on draft force and soil disturbance on natural grassland. The chamfers enhanced the cutting resistances for the tillage tines, but reduced the disturbed cross-section areas of the soil layer underground. For the tines with chamfered cutting edges, both the draft force and the area of disturbed cross-section increased with the depth increasing linearly with the R^2 value exceeding 0.78.

(3) The working depth affected the soil working resistance and disturbed cross-section area underground significantly ($P<0.05$), both draft force and disturbed cross-section area had good linear positive correlation relationship with the working depth, respectively. The specific draft force increased with the working depth increasing.

(4) V-shaped disturbed soil layer cross-sections were produced by very narrow tillage tines after tillage operation. Shank-type tillage tine with chamfers could cut and break the hardened soil layer on natural grassland with low disturbance and no pulling or dragging roots, indicating it could be an appropriate tillage tool applied for improving degraded natural grassland with low disturbance, but still need further surveys.

(5) The draft force, soil over-turning rate, area of disturbed cross-section, and specific draft force could reflect the tillage resistances coming from the soil layer and related disturbance characteristics produced by tillage tines on the grassland well, these parameters may become the evaluation indicators of the specialized tillage tools used for natural grassland, and supportive references for designing and optimizing related tillage tools for grassland.

ACKNOWLEDGEMENT

The authors were funded for this project by the National Natural Science Foundation of China (NSFC) (No. 51905277), the Inner Mongolia Natural Science Foundation (No. 2019BS05014), High-level Talent Scientific Research Project of Inner Mongolia Agricultural University (No. NDYB2018-7), the National Natural Science Foundation of China (NSFC) (No. 51405493), and the earmarked fund for China Agriculture Research System (CARS-34). They also received supports from Zhangjiakou Comprehensive Test Station of China Forage and Grass Research System.

REFERENCES

[1] Alvarez R., Steinbach H.S., (2009). A review of the effects of tillage systems on some soil physical properties, water content, nitrate availability and crops yield in the Argentine Pampas. *Soil and Tillage Research*, Vol.104, pp.1-15, Amsterdam/Netherlands;

[2] ASAE S313.3, (2009). Soil Cone Penetrometer. *ASABE*, St. Joseph Mich / America.

[3] Askari M., Shahgholi G., Abbaspour-Gilandeh Y., Tash-Shamsabadi H., (2013). The Effect of New Wings on Subsoiler Performance. *Applied Engineering in Agriculture*. Vol.32, pp. 353-362, USA,

[4] Bell L. W., Kirkegaard J. A., Swan A., Hunt J. R., Huth N. I., Fettell N. A., (2011). Impacts of soil damage by grazing livestock on crop productivity. *Soil and Tillage Research*, Vol.113, pp.19-29, Amsterdam/Netherlands

[5] Bueno J., Amiama C., Hernanz J.L., (2007). No-tillage drilling of Italian ryegrass (*Lolium multiflorum L.*): Crop residue effects, yields and economic benefits. *Soil and Tillage Research*, Vol. 95, pp. 61-68, Amsterdam/Netherlands.

[6] Chen H., Shao L., Zhao M., Zhang X., Zhang D., (2017). Grassland conservation programs, vegetation rehabilitation and spatial dependency in Inner Mongolia, China. *Land Use Policy*, Vol.64, pp. 429-439, England.

[7] De Boer H.C., Deru J.G.C., Van Eekeren N., (2018). Sward lifting in compacted grassland: effects on soil structure, grass rooting and productivity. *Soil and Tillage Research*, vol.184, pp. 317-325, Amsterdam/Netherlands.

[8] Godwin, R. J., (2007). A review of the effect of implement geometry on soil failure and implement forces. *Soil and Tillage Research*, vol.97, pp. 331-340, Amsterdam/Netherlands.

[9] Godwin R. J., O'Dogherty M.J., (2007). Integrated soil tillage force prediction models. *Journal of Terramechanics*, Vol.44, pp. 3-14, England.

[10] He C., You Y., Wang D., Wu H., Ye B., (2020). An experimental investigation of soil layer coupling failure characteristics on natural grassland by passive subsoiler-type openers. *INMATEH-Agricultural Engineering*, Vol. 61, Issue 2, pp.49-58, Bucharest/Romania.

[11] He C., You Y., Wang D., Wang G., Wu H., Gong S., (2016). Mechanical characteristics of soil-root composite and its influence factors in degenerated grassland (退化草地复合体力学特性与影响因素研究). *Transactions of the Chinese Society for Agricultural Machinery*, Vol.47, pp. 79-89, Beijing/China.

[12] ISO D. 11465, (1993). Soil quality—determination of dry matter and water content on a mass basis—Gravimetric method. Deutsches Institut für Normung Beuth, Berlin Google Scholar.

[13] Lal R., (2007). Evolution of the plough over 10,000 years and the rationale for no-till farming. *Soil and Tillage Research*, Vol.93, pp.1-12, Amsterdam/Netherlands.

[14] Liu G.X., He F., Wan L.Q., Li X.L., (2015). Management Regimen and Seeding Rate Modify Seedling Establishment of Leymus chinensis. *Rangeland ecology & management*, Vol.68, pp. 204-210, Lakewood/ America.

[15] Martınez L.J., Zinck J.A., (2004). Temporal variation of soil compaction and deterioration of soil quality in pasture areas of Colombian Amazonia. *Soil and Tillage Research*, Vol.75, pp.3-18, Amsterdam/Netherlands.

[16] MOA (Ministry of Agriculture of the People's Republic of China), (1996). Chinese Grassland Resource（中国草地资源）. Chinese Science and Technology Press, Beijing/China.

[17] MOMI (Ministry of Machinery Industry of the People's Republic of China). Chinese Standards. (2003). NY/T 740-2003: Field operation quality of ditchers（田间开沟机械作业质量）. MOMA, Beijing/China.

[18] MOMI (Ministry of Machinery Industry of the People's Republic of China). Chinese Standards. (1993). JB/T 7135.2-1993: Experimental Method of Tillage Implement for Leymus-chinensis Grassland(羊草地浅松耕犁 试验方法). MOMA, Beijing/China.

[19] Ramírez P.B., Calderón F.J., Fonte S.J., Bonilla C.A., (2019). Environmental controls and long-term changes on carbon stocks under agricultural lands. *Soil and Tillage Research*, Vol.186, pp. 310-321, Amsterdam/Netherlands.

[20] Su Y.Z., Zhao H.L., Zhang T.H., Zhao X.Y., (2004). Soil properties following cultivation and non-grazing of a semi-arid sandy grassland in northern China. *Soil and Tillage Research*, Vol.75, pp. 27-36, Amsterdam/Netherlands.

[21] Tang J., Davy A. J., Jiang D., Musa A., Wu D., Wang Y., Miao C., (2016). Effects of excluding grazing on the vegetation and soils of degraded sparse-elm grassland in the Horqin Sandy Land, China. *Agriculture, Ecosystems & Environment*, Vol. 235, pp.340-348, Amsterdam/Netherlands.

[22] Wang Z., Li L., Han X., Dong M., (2004). Do rhizome severing and shoot defoliation affect clonal growth of Leymus chinensis at ramet population level?. *Acta Oecologica*, Vol.26, pp. 255-260, Netherlands.

[23] You Y., Wang D., Liu J., (2012). A device for mechanical remediation of degraded grasslands. *Soil and Tillage Research,* Vol.118, pp. 1-10, Amsterdam/Netherlands.

[24] Zhao H.L., Zhou R.L., Zhang T.H., Zhao X. Y., (2006). Effects of desertification on soil and crop growth properties in Horqin sandy cropland of Inner Mongolia, north China. *Soil Tillage Research*. Vol.87, pp. 175–185, Amsterdam/Netherlands.

[25] Zhou J., Zhang Y., Wilson G.W., Cobb A.B., Lu W., Guo Y., (2017). Small vegetation gaps increase reseeded yellow-flowered alfalfa performance and production in native grasslands. *Basic and Applied Ecology*, Vol.24, pp.41-52, Jena/ Germany.

RESEARCH ON CROP INFORMATION EXTRACTION OF AGRICULTURAL UAV IMAGES BASED ON BLIND IMAGE DEBLURRING TECHNOLOGY AND SVM
/
基于无人机作物图像盲复原及 SVM 的作物信息提取研究

Zehai Xu [1)], Haiyan Song [1*)], Zhiming Wu [1)], Zefu Xu [2)], Shifang Wang [3)]
[1)] College of Agricultural Engineering, Shanxi Agricultural University, Taigu / China
[2)] School of Electrical Engineering, Beijing Jiaotong University, Beijing / China
[3)] Beijing Research centre for Agricultural Standards and Testing, Beijing / China
Tel: +86-0354-6288316; E-mail: haiyansong2003@163.com, 18434765476@163.com
DOI: https://doi.org/10.356.33/inmateh-64-03

Keywords**:** *blind image deblurring, re-weighted graph total variation (SVM), crop information extractions, SVM, UAV*

ABSTRACT
The blurring of crop images acquired by agricultural Unmanned Aerial Vehicle (UAV) due to sudden inputs by operators, atmospheric disturbance, and many other factors will eventually affect the subsequent crop identification, information extraction, and yield estimation. Aiming at the above problems, the new proposed combined deblurring algorithm based on the re-weighted graph total variation (RGTV) and L0-regularized prior, and the other two representative deblurring algorithms were applied to restore blurry crop images acquired during UAV flight, respectively. The restoration performance was measured by subjective vision, and objective evaluation indexes. The crop shape-related and texture-related feature parameters were then extracted, the Support Vector Machine (SVM) classifier with four common kernel functions was implemented for crop classification to realize the purpose of crop information extraction. The deblurring results showed that the proposed algorithm performed better in suppressing the ringing effect and preserving the image fine details, and retained higher objective evaluation indexes than the other two deblurring algorithms. The comparative analysis of different classification kernel functions showed that the Polynomial kernel function with an average recognition rate of 94.83% was most suitable for crop classification and recognition. The research will help in further popularization of crop monitoring based on UAV low-altitude remote sensing.

摘要
由于人为的突然输入，大气扰动以及许多因素将会导致农用无人机获取的作物图像出现模糊现象，最终会影响后续的作物识别，信息提取以及产量估计。针对这个问题，采用一种新提出的基于重加权总变分（RGTV）结合 L0 正则化先验的图像盲复原算法以及其他两种较具有代表性的去模糊算法分别对无人机在作业时获取到的作物图像进行复原处理。采用主观以及客观评价指数对复原效果进行评价。采用带有四种常见核函数的支持向量机分类器用于作物分类从而实现作物信息提取的目的。复原结果表明提出的算法能很好地抑制振铃效应以及保留图像的细节，并有着比另外两种算法较高的客观评价指数上。对不同核函数的分析表明：多项式核函数用于 94.83%的平均识别率是最适合作物的分类以及识别。研究将会帮助采用无人机低空遥感进行作物监测的推广提供一定的帮助。

INTRODUCTION
The rapid acquisition and analysis of crop information are the prerequisite and basis for carrying out precision agricultural practices (*Wang et al., 2014; Lan et al., 2017*). With the development of agricultural remote sensing technology, it has grown up to be an important means of obtaining farmland information in precision agriculture, as well as an important data source for yield estimation, crop type identification, and growth analysis (*Tian et al., 2013; Han et al., 2017*). Recently, agricultural UAV remote sensing platforms, with their characteristics of high timeliness, short operation cycle and high spatial resolution, become a reliable tool of agricultural monitoring (*Chlingaryan et al., 2018*; *Huang et al*., *2018; Garcia et al., 2020*).

---

[1] *Zehai Xu, As. M.S. Stud. Eng.; Haiyan Song* , Prof. Ph.D. Eng.; Zhiming WU, Prof. Ph.D. Eng.*
[2] *Zefu Xu, As. M.E. Stud. Eng.;*
[3] *Shifang Wang, As. M.E. Stud. Eng.*

However, the combined influence of atmospheric turbulence, UAV platforms shaking and operation mistakes will make the crop images be blurred and lose valuable information (*Zhang et al., 2012*), which will further affect the yield estimation, crop identification, and other crop-related studies *(Wang et al., 2018*). So far, there are few reports on crop information extraction based on blind image deblurring. Therefore, it is necessary to conduct research on restoration of the blurry crop images obtained during agricultural UAV flight.

Blind image deblurring, a major branch of digital image processing, has been studied extensively and advanced rapidly in remote sensing, text, face, nature, and other types of images in the past decades (*Fergus et al., 2006; Ma et al., 2009; Xu et al., 2017; Pan et al., 2017; Kong et al., 2017; Anger et al., 2019*). Early image deblurring studies mainly focused on the liner motion cases, which exploited parameter estimation methods to obtain the length and angle of the point spread function (PSF) for blind image restoration (*Tiwari et al., 2014*). However, the factors causing image degradation in reality are usually unknown and interactive, which leads to the difficulty of obtaining the PSF parameters (*Li et al., 2019*). In recent years, great progress has been made in blind image restoration algorithms which can be divided into three categories based on the operating principles. The first category is to exploit the regularization techniques to stabilize the restoration process via various priors learned from blur kernels and natural clear images. Then, image deblurring can be achieved by the alternating iterative algorithms (*Shan et al., 2008*). *Krishnan et al. (2011*) propose an image regularization term based on the l1/l2 norm, which can stabilize the kernel estimation process and obtain the satisfactory deblurring results. A simple yet effective L0-regularized prior based on intensity and gradient is adopted to reduce artifacts effectively, which does not require any complex processing techniques (*Pan et al., 2014*). *Pan et al. (2016),* inspired by the dark channel of blurred images that is less sparse, propose a dark channel prior for deblurring text, face, low-illumination and natural images, which does not require heuristic edge selections steps or any complex processing techniques in kernel estimation. *Bai et al. (2018)* design a reweighted graph total variation (RGTV) prior that can efficiently promote a bi-modal edge weight distribution given blurry patch. *Zhu et al. (2019)* apply a nonconvex second-order TV regularization model with linear constraints for remote sensing image restoration, which can preserve the edge information while avoiding the staircase effect. In addition to priors, the second category focus on sharp edge predictions for blur kernel estimation (*Tang et al., 2019*), which are more dependent on the image sharp edges. A combination of knife-edge detection and alternating minimization is applied for blind restoration of remote sensing images (*Shen et al., 2008*), which can stop the iterations at the best visual quality. However, the PSF estimation more relies on the existence of knife-edge features. *Chen et al. (2019)*, inspired by the observation that maximum value of local patch gradient will diminish after the blur process, propose a local maximum gradient prior for blind image deblurring. Chen et al. (2020) propose a novel method based on the non-local self-similarity for blind image deblurring, which can simultaneously capture the intrinsic structure correlation and spatial sparsity of an image. The third category based on deep learning combines neural network with blind image restoration to estimate the blur kernel (*Jidesh et al. 2018; Wang et al. 2018; Li et al., 2019*), which generally requires a lot of training data. Often, the lack of real blurry training data limits the application of this method to some extent.

The Support Vector Machine (SVM), a supervised machine learning technique, have been shown to perform well in non-linear, small sample data, and high-dimensional pattern recognition problems (*Tian et al., 2007*), which has been widely used in crop-related recognition problems as well (*Zhao et al., 2020*). *Li et al. (2012)* apply SVM to recognize wheat stripe rust and wheat leaf rust after segmentation by K-means clustering algorithm, which can successfully discriminate the two. *Li et al. (2020)* prove that the combination of recursive feature elimination algorithm based on SVM (SVM-RFE) feature subset and SVM model have the satisfactory effect on the classification of crops. *Bhatia et al. (2020)* propose a hybrid of Support Vector Machine (SVM) and Logistic Regression (LR) classifier for better prediction of powdery mildew disease in tomato plants.

In this paper, inspired by the idea of the first blind restoration algorithms, the new combined deblurring algorithm based on a more novel and universal RGTV prior and the L0-regularized intensity and gradient prior was proposed to restore blurry millet images obtained by agricultural UAV, and then the research on crop information extraction from the deblurred images with better deblurring performance was conducted. However, when extracting crop-related information, we observed the colour of millet spikes was similar to that of some senile leaves during the mid and late grain-filling stages, which might cause mistakes in crop yield estimation and other related studies.

Their shape-related and texture-related feature parameters with rotation scaling and translation (RST) invariance were extracted. The SVM classifier with different kernel functions was employed for classification to acquire the optimal recognition rate, so as to achieve more accurate crop information extraction.

MATERIALS AND METHODS

Millet images acquisition

The millet images for crop information extraction were obtained by a Phantom4 Advanced UAV at the foxtail millet planting base (millet was planted in late May and harvested in early October) in Zhongyang Village (37°28' N, 112°39' E), Taigu District, Shanxi Province, China. The camera was a FC6310 with a resolution of 5472×3648. The crop images were collected in a vertical manner. The UAV flew at a height of 4m with a speed of 3m/s to acquire the crop images on September 27, 2019, from 16:00 to 18:00 in the afternoon. The weather conditions during the period were good. The foxtail millet was in the mid and late grain-filling stages. Figure 1 shows a blurry foxtail millet image obtained during UAV flight.

Fig.1 - A blurry foxtail millet image obtained during UAV flight

The new combined deblurring algorithm based on RGTV prior and L0-regularized prior

The UAV images degradation process may be modeled by a convolution operation:

$$y = k \otimes x + n \tag{1}$$

where y is the observed blurry image, x is the latent sharp image, k is the unknown blur kernel (PSF), and n is random noise which is often modelled as Gaussian. Blind restoration is to recover the latent sharp image x and estimate the blur kernel k only given the blurry image y; the solution of the problem is not only unstable but also non-unique (*Bai et al., 2018*).

To cope with the problem, we present the image RGTV prior combined with the L0-regularized prior blind image restoration algorithm. According to the image degradation model, the maximum a posterior (MAP) framework was exploited to transform the blind image restoration problem into an optimization problem.

$$(\hat{x}, \hat{k}) = \arg\min_{x,k} \{\frac{1}{2}\|x \otimes k - y\|_2^2 + \lambda\|x\|_{RGTV} + \mu\|k\|_2^2\} \tag{2}$$

where λ, μ are positive regularization parameters, the first term is the squared L2-norm data-fidelity term. The second term is the regularization term on the latent images, which can efficiently promote bi-modal edge weight distribution of blurry images (*Bai et al., 2018*). The third term is used to regularize the solution of the blur kernel. We optimize (2) by solving the latent image and the blur kernel alternatively. Thus, we divided the problem into x sub-problem:

$$\arg\min_{x} \frac{1}{2}\|x \otimes k - y\|_2^2 + \lambda\|x\|_{RGTV} \tag{3}$$

After a certain number of iterations, not only the more accurate blur kernel is obtained, but we also get an intermediate latent image, which is a gray reconstructed blurry image with robust gradients, yet few details smoothed in the process of estimating the final blur kernel. Therefore, it cannot be regarded as the final restored image. For this reason, the non-blind restoration algorithm based on L0-regularized intensity and gradient prior, which does not require any complex filtering strategies to select salient edges, needs to be exploited to generate satisfactory deblurring performance (*Pan et al., 2014*).

Crop-related information classification using support vector machine

The support vector machine

Support Vector Machine (SVM), proposed by *Vapnik et al. in 1995* (*Vapnik, 2013*), is a supervised classifier. The core idea of SVM is to separate a given set of binary labelled training data with a hyper-plane that is maximally distant from them, which is mainly divided into the linear separable case and the nonlinear separable case (*Hasan et al., 2019*). Here, we focus on the non-linear separable case. To handle nonlinearly separable classes, a nonlinear transformation is used to map the original data points into a higher dimensional space, in which the data points are linearly separable (*Furey et al., 2000*). The corresponding classification decision function is:

$$f\left(x\right)=\operatorname{sign}\left(\sum_{i=1}^{n}a_i y_i K\left(x_i\cdot x\right)+b\right) \tag{4}$$

where sign( ) is the sign function, a_i is a Lagrange multiplier, b is the threshold of classification, K is the kernel function. Commonly used kernel functions include:

Linear kernel:

$$K\left(x,x_i\right)=x^t * x_i \tag{5}$$

Polynomial kernel:

$$K\left(x,x_i\right)=\left(x^t * x_i+b\right)^d, b>0 \tag{6}$$

Radial Basis Function kernel (RBF):

$$K\left(x,x_i\right)=\exp\left\{-\frac{\left|x-x_i\right|^2}{2\sigma^2}\right\}, \sigma\neq 0 \tag{7}$$

Sigmoid kernel:

$$K\left(x,x_i\right)=\tanh\left[\beta x^t x_i+\theta\right] \tag{8}$$

Establishment of SVM classification model

During the mid and late grain-filling stages, we observed that the colour of millet spikes was similar to that of the senile leaves. Directly extracting crop information during UAV flight might confuse, which could cause some mistakes in crop information extraction, yield estimation, and other crop-related researches. In view of the similarity of colour characteristics between millet spikes and senile leaves, the shape-related and texture-related feature parameters with RST invariance were extracted. Among them, the shape-related feature parameters included roundness (C) and Complexity (E); the texture-related feature parameters included Entropy (Ent), Angular Second Moment (Asm), Contrast (Con), and Correlation (Corr). Therefore, the SVM classifier was adopted to distinguish between the crop shape-related and texture-related feature parameters extracted from the millet spikes and leaves, respectively, so as to achieve more accurate information extraction from millet images.

To maximize presentation of the crop features using the extracted information as much as possible, the training samples applied to construct the classification model were taken from clear near-field images (the flying height of UAV was about 2 meters). Firstly, single complete millet spikes and leaves were extracted from the preprocessed crop images by image tool, each of which contained 30 samples. Then, their shape-related and texture-related feature parameters were extracted respectively. The obtained 60 sets of data were applied as inputs of the SVM to identify the best classification model, in which the millet spike samples were labelled as 1, and the leaf samples were labelled as 2. The LIBSVM-FarutoUltimate toolbox was employed to process the extracted feature parameters (Li, 2011). The training samples and the testing samples described in the 3.2 section were normalized by the scaleForClass function. Since the recognition effect of SVM is affected by the kernel function, penalty parameter c, and kernel function parameter g, each parameter of the SVM model was optimized by a grid search using the SVMForClass function, and the five-fold cross validation was used to prevent overfitting in the training process.

RESULTS AND DISCUSSION

The blind image deblurring results

Since the millet images acquired by agricultural UAV contain not only millet, but also weeds and soil, the restoration of the two will not play a significant role in the subsequent millet information extraction. Therefore, a set of blurry crop images was taken out, and the representative image blocks at 482×276 pixels with rich details and as many millet spikes as possible that were intercepted for efficient and fast image processing. We examined our proposed method on three blurry blocks and compared it to state-of-the-art natural image deblurring algorithms which could be detailed in the literature (*Krishnan et al., 2011; Pan et al., 2016*). In addition, in order to better measure the effect of the three deblurring algorithms, the same kernel size for all algorithms was set to estimate the blur kernel in each case. All the experiments were carried out in MATLAB 2017b with an Intel Core i5-6200U processor and 8GB RAM. The experimental results are shown in Figures 2-4, where Figure a represents the blurry image blocks, Figures b and c represent deblurring results based on normalized sparsity prior (*Krishnan et al., 2011*), dark channel prior (*Pan et al., 2016*), respectively. Figure d represents deblurring results restored by the new proposed algorithm.

From Figure 2, it can be seen that the algorithms based on the normalized sparsity prior (Figure (2b)) and the dark channel prior Figure (2c) can obviously restore the crop details, but the deblurring images have a little distortion. The reason leads to the phenomenon that there may be improperly estimated blur kernels, which makes the deblurred result still contain some ringing artifacts and unnatural visual effect. The visual comparisons show that the new proposed algorithm (Figure (2d)) is obviously better than *Krishnan et al. (2011), Pan et al. (2016)*, and can achieve a higher contrast ratio, which will facilitate crop information extraction.

a) Blurry crop image b) deblurring result of Krishnan et al., 2011

c) deblurring result of Pan et al., 2016 d) deblurring result the new proposed algorithm

Fig. 2 - Comparison of different blind image deblurring algorithms

As shown in Figure. 3, we can see that three deblurring algorithms can better restore the crop details. However, deblurring result based on the normalized sparsity prior Figure (3b), as well as the result based on the dark channel prior Figure (3c), contains obvious ringing artifacts at the edge of the image which decrease the performance of deblurring. As a contrast, the new proposed algorithm Figure (3d) performs better than other compared algorithms in suppressing ringing artifacts of the restored image and can robustly estimate blur kernel. The deblurring result is consistent with the research by *Bai et al. (2018)*.

a) Blurry crop image *b) deblurring result of Krishnan et al., 2011*

c) deblurring result of Pan et al., 2016 *d) deblurring result the new proposed algorithm*

Fig. 3 - Comparison of different blind image deblurring algorithms

As shown in Figure (4c), although a lot of crop details can be recovered, however, there still exists a little blur effect, which may be caused by the inaccuracy of estimated blur kernel. The algorithms based on the normalized sparsity prior Figure (4b) and new proposed algorithm can perform better in visual effect and crop details recovery, but the image restored by the new proposed algorithm Figure (4d) can obtain a clearer blur kernel.

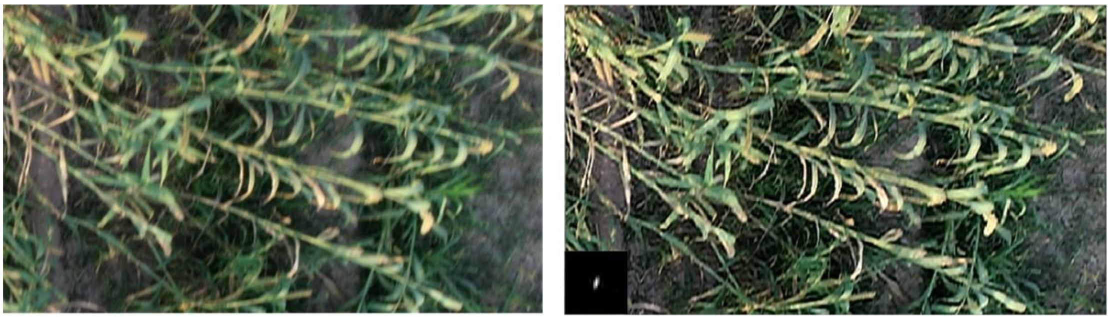

a) Blurry crop image *b) deblurring result of Krishnan et al., 2011*

c) deblurring result of Pan et al., 2016 *d) deblurring result the new proposed algorithm*

Fig. 4 - Comparison of different blind image deblurring algorithms

Apart from the subjective quality assessment, several objective evaluation criteria were also applied to further measure the deblurring performance of the algorithms. Due to the lack of original clear images, we employed three no-reference image quality assessment methods, namely, information entropy, standard deviation, and mean value, which can well measure the amount of information in an image. Generally, the bigger the assessment values, the higher the image quality (*Li et al., 2016*). The calculation results are shown in Tables 1-3.

It can be seen that three evaluation values of the new proposed algorithm are mostly higher than those of the other two algorithms.

At the same time, we can also observe that few values on the proposed algorithm's performance are lower than those of the other two algorithms, which indicates that there may still be some ringing artifacts in the restored images. In short, whether it is from subjective visual effects or objective evaluation indexes, the deblurring algorithm proposed in this paper has better quality than other algorithms.

Table 1

Blind evaluation index without reference quality of Figure 2

Parameter	Information Entropy	Standard deviation	Mean value
Blurred image	7.3245	$1.5852*10^3$	83.8473
Krishnan et al. (2011)	7.5028	$1.9701*10^3$	83.8664
Pan et al. (2016)	7.3850	$2.2949*10^3$	84.1945
Proposed algorithm	7.3808	$2.7058*10^3$	84.7155

Table 2

Blind evaluation index without reference quality of Figure 3

Parameter	Information Entropy	Standard deviation	Mean value
Blurred image	7.1739	$1.4642*10^3$	81.9876
Krishnan et al. (2011)	7.4185	$2.1479*10^3$	81.7898
Pan et al. (2016)	7.2781	$1.8428*10^3$	82.3977
Proposed algorithm	7.4327	$2.4052*10^3$	82.5726

Table 3

Blind evaluation index without reference quality of Figure 4

Parameter	Information Entropy	Standard deviation	Mean value
Blurred image	7.2867	1.7018*103	86.6493
Krishnan et al. (2011)	7.4696	2.9510*103	86.7686
Pan et al. (2016)	7.4506	2.5450*103	87.6612
Proposed algorithm	7.5612	2.5141*103	88.2280

Establishment of SVM test model

The single and complete millet spikes and leaves were intercepted from the deblurred images, each of which contained 12 samples. Two images from each category were displayed in Figure 5. Then, their shape-related and texture-related feature parameters were extracted, respectively. The extracted 24 sets of data were used to establish the SVM testing model, in which the millet spike samples were labelled as 1, and the leaf samples were labelled as 2.

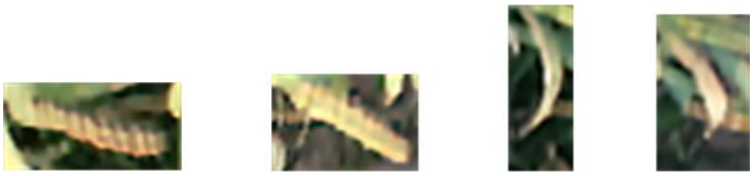

a) millet spike *b) millet spike* *c) senile leaf* *d) senile leaf*

Fig. 5 - The single complete millet spikes and leaves intercepted from the restored crop images

Recognition results of different kernel functions

The SVM with different kernel functions was applied to classify and recognize the millet spikes and leaves samples. The recognition results were shown in Table 4. The results show that the Polynomial kernel function has the best classification performance, and the average recognition rate for the training and testing of these two samples reached 94.83%.

The classification performance of Sigmoid kernel function was second, and the average recognition rate was 93.75%. The classification performance of the Linear kernel function and RBF kernel function was poorer with an average recognition rate of 89.58%. Therefore, the SVM classifier based on Polynomial kernel function was most suitable for distinguishing the millet spikes from the leaves.

Table 4

Results of image recognition of millet spikes and leaves using the SVMs with different kernel functions

Kernel function	Type	Sample		Recognition number		Recognition rate	
		Training sample	Testing sample	Training sample	Testing sample	Training sample	Testing sample
Linear	Millet spikes	30	12	30	10	100%	83.33%
	leaves	30	12	30	9	100%	75%
Polynomial	Millet spikes	30	12	29	10	96%	83.33%
	leaves	30	12	30	12	100%	100%
RBF	Millet spikes	30	12	30	10	100%	83.33%
	leaves	30	12	30	9	100%	75%
Sigmoid	Millet spikes	30	12	30	10	100%	83.33%
	leaves	30	12	30	11	100%	91.67%

As far as we know, crop growth monitoring and yield prediction by agricultural UAV is most commonly performed with the use of RGB (30%) and multispectral (59%) sensors (*Tsouros et al., 2019*), indicating that the implementation of precision agricultural via UAV equipped with RGB sensors has not been spread up so far. Our research about restoration of blurry crop images acquired during UAV flight equipped with RGB sensors and crop-related information extraction has achieved more satisfactory effect, which means that agricultural UAV equipped with RGB sensors for precision agriculture are relatively simple and feasible. This research will help in further promotion of crop monitoring based on UAV low-altitude remote sensing equipped with RGB sensors.

CONCLUSIONS

In this paper, in order to solve the problem that blurry millet images obtained during agricultural UAV flight resulting in the loss of useful information and affect the subsequent crop-related studies, we proposed a new and effective blind image deblurring algorithm based on the image RGTV prior combined with the L0-regularized intensity and gradient prior. Among them, the image RGTV prior, which can promote the bi-modal weight distribution of sharp images from blurry observations, was mainly adopted to obtain the more accurate blur kernel; the L0-regularized intensity and gradient prior was introduced to effectively acquire the final restored image.

The proposed algorithm achieved a highly competitive performance in comparison with other blind restoration methods (*Krishnan et al., 2011; Pan et al., 2016*). When extracting crop-related information from the images restored by proposed algorithm, however, the colour of the millet spikes was similar to that of senile leaves during the mid and late grain-filling stages, which would interfere with crop information extraction. Therefore, their shape-related and texture-related feature parameters with RST invariance were extracted, and the SVM classifier was adopted to distinguish the two.

The results showed that the Polynomial kernel function with an average recognition rate of 94.83% had the best classification performance. The research will provide a reliable basis and approach for realizing information monitoring and crop identification through UAV low altitude remote sensing platforms.

ACKNOWLEDGEMENTS

This study was supported by the National Key R&D Program of China (2018YFD0700300), the Key R&D Program of Shanxi Province (201903D221029), the Agricultural Science and Technology Achievements Transformation and Popularization Demonstration of Shanxi Province (SXNKTG201804).

We extent our thanks to Haiyan Song, Zhiming Wu, Zefu Xu and their colleagues for their reading and helpful comments on this manuscript.

REFERENCES

[1] Anger, J., Delbracio, M., & Facciolo, G. (2019). Efficient blind deblurring under high noise levels. Presentation at 2019 *11th International Symposium on Image and Signal Processing and Analysis*, Dubrovnik, Croatia.

[2] Bai, Y., Cheung, G., Liu, X., & Gao, W. (2018). Graph-based blind image deblurring from a single photograph. *IEEE Transactions on Image Processing*, 28(3), 1404-1418.

[3] Bhatia, A., Chug, A., & Singh, A. P. (2020). Hybrid SVM-LR Classifier for Powdery Mildew Disease Prediction in Tomato Plant. Presentation at 2020 *7th International Conference on Signal Processing and Integrated Networks, Noida*, India.

[4] Chen, L., Fang, F., Wang, T., & Zhang, G. (2019). Blind image deblurring with local maximum gradient prior. Presentation at *IEEE Conference on Computer Vision and Pattern Recognition*, Long Beach, CA, USA.

[5] Chen, X., Yang, R., Guo, C., Ge, S., Wu, Z., & Liu, X. (2020). Hyper-Laplacian Regularized Non-local Low-Rank Prior for Blind Image Deblurring. *IEEE Access*, 8, 136917-136929.

[6] Chlingaryan, A., Sukkarieh, S., & Whelan, B. (2018) Machine learning approaches for crop yield prediction and nitrogen status estimation in precision agriculture: A review. *Computers and electronics in agriculture*, 151, 61-69.

[7] Fergus, R., Singh, B., Hertzmann, A., Roweis, S.T., Freeman, W.T. (2006). Removing camera shake from a single photograph. *ACM Trans. Graph*, 25, 787-794.

[8] Furey, T. S., Cristianini, N., Duffy, N., Bednarski, D. W., Schummer, M., Haussler, D. (2000). Support vector machine classification and validation of cancer tissue samples using microarray expression data. *Bioinformatics*, 16(10), 906-914.

[9] Garcia Millan, V. E., Rankine, C., Sanchez-Azofeifa, G. A. (2020). Crop loss evaluation using digital surface models from unmanned aerial vehicles data. *Remote Sensing*, 12(6), 981.

[10] Han, W., Li, G., Yuan, M., Zhang, L., Shi, Z. (2017). Extraction method of maize planting information based on UAV remote sensing technology. *Transactions of the Chinese Society for Agricultural Machinery*, 48(1), 140-147. (in Chinese with English abstract).

[11] Hasan, M., Ullah, S., Khan, M.J., & Khurshid, K. (2019). Comparative analysis of SVM, ANN and CNN for classifying vegetation species using hyperspectral thermal infrared data. Presentation at International Archives of the Photogrammetry, *Remote Sensing & Spatial Information Sciences*, Enschede, The Netherlands.

[12] Huang, Y., Chen, Z., Tao, Y. U., Huang, X. Z., & Gu, X. F. (2018). Agricultural remote sensing big data: Management and applications. *Journal of Integrative Agriculture*, 17(9), 1915-1931.

[13] Jidesh, P., & Balaji, B. (2018). Adaptive non-local level-set model for despeckling and deblurring of synthetic aperture radar imagery. International Journal of Remote Sensing, 39(20), 6540-6556.

[14] Kong, J., Lu, K., & Jiang, M. (2017). A New Blind Deblurring Method via Hyper-Laplacian Prior. *Procedia Computer Science*, 107, 789-795.

[15] Krishnan, D., Tay, T., & Fergus, R. (2011). Blind deconvolution using a normalized sparsity measure. Presentation at *24th IEEE Conference on Computer Vision and Pattern Recognition*, Colorado Springs, CO, USA.

[16] Lan, Y., Shengde, C., & Fritz, B.K. (2017). Current status and future trends of precision agricultural aviation technologies. *International Journal of Agricultural and Biological Engineering*, 10(3), 1-17.

[17] Li, G., Ma, Z., & Wang, H. (2012). Image recognition of wheat stripe rust and wheat leaf rust based on support vector machine. *Journal of China Agricultural University*, 17(2), 72-79.

[18] Li, L., Shen, W., Gu, K., Wu, J., Chen, B., & Zhang, J. (2016). No-reference quality assessment of enhanced images. *China Communications*, 13(9), 121-130.

[19] Li, L., Pan, J., Lai, W.S., Gao, C., Sang, N., & Yang, M.H. (2019). Blind Image Deblurring via Deep Discriminative Priors. *International Journal of Computer Vision*, 127(8), 1025.

[20] Li, Y. (2011). *LIBSVM-FarutoUltimate version: a toolbox with implements for support vector machines based on Libsvm*. Software. Available at: https://www.ilovematlab.cn/thread-35262-1-1.html. Accessed 22 September 2019.
[21] Li, Y., Tofighi, M., Geng, J., Monga, V., Eldar, Y. C. (2019). *An algorithm unrolling approach to deep blind image deblurring*. arXiv preprint, arXiv:1902.03493.
[22] Li, Z., Zhao, Ji., Lan, Y., & Yang, H. (2020). Crop classification based on UAV visible image. *Journal of Northwest A & F University*, 48(06), 137-144+154. (in Chinese with English abstract).
[23] Ma, J., Le Dimet, F. X. (2009). Deblurring from highly incomplete measurements for remote sensing. *IEEE Transactions on Geoscience and Remote Sensing*, 47(3), 792-802.
[24] Pan, J., Dong, J., Tai, Y., Su, Z., Yang, M. (2017). Learning discriminative data fitting functions for blind image deblurring. Presentation at *2017 IEEE International Conference on Computer Vision*. Venice, Italy.
[25] Pan, J., Hu, Z., Su, Z., Yang, M.H. (2014). Deblurring Text Images via L0-Regularized Intensity and Gradient Prior. Presentation at *2014 IEEE Conference on Computer Vision and Pattern Recognition*, Columbus, OH, USA.
[26] Pan, J., Sun, D., Pfister, H., Yang, M.H. (2016). Blind image deblurring using dark channel prior. Presentation at 2016 *IEEE Conference on Computer Vision and Pattern Recognition*. Las Vegas, NV, USA.
[27] Shan, Q., Jia, J., Agarwala, A. (2008). High-quality motion deblurring from a single image. *ACM transactions on graphics (tog),* 27(3), 1-10.
[28] Shen, H., Zhao, W., Yuan, Q., Zhang, L. (2014). Blind restoration of remote sensing images by a combination of automatic knife-edge detection and alternating minimization. *Remote Sensing*, 6(8), 7491-7521.
[29] Tang, S., Zheng, W., Xie, X., He, T., Yang, P., Luo, L., Li, Z., Hu, Y., & Zhao, H. (2019). Multi-regularization-constrained blur kernel estimation method for blind motion deblurring. *IEEE Access*, 7, 5296-5311.
[30] Tian, Y. W., Li, T. L., Li, C. H., Piao, Z. L., Sun, G. K., & Wang, B. (2007). Method for recognition of grape disease based on support vector machine. *Transactions of the Chinese Society of Agricultural Engineering*, 23(6), 175-180.
[31] Tian, Z., Fu, Y., Liu, S. (2013). Rapid crops classification based on UAV low-altitude remote sensing. *Transactions of the Chinese Society of Agricultural Engineering*, 29(7), 109-116. (in Chinese with English abstract).
[32] Tiwari, S., Shukla, V. P., Biradar, S. R., Singh, A. K. (2014). Blur parameters identification for simultaneous defocus and motion blur. *CSI transactions on ICT*, 2(1), 11-22.
[33] Tsouros, D. C., Bibi, S., Sarigiannidis, P. G. (2019). A review on UAV-based applications for precision agriculture. *Information*, 10(11), 349.
[34] Vapnik, V. (2013). *The nature of statistical learning theory*. Springer science & business media.
[35] Wang, P., Luo, X., Zhou, Z., Zang, Y., Hu, L. (2014). Key technology for remote sensing information acquisition based on micro UAV. *Transactions of the Chinese Society of Agricultural Engineering*, 30(18), 1-12. (in Chinese with English abstract).
[36] Wang, R., Ma, G., Qin, Q., Shi, Q., Huang, J. (2018). Blind UAV images deblurring based on discriminative networks. *Sensors*, 18(9), 2874.
[37] Xu, F., Chen, Y., Peng, C., Wang, Y., Liu, X., He, G. (2017). Denoising of hyperspectral image using low-rank matrix factorization. *IEEE Geoscience and Remote Sensing Letters*, 14(7), 1141-1145.
[38] Zhang, C., Kovacs, J. M. (2012). The application of small unmanned aerial systems for precision agriculture: a review. *Precision agriculture*, 13(6), 693-712.
[39] Zhao, Li., Hou, F., Lyu, Z., Zhu, H., Ding, Y. (2020). Image recognition of cotton leaf diseases and pests based on transfer learning. *Transactions of the Chinese Society of Agricultural Engineering*, 36(7), 184-191. (in Chinese with English abstract).
[40] Zhu, J., Li, K., & Hao, B. (2019). Restoration of remote sensing images based on nonconvex constrained high-order total variation regularization. *Journal of Applied Remote Sensing*, 13(2), 022006.

DEVELOPMENT AND THERMAL EVALUATION OF DOUBLE DRUM DRYER FOR READY-TO-EAT FOOD PRODUCTS TO SUPPORT STUNTING PREVENTION
/
PENGEMBANGAN DAN EVALUASI TERMAL PENGERING DRUM GANDA UNTUK PRODUK MAKANAN SIAP SAJI DALAM MENDUKUNG PENCEGAHAN STUNTING

Dadang Dayat Hidayat[1)], Diang Sagita*[1)], Doddy Andy Darmajana[1)], Ashri Indriati[1)], Ari Rahayuningtyas[1)], Arie Sudaryanto[1)], Yose Rizal Kurniawan[1)], Pramono Nugroho[1)] [1]

[1)]Research Centre for Appropriate Technology, Indonesian Institute of Sciences

Tel: 6285719002251; E-mail: diang.sagita@lipi.go.id

DOI: https://doi.org/10.356.33/inmateh-64-04

Keywords: *design, double drum dryer, manufacture, stunting prevention*

ABSTRACT
The study aimed to develop a small-scale drum dryer to meet the small enterprises' demand in the context to produce ready-to-eat food products to support stunting prevention. The design, manufacture, and thermal evaluation of a double drum dryer had been carried out. The development stage consisted of sizing the main components, creating technical drawings, determining component materials, manufacturing, and performance tests. The dryer drum dimension was 500 mm in diameter and 400 mm in length and 20 mm in thickness. The capacity of the double drum dryer was 10 kg/batch. The double drum dryer was powered by a 3-phase electromotor 2.24 kW. There are three transmission systems applied, i.e. gearbox, chain-sprocket and belt-pulley. The feeding system applied was nip feeding. The heat source originated from the steamer using an electric heater. Results of the test showed that the double drum drying machine had worked well as expected. The temperature distribution of both drums was fairly uniform, and the temperature uniformity in the drum surface showed good uniformity (minimum gradient temperature). The double drum dryer was able to produce good characteristics of products in the form of ready-to-eat products made from several ingredients (i.e. millets and red bean) which contain high macro and micronutrient.

ABSTRAK
Penelitian ini bertujuan untuk mengembangkan drum dryer skala kecil untuk memenuhi kebutuhan usaha kecil dalam rangka memproduksi produk makanan siap saji untuk mendukung pencegahan stunting. Desain, pembuatan, dan evaluasi termal pengering drum ganda telah dilakukan. Tahap pengembangan terdiri dari pengukuran komponen utama, pembuatan gambar teknis, penentuan material komponen, pembuatan, dan uji kinerja. Dimensi drum pengering memiliki diameter 500 mm dan panjang 400 mm dan ketebalan 20 mm. Kapasitas pengering drum ganda adalah 10 kg/batch. Pengering drum ganda digerakkan oleh motor listrik 3-fase 2.24 kW. Ada tiga sistem transmisi yang diterapkan yaitu gearbox, rantai-sproket dan sabuk-puli. Sistem makan yang diterapkan adalah nip feeding. Sumber panas berasal dari steamer dengan menggunakan pemanas listrik. Hasil pengujian menunjukkan bahwa mesin pengering drum ganda telah bekerja dengan baik sesuai dengan yang diharapkan. Distribusi temperatur pada kedua drum cukup seragam, dan keseragaman suhu pada permukaan drum telah menunjukkan keseragaman yang baik (temperatur gradien minimum). Pengering drum ganda telah mampu menghasilkan karakteristik produk yang baik berupa produk siap saji yang terbuat dari beberapa bahan (mis. millet dan kacang merah) yang mengandung makro dan mikronutrien tinggi.

---

[1] *Dadang Dayat Hidayat, M.Eng.Sc.; Diang Sagita, M.Sc., Doddy Andy Darmajana, M.Sc.; Ashri Indriati, M.Sc.; Ari Rahayuningtyas, M.Sc.; Arie Sudaryanto, M.Agr.; Yose Rizal Kurniawan, M.Sc.; Pramono Nugroho, Ph.D.*

INTRODUCTION

Based on Basic Health Research results in 2013 and 2018, Indonesia's stunting prevalence reached 37.2% and 30.8%. With the efforts made by the government in 2019, the stunting rate dropped to 27.67 per cent *(Ministry of Health of the Republic of Indonesia, 2019)*.

The introduction of supplementation in weaning foods prepared from readily available and low-cost ingredients is vital to meet the growing children's requirements (*Saeeda et al., 2009*). Weaning food is one of the ready-to-eat food products to prevent stunting due to lack of good nutrition. These ready-to-eat food products require equipment and process technology that can answer these challenges. One of the technologies used to produce ready-to-eat food products is drying technology of drum dryer using.

Drum dryer is a type of dryer widely used in the food industry for drying various liquid, semi-liquid, and paste food ingredients. Several types of drum drying products include powdered milk, baby food, flour, fruit and vegetable pulp, honey, maltodextrin, yeast cream, and many other foods and non-food products *(Bonaui et al., 1996; Elmholt et al., 2007; Kasiri et al., 2004; Pua et al., 2007; Rodriguez et al., 1996; Tang et al., 2003*)*.* The dry product obtained is porous, easy to rehydrate, and ready to use (*Pua et al., 2007*). The dry products produced can be used as semi-finished products in milk, beverages, confectionery, and other industries (*Pua et al., 2007*). The purpose of drying is to extend the product's shelf life and reduce weight in transportation *(Pua et al., 2007*).

Drum dryers were first patented for use in the manufacture of pregelatinized starch in Germany by Mahler and Supf in 1921 *(Mujumdar, 1995)*. There are three types of cylinder type dryers: single-drum dryers, double drum dryers, and twin drum dryers. Based on the operation system, drum dryers are distinguished from open system dryers and vacuum dryers. Meanwhile, referring to the feeding method, there are four types of cylinder dryers, namely cylinder dryers with nip feed systems, splash feeds, dip feeds, and roller feeds (*Francis, 2000; Mujumdar, 1995; Tang et al., 2003*).

Some of the advantages of using drum dryers include: (a) relatively fast drying time, the thin film is spread over a large area resulting in fast heat and mass transfer, (b) the equipment is compact, uses relatively less space than other dryers, (c) short heating time, (d) the cylinder can be closed in a vacuum jacket, which allows the drying temperature to be reduced, and (e) the product is obtained in flakes, which are suitable for various purposes *(Choudhary, 2015)*. Other prior writings suggest that the advantages of using cylinder dryers are: (a) the product has good porosity and is easy to rehydrate, (b) drum dryers can dry very viscous slurry, such as gelatinized or cooked pastes and starches, which other methods cannot quickly dry, (c) drum dryers usually have high energy efficiency, (d) drying can be clean and hygienic, (e) drum dryers are easy to operate and maintain, and (f) are flexible and suitable for several other types of products *(Mujumdar, 1995)*.

There are also some disadvantages, including lack of control over (a) feed rate, (b) cylinder temperature, (c) film thickness, and (d) cylinder rotation speed *(Ahmed, 2013)*. Other publications say that some of the other disadvantages are: (a) Some products may not be able to dry out and do not form a good film on the cylinder surface, (b) some products, especially those containing high sugar, are not easily dredged from the cylinder surface, (c) the output relatively low compared to spray drying, (d) the cost of replacing the cylinder surface is quite expensive, (e) the possibility of the product being scorched due to direct contact with high temperatures on the cylinder surface, and (f) unable to process salty materials and corrosive materials (*Tang et al., 2003*).

Among the three types, single and double drum dryers are most often used for drying fruits and vegetables. Drum dryers are only used for drying materials that produce powder products. For materials sensitive to heat damage, a vacuum drum dryer can be used for reducing the drying temperature *(Mujumdar, 1995)*. The double drum dryer type has a higher production rate relative to other drum dryer types, it can handle products in a broader range and is more efficient (*Mujumdar, 1995; Okos et al., 1992*).

In Indonesia, drum dryer machines are generally imported from other country so that the costs are very high. Besides, the machine capacity is intended for large-scale businesses. Drum drying machines have not been developed especially for the needs of small and medium scale businesses in Indonesia. Therefore this research aimed to develop locally made drum dryers using available local materials in order to support the drying process of ready-to-eat food related to stunting prevention. The developed machine is expected to be appropriate with the small scale enterprise demand to produce high quality and standard ready-to-eat products.

MATERIALS AND METHODS

The development stage of the double drum drying machine consisted of a general description, sizing and determining the main components, creating technical drawings, manufacturing, and performing the functional test *(Hidayat et al., 2020)*.

Description of double drum drying machine

The double drum dryer, designed and constructed, is an open type (atmospheric) with a nip feeding system. Atmospheric double drum dryers are the most versatile and widely used type of drum dryer due to their products' versatility. This dryer type has a higher production rate, can handle a more comprehensive product range and is more efficient than other drum dryer types *(Mujumdar, 1995)*. Figure 1 shows an exploded view of a double drum dryer designed and constructed in this study.

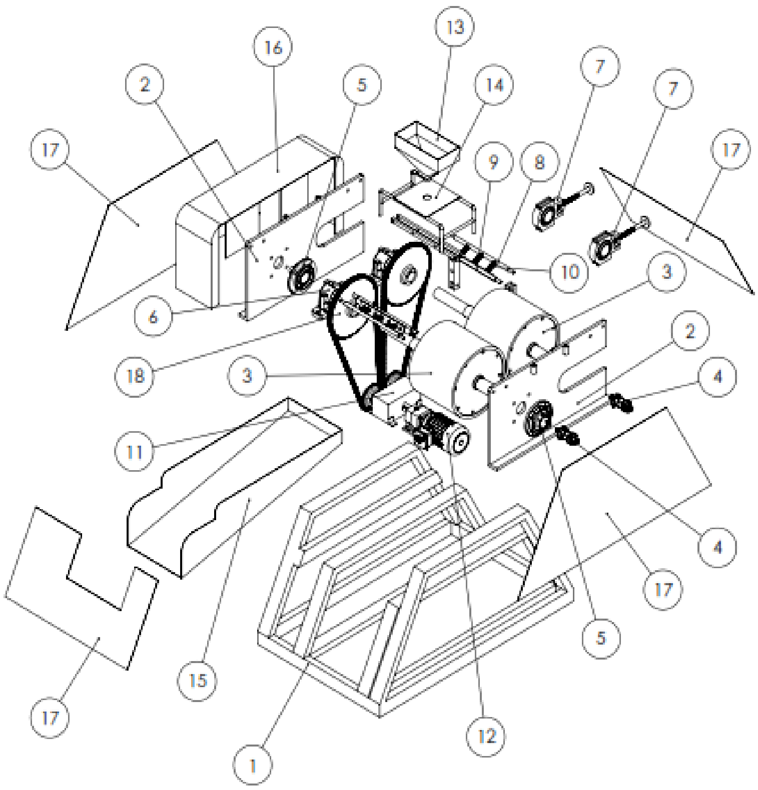

1. *Frame*
2. *Buttress*
3. *Drum*
4. *Rotary Joint*
5. *Pillow Block Bearing*
6. *Plummer Block Bearing*
7. *Pillow Block Bearing Adjuster*
8. *Support Shaft*
9. *Scraper*
10. *Springs*
11. *Gear Box*
12. *Electric Motor*
13. *Hopper*
14. *Hopper Stand*
15. *Product Release Chute*
16. *Transmission Cover*
17. *Frame Cover*
18. *Chain Sprocket*

Fig. 1 - An exploded view of the double drum dryer designed

The double drum dryer is classified as a conduction dryer. The drying process is obtained by transferring heat from the condensing steam inside the drum to the material covering its external surface (*Jurendić & Branko, 2012; Karapantsios, 2006*). Just like the name, the double drum dryer consists of two cylinders rotating against one another. The feeding system applied in this double drum dryer was nip feeding. The food material to be dried was prepared in the mixer by adding the desired components and water. After mixing, the liquid or semi-liquid food material was poured into the hopper. The material fell into the drum dryer surface and was equally distributed along the body by opening the tap. After about three-quarters of a drum revolution from the point of feeding, the material was dried, and then scraped off. The scraped off material fell into drop chute and was finally collected in the container.

Sizing of the main components

The main components of a double drum dryer need to be designed based on the criteria of the machine which has a capacity of 10 kg per batch. Sizing main components consisted of hopper dimension, drum mass and dimension, shaft, scraper, power source, and transmission system.

Hopper design

Hopper dimension is required to be designed according to hopper capacity target per batch. The hopper design is shown in figure 2 and the capacity is calculated using the equation (1)-(4).

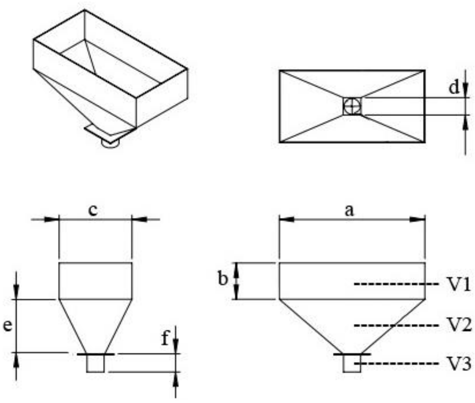

a = 40 cm
b = 10 cm
c = 20 cm
d = 4.7 cm
e = 15.3 cm
f = 5 cm

Fig. 2 - Orthogonal view of the hopper design

$$V_1 = a \times c \times b \text{ [cm}^3\text{]} \tag{1}$$

$$V_2 = \left[\frac{1}{3}(a \times c) \times e + \frac{1}{3}(d^2) \times e + \frac{1}{3}\sqrt{(a \times c) \times (d^2) \times e} \right] \text{ [cm}^3\text{]} \tag{2}$$

$$V_3 = \frac{\pi}{4} \times d^2 \times f \text{ [cm}^3\text{]} \tag{3}$$

$$\sum V = V_1 \times V_2 \times V_3 \text{ [cm}^3\text{]} \tag{4}$$

Results of calculation obtained that the gross volume of the hopper (ΣV) was 12827 cm^3 or 12.83 liters, taken into account 80% of capacity, the net volume for raw material is about 10 liters.

The statistical analysis results determined that the height of raw material in the hopper correlated quadratically with the volume. The correlation between the height of raw material and volume matched the equation of $y = 0.020x^2 - 0.237x + 0.768$, $R^2 = 1$, where X-axis is a height of material in the hopper, Y-axis is the volume of the raw material (figure 3).

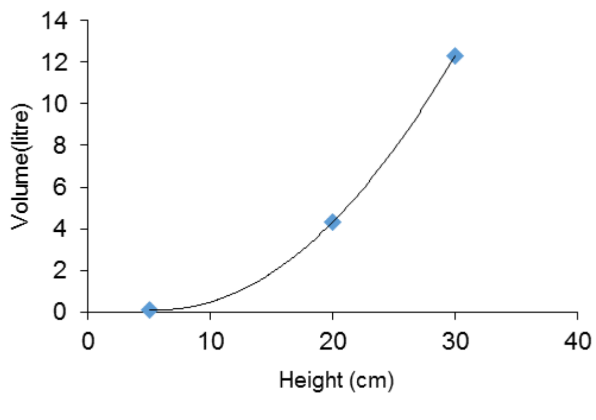

Fig. 3 - Correlation between height and volume of raw material in the hopper

Drum design

In developing a drum dryer, the drum is the most important part because the surface is where it comes into contact with the dried material so that the drum was constructed using cast iron (FCD 450). FCD 450 was chosen as it has a lower thermal expansion coefficient compared to stainless steel.

The coefficient of thermal expansion of FCD 450 and stainless steel are 10×10^{-6} K^{-1} and 17.3×10^{-6} K^{-1}, respectively. To increase hardness, durability, and avoid corrosion, FCD 450 was coated with chromium material. Drum design is shown in figure 4. The parameter of drum design consisted of surface area (A_D), drum volume (V_D) and drum mass (M_D), determined by using equation (5)-(7).

$$A_D = \pi \times D \times L \text{ [cm}^2\text{]} \quad (5)$$

$$V_D = A_D \times t \text{ [cm}^3\text{]} \quad (6)$$

$$M_D = V_D \times \rho \text{ [kg]} \quad (7)$$

where:

D is diameter of the drum, [m];

L – length of the drum, [m];

t – thickness of the drum, [m];

ρ – density of material [kg/m³]

Results of the calculation obtained that the surface area of the drum is 0.63 m^2, the volume of each drum is 0.0125 m^3, and the drum mass is 98 kg per drum (Cast iron density is 7874 kg/m^3). It means that the mass of the two drums is 196 kg.

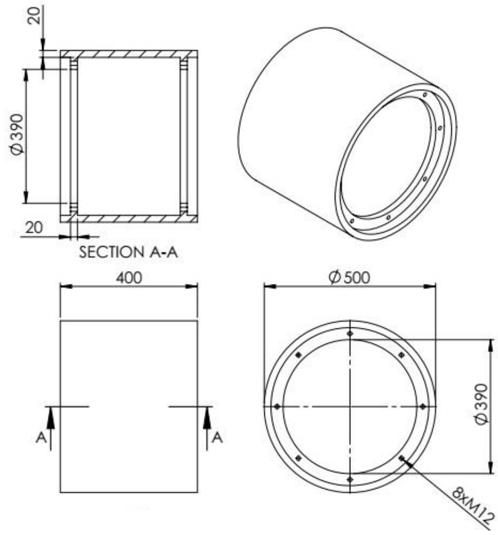

Fig. 4 - Drum dryer design and dimension (in mm)

Analysis of power needs

The electric motor is the source of power considered to be used to rotate the double drum part. In this case, the size of the motor needs to be calculated based on the mass of the double drum dryer part. Power needed *(P)* for rotating the drum dryer is calculated using equation (8)-(9).

$$T = M \times r \text{ [Nm]} \quad (8)$$

$$P = T \times \frac{2 \times \pi \times n}{60000} \text{ [kW]} \quad (9)$$

where,

T is torque, [Nm];

M – moment of force, [N];

r – radius of drum [m]

n – drum rotation, [rpm]

Based on some known parameters (i.e. drum mass is 98 kg, radius of the drum is 0.25 m, and the gravity is 9.81 m/s^2), the calculation of the torque value is 240.35 Nm. In this double dryer there are two drums so that the total torque is 480.7 Nm. Drum rotation is assumed to be at a maximum rotation of 10 rpm so the power obtained is 0.5 kW. Because there is a factor of motor efficiency that is assumed to be 60% and a safety factor of 2, the motor power required is 1.68 kW (2.25 HP) rounded to 3 HP.

Shaft design

Shaft design was carried out using the calculation method according to Sularso & Suga (2004). Shaft diameter is calculated using equation (10) and (11).

$$d_s = \left[\frac{5.1}{\tau_a} \times C_b \times K_t \times T \right]^{1/3} \text{ [m]} \quad (10)$$

$$\tau_a = \frac{\sigma_b}{Sf_1 \times Sf_2} \text{ [N/m}^2\text{]} \quad (11)$$

Where:

d_s is shaft diameter, [Nm];
C_b – bending load factor;
K_t – twisting load factor;
τ_a – allowable stress, [N/m²];
σ_b – tensile strength, [N/m²];
Sf_1 – safety factor due to shaft material;
Sf_2 – safety factor due to keyway

According to *(Sularso & Suga, 2004)*, the value of C_b and K_t depends on the load assumption that occurs on the shaft. In this case, the twisting load is assumed to be small so that the value of K_t is 1.5. There is also a possibility of bending loads so that the value of C_b is 2.3. Tensile strength of the shaft material is 4.8×10^8 N/m², Sf_1 is 6 and Sf_2 is 3. Based on the calculation, the minimum shaft diameter is 0.068 m or 68 mm, rounded to 70 mm.

Scraper

The material used for constructing a scraper was steel ST 25. To avoid damage to the dryer drum because of friction, the material of the scraper has to be softer than the drum. The hardness number of ST 25 is 123-183 HB and hardness number of FCD 450 is 143-217 HB. Scraper design is presented in figure 5.

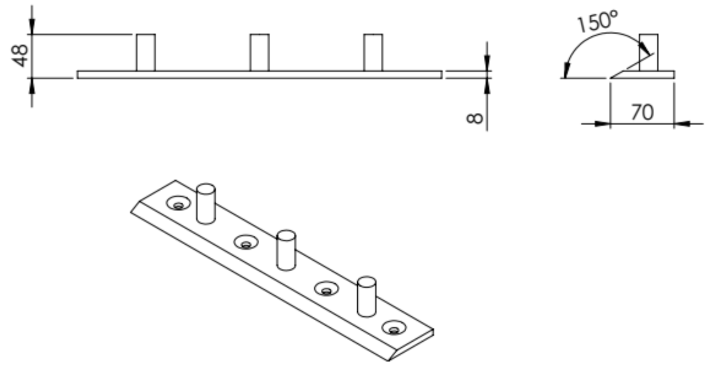

Fig. 5 - Scraper design and dimension (in mm)

Transmission system

There are three transmission systems applied in this double drum dryer, i.e. gearbox, belt-pulley and chain-sprocket. The transmission ratio of the gearbox used was 1:50, belt-pulley was 1:3, and chain-sprocket was 1:3. The rotation per minute of dryer drum theoretically was 3.22 rpm, due to losses occurred, the real rotation was 2.7 rpm. Various inverter frequency was used to adjust the rotation up to 0.5 rpm performed in 10 Hz frequency.

Evaluation of the drum dryer

There were two kinds of test conducted to evaluate the drum dryer i.e. functional test and performance test. Functional test was performed without using the test sample material. The parameter measured consisted of steam pressure and drum surface temperature. The heat source used to run the drum dryer was a steamer which uses 4500 watts of power. The steamer was set in a pressure range between 2 and 3.8 bar. When the pressure reaches the set point pressure, the electricity was automatically turn off and vice versa. There are three stages while operating the drum dryer: 1) turn on the steamer and wait until the pressure reaches the set point, 2) open the valve that connects the steamer to the drum, and it will drop the pressure, 3) wait until the pressure reaches the target and the drum dryer is ready to use. The steam pressure and drum temperature parameters of all stages were observed and evaluated to obtain parameters profile. The tool used for observing the drum temperature was infrared thermal imager (*Fluke TiS40*) with an accuracy of 0.1 °C.

Performance tests was conducted using two formulas of puree made from several ingredients which contain high nutrition that is specifically for toddlers in order to prevent stunting. The first formula consisted of red proso millet (*Panicum miliaceum* L.) 332.56 gr, red kidney bean (*Phaseolus vulgaris* L.) 262.5 gr, salt 8.74 gr, and water 3360 ml. The second formula consisted of white proso millet (*Panicum miliaceum* L.) 332.56 gr, red kidney bean (*Phaseolus vulgaris*) 262.5 gr, salt 8.74 gr, and water 3360 ml. The evaluation was only to observe the ability of the drum dryer to process puree into ready-to-eat products.

RESULTS

The prototype of double drum dryer

The prototype of double drum drying machine developed in this study is shown in figure 6, and the specification of the machine is presented in table 1.

Fig. 6 - The prototype of a double drum dryer

Table 1

Specification of a double drum dryer prototype

❑ Over all dimension	
• length	1600 mm
• width	1150 mm
• height	2050 mm
❑ Drum	
• length	400 mm
• diameter	500 mm
• thickness	20 mm
• material	Cast Iron FCD 450 Hardened with Chromium
❑ Scraper	
• length	500 mm
• width	56 mm
• thickness	8 mm
• material	ST 25, Zinc coated
❑ Power source	Electric motor 3 HP, 3 Phase, V 380 volt
❑ Transmission system	
• Gearbox ratio	1:50
• Sprocket ratio	1:3
• Pulley ratio	1:3
❑ Inverter	YD 101, 3 Phase 400 V, 0.4 -22 kW
❑ Drum rotation	0 – 3 rpm
❑ Feeding system	Nip
❑ Heat source	Electric steamer
❑ Capacity	10 kg/batch

Double drum dryer performance

A double drum dryer's operation stages included heating the steamer, opening the steam distribution valve to the dryer cylinder, and setting the condensate outlet. After the desired temperature had been reached, the material in the hopper was poured into the gap between the two cylinders, material feeding being managed by opening the tap in the hopper. The cylinder rotation was regulated by adjusting the inverter frequency.

The black line in figure 7 shows the pressure profile in the steamer, while the blue line shows the temperature at drum-1 and the red line shows the temperature at drum-2. Before the valve that connects the steam supply to the drum is opened, the pressure rises (stage 1). After the valve is opened, the pressure drops drastically (stage 2), and then the pressure rises again gradually (stage 3). The pressure on the steamer will also decrease when the steam trap tap is opened. The steam trap tap function is to remove the condensate in the dryer drum. When drying the material, pressure on the steamer and the temperature on the cylinder drum is relatively constant.

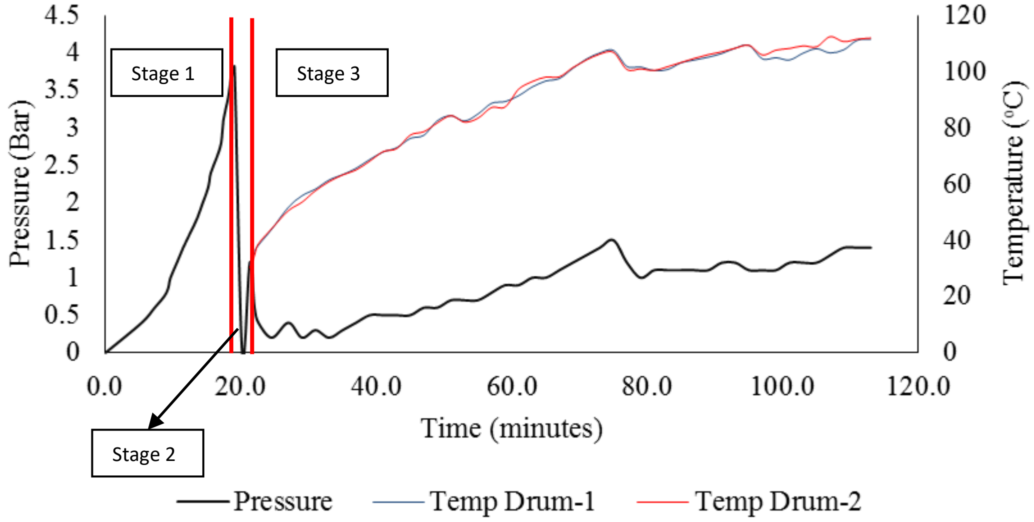

Fig. 7 - Profile of steam pressure and temperature on both drums during functional test

When drying, the temperature of both drums were collected to characterize the homogeneity of the heat distribution in both drums and were analyzed statistically. The paired t-test analysis results did not show a significant difference in the two cylinders' heat distribution. The statistical analysis results using paired t-test showed that the distribution of temperature in the two cylinders were not significantly different, t(48); p>0.05. The result of the temperature distribution in the both drums was also presented in figure 8. Beside the fact that the temperature of both drums was fairly uniform, the uniformity of temperature in the whole drum was also uniform according to figure 8.

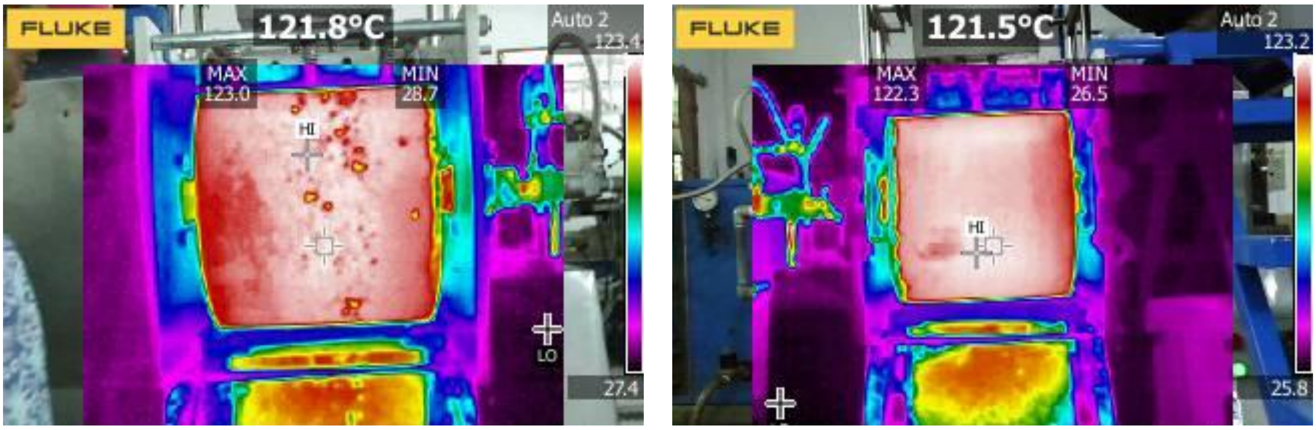

(a) Drum-1 (b) Drum-2

Fig. 8 - Distribution of temperature in the both drum

This study also investigated the relation between steam pressure and drum temperature. Based on figure 9, it is shown that there is a strong correlation between steam pressure and drum temperature (R^2 is 0.9667). For further experiments, the desired drum temperature can be set based on the pressure set at the beginning of the process.

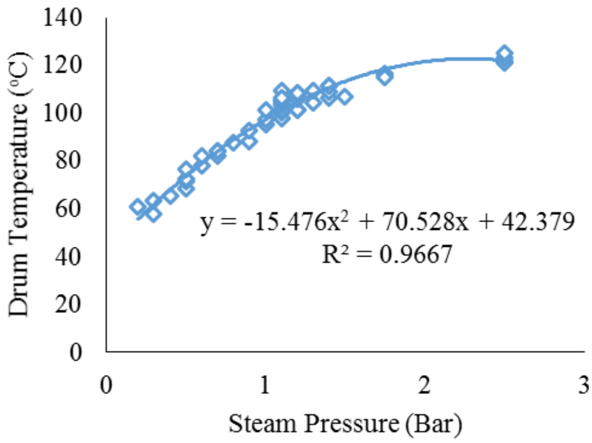

Fig. 9 - Correlation between steam pressure and drum temperature

Regarding the cylinder's rotation, the statistical analysis results obtained from the drum rotation correlated linearly with the frequency. The correlation between drum rotation and inverter frequency matched the equation of $y = 0.054x + 0.004$, $R^2 = 0.999$, where X-axis is a frequency (Hz) Y-axis is the rotation (rpm) as shown in figure 10.

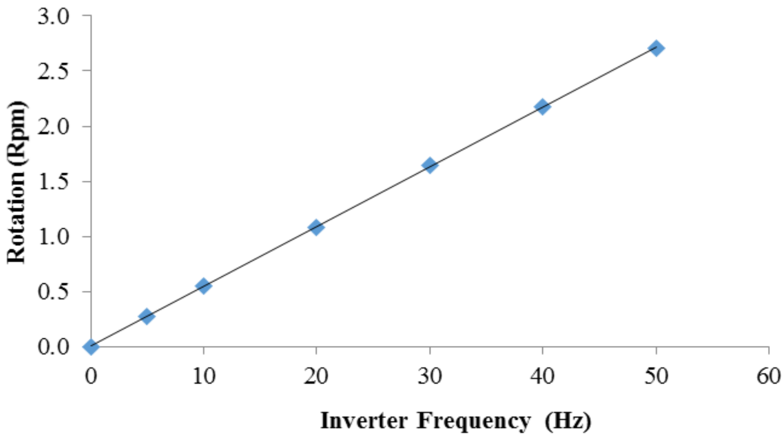

Fig. 10 - Correlation between drum rotation and inverter frequency

Figure 11 shows sample products of two formulas produced by a double drum dryer set at a temperature of 121°C (pressure of 2 Bars) and drum rotation of 1.6 rpm (30 Hz).

First formula Second formula

Fig. 11 - Thin-film product samples produced by the double drum dryer

The result shows that the double drum dryer has been able to produce good characteristics of both products in the form of ready-to-eat products made from several ingredients (i.e. millets and red bean) which contain high macro and micronutrient (*Kusumah et al., 2020; Shobana et al., 2013*). A combination of red kidney bean and proso millets can be used as ingredients to provide high-nutritional value in foods in the form of ready-to-eat food products that can be consumed by toddlers to prevent stunting problems. The ready-to-eat products can easily be produced by using drum drying technology.

CONCLUSIONS

A 10 kg/batch double drum dryer was developed and tested in this study. Dryer drum dimension was 400 mm length, 500 mm diameter and 20 mm thickness. The electromotor used to drive was 2.24 kW/3 phase. There were three transmission systems used, i.e. gearbox, sprocket-chain and belt-pulley. The rotation in processing was set by adjusting the inverter frequency. The double drum dryer designed and constructed had worked well, as expected. The temperature distribution of both drums was fairly uniform, and the temperature uniformity in the drum surface has shown good uniformity (minimum gradient temperature). The double drum dryer has been able to produce good characteristics of products in the form of ready-to-eat products made from several ingredients (i.e. millets and red bean) which contain high macro and micronutrient which are useful for preventing stunting in toddlers. Extensive performance evaluation is recommended to optimize the operational condition of double drum dryer in producing various formula of ready-to-eat food and other instant foods.

ACKNOWLEDGEMENT

Financial support from Indonesia Endowment Fund for Education, Ministry of Research and Technology, National Research and Innovation Agency (Indonesia) is gratefully acknowledged. We would like to appreciate all those who offered us the possibility to complete this research. We would also like to thank Teguh S., Maulana F., Dadang G., Iman R. and Taufik Y. for their help in constructing the prototype of this study.

REFERENCES

[1] Ahmed, M. A. T. (2013). *Presentation on Drying*. https://www.slideshare.net/abdullahtauheed/drying-final

[2] Bonaui, C., Dumoulin, E., Raoult-Wack, A.-L., Berk, Z., Bimbenet, J.-J., Courtois, F., Trystram, G., & Vasseur, J. (1996). Food drying and dewatering. *Drying Technology*, *14*(9), 2135–2170.

[3] Choudhary, P. (2015). *Drying of Food*. Indian Institute of Food Processing Technology. https://www.slideshare.net/choudharypintu13/drying-of-food

[4] Elmholt, S., Kristensen, E. F., & Thrane, U. (2007). Comparing the effect of continuous drying and drum drying on fungal contamination of bread grain (rye). *Biosystems Engineering*, *97*(3), 425–428.

[5] Francis, F. J. (2000). Dryers: Technology and Engineering. *Encyclopedia of Food Science and Technology. New York: Wiley*, 542–578.

[6] Hidayat, D. D., Sudaryanto, A., Kurniawan, Y. R., Indriati, A., & Sagita, D. (2020). Development and Evaluation of Drum Coffee Roasting Machine for Small-Scale Enterprises. *INMATEH Agricultural Engineering*, *60*(1), 79–88. https://doi.org/10.35633/inmateh-60-09

[7] Jurendić, T., & Branko, T. (2012). Mathematical Modeling of Conductive, Convective and Irradiative Drying of Cereal Based Baby Foods. *Journal of Agriculture and Food Technology*, *2*(8), 126–133.

[8] Karapantsios, T. D. (2006). Conductive drying kinetics of pregelatinized starch thin films. *Journal of Food Engineering*, *76*(4), 477–489.

[9] Kasiri, N. A., Hasanzadeh, M. A., & Moghadam, M. (2004). Mathematical modeling and computer simulation of a drum dryer. *Iranian Journal of Food Science & Technology*, *28*(B6), 679–687.

[10] Kusumah, S. H., Andoyo, R., & Rialita, T. (2020). Isolation and Characterization of Red Bean and Green Bean Protein using the Extraction Method and Isoelectric pH. *SciMedicine Journal*, *2*(2), 77–85. https://doi.org/10.28991/scimedj-2020-0202-5

[11] Ministry of Health of the Republic of Indonesia. (2019). *National Report for Basic Health Research (NRBHR) 2018*. Publishing Agency for Health Research and Development Agency.

[12] Mujumdar, A. S. (1995). *Handbook of industrial drying, revised and expanded* (Vol. 2). CRC Press.

[13] Okos, M. R., Narsimhan, G., Singh, R. K., & Weitnauer, A. C. (1992). Food Dehydration. In *Handbook of Food Engineering* (Vol. 1, pp. 1–10). Marcel Dekker Inc.

[14] Pua, C. K., Hamid, N. S. A., Rusul, G., & Rahman, R. A. (2007). Production of drum-dried jackfruit (Artocarpus heterophyllus) powder with different concentration of soy lecithin and gum arabic. *Journal of Food Engineering*, *78*(2), 630–636.

[15] Rodriguez, G., Vasseur, J., & Courtois, F. (1996). Design and control of drum dryers for the food industry. Part 1. Set-up of a moisture sensor and an inductive heater. *Journal of Food Engineering*, *28*(3–4), 271–282.

[16] Saeeda, R., Safdar, M. N., Amer, M., Nouman, S., Khalid, N., & Muhammad, A. (2009). Preparation and quality evaluation of nutritious instant baby food from indigenous sources. *Pakistan Journal of Agricultural Research*, *22*(1/2), 50–55.

[17] Shobana, S., Krishnaswamy, K., Sudha, V., Malleshi, N. G., Anjana, R. M., Palaniappan, L., & Mohan, V. (2013). Finger Millet (Ragi, Eleusine coracana L.). A Review of Its Nutritional Properties, Processing, and Plausible Health Benefits. In *Advances in Food and Nutrition Research* (1st ed., Vol. 69, pp. 1–39). Elsevier Inc. https://doi.org/10.1016/B978-0-12-410540-9.00001-6

[18] Sularso & Suga, K. (2004). *Basic Planning and Selection of Machine Elements* (*Dasar Perencanaan dan Pemilihan Elemen Mesin)*. Pradya Paramita.

[19] Tang, J., Feng, H., & Shen, G.-Q. (2003). Drum drying. In *Encyclopaedia of Agricultural, Food, and Biological Engineering* (pp. 211–214). Marcel Dekker, Inc., New York.

DEVELOPMENT AND EVALUATION OF FINGER WHEEL AND CUTTING DISC COMBINED DEVICE FOR STALK RETURNING
/
拨禾指轮-锯盘组合式秸秆还田装置的研制与评价

Zhang Zhilong[1,3], Yu Yongtao[1], Yang Qiyong[1], Geng Aijun*[1,3], Zhang Ji[1,2] [1]
[1] Shandong Agricultural University, College of Mechanical and Electronic Engineering/ China;
[2] Shandong Provincial Engineering Laboratory of Agricultural Equipment Intelligence/ China;
[3] Shandong Provincial Key Laboratory of Horticultural Machineries and Equipment/ China
Tel: +86-0538-8242339; E-mail: gengaj@sdau.edu.cn
DOI: https://doi.org/10.35633/inmateh-64-05

Keywords: *Stalk returning, Finger wheel, Sawtooth blade group, High speed photography, Test*

ABSTRACT

Stalk returning technology was an important way to preserve soil nutrients and reduce soil erosion. It was of great significance to improve the stalk chopping quality, reduce power consumption. On the basis of the previous research, the finger wheel and cutting disc combined device for stalk returning was developed, mainly composed of the sawtooth blade group, the finger wheel and the stalk lifting grid. The stalk was fed into the cutting area of the sawtooth blades by the rotation of the finger wheel, and the operation of the stalk chopping was completed under the combination of the sawtooth blade group and the finger wheel. The movement of stalks in the device with finger wheel and sawtooth blades was analysed by high speed photography, and the rotational speed of finger wheel, the rotational speed of sawtooth blade group, the stalk feeding speed had a great influence on the movement of the stalks. Through orthogonal test and verification test, the clamping angle was 20°, the rotational speed of sawtooth blade group was 800 min^{-1}, the stalk feeding speed was 1.45 m/s, the rotational speed of finger wheel was 110 min^{-1}, the cut length qualified rate was 92.47% and the cutting power was 529.97 W. The test results met the quality requirements of the Chinese national standard. The related research can provide reference for the research of stalk returning device.

摘要

秸秆还田技术是保持土壤养分、减少土壤侵蚀的重要手段。提高秸秆切碎质量，降低能量消耗具有重要意义。在前期研究的基础上，研制了拨禾指轮-锯盘组合式秸秆还田装置，主要由锯齿刀片组、指轮和分禾栅板组成。秸秆通过指轮的转动送入锯齿刀片组的切割区，在锯齿刀片组和指轮的组合下完成秸秆的切割。通过高速摄影分析了秸秆在指轮和锯齿刀片组中的运动，得到指轮转速、锯齿刀片组转速、秸秆进给速度对秸秆的运动有很大的影响。通过正交试验和验证试验，确定钳住角为20°，锯齿刀片组转速为800 min^{-1}，秸秆进给速度为1.45 m/s，指轮转速为110 min^{-1}，切割长度合格率为92.47%，切割功率为529.97 W。检测结果符合中国国家标准的质量要求。相关研究可为秸秆还田装置的研究提供参考。

INTRODUCTION

The North China Plain (NCP) is the main grain production area in China and the predominant cultivation model is winter wheat-summer maize double cropping system (*Ren B. et al, 2018*). Soil fertility has declined, and environmental problems such as soil erosion by wind and water have been caused for long term conventional tillage methods (*Blanco S.R. and Aguilar C. A., 2016; Topa D. et al, 2021*). In order to realize the protection of cultivated land, many scholars have conducted research on conservation tillage technology, and the government has gradually promoted the use of conservation tillage in NCP (*Dai X. et al, 2013*).

Conservation tillage is defined as an agricultural ploughing technology that leaves protective amount of residues on the soil surface, reduces water and wind erosion, and retains water and nutrients or other resources (*Lopez-Garrido R. et al, 2014; Klik A. and Rosner J., 2020*). The main content of conservation tillage includes stubble mulching, no-tillage fertilization and sowing, weed and pest control, subsoiling and topsoil operations (*Moyer J.R. et al,1994*). As a dry farming technology that saves costs and increases yield, conservation tillage has been widely used in arid and semi-arid areas (*He Jin et al, 2018*).

[1] *Zhang Zhilong, Lec. Ph.D. Eng.; Yu Yongtao; Yang Qiyong; Geng Aijun, Ph.D. Eng.; Zhang Ji*

Stubble mulching means retaining residues on the soil surface which is an important way to improve organic matter level in the soil, and reduce wind and water erosion (*Kim N. et al, 2021; Jia Honglei et al, 2015*). As an important part of conservation tillage technology, straw returning has been widely used in NCP (*Li H. et al, 2018*). Due to the short interval between summer corn harvesting and wheat sowing, the wheat seeds would not be firmly attached to the seed bed if the full corn stalks are returned to the field, resulting in no emergence or hanging roots during the seedling stage (*Li S. et al, 2006*). Moreover, the crude protein content in the stalk lower part is low, and the nutrition in the middle and upper part of the stalks is better which can be used as high-quality roughage for livestock, and the suitable harvest height for stalk as feed is 100cm above the ground (*Zhao H. et al, 2013; Wang M. et al, 2012*).

The research team conducted the study on the rational use of stalk in sections and developed a high stubble maize double header with a saw-disc chopping device which could harvest the middle and upper part of the stalks and leave the rest chopped as residues (*Zhang J. et al, 2018*). In order to further improve the feeding performance and chopping effect of the mechanism, the research team improved the design of the returning device based on the preliminary research and conducted a bench test to obtain the better parameters. The results could provide a reference for the design of stalk returning mechanism and the rational utilization of corn stalks.

MATERIALS AND METHODS

Device structure

The finger wheel and cutting disc combined device for stalk returning which was located at the front and lower part of the header mainly consisted of sawtooth blade group, finger wheel, stalk-lifting grid etc., as shown in Fig.1. The sawtooth blade group was composed of several sawtooth blades which were arranged in an inverted cone shape, coaxial with and located below the stalk cutter. The finger wheel was installed between the sawtooth blade group, and was located at a middle position of the sawtooth blade group. The stalk-lifting grid, which consisted of series of grids, was located at the end of the cutting area of the sawtooth blade group (the contact area between the sawtooth blade group and the stalk was regarded as the cutting area), and several grids were evenly located among the sawtooth blades.

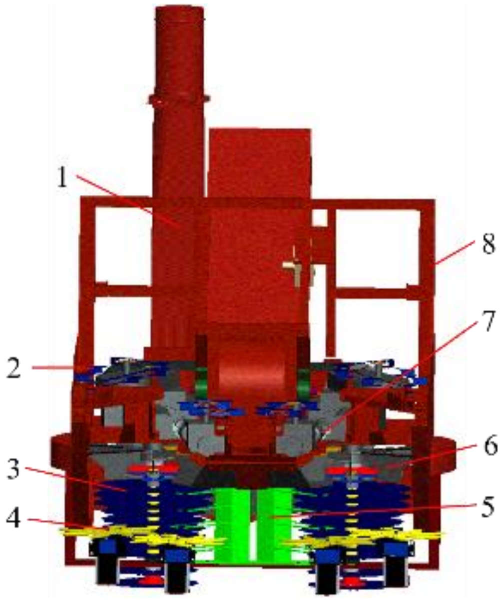

Fig. 1 - Finger wheel and cutting disc combined device for stalk returning

1. Throwing mechanism; 2.Gathering chain; 3.Sawtooth blade group; 4.Finger wheel; 5.Stalk-lifting grid; 6.Stalk cutter; 7.Snapping rollers; 8.Frame

The stalk returning device was driven by corn header and moved forward with the harvester. The plants were fed into the header, the upper part of the stalk was pulled down by the snapping rollers and chopped by the stalk cutter. The lower part of the stalk was fed into the sawtooth blade group, and chopped by rotating sawtooth blades with the support of the finger wheel. The lower part of the stalk was cut gradually from top to bottom as the rotation and forward movement of the sawtooth blades. When the incomplete cutting stalk contacted the stalk lifting grid, the stalk was cut by the sawtooth blades forcibly with the stalk lifting grid as the support, and then the stalks were chopped into pieces.

Analysis of key components

Sawtooth blade group

1.Structure parameter

The sawtooth blade group consisted of several sawtooth blades, a cutter shaft, a flange, a shaft sleeve, and a fixing nut, as shown in Fig.2. According to the stalk bending characteristics, the closer the stalk was to the root, the more bending strength the stalk would have (*Xin Shanglong, 2020*). The stalk would be pushed forward by the thrust force created by the sawtooth blades for the lower part of the stalk was fixed by the ground and the stalk could be taken as a cantilever beam. The upper stalk had not been completely cut off and the lower stalk would be sawed off the ground if the sawtooth blade diameter was the same, resulting in the fact that the upper stalk could not be completely sawed off. Therefore, the sawtooth blades were divided into 3 groups with the diameter decreasing from top to bottom in turn and showing an inverted cone shape. The two sawtooth blades were separated by an axle sleeve, and the cone angle was 22.6° (*Zhang J. et al, 2018*).

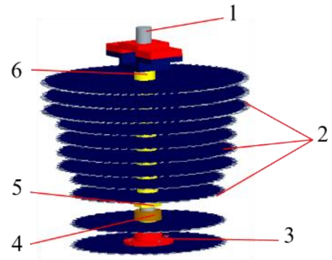

Fig. 2 - Sawtooth blade group

1.Cutter shaft; 2.Sawtooth blade; 3.Flange; 4.Self-aligning ball bearing; 5.Fixing nut; 6.Shaft sleeve

The distance between the blades was the key factor to determine whether the stalk could be cut and crushed. According to the preliminary experimental results of the research group, when the sawtooth blade spacing was greater than 30 mm, the stalks could only be cut into segments, and the sawtooth blade spacing was less than 30mm, the sawtooth blades had a crushing effect on the stalk. Therefore, the sawtooth blade spacing was taken as 25mm.

2. Force analysis of the stalk during cutting process

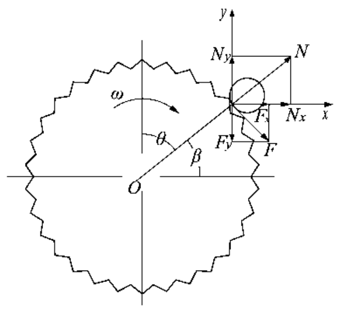

Fig. 3 - Force analysis of the stalk

The stalk was subjected to two forces, namely the tangential force *F* and the normal reaction force *N* acted on the stalk by the sawtooth blades (*Fan Guochang et al, 1998*).

The coordinate system was established with the contact point of the sawtooth blade and the stalk as the coordinate origin, and the force of the sawtooth blade to cut the stalk could be described as F_x+N_x and the force of the sawtooth blade to clamp the stalk could be described as F_y-N_y. It was obvious that the condition for the sawtooth blade to clamp the stalk and make stable cutting was $F_y>N_y$, that was:

$$F \cdot \cos\beta > N \cdot \sin\beta \tag{1}$$

that was

$$f > \tan\beta \tag{2}$$

where, β-clamping angle; f-friction coefficient between the sawtooth blade and the stalk.

The friction coefficient between the sawtooth blade and the stalk f was between 0.3 and 0.6 (*Lenaerts B. et al, 2014*), it could be obtained that β was between 17° and 31°. In this study, the optimum parameters of clamping angle β were determined by orthogonal test.

Finger wheel

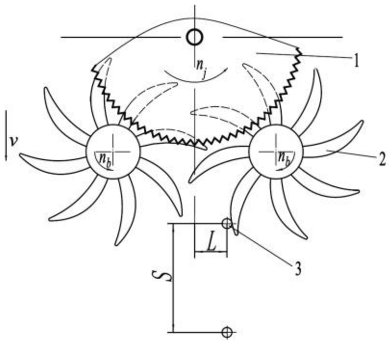

Fig. 4 - Schematic diagram of stalk feeding
1.Sawtooth blade; 2.Finger wheel; 3.Stalk

The finger wheel was arranged symmetrically in front of the sawtooth blade group, used to guide, feed the stalks to the sawtooth blade group and provide support for cutting to avoid missing cutting caused by stalk derivation which was induced by the centrifugal force generated by the sawtooth blade cutting the stalks. For this reason, the movement and the key parameters of the finger wheel was determined.

1. *The condition for orderly feeding of the stalks*

In order to cut the stalks smoothly, the stalks should be fed in an orderly manner by the finger wheel to avoid accumulation on the sawtooth blade group during the advancement of the header which would affect the cutting motion. The relative movement of the stalks in the feeding direction was shown in Fig.4.

Suppose that the stalk started to contact with the finger wheel from the position shown in Fig.4. In order to avoid feeding two plants to the finger wheel in the same time, the following relation should be satisfied:

$$\frac{S}{v} \geq \frac{60}{N \cdot n_b} \tag{3}$$

where, S is plant spacing, taking 250mm; v is forward speed, taking 1m/s; N is number of the finger, taking 8; n_b is rotational speed of finger wheel, min^{-1}.

It could be obtained：$n_b \geq 30$ min^{-1}.

2. *Parameters of the finger wheel*

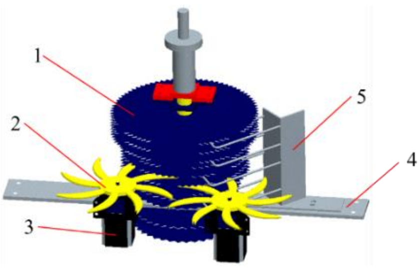

Fig. 5 - The position of finger wheel
1.Sawtooth blade group; 2.Finger wheel; 3.Motor; 4.Frame; 5.Stalk-lifting grid

The finger wheel was arranged between the sawtooth blades and driven by motor, as shown in Fig.5. In order to ensure that the stalks could be fed into the cutting position of the sawtooth blade group by finger wheel and the stalk leakage which was caused by collision from the finger wheel in the rotating process could be reduced, two finger wheels were set symmetrically in the front of the sawtooth blade group, a certain gap was set in the vertical direction and a certain overlap area was located between the two finger wheels. The outside diameter of the finger wheel was taken as 340 mm, and the centre distance of the two finger wheels was taken as 300 mm.

Stalk-lifting grid

The preliminary test showed that the finger wheel supported and assisted in cutting stalks in the forward direction, and most of the stalks would be cut under the joint action of the finger wheel and the sawtooth blades.

However, the stalk was subjected to a tangential force along the cutting direction in the process of cutting the stalks. If the stalk had not been completely cut by the sawtooth blades, the rest of the stalk would move along the cutting direction under the tangential force which could cause missing cutting the stalk. A stalk-lifting grid was designed at the end of the cutting area to avoid missing cutting, and the structure of the stalk-lifting grid was shown in Fig.6. The stalk-lifting grid was composed of a set of 6 mm round steel lifting rod which was interlaced with the sawtooth blade group.

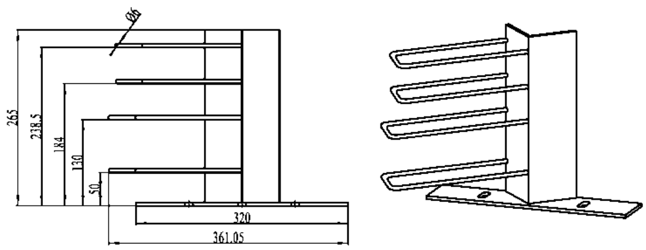

Fig. 6 - Stalk-lifting grid

Performance test

Test instruments and equipment

The experiment was carried out on a self-made test rig, which was composed of the stalk conveying device, the stalk returning device, the industrial computer and the motor, etc., as shown in Fig.7. The start and stop of the motor was controlled by the industrial computer, and the sawtooth blade group was driven by 7.5 kW variable-frequency adjustable-speed motor YVP132M-4. The finger wheels were respectively driven by the deceleration motor 4RK25GN-C. The conveying and feeding of the stalks were completed by the stalk conveying device.

The instruments used in the experiment included high-speed camera system and its analysis software Image-Pro Plus 6.3 (Cam Record 1000 high-speed camera, shooting frame speed of 1000-20000 fps, Optronis, Germany), YH502 dynamic torque sensor, light supplement lamp, electronic balance, meter ruler, vernier calliper, etc. The high-speed camera and light supplement lamp were shown in Fig.7.

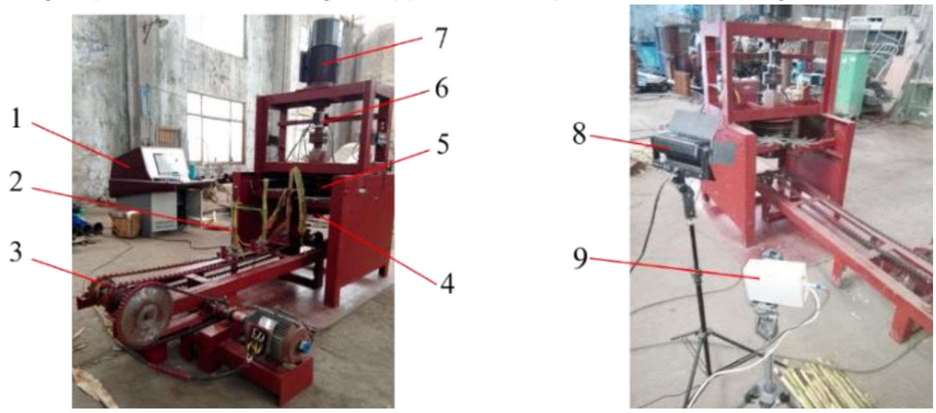

Fig. 7 - Stalk returning test rig

1. Industrial computer; 2. Stalks; 3. Stalk conveying device; 4. Deceleration motor 4RK25GN-C; 5. Stalk returning device; 6. Dynamic torque sensor YH502; 7. Variable-frequency adjustable-speed motor YVP132M-4; 8. Light supplement lamp; 9. High-speed camera

Test materials

The maize variety used in the experiment was Zhengdan 958, which was collected in the experimental field of Shandong Agricultural University, and the average moisture content of the stalks was 78.3 %. The stalks were cut from 10 cm above the soil surface, then the roots, tops were cut off, and the leaf sheathes, leaf covers were removed. The stalks which were 50 cm above the root were taken as the test samples. The average diameter of the big end and the small end of the stalks was respectively 22.34 mm, 19.21 mm.

Test methods and test indexes

The lower part of the stalks was fixed on the conveying device with clamps to put the stalks in a vertical state before the test. The rotation of the sawtooth blade group and the finger wheel was controlled by the industrial computer. After the rotational speed of the sawtooth blade group and the finger wheel was stabilized, the motor of the stalk conveying device was started, and the stalks were fed to the stalk returning device by the stalk conveying device. The stalks were cut by the sawtooth blade group with the support of the finger wheels.

The high-speed camera and its analysis software Image-Pro Plus 6.3 was used to collect and analyse the image information of the cutting area of the stalk returning device. The cutting power and cut length qualified rate were taken as performance test indexes.

1. Cutting power

The YH502 dynamic torque sensor was used to collect the torque information of the sawtooth blade group and the cutting power p_q was obtained by the equation (4-6).

$$P_q = P_z - P_k \tag{4}$$

$$P_z = \frac{T_z n}{9550} \tag{5}$$

$$P_k = \frac{T_k n}{9550} \tag{6}$$

where, T_k-idling torque, N·m; T_z-total operating torque, N·m; P_k-idling power, W; P_z-total operating power, W.

2. Cut length qualified rate

After the experiment, an electronic balance was used to weigh the total mass of the chopped stalks and the total mass of the chopped stalks the cutting length of which was more than 25 mm. The cut length qualified rate F_h could be obtained by equation (7).

$$F_h = \frac{m_z - m_b}{m_z} \tag{7}$$

where, m_z was the total mass of the chopped stalks, kg; m_b was the total mass of the chopped stalks the cutting length of which was more than 25 mm, kg.

Test plan

The theoretical analysis showed that the clamping angle β had a major influence on the stable and reliable cutting of the stalks, so the clamping angle β was taken as a factor for the performance test. In addition, the rotational speed of the finger wheel, stalk feeding speed (machine forward speed) and the rotational speed of the sawtooth blade group were selected as the test factors which had major influence on the test indexes.

After the single-factor test in the early stage, the operation effect was better when the rotational speed of the finger wheel was 80~140 min^{-1}, the stalk feeding speed was 1.1~1.80 m/s, the clamping angle was 15~25°, and the rotational speed of the sawtooth blade group was 700~900 min^{-1}. In order to determine the optimal combination, a four-factor and three-level orthogonal test was designed, and the factor level table was shown in Table 1.

Table 1

Test factors and levels

Levels	Factors			
	A Rotational speed of the sawtooth blade group (min^{-1})	**B** Stalk feeding speed (m·s^{-1})	**C** Rotational speed of the finger wheel (min^{-1})	**D** Clamping angle (°)
1	700	1.10	80	15
2	800	1.45	110	20
3	900	1.80	140	25

RESULTS

Motion analysis of the stalks in the stalk returning device

High-speed photography was used to analyse the motion of the stalks in the cutting process. After the preliminary experiment, the process of stalk cutting could be divided into two steps: stalk feeding and stalk chopping. The movement of the stalk in the feeding step was shown in Fig.8.

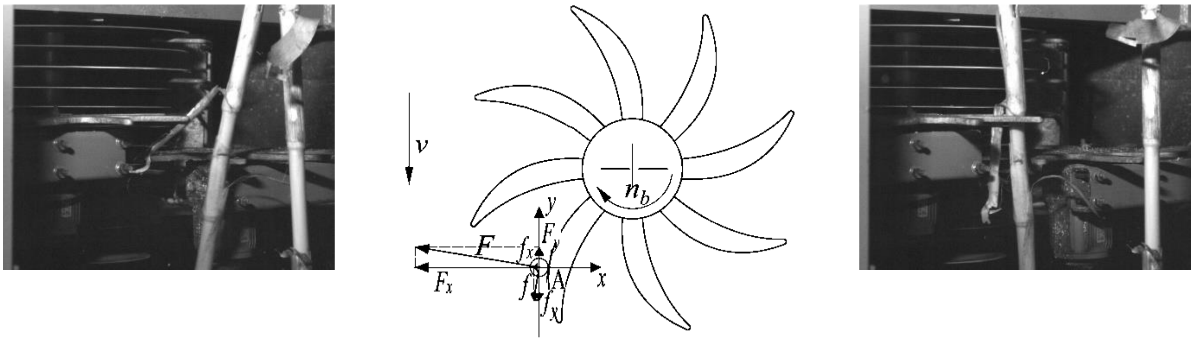

a) The stalk was grabbed by finger wheel in right side *b) Force analysis of the stalk contact with the right finger wheel* *c) The stalk was pushed by the left finger wheel*

Fig. 8 - The motion of the stalk in the feeding step

As the stalk returning device moved forward, the stalk was grabbed by the finger wheel and fed in the direction of the sawtooth blade group as shown in Fig.8a. The stalk was impacted by the right finger wheel, and the stress of the stalk was shown in Fig.8b. Suppose that the stalk was in contact with the finger wheel at point A. The stalk was affected by the thrust *F* and the friction force *f* of the finger wheel. The direction of the thrust *F* was the normal line of the contact point between the stalk and the finger wheel. The direction of the friction force *f* was the tangent direction of the contact point.

A coordinate system was established with the geometric centre of the stalk as the coordinate origin, the thrust force *F* and the friction force *f* on the stalk were decomposed towards the *x*-axis and the *y*-axis respectively. The horizontal force of the stalk was the resultant force of F_x and f_x. The resultant force in the left direction caused the stalk to accelerate and move to the left. In addition, the stalk also had a relative speed moving toward the sawtooth blade group. Therefore, the movement of the stalk was a combination of the movement to the left and the movement to the sawtooth blade group. When entering the movement area of the left finger wheel, the stalk would gradually move to the cutting area under the push of the left finger wheel, as shown in Fig.8c. It could be concluded from the above analysis that the rotational speed of the finger wheel and stalk feeding speed had a major influence on the motion of the stalk in the feeding step.

The movement of the stalk in the returning device during cutting step was shown in Fig.9. The bending resistance of the stalk indicated that the upper part of the stalk was more flexible than the lower part. The inverted cone structure of the sawtooth blade group made the upper part enter the cutting area first, as shown in Fig.9a. The stalk was subjected to the tangential force F_{ct}, the normal force F_{cn} of the sawtooth blade, and the supporting force F_p of the finger wheel. A coordinate system was established with the centre of the stalk as the coordinate origin, and the force of the stalk was decomposed in the horizontal and vertical directions, as shown in Fig.9b. The upper part of the stalk was cut by the sawtooth blade with the support of the finger wheel for the support force F_{py} on the stalk from the finger wheel in the *y*-axis direction. The stalk was subjected to the component force F_{ctx} of the tangential force and the component force F_{px} of the supporting force of the finger wheel in the *x*-axis direction, and the rotating direction of the finger wheel was the same as that of the sawtooth blade group. Therefore, after the upper part of the stalk was cut, the middle and lower parts of the stalk successively entered the right cutting area of the sawtooth blade group, as shown in Fig.9c.

The force of the stalk in the right cutting area was shown in Fig.9e. The stalk was subjected to the tangential force F_{dt} from the sawtooth blade, the normal force F_{dn} from the sawtooth blade, and the supporting force F_q from the finger wheel. The coordinate system was established with the centre of the stalk as the coordinate origin, and the forces on the stalk were decomposed. The stalk was subjected to the supporting force F_{qy} from the finger wheel and the component force F_{dty} of the tangential force in the *y*-axis direction.

Due to the supporting forces F_{qy} and F_{dty}, the stalk was clamped by the sawtooth blade group and the stalk would not be bounced under the component force F_{dny} of the normal force from the sawtooth blade. In the *x*-axis direction, the stalk was subjected to the horizontal component force F_{dtx} of tangential force, and the horizontal component force F_{dnx} of normal force, which caused the stalk to accelerate to the right, so that the stalk moved along the rotation direction of the sawtooth blade. Therefore, the stalk would move in the direction of rotation of the sawtooth blades under the combined action of the sawtooth blades and the finger wheel during the cutting process, as shown in Fig.9d. The chopped stalk segments were thrown along the direction of rotation of the sawtooth blade under the cutting forces from the sawtooth blades.

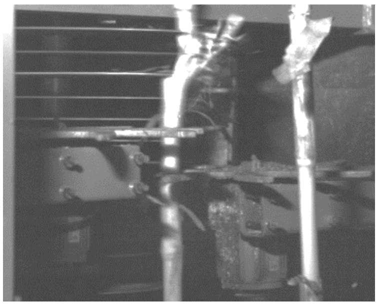

a) The upper part of the stalk was cut by the sawtooth blade group

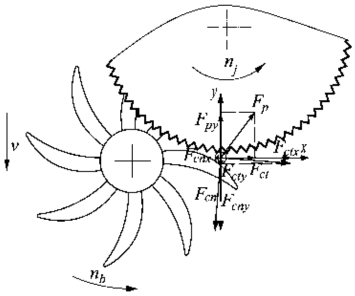

b) Force analysis of the upper part of the stalk

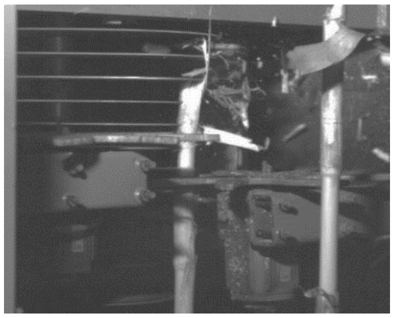

c) The middle part of the stalk was cut by the sawtooth blade group

d) The lower part of the stalk was cut by the sawtooth blade group

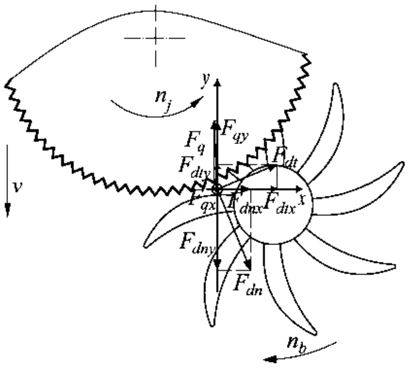

e) The force of the stalk during cutting process in the right cutting area

Fig. 9 - The motion of the stalk in the cutting process

During the cutting process, the cutting force from the sawtooth blades was related to the rotational speed of the sawtooth blade group. The higher the rotational speed of the sawtooth blade group was, the greater the cutting force from the sawtooth blade group would be. The stalks were pushed to the sawtooth blade group by the finger wheel, and cut by the sawtooth blade group with the finger wheel as the support. The rotational speed of the finger wheel would also affect the cutting effect of the stalk.

Analysis of orthogonal test results

Test results

The orthogonal test results were shown in Table 2.

Table 2

Test results

Test No.	Factors				Values	
	Rotational speed of the sawtooth blade group A (min^{-1})	Stalk feeding speed B (m·s^{-1})	Rotational speed of the finger wheel C (min^{-1})	Clamping angle D (°)	Cut length qualified rate (%)	Cutting power (W)
1	1	1	1	1	77.31	537.46
2	1	2	2	2	79.69	389.40
3	1	3	3	3	76.82	439.61
4	2	1	2	3	73.72	497.39
5	2	2	3	1	92.72	698.27
6	2	3	1	2	75.60	424.92
7	3	1	3	2	80.96	786.44
8	3	2	1	3	83.58	599.84
9	3	3	2	1	89.32	719.06

Variance analysis

In order to determine the influence of various factors on the test indexes, the variance analysis was carried out on each test index, as shown in Table 3.

Table 3

Variance analysis results

Index	Source of variance	Deviation sum of squares S	Degrees of freedom f	F ratio	Reliability α	F_α	Significance marker
Cut length qualified rate	Factor A	270.69	2	3.59	0.05	3.35	※
	Factor B	388.529	2	5.15	0.05	3.35	※
	Factor C	131.24	2	1.74	0.25	1.46	[※]
	Factor D	522.15	2	6.92	0.01	5.49	※※
	Error E	1018.04	27	—	—	—	—
	Sum	2330.65	35	—	—	—	—
Cutting power	Factor A	375780.12	2	17.92	0.01	5.49	※※
	Factor B	37865.53	2	1.8058	0.25	1.46	[※]
	Factor C	104196.97	2	4.97	0.05	3.35	※
	Factor D	135158.94	2	6.45	0.01	5.49	※※
	Error E	283086.78	27	—	—	—	—
	Sum	936088.34	35	—	—	—	—

$F_{0.25}(2,27)$ =1.46, $F_{0.10}(2,27)$ =2.51, $F_{0.05}(2,27)$ =3.35, $F_{0.01}(2,27)$ =5.49
$F_{factor}(2,27) > F_{0.01}(2,27)$, the influence of factor on the test index was highly significant, marked as ※※;
$F_{0.01}(2,27) \geq F_{factor}(2,27) > F_{0.05}(2,27)$, the influence of factor on the test index was significant, marked as ※;
$F_{0.10}(2,27) \geq F_{factor}(2,27) > F_{0.25}(2,27)$, the influence of factor on the test index was not significant but has an influence, marked as [※]

The results of the variance analysis showed that the clamping angle β had a highly significant effect on the cut length qualified rate among the four factors examined in the test, and the judgment reliability was 99%. The rotational speed of the sawtooth blade group and the stalk feeding speed had a significant influence on the cut length qualified rate and the judgment reliability was 95%. The rotational speed of the finger wheel had no significant influence on the cut length qualified rate, but it had an influence, and the judgment reliability was 75%. Therefore, the primary and secondary order of each factor affecting the cut length qualified rate was clamping angle (D), stalk feeding speed (B), rotational speed of the sawtooth blade group (A), rotational speed of the finger wheel (C).

The rotational speed of the sawtooth blade group and the clamping angle β had a highly significant effect on the cutting power, and the judgment reliability was 99%. The rotational speed of the finger wheel had a significant influence on the cutting power and the judgment reliability was 95%. The stalk feeding speed had no significant influence on the cutting power, but it had an influence, and the judgment reliability was 75%. Therefore, the primary and secondary order of each factor affecting the cutting power was rotational speed of the sawtooth blade group (A), clamping angle (D), rotational speed of the finger wheel (C) and stalk feeding speed (B).

When the optimal combination was determined, the cut length qualified rate should be set as a large value, and the cutting power as a small value. The cut length qualified rate was more important than the cutting power for the performance of the machine. Therefore, combined with the results of variance analysis, the optimal combination of the test was finally selected as D2, A2, B2 and C2, that was, the clamping angle was 20°, the rotational speed of the sawtooth blade group was 800 min^{-1}, the stalk feeding speed was 1.45 m/s, and the rotational speed of the finger wheel was 110 min^{-1}.

Verification test

In order to verify the effect of the optimal combination, the experimental conditions were set as follows: clamping angle was 20°, the rotational speed of the sawtooth blade group was 800 min^{-1}, the stalk feeding speed was 1.45 m/s, and the rotational speed of the finger wheel was 110 min^{-1}. Verification tests were carried out on the test rig, 3 plants were taken in each group of tests and repeated for 10 times. The test results were shown in Table 4.

Table 4

Verification test results

Test No.	Cut length qualified rate (%)	Cutting power (W)
1	92.40	507.96
2	91.34	551.31
3	93.15	590.89
4	94.94	536.23
5	89.72	563.56
6	89.64	518.32
7	97.58	490.99
8	90.86	417.49
9	89.67	563.56
10	95.38	559.40
Mean.	92.47	529.97

It could be obtained from Table 4 that the cut length qualified rate was 92.47% and the cutting power was 529.97 W. The qualified rate of chopped length was greater than the requirement of Chinese national standard NY/T 1004-2006. The views of the chopped stalks were shown in Fig.10.

Fig. 10 - Views of the chopped stalks

CONCLUSIONS

1. A finger wheel and cutting disc combined device for stalk returning was developed. The stalks were grabbed and held by the finger wheel and then fed into the sawtooth blade group. The stalks were crushed off the ground by the cooperation of the finger wheel and the sawtooth blade group.

2.The motion of the stalk in the stalk returning device was analysed by means of high-speed photography, and it was found that the rotational speed of the finger wheel, the rotational speed of the sawtooth blade group and the feeding speed had considerable impact on the motion of the stalk.

3. The test results showed that the operation effect of the stalk returning device was better when the clamping angle β was 20°, the rotational speed of the sawtooth blade group was 800 min^{-1}, the stalk feeding speed was 1.45 m/s, and the rotational speed of the finger wheel was 110 min^{-1}. A verification test was carried out and the test results showed that the cut length qualified rate was 92.47%, and the cutting power was 529.97 W in the optimized parameters combination.

ACKNOWLEDGEMENT

This work was supported by 13th Five-Year National Key R & D Program (2018YFD0300606), Shandong Provincial Key Science and Technology Innovation Engineering Project (2018CXGC0217).

REFERENCES

[1] Blanco S. R., Aguilar C. A., (2016), The erosion threshold for a sustainable agriculture in cultures of bean (*Phaseolus vulgaris L.*) under conventional tillage and no-tillage in Northern Nicaragua. *Soil Use and Management*, Vol.32, Issue 3, pp. 368-380, Málaga/Spain.

[2] Dai X., Li Y., Ouyang Z., Wang H., Wilson G.V, (2013), Organic manure as an alternative to crop residues for no-tillage wheat-maize systems in North China Plain. *Field Crops Research*, Vol.149, pp. 141-148, Beijing/China.

[3] Fan Guochang, Ma Damin, Ji Junjie, Liu Huanxin, (1998), Study on sawtooth cutters of double disk. *Journal of Hebei Agrotechnical Teachers College*, Vol.12, issue 2, pp.40-43. Shijiazhuang/China.

[4] He Jin, Li Hongwen, Chen H., Lu Caiyun, Wang Q, (2018), Research progress of conservation tillage technology and machine. *Transactions of the Chinese Society for Agricultural Machinery*, Vol.49, issue 4, pp.1-19. Beijing/China

[5] Jia Honglei, Wang Gang, Li Guo, Zhuang Jian, Tang Lie, (2015), Wind erosion control utilizing standing corn residue in Northeast China. *Soil and Tillage Research*, Vol.153, pp.112-119. Changchun/China.

[6] Kim N., Riggins C.W., Rodríguez-Zas S., Zabaloy M.C., Villamil M.B, (2021), Long-term residue removal under tillage decreases amoA-nitrifiers and stimulates nirS-denitrifier groups in the soil. *Applied Soil Ecology*. doi:10.1016/j.apsoil.2020.103730. Illinois/USA.

[7] Klik A., Rosner J., (2020), Long-term experience with conservation tillage practices in Austria: Impacts on soil erosion processes. *Soil and Tillage Research*, Vol.203, pp. 1-14, Vienna/Austria.

[8] Lenaerts B., Aertsen T., Tijskens E., Ketelaere B.D., Ramon H., Baerdemaeker J.D., Saeys, W, (2014), Simulation of grain-straw separation by Discrete Element Modeling with bendable straw particles. *Computers and Electronics in Agriculture*, Vol.101, pp.24-33. Leuven/Belgium.

[9] Li H., Dai M., Dai S., Dong X., (2018), Current status and environment impact of direct straw return in China's cropland-A review. *Ecotoxicology and Environmental Safety*, Vol.159, pp.293-300. Hefei/China.

[10] Li S., Wang K., Feng J., Xie R., Gao S., (2006), Factors affecting seeding emergence in winter wheat under different tillage patterns with maize stalk mulching returned to the field. *Acta Agronomica Sinica*, Vol.32, issue 3, pp.463-465. Beijing/China.

[11] López-Garrido R., Madejón E., Moreno F., Murillo J.M., (2014), Conservation tillage influence on carbon dynamics under Mediterranean conditions. *Pedosphere*, Vol.24, issue 1, pp.65-75. Seville/Spain.

[12] Moyer J.R., Roman E.S., Lindwall C.W., Blackshaw R.E, (1994), Weed management in conservation tillage systems for wheat production in North and South America. *Crop Protection*, Vol.13, issue 4, pp.243-259. Alberta/Canada.

[13] Ren B., Li X., Dong S., Liu P., Zhao B., Zhang J., (2018), Soil physical properties and maize root growth under different tillage systems in the North China Plain. *The Crop Journal*, Vol.6, issue 6, pp.669-676. Tai'an/China.

[14] Topa D., Cara I. G., Jităreanu G, (2021), Long term impact of different tillage systems on carbon pools and stocks, soil bulk density, aggregation and nutrients: A field meta-analysis. *CATENA*. Iasi/Romania. doi:10.1016/j.catena.2020.105102.

[15] Wang M., Zhong R., Zhou, D., (2012), Research on appropriate harvesting time of corn and utilization mode of straw forage. *Agricultural Research in the Arid Areas*, Vol.30, issue 3, pp.18-25. Changchun/China.

[16] Xin Shanglong, (2020), *Study on the mechanism and key technology of corn ear picking with vertical roller*. Gansu agricultural university, Lanzhou/China.

[17] Zhang J., Yu Y., Yang Q., Zhang J., Zhang Z., Geng A., (2018), Design and experiment of smashed straw unit for high stubble maize double header. *Transactions of the Chinese Society for Agricultural Machinery*, Vol.49, issue S1, pp.42-49. Tai'an/China.

[18] Zhao H., Ning T., Nie L., Wang B., Tian S., Li Z., (2013). Comparison of yields and nutrient compositions between different harvesting heights of maize stover. *Scientia Agricultura Sinica*, Vol.46, issue 20, pp.4354-4361. Tai'an/China.

AUTO LOAD-LEVELLING CONTROL OF A LARGE SPRAYER CHASSIS USING THE SLIDING MODE METHOD
/
基于滑模控制的大型喷雾机底盘自动调平方法研究

Yu Chen[1)], Jun Wu[2)], Shuo Zhang[1)], Jun Chen*[1)], Hui Xia[3)], Yahui Zhu [3)], Jiajun Wang [3)]
[1)] College of Mechanical and Electronic Engineering, Northwest A&F University, Yangling 712100, China;
[2)] Nanjing Research Institute for Agricultural Mechanization, Ministry of Agriculture and Rural Affairs, Nanjing 210014, China;
[3)] Jiangsu World Agriculture Machinery Co., Ltd, Danyang 212300, China;
Tel: +86 13572191773; E-mail: chenjun_jdxy@nwsuaf.edu.cn
DOI: https://doi.org/10.356.33/inmateh-64-06

Keywords: *Agricultural sprayer, Sliding mode variable structure, Air suspension, Auto load levelling control*

ABSTRACT
When a sprayer travels on a ramp or a rough road, the load exerted on each wheel changes. If an unbalanced wheel load is maintained for long periods of time, the wheels may slip, the sprayer's manoeuvrability is affected, and a rollover accident may occur. In this study, the air suspension of a self-propelled sprayer chassis was investigated, and the potential load imbalance conditions of the sprayer suspension were analysed. A mathematical model of the inflation/deflation of the suspension was established based on air nonlinear thermodynamics and vertical dynamics theory and a ¼-scale vertical dynamics model of the sprayer chassis was developed. A control strategy to balance the sprayer's wheel load was developed. Considering the nonlinear characteristics of the air suspension, a sliding mode variable structure control method was used to balance the wheel load. Simulation experiments were conducted under different working conditions. The simulation results showed that the sliding mode variable structure control provided good control response and precision. The proposed auto load-levelling controller was tested under different working conditions, including different roll and pitch angles and navigating a rough road; the controller successfully changed the load on each spring to ensure that the sprung mass of the suspension was equal and the wheel load was balanced. The results of this study provide reference information for auto load-levelling control of large sprayers.

摘要
喷雾机在凹凸路面或者坡道路面行驶时，导致各车轮负载会发生变化。长时间车轮负载的不平衡，不仅会使车轮出现打滑或失去操纵能力，更会导致侧翻事故的发生。本文以带空气悬架的大型高地隙自走式喷雾机为研究对象，分析喷雾机车轮可能发生载荷不平衡的工况。基于车辆动力学和空气热力学理论，建立了空气悬架充放气数学模型和 1/4 悬架垂向动力学模型。在此基础上，制定了喷雾机车轮负载平衡控制策略。考虑到空气悬架的非线性特性，采用滑模变结构控制，设计了车轮负载平衡控制器，并以不同工况为例，进行了仿真对比实验。通过仿真实验可以得到，滑模控制对模型参数的变化具有较好的鲁棒性，使其具有良好的控制响应和精度。同时，在侧倾、俯仰和凹凸路面三种工况下，通过本文设计的负载平衡控制器的干预和控制，各弹簧所受载荷也随之变化，最终使得整机左右两侧悬架簧载质量相等，各车轮负载达到平衡状态。通过本文研究，可为大型高地隙自走式喷雾机车轮负载平衡控制提供参考。

INTRODUCTION
As an important tool for preventing and eliminating crop diseases and insect pests, pesticide applications have become an important measure to improve crop yield (*Li X. et al., 2017*). The self-propelled sprayer is an essential piece of equipment to ensure secure food production and stable development of agriculture (*Tahmasebi M. et al., 2013; 2018*). With the advancement of agricultural mechanization and the implementation of large-scale farm cooperative management, high-power and high-efficiency field management machinery is needed to spray and fertilize large plots. An advanced sprayer with excellent performance allows for the precise, efficient, and intelligent management of field crops and has the characteristics of high efficiency, low injury risk, field friendliness, good comfort, and mobility. High-clearance self-propelled sprayers are important for spraying and fertilizing crops and are widely used due to their high efficiency, environmental protection capacity, and ease of use (*Chen Y. et al., 2020; Yuki S. et al., 2013; Baumhardt U. B. et al., 2017*).

Compared with the general agricultural machinery, the sprayer has complicated operating conditions and needs to be equipped with a special suspension system to improve its ride comfort, reduce the vibration, swing and rotation of the sprayer boom, thereby making the spray more uniform and reduce drift (*Herbst A. et al., 2018; Ilica A. et al., 2018; Gil E. et al., 2015*). Air suspension is widely used in sprayers because of its good nonlinear elastic characteristics, large suspension range, adjustable load capacity, and large load-bearing mass (*Melzi S. et al., 2014; Chen Y. et al., 2016*). Some sprayer manufacturers such as John Deere (*Carlson B. C. et al., 2011; Wubben T. M. et al., 2007*) and Hagie (*Schaffer J. A., 2002*) use a four-wheel independent vertical shaft air suspension system. A vertical shaft is connected between the wheel hub and the bottom of the airbag and the top of the airbag is attached to a sleeve connected to the vehicle frame through a gantry frame. As the sprayer travels over uneven road surfaces, the air springs are squeezed and stretched to reduce suspension buffer vibration. In order to ensure that the sprayer is adaptable to complex operating conditions, researchers have focused on the active or semi-active adjustment of the suspension by attaching an adjustable damper to the suspension, adding a highly stable device to the elastic element, or integrating a ground clearance adjustment device into the suspension (*Zatrieb J. et al., 2012; Li W. et al., 2018*).

A large self-propelled sprayer has a high operating speed and high ground clearance; the sprung mass and the content of the liquid change frequently during the spraying process (*Chen Y. et al., 2012*). The sprayer mass is in the range of ten to twenty tons and the width of the spray rod is twenty to fifty meters, significantly exceeding the size of regular vehicles and off-road vehicles (*Cui L. F. et al., 2018; 2019*). The sprayer is not only different from road vehicles, but also different from general non-road vehicles. When the sprayer is in the transport condition, the fast running speed requires that the sprayer suspension can fully dissipate the vibration energy transferred from the ground to the body to ensure sprayer comfort and smoothness. When the sprayer is in the spraying condition, the ground friendliness should be taken into account, that is, the excessive dynamic tire load should not be generated to prevent soil compaction and damage. When the sprayer is in the injection or spraying conditions, the body mass will change, at this time the suspension can adjust the body height in real time to ensure the driving stability. In addition, since the sprayer mostly adopts the "two pump + four motor" full hydraulic driving scheme, each wheel should have enough load to prevent wheel slip and tire wear. However, when the sprayer is driving on a ramp, the machine mass will shift to one side, which increases the wheel load on the lower side and the risk of overloading the wheel. The load is lower on the high side and the wheels may slip or lose control. Due to the high barycentre of high-clearance sprayers and the unbalanced load on both sides of the wheels, rollover accidents can easily occur. The imbalance of the wheel load not only has a large influence on the handling stability and safe operation of the sprayer but also affects the quality and efficiency of the sprayer operation. Therefore, measures must be taken to eliminate or reduce this effect.

In order to ensure the vehicle running stability and safety, researchers have studied the vehicle body height stability control and made some progress. Holbrook developed a method for the manual and automatic adjustment of the sprung mass height of the suspension to a predetermined reference height (*Holbrook G., 2010*). Hyunsup (*Kim H. et al., 2011*) applied the sliding mode control theory to design a non-linear controller for an air suspension based on body height adjustment. The controller monitored the height change of the car body in real time using a pressure sensor installed inside the four air springs and adjusted the height (height control) and the roll angle and pitch angle of the car body (levelling control). Simulations and experiments indicated that the controller improved the ride comfort and safety. In addition, electronically controlled air suspension systems have the disadvantages of overcharge, over-discharge, and sensor failure. Jang (*Jang I. et al., 2007*) used a failure protection algorithm to perform auxiliary correction control on the target height of the vehicle body. Yang conducted a detailed study on the relationship between the stiffness and height of the air spring and air charging and discharging and designed an electronically controlled air suspension system based on fuzzy proportional-integral-derivative (PID) control (*Yang Q. Y., 2008*). Wang conducted an analysis of the characteristics of the charge and discharge process of an air spring and divided the vehicle body height into high, medium, and low. A fuzzy control algorithm was used to control the vehicle body height depending on the road surface and speed of the vehicle (*Wang S. H. et al., 2013*).

However, these researches mainly focused on the control of the vehicle body height (*Wang S. H. et al., 2015; Jiang H. et al., 2015*), and there are few studies on the auto load-levelling control of agricultural sprayers. When the height of air suspension, hydropneumatic suspension and other nonlinear suspension is controlled, due to the strong nonlinearity and the variability of the suspension internal parameters, the general control method effect has a certain overshoot phenomenon (*Jiang H. et al., 2017; Chen Y. X. et al.,* *2015; Porumamilla H. et al., 2005*). The large high clearance self-propelled sprayer chassis mostly use air suspensions, the driving road conditions and operating conditions are complex and changeable. The precision and response speed of auto load-levelling control directly affect the safety and spray quality of the sprayer.

Therefore, in this study, the air suspension of a self-propelled sprayer chassis was taken as the object and potential load imbalance conditions of the sprayer suspension were analysed. An auto load-levelling control strategy of the sprayer chassis air suspension was developed. According to the nonlinear characteristics of air inflation/deflation process and law of gas thermodynamics, the mathematical model of the air spring inflation/deflation and ¼-scale vertical dynamic model of sprayer chassis air suspension were established. Based on the differential geometry theory, the ¼-scale suspension vertical dynamic model was globally linearized by the state feedback linearization method, and the sliding mode controller was designed in the linear domain. Through the inverse linear transformation, a nonlinear control algorithm for sprayer auto load-levelling in the original coordinate system was obtained. The simulation results show that the developed auto load-levelling control strategy and algorithm can efficiently and accurately control the load levelling of the high-clearance sprayer chassis suspension under various unfavourable working conditions to ensure the stability and safety of the sprayer.

MATERIALS AND METHODS

Analysis of sprayer operating conditions

In certain road conditions, the vertical load of the wheels will change, thereby reducing the adhesion of the wheels to the ground or a wheel(s) may not touch the ground. As shown in Fig. 1(a), it is assumed that when the sprayer is running, the rear left wheel enters a pit and the wheel is not suspended due to the use of an independent air suspension. Under the action of air pressure inside the air spring, the air spring is rapidly stretched. Therefore, the internal pressure and the load borne by the spring also decrease, ultimately reducing the adhesion of the wheel. This impacts the handling performance of the sprayer. Due to the use of a hydrostatic drive, when a drive wheel has less adhesion, the driving force is greater than the adhesion and the wheel will slip. Tire skid not only consumes a lot of power but also increases tire wear and soil damage. When the sprayer is driving on a ramp, as shown in Fig. 1(b), the mass of the machine will shift to one side, increasing the wheel load on the lower side and the risk of overloading the wheel. The load on the high side is reduced and the wheels may slip or lose control. Due to high barycentre of the high-clearance sprayer and the unbalanced load on both sides of the wheels, rollover accidents can easily occur. The load imbalance is caused by a change in the attitude of the sprayer body. When the sprayer body is in the levelling state, the mass of the body is distributed to each suspension system with equal mass. Since the suspensions are directly connected to the wheels, the load on each wheel is also equal. Therefore, the load balancing process of the sprayer wheel is equivalent to the process of its body levelling.

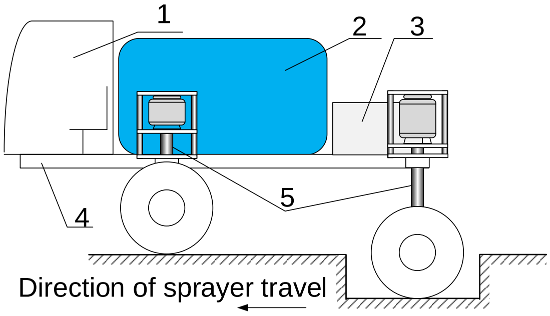

(a) Sprayer is driving on uneven roads

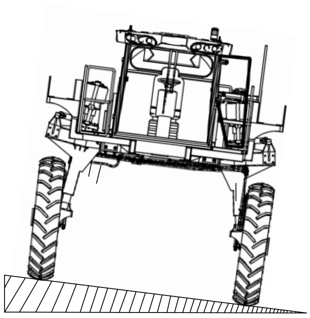

(b) Sprayer is driving on a ramp

1. cab; 2. liquid tank; 3. engine; 4. frame; 5. pneumatic suspension

Fig. 1 – Schematic diagram of load imbalance

Mathematical model

The air suspension of the sprayer chassis is inflated and deflated to adjust the body attitude and achieve load-levelling. In order to adjust the sprayer's load balance, a pneumatic system was designed, as shown in Fig. 2.

The pneumatic system consists of an air compressor, a pressure-regulating valve, an air dryer, an accumulator, four height sensors, four three-position three-way proportional solenoid valves, four air springs, and an air spring control unit. The compressed air required by the system is provided by an air compressor on the engine. The air compressor supplies clean, dry compressed air to the suspension system in an appropriate pressure range while ensuring that the air compressor has a suitable load condition and the impact on the engine performance is low. The pressure regulator switches between the operating and unloading state of the air compressor to regulate the system pressure. The air dryer absorbs moisture from the air and prevents the system components from getting wet. It can also be used to filter oil mist and particulate impurities in the air and to alleviate system component wear. The function of the accumulator is to buffer and store energy so that the air enters the suspension system smoothly.

The height sensor is installed beside each air spring. The controller controls the movement of the solenoid valve spool through an electrical signal output by the sensor to charge and discharge the air spring, adjust the height of the air spring, and achieve load-levelling of each wheel. When the height of the sprayer is increased by the air spring, the air passes from the accumulator and three-position three-way solenoid valve to the air spring. When the height is reduced, the air flows out from the air spring, passes through the three-position three-way solenoid valve, and then is vented to the atmosphere by an exhaust valve. Therefore, the mathematical model of the system includes three parts: the accumulator model, the fluid resistance model, and the air spring model.

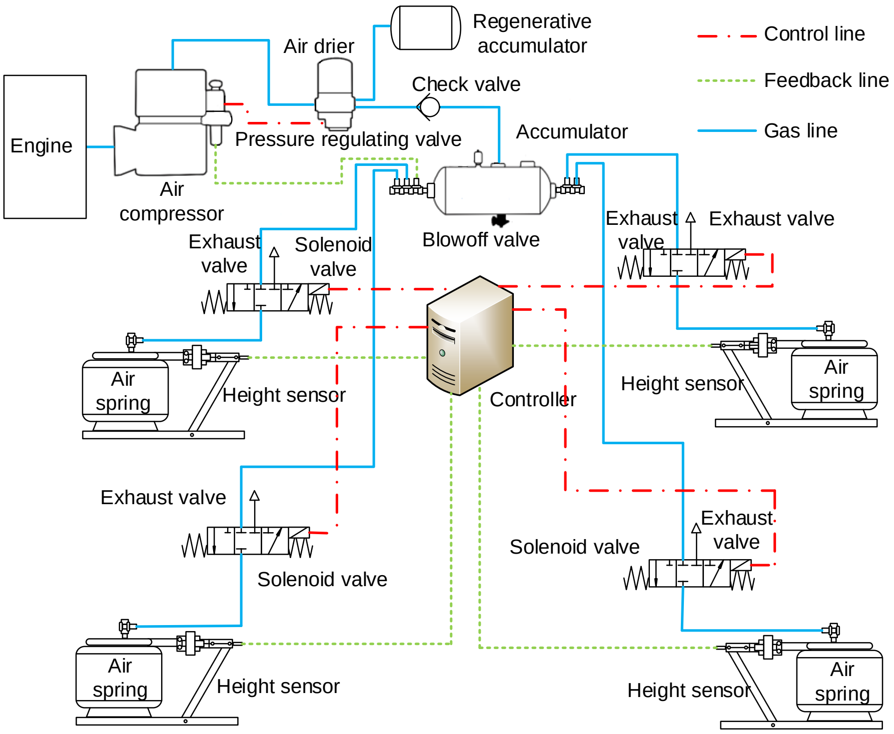

Fig. 2 - Schematic diagram of sprayer airflow line system

- **Accumulator model**

As the constant volume air source of the suspension system, the accumulator's charging process of the air spring can be regarded as a constant-volume air discharge process. The airflow out of the accumulator is considered negative airflow. Based on the mass continuity equation and the ideal gas state equation, it can be concluded that during the inflation of the air spring, the gas pressure changes in the accumulator are defined as:

$$\dot{p}_c = -\frac{nRT_{c0}}{V}\left(\frac{p_c}{p_{c0}}\right)^{\frac{n-1}{n}} G_c \tag{1}$$

In Eq. (1), p_c, T_{c0}, and p_{c0} are the absolute pressure, initial gas temperature and absolute pressure in the accumulator, respectively; the units are MPa, K, and MPa; V is the accumulator volume, m^3; refer to literature (*Carneiro J. F. et al., 2006*), the thermodynamic charging / discharging of air inside pneumatic suspensions are regarded as a polytropic process, n is the gas polytropic index that can be adjusted from 1 (isothermal process) to 1.4 (adiabatic process). According to literature (*Carneiro J. F. et al., 2006*), the value of n is 1.35 as a calculation example; R is a constant and the value is 287.1 J/(kg·K).

- **Fluid resistance model**

The air flows through the solenoid valves and the gas lines produce fluid resistance. The pressure-flow characteristics when airflow passes through the solenoid valve and pneumatic pipeline are equivalent to the pressure-flow characteristics when airflow passes through the throttle valve orifice. Therefore, the mass flow rate of air passing through the solenoid valve and pneumatic pipeline when the suspension is raised is:

$$G_c = \frac{c_d K p_c A_{K1} N_c}{\sqrt{T_c}} \tag{2}$$

When the suspension is lowered, the air in the air spring is directly discharged into the atmosphere through the solenoid valve. Therefore, the mass flow rate when air passes through the solenoid valve and the pneumatic pipe is:

$$G_k = -\frac{c_d K p_1 A_{K1} N_k}{\sqrt{T_1}} \tag{3}$$

where K is taken as a constant, which is a function of the polytropic exponent n for air. N_c and N_k are restriction factor, which are function of n and the up-stream and down-stream pressures.

When the suspension is raised, the up-stream and down-stream pressures are P_c and P_1, respectively.

When the suspension is lowered, the up-stream and down-stream pressures are $P1$ and P_a, respectively. T_c and T_1 are gas temperature in the Accumulator and air spring, respectively, the units are K. N_c, N_k, K can be obtained by the following formulas.

$$N_c = \left\{ \frac{\left(\frac{p_1}{p_c}\right)^{\frac{2}{n}} - \left(\frac{p_1}{p_c}\right)^{\frac{n+1}{n}}}{\frac{(n-1)}{2}\left(\frac{2}{n+1}\right)^{\frac{n+1}{n-1}}} \right\}^{\frac{1}{2}}, \quad N_k = \left\{ \frac{\left(\frac{p_a}{p_1}\right)^{\frac{2}{n}} - \left(\frac{p_a}{p_1}\right)^{\frac{n+1}{n}}}{\frac{(n-1)}{2}\left(\frac{2}{n+1}\right)^{\frac{n+1}{n-1}}} \right\}^{\frac{1}{2}}, \quad K = \left[\frac{n}{R}\left(\frac{2}{n+1}\right)^{\left(\frac{n+1}{n-1}\right)} \right]^{\frac{1}{2}}$$

- **Air spring model**

When the suspension is raised, a variable-mass variable-volume aeration process occurs in the air spring. The air mass flow from the accumulator to the air spring through the solenoid valve is defined as G_c and the air pressure inside the spring is:

$$\dot{p}_1 = -\frac{np_1}{V_1}\dot{V}_1 + \frac{nRT_{10}}{V_1}\left(\frac{p_1}{p_{10}}\right)^{\frac{n-1}{n}} G_c \tag{4}$$

Similarly, when the suspension is lowered, a variable-mass variable-volume deflation process occurs in the air spring. The change rate of the gas pressure inside the spring is:

$$\dot{p}_1 = -\frac{np_1}{V_1}\dot{V}_1 - \frac{nRT_{10}}{V_1}\left(\frac{p_1}{p_{10}}\right)^{\frac{n-1}{n}} G_k \tag{5}$$

- **Vertical dynamic model of sprayer suspension**

Equations (1) to (5) indicate that the vertical dynamics model of the ¼-scale suspension during inflation and deflation is:

$$\text{When the spring is inflated}\begin{cases} G_c = \dfrac{c_d K p_c A_{K1} N_c}{\sqrt{T_c}} \\ \dot{p}_c = -\dfrac{nRT_{c0}}{V}\left(\dfrac{p_c}{p_{c0}}\right)^{\frac{n-1}{n}} G_c \\ \dot{p}_1 = -\dfrac{np_1}{V_1}\dot{V}_1 + \dfrac{nRT_{10}}{V_1}\left(\dfrac{p_1}{p_{10}}\right)^{\frac{n-1}{n}} G_c \\ m_b(\ddot{x}_b + g) + c_s(\dot{x}_b - \dot{x}_t) = (p_1 - p_a)A_e \\ m_t\ddot{x}_t - c_s(\dot{x}_b - \dot{x}_t) - m_b g + k_t(x_t - w) + c_t(\dot{x}_t - \dot{w}) = -(p_1 - p_a)A_e \end{cases} \tag{6}$$

$$\text{When the spring is deflated}\begin{cases} G_{\mathrm{k}} = -\dfrac{c_{\mathrm{d}} K p_1 A_{\mathrm{k1}} N_{\mathrm{k}}}{\sqrt{T_1}} \\ \dot{p}_1 = -\dfrac{n p_1}{V_1}\dot{V}_1 - \dfrac{nRT_{10}}{V_1}\left(\dfrac{p_1}{p_{10}}\right)^{\frac{n-1}{n}} G_{\mathrm{k}} \\ m_{\mathrm{b}}(\ddot{x}_{\mathrm{b}} + g) + c_{\mathrm{s}}(\dot{x}_{\mathrm{b}} - \dot{x}_{\mathrm{t}}) = (p_1 - p_{\mathrm{a}})A_{\mathrm{e}} \\ m_{\mathrm{t}}\ddot{x}_{\mathrm{t}} - c_{\mathrm{s}}(\dot{x}_{\mathrm{b}} - \dot{x}_{\mathrm{t}}) - m_{\mathrm{b}} g + k_{\mathrm{t}}(x_{\mathrm{t}} - w) + c_{\mathrm{t}}(\dot{x}_{\mathrm{t}} - \dot{w}) = -(p_1 - p_{\mathrm{a}})A_{\mathrm{e}} \end{cases} \tag{7}$$

In Eqs. (1) to (7), p_a is atmospheric pressure and the value is 0.1 MPa; the other unmarked symbols meanings are listed in Tab.1.

Table 1

Symbols meaning in Eqs. (1) to (7)

Symbols/unit	Instructions	Symbols/unit	Instructions
p_c/ MPa	Absolute pressure in the accumulator	T_{c0}/ K	Initial gas temperature in the accumulator
p_{c0}/ MPa	Initial absolute pressure in the accumulator	V/ m³	accumulator volume
c_d	Throttle valve shrinkage coefficient	A_{k1}/ m²	The solenoid valve port area
T_c / K	Gas temperature in the accumulator	T_1/ K	Gas temperature in the air spring
p_1 / MPa	Absolute pressure in the air spring	m_b/ kg	Sprung mass
g / m·s^{-2}	Gravity acceleration	m_t/ kg	Unsprung mass
x_b/ m	Sprung mass displacement	x_t/ m	Unsprung mass displacement
V_1/ m³	Air spring volume	C_s/ N·s·m^{-1}	Suspension damping
T_{10}/ K	Initial gas temperature in the air spring	p_{10}/ MPa	Initial pressure in the air spring
k_t/ N·m^{-1}	Tire equivalent radial stiffness	A_e/ m²	Effective cross-sectional area of the air spring
w/ m	Road excitation	C_t/ N·s·m^{-1}	Tire equivalent radial damping

Controller design

- **Control strategy**

During automatic load-levelling, the adjustment range needs to be set in advance, as shown in Fig. 3. D_t is the adjustment amount. The value of D_t is related to the height difference between springs. D_t is obtained using Eq. (8).

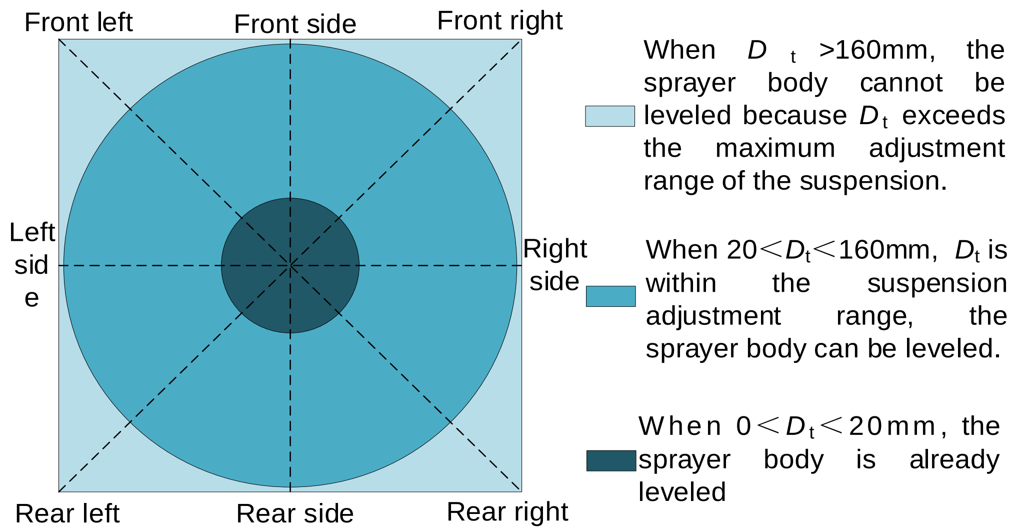

Fig.3 - Schematic diagram of load levelling adjusting range

$$D_{\mathrm{t}} = \begin{cases} \max(x_{\mathrm{bij}}) - \min(x_{\mathrm{bij}}) & \text{When the four springs are individually adjusted} \\ \varphi L & \text{When the sprayer climbs or downhill} \\ \theta B_{\mathrm{F}} & \text{When the sprayer drives along the ramp} \end{cases} \tag{8}$$

In Eq. (8), *ij* represents the four positions of the suspensions relative to the sprayer chassis, which is denoted as *FL, FR, RL*, and *RR. FL, FR, RL*, and *RR* represent front left, front right, rear left, rear right, respectively. θ and φ are the sprayer body roll angle and pitch angle measured by a gyroscope. L and B_F are the wheelbase and wheel track respectively. According to the load balancing requirements, combined with the characteristics of the air suspension structure, a load balancing control strategy for the large high-clearance self-propelled sprayer is developed. The strategy is shown in Fig. 4. The high-frequency and low-frequency limits of the bandpass filter are 0.05 Hz and 0.1 Hz, respectively. The bandpass filter filters out changes in body displacement caused by road surface excitation and sprung mass changes. The BLOCKTIMER allows the controller to compare changes in the adjustment D_t within 10 s to identify whether the sprayer is in a long-term load imbalance condition and makes adjustments to avoid frequent movement of the solenoid valve. In the initial state, the height difference of each spring is within 20 mm and the loads of the springs are in equilibrium. When the sprayer travels on uneven roads or slopes, the loads of the springs change under the weight of the body. When the height difference between springs caused by the load change is within the range of 20 mm, the controller recognizes that the sprayer is in a balanced load state. When the height difference between springs exceeds 160 mm, the controller alerts the driver that the machine load is not in the equilibrium state so that the driver uses caution when operating the sprayer. When the height difference between springs is in the range of 20~160 mm, the sprayer is in a load level state. In addition to the height sensor, a gyroscope is installed at the barycentre of the sprayer. The gyroscope measures the tilt angle of the sprayer in the front and rear directions or the left and right directions when the sprayer is operated on a slope. The controller calculates D_t based on the measured tilt angle and the wheelbase and wheel track of the sprayer. During load-levelling, the spring on the high side has priority of deflation and if load-levelling cannot be achieved, the spring on the low side is inflated. High side refers to the side with large sprung mass displacement value x_{bij} in the four suspensions of sprayer. Low side refers to the side with small sprung mass displacement value x_{bij} in the four suspensions of sprayer. Reducing the inflation time of the spring reduces the pumping time of the air compressor and extends the life of the compressor.

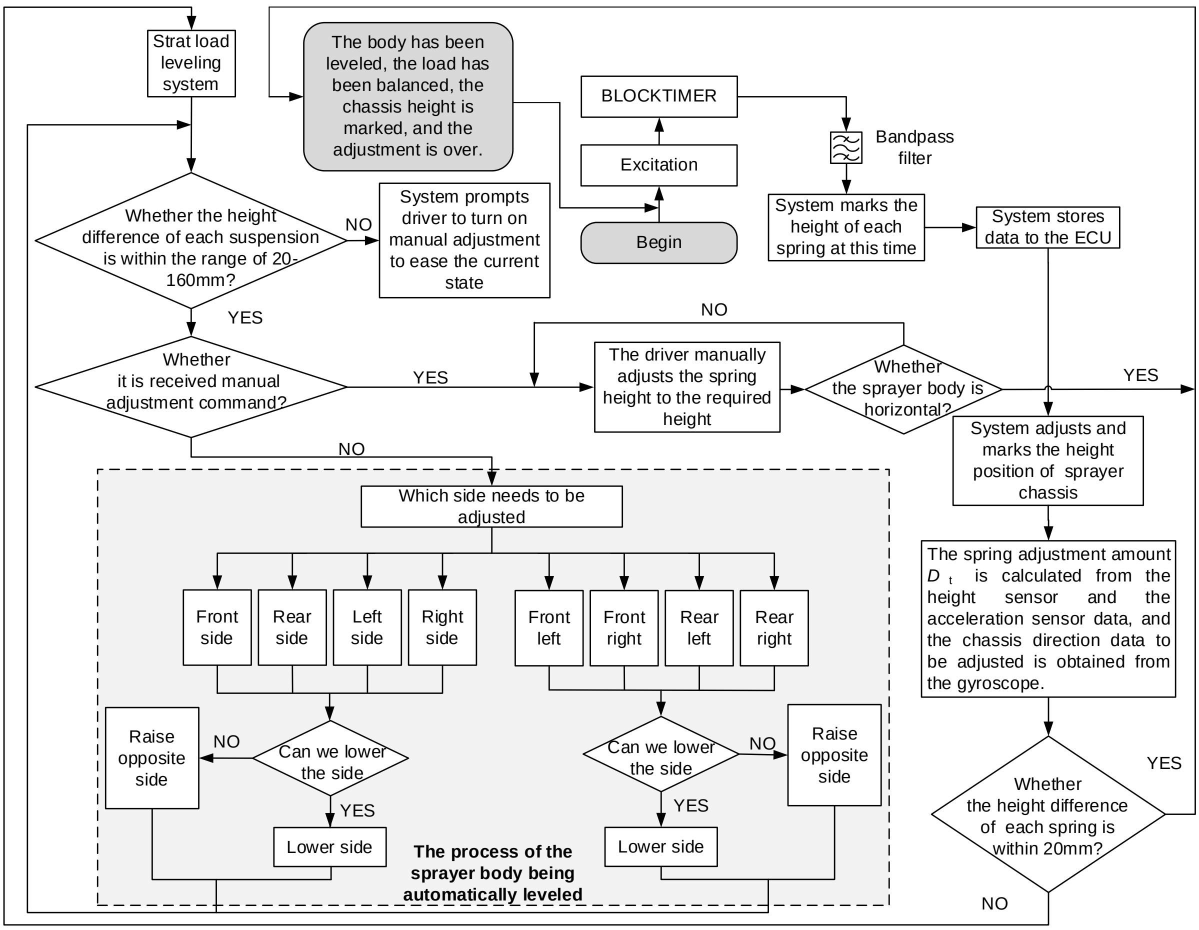

Fig. 4 - Control strategy of auto load levelling

- **Control algorithm**

The auto load-levelling control is based on the suspension height and body attitude, which are determined by the height sensors, the unsprung mass acceleration sensors, and the gyroscope. The amount of adjustment required for each spring is calculated and the springs are adjusted to achieve load-levelling of the suspensions. Therefore, auto load-levelling control requires a control algorithm to adjust the target height. The established load-levelling control strategy and the sliding mode control are used for the proposed auto load-levelling control algorithm, which is shown in Fig. 5. The u_{ij} is the control amount and x_{bijm} is the target height of each spring. In order to obtain the sprung mass displacement x_{bij} of the air suspensions, x_{ij} and x_{tij} need to be obtained. The x_{ij} could be obtained through the spring height sensor, and the x_{tij} could be obtained by the unsprung mass acceleration sensor.

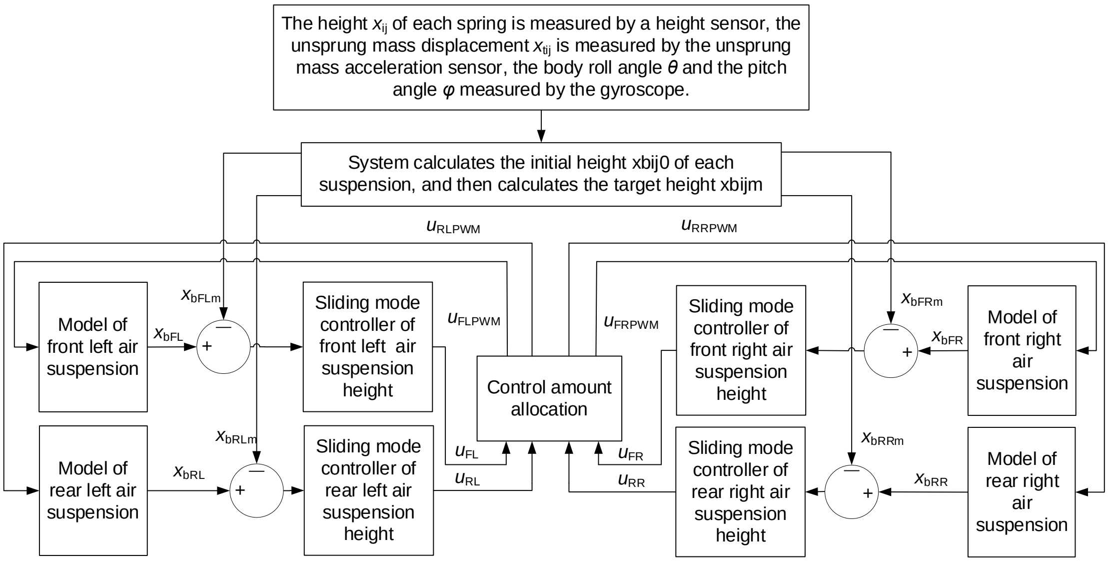

Fig. 5 - Control algorithm of auto load levelling

- **Auto load-levelling control model of the sprayer chassis**

We use the front left air suspension during inflation as an example; the system state variable is $\boldsymbol{x}_{FL}=[x_1\ x_2\ x_3\ x_4\ x_5]^T=[x_{bFL}\ \dot{x}_{bFL}\ x_{tFL}\ \dot{x}_{tFL}\ p_{1FL}]^T$.

The vertical dynamics model of the sprayer suspension model represents the state equation, as shown in Eq. (9).

$$\begin{cases} \dot{\boldsymbol{x}}_{FL} = f\left(\boldsymbol{x}_{FL}\right) + g(\boldsymbol{x}_{FL})u_{FL} \\ \boldsymbol{x}_{FL} = \left[x_{bFL} \quad \dot{x}_{bFL} \quad x_{tFL} \quad \dot{x}_{tFL} \quad p_{1FL}\right]^T \\ y = h\left(\boldsymbol{x}_{FL}\right) = x_{bFL} - x_{tFL} \end{cases} \tag{9}$$

$f(x_{FL})$ and $g(x_{FL})$ in Eq. (9) are expressed as:

$$f\left(\boldsymbol{x}_{FL}\right) = \begin{bmatrix} x_2 \\ \left(\left(x_5 - p_a\right)A_{eFL} - c_{dFL}\left(x_2 - x_4\right) - m_{bFL}g\right)/m_{bFL} \\ x_4 \\ \left(c_{dFL}\left(x_2 - x_4\right) - \left(\left(x_5 - p_a\right)A_{eFL} - m_{bFL}g\right) - k_{tFL}x_3 - c_{tFL}x_4\right)/m_{tFL} \\ -\left(np_{1FL}A_{eFL}\left(x_2 - x_4\right)\right)/V_{1FL} \end{bmatrix},\ g\left(\boldsymbol{x}_{FL}\right) = \begin{bmatrix} 0 \\ 0 \\ 0 \\ 0 \\ nRT_{1FL}/V_{1FL} \end{bmatrix}.$$

According to Eq. (9), Eq. (10) can be obtained from the theory of differential geometry.

$$L_{\mathrm{f}}h(\boldsymbol{x}_{\mathrm{FL}})=x_2-x_4,\ \ L_{\mathrm{f}}^{2}h(\boldsymbol{x}_{\mathrm{FL}})=f_2-f_4,\ \ L_{\mathrm{g}}h(\boldsymbol{x}_{\mathrm{FL}})=0,$$
$$L_{\mathrm{f}}^{3}h(\boldsymbol{x}_{\mathrm{FL}})=\left(\left(\frac{1}{m_{\mathrm{bFL}}}+\frac{1}{m_{\mathrm{tFL}}}\right)\left(A_{\mathrm{eFL}}f_5-c_{\mathrm{dFL}}f_2+c_{\mathrm{dFL}}f_4\right)\right)+\frac{\left(k_{\mathrm{tFL}}+c_{\mathrm{tFL}}\right)}{m_{\mathrm{tFL}}}\left(f_3+f_4\right), \tag{10}$$
$$L_{\mathrm{g}}L_{\mathrm{f}}h(\boldsymbol{x}_{\mathrm{FL}})=0,\ L_{\mathrm{g}}L_{\mathrm{f}}^{2}h(\boldsymbol{x}_{\mathrm{FL}})=\left(\frac{1}{m_{\mathrm{bFL}}}+\frac{1}{m_{\mathrm{tFL}}}\right)\frac{nRT_{\mathrm{1FL}}A_{\mathrm{eFL}}}{V_{\mathrm{1FL}}}\neq 0$$

According to Eq. (10), the relative order of the system is 3, which is smaller than the order of the equation state of the original system. Therefore, local feedback linearization processing can be performed on Eq. (9). We define the new system state variable $\boldsymbol{\vartheta}_{\mathrm{FL}}=[x_{\mathrm{bFL}}\text{-}x_{\mathrm{tFL}}\ \dot{x}_{\mathrm{bFL}}\text{-}\dot{x}_{\mathrm{tFL}}\ \ddot{x}_{\mathrm{bFL}}\text{-}\ddot{x}_{\mathrm{tFL}}]^{\mathrm{T}}$ in linear space. The state equation of Eq. (9) in linear space is as shown in Eq. (11). The relationship between the original control amount u_{FL} and the control amount υ_{FL} in the linear state is defined in Eq. (12).

$$\begin{cases}\dot{\vartheta}_{\mathrm{FL}}=\mathbf{A}\vartheta_{\mathrm{FL}}+\mathbf{B}\upsilon_{\mathrm{FL}}\\ y=\vartheta_{\mathrm{1FL}}\end{cases} \tag{11}$$

$$\upsilon_{\mathrm{FL}}=L_{\mathrm{f}}^{3}h(\boldsymbol{x}_{\mathrm{FL}})+L_{\mathrm{g}}L_{\mathrm{f}}^{2}h(\boldsymbol{x}_{\mathrm{FL}})u_{\mathrm{FL}} \tag{12}$$

A and **B** in Eq. (11) are expressed as:

$$\mathbf{A}=\begin{bmatrix}0&1&0\\0&0&1\\0&0&0\end{bmatrix},\mathbf{B}=\begin{bmatrix}0\\0\\1\end{bmatrix}.$$

The model obtained by feedback linearization is a third-order linear system. In the linear system, the new output error is defined as $e_{\mathrm{FL}}=\vartheta_{\mathrm{1FL}}\text{-}\vartheta_{\mathrm{1dFL}}$. The sliding surface can be set to:

$$s_{\mathrm{FL}}=\lambda_{\mathrm{FL}}^{2}e_{\mathrm{FL}}+2\lambda_{\mathrm{FL}}\dot{e}_{\mathrm{FL}}+\ddot{e}_{\mathrm{FL}} \tag{13}$$

In Eq. (13), λ_{FL} is the sliding mode coefficient and $\lambda_{\mathrm{FL}}>0$. The sliding mode control output υ_{FL} consists of an equivalent control amount υ_{FLeq} and a switching control amount υ_{FLsw}, that is,

$$\upsilon_{\mathrm{FL}}=\upsilon_{\mathrm{FLeq}}+\upsilon_{\mathrm{FLsw}} \tag{14}$$

The effect of the equivalent control is to drive the system state to move along the expected sliding mode surface (*Zhao Y. Z. et al., 2014; Jin M. et al., 2014; Assadsangabi B. et al., 2009; Zirkohi M. M. et al., 2015*) and keep the system at $\dot{s}_{\mathrm{FL}}$ =0. We use the derivative of Eq. (13) to obtain Eq. (15).

$$\begin{aligned}\dot{s}_{\mathrm{FL}}&=\lambda_{\mathrm{FL}}^{2}\dot{e}_{\mathrm{FL}}+2\lambda_{\mathrm{FL}}\ddot{e}_{\mathrm{FL}}+\dddot{e}_{\mathrm{FL}}\\&=\lambda_{\mathrm{FL}}^{2}\left(\dot{\vartheta}_{\mathrm{1FL}}-\dot{\vartheta}_{\mathrm{1dFL}}\right)+2\lambda_{\mathrm{FL}}\left(\ddot{\vartheta}_{\mathrm{1FL}}-\ddot{\vartheta}_{\mathrm{1dFL}}\right)+\left(\dddot{\vartheta}_{\mathrm{1FL}}-\dddot{\vartheta}_{\mathrm{1dFL}}\right)\\&=\lambda_{\mathrm{FL}}^{2}\left(\vartheta_{\mathrm{2FL}}-\dot{\vartheta}_{\mathrm{1dFL}}\right)+2\lambda_{\mathrm{FL}}\left(\vartheta_{\mathrm{3FL}}-\ddot{\vartheta}_{\mathrm{1dFL}}\right)+\left(\upsilon_{\mathrm{FLeq}}-\dddot{\vartheta}_{\mathrm{1dFL}}\right)\end{aligned} \tag{15}$$

Let $\dot{s}_{\mathrm{FL}}$ =0, then the equivalent control υ_{FLeq} can be expressed by Eq. (16).

$$\upsilon_{\mathrm{FLeq}}=\lambda_{\mathrm{FL}}^{2}\dot{e}_{\mathrm{FL}}+2\lambda_{\mathrm{FL}}\ddot{e}_{\mathrm{FL}}-\dddot{\vartheta}_{\mathrm{1dFL}} \tag{16}$$

The function of switching the control is to drive the system state to approach the sliding mode switching surface s_{FL} =0; the output of the switching control is defined in Eq. (17).

$$\upsilon_{\mathrm{FLsw}}=-\varepsilon_{\mathrm{FL}}\mathrm{sgn}\left(s_{\mathrm{FL}}\right) \tag{17}$$

In Eq. (17), $\varepsilon_{\mathrm{FL}}$ is the switching constant and sgn(s_{FL}) is a sign function. Equation (14) can be expressed as:

$$\upsilon_{\mathrm{FL}}=\lambda_{\mathrm{FL}}^{2}\dot{e}_{\mathrm{FL}}+2\lambda_{\mathrm{FL}}\ddot{e}_{\mathrm{FL}}-\dddot{\vartheta}_{\mathrm{1dFL}}-\varepsilon_{\mathrm{FL}}\mathrm{sign}\left(s_{\mathrm{FL}}\right) \tag{18}$$

Based on the Lyapunov stability condition, if the designed sliding mode control system is stable, the inequality (19) is correct.

$$\dot{\mathrm{V}}\left(s_{\mathrm{FL}}\right)=\frac{1}{2}\frac{\mathrm{d}}{\mathrm{d}t}s_{\mathrm{FL}}^{2}=s_{\mathrm{FL}}\dot{s}_{\mathrm{FL}}<-\eta_{\mathrm{FL}}\,|\,s_{\mathrm{FL}}\,| \tag{19}$$

In Eq. (19), η_{FL} is an arbitrarily small positive integer. The function of the equivalent control υ_{FLeq} is to ensure that $\dot{s}_{FL}$ =0; therefore, Eq. (19) can be expressed as:

$$s_{FL}\left(-\varepsilon_{FL}\text{sign}\left(s_{FL}\right)\right)<-\eta_{FL}\,|s_{FL}|\quad\Rightarrow\varepsilon_{FL}>\eta_{FL} \tag{20}$$

It is known from Eq. (20) that when $\varepsilon_{FL}>\eta_{FL}$, the sliding mode control system [29-30] is stable. In order to reduce the system chatter caused by the switching control in the auto load-levelling control system, the sign function in Eq. (17) can be replaced by the saturation function of Eq. (21).

$$\text{sat}\left(s_{FL}/\psi_{FL}\right)=\begin{cases}s_{FL}/\psi_{FL}, & |s_{FL}|\le\psi_{FL}\\ \text{sgn}(s_{FL}), & |s_{FL}|>\psi_{FL}\end{cases} \tag{21}$$

In Eq. (21), ψ_{FL} is the boundary layer thickness. According to Eq. (18), the output of the sliding mode controller in the linear state is obtained as shown in Eq. (22).

$$\upsilon_{FL}=\lambda_{FL}^{2}\dot{e}_{FL}+2\lambda_{FL}\ddot{e}_{FL}-\dddot{\vartheta}_{1dFL}-\varepsilon_{FL}\text{sat}\left(s_{FL}/\psi_{FL}\right) \tag{22}$$

Combined with Eqs. (12) and (22), the actual sliding mode control amount of the front left air suspension inflation is as shown in Eq. (23).

$$u_{FL}=\frac{-\lambda_{FL}^{2}\dot{e}_{FL}-2\lambda_{FL}\ddot{e}_{FL}+\dddot{\vartheta}_{1dFL}-L_f{}^{3}h\left(\boldsymbol{x}_{FL}\right)-\varepsilon_{FL}\text{sat}\left(s_{FL}/\psi_{FL}\right)}{L_gL_f{}^{2}h\left(\boldsymbol{x}_{FL}\right)} \tag{23}$$

Similarly, the actual sliding mode control amounts u_{FR}, u_{RL}, and u_{RR} of the front right, rear left, and rear right air suspension inflation processes are as shown in Eqs. (24)-(26), respectively.

$$u_{FR}=\frac{-\lambda_{FR}^{2}\dot{e}_{FR}-2\lambda_{FR}\ddot{e}_{FR}+\dddot{\vartheta}_{1dFR}-L_f{}^{3}h\left(\boldsymbol{x}_{FR}\right)-\varepsilon_{FR}\text{sat}\left(s_{FR}/\psi_{FR}\right)}{L_gL_f{}^{2}h\left(\boldsymbol{x}_{FR}\right)} \tag{24}$$

$$u_{RL}=\frac{-\lambda_{RL}^{2}\dot{e}_{RL}-2\lambda_{RL}\ddot{e}_{RL}+\dddot{\vartheta}_{1dRL}-L_f{}^{3}h\left(\boldsymbol{x}_{RL}\right)-\varepsilon_{RL}\text{sat}\left(s_{RL}/\psi_{RL}\right)}{L_gL_f{}^{2}h\left(\boldsymbol{x}_{RL}\right)} \tag{25}$$

$$u_{RR}=\frac{-\lambda_{RR}^{2}\dot{e}_{RR}-2\lambda_{RR}\ddot{e}_{RR}+\dddot{\vartheta}_{1dRR}-L_f{}^{3}h\left(\boldsymbol{x}_{RR}\right)-\varepsilon_{RR}\text{sat}\left(s_{RR}/\psi_{RR}\right)}{L_gL_f{}^{2}h\left(\boldsymbol{x}_{RR}\right)} \tag{26}$$

In Eqs. (24) to (26), λ_{FR}, λ_{RL}, and λ_{RR} are the sliding mode coefficients corresponding to the respective suspension controls. ε_{FR}, ε_{RL}, and ε_{RR} are the switching constants. ψ_{FR}, ψ_{RL}, and ψ_{RR} are the boundary thicknesses.

In addition, in the case of an unbalanced load of the sprayer, the load on each chassis suspension will change. It is assumed that if the sprayer is operating in a certain extreme condition, the roll angle and the pitch angle are θ and φ, respectively. The distance from the barycentre to the front and rear axles are a and b, respectively. According to θ, φ, a, b and the overall mass m_s, the sprung mass of each sprayer chassis suspension in the limit working condition can be calculated by Eq. (27).

$$\begin{cases}m_{sFL}=m_s\left(\dfrac{b}{2L}-\dfrac{\theta}{2}+\dfrac{\varphi}{2}\right)\\ m_{sFR}=m_s\left(\dfrac{b}{2L}+\dfrac{\theta}{2}+\dfrac{\varphi}{2}\right)\\ m_{sRL}=m_s\left(\dfrac{a}{2L}-\dfrac{\theta}{2}-\dfrac{\varphi}{2}\right)\\ m_{sRR}=m_s\left(\dfrac{a}{2L}+\dfrac{\theta}{2}-\dfrac{\varphi}{2}\right)\end{cases} \tag{27}$$

In Eq. (27), m_{sFL}, m_{sFR}, m_{sRL}, and m_{sRR} are the sprung masses of each suspension.

In the actual auto load-levelling control process of the sprayer chassis air suspension, according to equations (23) - (26), the controlled quantity u_{ij} of proportional solenoid valve is obtained when the suspension is inflated and deflated, and then the opening degree of the proportional solenoid valve is controlled by pulse width modulation (PWM) method. The actual switching state duty ratio of the proportional solenoid valve can be obtained by Eq. (28).

$$u_{\text{ijPWM}}=\begin{cases}1, & \text{When} \quad u_{\text{ij}}\geq\left|u_{0\max\text{ij}}\right| \\ u_{\text{ij}}/\left|u_{0\max\text{ij}}\right|, & \text{When} \quad 0<u_{\text{ij}}<\left|u_{0\max\text{ij}}\right| \\ 0, & \text{When} \quad u_{\text{ij}}\leq 0\end{cases} \tag{28}$$

In Eq. (28), u_{ijPWM} is the duty ratio of the proportional solenoid valve actual switching state. $u_{0\text{maxij}}$ is the product of the air mass flow and the unit control period when the solenoid valve is fully opened. The mass flow value required in the spring height control process can be converted into the duty cycle in the solenoid valve switch electrical signal, so as to control the solenoid valve more conveniently. The maximum control amount $u_{0\text{maxij}}$ of each suspension can be obtained by equation (29).

$$u_{0\text{maxij}}=\begin{cases}c_{\text{d}}KA_{\text{K1max}}p_{\text{c}}N_{\text{c}}/\sqrt{T_{\text{c}}} & \text{When the spring is inflated} \\ -c_{\text{d}}KA_{\text{K1max}}p_{\text{1ij}}N_{\text{k}}/\sqrt{T_{1}} & \text{When the spring is deflated}\end{cases} \tag{29}$$

In Eq. (29), A_{k1max} is the solenoid valve port area when the proportional solenoid valve connected to the spring is fully opened.

RESULTS AND DISCUSSION

Matlab/Simulink was used to develop the simulation model of the auto load-levelling control system. The simulation used fixed-step type, and the solving algorithm used ode3 (Bogacki-Shampine). The sampling frequency was 1000Hz and the sampling time was 6s in the simulation. Simulation parameters are shown in Tab. 2.

Table 2

Initial simulation parameters of auto load-levelling control

Parameters / unit	Instructions	Values	Parameters / unit	Instructions	Values
m_s / kg	Body mass	12000	T_{ij} / K	Internal spring temperature	293
V / km·h^{-1}	Speed	12	f / Hz	Sampling frequency	1000
B_F / m	Wheel track	3.2	t / s	Sampling time	6
a / m	Front axle distance from centroid	1.8	λ_{ij}	Sliding mode coefficient of each suspension	40.328
b / m	Rear axle distance from centroid	2.2	ε_{ij}	Switching constant of each suspension	16
V_1'	Rate of change in volume of the spring	0.518	Ψ_{ij}	Boundary thickness of each suspension	0.01
x_{0ij} / mm	Initial spring height	380	C_{sij} / N·s·m^{-1}	Suspension damping	2400
V_{10ij} / m^3	The initial working volume of the spring	0.01914	G / mm	Centroid height of sprayer	1620
m_{tij} / kg	Unsprung mass of each suspension system	300	k_{tij} / N·m^{-1}	Tire equivalent radial stiffness	560000
C_{tij} / N·s·m^{-1}	Tire equivalent radial damping	5700			

In order to verify the performance of the proposed sliding mode control method, the front left air suspension was increased by 0.08 m or reduced by 0.08 m from the design height of 0.38 m and the suspension height adjustments in the on-off control, PID control and sliding mode control were obtained, as shown in Fig. 6. The Ziegler-Nichols method was used to tune the PID controller parameters and selected the best PID control parameters. Through the tuning of PID control parameters, the proportional link coefficient k_P=25.4, the integral link coefficient k_I=15.8, and the differential link coefficient k_D=10.2. Fig. 6 (a) shows the lift of the front left air suspension. After 3 s, the target height of 0.46 m is reached under sliding mode control and the suspension heights in the on-off control and PID control are still being adjusted. After 3.5 s, the suspension height in the on-off control has stabilized at 0.47 m, exceeding the target height by 0.01 m. At this time, the height of the suspension under PID control accurately reaches the target height of 0.46 m. Fig. 6 (b) shows the lowering of the front left air suspension. After 3 s, the target height of 0.30 m is reached under sliding mode control. After 3.5 s, the suspension height in the on-off control has stabilized at 0.295 m, exceeding the target height by 0.005 m. At this time, the height of the suspension under PID control accurately reaches the target height of 0.30 m. The simulation results show that both the sliding mode control and PID control have higher precision, and both effectively solve the problems of "overcharging" and "over discharging" in the suspension height control process. However, compared with PID control, sliding mode control has a faster response speed and better robustness for air suspension system with strong nonlinearity.

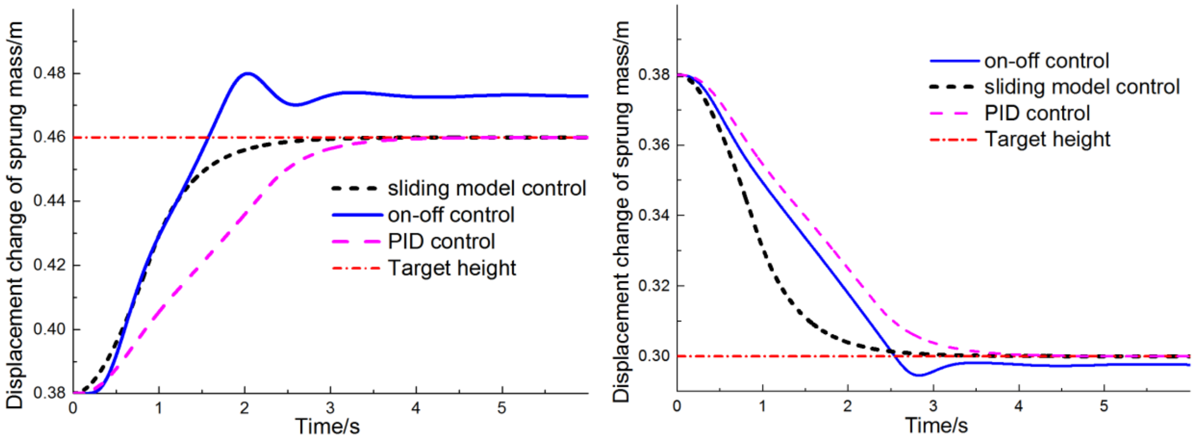

(a) The lift of the front left air suspension *(b) The lowering of the front left air suspension*

Fig. 6 - The suspension height adjustment effect in different control modes

In order to verify the performance of the auto load-levelling algorithm based on the sliding mode control, the sprayer is tested using different roll and pitch angles and rough road conditions; the roll angle, pitch angle, barycentre height, sprung mass of each suspension, and the height changes were analysed, as shown in Figs. 7-9. According to the sprayer auto load-levelling control strategy in Section 2.3.1 and the parameter data in Tab. 2, since the sprayer wheel track is 3.2m, the distance from the front axis to the centroid is 1.8m, the distance from the rear axis to the centroid is 2.2m, the centroid height is 1.62m, initial air spring height is 380mm, and the maximum height difference between the air springs should not exceed 160mm. By calculating the above parameters and obtaining that the maximum roll angle of the sprayer does not exceed 0.025rad, and the maximum pitch angle does not exceed 0.02rad.

Fig. 7 shows the changes in various parameters during auto load-levelling for a roll angle of 0.025 rad and a pitch angle of 0 rad. The auto load-levelling controller first deflated the two suspensions on the left side of the sprayer until the suspensions' heights were reduced from 2.08 m to 2.0 m. The heights of the two suspensions on the left and right sides were equal, as shown in Fig. 7(b). The body roll angle gradually decreased from 0.025 rad to 0 rad and the centroid height also decreased. The pitch angle fluctuated around 0 rad and the change was negligible, as shown in Fig. 7(a). When the suspension height on the left side changed, the load on each spring also changed; ultimately, the suspension's sprung mass on the left and right sides of the machine were equal and the load of each suspension reached an equilibrium state.

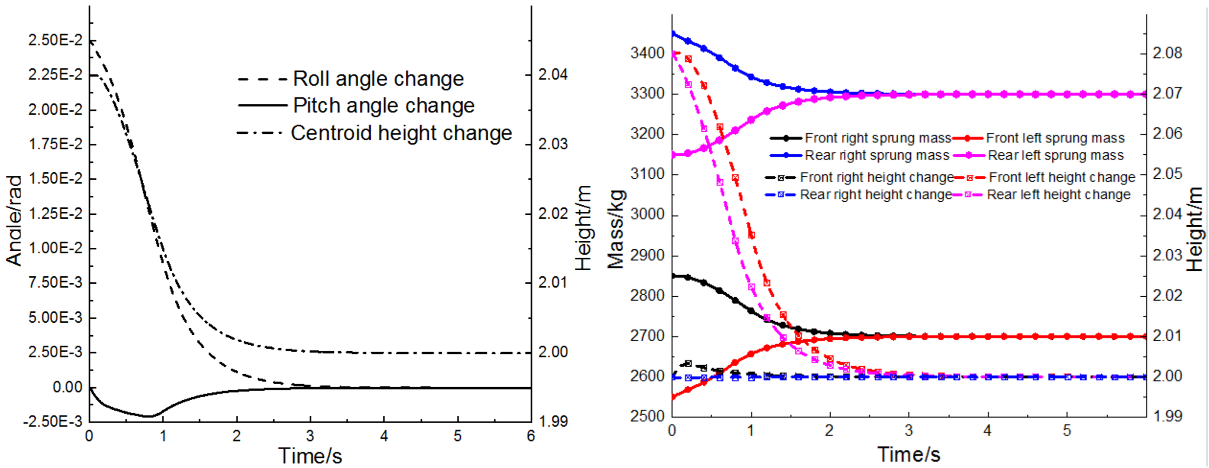

(a) Roll angle, pitch angle and centroid height changes *(b) Sprung mass and height changes*

Fig. 7 -Effect control of auto load-levelling during body rolling

Fig. 8 shows the changes in various parameters during auto load-levelling control for a roll angle of 0 rad and a pitch angle of 0.02 rad. Similar to the control process shown in Fig. 7, the auto load-levelling controller first deflated the two suspensions on the rear side of the sprayer until the suspensions' heights were reduced from 2.08 m to 2.0 m. The heights of the two suspensions on the front and rear sides were equal, as shown in Fig. 8(b).

The body pitch angle gradually decreased from 0.02 rad to 0 rad and the centroid height also decreased. The roll angle fluctuated around 0 rad and the change was negligible, as shown in Fig. 8(a). When the suspension height on the rear side changed, the load on each spring also changed; ultimately, the suspension's sprung mass on the front and rear sides of the machine were equal and the load of each suspension reached an equilibrium state.

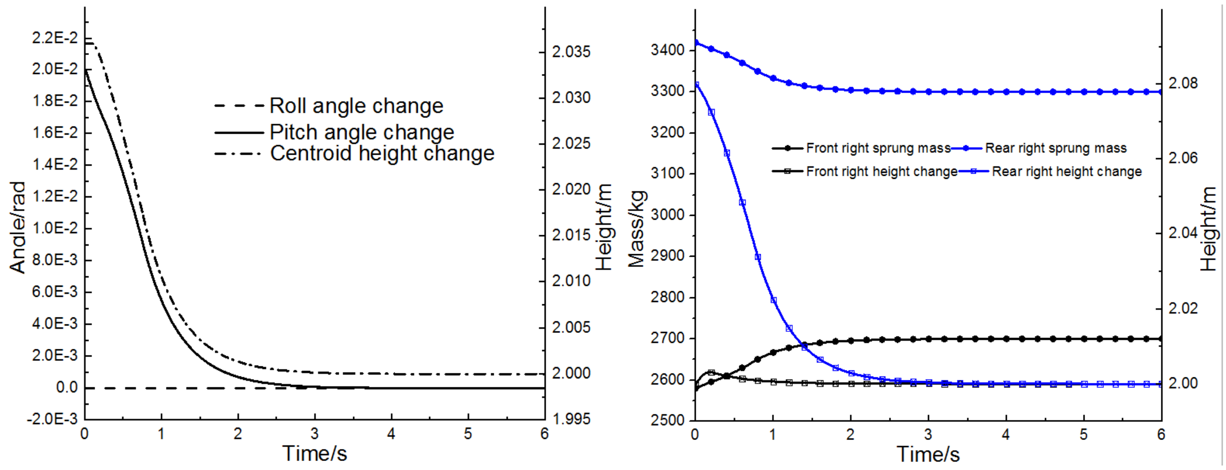

(a) Roll angle, pitch angle and centroid height changes *(b) Sprung mass and height changes*

Fig. 8 - Effect control of auto load-levelling during body pitching

Fig. 9 showed the changes in various parameters during auto load-levelling control for a roll angle of 0.025 rad and a pitch angle of 0.02 rad. The controller reduced the height of each suspension to 2.0 m. The auto load-levelling controller first inflated the front right suspension and deflated the other suspensions until all suspension heights reached the target height, as shown in Fig. 9(b).

The body roll angle and pitch angle gradually decreased from 0.025 rad and 0.02 to 0 rad, respectively. The centroid height also decreased, as shown in Fig. 9(a). Finally, the load on each suspension reached a balanced state.

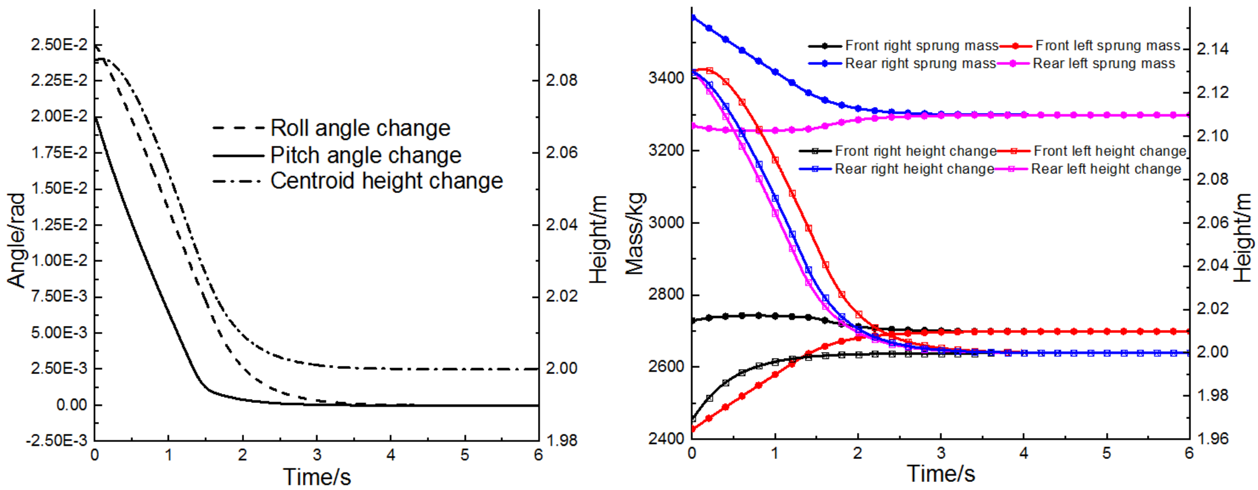

(a) Roll angle, pitch angle and centroid height changes *(b) Sprung mass and height changes*

Fig.9 - Effect control of auto load-levelling during sprayer running on the uneven road

CONCLUSIONS

During the sprayer operation, load imbalance will cause the wheels to slip or the machine to roll over, affecting the safe operation and handling stability of the sprayer. Auto load-levelling control is an important technology to improve sprayer performance. The following conclusions can be drawn:

(1) A model of the charge and discharge of the air suspension of a sprayer was established and a ¼-scale vertical dynamics model of the suspension was developed to lay a theoretical foundation for auto load-levelling control of a sprayer.

(2) The proposed auto load-levelling control algorithm with sliding mode effectively overcomes the problems of oscillation, "overcharging" and "over discharging" in the vehicle height control process, and has good accuracy, good control response and robustness to changes in the model parameters.

(3) The control strategy and algorithm meet the needs of auto load-levelling control and provide reference information for auto load-levelling control of self-propelled sprayers.

However, the above research mainly verified the proposed auto load-levelling control effect of the large self-propelled sprayer from a simulation perspective. Although the implementation method of applying pulse width modulation (PWM) to the proportional solenoid valve opening control in actual control was also proposed, its actual control effect needs to be further verified. In addition, since the high control activity of the sliding mode control method is the main factor restricting its practical application, it is necessary to further study the sliding mode control problem of the discrete-time system, the optimization problem of the sliding mode control parameters, or combined the sliding mode control with other control methods, such as fuzzy control for joint control to overcome the shortcomings of the current sliding mode control method, so as to better realize the auto load-levelling control actual vehicle application of the large self-propelled sprayer chassis air suspension.

ACKNOWLEDGMENT

The authors thank the editing team of EditorBar for improving the English language fluency of our paper. The work in this paper was supported by the Key Research and Development Program of Shaanxi Province (No. 2019ZDLNY02-01), the National Key Research and Development Program (No.2018YFD0701100-2018YFD0701102) and the China Postdoctoral Science Foundation (No.2018M643744).

REFERENCES

[1] Assadsangabi B., Eghtesad M., Daneshmand F., Vahdati N., (2009), Hybrid sliding mode control of semi-active suspension systems, *Smart Materials and Structures*, vol.18, pp.406-414.

[2] Baumhardt U. B., Airton D. S. A., Tenorio H. G. T., Ferreira C. C., Bedin P. R., (2017), Methodology for conception of cabins of agricultural machines: informational phase applied to a self-propelled sprayer, *Journal of the Brazilian Society of Mechanical Sciences and Engineering*, vol.39, pp.1683-1694.

[3] Carlson B. C., Young D. E., Baxter G. E., Anderson J. C., (2011), *Suspended axle for sprayer*, US, Patent 7938415.

[4] Carneiro J. F., De A. F. G., (2006), Reduced-order thermodynamic models for servo-pneumatic actuator chambers, *Proceedings of the Institution of Mechanical Engineers*, Part I: Journal of Systems and Control Engineering vol.220, pp.301-314.

[5] Chen Y., Chen L., Xu X., Huang C., (2015), Vehicle height control of electronic-controlled air suspension under random disturbance（随机干扰下电控空气悬架整车车身高度控制研究）, *Transactions of the Chinese Society for Agricultural Machinery*, vol.46, pp.309-315.

[6] Chen Y., Chen S., Du Y., Zhu Z., Mao E., (2016), Damping characteristics of chassis suspension system of high clearance agricultural machinery based on friction damper（基于摩擦阻尼的高地隙农机底盘悬架减振特性）, *Transactions of the CSAE*, vol.32, pp.51-57.

[7] Chen Y., Mao E., Li W., Zhang S., Song Z., Yang S., Chen J., (2020), Design and experiment of a high-clearance self-propelled sprayer chassis, *International Journal of Agricultural and Biological Engineering*, vol.13, pp.71-80.

[8] Chen Y., Zhang S., Mao E., Du Y., Chen J., Yang S., (2020), Height stability control of a large sprayer body based on air suspension using the sliding mode approach, *Information Processing in Agriculture* vol.7, pp.20-29.

[9] Cui L., Mao H., Xue X., Ding S., Qiao B., (2018), Optimized design and test for a pendulum suspension of the crop spray boom in dynamic conditions based on a six DOF motion simulator, *International Journal of Agricultural and Biological Engineering*, vol.11, pp.76-85.

[10] Cui L., Xue X., Ding S., Le F., (2019), Development of a DSP-based electronic control system for the active spray boom suspension, *Computers and Electronics in Agriculture*, vol.166, pp.1-9.

[11] Cui L., Xue X., Le F., Mao H., Ding S., (2019), Design and experiment of electro hydraulic active suspension for controlling the rolling motion of spray boom, *International Journal of Agricultural and Biological Engineering*, vol.12, pp.72-81.

[12] Gil E., Gallart M., Balsari P., Marucco P., Almajano M., Llop J., (2015), Influence of wind velocity and wind direction on measurements of spray drift potential of boom sprayers using drift test bench, *Agricultural and forest meteorology*, vol.202, pp.94-101.

[13] Herbst A., Osteroth H., Stendel H., (2018), A novel method for testing automatic systems for controlling the spray boom height, *Biosystems Engineering*, vol.174, pp.115-125.

[14] Holbrook G. (2010), *Method and system for adjusting a vehicle aligned with an artificial horizon*, EP, 7744099.

[15] Ilica A., Boz A., (2018), Design of a nozzle-height control system using a permanent magnet tubular linear synchronous motor, *Journal of Agricultural Sciences*, vol.24, pp.374-385.

[16] Jang I., Kim H., Lee H., Han S., (2007), Height control and failsafe algorithm for closed loop air suspension control system, *2007 International Conference on Control, Automation and Systems*, Seoul, pp.373-378.

[17] Jiang H., Yang Y., Wang Y., Xu X., Li M., (2017), Experimental study on height control and energy consumption characteristics of closed-loop air circuit interconnected air suspension system（气路闭环互联空气悬架车高控制与能耗特性试验）, *Journal of Central South University (Science and Technology)*, vol.48, pp.270-276.

[18] Jiang H., Yang Y., Xu P., Xu X., Li M., (2015), Vehicle height adjustment of closed-loop air circuit laterally interconnected air suspension system（气路闭环横向互联空气悬架车身高度调节）, *Journal of Beijing University of Aeronautics and Astronautics*, vol.41, pp.2010-2016.

[19] Jin M., Lee J., Ahn K., (2014), Continuous nonsingular terminal sliding-mode control of shape memory alloy actuators using time delay estimation, IEEE/ASME *Transactions on Mechatronics*, vol.20, pp.899-909.

[20] Kim H., Lee H., (2011), Fault-tolerant control algorithm for a four-corner closed-loop air suspension system, *IEEE transactions on industrial electrics*, vol.58, pp.4866-4879.

[21] Kim H., Lee H., (2011), Height and levelling control of automotive air suspension system using sliding mode approach, *IEEE transactions on industrial electrics*, vol.60, pp.2027-2041.

[22] Li W., Chen Y., Zhang S., Mao E., Du Y., Wen H., (2018), Damping characteristic analysis and experiment of air suspension with auxiliary chamber, *IFAC-PapersOnLine*, vol.51, pp.166-172.

[23] Li X., Wei X., Jia L., Chen X., Liu L., Zhang Y., (2017), Recognition of Crops, Diseases and Pesticides Named Entities in Chinese Based on Conditional Random Fields（基于条件随机场的农作物病虫害及农药命名实体识别）, *Transactions of the Chinese Society for Agricultural Machinery*, vol.48, pp.178-185.

[24] Melzi S., Negrini S., Sabbioni E., (2014), Numerical analysis of the effect of tire characteristics, soil response and suspensions tuning on the comfort of an agricultural vehicle, *Journal of Terramechanics*, vol.55, pp.17-27.

[25] Porumamilla H., Kelkar A., (2005), Robust control and μ analysis of active pneumatic suspension, *2005 American Control Conference*, pp.2200-2205.

[26] Schaffer J., (2002), *Steering system for variable height agricultural sprayer*. US, Patent 6371237.

[27] Schaffer J., (2002), *Wheel support system for agricultural sprayer*, US, Patent 6491306.

[28] Tahmasebi M., Gohari M., Mailah M., Abd R., (2018), Vibration suppression of sprayer boom structure using active torque control and iterative learning, part ii: experimental implementation, *Journal of Vibration and Control*, vol.24, pp.4740–4750.

[29] Tahmasebi M., Mailah M., Gohari M., Abd R., (2018), Vibration suppression of sprayer boom structure using active torque control and iterative learning, part i: modelling and control via simulation, *Journal of Vibration and Control*, vol.24, pp.4689–4699.

[30] Tahmasebi M., Rahman R., Mailah M., Gohari M., (2013), Roll movement control of a spray boom structure using active force control with artificial neural network strategy, *Journal of Low Frequency Noise Vibration and Active Control*, vol.32, pp.189–201.
[31] Wang S., Chen L., Sun X., (2013), A multi-mode switching control mode for semi-active air suspension（半主动空气悬架多模式切换控制模型的分析）, *Journal of Jiangsu University (Natural Science Edition)*, vol.34, pp.637-642.
[32] Wang S., Dou H., Sun X., Yin C., (2015), Vehicle height adjustment and attitude control of electronically controlled air suspension（电控空气悬架车高调节与整车姿态控制研究）, *Transactions of the Chinese Society for Agricultural Machinery*, vol.46, pp.335-342+356.
[33] Wubben T., Maiwald M., Carlson B., Anderson J., (2007), *High clearance vehicle suspension with twin spindles for transferring steering torque*, US, Patent 7168717.
[34] Yang Q., (2008), *Research on matching and inflation/deflating of suspension system in ECAS-Bus*（ECAS客车悬架系统的匹配与充放气研究）, Zhenjiang: Jiangsu University.
[35] Yuki S., Yasuda H., Matsubayashi T., Ishizhka H., (2013), Development of tractor automatic controlled boom sprayer using CAN-BUS, *IFAC Proceedings Volumes*, vol.46, pp.264-269.
[36] Zatrieb J., Kasler R., (2012), New generation of hydro-pneumatic suspension systems with adaptive damping, *SAE Technical Paper*, 2012-36-0016.
[37] Zhao Y., Wang Z., Chen S., (2014), Investigation of height control for air suspension system based on sliding mode method（基于滑模控制的空气悬架车高控制系统研究）, *Transactions of Beijing Institute of Technology*, vol.34, pp.1125-1129.
[38] Zirkohi M., Lin T., (2015), Interval type-2 fuzzy-neural network indirect adaptive sliding mode control for an active suspension system, *Nonlinear Dynamics*, vol.79, pp.513-526.

TEMPERATURE CONTROL SYSTEM FOR MINT DEHYDRATION IN DOUBLE-CHAMBER MARQUEE USING LINEAR ACTUATORS
/
SISTEMA PARA EL CONTROL DE TEMPERATURA, APLICADO A LA DESHIDRATACIÓN DE MENTA MEDIANTE ACTUADORES LINEALES Y MARQUESINA DE DOBLE

Jose Alfredo Palacio-Fernández*[1)], Bayardo Emilio Cadavid[1)], William Orozco[1)] [1]
[1)] Intituto técnologico Pasciual Bravo; GIIAM research group,
[*)] *Calle 73 # 73A – 226 Medellín Colombia*
E-mail: josealpa@pascualbravo.edu.co
DOI: https://doi.org/10.356.33/inmateh-64-07

***Keywords:** drying, plants, humidity, temperature, marquee*

ABSTRACT

The objective of this research was to determine the thermal performance of a solar dehydration system that allows controlling the temperature for the dehydration of aromatic herbs such as mint. The use of a double chamber marquee allowed obtaining high thermal values, even with low radiation levels. For temperature control, a system of vertical mobile beds was used in order to reach the programmed temperature. This temperature was monitored using an embedded Arduino-type system that allows both monitoring and controlling motors, as well as recording temperature information. It was possible to keep the temperature approximately constant at 40°C, the ideal value for drying aromatic and medicinal herbs.

RESUMEN

El objetivo de este trabajo fue determinar el desempeño térmico de un sistema de deshidratación solar que permita controlar la temperatura para el deshidratado de hierbas aromáticas como la menta. El uso de una marquesina de doble cámara, permitió obtener valores térmicos altos incluso con niveles de radiación baja. Para el control de temperatura se empleó un sistema de camas móviles en la dirección vertical que permita encontrar la temperatura programada. Esta temperatura se monitoreo empleando un sistema embebido tipo Arduino que permite tanto el monitoreo como el control de los motores y el registro de la información de temperatura. la temperatura se pudo mantener aproximadamente constante en 40°C cuyo valor es ideal en el secado de hierbas aromáticas y medicinales.

INTRODUCTION

Due to the increase in the world population, it is necessary to reformulate strategies that could improve agricultural production and, in turn, food security, both for humans and animals. Another factor to take into account is climate change, which does not guarantee harvests on a regular basis with the same precision of both the harvest date and the volume collected. To meet this demand, there must be greater regulation of production, or the food produced must have the ability to be stored after processing. Although continuous production is not possible, it is possible to store food for a certain period when dehydrated *(Singh et al., 2018*).

Although there are mechanical dryers that use fossil fuel-based energy, the cost of drying is relatively high, and access to the combustion source can be difficult for remote areas (*Boroze et al., 2014*) . Additionally, the use of such dryers creates an environmental problem caused by the emission of carbon dioxide. Some researches harness energy that wastes non-renewable sources: part of the energy produced that is wasted is used in another process, thus being a renewable method such as the one used by *(Cacua et al., 2016*), who, from a micro-trigeneration system, used the residual energy of the exhaust gases of a diesel engine for mint drying and cooling.

In general, there are various drying techniques, such as spraying, mechanical, electrical, solar drying, etc. These drying techniques are used worldwide for drying agricultural and non-agricultural products.

[1] *Jose Alfredo Palacio-Fernández, Ph.D. (c); Bayardo Emilio Cadavid, M.Sc.; William Orozco, M.Sc.*

Among these dryers, the solar greenhouse dryer has several advantages over other types that make it a good alternative (*Singh et al., 2018*). These not only reduce the consumption of fossil fuels for drying purposes, but also provide the best quality in organoleptic characteristics (*Patil & Gawande, 2016*).

Kaewkiew et al., (2012) evaluated the drying performance of a parabolic shaped greenhouse dryer in Ubon Ratchthani, Thailand. (*Kulanthaisami et al., 2009*) used an 18 m long and 3.75 m wide tunnel-type solar dryer to dry 5000 coconuts per batch. The plastic sheet was opaque to long-wave radiation. These radiations were trapped inside the dryer and raised the temperature of the tunnel. They used a single layer polyethylene film for the cover of the solar dryer, due to the economy of the material and its easy handling. The dryer wrapped in a polycarbonate sheet had a concrete surface of 160 m^2. 50 W photovoltaic modules were used to power 9 DC fans, provided to maintain the required air circulation. To evaluate the performance of the solar greenhouse dryer, 500 kg of chilies were dried inside. The moisture content was reduced from 74% to 9% in 3 days in a solar greenhouse dryer, compared to the 5 days taken by natural solar drying. Besides, a reduction in the time necessary to complete drying, better flavour and colour were also observed.

Morad et al., (2017) built three identical solar tunnel greenhouse dryers to dry mint with overall dimensions of 2000 mm long, 1000 mm wide and 800 mm tall. The leaves and whole plants were placed in a range of between 6 and 10 cm thick according to the different loads of mint in a wire net, which was installed at the bottom of the lot in a greenhouse. A fixed suction air fan was used, powered by an electric motor of 0.5HP (0.37 kW) at 3000 rpm. The fan was connected to a digital thermostat that was set to operate the fan when the indoor air temperature approached 50°C. The mint load analysed was 2kg/m^2. A drying time of fewer than 12 hours was noted.

On a smaller production scale, researches using solar dehydration through collectors and chimney-type drying chambers are common. The chimney-type drying chamber is commonly used for passive drying (natural convection mode), as shown in Fig. 1 (*Abdulmalek et al., 2018*). Hot updraft air is used to dry the product located in one or more trays arranged vertically at the bottom of the chimney.

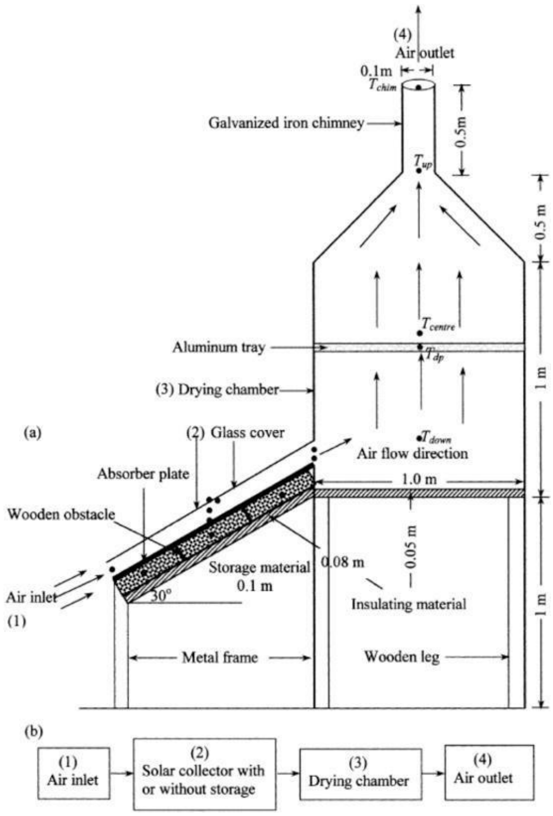

Fig. 1 - Solar dryer of chimney type drying chamber (*Abdulmalek et al., 2018*)

Solar collectors have not only been used for the drying process but also in refrigeration processes. For instance, (*Gil et al., 2017*) developed a solar-powered air conditioning system, also in pool heaters supported by vacuum tubes *(Roldan et al., 2013*). In general, collectors are a technology widely used in research that uses solar energy. A disadvantage could be that the drying volume is more limited than that processed with other technologies.

This is why a combination of technologies was used by *(Aymen et al., 2019*), who used both a collector and a marquee-type system, reaching temperatures close to 50°C in the case of the latter and 55°C in the case of the former, for maximum solar radiation of 800 W/m^2.

The temperature fluctuations that occur due to the rapid variations in radiation can be reduced by using materials with thermal storage. This is what authors (*Natarajan et al., 2017*) did, who analysed storage materials such as rock, sand, and aluminium fillers to identify the thermal performance of a tunnel type dryer and found that the thermal efficiency of the dryer without heat storage was 9.9%; the sand bed, 15.46%; the rock bed, 14.75%; and the aluminium fillers, 13.7%. This allows the sand bed to be identified as a good material for temperature storage. (*Abubakar et al., 2018*) used a black-painted rock bed to improve thermal absorption for a collector-type drying system, taking advantage of its low cost. For the collector dryer, the response of the system when the incident radiation is interrupted has been experimented, observing a first-order response to the dryer *(Deng et al., 2016*).

Solar dehydration systems are mainly used for drying plant material, in order to reduce the moisture content to levels that allow it to be stored for longer times without significantly reducing the active ingredients and the organoleptic characteristics. In the case of *Menta spicata* dehydration, the initial moisture content of 84% was analysed, as well as the final 10% (*Doymaz, 2006*). This study provides an analysis of the drying speed according to temperature.

Despite the fact that solar energy allows the thermal levels required in the dehydration process to be reached, it was necessary to reduce the humidity accumulated both by external filtration and by the number of plants or plant load to be processed. To extract excess moisture for both collector-type dryers just like (*Zaredar et al., 2018*), ventilators were used to produce forced airflow powered by photovoltaic solar panels, the forced ventilation in tunnel-type greenhouse or marquee systems (*Barnwal & Tiwari, 2008*)(Fig. 2), (*Morad et al., 2017*; *Chauhan et al., 2018*).

Fig. 2 - Hybrid photovoltaic-thermal (PV/T) dryer (*Barnwal & Tiwari, 2008*)

The literature consulted showed different methods that use solar energy as the main source of energy with a load capacity that varies depending on the form of heat concentration and that generally seek to be as economical as possible. This research employed some techniques developed in marquee-type dehydrators, modifying heat concentration. A double chamber structure is proposed for the dehydration of aromatic and medicinal plants, which allows to store them in an intermediate chamber embedded within another, thus serving as a thermal mattress, during hours of low radiation flow and which will simultaneously improve thermal levels inside.

The temperatures reached inside the system were recorded, which were above 65°C in the hours of greatest radiation in the upper part of the system, remaining as such at the intermediate level of dehydration, and above 40°C between 8 AM and 5 PM on days with little cloud cover.

Finally, temperature control close to 40°C was achieved for most of the day using a system of mobile beds controlled by linear actuators.

MATERIALS AND METHODS

This research was based on a need to preserve food with a novel methodology that can be transferred through education, ease of use, and that can be replicated in the future, including the ability to choose and adapt it to local conditions, and integrate it into the technology from the region.

This is basically what is known as technology transfer (*Londoño-Gallego et al., 2018*). Currently, this stage of the project corresponds to the second replica of a prototype implemented in another region of the Antioquia department in Colombia.

The analysed system was made of a structure of 2.5 m x 3.0 m x 2.8 m, as shown in Fig. 3 (taken from (*Palacio-Fernández & Cadavid, 2019*). The construction material was PVC for the structure and high-density polyethylene plastics for the inner chamber and the outer chamber, dark and transparent respectively. It sought to capture as much heat as possible between the transparent and dark plastic, taking advantage of the greenhouse effect, and thus to be transferred to the internal chamber gradually, allowing a smooth variation in temperature given sudden changes in radiation.

Fig. 3 - Double-layer polyethylene marquee used

A 60 cm linear stroke actuator was used to control the temperature (see Fig. 4), which allowed the beds to search for the appropriate temperature at the top during low radiation hours, and at the bottom during high radiation hours. The lower forced ventilation system allows excess moisture to be evacuated, since, although the temperature at the bottom is lower than that which occurs at the ceiling level, the current humidity is the opposite, and the excess humidity in the lower part tends to be quite high mainly at the beginning of the dehydration process.

Fig. 4 - Linear actuator for vertical movement of beds

RESULTS

Although the radiation values recorded by the early warning system of the city of Medellín (SIATA, n.d.) were not the best for experimentation on June 21 and 22, 2019, which were the dehydration dates (see Fig. 5), it was possible to achieve thermal values in the beds above 40°C, which allowed maintaining close control at this temperature, as suggested by (*Castro-Restrepo et al., 2013*). Fig. 7 shows the level close to 40°C that was achieved with the linear actuators when temperatures above 40°C were reached inside.

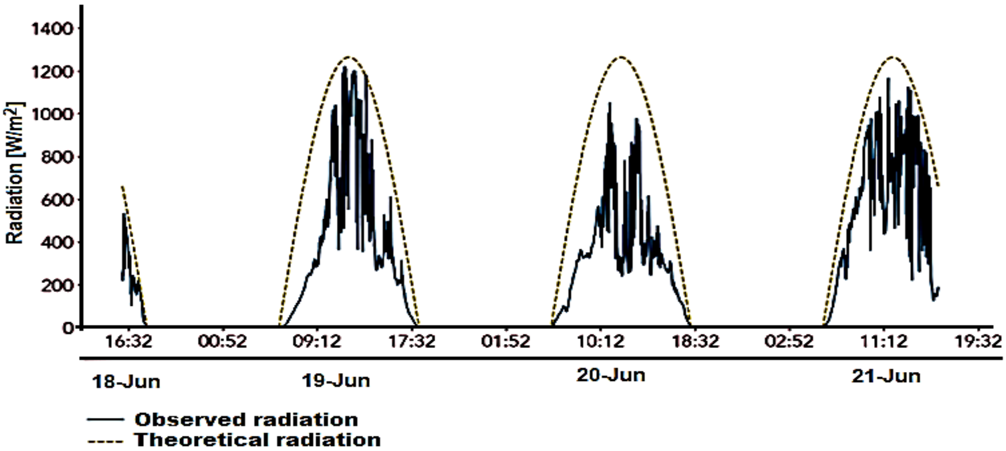

Fig. 5 - Radiation: SIATA tower pyranometer

The data was acquired and the system controlled by shield-type acquisition cards for Arduino Leonardo (see Fig. 6). This allows to control the process (Arduino Leonardo at level 1) and store the information and time of control events through Shield (level 3). Levels 2 and 4 are control cards for vertical linear actuators and for forced ventilation systems, and humidity and temperature sensors built by the authors of this article.

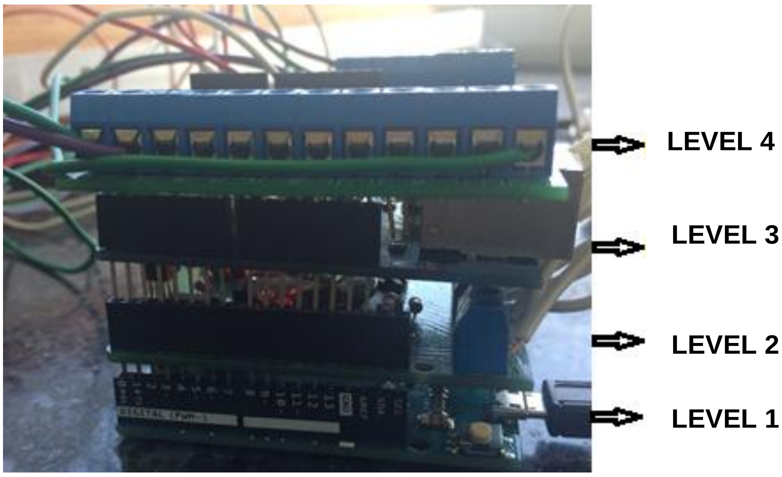

Fig. 6 - Data acquisition system

The data acquired (Fig. 7) show the scope of the constant temperature at 40°C reached during the interval of greatest radiation that allowed thermal levels greater than 40°C inside.

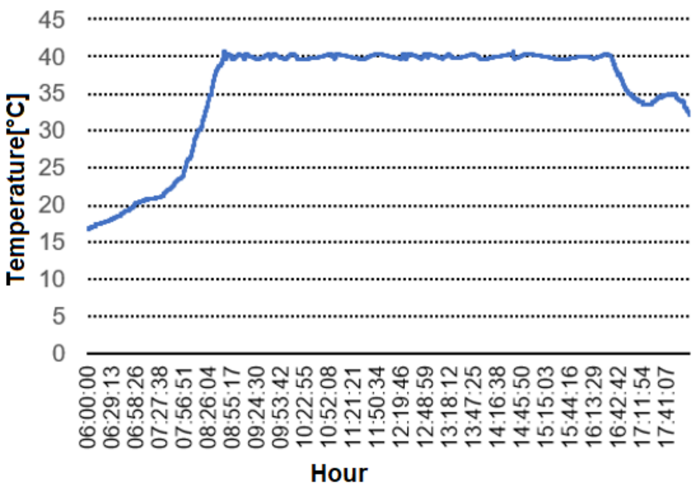

Fig. 7 - Controlled temperature, of approximately 40°C during 8 hours in a day

Fig. 8 shows the state of the fresh (a) and dehydrated (b) plants after the first day of drying for the test material, with the mint –still leaved– in the upper bed. The beds include a real-time weighing system that is recorded together with the environmental variables.

(a) (b)

Fig. 8 - Fresh and dehydrated mint

The mass loss of mint when it is dehydrated with the stem separately, compared to the dehydration with the attached stem, showed a small difference. In Fig. 9, two halves with equal mass were distributed in three beds and two divisions. The mint was placed in one of them with the stems and loose leaves, and in the other, the mint was placed without leafing. The mass of the loose leaves was 1000 g and the mass of the mint without leafing was 1000 g. The mass was analysed on a drying day which registered 389 grams for the mint with stem and 365 for the loose leaves. Mass losses of 65.1% in the former and 63.5% in the latter were achieved.

Fig. 9 - Distribution in each bed, equal mass in each one

When the moisture content decreases, the product changes mass, even though the dry matter remains constant (*García Navarrete, 2014*). The amount of water removed during the drying process was calculated using equation 1.

$$CH_f = 100 - \frac{w_i\left(100 - CH_i\right)}{w_f} \tag{1}$$

Where: w_i : initial mass (g)

w_f : final mass (g)

CH_i : initial moisture content [%]

CH_f final moisture content [%]

At the end of the first day, with an initial mass of 1000 g of loose leaves, a final mass of 365 grams and a final humidity (CHF) of 29.28% were obtained. On the second day, the same material had a final mass of 315 grams and a final humidity (CHF) of 12.11%. The values were average since there were beds in which leaves were placed separated from the stem, and others which included leaves attached to the stem.

CONCLUSIONS

Solar dehydration systems can be economically efficient due to the primary energy that feed them, and they can also be technically efficient if systems with good capacity for capturing and storing energy are built.

The use of mobile beds in a vertical displacement allows performing temperature control, even with sudden changes in radiation.

A little more moisture loss is registered if the mint is defoliated before dehydrating, although the process of removing the dried leaf is faster.

The control was not performed with the possibility that the beds reached the ceiling, due to the length of the actuators. With longer actuators or with another type of system, the temperature control spectrum could be extended during the day.

ACKNOWLEDGEMENT

Thanks to the Institución Universitaria Pascual Bravo, GIIAM research group and the Dirección de Tecnología e Innovación from the same institution for their collaboration for the realization of this Project.

REFERENCES

[1] Abdulmalek, S. H., Assadi, M. K., Al-Kayiem, H. H., & Gitan, A. A. (2018). A comparative analysis on the uniformity enhancement methods of solar thermal drying. *Energy*, 148, 1103–1115.

[2] Abubakar, S., Umaru, S., Kaisan, M. U., Umar, U. A., Ashok, B., & Nanthagopal, K. (2018). Development and performance comparison of mixed-mode solar crop dryers with and without thermal storage. *Renewable Energy*, 128, 285–298.

[3] Aymen, E. L., Hamdi, I., Kooli, S., & Guizani, A. (2019). Drying of red pepper slices in a solar greenhouse dryer and under open sun: Experimental and mathematical investigations. *Innovative Food Science & Emerging Technologies*, 52, 262–270.

[4] Barnwal, P., & Tiwari, G. N. (2008). Grape drying by using hybrid photovoltaic-thermal (PV/T) greenhouse dryer: an experimental study. *Solar Energy*, *82*(12), 1131–1144.

[5] Boroze, T., Desmorieux, H., Méot, J.-M., Marouzé, C., Azouma, Y., & Napo, K. (2014). Inventory and comparative characteristics of dryers used in the sub-Saharan zone: Criteria influencing dryer choice. *Renewable and Sustainable Energy Reviews*, 40, 1240–1259.

[6] Cacua, K., Olmos-Villalba, L., Herrera, B., & Gallego, A. (2016). Experimental evaluation of a diesel-biogas dual fuel engine operated on micro-trigeneration system for power, drying and cooling. *Applied Thermal Engineering*, 100, 762–767.

[7] Castro-Restrepo, D., Díaz-García, J. J., Serna-Betancur, R., Martínez-Tobón, M. D., Urrea, P. A., Muñoz-Durango, K., & Osorio-Durango, E. J. (2013). *Cultivation and production of aromatic and medicinal plants*.

[8] Chauhan, P. S., Kumar, A., & Nuntadusit, C. (2018). Heat transfer analysis of PV integrated modified greenhouse dryer. *Renewable Energy*, 121, 53–65.

[9] Deng, J., Ma, R., Yuan, G., Chang, C., & Yang, X. (2016). Dynamic thermal performance prediction model for the flat-plate solar collectors based on the two-node lumped heat capacitance method. *Solar Energy*, 135, 769–779.

[10] Doymaz, I. (2006). Thin-layer drying behaviour of mint leaves. *Journal of Food Engineering*, 74(3), 370–375.

[11] García Navarrete, F. J. (2014). Evaluation of the effects of the drying process on the quality of Stevia (Stevia rebaudiana Bertoni) and Peppermint (Mentha spicata). *Departamento de Ingenier{\'\i}a Civil y Agr{\'\i}cola*.

[12] Gil, J. C., Orrego, J. H. G., Roldán, C. A. I., Salazar, R. T., & Chejne, D. A. L. (2017). Integration of energy efficient technologies in air conditioning systems operated with thermal energy. *Revista CINTEX*, 22(1), 83–96.

[13] Kaewkiew, J., Nabnean, S., & Janjai, S. (2012). Experimental investigation of the performance of a large-scale greenhouse type solar dryer for drying chilli in Thailand. *Procedia Engineering*, 32, 433–439.

[14] Kulanthaisami, S., Subramanian, P., Mahendiran, R., Venkatachalam, P., Sampathrajan, A., & others. (2009). Drying characteristics of coconut in solar tunnel dryer. *Madras Agric. J*, 96(1/6), 265–269.

[15] Londoño-Gallego, J. A., Restrepo, S. M. V., Rodríguez, M. E. V., Cuartas, F. D. J. F., & Viana-Rúa, N. E. (2018). Identification of types, models and technology transfer mechanisms that leverage innovation. *CINTEX Journal*, 23(2), 13–23.

[16] Morad, M. M., El-Shazly, M. A., Wasfy, K. I., & El-Maghawry, H. A. M. (2017). Thermal analysis and performance evaluation of a solar tunnel greenhouse dryer for drying peppermint plants. *Renewable Energy*, 101, 992–1004.

[17] Natarajan, K., Thokchom, S. S., Verma, T. N., & Nashine, P. (2017). Convective solar drying of Vitis vinifera & Momordica charantia using thermal storage materials. *Renewable Energy*, *113*, 1193–1200.

[18] Palacio-Fernández, J. A., & Cadavid, B. E. (2019). Remote monitoring of environmental variables in a solar dryer, an IoT bet applied to agriculture. *Sostenibilidad, Cultura y Sociedad*, 231–250.

[19] Patil, R., & Gawande, R. (2016). A review on solar tunnel greenhouse drying system. *Renewable and Sustainable Energy Reviews*, 56, 196–214.

[20] Roldan, C. A. I., Río, D., & o Rico, S. (2013). Development of a mathematical model for energy optimization in pool heating systems. *CINTEX Journal*, 18, 187–203.

[21] SIATA. (n.d.). *Sistema de Alerta Temprana del valle de Aburrá.* 2019. Retrieved June 21, 2019, from https://siata.gov.co/siata_nuevo/

[22] Singh, P., Shrivastava, V., & Kumar, A. (2018). Recent developments in greenhouse solar drying: a review. *Renewable and Sustainable Energy Reviews*, 82, 3250–3262.

[23] Zaredar, A., Effatnejad, R., & Behnam, B. (2018). Construction of an indirect solar dryer with a photovoltaic system and optimised speed control. *IET Renewable Power Generation*, 12(15), 1807–1812.

IMPACT OF VIBRATION ON TILLAGE PERFORMANCE OF SUBSOILERS USING THE DISCRETE ELEMENT METHOD (DEM)
/
振动对深松机耕作性能影响的离散元法研究

Shi Zhiming, Chen Tonghao, Li Shoutai, Yang Ling, Yang Mingjin*) [1]
Southwest University, College of Engineering and Technology, Chongqing Key Laboratory of Agricultural Equipment for Hilly and Mountainous Regions / P. R. China
*Correspondence: Tel: +86-13883002509; E-mail: ymingjin@swu.edu.cn
DOI: https://doi.org/10.35633/inmateh-64-08

Keywords: *subsoiling, vibration, tillage performance, DEM, field experiment*

ABSTRACT
Plow pan is one of the main obstacles to high production of agricultural plants in Chongqing, China. As a minimal tilling method, subsoiling can break the plow pan and help the growth of agricultural plants. There are two subsoiling methods: vibrating subsoiling (VS) and traditional subsoiling (TS). A soil model with upland field features in Chongqing was established for DEM-based simulation. The simulation was validated by field experiments, in items of soil looseness, coefficient of soil disturbance, and cross-section of tillage, the errors of the simulated and experimental values of the soil looseness and soil disturbance coefficient of TS and VS were 12.9% and 14.7%, respectively. Compared with TS, VS resulted in lower soil looseness, higher coefficient of soil disturbance, smaller width of upper furrow, and lighter damage of tillage layer, and no obvious overturn of soil blocks was observed for the VS. Compared with TS, vibration helps improve the tillage performance of subsoilers.

摘要
犁底层是中国重庆地区农业高产的主要障碍之一。作为一种少耕方法，深松可以打破犁底层，并有助于农业作物生长。有两种深松法：振动深松法和传统深松法。用离散元法建立了重庆地区田间土壤模型。通过田间试验，在土壤膨松度，土壤扰动系数和耕作横截面方面对仿真结果进行了验证，TS和VS后的土壤膨松度和土壤扰动系数的仿真值和实验值的误差分别为12.9%和14.7%。与传统深松相比，振动深松降低了土壤膨松度，增加了土壤扰动系数，减小了上部沟形宽度，对土壤耕作层破坏较小，地表无明显翻土。与传统深松相比，振动有助于提高深松机的耕作性能。

INTRODUCTION
Small handheld tillers are universally employed in Chongqing, China. More than 99.5% of power tillers are of small handheld tillers in Chongqing since riding power tillers are unsuitable for tilling operation in the small hilly farmlands. Plow pan with thickness of 5-10 cm was formed by long term tillage of small handheld tillers, and it was one of the main obstacles to high production of agricultural plants (*Ma C. et al, 2017; Geroy I.J. et al, 2011*). Subsoiling, as a minimal tilling method (*Sun J.Y. et al, 2018*), can break the plow pan, improve the soil structure, and then help the growth of agricultural plants (*Hang C.G. et al, 2017*).

Vibration, electroosmosis and bionic method are main approaches to reducing traction resistance in subsoiling (*Sun J.Y. et al, 2018*). According to whether vibration occurs during operation, subsoiling was divided into vibrating subsoiling (VS) and traditional subsoiling (TS). The latter was a non-vibrating subsoiling method (*Liu X.H. et al, 2014*). As for VS, a periodic vibration was applied to the subsoiler in the vertical direction, and the vibration affected traction resistance, power consumption and tillage performance (*Niyamapa T. et al, 2010*).

While considering the soil disturbance, how to choose the subsoiling method is a problem that needs attention. However, the present research focuses on the drag reduction effect of VS, the influence of different vibrating sources, and subsoiling machine structure and other factors on subsoiling effect.

---
[1] *ZM Shi, Ms.; TH Chen, Ms.; ST Li, Ms.; L Yang, Prof.; MJ Yang, Prof.*

Few comprehensive simulation and experiment methods were used to comprehensively analyze the impact of VS and TS on soil disturbance behavior, soil furrow shape.

At present, most of the researches on soil subsoiling were carried out by using direct measurement method of field experiment or soil bin experiment and finite element method simulation. The direct measurement method was limited by factors such as weather, time, manpower and material resources. The finite element method was mainly for continuous media, and the soil could only be studied as a whole object. While the soil belongs to a discontinuous medium, the finite element method could not accurately analyze the interaction between subsoiler and soil particles, and it could not analyze the movement of soil particles after subsoiling to evaluate the soil subsoiling effect (*Mouazen A.M. et al, 1999*). Discrete element method (DEM), as a general method to study the discontinuous medium, could well solve the deficiencies of finite element method in the study of soil subsoiling (*Kasisira L.L. et al, 2006*).

The arc-shaped subsoiler had excellent farming performance compared with the linear shape under the condition of small length-to-depth ratio due to its convenient production and strong crushing ability. Therefore, the arc-shaped subsoiler was selected as the experiment machine in this study. According to the physicochemical properties of cultivated soil and the requirements of subsoiling operation in Chongqing hilly and mountainous area, the soil model was established based on the DEM, and the effects of VS and TS on soil disturbance behavior, soil furrow profile were analyzed.

MATERIALS AND METHODS

Move model

Subsoiler move

VS tilled the soil under the joint action of the vibrating element and the soil resistance. The periodic reciprocating vibrating element transmitted the force to the shank to drive the tine. The vibrating soil cutting was realized at locations of tine face and tine edge.

Compared with TS, the VS had one more periodic motion in the vertical direction. The equation of motion of vibrating subsoiler was simplified as:

$$x = v \cdot t \text{ , [mm]} \tag{1}$$

$$y = A \cdot \sin \omega t \text{ , [mm]} \tag{2}$$

where:

v is the horizontal movement speed, [mm/s];

t is the time, [s];

A is the amplitude, [mm];

ω is the angular velocity, [rad/s].

Soil move

The traditional subsoiler could be regarded as rigid, and it completes soil cutting, crushing, lifting and other actions at the same time under the drive of traction power (*Li X. et al, 2012*). The subsoiler moved forward, and the soil was periodically fractured along the shear surface under the cutting edge of the subsoiler, then the soil was partially lifted due to the mutual squeezing action (*Guo Z.J. et al, 2001*). The forces acting on the soil at this time included the frictional force, shearing force, squeezing force and the cutting force of the tine edge. The sum of the horizontal components of these forces was the resistance received by subsoiler during the tillage process (*Li B. et al, 2018*). The cutting process of traditional subsoiler in the soil was simplified to a low-speed moving inclined surface in the soil. The basic feature of this effect was that the soil repeatedly fails due to shearing, and the soil was repeatedly compressed to form many small soil blocks (*Momozu M. et al, 2002*), as shown in Fig. 1a.

In the case of VS, the subsoiler changed from one-dimensional cutting to two-dimensional vibration cutting. The original single motion process of the subsoiler was divided into two different stages: shearing the soil and lifting the soil (*Shmulevich, I., 2010*). After the subsoiler entered the soil, it rotated due to soil resistance and compresses the elastic element. The elastic element accumulated energy. After the soil reached the yield limit, the soil was broken, and the elastic element released energy to make the subsoiler rotate to complete the shearing process. After the soil was broken, the elastic element further released energy to make the subsoiler complete the lifting of the soil. At this time, the force of the soil on the subsoiler was almost perpendicular to the direction of traction, so the resistance was greatly reduced, as shown in Fig. 1b.

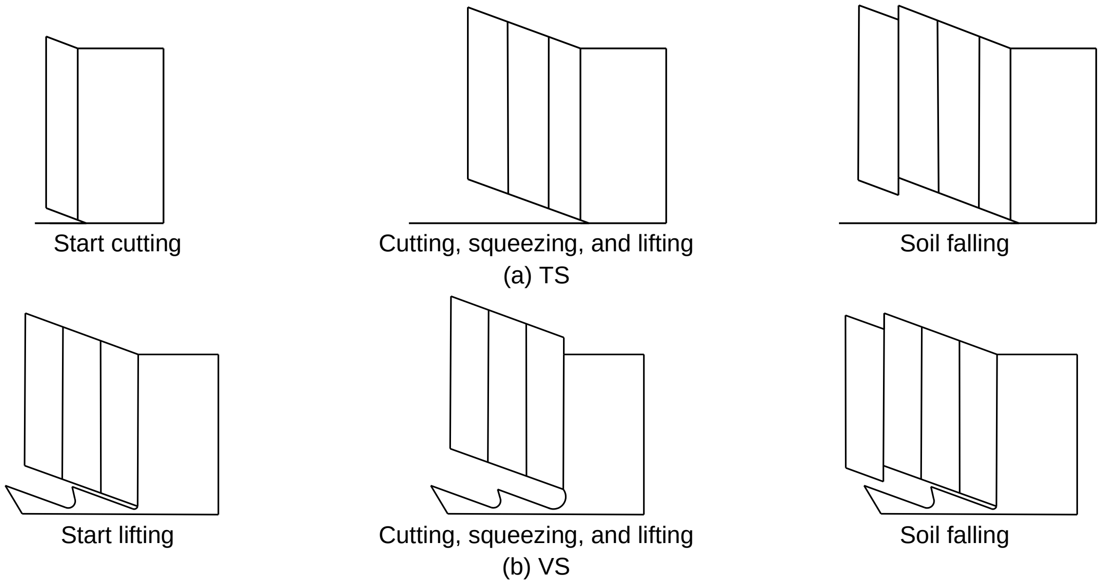

Fig. 1 - Soil move under TS and VS

Subsoiling simulation

Experiment method

In this study, DEM was used for simulation experiments, combined with the soil quality and physicochemical properties of the hilly and mountainous areas of Chongqing. A soil bin model was established in the software of EDEM (Engineering Discrete Element Method), and the geometric model of the subsoiler created was imported. After completion, the simulation experiment was started, and the results were exported and analyzed.

Subsoiler model

According to the Chinese standard (JB/T9788-1999), an arc-shaped subsoiler was selected for the experiment, and the subsoiler consisted of an arc-shaped shank and a chisel-shaped tine, as shown in Fig. 2. The subsoiler installation height *H* was 680mm, the straight shank height H_1 was 320mm, the shank width *b* was 60mm, the tine length *L* was 165mm, the arc-shaped shank radius *R* was 303mm, and the tine blade angle *α* was 20°.

In order to ensure the accuracy of the simulation, the three-dimensional structural model of the subsoiler for simulation was established by using software of Creo3.0 with ratio of 1:1 and saved it in igs. format.

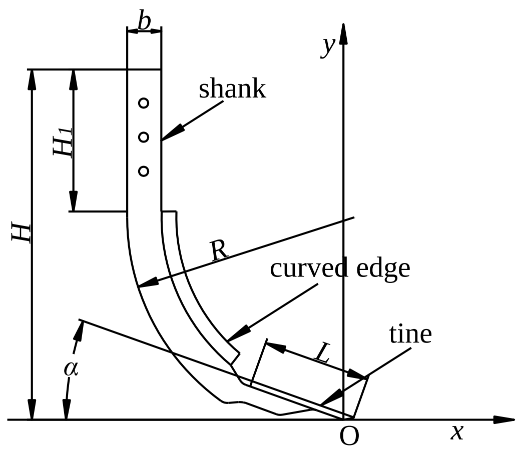

Fig. 2 - Schematic diagram of subsoiler

Soil particle and soil contact model

In order to make EDEM simulation experiments reliable, it was necessary to create a more accurate virtual soil model. Soil particles were mainly composed of lump, nuclei, and column (Yang, Q. et al, 2019). Using the self-contained particles (3mm in diameter) in the EDEM as the basic structural unit, models of lump, nuclear and columnar soil particle were obtained (*Tadesse, D., 2010*), as shown in Fig. 3.

Considering the type of purplish soil in the hilly and mountainous regions of Chongqing, the Hertz-Mindlin with Bonding model in EDEM was used to create a contact model between soil particles.

This model made the particles had bond like the actual soil hydraulic bridge force in the field (as shown in Fig. 3e), which could withstand a certain amount of force and torque (*Wang Y., 2014*).

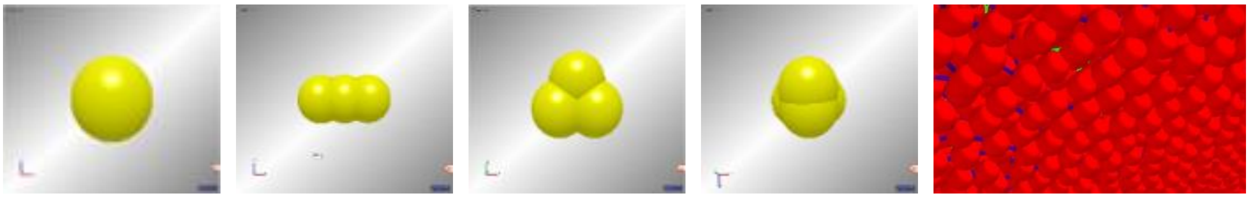

(a) Lump 1 (b) Column (c) Nuclei (d) Lump 2 (e) Bonding between particles

Fig. 3 - Model of soil particles and their bonding model

Soil model parameters

The main parameters of the selected soil contact model included the coefficient of restitution, the dynamic and static friction coefficients of soil to soil and soil to subsoiler. The parameters were mainly from data in the references (*Wang Y., 2014; Ucgul M. et al, 2014*).

The main parameters of the soil bin model were listed in Table 1.

Table 1

Main parameters of soil bin model

Parameter	Value	Parameter	Value
Soil bin dimensions (length, width, height) [mm]	1000×1200×400	Coefficient of static friction of soil-soil	0.55
Subsoiler speed [mm/s]	830	Coefficient of restitution of soil-65Mn steel	0.35
Tillage depth [mm]	250	Coefficient of rolling friction of soil-65Mn steel	0.09
Soil particle density [kg/m^3]	1920	Coefficient of static friction of soil-65Mn steel	0.55
Poisson's ratio of soil	0.4	Radius of the filling element [mm]	3
Shear modulus of soil [Pa]	1×10^7	Number of soil particles	680000
Density of 65Mn steel [kg/m^3]	7830	Acceleration of gravity [m/s^2]	9.81
Poisson's ratio of 65Mn steel	0.35	Simulation time [s]	10
Shear modulus of 65Mn steel [Pa]	7.27×10^{10}	Amplitude [mm]	20
Coefficient of restitution of soil-soil	0.3	Frequency [Hz]	4
Coefficient of rolling friction of soil-soil	0.35	Angular velocity [rad/s]	8π

EDEM modeling

In order to ensure the simulation in consistency with the field experiment, according to the depth and width of the subsoiling, a soil bin model with dimensions of 1000 mm × 1200 mm × 400 mm (length × width × height) was created in EDEM, as shown in Fig. 4.

After the simulation parameter setting was completed, the soil particles were dynamically generated by the particle factory in the EDEM, and then the particles were settled and bonded to form a bond between the particles. In real soil particles, the size of soil particles of different types was not the same.

In order to make the soil bin model closer to the real soil, the size of soil particles generated was in normal distribution (*Wang, Y. 2014*).

Then import the 3D model of the subsoiler into the EDEM, set motion parameters of the subsoiler and the tillage depth to 250mm. After the simulation was completed, the data of TS and VS were saved.

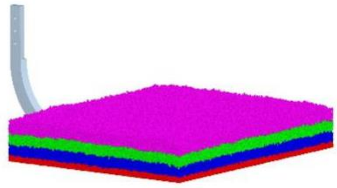

Fig. 4 - EDEM simulation soil model

Field experiment

Experiment site and materials

The experiment site located at the experimental field next to the engineering training center of Southwest University, with length of 15 m and width of 6.5 m. The soil in the experimental field was purplish soil.

Experimental process

Before the experiment, the experimental field was simply treated, the soil debris such as grass roots and stones were removed, and leveling treatment was carried out. The measurement of the basic parameters of the soil in the experimental field was completed according to the experiment requirements. The average of the measurement results is shown in Table 2.

Table 2

Soil parameters of experiment field

Parameter	Density [kg/m^3]	Moisture content [%]	Firmness [Pa]
Value	1920	36.5	642700

After the soil parameter measurement was completed, the TS and VS were experimented in turn. The traction power was from a riding type tractor (Dongfanghong LX2004, China). According to requirements of subsoiling of farming soil in Chongqing, the moving speed of subsoiler was selected as 830 mm/s with the tillage depth 250mm. After tilling operation, a self-made simple soil cross-sectional profile measuring instrument was used to measure the soil data of different subsoiler. In order to ensure the accuracy of the measurement results, the soil data under the action of each subsoiler were measured in three different positions with an interval of 1.0m, and the soil data were recorded, as shown in Fig. 5.

(a) TS (b) VS (c) Measurement after subsoiling

Fig. 5 - Scenery of field experiment

RESULTS

Comparative analysis of soil disturbance

In order to study the impact of TS and VS on the soil disturbance behavior of different soil layers, the longitudinal sections at tilling time 0.05 s, 0.25 s, 0.45 s, 0.65 s, and 0.85 s were selected and plotted, as shown in Fig. 6. The effects of subsoiling on the overall soil disturbance were obtained as well, as shown in Fig. 7. Compared with TS, VS had one more vertical motion of sine vibration, and its vibration parameters were listed in Table 1.

As seen from Figs. 6 and 7, different subsoiling mechanisms of VS and TS were observed. Firstly, for TS, the subsoiler moved forward under the action of traction. The tine and the curved cutting edge of the subsoiler successively contacted the plow pan in the soil.

The cutting and squeezing of the plow pan made it rise and break down at the same time, which disturbed the cultivated layer (magenta particles in Fig. 6) and formed a certain ridge on the surface. As the subsoiling progressed, the ridge formed on the ground broke and failed under the shearing action of the shank, and finally backfilled into the subsoiling soil pit under the gravity. Secondly, for VS, the subsoiling process was divided into two different stages: shearing and lifting the soil. The subsoiler moved forward under the action of traction. The tine and the curved edge of the subsoiler contacted successively the plow pan in the soil. The shearing and squeezing of the plow pan caused it to break and fail. Due to the presence of vibration, the plow pan was sheared, squeezed, and lifted. With the tilling of the soil, the shear plane periodically sheared and lifted, which formed a periodic intermittent shear plane. Compared with TS, VS had a larger disturbance range on the soil particles of the plow pan, and the effect of loosening soil was strengthened.

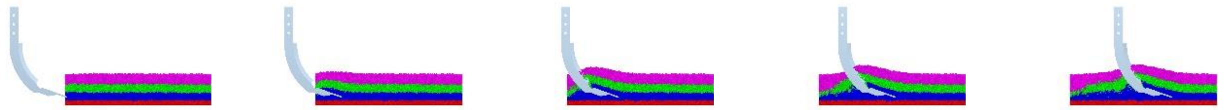

t= 0.05s t= 0.25s t= 0.45s t= 0.65s t= 0.85s

(a) TS at different time points

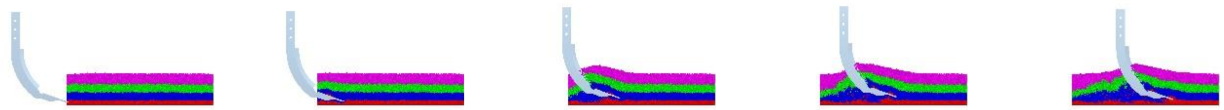

t= 0.05s t=0.25s t= 0.45s t= 0.65s t= 0.85s

(b) VS at different time points

Fig. 6 - The effects of subsoiling on the vertical disturbance of each layer of soil

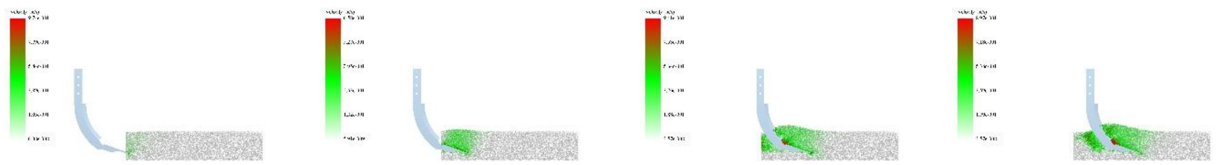

t= 0.05s t= 0.25s t= 0.45s t= 0.65s

(a) TS at different time points

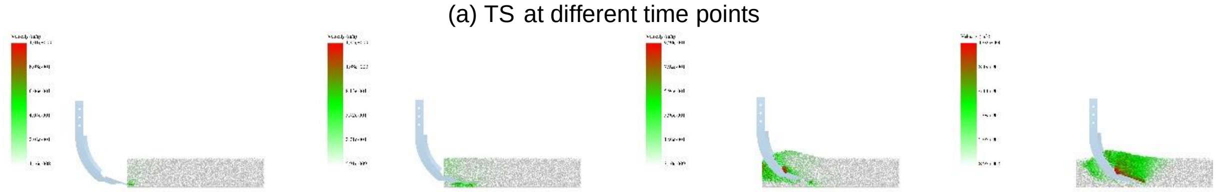

t= 0.05s t= 0.25s t= 0.45s t= 0.65s

(b) VS at different time points

Fig. 7 - The effects of subsoiling on the overall soil disturbance range

Analysis of soil disturbance effect

The soil looseness and soil disturbance coefficient were commonly used to evaluate the disturbance effect of soil (*Hang, C. G. et al, 2017*). The effect of soil disturbance after subsoiling was shown in Fig. 8. The soil looseness and soil disturbance coefficient were expressed as:

$$\rho = \frac{A_h - A_q}{A_q} \times 100\%\text{, [\%]} \tag{3}$$

$$y = \frac{A_s}{A_q} \times 100\%\text{, [\%]} \tag{4}$$

where:

ρ is the soil looseness, [%];

A_h is the cross-sectional area formed by the post-tillage soil surface and the boundary of the standard furrow described in Chinese Standards for Subsoiling Implements (JB/T10295-2014), [mm^2];

A_q is the cross-sectional area formed by the un-tilled soil surface and the boundary of the standard furrow, [mm^2]; y is the soil disturbance coefficient, [%];

A_s is the cross-section area formed by the un-tilled soil surface and the actual furrow from field experiment, [mm^2].

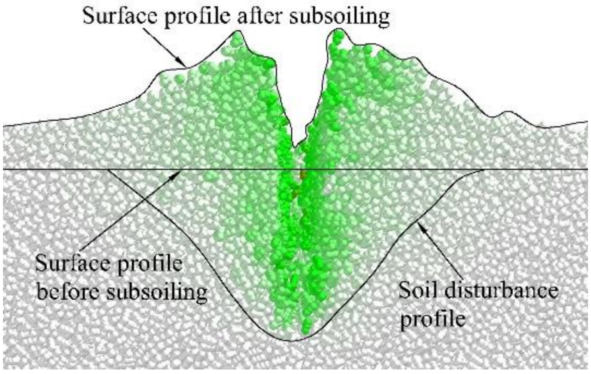

Fig. 8 - Effect diagram of soil disturbance

The profile of soil disturbance after subsoiling was shown in Fig.9. According to provisions of the Chinese standard (GB/T 24675.2-2009) “Conservation Tillage Machine-Subsoiler”, the quality evaluation of subsoiling should meet requirements: operation was soil looseness within range of 10%-40%, and soil disturbance coefficient larger than 50%. The simulation and experiment values and relative errors of soil looseness and soil disturbance coefficient after TS and VS were calculated from equations (3) and (4), as listed in Table. 3.

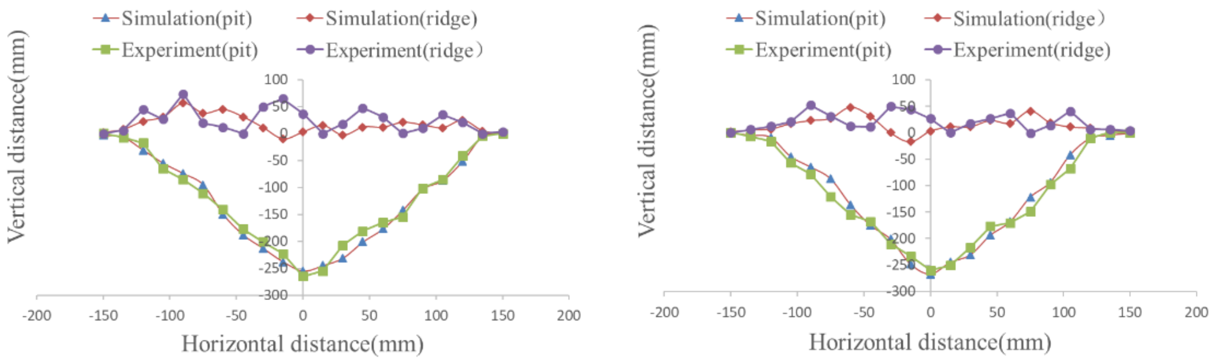

(a) TS (b) VS

Fig. 9 - Effect of subsoiling on soil disturbance profile

Table 3

Simulation and experiment results of soil looseness and disturbance coefficient

Subsoiling method	Soil looseness			Soil disturbance coefficient		
	Simulation value [%]	Experiment value [%]	Relative error [%]	Simulation value [%]	Experiment value [%]	Relative error [%]
TS	27.1	24.4	11.1	62.1	54.2	14.6
VS	26.5	23.3	13.7	65.3	56.5	15.6

As seen from Table 3, the soil disturbance after VS and TS met requirements of provisions of the Chinese standard. Compared with TS, VS had a smaller soil looseness and a larger soil disturbance coefficient. In addition, the mean errors of the simulated and experimental values of the soil looseness and soil disturbance coefficient of TS and VS were 12.9% and 14.7%, respectively. Then, the simulation model in this study could reveal the disturbance behavior of soil during the actual subsoiling process with good agreements.

The effect of subsoiling on furrow profile

The experiment and simulation results of the furrow profile after TS and VS were calculated and summarized, as listed in Table 4. The furrows of simulation and experiment were shown in Fig. 10. As seen from Table 4, TS and VS had significant influence on the V-shaped soil furrow. Compared with TS, the width of the upper furrow profile after the VS was obviously smaller, but there was no significant difference in the width of the lower furrow profile. As seen from Fig. 11, compared with TS, VS had less damage to the cultivated soil layer, and there was no significant overturning of the soil surface, which was beneficial to improve the soil's ability to store water and maintain moisture, and helpful for increase of crop yield.

Table 4

Width of furrow after subsoiling

Subsoiling method	Upper furrow width		Lower furrow width	
	Simulation value [mm]	Experiment value [mm]	Simulation value [mm]	Experiment value [mm]
TS	245	293	64	71
VS	213	247	61	75

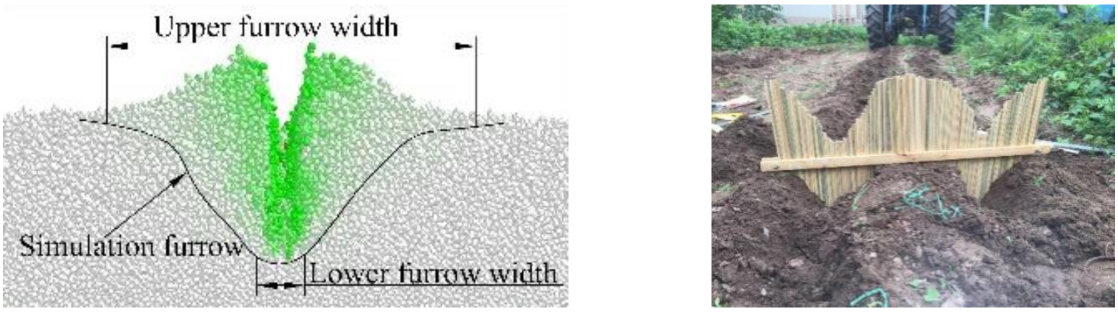

(a) Simulation furrow (b) Field experiment furrow

Fig. 10 - Furrow measurement after subsoiling

(a) Surface after TS (b) Surface after VS

Fig. 11 - Soil surface after subsoiling

CONCLUSIONS

Based on soil type in Chongqing, China, a soil model was established using EDEM and combined with field experiments. The effects of TS and VS on soil disturbance behavior, furrow profile were studied and analyzed. Main conclusions were drawn as follows:

(1) The DEM can accurately simulate the disturbance in the process of soil subsoiling, with good consistence with field experiment. The errors of the simulated and experimental values of the soil looseness and soil disturbance coefficient of TS and VS were 12.9% and 14.7%, respectively. Compared with TS, the soil of VS had less soil looseness and larger soil disturbance coefficient.

(2) TS and VS had a great impact on the furrow profile. Compared with TS, the width of the upper furrow profile of VS was obviously smaller, VS had less damage to the cultivated soil layer, and there is no obvious overturning of soil and lump on the surface. There was no significant difference in the width of the lower furrow profile between TS and VS.

ACKNOWLEDGEMENTS

The study was funded by Fundamental Research Funds for Central Universities, China (No.XDJK2018AC001) and Chongqing Science & Technology Commission (No. CSTC2016SHMSZX80037).

REFERENCES

[1] Geroy, I. J., Gribb, M. M., Marshall, H. P., Chandler, D. G., Benner, S. G. (2011). Aspect influences on soil water retention and storage. *Hydrological Processes*, Vol.25, Issue 25, pp.3836-3842, Ed. Southwest University; http://dx.doi.org/10.1002/hyp.8281.

[2] Guo, Z. J., Tong, J., Zhou, Z. L., Ren, L. Q. (2001). Status and prospect of subsoiler technology research (深松技术研究现状与展望). *Transactions of the Chinese Society of Agricultural Engineering*, Vol.17, Issue 6, pp.169-174, Ed. Chinese Society of Agricultural Engineering, Beijing/P.R.C.

[3] Hang, C. G., Huang, Y. X., Zhu, R. X. (2017). Analysis of the movement behavior of soil between subsoilers based on the discrete element method. *Journal of Terramechanics*, Vol.74, Issue 12, pp.35-43, Ed. Elsevier Sci Ltd, Oxford/England. https://doi.org/10.1016/j.jterra.2017.10.002.

[4] Kasisira, L. L., Plessis, H. L. M. D. (2006). Energy optimization for subsoilers in tandem in a sandy clay loam soil. *Soil & Tillage Research*, Vol.86, Issue 2, pp.185-198, Ed. Elsevier Sci Ltd, Oxford/England. https://doi.org/10.1016/j.still.2005.02.031.

[5] Liu, X. H., Yu, Y., Qiu, L. C. (2014). Design and experimental study on the vibration subsoiler. *Applied Mechanics & Materials*, Vol.707, Issue 12, pp.356-359, Ed. Helen Zhang, M. Han and X.J. Zhao. https://doi.org/10.4028/www.scientific.net/AMM.707.356.

[6] Li, X., Fu, J., Zhang, D., Cui, T., Zhang, R. (2012). Experiment analysis on traction resistance of vibration subsoiler (基于振动减阻原理的深松机牵引阻力试验). *Transactions of the Chinese Society of Agricultural Engineering*, Vol.28, Issue 1, pp.32-36, Ed. Chinese Society of Agricultural Engineering, Beijing/P.R.C.

[7] Li, B., Chen, Y., Chen, J. (2018). Comparison of two subsoiler designs using the discrete element method (DEM). *Transactions of the Asabe*, Vol.61, Issue 5, pp.1529-1537, Ed. American Society of Agricultural and Biological Engineers. DOI:10.13031/trans.12629.

[8] Ma, C., Meng, H., Kan, Z., Qi, J., (2017), The research current situation and development countermeasure of the orchard organic fertilizer deep application of disc ditching machine. *Journal of Agricultural Mechanization Research*, Vol.39, Issue 10, pp.12-17, 28.

[9] Mouazen, A. M. (1999). Finite element analysis of subsoiler cutting in non-homogeneous sandy loam soil. *Soil & Tillage Research*, Vol.51, Issue 1-2, pp.1-15, Ed. Elsevier Sci Ltd, Oxford/England. https://doi.org/10.1016/S0167-1987(99)00015-X.

[10] Momozu, M., Oida, A., Yamazaki, M., Koolen, A. J. (2002). Simulation of a soil loosening process by means of the modified distinct element method. *Journal of Terramechanics*, Vol.39, Issue 4, pp.207-220, Ed. Elsevier Sci Ltd, Oxford/England. https://doi.org/10.1016/S0022-4898(03)00011-9.

[11] Niyamapa, T., Namikawa, K. (2010). Force mechanics and soil disturbance of vibrating tillage tool. *Journal of Terramechanics*, Vol.37, Issue 3, pp.151-166, Ed. Elsevier Sci Ltd, Oxford/England. https://doi.org/10.1016/S0022-4898(00)00005-7.

[12] Sun, J. Y., Wang, Y. M., Ma, Y. H., Tong, J., Zhang, Z. J. (2018). DEM simulation of bionic subsoilers (tillage depth >40 cm) with drag reduction and lower soil disturbance characteristics. *Advances in Engineering Software*, Vol.119, Issue 5, pp.30-37, Ed. Elsevier Sci Ltd, Oxford/England. https://doi.org/10.1016/j.advengsoft.2018.02.001.

[13] Shmulevich, I. (2010). State of the art modeling of soil–tillage interaction using discrete element method. *Soil & Tillage Research*, Vol.111, Issue 1, pp.41-53, Ed. Elsevier Sci Ltd, Oxford/England. https://doi.org/10.1016/j.still.2010.08.003.

[14] Tadesse, D. (2010). Modelling soil structure, soil strength and material properties in DEM. *Advanced Engineering Materials*, Vol.13, Issue 1-2, pp.57-63, Ed. National Academic Research and Collaborations Information System. http://dx.doi.org/10.1002/adem.201000169.

[15] Ucgul, M., Fielke, J. M., Saunders, C. (2014). Three-dimensional discrete element modelling of tillage: determination of a suitable contact model and parameters for a cohesionless soil. *Biosystems Engineering*, Vol.121, Issue 5, pp.105-117, Ed. Elsevier Sci Ltd, Oxford/England. https://doi.org/10.1016/j.biosystemseng.2014.02.005.

[16] Wang, Y. Simulation analysis of structure and effect of the subsoiler based on DEM (基于离散元法的深松铲结构与松土效果研究), Master thesis of Jilin Agriculture University. 2014.
[17] Yang Q., Li, Z., Li H., He J., Wang Q., Lu C., (2019), Numerical Analysis of Particle Motion in Pneumatic Centralized Fertilizer Distribution Device Based on CFD-DEM. *Transactions of the Chinese Society for Agricultural Machinery*, Vol.50, Issue 8, pp.81-89, Ed. Chinese Society of Agricultural Engineering, Beijing/P.R.C.

EXPERIMENTAL VALIDATION OF COMBINED TRIP ESTIMATOR FOR SMALL POWER ELECTRIC TRACTOR
/
VALIDAREA EXPERIMENTALĂ A ESTIMATORULUI DE PARCURS COMBINAT LA TRACTORUL ELECTRIC DE PUTERE MICĂ

Tudor Emil[1]; Matache Mihai Gabriel*[2]; Sburlan Ion Cătălin[1]; Vasile Ionuț[1]; Cristea Mario[2] [1]
[1] INCDIE ICPE-CA / Romania;
[2] INMA Bucharest / Romania;
Tel: +40722235842 E-mail: gabimatache@yahoo.com
DOI: https://doi.org/10.35633/inmateh-64-09

Keywords: *electric tractor, trip estimator, mixed load, efficiency*

ABSTRACT

The combined use of the electric tractor in high-speed travel and high-torque towing must involve a trip range estimation and an optimal driving behavior of the vehicle. The paper proposes an estimation method based on the measured usable energy reserve and on prediction of the power consumption for the two selected operating modes: rolling and towing. As driver's interface will be used an interactive graphical display which can be used for the initial settings and further adjustments of some of the working parameters. The demonstrations are sustained by trip recordings used for calibration process and for error mitigation.

REZUMAT

Folosirea combinată a tractorului electric în regim de deplasare cu viteză ridicată și în regim de tractare cu cuplu mare trebuie să implice o estimare a parcursului rămas și recomandări pentru modul de conducere al vehiculului. Lucrarea propune o metodă de estimare a autonomiei bazată pe măsurarea rezervei de energie disponibile și pe predicții ale consumului în cele două moduri de funcționare specifice: deplasare și tractare. Pentru interfața cu utilizatorul se folosește un afișor grafic care permite setările inițiale și ajustările ulterioare ale unor parametri. Demonstrațiile sunt susținute de înregistrările utilizate în timpul procesului de calibrare și pentru atenuarea erorilor.

INTRODUCTION

Users of the new vehicles, by now, are struggling to deal with the range anxiety which is involved by the new energy storage used for powering the electric vehicles (EV). Range anxiety is a driver's fear of being stranded by a depleted EV battery. For now, the classical indication regarding the remaining range of the Internal Combustion Engine vehicles (ICE) was the remaining volume of the gas tank (the "fuel" gauge on the dashboard instrument) and some range estimator located in the Board Computer (CB) based on recorded mileage and recorded gas consumption over a trip counter which can be restarted by the driver. Due to their relative estimation, some methods to avoid excessive usage of this estimators and to mitigate the trust of the driver in the trip estimator, both the trip estimation and the remaining tank gas reserve are not valid for the last 5 liters of gas in the tank, being replaced by a yellow warning which asks for immediate refueling.
Meanwhile, the traction battery of the electric vehicle is dealing with similar information, as the State of Charge (SOC) of the battery, expressed in kWh.

By analyzing the traction power requested by a vehicle, in (*Kuew and Leong*, *2014*)

$$P = mav + mgv\sin\propto + C_{RR}mgv\cos\propto + \frac{1}{2}\rho C_D A v^3 \tag{1}$$

the authors consider the mass *m*, the acceleration *a*, the slope of the road *α*, the aerodynamic coefficients and the air viscosity.

The formula is complex and cannot be used for online calculation of the range of a special vehicle, being more usable when we need to estimate the energy requirements over an imposed trip (like a bus line) in order to decide the energy level needed to be available in the battery when starting a new trip, especially if the vehicle is located in an isolated area with special precautions about the available energy *(Maican et al., 2019)*.

[1] *Tudor E., Ph.D. Eng.; Matache M. G., Ph.D. Eng.; Sburlan I. C, Mst. Eng.; Vasile I., Mst. Eng.; Cristea M., Ph.D. Stud. Eng.*

MATERIALS AND METHODS

Methods for state of charge measurement

As a fact, the trip estimation is based on measured SOC value and an energy consumption prediction. The methods for measuring the SOC are described widely in the literature, are subject of continuously improving and the SOC methods are becoming more and more accurate. The SOC estimator is well described in the literature *(Yong Tian et al., 2016)* describing four popular model-based SOC estimation algorithms, namely extended Kalman filter, unscented Kalman filter (UKF), sliding mode observer and nonlinear observer (NLO), which are compared in terms of prediction accuracy, tracking ability to initial SOC error, and computation complexity.

As the Li-Ion batteries have different topologies, the battery builder is providing the electronic Battery Management System (BMS) which performs various tasks as:

- Cell voltage balancing (active or passive);
- Temperature monitoring, including fan control for ventilation and for overtemperature protection;
- Voltage monitoring, including over-voltage or under-voltage monitoring, charger voltage request, max pack voltage;
- Current monitoring, including over-current protection and charging current protection;
- State of charge estimation, using pack voltage, pack current and pack temperature;
- State of Health estimation, using pack voltage and pack current;
- Charger limits for voltage and current, provided by CAN communication and by analog output signal;
- DC contactor control for protection of the battery;
- The protection system contains a DC fuse for overcurrent and short circuit protection.

One of the most popular methods used by BMS systems *(P. A. Topan et al., 2016; ORION, 2020; D. Xu et al., 2010)* to calculate a battery pack's state of charge (SOC) is coulomb counting (keeping track of the amount of current that has entered or left the battery pack). This method requires the use of a current sensor and generally tracks the state of charge of the battery pack quite well provided that the capacity of the battery is known, and the current sensor is accurate. Also, the BMS uses a secondary SOC correction algorithm using the measured open circuit voltage of the highest and lowest cells (the voltage as if the cell were at rest) and compares them to a table of known voltages. If the BMS has previously been calculating the state of charge at a lower value, it can correct the state of charge calculation based on this information. The BMS will always use the highest open circuit cell voltage (to drift up) and lowest open circuit cell voltage (to drift down) for these calculations so that the pack is properly protected. This helps improving the accuracy of the calculated state of charge.

In addition to the correction drift points that are programmed in, the BMS can also correct the calculated state of charge when a charge cycle completes.

The SOC measurements are more accurate as the battery is in new-condition, and when the battery is worn, the cells will have different open-circuit voltage and less capacity, thus making the full-charge status reached in lesser time, with less energy stored. A new parameter is then used when the energy availability of the traction battery has to be measured: the State of Health (SOH), which is 100% at the new battery and below for the worn one. This parameter must be considered when computing the available range of the whole vehicle, and the SOH parameter has to be verified for range estimation.

Trip estimator based on electric power consumption

Some authors are imposing the trip, including road conditions, by willing to estimate the remaining SOC at the arrival at the end of the trip (*K. Sarrafan et al., 2017; V. R. Tannahill et al., 2016*). Those methods are mainly an estimator regarding consumption.

We are using the SOC estimator described below to obtain the on-line SOC status. This is determined by subtracting the electric energy consumption and by adding the electric energy regeneration (coulomb tracking). For trip estimator we can use the following data:

- SOC_0 at starting point (provided by BMS);
- SOC at actual point (provided by BMS);
- Energy loss (by integration of the energy consumption);
- x_0 Initial trip (km) (provided by Bord Computer (CB));
- x Actual trip (km) (provided by CB);
- Initial time (from both BMS and CB)
- Actual time (from both BMS and CB);
- x_{max} Maximum trip (from CB).

The estimation of the remaining trip is to be made by the bord computer CB and must be presented to the driver. One method is to calculate the remaining range, in *km*, using the formula:

$$x_{max} = x + (SOC - SOC_{min}) \cdot \frac{x - x_0}{SOC_0 - SOC} \quad (2)$$

Where the SOC_{min} is the minimum discharge state of the battery (usually 20%).

This method is close to the ICE range estimator, considering the reset of the counter at the beginning of each trip, as being equivalent to full recharge of the electric vehicle. However, this method lacks in accuracy due to the pour resolution of the km counter and offers less information about the driving mode, being effective only for constant load and constant trip.

Electric tractor presentation

Our trip estimator must solve the range anxiety of an electric tractor prototype driver, tractor showed in Fig. 1, which must operate a small demonstrator with the following characteristics:

- Mass 1210 kg;
- Traction (AC motor) PS2 = 32 kW;
- Transmission 8+1 speeds;
- Maximum speed 26 km/h;
- Traction battery voltage Vbatt = 141 Vdc;
- Traction battery energy Ebatt = 17.28 kWh;
- Maximum current Ibatt < 121 Adc.

Fig. 1 - Electric tractor prototype

The main functions of the electric tractor are:

- Road transfer from the charging point / workshop to the operation area, using the high-speed gear, by using up-to 10% of the stored energy;
- Ploughing or towing loads as requested, using the high-torque gear;
- Returning to charging point with high-speed gear.

The main components of the electric drivetrain *(Cristea et. Al, 2020)* are connected as provided in Fig. 2. The tractor has an AC traction motor TM driven by a traction power converter TPC powered from a traction battery BAT2 connected though DC contactors contained in connection box CONB. Charging of the battery is controlled by the On-board charger OBCC which is supplied from the 220Vac network through Mode 2 connector MOD2.

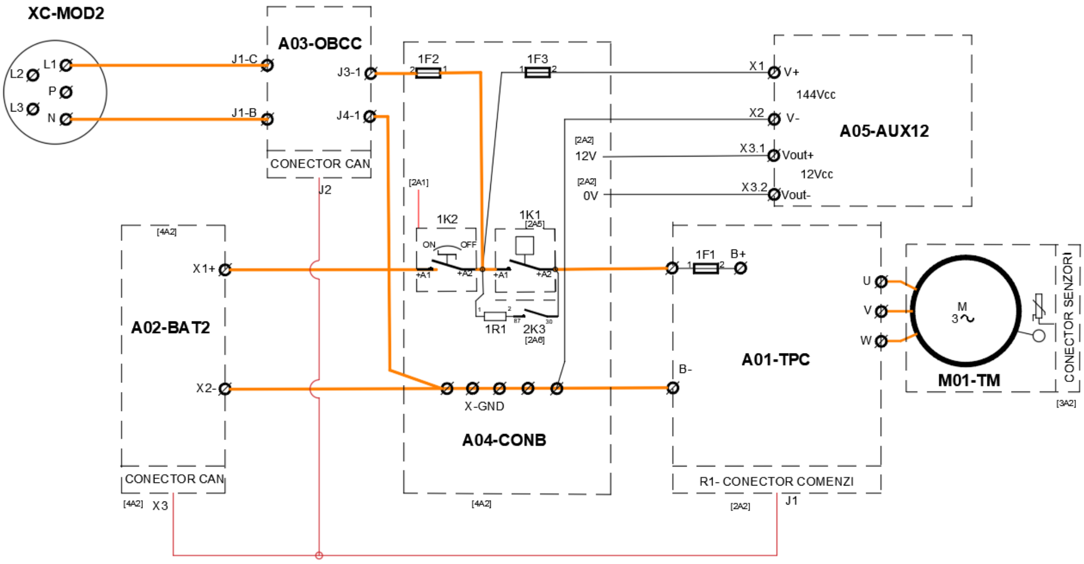

Fig. 2 - Main electric diagram of the electric tractor

Control electronics are supplied from traction battery using a DC-DC galvanic-insulated converter AUX12, thus making obsolete the 12Vdc primary battery of the tractor.

Measuring the State of Charge from Battery Management System

The BMS electronic unit is designed with the aim to provide enough information via serial CAN communication in order to organize multiple battery units connected in series or in parallel on the EV for range extension. The data is provided on-line and is designated to be used by a master-BMS unit or, directly, by the external connected electronic units as the battery charger and the traction converter. A special software was developed in order to extract the most important data exchanged on the CAN communication line between the battery, charger and traction converter. A caption of the Romanian interface of the software is presented in Fig. 3.

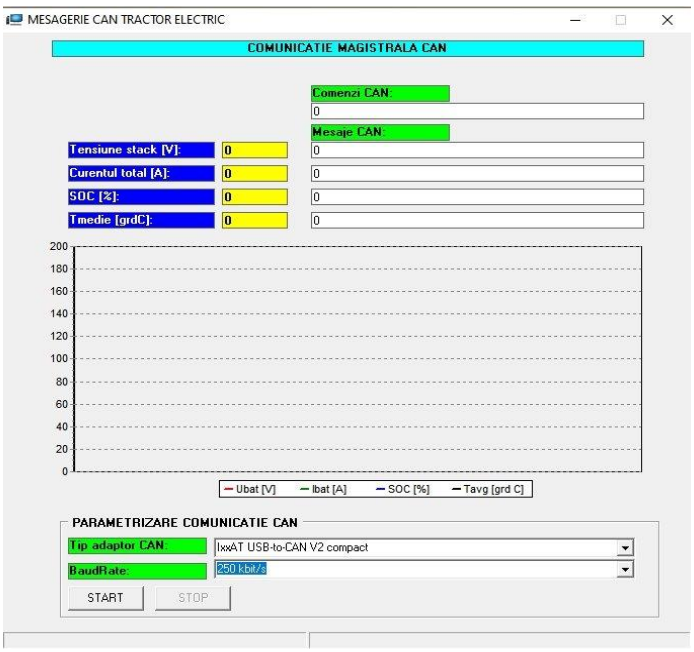

Fig. 3 - Communication software for data recording

In the figure below is presented a charging log-file recorded from a 1 ½ hour charging from SOC 51% up to SOC 89%, using a 6.6 kWh charger. The maximum charging current was set up at 32 A using a regular 240 Vac power supply.

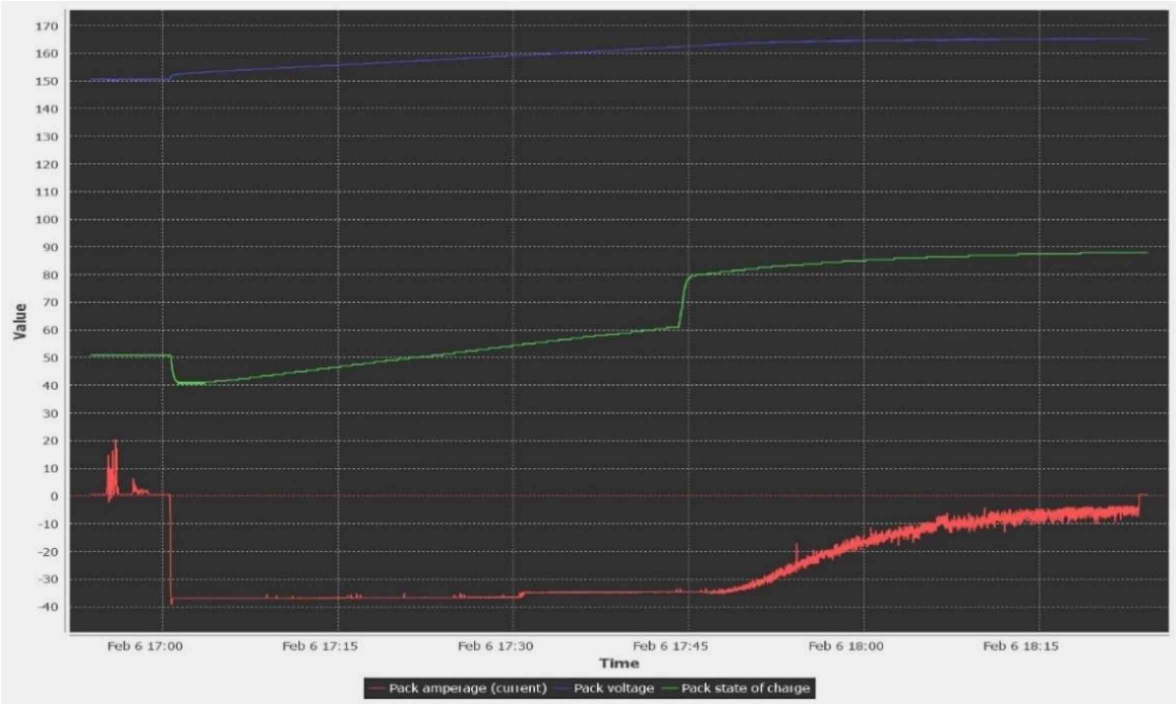

Fig. 4 - Charging battery in time - Current, Voltage and SOC using 15 min grid

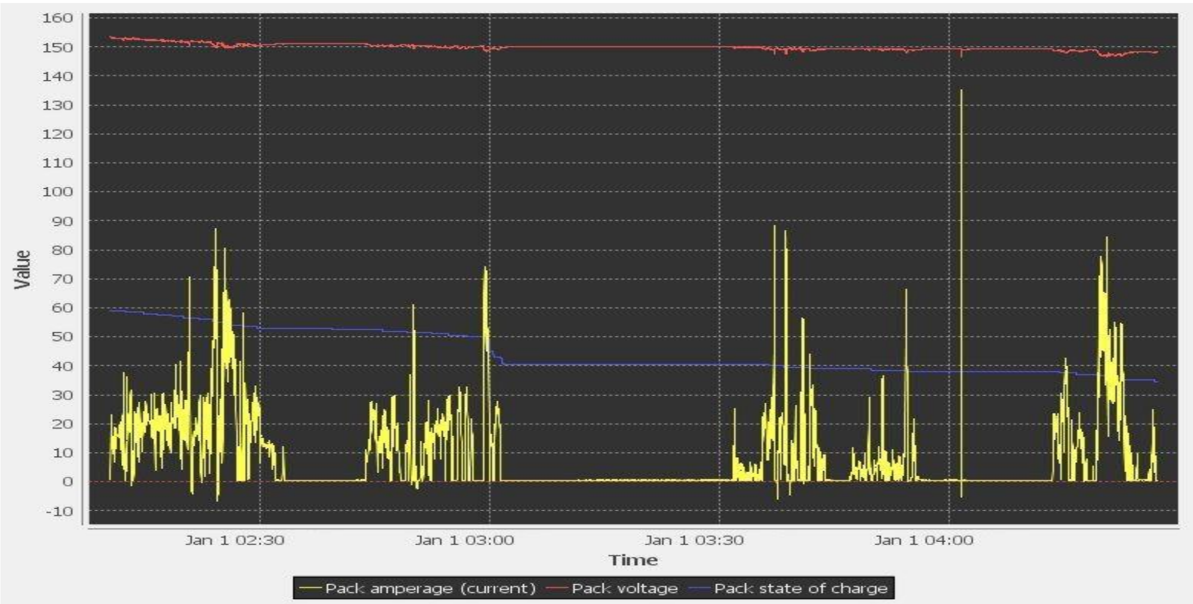

Fig. 5 - Discharging battery in time - Current, Voltage and SOC using 15 min grid

In Fig. 5 is presented a working current diagram, where we can see the SOC depletion from 59% down to 35% in only one hour of ploughing. There could be observed peaks of up to 90 A drawn from the battery with a drop of 6 Volts from the total pack voltage. Also there are periods with very low current consumption which are corresponding to the process of taking out the plough from the soil and reversing the ploughing direction by turning the tractor.

RESULTS

As observed in Table 1 and in Table 2, our tractor does not have a reliable trip counter expressed in km. The main trip counter resides in the traction controller, and is based on computation related to the number of revolutions performed by the rotor of the traction motor. As our tractor has to maintain a classical gearbox and a differential redactor in order to provide both high torque and high-speed service, then the trip becomes more difficult to be estimated. Furthermore, the tractor is a vehicle which operates often in sliding mode (Table 1, column 4) as it must operate on soil. Then, the actual trip is much lesser than the real one because of the sliding of the tractive wheels.

Table 1

Electric tractor autonomy for ploughing works

Experiment no.	Electric power input Pe, W	Tractor autonomy, h	Ploughing productivity, ha/h	Total ploughed surface, ha
0	*1*	*2*	*3*	*4*
1	3454	5.00	0.09	0.46
2	4594	3.76	0.09	0.33
3	7354	2.35	0.08	0.20
4	7940	2.18	0.18	0.39
5	9702	1.78	0.17	0.31
6	12602	1.37	0.17	0.23
7	11487	1.50	0.25	0.38
8	14435	1.20	0.24	0.29
9	19147	0.90	0.22	0.20

Table 1

Experimental results obtained for draft force

Experiment no.	Working depth, m	Actual working speed, m/s	Mean draft force, N	Travel reduction ratio TRR, %
0	*1*	*2*	*3*	*4*
1	0.10	0.50545	3822	8.1
2	0.15	0.48895	5728	11.1
3	0.2	0.4719	7527	14.2
4	0.10	0.9988	3884	9.2
5	0.15	0.9526	5801	13.4
6	0.2	0.8954	7644	16.6
7	0.10	1.4032	3926	12.3
8	0.15	1.3392	5844	16.3
9	0.2	1.2608	7789	23.2

One can notice that the reference for tractors autonomy is the operation time (in hours) (*G. A. Golub et al.*, *2019*). Also, from Table 1 is possible to compare and discover that the power consumption is proportional with the operational speed (compare data from column 1, records 1, 4 and 7 corresponding to the same working depths at different speeds). Regarding the SOC measurements, some aspects must be interpreted. In Fig. 4, there are two specific areas to be analyzed: The SOC drop is determined by a minimum cell voltage and the 10% is missing from the reported value, but is re-displayed when the cell voltages restored to normal values due to active cell balancing; When the SOC is more than 80%, the charging current is gradually reduced by the charger, as instructed via the CAN bus by the battery.

Combined dynamic measurements Method 1 – trip estimator based on recorded consumption

We transferred the data imported from CAN communication (Fig. 5) into spreadsheet software and some data analysis was performed.

The goal is to provide accurate trip estimator for the driver, regarding the actual (recorded) consumption of the tractor which was related to the load characteristics. The diagram below presents the current provided by the battery in time – expressed in seconds. For a correct evaluation we provide an integrated value of the current over the last 60 seconds, using the Moving Average Method (*Ilmiawan et al., 2014)*.

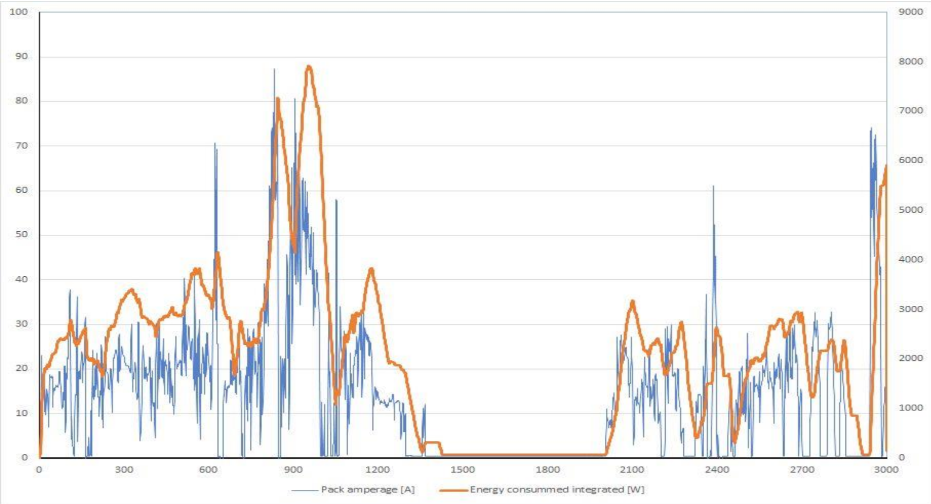

Fig. 6 - DC current [A] and Power measurement [W] with 60s moving average in time [s]

As the diagrams show a high variation in the output function, we cannot use the values presented in Fig. 6, for the estimation of the remaining trip. Current [A] multiplied by the pack voltage [W] is filtered and integrated over a 600s time interval. The moving average value is presented in the following diagram.

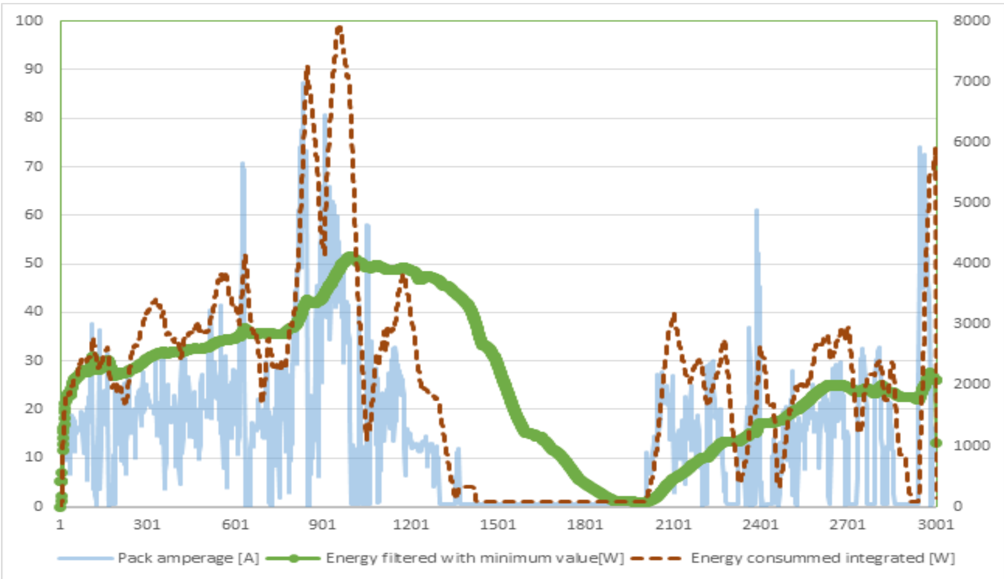

Fig. 7 - DC current [A] and Power measurement [W] with 600s moving average in time [s]

One can see that, if we intent to predict the remaining energy for the remaining trip estimation at moment *n*, the equation (4) has to be used, and, since the value of the integrator factor k_n is a divider, we must consider a minimum value for this factor. In this case we shall consider a value of 1054W that we chose as the smallest value of instantaneous power when the tractor marches with no load.

$$t_n = Ptot\frac{SOC-SOC_0}{k_n} \qquad (3)$$

Where:

- Ptot is the total power, in this case Ptot=120Ah*144V=17280Wh;
- SOC is the actual value reported;
- SOC_0 is the final energy reserve provided by the battery manufacturer (usual value is 20%);
- k_n is the integrated power representing the medium power consumption for the last *m* records of Δt.

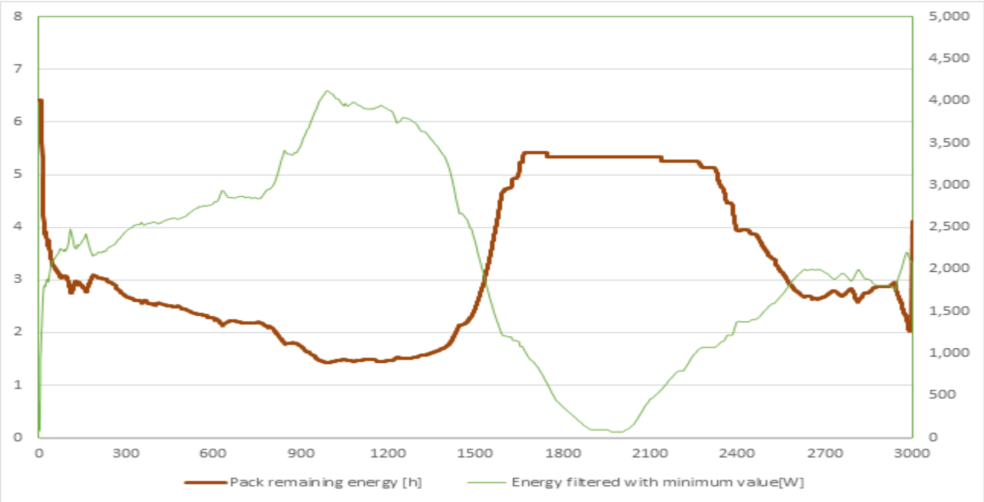

Fig. 8 - Estimating remaining trip [h] according to the average 600s load [W]

$$k_n = \frac{1}{m*\Delta t}\sum_{i=n-m}^{n} Pi \tag{4}$$

Applying the relation (3) and (4) on the example presented in Fig. 6 and Fig. 7, we will have the following predictions regarding the remaining operational time, Fig. 8.

Method 2 – trip estimator based on energy reserve with predefined and recorded measurements

The method consists in using the equation 3 and needs setting one energy consumption factor for minimum load k_{min} and other for maximum load k_{max}. There are two trip expectations, the minimum t_{load} and the maximum t_{free}.

$$t_{free} = Ptot\frac{SOC-SOC_0}{k_{min}} \tag{5}$$

$$t_{load} = Ptot\frac{SOC-SOC_0}{k_{max}} \tag{6}$$

Fig. 9 presents the evolution of the remaining time evaluation starting with the values of the SOC, with a 20% reserve, and with an average consumption of 1052 W/s measured during the tests while the tractor runs free and a maximum consumption of 4208 W/s while ploughing.

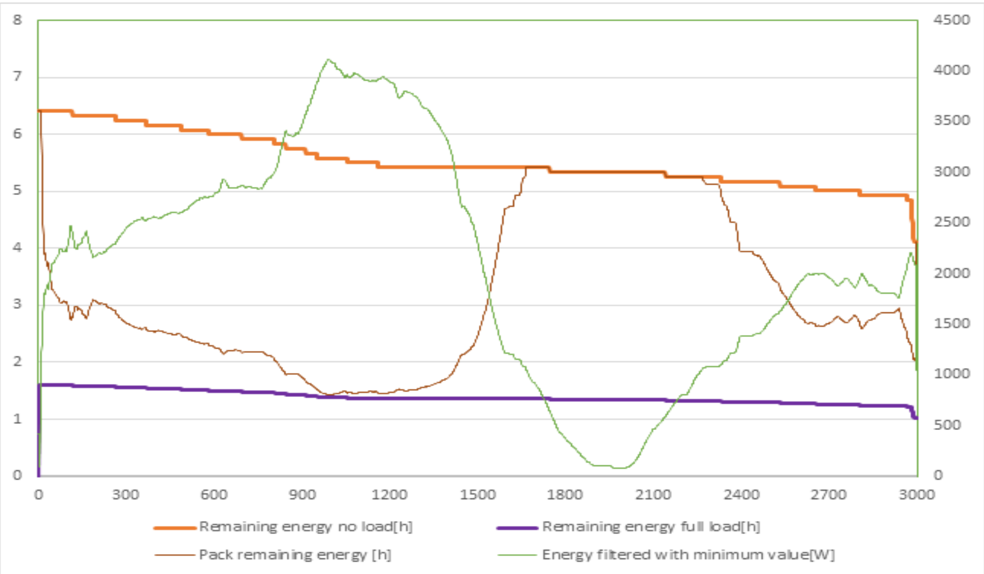

Fig. 9 - Preset consumption from load/no-load characteristics - trip estimation (s)

Method 3 – combined trip estimator based on predefined and recorded measurements and energy reserve introduction

The third method is proposed and tested on the track with mixed loads.

The trip estimator is very important for the ploughing activity, where a correlation between the SOC and the ploughing effort must be made. No lesser is the trip estimator for the return home energy reserve needed to avoid stalling the tractor on the field, Fig. 10.

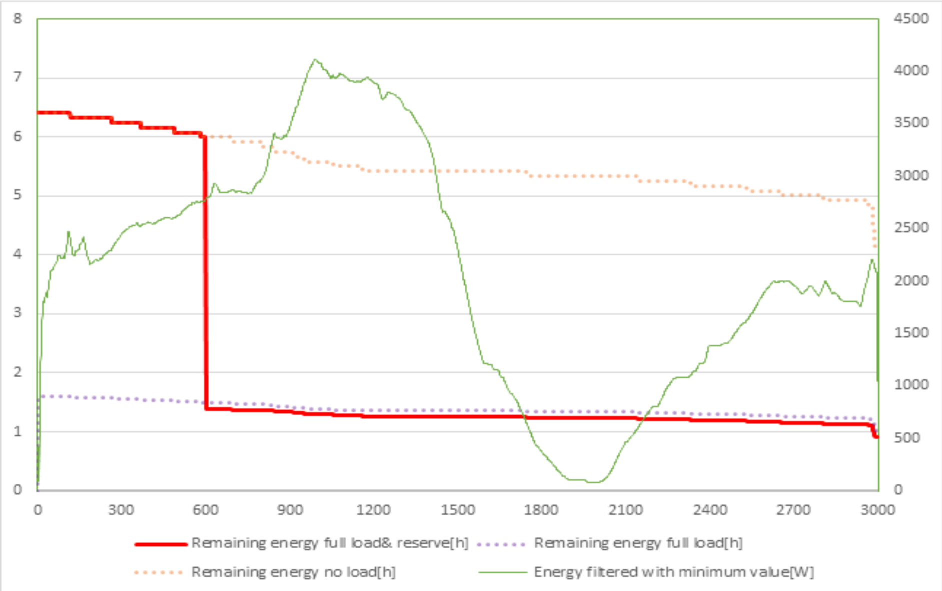

Fig. 10 - Trip estimation with return home reserve set before starting ploughing

Our proposal was to set an energy reserve for return home, via the human interface. Then, the estimation with method 1 or method 2 could be shown on screen as the "remaining working time". We selected the first 600s for the trip, and the rest for the ploughing (higher currents). The energy reserve was about 2.5% of SOC, because the test was performed near the garage.

CONCLUSIONS

- The goal of the trip estimator is to provide the remaining working time until depletion of the battery. Also, saving the information about the energy consumption recorded over the road trip from the garage to the working area is useful for retaining same amount of energy for the returning path.
- The experiments performed with the tractor prototype were recorded and analyzed. The moving average method must be used for on-line energy consumption measurements, by using the energy integrated over 1 minute or 10 minutes.
- The maximum consumption and the minimum consumption rates are a fair enough instrument for trip estimator. For convenience, the display can also show the value of the remaining time, and the driver can use the one which is close to the operation performed. The average value from full charge can be used, but only for operations at constant load.
- The trip estimator for a wide type of working tasks, like the tractor has, can be instructed to provide also range in km, but the usage in the agricultural works operates with remaining working hours, and so do our methods proposed and tested with the tractor prototype.

ACKNOWLEDGEMENT

This work was supported by a grant of the Romanian Research and Innovation Ministry, through Sectoral Plan, contract no. 1PS/2019 and through Programme 1 – Development of the national research development system, subprogramme 1.2 – Institutional performance – Projects for financing excellence in RDI, contracts no. 16PFE and 30PFE.

REFERENCES

[1] Chew K. W., Leong C.H., (2014), ”Contour Data Acquisition System For Electric Vehicle Distance Estimation System”, *Journal of Marine Science and Technology*, Vol. 22, No. 6, pp. 700-704 DOI: 10.6119/JMST-014-0321-6;

[2] Cristea M., Matache M.G., Sorică C., Biriş S.Şt, Ungureanu N., Cristea R.D., (2020), “Study on the behavior of a battery mounted on an electric tractor prototype” / “Studiu privind comportamentul unei baterii de acumulatori montată pe un prototip de tractor electric” *INMATEH Agricultural Engineering*, Vol 62, No 3, pp. 19–28 DOI:10.35633/inmateh-62-02

[3] Golub G.A., Chuba V.V., Marus O.A., (2019), “Modeling of transition processes and fuel consumption by machine-tractor unit using biofuel” / “моделювання перехідних процесів та витрат палива машинотракторним агрегатом при застосуванні дизельного біопалива” - *INMATEH Agricultural Engineering*, Vol 58, No. 2, pp. 45-56 DOI: 10.35633/inmateh-58-05

[4] Ilmiawan A. F., Wijanarko D., Arofat A. H., Hindersyah H., Purwadi A., (2014), "An easy speed measurement for incremental rotary encoder using multi stage moving average method", *2014 International Conference on Electrical Engineering and Computer Science (ICEECS)*, Kuta, pp. 363-368, DOI: 10.1109/ICEECS.2014.7045279;

[5] Matache M. G., Cristea M., Găgeanu I., Zapciu A., Tudor E., Carpus E., Popa L. D.,(2020), ”Small Power Electric Tractor Performance During Ploughing Works” – “Performanţele unui tractor electric de putere mică în timpul lucrărilor de arat”, *INMATEH Agricultural Engineering* , Vol 60, No 1, pp. 123–129 (2020) DOI:10.35633/inmateh-60-14;

[6] Maican E., Vlădut V., Vîlcu C., Sorică C., Marin D., Mirea D.P., Bogăţeanu R. – (2019) – “Hybrid renewable energy systems for isolated farms. A review” / “Sisteme hibride de energie regenerabilă pentru fermele insularizate. O trecere in revistă” *INMATEH Agricultural Engineering*, Vol 59, No 3, pp. 77-92 DOI:10.35633/inmateh-59-09;

[7] Sarrafan K., Sutanto D., Muttaqi K. M., Town G., (2017), "Accurate range estimation for an electric vehicle including changing environmental conditions and traction system efficiency" *IET Electrical Systems in Transportation*, vol. 7, (2) pp. 117-124;

[8] Tannahill V. R., Muttaqi K. M., Sutanto D., (2016); "Driver alerting system using range estimation of electric vehicles in real time under dynamically varying environmental conditions" *IET Electrical Systems in Transportation*, vol. 6, (2) pp. 107-116;

[9] Topan P.A., Nisvo-Ramadan M., Fathoni G., Cahyadi A.I., Wahyunggoro O., (2016), ”State of Charge (SOC) and State of Health (SOH) Estimation on Lithium Polymer Batteryvia Kalman Filter”, *2nd International Conference on Science and Technology-Computer (ICST)*, Yogyakarta, Indonesia, doi: 10.1109/ICSTC.2016.7877354;

[10] Xu D., Wang L. and Yang J., (2010), "Research on Li-ion Battery Management System," *2010 International Conference on Electrical and Control Engineering*, Wuhan, China, 2010, pp. 4106-4109, doi: 10.1109/iCECE.2010.998;

[11] ****ORION BMS 2 operational Manual* https://www.orionbms.com/, (2020).

MECHANICAL CHARACTERISTICS OF THE RUBBED MAIZE STRAW DURING SCREW CONVEYING
/
揉碎玉米秸秆螺旋输送过程中的力学特性研究

Wulantuya; Wuyuntana; Wang Hongbo*; Guo Wenbin; Wang Chunguang; Qinglin
College of Mechanical and Electrical Engineering, Inner Mongolia Agricultural University, Hohhot / China
Tel: +86 13739981395; E-mail: wanghb@imau.edu.cn
DOI: https://doi.org/10.356.33/inmateh-64-10

Keywords: *rubbed maize straw, mechanical characteristics, screw conveying, experiment*

ABSTRACT
In order to reduce the power consumption of screw conveyor and to improve the productivity, this study investigated such mechanical characteristics of rubbed maize straw as coefficient of sliding friction, angle of repose, internal friction coefficient, cohesion, flow function value and compressible coefficient with respect to its moisture content and density. An experiment was designed and consists of a sliding friction characteristic test-bed, a direct shear apparatus, a self-made device with adjustable density and compression. The results showed that: the coefficient of sliding friction increases with the increase of moisture content and density; the angle of repose and internal friction coefficient each increases with increasing moisture content respectively; there is no significant effect between the moisture content and the cohesion of rubbed maize straw; the flow function value goes up with the increase of the moisture content; also the increase of the moisture content leads to the increased bulk density due to the reduced materials gap and the increased compression coefficient, which makes it hard to compress. The equation of pressure and density was found, and it is suitable for the analysis of compression characteristic of rubbed maize straw. The research results lay a theoretical foundation and a basis for the further study on mechanical properties of maize straw.

摘要
为了减少螺旋输送机的功耗并提高生产率，采用滑动摩擦特性试验台，直切仪、自行研制的密度调节装置和压缩装置试验研究了揉碎玉米秸秆的滑动摩擦系数、休止角、内摩擦系数、粘聚力、流动函数值和可压缩系数等力学特性与含水率、密度之间的关系。结果表明:滑动摩擦系数随着含水率和密度的增加而增大,休止角和内摩擦系数随含水量的增加而增大,含水率对揉碎玉米秸秆粘聚力的影响不显著,流动函数值随含水率的增加而增大,随着含水率的增加物料间的间隙减小、压缩系数增大、堆积密度增大，使物料难以压缩。获得了压强和密度的关系式，该式也适合揉碎玉米秸秆的压缩特性的分析。研究结果可为玉米秸秆力学性能的研究奠定了理论基础。

INTRODUCTION
The rubbing of corn stalks is a processing technology that emerged in China in the 1980s *(Lin Li et al, 1997)*. The straw rubbing process not only separates cellulose, hemicellulose and lignin, but the longer straw silk can prolong its residence time in the rumen of ruminants, which is beneficial to the digestion and absorption for livestock, thus improving both the feed intake of straw and digestibility. Straw rubbing is a simple, efficient and low-cost processing method. The processing efficiency is about 1.2 to 1.5 times that of straw crushing. The rubbed maize straw is a soft, fluffy silk with suitable length and thickness, which can be fed directly, and the feeding rate can reach more than 90%. While it can also be further processed to produce high quality roughage, such as silage, micro-storage, ammoniation, alkalization, briquetting and puffing treatment, etc. (*Tianshu Chu et al, 2016; Cailong Ma et al, 2018; Shuangxia Zhang et al, 2016)*.

The screw conveyor is essential equipment in the treatment of rubbed maize straw. The conveying performance will directly affect the quality and productivity of the processing, and as well affect the performance of screw conveyor. Previous studies have shown that the mechanical properties of rubbed maize straw inevitably affect the working performance of screw conveyor *(Wulantuya et al, 2015; Wulantuya et al, 2016;*

Wulantuya, Lecturer; Wuyuntana, Associate Professor; Hongbo Wang, Associate Professor, Correspondent author; Wenbin Guo, Associate Professor; Chunguang Wang, Professor; Qinglin, Teaching assistant*

Wulantuya et al, 2020). While there have been few studies on the mechanical properties of rubbed maize straw, similar research on rice straw, crushed straw and soybean stalk is common *(Chevanan et al, 2009).* Shinners et al. studied the effects on the sliding friction coefficient of stalks and static friction coefficient of chopped grasses with regard to water content, pressure, relative velocity and material type of straw *(Shinners et a, 1991; Joseph et al, 2008; Kakitis et al, 2005)*. Larsson et al *(2010)* studied the influence of moisture content and pressure on the dynamic friction coefficient of straw, and established a model to analyse its influence. Phani et al. *(2010)* studied the variation of friction coefficient of crushed straw of barley, rapeseed, oat and wheat respectively, with untreated raw and through steam explosion. Yishui Tian et al. studied the fluidity by Carr index evaluation method assuming a straw with a length of 5-30mm as a bulk with a large particle size distribution *(Yishui Tian et al, 2011; Zonglu Yao et al, 2012)*. Xin Fang et al. *(2012)* made a self-made bevelling instrument and researched the effects of moisture content on the sliding friction between finely shredded soybean straw and different materials. Haitao Chen et al. *(2013)* studied the flow dynamics characteristics of straw materials following refining treatment, which detailed the internal friction angle, cohesion and flow function values of rice straw.

The mechanical properties of straw materials refer to the friction, flow and compression characteristics, in which friction is expressed by sliding friction angle, rolling stability angle, angle of repose and internal friction angle, flow by internal friction angle, cohesion, flow function value representation, compression expressed in terms of compressibility coefficients *(Yuming Guo et al, 2005)*.

In this study the test was conducted to obtain the mechanical characteristics and corresponding parameters of rubbed maize straw by using a direct shear apparatus, sliding friction characteristic test-bed, self-made adjustable density device and compression device. The moisture content and density of rubbed maize straw has an effect on its mechanical characteristics, and the influence law was obtained. This data provides the necessary theoretical basis and technical basis for the design and optimization of rubbed maize straw conveying machinery.

MATERIALS AND METHODS

Materials

The maize straw was obtained from the suburbs of Hohhot, China and was rubbed using a 9R-40 type rubber *(Designed and manufactured by Inner Mongolia Agricultural University)*. Rubbed maize straw was less than 180 mm long and 2-8 mm wide, as shown in Fig.1. The moisture content of the rubbed maize straw was tested by moisture meter *(Hebi Electronic Research Institute Co., Ltd. DYSF-8000W automatic moisture analyser, Henan, China)*. The initial average moisture content of the straw was 15.76%. According to the test requirements, each of the ground straws was conditioned to moisture contents of 22.36%, 31.82%, 42.27%, and 52.87% *(w.b)* by adding appropriate amounts of distilled water to the samples contained in Ziploc bags and stored in a cool room at 4℃ for 24 h. The calculation formula for the moisture content of the material was shown in Eq. 1 below. The mechanical properties test was performed after the moisture content of the straw was uniform.

$$M = \frac{m_1 - m_2}{m_1} \times 100\% \tag{1}$$

where: M is wet basis moisture content, m_1 is the mass of fresh materials, m_2 is the mass of dry materials.

Fig. 1 - Test samples

Devices

The experimental devices were a test-bed for sliding friction characteristics, a self-made density-adjustable device, a direct shear test apparatus, and a compression device, as shown in Fig.2- Fig.5. Besides, there was also a iHP-2K push-pull force meter produced by Yueqing Aidebao Instrument Co., Ltd. The balance scales produced by Beijing Fums Technology Development Co., Ltd. has an accuracy of 0.01g and a measuring range of 6 kg.

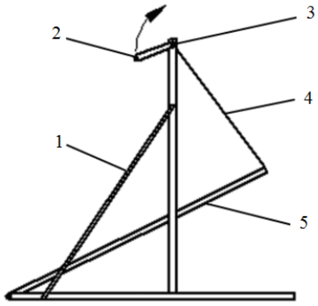

Fig. 2 - Sliding friction characteristic test-bed
1 – Studdle; 2 – Handle; 3 – Winding shaft; 4 – Rope; 5 – Sideling plane

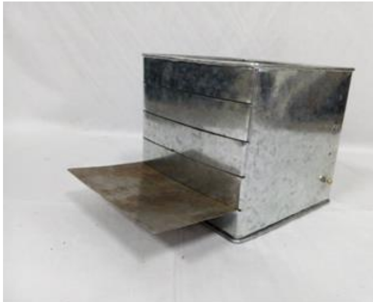

Fig. 3 - The density controller

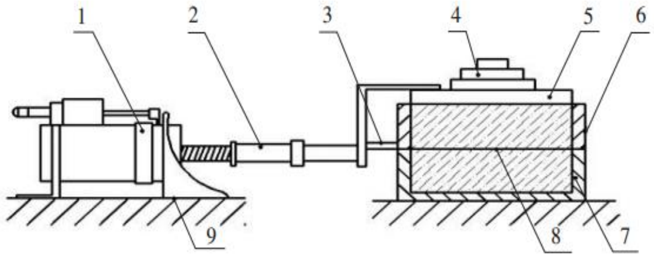

Fig. 4 - Direct shear test apparatus
1 – Load device; 2 – Dynamometer; 3 – Load pole; 4 – Compaction load; 5 – Cap; 6 – Shear cell; 7 – Base; 8 – Shear plane; 9 – Bottom plane

Fig. 5 - Material compression test unit

Experimental Methods

The mechanical properties of rubbed maize straw are subject to many factors. The friction characteristic is mainly related to such factors as moisture content and density. The moisture content will affect the flow characteristics as well as the compression characteristics of rubbed maize straw. The selected experimental factors and levels are shown in Table 1. Each test was replicated 10 times, and the results were averaged.

Table 1

Test factors and levels

Moisture Content [%]	Density [kg/m^3]
15.76	76.8
22.36	96
31.82	128
42.27	192
52.87	384

Method for sliding friction coefficient determination

Five groups of rubbed maize stalks with different moisture contents were taken as test materials. 1.2 kg of rubbed maize stalks were placed in the density controller for each test, and the volume of the material was changed by inserting plates to different positions so as to obtain five different densities. The sliding friction coefficient test was carried out at different densities respectively.

Method for determining the angle of repose

Determination of the angle of repose of rubbed maize straw with five different moisture contents by the tilt method.

Method for measuring internal friction angle, cohesion force and flow function value

Determination of the angle of repose of rubbed maize straw with five different moisture contents by the tilt method. Set the pre-compacting positive load to 200 kPa, then at 200, 150, 100, 50 kPa. Direct shearing is carried out step by step under positive load conditions of 4 grades. This method refers to GB/T4934.1-2008 for specific operation procedures, which is a China National Standard Test Method.

Excel 2003 software was used, the positive load value as the x-axis, and the corresponding shear load value as the y-axis. The scatter diagram was plotted and the trend line was added, linear regression equation was fitted. This trend line is the Moire envelope, and the regression equation can be regarded as the expression of the Moire envelope, expressed by the formula (2), and then the internal friction angle and the value of cohesion were obtained.

$$\tau = c + \sigma \tan\varphi \tag{2}$$

where:

τ is the shear stress; c is the unitary cohesion; σ is the normal stress, φ is the internal friction angle.

Under certain pre-compaction conditions, the flow function value of rubbed maize straw was obtained by formulas (3), (4) and (5).

$$FF = \frac{\sigma_1}{\sigma_c} \tag{3}$$

where:

σ_1 is the maximum main stress; σ_c is the unconfined yield stress.

$$\sigma_c = \frac{2c(1+\sin\varphi)}{\cos\varphi} \tag{4}$$

$$\sigma_1 = \left(\frac{A - \sqrt{A^2 \sin^2\varphi - \tau_0{}^2 \cos^2\varphi}}{\cos^2\varphi} \right) \times (1+\sin\varphi) - \left(\frac{c}{\tan\varphi} \right) \tag{5}$$

where:

$A=\sigma_0+c/\tan\varphi$; σ_0 is the maximum normal stress corresponding to the pre-compacting load;

τ_0 is the shear stress corresponding to the maximum normal stress.

Method for determining coefficient of compressibility

The rubbed maize straw is a soft, loose viscoelastic body with a large random shape and size. In order to improve the measurement accuracy, 20 samples were taken and filled at each moisture content without any pre-compaction. The box body is weighed and then the bulk density of the material is calculated. The formula is as follows:

$$\rho_a = \frac{M - m_X}{V_X} \tag{6}$$

where:

ρ_a is the bulk density of material;

M is the total mass of materials and cabinets;

m_X is the mass of the cabinet;

V_X is the volume of the box.

The measurement of the material density was repeated 10 times for each sample and the result was averaged. Finally, the average of the density obtained from the repeated test of 20 samples with the same moisture content averaged as the final density.

Five groups of rubbed maize straw with different moisture contents were taken as test materials, and 20 samples were taken from each group. The mold filled and the upper template covered without any pre-compaction. The push-pull force gauge *(HP-2K type)* applies different pressures *(during the screw conveying process, the pressure of the rubbed maize straw is 30-200 N)* and the distance between the upper surface of upper template and the upper edge of mold under different pressures were measured to calculate the volume of the material. Then the material density corresponding to each pressure value is calculated. The experimental data was analysed using MATLAB 2014 *(Math Works, Natick, MA, USA)*.

RESULTS AND DISCUSSION

Effects of moisture content and density on the sliding friction coefficient

Fig.6 shows the relation between moisture content and sliding friction coefficient of rubbed maize straw with different densities. Take five different densities from 76.8 kg/m³ to 384 kg/m³ and observe the result when the moisture content of the material varies from 15.76% to 52.87%. It is obvious that the sliding friction coefficient of rubbed maize straw is gradually increasing with the increase of moisture content. Many related studies have shown that the friction coefficient is related to the material, smoothness and humidity of the contacting objects and is subject to moisture content. The main reason is that as the moisture content increases, a thin liquid film was formed on the contact surface *(by adsorption or deposition)* and thus generating a meniscus force around the surface and consequently increased frictional force. Therefore, when sliding occurs, both the sliding friction angle and the friction coefficient increase. In addition, as the moisture content increases, the material is more likely to adhere to the contact surface, resulting in increased resistance to frictional sliding between the material and the steel sheet.

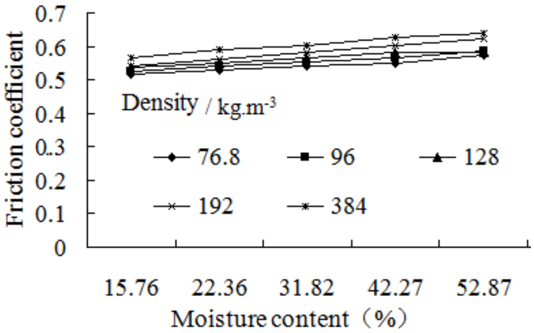

Fig. 6 - Relation between moisture content and friction coefficient

By the mathematical statistics analysis software MATLAB, the relation between the moisture content of the material and the friction coefficient was obtained, as shown in Table 2.

Table 2

Functional relation between moisture content and friction coefficient

Density [kg/m³]	Moisture Content [%]	Fitting Equation	R^2
76.8	15.76~52.87	$y = 0.0015x + 0.4918$	0.9391
96	15.76~52.87	$y = 0.0017x + 0.4977$	0.9934
128	15.76~52.87	$y = 0.0018x + 0.507$	0.996
192	15.76~52.87	$y = 0.0022x + 0.5102$	0.9878
384	15.76~52.87	$y = 0.002x + 0.5401$	0.9778

Note: y is the sliding friction coefficient, x, is the moisture content.

Fig.7 shows the relation between density and friction coefficient at different moisture content values. With the moisture content changing from 15.76%-52.87%, the sliding friction coefficient between the material and the steel plate increased with the material density in the range of 77.8-384kg/m³. The main reason for this effect is that the rubbed maize straw is soft and fluffy, and there is gap between them. For a certain amount of materials, increasing density squeezes the gap between them so that the area of contact surface between material and steel plate increases. As a result, increasing adhesion leads to increasing friction coefficient.

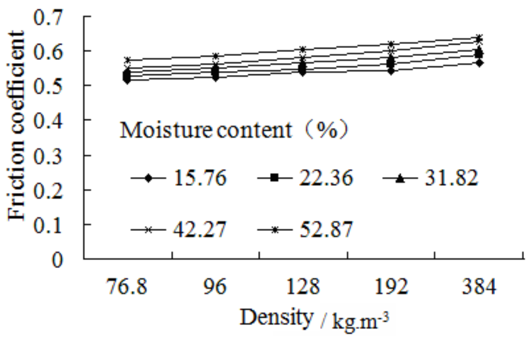

Fig. 7 - Relation between density and friction coefficient

Through the mathematical analysis by MATLAB, the relation between the density of the material and the friction coefficient was obtained, as shown in Table 3.

Table 3

Functional relation between density and friction coefficient

Moisture Content [%]	Density [kg/m³]	Fitting Equation	R^2
15.76	76.8～384	$y = 0.002x + 0.5104$	0.9583
22.36	76.8～384	$y = 0.002x + 0.5182$	0.9651
31.82	76.8～384	$y = 0.002x + 0.534$	0.8544
42.27	76.8～384	$y = 0.002x + 0.5433$	0.8778
52.87	76.8～384	$y = 0.002x + 0.5717$	0.8838

Note: y is the sliding friction coefficient, x, is the density.

Effect of moisture content on the angle of repose

Fig.8 shows the relation between moisture content and the angle of repose. It can be seen from Fig.8 that as the moisture content increased, the angle of repose for the rubbed maize straw increased. The reason is that after the moisture content increases, the surface of the rubbed maize straw is wet, and the viscosity between the materials is increased, which making it easier to pile up, and its scattering and fluidity are obviously weakened.

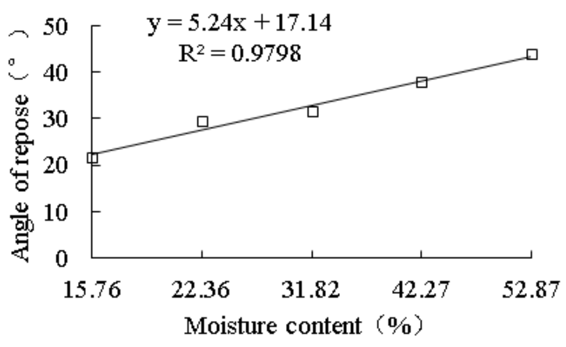

Fig. 8 - Angle of repose of materials under different moisture content

Effect of moisture content on the flow characteristics

As shown in Fig.9, with the increase of moisture content, the internal friction coefficient increased, which was consistent with the previous test results. The internal friction coefficient is one of the indicators for measuring the interaction force between materials. For rubbed maize straw, the internal friction coefficient is one of the main causes for material compression and aggregation. As the moisture content increases, the adhesion force between materials increases, resulting in an increase in internal frictional resistance.

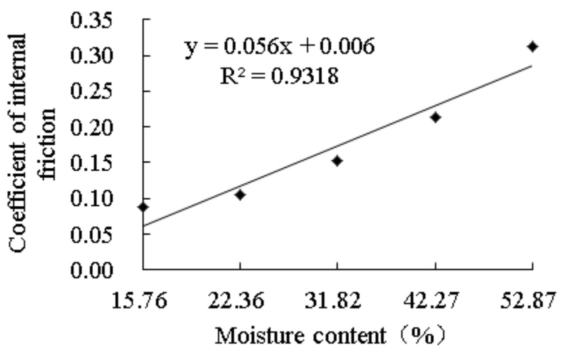

Fig. 9 - Internal friction coefficient of materials under different moisture content

As shown in Fig.10, with the increase of moisture content, the cohesion of the rubbed maize straw fluctuates, and the flow function value increases steadily. Under the conditions of this study, the moisture content is not the main factor affecting cohesion of rubbed maize straw. There are few studies on the relation between moisture content and cohesion. Some research showed that the physical and compression properties of the material are the main factors affecting the cohesion.

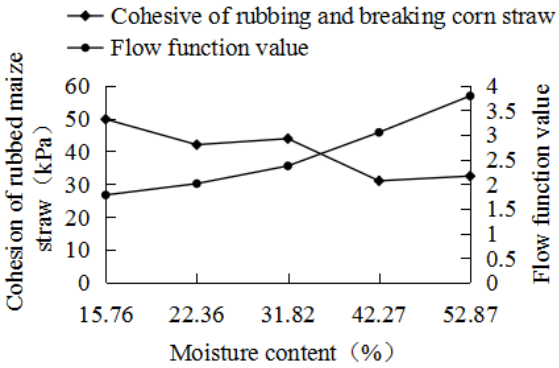

Fig. 10 - Flow characteristic of materials under different moisture content

Effect of moisture content on the compressibility

In deriving the mathematical model of the productivity and power consumption of the screw conveyor, the relation between pressure and density is used, which involves the compressible coefficient C_o of the material, so it is necessary to study this coefficient *(Wulantuya et al, 2020)* .

The following relation exists between the pressure and density of the material. The bulk density of the materials with five different moisture contents and the density values of the materials under different pressures are substituted into the above formula respectively to obtain a function of density and pressure, and the function is further combined with the test curve to obtain the compressibility factor of rubbed maize straw. The compression test curves of rubbed maize straw under five moisture contents are shown in Fig.11.

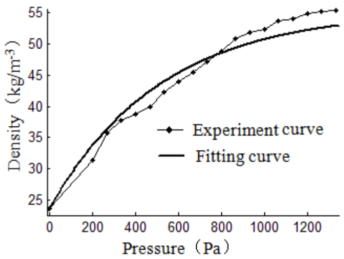

(a) Moisture content 15.76%

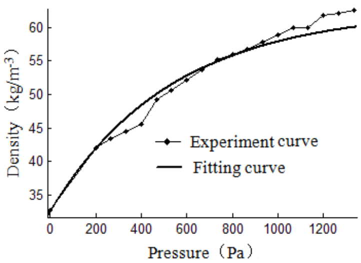

(b) Moisture content 22.36%

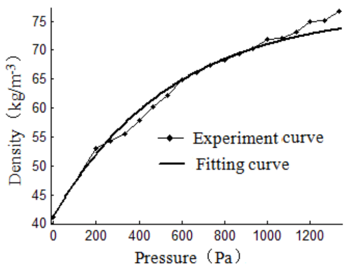

(c) Moisture content 31.82%

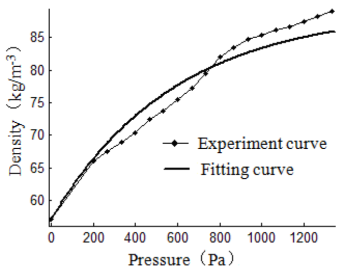

(d) Moisture content 42.27%

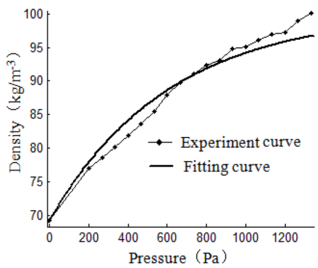

(e) Moisture content 52.87%

Fig. 11 - Relation between density and pressure under different moisture content

The equations and compressibility values for different moisture contents are shown in Table 4.

Table 4

Equation and the value of C_0 under different moisture content

Moisture Content[%]	Fitting Equation	C_0
15.76	$y=55.27-(55.27-23.73)\cdot e^{-C_0x}$	0.001929
22.36	$y=62.51-(62.51-32.85)\cdot e^{-C_0x}$	0.001865
31.82	$y=76.82-(76.82-41.23)\cdot e^{-C_0x}$	0.001812
42.27	$y=89.06-(89.06-57.2)\cdot e^{-C_0x}$	0.001713
52.87	$y=100.12-(100.12-69.4)\cdot e^{-C_0x}$	0.001639

The compression coefficient C_o is a characteristic parameter of the material itself, which reflects the difficulty of compressing the material, and is related to the type of material, the size of the particle, and the moisture content. According to the relevant literature, the greater the compression coefficient, the easier the material is compacted, and the smaller the compressible coefficient, the harder it is to compact the material *(Canjun Huang, 2013)*.

From Table 4 and the results of the bulk density test, it is known that as the moisture content increases, the bulk density of the rubbed maize straw increases, the gap between the materials becomes smaller, the compressibility coefficient decreases, and the material is not easily compressed, which is in accordance with the rules above. The relation between pressure and density is as follows. It is also suitable for the analysis of the compressive properties of rubbed maize straw.

$$\rho=\rho_m-(\rho_m-\rho_a)\cdot e^{-C_0P} \tag{7}$$

where:

$A=\sigma_0+c/\tan\varphi$;

σ_0 is the maximum normal stress corresponding to the pre-compacting load;

τ_0 is the shear stress corresponding to the maximum normal stress

CONCLUSIONS

After analysing the influence of the moisture content on coefficient of sliding friction, the results showed that when the density of the rubbed maize straw was 77.8 to 384 kg/m^3 and the moisture content of the material was in the range of 15.76% to 52.87%, as the moisture content increased, the coefficient of sliding friction increased gradually. Through the analysis of MATLAB, the relation between the moisture content of the material and the friction coefficient was obtained. The fitting coefficient of determination was greater than 0.97.

After analysing the influence of the density on friction coefficient, the results showed that when the moisture content of the material was 15.76% to 52.87%, the density of the material was in the range of 77.8 to 384 kg/m^3, as the density increased, the coefficient of sliding friction increased gradually. Through the analysis of MATLAB, the relation between the moisture content of the material and the friction coefficient was obtained. The fitting coefficient of determination was greater than 0.97.

After analysing the influence of the moisture content of rubbed maize straw on angle of repose, the results showed that as the moisture content increased, the angle of repose increased.

After analysing the influence of the moisture content on internal friction coefficient, cohesion and flow function value, the results showed that with the increase of moisture content, the internal friction coefficient increased, the cohesion fluctuated and the flow function value increased too.

After analysing the influence of the moisture content of rubbed maize straw on the compression coefficient, the result showed that with the increase of the moisture content, the bulk density increased due to the decrease of materials gap and the compression coefficient, resulting in smaller compressibility. The equation of pressure and density, is suitable for the analysis of compression character of rubbed maize straw.

ACKNOWLEDGEMENT

The research was supported by the Inner Mongolia Natural Science Foundation (No. 2020BS05022) and the High-level Talent Introduction Fund Project of Inner Mongolia Agricultural University (205-206050).

REFERENCES

[1] Canjun Huang, (2013), *Study on continuous explosion mechanism and technology of discarded biomass spiral booster (废弃生物质螺旋增压式连续闪爆过程机理及技术研究),* PhD Thesis, South China University of Technology, Guangzhou/China;

[2] Chevanan, N., Womac, A.R., Bitra, V.S.R., Yoder, D.C., Sokhansanj, S., (2009), Flowability parameters for chopped switchgrass, wheat straw and corn stover, *Powder Technology*, Vol.193, no.1, ISSN 00325910, pp.79-86, Elsevier, Lausanne/Switzerland;

[3] Cailong Ma, (2018), *Improved Design of 9RS-2 Straw Kneading Machine (9RS-2 型秸秆揉丝机的改进设计)*, MSc Thesis, Gansu Agricultural University, Lanzhou/China;

[4] Enchen Jiang, Leiming Xiong, Mingfeng Wang, Xulin Su, Xinhui Guo, Chuang Zhao, (2014), Development of biomass pyrolysis volatiles fractional condenser, *Journal of Northeast Agricultural University*, Vol.45, no.5, ISSN 10059369, pp.110-115, Heilongjiang/China;

[5] Haitao Chen, Ying Zhang, Zhenhua Huang, Xin Fang, Lixia LI, (2013), Effect of different moisture contents on flowability parameters of chopped rice straw (含水率对水稻秸秆流动力学特性的影响), *Journal of Northeast Agricultural University,* Vol.44, no.11, ISSN 10059369, pp.90-94, Heilongjiang/China;

[6] Joseph, S.t., (2008), Friction coefficients of chopped forages, *American Society of Agricultural and Biological Engineer*, Vol.26, no.9, pp.1-2, ASABE/U.S.A.;

[7] Kakitis, A., Nulle. I., (2005), Friction of chopped straw, *AGRIS*, Vol.113, no.16, pp.98-107, AGRIS/U.S.A.;

[8] Lingxin Geng, Lijuan Zhang, Qingxiang Shi, Chang'an Ni, Feng Jing, (2011), Parameters optimization of long-straws vertical cutting table based on double helix mechanism, *Transactions of the Chinese Society for Agricultural Machinery*, Vol.42, no.s1, ISSN 10001298, pp.10-13, Beijing/China;

[9] Lin Li, Mingshao Yang, Chuanguang Wang, Weifeng Liu, Qiurong Zhao, (1997), The manufacture & testing of 9R-40 rubber (9R-40 型揉碎机的研制与试验)*, Journal of Inner Mongolia Institute of Agriculture & Animal Husbandry*, Vol.18, no.3, ISSN 10093575, pp.69-74, Inner Mongolia /China;

[10] Larsson, S.H., (2010), Kinematic wall friction properties of reed canary grass powder at high and low normal stresses, *Powder Technology*, Vol.198, no.1, ISSN 00325910, pp.108-113, Elsevier, Lausanne/Switzerland;

[11] Phani, A., Lope, T., Greg, S., (2010), Physical and Frictional properties of non-treated and steam exploded barley, canola, oat and wheat straw grinds, *Powder Technology*, Vol.201, no.3, ISSN 00325910, pp.230-241, Elsevier, Lausanne/Switzerland;

[12] Ran Li, Wei Long, (2014), Fuel delivery system layout design of grey straw biomass power plant (灰色秸秆生物质电厂燃料输送系统布置设计), *Jilin Electric Power*, Vol.42, no.3, ISSN 10095306, pp.55-56, Jilin/China;

[13] Shinners, K.J., Koegel, R.G., Lehman, L.L., (1991), Friction coefficient of alfalfa, *Transactions of the ASABE*, Vol.34, no.1, pp.33-37, ASABE/U.S.A.;

[14] Shuangxia Zhang, Qiang Xu, (2016), Study of 9ZS－4 forage grass crushing machine and its design (9ZS-4 饲草揉碎机的研究设计), *Machine Building & Automation*, Vol.45, no.5, ISSN 16715276, pp.147-149, Nanjing/China;

[15] Tianshu Chu, Zengling Yang, Lujia Han, (2016), Analysis on satisfied degree and advantage degree of agricultural crop straw feed utilization in China, *Transactions of the Chinese Society of Agricultural Engineering,* Vol.32, no.22, pp.1-9, Beijing/China;

[16] Wulantuya, Chunguang Wang, Shaohua Qi, Jianguo Yan, Jinlian Wang, (2015), Test and analysis of performance of screw conveyor for rubbing and breaking corn straw, *Transactions of the Chinese Society of Agricultural Engineering*, Vol.31, no.21, ISSN 10026819, pp.51-59, Beijing/China;

[17] Wulantuya, Chunguang Wang, Shaohua Qi, Xiaorong Wang, Haichao Wang, Jinlian Wang, (2016), Theoretical model analysis and test of screw conveyor for rubbing and breaking corn straw, *Transactions of the Chinese Society of Agricultural Engineering*, Vol.32, no.22, ISSN 10026819, pp.18-26, Beijing/China;

[18] Wulantuya, Hongbo Wang, Chunguang Wang, Qinglin, (2020), Theoretical analysis and experimental study on the process of conveying agricultural fibre materials by screw conveyors, *Engenharia Agrícola*, vol.40, no.5, pp.589-594, ISSN 18094430, Jaboticabal/Brazil;

[19] Xin Fang, Haitao Chen, Zhenhua Huang, Lixia Li, (2012), Sliding friction characteristic of different moisture content of soybean stalk with different materials (不同含水率大豆秸秆与不同材料间滑动摩擦特性的研究), *Soybean Science*, Vol.31, no.5, ISSN 10009841, pp.838-841, Beijing/China;

[20] Yishui Tian, Zonglu Yao, Shuangping Ouyang, Lixin Zhao, Haibo Meng, Shulin Hou, (2011), Physical and chemical characterization of biomass crushed straw (切碎农作物秸秆理化特性试验), *Transactions of the Chinese Society for Agricultural Machinery*, Vol.42, no.9, ISSN 1000-1298, pp.124-128,145, Beijing/China;

[21] Yuming Guo, Hongmei Yuan, Decong Zheng, (2005). A review on application and development of agricultural material mechanics (农业工程科技创新与建设现代农业—2005 年中国农业工程学会学术年会论文集第一分册), *Proceedings of the annual conference of Chinese society of agricultural engineering*, pp.426-461, Guangzhou/China;

[22] Zonglu Yao, Shuangping Ouyang, Haibo Meng, Lixin Zhao, Yishui Tian, (2012), Flow characterization of biomass particle straw (颗粒状秸秆物料流动特性试验), *Transactions of the Chinese Society for Agricultural Machinery*, Vol.43, no.7, ISSN 10001298, pp.112-116, Beijing/China.

PERFORMANCE ANALYSIS AND TECHNOLOGY OPTIMIZATION OF INFRARED DRYING OF SWEET POTATO SLICE
/
甘薯片近红外干燥性能评价和工艺优化

Xie, SY[1)]; Yang, ZR[2)]; Yang, L[1)]; Li, ST[1)]; Wang, JL[3)]; Yang, MJ*[1)] [1]

[1)] Chongqing Key Laboratory of Agricultural Equipment for Hilly and Mountainous Regions, College of Engineering and Technology, Southwest University, Chongqing 400715;

[2)] Xi'an Guide Technology Co. Ltd, Xi'an 710065, China;

[3)] Nanjing Institute of Agricultural Mechanization, Ministry of Agriculture and Rural Affairs, Nanjing 210014, China;

*Correspondence: Tel: +86-13883002509; E-mail: ymingjin@swu.edu.cn

DOI: https://doi.org/10.35633/inmateh-64-11

Keywords: *IR drying, drying performance, technology optimization, temperature-varying, analysis of variance, sweet potato*

ABSTRACT

Sweet potato (Ipomoea batatas L.) is an important tuber crop for the daily consumption. Efficient processing must be taken to reduce wastage, and to improve quality and extend shelf period of sweet potato products. Infrared (IR) drying has advantages of high drying rate, good uniformity, and high production efficiency. A laboratory infrared (IR) dryer was developed to study the drying performance of sweet potato slice and its technology optimization in this paper. Single-factor, orthogonal, and temperature-varying experiments of IR drying of sweet potato slice were conducted sequentially. Temperature, slice thickness and steaming time were defined as control factors, and effective moisture diffusivity (EMD), total color change (TCC), specific energy consumption (SEC) and drying time were defined as evaluation indexes. Same weights were applied to the synthetic evaluation index (SEI). Experiment results and statistical analysis showed that: temperature-varying IR drying technology of temperature-decrease mode, under drying conditions of 70ºC (75min) - 65ºC (to end), showed the best drying performance; the optimal combinations for temperature-constant were slice thickness 3 mm, temperature 70ºC, and steaming time 6 min; Midilli et al. model gave the best approximation to experimental data of moisture ratio, with coefficient of determination 0.99933, reduced Chi-square 0.00007, and root mean square error (RMSE) 0.00838; high temperature (75ºC) and large slice thickness (9 mm) were not suitable for IR drying of sweet potato slice. The results of this study can provide references for research on IR drying technology and design of IR dryer for sweet potato slice.

摘要

甘薯是一种日常食用的重要根茎类作物。为了降低损坏、提高品质和延长储藏期，需对甘薯进行有效的加工处理。近红外干燥具有干燥速率快、均匀性好和效率高等优点。本文开发了一套实验用近红外干燥机用于甘薯片的干燥性能和工艺优化研究。依次对甘薯片进行近红外干燥的单因素试验、正交试验和变温试验。以温度、甘薯片厚度和蒸制时间为控制因子，有效水分扩散系数、总色差、比能耗和干燥时间为评价指标。对各评价指标赋予均等权重后得到综合指标。实验结果和数据分析表明：70 ºC (75min) - 65 ºC (至结束)的降温模式变温干燥工艺具有最佳干燥性能；常温干燥工艺的最优控制因子参数组合为：甘薯片厚度 3mm、温度 70 ºC、蒸制时间 6min；Midilli 模型对水分比的实验数据具有最佳拟合近似度，其决定系数 0.99933、卡方 0.00007、平均根方误差 0.00838；高的温度（75 ºC）和大的甘薯片厚度（9mm）不适合用于甘薯片的近红外干燥。本文研究结果可为基于甘薯片近红外干燥工艺和干燥机设计提供参考。

INTRODUCTION

Sweet potato (*Ipomoea batatas* L.) is an important tuber crop of the genus Convolvulaceae and it is broadly planted in Asia, Africa, and South America (*Liu, B. et al, 2020*). According to FAO, China ranks the first in annual planting area and production, and they are 2.374×10^6 ha and 5.199×10^7 tons in 2019. Sweet potato contains enormous amount of starch, protein, minerals, dietary fibers, and vitamins (*Song, F. et al, 2019; Rashid M. T. et al, 2020*). It can be consumed as staple food, snacks or bakery products (*Hanim, A. B. M. et al, 2014*). In addition, sweet potato can regulate blood sugar, improve immunity function and prevent

[1] *SY Xie, Prof.; ZR Yang, Ms.; L Yang, Prof.; ST Li, Ms.; JL Wang, Ms.; MJ Yang, Prof.*

cancer (*Wang, S. et al, 2016*). However, sweet potato is seasonal, and fresh sweet potato is susceptible to microbial activities because of high moisture content. These microbial activities lead to degradation and spoilage (*Onwude, D. I. et al, 2019*). Timely processing or preservation operations must be taken to reduce wastage, and to improve quality and extend shelf period of products.

Drying is an important and effective operation to remove moisture from fresh agricultural products. It implies simultaneous heat and mass transfer (*Rojas, M. L. & Augusto, P. E. D., 2018; Stasiak, M. et al, 2020*). Hot-air drying is the most common method for agricultural products, with main drawbacks of undesirable changes in physics, chemics, structure, nutrition, and color (*Ren, G. et al, 2020*). Infrared (IR) drying is used to heat materials by absorption of IR energy in the form of resonance between the electromagnetic radiation frequency and inherent frequency of the moisture in the materials, with advantages of high drying rate, good uniformity, and high production efficiency (*Huang, X. et al, 2021; Li, B. et al, 2019*). IR drying has been successfully applied to sweet potato slice, but its applications were mainly combined with other drying methods, such as hot-air drying (*Onwude, D. I. et al, 2018*), freeze drying (*Song, F. et al, 2019*), and hot-press drying (*Oh, S. et al, 2017*). However, an improper drying operation also causes the quality decline of dried products (*Zhang, M. et al, 2017*).

Doymaz et al. (2012) investigated the effect of IR power levels of 104, 125, 146 and 167 W on drying kinetics and rehydration ratio of sweet potato slice. The increase in the power level decreased the drying time. The highest rehydration ratio was obtained in the power level of 146 W. Logarithmic model gave a better fit of drying kinetics. *Onwude et al.* (2019) examined the performance of different combined IR and hot-air drying strategies for sweet potato slice, including simultaneous IR and hot-air drying, two-stage sequential hot-air and IR drying, two-stage sequential IR and hot-air drying, and intermittent IR and hot-air drying. Strategy of Intermittent IR and hot-air drying was the most suitable strategy for sweet potato slice. Wu et al. (2020) evaluated the influence of ultrasonic (US) pre-treatment on drying kinetics and quality of sweet potato slice in IR freeze drying. The US pre-treatment improved the quality of dried sweet potato slice and decreased the drying time. *Onwude et al.* (2021) developed a fully coupled multiphase model for combined IR-convective drying of sweet potato slice. The multiphase model showed the advantage in swift quantification of phase change and impact of operating parameters. Nevertheless, there are few publications on the performance-based technology optimization of IR drying of sweet potato slice.

The aim of this study was to (1) determine the levels of control factors that affect performance of IR drying of sweet potato slice, (2) find the optimal combinations for temperature-constant IR drying technology for sweet potato slice, (3) select the best model to fit experimental data with good approximation, and (4) determine the best temperature-varying IR drying technology with high performance of SEI.

MATERIALS AND METHODS

Materials

Samples of fresh sweet potato (*Ipomoea batatas L.*) were handpicked and purchased. Rotten and damaged samples were removed, and physically similar samples were stored at 4-8ºC in a sealed dark bag in a refrigerator (BC/BD-195HE, Henan Xinfei Electrical Appliance Co., Ltd., China). The initial moisture content of the samples was measured in accordance with Chinese standard “Determination of moisture in foods” (*China National Standardizing Committee, 2016*). The initial moisture was found to be 72.0 % - 76.1 % w.b.

Before each experiment, the samples were taken out of the refrigerator, washed, hand peeled and sliced. The sliced samples were color-fixed with color fixative of 0.3% citric acid + 0.1% ascorbic acid + 99.6% water (w/w) for 30 min (*He, J. et al, 2013*). Then, the sliced samples were steamed at 100ºC by a thermostat water bath (DF-101S-2L, Shanghai Pailan Instrument Equipment Co., Ltd., China). A laboratory IR dryer was developed for drying the pre-treated slices. It consists of control panel, temperature sensors, IR heaters, screen mesh (material tray), mesh stand, air inlet, air outlet, and drying chamber with 500 × 260 mm in cross section and 260 mm in height, as shown in Fig. 1. The screen mesh is placed between 2 temperature sensors with precision of ± 0.5ºC (DS18B20, Dallas Semiconductor Inc., USA). Two IR heaters of carbon fiber quartz (YH-001, Jiuerbao Optoelectronics Technology Co., Ltd., China), 300 W per heater, are fixed on the ceiling of the drying chamber. Energy consumption was measured by an electric power monitor (P08S-10, Xincheng Electronic Company Introduction, China). Total color change (TCC) was measured by a colorimeter (NR60CP, Shenzhen 3nh Technology Co., Ltd., China) after dried samples being powdered by a pulverizer (FW100, Tianjin Taisite Instrument Co., Ltd., China).

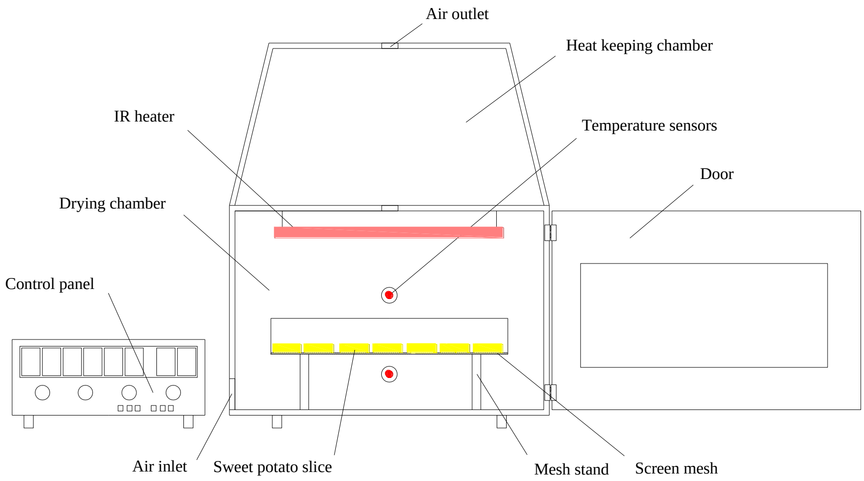

Fig. 1 - Schematic diagram of the IR dryer

Methods

Experiment arrangement

Single-factor experiment, orthogonal experiment and temperature-varying experiment were conducted in this study.

As for single-factor experiment, it was conducted to investigate the effect of individual control factor on performance of IR drying of sweet potato slice while levels of other factors remained constant, and the experiment arrangement was designed as listed in Table 1. Define temperature as factor A, slice thickness as factor B, and steaming time as factor C. No. 2, No.5 and No. 10 had the same combinations of factorial levels. Nevertheless, they kept in different rows in the table for the convenience of statistical analysis and presentation of results. Evaluation indexes included effective moisture diffusivity (EMD), TCC, Specific energy consumption (SEC), and drying time. Thereafter, normalization was applied to all evaluation indexes and equal weights were given to each evaluation index to obtain the SEI. The smaller the SEI is, the better the IR drying process is. The SEI was expressed as:

$$E_{\mathrm{s}} = w_1\left(1 - D_{\mathrm{e}}'\right) + w_2\Delta E' + w_3 E' + w_4 t_{\mathrm{d}}' \tag{1}$$

where

E_{s} is SEI, [dimensionless];

D_{e}' – normalized EMD, [dimensionless];

$\Delta E'$ – normalized TCC, [dimensionless];

E' – normalized SEC, [dimensionless];

t_{d}' – normalized drying time, [dimensionless];

w_1, w_2, w_3, and w_4 – weights for EMD, TCC, SEC, and drying time, respectively, [dimensionless].

Table 1

Single-factor experiment arrangement and results

No.	Factor A [°C]	Factor B [mm]	Factor C [min]	Experiment results				SEI
				EMD [×10^{-10}m^2/s]	TCC	SEC [kJ/g]	Drying time [min]	
1	60	3	6	5.112	19.548	108.758	108.094	0.4843
2	65			6.027	19.219	102.543	75.028	0.4017
3	70			6.567	20.016	100.144	89.136	0.4248
4	75			9.888	22.829	81.537	59.057	0.3724
5	65	3	6	6.027	19.219	102.543	75.028	0.4017
6		5		12.404	16.496	127.814	136.866	0.2498
7		7		13.950	19.184	160.973	219.457	0.4144
8		9		14.566	18.646	173.761	345.967	0.5849
9	65	3	4	5.721	19.808	112.011	80.738	0.4636
10			6	6.027	19.219	102.543	75.028	0.4017
11			8	7.125	19.832	110.027	84.659	0.4258
12			10	5.008	20.891	114.354	92.778	0.5418

As for orthogonal experiment, it was conducted to investigate the significance of each factors on performance of IR drying of sweet potato slice, and to optimize process of the IR drying technology. Levels of main control factors were defined according to single-factor experiment, as listed in Table 2. Experiment arrangement was designed in accordance with an appropriate orthogonal array $L_9(3^4)$, as listed in Table 3.

Table 2

Control factors and their levels

Levels	Control factors		
	Temperature A [°C]	Slice thickness B [mm]	Steaming time C [min]
1	60	3	4
2	65	5	6
3	70	7	8

Table 3

Orthogonal experiment arrangement and results

No.	Factor A	Factor B	Factor C	Error	Experiment results				SEI
					EMD [$\times 10^{-10}$m^2/s]	TCC	SEC [kJ/g]	Drying time [min]	
1	1	1	1	1	4.945	25.969	103.954	112.333	0.5617
2	1	2	2	2	7.539	20.116	130.074	223.117	0.6020
3	1	3	3	3	10.138	16.975	158.461	293.036	0.6595
4	2	1	2	3	6.173	20.886	97.998	89.275	0.3806
5	2	2	3	1	9.634	18.194	147.445	161.813	0.5054
6	2	3	1	2	13.013	16.706	167.346	208.887	0.5236
7	3	1	3	2	6.402	13.989	144.533	77.179	0.3814
8	3	2	1	3	12.202	15.940	136.650	127.160	0.3229
9	3	3	2	1	16.155	15.611	168.969	162.070	0.3822

As for temperature-varying experiment, it was conducted to investigate the advantages of temperature-varying drying technology in final product quality and energy consumption. Two drying modes, namely temperature-decrease mode, and temperature-increase mode, were investigated, both modes having 3 different drying conditions. The slice thickness was 3 mm, and the steaming time was 6 min. Experiment arrangement was designed based on single-factor experiment and orthogonal experiment, as listed in Table 4. Since TCC and SEC were the major factors considered for a practical IR drying process, evaluation indexes of TCC and SEC were employed to calculate the SEI.

Table 4

Temperature-varying experiment arrangement and results

No.	Drying modes	Drying conditions	TCC	SEC [kJ/g]	SEI
1	Temperature-decrease	70ºC (75min) - 60ºC (to end)	18.508	73.458	0.5000
2		70ºC (75min) - 65ºC (to end)	17.763	75.905	0.2678
3		65ºC (105min) - 60ºC (to end)	18.006	93.485	0.5357
4	Temperature-increase	65ºC (105min) - 70ºC (to end)	17.063	101.819	0.2965
5		60ºC (120min) - 70ºC (to end)	17.907	108.076	0.6539
6		60ºC (120min) - 65ºC (to end)	18.340	121.278	0.9416

Data treatment

The samples of sweet potato slice were weighed every 5 min during the 1st hour of IR drying, every 15 min during the 2nd hour, and every 30 min till the end of drying. The drying ended when neighbor weighing of mass change was less than 0.02 g. Three replications were conducted for each experiment.

Moisture ratio (MR) and drying rate (DR) are expressed as (*Chandrasekar, M. et al, 2018*):

$$MR = \frac{M_t}{M_0} \tag{2}$$

$$DR = \frac{M_t - M_{t+\Delta t}}{\Delta t} \tag{3}$$

where

MR is moisture ratio, [dimensionless];

DR – drying rate, [% d.b./min];

M_0 – initial moisture content [% d.b.];

M_t – instantaneous moisture content [% d.b.];

t – time [min].

EMD is expressed as (*Guine, R. P. F. et al, 2017*):

$$\ln MR = \ln\frac{8}{\pi^2} - \frac{\pi^2 D_e t}{L^2} \tag{4}$$

where

D_e is effective moisture diffusivity, [m²/s];

L – layer thickness, [m].

TCC between dried and fresh material is calculated as (*Pasławska, M. et al, 2020*):

$$\Delta E = \sqrt{(\Delta L^*)^2 + (\Delta a^*)^2 + (\Delta b^*)^2} \tag{5}$$

where

Δ*E* is total color change, [dimensionless];

Δ*L**, Δ*a**, and Δ*b** – changes of lightness, greenness, and yellowness between dried and fresh material, respectively, [dimensionless].

SEC is defined as the ratio of energy consumption for removing of a unit mass of moisture in the material, and it is expressed as:

$$E = \frac{Q}{m} \times 3600 \tag{6}$$

where

E is specific energy consumption [kJ/g];

Q – energy consumed, [kW·h];

m – mass of moisture removal, [g].

Mathematical thin layer drying models were used for the approximation of moisture ratio of orthogonal experiment, as listed in Table 5. Coefficient of determination (R^2), reduced Chi-square (χ^2) and root mean square error (RMSE) were applied to evaluate accuracy of the approximation (*Yang, L. et al, 2019*). The model that gave the best approximation was employed to calculate drying time of each experiment. The drying time was defined as the time when moisture content of the sweet potato slices decreased to 10% d.b., the safe storage level of dried sweet potato slices.

Table 5

Mathematical thin layer drying models used for the approximation

Model	Model name	Equations		References
1	Page	$MR = \exp(-kt^n)$	(7)	*Page, G. 1949*
2	Two-term	$MR = a\exp(-k_1 t) + b\exp(-k_2 t)$	(8)	*Henderson, S. M., 1974*
3	Verma et al.	$MR = a\exp(-kt) + (1-a)\exp(-gt)$	(9)	*Verma, L. R. et al, 1985*
4	Midilli et al.	$MR = a\exp(-kt^n) + bt$	(10)	*Midilli, A. et al, 2002*
5	Hii et al.	$MR = a\exp(-bt^c) + d\exp(-gt^c)$	(11)	*Hii, C. et al, 2009*

Note: *a*, *b*, *c*, *d*, *g*, *k*, k_1, k_2, *n* are parameters, [dimensionless].

RESULTS AND DISCUSSIONS

Single-factor experiment

The profiles of moisture ratio and drying rate of sweet potato slice at different drying conditions by single-factor experiment were plotted, as shown in Fig. 2. The corresponding values of EMD, TCC, SEC, drying time and SEI were calculated, as listed in Table 1. The comparisons of the drying performance at different drying conditions were plotted, as shown in Fig. 3. The drying time was calculated by *Midilli et al.* model (Model 4 in Table 5) which showed the best approximation of moisture ratio during the IR drying of sweet potato slice.

As seen from Fig. 2, the moisture ratio decreased with the increase of time processed. The drying rate decreased with the decrease of moisture ratio, except for the initial drying period. During the initial drying period, the moisture ratio was high and the sweet potato slice required to be heated to drying temperature that was set for each experiment, which affected the changes of moisture ratio and drying rate in this period. There was no constant drying rate stage for sweet potato slice. The higher the drying temperature was, the shorter the drying time was required. Steaming time had little effect on the changes of moisture ratio and drying rate. Nevertheless, steaming benefited nutritious quality of the sweet potato slice (*Trancoso-Reyes, N. et al, 2016*), pre-treatment of steaming was kept in the IR drying technology of this study. As seen from Fig. 3, slice thickness had strong effects on EMD and drying time, temperature had certain effects on them, and steaming time had a small effect on them. The larger the slice thickness was, the higher the EMD and drying time were; the higher the temperature was, the higher the EMD was, and the lower the drying time was. All control factors had a small effect on TCC, except for the effect of temperature at 75ºC and slice thickness of 5 mm. Slice thickness had a strong effect on SEC, temperature had a certain effect on SEC, and steaming time had a small effect on SEC.

The larger the slice thickness was, the higher the SEC was. As for SEI, the effect of temperature was the strongest among all control factors.

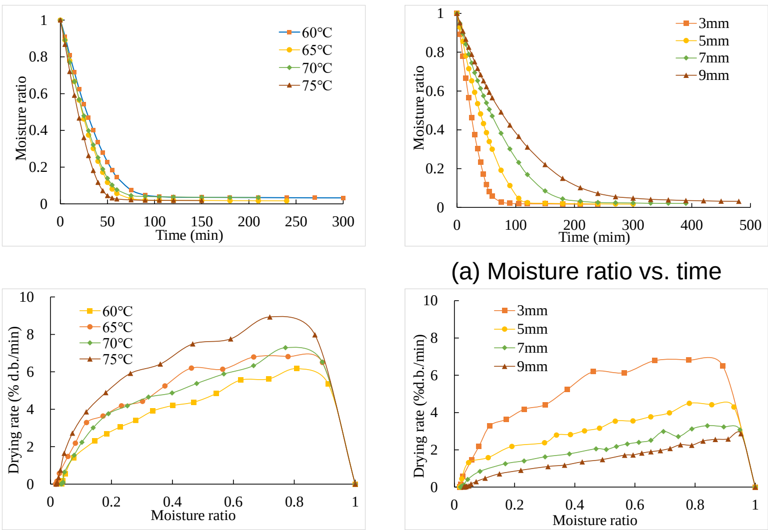

(a) Moisture ratio vs. time

(b) Drying rate vs. moisture ratio

Fig. 2 - Drying curves of sweet potato slice by single-factor experiment

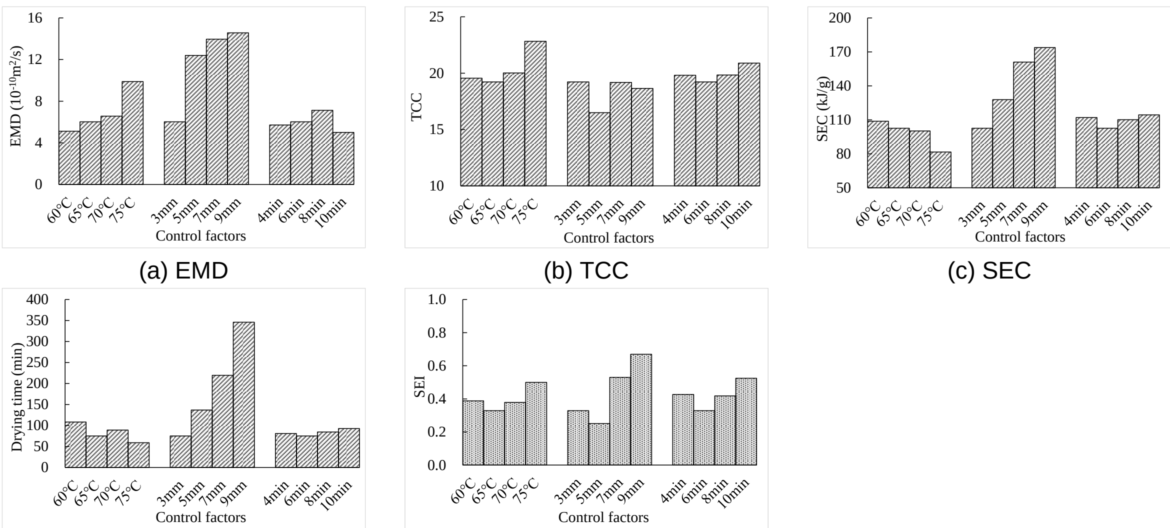

(a) EMD (b) TCC (c) SEC

(d) Drying time (e) SEI

Fig. 3 - Drying performance of sweet potato slice by single-factor experiment

Orthogonal experiment

According to single-factor experiment results and the corresponding analysis, levels of temperature 75ºC, slice thickness 9 mm, and steaming time 10 min were not considered in the orthogonal experiment. The profiles of moisture ratio and drying rate of sweet potato slice of different runs by orthogonal experiment were plotted, as shown in Fig. 4. The corresponding values of EMD, TCD, SEC, drying time and SEI were calculated, as listed in Table 3. The visual observations of dried sweet potato slice of different runs were presented, as shown in Fig. 5 a. As seen from Fig. 4, The profiles of moisture ratio and drying rate of sweet potato slice by orthogonal experiment were similar with those by single-factor experiment.

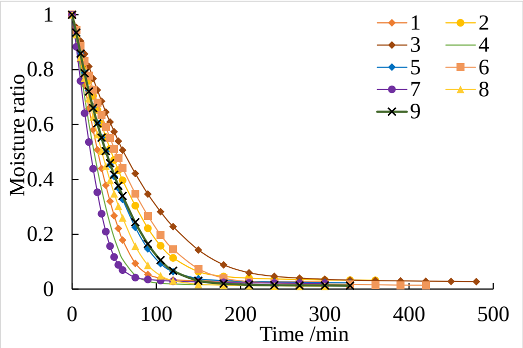

(a) Moisture ratio vs. drying time

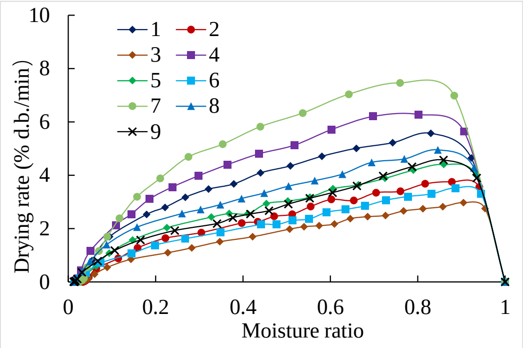

(b) Drying rate vs. moisture ratio

Fig. 4 - Drying curves of sweet potato slice by orthogonal experiment

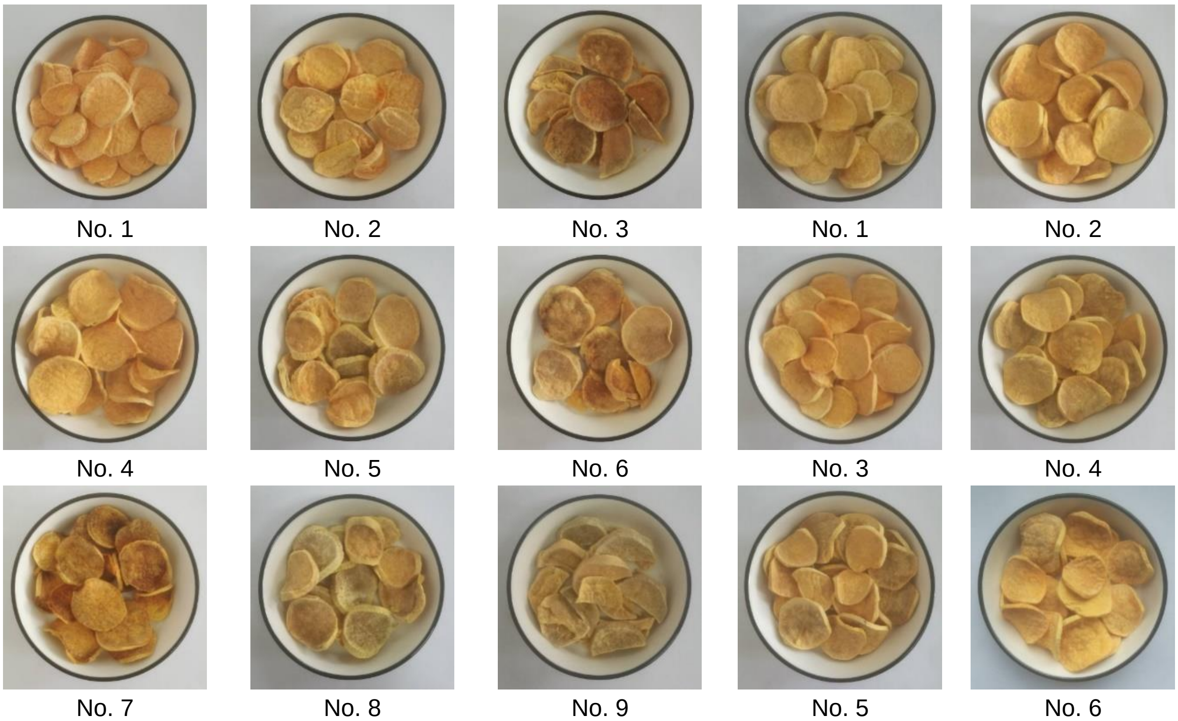

(a) Orthogonal experiment (b) Temperature-varying experiment

Fig. 5 - Visual observations of dried sweet potato slice of different runs

Analysis of variance (ANOVA) was performed to obtain the effects and their significance level of each control factor on the individual evaluation indexes and the SEI. The results of ANOVA were presented, as listed in Table 6. As seen from Table 6, slice thickness had a significant effect on EMD at confidence level 97.06%. Temperature had a significant effect on EMD at confidence level 91.08%. Slice thickness had a significant effect on drying time at confidence level 95.48%. Temperature had a significant effect on drying time at confidence level 90.83%. Slice thickness had a significant effect on SEC at confidence level 90.20%. As for SEI, temperature had a significant effect at confidence level 96.29%.

Table 6

Analysis of variance

Evaluation indexes	Source of variance	Degree of freedom	Sum of squares	Mean sum of square	F-ratio	Critical F-ratio
EMD	Factor A	2	24.555	12.277	10.207	$F_{0.0892}(2, 2) = 10.207$(*)
	Factor B	2	79.311	39.655	32.967	$F_{0.0294}(2, 2) = 32.967$*
	Factor C	2	3.290	1.645	1.368	$F_{0.4223}(2, 2) = 1.368$
	Error	2	2.406	1.203	/	/
	Total	8	109.561	/	/	/
TCD	Factor A	2	51.646	25.823	3.719	$F_{0.2119}(2, 2) = 3.719$
	Factor B	2	22.386	11.193	1.612	$F_{0.3828}(2, 2) = 1.612$
	Factor C	2	16.557	8.279	1.192	$F_{0.4562}(2, 2) = 1.192$
	Error	2	13.885	6.943	/	/
	Total	8	104.475	/	/	/
SEC	Factor A	2	570.327	285.163	1.428	$F_{0.4119}(2, 2) = 1.428$
	Factor B	2	3674.281	1837.141	9.199	$F_{0.0980}(2, 2) = 9.199$(*)
	Factor C	2	530.640	265.320	1.329	$F_{0.4294}(2, 2) = 1.329$
	Error	2	399.407	199.703	/	/
	Total	8	5174.654	/	/	/
Drying time	Factor A	2	11759.538	5879.769	9.900	$F_{0.0917}(2, 2) = 9.900$(*)
	Factor B	2	25098.674	12549.337	21.130	$F_{0.0452}(2, 2) = 21.130$*
	Factor C	2	1221.226	610.613	1.028	$F_{0.4931}(2, 2) = 1.028$
	Error	2	1187.819	593.909	/	/
	Total	8	39267.256	/	/	/
SEI	Factor A	2	0.091	0.045	25.928	$F_{0.0371}(2, 2) = 25.928$*
	Factor B	2	0.010	0.005	2.787	$F_{0.2641}(2, 2) = 2.787$
	Factor C	2	0.006	0.003	1.709	$F_{0.3691}(2, 2) = 1.709$
	Error	2	0.004	0.002	/	/
	Total	8	0.110	/	/	/

Notes: * indicates the significance of effect at confidence level higher than 95%; (*) indicates the significance of effect at confidence level higher than 90%.

According to statistics of range analysis (*Yang, L. et al, 2019*), the optimal combinations of control factors' levels for individual evaluation indexes and SEI were obtained as: EMD: B3A3C1; TCD: A3B3C2; SEC: B1A3C2; drying time: B1A3C1; SEI: B1A3C2. The sequence of characters in the combinations indicated the significance of the control factor with a decrease mode. The numbers in the combinations indicated the levels of the corresponding control factors. Therefore, the optimal combinations for SEI were slice thickness 3 mm, temperature 70ºC, and steaming time 6 min.

The experimental data of moisture ratio of the orthogonal experiment were fitted into the selected mathematical models (Table 5). The model parameters and accuracy of approximation were shown in Table 7. The higher the R^2 values and the lower the χ^2 and RMSE values were, the better the approximation was (*Wang, Z. F. et al, 2007*). As seen from Table 7, Midilli et al. model (Model 4) gave the best approximation to experimental data of moisture ratio, with R^2 0.99933, χ^2 0.00007, and RMSE 0.00838. To validate the effectiveness of Midilli et al. model, experiments of combinations that were different from those in Table 3 were conducted. The profiles of experimental and calculated moisture ratio at different drying conditions were plotted, as shown in Fig. 6. The experimental results agreed well with calculated data (mean coefficient of determination 0.99857, mean relative error 12.15%), and the accuracy of the approximation was presented, as listed in Table 8.

Temperature-varying experiment

The profiles of moisture ratio and drying rate of sweet potato slice at different drying conditions by temperature-varying experiment were plotted, as shown in Fig. 7. The visual observations of dried sweet potato slice of different technology were presented, as shown in Fig. 5 b. The corresponding values of TCD, SEC, and SEI were calculated, as listed in Table 4. Same weights were applied to TCD and SEC for the calculation of SEI. As seen from Table 4, drying mode of temperature-decrease, namely, No. 2 under drying conditions of 70ºC (75min) - 65ºC (to end) showed the minimum SEI 0.2678. Then, drying mode of No.2 was the optimal temperature-varying drying technology. If same weights were applied to results of No. 2 and No. 3 in Table 1, their resultant values of SEI were 0.3288 and 0.3287, respectively. Therefore, there were 18.55 % and 29.28% decrease of SEI by the optimal temperature-varying drying technology compared to the optimal traditional temperature-constant drying technologies 65ºC and 70ºC, respectively. The experiments of No. 2 and No. 3 were the temperature-constant IR drying technologies under same conditions of slice thickness 3 mm and steaming time 6 min as temperature-varying IR drying technology, while their temperatures were 65ºC and 70ºC, respectively.

Table 7

Statistical analysis of mathematical models

Model	Parameters	values No. 1	No. 2	No. 3	No. 4	No. 5	No. 6	No. 7	No. 8	No. 9	Mean values
1	k	0.00960	0.00945	0.00795	0.01072	0.00944	0.00799	0.01431	0.00897	0.01025	/
	n	1.25783	1.12191	1.08799	1.28723	1.16915	1.13689	1.26790	1.22587	1.14359	/
	R2	0.99753	0.99781	0.99855	0.99882	0.99809	0.99914	0.99686	0.99894	0.99911	0.99832
	χ2	0.00026	0.00024	0.00017	0.00012	0.00021	0.00010	0.00030	0.00012	0.00010	0.00018
	RMSE	0.01618	0.01553	0.01313	0.01117	0.01449	0.01006	0.01726	0.01087	0.00996	0.01318
2	a	-477.704	-0.24228	-0.14477	-40.3014	47.8823	-25.0392	72.8883	95.6354	27.5444	/
	b	478.699	1.23978	1.14322	41.2945	-46.8867	26.0344	-71.8932	-94.6424	-26.5473	/
	k1	0.04577	0.04909	0.04172	0.05601	0.03104	0.02339	0.06471	0.03804	0.02931	/
	k2	0.04570	0.01866	0.01325	0.05498	0.03143	0.02291	0.06537	0.03831	0.02990	/
	R2	0.99739	0.99778	0.99856	0.99873	0.99812	0.99928	0.99668	0.99900	0.99921	0.99831
	χ2	0.00028	0.00024	0.00017	0.00013	0.00021	0.00008	0.00031	0.00011	0.00009	0.00018
	RMSE	0.01661	0.01562	0.01308	0.01162	0.01438	0.00920	0.01775	0.01054	0.00934	0.01313
3	a	537.501	1.24476	1.14546	503.288	1289.708	-161.250	-124.412	-545.642	1337.069	/
	k	0.04550	0.01868	0.01326	0.05510	0.03102	0.02298	0.06494	0.03787	0.02945	/
	g	0.04556	0.04785	0.04073	0.05518	0.03104	0.02291	0.06465	0.03783	0.02946	/
	R2	0.99751	0.99788	0.99861	0.99877	0.99819	0.99930	0.99683	0.99902	0.99924	0.99837
	χ2	0.00026	0.00023	0.00016	0.00013	0.00020	0.00008	0.00030	0.00011	0.00008	0.00017
	RMSE	0.01623	0.01528	0.01283	0.01143	0.01410	0.00910	0.01734	0.01044	0.00916	0.01288
4	a	0.98850	0.98943	0.99131	0.98738	0.98525	0.98588	0.99014	0.98472	0.98880	/
	k	0.00801	0.00752	0.00640	0.00921	0.00756	0.00660	0.01253	0.00748	0.00891	/
	n	1.30785	1.18113	1.14118	1.32834	1.22499	1.18059	1.30771	1.26985	1.17707	/
	b	0.00011	0.00010	0.00006	0.00007	0.00008	0.00003	0.00017	0.00003	0.00003	/
	R2	0.99931	0.99958	0.99976	0.99928	0.99926	0.99945	0.99888	0.99913	0.99930	0.99933
	χ2	0.00007	0.00005	0.00003	0.00008	0.00008	0.00006	0.00011	0.00010	0.00008	0.00007
	RMSE	0.00854	0.00683	0.00533	0.00877	0.00904	0.00802	0.01029	0.00984	0.00879	0.00838
5	a	0.95283	0.99285	0.00730	0.90394	0.93144	0.91810	0.95821	0.87313	0.86603	/
	b	0.00629	0.00885	-0.00132	0.00464	0.00506	0.00375	0.01017	0.00275	0.00331	/
	c	1.35618	1.13585	1.13838	1.48775	1.30370	1.28985	1.35348	1.48873	1.38033	/
	d	0.04758	0.00715	0.98453	0.09550	0.06872	0.08087	0.04183	0.12488	0.13287	/
	g	0.09754	0.36186	0.00649	0.06140	0.06906	0.04594	0.20015	0.03467	0.03394	/
	R2	0.99729	0.99749	0.99974	0.99907	0.99809	0.99935	0.99650	0.99953	0.99945	0.99850
	χ2	0.00029	0.00028	0.00003	0.00010	0.00021	0.00008	0.00033	0.00005	0.00006	0.00016
	RMSE	0.01692	0.01663	0.00553	0.00993	0.01449	0.00876	0.01823	0.00721	0.00779	0.01172

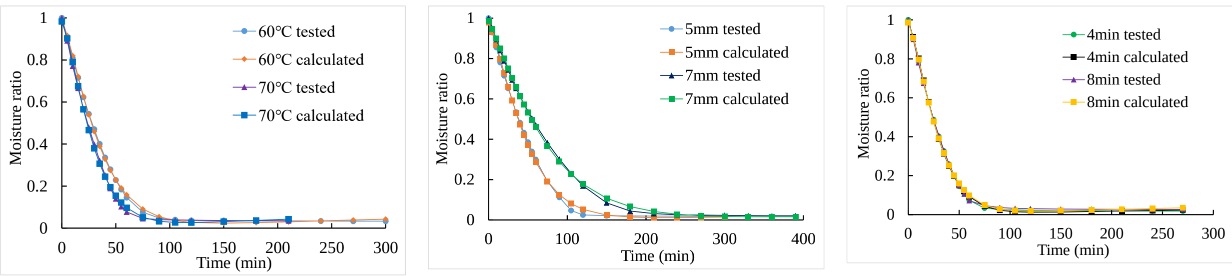

(a) Different temperature (b) Different slice thickness (c) Different steaming time

Fig. 6 - Validation of Midilli et al. model under different drying conditions

Table 8

Accuracy of the approximation of Midilli et al. model under different drying conditions

No.	Factor A [°C]	Factor B [mm]	Factor C [min]	R^2	Relative error [%]
1	60	3	6	0.99915	9.42
2	70			0.99810	10.59
3	65	5	6	0.99806	16.17
4		7		0.99899	9.87
5	65	3	4	0.99890	13.48
6			8	0.99823	13.38

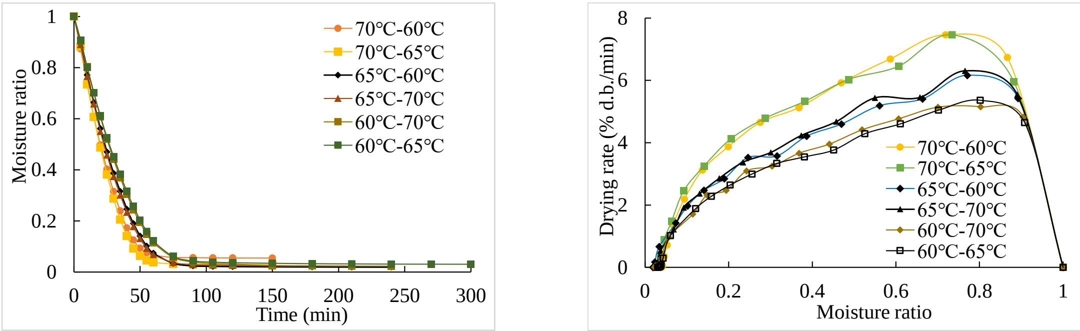

(a) Moisture ratio vs. drying time (b) Drying rate vs. moisture ratio

Fig. 7 - Drying curves of sweet potato slice by temperature-varying experiment

CONCLUSIONS

A laboratory IR dryer was developed to study the drying characteristics of sweet potato slice, to investigate the effects of control factors and their significance on drying performance, and to optimize the IR drying technology. Main conclusions were drawn as follows:

- Temperature-varying IR drying technology of temperature-decrease mode, under drying conditions of 70ºC (75min) - 65ºC (to end), showed the best drying performance while considering TCD and SEC, with 18.55% and 29.28% decrease of SEI compared to temperature-varying IR drying technologies of 65ºC and 70ºC, respectively.

- The significance order of the effects of control factors on the SEI was: temperature, slice thickness and steaming time, in a sequence of decrease. Temperature was significant at confidence level 96.29%. The optimal combinations for temperature-constant were slice thickness 3 mm, temperature 70ºC, and steaming time 6 min.

- Midilli et al. model gave the best approximation to experimental data of moisture ratio, with R2 0.99933, χ2 0.00007, and RMSE 0.00838. The results of validation experiment agreed well with calculated data of Midilli et al. model, with R2 0.99857 and mean relative error 12.15%.

- Temperature of 75ºC and slice thickness of 9 mm were not suitable for IR drying of sweet potato slice because the former resulted in high TCD and the latter resulted in high SEC. Steaming time had little effect on the IR drying performance.

ACKNOWLEDGEMENTS

The study was funded by Chongqing Science and Technology Bureau (cstc2019jscx-gksbx0108); Chongqing Municipal Education Commission (kjcx2020002); Key Lab of Modern Agricultural Equipment, Ministry of Agriculture and Rural Affairs, China (ht20200705).

REFERENCES

[1] Chandrasekar M., Senthilkumar T., Kumaragurubaran B., Fernandes, J. P., (2018). Experimental investigation on a solar dryer integrated with condenser unit of split air conditioner (A/C) for enhancing drying rate. *Renewable Energy*, Vol. 122, pp. 375-381, England, DOI: 10.1016/j.renene.2018.01.109;

[2] Doymaz İ., (2012). Infrared drying of sweet potato (*Ipomoea batatas* L.) slices. *Journal of Food Science and Technology*, Vol. 49, Issue 6, pp. 760-766, New Delhi / India, DOI: 10.1007/s13197-010-0217-8;

[3] Guine R. P. F., Brito M. F. S., Ribeiro J. R. P., (2017). Evaluation of mass transfer properties in convective drying of kiwi and eggplant. *International Journal of Food Engineering*, Vol. 13, Issue 7, pp. 1-13, Berlin/Germany, DOI: 10.1515/ijfe-2016-0257;

[4] Hanim A. B. M., Chin N. L., Yusof Y. A., (2014). Physico-chemical and flowability characteristics of a new variety of Malaysian sweet potato, VitAto flour. International Food Research Journal, Vol. 21, Issue 5, pp. 2099-2107, ISSN 1985-4668;

[5] He J., Cheng L., Hong Y., Gu Z., Li Z., (2013). Optimization of compound color fixative without sulfur during sweet potato flour processing (甘薯全粉加工中无硫复合护色工艺优化). *Transactions of the Chinese Society of Agricultural Engineering*, Vol. 29, Issue 9, pp. 275-284, Chinese Society of Agricultural Engineering, Beijing/P.R.C.; DOI: 10.3969/j.issn.1002-6819.2013.09.035;

[6] Henderson S. M., (1974). Progress in developing the thin layer drying equation. *Transactions of the American Society of Agricultural Engineers*, Vol. 17, pp.1167-1172, USA, ISSN: 0001-2351;

[7] Hii C. L., Law C. L., Cloke M., (2009). Modeling using a new thin layer drying model and product quality of cocoa. *Journal of Food Engineering*, Vol. 90, Issue 2, pp. 191-198, England, DOI: 10.1016/j.jfoodeng.2008.06.022;

[8] Huang X., Li W., Wang Y., Wan F., (2021). Drying characteristics and quality of stevia rebaudiana leaves by far-infrared radiation. *LWT-Food Science and Technology*, Vol. 140, 110638, Ed. ELSEVIER, Amsterdam/Netherlands, DOI: 10.1016/j.lwt.2020.110638;

[9] Li B., Lin J., Zheng Z., Duan H.; Li D., Wu M., (2019). Effects of different drying methods on drying kinetics and physicochemical properties of Chrysanthemum morifolium Ramat. *International Journal of Agricultural and Biological Engineering*, Vol. 12, Issue 3, pp. 187-193, Beijing/PRC, DOI: 10.25165/j.ijabe.20191203.4820;

[10] Liu B., Lyu X., Wang C., Sun J., Jiang W. (2020). Process optimization of high temperature and short time hot air treatment to promote the callus formation of sweet potatoes (高温短时热空气处理促进甘薯愈伤的工艺优化). *Transactions of the Chinese Society of Agricultural Engineering*, Vol.36, Issue 19, pp.313-322, Beijing/PRC, DOI: 10.11975/j.issn.1002-6819.2020.19.036;

[11] Midilli A., Kucuk H., Yapar Z., (2002) A new model for single layer drying. *Drying Technology*, Vol. 20, Issue 7, pp. 1503-1513, USA, DOI: 10.1081/DRT-120005864;

[12] Oh S., Ramachandraiah K., Hong G. P., (2017). Effects of pulsed infra-red radiation followed by hot-press drying on the properties of mashed sweet potato chips. *LWT-Food Science and Technology*, Vol. 82, pp. 66-71, Ed. ELSEVIER, Amsterdam/Netherlands, DOI: 10.1016/j.lwt.2017.04.023;

[13] Onwude D. I., Hashim N., Abdan K., Janius R., Chen G. N., (2018). The effectiveness of combined infrared and hot-air drying strategies for sweet potato. *Journal of Food Engineering*, Vol. 241, Jan., pp. 75-87, Ed. ELSEVIER, Netherlands, DOI: 10.1016/j.jfoodeng.2018.08.008;

[14] Onwude D. I., Hashim N., Abdan K., Janius R.; Chen G.N., (2019). Experimental studies and mathematical simulation of intermittent infrared and convective drying of sweet potato (*Ipomoea Batatas* L.). *Food and Bioproducts Processing*, Vol. 114, pp. 163-174, England, DOI: 10.1016/j.fbp.2018.12.006;

[15] Onwude D. I., Hashim N., Abdan K., Janius R., Chen G. N., Kumar C., (2018). Modelling of coupled heat and mass transfer for combined infrared and hot-air drying of sweet potato. *Journal of Food Engineering*, Vol. 228, pp. 12-24, England, DOI: 10.1016/j.jfoodeng.2018.02.006;

[16] Onwude D. I., Hashim N., Chen G., Putranto A., Udoenoh N. R., (2021). A fully coupled multiphase model for infrared convective drying of sweet potato. *Journal of the Science of Food and Agriculture*, Vol. 101, Issue 2, pp. 398-413, Ed. WILEY, NJ/USA, DOI: 10.1002/jsfa.10649;

[17] Page G., (1949). Factors influencing the maximum rates of air-drying shelled corn in thin layer (MSc Thesis). Purdue University, WEST LAFAYETTE, IN/USA;

[18] Pasławska M., Sala K., Nawirska-Olszańska A., Stepien B., Plaskowska E., (2020). Effect of different drying techniques on dehydration kinetics, physical properties, and chemical composition of lemon thyme. *Natural Product Communications*, Vol. 15, Issue 2, pp. 1-12, USA, DOI: 10.1177/1934578X20904521;

[19] Rashid M. T., Jatoi M. A., Safdar B., Wali A., Aadil R. M., Sarpong F., Ma H. L., (2020). Modeling the drying of ultrasound and glucose pretreated sweet potatoes: the impact on phytochemical and functional groups. *Ultrasonics Sonochemistry*, Vol. 68, No. 105226, Ed. Elsevier, Netherlands, DOI: 10.1016/j.ultsonch.2020.105226;

[20] Ren G, Zhang L, Zeng F, Li Y. B., Li L. L., Duan X., (2020). Effects of hot air drying temperature and tempering time on the properties of maize starch. *International Journal of Agricultural and Biological Engineering*, Vol. 13, Issue 6, pp. 236-241, PRC, DOI: 10.25165/j.ijabe.20201306.3362;

[21] Rojas M. L., Augusto P. E. D., (2018). Ethanol and ultrasound pre-treatments to improve infrared drying of potato slices. *Innovative Food Science & Emerging Technologies*, Vol. 49, pp. 65-75, Ed. ELSEVIER SCI LTD, OXON/ England, DOI: 10.1016/j.ifset.2018.08.005;

[22] Song F., Xu Y., Zhang J., Qi Y., Zhang Y., (2019). Research on the effects of different drying conditions on quality of potato powder (不同干燥条件对马铃薯粉品质影响的研究). *Cereals & Oils*, Vol. 32, Issue 8, pp. 79-82, Ed. SHANGHAI INSTITUTE OF FOOD SCIENCE, SHANGHAI/PRC, ISSN: 1008-9578;

[23] Stasiak M., Musielak G., Mierzwa D., (2020). Optimization method for the evaluation of convective heat and mass transfer effective coefficients and energy sources in drying processes. *Energies*, Vol. 13, Issue 24, No. 6577, Switzerland, DOI: 10.3390/en13246577;

[24] Trancoso-Reyes N., Ochoa-Martinez L. A., Bello-Perez L. A., Morales-Castro J., Estevez-Santiago R., Olmedilla-Alonso B., (2016). Effect of pre-treatment on physicochemical and structural properties, and the bioaccessibility of β-carotene in sweet potato flour. *Food Chemistry*, Vol. 200, pp. 199-205, Ed. Elsevier SCI LTD, Oxon/ England, DOI: 10.1016/j.foodchem.2016.01.047;

[25] Verma L. R., Bucklin R. A., Endan J. B., Wratten F. T., (1985). Effects of drying air parameters on rice drying models. *Transactions of the American Society of Agricultural Engineers*, Vol. 28, pp. 296-301, USA, ISSN: 0001-2351;

[26] Wang S., Nie S., Zhu F., (2016). Chemical constituents and health effects of sweet potato. *Food Research International*, Vol. 89, pp. 90-116, Ed. Elsevier, Netherlands, DOI: 10.1016/j.foodres.2016.08.032;

[27] Wang Z. F., Sun J. H., Liao X. J., Chen F., Zhao G. H., Wu J. H. Hu X. S., (2007). Mathematical modeling on hot air drying of thin layer apple pomace. *Food Research International*, Vol. 40, Issue 1, pp. 39-46, Ed. Elsevier, Netherlands, DOI: 10.1016/j.foodres.2006.07.017;

[28] Wu X., Zhang M., Le Y., Yu, D. X., (2020). Influence of ultrasonic pretreatments on drying kinetics and quality attributes of sweet potato slices in infrared freeze drying (IRFD). *LWT-Food Science and Technology*, Vol. 131, No. 109801, Ed. Elsevier, Amsterdam/Netherlands, DOI: 10.1016/j.lwt.2020.109801;

[29] Yang L., Yin X.F., Li S.T., Wu D. K., Xie S. Y, Yang M. J, (2019). Effects of osmotic dehydration and process conditions on infrared drying: application to drying of chili pepper. *International Agricultural Engineering Journal*, Vol. 28, Issue 3, pp. 266-275, Beijing/PRC, ISSN: 0858-2114;

[30] Zhang M., Chen H., Mujumdar A. S., Tang J. M., Miao S., Wang Y. C., (2017). Recent developments in high-quality drying of vegetables, fruits, and aquatic products. *Critical Reviews in Food Science and Nutrition*, Vol. 57, Issue 6, pp. 1239-1255, USA, DOI: 10.1080/10408398.2014.979280;

[31] *** China National Standardizing Committee, (2106). GB 5009.3-2016, D*etermination of moisture in foods*. Beijing: Chinese Standard Press, PRC.

REMOTE MONITORING OF ENERGY PRODUCTION AND EFFICIENCY OF AN OFF-GRIDD PHOTOVOLTAIC SYSTEM
/
MONITORIZAREA DE LA DISTANTA A PRODUCTIEI DE ENERGIE SI A EFICIENTEI UNUI SISTEM FOTOVOLTAIC OFF-GRIDD

Rădoi Radu-Iulian *1); Dumitrescu Liliana 1); Chiriță Alexandru-Polifron 1); Vlăduț Nicolae-Valentin 2)
1)Hydraulics and Pneumatics Research Institute INOE 2000-IHP, Bucharest, Romania
2)National Institute of Research – Development for Machines and Installations Designed for Agriculture and Food Industry – INMA Bucharest, Romania
Tel: 0213363991; E-mail: radoi.ihp@fluidas.ro
DOI : https://doi.org/10.356.33/inmateh-64-12

Keywords: *Renewable energy, remote data monitoring, monitoring software, solar energy*

ABSTRACT
In remote locations where people are required to live, such as weather stations in mountain areas, astronomical observatories etc., it is necessary to provide electricity for the operation of equipment and for domestic needs. The optimal solution is the use of photovoltaic energy. Owners of solar systems can remotely monitor the operation of the photovoltaic plant via the Internet (LTE, LoRa). The operating parameters of the solar installation can be seen in real time or can be adjusted. The article presents theoretical aspects, the hardware structure of monitoring equipment and remote monitoring software, which allow the analysis of the production and efficiency of the photovoltaic (PV) installation.

REZUMAT
În locațiile îndepărtate în care oamenii trebuie să locuiască, cum ar fi stațiile meteo din zonele montane, observatoarele astronomice etc., este necesar să se furnizeze energie electrică pentru funcționarea echipamentelor și pentru nevoile casnice Soluția optimă este utilizarea energiei fotovoltaice. Proprietarii de sisteme solare pot monitoriza de la distanță funcționarea centralei fotovoltaice prin Internet (LTE, LoRa). Parametrii de funcționare ai instalației solare pot fi vizualizați în timp real sau pot fi reglați. Articolul prezintă aspecte teoretice, legate de structura hardware a echipamentelor de monitorizare și software-ul de monitorizare la distanță, care permit analiza producției și a eficienței instalației fotovoltaice.

INTRODUCTION
Monitoring of the photovoltaic systems is useful for maintenance or for improving the performances of energy production. In order to be able to monitor the operation of the solar system, the equipment (e.g. solar charger, inverter) must be provided with communication interfaces. By means of additional hardware equipment and software applications, remote monitoring can be performed directly through the local network or through the Internet (LTE, LoRa). In other papers that addressed the monitoring of PV systems, the authors used wireless systems (Andreoni et al., 2012) or data acquisition system (DAS) (Meyer et al., 2020) for remote monitoring and control for microgrid applications. In the first mentioned work, the authors present a flexible, robust and reliable measurement and control system based on wireless sensor network (WSN) architecture. The wireless communication technology utilizes a full duplex digital system using the ZigBee protocol, based on the IEEE 802.15.4 standard for Wireless Personal Area Network (WPAN). In the second paper, the authors present a data acquisition system (DAS) for monitoring electrical and meteorological parameters for a microgrid system composed of three PV systems. Electrical and meteorological data are automatically recorded using two data loggers, and the data is periodically downloaded via Wi-Fi to a personal computer for analysis.

In this article, the authors present the hardware structure of a monitoring equipment and a virtual instrument developed for monitoring a PV system from a remote location. The photovoltaic system is located on a mooring pontoon in the Danube Delta. For the purpose of remote monitoring, the equipment is connected to the internet via a Venus GX unit from Victron Energy. At the location of the pontoon, the internet was provided with an LTE router.

---

[1] *Radu-Iulian Rădoi, Scientific researcher II*

MATERIALS AND METHODS

Photovoltaic system

In Romania there are favourable conditions for the production of solar energy, the potential being on average 1500 kWh /m^2/an. *(***)*

A solar installation installed by the authors on a mooring pontoon (Fig. 1) in an isolated area of the Danube Delta is equipped with a remote monitoring system of operating parameters. Through the monitoring system, the operating parameters of the PV system can be seen or the system parameters can be changed.

The parameters of the PV installation are: solar power, solar voltage and current, voltage, current and battery temperature. The system parameters can be: AC input current limit, battery monitor, DC input low shut-down, DC input pre-alarm, shut-down on SOC (state of charge) limit, absorption voltage, float voltage, charge current, ESS (energy storage system) grid set point and others. The area of photovoltaic panels is dimensioned, by the amount of electrical energy to be supplied by photovoltaic panels in one day so that to supply electrical loads in the amount of 1.1 kW. 1.1 kW ·24 h = 26.4 kWh.

In order to achieve a 27 kWh average production capacity in any season during a calendar year, 30 photovoltaic panels of 265 W are needed. The electricity produced during the day is stored in 12 batteries with the following characteristics: voltage U = 12 V, capacity C = 220 Ah. The energy stored by them is E = U [V]· C [Ah] · 12 = 12 V · 220 Ah · 12 = 31680 Wh. To prolong the battery life to 1000 discharge cycles specific to gel batteries, the battery state of charge must be maintained at 60%. Then, the available battery energy is E_b = 31.68 kWh · 40% = 12.67 kWh, which can ensure consumption for about 12 hours without sun. For batteries charging, a charger model SmartSolar 250/100 produced by Victron Energy is used, and for energy management and for DC/AC conversion (inverter), a Quattro 48/8000 unit also from Victron Energy is used.

Fig. 1 - Solar installation located on a mooring pontoon in the Danube Delta

For the purpose of remote monitoring, the pieces of equipment are connected to the internet via a Venus GX unit. At the site of the pontoon, the internet was provided with an LTE router.

Theoretical aspects

The current – voltage curves of a PV module describes the ability to convert energy under given conditions of irradiance and temperature. A PV cell is a p-n junction with features similar to a diode *(*)*. When the cell is illuminated, photons excite electrons in it and a current is generated. This is known as the photovoltaic effect. The current of a PV cell can be modeled:

$$I = I_0\left[exp\left(\frac{qV}{nkT}\right) - 1\right] - I_L \tag{1}$$

The parameters used to characterize the output of solar cells are the short circuit current (I_{sc}) - current with zero voltage and the open circuit voltage (V_{oc}) - maximum voltage with zero current *(Mori et al., 2020)*. This value increases logarithmically with increased sunlight. At $I = 0$:

$$V_{OC} = \frac{nkT}{q}\ln\left(\frac{I_L}{I_0} + 1\right) \tag{2}$$

The current – voltage curve is characterized by the following parameters *(Moulin et al., 2019; *****)*:

- Maximum power point (MPP) - designated as the rated power of a photovoltaic cell, is the point on the current-voltage curve at which it operates at maximum power. For MPP, both the rated current (I_{MPP}) and the rated voltage (V_{MPP}) are specified.

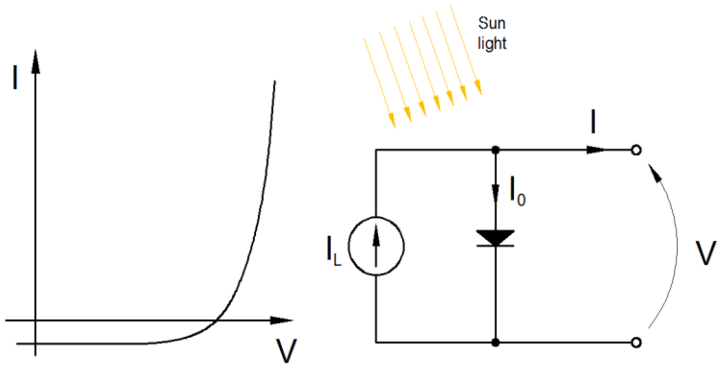

Fig. 2 - Current – voltage characteristics of a p-n junction subject to illumination

- The short-circuit current (I_{SC}), which varies depending on the technology used to build the cell. An important feature of the short-circuit current of the cell is that it is linearly dependent on irradiance.

- Open Circuit Voltage (V_{OC}) - represents the voltage at the terminals of the cell when it has no load. V_{OC} is also dependent on the material from which the cell is made.

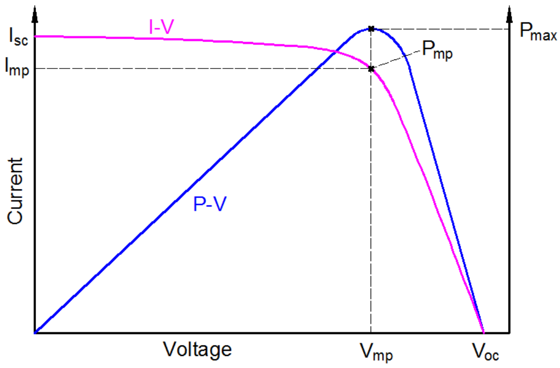

Fig. 3 - The current – voltage and P – V curves of a photovoltaic cell

The solar irradiance incident to a solar panel is the most important factor in amount of power a solar cell can generate. The amount of irradiation affects the short-circuit current drastically, while the open-circuit voltage remains almost unchanged. The maximum power point MPP tracks very closely with the irradiance incident to the solar cell and it is proportional to the irradiance *(****)*.

The fill factor FF is a qualitative size used to characterize solar cells. Assuming an ideal I-V curve, rectangular in shape, in which the point of maximum power is obtained by multiplying the values of the short-circuit current and the open-circuit voltage, the filling factor represents the deviation of the real characteristic from the ideal one. From a geometric point of view, the filling factor represents the ratio between the surfaces formed by the two characteristics in the system of orthogonal axes. The value for fill factor FF has the following calculation formula:

$$FF = \frac{P_{MPP}}{V_{OC} \cdot I_{SC}} = \frac{\eta \cdot A_C \cdot E}{V_{OC} \cdot I_{SC}} \tag{3}$$

Solar Cells Efficiency

The conversion efficiency of photovoltaic cells represents their electricity flow in relation to the energy absorbed by the incident solar radiation *(Mehmet and Furkan, 2011; Cristescu et al., 2017; Meyer et al., 2020)*. This is calculated by dividing the peak electric power of the cell expressed in W by the power density of the incident radiation when the maximum power is reached expressed in W/m^2 and at the cell surface expressed in m^2:

$$\eta = \frac{P_{MPP}}{A_C \cdot E} \tag{4}$$

In the production of photovoltaic cells, given the dependence of their electrical characteristics on temperature and radiation spectrum, the conversion efficiency is determined according to standardized test conditions STC - Standard Test Conditions *(**)*. These assume a temperature of 25°C with a tolerance of ±

2°C, the incident irradiance of 1000W/m^2 and the spectral distribution of the radiation corresponding to an air mass index AM 1.5. The STC's correspond to a clear day in which the Sun has an elevation angle of 41.81° and the cell is oriented towards it, at an angle of 37°.

The efficiency of a solar cell is determined as the fraction of incident power which is converted to electricity and is defined as:

$$P_{MPP} = V_{OC} \cdot I_{SC} \cdot FF \tag{5}$$

where: V_{OC} is the open circuit voltage;
I_{sc} is the short circuit voltage;
FF is the fill factor

$$\eta = \frac{V_{OC} \cdot I_{SC} \cdot FF}{P_{in}} \tag{6}$$

The power of incident solar radiation can be measured using a light sensor placed locally or from a nearby weather station. (Fig. 4).

The efficiency of a photovoltaic installation can be determined in real time with a software algorithm that takes into account the surface of the photovoltaic installation, rated power of solar panels and the locally measured temperature and sun luminosity *(Attari et al., 2016; Filippo et al., 2013; Nanjannavar, 2013; Suresh et al. 2014).*

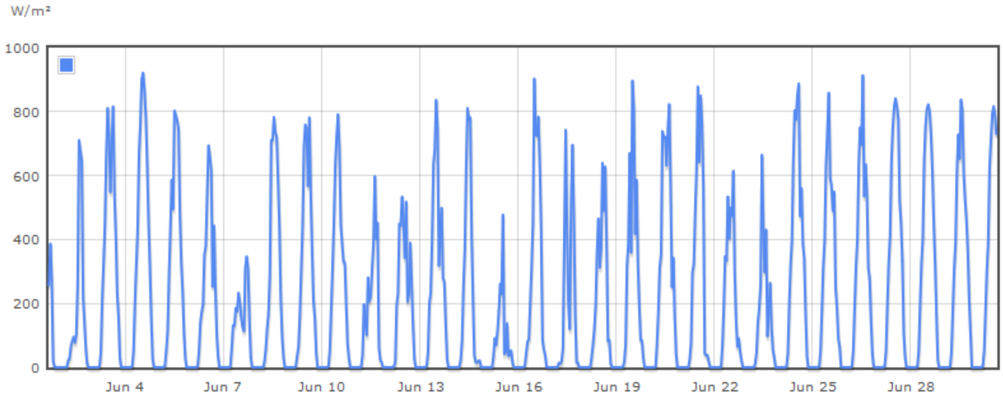

Fig. 4 - Records of the solar power peak for June 2020 at PV plant location (aprs.fi/weather Luminosity)

PV system monitoring

High-performance equipment for solar installations such as solar chargers or inverters have Serial, Ethernet, CAN or Modbus communication ports. These devices can be connected to the internet through gateways. Some companies producing equipment for solar photovoltaic systems also provide modules for transmitting operating parameters via the Internet. The equipment of the solar installation transmits data in real time by means of these communication devices, thus being able to monitor the state of charge of the batteries, the voltage and the current delivered by the solar panels, the temperature of the batteries and the state of operation of the inverter *(Andreoni et al., 2012)*. Through a console, the operating parameters of the solar system can be changed or one can upload configuration files.

Individual equipment equipped with a communication port can also be connected to the internet. Thus, an MPPT solar charger from Victron Energy (Fig. 5) can be connected to the Internet via a gateway module. In Figure 6 it can be seen the realization of a communication module for a solar charger. Serial data from the pins of VE.Direct port of the charger are converted to RS232 and connected to an RS232-Ethernet gateway module, model WIZ110SR from Wiznet.

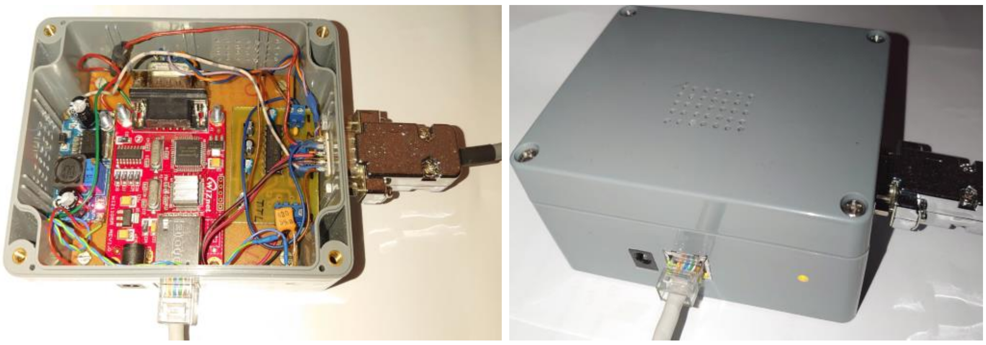

Fig. 5 - TCP/IP gateway module for solar charger

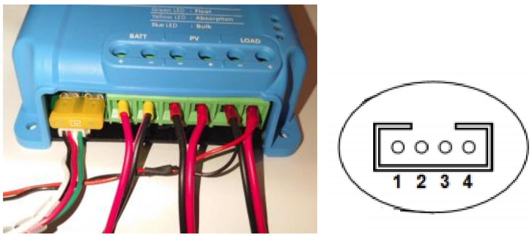

Pin	Function
1	GND
2	VE.Direct-TX
3	VE.Direct-RX
4	Power +

Fig. 6 - VE. Direct serial port on Victron solar charger

The gateway module connects to the internet via a router (Fig. 7) which is configured with port forwarding. The gateway module is configured as TCP server mode, has an IP configured, an ethernet communication port and the COM port through which the communication with the solar charger is made.

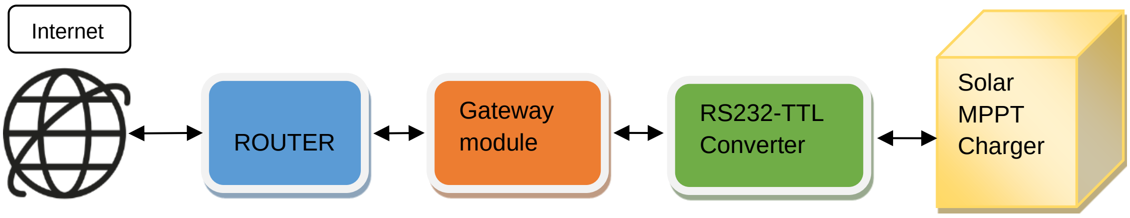

Fig. 7 - The way to connect the solar charger to the internet

The authors have developed a software tool in the LabView environment with which the parameters provided by the solar charger by serial port (Fig. 8) can be monitored, via the Internet. It has an interface through which the header of the monitored values can be set. Values with the correct pattern are represented graphically. For example, the “VPV” parameter which is the voltage from the solar panel has the value transmitted serially: 14110 (mV).

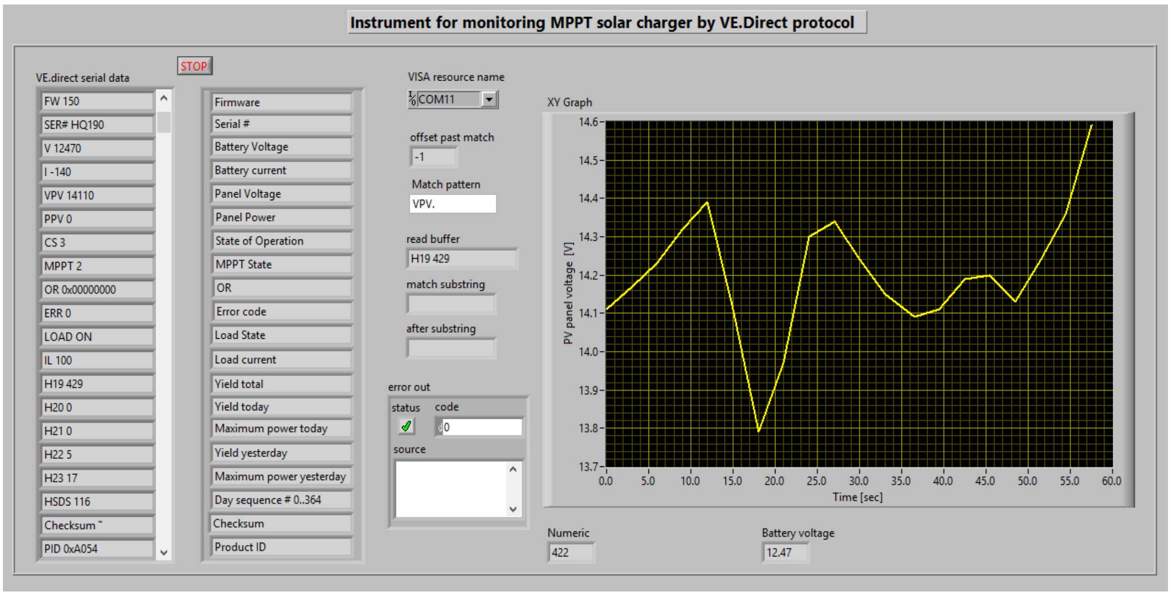

Fig. 8 - Software tool for monitoring the solar charger

Solar installations connected to the Internet through a monitoring system equipped with Modbus TCP service can be monitored using software applications that read the values of the registers from remote units ID’s. A GX monitoring system from Victron Energy has the unit ID and services in Table 1.

Table 1

Modbus TCP services	
com.victronenergy.hub4 com.victronenergy.hub4	Unit ID: 100
BlueSolar Charger MPPT com.victronenergy.solarcharger	Unit ID: 239
com.victronenergy.system com.victronenergy.system	Unit ID: 100
MultiPlus Com.victronenergy.vebus	Unit ID: 246

By unit ID 246, VE.Bus state (0=Off; 1=Low Power; 2=Fault; 3=Bulk; 4=Absorption; 5=Float; 6=Storage; 7=Equalize; 8=Passthru; 9=Inverting; 10=Power assist; 11=Power supply; 252=Bulk protection) and battery temperature can be monitored. By unit ID 239, MPPT charger status, PV voltage; PV power and PV current can be monitored. By Unit ID 100, battery voltage, battery current, battery power and SOC – state of charge can be monitored *(Sivagami and Jothiswaroopan, 2020; Vargas et al., 2019)*.

An application for the complete monitoring of the photovoltaic system was also developed, in the LabView environment which monitor the PV system via Modbus TCP. The virtual instrument has the block diagram in Figure 9 and the front panel from Figure 10. In the application window the user can select the parameters that can be displayed on the graph and the recorded data can be saved in files.

The block diagram of the instrument for monitoring the photovoltaic installation uses a TCP master function through which unit IDs of the PV system are accessed, and on the basis of the registers the operating parameters of the photovoltaic system for electricity production are read. The data read from the devices are processed and displayed on the dials and on the graph. The curves displayed on the graph can be selected by means of a selection block made with the "case structure" function.

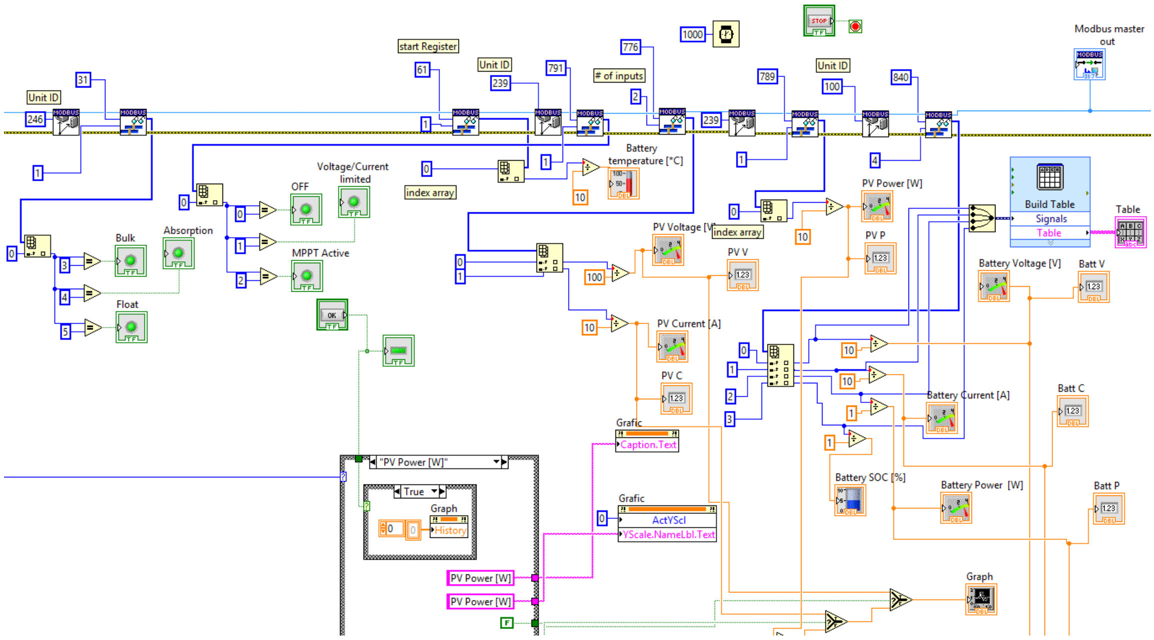

Fig. 9 - Block diagram of the instrument for monitoring PV installation made in LabView

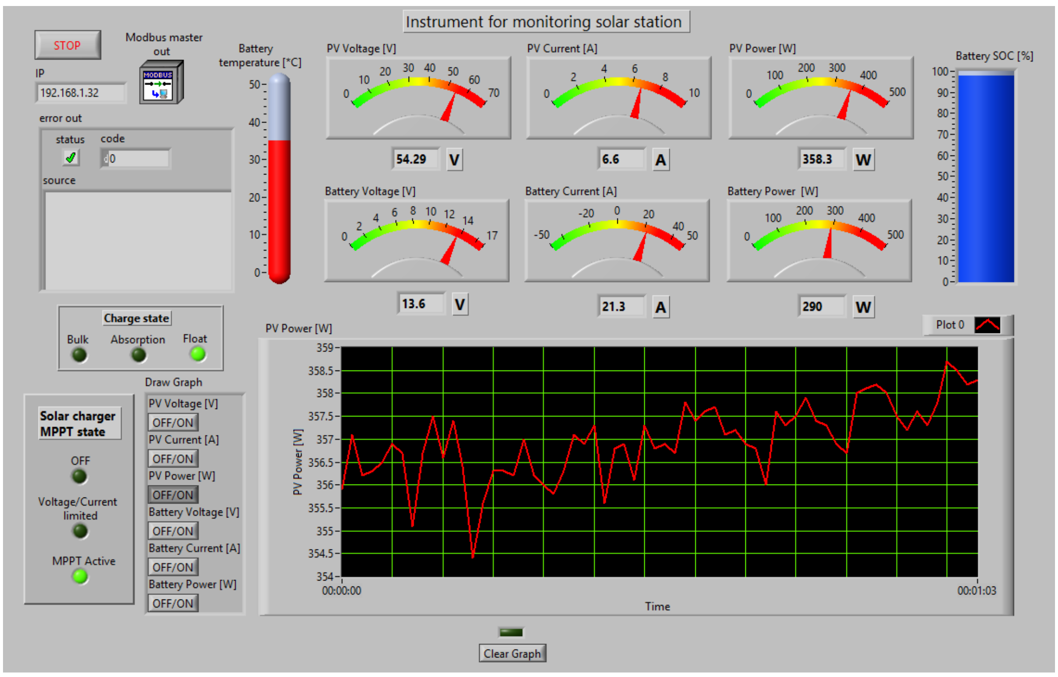

Fig. 10 - Front panel of the virtual instrument for monitoring PV installation

The block diagram of the instrument for monitoring the photovoltaic installation uses a TCP master function through which unit IDs of the PV system are accessed, and on the basis of the registers the operating parameters of the photovoltaic system for electricity production are read. The data read from the devices are processed and displayed on the dials and on the graph. The curves displayed on the graph can be selected by means of a selection block made with the "case structure" function.

RESULTS

The following is the data recorded for June 2020 by monitoring the remote PV plant. Figure 11 shows the curves drawn for the production of solar energy and PV power. The graph shows that in the middle of the month, productions of 10 kWh were obtained.

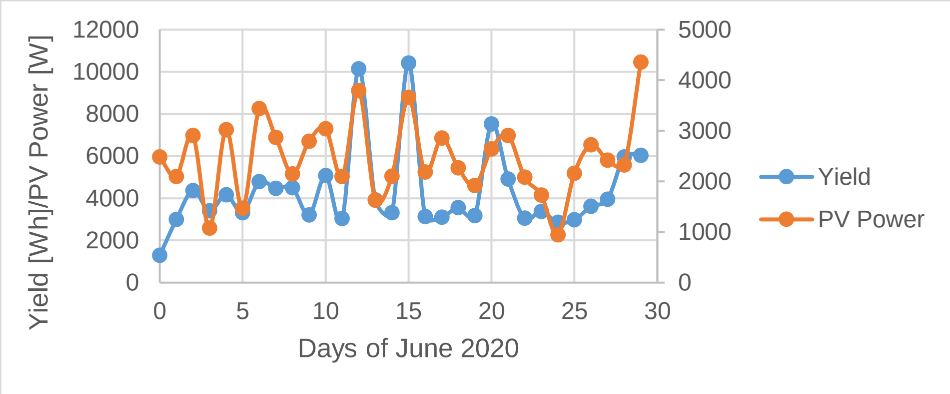

Fig. 11 - Solar Yield / PV Power

Figure 12 shows the voltage variation provided by the solar panels for June 2020.

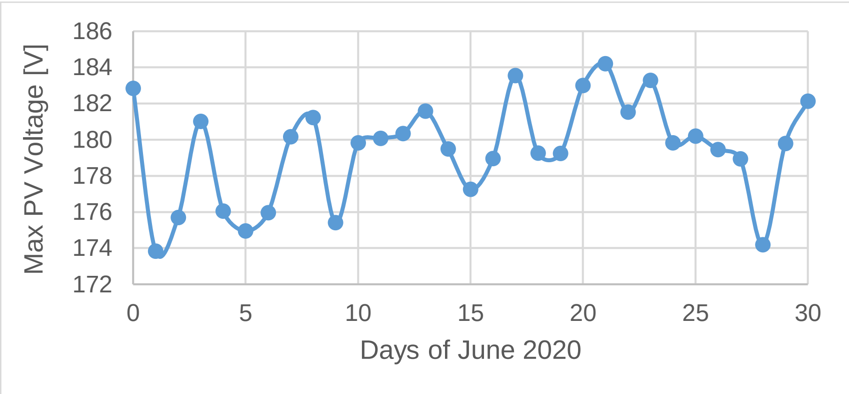

Fig. 12 - Maximum PV Voltage

The variation curve of the maximum battery voltage can be found in figure 13. It can be seen that once in 7 days the battery charging system raises the voltage to ~ 14.5 V when the batteries enter Cycle service with absorption mode.

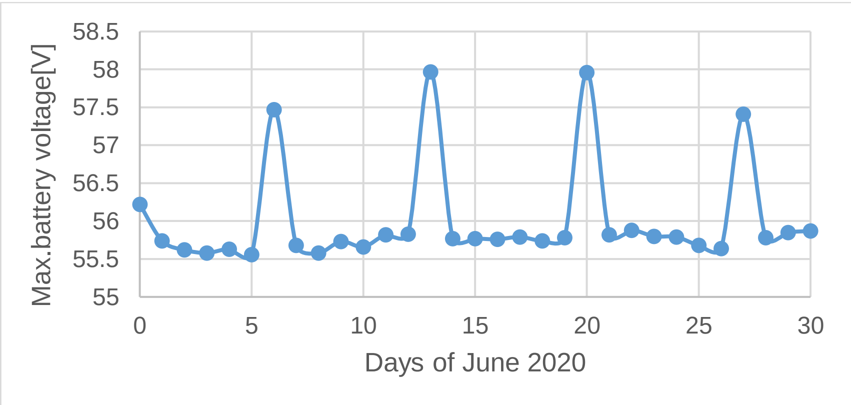

Fig. 13 - Maximum battery voltage

Figure 14 shows the variation of the battery temperature for June 2020. The temperature of the batteries oscillates by a few degrees between night and day when the batteries are charged. It is found that the temperature of the batteries has an increasing trend towards the end of the month with the warming of the weather.

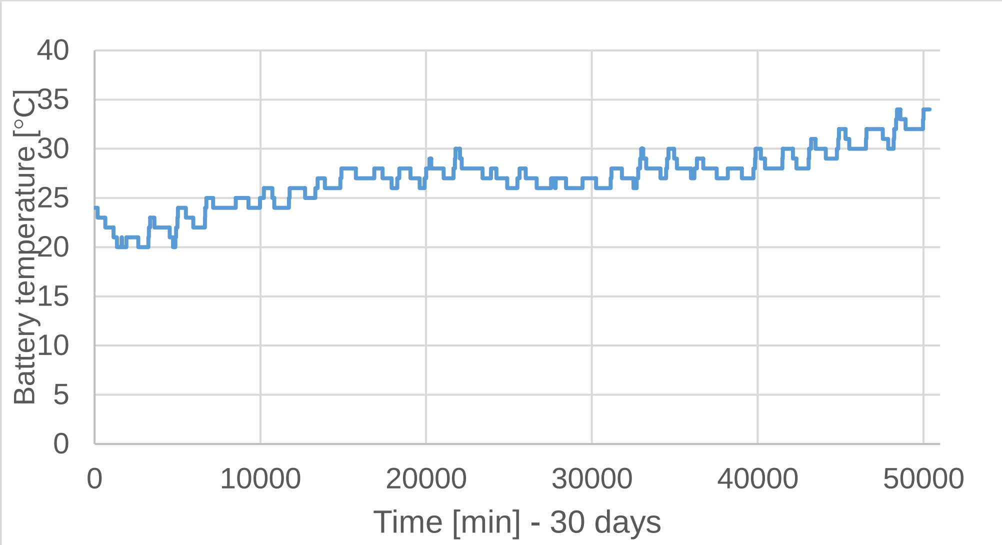

Fig. 14 - Battery temperature variation

In Figure 15 is a diagram with battery voltage, PV current and PV power made with data for a period of 24 days, data that were downloaded from the VRM portal of Victron Energy.

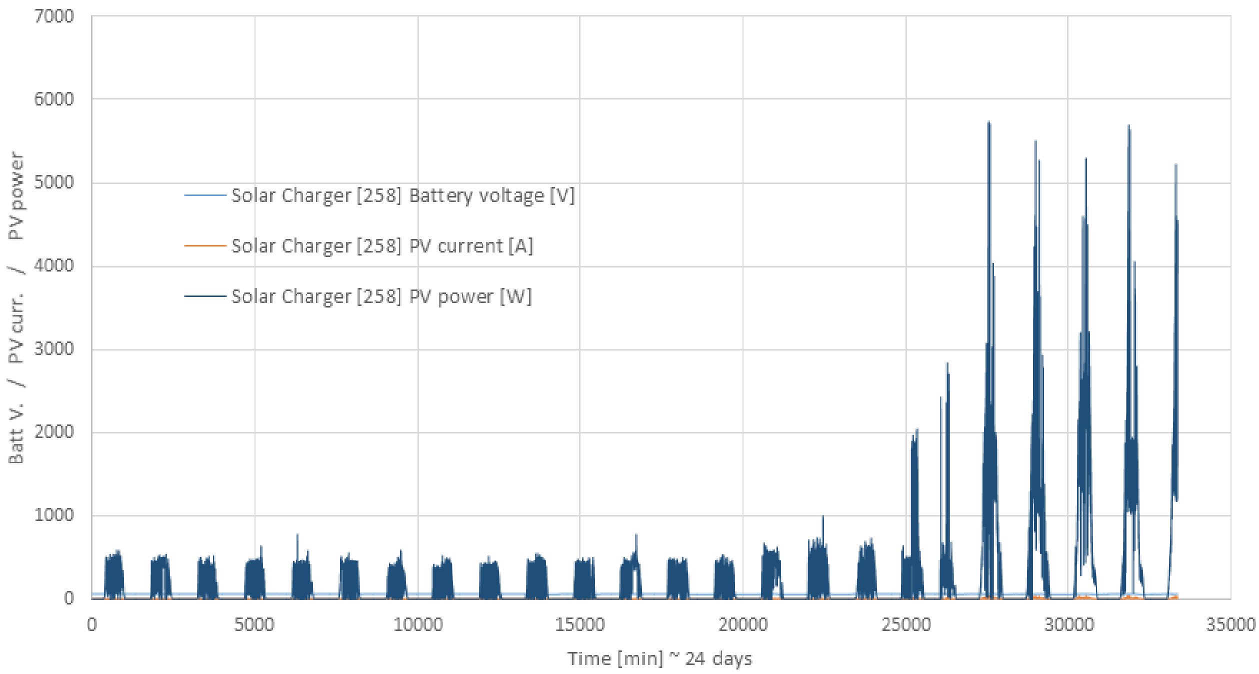

Fig. 15 - Battery voltage, PV current and PV power for 24 days

CONCLUSIONS

In order to be able to optimize the energy production of a photovoltaic installation, it is necessary to monitor the operating parameters. If the installation is located in a remote area and is not serviced by personnel with technical knowledge, monitoring can be done remotely.

By transmitting the operation data of the solar installation to a cloud server, the operation history of the PV installation can be kept.

By remote monitoring, some measures to improve the performances of the installation can be taken. For example, if there is a deterioration in energy production, this may be due to the dirt covering the solar panels and measures may be taken to clean the panels.

By connecting the equipment of the photovoltaic installation to the internet, some operating parameters can be changed remotely and alarms can be received in case of abnormal operation.

With the help of a software instrument, the operation of a photovoltaic plant placed in a remote location can be watched live.

ACKNOWLEDGEMENT

This paper has been funded by the Romanian Ministry of Research and Innovation under Nucleu Programme, Financial Agreement no. 19N/2019, Ad 9/2020, Project code PN 19-18.01.01, Phase 15 “Contributions to the modernization of the fluid power field by integrating intelligent equipment in the systems compatible with the automation solutions of the future, which is part of the Industry 4.0 concept”, while the scientific results have been obtained in the framework of a project co-financed by the European Union through the European Regional Development Fund, under Competitiveness Operational Programme 2014-2020, Priority Axis 1: Research, technological development and innovation (RD&I) to support economic competitiveness and business development, Action 1.1.4 – Attracting high-level personnel from abroad in order to enhance the R&D capacity, project title: *Establishing a high level proficiency nucleus in the field of increasing renewable energy conversion efficiency and energy independence by using combined resources*, project acronym: CONVENER, Financial agreement no. 37/02.09.2016.

REFERENCES

[1] Andreoni, M., Mantinan, F.J., Molina, M.G. (2012), Implementation of wireless remote monitoring and control of solar photovoltaic (PV) system, *Sixth IEEE/PES Transmission and Distribution Conference and Exposition*, DOI:10.1109/TDC-LA.2012.6319050

[2] Attari, K., Elyaakoubi, A., Asselma, A. (2016), Performance analysis and investigation of a grid-connected photovoltaic installation in Morocco, Online at www.sciencedirect.com, Elsevier.

[3] Cristescu, C., Dumitrescu, C., Dulgheru, V., Popescu, T.C., (2017), Increasing energy efficiency and optimizing the operation of systems that produce clean energy from renewable sources. *Hidraulica Magazine 3*, pp. 62–73.

[4] Filippo, S., Fabio, C., (2013), Monitoring and checking of performance in photovoltaic plants: a tool for design, installation and maintenance of grid connected systems. *Renew Energy* 60.

[5] Mehmet, E. M., Furkan, D., (2011), *A review of the factors affecting operation and efficiency of photovoltaic based electricity generation systems*. Online at www.sciencedirect.com, Elsevier.

[6] Meyer, E.L., Apeh, O.O., Overen, O.K., (2020) Electrical and Meteorological Data Acquisition System of a Commercial and Domestic Microgrid for Monitoring PV Parameters, *Applied sciences-Basel*, 10 (24), Article Number: 9092, DOI: 10.3390/app10249092, https://www.mdpi.com/2076-3417/10/24/9092

[7] Moulin, N., Amara, M., Mandorlo, F., Lemiti, M., (2019), Tunnel junction I(V) characteristics: Review and a new model for p-n homojunctions, *Journal of applied physics*, 126 (3), Article Number: 033105, DOI: 10.1063/1.5104314, https://www.researchgate.net/

[8] Mori, R., Tezuka, N., Imamura, T., Tanaka, K., (2020), Fabrication of a transparent p-n junction using CuBr1-xIx and ZnO nanorods, *Japanese journal of applied physics,* Volume: 59 (SC), Article Number: SCCB09, DOI: 10.7567/1347-4065/ab4a9f https://apps.webofknowledge.com/

[9] Nanjannavar, V., Gandhi, P., Patel, N., LabVIEW based PV cell Characterization and MPPT under Varying Temperature and Irradiance Conditions, *Nirma University International Conference on Engineering, NUiCONE*, 2013.

[10] Sivagami, P., Jothiswaroopan, N. M., (2020*), IOT based statistical performance improvement technique on the power output of photovoltaic system, Journal of ambient intelligence and humanized computing,* 10.1007/s12652-020-01954-8, https://link.springer.com/article/10.1007/s12652-020-01954-8

[11] Suresh, S., Rakesh, K., Vivek, V., (2014). Performance analysis of 58kW grid-connected roof-top solar PV system. In*: Power India International Conference*, PIICON, 6^{th} IEEE.

[12] Vargas, L. A., Fuentes, M., Vivar, G. M., Munoz, R., Francisco, J., (2019), Low-Cost Datalogger Intended for Remote Monitoring of Solar Photovoltaic Standalone Systems Based on Arduino (TM)*, IEEE Sensors journal*, 19 (11), 4308-4320, DOI: 10.1109/JSEN.2019.2898667, https://www.researchgate.net/

[13] * Bowden, S, Honsberg, C., *Photovoltaic Education*. In http://www.pveducation.org/.

[14] ** Coulee Ltd., *Standard test conditions of a PV module*. Online at: https://couleenergy.com/standard-test- conditions-of-pv-module.
[15] *** *Global irradiation and electricity potential*. In https://re.jrc.ec.europa.eu/pvg_download/map_index.html.
[16] **** *Leonics Co, Basics of MPPT Solar Charge Controller*. In http://www.leonics.com/support/article2_14j/ articles2_14j_en.php.
[17] ***** Solmetric Corporation, *Guide to Interpreting I-V Curve Measurements of PV Arrays*. *Application Note PVA-600-1*, 2011.

STUDY ON FILLING PERFORMANCE OF HOLE FERTILIZATION DEVICE AND OPTIMIZATION OF CAVITY
/
穴施肥装置充肥性能研究及肥腔优化

Zhiqi Zheng[1)], Tao Wang[1)], Zhengdao Liu[*1)], Qingjie Wang[2)] Hongbo Zhao[1)] Suyuan Liu[1)]

[1)] College of Mechanical and Electronic Engineering, Northwest A&F University, Yangling 712100, China;
[2)] College of Engineering, China Agricultural University, Beijing 100083, China;
Tel: +86029 87092064; E-mail: liuzd@nwafu.edu.cn
DOI: https://doi.org/10.35633/inmateh-64-13

Keywords: *hole fertilization, fertilizer filling, discrete element method, cavity, structure optimization*

ABSTRACT
Hole fertilization is an effective method to improve the utilization rate of chemical fertilizer. In order to improve the accuracy and stability of the amount of fertilizer discharging for the hole fertilization device, this paper proposed the method of rotary filling by notched disk, designed a hole fertilization device with notched disk, and completed the structure design of the device and cavity. Through the dynamic analysis of fertilizer particles in the process of fertilizer filling, this study found that the interface span of fertilizer cavity, the rotational speed of fertilizer disk, and the amount of fertilizer applied in each hole are the main factors affecting the performance of filling. Then, this study carried out the three-factor quadratic orthogonal rotation combination simulation test to optimize the structure of the cavity. The test used the discrete element method with interface span of fertilizer cavity, the rotational speed of fertilizer disk, and the amount of fertilizer applied in each hole as test factors and the accuracy and variation coefficient of filling amount as evaluation indexes. Results showed that the optimal performance was obtained when the cross section span of the cavity was 13.58°, the opening width was 29.56 mm, and the depth was 22.08 mm. The field validation showed that the average accuracy of filling amount per hole was 97.67%, and the average variation coefficient was 1.90%. The performance of fertilizer discharge satisfied the design requirements, and agreed with the law of the simulation results. The research results could provide a theoretical basis for the design of hole fertilization device and the improvement of filling performance.

摘要
穴施肥技术是提高化肥利用率的有效手段，为提高穴施肥装置排肥量准确性和稳定性，本文提出了腔盘回转取肥法，并设计了腔盘式穴施肥装置，完成了排肥盘及肥腔的结构设计。重点围绕取肥环节，通过对取肥过程肥料颗粒的动力学分析，明确了肥腔界面跨度，排肥盘转速和每穴施肥量是影响取肥性能的主要因素；采用离散元法，以上述因素为试验因素，以排肥量准确度和变异系数为评价指标，进行了三因素二次正交旋转组合仿真试验，完成了肥腔结构优化，当肥腔截面跨度为 13.58°，开口宽度为 29.56 mm，深度为 22.08 mm 时取肥性能最优。田间验证试验表明，每穴排肥量准确度平均为 97.67%，变异系数平均值为 1.90%，排肥性能满足设计要求，且与仿真结果规律相同。研究结果可为穴施肥装置的设计及取肥性能的提升提供理论依据。

INTRODUCTION
At present, grain fertilizer is the main source for corn fertilization. However, in the seedling stage, the area of maize root is still small. Thus, the fertilizer between adjacent plants is not easy to be absorbed, resulting in low fertilizer utilization rate (*Zhu et al., 2016; Liu et al., 2019*). The hole fertilization technology is an effective method to improve the utilization rate of corn fertilizer, because this technology directly applies a certain amount of chemical fertilizer nearby the seed and limits it in a certain length range according to the law of corn fertilizer needs. (*Jiang et al., 2018; Tang et al., 2019; Zhang et al., 2020*)

In order to achieve precision hole fertilization of corn, related scholars have carried out a series of studies on hole fertilization device. For instance, Great Plains Mfg. Inc. has developed the AccuShot Corn Liquid Fertilizer Precision Hole Planter for liquid fertilizer. Wang et al. (*2018a, 2018b*) adopted a planetary gear pot-tying and spraying mechanism to achieve the hole application of rice liquid fertilizer. However, granular fertilizer is still the main type of fertilizer in China and many other countries. Thus, it is necessary to develop fertilizer device to improve the utilization rate of granular fertilizer.

Around the particle fertilizer hole application device, *Hu et al.* (*2016*) adopted rotary retaining blocks to achieve intermittent fertilizer discharge, and the performance test met the design requirements at a forward speed of 2.88 km/h. *Wang et al.* (*2020*) implemented intermittent discharge of fertilizer by installing a stopper with a hole at the discharge opening, with a working speed ranging from 1.8 km/h to 3.6 km/h. *Zhang et al.* (*2018*) adopted the opening and closing of the turning plate to achieve intermittent fertilization. The variation coefficient of fertilizer application amount per hole was 0.09 in their study. *Yuan et al.* (*2018*) designed a spoon-wheel hole fertilizer discharge device, with an experimental advance speed of 1.8 km/h. *Li et al.* (*2018*) designed an electrically driven external groove-wheel hole fertilizer discharge device, and the average pass rate of hole fertilizer application was 87.49% when the advancing speed was 2.48 km/h. Fertilizer quantitative distribution was achieved through different structures in the above studies, but the operating speed was all at 4 km/h.

Therefore, in order to ensure the fertilizer filling performance of the hole fertilization device at different operating speeds, this study aimed to propose the cavity and disc rotation fertilizer filling method to ensure the fertilizer filling performance of the hole fertilization device at different operating speeds. The following steps were carried out to achieve the main purpose of this study. First, we designed the cavity and disc type hole fertilization device and the structure of fertilizer discharging disk and fertilizer cavity. Then, this study optimized the fertilizer cavity structure through theoretical analysis and simulation calculation to improve the accuracy and stability of the amount of fertilizer discharging for hole fertilization device. We believed the study could provide theoretical basis for the design of hole fertilization device and the improvement of fertilizer filling performance.

MATERIALS AND METHODS

Structure and working principle of corn hole fertilization device

The structure of corn hole fertilization device is shown in Fig.1. The hole fertilization device is fixed on the front beam of the corn fertilization seeder and used with the sowing monomer. It is mainly composed of frame, colter, secondary fertilizer box, fertilizer discharging disk, cleaning mechanism, protecting chamber, pneumatic delivery mechanism, regulating mechanism fertilization amount, and transmission mechanism.

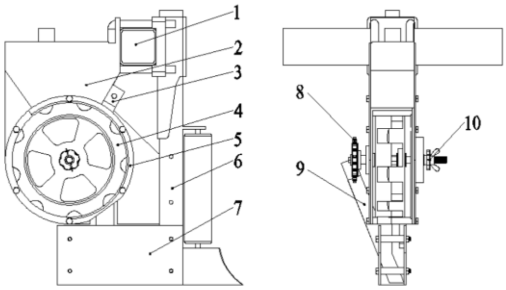

Fig. 1 - Overall structure of hole fertilization device

1) Front beam; 2) Secondary fertilizer box; 3) Fertilizer cleaning mechanism; 4) Fertilizer discharging disk; 5) Fertilizer protecting chamber; 6) Colter; 7) Soil retaining plate; 8) Drive sprocket; 9) Pneumatic delivery mechanism; 10) Regulating mechanism fertilization amount

The colter of the hole fertilization device adopts the no-tillage colter to prevent blockage, and the fertilizer bed is opened in the soil. The colter was designed with a soil retaining plate, so that the back end of the colter can maintain a complete trench type within a certain distance. The process of fertilizer from the box into the bed can be divided into four stages of filling, cleaning, transport and delivery. Driven by the driving force, the fertilizer discharge disk rotates around the central axis in the fertilizer protecting chamber and the secondary fertilizer box. When the fertilizer cavity passes through the secondary fertilizer box, it is filled with fertilizer. When the fertilizer cavity leaves the secondary fertilizer box with the fertilizer, the excess fertilizer is cleared out by the fertilizer cleaning mechanism and enters the fertilizer protecting chamber. The gap between the plate of the fertilizer protecting chamber and the fertilization cavity is less than the diameter of fertilizer particles. Fertilizers are always kept in the cavity in a lump-like form and transported to the fertilizer delivery mechanism at the bottom of the fertilizer care chamber with the rotation of the fertilizer discharge chamber and plate. Fertilizer delivery mechanism is connected with the fan, the lump-like fertilizer in the fertilizer cavity is discharged out of the fertilizer cavity and quickly delivered to the fertilizer ditch under the action of air flow and dead weight, and the hole type fertilizer discharge is completed.

Structure design of fertilizer discharge disk and cavity

Fertilizer discharging disk is the main carrier for carrying fertilizer. It is mainly composed of the main disk of fertilizer discharging, the auxiliary disk of fertilizer discharging, the main shaft of fertilizer discharging disk and the auxiliary shaft of fertilizer discharging disk. Fertilizer discharging disk is installed in the fertilizer protecting cavity. Its structure and installation method are shown in Fig. 2. A number of notches are distributed around the main plate, and the same number of matching bulges are distributed around the auxiliary plate. There is a hexagonal hole at the end of the main shaft, and the hexagonal shaft at the end of the auxiliary shaft is matched with the hexagonal hole. The main disk is fixed on the main shaft by a flat key and a clamp spring, and the secondary disc is installed on the secondary shaft in the same way. The main shaft and the auxiliary shaft are respectively installed on the wall of the fertilizer cavity and the side cover of the fertilizer cavity, so that the fertilizer discharge disk rotates in the fertilizer cavity. Main plate and auxiliary plate through the six-party axis and six square hole together, the disc gap and pair of disc bulge formed by the area is the fat cavity, deputy plate in fertilizer consumption by adjusting mechanism can be the main shaft of the six-party hole axial movement, change the raised amount of overlap and gap can adjust the cavity volume, and then adjust the single cavity fertilizer consumption.

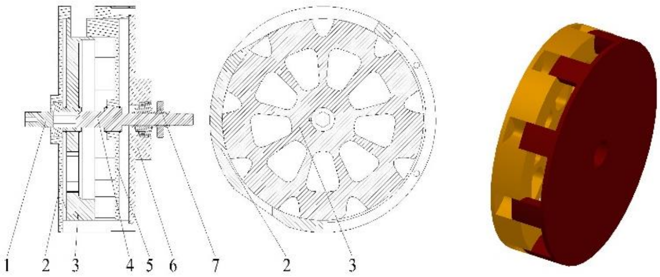

Fig. 2 - Structure diagram and three-dimensional shape of discharging fertilizer disk

1) Main shaft; 2) Wall of protecting chamber; 3) Main disk; 4) Auxiliary shaft; 5) Auxiliary disk; 6) Side cover; 7) Regulating mechanism of fertilization amount

Fertilizer cavity is the most important part of fertilizer disk, and its structural parameters will directly affect the movement of fertilizer group in the process of fertilizer discharging, especially in the stage of fertilizer collecting, the structure of fertilizer cavity has a great influence on the performance of fertilizer collecting disk. The cavity of the fertilizer discharging disk is surrounded by the notch of the main disk and the bulge of the auxiliary disk. In order to facilitate the filling and discharging of fertilizer, the cross section of the fertilizer chamber is generally curved and open-shaped. The shape of the fertilizer cavity was obtained by using the spline curve in Cro/E, as shown in Fig.3. The spline curve used in Cro/E is B-spline curve, and the cross section shape of the fertilizer cavity is determined by A, B and C, and its structural parameters include the cross section span and depth of the fertilizer cavity.

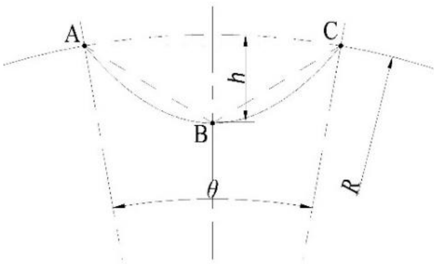

Fig. 3 - Structure drawing of fertilizer cavity

where: θ is the cross section span of fat cavity, (°);

R is the diameter of fertilizer discharging disk, mm;

h is the depth of cavity, mm.

In China, corn strip fertilization is generally applied in the range of 300 kg/hm^2 to 750 kg/hm^2 (*Rinnan et al., 2007; Cozzolino et al, 2006*). *Jiang et al.* (*2018*) showed that compared with strip fertilization, summer corn hole fertilization could improve nitrogen fertilizer performance use efficiency by 12.4% and phosphorus fertilizer performance use efficiency by 27.2%. Therefore, in this paper, when setting the maximum amount of fertilizer applied to each hole, the maximum amount of fertilizer applied by strip fertilization method was calculated as 80%. When the sowing row spacing of corn was generally 600 mm and the planting spacing was 250 mm, the maximum amount of fertilizer applied in each hole was calculated as 9 g. The measured bulk density of fertilizer particles is 8.3×10^{-4} g/mm^3, the maximum adjustment length of fertilizer chamber is 30 mm, and the calculated cross-section area of fertilizer chamber is 361.43 mm^2, rounded to 360 mm^2.

In the fertilizer filling stage, the fertilizer chamber rotates along with the discharge disk through the secondary fertilizer box, and the fertilizer in the secondary fertilizer box is filled into the fertilizer chamber under the disturbance of its own gravity and the fertilizer disk. The force and movement of fertilizer particles in the filling process are mainly affected by the rotating speed of fertilizer disk, the thickness of fertilizer in the secondary fertilizer box and the depth of fertilizer chamber. In the actual work process, the secondary fertilizer box is always full of fertilizer, and the accumulation thickness of fertilizer in the secondary fertilizer box is only used as the test condition, not as the test factor. Therefore, this paper will take the cross section span of the fertilizer chamber, the speed of the fertilizer disk and the thickness of the fertilizer chamber as the test factors to study the influence rules of the three factors on the performance of the fertilizer chamber.

Experiment design

In this paper, the discrete element method is used to simulate and analyze the process of fertilizer filling. Fertilizer plate simulation model and fertilizer simulation model were established by using Cro/E and EDEM software respectively. The fertilizer used in the experiment is a compound fertilizer commonly used in corn in North China, and the manufacturer is Hebei Zhongren Fertilizer Group Co., Ltd., with a moisture content of 4.37%. The particle shape is nearly spherical, the diameter distribution conforms to the normal distribution, the central value is 2.967 mm and the standard deviation is 0.25. The material contact and intrinsic parameters are shown in Table 1.

Table 1

Material contact and intrinsic parameters

Attribute	The fertilizer particle	Metal components
Poisson's ratio	0.25	0.269
Shear modulus (Pa)	0.29×10^9	8.12×10^{10}
density (kg/m^3)	1490	7890
Coefficient of restitution	0.40 (Fertilizer particle – Fertilizer particle)	0.50(Particle - metal construction)
Static friction coefficient	0.43 (Fertilizer particle – Fertilizer particle)	0.50(Particle - metal construction)
Rolling friction factor	0.05 (Fertilizer particle – Fertilizer particle)	0.01(Particle - metal construction)

This paper took the end span of fertilizer cavity, the speed of fertilizer disk and the amount of fertilizer applied in each hole as the test factors. Using the variation coefficient of the average amount of fertilizer applied and the amount of fertilizer applied per hole as the evaluation index, a three-factor quadratic orthogonal rotation combination test was carried out.

(1) Cross section span of fertilizer cavity

Since the cross section area of the cavity is determined to be 360 mm^2, the cross section span of the cavity determines the opening width and depth of the cavity section. In order to avoid too small opening width, which may affect fertilizer filling into the fertilizer chamber, the opening width and depth of the fertilizer chamber are equal, that is, the opening width of 23.3 mm is the minimum width, and the corresponding minimum cross section span of the fertilizer chamber is 10.70°. The minimum depth was 4 times the average particle diameter (2.967 mm), i.e., the maximum width was 40.1 mm, and the corresponding maximum span was 20.29 mm, in order to avoid the shallow cavity causing the particle size in the fertilizer cavity to be less than the theoretical application amount. Therefore, the cross section span of the fertilizer cavity in the test is 10° to 20°.

(2) Speed of fat plate

The rotating speed of fertilizer disk is determined by the advancing speed of the machine and tools, the spacing of sowing plants and the number of fertilizer cavities of fertilizer disk etc., and its calculation formula is:

$$n_p = \frac{v}{60\ l_p N} \times 10^6 \tag{1}$$

Where:

n_p is the speed of fertilizer discharging disk, r/min; l_p is the spacing of sowing plants, mm; v is the forward speed of the machine and tools, km/h; N is the number of fertilizer cavities in the fertilizer discharging disk.

The maximum cross section span of fertilizer chamber is 20°. In order to ensure that the distribution length of fertilizer in each hole in the soil is not more than half of the planting distance, the interval Angle between each fertilizer chamber must be greater than 2 times of the cross section span of fertilizer chamber. If the interval between adjacent fertilizer chambers is 40°, the number of fertilizer cavities in fertilizer discharge disk is 9. The planting spacing of maize was 250 mm, the forward speed of the machine was 3~8 km/h, and the speed range of the fertilizer disk was 22.22 r/min to 59.26 r/min. Therefore, the speed range of compost plate in the test was 20 r/min to 60 r/min.

(3) The amount of fertilizer applied to each point

When the cross section area of the cavity is determined, the amount of fertilizer applied to each hole is determined by the thickness of the cavity. The maximum adjustment distance of the fertilizer chamber is 30 mm, corresponding to the maximum fertilization amount of each hole which is 9 g. Since the thickness of the fertilizer chamber must be greater than zero, the minimum value is 5 mm, corresponding to the minimum fertilization amount of each hole which is 1.5 g. Therefore, the range of fertilizer application per hole in the test was 1.5 g to 9 g.

According to the ternary quadratic orthogonal rotation test design method, the horizontal coding of test factors is obtained, as shown in Table 2.

Table 2

Factor level coding table

The level	factors		
	Fertilizer cavity section span X_1 (°)	Fertilizer discharging disk rotational speed X_2 (r/min)	Fertilization amount per hole X_3 (g)
γ	20	60	9
1	17.97	51.89	7.48
0	15	40	5.25
-1	12.03	32.16	3.02
-γ	10	20	1.5
Δ*j*	2.97	14.86	2.23

The test indexes include variation coefficient and accuracy of fertilization amount. The test method is shown in Fig. 4. In the post-treatment stage, a Mass flow sensor was added below the exit of the secondary fertilizer box. The area covered by the Mass flow sensor should be larger than the cross section area of the fertilizer chamber, and there could only be one fertilizer cavity in the area at the same time, so the diameter of the Mass flow sensor was 20 mm. The change of the total fertilizer particle mass in the sensor covered area with time was recorded during the process of each fertilizer cavity passing through the sensor.

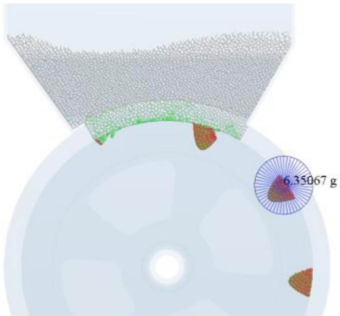

Fig. 4 - Grid bin group and mass flow sensor location

Calculation formula of each index:

(1) Variation coefficient of filling amount in each cavity

$$C_V = \frac{\sqrt{\frac{1}{n_1}\sum_{i=1}^{n_1}(m_{imax} - \overline{m}_{max}}}{\overline{m}_{max}} x100\ \% \tag{2}$$

Where: n_1 is the number of fertilizer cavity passing through the mass flow sensor in the simulation period (excluding the first and last one); m_{imax} is the maximum mass in the sensor area during the process of the cavity passing through the mass flow sensor, g; m_{max} is the arithmetic mean of m_{imax}, g.

(2) Accuracy of filling amount in each cavity

$$\zeta = \frac{\sum_{i=1}^{n_1 \Sigma} m_{imax}}{n_1 M_h \%} \tag{3}$$

Where:

M_h is the theoretical fertilizer application rate per hole, g.

In order to ensure continuous fertilizer supply throughout the whole simulation test process, and there is still enough residual fertilizer stored in the fertilizer box, the total mass of particles generated in the fertilizer box is set as 3 kg. The simulation time step was set as 15% Rayleigh time step, the output time step was 0.01 s, the grid size was 5.44 mm, and the total length of simulation time was 5 s.

RESULTS

Expert Design 8.0.6 software was used to design the experiment and record the test results. The test scheme and results are shown in Table 3. After the experiment, quadratic regression analysis was conducted on the test results and multiple regression fitting was performed to obtain the regression equations of the Variation coefficient of fertilizer discharge rate Y_1 and the accuracy of filling amount rate Y_2 at each hole.

Table 3

Test scheme and results

Test serial number	Fertilizer cavity section span X_1	Fat disk rotational speed X_2	Fertilization amount per hole X_3	Variation coefficient of filling amount Y_1 (%)	Accuracy of filling amount Y_2 (%)
1	-1	-1	-1	2.24	81.32
2	1	-1	-1	2.55	76.92
3	-1	1	-1	3.23	74.10
4	1	1	-1	4.00	70.24
5	-1	-1	1	1.67	87.60
6	1	-1	1	1.5	82.16
7	-1	1	1	1.27	84.22
8	1	1	1	2.24	77.92
9	-1.682	0	0	1.85	83.76
10	1.682	0	0	2.96	74.04
11	0	-1.682	0	1.63	85.19
12	0	1.682	0	2.32	79.87
13	0	0	-1.682	4.35	68.55
14	0	0	1.682	1.27	85.10
15	0	0	0	1.95	82.74
16	0	0	0	1.88	81.11
17	0	0	0	1.70	80.59
18	0	0	0	2.23	83.24
19	0	0	0	1.82	81.93
20	0	0	0	2.18	83.74
21	0	0	0	1.79	82.37
22	0	0	0	1.83	81.52
23	0	0	0	2.07	83.21

Significance analysis of variation coefficient of filling amount (Y_1)

The software Design Expert 8.0.6 was used to conduct variance analysis on the test results, and the results are shown in Table 4. As can be seen from Table 4, the test model is extremely significant (P < 0.01). Among the main factors, the section span of fertilizer cavity, the rotational speed of fertilizer disk and the amount of fertilizer application all had extremely significant effects on the variation coefficient of filling amount at each hole, and the order of influence of each factor on the variation coefficient of filling amount was X_3>X_2>X_1. Among the interaction terms, X_2X_3 has a very significant effect on the variation coefficient of filling amount, X_1X_2 has a significant effect, but X_1X_3 has no significant effect. In the quadratic term, X_3^2 has a very significant effect on the variation coefficient of filling amount, and X_1^2 has a significant effect. After incorporating the non-significant factors into the residual items, variance analysis was conducted again. The results are shown in Table 4. The regression equation between each factor and indicator is:

$$Y_1 = 8.056 - 0.632X_1 - 0.009X_2 - 0.562X_3 + 0.006X_1X_2 - 0.010X_2X_3 + 0.017{X_1}^2 + 0.058{X_3}^2 \tag{4}$$

Where: X_1 represents the cross section span of fertilizer cavity, X_2 represents the rotating speed of fertilizer plate, and X_3 represents the amount of fertilizer application.

The loss of fit test for the above regression equation shows that P > 0.1 is not significant, which proves that there is a significant quadratic relationship between the test index and the test factors.

Table 4

Variance analysis of variation coefficient of filling amount

Sources of variation	Sum of squares	Degrees of freedom	The mean square	F	P
Model	12.819/12.809	9/7	1.424/1.830	28.399/41.446	<0.0001***/<0.0001***
X_1	1.028/1.028	1/1	1.028/1.028	20.495/23.282	0.0006***/0.0002***
X_2	1.137/1.137	1/1	1.137/1.137	22.668/25.751	0.0004***/0.0001***
X_3	8.104/8.104	1/1	8.104/8.104	161.567/183.541	<0.0001***/<0.0001***
X_1X_2	0.320/0.320	1/1	0.320/0.320	6.380/7.248	0.0253**/0.0167**
X_1X_3	0.010	1	0.010	0.195	0.6657
X_2X_3	0.551/0.551	1/1	0.551/0.551	10.991/12.486	0.0056***/0.0030***

Table 4
(continuation)

Variance analysis of variation coefficient of filling amount

Sources of variation	Sum of squares	Degrees of freedom	The mean square	*F*	*P*
X_1^2	0.342/0.342	1/1	0.342/0.342	6.824/7.757	0.0215**/0.0139**
X_2^2	0.0004	1	0.0004	0.009	0.9268
X_3^2	1.336/1.336	1/1	1.336/1.336	26.635/30.267	0.0002***/< 0.0001***
Lost to poor	0.383/0.393	5/7	0.077/0.056	2.280/1.672	0.1437/0.2432
error	0.269/0.269	8/8	0.034/0.034		

notes：The figures under "/" are the results of ANOVA after excluding the insignificant factors："***" means extremely significant（$P < 0.01$）；"**" means significant（$0.01 < P < 0.05$）；"*" means more significant（$0.05 < P < 0.1$），It is the same in the following.

Significance analysis of accuracy of filling amount (Y_2)

The results of variance analysis of Y_2 for fertilizer discharge accuracy are shown in Table 5. As can be seen from Table 5, the experimental model was significant (P < 0.01). Among the main factors, the cross section span of fertilizer cavity, the rotating speed of fertilizer disk and the fertilizing amount all had extremely significant effects on the accuracy of filling amount. Among the interaction terms, X_2X_3 had a significant effect on the accuracy of filling amount, while the other interaction terms had no significant effect. In the quadratic term, both X_1^2 and X_3^2 have extremely significant effects on the Variation coefficient of fertilizer discharge, while X_2^2 has no significant effects. After incorporating the non-significant factors into the residual items, variance analysis was conducted again. The results are shown in Table 5, and the regression equation between each factor and indicator is

$$Y_2 = 82.33 - 2.66X_1 - 2.23X_2 + 4.18X_3 + 0.79X_2X_3 - 1.18{X_1}^2 - 1.91{X_3}^2 \tag{5}$$

The loss of fit test for the above regression equation shows that P > 0.1 is not significant, which proves that there is a significant quadratic relationship between the test index and the test factors.

Table 5

Variance analysis of accuracy of filling amount

Sources of variation	Sum of squares	Degrees of freedom	The mean square	*F*	*P*
Model	490.304/488.603	9/6	54.478/81.434	37.046/62.589	<0.0001***/<0.0001***
X_1	96.736/96.736	1/1	96.736/96.736	65.783/74.350	<0.0001***/<0.0001***
X_2	67.969/67.969	1/1	67.969/67.969	46.221/52.241	<0.0001***/<0.0001***
X_3	239.187/239.187	1/1	239.187/239.187	162.653/183.837	<0.0001***/<0.0001***
X_1X_2	0.013	1	0.013	0.009	0.9271
X_1X_3	1.514	1	1.514	1.029	0.3288
X_2X_3	4.930/4.930	1/1	4.930/4.930	3.352/3.789	0.0901*/0.0694*
X_1^2	22.080/22.109	1/1	22.080/22.109	15.015/16.992	0.0019***/0.0008***
X_2^2	0.174	1	0.174	0.118	0.7365
X_3^2	58.115/58.162	1	58.115/58.162	39.520/44.702	<0.0001***/<0.0001***
Lost to poor	10.055/11.755	5/8	2.011/1.469	1.775/1.297	0.2241/0.3609
error	9.062/9.062	8/8	1.133/1.133		

According to the significance analysis, X_1X_2 and X_2X_3 had significant effects on the variation coefficient of fertilization rate, and X_2X_3 had significant effects on the accuracy of fertilization rate. Through data processing with Desk-Expert 8.0.6, the response surface of interaction effect on the variation coefficient and accuracy of fertilizer filling was obtained.

As for the variation coefficient of fertilizer quantity, the interaction between the speed of fertilizer plate and the section span of fertilizer cavity is shown in Fig. 5a. When the rotational speed of each fertilizer cavity is fixed, the variation coefficient of fertilizer quantity decreases first and then increases with the cross section span of the fertilizer cavity, and the optimal cross section span of the fertilizer cavity is 12° to 15°. When the cross section span of the fertilizer cavity is fixed, the variation coefficient of fertilizer quantity increases with the increase of the speed of the fertilizer disk, and the optimal speed range of the fertilizer disk is 40 r/min to 55 r/min.

For the variation coefficient of fertilization amount, the interaction between the speed of fertilizer plate and the amount of fertilizer applied in each hole is shown in Fig. 5b. When the amount of fertilizer was fixed in each hole, the variation coefficient of fertilization amount increased with the increase of the speed of fertilizer disk, and the optimal range of the speed of fertilizer disk was 40 r/min to 60 r/min.

When the rotational speed of fertilizer plate was fixed, the variation coefficient of fertilization amount decreased with the increase of fertilization amount in each hole, and the optimal range of fertilization amount in each hole was 7 g to 8 g.

As for the accuracy of fertilizer filling, the interaction between the speed of fertilizer plate and the amount of fertilizer applied in each hole is shown in Fig. 5c. When the amount of fertilizer was fixed in each hole, the accuracy of fertilization amount decreased with the increase of the speed of fertilizer disk, and the optimal range of the speed of fertilizer disk was 40 r/min to 60 r/min. When the rotational speed of the fertilizer disk was fixed, the accuracy of fertilizer filling increased with the increase of fertilization amount in each hole, and the optimal range of fertilization amount in each hole was 6 g to 8 g.

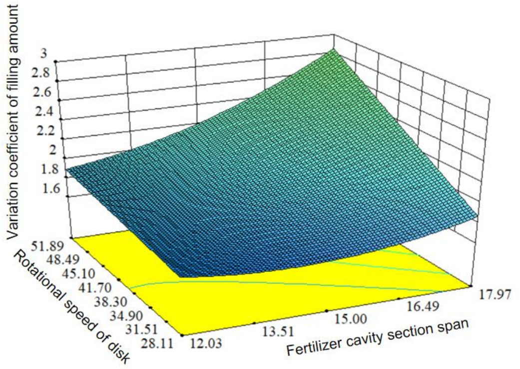

(a) Variation coefficient of filling amount influenced by X_1X_2

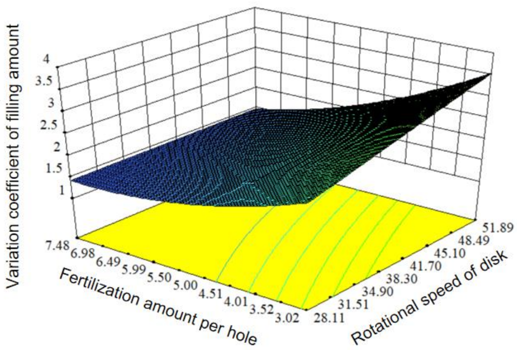

(b) Variation coefficient of filling amount influenced by X_2X_3

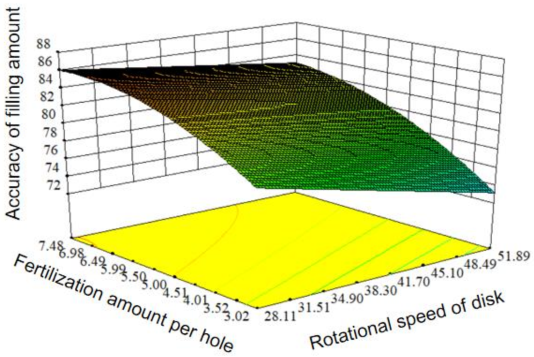

(c) Accuracy of filling amount influenced by X_2X_3

Fig. 5 - Response surface of interaction to test index

In order to obtain the optimal structural parameters of the fat cavity, the optimization module of Design Expert 8.0.6 software was used to solve the constraint objective optimization of the above two regression models. In order to make the fertilizer disk meet the requirements of various forward speeds and fertilization amount, the difference values of the speed of fertilizer disk and fertilization amount of each hole were taken when selecting the optimal constraint conditions, objectives and constraint functions. That is, the rotational speed of the fertilizer disk is 50 r/min, and the fertilization amount per hole is 3 g.

The final objective function is:

$$\begin{cases} \min Y_1(X_1, X_2, X_3) \\ \max Y_2(X_1, X_2, X_3) \\ \text{s.t.} \begin{cases} 12 \le X_1 \le 15 \\ X_2 = 50 \\ X_3 = 3 \end{cases} \end{cases} \tag{6}$$

The objective function was optimized and solved. The results were as follows: when the cross section span of the fertilizer cavity was 12.35°, the rotational speed of the fertilizer disk was 50 r/min, and the fertilization amount per hole was 3 g, the variation coefficient of fertilization amount was 3.20%, and the accuracy of fertilization amount was 75.05%. Fertilizer application rate in each hole and fertilizer disk speed were changed to the optimal values under operating conditions, that is, fertilizer discharge disk speed was 20 r/min, fertilizer application rate in each hole was 9 g, the variation coefficient of fertilization amount was 1.89%, and the accuracy of fertilization amount was 86.93%.

When the cross section span of the fertilizer cavity is 12.35°, the accuracy of fertilizer filling varies from 75.05% to 86.93% with the change of the rotational speed of the fertilizer disk (the moving speed of the machine) and the fertilizer application amount per hole. In order to keep the accuracy of the fertilizer disk near 100% and the diameter of the fertilizer disk unchanged, the opening width and depth of the section of the fertilizer cavity are increased to 1.23 times of the original. That is, after the final optimization, the cross section span of the cavity is 13.58°, the opening width of the cavity is 29.56 mm, and the depth of the cavity is 22.08 mm.

The verification test was carried out under the operating conditions of the central group, namely, the rotational speed of the fertilizer disk was 40 r/min, and the fertilization amount applied to each hole was 5.25g. The test results showed that the average fertilization amount was 5.221 g, the accuracy of fertilization amount was 98.45%, and the variation coefficient of fertilization amount was 1.74%, which met the design requirements.

Verification test

The field performance test was carried out in April 2019. The experimental site was selected at the Cultivated Land Conservation Observation and Experiment Station in North Hebei, China Agricultural University, located in Dongchengfang Town, Zhuozhou City, Hebei Province (115° 56'E, 39° 28'N). In order to test the operating performance of the machine under different operating conditions, the forward speed of the machine was selected as the test factor for single factor test. Fertilizer application rate was set at 6 g/plant, the advancing speed of the machine was 3, 4, 5 and 6 km/h, respectively. The operating length of each group was 100 m, among which the middle 60 m was the stable operation area. During the test, the seeding depth and fertilization depth were measured after the normal operation of the seeder. Since it is difficult to observe and sample after the fertilizer is placed in the soil, the depth of sowing fertilization is adjusted to 0 during the test to make the seeds and fertilizer fall on the surface, as shown in Fig. 6.

Fig. 6 - Seed and fertilizer distribution

The experimental results showed that when the application amount was 6 g per hole and the moving speed of the machine was 3, 4, 5 and 6 km/h, the actual fertilizer discharge amount per hole was 5.88, 5.79, 5.91 and 5.86 g, respectively. The variation coefficients of the application amount per hole were 2.39%, 1.78% and 1.52%, respectively, which did not show significant difference. The average amount of fertilizer applied in each hole was 5.86 g, the average accuracy of filling amount was 97.67%, and the average variation coefficient of fertilizer application in each hole was 1.90%. The performance of fertilizer discharge met the design requirements, and the law was the same with the simulation results, which verified the accuracy of the simulation test.

CONCLUSIONS

(1) This study put forward the rotation of cavity and plate for fertilizer extraction according to the agronomic requirements of corn hole fertilization and sowing. Meanwhile, this study designed the overall structure of the cavity fertilization device, the fertilizer discharging plate, and fertilizer cavity. Through the dynamic analysis of fertilizer particles in the process of fertilizer filling, we found that the main factors affecting the performance of fertilizer filling were the cross section span of fertilizer cavity, the rotational speed of fertilizer disk, and the amount of fertilizer applied in each hole.

(2) The discrete element method was used to carry out the three-factor quadratic orthogonal rotation combination test. The effects of the cross section span of the fertilizer cavity, the speed of the fertilizer disk, and the application rate of fertilizer per hole on the variation coefficient and accuracy of fertilizer filling were

studied. The structure of the fertilizer cavity was optimized. The cavity performed the best when the cross section span of the cavity is 13.58°, the opening width of the cavity is 29.56 mm, and the depth of the cavity is 22.08 mm.

(3) The verification test in the corn field showed that the average accuracy of filling amount in each hole was 97.67%, and the average variation coefficient of fertilizer application in each hole was 1.90%. The fertilizer discharge performance satisfied the design requirements, and agreed with the law in the simulation results, which verified the accuracy of the simulation test.

ACKNOWLEDGEMENT

This work was supported by the National Key R & D Program - Key Techniques and Equipment for Precision Sowing and Precision-deep Fertilization in Northern China (Grant No. 2016YFD0200600).

REFERENCES

[1] Cozzolino D., Morón A., (2006), Potential of near-infrared reflectance spectroscopy and Chemometrics to predict soil carbon fractions. *Soil & Tillage Research*, vol. 85, issue 1, pp. 78-85.

[2] Hu H., Li H., Wang Q. et al., (2016), Design and experiment of a topdressing machine for deep application of maize at fixed point between rows. *Transactions of the Chinese Society of Agricultural Engineering*, vol. 32, issue 24, pp. 26-35.

[3] Jiang C., Wang H., Lu D. et al., (2018), The yield and nutrient absorption and utilization efficiency of summer maize were improved by one-time application of urea in root zone. *Transactions of the Chinese Society of Agricultural Engineering*, vol. 34, issue 12, pp. 146-153.

[4] Li S., (2018), Design and experiment of side deep burrow fertilization device with electromechanical drive for precision burrow direct seeding of rice, *Northeast Agricultural University*.

[5] Liu Z., Zhao Y., Guo S. et al., (2019), Enhanced crown root number and length confers potential for yield improvement and fertilizer reduction in nitrogen-efficient maize cultivars, *Field Crops Research*, vol. 241, pp. 107562.

[6] Luo X., Liao J., Hu L., et al., (2016), Raise agricultural mechanization level to promote agricultural sustainable development. *Transactions of the Chinese Society of Agricultural Engineering*, vol. 32, issue 01, pp. 1-11.

[7] Rinnan R., Rinnan S., (2007), Application of near infrared reflectance (NIR) and fluorescence spectroscopy to analysis of microbiological and chemical properties of arctic soil. *Soil Biology & Biochemistry*, vol. 39, issue 07, pp. 1664-1673.

[8] Tang H., Wang J., Xu C., et al., (2019), Research progress analysis on key technology of chemical fertilizer reduction and efficiency increase, *Transactions of the Chinese Society for Agricultural Machinery*, vol. 50, issue 4, pp. 1-19.

[9] Wang J., Li S., Z. Z., (2018a), Design and experiment of side deep burrow fertilization system with electromechanical drive for precision burrow direct seeding of rice (English). *Transactions of the Chinese Society of Agricultural Engineering*, vol. 34, issue 08, pp. 43-54.

[10] Wang J., Zhou W., Bai H., (2018b), Design and Test of Differential Bidirectional Fertilizer Supply and Distribution Device for Liquid Fertilizer Deep applicator. *Transactions of the Chinese Society for Agricultural Machinery*, vol. 49, issue 06, pp. 105-111.

[11] Wang Z., Liang C., Wang H., (2020), Design and experiment of corn variable hole fertilization test bed. *Mechanization research*, vol. 42, issue 04, pp. 166-169.

[12] Yuan W., Li K., Jing C., (2018), Design and test of hole fertilizer dispenser. *Mechanization research*, vol. 40, issue 1, pp. 145-149.

[13] Zhang L., Song H., Chen X., et al., (2020), Primary study on nutrient migration under hole fertilization in soils, *Soils*, vol. 52, issue 6, pp. 1145-1151.

[14] Zhang J., Liu H., Gao J., (2018), SPH simulation and experiment of maize delamination positive hole fertilization and precision seeder. *Transactions of the Chinese Society for Agricultural Machinery*, vol. 49, issue 9, pp. 66-72.

[15] Zhou W., Sun X., Liu Z., et al., (2020), Simulation analysis and test of interaction between needle body and soil of liquid fertilizer hole applicator. *Transactions of the Chinese Society for Agricultural Machinery*, vol. 51, issue 4, pp. 87-94.

[16] Zhu S., Jorge M. V., Daniel K. M., (2016), Nitrogen fertilizer rate affects root exudation, the rhizosphere microbiome and nitrogen-use-efficiency of maize, *Applied Soil Ecology*, vol. 107, pp. 324-333.

DESIGN AND EXPERIMENT OF A SELF-PROPELLED CRAWLER-POTATO HARVESTER FOR HILLY AND MOUNTAINOUS AREAS
/
丘陵山区履带自走式马铃薯收获机设计与试验

JianGuo Zhou[1)], ShuMing Yang[2)], MaoQiang Li[3)], Zhi Chen[4)], JianDong Zhou[5)], ZeNing Gao[1)], Jun Chen*[1)] [1]

[1)] College of Mechanical and Electronic Engineering, Northwest A&F University, Yangling 712100, China;
[2)] College of Mechanical Engineering, Ningxia University, Yinchuan 750021, China;
[3)] College of Mechanical and Electrical Engineering, North Minzu University, Yinchuan 750021, China;
[4)] Ningxia Zhiyuan Agricultural Equipment Co., Ltd., Wuzhong 751100, China;
[5)] Agricultural Mechanization Technology Extension Station of Ningxia Hui Autonomous Region, Yinchuan 750021, China
Tel: +86 135721917773; E-mail: chenjun_jdxy@nwsuaf.edu.cn
DOI: https://doi.org/10.35633/inmateh-64-14

***Keywords:** hilly and mountainous area, self-propelled, potato harvester, finite element analysis*

ABSTRACT
A self-propelled crawler and potato harvester was designed, with the terrain characteristics of both hilly and mountainous areas considered, to address the low degree of mechanization, markedly low potato harvesting rate, and high labor intensity of potato harvesting in hilly and mountainous areas. The harvester could complete the tasks of digging potatoes, separating them from the soil, transporting potatoes, and collecting them in a single operation. Finite element analysis was conducted on major parts, such as the digging shovel and the frame, based on the overall structure and working principle of the harvester. A field experiment was then conducted. The results of the finite element analysis showed that the maximum stress of the digging shovel was 37.969MPa, the maximum strain was 1.846×10^{-4}, and the total deformation was 0.8041mm. These measurements were within a safe range. The field experiment results showed that potato harvesting rate, bruising rate, and damage rate were 98.54%, 1.51%, and 1.31%, respectively that is, higher than the national standards for potato harvesters. The potato harvester exhibited reliable walking performance and harvesting performance, which could provide a reference for research on the mechanization of potato harvesting in hilly and mountainous areas.

摘要
针对丘陵山区马铃薯收获的机械化程度低、明薯率低和劳动强度大的问题，结合丘陵山区地形特点，设计了一种履带自走式马铃薯收获机。该收获机能够一次性完成丘陵山区单垄双行马铃薯的挖掘、薯土分离、输送和集薯装箱的工作。在阐述收获机整体结构和工作原理的基础上，完成对挖掘铲和机架等关键部件的有限元分析，并进行了田间收获试验。有限元分析结果表明，挖掘铲的最大应力为 37.969MPa，最大应变为 1.846×10^{-4}，总变形为 0.8041mm，均在安全范围内。田间试验结果表明，该收获机明薯率为 98.54%，破皮率为 1.51%，伤薯率为 1.31%，各项数据指标均符合马铃薯收获机国家标准的要求。该马铃薯收获机通过性能和收获性能良好，为丘陵山区复杂地形马铃薯全程机械化收获的研究提供参考。

INTRODUCTION
Potatoes are cultivated worldwide, and China has a long history of potato cultivation *(Xu et al., 2018; Zaheer et al., 2016)*. Potatoes present several advantages, such as fast growth, high yield, and high nutritional content *(Darooghegi et al., 2020; Tian et al., 2016)*. With the development of the potato staple food strategy in China, potato planting area and yield have increased year by year *(Li et al., 2020; Zhou et al., 2021)*. The two data points currently rank first globally. In 2019, the potato planting area in China exceeded 5.3×10^5 hectares, and fresh potatoes output exceeded 1.1×10^9 kilograms. However, relative to that of agriculturally developed countries, the technical skills of potato harvesters remain relatively backward *(Li et al., 2020; Wei et al., 2019)*. The mechanization degree of potato harvesting in major potato-producing areas in China, particularly hilly and mountainous areas, is considerably lower than that in plain areas *(Liu et al., 2020)*.

[1] *Jianguo Zhou, M.S. Stud. Eng.; Shuming Yang, Prof. Ph.D. Eng.; Maoqiang Li, T.A. Eng.; Zhi Chen, Chair. Eng.; Jiandong Zhou, A. Stat. Mast. Eng.; Zening Gao, M.S. Stud. Eng.; Jun Chen, Prof. Ph.D. Eng.*

Numerous studies have been conducted on potato harvesters locally and globally *(Novikov et al., 2018; Uspenskiy et al., 2018; Yang et al., 2020)*. Potato harvesting can be divided, depending on the planting terrain, into the combined harvesting mode and segmented harvest mode *(Tseplyaev et al., 2018)*. The combined harvesting mode is mainly promoted in large and medium plain areas. Combined potato harvesters are not suitable for hilly and mountainous areas because of complex terrain and narrow land plots; moreover, they are generally costly. Therefore, the segmented harvesting mode is currently the primary mode adopted for hilly and mountainous areas *(Wei et al., 2019; Zhang et al., 2021)*. That is, potatoes are first dug out and then picked up. Mechanized operation in potato excavation has been realized. Various excavators, including self-propelled potato excavators and traction excavators, have been developed in many universities *(Baybulatov et al., 2020; Wan et al., 2019; Yang et al., 2016).* However, potato picking mainly relies on manual work. In hilly and mountainous areas, the application of the segmented harvesting mode is impeded by low efficiency and high costs, directly affecting the healthy and sustainable development of the potato industry *(Hrushetsky et al., 2019; Zhao et al., 2016)*.

To address the aforementioned problems, a harvester that can complete the tasks of digging and collecting potatoes in a single operation was designed. The size limit and functional requirements for the harvester were determined by assessing the potato planting environment in hilly and mountainous areas. In this study, the overall structure of the harvester was designed, the key components were analyzed, the harvester prototype was processed, and the field experiment was performed.

MATERIALS AND METHODS

Overall structure and working principle

As shown in Figure 1, the potato harvester mainly consists of the following: a cab, a frame, a crawler chassis, a depth limiting wheel, a digging shovel, a wave chain rod, a baffle, a transmission chain, and a collecting box. The wave chain rod, baffle, and transmission chain comprise the conveying device. The digging shovel and the depth limiting wheel are fixed in front of the conveying device. The cab, conveying device, and collecting box are fixed above the crawler chassis via the frame. The overall structure of the potato harvester provides advantages, including a moderate size and compact arrangement.

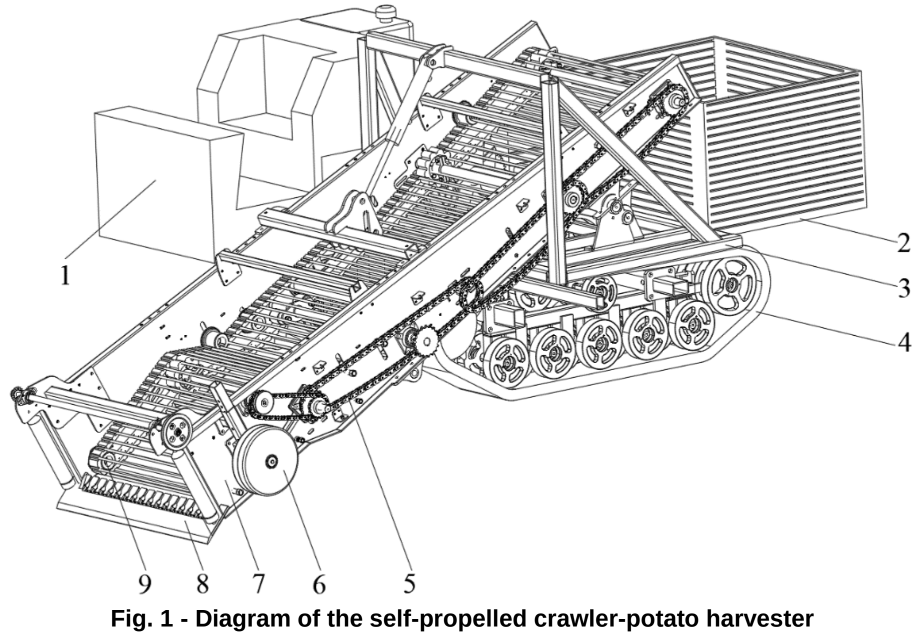

Fig. 1 - Diagram of the self-propelled crawler-potato harvester

1) cab; 2) collecting box; 3) frame; 4) crawler chassis; 5) transmission chain; 6) depth limiting wheel; 7) baffle; 8) digging shovel; 9) wave chain rod

The driver controls the potato harvester to move forward steadily, and the crawler chassis runs smoothly. Potatoes are dug out of the soil by using a digging shovel. The depth limiting wheel can ensure that the digging shovel is in the appropriate depth. The transmission chain drives the wave chain rod to rotate. Owing to vibration, the soil block progressively decreases. When the soil block is smaller than the gap of the wave chain rod, it falls back to the ground, prompting the separation of potatoes and the soil block. Potatoes are then transported in the back. When the collection box is filled with potatoes, it requires replacement.

The aforementioned process is repeated until the entire harvesting process is completed. The main technical parameters of the potato harvester are listed in Table 1.

Table 1

Main technical parameters of the self-propelled crawler-potato harvester

Technical parameters	Value	Units
Overall dimensions (length× width× height)	5200×2750×2750	mm
Overall weight	2970	kg
Auxiliary power	74	kW
Digging depth	100-300	mm
Working width	800	mm
Working speed	0.5-0.7	$m \cdot s^{-1}$

Finite element analysis

Finite element analysis is often used in the analysis of the stress and strain of the research object to improve reliability *(Issa et al., 2020)*. The solution process of finite element analysis typically includes the pre-processing, load-solving, and post-processing modules *(Yu et al., 2015)*. The main function of the pre-processing module is to define the material properties and divide the grid cells. The main function of the load-solving module is to add load constraints and displacement constraints. The solution is then completed computationally. The post-processing module mainly views the stress and strain analysis results. The weak structure of the design can be identified by finite element analysis. The design is then optimized in size and material. The aforementioned procedure is repeated, ultimately enhancing the design.

The digging shovel, one of the principal parts of a potato harvester, generally penetrates the soil at an angle of 20°-25° *(Fan et al., 2019)*. As the harvester moves forward, the potatoes and the soil are dug out together. The reliability of the digging shovel directly affects the working efficiency of the harvester. Consistent with the previously described steps, a finite element analysis of the digging shovel was conducted, and the software used was ANSYS 2020. Defined as 45 steel, the material of the digging shovel was evaluated; the results are listed in Table 2. As shown in Figure 2, the grid cell size of the digging shovel is 5mm, the number of nodes is 3.7778×10^4, and the number of cells is 2.0012×10^4. Figure 3 shows that the maximum stress value of the digging shovel is 37.969 MPa, which is considerably less than 355 MPa (yield strength of 45 steel). Figures 4 and 5 show that the maximum strain of the digging shovel is 1.846×10^{-4}, and the total deformation is 0.8041 mm, which fall within the safe range. Therefore, the design of the digging shovel can ensure its continuous and stable work.

Table 2

Main material properties of 45 steel

Parameters	Value	Units
Elastic modulus	2.09×10^5	MPa
Poisson's ratio	0.269	-
Mass density	7.89×10^3	$kg \cdot m^3$
Yield strength	355	MPa

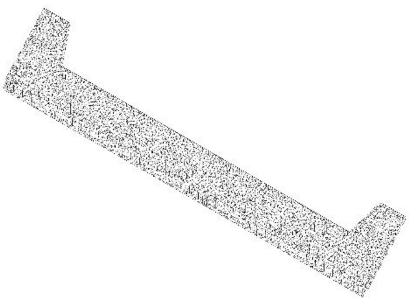

Fig. 2 - Mesh generation of the digging shovel

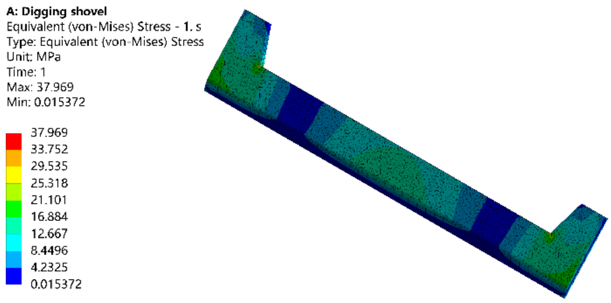

Fig. 3 - Stress nephogram of the digging shovel

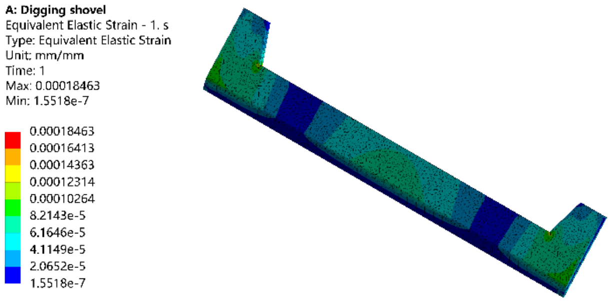

Fig. 4 - Strain nephogram of the digging shovel

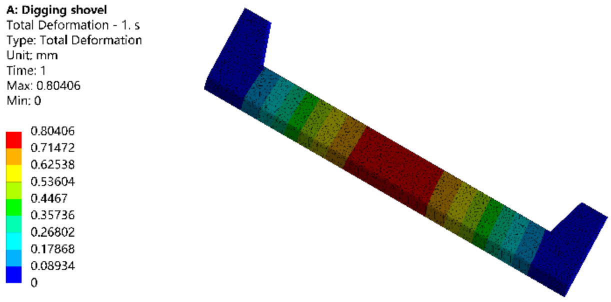

Fig. 5 - Total deformation nephogram of the digging shovel

The frame is also one of the principal components of a potato harvester *(Shen et al., 2020)*. A cab and a collection box are usually fixed above the frame, and a crawler chassis is connected below the frame. The reliability of the frame structure directly affects the stability of the whole harvester. As shown in Figure 6, the frame has a symmetrical structure to facilitate processing. The frame material was also 45 steel. The finite element analysis results of the frame are presented in Figures 7-9. The following characteristics of the frame were within the safe range: maximum stress, 13.946 MPa; maximum strain, 6.836×10^{-5}; and total deformation, 4.887×10^{-3} mm. Therefore, the frame can ensure a reliable connection.

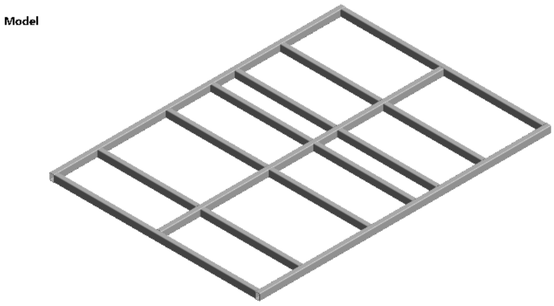

Fig. 6 - Schematic of the frame

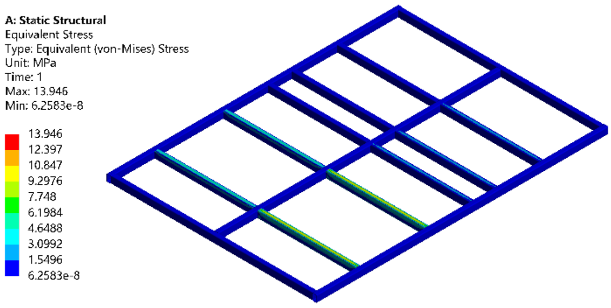

Fig. 7 - Stress nephogram of the frame

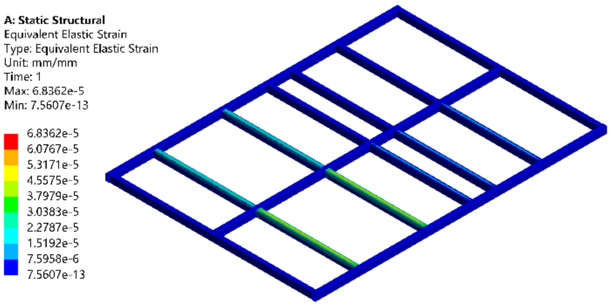

Fig. 8 - Strain nephogram of the frame

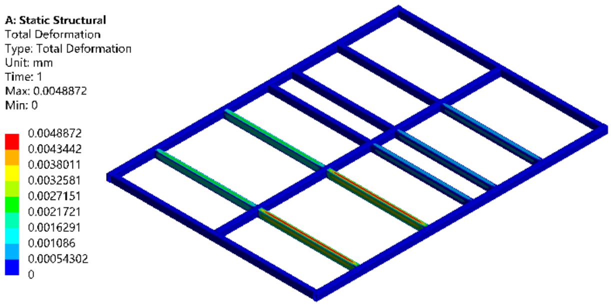

Fig. 9 - Total deformation nephogram of the frame

Performance evaluation

In accordance with relevant standards for the NYT648-2015 potato harvester, the performance of the harvester was evaluated by calculating the harvesting rate, bruising rate, and damage rate *(Chen et al., 2020; Qi et al., 2017)*. The experiment was designed as follows: five areas of the experimental field were randomly selected, with each field measuring 30 m in length. Five plots were randomly selected from each field, with each plot measuring 3 m in length. One plot was randomly selected from each field for harvesting experiments repeated five times. The evaluation indexes were then calculated based on the following formulas:

$$L_1 = \frac{M_1}{(M_1 + M_2)} \times 100\% \tag{1}$$

$$L_2 = \frac{M_3}{(M_1 + M_2)} \times 100\% \tag{2}$$

$$L_3 = \frac{M_4}{(M_1 + M_2)} \times 100\% \tag{3}$$

where:

L_1 is potato harvesting rate, %; L_2 is potato bruising rate, %; L_3 is potato damage rate, %; M_1 is the quantity of excavated potatoes, kg; M_2 is the quantity of potatoes that have not been excavated, kg; M_3 is the quantity of potato with broken skin, kg; M_4 is the quantity of the damaged potatoes, kg.

RESULTS AND ANALYSIS

Field experiment

To verify whether the self-propelled crawler-potato harvester can meet the requirements, a field experiment was conducted in Xiji County, Guyuan City, Ningxia on October 25, 2020. As shown in Figure 10, the experimental field is a hilly and mountainous area where a large number of potatoes are planted. The experimental field was located at 105.73° E and 35.96° N. The rainfall was 0.0 mm and the soil water content was 20%.

Fig. 10 – The experimental field

Qingshu No.9 is planted in the experimental field from April to May and harvested from September to October every year. The experiment equipment and instruments mainly included a self-propelled crawler-potato harvester, a stopwatch, a tape measure, a digital vernier caliper, a digital display platform scale, and a record book. The process of the field experiment is illustrated in Figures 11 and 12.

Fig. 11 - Potato harvester in motion

Fig. 12 - Potato harvester at work

Data analysis

The experimental data are listed in Table 3. The results of the field experiment showed that potato harvesting rate was 98.54%, the bruising rate was 1.51%, and the damage rate was 1.31%. All harvester indexes met the requirements for national harvester quantity evaluation. The effect of the harvester operation is shown in Figure 13.

Table 3

Data and results of the field experiment

Serial number	Harvesting rate (%)	Bruising rate (%)	Damage rate (%)
1	98.58	1.45	1.28
2	98.59	1.53	1.31
3	98.35	1.52	135
4	98.53	1.55	1.27
5	98.65	1.48	1.34
Average value	98.54	1.51	1.31

Fig. 13 – Potato harvester operation effect

CONCLUSIONS

(1) A self-propelled crawler-potato harvester was designed for potato harvesting in hilly and mountainous areas, which could complete the excavation and collection of potatoes in a single operation.

(2) The results of finite element analysis showed that the maximum stress and strain of the digging shovel and the frame met the safety requirements. The results of field experiments showed that the harvesting rate was 98.54%, the bruising rate was 1.51%, and the damage rate was 1.31%, which were superior to the national standards for potato harvesters.

(3) It is of great significance to improve the degree of potato harvesting mechanization and promote the sustainable and healthy development of the potato industry in hilly and mountainous areas.

ACKNOWLEDGEMENT

This research was supported by the Foreign Science and Technology Cooperation Special Project of Ningxia Hui Autonomous Region Key Research and Development Program (No. 2019BFF02003).

REFERENCES

[1] Baybulatov, T. S., Aushevent, M. K., Khamkhoev, B. I., & Tsechoeva, A. K., (2020), Results of studies of a potato digger with rod burning working bodies, *in 2020 International Conference on World Technological Trends in Agribusiness*, vol. 624, doi: 10.1088/1755-1315/624/1/012057.

[2] Chen, X. S., Chen, T., Wu, T., Ma, X., Zeng, L. C., & Chen, L. T., (2020), Design and experiment on harvester for winter planting potato of straw coverage, *Jilin Daxue Xuebao (Gongxueban) / Journal of Jilin University (Engineering and Technology Edition)*, vol. 50, issue 2, pp. 749-757, doi: 10.13229/j.cnki.jdxbgxb20181022.

[3] Darooghegi, M. M., Milajerdi, A., Sheikhi, A., & Azadbakht, L., (2020), Potato consumption and risk of all cause, cancer and cardiovascular mortality: a systematic review and dose-response meta-analysis of prospective cohort studies, *Critical Reviews in Food Science and Nutrition*, vol. 60, issue 7, pp. 1063-1076, doi: 10.1080/10408398.2018.1557102.

[4] Fan, Y., Zhao, P., Qiu, L. C., & Meng, T. T., (2019), Simulation analysis and experiment on performance of bionic potato digging shovel, *International Agricultural Engineering Journal*, vol. 28, issue 1, pp. 208-218.

[5] Hrushetsky, S. M., Yaropud, V. M., Duganets, V. I., Duganets, V. I., Pryshliak, V. M., & Kurylo, V. L., (2019), Research of constructive and regulatory parameters of the assembly working parts for potato harvesting machines, *INMATEH Agricultural Engineering*, vol. 59, issue 3, pp. 101-110, doi: 10.35633/INMATEH-59-11.

[6] Issa, I. I. M., Zhang, Z. G., El-Kolaly, W., Yang, X., & Wang, H., (2020), Design, Ansys analysis and performance evaluation of potato digger harvester, *International Agricultural Engineering Journal*, vol. 29, issue 1, pp. 60-73.

[7] Li, T., Yang, M. L., Zhang, X., Zhang, E. G., Cheng, X. T., & Wang, X. L., (2020), Potato production technology and difference of mechanization level in northwest china, *Nongye Jixie Xuebao/Transactions of the Chinese Society for Agricultural Machinery*, vol. 51, pp. 307-313, doi: 10.6041/j.issn.1000-1298.2020.S1.036.

[8] Li, Z., Chang, Q., Liu, J. Z., & Dong, X. J., (2020), Development status and trend of domestic and overseas potato harvesters, *Modern Manufacturing Technology and Equipment*, vol. 56, issue 09, pp. 207-208, doi: 10.16107/j.cnki.mmte.2020.0897.

[9] Liu, P. L., Zhou, Y., Sun, K., & Fang, Z., (2020), Priority analysis on the production layout of potato in China, *International Journal of Sustainable Development and Planning*, vol. 15, issue 7, pp. 1081-1087, doi: 10.18280/IJSDP.150712.

[10] Novikov, N. N., Rembalovich, G. K., Kostenko, M. Y., Byshov, D. N., Lapin, D. A., & Kostenko, N. A., (2018), To the question of the potato harvester reliability, *Tekhnika i oborudovanie dlya sela*, 9, 25-28.

[11] Qi, J. T., Li, Y. P., Meng, H. W., Kan, Z., Wang, L. H., Chen, S. J., & Gong, W. D., (2017), Design and experiment of 4UM-2 potato harvester, *International Agricultural Engineering Journal*, vol. 26, issue 4, pp. 166-174.

[12] Shen, H. Y., Wang, B., Hu, L. L., Wang, G. P., Ji, L. L., Shen, G. W., & Wu, T., (2020), Design of potato connecting and conveying mechanism for 4UZL-1 type sweet potato combine harvester, *Nongye Gongcheng Xuebao/Transactions of the Chinese Society of Agricultural Engineering*, vol. 36, issue 17, pp. 9-17, doi: 10.11975/j.issn.1002-6819.2020.17.002.

[13] Tian, J. H., Chen, J. C., Ye, X. Q., & Chen, S. G., (2016), Health benefits of the potato affected by domestic cooking: A review, *Food Chemistry*, vol. 202, pp. 165-175, doi: 10.1016/j.foodchem.2016.01.120.

[14] Tseplyaev, A. N., Abezin, V. G., & Skripkin, D. V., (2018), Technology of potato harvesting by combine harvester, *Izvestiya Nizhnevolzh Agricultural University Complex: Science and Higher Professional Education*, issue 1, pp. 276-284, doi: 10.32786/2071-9485-2018-01-276-284.

[15] Uspenskiy, I. A., Rymbalovich, G. K., Kostenko, M. U., & Beznosyuk, R. V., (2018), Assessment of prospective technological schemes potato harvester, *Izvestiya Nizhnevolzh Agricultural University Complex: Science and Higher Professional Education*, issue 1, pp. 262-269, doi: 10.32786/2071-9485-2018-01-262-269.

[16] Wan, E. C., Shang, S. Q., Wang, D. W., He, X. N., & Liu, X. D., (2019), Design and test of tractive potato combined harvester, *Journal of Agricultural Mechanization Research*, vol. 41, issue 07, pp. 80-84, doi: 10.13427/j.cnki.njyi.2019.07.015

[17] Wei, Z. C., Li, H. W., Su, G. L., Sun, C. Z., Liu, W. Z., & Li, X. Q., (2019), Development of potato harvester with buffer type potato-impurity separation sieve, *Nongye Gongcheng Xuebao/Transactions of the Chinese Society of Agricultural Engineering*, vol. 35, issue 8, pp. 1-11, doi: 10.11975/j.issn.1002-6819.2019.08.001.

[18] Wei, Z. C., Li, H., Sun, C., Su, G., Liu, W., & Li, X., (2019), Experiments and analysis of a conveying device for soil separation and clod-crushing for a potato harvester, *Applied Engineering in Agriculture*, vol. 35, issue 6, pp. 987-996, doi: 10.13031/aea.13283987.

[19] Xu, D., Liu, H., Jin, C. Y., Cao, C. M., Li, W. G., Zeng, F. K., Zhao, Y. C., & Liu, G., (2018), A new potato variety grown in China suitable for raw eating, *European Food Research and Technology*, vol. 244, issue 5, pp. 851-860, doi: 10.1007/s00217-017-3009-9.

[20] Yang, R. B., Yang, H. G., Shang, S. Q., Xu, P. X., Cui, G. P., & Liu, L. H., (2016), Design and test of poking roller shoving type potato harvester, *Nongye Jixie Xuebao/Transactions of the Chinese Society for Agricultural Machinery*, vol. 47, issue 7, pp. 119-126, doi: 10.6041/j.issn.1000-1298.2016.07.017.

[21] Yang, X. P., Wei, H. G., Zhao, W. Y., Jiang, Y. W., Dai, L. X., & Huang, X. P., (2020), Design and experiment of 4U-1600 set of pile type potato digger, *Nongye Jixie Xuebao/Transactions of the Chinese Society for Agricultural Machinery*, vol. 51, issue 6, pp. 83-92, doi: 10.6041/j.issn.1000-1298.2020.06.009.

[22] Yu, H. L, Zhao, X. S., Sang, Y. Y., & Wu, T., (2015), Parametric modeling and moving simulation of vibrating screen and tubers on potato harvester, *Advance Journal of Food Science and Technology*, vol. 7, issue 6, pp. 474-478, doi: 10.19026/ajfst.7.1343.

[23] Zaheer, K., & Akhtar, M. H., (2016), Potato production usage and nutrition a review, *Critical Reviews in Food Science and Nutrition*, vol. 56, issue 5, pp. 711-721, doi: 10.1080/10408398.2012.724479.

[24] Zhang, Z. G., Wang, H. Y., Li, Y. B., Yang, X., Ibrahim, I., & Zhang, Z. D., (2021), Design and experiment of multi-stage separation buffer potato harvester, *Nongye Jixie Xuebao/Transactions of the Chinese Society for Agricultural Machinery*, vol. 52, issue 2, pp. 96-109, doi: 10.6041/j.issn.1000-1298.2021.02.009.

[25] Zhao, J. F., Zhang, Y. H., Qian, Y. L., Pan, Z. H., Zhu, Y. J., Zhang, Y., Guo, J. P., & Xu., L. G., (2016), Coincidence of variation in potato yield and climate in northern China, *Science of the Total Environment*, vol. 573, pp. 965-973, doi: 10.1016/j.scitotenv.2016.08.195.

[26] Zhou, X. Y., Shen, C., Zhang, J., Cheng, G. D., Liu, Y., Wang, Y. H., Kong, F. T., & Wu, J. Z., (2021), Analysis of potato market in China in 2020 and prospects in 2021, *Chinese vegetables*, issue 03, pp. 1-3, doi： 10.19928/j.cnki.1000-6346.2021.0013.

CFD MODELING OF AERODYNAMIC FLOW IN A WIND TURBINE WITH VERTICAL ROTATIONAL AXIS AND WIND FLOW CONCENTRATOR

/

CFD МОДЕЛЮВАННЯ АЕРОДИНАМІЧНОГО ПОТОКУ У ВІТРЯНІЙ ТУРБІНІ З ВЕРТИКАЛЬНОЮ ВІССЮ ОБЕРТАННЯ І КОНЦЕНТРАТОРОМ ВІТРОВОГО ПОТОКУ

Gorobets V.G.[1)], Trokhaniak V.I.[1)], Masiuk M.Yu.[1)], Spodyniuk N.A.[1)], Blesnyuk O.V.[2)], Marchishina Ye.I.[1)] [1]

[1)] National University of Life and Environmental Sciences of Ukraine / Ukraine;

[2)] Kharkiv Petro Vasylenko National Technical University of Agriculture / Ukraine.

Tel: +380673513082; E-mail: Trohaniak.v@gmail.com

DOI: https://doi.org/10.356.33/inmateh-64-15

Keywords: *wind turbine, CFD, wind flow concentrator, speed, pressure*

ABSTRACT

In order to improve the aerodynamic characteristics by increasing the energy of the wind flow of wind turbines with a vertical rotational axis, a special device - wind flow concentrator was proposed. The concentrator contains channels with a curved contour, which are installed around the rotor. To study the hydrodynamic parameters of the wind flows concentrator depending on the ratio between the input and output geometric characteristics of the channels, as well as the angles of entry and exit methods of mathematical modeling are used. Based on the method of quadratic rotational design of orthogonal combinations, using three-dimensional numerical simulation, the aerodynamic characteristics of the wind flow concentrator for a vertical axis wind turbine were investigated.

РЕЗЮМЕ

Для покращення аеродинамічних характеристик підвищення енергії вітрового потоку вітротурбін з вертикальною віссю обертання було запропоновано спеціальний пристрій «концентратор вітрових потоків» з каналами, що мають криволінійний контур, які встановлюються навколо ротора. Методами математичного моделювання проведені дослідження гідродинамічних параметрів концентратора вітрових потоків в залежності від співвідношення між вхідними і вихідними геометричними характеристиками каналів, а також кутами входу та виходу. На основі методу квадратичного поворотного проектування ортогональних комбінацій, за допомогою тривимірного чисельного моделювання були досліджені аеродинамічні характеристики концентратора вітрових потоків для вертикально-осьової вітроелектричної установки.

INTRODUCTION

At present, in energy production is used the combustion of coal, crude oil and natural gas refining products. However, gradual depletion of natural resources, their rise in price, along with climate change, which is caused by harmful emissions from traditional energy sources have become major problems for countries around the world. Because of this problem, the main efforts of energy sector are directed at transition to new energy production technologies.

Most countries have committed themselves to reducing harmful emissions into environment under the United Nations Framework Convention on Climate Change and the Kyoto Protocol. Therefore, one of the most important energy problems is the development and implementation of energy efficient and safe technologies for obtaining heat and electricity. These technologies include the development of energy devices that use environmental energy - solar and wind energy, soil energy, and so on. These devices are called alternative or renewable energy sources.

---

[1] *Gorobets V.G., Head of Dep. DSc. Eng.; Trokhaniak V.I., Assoc. Prof. Ph.D. Eng.; Masiuk M.Yu., Ph.D. Student; Spodyniuk N.A., Assoc. Prof. Ph.D. Eng.; Blesnyuk O.V., Assoc. Prof. Ph.D. Eng.; Marchishina Ye.I., Assoc. Prof. Ph.D. Eng.*

One of the directions of progress in renewable sources is the development of devices that use wind energy - wind power plants. Based on design features of the wind turbine, there are installations with a horizontal rotational axis of the rotor and vertical axis wind turbines. The most widespread are wind turbines with a horizontal axis of the flow, which have a large capacity. One of the disadvantages of these plants, unlike vertical axis wind turbines, is the low efficiency at small wind speeds.

In the design of vertical axis wind turbine two types of rotors have been proposed: Savonius and Darya rotors, differing in the shape of the blades used in them. Further, the main efforts of researchers were focused on the rotors development with improved hydrodynamic characteristics. In particular, the authors of *Seki K. (1981)* developed a special profile of the wing of a vertical axis wind turbine, which was used on an operating wind turbine in Japan. A number of researchers have changed the shape of the aerodynamic profile of the blades, which would improve their starting characteristics at low wind speeds (*Zamani M. et al., 2016*). Studies of straight-bladed vertical axis wind turbine were carried out. In addition to changing the profile of the wing, they used, in particular, a wavy leading edge, a wavy trailing edge, and a flexible blade (*Favier J. et al. 2012; Zhenyu W. et al., 2018*). However, given the difficulties of practical manufacture of this type of blades, they need further improvement.

Another way to improve characteristics of a vertical axis wind turbine is to change the traditional design of straight blades in order to improve their performance and reduce aerodynamic resistance at low and high wind speeds. In particular, *Abdalrahman G. et al., (2017),* studied the effect of changing the pitch angle of the blades on the efficiency of wind turbines at different values of wind speeds. An analysis of the forces acting on the blade, which has a different pitch angle at the same speed of the blade (tip) edge during rotation was performed. The law of variation of rotational speed of the blades depending on the blade pitch angle was obtained.

Installation of wind flow concentrators on the rotor has been the most common area of research in recent years, which was mainly to improve the conditions of self-starting of the rotor. *Ji J.F., et al., (2012)*, proposed a variety of vertical axis wind turbine with wind shields, mounted around a vertical axis wind turbine with straight blades. These wind shields direct the incoming wind flow straight to the surface of the blades, which increases the rotational speed of the rotor. The research results have shown that these devices make it possible to improve the starting characteristics and power of wind turbines. Similarly, *Xiaohang W. et al. (2018)* patented a V-shaped orienting screen for power devices, generating electricity with the simultaneous use of solar and wind energy. Experimental studies have shown that self-starting characteristics and rotational speed of the blades of the vertical axis wind power plant when using V-shaped orienting screens were much better compared to a vertical axis wind power plant without an orienting screen.

Wong K.H. et al., (2018) studied the aerodynamic characteristics and the field of wind flow velocities using narrowing screens, which were located in the lower and upper part of the wind turbine. The use of this type of screens increased the wind flow velocity, as well as reduced the initial speed of the turbine.

The paper published by *Li Q. et al., (2021)* investigated the evaluation of the aerodynamic performance and vortex characteristic of a straight-bladed Vertical Axis Wind Turbine (VAWT) in the spanwise direction. To observe the aerodynamic forces characteristics, pressures acting on the blade surface were measured by a multiport pressure measurement device. Pressure measurement was carried out in the spanwise sections of $z/(H/2)$ = 0, 0.4, 0.70, 0.8 and 0.90 with wind tunnel experiments. This study provided a better understanding of the development of aerodynamic forces and vortex characteristic through pressure measurements and panel method calculations.

In this study, a conceptual co-axial contra-rotating vertical axis wind turbine (CR-VAWT) is conceived by splitting the single conventional vertical axis wind turbine blade length into two equal lengths forming two rotors separated by a small distance about the same axis of rotation. The available literature lacks much systematic investigation to find the best possible numerical setting and to extract an in-depth understanding of dominant factors limiting the aerodynamic performance of the CR-VAWT using CFD, which constitutes the primary focus for the present study. The present adopted concept of CR-VAWT is found to have negligible aerodynamic torque and side-side force action at the tower base (*Poguluri S.K. et al., 2021*).

The paper *Orlando A. et al., (2021)* discusses the response and fatigue damage of the supporting tower of a small vertical axis wind turbine subject to stationary and non-stationary excitation due to wind, turbine rotation, emergency stop and start. The emphasis of this paper is put on two main aspects: the use of full scale data and the detection of isolated events of non-stationary vibrations, the effects of which can be disregarded when using stress time-histories of 10 min - 1 h.

The floating vertical axis wind turbine (VAWT) is considered as a competitive device in the utilization of offshore wind energy. However, the platform pitch motion would affect its aerodynamic behavior. In this paper, the aerodynamic performance of a floating φ-type VAWT under pitch motion is investigated by using the Improved Delayed Detached Eddy Simulation SST turbulence model. The results showed that the averaged net power coefficient increment of about 1.5%–15% could be obtained under platform pitch motions, and the fluctuation of aerodynamic loads was found to increase (*Su J. et al., 2021*).

Authors *Hohman T.C. et al., (2020)* present the results of an experimental study of the effects of blade sweep on the wake characteristics of VAWTs performed using high resolution particle image velocimetry. Several sweep configurations were tested while holding the turbine solidity constant. As the sweep angle was increased, dynamic stall was reduced, which could yield a potential reduction in the amplitude of cyclical torque variations. Increased sweep also resulted in a more uniform wake exhibiting a faster wake recovery, and an increase in the planform energy flux in the turbine wake when compared to the straight-bladed turbine. The results support previous suggestions that the power generation of VAWT farms is bounded by the planform energy flux from above.

Authors of *Ipate G. et al., (2020)* worked on the numerical study of the effects of the fluid interaction with the blades of the working bodies of the renewable energy conversion systems. The paper presents the results of numerical research regarding the influence of the blade shape (straight), the number of blades (2, 3, 4) or the wind speed in the area on the output power of the small capacity wind turbines.

MATERIALS AND METHODS

One of the best designs of the wind flow concentrator is the truncated-cone-shaped wind gathering device with orienting channels, which is shown in Fig. 1. The wind flows concentrator consists of confuser-type narrowing channels system. The upper and lower parts of these channels are closed by conical surfaces, which make it possible to concentrate the wind flow in the direction of the rotor. According to the equation of flow continuity in incompressible liquid (gas) (*Li Y. et al., 2018*), the use of confuser-type narrowing channels increases the flow velocity and improves the concentration of wind flow energy in the direction of the rotor. The geometry of channel orienting shoulder blades should be chosen to direct the wind flow at optimal angle of attack on the turbine blade. The proposed design of wind flow concentrator is universal and works regardless of the wind direction, which flows through the orienting channels of confuser-type, where its speed increases due to Venturi effect. As a result of using this type of device it is possible to get more wind flow power per unit area for any wind direction, which increases the wind turbine productivity. Given the fact that electromagnetic moment and power of a wind turbine are proportional to the square and cube of the wind speed, respectively, the use of a wind flow concentrator will improve the aerodynamic characteristics of a vertical axis wind turbine.

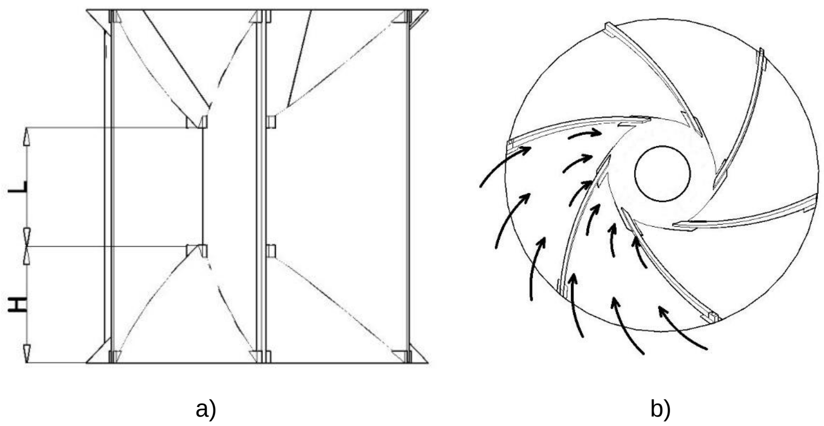

a) b)

Fig. 1 – Appearance of the wind flow concentrator
a) side view, b) sectional view (top)

Further, experimental studies of the wind flow concentrator will be carried out in a wind tunnel, which has the following characteristics - the size of the working area of 0.3×0.3 m, the range of changes in wind speed in the working area from 0 to 18 m/s. Based on these characteristics, a model of the rotor of wind flow concentrator was selected and designed with the following parameters, which are shown in table 1.

Structural parameters of the wind flow concentrator **Table 1**

Value	Dimensionality	Quantity
Cone height *H*	m	0.1
The height of the working area *L*	m	0.1
The thickness of the blade *l*	m	0.002
The size of the working area *L*x*R*	m	0.1x0.1
The area of the inlet of the channel S_1	m^2	0.0471
The area of the outlet of the channel S_2	m^2	0.0052

The general concept of the wind flow concentrator is to increase the energy of wind flow per unit area, increasing torque over the entire area of the blades, reducing the turbulence of the oncoming flow and stabilizing the rotor speed. The characteristics of the wind flow concentrator can be found by modeling the aerodynamic flows using CFD modeling included in the commercial package ANSYS Fluent.

Modeling of hydrodynamic flows is based on the solution of three-dimensional Navier-Stokes equations (*Gorobets V.G. et al., 2018; Khmelnik S.I., 2018;*), in which the laws of conservation of mass and momentum are formulated. A standard k-ε turbulence model was used (ANSYS, 2017; *Gorobets V.G. et al., 2018*). The computational area of the design of the wind flow concentrator is divided into cells. The numerical algorithm for solving the Navier-Stokes equations is based on use of the finite volume method, and the calculation of equations is performed for each cell in the computational domain. ANSYS Meshing software was used to create a three-dimensional grid for the computational model.

The Navier-Stokes equations for the turbulent flow of an incompressible liquid (gas) are as follows:

$$\left.\begin{aligned}
&\rho\left(\frac{\partial u}{\partial t}+u\frac{\partial u}{\partial x}+v\frac{\partial u}{\partial y}+w\frac{\partial u}{\partial z}\right)=-\frac{\partial p}{\partial x}+\mu\left(\frac{\partial^2 u}{\partial x^2}+\frac{\partial^2 u}{\partial y^2}+\frac{\partial^2 w}{\partial z^2}\right),\\
&\rho\left(\frac{\partial v}{\partial t}+u\frac{\partial v}{\partial x}+v\frac{\partial v}{\partial y}+w\frac{\partial v}{\partial z}\right)=-\frac{\partial p}{\partial y}+\mu\left(\frac{\partial^2 v}{\partial x^2}+\frac{\partial^2 v}{\partial y^2}+\frac{\partial^2 w}{\partial z^2}\right),\\
&\rho\left(\frac{\partial w}{\partial t}+u\frac{\partial w}{\partial x}+v\frac{\partial w}{\partial y}+w\frac{\partial w}{\partial z}\right)=-\frac{\partial p}{\partial z}+\mu\left(\frac{\partial^2 w}{\partial x^2}+\frac{\partial^2 w}{\partial y^2}+\frac{\partial^2 w}{\partial z^2}\right)
\end{aligned}\right\}$$

$$\frac{\partial u}{\partial x}+\frac{\partial v}{\partial y}+\frac{\partial w}{\partial z}=0. \tag{1}$$

The following boundary conditions are set on the walls of the channels and at its entrance and exit:

$$\begin{aligned}
&u(t=0)=v(t=0)=w(t=0)=0;\\
&at\quad x=x_{wall},\ y=y_{wall};\ z=z_{wall};\quad u=v=w=0,\ \frac{\partial u_{wall}}{\partial \bar{n}}=\frac{dv_{wall}}{\partial \bar{n}}=\frac{dw_{wall}}{\partial \bar{n}}=0,\\
&at\quad x=x_{ent};\ y=y_{ent};\ z=z_{ent};\quad u_{ent}=v_{ent}=w_{wall}=W_0;\\
&at\quad x=x_{exit};\ y=y_{exit};\ z=z_{exit};\quad \frac{\partial u_{exit}}{\partial x}=\frac{\partial v_{exit}}{\partial y}=\frac{\partial w_{exit}}{\partial z}=0.
\end{aligned} \tag{2}$$

For the given model, the following designations are accepted: *x,y,z* – Cartesian coordinates; *t* – time; *u,v,w* – speed components; *ρ* – air density; $\bar{n}$ –normal vector on the walls of the channels; the indices wall denote the walls of the channels; *ent, exit* – entrance and exit of channels; W_0 – air speed at the entrance to the channels.

Given the three-dimensionality of hydrodynamic air flows, it is necessary to consider a three-dimensional calculation model. The computational area for the wind flow concentrator is shown in Fig.2. The center of the counting system is the center of the rotor, and the direction of wind flow runs along the axis *0x*. The central rotational axis of the wind turbine is the axis *0z*. The length of the computational domain was taken equal to 1500 mm in the flow direction, and the cross-sectional area was taken equal to 290x290 mm, corresponding to the size of the wind flow concentrator, which will be used in the future for experimental studies in the wind tunnel. At the entrance to the computational domain, the wind flow velocity is constant and equal to 1 m/s. At the exit of the domain was set the value of the pressure, which is equal to atmospheric pressure. Standard conditions for flow adhesion are set on the side, upper and lower surfaces of the wind flow concentrator.

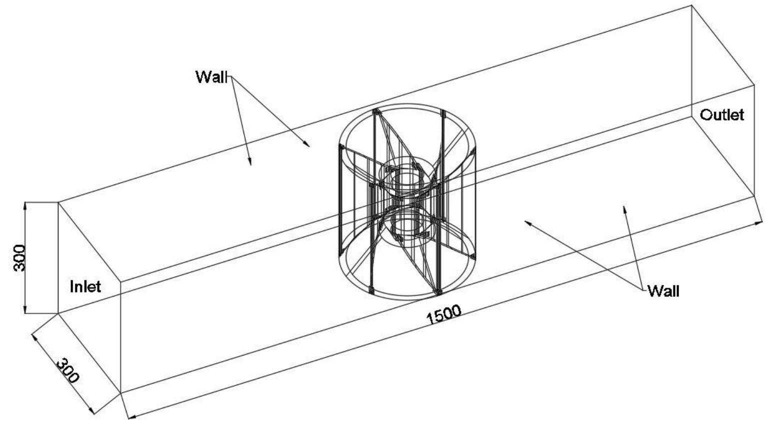

Fig. 2 – Computational domain scheme

In the computational model, a tetragonal unstructured grid was set, which is shown in Fig. 3. This type of grid has the greatest adaptability and high accuracy for modeling a wind turbine.

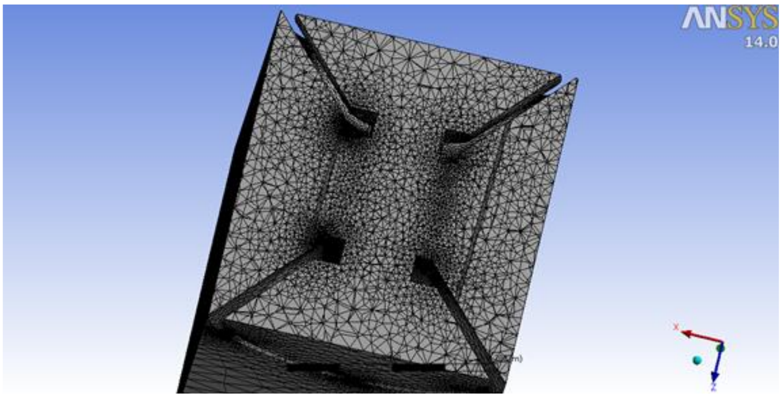

Fig. 3 – Estimated mesh

RESULTS

As a result of the numerical simulation in the wind flow concentrator, the velocity field for the cross section along the axis 0z and the longitudinal section of the axis 0y was obtained (see Fig. 4).

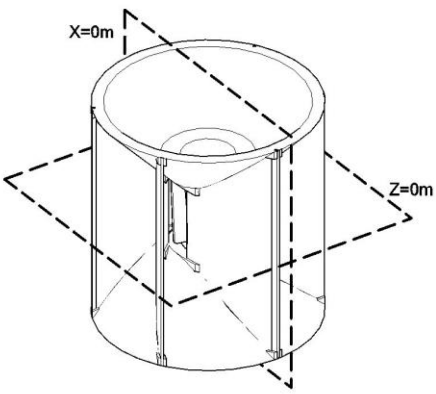

Fig. 4 – The location of the cross section in the numerical calculation model

The results obtained on the basis of numerical modeling of hydrodynamic processes in the inner part of the wind flow concentrator for the velocity field in the cross section of the working area are presented in Fig. 5-6. As can be seen from the figure, a significant increase in air velocity with maximum values at certain points up to 18 m/s is observed in the inner part of the wind flow concentrator. The average air velocity in the inner part of the wind flow concentrator is about 11 m/s. At the exit of the wind flow concentrator, increased turbulence can be observed (Fig. 6).

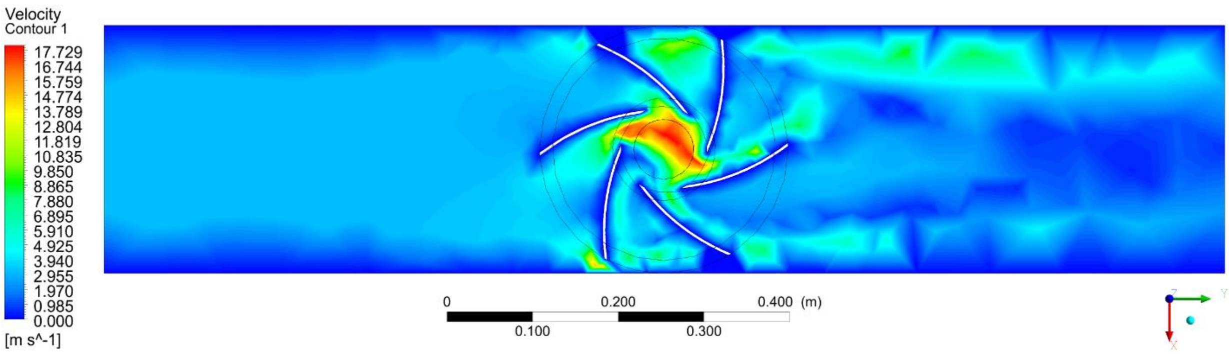

a)

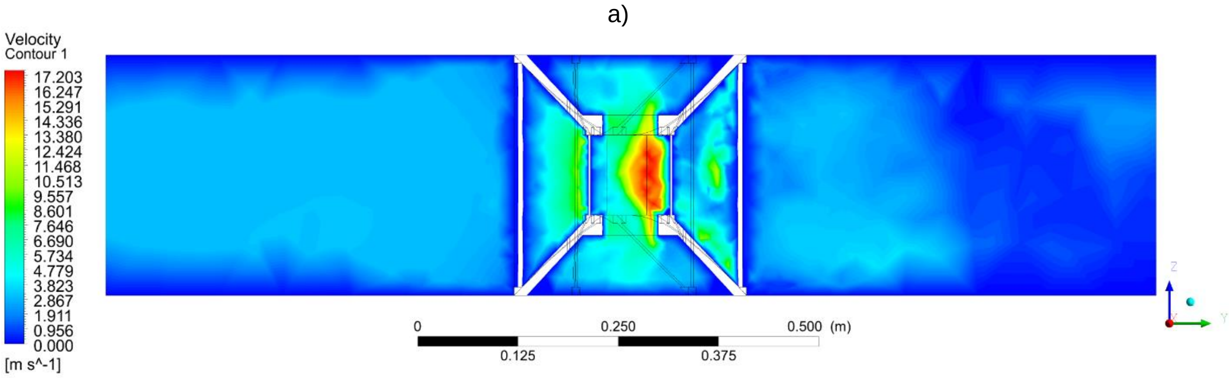

b)

Fig. 5 – The velocity field in the cross section along the axis *0z* (a) and the longitudinal section of the axis *0x* (b) of the wind flow concentrator, m/s

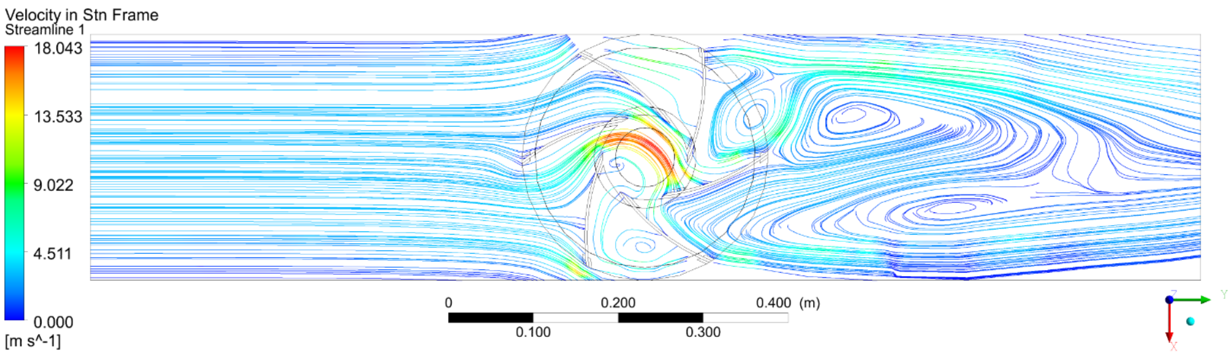

a)

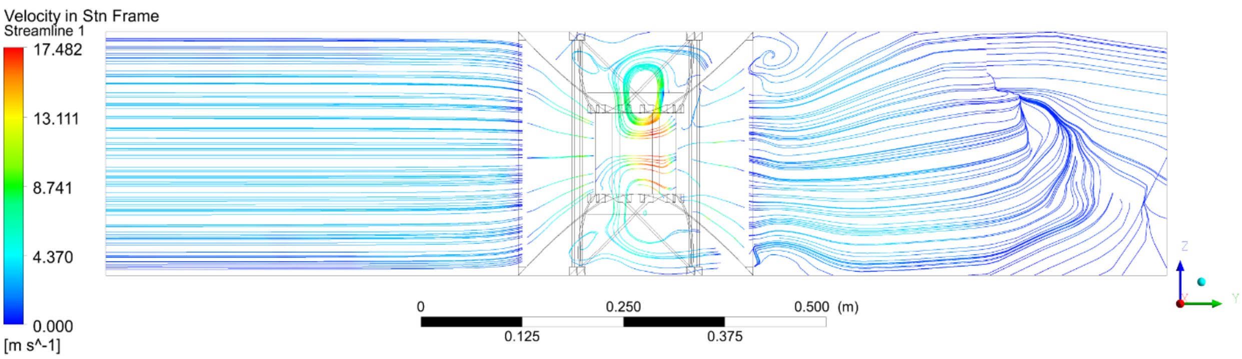

b)

Fig. 6 – Current lines in the cross section along the axis *0z* (a) and the longitudinal section of the axis *0x* (b) of the wind flow concentrator, m/s

The pressure drop is insignificant and reaches 432 Pa (Fig. 7).

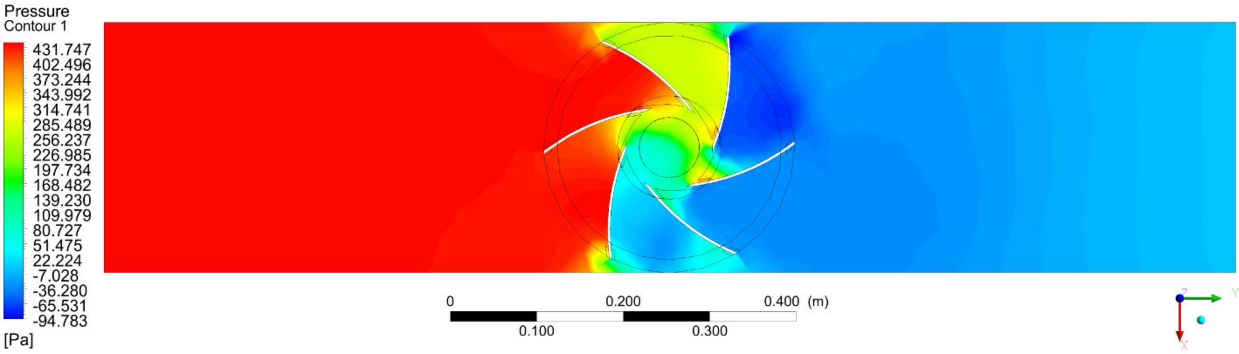

a)

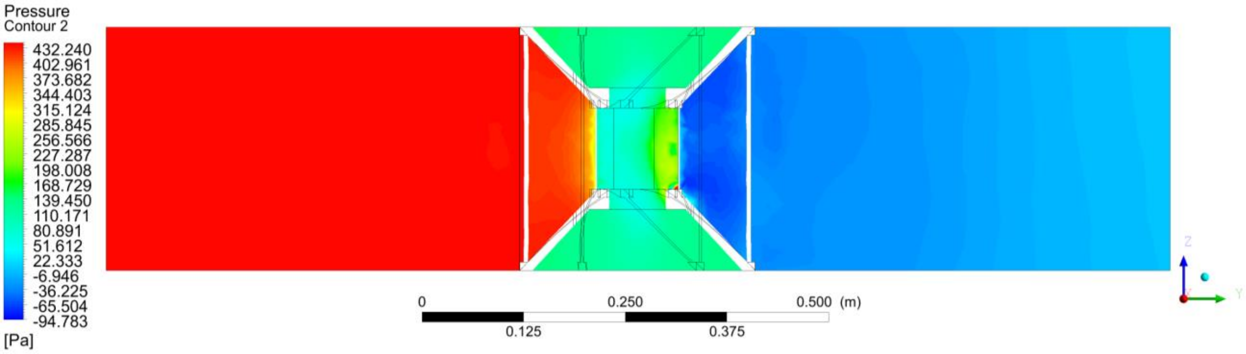

b)

Fig.7 – Pressure loss in the cross section along the axis *0z* (a) and the longitudinal section of the axis *0x* (b) of the wind flow concentrator, Pa

Analysis of the results of numerical modeling of hydrodynamics processes in wind flow concentrator shows that the use of these devices leads to increase the wind flow energy in the cross-section per unit cross-sectional area, as well as to raise the torque, which leads to the increase in rotor speed. Application of proposed design of the wind flow concentrator makes it possible to increase the productivity of vertical axis wind turbines and use them at low wind speeds.

CONCLUSIONS

1. An innovative device is presented - a wind flow concentrator which can be used to increase the productivity of a vertical axis wind turbine. The wind flow concentrator was designed to increase the energy of the oncoming wind flow, to raise the rotor torque and the use of wind flow energy in a wind turbine at low wind speeds. The wind flow concentrator is universal and works regardless of the wind direction, which flows through the orienting channels of confuser-type, where its speed increases due to Venturi effect.

2. CFD modeling of aerodynamic flows using the commercial package ANSYS FLUENT was performed. The velocity fields and pressure changes in the investigated design of the wind flow concentrator are obtained. In the inner part of the wind flow concentrator there is a significant increase in air velocity, which increases the rotational speed of the rotor.

3. The proposed design of the wind flow concentrator can be used in a vertical axis wind turbine in order to increase its productivity. Using a wind flow concentrator with a vertical axis wind turbine, in contrast to a wind turbine with a horizontal rotational axis of the rotor, makes it possible to apply wind turbines in areas with low wind speeds.

REFERENCES

[1] Abdalrahman G., Melek W., Lien F.S., (2017), Pitch Angle Control for Small-Scale Darrieus Vertical Axis Wind Turbine with Straight Blades (H-type VAWT), *Renewable Energy,* vol. 114, pp. 1353-1362, https://doi.org/10.1016/j.renene.2017.07.068, United Kingdom;

[2] ANSYS, (2017), *ANSYS Fluent Theory Guide. Release 18.2*, Published in the USA, 832 p.;

[3] Favier J., Pinelli A., Piomelli U., (2012), Control of the separated flow around an airfoil using a wavy leading edge inspired by humpback whale flippers, *Comptes Rendus Mécanique*, vol. 340, pp. 107-114, https://doi.org/10.1016/j.crme.2011.11.004, Paris/France;

[4] Gorobets V.G., Bohdan Yu.O., Trokhaniak V.I., Antypov I.O., (2018), Experimental studies and numerical modelling of heat and mass transfer process in shell-and-tube heat exchangers with compact arrangements of tube bundles, *MATEC Web of Conferences*, vol. 240, 02006, https://doi.org/10.1051/matecconf/201824002006, Cracow/Poland;

[5] Gorobets V.G., Trokhaniak V.I., Antypov I.O., Bohdan Yu.O., (2018), The numerical simulation of heat and mass transfer processes in tunneling air ventilation system in poultry houses, *INMATEH: Agricultural Engineering*, vol. 55, no. 2, pp. 87-96, Bucharest/Romania;

[6] Hohman T.C., Martinelli L., Smits A.J., (2020), The effect of blade geometry on the structure of vertical axis wind turbine wakes, *Journal of Wind Engineering and Industrial Aerodynamics*, vol. 207, 104328, https://doi.org/10.1016/j.jweia.2020.104328, Netherlands;

[7] Ipate G., Constantin G.A., Biris S.S., Voicu G., Rusanescu C.O., Stefan V., (2020), Numerical 3D analysis of a mini wind turbine with horizontal axis, for implementation in agricultural farms, *INMATEH: Agricultural Engineering*, vol. 63, no. 2, pp. 325-332, https://doi.org/10.35633/inmateh-62-34, Bucharest/Romania;

[8] Ji J.F., Deng Z.Y., Jiang L., (2012), Optimization design of a 5 kW lift type vertical axis wind turbine with wind shield-growth patterns, *Journal Engineering Thermophysics*, vol. 33, no. 7, pp. 560-564, Russian Federation;

[9] Khmelnik S.I., (2018), Navier-Stokes equations. On the existence and the search method for global solutions, *Mathematics in Computers – MiC*, 134 p., Bene-Ayish/Israel;

[10] Li Q., Cai C., Maeda T., Kamada Y., Shimizu K., Dong Y., Zhang F., Xu J., (2021), Visualization of aerodynamic forces and flow field on a straight-bladed vertical axis wind turbine by wind tunnel experiments and panel method, *Energy,* vol. 225, 120274, https://doi.org/10.1016/j.energy.2021.120274, United Kingdom;

[11] Li Y., Zhao S., Tagawa K., Feng F., (2018), Starting performance effect of a truncated cone-shaped wind gathering device on small-scale straight-bladed vertical axis wind turbine, *Energy Conversion and Management*, vol. 167, pp. 70-80, https://doi.org/10.1016/j.enconman.2018.04.062, United Kingdom;

[12] Orlando A., Pagnini L., Repetto M.P., (2021), Structural response and fatigue assessment of a small vertical axis wind turbine under stationary and non-stationary excitation, *Renewable Energy,* vol. 170, pp. 251-266. https://doi.org/10.1016/j.renene.2021.01.123, United Kingdom;

[13] Poguluri S.K., Lee H., Bae Y.H., (2021), An investigation on the aerodynamic performance of a co-axial contra-rotating vertical-axis wind turbine, *Energy*, vol. 219, 119547, https://doi.org/10.1016/j.energy.2020.119547, United Kingdom;

[14] Seki K., (1981), Vertical axis wind turbine designed aerodynamically at Tokai University, *Periodica Polytechnic Mechanical Engineering,* vol. 25, no. 1, pp 47-56, Budapest/Hungary;

[15] Su J., Li Y., Chen Y., Han Z., Zhou D., Zhao Y., Bao Y., (2021), Aerodynamic performance assessment of φ-type vertical axis wind turbine under pitch motion, *Energy*, vol. 225, 120202, https://doi.org/10.1016/j.energy.2021.120202, United Kingdom;

[16] Trokhaniak V., Klendii O., (2018), Numerical simulation of hydrodynamic and heat-mass exchange processes of a microclimate control system in an industrial greenhouse. *Bulletin of the Transilvania University of Brasov, Series II: Forestry, Wood Industry, Agricultural Food Engineering*, vol. 11 (60), no. 2, pp. 171-184, Brasov/Romania;

[17] Wong K.H., Chong W.T., Sukiman N.L. (2018), Experimental and simulation investigation into the effects of a flat plate deflector on vertical axis wind turbine, *Energy Conversion and Management*, vol. 160, pp. 109-125, https://doi.org/10.1016/j.enconman.2018.01.029, United Kingdom;

[18] Xiaohang W., Wentong C., Kokhoe W., Liphuat S., Sinchew P., Saihin L., Chin-Tsan W., (2018), Preliminary Performance Tests and Simulation of a V-Shape Roof Guide Vane Mounted on an Eco-Roof System, *Energies*, vol. 11, no. 10, 2846; https://doi.org/10.3390/en11102846, Basel/Switzerland;

[19] Zamani M., Javad M.M., Rasoul V.S., (2016), Starting torque improvement using J-shaped straight-bladed Darrieus vertical axis wind turbine by means of numerical simulation, *Renewable Energy*, vol. 95, pp. 109–126, https://doi.org/10.1016/j.renene.2016.03.069, United Kingdom;

[20] Zhenyu W., Yuchen W., Mei Z., (2018), Improvement of the aerodynamic per blades using CFD and Taguchi method, *Energy Conversion and Management*, vol. 177, pp. 107-121, http://dx.doi.org/10.1016/j.enconman.2018.09.028, United Kingdom.

RESULTS OF TECHNOLOGYCAL PARAMETERS OPTIMIZATION FOR THE CURD FILTER – PRESSING EQUIPMENT
/
ААРЦ ШАХАХ ТӨХӨӨРӨМЖИЙН ТЕХНОЛОГИЙН ҮЗҮҮЛЭЛТИЙГ ОНОВЧИЛСОН ДҮН

Amgalanzul Jargalsaikhan[1)], Baatarkhuu Dorjsuren[*)] [1]
[1)] School of Engineering and Technology, Mongolian University of Life Sciences, Ulaanbaatar / Mongolia
Tel: 976 – 8800 – 3201; E-mail: elec_eng@muls.edu.mn
DOI: https://doi.org/10.356.33/inmateh-64-16

***Keywords:** moisture, weight, duration, pressure*

ABSTRACT
Mongolia has a large nomadic culture which has existed for thousands of years. Nomadic herders spend much of their time producing milk and dairy products, including Aaruul, or dried yogurt curd, which is a local dairy product unique to Mongolia. There are several steps in the production of Aaruul from raw milk to the final dried curd, including an overnight filtration process. The main objective of this study was to optimize the curd filter pressing process for a newly designed apparatus, to establish the best time, pressure and weight of the curd. The apparatus tested could halve the time of current filtration methods. This study also demonstrated a more precise mathematical model of operating parameters of the pneumatic filter pressing device, measuring curd weight, compression pressure and time.

ХУРААНГУЙ
Монгол улс олон мянган жилийн турш оршин тогтнож ирсэн нүүдэлчдийн томоохон соёлтой. Нүүдэлчин малчид сүү, сүүн бүтээгдэхүүн, түүний дотор ааруул буюу хатаасан тарагны ааруул үйлдвэрлэхэд ихээхэн цаг хугацаа зарцуулдаг бөгөөд ааруул нь Монгол орны өвөрмөц онцлогтой орон нутгийн сүүн бүтээгдэхүүн юм. Түүхий сүүнээс эцсийн бүтээгдэхүүн болох ааруулыг хийхэд хэд хэдэн шат дамжлагатай байдаг. Энэхүү судалгааны ажлын гол зорилго нь шинээр зохион бүтээсэн төхөөрөмжийн аарц шахах процессыг оновчтой болгох, аарц шахах хамгийн тохиромжтой хугацаа, даралт, жинг тогтоох явдал байв. Туршилт хийсэн төхөөрөмж нь аарц шахах уламжлалт аргын хугацааг хоёр дахин багасгах боломжтой. Хийн шахуурга бүхий аарц шахах төхөөрөмжийн ашиглалтын үзүүлэлтүүд болох аарцны жин, шахах даралт, хугацаа зэргээс хамааруулан аарцны чийгийг тодорхойлон, математик загвар гаргаж, оновчтой утгуудыг тогтоолоо.

INTRODUCTION
Traditional Mongolian dairy products are consumed not only as important energy sources, but as traditional medicines *(Takeda et al., 2013; Won-Young Cho et al., 2020).* Dairy products are an important source of everyday nutrition for Mongolians. For generations, herders have been making dairy products from raw milk from their cattle using conventional home methods. Mongolians widely use high-protein dried curds that are well suited to the needs of people living in the arid climates of Central Asia (*Indra, 1983)*. Dried curd (Aaruul) is made of curdled milk that has been air-dried in direct sunlight. It is consumed as a snack, is sometimes flavored with sugar and berries, and has a long shelf-life which is perfectly suited to the nomadic lifestyle (*Daginger, 2015*). The composition of Mongolian cow milk varies depending on geographical location and type of plant species livestock consume (*Narangerel and Narangerel, 2009*).

According to the National Statistics Office the average annual consumption of dairy products per capita, between 2014 and 2017 had reduced from 415.45g per day to 136.5g per day or 67.1% in the capital city and from 667.6g per day to 380.9g per day or 42.9% in the country side *(Indicators for food security statistics, 2014; Indicators for food security statistics, 2017).*

[1] *Amgalanzul Jargalsaikhan, Ph.D. stud.; Baatarkhuu Dorjsuren, ass.prof., Ph.D.*

In 2018, the number of herder households decreased by 37 and the percentage of herders decreased by 4.9% compared to the previous year in Mongolia (*Indicators for food security statistics,* 2018). At the same time, the consumption of dairy products has fallen year by year, and 50% of the total dairy consumption has been supplied by imported products *(Indicators for food security statistics, 2017)*. Cattle farming is hard job due to the fact that it depends on weather and grasslands. So, to bring innovative technologies to increase efficiency of dairy products for cattle farming is essential.

Every herder households are able to supply certain percentage of dairy products by processing their milk and dairy products in summer and fall using modern techniques under traditional technologies. The aaruul (shaped and dried curd) making process, including curd filter pressing and drying, takes 4-5 days since the beginning.

Aaruul is one of the protein dairy products and as a Standard of general technical requirements (MNS 4230:2005), dairy protein contains not less than 14 per cent of the total protein derived from milk casein protein and whey milk produced by conventional and industrial methods. Table 1 describes some physical and chemical properties of curd products. As noted, the technical requirements for curds, which are a type of protein milk, are slightly sour or sweaty, have their own truly unique flavors, white or light yellow color, free from whey milk and even medium density *("Standards of general technical requirements for protein dairy. MNS 4230:2005", 2005).*

Table 1

Physical and chemical properties of curd products

Type of protein products	Parameters				
	Moisture, not less than %	**Protein,** %	**Fat,** %	**Sweetness,** %	**Acidity,** °T
Curd and curd's product	55.0	14.0 – 25.0	0.5 – 18.0	1.5 – 25.0	200 – 270
Aaruul	10.0 – 20.0	30.0 – 40.0	0.5 – 30.0	2.0 – 30.0	180 – 270

Numerous scientific studies have been conducted on the physical and chemical properties of dairy products and their use, composition and structure.

As noted in the scientific basics of Mongolian industrialized technology of dairy products, Damdinsuren et al. pointed out that the technology of curd filtration was suitable at a temperature of 90-95°C *(Damdinsuren, 2002).*

However, no research has been done on techniques and equipment for curd filter pressing, in particular on compression. Simplification of herder milk treatment, especially curd filter - pressing, curd forming and drying, will increase the efficiency of production and consumption of dairy products. Families are able to sell them on the market to expand profits and contribute to the growth of their household businesses. The aim of this study was therefore to design a curd filter - pressing machine for herder households and to determine the optimum values of the main parameters.

MATERIALS AND METHODS

Tsagaa (boiled yogurt) was made from cow milk under domestic conditions and curds were obtained and used for compression experiments *(Indra, 1983).* After the yogurt was boiled and cooled, it was placed in a cloth bag, the whey milk was drained, and it was prepared for the filter pressing test.

In August, measured portions of 400 liters of cow milk from a herder household of Batsumber soum, Tuv aimag were used in the research.

In the case of a herder household, the filtered curd is placed between two plates, pressed with a load of 20 to 30 kg for 12 hours to release the whey. To facilitate this operation, a pneumatic pump experimental machine was developed and a curd pressing test was carried out.

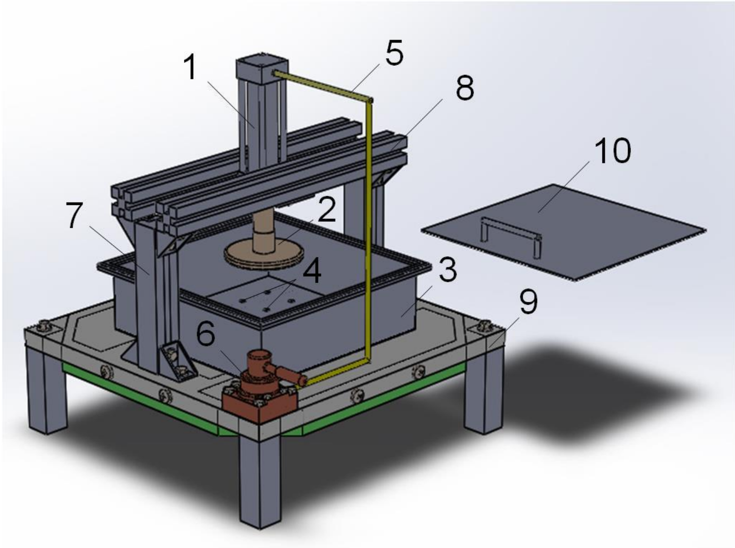

Fig. 1 - Curd pressing device with air pump

1 – pneumatic cylinder, 2 – pressing plate, 3 – drainage vessel, 4 – whey drainage holes, 5 – plastic tube, 6 – hydraulic valve, 7 – vertical pillar, 8 – horizontal pillar, 9 – base platform, 10 - square lid

The curd filter pressing experiment was performed using the method of planning and experiments for multi factor parameters. The mathematic statistic processing had to be done by the results of experiments to create the mathematical model of multivariate regression.

The general model of the second-order regression equation for the three factor experiment can be written as follows for the curd filter pressing:

$$y_i = b_o + b_1x_1 + b_2x_2 + b_3x_3 + b_{12}x_1x_2 + b_{13}x_1x_3 + b_{23}x_2x_3 + b_{11}x_1^2 + b_{22}x_2^2 + b_{33}x_3^2 \quad (1)$$

where: $b_o, b_1, \cdots b_{33}$ – equation coefficients; x_1, x_2, x_3 – factors

The effects of the regression coefficients of the mathematical model can be tested according to the T critical value:

$$t_T = (b_i) = \frac{|b_i|}{\sigma\{b_i\}} < t_x \quad (2)$$

where: t_T – calculated T critical value, t_x – T critical value, b_i – regression coefficient, $\sigma\{b_i\}$ – average squared deviation.

The similarity of the regression model can be tested by F distribution:

$$F_T = \frac{\sigma^2_{sim}\{y\}}{\sigma^2\{y\}} < F_x \quad (3)$$

where: F_T – Calculated F critical value, F_x – critical value of F distribution, $\sigma^2_{sim}\{y\}$ – value of the dispersion of similarity when repeated at the main test point, $\sigma^2\{y\}$ – dispersion of outlet parameter.

The optimal values of the multi-factored model was determined with the minimum values of the input factors as reported by Avdai and Enkhtuya (*Avdai and Enkhtuya, 2017*).

RESULTS & DISCUSSION

In order to select a suitable material for curd compression, the curd was prepared using the traditional method which was applied to three different commonly used bag fabrics of the same size, filtered and pressed at the same time.

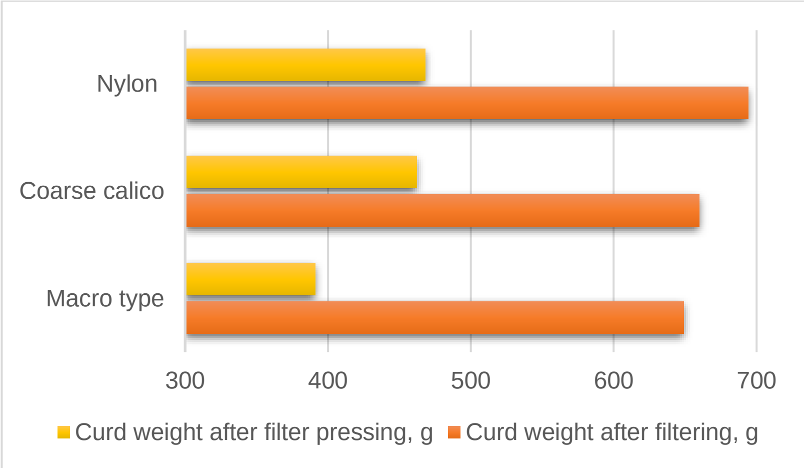

Fig. 2 – Curd weight after filtering and pressing, by three different materials

As seen in Figure 2, after filtration, the curd weight with nylon bag was 6.5% higher than the curd weight with macro type bag and 2.7% higher than that of the curd weight with coarse calico bag. Otherwise, nylon material has pretty poor filtration or less leakage.

After pressing, the weight of the curd with nylon material was 16.4% greater than the curd weight with macro type bag and 2.7% more than the curd weight with coarse calico bag .

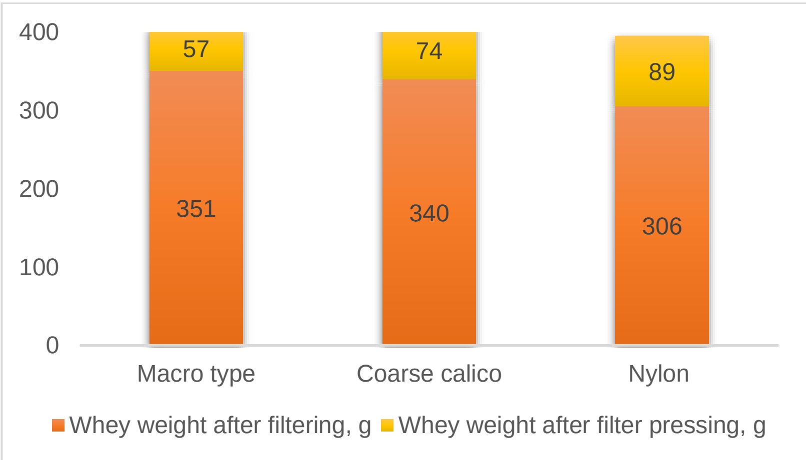

Fig. 3 – Whey weight after filtering and pressing

As shown in Figure 3, during the filtration process, more whey was released from the macro type of texture bag than from other bags, but more of the whey was discharged from the nylon bag than other bags during the pressing process. Even still, the highest release of whey was found when the coarse calico bag was used for both operations with 414 g of 1000 g curd. The coarse calico bag was therefore chosen for further experiments with a filter pressing machine. Honeycomb type cotton is a material used to pack the curd of cheese and it was determined that the porous material with pores of 2.67 mm^2 can be used too *(Oyunjargal, 2010*). The general design of the objectives of the main parameters for the operation of the machine was chosen as follows in Figure 4.

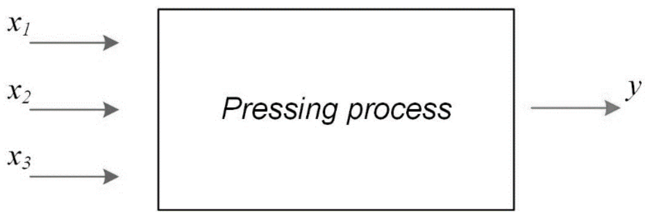

Fig. 4 – General design of objectives

Inlet parameters: x_1 *– curd weight;* x_2 *– pressure;* x_3 *– duration; outlet parameter:* y*– curd moisture, %.*

$$y\text{=f}(x_1, x_2, x_3) \rightarrow 55 - 80\%$$

Parameter levels that represent y-value are determined not only by the values of X_{imax}, X_{imin}, but by box planning or second-order rotatable planning with 3rd and 5th grade changes *(Avdai and Enkhtuya, 2017).* Optimum values of the inlet parameters are defined by the preliminary tests as demonstrated in Table 2.

Table 2

Experimental conditions

Effective parameters	**Changed values of effective parameters**					J_i
	$-x_a$	x_{imin}	x_{i0}	x_{imax}	$+x_a$	
	-1.682	-1	0	+1	+1.682	
Curd weight X_1, kg	0.182	2	2.5	3	4.682	0.5
Filter pressing pressure X_2, kg cm^{-2}	1.318	3	4	5	6.682	1
Duration X_3, min	118	120	150	180	181.682	30

The moisture content of the filter pressed curd must not be less than 55% as shown in Table 1.

The moisture value of the filter pressed curd is determined by the standard 'Method for the determination of moisture and dry matter in milk and milk products' MNS 401: 75 *("Standard of method for determination of moisture and dry matter in dairy products. MNS 0401:1975", 2009)*. The data obtained from the curd pressing experiment in the filter cloth are presented in table 3.

Table 3

Experimental matrix and the results

№	**Standard matrix**			**Experimental matrix**			**Outlet parameters**
	Inlet parameters			Real values of inlet parameters			
	x_1	x_2	x_3	X_1	X_2	X_3	y
1	-	-	-	2	3	120	66.6
2	+	-	-	3	3	120	66.6
3	-	+	-	2	5	120	64.6
4	+	+	-	3	5	120	64.4
5	-	-	+	2	3	180	62
6	+	-	+	3	3	180	65.3
7	-	+	+	2	5	180	59.4
8	+	+	+	3	5	180	62.9
9	-1.682	0	0	0.182	4	150	57.8
10	+1.682	0	0	4.682	4	150	68.3
11	0	-1.682	0	2.5	1.318	150	69.6
12	0	+1.682	0	2.5	6.682	150	64.25
13	0	0	-1.682	2.5	4	118	63.2
14	0	0	+1.682	2.5	4	181.682	59.4
15	0	0	0	2.5	4	150	58.9
16	0	0	0	2.5	4	150	60.2
17	0	0	0	2.5	4	150	64.1
18	0	0	0	2.5	4	150	65.3
19	0	0	0	2.5	4	150	62.5
20	0	0	0	2.5	4	150	64.7

The mathematical processing of the numerical values of the measurements was governed by the law of normal distribution, and the calculated value of the $Shapiro\ and\ Wilka\ W$ criteria was $W_T = 71.23$, which allowed the value in the table to be greater than $W_X = 0.96$. The calculated value of the $Cochrane$ criteria G, $G_T = 0.203$ is less than that of the table, $G_X = 0.2705$, indicating that the dispersion is homogeneous. Regression coefficients for factor dependence has been determined and a multivariate regression model (eq.4) for dependence has also been obtained.

$$y = 62.5494 + 1.9516x_1 - 1.3321x_2 - 1.3902x_3 + 1.5667x_2^2 - 0.4228x_3^2 \quad (4)$$

When the regression model was tested by Fisher's test, the calculated value of the test was $F_T = 0.56$, and $F_T < F_X = 2.71$, so our model proved to be similar.

We put following values to obtained regression model and defined the real model (eq.5):

$$x_1 = \frac{X_1 - 2.5}{0.5};\ x_2 = \frac{X_2 - 4}{1};\ x_3 = \frac{X_3 - 150}{30}$$

$$y = 79.546 + 3.903X_1 - 13.858X_2 + 0.095X_3 + 1.565X_2^2 - 0.00047X_3^2 \quad (5)$$

Figure 5 shows the correlation of the curd moisture (y) from the curd weight (X_1) and the pressure of the pressed curd.

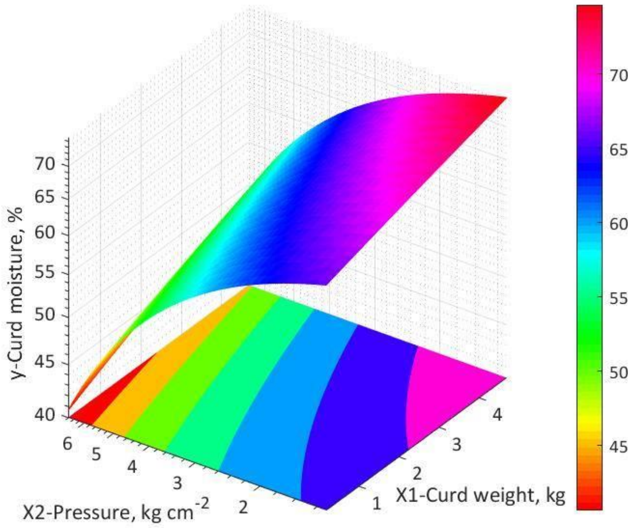

Fig. 5 – The moisture reflecting surface of pressed curd and its correlation graph $y = f(X_1, X_2)$

It shows that when the pressure (X_2) increases, the curd moisture (y) declines, when the curd weight (X_1) rises, the curd moisture (y) increases, respectively. The maximum value of the pressure (X_2) and the minimum value of the curd weight (X_1) can be seen in Figure 5 to hold the curd moisture (y) at between 55 – 60%.

Figure 6 shows how the pressed curd moisture (y) changes by the variation of curd weight (X_1) and pressing time (X_3).

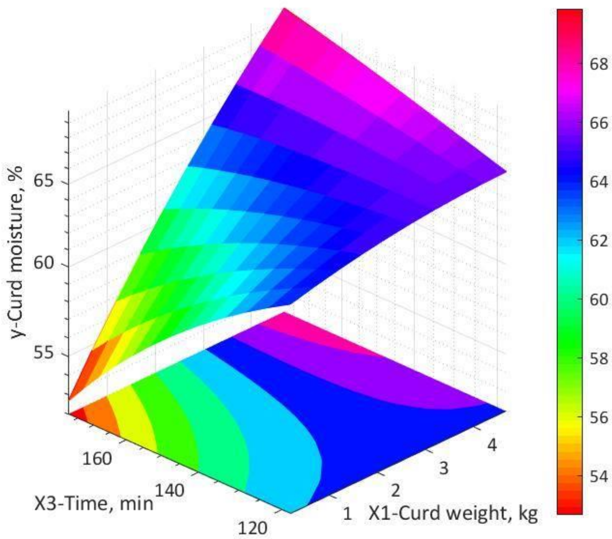

Fig. 6 – The moisture reflecting surface of pressed curd and its correlation graph $y = f(X_1, X_3)$

The Figure 6 describes that when the pressing time (X_3) increases, the curd moisture (y) decreases and when the curd weight (X_1) increases, the curd moisture (y) increases, respectively. To hold the curd moisture (y) in-between 55 – 60% the minimum value of the curd weight (X_1) and the maximum value of the curd pressing time (X_3) can be observed in Figure 6.

As presented in Figure 7, the pressed curd moisture (y) changes due to the variation of the curd pressing pressure (X_2) and the pressing time (X_3).

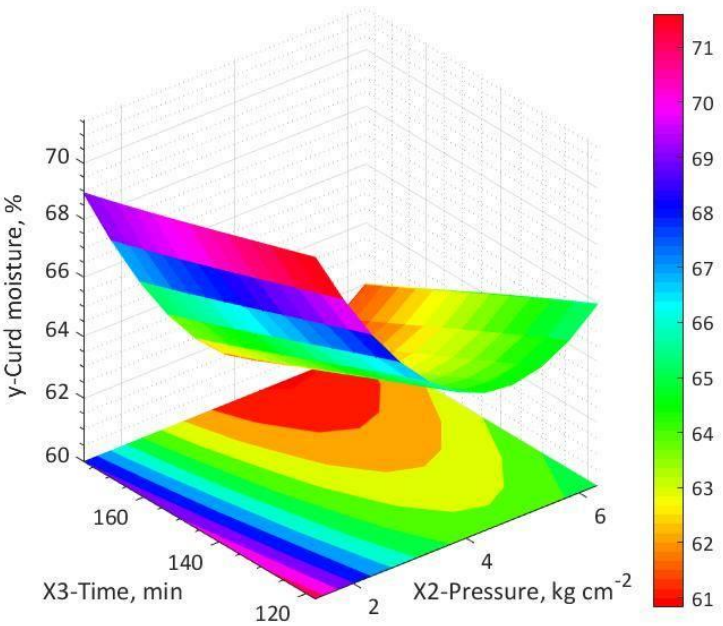

Fig. 7 – The moisture reflecting surface of pressed curd and its correlation graph $y = f(X_2, X_3)$

Figure 7 demonstrates that when the pressing pressure (X_2) and the curd pressing time (X_3) increases, the curd moisture (y) decreases. When the curd moisture content is (y) between 55-60 percent, the maximum value of the curd pressing pressure value (X_2) and the curd pressing time (X_3) could be seen in Figure 7.

By dissociative steps method, the optimum inlet values, when the outlet value is at minimum level, are determined from the real model and the results are shown below $X_1 = 2\,kg$, $X_2 = 5\,kg\,cm^{-2}$, $X_3 = 180\,min$, curd moisture $y = 59\%$. Oyunjargal and her team has developed a model of the cheese pressing process and studied the process of cheese formation rheology and structure. According to the results of this study, the method of liquid pressing used was 8 times shorter in terms of time compared to traditional methods of cheese pressing *(Oyunjargal, 2010)*.

CONCLUSIONS

In the experiment of selecting a convenient material for filtering and filter pressing of curd prepared by conventional method, the highest whey milk releasing material was coarse calico.

Based on the specific moisture content, the values of weight, filter pressure and pressing time using the air pump for curd pressing have been optimized and the mathematical model has been defined. The pressure and weight values were determined as the most effective parameters during the experiments.

The optimal values of the inlet parameters of the curd filter pressing process are calculated as 2 kg of curd weight, 5 kg cm^{-2} (0.49 MPa) of pressing pressure and 3 hours of pressing time to be 59% of the curd moisture content. The moisture content of the curd is 59%, which meets the requirement for moisture content of protein dairy products.

The results show that we are able to reduce the filter pressing time by half compared to the traditional method by using a machine. The machine was invented to save the time and human labor for curd making process. It can be seen that the time required for herder households to filter pressing curd can be halved and the productivity of curd production can be increased.

REFERENCES

[1] Avdai Ch., Enkhtuya D., (2019), *Mathematical methods of experimental planning and its application in research study*, Ulaanbaatar, Mongolia: MUST Printing, ISBN 978-99929-844-1-4, pp. 163-295;

[2] Daginder E., Pickova J., (2015), *AARUUL – A Mongolian Dried Curdled Milk – Evaluation of the consumer acceptance and the health aspect,* MSc Thesis, Swedish University of Agricultural Sciences / Sweden;

[3] Damdinsuren L., (2002), *Scientific bases for elaboration of Mongolian dairy product's industrialzed technology,* ScD dissertation, Mongolian University of Science and Technology / Mongolia;

[4] Indra R., (1983), *Milk and Dairy Products,* Ulaanbaatar, Mongolia: pp. 149-158;

[5] Narangerel Ch., Narangerel M., (2009), *Milk processing handbook*, Ulaanbaatar, Mongolia, pp. 8-11;

[6] Oyunjargal Ch., (2010), *Research on the process of pumping Mongolian cheese and optimization of device parameters, PhD dissertation,* Mongolian University of Science and Technology / Mongolia;

[7] Takeda Sh., Fujimoto R., Takenoyama Sh., Takeshita M., Kikuchi Yu., Tsend-Ayush Ch., Dashnyam B., Muguruma M., Kawahara S., (2013), Application of probiotics from mongolian dairy products to fermented dairy products and its effects on human defecation, *Food Science and Technology Research*, vol.19, no.2, doi: 10.3136/fstr.19.245, ISSN: 13446606, pp. 245–253;

[8] Won-Young Cho, Go-Eun Hong, Ha-Jung Lee, Su-Jung Yeon, Hyun-Dong Paik, Y. Z. H. and C.-H. L., (2020), Effect of Yogurt Fermented by Lactobacillus Fermentum TSI and L. Fermentum S2 Derived from a Mongolian Traditional Dairy Product on Rats with High-Fat-Diet-Induced Obesity, *Foods*, vol.9, no.(5), doi: https://doi.org/10.3390/foods9050594, ISSN 2304-8158, pp. 594.

[9] ****Indicators for food security statistics,* (2014), National statistical office of Mongolia, Mongolia, pp. 33-34;

[10] ****Indicators for food security statistics,* (2017), National statistical office of Mongolia, Mongolia, pp.11.

[11] ****Standard of method for determination of moisture and dry matter in dairy products*, MNS 0401:1975" (2009), Mongolian Agency for Standardization and Metrology, Mongolia, pp. 1-3;

[12] ****Standards of general technical requirements for protein dairy*, MNS 4230:2005" (2005), Mongolian Agency for Standardization and Metrology, Mongolia, pp. 1-3.

CONSTRUCTION OF A DISCRETE ELEMENT MODEL OF BUCKWHEAT SEEDS AND CALIBRATION OF PARAMETERS
/
荞麦籽粒离散元模型构建及参数标定

Bing Xu, Yanqing Zhang, Qingliang Cui*, Shaobo Ye, Fan Zhao
College of Agricultural Engineering, Shanxi Agricultural University, Taigu/China
Tel: +86-0354-6288906; E-mail: glcui@126.com
DOI: https://doi.org/10.356.33/inmateh-64-17

Keywords: *buckwheat seeds, discrete element, repose angle, parameter calibration, optimal design*

ABSTRACT

In view of the lack of seeds contact parameters that can be used as a reference for the design of key mechanical components such as buckwheat planting, harvesting, and processing, this study combines simulation optimization design experiments and physical experiments to calibrate the parameters of simulated discrete element of buckwheat seeds. The non-spherical particle model of buckwheat seeds was established using the automatic filling method, and the simulation accumulating test and physical accumulating test were carried out using the bottomless conical cylinder lifting method; the repose angle of buckwheat seeds was taken as the response value, and the initial parameters were screened for significance based on the Plackett-Burman test; and a second-order regression model of the error value for the repose angle and the significance parameter was established based on the steepest climb test and Box-Behnken test. On this basis, the minimum error value of the repose angle was used as the goal to optimize the significance parameter, the optimal combination of contact parameters was obtained, and parameter validation tests were carried out. The significance screening test showed that the buckwheat-buckwheat static friction coefficient, the buckwheat-stainless steel rolling friction coefficient, and the buckwheat-stainless steel restitution coefficient had significant effects on the repose angle of buckwheat ($P<0.05$). The optimization test showed that the buckwheat-buckwheat static friction coefficient was 0.510, the buckwheat-stainless steel rolling friction coefficient was 0.053, and the buckwheat-stainless steel restitution coefficient was 0.492. The validation test showed that the repose angle of buckwheat seeds under such parameter was 25.39°, and the error with the repose angle of the physical test was 0.55%, which indicated that the optimal parameter combination was reliable. This study could provide a seed model and simulation contact parameters for the research and development of buckwheat sowing, threshing and hulling machinery.

摘要

针对可供荞麦种植、收获、加工等机械关键部件设计参考的籽粒接触参数缺乏的现状，本研究结合仿真优化设计试验与物理试验对荞麦籽粒进行离散元仿真参数标定。采用自动填充法建立了荞麦籽粒非球颗粒模型，并采用无底锥筒提升法进行了仿真堆积试验与物理堆积试验；以荞麦籽粒休止角为响应值，基于 Plackett-Burman 试验对初始参数进行了显著性筛选；基于最陡爬坡试验与 Box-Behnken 试验建立了休止角误差值与显著性参数的二阶回归模型，此基础上以休止角误差值最小为目标，对显著性参数进行寻优，得到了接触参数最优组合，并进行参数验证试验。显著性筛选试验表明：荞麦-荞麦静摩擦因数、荞麦-不锈钢滚动摩擦因数、荞麦-不锈钢恢复系数对荞麦休止角影响显著（$P<0.05$）。优化试验表明：荞麦-荞麦静摩擦因数为 0.510，荞麦-不锈钢滚动摩擦因数为 0.053，荞麦-不锈钢恢复系数为 0.492。验证试验表明：此参数下荞麦籽粒休止角为 25.39°，与物理试验休止角的误差为 0.55%，表明最优参数组合可靠。本研究可为荞麦播种、脱粒、脱壳等机械研发提供籽粒模型及仿真接触参数。

INTRODUCTION

Buckwheat is a crop for both food and medicine, and also an important ration variety for improving dietary structure *(Zhang et al., 2017; Zhang et al., 2020)*. In 2018, the buckwheat production in China accounted for 39.1% of the world's total output, which is an important source of income for farmers in China's alpine and hilly areas. As a coarse cereal, buckwheat currently has few dedicated machinery and equipment

As Lec. Bing Xu, As Lec. Ph.D. Eng. Yanqing Zhang, Prof. Ph.D. Eng. Qingliang Cui

for production and processing *(Sun et al., 2018; Lu et al., 2020)*. The development of machinery and equipment dedicated to sowing, harvesting, and processing of buckwheat is an important way to promote its industrial development. The collection of the mechanical characteristic parameters of buckwheat seeds in an objective and accurate way is the prerequisite for the development of the machinery and equipment.

Discrete element method is a numerical method for calculating the mechanical behaviour of bulk materials. It is originally used to deal with geotechnical engineering problems abroad *(Wang et al., 2010)*. Repose angle is an important index to measure the friction characteristics of bulk materials. It is the natural slope of the pile when the materials are stacked in the horizontal plane. In recent years, many researchers have focused on the physical stacking of different agricultural bulk materials and simulation stacking based on discrete element method to calibrate the materials parameters through response surface optimization experiments with repose angle as the response value. *Gonzlez-Montellano C. et al.* built a discrete element model for corn kernels *(Gonz lez-montellano C. et al., 2012)*. Researchers used EDEM software to establish a discrete element model of potato, corn kernel, wheat flour, quinoa, and coated cotton-seeds, and performed the parameter calibration *(Liu et al., 2018; Wang et al., 2018; Li et al., 2019; Zhang et al., 2019; Liu et al., 2020; Wang et al., 2021)*. *Guo Xiaojun et al.* used EDEM software to simulate the seed metering effect of sunflower seeding unit under different conditions *(Guo et al., 2019)*. *Li Bing et al.* used EDEM software to simulate the screening process of the tea fresh leaf classifiers, and obtained the drum inclination and rotation speed for a good screening effect of the equipment *(Li et al., 2019)*. *Hou Zhanfeng, Dai Nianzu, et al*, used the discrete element method to simulate the seed and powder mixing uniformity of pelleting coating machine under the action of vibration force field, and obtained the optimal working parameters of pelleting coating machine *(Hou et al., 2020; Dai et al., 2021)*. *Jia Shuanglin et al*, used the Watershed algorithm and EDEM (EM solutions EDEM) algorithm to build a maize granule recognition model for large-scale and intelligent seed metering *(Jia et al., 2021)*. The use of discrete element method to simulate the mechanical behaviour of buckwheat seeds in sowing, threshing, and hulling machinery provides a reference for the development and performance prediction of related components.

In view of the lack of seeds contact parameters that can be used as a reference for the design of key mechanical components such as buckwheat planting, harvesting, and processing, this paper proposed a method to approximate the geometric model of buckwheat seeds with two triangular pyramids with different heights with the bottom planes connected. EDEM can be used for the analysis of particles in different shapes. The particle models that come with the EDEM system appear in only the single-ball, double-ball, three-ball, four-ball square and four-ball straight line models. The particle in other shapes requires manual filling. This paper used an automatic filling method to establish a non-spherical particle model of the buckwheat seeds, and adopted such model to conduct a significant screening test with the repose angle as the response value. A steep-climbing test was conducted for the significance factor, so as to determine the optimal value interval of the significance factor. The relative error of the repose angle was taken as the response value to conduct the Box-Behnken test in order to calibrate the contact parameters, and the parameter validation test was performed with the physical test.

MATERIALS AND METHODS

Test equipment and instruments

The rapid moisture analyser GAC2100AGRI (DICKEY-john Corporation, error ±0.2%) was used to measure the moisture content of the seeds. SU5000 scanning electron microscope was used to observe the morphological structure of seed section. The digital display vernier calliper (with the precision of 0.01 mm) was used to measure the seed size. The repose angle measuring device included a conical cylinder (diameter for a small opening: 30mm, and for a big opening: 80mm, the height is 120mm), and a baseplate (300mm×300mm), made of stainless steel. The digital angle ruler (with an accuracy of 0.05°) was used to measure the repose angle of the physical seeds accumulating test.

Test materials and repose angle physical test

This test took buckwheat seeds at harvest as the research subject. The materials for the test were selected from the coarse cereals experimental field of the College of Agricultural Engineering of Shanxi Agricultural University. Before the test, the materials were removed from impurities, shredded seeds and damaged seeds and dried. The moisture content of the seeds was measured to be 12.57%.

The repose angle physical test of buckwheat seeds was carried out in the laboratory using the bottomless conical cylinder lifting method according to the references *(Li et al., 2010)*. During the test, the baseplate was placed on the horizontal test bench, and the conical cylinder was placed on the baseplate with the small opening facing down, and the conical cylinder was filled with buckwheat seeds, as shown in Fig. 1a. The conical cylinder was slowly lifted in the direction perpendicular to the baseplate, and such procedure was repeated for 5 times. After each accumulating test, the digital angle ruler was used to measure the supplementary angle of the two repose angles on the accumulating plane at 180° intervals, as shown in Fig. 1b. The result of each test was the average of two repose angles. The results for the five tests were 25.600°, 25.725°, 24.800°, 24.650° and 25.475°. The final result was the average of the five test results, namely 25.25°, and the standard deviation was 0.49°.

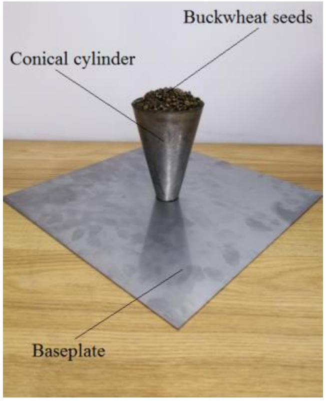

a) Measuring device of repose angle

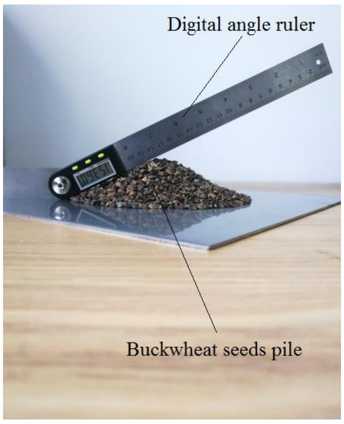

b) Measurement of repose angle

Fig. 1 - Physical accumulating test

Simulation Test

Construction of discrete model of buckwheat seeds

A geometric model of buckwheat seeds should be established ahead of the discrete element model of buckwheat seeds. Observation of the buckwheat seeds found that the bottom of the buckwheat seeds was not a plane in the strict sense, as shown in Fig. 2a. In this paper, the geometric model of buckwheat seeds is approximated by two triangular pyramids with different heights and connected bottom planes. The preliminary research by the research group determined the shape characteristics of buckwheat seeds *(Sun et al., 2018)*. The outline of buckwheat seeds was shown in Fig. 2b, where h_1 is the height of the upper triangular pyramid and h_2 is the height of the lower triangular pyramid.

a) Picture of the buckwheat seeds

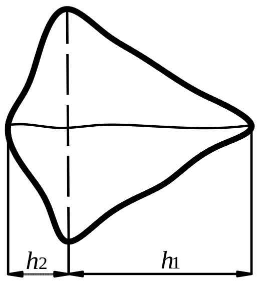

b) Outline of the whole buckwheat seeds

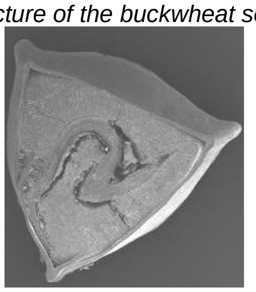

c) Scanning electron microscopy of the buckwheat seeds section

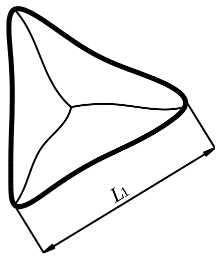

d) Outline of the buckwheat seeds section

Fig. 2 - Shape and section of buckwheat seeds

The cross section of the connected surface of buckwheat seeds observed under the electron microscope was shown in Fig. 2c. It could be seen that the connected surface was approximately an equilateral triangle. The cross-sectional schematic diagram of buckwheat seeds was shown in Fig. 2d, where L_1 is the side length of the connected surface. Based on this approximate method, the characteristic size of buckwheat seeds was measured. The specific measurement method was as follows: 10 firm seeds without visible damages were selected from the harvested seeds as samples. The digital display vernier calliper was used to measure the characteristic size of the samples, and the average value was calculated. The average value of h_1 was 4.22mm and 1.31mm for h_2, and the average value of L_1 was 5.50mm. A three-dimensional model was established in the Inventor according to the characteristic size of buckwheat seeds.

The buckwheat seeds shape is not spherical or ellipsoid like ordinary rice grains. It has sharp edges and corners, which is not easy for manual filling. In this paper, EDEM particle factory was used for automatic filling, and the three-dimensional Inventor model of buckwheat seeds established was converted into STL format and imported into EDEM as the filled model. According to the characteristic size of buckwheat seeds, it was determined that the particle factory would use the single-sphere particles with a radius of 0.3mm. The filling process was shown in Fig. 3a, and the filling result was shown in Fig. 3b. After the dynamic filling in the particle factory was completed, the sphere centre coordinates and radius data of each spherical particle were generated. In order to eliminate the gap between the small balls after filling, the radius of the spherical particle would be doubled when the sphere centre coordinates remained unchanged. The data processed were imported into EDEM to generate a buckwheat seeds bonding model, as shown in Fig. 3c. Such model was saved as a buckwheat seeds template.

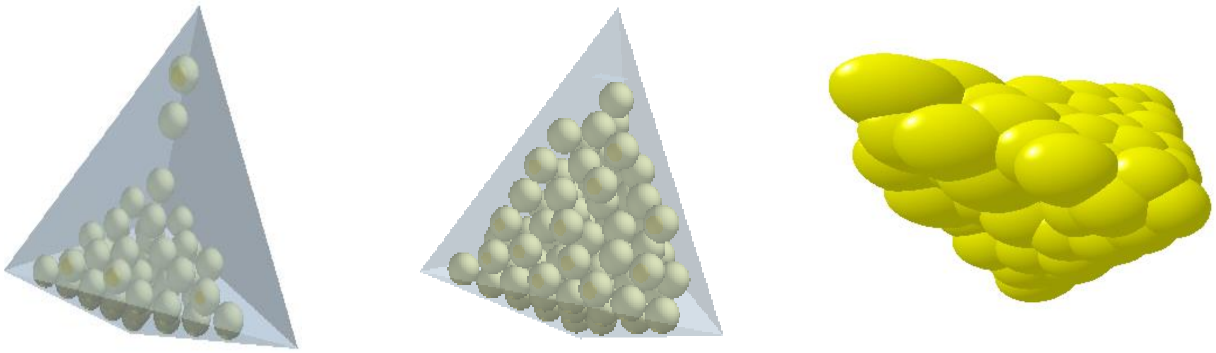

a) Filling process *b) Completion of filling* *c) Bonding model of buckwheat seeds*

Fig. 3 - Construction of discrete element model for buckwheat seeds

Simulation parameters

EDEM 2018 software was used for simulated accumulating. Plackett-Burman test was designed to perform the significance screening of the simulation contact parameters by taking the repose angle of buckwheat seeds on the stainless steel plate as the response value. References to the literature *(Li et al.,2019)* determined that the discrete element simulation parameters of stainless steel were as follows: stainless steel Poisson’s ratio was 0.29, the shear modulus was 70,000 MPa, and the density was 8,000 Kg/m^3.

The main contact parameters of buckwheat seeds and stainless steel were used as the test factors, and three Virtual variables were introduced to estimate the error *(Xu et al., 2010)*. According to relevant research literature on buckwheat, buckwheat seeds, and rice grains at home and abroad *(Li et al., 2019; Zhang et al., 2019)*, the levels of these test factors were determined, as shown in Table 1.

Table 1

The parameters of Plackett Burman test

Parameters	low-level	high-level
Poisson's ratio of buckwheat *A*	0.3	0.45
Shear modulus of buckwheat *B*	300	450
Buckwheat-buckwheat restitution coefficient *C*	0.48	0.72
Buckwheat-buckwheat static friction coefficient *D*	0.24	0.36
Buckwheat-buckwheat rolling friction coefficient *E*	0.008	0.012
Buckwheat-stainless steel restitution coefficient *F*	0.4	0.6
Buckwheat-stainless steel static friction coefficient *G*	0.448	0.672
Buckwheat-stainless steel rolling friction coefficient *H*	0.016	0.024
Virtual variable *J*	-1	1
Virtual variable *K*	-1	1
Virtual variable *L*	-1	1

Simulation model of the repose angle

The particles for the simulated accumulating test were the buckwheat seeds template established above. The conical cylinder and baseplate models of the same material and size as those in the laboratory accumulating process were established in EDEM. The small opening end of the conical cylinder was placed on the baseplate, and the conical cylinder was statically filled with buckwheat seeds, as shown in Fig. 4a. After filling, the conical cylinder was moved upwards perpendicular to the baseplate. The lifting speed of the conical cylinder was 0.02m/s, as shown in Fig. 4b.

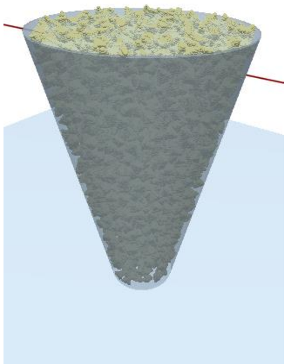

a) Static particles filling

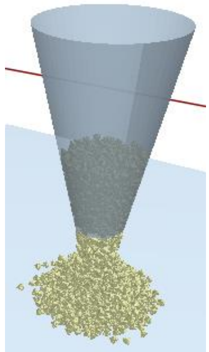

b) The accumulating process of particles

Fig. 4 - Simulation test of accumulating process

Measurement of repose angle of simulation test

After the simulation of the accumulating process, the left half of the seeds pile image in the accumulating test was subjected to processing in order to obtain the repose angle of the accumulating test *(Cai et al., 2019)*, as shown in Fig. 5a. First, Fig. 5a was subjected to gray processing to obtain Fig. 5b, and then the binarization processing of Fig. 5b brought Fig. 5c. Fig. 5d was obtained by edge detection of Fig. 5c. The edge curve was simulated by a straight line, as shown in Fig. 5e. The angle of the fitted straight line was exported. The repose angle on the right half of the seeds pile was obtained with the same method. The repose angle of each simulated accumulating process was the average value of the repose angles on the left and right sides.

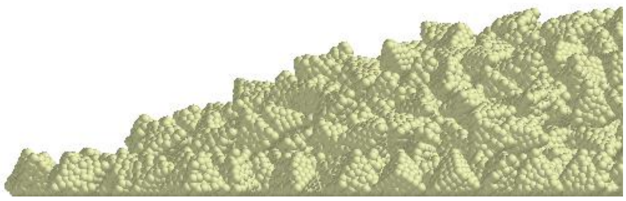

a) The left half image of the seeds pile

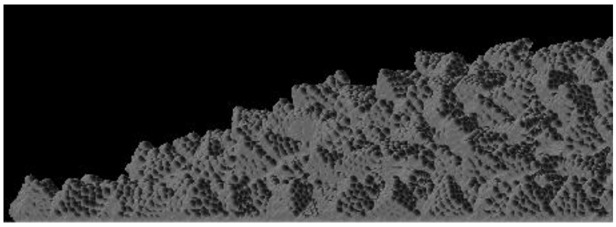

b) Grayscale image

c) Binary image

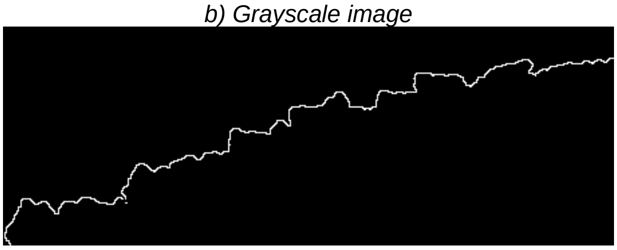

d) Edge detection image

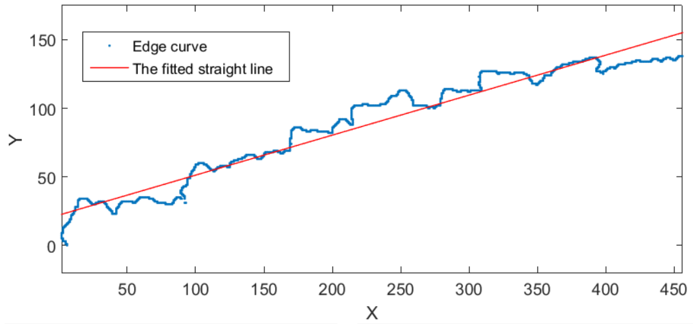

e) Linear fitting

Fig. 5 - Image processing of buckwheat seeds pile

RESULTS

Plackett-Burman test

Plackett-Burman test design was carried out using Design expert 10.0.4 software. The test plan and results were shown in Table 2.

Table 2

The design and results of Plackett Burman test

Number	*A*	*B*	*C*	*D*	*E*	*F*	*G*	*H*	*J*	*K*	*L*	Repose angle / (°)
1	-1	1	1	-1	1	1	1	-1	-1	-1	1	18.49
2	-1	-1	-1	-1	-1	-1	-1	-1	-1	-1	-1	18.87
3	1	1	-1	-1	-1	1	-1	1	1	-1	1	19.27
4	1	1	1	-1	-1	-1	1	-1	1	1	-1	19.32
5	-1	-1	1	-1	1	1	-1	1	1	1	-1	19.53
6	1	-1	-1	-1	1	-1	1	1	-1	1	1	21.33
7	-1	-1	-1	1	-1	1	1	-1	1	1	1	22.24
8	1	1	-1	1	1	1	-1	-1	-1	1	-1	22.38
9	1	-1	1	1	1	-1	-1	-1	1	-1	1	22.82
10	1	-1	1	1	-1	1	1	1	-1	-1	-1	23.50
11	-1	1	1	1	-1	-1	-1	1	-1	1	1	23.81
12	-1	1	-1	1	1	-1	1	1	1	-1	-1	24.31

The Design expert 10.0.4 software was used to analyse the variance of the test data, and the results were shown in Table 3.

Table 3

Analysis of variance

Source	Effect	Sum of squares	Contribution %	*F*	*P*
Model	/	49.31	/	84.79	0.0019
A	0.23	0.16	0.32	2.15	0.2387
B	-0.12	0.042	0.085	0.58	0.5024
C	-0.15	0.072	0.15	0.99	0.3928
D	3.71	41.26	83.29	567.49	0.0002
E	0.31	0.29	0.58	3.92	0.1420
F	-0.84	2.13	4.29	29.23	0.0124
G	0.42	0.53	1.06	7.22	0.0746
H	1.27	4.85	9.79	66.73	0.0038

It could be seen from Table 3 that the model was significant. The buckwheat-buckwheat static friction coefficient *D*, buckwheat-stainless steel rolling friction coefficient *H* and buckwheat-stainless steel restitution coefficient *F* had significant effects on the repose angle ($P<0.05$), while other factors were not significant ($P>0.05$).

Steep climbing test

A steep-climbing test was carried out to determine the best range of buckwheat-buckwheat static friction coefficient *D*, buckwheat-stainless steel rolling friction coefficient *H* and buckwheat-stainless steel restitution coefficient *F*. The level of significant factors in the test fell in the range of the low and high levels given in Table 1. The values were taken according to the arithmetic sequence, and the levels of other insignificant factors were taken as the middle value of the high and low levels in Table 1. The design plan and results of the steep climbing test were shown in Table 4.

Table 4

Experimental parameters and results of steep slope climbing

Number	*D*	*H*	*F*	Repose angle (°)	Relative error *φ* %
1	0.24	0.016	0.40	20.49	18.85
2	0.36	0.032	0.45	22.01	12.83
3	0.48	0.048	0.50	25.40	0.59
4	0.60	0.064	0.55	26.52	5.00

It could be seen from Table 4 that the optimal interval of buckwheat-buckwheat static friction coefficient *D* was 0.36-0.60, 0.032-0.064 for the buckwheat-stainless steel rolling friction coefficient *H* and 0.45-0.55 for the buckwheat-stainless steel recovery coefficient *F*.

Box-Behnken test

Test design and results

In order to obtain the optimal combination of buckwheat-buckwheat static friction coefficient *D*, buckwheat-stainless steel rolling friction coefficient *H* and buckwheat-stainless steel restitution coefficient *F*, the Box-Behnken response surface test was performed with the relative error value of the repose angle as the response value, and the factor levels of the steep-climbing tests 2, 3 and 4 were taken as the low, medium and high levels of the corresponding factors in the Box-Behnken response surface test, respectively. The Box-Behnken test design and results were shown in Table 5.

Table5

The design and results of Box-Behnken test

Number	*D*	*H*	*F*	Repose angle (°)	Relative error φ %
1	0.48	0.032	0.55	24.49	3.01
2	0.6	0.048	0.45	25.11	0.55
3	0.48	0.064	0.45	24.25	3.96
4	0.48	0.048	0.5	24.95	1.19
5	0.36	0.048	0.55	23.28	7.80
6	0.48	0.032	0.45	24.04	4.79
7	0.48	0.048	0.5	25.07	0.71
8	0.36	0.064	0.5	23.65	6.34
9	0.36	0.048	0.45	23.46	7.09
10	0.48	0.048	0.5	25.35	0.40
11	0.6	0.032	0.5	24.67	2.30
12	0.6	0.064	0.5	25.38	0.51
13	0.36	0.032	0.5	23.10	8.51
14	0.6	0.048	0.55	25.19	0.24
15	0.48	0.064	0.55	24.74	2.02

Analysis and optimization of model variance

The Box-Behnken test results were analysed and the second-order regression model of the repose angle error value and the buckwheat-buckwheat static friction coefficient *D*, the buckwheat-stainless steel rolling friction coefficient *H* and the buckwheat-stainless steel restitution coefficient *F* were established.

The regression equation is:

$$\begin{aligned}\varphi &= 302.95 - 218.92D - 902.19H - 886.67F + 62.50DH + \\ &102.50DF + 1162.50HF + 143.17D^2 + 2799.48H^2 + 784.67F^2\end{aligned} \tag{1}$$

The analysis of the model variance was shown in Table 6.

Table 6

Variance analysis of regression equation of Box-Behnken test

Source	Sum of square	Mean square	*F*	*P-value*
Model	120.09	13.34	117.10	< 0.0001
D	85.41	85.41	749.60	< 0.0001
H	1.01	1.01	8.85	0.0310
F	0.18	0.18	1.58	0.2643
DH	0.058	0.058	0.51	0.5089
DF	1.51	1.51	13.28	0.0148
HF	3.46	3.46	30.36	0.0027
D^2	15.69	15.69	137.74	< 0.0001

Table 6
(continuation)

Variance analysis of regression equation of Box-Behnken test

Source	Sum of square	Mean square	*F*	*P-value*
H^2	1.90	1.90	16.64	0.0095
F^2	14.21	14.21	124.70	0.0001
Residual	0.57	0.11	/	/
Lack of Fit	0.25	0.084	0.53	0.7043
Pure Error	0.32	0.16	/	/
Cor Total	120.66	/	/	/
R^2=0.9953, Adj-R^2=0.9868				

It could be seen from Table 6 that the fitting model had P<0.0001, the determination coefficient R^2=0.9953, and the correction determination coefficient Adj-R^2=0.9868, which were all close to 1, indicating that the regression model of the repose angle error value was extremely significant. The coefficients *D*, *HF*, D^2, H^2, and F^2 had extremely significant effects on the repose angle error, and the coefficients *H*, and *DF* had significant effects on the repose angle error, and other coefficients were not significant. Taking the minimum relative error value as the optimal goal, the established regression model was used to get the optimal solution: buckwheat-buckwheat static friction coefficient *D* was 0.510, and buckwheat-stainless steel rolling friction coefficient *H* was 0.053, and buckwheat-stainless steel rolling friction coefficient *F* was 0.492.

Simulated validation

Three simulation accumulating tests were performed with the calibrated parameters, and the repose angle was measured. The results were 24.97°, 25.67°, and 25.53°, respectively, and the average value was 25.39°. The error with the repose angle measured in the physical test was 0.55%. The test comparison map was shown in Fig. 6. The validation results showed that the methods to establish the discrete element and calibrate the parameters of buckwheat seeds were feasible.

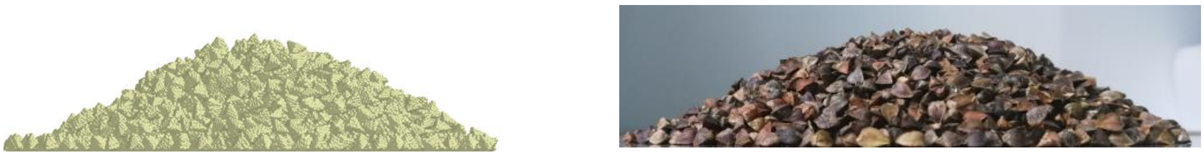

a) Simulation test b) Physical test

Fig. 6 - Comparison of simulation and Physical test

CONCLUSIONS

(1) According to the characteristic size of buckwheat seeds, a three-dimensional Inventor model of the buckwheat seeds is established, and a discrete element model of non-spherical particles of buckwheat seeds is established by the particle filling method in EDEM.

(2) The discrete element model of buckwheat seeds is used for simulated accumulating process. The repose angle is used as the response value for the significant screening test. The results show that the buckwheat-buckwheat static friction coefficient, buckwheat-stainless steel rolling friction coefficient, and buckwheat-stainless steel restitution coefficient have significant effects on the repose angle of buckwheat (P<0.05).

(3) The results of steep climbing test showed that the buckwheat-buckwheat static friction coefficient is 0.36-0.60, the buckwheat-stainless steel rolling friction coefficient is 0.032-0.064, and the buckwheat-stainless steel restitution coefficient is 0.45-0.55.

(4) A second-order regression model of the repose angle error and the significance parameter is established with the Box-Behnken test. The minimum relative error value of the repose angle is taken as the goal, and the significance parameters are optimized, in order to obtain the optimal combination: the buckwheat-buckwheat static friction coefficient is 0.510, the buckwheat-stainless steel rolling friction coefficient is 0.053, and the buckwheat-stainless steel restitution coefficient is 0.492. The calibrated parameters are used in the simulation test, and the average repose angle is 25.39°, with an error of 0.55% compared with the repose angle in the physical test.

(5) This research can provide a seed model and the simulation contact parameters for the research and development of buckwheat sowing, threshing and hulling machinery.

ACKNOWLEDGEMENTS

This research, titled “Construction of a Discrete Element Model of Buckwheat Seeds and Calibration of Parameters”, was funded by the National Key Research and Development Project of China (2016YFD0701801) and Doctoral Research Project of Shanxi Province (SXYBKY2019048) and Science and Technology Innovation Fund of Shanxi Agricultural University (2017015 and 2017018) and Scientific and technological innovation projects of higher disciplines in Shanxi Province (2020L0153).

REFERENCES

[1] Cai L.M., (2019), *Digital image processing Using MATLAB* (数字图像处理——使用 MATLAB 分析与实现), ISBN 9787302515043, Tsinghua University Press, Beijing/P.R.C.

[2] Dai H.Z., (2021), Numerical simulation and experiment of vibration pelletizer based on EDEM (基于 EDEM 振动丸化包衣机的数值模拟与试验). *INMATEH Agricultural Engineering*, Vol.63, Issue 1, pp. 469-478, Bucharest/Romania;

[3] Gonzalez-Montellano C., (2012), Determination of the mechanical properties of maize grains and olives required for use in DEM simulations. *Journal of Food Engineering*, Vol. 111, Issue 4，pp.553-562, Netherlands;

[4] Guo X.J., (2019), Simulation research on spoon-type seed metering device of sun flower seed based on EDEM (基于 EDEM 的勺轮式葵花排种器离散元仿真研究). *Journal of Chinese Agricultural Mechanization*, Vol.40, Issue 2, pp.19-24, Nanjing/P.R.C.;

[5] Hou Z.F., (2020), Numerical simulation and experimental study on pelleting motion law of agropyron seeds under vibration force field(振动力场作用下冰草种子丸化运动规律数值模拟与试验研究). *INMATEH Agricultural Engineering*, Vol.62, Issue 3, pp. 299-308, Bucharest/Romania;

[6] Jia S.L., (2021), Simulation analysis and construction of maize seeder model based on EDEM (em solutions EDEM) (基于 EDEM 的玉米排种器模型构建与仿真分析). *INMATEH - Agricultural Engineering*, Vol.63, Issue 1, pp. 365-374, Bucharest/Romania;

[7] Li Y.X., (2019), Parameter calibration of wheat flour for discrete element method Simulation based on particle scaling (基于颗粒缩放的小麦粉离散元参数标定). *Transactions of the Chinese Society of Agricultural Engineering*, Vol.35, Issue 8, pp.320-327, Beijing/P.R.C.;

[8] Li B., (2019), Research on Screening Rate of Fresh Tea Leaves Classifier Based on EDEM (基于 EDEM 的茶鲜叶分级机的筛分率的研究). *Journal of Tea Science*, Vol.39, Issue 4, pp.484-494, Hangzhou/P.R.C.;

[9] Li M.S., (2019), Design and Test of a Seed Metering Device for Buckwheat Seeder Based on the Discrete Element Method(基于离散单元法的荞麦播种机排种器设计与试验). *Journal of Southwest Agricultural University*, Issue 4, pp.78-85, Chongqing/P.R.C.;

[10] Liu W.Z., (2018), Calibration of Simulation Parameters for Potato Minituber Based on EDEM (基于离散元的微型马铃薯仿真参数标定). *Transactions of The Chinese Society of Agricultural Machinery*, Vol.49, Issue 5, pp. 125- 135+142, Beijing/P.R.C.;

[11] Liu F., (2020), Analysis and calibration of quinoa grain parameters used in a discrete element method based on the repose angle of the particle heap (基于堆积试验的藜麦离散元参数分析及标定). *INMATEH - Agricultural Engineering*, Vol.61, Issue 2, pp.77-86, Bucharest/Romania;

[12] Lu Q., (2020), Problems and Thoughts on Mechanized Harvesting Technology of Buckwheat in China (我国荞麦机械化收获技术问题与思考). *Agricultural engineering*, Vol.10, Issue 01, pp.6-9, Beijing/P.R.C.;

[13] Qinliang Li, (2010), The research of granular piling and bulk material transfer process using DEM Simulation (颗粒堆积性质和散状物料转载过程的 DEM 仿真研究). Northeastern University, Shenyang/P.R.C.;

[14] Sun J.X., (2018), Experimental study on biomechanical properties of buckwheat grain and viscoelastic properties of buckwheat powder (荞麦籽粒生物力学性质及内芯黏弹性试验研究). *Transactions of the Chinese Society of Agricultural Engineering*, Vol.34, Issue 12, pp.287-298, Beijing/P.R.C.;

[15] Wang L., (2021), A general modelling approach for coated cotton-seeds based on the discrete element method (基于多目标优化的包衣棉种离散元接触参数标定). *INMATEH - Agricultural Engineering*, Vol.63, Issue 1, pp. 221-230, Bucharest/Romania;

[16] Xu X.H., (2010), *Experimental design and application of design expert and SPSS* (试验设计与 Design-Expert、SPSS 应用), ISBN 9787030278678, Science Press, Beijing/P.R.C.;

[17] Zhang J., (2020), Establishment of Rapid Detection Model of Buckwheat Nutritional Components Based on Near Infrared Spectroscopy (基于近红外建立荞麦营养成分快速检测模型). *Journal of the Chinese Cereals and Oils Association*, Vol.35, Issue 6, pp.151-158, Beijing/P.R.C.;

[18] Zhang Y.W., (2017), Principal component analysis and comprehensive evaluation of protein and amino acid in different varieties of buckwheat and buckwheat sprout (不同种荞麦发芽前后蛋白质及氨基酸变化主成分分析与综合评价). *Food and Fermentation Industries*, Vol.43, Issue 7, pp.214-221, Beijing/P.R.C.;

[19] Wang G.Q., (2010), *Discrete element method and its application in EDEM* (离散单元法及其在 EDEM 上的实践), ISBN 9787561227978, Northwestern Polytechnic University Press, Xi'an/P.R.C.;

[20] Wang M.M., (2018), Research of discrete element modeling method of maize kernel based on EDEM (基于 EDEM 的玉米子粒建模方法的研究). *Journal of Henan Agricultural University*, Vol.52, Issue 1, pp.80-84+103, Zhengzhou/P.R.C.;

[21] Zhang C., (2019), The Measurement of Contact Parameters of Buckwheat Rice Screening Material and Discrete Element Simulation Calibration (荞麦米筛分物料接触参数测量与离散元仿真标定). *Journal of Agricultural Mechanization Research*, Vol.41, Issue 1, pp.46-51, Haerbin/P.R.C.;

DESIGN AND TEST OF NEGATIVE PRESSURE CHAMBER ROTARY BUCKWHEAT SEED METERING DEVICE

/

气室旋转式荞麦精密排种器的设计与试验

Shaobo Ye, Decong Zheng*), Wei Li, Qi Lu, Yuanqing Yang, Yun Liu, Bing Xu *)
College of Agricultural Engineering, Shanxi Agricultural University, Taigu/China
Tel: +86-0354-6288339; E-mail: zhengdecong@126.com
DOI: https://doi.org/10.356.33/inmateh-64-18

Keywords: *buckwheat, negative pressure, chamber rotary, metering device*

ABSTRACT

A negative pressure chamber rotary precision seed metering device was designed to achieve the buckwheat precision sowing goal, solving the problems of traditional negative pressure chamber poor sealing and air suction seed metering device high power consumption. The planting plate of the device was fixedly connected with the shell of the air chamber forming a negative pressure chamber, which rotates around an axis. A planting plate suitable for buckwheat seed metering was designed. Single factor test and response surface test were carried out on the seed metering device. Results showed that the buckwheat precision seed metering achieved best performance when the negative pressure, suction hole diameter and rotation speed was 2.4 kPa, 2.0 mm and 25 r/min respectively. The qualified index, multiples index and miss-seeding index were respectively 88.32%, 7.35%, and 4.33%, which met the technical requirements of buckwheat precision sowing. The results of the study provided references for the design and application of buckwheat precision seed metering device.

摘 要

为实现荞麦精量化播种，解决传统气吸式排种器负压气室密封差、功耗较高等问题。设计一种气室旋转式精量排种器，该排种器排种盘与气室后壳固定连接形成负压气室，工作时负压气室绕排种轴旋转，具有转动能耗小、气密性好等特点，并设计了适合于荞麦排种的排种盘。利用该排种器进行台架试验，以合格指数、重播指数、漏播指数为评价指标，气室真空度、排种孔孔径、排种盘转速为试验因素进行单因素试验和响应面试验。结果表明，在排种器气室负压值 2.4kPa、排种盘孔径 2.0mm、排种盘转速 25r/min 的组合下，荞麦精量排种效果较好，单粒精密排种合格指数 88.32%，重播指数 7.35%，漏播指数 4.33%，满足荞麦精量化播种技术要求。本研究可以为荞麦精量化排种器的设计和应用提供参考。

INTRODUCTION

Buckwheat belongs to *Polygonaceae* family, with high nutritional value *(Gim é Nez Bastida, 2015)*, which is widely cultivated all over the world *(Zhou M., 2018).* Buckwheat seeds are small in size, irregular in geometry, difficult to sow, and lack suitable sowing equipment, which seriously restricts the development of buckwheat. At present, buckwheat is still sown manually in most areas of China, which is inefficient. In some areas, the existing bulk crop sowing machines are used for sowing buckwheat, most of which are mechanical seed metering devices. There are some shortcomings such as low precision, easy damage, poor stability and unsuitable for high-speed operation *(Bu Y. et al, 2016; Du W.W. et al, 2016)*. Therefore, it is of great significance to develop a precision seed metering device suitable for buckwheat characteristics to improve the development of buckwheat industry.

Air suction seed metering device is a relatively advanced seed metering device due to its loose requirements on seed size, small seed damage, strong adaptability and high sowing speed *(Weirich N. P. H. et al, 2012; Han D. D. et al, 2018)*. *Nal I. et al* described the mechanism of seed adsorption according to the basic principles of hydrodynamics and seed Aerodynamics *(Nal I. et al, 2014)*. *Yazgi A.* and *Degirmencioglu A.* studied the effect of different number of holes on seed spacing uniformity of air suction metering device *(Yazgi A. and Degirmencioglu A., 2014)*. *Zhang Kaixing et al.* designed a double disk air suction seed metering device with variable particle size. Through the rotary combination of the two disks, the metering plates with different apertures were transformed, which improved the versatility of the metering device

*) *Shaobo Ye, As. Lec. M.S. Eng.; Decong Zheng*, Prof. M.S. Eng.; Wei Li, Ph.D. Stud. Eng.; Qi Lu, Lec. M.S. Eng.; Yuanqing Yang, Lec. M.S. Eng.; Yun Liu, Lec. M.S. Eng.; Eng.Bing Xu, Lec. M.S.*

(*Zhang K. X. et al, 2020*). Kverneland Company has developed a kind of air suction seed metering plate, which is connected with the shell of the chamber to form a negative pressure chamber. While working, the negative pressure chamber rotates synchronously with the seed metering shaft, which can effectively solve the problems of sealing gasket prone to be worn out and the high energy consumption of the seeder.

In the study, the design is further improved on the basis of Kverneland's seed metering device. The planting plate and the shell of air chamber are fixed and connected, and the annular sealing gasket is installed between the planting plate and the negative pressure chamber to further improve the gas tightness of the negative pressure chamber; some other structures and working parameters are also optimized. Meanwhile, a planting plate suitable for buckwheat seed is designed. Finally, bench test was made to find the best working parameters of the buckwheat seed metering device. The study may provide theoretical basis for the design and application of buckwheat precision seed metering device.

MATERIALS AND METHODS

Structure and working principle of seed metering device

- **Structure of seed metering device**

The negative pressure chamber rotary buckwheat seed metering device mainly consists of rear shell, shell of air chamber, air chamber gasket, planting plate, seed-stirring plate, front shell and other parts, as shown in Fig.1. There is a hollow shaft on rear shell used as an air inlet, and the bearing is installed on the shaft. The left side of the planting plate is fixedly connected with the outer ring of the air chamber shell to form a negative pressure chamber. The inner ring of the air chamber shell is fixedly connected with the sprocket wheel, the bearing outer ring is installed in the sprocket and the inner ring is installed on the shaft on the rear shell. The negative pressure chamber is in clearance fit with rear shell and front shell, so that the negative pressure chamber can rotate around the shaft on rear shell. The annular sealing gasket is installed between the planting plate and the annular groove on the air chamber shell to enhance the sealing performance of the negative pressure chamber. The right side of the planting plate is installed with a seed-stirring plate. The front shell includes a feed port and a seed metering port. The front shell, the isolation seed board and the planting plate form a seed chamber.

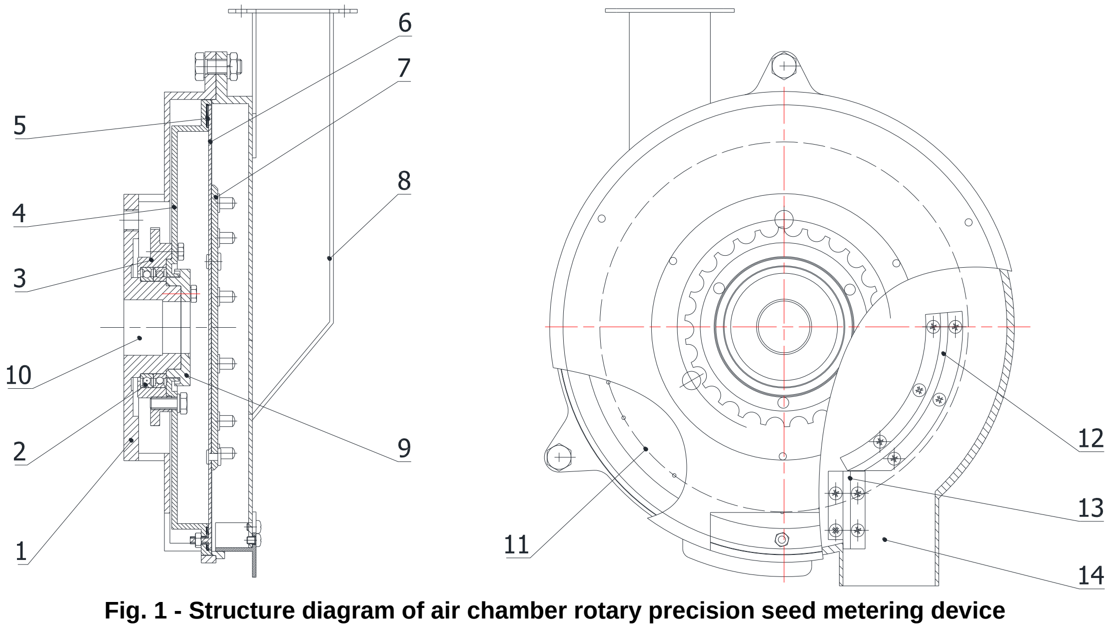

Fig. 1 - Structure diagram of air chamber rotary precision seed metering device

1: Rear shell; 2: Bearing; 3: Sprocket; 4: Air chamber shell; 5: Air chamber gasket; 6: Planting plate; 7: Seed-stirring plate 8: Front shell; 9: End cap; 10: Air inlet; 11: Suction hole; 12 Isolation seed board; 13: Seed unloading board; 14: Seed metering port

- **Working principle of the seed metering device**

When the metering device works, the seeds in the seed box fill the seed chamber through the feeding port. The sprocket drives the negative pressure chamber to rotate and the seeds in the seed chamber are in a discrete state affected by the seed-stirring plate. The negative pressure chamber is connected with the fan through a pipe installed on the air inlet, and a negative pressure is formed in negative pressure chamber under the action of the fan. The seeds are absorbed on the planting plate under the action of negative pressure air flow in the suction hole to complete the seed filling process.

The negative pressure chamber continues to rotate, and the seeds continue to be adsorbed on the planting plate under the action of the negative pressure air flow. When the seed is rotated to the position of seed unloading board, the seed is separated from the planting plate under the action of the seed unloading board, and the seed drops in the seed metering port by its own gravity.

Seed metering device main structure parameters design

- **Design of the buckwheat planting plate**

Planting plate is the core component of seed metering device *(St. Jack D. et al, 2013)*. The parameters of planting pate directly affect the working performance of seed metering device. The main performance parameters include the diameter of planting plate, the number of suction holes, and the diameter of suction holes *(Jia H. L. et al, 2018).*

The larger the diameter of planting plate, more suction holes can be set, which can reduce the linear speed of the planting plate and facilitate the seed adsorption, but the larger the diameter, the larger the overall size and energy consumption of the seed metering device. Considering the working performance and overall size of buckwheat seed metering device, the diameter of planting plate is 200 mm, the thickness is 1.5 mm, and the number of suction holes is 50.

The speed of planting plate directly affects the seeding efficiency and the linear speed of planting plate *(Zeliha Bereket Barut and Aziz Özmerzi, 2004)*. If the rotation speed of the planting plate is too high, the linear speed at the suction hole is large, and it is too short for the suction holes to pass through the seed filling area, or the seeds that have been adsorbed fall due to large collision force, which is easy to cause missing sowing phenomenon. The linear speed of the suction hole on planting plate should not exceed 0.35 m/s.

The rotation speed n_p and the linear speed v_p of planting plate are calculated as follows:

$$n_p = \frac{60 v_m}{SZ} \quad \text{[r/min]} \tag{1}$$

$$v_p = \frac{\pi d_p v_m}{SZ} \quad \text{[m/s]} \tag{2}$$

where: v_m is the operating speed of the seeder (m/s); S is the plant spacing (hole spacing) (m); Z is the number of suction holes on the planting plate; d_p is the diameter of the planting plate (m).

The relevant research shows that, the different planting methods and planting density of buckwheat have no significant difference on the performance value of buckwheat agronomic traits *(Li C.H. et al, 2019)*. At present, there is no specific standard for buckwheat precise planting. According to the planting density of about 700,000 buckwheat plants per hectare, the row spacing is 30 cm and the plant spacing is 4-6 cm. When the forward speed of the seeder is 3.6 km/h, the displacement formula can be used to calculate the row line speed v_p of 0.16 m/s, and the rotation speed of planting plate n_p is 20~30 r/min.

The seed suction hole diameter d is determined by the size of seed.

The empirical formula is as follows:

$$d = (0.64...0.66)b \quad \text{[mm]} \tag{3}$$

where: *b* is the average width of seeds (mm).

Due to the small sphericity of buckwheat seed, the difference of length, width and thickness in triaxial dimension is large. In order to avoid blockage of seed suction hole, the average width is calculated according to the average value of seed thickness. The minimum thickness range of buckwheat seeds of different varieties is about 2.93 ~ 4.32 mm *(Sun J.X. et al, 2018)*.

The diameter of seed suction hole is 1.38 ~ 2.38 mm calculated by the formula (3).

- **Negative pressure chamber design**

The design of negative pressure chamber mainly considers the consistency of vacuum degree and air tightness. The negative pressure chamber is an annular structure, so the negative pressure is uniform and consistent. When the traditional air suction seed metering device works, the air chamber shell is fixed and the planting plate rotates. The continuous friction between the planting plate and the air chamber shell causes high energy consumption and poor working stability. When the designed seed metering device works, the planting plate rotates synchronously with the air chamber shell. The design has the advantages of low energy consumption and low negative pressure requirements.

As shown in Fig.2, the right end face of the air chamber shell is provided with an annular groove, which is used to install the sealing gasket. The planting plate and the air chamber shell are closely matched. A negative pressure chamber with good sealing is formed, which can effectively reduce the Eddy current loss caused by the negative pressure airflow and reduce the negative pressure requirements during the operation of the seed metering device.

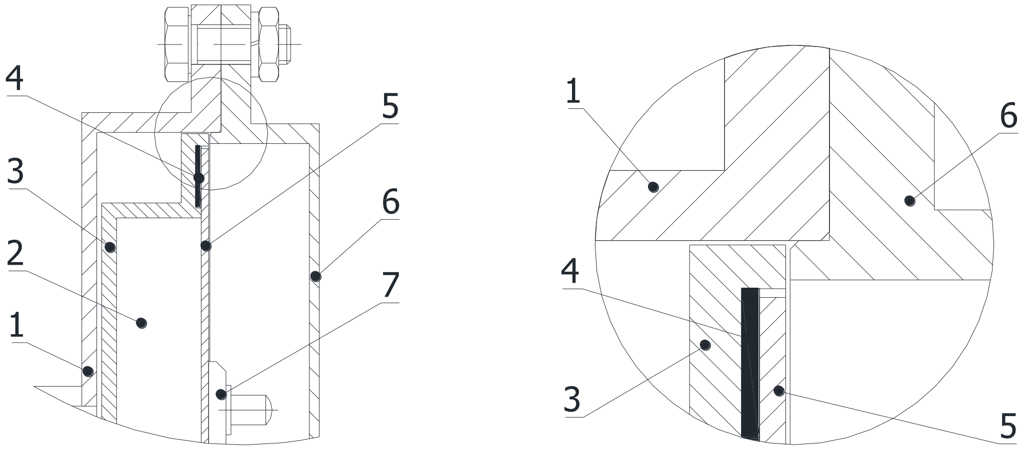

Fig. 2 - Diagram of shell positioning

1-Rear shell; 2- Negative pressure chamber; 3- Air chamber shell; 4- Air chamber gasket; 5- Planting plate; 6- Front shell; 7- Seed-stirring plate

- **Positioning structure design of seed metering device shell**

The position of the seed metering device shell directly affects the stability of the seed metering device. The front shell and the planting plate form the seed chamber through the clearance. Due to the small size of buckwheat seeds, it is particularly important to design the shell positioning reasonably.

As shown in Fig.2, an annular positioning boss is set on the inner wall of the front shell. The front shell positioning boss is closely matched with the right end face and inner surface of the rear shell, so that the positioning of the seed metering device shell is accurate during installation. In addition, there is a 0.5mm gap between the left end face of the front shell boss and the right end face of the air chamber shell, a 0.5mm gap between the inner surface of the rear shell and the outer surface of the air chamber shell, which ensures the chamber shell has no friction with the front and back shells during rotation, and at the same time, the buckwheat seeds cannot be jammed into the gap and damaged.

- **Vacuum degree design of air chamber**

On the air suction seed metering disk rotating in the vertical plane, the stress of the adsorbed seeds is shown in Fig.3. At least the following conditions should be met when a seed is adsorbed by a suction hole:

$$P_0 d / 2 \geq GC \tag{4}$$

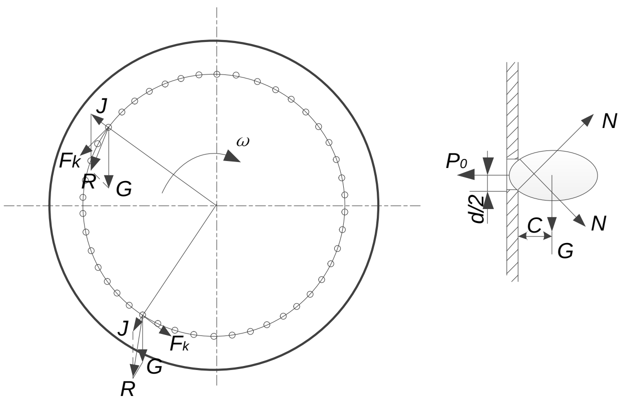

Fig. 3 - Force analysis of seed on suction hole

P_0 – Suction; G - Seed gravity; F_k - Air resistance; J - Centrifugal inertia force; d -Diameter of suction holes; C - The distance between seed barycentre and planting plate

Considering the distribution of seeds in the seed suction area, the collision between seeds, the external environment and the working stability reliability coefficient K_2, the maximum vacuum degree

H_{cmax} required by the negative pressure chamber can be calculated under the maximum limit condition according to the following formula.

$$H_{c\max} = \frac{80K_1K_2mgC}{\pi d^3}\left(1+\frac{v^2}{gr}+\lambda\right) \tag{5}$$

where: m is the mass of a seed (kg); v is the linear velocity at the centre of the suction hole (m/s); r is the rotation radius (m); g is the acceleration of gravity (m/s^2); λ is the comprehensive coefficient of friction resistance of seeds, λ = (6…10) tan θ, θ are the natural repose angle of seeds; K_1 is the reliability coefficient of seed suction, taking 1.8; K_2 is the external condition coefficient, taking 1.8.

Substituting the corresponding data, it can be calculated that the maximum vacuum degree H_{cmax} required by the air suction buckwheat seed metering device is about 3.6 kPa *(Sun J.X. et al, 2018).*

Test and result analysis

- **Test preparation**

Heifeng No.1 Tartary buckwheat seed was selected as the research object. The seed metering device was a designed negative pressure chamber rotary seed metering device. The test equipment was JPS-12 type seed metering device performance test bench developed by Heilongjiang Agricultural Machinery Engineering Research Institute. As shown in Fig.4, during the test, the seed metering device is fixed on the test bench, the sprocket wheel of the seed metering device and the driving shaft of the test bed are driven by chain, and the air inlet is connected with the negative pressure ventilation pipe of the test bench.

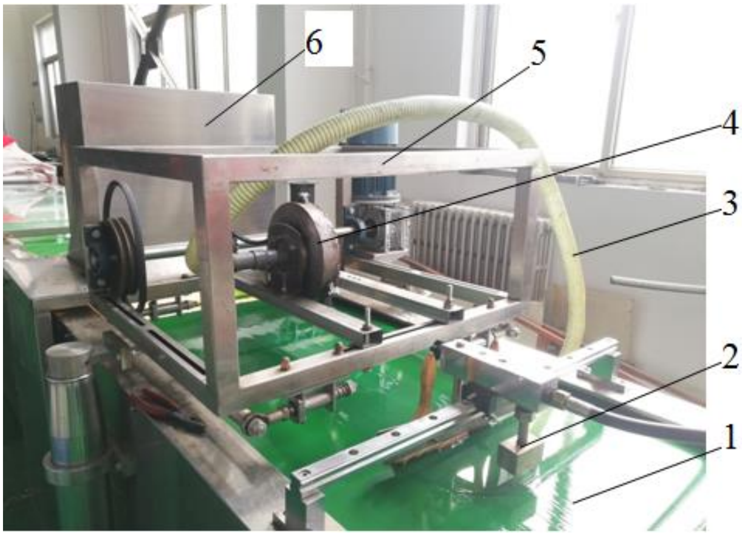

(a) Performance test bench of seed metering device

(b) Seeds distribution on seed bed belt

Fig. 4 - Bench test

1-Seed bed belt; 2-Oil nozzle; 3-Suction pipe; 4-Seed metering device; 5-Bench; 6-Camera box

The seed characteristic parameters of Heifeng No.1 Tartary buckwheat were measured as shown in Table 1.

Table 1

Seed characteristic parameters of Tartary buckwheat Heifeng No.1

Variety	Length / mm	Width / mm	Height / mm	1000-grain weight / g
Heifeng No.1 Tartary buckwheat	4.98	3.27	3.21	21

- **Test method**

In the process of bench test, the seed bed belt moves forward at the speed of 3.6km/h to simulate the field moving of the seeder. At the same time, oil is sprayed on the seed bed belt to avoid the jumping of the falling buckwheat seeds *(Karayel D et al, 2006)*. The seeds are discharged from the seed metering device and fall on the advancing seed bed belt. When passing through the camera box, the seed distribution is recorded, and finally the data is processed on the computer. Each experiment was repeated three times, and the distribution of seeds on 30 m seed bed belt was counted.

The qualified index, multiple index and miss-seeding index were taken as the detection indexes, and the diameter of suction hole, the negative pressure of air chamber and the speed of planting plate were taken as the test factors to carry out the seed metering device performance test. The calculation formula of qualified index, multiples index and miss-seeding index is as follows:

$$\begin{cases} R1 = \dfrac{n_1}{N} \times 100 \\ R2 = \dfrac{n_2}{N} \times 100 \\ R3 = \dfrac{n_0}{N} \times 100 \end{cases} \tag{6}$$

In the formula, $R1$ is the qualified index; n_1 is the number of single seed holes; N is the number of theoretical seed rows; $R2$ is multiples index; n_2 is the number of multiple seed holes; $R3$ is the miss-seeding index; n_0 is the number of zero seed holes.

- **Design of single factor test**

In the single factor test of seed suction hole diameter, the rotation speed of planting plate was set at 20 r/min, the negative pressure of air chamber was 2.4kPa, the diameter of suction hole was 1.5, 2.0 and 2.5mm as the experimental factor level. In the single factor test of the speed of planting plate, the planting plate with 1.5mm diameter of suction hole was selected, the negative pressure value of air chamber was set at 2.4kPa, and the rotating speed levels were 16, 18, 20, 22, 24, 26 and 28 r/min. In the single factor experiment of negative pressure, the diameter of seed suction hole was 2 mm, the rotation speed of planting plate was set at 24 r/min, and the horizontal values of negative pressure factors were 2.0, 2.2, 2.4, 2.6, 2.8 and 3.0 kPa, respectively.

- **Design of response surface test**

In order to further research the influence of various factors and their interaction on the buckwheat seed metering device performance, and determine its reasonable working parameters, the *BBD* (*Box Behnken design*) response surface test was carried out. The *BBD* response surface was carried out with the speed of seed metering plate, the diameter of suction hole and negative pressure as the test factors, and the qualified index, multiples index and miss-seeding index were used as evaluation indexes. According to the theoretical analysis results and the optimal range of single factor test, the coding values of BBD response surface test factors are shown in Table 2.

Table 2

Factor level table of the BBD response surface test

code	**Diameter: A / mm**	**Rotational speed: B / （r·min^{-1}）**	**Negative pressure: C / kPa**
1	1.5	18	2.4
0	2.0	22	2.8
-1	2.5	26	3.2

RESULTS

Results and analysis of the single factor test

The effect of suction holes diameter on the performance of seed metering device is shown in Fig.5 (a). When the diameter of seed suction hole is 2.0 mm, the performance of seed metering device is the best. When the diameter of the suction hole is 1.5mm, the miss-seeding index is higher. Because of the suction hole is small, the negative pressure air flow through the suction hole is insufficient, causing the decrease of seed adsorption. When the diameter of suction hole was 2.5mm, the qualified index was lower, and the replaying index was higher, which indicated that the number of seeds adsorbed by suction hole increased when the diameter was larger.

As shown in Fig.5 (b), with the increase of the speed of the seed metering plate, the qualified index of the metering device first stabilized and then decreased. The multiples index fluctuated up and down within a smaller range, and the miss-seeding index showed a gradual increase trend. When the rotation speed of planting plate is lower than 26 km/h, the performance of seed metering performance is better. The results showed that with the increase of rotating speed, when the linear velocity at the suction hole was too high, the time for the suction hole to pass through the seed filling area was short, and the suction hole was too late to absorb seeds, or the adsorbed seeds were easy to drop after being impacted by other seeds, thus resulting in missed sowing. However, considering the factors such as seeding efficiency and seed spacing, the rotation speed should not be too low.

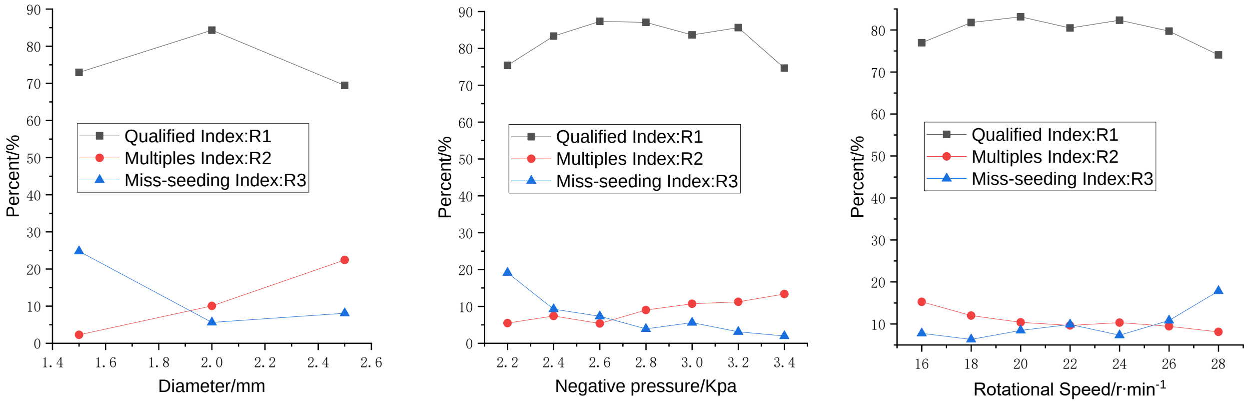

(a) (b) (c)

Fig. 5 - Effect of single factor on seeding performance

Fig.5 (c) showed that with the increase of negative pressure, the qualified index of seeding performance increased at first and then decreased, the multiples index increased continuously, and the miss-seeding index decreased gradually. When the negative pressure was 2.4…3.2 kPa, the adsorption effect of suction hole on buckwheat seed was better. The qualified index reached the maximum when the negative pressure was 2.4 kPa. Considering that the missing sowing index should not be too high, the vacuum degree of air chamber required by seed metering device should be greater than 2.4 kPa, less than the maximum vacuum degree of H_{cmax} of 3.6 kPa.

Results and analysis of response surface test

According to the requirements of *BBD* response surface with three factors and three levels, a total of 17 groups of tests were conducted. The test scheme and statistical results are shown in Table 3.

Table 3

Scheme and results of the test

Group	A	B	C	Qualified Index: R1 / %	Multiples Index: R2/%	Miss-seeding Index: R3 / %
1	1	0	-1	75.63	12.16	11.21
2	-1	1	0	73.80	2.83	23.37
3	0	-1	1	84.75	10.87	4.38
4	1	-1	0	68.31	24.71	6.98
5	0	1	-1	72.91	9.25	17.84
6	0	0	0	85.26	9.41	5.33
7	0	1	1	81.76	9.32	8.92
8	-1	0	1	83.47	4.17	12.36
9	0	0	0	87.48	7.87	4.65
10	1	0	1	64.21	30.18	5.61
11	0	0	0	88.69	6.82	4.49
12	0	0	0	86.32	9.75	3.93

Table 3
(continuation)

Group	A	B	C	Qualified Index: R1 / %	Multiples Index: R2 / %	Miss-seeding Index: R3 / %
13	-1	0	-1	70.93	3.53	25.54
14	1	1	0	70.35	19.57	10.08
15	0	0	0	88.15	4.22	7.63
16	-1	-1	0	79.18	4.10	16.72
17	0	-1	-1	77.93	14.48	7.59

Regression analysis was carried out on the test results. The influence of each factor and its interaction on the qualified index, multiples index and miss-seeding index of the metering device is shown in table 4. The three regression models of qualified index $R1$, multiples index $R2$ and miss-seeding index $R3$ were significant, among which the regression model of miss-seeding index was highly significant (P < 0.0001), and the R-squared values of $R1$, $R2$ and $R3$ were 0.9612, 0.9190 and 0.9757, respectively, indicating that the fitting regression model has high reliability. The lack of fit was not significant (P > 0.05). The response surface equation is obtained as follows:

$$\begin{cases} R1 = 87.18\text{-}3.61A\text{-}1.42B{+}2.1C{+}1.85AB\text{-}5.99AC{+}0.51BC{+}10.02A^2 - 4.25B^2 - 3.60C^2 \\ R2 = 7.61{+}9A\text{-}1.65B{+}1.77C\text{-}0.97AB{+}4.1AC{+}0.92BC{+}3.48A^2 + 1.7B^2 + 1.66C^2 \\ R3 = 5.21\text{-}5.51A{+}3.07B\text{-}3.86C\text{-}0.89AB{+}1.9AC\text{-}1.43BC{+}6.54A^2 + 2.54B^2 + 1.93C^2 \end{cases} \tag{7}$$

Table 4

Significance analysis of different factors on performance indices

source	Qualified Index: *R1*				Multiples Index: *R2*				Miss-seeding Index: *R3*			
	SS	DF	F-Value	P-Value	SS	DF	F-Value	P-Value	SS	DF	F-Value	P-Value
Model	914.78	9	19.26	**0.0004**	869.08	9	8.83	**0.0045**	704.01	9	31.25	**<0.0001**
A	104.26	1	19.76	0.0030	665.94	1	60.88	0.0001	243.21	1	97.18	<0.0001
B	16.10	1	3.05	0.1241	21.75	1	1.99	0.2014	75.28	1	30.08	0.0009
C	35.24	1	6.68	0.0362	24.92	1	2.28	0.1749	119.43	1	47.72	0.0002
AB	13.76	1	2.61	0.1503	3.74	1	0.34	0.5769	3.15	1	1.26	0.2989
AC	143.52	1	27.20	0.0012	67.08	1	6.13	0.0424	14.36	1	8.74	0.0478
BC	1.03	1	0.20	0.6719	3.39	1	0.31	0.5953	8.15	1	3.26	0.1141
A^2	423.06	1	80.18	<0.0001	51.12	1	4.67	0.0674	180.06	1	71.95	<0.0001
B^2	75.92	1	14.39	0.0068	12.23	1	1.12	0.3255	27.21	1	10.87	0.0132
C^2	54.45	1	10.32	0.0148	11.63	1	1.06	0.3368	15.76	1	6.30	0.0404
Lack of fit	29.20	3	5.03	**0.0763**	18.85	3	3.77	**0.1162**	9.18	3	1.47	**0.3500**

According to the factor effect test of each response surface, the significant influence of test factors on qualified index $R1$, multiples index $R2$ and miss-seeding index $R3$ from large to small is seed suction hole diameter *A*, negative pressure *C* and rotation speed of planting plate *B*. The factors *A* and *C* had significant effects on qualified index $R1$, multiples index $R2$ and miss-seeding index $R3$, while factor *B* had no significant effect on pass index $R1$ and multiples index $R2$ (*P < 0.05*), but had significant effect on missed seeding index $R3$.

The *P* values of *AC* in the three regression models were all less than 0.05, indicating that the interaction between the diameter of suction hole *A* and the negative pressure *C* had significant influence on the qualified index $R1$, multiples index $R2$ and miss-seeding index $R3$. As shown in Fig.6, when the rotational speed is 22 r/min, the interaction of factor *A* and factor *C* affects the qualified index $R1$, multiples index $R2$ and miss-seeding index $R3$, respectively. It can be seen from the figure that with the increase of suction hole diameter a and negative pressure *B* of air chamber, the qualified index $R1$ increases at first and then decreases, and the repeat index $R2$ and miss seeding index $R3$ show a trend of small first and then increase. The main reason is that the diameter of seed suction hole a and negative pressure *B* of air chamber directly affect the strength of negative pressure air flow through the suction hole, thus affecting the seed adsorption capacity of the suction hole. When the diameter of seed suction hole is selected properly and the negative pressure value of air chamber is moderate, the seed adsorption performance is the best and the working performance of seed metering device is good.

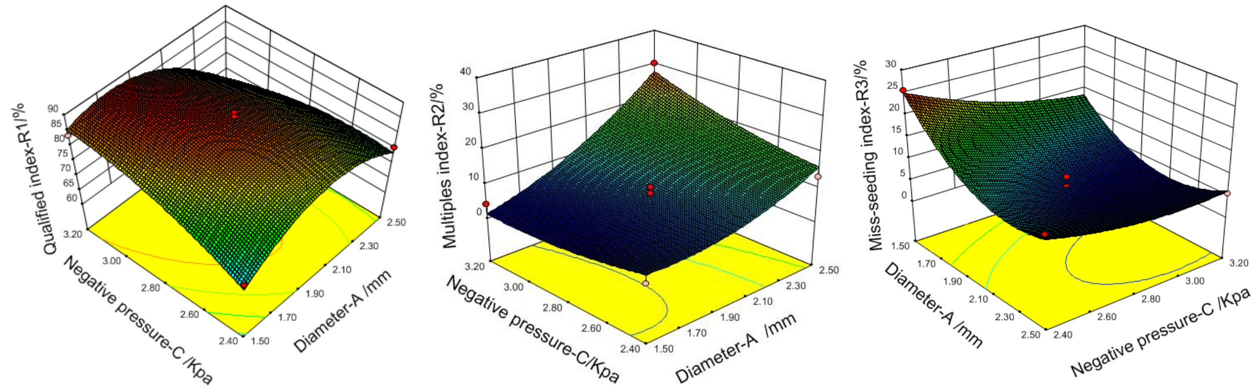

Fig. 6 -The influence of experimental factors on performance of seed metering device

Optimization of working parameters

When the seed metering device works, it is necessary to meet the requirements of high qualified index, low multiples index and low miss-seeding index. In addition, the appropriate multiples index can ensure the survival rate of buckwheat seedlings. The comprehensive indexes of qualified index $R1$, multiples index $R2$ and miss-seeding index $R3$ are used to establish the optimization function. The qualified index $R1$ should be greater than 80%, the multiples index should be less than 15%, the miss-seeding index should be less than 8%, and the diameter of suction hole was set to 2.0 mm. Using the numerical optimization module of Design Expert, the optimal solution is as follows: the diameter of suction hole is 2.0mm, the rotation speed of planting plate is 21.40 r/min, and the negative pressure is 2.91 kPa, the qualified index $R1$ is 87.58%, the multiples index $R2$ is 8.49%, and the miss-seeding index R3 is 3.93%. Based on the optimal combination of working parameters, the verification test was repeated for 5 times, and the approximate test results were obtained. The qualified index was 88.32%, the multiples index was 7.35%, and the miss-seeding index was 4.33%, which met the technical requirements of precision sowing.

CONCLUSIONS

(1) The structure of Kverneland air suction seed metering device was improved. A kind of negative pressure chamber rotary precision seed metering device was designed. The planting plate rotated synchronously with the air chamber shell forming a negative pressure chamber. An annular sealing gasket was installed between the air chamber shell and the planting plate to further improve the air tightness of the negative pressure chamber. Buckwheat planting plate was designed according to buckwheat seeds physical and mechanical characteristics. The main parameters of the metering device were analysed.

(2) The results of single factor test showed that the seed metering performance was better when the diameter of suction hole was 2 mm, the miss-seeding index increased obviously when the rotation speed of planting plate was higher than 26 r/min, and the suction hole had better seed adsorption effect when the negative pressure was greater than 2.4 kPa. The results of response surface test showed that

the order of significant influence of each factor on qualified index, multiples index and miss-seeding index was the diameter of suction hole, negative pressure and rotation speed of planting plate. The interaction between diameter of suction hole and negative pressure had significant influence on the performance of seed metering device. The results showed that the optimal combination of the factors was: the diameter of suction hole was 2 mm, the negative pressure was 2.91kPa, and the rotation speed was 21.4 r/min. Under the combination, the qualified index was 88.32%, the multiples index was 7.35%, and the miss-seeding index was 4.33%, which met the technical requirements of buckwheat precision sowing.

ACKNOWLEDGEMENT

This work was supported by the Major Special Projects for the Construction of China Modern Agricultural Industrial Technology System (No. CARS-07-D-2). Youth Science and Technology Innovation Project of Shanxi Agricultural University (No. 2017021). Science and Technology Innovation Project of Shanxi Colleges and Universities (No. 2020L0153).

REFERENCES

[1] Bu Y., (2016). Development of big ridge double row buckwheat seeder (大垄双行荞麦播种机的研制). *Agricultural research in arid areas*, Vol.34, Issue3, pp. 281-290, Xi'an / P.R.C.;

[2] Du W. W., (2017), Research status and development trend of small seed precision seeder (小粒种子精量播种机研究现状及发展趋势). *Agricultural Engineering*, Vol.7, Issue6, pp. 9-13, Beijing / P.R.C.;

[3] Giménez-Bastida J.A. et al. (2015), Buckwheat as a Functional Food and Its Effects on Health. *J Agric Food Chem*, Vol. 63, Issue 36, pp. 896-913, Washington DC /USA;

[4] Han D. D., (2018). DEM-CFD coupling simulation and optimization of an inside-filling air-blowing maize precision seed-metering device. *Computers and Electronics in Agriculture*, Ed. Elsevier BV, vol.150, pp.426-438, Oxford / U.K.;

[5] Jia H.L., (2018). Design and key parameter optimization of an agitated soybean seed metering device with horizontal seed filling. *International Journal of Agricultural and Biological Engineering*, Vol.11, Issue 2, pp.76-87, Beijing/P.R.C.;

[6] Karayel D. (2006), Laboratory measurement of seed drill seed spacing and velocity of fall of seeds using high-speed camera system [J]. *Computers & Electronics in Agriculture*, Vol.50, Issue 2, pp.89-96, Oxford / U.K.;

[7] Li C.H., (2019), Effects of different sowing methods and planting densities of buckwheat on weeds and buckwheat yield (荞麦不同播种方式和种植密度对田间杂草及荞麦产量的影响), *Journal of Weeds*, Vol.37, Issue 3, pp.36-41, Nanjing/P.R.C.;

[8] Nal I, (2014). An evaluation of seed spacing accuracy of a vacuum type precision metering unit based on theoretical considerations and experiments [J]. *Turkish Journal of Agriculture & Forestry*, Vol.36, pp.133-134, Ankara/Turkey;

[9] St. Jack D., (2013). Precision metering of Santalum spicatum (Australian Sandalwood) seeds [J]. *Biosystems Engineering*, vol. 115, issue 2, pp. 171-183; San Diego/USA

[10] Sun J.X, (2018), Experimental study on biomechanical properties and viscoelasticity of buckwheat kernel [J], *Journal of Agricultural Engineering*, 34(23):287-298. Vol.34, Issue 23, pp.287-298, Beijing/P.R.C.;

[11] Weirich N.P.H., (2012). Comparison of metering mechanisms of corn seed. *Engenharia Agrícola*, 32(5): 981-988. Jaboticaba/Spain;

[12] Yazgi A., Degirmencioglu A., (2014). Measurement of seed spacing uniformity performance of a precision metering unit as function of the number of holes on vacuum plate. *Measurement*, Vol.56, pp. 128-135, Ed. Elsevier, Oxford /U.K.;

[13] Zeliha Bereket Barut, Aziz Özmerzi, (2004), Effect of different operating parameters on seed holding in the single seed metering unit of a pneumatic planter. *Turkish Journal of Agriculture & Forestry*, Vol.28, Issue 6, pp.435-441, Ankara/Turkey;

[14] Zhang K.X, (2020), Design and test of variable diameter pneumatic drum type bean seed metering device, *INMATEH-Agricultural Engineering*, Vol.60, Issue 1, pp.9-18, Bucharest/Romania;

Zhou M. (2018). Buckwheat germplasm in the world. *Overview of Buckwheat Resources in the World*. Ed. Elsevier, Beijing/P.R.C.

DESIGN AND PARAMETER OPTIMIZATION OF WATER-RETAINING MOULDING DEVICE FOR STRAW AND COW DUNG MIXED MATERIALS
/
秸秆-牛粪混合物料保水成型装置设计与参数优化

Wang Tiejun [1,2], Wang Ruili [1)] , Yu Jin [1)], Gong Yuanjuan [1)], Wang Tieliang *[2)] [1]
[1)] Shenyang Agricultural University, College of Engineering, Shenyang / China;
[2)] Shenyang Agricultural University, College of Water Conservancy, Shenyang / China
Tel: +8613840004545; E-mail: tieliangwang@syau.edu.cn
DOI: *https://doi.org/10.356.33/inmateh-64-19*

Keywords: *agricultural waste; water-retaining moulding; device design; parameter optimization; response surface*

ABSTRACT
A hydraulic horizontal water-retaining moulding device for mixed materials was designed and optimized. The effect of compression process parameters of the mixture of straw and cow dung on the effect of water retention moulding was analysed through experiment. The suitable value range and critical value of process parameters were obtained. The main power and structural parameters of the hydraulic system in the mixture compression unit were designed and calculated. Appropriate hydraulic and control components were selected. A test prototype of the hydraulic horizontal mixed material compressor machine was manufactured. Through the method of combination experiment and response surface optimization, the optimal combination of working parameters of the hydraulic horizontal water-retaining moulding device was obtained and verified. The dimensional stability of small-scale compost blocks made by the compressor could reach 84.71% under the condition of 250 mm/min for the compression speed, 55 kg for the feed amount and 200 s for the holding time.

摘要
设计并优化了一种液动卧式混合物料保水成型装置。试验分析秸秆与牛粪混合物料的压缩过程参数对保水成型效果的影响规律，得出过程参数适宜取值范围与临界值，并设计了装置液压系统主要动力与结构参数，选配适宜的液压与控制元件，制造液动卧式混合物料压缩试验样机；通过组合试验与响应面优化结合的方法，得出并验证液动卧式保水成型装置较优的工作参数组合：压缩速度250 mm/min、喂入量55 kg、保压时间200 s，此条件下所制得微贮块的尺寸稳定性可达到84.71%。

INTRODUCTION
The mixed straw and cow dung is a kind of dispersed and viscoelastic material that can rebound after compression. It is necessary to overcome the viscoelastic properties of the material and maintain proper moisture, during the compression process (*Wang et al., 2021a*). The existing compression moulding equipment is not completely suitable for the water-retaining moulding of the mixture material in the small-scale compost production with localized straw and cow dung (*Wang et al., 2021b*). The stress relaxation change and suitable pressure range of the moulding process of the mixed materials of straw and cow dung under suitable moisture conditions are different from the single material of straw or cow dung, which has an important impact on the quality of small-scale compost production and the productivity of compression moulding device (*Robert et al., 2012*). Researchers discussed the raw materials and technology of biomass small-scale blocks (*Moiceanu et al., 2015; Zhang et al., 2017; Voicu et al., 2019*). In particular, many studies have been carried out on the moulding mechanism and compression characteristics of the single straw material (*Nehru et al., 2010; Carone et al., 2011; Niccolò et al., 2019; Liang et al., 2020*). Pressure keeping and strain keeping are two key processes to enhance the dimensional stability of compressed straw (*Jia et al., 2020*). *Mirko et al*. (*2017*) compression tests were performed and they found traditional baling systems were not adequate to guarantee a good control on the linear dimensions and on the density of the bales since bale length had a great variability. *K. Theerarattananoon et al.* (*2011*) and *Kazuei et al.* (*2014*) have shown that the initial water content was an important factor affecting the productivity of straw briquettes, as the water content of the briquettes increases, their bulk density and true density decrease.

---

[1] *Tiejun Wang, Ph.D.; Ruili Wang, Assoc. Prof. Ph.D.; Jin Yu, Postgraduate Stud.; Yuanjuan Gong, Prof. Ph.D.; Tieliang Wang, Prof. Ph.D.*

In order to explore the influence of compression parameters in the water-retaining moulding process of the straw and cow dung mixed material, the appropriate value range and critical value of the key process parameters through the single factor experiment of the experiment bench and data acquisition system were determined. The hydraulic power system of the water-retaining moulding device was designed biased on the single factor experiment results. Moreover, through the three-dimensional quadratic regression orthogonal rotation combined experiment and field verification test, the working parameters of the prototype were optimized, and the working performance was verified.

MATERIALS AND METHODS

Examination conditions and methods

The experiment was conducted at the Key Laboratory of Agricultural Mechanization Engineering of Liaoning Province in Shenyang Agricultural University. The experiment maize straw was harvested in 2018 at North Mountain Scientific Research Base of Shenyang Agricultural University, and the experiment cow dung was taken from surrounding farmers. Before the experiment, it was randomly sampled and determined the moisture content range of maize straw and cow dung stored under natural conditions, using an electronic analytical balance (Germany Sartorius QUINTIX224-1CN) and a halogen fast moisture meter (Shenzhen Guanya Electronic Technology Co., Ltd. SFY-60) and other equipment. The ratio of straw to cow dung was 3:2 during the experiment. The self-made rubbing filament machine and mixer were used to pre-treat the materials to the moisture content level range of (60±2) %.

Single factor experimental design

The microcomputer-controlled two-way electronic universal testing machine (Jinan Dongfang Testing Instrument Co., Ltd. WSDS-50) and a self-made mould were used to conduct an experimental study on the water-retaining moulding process of the straw and cow dung mixed material. The water retention rate, compression rate and deformation rate were taken as the evaluation index of water-retaining moulding effect experiment indexes. Calculate the experiment index value according to formula (1), (2), and (3) respectively.

$$Y_1 = (1 - \frac{w_0 - w_1}{w_0}) \times 100 \tag{1}$$

$$Y_2 = \frac{V_0 - V_1}{V_0} \times 100 \tag{2}$$

$$Y_3 = \frac{V_2 - V_1}{V_1} \times 100 \tag{3}$$

where Y_1 is the water retention rate, %; w_0 is the moisture content of the material before compression, %; w_1 is the moisture content of the material after compression, %; Y_2 is the compression rate, %; V_0 is the material volume before compression, m^3; V_1 is the material volume after compression, m^3; Y_3 is the deformation rate, %; V_2 is the material relaxation volume after being placed for 72 h, m^3.

Take one kilogram of mixed material as a sample, carry out the single factor examination with the same compression time, and calculate the material moisture content and volume before compression, and the material moisture content and volume after compression. The relaxation volume was obtained by calculating the maximum size of the small-scale block in each direction of length, width, and height after being placed for 72 h. All the results were kept to two decimal places. The small-scale block sample compressed by single factor examination was shown in Figure 1.

Fig. 1 - Single factor examination compressed small-scale block sample

The examination factors and levels were shown in Table 1, and each examination number was subjected to 3 repeats. During the pressure single factor examination, the values of the non-variable factor examination were: compression speed 300 mm/min, and the pressure holding time 150 s; in the single factor examination process of the compression speed, the non-variable factor examination values were: pressure 18 kN, pressure holding time 150 s; in the single factor examination process of the pressure holding time, the values of the non-variable factor examination were: pressure 18 kN, compression speed 300 mm/min.

Table 1

Factors and levels of single factor experiment

Experimental factors		**Experimental levels and number**								
		1	**2**	**3**	**4**	**5**	**6**	**7**	**8**	**9**
Pressure	[kN]	6	9	12	15	18	21	24	27	30
Compression speed	[mm·min^{-1}]	100	150	200	250	300	350	400	450	500
Pressure holding time	[s]	30	60	90	120	150	180	210	240	270

Design of hydraulic mechanism of the hydraulic horizontal mixed material compression device

The hydraulic compression device of the mixed materials was mainly composed of an electric motor, a compression mechanism, a hydraulic system and a control system, as shown in Figure 2. The whole machine was equipped with three hydraulic execution units, which were used to drive the pressing plate to move and compress the material, drive the baffle plate to move and open-close the discharge port and drive the push plate to move the small-scale block. The three hydraulic units were composed of the pressing plate, flange and hydraulic pressure. The compression hydraulic cylinder was arranged in parallel with the opening and closing hydraulic cylinder. The discharge hydraulic cylinder and the compression hydraulic cylinder were arranged vertically. The machine design dimensions (length × width × height) were 2 600 mm×1 600 mm×1 200 mm, the compression chamber capacity was 0.26 m^3, the power input was 3.0 kW, and the overall weight was about 600 kg.

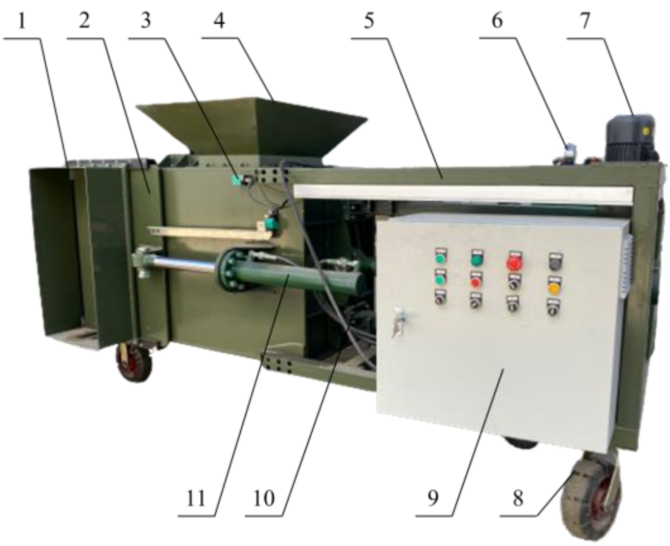

Fig. 2 - Structure schematic diagram of the hydraulic horizontal mixed material compression device
1-Discharge port; 2-Discharge baffle; 3-Sensor; 4-Feed inlet; 5-Frame; 6-Pressure gauge; 7-Motor; 8-Walking wheel; 9-Control cabinet; 10-Compression hydraulic cylinder; 11-Opening and closing hydraulic cylinder

The hydraulic mechanism had an important influence on the overall performance of the compressor, which was designed to include the selection and verification of hydraulic cylinders and system power components. The hydraulic system was mainly composed of hydraulic pump, electromagnetic reversing valve, hydraulic control one-way valve, sequence valve, overflow valve, hydraulic cylinder, oil tank, etc. When working, the motor drove the hydraulic pump coaxially, and the pressure was sent to the oil block through the high-pressure oil pipeline. It was connected in parallel with the compression hydraulic cylinder, the opening and closing hydraulic cylinder and the discharge hydraulic cylinder, and was connected with the Rexroth three-position four-way solenoid valve and two-position four-way solenoid valve.

The two-way solenoid reversing valve was connected in series with the two-position two-way manual reversing valve. At the same time, an electromagnetic relief valve was installed at the outlet of the high-pressure oil circuit to ensure the oil pressure in the system. When working at low pressure, the small load hydraulic cylinder (opening and closing hydraulic cylinder) could quickly enter and exit the oil and reduce the power of the motor.

In the compression process of the straw and cow dung mixed materials, the force of the compression mechanism was mainly the force acting on the pressure plate, including the friction between the material and the compression chamber when the pressure plate pushes the material, and the reaction of the material resisting deformation to the pressure plate force, and both of them changing with the increase of the compression process. Under the condition that the preload load was ignored, the solenoid hydraulic valves in the hydraulic system didn't interfere with each other's control of the advance and retreat routes, and the reciprocating speed of the hydraulic oil was the same. The calculations of the unit hydraulic cylinder working load ***F*** (kN), cylinder bore *D* (mm) and piston rod diameter *d* (mm) were based on equations (4), (5), and (6), respectively.

$$F = s \cdot P \tag{4}$$

$$D = \sqrt{\frac{4F}{\pi P_0}} \tag{5}$$

$$d = D\sqrt{\frac{\varphi - 1}{\varphi}} \tag{6}$$

where, P is the maximum pressure required for the hydraulic cylinder working, MPa; s is the pressure plate area, m^2; P_0 is the working pressure of the system, MPa; φ is the ratio of the round-trip speed of the hydraulic cylinder.

Taking the working pressure of the system as 10 MPa (*Chinese Academy of Agricultural Mechanization, 2007*), the ratio of the round-trip speed of the hydraulic cylinder φ=2 (*Wen, 2014*). It can be seen from the single factor examination that under the conditions of a suitable maximum pressure of 24 kN and an examination mould platen area of 0.04 m^2, the maximum pressure P required for the compression of the hydraulic cylinder and the push out of the hydraulic cylinder was 0.6 MPa. The main design parameters of the hydraulic cylinder were shown in Table 2.

Table 2

Main design parameters of hydraulic cylinder

Design parameter		Compression unit	Open and close unit	Discharge unit
Platen area *s*	[m^2]	0.30	0.24	0.24
Maximum pressure required for hydraulic cylinder work *P*	[MPa]	0.6	0.1	0.6
Working load *F*	[kN]	180	24	144
Calculated value of cylinder inner diameter *D*	[mm]	151.33	55.68	135.28
Calculated value of piston rod diameter *d*	[mm]	107.06	39.09	95.76
Selection value of cylinder inner diameter *D*	[mm]	160	63	140
Selection value of piston rod diameter *d*	[mm]	110	45	100
Piston stroke *l*	[mm]	900	430	600

Combination experimental design

The combination experiment was conducted at the Northeast Facility Horticultural Engineering Scientific Observation and Experimental Station of Shenyang Agricultural University. The stability of the small-scale block after 72 hours of standing and stacking was investigated for the moulding effect of the hydraulic horizontal mixed material compression device.

The dimensional stability of the small-scale block was selected as the experimental index (*Xin et al., 2017*), calculated according to formula (7).

$$Y_4 = (1 - \frac{V_2 - V_1}{V_1}) \times 100 \quad (7)$$

where Y_4 is the dimensional stability, %; the material volume after compression V_1 in this combination experiment was 0.12 m³.

The experiment selected the compression speed, feeding amount and pressure holding time as the experiment factors, and carries out the ternary quadratic regression orthogonal rotation combination experiment. According to the analysis of the single factor experiment results, the value range of each factor and the experiment factor levels were shown in Table 3. In order to reduce the experiment operation error, the round integer in the parentheses in Table 3 was taken as the experiment value. The experiment process was shown in Figure 3.

Table 3

Factors and levels of combination experiment

Levels	Factors		
	Compression speed [mm·min⁻¹]	Feeding amount [kg]	Pressure holding time [s]
	x_1	x_2	x_3
1.682	400	150	210
1	339.18 (340.00)	129.73（130.00）	197.84（198.00）
0	250	100	180
-1	160.82 (160.00)	70.27 (70.00）	162.16（162.00）
-1.682	100	50	150
△j	89.18 (90.00)	29.73 (30.00)	17.84（18.00）

Fig. 3 - Experimental process

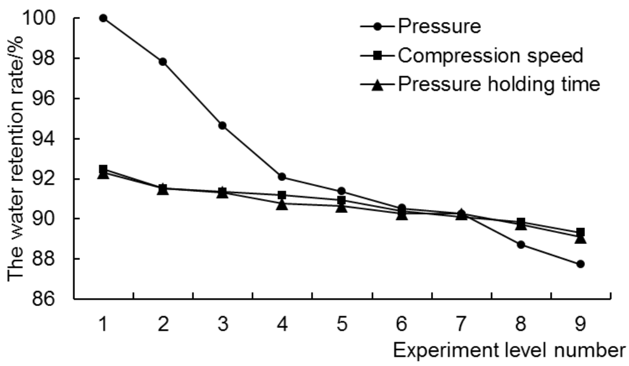

Fig. 4 - Statistical graph of single factor experimental results of the influence of compressed parameters on water retention rate

RESULTS

Single factor experiment results and analysis

Figure 4 shows the statistical diagram of the single factor experiment results of the influence of compression process parameters on the water retention rate. It can be seen from the diagram that the water retention rate decreased with the increase of pressure, compression speed and pressure retention time, and the decrease was larger with the increase of pressure. With the increase of compression speed and pressure holding time, the decrease was relatively gentle, and it was greater than 85% within the range of experiment parameters. When the pressure was 6-24 kN, the compression speed was 100-400 mm/min, and the pressure holding time was 30-210 s, the water retention rate of small-scale blocks was above 90%, and this range was regarded as a more suitable process parameter range for water-retaining of small-scale blocks.

Figure 5 shows the statistical diagram of the single factor experiment results of the influence of compression process parameters on the compression ratio. It can be seen from the figure that the compression ratio increased with the increase of pressure, compression speed and pressure holding time, and the increase with pressure increases is larger.

The increase in compression speed and holding time was relatively gentle, and was higher than 55% within the range of experiment parameters. When the pressure was 21-30 kN, the compression speed was 100-500 mm/min, and the holding time was 30-270 s, the material compression rate was above 65%, and this range was regarded as a more suitable process parameter range for material compression.

Figure 6 shows the statistical diagram of the single factor experiment results of the influence of compression process parameters on the deformation rate. It can be seen from the figure that the deformation rate first decreased and then increased with the increase of pressure, and the change was small with the increase of compression speed, and with the increase of pressure holding time. The deformation rates were all below 50% within the range of experiment parameters. When the pressure was 24 kN, the compression speed was 100-500 mm/min, and the pressure holding time was 150-240 s, the deformation rate was below 15%. This range was regarded as the process parameter range which was more suitable for the small-scale block to keep the shape stable.

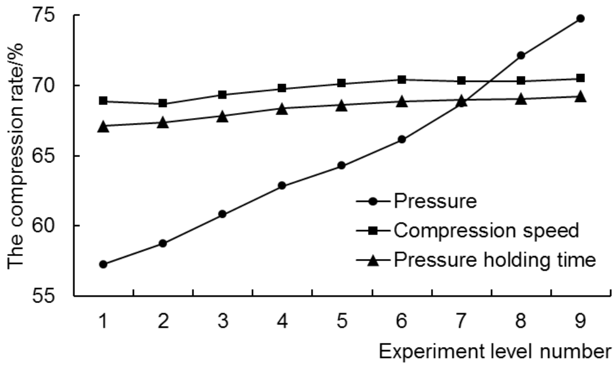

Fig. 5 - Statistical graph of single factor experimental results of the influence of compressed parameters on compression rate

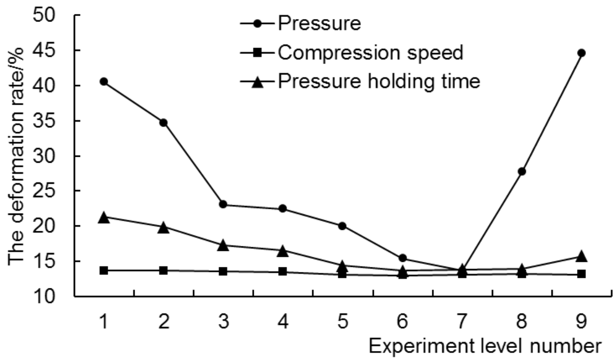

Fig. 6 - Statistical graph of single factor experimental results of the influence of compressed parameters on deformation rate

The reason for the above phenomenon was that under the same compression speed, the straw filaments in the mixture material had strong viscoelasticity, and the compressibility of the mixture material was negatively related to the pressure. After compression, the elasticity was stronger and the residual stress was larger, and the amount of stress relaxation also increased. When the pressure was at a higher level, the mixture material was further compacted after holding pressure, the material properties changed from viscoelastic deformation to yield deformation, and the compression performance and resistance to deformation of the mixture material were enhanced; with the increase of the compression process parameters, the mixture material after compaction and then compression, the water was pressed out, and the water retention performance of the mixture material was reduced.

Combination experiment results and analysis

The combination experiment plan and results were shown in Table 4. By using Design-Expert software, the quadratic polynomial regression model among the compression speed (X_1), feeding amount (X_2), pressure holding time (X_3), and dimensional stability (Y_4) were established for multiple regression analysis. The regression model was shown as formula (8).

$$Y_4=-82.87-1.98X_1-3.15X_2+1.49X_3-1.69X_1X_2-0.30X_1X_3-1.22X_2X_3-1.871X_1^2-2.53X_2^2+0.38X_3^2 \quad (4)$$

Table 4

Experimental plan and results

No.	Compression speed [mm·min^{-1}]	Feeding amount [kg]	Pressure holding time [s]	Y_4 [%]
1	1	1	1	71.25
2	1	1	-1	72.94
3	1	-1	1	85.30
4	1	-1	-1	80.37
5	-1	1	1	79.26
6	-1	1	-1	78.01
7	-1	-1	1	84.80
8	-1	-1	-1	80.43
9	1.682	0	0	73.05

Table 4 (continuation)

No.	Compression speed [mm·min-1]	Feeding amount [kg]	Pressure holding time [s]	Y4 [%]
10	-1.682	0	0	81.57
11	0	1.682	0	71.39
12	0	-1.682	0	79.49
13	0	0	1.682	87.08
14	0	0	-1.682	80.25
15	0	0	0	83.54
16	0	0	0	82.66
17	0	0	0	82.51
18	0	0	0	81.14
19	0	0	0	83.79
20	0	0	0	82.73
21	0	0	0	83.87
22	0	0	0	82.25
23	0	0	0	83.43

Significance test and analysis of variance were performed on the obtained ternary quadratic regression equation, and the results were shown in Table 5. It can be seen from the table that the primary and secondary order of the influence of each experiment factor on the dimensional stability was feeding amount > compression speed > pressure holding time. The compression speed (x_1), feeding amount (x_2) and pressure holding time (x_3) had extremely significant effects on the dimensional stability (P<0.01); the quadratic term of compression speed (x_1^2) and feeding amount (x_2^2) had extremely significant impact on the dimensional stability (P<0.01). In the interaction of factors, the interaction of compression speed and feeding amount (x_1x_2) had extremely significant impact on the dimensional stability (P<0.01), the interaction of feeding amount and pressure holding time (x_2x_3) had significant impact on the dimensional stability (P<0.05). The determination coefficient R^2=0.95, the regression equation significance level F_R=30.39, the lack of fit test F_{Lf}=3.48, P=0.0574, were all greater than 0.05 and the difference was not significant, indicating that the regression equations Y_4 was statistically significant.

The optimized regression equation after excluding insignificant terms such as x_1x_3 and x_3^2 of Y_4 at the significance level of P=0.05 was:

$$Y_4=-82.87-1.98X_1-3.15X_2+1.49X_3-1.69X_1X_2-1.22X_2X_3-1.871X_1^2-2.53X_2^2 \quad (6)$$

Table 5

Data significance experiment and analysis of variance

Source of variation	Dimensional stability Y_4				
	SS	DF	MS	*F value*	*P value*
Model	413.68	9	45.96	30.39	< 0.0001**
X_1	53.28	1	53.28	35.22	< 0.0001**
X_2	135.86	1	135.86	89.81	< 0.0001**
X_3	30.32	1	30.32	20.05	0.0006**
X_1X_2	22.82	1	22.82	15.09	0.0019**
X_1X_3	0.71	1	0.71	0.47	0.5068
X_2X_3	11.86	1	11.86	7.84	0.0150*
X_1^2	55.44	1	55.44	36.65	< 0.0001**
X_2^2	101.78	1	101.78	67.29	< 0.0001**
X_3^2	2.27	1	2.27	1.5	0.2420
Remaining	19.66	13	1.51		
Lack of Fit	13.48	5	2.7	3.48	0.0574
Pure Error	6.19	8	0.77		
Sum	433.34	22			

Analysis of influencing factors

The calculation results of the response surface of each experiment factor and its interaction on the experiment index were shown in Figure 7.

Figure 7a shows the response surface diagram of the influence of the interaction between the compression speed and the feeding amount on the dimensional stability when the pressure holding time was 0 level (180 s). The analysis showed that when the compression speed was constant and at the lower level of the experimental range, and the feeding amount gradually increased within the experimental range, the dimensional stability first improved and then decreased. When the compression speed was constant at the higher-level range of the experimental range, and the feeding amount gradually increased within the experimental range, the dimensional stability gradually decreased. When the feeding amount was constant and at the lower level range of the experimental range, and the compression speed was in the experimental range gradually increased, the dimensional stability first increased and then decreased. When the feeding amount was constant and at the higher level of the experimental range, and the compression speed gradually increased at the experimental range, the dimensional stability gradually decreased. The dimensional stability peak appeared at the middle horizontal interval. This might be because when the feeding amount was large, the compression amount of the material unit in the mixture would increase, and the friction and cohesive force between the material units would be strengthened, the stress relaxation would increase, so that the compaction of the small-scale block after compression would be increased. On the other hand, a higher compression speed increased the start time of viscous strain in the small-scale block after compression, and the residual stress relief time in the small-scale block was relatively reduced, thereby increasing the stress relaxation after compression and reducing the dimensional stability of the small-scale block.

Figure 7b shows the response surface diagram of the influence of the interaction between the compression speed and the pressure holding time on the dimensional stability when the feeding amount was 0 level (100 kg). The analysis showed that when the compression speed was constant and at the lower level of the experimental range, when the pressure holding time gradually increased within the experimental range, the dimensional stability first increased and then decreased. When the compression speed was constant, and at the higher level range of the experimental range, when the pressure holding time gradually increased within the experimental range, the dimensional stability gradually decreased; when the pressure holding time was constant and the compression speed gradually increased within the experimental interval, the dimensional stability increased first slightly lowered. This may be because under the same feeding amount, the stress increase relaxation caused by the compression speed increase and the stress relaxation decrease caused by the pressure holding time increase gradually offset with the compression process, so the interaction of the two factors on the dimensional stability of the small-scale block was not obvious.

Figure 7c shows the response surface diagram of the influence of the interaction between the feeding amount and the pressure holding time on the dimensional stability when the compression speed was 0 level (250 mm·min^{-1}). The analysis showed that when the feeding amount was constant and at the lower level of the experimental range, and the pressure holding time gradually increased within the experimental range, the dimensional stability did not change significantly. When the feeding amount was constant, and at the higher level of the experimental range, and the pressure holding time gradually increased within the experimental interval, the dimensional stability gradually decreased; when the pressure holding time was constant and the feeding amount gradually increased within the experimental range, the dimensional stability was gradually improved. This may be because the holding pressure could significantly reduce the residual stress in the small-scale block after decompression, thereby reducing the stress relaxation after compression and improving the dimensional stability of the small-scale block; the increase in the feeding amount increased the irreversible viscous reverse strain produced by the mixture materials. The viscoelasticity of the mixture materials was reduced, the yield deformation was increased, the residual stress was reduced, and the dimensional stability of the small-scale block was further improved.

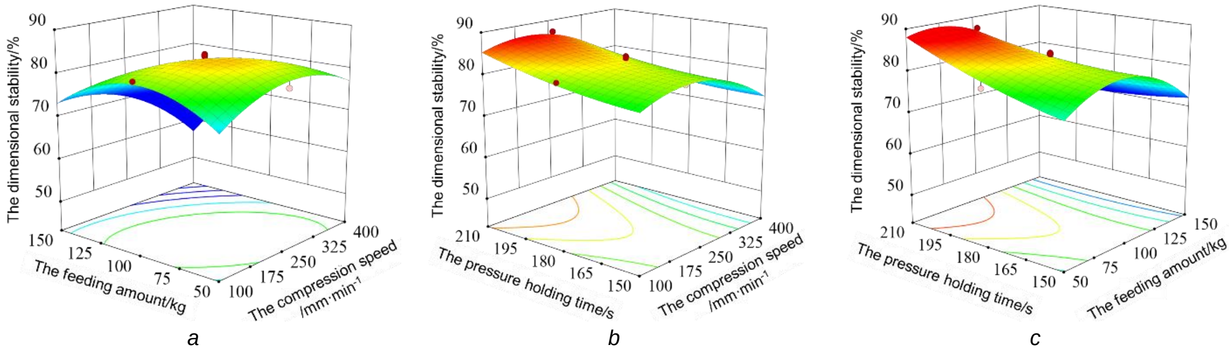

Fig. 7 - Response surface analysis of the factor interaction effect on the index

Parameter optimization and verification test

Set the target parameter the dimensional stability to maximize, and the factors parameter to the range of experiment to establish the optimal mathematical model formula for constraints as formula (9). Solve the optimal working parameter combination of the hydraulic horizontal mixed material compression device: the compression speed was 250.56 mm·min^{-1}, the feeding amount was 56.26 kg and the pressure holding time was 205.07 s, the overall operation effect being the best. The predicted dimensional stability will be 87.39%.

$$\begin{cases} \max \ Y_4(x_1, x_2, x_3) \\ s.t. \begin{cases} 100 \le x_1 \le 400 \\ 50 \le x_2 \le 150 \\ 150 \le x_3 \le 210 \end{cases} \end{cases} \tag{9}$$

In order to further verify the reliability and applicability of the mathematical model, the optimization results were tested and verified under the same experiment conditions, while the actual test results and the model prediction values were analysed for error. Considering the operability of the test, the optimization results were adjusted as follows: the compression speed was 250 mm·min^{-1}, the feeding amount was 55 kg and the pressure holding time was 200 s, and three repeated tests were carried out to obtain the best working parameter combination. The average values of the test values of dimensional stability was 84.71%, which was close to the predicted values of the model. The relative error between the actual and predicted values didn't exceed 3%, indicating the established model and analysis results were valid.

CONCLUSIONS

In this paper, a hydraulic horizontal mixed material compression device was developed to solve the problems of water easily loss and compression molding effectiveness slightly poor during the mixed materials compression process in the fertilizer production, according to the suitable pressure and intensity of pressure of the water-retaining moulding, the hydraulic system parameters were designed and calculated. The structure and working parameters of the compressor had been optimized through experiments. The water retention rate, compression rate, deformation rate and dimensional stability were taken as the water-retaining moulding effect experiment indexes, and the pressure, compression speed, feeding amount and pressure holding time under the composition condition of maize straw and cow dung was studied. The following conclusions were drawn:

1) The single factor experiment analysed the appropriate value range of the compression process parameters, and integrated the influence of each compression process parameter on the water-retaining moulding effect of the mixture material. The more appropriate process parameter range was 24 kN of the pressure, 100-400 mm·min^{-1} of the compression speed, and 150-210 s of the pressure holding time. The water retention rate of the small-scale block in this range was above 90%, the compression rate was above 65%, and the deformation rate was below 15%.

2) The combination experiment showed that the primary and secondary factors affecting dimensional stability are feeding amount > compression speed > pressure holding time, and the interaction of the factors was compression speed and feeding amount, feeding amount and pressure holding time. A response surface model was established, and the device's best working parameters were optimized through experiments. The optimization and verification results showed that the optimal working parameters combination of the hydraulic horizontal mixed material compression device was a compression speed of 250 mm·min^{-1}, a feeding amount of 55 kg, and a pressure holding time of 200 s. The average value of the actual value of the dimensional stability under this condition was 84.71%, which met the design requirements.

ACKNOWLEDGEMENT

The study was supported by the Key R&D Guidance Plan Project of Liaoning Province (2019JH8/10200019) and the Higher Education Research Budget Project of Liaoning Province (LSNFW201909). The authors thank relevant scholars for their assistance in the literature.

REFERENCES

[1] Carone M.T., Pantaleo A., Pellerano A., (2011), Influence of process parameters and biomass characteristics on the durability of pellets from the pruning residues of Olea European L. *Biomass & Bioenergy*, Vol.35, pp. 401-410, Oxford/England.

[2] Chinese Academy of Agricultural Mechanization Sciences, (2007), Agricultural Machinery Design Manual. *China Agricultural Science and Technology Press*, Beijing/China.

[3] Jia Honglei, Chen Tianyou, Zhang Shengwei, et al., (2020), Effects of pressure maintenance and strain maintenance during compression on subsequent dimensional stability and density after relaxation of blocks of chopped corn straw. *BioResources*, Vol.15, Issue 2, pp. 3717-3736, North Carolina/United States.

[4] K. Theerarattananoon, F. Xu, J. Wilson, et al., (2011), Physical properties of pellets made from sorghum stalk, corn stover, wheat straw, and big bluestem. *Industrial Crops and Products*，Vol.33, Issue 2, pp. 325-332, Amsterdam/Netherlands.

[5] Kazuei Ishii, Toru Furuichi, (2014), Influence of moisture content, particle size and forming temperature on productivity and quality of rice straw pellets. *Waste Management*, Vol.34, Issue 12, pp. 2621-2626, Oxford/England.

[6] Lixian Zhang, Zhongping Yang, Qiang Zhang, et al., (2017), Mechanical behaviour of corn stalk pith: an experimental and modeling study. *INMATEH—Agricultural Engineering*, Vol.51, Issue 1, pp.39-48, Bucharest/Romania.

[7] Mirko Maraldi, Luisa Molari, Nicolò Regazzi, et al., (2017), Analysis of the parameters affecting the mechanical behaviour of straw bales under compression. *Biosystems Engineering*, Vol.160, pp. 179-193, San Diego/United States.

[8] Moiceanu G., Voicu Gh., Paraschiv G., (2015), Mechanical properties of energetic plant stems - review. *INMATEH—Agricultural Engineering*, Vol.45, Issue 1, pp.149-156, Bucharest/Romania.

[9] Nehru Chevanan, Alvin R. Womac, Venkata S.P. Bitra, et al., (2010), Bulk density and compaction behaviour of knife mill chopped switchgrass, wheat straw, and corn stover. *Bioresource Technology*, Vol.101, Issue 1, pp. 207-214, Oxford/England.

[10] Niccolò Pampuro, Giorgia Bagagiolo, Eugenio Cavallo, (2019), Energy requirements for wood chip compaction and transportation. *Fuel*, Vol.262, 16618, Oxford/England.

[11] Robert Samuelsson, Sylvia H. Larsson, Mikael Thyrel, et al., (2012), Moisture content and storage time influences the binding mechanisms in biofuel pellets. *Applied Energy*, Vol.99, pp. 109-115, Oxford/England.

[12] Voicu Gh., Moise V., Popa L., (2019), Kinematic analysis of a mechanism, with articulated precompaction bars, of municipal solid waste collecting machines. *INMATEH—Agricultural Engineering*, Vol.59, Issue 3, pp.93-100, Bucharest/Romania.

[13] Xin Mingjin, Chen Tianyou, Zhang Qiang, et al., (2017), Parameters optimization for moulding of vegetable seedling substrate nursery block with rice straw. *Transactions of the Chinese Society of Agricultural Engineering (Transactions of the CSAE)*, Vol.33, Issue 16, pp. 219-225, Beijing/China.

[14] Wang Ruili, Yu Jin, Wang Tiejun, et al., (2021a), Experimental study on moulding technology for a mixture of corn straw and cow manure. *BioResources*, Vol.16, Issue 1, pp. 1740-1756, North Carolina/ United States.

[15] Wang Tiejun, Wang Ruili, Sun Junde, et al., (2021b), Parameter optimization of the small-scale compost technology with localization maize stover and livestock manure. *Transactions of the Chinese Society of Agricultural Engineering (Transactions of the CSAE)*, Vol.37, Issue 2, pp. 251-257, Beijing/China.

[16] Wen Bangchun, (2014), Mechanical Design Manual (5th Edition). *Mechanical Industry Press*, Beijing/China.

INTELLIGENT FAULT MONITORING SYSTEM OF NEW ENERGY TRACTOR ENGINE FOR BIG DATA
/
面向大数据新能源拖拉机发动机智能故障监测系统

Beibei Qi
Xinxiang Vocational and Technical College，Xinxiang, Henan, 453002, China
**E-mail: cii67757@163.com*
DOI: https://doi.org/10.35633/inmateh-64-20

Keywords: *tractor, engine, intelligent fault monitoring, artificial intelligence, big data*

ABSTRACT
Tractor engine has complex working environment and many parts. In the process of use, with the increase of service mileage and working hours, parts will wear to a certain extent, resulting in some engine failures. Using modern fault diagnosis technology to know the working performance of tractor engine in time, and to judge whether each component is in or will be in any fault state, is of great importance and practical significance for the research of fault diagnosis technology theory and diagnosis system of tractor engine. Taking the engine of new energy tractor as the research object, the principle and monitoring method of engine intelligent fault diagnosis are introduced. Then, based on big data and neural network technology, the engine intelligent fault monitoring system of new energy tractor for big data is designed. The fault diagnosis system of tractor engine based on artificial intelligence and big data technology realizes the functions of database and signal analysis, which improves the real-time and accuracy of the system.

摘要
拖拉机发动机工作环境复杂，零部件多。在使用过程中，随着使用里程和工作时间的增加，零件会有一定程度的磨损，导致一些发动机故障。利用现代故障诊断技术及时了解拖拉机发动机的工作性能，判断各部件是否处于或将处于任何故障状态，对拖拉机发动机故障诊断技术理论和诊断系统的研究具有重要的现实意义。以新能源拖拉机发动机为研究对象，介绍了发动机智能故障诊断的原理和监测方法。然后，基于大数据和神经网络技术，设计了新能源拖拉机发动机大数据智能故障监测系统。基于人工智能和大数据技术的拖拉机发动机故障诊断系统实现了数据库和信号分析功能，提高了系统的实时性和准确性。

INTRODUCTION
In recent years, with the encouragement of national purchase subsidy policy, there are more and more users of agricultural tractors, which greatly promotes the rapid development of rural economy *(Jafari M. J. et al., 2020)*. Tractor engine has complex working environment and many components. In the process of use, with the increase of mileage and working hours, the components will wear to a certain extent, resulting in some engine failures *(Chen Y. M. et al., 2021)*. Tractor engine is a complex system, and its failure rate accounts for more than 90% of the total vehicle failure rate, which is the most prone component of tractor. Tractor failures are various, and the causes of failures are also complicated. A fault may show multiple signs, and one sign may reflect multiple faults *(Dong J. H. et al., 2018; Wang Yingbo et al., 2021)*. In order to avoid serious accidents, the use of modern fault diagnosis technology to timely understand the working performance of tractor engine, judge whether the components are in or about to be in what fault state, the research of tractor engine fault diagnosis technology theory and diagnosis system has a very important and practical significance *(Jhih Y. C. et al., 2021; Qiuju X. et al., 2021; Rulli F. et al., 2021)*. Agricultural tractors provide great convenience for farmers, reduce labour intensity and production costs *(Wei W. et al., 2021)*. In the agricultural production and transportation work, agricultural tractors will have a variety of faults. As tractor operators, it is very important to understand and master the causes of common faults and maintenance methods *(Yu L. C. et al., 2021)*. It is particularly important to adopt effective strategies for fault diagnosis of tractor engine to remind the driver of correct use and timely maintenance *(Cheng R. et al., 2018)*.

When the tractor breaks down, observe the fault performance, adopt specific fault detection methods according to different fault performance, determine the cause of the fault, and finally determine the troubleshooting method *(Gultyaeva E., Shaydayuk E., Gannibal P., 2021)*.

At present, the engine fault diagnosis system in our country is still lack of a universal platform integrating multiple parameter acquisition, analysis and processing, diagnosis and reasoning. At the same time, when analysing the nonlinear relationship between fault phenomenon and fault cause, the existing fault diagnosis theory cannot be simply applied to the fault diagnosis system *(Martínez-Moreno F. et al., 2021)*. In order to achieve the purpose of fault diagnosis of tractor engine without disassembly and improve the diagnosis efficiency, an artificial intelligence fault detection method based on neural network is proposed and a tractor engine vibration signal acquisition system is constructed *(Gross G. et al., 2018)*. Taking the new energy tractor engine as the research object, this paper introduces the engine intelligent fault diagnosis principle and monitoring method, and then designs an intelligent fault monitoring system for new energy tractor engine based on big data and neural network technology. When analysing the cause of failure, we should be good at thinking, observe the failure phenomenon, and analyse it in sections according to the relationship between various parts *(Jensen R., 2021)*. We should also follow the principle of simplicity to complexity, from the outside to the inside. We should first analyse the simple and superficial reasons, then consider the complex and internal reasons, first find the probable and common reasons, and then check the unlikely parts to avoid unnecessary disassembly *(Nouiri M. et al., 2018)*.

Agricultural tractors bring great convenience to farmers, reduce labour intensity and reduce production costs. However, it is inevitable that agricultural tractors will fail during operation, which seriously affects the storage and transportation. Based on this, based on the analysis of the common faults of agricultural tractors, this paper puts forward the detection and elimination methods of tractor faults. For a certain fault, there may be many reasons, but because tractor is the unity of many parts working in coordination, the organic connection between them determines that there are certain regularity in various fault reasons. Therefore, according to the specific situation and use experience of tractors, the causes of faults can be found out through scientific analysis and judgment. Using artificial intelligence can improve the analysis process and get a fault diagnosis model that can solve practical problems, thus effectively improving the accuracy and efficiency of fault diagnosis. The method in this paper can effectively diagnose the engine faults of new energy tractors, with high diagnostic accuracy, and can provide reference for engine fault diagnosis and maintenance personnel. Tractor engine fault diagnosis system based on artificial intelligence and big data technology comprehensively uses signal acquisition technology, signal processing technology, database technology, neural network technology and artificial intelligence expert system, realizes the processing function of database and powerful signal analysis, and improves the real-time diagnosis and diagnosis accuracy of the system.

In agricultural production and transportation, agricultural tractors will have various faults. As tractor operators, it is very important to understand and master the causes of common faults and maintenance methods. Literature thinks that to check the faults of tractors, we should first observe the fault phenomena, determine the main causes of the faults through analysis and judgment, and then eliminate them. Literature points out that modern fault real-time detection is a comprehensive technology, which can analyse the faults of machines by signal processing and data analysis according to the fault characteristics and vibration laws of machines. Literature points out that a fault may show multiple signs, and one sign may reflect multiple faults, which brings some difficulties to fault analysis. Literature uses big data and neural network algorithms to design a new energy tractor engine intelligent fault monitoring system. The main tasks of engine fault detection are: use the various feature indicators collected by the sensor to determine whether the machine is working in a normal state; classify the fault characteristics to accurately determine the faulty parts and provide a theoretical basis for rapid maintenance; use data Technologies such as analysis, probability theory and big data can predict engine failures and realize the health management of machinery and equipment. Literature uses field test methods to verify the rapid diagnosis system of tractor faults. The test results show that the use of artificial intelligence diagnosis method can not only effectively improve the accuracy of the system, but also the response of the diagnosis system is faster, and the stability of normal work can still be maintained in harsh on-site environments such as exposure, vibration, and dust.

MATERIALS AND METHODS

Principle of fault diagnosis

There are many types of faults in agricultural tractors, which generally include five aspects:

1) Abnormal appearance. The exhaust emits black smoke, white smoke or blue smoke, the tractor leaks oil, air and water, the front wheel swings while driving, and the lights flicker. 2) Abnormal sound. Abnormal sound, knocking sound, air blasting sound, hoarseness of horns, etc. 3) Abnormal temperature. Overheating

of engine, overhigh temperature of cooling water, overhigh oil temperature of gearbox or rear axle, overheating of brake, etc. 4) Abnormal consumption. Excessive consumption of fuel oil, engine oil and cooling water, abnormal increase or rapid decrease of oil level in oil pan, etc. 5) Abnormal function. Difficulties in starting, difficulty in shifting or shifting gears, steering and braking failure, etc.

With the rapid development of mobile Internet technology, artificial intelligence, big data technology stand in the development of tuyere, more and more big data application services emerge. For such a complex tractor system, a small part problem may affect the operation of the whole machine. As the core of the whole system, the engine is easy to be damaged and led to serious mechanical failure. Through the observation of the tractor's appearance, if there is any abnormality, such as the tractor inclines on the flat road, the tire has abnormal wear, scratches, and parts are lost, the operator should be alert. No matter what part of the component, no matter what degree of failure occurs, it will lead to the change of the whole system function, and this change will be directly reflected in the change of parameters. When you feel that the temperature is too high during driving, or when you stop halfway for inspection, if you touch the temperature of various parts of the vehicle abnormally, such as the brake drum, tire, rear axle housing, transmission housing, etc., the temperature makes your hands unbearable, which indicates that the tractor is faulty. The clearance of each part of tractor has its standard value. If the clearance is too large or too small, it indicates that there is a fault. All kinds of oil consumption of tractors have a standard range. If the oil consumption increases obviously, the tractor has hidden faults. Because of the huge tractor system, the parameter information in the running process will be very complex, so in fault diagnosis, we should first extract useful fault features and remove useless parameters. Because the fault cannot be directly judged according to the extracted characteristic parameters, it is necessary to further analyse the parameters and extract the fault symptom information. With the above foundation, fault types can be identified and classified. The fault diagnosis process is shown in Figure 1.

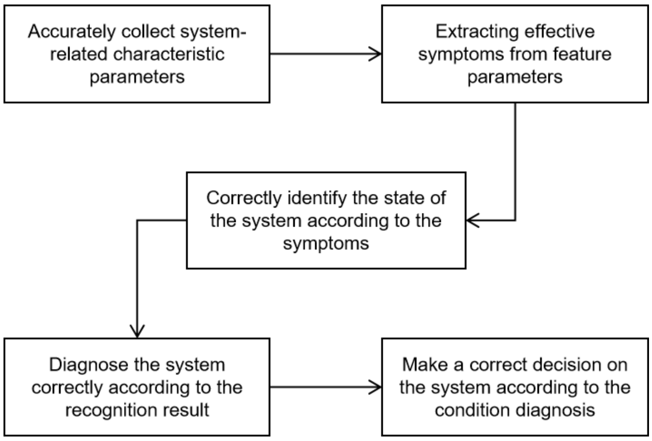

Fig. 1 - Schematic diagram of fault diagnosis process

In order to improve the accuracy of tractor engine fault diagnosis, based on the classification of big data, this paper uses neural network to analyse and judge it. The process of fault diagnosis is complicated, and the most important thing is to diagnose the fault state of the system according to the fault symptom.

Most of modern agricultural tractors use electronically controlled multi-point fuel injection engines, and engine failures, especially cylinder failure, are generally caused by oil or fire failure of one cylinder of the engine. In engine fault detection, the fault of engine can be judged by analysing the characteristics of vibration signals. For tractors, during their operation, the parameters such as heat and vibration will change continuously. Sensors are used to collect these pieces of information, including vibration frequency, displacement of machinery and equipment, instantaneous engine speed, acceleration, temperature, voltage and current, etc. If the tractor has faults, the fault information can be extracted from these parameters. Signal processing mainly includes the use of Fourier, wavelet and other methods to amplify, denoise, transform and other processing. In engine fault detection, due to the influence of noise background in test signal, data redundancy will be generated. The speed and accuracy of engine fault diagnosis can be effectively improved by using artificial intelligence database algorithm. The design framework is shown in Figure 2.

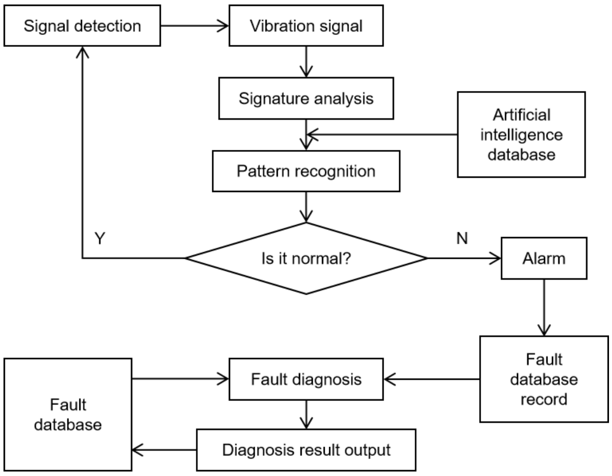

Fig. 2 - The framework of the engine fault diagnosis system

The trained neural network model is used to detect the special diagnosis of known faults, and the known faults and the detected faults are compared to judge whether the model is accurate or not. When the engine is found to have faults, if the engine has faults, the fault experience database of artificial intelligence database can be used to identify the types of faults.

Engine fault diagnosis framework is mainly divided into signal detection, signal recognition, feature analysis, artificial intelligence database and fault database. Among them, signal collection and analysis is the main part of fault analysis system, and the efficiency of pattern recognition can be improved by using artificial intelligence database. When the machine is in normal operation, it is necessary to predict and judge the state of the machine in a certain time in the future through a series of parameters. In the process of fault identification and classification, according to the collected fault symptoms, various identification algorithms and models are adopted to carry out accurate fault diagnosis. The common faults of fault diagnosis system can be analysed by virtual simulation, and the experience database of diagnosis system can be established by using the results of simulation analysis, at the time of diagnosis. When there is a fault signal, the signal characteristics and fault information are compared quickly to get the signal diagnosis results. Figure 3 shows the structure of artificial intelligence virtual platform for fault diagnosis.

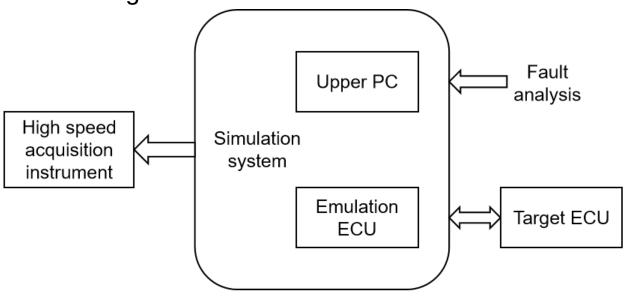

Fig. 3 - Fault diagnosis artificial intelligence virtual platform structure

The main signals collected in tractor engine fault diagnosis are speed and vibration signals. After these data are processed, the subroutine of algorithm can be used to judge the fault type.

Detection method of tractor fault

Sensory identification method mainly refers to judging the fault location of tractor through sensory organs without using other measuring tools and instruments. In order to achieve this, we need the appraisers to accumulate rich experience. The appraiser mainly judges the colour, water and oil of tractor exhaust by looking at it to see if there is water leakage, gas and oil; Through ear listening, it is mainly to judge the sound after the tractor when it is started, and check whether the sound of the chassis is abnormal; Judging the temperature of tractor body by hand touch, whether the body runs flexibly; Judging whether there is burnt smell or abnormal smoke exhaust smell during tractor operation by sniffing.

The comparative method is to check the same parts, that is, to replace them again, in order to compare the changes of parts before and after checking to judge whether the replaced parts are in normal condition. If it is suspected that the fuel injector, oil pressure gauge and other components are not working properly, they can be replaced with good technical status for comparison to determine whether the components are normal. If there is a problem with the tractor injector components, the adjustment method should be used to compare the technical status of the operation to determine whether the components are operating normally.

The method of test and proof is to use the working method of changing a certain position or observe the change of the fault in the working state, and judge the fault position directly. For example, the diesel engine cannot be started normally. It is suspected that the cylinder sleeve and piston have worked for a long time, which leads to serious wear and abnormal compression. The cylinder and piston need to be checked to see if the wear is not working properly due to long-term operation. To judge whether this is the case, a small amount of engine oil can be injected into the cylinder, and the compression performance can be checked after several revolutions. If it is determined that this is the reason, a small amount of engine oil can be injected into the cylinder to check whether the compression performance is good after running several times.

Intelligent fault diagnosis method

Intelligent algorithm based on confidence weight and artificial neural network is the most commonly used artificial intelligence algorithm at present, but there is little research on tractor fault diagnosis. It is a new attempt to use artificial intelligence algorithm in engine fault diagnosis. In order to find out the faults, necessary inspection means and methods should be provided. The state of tractor is related to environmental temperature, pressure, machine vibration frequency, voltage value, current value and other parameters, and this relationship is very complex, so it is necessary to use neural network for fault diagnosis of tractor uncertainty. Through observation, understand the main phenomenon of the fault, but also in-depth and detailed analysis of these phenomena, in order to determine the location and cause of the fault. After using big data to construct fault features, neural network can be used to identify and judge them. The diagnosis architecture of tractor transmitter based on big data is shown in Figure 4.

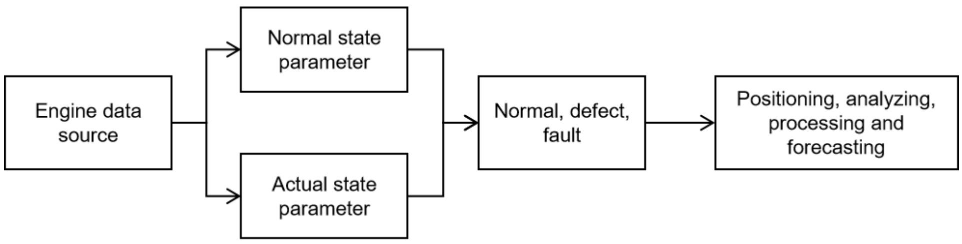

Fig. 4 - Tractor transmitter diagnosis architecture based on big data

Neural network is a mathematical model established by researchers to simulate human brain thinking and analysing problems. It uses the methods of gradient descent and weight updating to obtain the minimum error function. Using neural network subnet, tractor engine faults can be measured from different aspects, and local information fusion can be completed. Using information fusion decision neural network, the diagnosis results of subnet can be output. The fault parameters of tractor engine mainly include fuel supply time, fuel injection pressure, sealing of plunger pair and outlet valve, which are also included in the vibration signal of engine. After repeated learning and training, a set of weights is generated to call the test samples, so as to predict the characteristics of the target object. The structure of neural network model is shown in Figure 5.

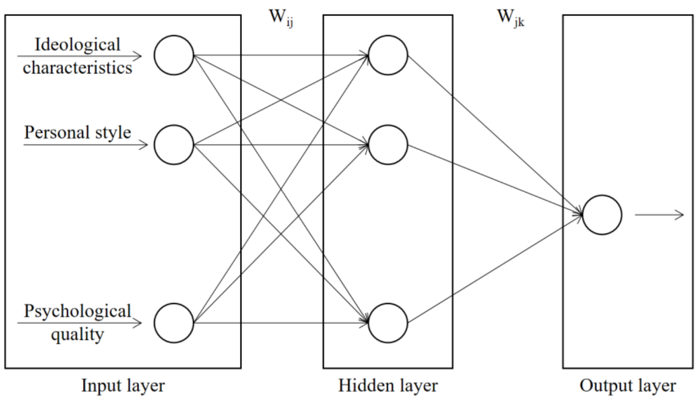

Fig. 5 - Comprehensive quality evaluation model

A three-layer BP network can be used to complete any n-dimensional to m-dimensional mapping. The number of neurons in the hidden layer $s=\sqrt{n+m}+a$, where n and m are the number of nodes in the input and output layers, respectively. The activation function of the hidden layer neuron is selected as the hyperbolic tangent function, and the function form is:

$$f(x)=\frac{e^{x}-e^{-x}}{e^{x}+e^{-x}} \tag{1}$$

The activation function of the output layer uses the Sigmoid activation function, and the form of the function is:

$$f(x)=\frac{1}{1+e^{-x}} \tag{2}$$

The induced local domain of a certain neuron j in the hidden layer is:

$$v_j(p)=\sum_{i=1}^{n} w_{ij}x_i-\theta_j \tag{3}$$

The induced local domain of a certain neuron k in the output layer is:

$$v_k(p)=\sum_{j=1}^{s} w_{jk}v_j(p)-\theta_k \tag{4}$$

In which n and s are the number of neurons in the input layer and the hidden layer respectively. In engine fault diagnosis, multisensor can be used as integrated neural network. In actual fault diagnosis, information fusion includes local fusion and global fusion, so neural network can also be in series and parallel. In order to find out the main reference that affects the performance, the neural network learning method of artificial intelligence and nonlinear mapping can be used to establish the model of engine parameters and performance evaluation. Each neuron can receive the signal from the upper layer, and after processing, it can output the result to the next layer through a related function. Therefore, a neuron can be regarded as a mathematical function with certain analysis, and a neural network is composed of numerous such networks. The system uses signal acquisition technology, signal processing technology, neural network technology and artificial intelligence expert system to realize the rapid and accurate judgment of engine fault.

RESULTS

Tractor working environment is complex, and noise is the main factor affecting signal fault diagnosis. Therefore, tractor engine fault diagnosis system firstly classifies the original training samples by using dynamic clustering artificial intelligence method, and obtains different groups. Then, the classified samples are trained in the subnet of neural network, and the corresponding weights and thresholds are obtained to form the empirical knowledge base of engine fault diagnosis. Figure 6 shows the fault detection process of tractor engine based on artificial intelligence and big data.

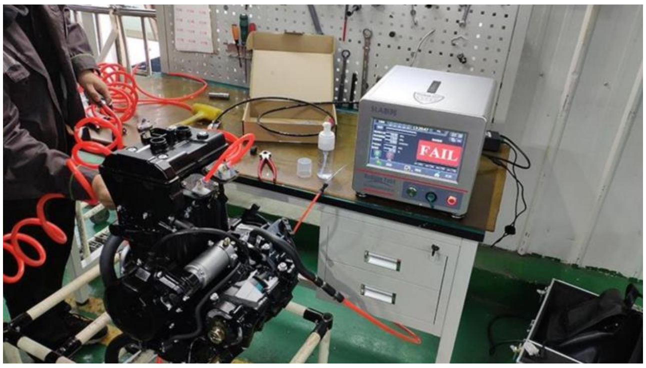

Fig. 6 - Failure detection of tractor engine

The decision algorithm of the confidence weight database is adopted for the judgment of the engine fault type. The basic principle is to assume that the artificial neural network forms a fault vector $G=[G_{1i}, G_{2i,...}, G_{mi}]$. Its confidence weight vector for engine failure is $Z=[Z_{1i}, Z_{2i,...}, Z_{mi}]$., then the parallel combination of subnets is $N_n=[NN_1, NN_{2,...}, NN_m]$., thus forming the fault matrix G and the confidence weight matrix z, and the confidence matrix is assigned to each subnet, namely:

$$G=\begin{bmatrix} g_{11} & g_{12} & \cdots & g_{1m} \\ g_{21} & g_{22} & \cdots & g_{2m} \\ \cdots & & & \\ g_{n1} & g_{n2} & \cdots & g_{nm} \end{bmatrix} \tag{5}$$

$$z=\begin{bmatrix} z_{11} & z_{12} & \cdots & z_{1m} \\ z_{21} & z_{22} & \cdots & g_{2m} \\ \cdots & & & \\ z_{n1} & z_{n2} & \cdots & z_{nm} \end{bmatrix} \tag{6}$$

The fusion output is:

$$Y=G\cdot R \tag{7}$$

Therefore, the probability of occurrence of the i-th fault is:

$$g_i=g_{i1}z_{1i}\hat{+}g_{i2}z_{2i}\hat{+}\ldots\hat{+}g_{in}z_{ni} \tag{8}$$

For the decision fusion of the two sub-networks, the fusion result is:

$$g_i=g_{i1}z_{1i}\hat{+}g_{i2}z_{2i} \tag{9}$$

Since $g_{i1<1}, z_{i1<1}, g_{i1>} g_{max}= g_{i1} z_{1i}$, so we can deduce:

$$g_{i1}>g_{\max}=\max\{g_{i1}z_{1i},g_{i2}z_{2i},\ldots,g_{in}z_{ni}\} \tag{10}$$

The final output result can be expressed as:

$$Y=\max\{g_i\} \tag{11}$$

Or any fusion result g_i that is larger than a certain threshold may fail, so the fault detection of tractor engine can be realized by using this principle.

The neural network of tractor engine fault is trained by gradient method. After 3000 iterations of training, the actual calculated network error will be obtained. The sample training is shown in Table 2.

Table 1

Training results of neural network samples

Fault	Output node				
	1	2	3	4	5
Blocked oil path	-0.015	0.184	-0.005	-0. 028	-0.113
Fuel injector failure	1.036	0.255	0.041	0.017	0.252
Tubing rupture	-0.121	0.788	0.005	0.019	0.211
The flywheel is stuck	-0.033	0.122	0.354	0.011	0.125
Air pump channeling oil	0.028	-0.355	0.003	1.051	-0.552
Piston wear	-0.019	0.327	O.251	-0.004	0.666

The field test is to verify the tractor in the real working environment, test the performance of the tractor engine fault diagnosis system, test the overall performance and reliability of the system, and finally realize the practicability and accuracy of the tractor engine fault diagnosis system. As shown in Figure 7, in the field test, the light will have a certain impact on the LCD display of the engine fault diagnosis system, resulting in the display is not clear, so the time period with weak light in the morning and evening is selected.

Fig. 7 - Schematic diagram of field acceptance experiment

In order to verify the reliability and stability of the intelligent fault monitoring system for new energy tractor engines facing big data, 10 new energy tractor engines with faults were diagnosed and analysed. A fault signal collected from new energy tractor engine is shown in Figure 8.

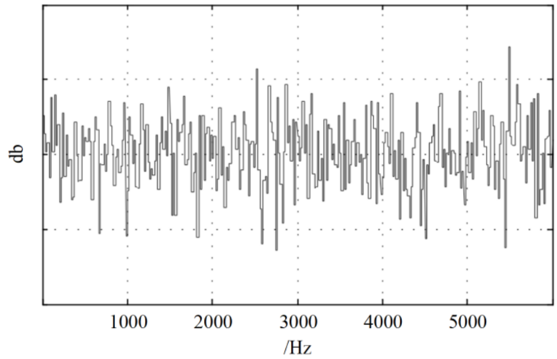

Fig. 8 - The original data of the fault signal

In order to overcome the influence of noise on the experimental results, the artificial intelligence filtering method is used to filter the experimental signals. In the aspect of engine fault signal edge extraction, the wavelet transform has the characteristic of adjustable time-frequency window to approximate any detail part of the signal, and the edge signal and noise are gradually separated by multi-scale. First, the signal is decomposed by two-dimensional wavelet:

$$f(x,y)= f_0(x,y)= f_J(x,y)+\sum_{i=1}^{J} g_j(x,y) \tag{12}$$

f_J is the projection of $f(x,y)$ on space V_J^2 , and:

$$g_j(x,y)=\sum_{k,m}\left[d^1_{j,k,m}\varphi_{j,k}(x)\psi_{j,m}(y)+d^2_{j,k,m}\varphi_{j,k}(x)\psi_{j,m}(y)+d^3_{j,k,m}\varphi_{j,k}(x)\psi_{j,m}(y)\right] \tag{13}$$

$j=1,\ldots J$ is the details in three directions.

Then establish the correlation coefficient $\omega^1_{j,k,m}$ and $d^1_{j,k,m}, d^2_{j,k,m}, d^3_{j,k,m}$ for dynamic comparison, select the three-direction wavelet coefficients to filter out the noise, and then perform edge extraction. After signal processing, the signal shown in Figure 9 is obtained.

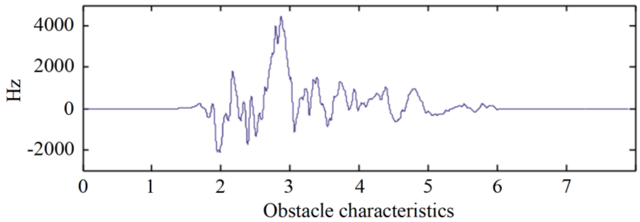

Fig. 9 - Data after fault signal processing

After using neural network algorithm for fault diagnosis, the fault diagnosis results shown in Table 2 are obtained.

Table 2

Fault diagnosis results

Fault	Diagnostic results	Actual results	Accuracy (%)
Blocked oil path	2	2	100
Fuel injector failure	7	5	100
Tubing rupture	3	2	100
The flywheel is stuck	3	3	100
Air pump channeling oil	5	6	100
Piston wear	3	2	100

It can be seen from the table that the intelligent fault monitoring system for new energy tractor engine facing big data can accurately diagnose faults, and the diagnosis results are consistent with the actual results, which can provide reference for engine fault diagnosis and maintenance personnel. Wear and oil leakage occurs at the joint of the convex head at both ends of tractor high-pressure oil pipe, fuel injector and oil outlet valve. A round copper skin can be cut from the waste gas cylinder pad, and a small hole can be pierced in the middle for grinding and sliding, so that the urgent need can be solved by placing it between convex pits. In this experiment, artificial intelligence method was used to process the acquisition results, and the curve of diagnosis results at high resolution was obtained. The test results show that the panel of the engine fault monitoring system can display the result curve of tractor engine fault diagnosis in real time, which verifies the feasibility and correctness of the fault diagnosis monitoring algorithm. Using artificial intelligence diagnosis method can not only effectively improve the accuracy of the system, but also make the diagnosis system respond more quickly. In order to solve the problem that the engine oil pump can't pump oil at the first start of the locomotive after overhaul, the oil filter or oil outlet pipe should be removed, and then the oil injector should be used to fill the oil from the oil outlet hole of the locomotive body. The oil filter or oil pipe leading to the oil indicator should be installed immediately, and the oil will pump up after starting. From the whole experiment, it is found that the tractor engine fault diagnosis system can achieve stable working state in the whole working cycle, and can still maintain normal working stability in the harsh field environment such as exposure, vibration and dust.

CONCLUSIONS

Tractors are widely used. In agricultural production, tractors and farm tools can complete farmland operations such as ploughing, raking, sowing, intertillage and harvesting. In addition, tractors can be used for farmland capital construction such as ditching, bulldozing and levelling, and can also be used for agricultural transportation, as well as fixed operations such as pumping threshing and processing of agricultural and sideline products. In agricultural production, increasing the number of agricultural tractors and improving their quality, and strengthening the management and maintenance of tractors during operation are conducive to the further development of agricultural mechanization in China.

In order to overcome the technical difficulties of tractor engine fault detection under strong noise background and improve the accuracy and detection efficiency of engine fault diagnosis, an artificial intelligence fault detection method based on neural network is proposed, and a tractor engine vibration signal acquisition and fault analysis and processing system is constructed. Taking the engine of new energy tractor as the research object, the principle and monitoring method of engine intelligent fault diagnosis are introduced. Then, based on big data and neural network technology, the engine intelligent fault monitoring system of new energy tractor for big data is designed. Using artificial intelligence diagnosis method can not only effectively improve the accuracy of the system, but also the response of the diagnosis system is faster and the adaptive ability to the environment is stronger. The system can effectively diagnose the engine fault of new energy tractor, and the diagnosis accuracy is high, which can provide reference for engine fault diagnosis and maintenance personnel. The increase of tractor quantity, the improvement of tractor quality and the reasonable use, maintenance and management are of great significance to the realization of Agricultural Mechanization in China.

REFERENCES

[1] Chen Y. M., Song H. Y., Zhao R., Su Q., (2021), CFD-based simulation and model verification of peaches forced air cooling on different air supply temperatures. *INMATEH Agricultural Engineering*, Vol. 63, Issue 1, pp. 61-72. Romania. https://doi.org/10.35633/inmateh-63-06

[2] Cheng R., Jin Y., (2018), A social learning particle swarm optimization algorithm for scalable optimization. *Information Sciences,* Vol. 291, Issue 6, pp. 43-60. Netherlands;

[3] Dong J. H., Li W., Yang Z. R., (2018), Analysis and optimization of torsional vibration of 3-cylinder engine crankshaft system based on virtual prototype. *Automotive Engine*, Vol. 235, Issue 02, pp. 64-70. United Kingdom;

[4] Martínez-Moreno F., Giraldo P., del Mar Cátedra M., Ruiz M., (2021), Evaluation of leaf rust resistance in the Spanish core collection of tetraploid wheat landraces and association with ecogeographical variables. *MDPI (Agriculture),* Vol. 11, Issue 4, pp. 277. Switzerland. https://doi.org/10.3390/agriculture11040277

[5] Gultyaeva E., Shaydayuk E., Gannibal P., (2021), Leaf Rust Resistance Genes in Wheat Cultivars Registered in Russia and Their Influence on Adaptation Processes in Pathogen Populations. *MDPI.* Vol. 11, Issue 4, pp. 319. Switzerland;

[6] Gross G., Hoffmann A., (2018), Therapeutic strategies for tendon healing based on novel biomaterials, factors and cells. *Pathobiology,* Vol. 80, Issue 4, pp. 203-210. Switzerland;

[7] Wang Yingbo, Li Hongwen, Wang Qingjie, He Jin, Lu Caiyun, Liu Peng, Yang Qinglu, (2021), Experiment and parameters optimization of seed distributor of mechanical wheat shooting seed-metering device. *INMATEH Agricultural Engineering*, Vol. 63, Issue 001, pp. 29-40. Romania. https://doi.org/10.35633/inmateh-63-03

[8] Jafari M. J., Pouyakian M., Hanifi S. M., (2020), Reliability evaluation of fire alarm systems using dynamic Bayesian networks and fuzzy fault tree analysis. *Journal of Loss Prevention in the Process Industries*, Issue 67, pp. 104229. Netherlands;

[9] Jensen R., (2021), The Restless and Relentless Mind of Wes Jackson: Searching for Sustainability. University Press of Kansas. *JSTOR*. USA;

[10] Jhih Y. C, Hsin C. C., Chih W. C., Kai M. Y., (2021), Relationship between Antioxidant Components and Oxidative Stability of Peanut Oils as Affected by Roasting Temperatures. *MDPI (Agriculture)*, Vol. 11, Issue 004, pp. 300. Switzerland. doi.org/10.3390/agriculture11040300

[11] Nouiri M., Bekrar A., Jemai A., (2018). An effective and distributed particle swarm optimization algorithm for flexible job-shop scheduling problem. *Journal of Intelligent Manufacturing,* Vol. 2, Issue 3, pp. 11-13. Netherlands;

[12] Qiuju X., Fanyi L., Ming J. Y., Jun L., Shang H. Y., Shou Y. X., (2021), DEM simulation and evaluation of well cellar making performance of opener with large socket. *Machine Design*, Vol. 63, Issue 01, pp. 41-50. Romania. https://doi.org/10.35633/inmateh-63-04

[13] Rulli F., Barbato A., Fontanesi S., (2021), Large eddy simulation analysis of the turbulent flow in an optically accessible internal combustion engine using the overset mesh technique. *International Journal of Engine Research*, Vol. 22, Issue 5, pp. 1440-1456. England;

[14] Wei W., Yuan J. G., Xue W. B., (2021), Detection system for feeding quantity of mobile straw granulator based on power of screw conveyor. *INMATEH Agricultural Engineering*, Vol. 63, Issue 1, pp. 09-18. Romania;

[15] Yu L. C., Meng Z., Z L., Yu B. L., Li L. Y., Qiang J. P., Xiang Y., (2021), Design and experiment of seed agitator for vertical disk seed metering device. *INMATEH Agricultural Engineering*, Vol. 63, Issue 1, pp. 177-186. Romania. https://doi.org/10.35633/inmateh-63-01

INTEGRATION OF SUBSURFACE IRRIGATION AND ORGANIC MULCHING WITH DEFICIT IRRIGATION TO INCREASE WATER USE EFFICIENCY OF DRIP IRRIGATION

دمج الرى تحت السطحي والتغطية العضوية مع الرى الناقص لزيادة كفاءة استخدام المياه للرى بالتنقيط

Moataz Elnemr

Department of Agricultural Engineering, Faculty of Agriculture, Damietta University/ Egypt
Tel: +201101007863; E-mail: moknemr@agr.du.edu.eg

DOI: https://doi.org/10.35633/inmateh-64-21

Keywords: *deficit irrigation, subsurface drip irrigation, rice straw mulching, water use efficiency, tomato yield.*

ABSTRACT

This study aimed to integrate the ability of organic mulching (rice straw) and subsurface irrigation with deficit irrigation to save soil moisture content (SMC) and increase water use efficiency (WUE). A field experiment was carried out during 2019 on tomato crop in sandy soil. The variables included four levels of irrigation namely 70, 80, 90, and 100% of crop evapotranspiration (ET_c) with three irrigation techniques which were subsurface drip irrigation (SSD), mulched surface drip irrigation (MD), and mulched subsurface drip irrigation (MSSD). The treatments of MSSD showed earlier maturity of tomato crop and longer picking period if compared to MD and SSD treatments. MSSD showed higher ability to save (SMC) than other irrigation techniques. Reduction of applied water from 100 to 70% ET_c led to a decrease in tomato yield by 23.32% at MSSD compared to 28.47%, and 26.23% for MD, and SSD respectively. The highest WUE was at MSSD70 with 5.92 kg/m^3 while the least was 4.21 kg/m^3 with SSD100. The highest benefit/cost ratio was 9.03 with the treatment SSD70 while the highest profit of water unit was 2.19 US\$/m^3 with MSSD70. MSSD can be used with 90% of ET_c without any significant difference in tomato crop while it can be used with 70% ET_c to obtain higher WUE. The study recommended integrating rice straw mulching and subsurface drip irrigation with deficit irrigation as a strategy to save irrigation water and obtain the maximum possible benefits of water unit whether related to tomato yield or its revenue.

ملخص

تهدف هذه الدراسة الى دمج قدرة التغطية العضوية (قش الأرز) والرى التحت سطحي مع الرى الناقص في المحافظة على المحتوى الرطوبي للتربة لزيادة كفاءة استخدام المياه. تم اجراء تجربة حقلية خلال عام 2019 على محصول الطماطم في تربة رملية. شملت المتغيرات أربعة مستويات من مياه الرى وهى 90،80،70، 100% من الاستهلاك المائي للمحصول باستخدام ثلاث تقنيات للرى وهى الرى بالتنقيط التحت سطحي والرى بالتنقيط السطحي مع التغطية بالإضافة للرى التحت سطحي المغطى. أظهرت معاملات الرى بالتنقيط التحت سطحي المغطى نمو مبكر لمحصول الطماطم وفترات حصاد أطول مقارنة بمعاملات الرى بالتنقيط السطحي المغطى والرى التحت سطحي. أظهر الرى بالتنقيط التحت سطحي المغطى قدرة أكبر على الحفاظ على المحتوى الرطوبي للتربة مقارنة بالتقنيتين الأخريين. تخفيض مياه الرى من 100% الى 70% من الاستهلاك المائي أدى الى نقص محصول الطماطم بنسب 23.32، 28.47، 26.23% من أعلى قيمة انتاجية تم الحصول عليها لكل من معاملات الرى تحت سطحي المغطى ، والسطحي المغطى، والرى التحت سطحي على الترتيب. بلغت أعلى قيمة لكفاءة استخدام المياه 5.92 كج/م^3 للرى التحت سطحي المغطى عند النسبة 70% بينما بلغت أقل قيمة لكفاءة استهلاك المياه 4.21 كج/م^3 للرى التحت سطحي مع النسبة 100% من الاحتياجات المائية للمحصول. بلغت أعلى نسبة عائد الى التكاليف 9.03 لمعاملة الرى تحت سطحي المغطى مع 70% من الاحتياجات المائية وحققت نفس المعاملة أقصى ربح من وحدة المياه وبلغ 2.19 دولار أمريكي /م^3. يمكن استخدام الرى تحت سطحي المغطى بقش الأرز مع النسبة 90% من الاستهلاك المائي للمحصول دون انخفاض محصول الطماطم بشكل معنوي ويمكن استخدام نفس التقنية مع النسبة 70% للخصول على كفاءة أعلى لاستخدام المياه. أوصت الدراسة بدمج التغطية بقش الأرز مع الرى التحت سطحي والرى الناقص كاستراتيجية للحفاظ على مياه الرى وتحقيق أقصى عائد من وحدة المياه سواء لإنتاج محصول الطماطم أو لتحقيق أفضل ربح مادي.

INTRODUCTION

Agricultural activities which are necessary to assure human needs withdraw about 70-95% of fresh water *(Evans and Sadler, 2008; FAO, 2012)*. Irrigated agriculture extends over 270 Mha and provides 40 to 45% of the world needs of food and fibers *(Douh and Boujelben, 2011)*. It is necessary to apply all possible strategies and techniques to achieve sustainability of water resources and agricultural production (*Morison et al., 2008*). Drip irrigation system as a modern irrigation system has the feature of saving irrigation water and obtaining higher yield which means higher water use efficiency *(Aujla et al., 2007; Ibragimov et al., 2007)*. In the way to maximize water use efficiency of drip irrigated crops; it is logic to think about how to reduce irrigation water loss to apply least possible amount of irrigation water in parallel with obtaining the maximum possible crop yield.

Deficit irrigation can appear as an acceptable solution to save irrigation water and obtain higher water use efficiency especially when the water resources are limited *(Kirda et al., 1999)*. On the other hand, water deficiency is an adverse aspect for crop production *(Wu et al., 2008)*. The studies made by (*Romero et al., 2004; Al-Omrana et al., 2005; García–Tejero et al, 2011; Çolaka et al., 2018; Mele, 2019; Abdelkhalik et al., 2020; Mattar et al., 2020)* proved that deficit irrigation leads to increase water use efficiency despite the reduction in crop yield if compared to full irrigation. Deficit irrigation should be regulated and well managed to minimize the reduction of crop productivity as possible. Using deficit irrigation requires minimizing the irrigation water loss especially evaporation from soil surface to ensure that the plant obtains greatest potential benefit from applied water.

Subsurface drip irrigation has the advantage of saving water if compared to surface drip irrigation *(Lamm and Trooien, 2003; Patel and Rajput, 2007; Badr et al., 2010; Abed EL-Hamied et al., 2017; Umair et al., 2019)*. The use of subsurface drip irrigation supports crop production process with many advantages like applying water and nutrients in the most sensitive part of the root zone, weed control, and dry soil surface which results in higher yield with minimal water loss *(Encisco et al., 2005; Lamm and Camp, 2007; Patel and Rajput, 2007; Patel and Rajput, 2008; Selim et al., 2009; Thompson et al., 2009)*.

Surface mulching whether using organic or inorganic materials gives the advantages of keeping soil moisture, reducing salts accumulation, and controlling weeds. Organic mulch has the ability to control soil temperature, improve physical and chemical properties of the soil, and enhance soil biological activity *(Deng et al., 2006; Ramakrishna et al., 2006)* if compared to inorganic mulch *(Al-Wahaibi et al., 2007; Al-Rawahy et al., 2011)*.

Rice straw has the features of organic mulch beside its availability and low-cost in the local Egyptian agricultural environment, which causes avoidance of profits reduction resulted from the increase of total farming costs. (*Abo-Ogiala and Khalafallah, 2019)* mentioned that rice straw mulch could save 50% of water requirements of grapes because of its role in saving soil moisture. (*Abdel-Raouf and Ragab, 2018)* studied the effect of using deficit irrigation and rice straw mulching with partial root drying strategy for maize crop irrigated with drip irrigation system. Their results indicated that rice straw mulching helped to obtain higher water use with deficit irrigation due to the ability of retaining soil moisture and reducing evaporation loss.

Integration of subsurface irrigation and organic mulching with deficit irrigation is expected to increase the benefits of saving irrigation water for each technique more than if they are used individually.

Applying this proposed integration to a highly drought-sensitive crop like tomato *(Shao et al., 2015; Cui et al., 2020)* is expected to demonstrate the effect of using less amounts of irrigation water on crop yield and water use efficiency clearly. The aim of this study is using deficit irrigation and integrating it with subsurface irrigation and rice straw mulching to investigate for which level they can reduce the effect of water stress on tomato crop yield in order to obtain higher water use efficiency with drip irrigation system.

MATERIALS AND METHODS

Description of the study area and agronomic practices

Field experiment was carried out in a private farm (30.32^{o}N, 30.63^{o}E) in Khataba village, Menoufia governorate, Egypt under sandy soil conditions. Table 1 shows the physical properties of the experiment soil. Tomato crop (super strain, B) was cultivated during the summer season of the year 2019. Tomato seedlings were transplanted in the middle of February and then moved to the permanent soil on April 5th.

Table 1

Some physical properties of the experiment soil

Depth, [cm]	Particle size distribution, [%]			Texture	Field capacity, [%]	Permanent wilting point, [%]
	Sand	Silt	Clay			
0-15	89.94	0.45	9.61	Sandy	9.8	4.8
15-30	89.71	0.45	9.84	Sandy	10.2	5.0
30-45	88.51	3.24	8.28	Sandy	10.9	5.1
45-60	87.82	4.22	7.96	Sandy	11.5	5.5

Table 2 shows chemical characteristics of irrigation water while chemical properties of the experiment soil are listed in Table 3. The experiment area was ploughed two times before planting; each of them was perpendicular to the direction of the other. Organic manure and super phosphate were added to the soil during ploughing in rates of 72 m^3/ha, and 960 kg/ha respectively. Application of fertilizers to the soil was made through fertigation technique by adding fertilizers with required amounts to the fertilizers tank of the farm which was connected to the irrigation network. 720 kg/ha of ammonia sulphate and potassium sulphate were added in three batches with irrigation water starting from the first irrigation process with 20 days interval. The level of soil surface was completely horizontal with no slope.

Table 2

Chemical properties of irrigation water

EC, [dS/m]	Cations, [m_{eq}/l]					Anions, [m_{eq}/l]		
	pH	Na	K	Ca	Mg	HCo_3	Cl	SO_4
0.41	7.5	2.3	0.3	2.3	2.1	0.6	3.9	2.4

Table 3

Some Chemical properties of experiment soil

EC, [dS/m]	pH	Organic matter, [%]	CaCo3, [%]
4.2	7.68	0.69	27

Experimental design and layout

The variables of this study included four levels of irrigation (*IL*) namely 100, 90, 80, and 70% of crop evapotranspiration *(ET_c)* and three drip irrigation techniques (*IRT*) which were subsurface drip irrigation *(SSD)*, mulched surface drip irrigation (*MD*), and mulched subsurface drip irrigation *(MSSD)*. The statistical design was split-plot. Drip irrigation technique was the main plot while the irrigation level was sub-plot with three replicates for each treatment. Statistical analysis and Duncan's means comparison test was carried out using Cropstat 7.0 and MstatC computer software, respectively.

Dimensions of the experiment area were 70m length and 50m width. The layout of the experiment was as shown in Figure 1.

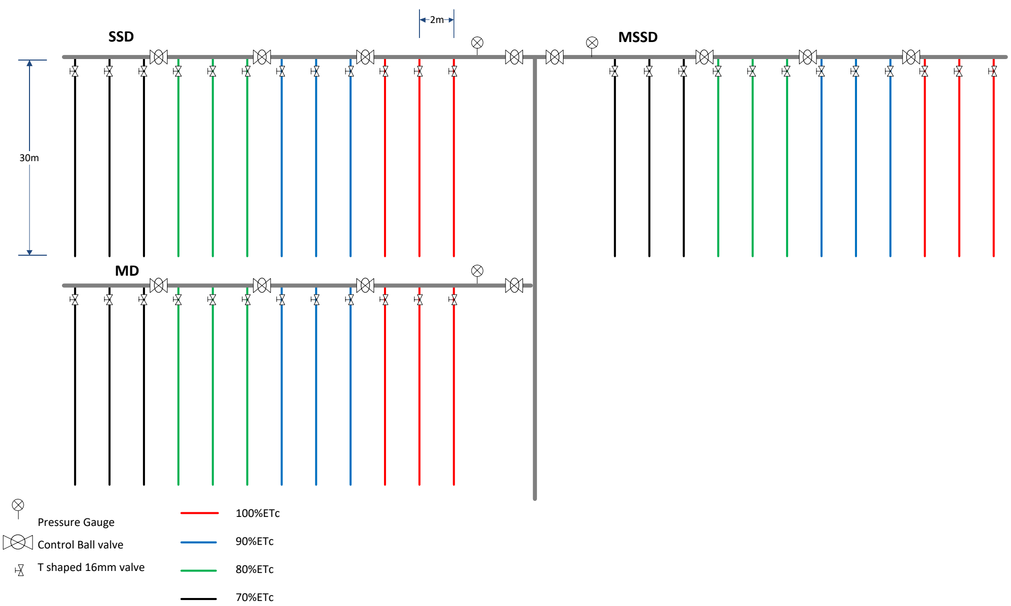

Fig. 1– Schematic drawing for the layout of experiment and irrigation network

Manifolds were PVC pipes with 63mm inner diameter. Polyethylene laterals 30m long and 16mm inner diameter had built-in emitters with 50 cm spacing. Laterals spacing was 2m. Subsurface drip irrigation laterals were laid manually at 20 cm depth from soil surface.

The beginning of each lateral was provided with T-shaped 16mm plastic valve and the end of each lateral was closed by an end cap. Rice straw covered the whole length of mulched treatments' laterals with a rate of 0.3 kg/m^2. The operating pressure of the irrigation network was 200 kPa and the irrigation frequency was every 72 hours. Irrigation treatments started after moving seedlings to the permanent soil.

Crop water requirement

Crop water requirement was calculated basing on climate data collected from Tahrir meteorological station (30.70ºN, 30.65ºE) which covers the experiment area. Table 4 shows the used climate data during the growing season. FAO Cropwat 8.0 computer program was used to calculate the reference evapotranspiration *(ET_o)*. Crop evapotranspiration *(ET_c)* was calculated according to Equation 1.

$$ET_c = ET_\circ . K_c \tag{1}$$

Where: K_c is crop coefficient.

Crop coefficient values of tomato were 0.6, 1.15, and 1.95 for initial, middle, and end of growing season respectively *(FAO, 1998).*

Table 4

Climate data and reference evapotranspiration (ET_o) values

	April	May	June	July	August
Minimum Temperature, [ºC]	11.40	14.10	17.50	19.50	19.40
Maximum Temperature, [ºC]	28.20	31.80	34.60	34.70	34.60
Sunshine hours, [h/day]	8.65	9.80	10.83	10.59	10.12
Wind speed, [m/s]	2.59	2.50	2.20	1.09	1.09
Solar radiation, [MJ/m^2/day]	21.67	24.48	26.2	25.69	24.10
Relative humidity, [%]	56.19	53.57	55.75	63.55	65.67
Precipitation, [mm/month]	2.00	0.00	0.00	0.00	0.00
ET_o, [mm/day]	4.42	5.39	5.94	5.65	5.26

Soil moisture content variation

The main purpose of measuring soil moisture content was to investigate the ability of each treatment to reduce soil moisture loss which is expected to help in reducing the possible negative effect of deficit irrigation on crop production. Soil moisture content was measured at 0, 12, 24, and 48 hours after irrigation. 3 cm diameter 4.5 cm height gypsum blocks were made using anti saline gypsum formula to measure the soil moisture content. Every gypsum block had two shielded steel cables 70 cm length which were immersed vertically in the blocks. 6 gypsum blocks were immersed horizontally under emission point with 10cm vertical spacing to measure the vertical distribution of soil moisture through 60 cm depth of the root zone as shown in Figure 2. Every cable had a label mentioning its measuring depth. The electric resistance between the two cables was used to describe the soil moisture content. The average of the readings of the six gypsum blocks described the soil moisture content of the root zone. Measurement of the soil moisture content was in one position in the middle of one lateral from each treatment

A calibration process has been made to detect the soil moisture content value facing each electric resistance. Twelve soil samples with a volume of 200 ml for each one were collected from the experiment area, and wetted with different amounts of water to make a variation in moisture content. The electric resistance reading was recorded and the soil moisture content was calculated using gravitational method. All the used gypsum blocks have been made with the same dimensions and materials.

Fig. 2– Soil moisture measurement using gypsum blocks

Crop yield and water use efficiency

Tomato crop harvesting of each treatment started when fruits reached the acceptable marketing size and color. The average yield of the three replicates described the total crop yield. Water use efficiency (WUE) described the tomato crop yield per volumetric unit of irrigation water. Water use efficiency was calculated referring to *Rodrigues and Pereira, 2009* as follows:

$$WUE = \frac{Y}{W_A} \tag{2}$$

Where: WUE is water use efficiency, [kg/m^3];
Y= Crop yield, [kg/ha];
W_A= Amount of applied water, [m^3/ha].

Profits

Total annual costs of agronomic practices and network operation were calculated referring to *Buchanan and cross, 2002*. The total costs were the summation of fixed costs and total variable costs. Fixed costs included annual depreciation of the irrigation network components, investment costs, and taxes and insurance. Scrap value was 10% of the initial cost of the network components. Annual interest ratio was 7.75% referring to the data of Egyptian Central Bank in 2019. Taxes and insurance was 2% of the initial cost.

Variable costs included the cost of repairs and maintenance, energy, labor, and any additive costs. Repairs and maintenance cost was considered to be equal to the total depreciation cost. The source of energy was diesel fuel with a price of 0.41 US$/l. Labor cost was 6US$/person/day with 8 hours daily working duration.

Additive costs included seeds and seedlings, rice straw, chemicals, agronomic practices and manual harvesting. Gross revenue of tomato crop was calculated to determine the benefit–cost (B/C) ratio. Total profits were divided by total applied water of each treatment to investigate the revenue of each unit of water volume. Referring to the Egyptian market and conversion price of US$ to Egyptian pound, the price of selling tomato from the farm after finishing harvesting was 0.37 US$/kg in average during the harvesting period.

RESULTS AND DISCUSSION

Growing season duration

Combining rice straw mulching and subsurface drip irrigation led to shorten the maturity period followed by mulched drip irrigation and subsurface drip irrigation, respectively. Data listed in Table 5 showed the total number of days of growing season including the time period after planting till reaching maturity stage (D_{mat}) and the duration of harvesting period (P_{har}). The results showed that rice straw mulching had an effect on accelerating the maturity of tomato fruit. Both mulched techniques had fewer days till reaching maturity if compared to subsurface drip irrigation treatments. The longest maturity period was at the treatment *SSD70* while the shortest was at *MSSD100* and *MSSD90* which was 56 days. The less amount of applied water, the longer maturity period observed.

These results might refer to the additional feature of rice straw mulching to make a modification to soil temperature beside saving water especially in early stage of tomato growing *(Yang et al., 2006; Abd El-Kader et al., 2010; Al-Rawahy et al., 2011)*. The treatment *MSSD100* showed the longest harvesting period by 98 days while the treatment *SSD70* had the shortest harvesting period by 52 days.

Table 5

Number of days required to reach maturity and the total duration of harvesting period and growing season

IL, [% of ET_c]	SSD			MD			MSSD		
	D_{mat}	Total	P_{har}	D_{mat}	Total	P_{har}	D_{mat}	Total	P_{har}
70	74	126	52	68	130	62	61	131	70
80	71	126	53	66	131	75	58	135	77
90	67	138	71	62	142	80	56	147	91
100	65	148	83	58	150	92	56	154	98

Soil moisture content variation

The integration between rice straw mulching and subsurface drip irrigation showed the highest ability to save soil moisture content and reduce its loss. The average values of soil moisture content during 48 hours revealed that reducing amount of applied water will reduce the loss of soil moisture. These results were in agreement with the results of (*Wang et al., 2012*). Figures 3 and 4 showed the variation of soil moisture content for different *IRT*s and *IL*s. There was a variation on initial soil moisture content after irrigation directly with the same amounts of applied water. This was due to a little variation in soil moisture content before irrigation despite the precautions taken to make this variation at minimum value. Any way this measurement was to evaluate the ability of each technique on saving moisture not to detect the moisture value itself. For subsurface drip irrigation; the rate of moisture loss in 100% amount was greater than other amounts. After 48 hours of irrigation, the values of soil moisture content were very close at all irrigation levels. The soil moisture content values of mulched drip irrigation indicated that the loss of soil moisture was greater than subsurface drip irrigation. Despite the ability of rice straw mulching to save water subsurface drip irrigation showed better ability to save irrigation water if compared to rice straw mulching because of the minimal evaporation loss from soil surface *(Abo-Ogiala and Khalafallah, 2019)*

Combining rice straw mulching and subsurface drip irrigation led to increase the benefits of the two techniques for saving water. In the *MSSD* treatments, the loss of moisture content at all levels of irrigation was less than the two other irrigation techniques. The soil moisture content of the treatment *MSSD70* was stable and nearly constant after 12 hours of irrigation till 48 hours. The minimum variation in soil moisture content was at the treatment MSSD70 while the maximum recorded variation was at the treatment MD100.

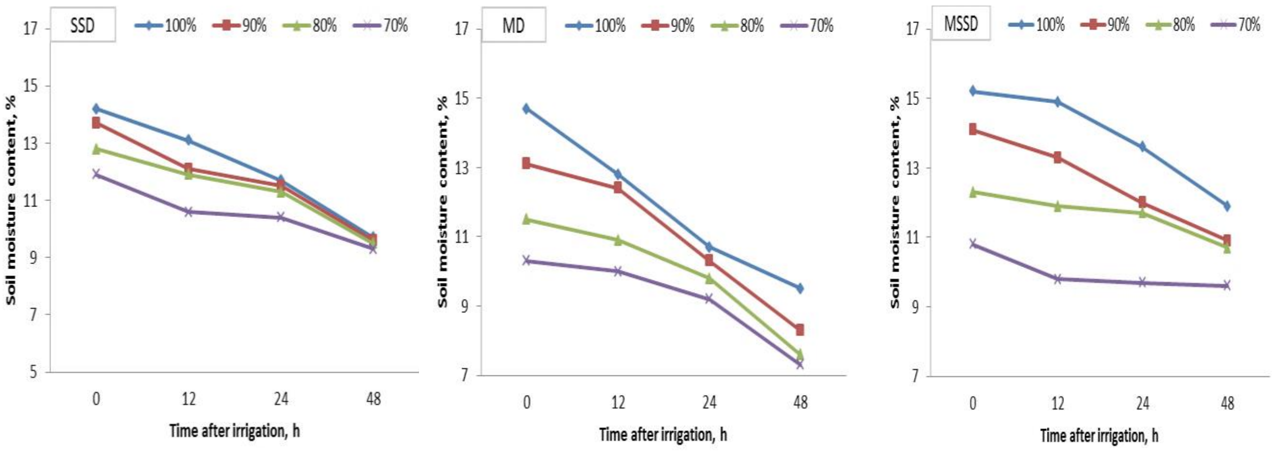

a) b) c)

Fig. 3– Soil moisture content at different irrigation techniques and irrigation levels

a. Subsurface drip irrigation; b. Mulched drip irrigation; c. Mulched subsurface drip irrigation

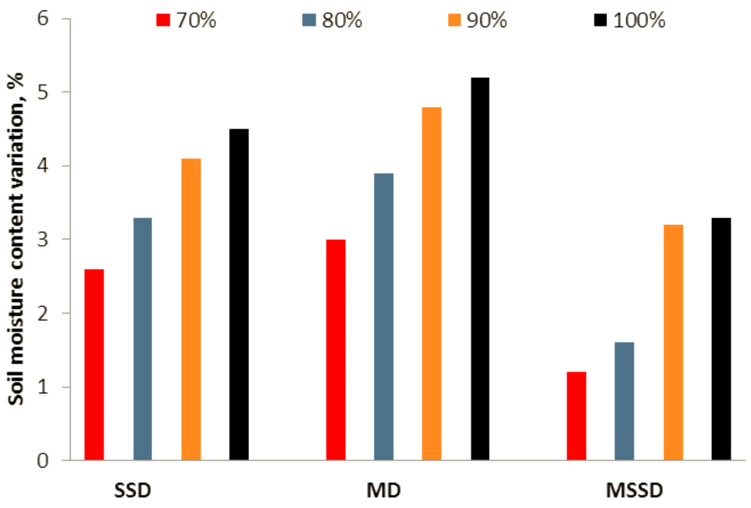

Fig. 4 – Comparison between soil moisture variation with different irrigation techniques and amounts of applied water after 48 hours of irrigation

Crop yield

The statistical analysis of the crop yield data showed that both of irrigation technique and irrigation level had a highly significant effect on tomato yield as shown in Table 6. The interaction between the two previously mentioned factors had no significant effect on crop yield. The non-significant effect of the interaction between irrigation technique and amount of applied water might be due to the effect of all proposed *IRT*s on reducing deficit irrigation impact on crop yield because of their ability to save moisture content.

Table 6

Analysis of variance for the effect of experimental variables on tomato crop yield.

Source of variation	DF	Sum of squares	Mean squares	F ratio
IRT	2	320.496	160.248	26.04**
IL	3	941.216	313.739	50.98**
IRT*IL	6	20.596	3.433	0.56 ns
Residuals	24	147.691	6.154	

***= Significant at 1% level; ns= not significant*

Tomato crop yield values listed in Table 7 clarified that tomato yield was directly proportional to the amount of applied water which was in agreement with the study of *Al-Ghobari and Deweidar (2018*) on tomato crop. The highest crop yield was 56.22 Mg/ha at *MSSD100* while the least obtained crop yield was 36.92 Mg/ha at *SSD70*. For all amounts of applied water, mulched subsurface drip irrigation gave the highest crop yield followed by mulched surface drip irrigation and the least values were with subsurface drip irrigation. Subsurface drip irrigation showed the ability of saving soil moisture content more than rice straw mulching; but rice straw mulching treatments recorded higher yield values because of the additive feature of modifying soil temperature. Reduction in the mount of applied water from 100 to 70% ET_c led to decrease the tomato yield by 23.32%, 28.47%, and 26.23% of the highest obtained yield with *MSSD*, *MD*, and *SSD* respectively. There was no significant difference between the treatments *MSSD100* and *MSSD90* while there was a significant difference between the same amounts of applied water with *MD* and *SSD*. This might clarify the effect of combining subsurface drip irrigation and rice straw mulching on reducing the effect of deficit irrigation on tomato yield when compared to using subsurface drip irrigation and mulched surface drip irrigation individually.

Table 7

Tomato crop yield, [Mg/ha] for the different irrigation techniques and levels

***IL*, [% of ET$_c$]**	**SSD**	**MD**	**MSSD**
70	36.92 g	38.13 g	43.11 ef
80	39.16 fg	44.95 de	48.76 cd
90	45.14 de	48.25 cd	52.38 abc
100	50.05 bc	53.31 ab	56.22 a

Least significant difference (L.S.D) at 5% level= 4.180

Amount of applied water and water use efficiency

Table 8 showed total amounts of applied water during growing season of each treatment and the values of WUE. The largest amount of applied water was 12405.72 m^3/ha for the treatment *MSSD100* while the least amount was 6982.92 m^3/ha for the treatment *SSD*70. The variation between same irrigation levels with different *IRT*s was because of the previously mentioned difference in growing season duration between treatments.

Table 8

Amount of applied water, [m^3/ha] and Water use efficiency, [kg/m^3] for different treatments

IL, [% of ET_c]	SSD		MD		MSSD	
	W_A	WUE	W_A	WUE	W_A	WUE
70	6982.92	5.29 bcd	7225.93	5.28 bcd	7286.69	5.92 a
80	7980.48	4.91 de	8327.64	5.40 bc	8466.50	5.76 ab
90	9915.37	4.55 efg	10227.82	4.72 ef	10618.37	4.93 cde
100	11884.98	4.21 g	12145.35	4.39 fg	12405.72	4.53 efg

Least significant difference (L.S.D) at 5% level= 0.482

The highest water use efficiency was at *MSSD70* while the least was at *SSD100*. Deficit irrigation led to increase WUE for all treatments (*Abd El-Mageed and Semida, 2015; Zhang et al., 2017*). The only exception for this was the treatment *MD80* which gave higher WUE than *MD70* because of the significant difference between crop yield values of the previously mentioned treatments and lower water consumption difference if compared to the consumed water of the same two percentages with the other two irrigation techniques. Reducing amount of applied water from 100 to 70% ET_c led to increase water use efficiency by 30.68, 20.27, and 25.65% of the WUE value at 100% ET_c amount for *MSSD*, *MD*, and *SSD* respectively which recorded the least value of WUE at all *IRT*s. There are research evidences about the ability of deficit irrigation to show higher water use efficiency values, especially if the moisture stress resulting from the deficit is not so severe (*Igbadun et al., 2006; Saad et al., 2018*). The question appeared here which irrigation technique helped to get the benefits of deficit irrigation for increasing WUE. *MSSD* showed higher ability to get the best benefit of unit of water if compared to *MD* and *SSD*. This feature may help to use deficit irrigation in arid areas and all cases of limited water resources when saving water is more important than the obtained yield as recommended by *García–Tejero et al., (2011*).

There was no significant difference between the WUE values of the treatments *MSSD70*, and *MSSD80* which had the highest value of WUE. There was no significant difference between WUE values for the other two irrigation techniques with the same amount of applied water. This result clarified the ability of the three *IRT*s to increase water use efficiency with deficit irrigation by keeping the reduction in tomato crop yield at minimum possible level with a clear distinction for the integration between subsurface and rice straw mulching with deficit irrigation.

Table 9 showed the analysis of variance for the effect of different *IRTs* and *ILs* on water use efficiency. Both of irrigation technique and amount of applied water had a highly significant effect on water use efficiency. Despite the clear variation in amounts of applied water for different treatments but the interaction between the *IRT* and IL did not show a significant effect on water use efficiency. This might also clarify the role of the experimental *IRTs* in reducing the negative effect of water stress on tomato crop yield.

Table 9

Analysis of variance of the effect of experimental variables on water use efficiency

Source of variation	DF	Sum of squares	Mean squares	F ratio
IRT	2	1.82	0.91	11.13**
IL	3	7.44	2.48	30.29**
IRT*IL	6	0.46	0.076	0.93 ns
Residuals	24	1.96	0.082	

***= Significant at 1% level; ns= not significant*

Profits

The main differences in costs between all treatments were due to the costs of energy, labor, and mulching. For all irrigation techniques, the total costs followed a descending order with the amounts 100, 90, 80, and 70% ET_c respectively, as shown in Table 10. This was due to the longer operation time period which increased energy consumption.

Total costs of rice straw mulched drip irrigation were higher than the treatments of subsurface drip irrigation. This is due to the additional costs of mulching material and longer growing season which needed more energy and labor (*Tiwari et al., 2003*). The treatments of MSSD had the highest costs when compared to the corresponding treatments at both *SSD* and *MD*. The maximum benefit was *20801.4* US$/ha for the treatment *MSSD100* while the least one was 13660.4 US$/ha for the treatment SSD70. The highest B/C ratio was 9.03 for the treatment SSD80 while the least one was 7.91 for the treatment MD70. Despite the higher tomato yield of *MSSD* compared to *MD* and *SSD*, it did not record the highest B/C ratio. This was mainly due to the costs of burying drip laterals, rice straw mulching, longer season which meant higher costs for energy and harvesting labor.

The maximum B/C ratio for *MSSD*, *MD*, and *SSD* were at the percentages 80, 90, and 80% ET_c respectively. The previous result pointed out to the ability of the three techniques to be profitably integrated with deficit irrigation regardless the different recommended percentage of water stress for each one. The reduction in the amount of applied water from 100 to 70%ET_c led to decrease the benefits of *MSSD*, *MD*, and *SSD* by 23.32%, 28.47%, and 26.23% of maximum benefit at each irrigation technique respectively. The less difference in benefits at *MSSD* referred to the less difference in crop yield with this irrigation technique. The profits of water unit pointed out that the maximum obtained profit of water unit was 2.19 US$/m3 for the treatment *MSSD70* while the least one was 1.56 US$/m^3 for *SSD100*. The maximum water profit for *MD* was 2.0 US$/m^3 with 80% ET_c ratio while it was 1.96 US$/m^3 for *SSD* with 70% ET_c ratio. This also confirmed the ability of the three techniques to maximize the profits of water unit when implementing deficit irrigation with a rational advantage for the combination between rice straw mulching and subsurface drip irrigation to be integrated with deficit irrigation.

Table 10

Total annual costs and benefits of tomato crop during the growing season, [US$/ha]

	SSD				***MD***				***MSSD***			
	70	***80***	***90***	***100***	***70***	***80***	***90***	***100***	***70***	***80***	***90***	***100***
Total fixed costs	360.26	360.26	360.26	360.26	360.26	360.26	360.26	360.26	360.26	360.26	360.26	360.26
Energy	14.92	25.03	36.76	43.80	15.96	26.31	37.66	44.20	15.98	26.84	38.27	44.55
Labor	936.00	954.00	1278.00	1494.00	1116.00	1350.00	1440.00	1656.00	1260.00	1386.00	1638.00	1764.00
Repairs and maintenance	116.64	116.64	116.64	116.64	116.64	116.64	116.64	116.64	116.64	116.64	116.64	116.64
Additives	92.81	148.14	231.99	271.20	175.37	212.14	226.29	260.23	198.00	217.80	257.40	277.20
Total variable cost	1160.37	1243.81	1663.39	1925.64	1423.97	1705.09	1820.58	2077.07	1590.62	1747.28	2050.31	2202.39
Total cost	1520.63	1604.07	2023.65	2285.90	1784.23	2065.35	2180.84	2437.33	1950.88	2107.54	2410.57	2562.65
Benefits	13660.4	14489.2	16701.8	18518.5	14108.1	16631.5	17852.5	19724.7	15950.7	18041.2	19380.6	20801.4
B/C ratio	8.98	9.03	8.25	8.10	7.91	8.05	8.19	8.09	8.18	8.56	8.04	8.12
Water profits US$/m^3	1.96	1.82	1.68	1.56	1.95	2.00	1.75	1.62	2.19	2.13	1.83	1.68

CONCLUSIONS

Combining rice straw mulch with subsurface drip irrigation had a significant effect on crop yield and water use efficiency with deficit drip irrigated tomato. Using rice straw mulching with subsurface drip irrigation impacted on saving soil moisture content especially at 70, and 80% ET_c. This feature helped to speed crop maturity and increase crop yield with all *MSSD* amounts of applied water. Both of irrigation technique and amount of applied water had a highly significant effect on crop yield and water use efficiency. The previously mentioned factors showed no significant effect of the interaction between them neither on crop yield nor on water use efficiency. Deficit irrigation can be used till 90% ET_c with *MSSD* without any significant difference on crop yield. In order to obtain the maximum WUE; *MSSD* can be used with 70% ET_c. The maximum B/C ratio was at the treatment *SSD80* while the maximum profit of water unit was at *MSSD70*. Future studies are recommended to use *MSSD* on crops less sensitive to water stress as it is expected to use higher deficit irrigation levels. Also there is a need for more studies on the integration between subsurface drip irrigation, rice straw mulch, and deficit irrigation on different crops in different soil types and climate conditions especially in arid areas where water supplies are limited, in order to maximize the benefits of water unit whether related to crop yield production or economic profits.

REFERENCES

[1] Abd El-Kader, N., Derbala, A., Ahmed, M. E. M., (2010), Influence of mulching and some micro-nutrients usage on soil temperature, soil moisture, growth and cowpea yield. *Research Journal of Agriculture and Biological Sciences*, vol. 4, pp. 505-513.

[2] Abd El-Mageed, A., Semida, W. M., (2015), Effect of deficit irrigation and growing seasons on plant water status, fruit yield and water use efficiency of squash under saline soil. *Scientia Horticulturae*, vol. 186, pp. 89–100.

[3] Abdelkhalik, A., Pascual, B., Nájera, I., Domene, M. A., Baixauli, C., Pscual-Seva, N., (2020), Effects of deficit irrigation on the yield and irrigation water use efficiency of drip-irrigated sweet pepper (Capsicum annuum L.) under Mediterranean conditions. *Irrigation Science*, vol. 38, pp. 89-104.

[4] Abdelraouf, R. E., Ragab, R., (2018), Applying partial root drying drip irrigation in the presence of organic mulching. Is that the best irrigation practice for arid regions? Field and modelling study using the SALTMED model. *Irrigation and Drainage*, vol. 67, pp. 491-507.

[5] Abed EL-Hamied, S. A., Zaen El-Deen, E. M. A., El-Hagarey, M. E., (2017), Management of irrigation systems to improve productivity and quality of grapevine under desert conditions. *Journal of Agriculture and Veterinary Science*, vol. 10, no. 10, pp. 77-90.

[6] Abo-Ogiala, A. M., Khalafallah, N. E., (2019), Effect of rice straw mulching on water use efficiency, growth, yield and quality of King Ruby grape under Surface Irrigation. *Egyptian Journal of Horticulture*, vol. 46, no. 1, pp, 29–39.

[7] Al-Ghobari, H. M., Dewidar, A. Z., (2018), Integrating deficit irrigation into surface and subsurface drip irrigation as a strategy to save water in arid regions. *Agricultural Water Management*, 209: 55–61.

[8] Al-Omrana, A. M., Shetaa, A. S., Falataha, A. M., Al-Harbi, A. R., (2005), Effect of drip irrigation on squash (Cucurbita pepo) yield and water-use efficiency in sandy calcareous soils amended with clay deposits. *Agricultural Water Management*, vol. 73, pp. 43–55.

[9] Al-Rawahy, S. A., Al-Dhuhli, H. S., Prathapar, S. A., AbdelRahman, H., (2011), Mulching material impact on yield, soil moisture and salinity in saline-irrigated sorghum plots. *International Journal of Agricultural Research*, vol. 6, no. 1, pp. 75-81.

[10] Al-Wahaibi, N. S., Hussain, N., Al-Rawahy, S. A., (2007). Mulching for sustainable use of saline water to grow tomato in Sultanate of Oman. *Science International*, vol. 19, pp. 79-81.

[11] Aujla, M. S., Thind, H. S, Buttar, G. S., (2007), Fruit yield and water use efficiency of eggplant (Solanum melongema L.) as influenced by different quantities of nitrogen and water applied through drip and furrow irrigation. *Scientia Horticulturae*, vol. 112, pp. 142–148.

[12] Badr, M. A., Abou Hussein, S. D., El-Tohamy, W. A., (2010), Efficiency of Subsurface Drip Irrigation for Potato Production Under Different Dry Stress Conditions. *Gesunde Pflanzen*, vol. 62, pp. 63–70.

[13] Buchanan, R. J., Cross, T. L., (2002), *Irrigation cost analysis hand book*. Agricultural Extension Service, The University of Tenessee. PB1721.

[14] Çolaka, Y. B., Yazar, A., Gönena, E., Eroğlua, C., (2018), Yield and quality response of surface and subsurface drip-irrigated eggplant and comparison of net returns. *Agricultural Water Management*, vol. 206, pp. 165–175.

[15] Cui, J., Shao, G., Lu, J., Keabetswe, L., Hoogenboom, G., (2020), Yield, quality and drought sensitivity of tomato to water deficit during different growth stages. *Scientia Agricola*; 2020, vol. 77, no. 2, https://dx.doi.org/10.1590/1678-992x-2018-0390. 2020. e20180390.

[16] Deng, X. P., Shan, L., Zhang, H. P., Turner, N. C., (2006), Improving agricultural water use efficiency in arid and semiarid areas of China. *Agricultural Water Management*, *vol.* 80, no. 1-3, pp. 23-40.

[17] Douh, B., Boujelben, A., (2011). Improving water use efficiency for a sustainable productivity of agricultural systems with using subsurface drip irrigation for maize (Zea mays L.), *Journal of Agricultural Science and Technology* B1 (JAST), pp. 881-888.

[18] Enciso, J. M., Colaizzi, P. D., Multer, W. L., (2005), Economic analysis of subsurface drip irrigation lateral spacing and installation depth for cotton. *Transactions of the American Society of Agricultural Engineering*, vol. 48, no.1, pp. 197–204.

[19] Evans, R. G., Sadler, E. J., (2008), Methods and technologies to improve efficiency of water use. *Water Resources Research*. Vol. 44, pp. 1–15.

[20] FAO, (1998), Crop evapotranspiration - guidelines for computing crop water requirements, *FAO Irrigation and Drainage* Paper 56.

[21] FAO, (2012), Coping with water scarcity - An action framework for agriculture and food security. *FAO water report* No.38.

[22] García–Tejero, I., Romero-Vicente, R., Jimenez-Bocanegra, J. A., Martınez-Garcıa, G., Duran-Zuazo, V. H., Muriel-Fernandez, J. L., (2011), Response of citrus trees to deficit irrigation during different phenological periods in relation to yield, fruit quality, and water productivity. *Agricultural Water Management*, vol. 97, pp. 689–699.

[23] Ibragimov, N. S., Evett, R., Esanbekov, Y., Kamilov, B. S., Mirzaev, L., Lamers, J. P. A., (2007), Water use efficiency of irrigated cotton in Uzbekistan under drip and furrow irrigation. *Agricultural Water Management*, vol, 90, pp. 112–120.

[24] Igbadun, H. E., Mahoo, H. F., Tarimo, A. K. P. R., Salim, B. A., (2006), Crop water productivity of an irrigated maize crop in Mkoji sub-catchment of the Great Ruaha River Basin, Tanzania. *Agricultural Water Management*, vol. 85, pp. 141–150.

[25] Kirda, C., Moutonnet, P., Hera, C., Nielsen, D. R., (1999), Crop yield response to deficit irrigation scheduling based on plant growth stages showing water stress tolerance. *Dordrech*, The Netherlands, Kluwer academic publishers.

[26] Lamm, F. R., Camp, C. R., (2007), Maintenance. In: Lamm F. R., Ayars, J. E., Nakayama, F. S. (eds) Microirrigation for crop production. Design, operation and management. *Elsevier*, Amsterdam, pp. 473–551.

[27] Lamm, F. R., Trooien, T. P., (2003), Subsurface drip irrigation for corn production: a review of 10 years of research in Kansas. *Irrigation Science*, vol, 22, pp 3-4, pp. 195–200.

[28] Mattar, M. A., Zin El-Abedin, T. K., Alazba, A. A., Al-Ghobari, H. M., (2020). Soil water status and growth of tomato with partial root-zone drying and deficit drip irrigation techniques. *Irrigation Science*, vol, 38, pp. 163-176.

[29] Mele, A., (2019), Water use efficiency and nitrogen use efficiency in drip and deficit drip irrigated sugar beets (BETA VULGARIS). M.Sc thesis. *Jordan College of Agricultural Sciences and Technology*, California State University, Fresno.

[30] Morison, J. I. L., Baker N. R., Mullineaux, P. M., Davies, W. J., (2008), Improving water use in crop production. *Philosophical Transactions of The Royal Society* B, vol. 363, pp. 639–658.

[31] Patel, N., Rajput, T. B. S., (2007), Effect of drip tape placement depth and irrigation level on yield of potato. Agricultural Water Management, vol. 88, pp. 209–223.

[32] Patel, N., Rajput, T. B.S., (2008), Dynamics and modeling of soil water under subsurface drip irrigated onion. *Agricultural Water Management*, vol. 95, no. 12, pp. 1335 –1349.

[33] Ramakrishna, A., Tam, H. M., Wani, S. P, Long, T. D., (2006), Effect of mulch on soil temperature, moisture, weed infestation and yield of groundnut in northern Vietnam. *Field Crops Research*, vol. 95, no. 2-3, pp. 115-125.

[34] Rodrigues, G. C., Pereira, L. S., (2009), Assessing economic impacts of deficit irrigation as related to water productivity and water costs. *Biosystems Engineering*, vol. 103, pp. 536-551.

[35] Romero, P., Botia, P., Garcia, F., (2004), Effects of regulated deficit irrigation under subsurface drip irrigation conditions on vegetative development and yield of mature almond trees. *Plant and Soil*, vol. 260, pp. 169–181.

[36] Saad, A. F., Adel, A. S., Mokhtar, A. M., (2018), Influence of deficit irrigation using saline water on yield of tomato under two irrigation systems. *Alexandria Science Exchange Journal*, vol. 39, no. 1, pp. 35-47.

[37] Selim, E. M., Mosa, A. A., El-Ghamry, A. M., (2009), Evaluation of humic substances fertigation through surface and subsurface drip irrigation systems on potato grown under Egyptian sandy soil conditions. *Agricultural Water Management*, vol. 96, pp. 1218–1222.

[38] Shao, G. C., Deng, S., Liu, N., Wang, M. H., She, D. L., (2015), Fruit quality and yield of tomato as influenced by rain shelters and deficit irrigation. *Journal of Agricultural Science and Technology*, vol. 17, pp. 691-704

[39] Thompson, T. L., Pang, H. C., Li, Y. Y., (2009), The potential contribution of subsurface drip irrigation to water-saving agriculture in the western USA. *Agricultural Sciences in China*, vol. 8, no. 7, pp. 850–854.

[40] Tiwari, K. N., Singh, A., Mal, P. K., (2003), Effect of drip irrigation on yield of cabbage (Brassica oleracea L. var. capitata) under mulch and non-mulch conditions. *Agricultural water management*, vol. 58, pp. 19-28.

[41] Umair, M., Hussain, T., Jiang, H., Ahmad, A., Yao, J., Qi, Y., Zhang, Y., Min, L., Shen, Y., (2019), Water saving potential of subsurface drip irrigation for winter wheat. *Sustainability*, vol. 11, pp. 2978-2992.

[42] Wang, S., Fu, B. J., Gao, G. Y., Yao, X. L., Zhou, J., (2012), Soil moisture and evapotranspiration of different land cover types in the Loess Plateau, China. *Hydrology and Earth System Sciences*, vol.16, pp. 2883-2892.

[43] Wu, F., Bao, W., Li, F., Wu, N., (2008), Effects of drought stress and N supply on the growth, biomass partitioning and water use efficiency of Sophora davidii seedlings. *Environmental and Experimental Botany*, vol 63, no.1, pp. 248-255.

[44] Yang, Y., LIU, X., LI, W., LI, C., (2006), Effect of different mulch materials on winter wheat production in desalinized soil in Heilongjiang region of North China. Journal of Zhejiang University SCIENCE B, vol. 7, no. 11, pp. 858-867.

[45] Zhang, H., Xiong, Y., Huang, G., Xu, X., Huang, Q., (2017), Effects of water stress on processing tomatoes yield, quality and water use efficiency with plastic mulched drip irrigation in sandy soil of the Hetao Irrigation District. *Agricultural Water Management*, vol. 179, pp. 205–214.

TECHNICAL AND TECHNOLOGICAL SOLUTIONS FOR PREPARING FLAX RAW MATERIALS FOR PROCESSING
/
ТЕХНІКО-ТЕХНОЛОГІЧНІ РІШЕННЯ ПІДГОТОВКИ ЛЛЯНОЇ СИРОВИНИ ДО ПЕРЕРОБКИ

Berezovsky Yu.[1)], Kuzmina T.[1)], Yedynovych M.[1)], Boyko G.[1)], Lyalina N.[2)], Holovenko T.[3)]
[1)] Kherson National Technical University, Kherson / Ukraine;
[2)] Kyiv National University of Construction and Architecture, Kyiv / Ukraine;
[3)]Lutsk National Technical University, Lutsk / Ukraine
Tel: +38 (099) 023-62-32; E-mail: berezov.sky.ua@gmail.com
DOI: https://doi.org/10.35633/inmateh-64-22

Keywords: *flax; retted straw; storage methods; humidity; preservation.*

ABSTRACT
The article contains theoretical and experimental researches in the field of the preservation of flax raw material of high moisture content. In the article, factors that are worsening the quality of flax raw material, resulting in non-observance of agrotechnical and technological requirements of preparing, collecting, harvesting the stem material, adverse weather conditions and other factors, are considered. The objective of this paper is to study the influence of preservation agents' concentrations and of hollow structure device on the quality of flax raw material during long-time storage. In the article, the influence of aqueous preservatives' concentration, humidity, storage length on the quality of fibrous products, obtained as a result of processing stem material, is analyzed. The influence of the device of hollow structures, as an alternative to preservatives, on the storage process of bast crops stem material was evaluated. The method of flax retted straw storage is described, actions of the main factors influence on the strength of fibers are analyzed. It is demonstrated, that prolongation of flax raw material preservation time can be made by using preservatives without considerable wastes of quality.

РЕЗЮМЕ
Стаття містить теоретичні та експериментальні дослідження в галузі збереження лляної сировини підвищеної вологості. У статті розглянуто фактори погіршення якості лляної сировини, що пов'язані з недотримання агротехнічних та технологічних вимог підготовки, збирання, заготівлі стеблового матеріалу, несприятливими погодними умовами та іншими факторами. Завданням роботи є вивчення впливу консервантів та установки порожнистих структур на якість лляної сировини при тривалому зберіганні. У статті проаналізовано вплив концентрації водних розчинів консервантів, вологості, терміну зберігання на якість волокнистої продукції, отриманої у результаті переробки стеблового матеріалу. Здійснено оцінку впливу установки порожнистих структур, як альтернативи консервантам при зберіганні стеблового матеріалу луб'яних культур. Описано методику проходження зберігання лляної трести, проаналізовано дії основних факторів впливу на міцність волокна. Доведено, що використання консервантів дає можливість подовжити термін зберігання лляної сировини без значних втрат її якості.

INTRODUCTION
The production of industrial crops occupies an important place in the modern world economy. Crops that require further industrial processing are considered technical. These include fiber, sugar, oil, tannin, and rubber-bearing crops. Fiber crops are one of the most important industrial crops *(Holovenko T.N. at. al., 2018; Roland J. at. al., 1996)*. They comprise cotton, flax, hemp, abacus, jute, and sisal. The world leaders in flax production are France, Russia, Poland, Germany, Belgium, leading producers of hemp are Canada, China, abacus - the Philippines, jute - India, Bangladesh, and sisal - Tanzania, Kenya, and Brazil.

One of the traditional industrial crops having long been cultivated in Ukraine is flax. "Flax fiber is suitable for the production of non-woven materials, technical textiles and paper" (*Dudarev I. at. al., 2020*). "Studies have shown the prospects of using small-sized fuel rolls from oleaginous flax waste as a new type of solid biofuel" (*Yaheliuk S. at. al., 2020*)". It is a valuable raw material for textile, construction, pulp and paper, pharmaceutical and other industries.

Under the development of industrial production of synthetic fibers, expanding their range, the value of economic and hygienic properties of flax fiber remains unchanged *(Abbar B. at. al., 2017; Berezovsky Yu.V., 2018).*

The general technology at the enterprises of primary processing provides drying of raw materials with high moisture content on drying installations to normalized values and its further storage in a fluffed state separately from the main amount of raw materials and its immediate processing *(Dudarev I. at. al., 2020)*.

The loss of raw materials during storage is mainly due to excessive moisture content, which is a consequence of the improper preparation and stacking of raw materials, raw materials harvesting in autumn and spring when humidity is extremely high. With the high moisture content of the raw material, the temperature inside the stacks rises, which is accompanied by self-heating of the material and makes it unusable. Therefore, in the process of long-term storage, it is important to ensure the preservation of the quality of flax raw materials due to the negative activity of a large number of cellulose-destroying fungi and bacteria, which significantly reduce the technological value of fiber *(Didukh V.F. at. al., 2008)*.

Microbiological processes that cause complete damage to flax fiber during storage have been studied by various scientists *(Khilevich V.S., 1992; Kyryliuk R.M., 1994; Ostrik N.M., 1983)*. Microbes have been shown to cause hydrolytic dissolution of proteins and other nitrogenous organic substances by proteases. The decomposition of the constituent substances is possible only when the destructive microorganisms have all the necessary conditions for their development: the optimum temperature, moisture content, the appropriate reaction of the environment, the necessary nutrients, and other factors. Low temperatures slow down biochemical processes, so at "a temperature of 5°C, the biological processes completely stop and the straw is kept in the state of natural preservation *(Kuzmina T.O. at. al., 2018)*". Freshly harvested straw is more resistant to pectin-destroying fungi than dried flax stems, and the preservation of quality indicators of flax raw materials can be carried out at a moisture content of no more than 25%, and in a roll - no more than 23%; this rule often forces to leave raw materials on flax harvesting sites, which can lead to the loss of fiber strength.

Theory and practice of harvesting and storage of flax and hemp raw materials, the application of new forms of packaging and technological equipment, the use of high-performance equipment for the preparation and processing of bast raw materials, which are presented in *(Gopu R. Nair at. al.; 2013; Mankowski J. at. al., 2018; Mukhin V.V., 1985; Kuzmina T.O. at. al., 2018)*, give grounds to assert that at the present stage of light industry development in Ukraine obtaining significant results in the flax and hemp processing is possible only by addressing the issue of ensuring the initial quality characteristics of raw materials, compliance with the necessary technological parameters, guaranteeing the preservation of physical and mechanical properties, implementing innovative solutions to the problems of preparation, storage, and processing in the industry taking into account anatomic and physical and mechanical properties of bast crops. "Under certain investment attraction conditions and introducing innovative technologies the industry will acquire considerable potential, which will help to increase the domestic raw materials competitiveness, leading to flax and hemp production revival (*Berezovsky Yu.V. at. al., 2020)"*.

World experience in the preservation of products, characterizing the effect of negative microflora suppression, distinguishes mainly the chemical method of exposure using chemicals; temperature method providing the regulation of storage temperature; method of storage in gaseous media in a controlled atmosphere - with the selection of gas and temperature parameters. "Chemical or biological preservation can provide much less dependence of storage technology on changing weather conditions *(Kuzmina T.O. at. al., 2018)*". Each method in its own way characterizes the impact on the destructive microflora, their nature and degree of influence depend on the nature and concentration of substances, processing conditions, integrity, and controllability of storage facilities, as well as the quantitative and qualitative composition of microflora, which determines the relevant economic indicators, efficiency and use of special complex equipment.

As the artificial drying of flax raw materials is not currently widely used in practice due to significant heat costs and metal consumption of equipment, the domestic processing industry needs to find and develop a new rational economic technology for storing flax retted straw of high-moisture content.

Based on the theoretical and experimental studies performed, the inefficiency of using traditional technology of preparation, storage, and processing of domestic bast crops has been established, which is due to the significant dependence of fiber on the initial state of raw material, especially moisture content, development of cellulose-destroying processes in the stem material. Analysis of technical and technological perspectives revealed in *Berezovsky Yu.V. (2018)*, indicates that to obtain high-quality fiber at the end of the production process chain, highly dimensional equipment is used that requires significant energy costs, which, to date, is simply impractical and virtually causes economic inefficiency of this approach. Therefore, "introduction of resource-saving technology will increase the profitability of linseed cultivation" *(Dudarev I. at. al., 2020)*.

Currently, some discussions are taking place and the relevant scientific basis of modern technologies are being developed for harvesting, preparation, storage, processing of bast raw materials, use of high-tech modern equipment for bast material preparation, application and implementation of special measures and effective ways to preserve qualitative and quantitative characteristics of flax straw and retted straw *(Bobyr S. at. al., 2014; Dudarev I. at. al., 2020)*. However, to date, such issues have not been sufficiently resolved from the standpoint of rational use, feasibility, and versatility of application for different types of bast raw materials.

It has been found that many scientists are involved in the preparation, harvesting, and storage of bast crops, but no reliable methods or techniques have yet been established. Nowadays, in foreign and domestic practice for prolonged storage, a range of promising chemical compounds is used that has antioxidant, fungicidal, and bactericidal properties that inhibit the activity of the microflora, as well as desiccants *(Bobyr S. at. al., 2014; Kuzmina T.O. at. al., 2018)*, which dehydrate and dry the stem material, absorb or chemically bind water within, but many storage issues still remain unresolved. Therefore, there is a need to continue the search for new technologies that would ensure the preservation of the physical and mechanical properties of flax raw materials and would be affordable and cost-effective.

Solving the issue of finding available preservatives, that can affect the viability of microorganisms and ensure the preservation of the quality of flax raw materials in the long run, is necessary for the domestic processing branch of the light industry. Development and introduction of accessible and effective technology of preservation of flax retted straw in production allow optimizing the process of storage of flax raw materials of high moisture content, to establish rational storage terms of bast fiber without considerable quantitative and qualitative losses during preparation and primary processing.

MATERIALS AND METHODS

Today, the textile industry remains the main consumer of flax stems. Given that the world market for silk is becoming more expensive every year, the prospects for textile producers are growing. At the same time, Ukrainian scientists predict that after setting up processing facilities, Ukraine may sow flax up to 25-30 thousand hectares in the next 5-10 years. The European Union has refused to import Canadian modified oilseed flax. Therefore, there is a deficit in Europe, which can be offset by purchasing flax from Ukraine and other neighboring countries *(Berezovsky Yu.V. 2018)*. World flax production and flax seed exports in 2019-2020 reached 3.11 million tons. According to OilWorld experts, world flax seed production in the 2020-21 marketing year could increase to 3.29 million tons *(Agronews.Ua, 2021).* Ukrainian producers can only benefit from this deficit - they now have every chance to take a worthy place in the world flax market, but the dynamics of changes in flax sown areas in Ukraine for 2000-2019 is still far from being optimistic (Fig. 1).

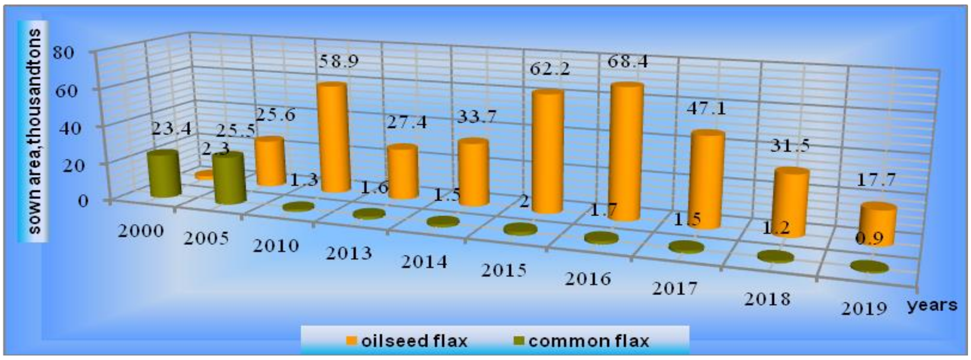

Fig. 1 - Dynamics of flax sown areas in Ukraine for the period 2000-2019 (constructed according to the Ukrainian State Statistics Service)

In order to achieve far-reaching opportunities, domestic production needs to solve the problems associated with harvesting, preparation, and storage of bast raw materials, as it is at these stages that a significant amount of it is lost. It is known that the decrease in the quality of flax retted straw is associated with untimely spreading or removing it from rettery, during which due to adverse weather conditions, destructive microflora causes significant damage to flax production. During the process of aging and storage of wet flax material, there is a change in its chemical composition and physical and mechanical properties, its strength is lost, the separability increases *(Khilevich V.S., 1992; Kuzmina T.O. at. al., 2018)*.

It is important not only to process the entire yield of flax straw into a quality retted straw but also to preserve the quality of the retted straw already obtained by spreading in the process of long-term storage in flax plants after mass harvesting. Due to the high infestation of fungi and bacteria, and the increased moisture content, the retted straw rapidly loses quality indicators and the technological value of the fiber decreases *(Bobyr S. at. al., 2014; Kuzmina T.O. at. al., 2018).*

There are several ways to store flax raw materials with high moisture content. The storage of bast material is achieved by bringing it to the normatively accepted condition in terms of moisture content during drying or by treatment with chemical and biological substances. Conventional natural drying processes are complicated by the high density of the material in the packaging rolls, so artificial drying is a reliable technology for storing bast material. Although due to the significant energy consumption as a method of maintaining the quality of raw materials, it has been more widely used abroad than in Ukraine. In world practice, fungicides and antiseptics are used for chemical plant protection. Fungicides are used against fungi, bacterial and viral diseases, often for seed treatment. Antiseptics are substances that affect microorganisms. They are used in various sectors of the economy as additives to the material that permeates it. Thus, the action of ammonia, ammonia salts during storage is manifested as the action of fungicide, bactericide, rodenticide and fibrilizer, and chemicals show technical and economic efficiency.

The research of American scientists in the direction of product storage is of interest. They followed an unconventional way of extending the storage term of agricultural products, using a chitin substance contained in the shell of arthropods *(Semakov V.V., 1994)*. This substance in the form of a chitin derivative dissolved in water is sprayed as an aerosol, forming a semipermeable shell on the surface of the products. Researchers at the University of Washington justify the principle of chitosan action slowing down of the process of respiration of products during storage, which protects them from fungal infections.

American scientists describe two more non-traditional methods of plant protection, the effect having been tested in laboratory and field conditions. One of them is the use of so-called coniferous wax as a protective layer, which is a by-product of chemical processing of pine and spruce needles *(Semakov V.V, 1994)*. Sprayed similarly to chitosan, the wax forms a thin film on the product surface, inhibiting the passage of oxygen and metabolic products, and the use of water-gasoline emulsion of chlorophyll-carotene paste, which is obtained from pine and spruce needles, resulting in prolonged storage.

Practice shows that in order to obtain high-quality end products of flax processing during storage of flax raw material with high moisture content, it is necessary to constantly monitor its condition, which is often influenced by natural factors and the microflora that surrounds and develops under appropriate conditions. One way to reduce such losses may be to increase the use of balers by harvesting flax straw and high moisture content retted straw using preservatives that reduce the technology's dependence on weather conditions. Applying liquid preservatives in the roll forming process enables more uniform distribution of preservatives within the raw material *(Boyarchenkova M.M. at. al., 1988; Khilevich V.S., 1992)*.

In domestic practice, biologically active substances "Trichodermin" and "Fitosporin-M" *(Bobyr S. at. al., 2014; Kuzmina T.O. at. al., 2018)*, which have a fungicidal and bactericidal effect against cellulosolytic fungi and bacteria, have been successfully used for the storage of oil flax stems. In spite of the practical significance of these results, such studies are inherent in the stem material of oilseed flax in the southern regions of the country, which differs significantly in the properties and conditions of common flax straw and retted straw, which is the main source of flax fiber.

The use of technology for preserving high-moisture retted straw can reduce the cost of manual labor for harvesting raw materials in adverse weather conditions, significantly reduce energy consumption for artificial drying, and loss of fiber flax products.

All known preservatives used for storage of high-moisture retted straw do not have a set of necessary properties: efficiency, environmental safety and cheapness. That is why the development of effective ways to preserve the quality of flax raw materials is still quite relevant in modern conditions.

The studies on determining the effectiveness of preservatives, means, and methods of flax storage were guided by feasibility, ease of use, efficiency, and safety. Instrumental standard methods were used to verify the qualitative characteristics of flax raw material samples. During the experiments, the principle of a single difference was followed. At some research sites, treatment with preservative solutions, roll formation, and further studies were performed within one day, using the same instruments and equipment.

During the research, common flax varieties "Eskalina", "Charivny" were used, which were grown in farms and research areas of Zhytomyr region, and the soil growing conditions were typical for the flax zone. Flax cultivation for experiments was carried out in compliance with all technological conditions.

Typical flax stems, similar in morphological features to the predominant number of raw materials, were selected for the research. Initial research was performed on industrial packaging (rolls) of flax raw materials, and subsequent studies were carried out on small batches weighing 50 g with a density of 125 kg/m^3, allowing observing changes in flax stems, to determine the main regularity and causes of these changes, as well as the effectiveness of certain techniques. The mode of the storage process was applied at a temperature range of 15-20°C and relative moisture content of about 60-65%.

Aqueous solutions of carbamide, ammonium nitrate, aethonium, sodium carbonate, sodium chloride, and methanol were used as preservatives. The optimal distribution of preservative on flax stems is ensured by a specially designed cylindrical wing-shaped ejector (Fig. 2), and an irrigation system, which is installed above the place of formation of the flax retted straw roll *(Chursina, L.A., 2002).* The process of storage of high-moisture flax retted straw with the use of installation of hollow structures imitating beehives was also investigated. The section of the installation of hollow structures is shown in Fig. 3.

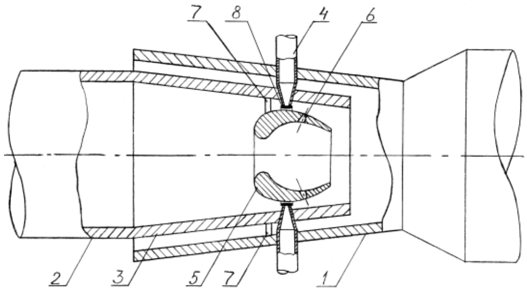

Fig. 2 - Ejector

1 - housing; 2 - active medium intake; 3 - duct reducer unit; 4 - passive medium intake;
5 - streamlined body; 6 - slit; 7 - rod; 8 - slot-shaped nozzle

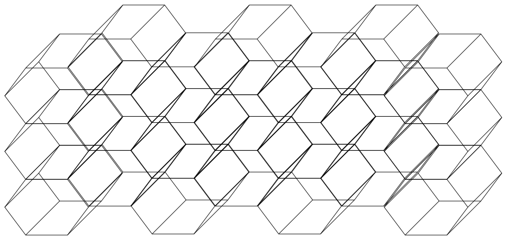

Fig. 3 – Cross-section of the installation part of hollow structures

The main components of the installation are hexagonal tubes, which can be made of different materials, with an inner diameter of 0.012 m. The hexagonal tubes are tightly connected and installed in a vertical position, which allows reproducing beehives. In this structure, an air flow is directed to the retted straw mass, which provides an aerobic storage environment.

To determine the effectiveness of the use of chemicals that were selected for research on the preservation of flax retted straw, the search for the optimal concentration of the above substances was carried out. According to the results of the scientific research scientists *(Boyarchenkova M.M. at. al., 1988; Khilevich V.S., 1992; Kyryliuk R.M., 1994)*, it was determined that the most expedient and cost-effective is the concentration of aqueous solutions of preservatives, not exceeding 10%. Therefore, the effectiveness of aqueous solutions of carbamide, ammonium nitrate, worked-out aethonium, sodium carbonate, sodium chloride, and methanol was investigated at the above concentration at retted straw moisture content of 30% and the duration of storage of high-moisture retted straw of 30 days (Table 1).

Table 1

Change in physical and mechanical parameters of retted straw under the influence of preservatives

Preservative type	Physical and mechanical parameters of retted straw		
	separability, conventional units	flexibility, mm	breaking load, daN
Carbamide	6.7	44	16.8
Ammonium nitrate	6.9	47	14.7
Aethonium	7.6	68	8.6
Sodium carbonate	8.1	53	5.7
Sodium chloride	8.3	64	2.6
Methanol	7.7	45	13.0
Initial indicators of retted straw	6.0	36.6	16.0
Control (without preservative)	8.8	74	3.1

RESULTS

The results of studies showed the ineffectiveness of the use of such preservatives as sodium carbonate and sodium chloride. They did not provide storage of high moisture content retted straw even for 30 days. But the preservative efficiency of aqueous solutions of carbamide, ammonium nitrate, worked-out aethonium, methanol was revealed. Although the aqueous solution of methanol showed a good preservative effect, it was excluded from the study due to environmental safety considerations. To conduct further research to identify optimal storage conditions for flax retted straw, the preservatives represented by aqueous solutions of carbamide, ammonium nitrate, worked-out aethonium were selected as the most effective, environmentally friendly, and feasible.

Based on a preliminary analysis of theoretical and practical research data and the application of mathematical experiment design, the following levels of variation of the above factors were determined: concentration of substances C, % (7.6; 8.8; 10); storage term T, days (30; 45; 60); moisture content in retted straw W, % (25; 30; 35). During the study, it was found that the lowest concentration of preservatives at which the preservative effect is observed is 7.6 %.

The results of research indicate that the flax raw material obtained from flax stems during storage using preservatives has higher physical and mechanical properties compared to flax raw material not having been treated. It was found that all the quality characteristics change during storage depending on the type of preservative. The values of physical and mechanical parameters indicate the possibility of storing retted straw of high moisture content. Thus, when using an aqueous solution of carbamide, positive results were obtained in options at the following levels of factor variation: 1) C = 7.6%; T = 45 days; W = 35%; 2) C = 7.6%; T = 60 days; W = 35%. Aqueous solution of ammonium nitrate also proved to be an effective preservative, when used, the physical and mechanical properties of flaxseed are at the appropriate level, except when the levels of factor variation are as follows: 1) C = 7.6%; T = 30 days; W = 25%; 2) C = 7.6%; T = 45 days; W = 30%; 3) C = 7.6%; T = 45 days; W = 35%; 4) C = 7.6%; T = 45 days; W = 30%; 5) C = 7.6%; T = 45 days; W = 35%.

Studies to identify the effect of aethonium on the storage process of flax retted straw were conducted at the same levels of variation as in previous research options. Based on the results obtained, it can be argued that worked-out aethonium proved to be a short-acting preservative. Aethonium significantly affects the process of storage for only 30 days. In comparison with the control, this preservative retains the physical and mechanical properties of flax retted straw only for a short period of storage. To increase the efficiency of the preservative force during a longer storage period, it is necessary to use aethonium of a higher concentration, but this leads to an increase in the cost of preserving high-moisture flax raw material.

As a result of the research analysis, it was revealed that in some cases at the specified concentration of the preservative solution and the established term of storage with an increase in flax retted straw moisture content its strength increases, although without application of preservatives the opposite process occurs. This trend can be explained by the fact that a sufficiently high solution concentration and long-term storage with increasing moisture content of flax raw materials facilitates the penetration of preservatives through the tissues of the stem to the inner cavity. At the same time, preservation occurs both in the middle of flax retted straw stems and outside them. At low retted straw moisture content, only external preservation of tissue occurs. Rotting and mold fungi can grow freely without hindrance, i.e. the conservation is not properly performed.

When comparing the effectiveness of the three preservatives, it should be noted that carbamide has the best and longer-lasting effect on the storage process of flax retted straw of high moisture content.

Installation of hollow structures, as well as the use of preservatives, is effective in storing flax retted straw of high moisture content. Although it should be noted that the use of this installation contributes to the preservation of physical and mechanical properties of flax raw materials but not for the entire storage period. Thus, for 30 days the physical and mechanical parameters of the retted straw remained at the proper level, at a sample moisture content of 25%, 35%, and at 45% there is a significant decrease, which does not meet the requirements of regulatory and technical documentation. For a longer period of 45; 60 days, the preservation of retted straw quality is observed only at the flax moisture content of 25%, and at other levels of moisture content there is an abrupt decrease in strength.

Comparison of the results of studies obtained using preservatives and the installation of hollow structures shows that the best effect of maintaining the quality of flax raw materials is achieved with the use of the aqueous solution of carbamide as preservative.

Since in the study on the storage of high moisture content flax retted straw, the best results were obtained with the use of carbamide, the mathematical model of the retted straw storage process was developed on the basis of experimental data using the specified preservative. The main indicator of the flax retted straw quality during storage is the breaking load, which characterizes the fiber strength, so this indicator was chosen as the initial criterion.

Based on the results of the study, a mathematical model of the retted straw storage process using an aqueous solution of carbamide was obtained in the form of a corresponding regression equation in coded and natural form, which allows determining the breaking load during the storage of flax retted straw of high moisture content:

The regression equation in natural variables is presented as follows (1):

$$P = 9{,}791 + 0{,}388C + 0{,}736T - 1{,}026W + 0{,}04CT + 0{,}265\ CW - 0{,}033TW - 0{,}377C^2 - 0{,}0015T^2 - 0{,}002W^2, \quad (1)$$

Where: P – breaking load, daN;

C – preservative concentration, %;

T – storage term, days;

W – moisture content in flax retted straw, %.

After obtaining a relevant model of the storage process of flax retted straw using an aqueous solution of carbamide, the response surfaces describing the storage process of high moisture content flax retted straw were investigated and the optimal values of the factors influencing this process were determined. For this purpose, graphical dependences of the strength of flax retted straw on the influence factors were developed. The shape of the surface was determined by the canonical equation to which the equation of the second-order polynomial describing this surface is reduced. Two-dimensional cross-sections were investigated to determine the type of response surface.

Based on the obtained mathematical model of the retted straw storage process, diagrams of the dependences of the breaking load on the concentration of carbamide solution, storage duration, moisture content of the flax retted straw were built, that are presented in Fig 4; 5; 6. Dependence diagrams are built in such a way that only one factor varies, the influence of which on the optimizing value is studied, and other factors remain at the basic level of variation. Fig. 4 shows how the retted straw strength changes with the variation of the preservative solution concentration, which is to ensure the storage of flax retted straw.

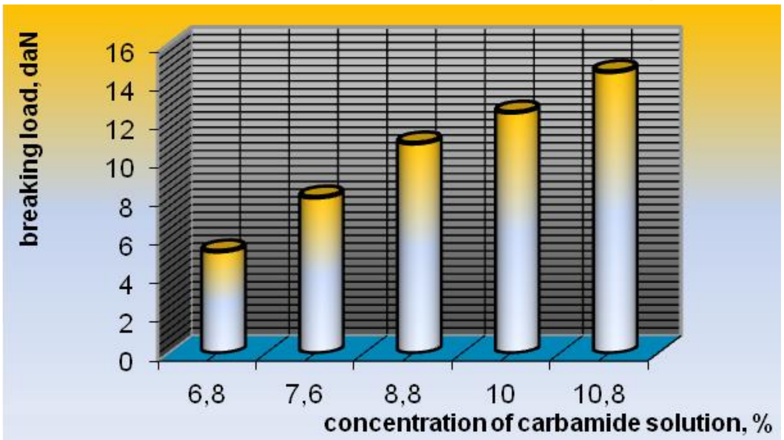

Fig. 4 - Dependence of strength of the high moisture content flax retted straw on the concentration of carbamide aqueous solution at T = 45 days; W = 30%

The diagram (Fig. 4) shows that the output parameter is directly dependent on the specified factor. As the concentration of the preservative increases, the probability of obtaining a fiber with the appropriate value of the strength index increases. Therefore, it is necessary to further determine the optimal value of a specified factor, at which it would be possible to ensure the storage of flax retted straw of high moisture content.

Fig. 5 shows how the retted straw strength changes with the changes in storage duration of flax retted straw of high moisture content. It is seen that within 30 days there is a rather sharp decrease in fiber strength, and in the next 30 days it stabilizes somewhat. After a period of 60 days of storage, the strength of the fiber again decreases quite rapidly. The diagram shows a short period of 30-45 days, during which the strength of the fiber is in a fairly stable state, i.e. it is possible to assume that these are the best storage conditions for flax retted straw under the influence of this factor.

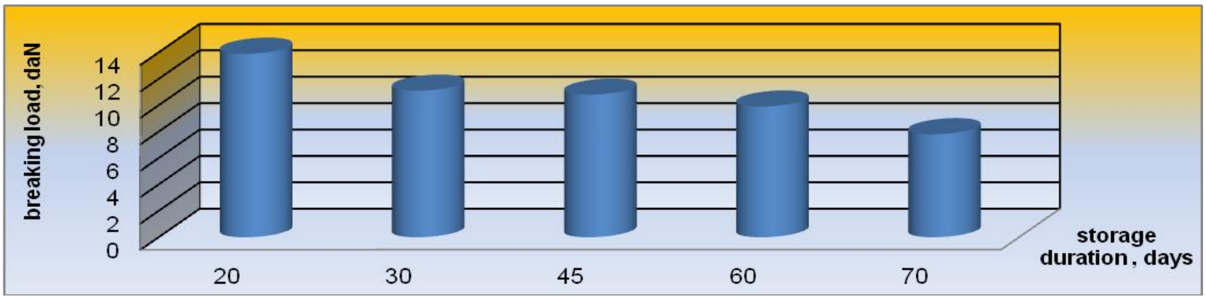

Fig. 5 - Dependence of the strength of flax retted straw on the storage duration at C = 8.8%; W = 30%

When superimposing two diagrams of dependences, it is possible to identify the optimal storage conditions of the flax retted straw of high moisture content under the action of the two above-mentioned influence factors. The most favorable conditions for obtaining fiber of high quality can be considered the preservative concentration C = 7÷9%; storage term T = 30÷45 days; moisture content W = 30%.

Fig. 6 shows how the retted straw strength changes with the changes in the moisture content of the flax material. Analysis of the diagram indicates that the initial parameter is inversely related to a specified factor, i.e. increasing moisture content of the flax material leads to the decrease in the strength of the fiber obtained by processing. Thus, it is necessary to further determine the optimal value of a specified factor at which it would be possible to ensure the storage of flax retted straw of high moisture content. On the diagram it is possible to allocate an interval at W = 25÷35% on which fiber strength values decrease not so rapidly, it is possible to consider this stage of changing moisture content in flax retted straw optimum.

The diagrams in Figs. 4; 5; 6 show that the flax fiber strength varies according to a certain law depending on the factors that influence it. As expected, the strength is significantly affected by all these factors, especially the preservative solution concentration and the moisture content in the material. It should be noted that when stabilizing the two factors at the main level, these dependencies are almost linear, which indicates the identity in the laws of change in fiber strength.

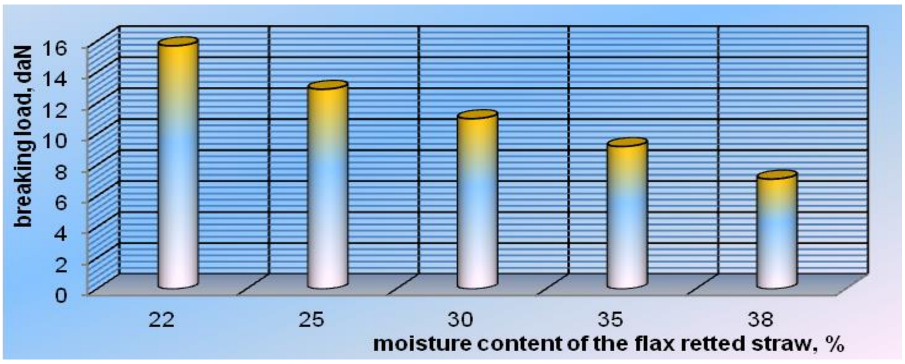

Fig. 6 - Dependence of the flax retted straw strength on the moisture content at C = 8.8%; T = 45 days

Graphs of one-dimensional cross-sections do not contradict the generally accepted provisions. Thus, when using a preservative aqueous carbamide solution of a higher concentration, the strength of the flax fiber will remain quite significant. With increasing storage term or moisture content in the material at other constant indicators of the influence factors, a decrease in the strength of the flax retted straw occurs.

For a more detailed consideration of the dependences of the retted straw strength on the carbamide solution concentration, the moisture content in flax retted straw, duration of storage, and determination of the optimal mode of storage technology of high moisture content retted straw, a two-dimensional cross-section of the response surfaces was used. The storage process of high moisture content retted straw when using an aqueous carbamide solution is characterized by hyperbola contour lines. According to the analysis of the response surfaces, it was found that the maximum values of flax retted straw moisture and the preservative solution concentration allow obtaining the minimum values of strength; the area of optimal strength ($y \rightarrow$max) is set at minimum values of moisture and insignificant values of preservative concentration. The hyperbola contour lines are descending.

From a practical point of view, increasing the concentration by more than 10% is not appropriate; therefore, the change in strength at the given concentration below C = 10% was verified. For a complete picture of the phenomena that occur during storage of flax retted straw of high moisture content with the use of carbamide, the effect of its aqueous solution on a constant concentration at the level of C = 7.6% was evaluated. Given the above, a study of the cross-section of the construction of hyperbola curved lines was carried out (Fig. 7).

According to the performed analysis, it was found that the hyperbola contour lines both under the constant factor of storage term (T) and the constant factor of the preservative solution concentration (C) are descending. Herewith, the range of optimal strength values at T = 45 days is set at minimum values of material moisture and insignificant values of preservative concentration, and at C = 7.6% and C = 10% - at maximum values of storage duration and material moisture.

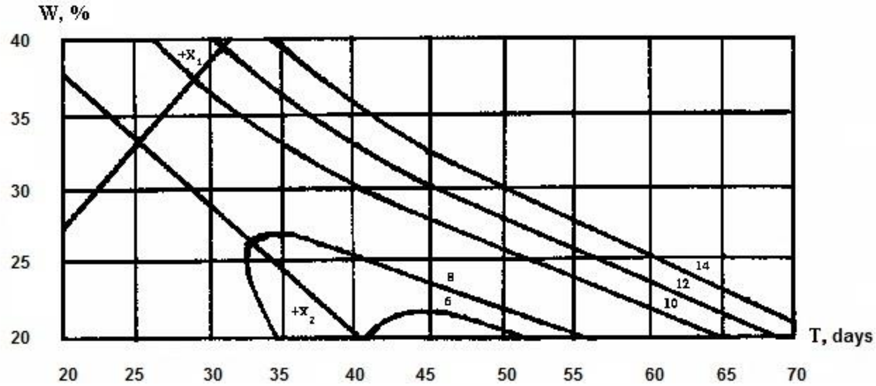

Fig. 7 - Two-dimensional cross-section of the response surface at C = 7.6%

Comparison of two-dimensional cross-sections allowed determining the optimal values of all influencing factors. In the study of the mathematical model in various storage modes, different types of two-dimensional cross-sections were obtained: when fixing the moisture factor and varying the other two, an ellipse was obtained, in other cases, the same values of input parameters resulted in a hyperbola. This made it possible to more deeply consider and imagine the course of processes, enabled to study the dependence of optimization parameters not only on the factors influencing the process but also on their interaction. The generalization of the experiment results, the analysis of one-dimensional and two-dimensional cross-sections gave grounds to assert that the process of storage of flax retted straw of high moisture content should take place under the following rational storage conditions:

- the moisture content of flax material should not exceed 35%;
- it is advisable to leave flax retted straw of high moisture content for storage for up to 45 days;
- to use a preservative aqueous solution of carbamide with a concentration range of 8.8-10%.

In the analysis of one-dimensional and two-dimensional cross-sections of the response surfaces of the mathematical storage process model of high-moisture flax retted straw, a certain variable regularity is observed in a specific change area of input parameters. It was established that the strength of flax fiber obtained by processing retted straw is linearly dependent on the concentration of the preservative aqueous solution, as well as on the moisture content of the material described by the empirical equations.

CONCLUSIONS

According to the results of scientific and theoretical research, it was determined that the most expedient and cost-effective way to store flax retted straw of high moisture content is the use of preservatives, such as an aqueous solution of carbamide. This is due to the fact that artificial drying of raw materials is not used in practice because of significant energy and material costs; the recommended technology is simple, reliable, and cheap, aqueous solution of carbamide as a preservative can ensure the quality of flax raw material at the appropriate level.

It was established that such preservatives as carbamide, ammonium nitrate, worked-out aethonium inhibit the activity of cellulose-destructive microorganisms, and thus ensure the preservation of physical and mechanical properties of flax retted straw. It was found that to obtain positive results of storing retted straw when using the technology of treatment of flax retted straw stems with carbamide, it is necessary to apply 150 ml of its preservative aqueous solution per 1 kg of flax material, which will ensure maximum irrigation of packaging and penetration of preservatives into stems.

When using a preservative solution of carbamide, it was found that the quality of flax retted straw remains high for up to 60 days. It was theoretically and experimentally proved that increasing the concentration of carbamide over 10% to maintain the quality of flax raw material is not feasible and thus irrational. The best results of preserving the quality of flax retted straw are achieved when using preservative solutions with a concentration of 8.8%, which can be considered as close as possible to the optimum value if the moisture content in flax material does not exceed 35% and storage term is 60 days.

It was found that the installation of hollow structures provides storage of flax retted straw of high moisture content, it is environmentally friendly and can present an alternative to the use of chemical preservatives.

REFERENCES

[1] Abbar, B., Alem A., Pantet A., Marcotte S., Ahfir N.-D., Duriatti D., (2017), Experimental investigation on removal of suspended particles from water using flax fiber geotextiles, *Environmental Technology*, V. 38, № 23, 2964-2978;

[2] Berezovsky, Yu.V., (2018), Technical solution for scutching the raw bast material (Технічні рішення процесу тіпання луб'яної сировини), *Science and innovation*, V. 14, № 1, 26-39;

[3] Berezovsky, Yu., Kuzmina, T., Lialina, N., Yedynovych, M., Lobov, O., (2020), Technical and technological solutions for producing fiber from bast crops, *INMATEH - Agricultural Engineering*. Vol. 60, №. 1, 137-146;

[4] Bobyr, S.V., Kuzmina, T.O., Rastorhueva, M.Y., (2014), Preservation of quality parameters of the straw of oil flax in the conditions of the southern of Ukraine (Сохранность качественных показателей соломы льна масличного в условиях юга Украины), *Vestnik of Vitebsk State Technological University,* № 26, 29-37;

[5] Boyarchenkova, M.M., Mareeva, Z.I., (1988), Use of chemicals as preservatives for wet flax raw material (Использование химических веществ в качестве консервантов влажного льносырья), *Breeding, seed production and agrotechnology of flax cultivation*, 167-170;

[6] Chursina, L.A., Berezovsky, Yu.V., (2002), *Ejector (Ежектор).* Ukraine, Patent, № 49617;

[7] Didukh, V.F., Dudarev, I.M., Kirchuk, R.V., (2008), *Harvesting and primary processing of flax (Збирання та первинна переробка льону-довгунця)*, Lutsk / Ukraine, "LNTU" Publishing House; ISBN 978-966-7667-84-9;

[8] Dudarev, I., Say, V., (2020), Development of resource-saving technology of linseed harvesting. *Journal of Natural Fibers*, 17 (9), 1307-1316;

[9] Gopu, R. Nair, Denis Rhoand, G.S., Vijaya Raghavan, (2013), Application of electro-technologies in processing of flax fiber. *Fibers*, 1 (2), 21-35;

[10] Grebennikov, V.S., (1990), Aliens in honeycombs (Инопланетяне в сотах), *Nature and man*, № 8, 22-27.

[11] Holovenko, T.N., Tikhosova, H.A., Bogdanova, O.F., Shovkomud, A.V., (2018), Analysis of the state of light industry in Ukraine (Анализ состояния легкой промышленности Украины), *Proceedings of higher educational institutions. Textile Industry Technology*, Issue 5 (377), 251-254;

[12] Khilevich, V.S., (1992), *Changes in the preservation of flax products during storage and measures to increase (Изменение сохраняемости льнопродукции при ее хранении и мероприятия по повышению)*. Kyiv / Ukraine, "UkrINTEI" Publishing House;

[13] Kuzmina, T.O., Yedynovych, M.B., Berezovsky, Yu.V., Bobyr, S.V., Yevtushenko, V.V., Rudenko, I.A., (2018), Application of biologically active substances to storage of oil flax straw (Застосування біологічно активних препаратів для зберігання соломи льону олійного), *Science and innovation*, V. 14, № 4, 26-39;

[14] Kyryliuk, R.M., (1994), *Changing the quality of flax raw material during cooking and storage (Зміна якості льонотрести в процесі приготування і її зберігання),* Ph.D. dissertation, Kyiv/Ukraine; Ukrainian State Agrarian University;

[15] Mankowski, J., Maksymiuk, W., Spychalski, G., Kolodziej, J., Kubacki, A., Kupka, D., Pudelko, K., (2018), Research on new technology of fiber flax harvesting. *Journal of Natural Fibers*, 15 (1), 53-61;

[16] Mukhin, V.V., (1985), Dosing with liquid chemical preservatives of flax in pressing of rolls (Дозирование жидких химических консервантов при прессовании льна в рулоны), *XXII International Symposium "Economy, mechanization and primary processing"*, Kyiv/Ukraine, 64-68;

[17] Ostrik, N.M., (1983), *Improvement of the technology of post-harvest processing and storage of flax raw materials (Усовершенствование технологии послеуборочной обработки и хранения льносырья)*, Ph.D. dissertation, Kyiv/Ukraine; Ukrainian Academy of Agricultural Sciences;

[18] Roland, J., Mosiniak, M., Roland, D., (1996), Dynamics of the cellulose microfibrils orientation in the cell wall of the flax fibers. *Acta Botanica Callica*; V. 142, № 5, 463-484;

[19] Semakov, V.V., (1994), Unconventional ways (Нетрадиционные способы), *Plant protection*, 3, 16-17;

[20] Yaheliuk, S., Didukh, V., Busnyuk, V., Boyko, G., Shubalyi, O., (2020), Optimization on efficient combustion process of small-sized fuel rolls made of oleaginous flax residues, *INMATEH - Agricultural Engineering*. V. 62, №. 3, 361-368;

[21] *** Demand for flax seeds is growing in Ukraine (В Україні зростає попит на насіння льону). *Agronews.Ua.* URL: https://agronews.ua/news/v-ukraini-zrostaie-popyt-na-nasinnia-lonu/. Last accessed: 10.02.2021);

[22] ***State Statistics Service of Ukraine, (2020), URL: http://www.ukrstat.gov.ua.

RESEARCH OF THE BURROWING SHARE OF A MACHINE FOR HARVESTING VEGETABLES AND ONIONS UNDER LABORATORY CONDITIONS
/
ИССЛЕДОВАНИЯ ПОДКАПЫВАЮЩЕГО ЛЕМЕХА МАШИНЫ ДЛЯ УБОРКИ ОВОЩНЫХ КУЛЬТУР И ЛУКА В ЛАБОРАТОРНЫХ УСЛОВИЯХ

Dorokhov A.S., Sibirev A.V.*), Aksenov A.G., Sazonov N.V. [1]
FSBSI "Federal Scientific Agronomic and Engineering Centre VIM"/ Moscow, Russia
Telephone: 89645843518; E-mail: sibirev2011@yandex.ru
DOI: https://doi.org/10.35633/inmateh-64-23

Keywords: *onions, digging share, soil admixtures, experimental studies*

ABSTRACT
It was found that the extraction of a tuberous heap, namely potatoes, with a digging working body with a movable frame, has the most significant drawback, which is that when the depth of the burrowing share tip is changed, the angle of its inclination changes, which negatively affects the chipping of the soil layer and leads to the deterioration of the transportation of the excavated soil layer to the separating working bodies, for which it is necessary to determine and clarify the main technological and design parameters of the developed intake plough share for digging / picking up root crops and bulbs due to the fact that potato tubers and onion bulbs have different size and mass and physical and mechanical properties. A method has been developed for determining the amount of supply of a heap of onion sets from the surface of the digging share to the separating working bodies, the required soil moisture necessary for research. The methodology and results of experimental studies to determine the decrease in the content of soil impurities in the gathering heap of onions are presented, the main statistical characteristics of the experiment are reflected. Based on the results of the screening experiment, significant factors have been established that have a decisive effect on the selected optimization criterion: spring preload, determined by the spring length and the forward speed of the digging share. It was found that the minimum possible amount of soil impurities when extracting onions from the soil is 24.8%. It depends on the values of the investigated factors, values that should be set in the interval: the length of the spring L_{PPR} *=0.02-0.04 m and the speed of the moving share* v_L *=1.2-1.4 m/s.*

РЕЗЮМЕ
Установлено, что извлечение клубненосного вороха, а именно – картофеля подкапывающим рабочим органом с подвижной рамкой, имеет наиболее значимый недостаток, заключающийся в том, что при изменении величины заглубления носка подкапывающего лемеха происходит изменение угла его наклона, что отрицательно сказывается на скалывании почвенного слоя и приводит к ухудшению транспортирования подкопанного почвенного пласта на сепарирующие рабочие органы, для чего необходимо определить и уточнить основные технологические и конструктивные параметры разработанного приемного лемеха для подкапывания/ подбора корнеплодов и луковиц в связи с тем, что клубни картофеля и луковицы лука-севка обладают различными размерно-массовыми и физико-механическими свойствами. Разработаны методика по определению величины подачи вороха лука-севка с поверхности подкапывающего лемеха на сепарирующие рабочие органы, требуемой влажности почвы, необходимой для проведения исследований. Представлены методика и результаты экспериментальных исследований по определению снижения содержания почвенных примесей в сходовом ворохе лука, отражены основные статистические характеристики эксперимента. По результатам отсеивающего эксперимента установлены значимые факторы, оказывающие определяющее влияние на выбранный критерий оптимизации: поджатие пружины, определяемое длиной пружины и поступательная скорость движения подкапывающего лемеха. Установлено, что минимально возможное количество почвенных примесей при извлечении лука из почвы составляет 24,8%. Это зависит от значений исследуемых факторов, значения которых должны устанавливаться в интервале: длина пружины L_{PPR}*=0.02 - 0.04 м и скорость движения подкапывающего лемеха* v_L *= 1.2-1.4 м/с.*

---
[1] *Dorokhov A.S., Prof. PhD. Eng.Sc.; Sibirev A.V., PhD. Eng.Sc.; Aksenov A.G., PhD. Eng.Sc.; Sazonov N.V., Eng.Sc.*

INTRODUCTION

When a swath of onion set at the surface of a field is formed by an onion harvester, onions interact with each other and with the surface of the soil *(Lobachevsky Ya.P. et al, 2016; Laryushin A.M., 2010; Protasov A.A., 2011; Reingart E.S., 1995; Sorokin A.A., 2006).* In the process of onions extraction from the soil, onion harvester advances progressively. This prevents a swath of onion set from having a large height and thus increases the share of damaged bulbs (since the increase of the swath leads to a decrease of bulb falling height and the degree of mechanical impact on lower bulbs being hit, whereas the number of onion set bulbs within the swath layer increases). Limiting rollers formed by the packing roller of the onion harvester prevent excessive growth of the width of onion set swath and thus prevent bulbs from scattering (*Protasov A.A., 2011*).

The analysis of the designs of existing machines for harvesting root crops and onions, as well as patent and technical literature, presented below, revealed shortcomings in the design of the digging parts of machines for harvesting root crops and bulbs, which do not allow ensuring a high-quality performance of the technological process separation of commercial products, and also lead to an increase in energy costs for harvesting, due to the increased rise of the soil layer together with commercial products (*Farhadi R. et al, 2012*).

Known machine for harvesting potatoes consist of basic elements, namely: an undercutting share, a separating bar elevator and support rods (*Tauseef A.M., et al, 2014*).

The main distinguishing feature of the harvester presented above is the design of the undercutting implement 1 (Fig. 1).

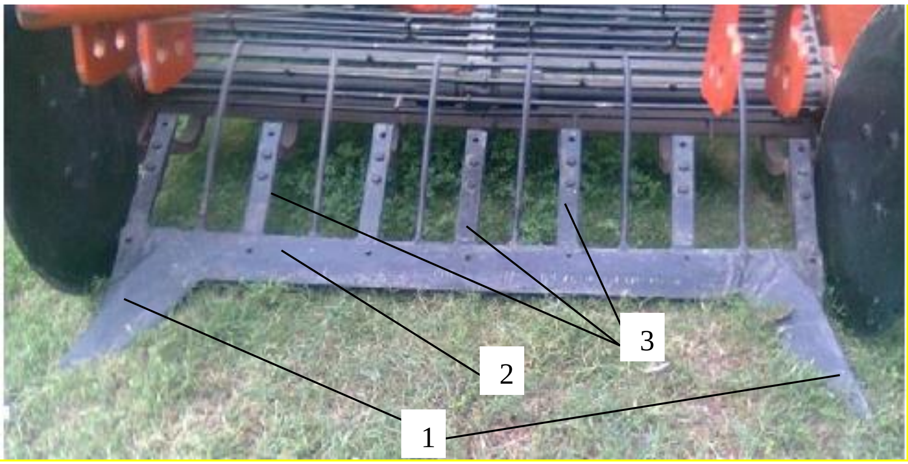

Fig. 1 - General view of the sub-digging body

1 – ripping element; 2 – digging element; 3 –pre-separation slotted holes

The underfloor working body is a combination of loosening *1* and undercutting *2,* elements with pre-separation slotted holes *3,* formed by the working surface of the undercutting element 2.

The loosening element *1* of the digging working body carries out preliminary loosening of the soil layer being dug in order to reduce the supply of soil clods to the separating working bodies, and therefore, intensifying the process of cleaning root crops from commensurate soil clods, as well as reducing the amount of damage to marketable products from collisions with soil clods on the rods cleaning machine. The digging element *2* carries out the extraction of root crops from the soil in the preliminary separation through the slotted holes *3*.

The disadvantages of this digging part include increased losses of root crops through the slotted holes *3* of the digging element *2*; in addition, this design of the digging working body does not reduce the amount of damage to the separated products on the bar elevator due to insufficient loosening of the soil layer of root crops location.

There is a known design of an undercutting working body, in which the front part of the bar elevator web on the part of the undercutting share vibrates in the vertical plane, when the underburned share mounting bracket acts on the supporting roller, which provides an additional force effect on the soil layer, and thereby intensifies the process of soil and plant impurities separation (*Natenadze N., 2016*).

The disadvantages of the known design of the digging working body include increased damage to root crops during the transition from one cascade to another, as well as the impossibility of dispersing a heap of root crops over the entire width of the conveyor.

Analysis of the technical means of mechanized harvesting of root crops allows us to conclude that the functioning elements of the harvesting machine with various types of separation intensifiers do not provide quality indicators for harvesting root crops in terms of such indicators as completeness of separation and damage to root crops.

The aim of the research is experimental research of the power effect of the digging share during mechanized onion harvesting. This need is due to the desire to reduce the traction and specific traction resistance of agricultural implements, which requires a constant search for more advanced, in terms of energy intensity, working bodies and technologies for field work. So, the use of working bodies of one type or another determines the predominance of a certain type of deformation of the soil layer. And since the soil resists differently to different types of influences, this leads to a decrease or increase in its resistivity (*Dorokhov A.S. et al, 2020*).

MATERIALS AND METHODS

The laboratory study program involved a study of the intake plough share used to lift and pick up roots. This was carried out in order to determine optimal values of its structural and process parameters that would ensure maximum thoroughness of harvest of root crops and onions with minimum pickup of soil impurities by separating working tools *(Devsh K., Ashok T., 2017; Koga N. et al 2013; Lü J.Q. et al, 2016).*

To study the volume of a root crop and onion heap transported from the surface of the intake plough share for subsequent lifting and pickup of root crops by the separating working tools of the harvester, research activities were carried out in the Penza Region in 2018 and 2019.

Stuttgarter Riesen onion seeds were planted according to the row/strip cropping system (six 45+25 cm rows), which calls for guess row and tractor wheel spacings of 50 cm and other spacings equal to 40 cm (*Hevko R.B., 2016*).

The quality of lifting of root crops and onions by the intake plough share used to lift/pickup root crops depends on a number of factors *(Dorokhov A.S. et al, 2020)*. In view of this, laboratory studies were carried out using the multifactorial experiment method, at the setup installed at a mobile soil channel (Fig. 2).

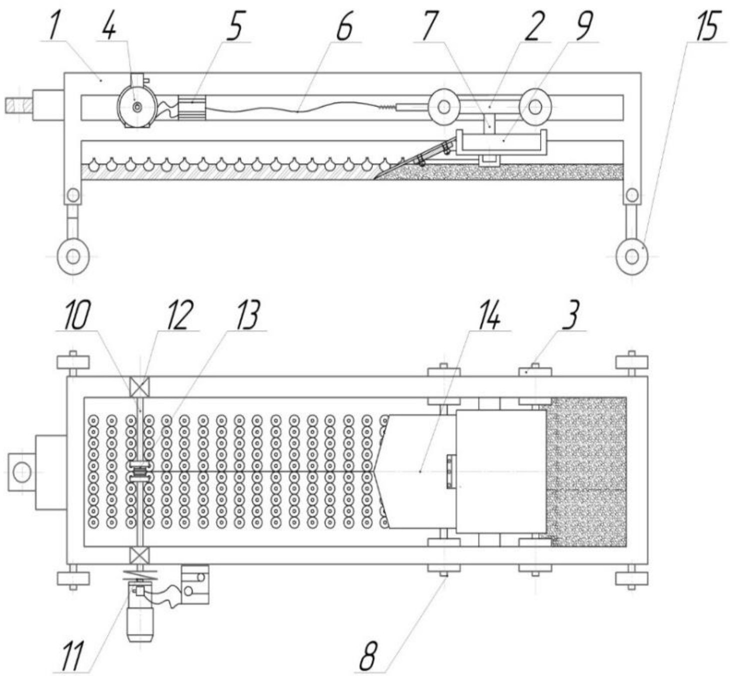

Fig. 2 – Diagram of the laboratory setup for determining the supply speed of onion heap to the digging plough share

1 – guide; 2 – driven trolley; 3 – steel roller; 4 – electric motor; 5 – frequency converter; 6 – rope connection; 7 – mounting rack; 8 – trolley axis; 9 – heap collection tray; 10 – trolley drive shaft; 11 – safety clutch; 12 – bearing; 13 – coil with restrictive flanges; 14 – digging plough share; 15 – supporting wheels

To determine the speed Q_{Bp} (the flow of a heap of onion sets and soil impurities from the surface of the digging share to the separating workers) of onion heap feed to the digging plough share of the root crop and onion harvester, a laboratory setup in the form of a mobile soil channel was used.

This made it possible to study qualitative indicators of digging working tools' operation on soils having varying physical and mechanical composition.

The setup used was a welded structure consisting of guides *1* with the driven carriage *2* moving along them. The carriage was mounted on four wheels *3* and driven by the electric motor *4* equipped with the frequency converter *5*, via the flexible rope connection *6*. The digging plough share *14* and the heap collection tray *9* were attached to the mounting rack *7* which was installed on the driven trolley *2*.

The driven trolley *2* moved along the guides *1* on the steel rollers *3* with the diameter of 0.15 m by means of an electric drive comprising the asynchronous electric motor *4* and the frequency converter *5*. This made it possible to control both the rotation frequency of the electric motor shaft and the direction of shaft rotation.

The method for determining Q_{Bp} the value of onion set heap feed speed from the surface of the digging plough share to the separating working tools is as follows. To account for soil moisture during the studies, it was measured using the method described below.

To ensure the soil moisture level required for the studies, the soil was moistened using surface irrigation, then kept for several hours until the required moisture level was achieved within the soil layer corresponding to the bulb lifting depth.

In accordance with the experiment plan, experiments were carried out with the soil moisture level corresponding to the required value.

A mobile soil channel was mounted on the experimental onion-planting plot (Fig. 3). The digging plough share *7* (standard grasp width 1.2 m) was mounted on the driven trolley *2* at the mobile soil channel to achieve the digging h_L depth within the range of 0.02 m to 0.05 m, and the variation interval of 0.01 m by moving the mounting rack *7* along the driven trolley *2*.

Fig. 3 – General View of the Laboratory Setup for Determining the Feed Speed of Onion Set Heap onto the Digging Plough Share

1 – guide; 2 – driven trolley; 3 – steel roller; 4 – electric motor; 5 – frequency converter; 6 – rope connection; 7 – mounting rack; 8 – trolley axis; 9 – heap collection tray; 10 – trolley drive shaft; 11 – safety clutch; 12 – bearing; 13 – coil with restrictive flanges; 14 – digging plough share; 15 – power supply

Seed onion heap collection tray *9* was rigidly attached to the digging plough share.
After that, the driven trolley *2* was set in motion, its travel speed was changed in increments of 0.2 m/s from the minimum value of 0.4 m/s to the limit value of 1.8 m/s.

After the driven trolley *2* passed the experimental plot, the onion-soil heap was removed from the tray *9* and weighed on an electronic scale (model MK - 15.2 - A21) (the weight of bulbs and soil impurities was determined separately).

When studying the intake plough share used for lifting/pickup of root crops and onions to determine qualitative characteristics of its operation, the content of soil impurities in the resulting heap M_P was assumed as the optimization criteria, characteristics of bulb damage W_L and loss P_L were assumed as limiting parameters (*Dorokhov A.S. et al, 2020*).

The value of the optimization criterion M_{Π} was determined using the following dependency:

$$M_P = \frac{M_{BL} - M_L}{M_{BL}} \cdot 100\%, \quad (1)$$

where M_{BL} – is the mass of onions, mass of soil impurities, mass of vegetable impurities [kg];

M_L – is the mass of onion set [kg].

According to the results obtained during studies of reduction of over consolidated soil delivery to the separating working tools of a potato harvester carried out by F. N. Gallyamov, the highest level of cleanliness of the resulting heap with the acceptable share of tuber loss of up to 3% was achieved at the travel speed of $v_L = 1.2$ m/s, spring stiffness F_{PR} =of 25 kN/m (P – spring, R – rate) and spring load of 0.05 m (*Gallyamov F.N., 2004)*.

The results obtained by *F.N. Gallyamov* applied to tuberiferous heap of potatoes picked up by a digging working tool with a movable frame. This type of working tool has the following drawback - changing the depth of the digging plough share's toe results in variation of its inclination angle, which impacts the quality of the soil layer shearing and transportation of the extracted soil slice to working tools adversely. This led to the necessity to determine and clarify main process and design parameters of the developed intake plough share for lifting/pickup of root crops and onions since potato tubers and onion set bulbs have different sizes and weights, as well as physical and mechanical properties.

Thus, in our case, in order to ensure that the plough share's toe is buried to the maximum depth of 6 cm, down to the minimum depth of onion set bulb location within soil of 3 cm, it is necessary to set spring stiffness to F_{PR} =20 kN/m.

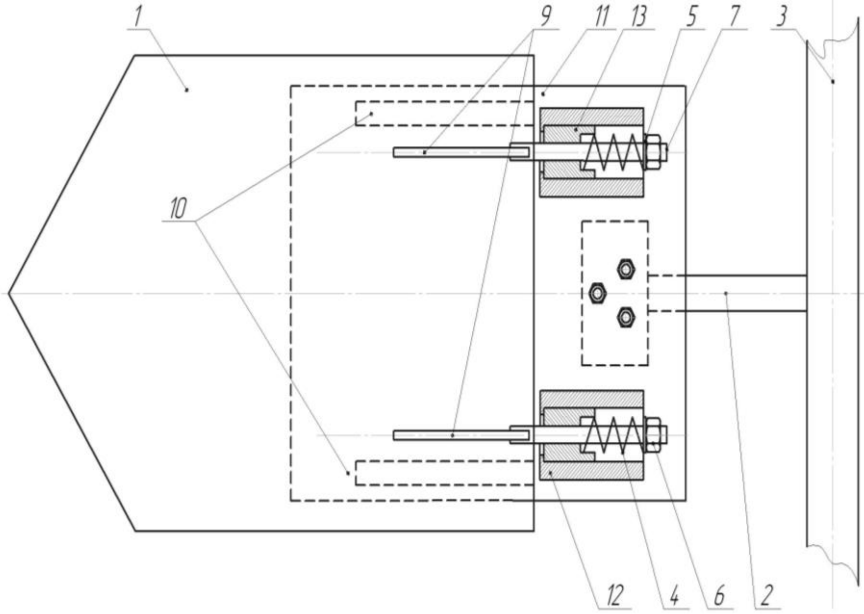

Fig. 4 – Structural and Process Diagram of Intake Plough Share for Lifting/Pickup of Root Crops and Onions

1 – plough share; 2 – bracket; 3 – frame; 4 – elastic support element; 5 – gasket; 6 – nut; 7 – rod; 8, 9 – plungers; 10 – guides; 11 – base plate; 12 – bushing

Based on the results of the screening experiment performed to reveal the most important factors affecting the selected optimization criteria, we distinguished the following two criteria:

- spring load L_{PPR}, [m];
- travel speed of the digging plough share v_L, [m/s].

The working travel speed of the trolley was determined based on the length of the registration plot (4 m) and the time required to complete a passage:

$$v_L = \frac{S_T}{t_T}, \quad (2)$$

where:

S_T – is the distance covered by the trolley, [m];

t_T – is the distance passage time, [s].

The spring L_{PPR} was loaded by relocating the nut *6* along the rod *7*.

Three levels were selected for each factor: lower, upper and base – zero level. After that, factor variation interval was determined (Table 1) and the multifactorial experiment was conducted according to the experiment plan 2^3 (Table 1).

Table 1

Factor Variation Levels when Determining Qualitative Characteristics of Root Crop and Onion Lifting/Pickup Intake Plough Share Operation

<table>
<tr><th rowspan="4">Level of variation</th><th colspan="2">Variable Factors</th><th>Optimization Criteria</th></tr>
<tr><th>Spring load L_{PPR}, m</th><th>Progressive speed of the digging plough share v_L, m/s</th><th rowspan="3">Content of soil impurities in the resulting heap M_P, %</th></tr>
<tr><th colspan="2">Variability interval, Δx_i</th></tr>
<tr><td>0.02</td><td>0.2</td></tr>
<tr><td>upper (+1)</td><td>0.06</td><td>1.6</td><td rowspan="4">Y</td></tr>
<tr><td>lower (-1)</td><td>0.02</td><td>1.2</td></tr>
<tr><td>base (0)</td><td>0.04</td><td>1.4</td></tr>
<tr><td>Designations</td><td>X_1</td><td>X_2</td></tr>
</table>

The studies were carried out with the aim of determining the effect of process parameters (L_{PPR} and v_L) of the root crop and onion lifting/pickup intake plow share on the amount of soil impurities in the resulting heap M_P in a laboratory environment.

Table 2

Two-Factor Experiment Planning Matrix

<table>
<tr><th rowspan="3">Designation</th><th colspan="2">Factors</th></tr>
<tr><th>Spring load L_{PPR}, m</th><th>Progressive speed of the digging plough share v_L, m/s</th></tr>
<tr><th>X_1</th><th>X_2</th></tr>
<tr><td>1</td><td>-1</td><td>-1</td></tr>
<tr><td>2</td><td>1</td><td>-1</td></tr>
<tr><td>3</td><td>-1</td><td>1</td></tr>
<tr><td>4</td><td>1</td><td>1</td></tr>
<tr><td>5</td><td>1</td><td>0</td></tr>
<tr><td>6</td><td>-1</td><td>0</td></tr>
<tr><td>7</td><td>0</td><td>1</td></tr>
<tr><td>8</td><td>0</td><td>-1</td></tr>
<tr><td>9</td><td>0</td><td>0</td></tr>
<tr><td>10</td><td>0</td><td>0</td></tr>
<tr><td>11</td><td>0</td><td>0</td></tr>
<tr><td>12</td><td>0</td><td>0</td></tr>
<tr><td>13</td><td>0</td><td>0</td></tr>
</table>

After the results of the multifactorial experiment were processed by STATISTICA 6.0 software, response function values were obtained.

RESULTS

The content of soil impurities in the resulting heap M_P depending on the varied factors, and an adequate encoded mathematical model describing the dependency M_P=f(L_{PPR}, v_L) of onion and soil heap input on the selected factors was developed.

$$Y = 25.23 + 0.12x_1 + 1.63x_2 - 0.001x_1^2 - 0.015x_2^2 - 0.03x_1x_2 \tag{3}$$

The adequacy of the presented model was verified using statistical analysis of the regression equation. The results of statistical characteristic calculations are shown in Table 3.

The coordinates of the yield surface were determined by differentiating the equation (3) and solving the following system of equations:

$$\begin{cases} \dfrac{dy}{dx_1} = 0.12 - 0.002x_1 - 0.03x_2 = 0, \\ \dfrac{dy}{dx_2} = 1.63 - 0.03x_2 - 0.03x_1 = 0. \end{cases} \tag{4}$$

By solving the system of equations (8), we determined the coordinates of the encoded response function's surface center: $x_1 = -86.25,\ x_2 = 9.75$ (decoded results are: L_{PPR}=0.032 м, v_L =1.4 m/s).

Table 3

Statistical Characteristics of Experimental Error

No.	Y_1	Y_2	Y_3	$\overline{Y_u}$	$\widehat{Y_u}$	S_y^2	S_{LF}^2	$(Y_u - \widehat{Y_u})^2$
1	23.9	24.2	24.2	24.2	23.43	0.7	0.381	1.413
2	23.1	22.7	22.9	22.9	23.73	1.06	0.581	2.131
3	23.8	23.9	23.7	23.8	26.75	1.08	0.589	2.162
4	22.3	22.5	22.1	22.3	26.93	0.04	0.021	0.081
5	24.2	24.2	23.9	24.1	25.34	0.03	0.016	0.063
6	25.3	24.8	25.2	25.1	25.11	0.06	0.033	0.124
7	25.3	25.4	25.2	25.3	26.84	1.48	0.807	2.961
8	22.8	22.6	22.7	22.7	23.61	1.24	0.675	2.475
9	25.4	25.6	25.2	25.4	25.23	0.08	0.045	0.166
10	25.3	25.0	25.3	25.2	25.23	0.03	0.017	0.062
11	25.4	25.2	25.3	25.3	25.23	0.01	0.009	0.034
12	25.1	25.1	25.4	25.2	25.23	0.03	0.017	0.062
13	25.2	25.2	25.5	25.3	25.23	0.03	0.021	0.074
Σ	-	-	-	316.8	-	5.871	3.212	11.81

By applying values x_1 and x_2 to the equation (7), we obtained the value of the response function at the center of the surface.

$$Y_S = 24.86 \tag{5}$$

By applying canonical transformation of the equation (7), we obtained the equation in its canonical form:

$$Y - 24.86 = 0.0015x_1^2 - 0.471x_2^2 \tag{6}$$

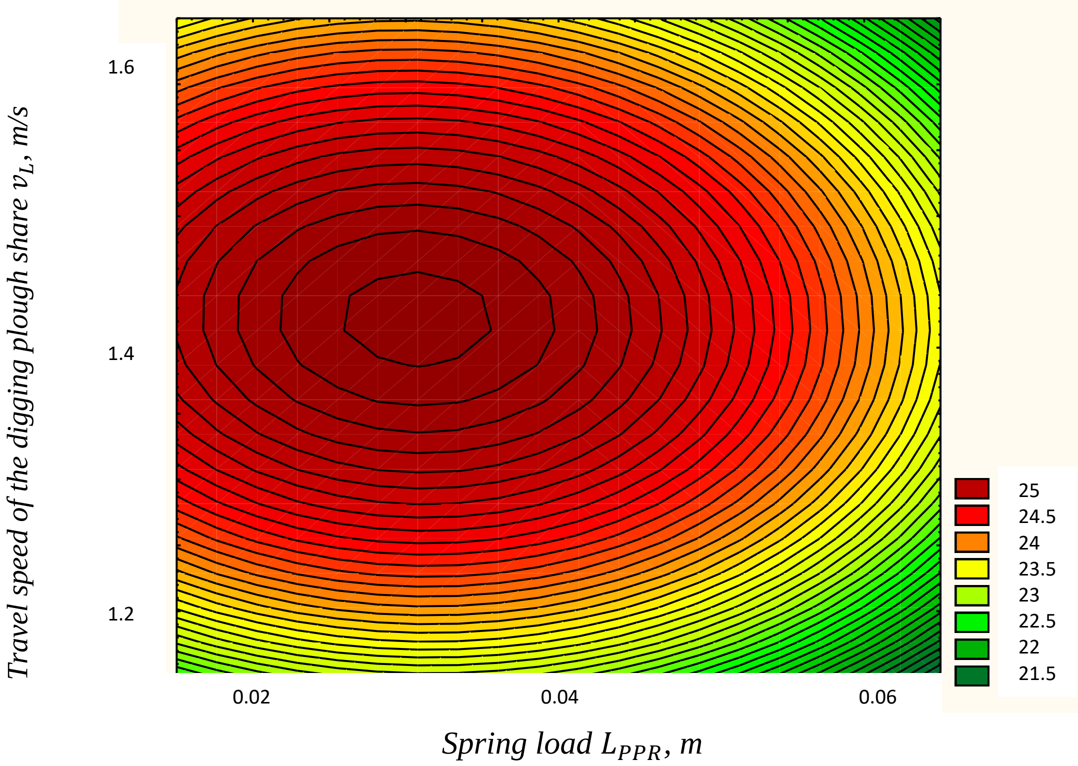

Fig. 5 - Two-Dimensional Section of the Response Surface Characterizing the Dependency of Content of Soil Impurities in the Resulting Heap (in %) from the Spring Load and Travel Speed of the Digging Plough Share

Axis turning axle is:

$$\mathrm{tg}\, 2\alpha_2 = \frac{0.005}{0.11 - 0.005} = 0.047 \tag{7}$$

Angle α_2= - 1.26 °.

By applying various values of the response function (3), we obtained contour plot (ellipse) equations. Calculation results are shown in Fig. 5.

CONCLUSIONS

The results of the screening experiment made it possible to determine the significant factors that have a decisive influence on the selected optimization criterion: spring preload, determined by the spring length and the forward speed of the digging share.

It was found that the minimum possible amount of soil impurities when extracting onions from the soil is 24.8%. It depends on the values of the investigated factors, the values of which should be set in the interval: spring length L_{PPR}=0.02 - 0.04 m and the speed of movement of the undercutting share v_L = 1.2-1.4 m/s.

ACKNOWLEDGEMENT

«The reported study was funded by RFBR, project number 19-316-90068».

REFERENCES

[1] Devsh K., Ashok T. (2017), Performance evaluation of tractor drawn potato digger cum-elevator, *International Journal of Agricultural Science and Research*, Issue number 7(2), pp. 433 – 448, Tehran / Iran;

[2] Dorokhov A.S., Sibirev A.V., Aksenov A.G. (2020), Investigation of the performance indicators of the receiving ploughshare for digging / picking up root crops and bulbs in laboratory conditions (Исследование показателей качества работы приемного лемеха для подкапывания/подбора корнеплодов и луковиц в лабораторных условиях), *Agricultural scientific journal*, Issue number 7: pp.70 – 74. Saratov / Russia;

[3] Farhadi R., Sakenian N., Azizi P. (2012), Design and construction of rotary potato grader, *Bulgarian Journal of Agricultural Science*, Issue number 2, pp. 304 – 314, Sofia / Bulgaria*;*

[4] Gallyamov F.N. (2004), *Development and optimization of the parameters of the device for controlling the depth of travel of the undercutting working bodies of potato harvesters (Разработка и оптимизация параметров устройства регулирования глубины хода подкапывающих рабочих органов картофелеуборочных машин)*, dissertation Candidate of Engineering, Orenburg / Russia;

[5] Hevko R.B., Tkachenko I.G., Synii S.V., (2016), Development of design and investigation of operation processes of small-scale root crop and potato harvesters, *INMATEH-Agricultural Engineering*. Vol. 49 (2), pp. 53-60, Bucharest / Romania;

[6] Koga N., Kajiyama T., Senda K., Iketani S, Tamiya S, Tsuda, S., (2013), Energy efficiency of potato production practices for bioethanol feedstock in northern Japan, *European Journal of Agronomy*, Issue number 44(1), pp. 1–8, Amsterdam / Netherlands;

[7] Lü J.Q., Shang Q.Q., Yang Y., Li Z.H., Li J.C., Liu Z.Y. (2016), Design optimization and experiment on potato haulm cutter, *Transactions of the CSAM*, Issue number 47(5), pp.106–114, London / United Kingdom*;*

[8] Lobachevsky Ya.P., Emelyanov P.A., Aksenov A.G., Sibirev A.V., (2016), Onion production machine technology (Машинная технология производства лука), *Monograph, FSBSI "Federal Scientific Agronomic and Engineering Centre VIM".* 168 p. Moscow / Russia;)

[9] Laryushin A.M. (2010), *Energy-saving technologies and technical means for onion harvesting (Энергосберегающие технологии и технические средства для уборки лука), dissertation Doctor of Engineering,* Penza / Russia*;*

[10] Nappe Mordi N. Al-Dosary (2016), Potato harvester performance on tubers damage at the eastern of Saudi Arabia, *Agricultural engineering international: CIGR Journal*, Issue number 18(2), pp. 32–42, Beijing / China*;*

[11] Natenadze N. (2016), The design and theoretical justification of a vibratory digger shovel, *Scientific technical union of mechanical engineering Bulgarian association of mechanization in agriculture*, Issue number 5, pp. 9–12, Sofia / Bulgaria*;*

[12] Protasov A.A., (2011), A functional approach to the development of an onion harvester (Функциональный подход к созданию лукооуборочной машины), *Herald of the Federal State Higher Vocational Education Institution Moscow State Agricultural Engineering University named after V. P. Goryachkin*, Issue number 2 (47), pp. 37-43, Moscow / Russia;

[13] Reingart E.S., Sorokin A.A., Ponomarev A.G., (2006), The new generation of standardized potato harvesters (Унифицированные картофелеуборочные машины нового поколения), *Tractors and agricultural machinery*, Issue number 10, pp. 3-5, Moscow / Russia;

[14] Sorokin A.A., (2006), Theory and calculation of potato harvesters (Теория и расчет картофелеуборочных машин), *Monograph, FSBSI "Federal Scientific Agronomic and Engineering Centre VIM".* 159 p. Moscow / Russia;

[15] Sun D.X., Zhang A.M., Gong J.X. (2016), Design and experiment on 1SZL-250A type subsoiling rotary tillage fertilizer combined soil working machine, *Journal of Chinese Agricultural Mechanization*, Issue number 37(4): pp. 1–6. Beijing / China*.*

[16] Tauseef A. M., Ghafoor A., Munir A., Iqbal M., Ahmad M. (2014), Design modification and field testing of groundnut digger, *Asian Journal of Science and Technology*. Issue number 5: pp. 389–394. Tamil Nadu / India.

EFFECT OF FRUIT AND VEGETABLE BLANCHING AND COMPRESSION ON THE LOSS OF MULTILAYER CHIPS
/
ВПЛИВ БЛАНШУВАННЯ ТА СПРЕСОВУВАННЯ ФРУКТІВ І ОВОЧІВ НА ВТРАТИ БАГАТОШАРОВИХ ЧИПСІВ

Dudarev Igor*), Panasyuk Svitlana, Taraymovich Iryna, Say Volodymyr
Lutsk National Technical University / Ukraine
Tel: +38(096)0403755; E-mail: i_dudarev@ukr.net
DOI: https://doi.org/10.356.33/inmateh-64-24

Keywords: *fruit chips, vegetable chips, blanching time, chips loss, chips technology*

ABSTRACT
Chips are a useful and popular product that is produced in most countries of the world. The main processes of traditional chips technology are slicing fruits and vegetables into thin slices, blanching and drying slices. Multilayer chips are formed from several layers of different materials (fruits, vegetables and seeds). For forming of such chips, it is important that the layers of different materials stick together well. Studies have shown that the material type and blanching time significantly affect the adhesion of material and loss of chips. Also, effect of compression of raw material layers on the chips loss was studied.

АНОТАЦІЯ
Фруктові та овочеві чипси – це корисний і популярний продукт, який виробляється в більшості країн світу. Основними процесами традиційної технології виробництва чипсів є нарізування фруктів та овочів на тонкі скибочки, бланшування та сушіння скибочок. Багатошарові чипси формуються із декількох шарів різної сировини, такої як фрукти, овочі та насіння. Для формування таких чипсів важливо, щоб шари різної сировини добре злипалися. Експериментальні дослідження продемонстрували, що вид сировини та час її бланшування суттєво впливають на липкість сировини та втрати чипсів. Також досліджувався вплив спресовування шарів сировини на втрати чипсів.

INTRODUCTION
Chips are very popular type of snack food in most countries of the world. A broad variety of chips made by different technologies are available in the market. An assortment of chips includes potato chips, corn chips, tortilla chips, fruit chips, vegetable chips etc. Chips may be classified according to raw materials used in their production (fruits, vegetables, corns etc.) and specific unit operations (baking, drying, extrusion, frying etc.) for their manufacture *(Pedreschi et al., 2018)*. New types of chips and technologies for their manufacture are constantly being developed by scientists and snack food producers. In particular, the apple chips technology using osmotic pre-treatment in cherry or apple concentrated juices before convection drying was developed, which enriches chips with additional natural nutrients and improves their color and taste *(Kowalska et al., 2018)*.

Fruit and vegetable chips are the most useful types of snack food for the human body. The manufacturing technology of such chips, as well as potato chips *(Pedreschi et al., 2007)*, includes the processes of washing, peeling, sorting, cutting into slices and blanching of raw materials. But in contrast to the potato chips manufacturing technology, where potato slices are fried, in the production of fruit and vegetable chips, technology involves the drying process of fruit and vegetable slices.

It is known that drying is one of the most common techniques used to preserve food *(Prawiranto et al., 2019)*. Drying of fruits and vegetables is a complicated process *(Diamante et al., 2010)* and involves simultaneous mass and heat transfer accompanied by physical and structural changes *(Senadeera et al., 2000)*. Also, drying process reduces water activity of fruits and vegetables products, which inhibits microbial growth and decreases degradative reactions, resulting in higher stability *(Abano et al., 2019)*. Dehydration, which occurs during fruits and vegetables drying in thin-layer, leads to a change in textural characteristic of finished products *(Ramos et al., 2003)*. For consumers, the texture is one of the most significant quality characteristic of chips since the texture makes a dominant contribution to the overall quality and acceptability

(Kayacier and Singh, 2003). Therefore, it is very important that the changes, which occur during fruits and vegetables drying, do not lead to a significant deterioration in the quality properties of chips compared to the quality properties of fresh fruits and vegetables.

In the food industry, different drying methods are applied, including solar drying, convective drying, microwave drying, osmotic dehydration, freeze drying, spray drying, superheated steam drying, and vacuum drying *(Sagar and Suresh Kumar, 2010)*. An optimal drying method should be cost effective, and must have a shorter drying time with minimum damage to the product. For dehydration of fruits and vegetables, some new drying technologies were developed, such as infrared radiation drying, microwave drying, radio frequency drying, electrohydrodynamic drying, dielectric drying, and hybrid drying methods combining two or more different drying techniques *(Zhang et al., 2017)*. Due to the unique characteristics of fruits and vegetables, there are different choices for the dehydration process and each one has certain characteristics that affect the drying behavior and the final foodstuff quality *(Santos and Silva, 2008)*. The various conditions affecting the drying of sliced fruits and vegetables include air velocity, drying temperature, size and shape of slices, slice thickness and the relative humidity *(Onwude et al., 2016)*.

Blanching is an important technological operation for preparing fruits and vegetables for drying, because blanching has resulted in increasing the drying rate of products *(Dandamrongrak, 2003)*. In particular, it is determined that steam treatment shortens the drying process by 20 – 30% than the raw fruit dehydration *(Husarova and Shapar, 2017)*. The main purpose of blanching is to inactivate enzymes responsible for deterioration of fresh fruits and vegetables such as peroxidase and polyphenol oxidases *(Aktas et al., 2007)*. Thermal processing of fruits and vegetables has pronounced effects on the cell structure, often negatively affecting the final textural properties of the product *(Neri et al., 2011)*. Also, temperature and blanching time significantly reduced in bioactive components, and firmness of fruits and vegetables *(Eyarkai Nambi et al., 2016)*. The color of fruits and vegetables changes considerably during blanching *(Tijskens et al., 2001)*. Quality characteristics of fruits and vegetables after blanching depend on the method of blanching and the initial properties of fresh raw materials.

The various types of blanching methods include water blanching, steam blanching, vacuum steam blanching, in-can blanching, microwave blanching and hot-gas blanching *(Selman, 1994)*. Blanching parameters, such as temperature and blanching time, depend on the quality characteristics of raw materials and subsequent technological processes of chips manufacturing. For example, blanching at a high temperature and short time is recommended for vegetable soybeans *(Song et al., 2003)* and the best blanching parameters for carrots are temperature of hot water about 95ºC and blanching time about 5 min *(Shivhare et al., 2009)*. Typically, the blanching process utilizes temperatures around 75 – 95ºC *(Selman, 1994)* for times of about 1 – 10 min *(Xiao et al., 2017)*, depending on the product requirements.

The influence of different methods of blanching on the finished product quality has been studied by scientists. Thus, vegetables blanched with microwave energy are more nutritious than those heated to the same temperature by conventional water blanching *(Ramesh et al., 2002)*. Also, a vitamin C decrease is not observed in microwaved broccoli *(Severini et al., 2016)*. The thermosonication is a potential alternative to conventional thermal treatments, the impact of which on food quality attributes is lower than the ones observed with heat blanching *(Alexandre et al., 2011)*.

When forming foods, such as multilayer chips from different layers of raw materials, it is important that the layers stick together well. There are many food-related and non-food related factors and forces, which affect the stickiness (adhesion) of food materials, such as moisture content, temperature, viscosity and type of the food, compression of a food system, and a combined effect of adhesive and cohesive forces *(Adhikari et al., 2001)*. Researches have proposed various methods to determine a food material adhesion, but the simplest method is to weigh the material remaining on the contact surface *(Michalski et al., 1997)*.

The aim of the study is to determine the effect of fruit and vegetable blanching and compression of raw material layers on the loss of multilayer chips.

MATERIALS AND METHODS

Sample preparation

Multilayer chips can be made from different combinations of fruits, vegetables and seeds. Loss of multilayer chips during technological processes depends on the fruits and vegetables properties and processing regimes of chips production. Multilayer chips were formed from two or three layers of fruits, vegetables and seeds. The first layer (the main layer) of all types of chips was formed from a rectangular-shaped slice of fruit or vegetable. For the main layer, slices of fruit and vegetables were blanched.

The first layer is the basis of multilayer chips, because all other layers were formed on it. The second layer of all types of chips was formed by breading of one slice side with crushed seeds. As a raw material for the second layer of chips, flax seeds were used, which contain a large amount of nutrients and lignin, which ensures the bonding of the layers of chips. The third layer of three-layer chips was formed from grated fruits or vegetables. Grated vegetables were blanched and grated fruits were not blanched.

Local raw fruits, vegetables and seeds such as zucchini, carrots, apples and flax seeds were used to form the multilayer chips. Flax seeds, fresh fruit and vegetables purchased from local markets were randomly sampled. Fruits and vegetables were cleaned, peeled and sliced into rectangular-shaped slices with dimensions $a \times a$ and thickness h (fig. 1, a). The slice surface did not contain peel. The slice thickness h was as follows: for zucchini slices – 3 mm, 5 mm and 7 mm; for carrot slices – 1 mm, 2 mm and 3 mm; for apple slices – 2 mm, 3 mm and 5 mm. The slice dimensions $a \times a$ were as follows: for zucchini slices – 3 cm $\times$ 3 cm; for carrot and apple slices – 2 cm $\times$ 2 cm. The area s of the slice surface, which was breaded with crushed seeds, was as follows: for zucchini slices – 9 cm^2; for carrot slices – 4 cm^2; for apple slices – 4 cm^2.

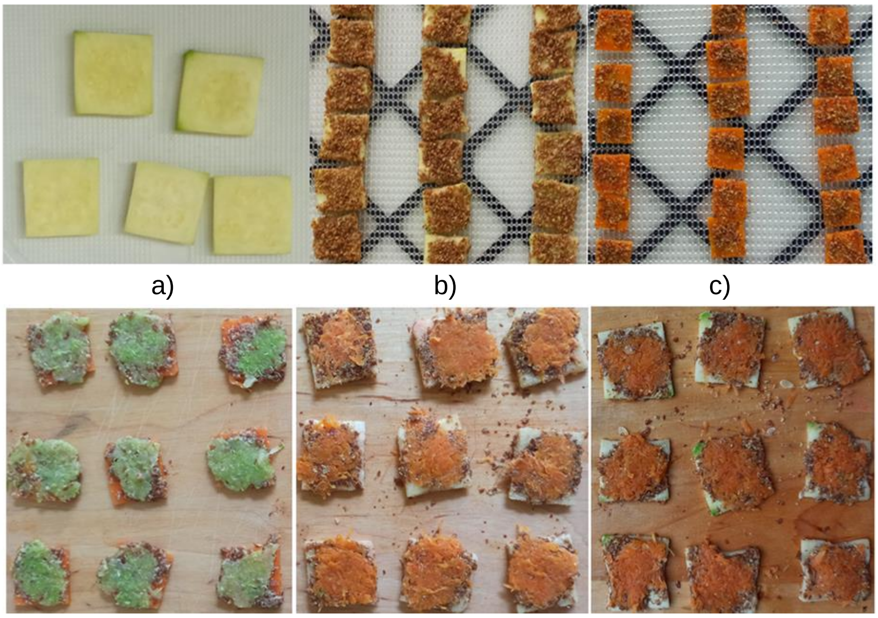

a) b) c)

d) e) f)

Fig. 1 - Rectangular-shaped zucchini slices (a), and formed samples of some types of two-layer chips, such as ZF (b) and CF (c), and three-layer chips, such as CFZ (d), AFC (e) and ZFC (f)

For the second layer of chips flax seeds were crushed. The percentage of seed particles, which was determined by the sieve method on sieves with round orifices, was for seed particle size: more than 3 mm – 1.9%; from 2 mm to 3 mm – 54.8%; from 1.1 mm to 2 mm – 40%; from 0.5 mm to 1.1 mm – 3.1%; from 0.25 mm to 0.5 mm – 0.2%.

For the third layer of chips, fruits and vegetables were grated. The sizes of the grated raw materials were as follows: the length – less than 10 mm; the width – less than 5 mm; thickness – less than 1 mm.

Three variants of two-layer chips were studied (fig. 1, b, c):

- the first layer of chips was formed by a zucchini slice, and the second layer was formed by crushed flax seeds (the designation of the variant is ZF);
- the first layer of chips was formed by a carrot slice, and the second layer was formed by crushed flax seeds (the designation of the variant is CF);
- the first layer of chips was formed by an apple slice, and the second layer of was formed by crushed flax seeds (the designation of the variant is AF).

Nine variants of three-layer chips were also studied:

- the first layer of chips was formed by a carrot slice, and the second layer was formed by crushed flax seeds, and the third layer was formed by grated carrot (the designation of the variant is CFC);
- the first layer of chips was formed by a carrot slice, and the second layer was formed by crushed flax seeds, and the third layer was formed by grated zucchini (the designation of the variant is CFZ (fig. 1, d));
- the first layer of chips was formed by a carrot slice, and the second layer was formed by crushed flax seeds, and the third layer was formed by grated apple (the designation of the variant is CFA);

- the first layer of chips was formed by an apple slice, and the second layer was formed by crushed flax seeds, and the third layer was formed by grated apple (the designation of the variant is AFA);
- the first layer of chips was formed by an apple slice, and the second layer was formed by crushed flax seeds, and the third layer was formed by grated zucchini (the designation of the variant is AFZ);
- the first layer of chips was formed by an apple slice, and the second layer was formed by crushed flax seeds, and the third layer was formed by grated carrot (the designation of the variant is AFC (fig. 1, e));
- the first layer of chips was formed by a zucchini slice, and the second layer was formed by crushed flax seeds, and the third layer was formed by grated zucchini (the designation of the variant is ZFZ);
- the first layer of chips was formed by a zucchini slice, and the second layer was formed by crushed flax seeds, and the third layer was formed by grated apple (the designation of the variant is ZFA);
- the first layer of chips was formed by a zucchini slice, and the second layer was formed by crushed flax seeds, and the third layer was formed by grated carrot (the designation of the variant is ZFC (fig. 1, f)).

Instruments

During study, the main laboratory equipment was used, such as: slicer GORENJE R 506 E; dehydrator Excalibur 4926T Black; grinder Hamilton Beach Fresh Grind 4.5 oz; laboratory drying cabinet CNOL-3,5.3,5.3,5/3,5; thermometer Testo 405V1; laboratory balances FEN-V2003.

Moisture content determination

Moisture content of fruits and vegetables and multilayer chips was determined by standard method *(AOAC Official Method)*. Moisture content of fruits and vegetables was as follows: for zucchini – 94.9%; for carrots – 91.2%; for apples – 93.7%; for flax seeds – 6.4%. Moisture content of multilayer chips of all variants was between 6.3% and 8.5%.

Blanching of fruit and vegetable slices

Blanching of fruit and vegetable slices and grated vegetables was carried out by steam at a temperature of 85 – 95ºC. Blanching time t was as follows:

- for zucchini slices: 1 min, 2 min, 3 min and 5 min (h = 3 mm); 2 min, 3 min, 5 min, 7 min (h = 5 mm); 3min, 5 min, 7 min and 9 min (h = 7 mm);
- for carrot slices – 3 min, 5 min, 7 min and 9 min (h = 1 mm, h = 2 mm, h = 3 mm);
- for apple slices – 1 min, 2 min, 3 min and 5 min (h = 2 mm, h = 3 mm, h = 5 mm).

The time t of grated vegetable blanching was as follows: for grated zucchini – 2 min; for grated carrot – 3 min. Grated apples were not blanched.

Adhesion index determination

During the study, it was necessary to determine the adhesion index of fruits and vegetables and the ability of the chips layers to be joined and not crumble into crumbs after drying. Therefore, the effect of blanching time on the adhesion of the crushed seeds to chips first layer was determined. After blanching, the sample of sliced fruits or vegetables was weighed and breaded on one side with crushed seeds. After breading, the sample was weighed again. In the control variant (without blanching), the sample was weighed twice before and after breading. The adhesion index of sliced fruits and vegetables was calculated by the equation:

$$\lambda = (m_2 - m_1) / s, \tag{1}$$

where: λ is an adhesion index of sliced fruits and vegetables, g·cm^{-2}; m_1 is a mass of the sample of sliced fruits or vegetables before breading, g; m_2 is a mass of the sample of sliced fruits or vegetables after breading, g; s is the breaded surface area of the sample, cm^2.

Compression of chips layers

After forming samples of multilayer chips, the samples were compressed with a load of a certain mass m. Since the area s of the sample of multilayer chips (the size $a \times a$ of the first layer) and the force F of compression were known, the pressure on the sample was calculated by the equation:

$$P = mg / s = F / s, \tag{2}$$

where: P is a pressure on the sample of multilayer chips, Pa; m is a mass of load, kg; g is an acceleration of gravity, m·s^{-2}; F is a force of compression, N; s is a surface area of the sample of multilayer chips, m^2.

During the study, the pressure P on the sample of chips was as follows: 4.0 kPa, 4.9 kPa and 5.5 kPa.

Drying of multilayer chips samples

The convective method of drying was used for multilayer chips samples drying. For all types of multilayer chips, the drying temperature was about 63ºC. For two-layer chips (fig. 2, a, b, c), the drying time was as follows: for chips with the first layer made of zucchini – 5.5 h; for chips with the first layer made of apple – 4.0 h; for chips with the first layer made of carrot – 3.0 h. For all variants of three-layer chips (fig. 2, d, e, f), the drying time was about 6.5 h.

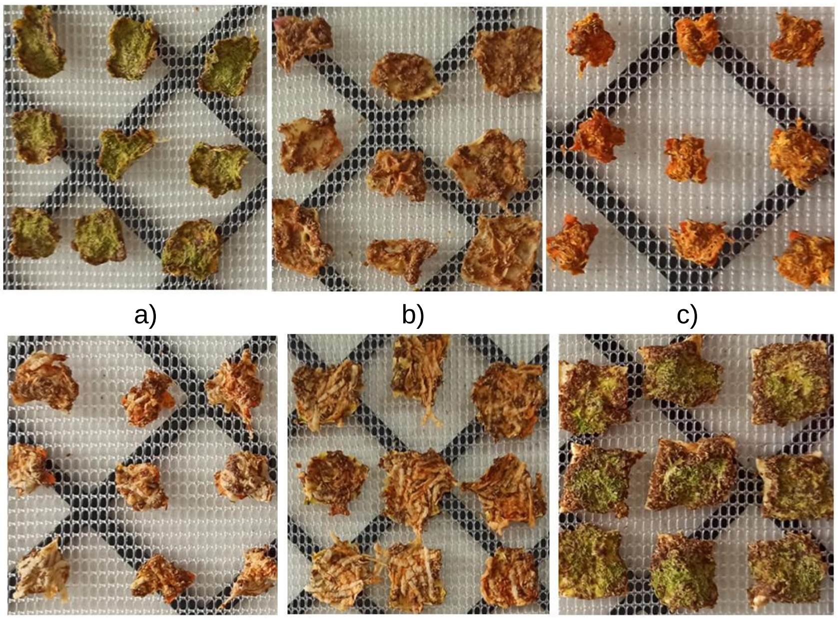

a) b) c)

d) e) f)

Fig. 2 - Dried two-layer chips, such as ZF (a), AF (b) and CF (c), and dried three-layer chips, such as CFA (d), ZFA (e) and AFZ (f)

Determination of multilayer chips loss

Multilayer chips loss was determined after drying and cooling of the samples. For this purpose, samples of chips were placed in the parallelepiped-shaped container with dimensions 30 cm × 30 cm × 5 cm. The container rotated about 100 times and shook intensely, as a result of which the chips moved on its inner surfaces. In this way, the movement of chips on the working surfaces of the technological equipment was simulated. During the container rotating and shaking, crumbs of chips were formed. These crumbs are the losses of multilayer chips. After container rotating and shaking, multilayer chips and crumbs were weighed separately. Multilayer chips loss was calculated by the equation:

$$\eta = m_4 \cdot 100 \,/\, (m_3 + m_4), \tag{3}$$

where:

η is a chips loss, %; m_3 is a mass of multilayer chips after container rotating and shaking, g; m_4 is a mass of chips crumbs after container rotating and shaking, g.

Statistical analysis

The experimental data were processed using the methods of mathematical statistics *(Steel et al., 1997)* and computer software Mathcad 14. The coefficient of determination r^2 was also calculated.

RESULTS

Fig. 3, a presents the effect of zucchini slice blanching time t on the adhesion of crushed flax seeds to zucchini slices. Regardless of the zucchini slice thickness h, the adhesion index λ of blanched zucchini slices was greater than the adhesion index of non-blanched zucchini slices (the control variant). The results of the study show that the blanching time t significantly affects the adhesion index λ. With the time of the zucchini slice blanching up to 2 min, the adhesion index of the zucchini slices increased to 0.047 g·cm^{-2} (h = 3 mm) and to 0.054 g·cm^{-2} (h = 5 mm). For zucchini slices with a thickness of 7 mm the maximum adhesion index was 0.056 g·cm^{-2}. This value of the adhesion index was achieved with a blanching time of 5 min.

Regardless of the slice thickness, the increase in the blanching time more than 2 min (h = 3 mm, h = 5 mm) and more than 5 min (h = 7 mm) led to a decrease in the adhesion index of zucchini slices.

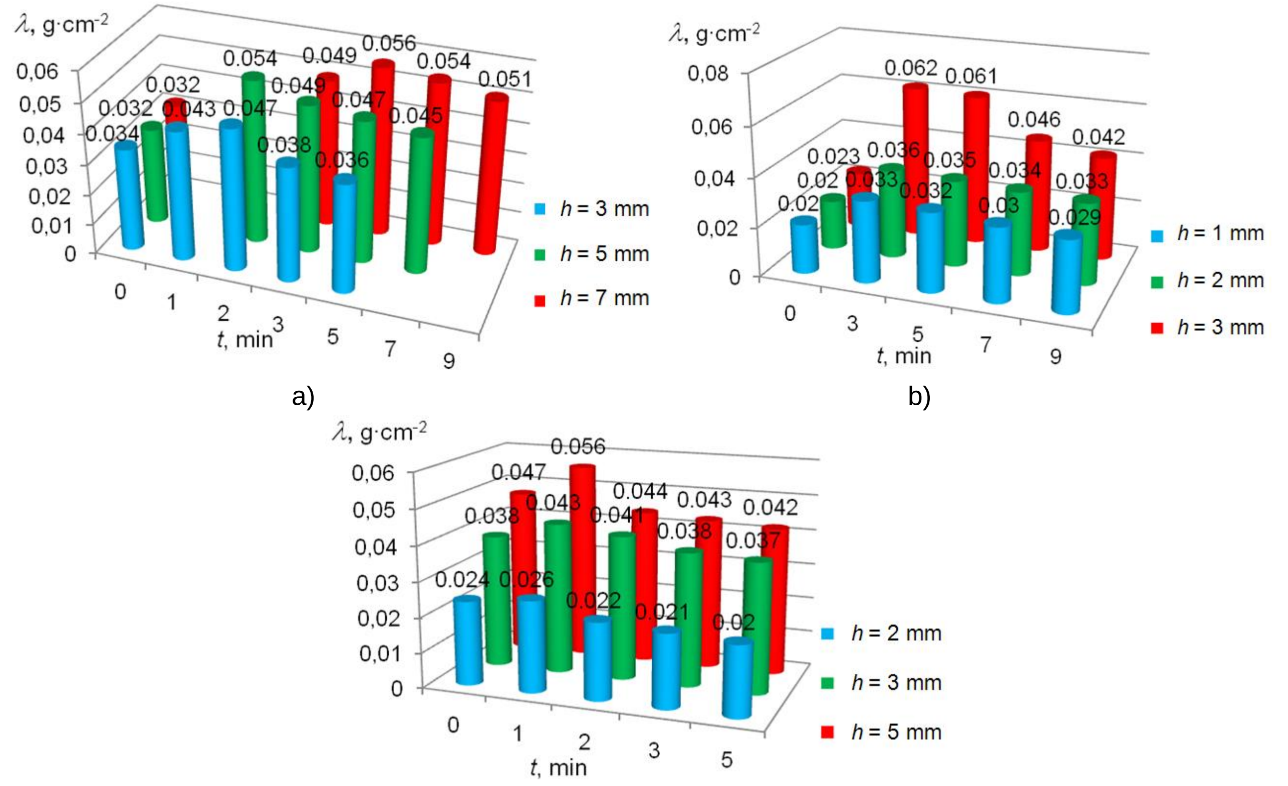

c)

Fig. 3 - Effect of slice blanching time *t* on the adhesion index λ of slices with thickness *h*: zucchini slices (a); carrot slices (b); apple slices (c)

Fig. 3, b presents the effect of carrot slice blanching time t on the adhesion index λ of carrot slices. For all variants of the study, the adhesion index of blanched carrot slices was greater than the adhesion index of non-blanched carrot slices. In the case of carrot slice blanching of 3 min, the adhesion index was the highest: for slice thickness of 1 mm – λ = 0.033 g·cm^{-2}; for slice thickness of 2 mm – λ = 0.036 g·cm^{-2}; for slice thickness of 3 mm – λ = 0.062 g·cm^{-2}. Increasing blanching time more than 3 min led to a decrease in the adhesion index of carrot slices.

Fig. 3, c presents the effect of apple slice blanching time t on the adhesion index λ of apple slices. In the case of apple slice blanching about 1 min, the adhesion index was the highest: for the slice thickness of 2 mm – λ = 0.026 g·cm^{-2}; for the slice thickness of 3 mm – λ = 0.043 g·cm^{-2}; for the slice thickness of 5 mm – λ = 0.056 g·cm^{-2}. Increasing blanching time more than 1 min caused a decrease in the adhesion index to the level of the adhesion index of non-blanched apple slices.

Fig. 4, a shows the results of determination of chips (ZF) loss η. In case of zucchini slice thickness of 3 mm, the chips (ZF) had the smallest loss in the variant of blanching time of 2 min, which was about 9.3%. In the case of zucchini slice thickness of 5 mm, the smallest loss of chips was about 9.2% in the variant of blanching time of 3 min. And, in the case of zucchini slice thickness of 7 mm, the smallest loss of chips was about 9.5% in the variant of blanching time 5 min. Regardless of the zucchini slice thickness, the highest chips loss was observed in variants with non-blanched zucchini slices (h = 5 mm, h = 7 mm) and with blanching time of 5 min (h = 3 mm). Thus, in the variants with a high adhesion index of blanched zucchini, the loss of chips was the smallest.

Analysis of chips loss indicates that the highest loss η of two-layer chips (CF) was in variants with blanching time of carrot slices about 9 min (fig. 4, b). The smallest loss of chips (CF) was in variants in which blanched slices of carrot had the highest adhesion index λ. Thus, the smallest loss of two-layer chips (CF) was in variants with the blanching time about 3 min: for carrot slice thickness of 1 mm – η = 14.1%; for carrot slice thickness of 2 mm – η = 13.6%; for carrot slice thickness of 3 mm – η = 13.3%. It should be noted that the loss of chips (CF) decreased with increasing slice thickness. But, in the case of blanching time of 3 min, the loss of chips did not differ significantly for different variants of carrot slice thickness.

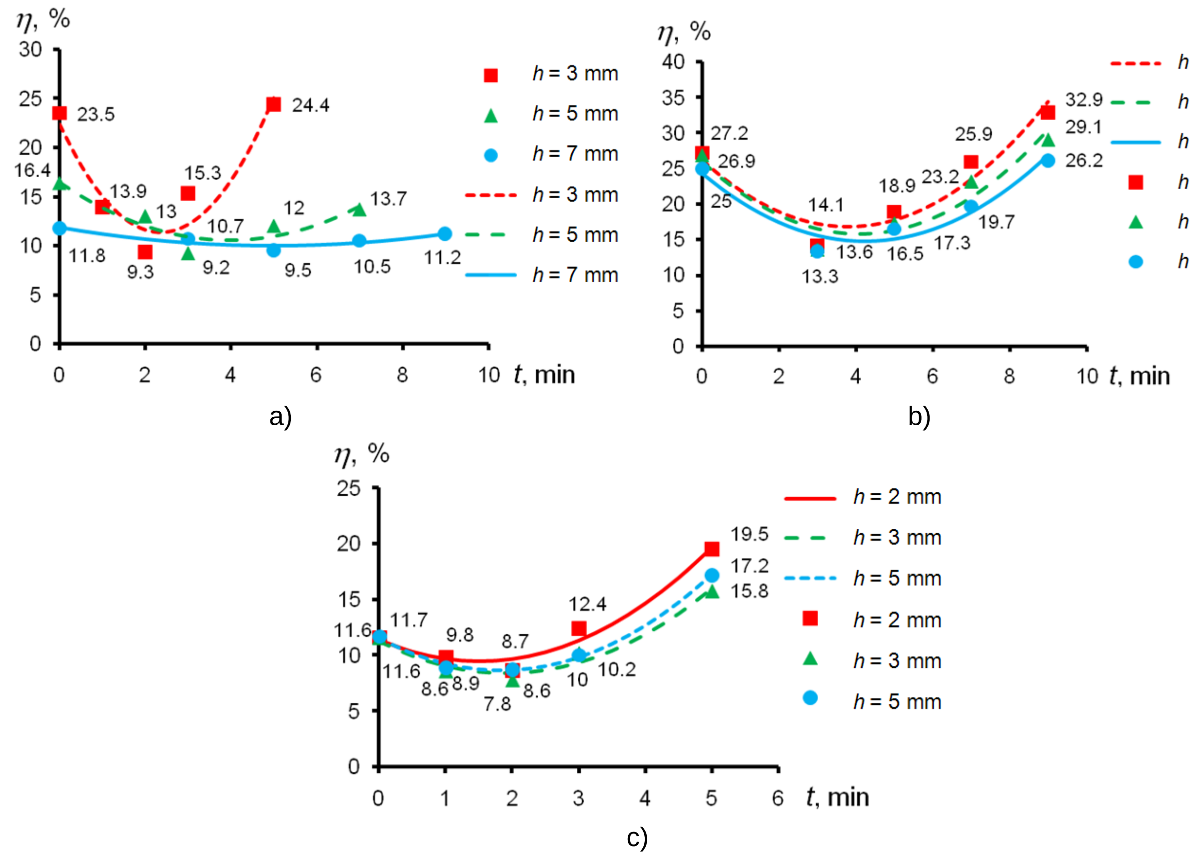

Fig. 4 - Effect of slice blanching time *t* on the loss η of two-layer chips with thickness of the main layer *h*: a) – chips (ZF); b) – chips (CF); c) – chips (AF)

In the fig. 4, c the results of determination of chips (AF) loss η is presented. In the variants with the longest time *t* of apple slice blanching, loss of two-layer chips (AF) was the highest. These are the same variants, which had the smallest adhesion index λ of blanched apple slices. The highest loss of two-layer chips (AF) was as follows: for apple slice thickness of 2 mm – η = 19.5%; for apple slice thickness of 3 mm – η = 15.8%; for apple slice thickness of 5 mm – η = 17.2%. Variants of chips with the high adhesion index λ of blanched apple slices had the smallest loss of chips (AF). So, in case of apple slice blanching time of 2 min, the loss of chips (AF) was the smallest: for apple slice thickness of 2 mm – η = 8.6%; for apple slice thickness of 3 mm – η = 7.8%; for apple slice thickness of 5 mm – η = 8.7%.

As a result of processing of experimental data, the equations describing effect of blanching time *t* (min) on the loss η (%) of two-layer chips were received:

- for chips (ZF) with thickness of the main layer *h* = 3 mm, *h* = 5 mm and *h* = 7 mm (fig. 4, a):

$$\eta = 1.974t^2 - 9.332t + 22.41,\ r^2 = 0.892, \quad (4)$$

$$\eta = 0.374t^2 - 2.968t + 16.44,\ r^2 = 0.814, \quad (5)$$

$$\eta = 0.076t^2 - 0.757t + 11.89,\ r^2 = 0.845, \quad (6)$$

- for chips (CF) with thickness of the main layer *h* = 1 mm, *h* = 2 mm and *h* = 3 mm (fig. 4, b):

$$\eta = 0.647t^2 - 4.911t + 26.15,\ r^2 = 0.907, \quad (7)$$

$$\eta = 0.608t^2 - 4.971t + 25.93,\ r^2 = 0.897, \quad (8)$$

$$\eta = 0.535t^2 - 4.525t + 24.32,\ r^2 = 0.927, \quad (9)$$

- for chips (AF) with thickness of the main layer *h* = 2 mm, *h* = 3 mm and *h* = 5 mm (fig. 4, c):

$$\eta = 0.839t^2 - 2.541t + 11.42,\ r^2 = 0.967, \quad (10)$$

$$\eta = 0.795t^2 - 3.027t + 11.26,\ r^2 = 0.964, \quad (11)$$

$$\eta = 0.859t^2 - 3.15t + 11.53,\ r^2 = 0.996. \quad (12)$$

The diagram (fig. 5, a) shows the effect of the pressure P of layer compression on the loss η of multilayer chips (ZFA, ZFC, ZFZ). Zucchini slices with thickness of 3 mm, which were blanched for 2 min, formed the first layer of multilayer chips (ZFA, ZFC, ZFZ). Analysis of the experimental data shows that the chips layers adhered better at higher pressure. Increase in pressure from 4.0 kPa to 5.5 kPa led to a decrease in multilayer chips loss: for chips (ZFZ) – from 13.2% to 7.8%; for chips (ZFC) – from 12.6% to 10.8%; for chips (ZFA) – from 8.7% to 7.3%.

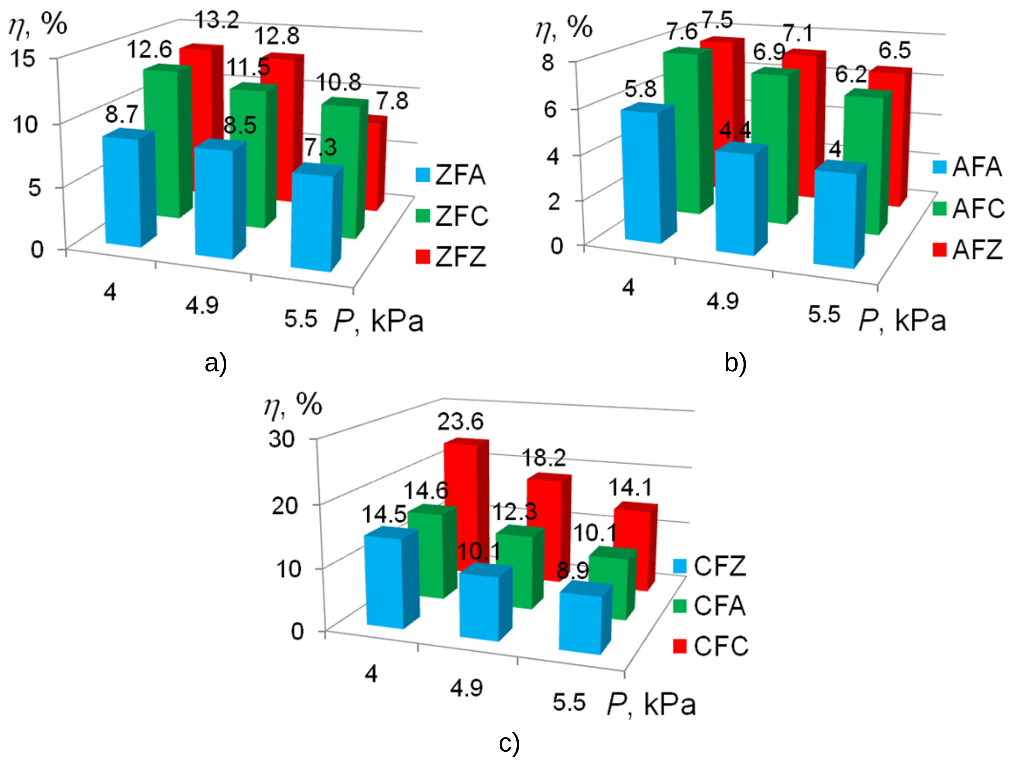

Fig. 5 - Effect of the pressure *P* of layer compression on the loss η of multilayer chips:
a) – ZFA, ZFC, ZFZ; b) – AFA, AFC, AFZ; c) – CFZ, CFA, CFC

The diagram (fig. 5, b) shows the effect of the pressure P of layer compression on the loss η of multilayer chips (AFA, AFC, AFZ). Apple slices with thickness of 3 mm, which were blanched for 2 min, formed the first layer of multilayer chips (AFA, AFC, AFZ). For multilayer chips (AFA, AFC, AFZ), increase in pressure from 4.0 kPa to 5.5 kPa led to a decrease in multilayer chips loss: for chips (AFA) – from 5.8% to 4.0%; for chips (AFZ) – from 7.5% to 6.5%; for chips (AFC) – from 7.6% to 6.2%.

The diagram (fig. 5, c) shows the effect of the pressure P of layer compression on the loss η of multilayer chips (CFZ, CFA, CFC). Carrot slices with thickness of 1 mm, which were blanched for 3 min, formed the first layer of multilayer chips (CFZ, CFA, CFC). Analysis of the experimental data shows that increase in pressure from 4.0 kPa to 5.5 kPa led to a decrease in multilayer chips loss: for chips (CFC) – from 23.6% to 14.1%; for chips (CFZ) – from 14.5% to 8.9%; for chips (CFA) – from 14.6% to 10.1%.

One of the goals of blanching of sliced fruits and vegetables, which formed the first layer of multilayer chips, is to ensure the high value of the adhesion index. In this case, the layers of chips will stick together. For the studied slices of zucchini, carrots and apples, the adhesion index increases with short-term blanching and decreases with long-term blanching. Also, it is important to remember that prolonged blanching causes the loss of nutrients and vitamins. So, the blanching should be as short a time as possible.

Analysis of the experimental data shows that apples and zucchini are the most suitable raw fruit and vegetable for the first layer of multilayer chips because the loss of such chips will be the smallest. In case of using zucchini and apples for first layer forming, the recommended thickness of zucchini and apple slices is about 3 mm and blanching time is about 2 min.

Experimental data show that increasing the pressure P from 4.0 kPa to 5.5 kPa reduced the loss η of multilayer chips because the layers of chips adhered better and less crumbs were formed after chips drying. Also, experimental data show that the chips, in which the first layer was formed by carrot slices, had the largest loss of chips.

CONCLUSIONS

During the production of multilayer chips, steam blanching of fruit and vegetable slices for 2 – 3 min at 85 – 95ºC causes an increase in adhesion index of sliced fruits and vegetables. Steam blanching of sliced fruits and vegetables in combination with the compression of the chips layers reduces the chips loss that is possible due to chips crushing and destruction during technological processes. Chips loss is a production waste that can be reused after grinding as a raw material for fruits and vegetables breading.

For the multilayer chips production, the recommended thickness of fruit and vegetable slices and blanching time depend on the type of fruits and vegetables: for first layer made of apples or zucchini, it is recommended to slice fruit and vegetable with the slice thickness of 3 mm and blanch slices for 2 min; for first layer made of carrots, it is recommended to slice carrots with the slice thickness of 1 mm and blanch carrot slices for 3 min. The second layer of multilayer chips can be formed by breading of one side of the main layer of chips with crushed flax seeds. The recommended seed particle size ranges from 1.1 mm to 2.0 mm. The third layer of multilayer chips can be formed of a thin layer of grated fruits or vegetables (zucchini, apples, carrots, etc.), which (vegetables) were blanched for about 2 – 3 min. For better adhesion of layers of multilayer chips, the recommended pressure of chips layers' compression is about 5.5 kPa. So, at the recommended parameters of processing of multilayer chips, the chips loss will be the smallest.

REFERENCES

[1] Abano, E. E., Amoah, R. S., & Opuku, E.K. (2019). Temperature, microwave power and pomace thickness impact on the drying kinetics and quality of carrot pomace. *Journal of Agricultural Engineering*, *50*(1), 28–37. http://doi.org/10.4081/jae.2019.872

[2] Adhikari, B., Howes, T., Bhandari, B. R., & Truong, V. (2001). Stickiness in foods: a review of mechanisms and test methods. *International Journal of Food Properties*, *4*(1), 1–33. http://doi.org/10.1081/JFP-100002186

[3] Aktas, T., Fujii, S., Kawano, Y., & Yamamoto, S. (2007). Effects of pretreatments of sliced vegetables with trehalose on drying characteristics and quality of dried products. *Trans IChemE, Part C*, *Food and Bioproducts Processing*, *85*(C3), 178–183. http://doi.org/10.1205/fbp07037

[4] Alexandre, E. M. C., Santos-Pedro, D. M., Brandao, T. R. S., & Silva, C. L. M. (2011). Study on thermosonication and ultraviolet radiation processes as an alternative to blanching for some fruits and vegetables. *Food and Bioprocess Technology*, *4*, 1012–1019. http://doi.org/10.1007/s11947-011-0540-8

[5] AOAC Official Method 934.06 – *Moisture in Dried Fruits*.

[6] Dandamrongrak, R., Mason, R., & Young, G. (2003). The effect of pretreatments on the drying rate and quality of dried bananas. *International Journal of Food Science and Technology*, *38*(8), 877–882. http://doi.org/10.1046/j.0950-5423.2003.00753.x

[7] Diamante, L. M., Ihns, R., Savage, G. P., & Vanhanen, L. (2010). Short communication: a new mathematical model for thin layer drying of fruits. *International Journal of Food Science & Technology*, *45*(9), 1956–1962. http://doi.org/10.1111/j.1365-2621.2010.02345.x

[8] Eyarkai Nambi, V., Gupta, R. K., Kumar, S., & Sharma, P. C. (2016). Degradation kinetics of bioactive components, antioxidant activity, color and textural properties of selected vegetables during blanching. *Journal of Food Science and Technology*, *53*(7), 3073–3082. http://doi.org/10.1007/s13197-016-2280-2

[9] Husarova, O., & Shapar, R. (2017). The features of fruits drying in the production of natural chips. In *Proceeding on the 7th International youth science forum "Litteris et artibus"*. Lviv, Ukraine. Lviv Polytechnic Publishing House, 44–45. ISBN 978-966-941-108-2.

[10] Kayacier, A., & Singh, R. K. (2003). Textural properties of baked tortilla chips. *LWT – Food Science and Technology*, *36*(5), 463–466. http://doi.org/10.1016/s0023-6438(02)00222-0

[11] Kowalska, H., Marzec, A., Kovalska, J., Samborska, K., Tywonek, M., & Lenart, A. (2018). Development of apple chips technology. *Heat and Mass Transfer*, *54*, 3573–3586. http://doi.org/10.1007/s00231-018-2346-y

[12] Michalski, M.-C., Desobry, S., & Hardy, J. (1997). Food materials adhesion: a review. *Critical Reviews in Food Science and Nutrition*, *37*(7), 591–619. http://dx.doi.org/10.1080/10408399709527791

[13] Neri, L., Hernando, I. H., Perez-Munuera, I., Sacchetti, G., & Pittia, P. (2011). Effect of blanching in water and sugar solutions on texture and microstructure of sliced carrots. *Journal of Food Science*, *76*(1), 23–30. http://doi.org/10.1111/j.1750-3841.2010.01906.x

[14] Onwude, D. I., Hashim, N., Janius, R. B., Nawi, N. M., & Abdan, K. (2016). Modeling the thin-layer drying of fruits and vegetables: a review. *Comprehensive Reviews in Food Science and Food Safety*, *15*(3), 599–618. http://doi.org/10.1111/1541-4337.12196

[15] Pedreschi, F., Cortes, P., & Mariotti, M. S. (2018). Potato crisps and snack foods. *Reference Module in Food Science*. http://doi.org/10.1016/B978-0-08-100596-5.21137-2

[16] Pedreschi, F., Moyano, P., Santis, N., & Pedreschi, R. (2007). Physical properties of pre-treated potato chips. *Journal of Food Engineering*, *79*(4), 1474–1482. http://doi.org/10.1016/j.foodeng.2006.04.029

[17] Prawiranto, K., Defraeye, T., Derome, D., Buhlmann, A., Hartmann, S., Verboven, P., Nicolai, B., & Carmeliet, J. (2019). Impact of drying methods on the changes of fruit microstructure unveiled by X-ray micro-computed tomography. *RSC Advances*, *9*, 10606–10624. http://doi.org/10.1039/c9ra00648f

[18] Ramesh, M. N., Wolf, W., Tevini, D., & Bognar, A. (2002). Microwave blanching of vegetables. *Journal of Food Science*, *67*(1), 390–398. http://doi.org/10.1111/j.1365-2621.2002.tb11416.x

[19] Ramos, I. N., Brandao, T. R. S., & Silva, C. L. M. (2003). Structural changes during air drying of fruits and vegetables. *Food Science and Technology International*, *9*(3), 201–206. http://doi.org/10.1177/1082013030335522

[20] Sagar, V. R., & Suresh Kumar, P. (2010). Recent advances in drying and dehydration of fruits and vegetables: a review. *Journal of Food Science and Technology*, *47*(1), 15–26. http://doi.org/10.1007/s13197-010-0010-8

[21] Santos, P. H. S., & Silva, M. A. (2008). Retention of vitamin C in drying processes of fruits and vegetables – a review. *Drying Technology: An International Journal*, *26*(12), 1421–1437. http://doi.org/10.1080/07373930802458911

[22] Selman, J. D. (1994). Vitamin retention during blanching of vegetables. *Food Chemistry*, *49*(2), 137–147. http://doi.org/10.1016/0308-8146(94)90150-3

[23] Senadeera, W. Bhandari, B. R., Young, G. S., & Wijesinghe, B. (2000). Physical property changes of fruits and vegetables during hot air drying. In Mujumdar, A.S. (Ed.) *Drying technology in agriculture and food sciences*. USA, Science Publishers, 149–166. ISBN 1-57808-148-3.

[24] Severini, C., Giuliani, R., De Filippis, A., Derossi, A., & De Pilli, T. (2016). Influence of different blanching methods on color, ascorbic acid and phenolics content of broccoli. *Journal of Food Science Technology*, *53*(1), 501–510. http://doi.org/10.1007/s13197-015-1878-0

[25] Shivhare, U. S., Gupta, M., Basu, S., & Raghavan, G. S. V. (2009). Optimization of blanching process for carrots. *Journal of Food Process Engineering*, *32*, 587–605. http://doi.org/10.1111/j.1745-4530.2007.00234x

[26] Song, J.-Y., An, G.-H., & Kim, C.-J. (2003). Color, texture, nutrient contents, and sensory values of vegetable soybeans [Glycine max (L.) Merrill] as affected by blanching. *Food Chemistry*, *83*(1), 69–74. http://doi.org/10.1016/S0308-8146(03)00049-9

[27] Steel, R. G. D., Torrie, J. H., & Dicky, D. A. (1997). *Principles and procedures of statistics: a biometrical approach*. 3rd ed. New York, USA. McGraw Hill, Inc. Book Co., 666 p. ISBN 0070610282.

[28] Tijskens, L. M. M., Schijvens, E. P. H. M., & Biekman, E. S. A. (2001). Modelling the change in color of broccoli and green beans during blanching. *Innovative Food Science & Emerging Technologies*, *2*(4), 303–313. http://doi.org/10.1016/S1466-8564(01)00045-5

[29] Xiao, H.-W., Pan, Z., Deng, L.-Z., El-Mashad, H. M., Yang, X.-H., Mujumdar, A. S., Gao, Z.-J., & Zhang, Q. (2017). Recent developments and trends in thermal blanching – a comprehensive review. *Information Processing in Agriculture*, *4*(2), 101–127. http://doi.org/10.1016/j.inpa.2017.02.001

[30] Zhang, M., Chen, H., Mujumdar, A. S., Tang, J., Miao, S., & Wang, Y. (2017). Recent developments in high-quality drying of vegetables, fruits, and aquatic products. *Critical Reviews in Food Science and Nutrition*, *57*(6), 1239–1255. http://doi.org/10.1080/10408398.2014.979280

DESIGN AND PERFORMANCE TEST OF DIRECT SEED METERING DEVICE FOR RICE HILL
/
水稻穴直播排种器设计与性能试验

Tian Liquan[1, 2), Xiong Yongsen*[1, 2), Ding Zhao[1)], Su Zhan[1)] [1]

[1)] College of Engineering, Jinhua Polytechnic, Jinhua, 321017 / China

[2)] Key Laboratory of Crop Harvesting Equipment Technology of Zhejiang Province, Jinhua, 321017/China

Tel: 15888993199; E-mail: tlqbuct@foxmail.com

DOI: https://doi.org/10.35633/inmateh-64-25

***Keywords**: direct seeding in rice hill; seed-metering device; spiral groove; design; test*

ABSTRACT

In order to meet the requirements of rice field precision direct seeding in rows and hills, a spiral grooved seed metering device for rice field precision direct seeding in hills is designed. The Matlab software is used to study the movement trajectory of rice buds in the spiral groove during the seeding process. Based on the quadratic regression-orthogonal rotation combination design, and taking the working speed of the seeding wheel, the spiral groove length and the helix angle of the spiral groove as the test factors, as well as the qualified rate of hill diameters, the qualified rate of hill grains and the miss-seeding rate as the indicators, the seed metering performance is tested by JPS-12 metering device test bench. The test data are analyzed by using Design-Expert 6.0.10 software to obtain a mathematical model between the factors and indicators. The test results show that when the spiral groove rise angle is 71.0°, the spiral groove length is 10.8mm, and the working speed of the metering wheel is 23.2r/min, the qualified rate of hill diameter, qualified rate of hill grains and miss-seeding rate are 91.06%, 94.64% and 3.64% respectively. The seeding performance meets the agronomic requirements of rice field seeding.

摘要

为满足水稻田间精量成行成穴机械直播的要求，设计了一种螺旋槽式水稻田间精量穴直播排种器。应用 Matlab 软件对排种过程中螺旋槽内水稻芽种的运动轨迹进行了研究。采用二次回归正交旋转组合设计，以排种轮工作转速、螺旋槽长度、螺旋槽升角为试验因素，穴径合格率、穴粒数合格率和漏播率为指标，利用 JPS-12 型排种器检测试验台对排种性能进行试验，并运用 Design-Expert6.0.10 软件对试验数据进行分析，得到因素与指标之间的数学模型。试验结果表明：当螺旋槽升角为 71.0°、螺旋槽长度为 10.8mm 和排种轮工作转速为 23.2r/min 时，穴径合格率、穴粒数合格率和漏播率分别为 91.06%、94.64%和 3.64%，排种性能满足水稻田间播种的农艺要求。

INTRODUCTION

Mechanized rice planting mainly includes transplanting and direct seeding. Direct seeding of rice does not require seedlings, and it saves the process of seedlings rising, seedlings pulling and seedlings transplanting during transplantation. It is a labor-saving, cost-saving and energy-saving planting method (*Yin, 2020; Yang, 2020; Wang et al., 2020; Hevko et al., 2018*). Mechanized precision hill direct seeding in the rice field makes the population size of rice field small. Rice plants are evenly distributed in the population, with better ventilation and light transmission, no damage to the root system, well-developed individual root system, more effective tillers, high ear-forming rate and increased yield (*Huang et al., 2020; Dudarev et al., 2017; Arzu and Adnan, 2014*).

Therefore, the precision direct seeding technology of rice that can be used for both rows and hills has become the development direction of mechanized rice planting (*Xing et al., 2020; Xing et al., 2018*). At present, researches on some mechanical seeding technologies, such as rice electromagnetic vibration plug seeding technology, pneumatic suction tube seeding technology, auger seeding technology, seeding belt technology and seed rope technology, have been reported (*Zhang et al., 2018; Liu et al., 2019; Zheng et al., 2018*).

---

[1] *Tian Liquan, Associate Professor; Xiong Yongsen, Prof; Ding Zhao, Ph.D; Su Zhan, Ph.D;*

However, the structure of seeding device in the above technologies is complex, and the operation is inefficient and the cost is high (*Liu et al., 2017; Zhou et al., 2016*; *Vasylkovska et al., 2019)*. Since 1970s, the research on rice direct seeding metering device has been carried out in China. *Luo et al*. (2008) designed a hill wheel rice direct seeding metering device with two seed filling chambers, but it is difficult to adjust the seeding rate (*Ren et al., 2009; He et al., 2019; Luo et al., 2007*). *Lu et al. (2018)* designed a rice seedling seeder and *Yuan (2006)* developed an air suction vertical tray rice precision seeder (*Lu et al., 2018; Trokhaniak et al., 2020*). The two researches mainly solve the needs of rice transplanting and seedling rising, which is difficult to meet the needs of field direct seeding (*Zhang et al., 2020; Cao et al., 2015*).

In order to meet the requirement of precision seeding and facilitate the adjustment of seeding rate, a spiral grooved seed metering device for rice field precision direct seeding in hills was designed. Its working process was analyzed theoretically and the structural parameters of key components were optimized. Taking the rice seeds as the example, the best combination of various parameters of the seed metering device was obtained to provide a reference for the design of the whole machine.

MATERIALS AND METHODS

Threshed maize mixtures and models of cleaning device

The structure of the seed metering device is shown in Figure 1. It is mainly composed of a spiral grooved metering wheel, a seed metering wheel cover, a seed cleaning roller brush, a seed protection arc plate, a seed pusher blade, a seed metering wheel positioning sleeve, a cover plate and a sprocket. The seed metering device is installed to the bottom of the seed box through the assembly hill. After determining the working length of the spiral grooved seeding wheel in the metering device (that is, the length of the spiral groove section), fasten the metering wheel positioning sleeve on the main shaft to make the spiral grooved metering wheel unable to move along the axis of the spindle. The seed cleaning sprocket and the driving sprocket are connected by a chain, and the rotation direction of the seed cleaning roller brush and the seed metering wheel are opposite. The seed protection device adopts an elastic seed protection arc plate, so that the short arc surface of the seed protection arc plate is in contact with the seed cleaning roller brush, and the long arc surface is in contact with the spiral grooved seeding wheel. Put the seed pushing blade into the circumferential ring groove cut on the spiral grooved seeding wheel, so that the pushing blade and the bottom of the ring groove are closely attached to improve the seeding effect.

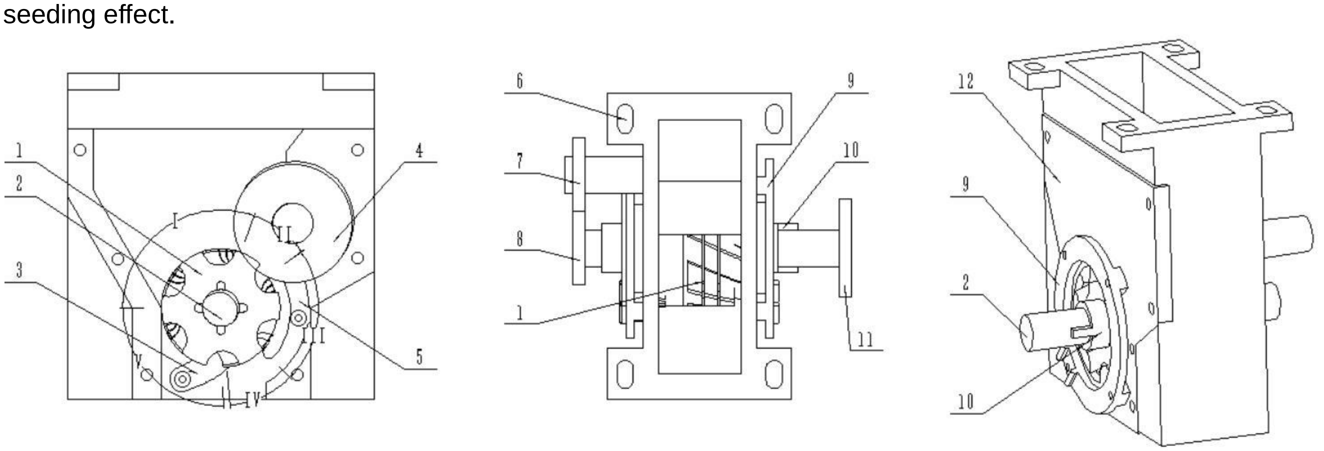

(a) Main view (removal of cover plate) (b) top view (c) Isometric view

Fig. 1- Sketch of seed-metering device

I-Filling area II-cleaning area III- Protected area IV-Seeding area V-idle running

1. Spiral grooved seeding wheel; 2.Spindle; 3.Seed pusher blade; 4.Seed cleaning roller brush; 5.Seed protection arc plate; 6. Upper assembly hole; 7.Seed cleaning sprocket; 8.Drive sprocket; 9. Cover plate of seeding wheel; 10. Positioning sleeve of seeding wheel; 11.Spindle sprocket; 12.Cover plate

Working principle

Operation of the seed metering device can be divided into four stages: seed filling, seed cleaning, seed protection and seeding. As shown in Figure 1a, the rice buds are filled from the seed box into the seed metering device during operation. The spindle sprocket is powered by the machinery to rotate, and the coaxial drive sprocket drives the clearing sprocket to rotate. In the filling area of the seed metering device, the rice buds are filled into the spiral grooved seeding wheel. The buds filled in the spiral groove enter the seed clearing area with the rotation of the seed metering wheel, and the clearing roller brush removes the excess buds outside the spiral groove hook spoon. The cleared buds remain in the seed filling area for secondary seed filling. After passing through the seed cleaning area, the buds enter the seed protection area with the spiral groove. The seed protection device adopts an elastic seed protection arc plate to ensure the distance between the seed protection arc plate and the seed metering wheel. This cannot only prevent the sprout from getting stuck in the spiral grooved seed metering wheel and the protection arc plate and causes knocks when the distance is too small, but also reduces the abrasion of the buds on the protection arc plate. After passing through the seed protection area, the buds rotate with the seeding wheel to the seeding area; the buds are separated from the spiral groove by the pusher blade and reach the paddy field ground to complete the seeding.

Design and analysis of key components of the seed metering device

Spiral grooved seeding wheel

The spiral grooved seeding wheel is one of the key components of the seed metering device, and the design of its structural shape and size parameters directly affects the seeding performance. As shown in Figure 2, the seeding wheel is composed of a spiral groove section I and a cylindrical section II with the same diameter. The spoons of the spiral groove section are evenly distributed on the cylindrical surface according to the spiral line pattern. A number of circumferential ring-shaped shallow grooves are cut on the spiral groove section. A spindle hole is set in the center of the seeding wheel, which moves along the spindle through the hole. The positioning sleeve can adjust the length of the spiral groove section in the seeding shell, thereby achieving the purpose of adjusting the seeding volume.

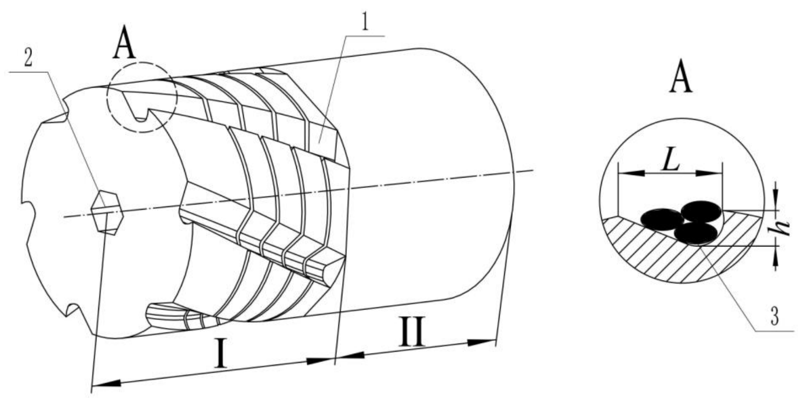

Fig.2-Sketch of seeding wheel

1. spiral groove; 2.spindle hole; 3.buds

The cross section of the spiral groove segment is a spoon profile formed by arc lines. Where, L is the opening width of the spoon profile, and its value is determined by the length of the longest rice buds. The opening width of the spoon should be 1.1 times the maximum length of buds. h is the depth of spoon, its size affects the uniformity of the seeding wheel, and the value should be greater than the maximum value of the thickness and width of the buds. In order to ensure that at least 3 buds are filled into the spoon, the depth h of the spoon should be 1.4 times the maximum thickness and width of the buds. In order to facilitate the filling and discharge of rice buds from the spoon, the design principle of the contour parameters of the hook-spoon is as follows:

$$\begin{cases} L = 1.1\ l_{max} \\ h = 1.4\ w_{max} \end{cases} \tag{1}$$

where: l_{mxa}—Maximum length of rice buds, mm; w_{max}—Maximum depth of rice buds, mm.

In order to increase the adaptation range of the spoon-shaped profile of the spiral groove, and optimize the design of reasonable structural parameters, the rice seed Longjing 36 that has a wide range of direct seeding in Heilongjiang was selected. 1000 seeds were randomly selected and soaked to promote germination, so as to make them appear white.

The material characteristics of the buds were measured, and the average value of statistical data and more are shown in Table 1.

The diameter of seeding wheel and the spoons of spiral grooved seeding wheel are important factors that affect the quality of seeding. The single-factor pre-test shows that the diameter of the seeding wheel is small, and the number of evenly distributed spiral grooved scoops is also small. To ensure the required hill spacing during seeding, the rotation speed of the seeding wheel needs to be increased *(Liu et al., 2019)*. However, the rotation speed of the seeding wheel is too large, the time for the spiral grooved spoon to pass through the filling area becomes short, and the buds cannot be filled into the spoon in time, which easily causes miss-seeding. Therefore, the diameter of the seeding wheel should be large. However, too large diameter of seeding wheel will result in the increase of size and mass of the seed metering device. Therefore, the radius of the seed metering wheel is 40mm, and the spiral grooved spoons are 6.

Table 1

Material Characteristics of Longjing36

Parameter	Value
Quality of thousand grains (kg)	36.7×10^{-3}
Moisture content (%)	21.8
Natural angle of repose (°)	36.6
Length×width×thickness / (mm×mm×mm)	8.08×3.26×2.29

Dynamic analysis of seed filling of spiral grooved spoon

With the rotation of the seeding wheel, the water rice sprouts and seeds in the seed filling area are driven by the outer wall of the spiral groove and filled into the spoon. There should be a velocity difference between the tangential of the spiral grooved spoon and the outer wall of the spoon, otherwise the normal seed filling of the spoon cannot be guaranteed. Meanwhile, the time for the buds to enter the spiral grooved spoon is one of the main factors affecting the filling performance. If the time that buds enter the spiral grooved spoon is too long, they cannot quickly enter the spiral grooved spoon, resulting in insufficient seed filling and increasing the miss-seeding rate. Therefore, it is necessary to analyze the filling process and explore the relationship between the design parameters of the spiral grooved spoon, the parameters of the buds and the filling time. The coordinate system is established with the centroid of the buds as the coordinate origin and the normal direction of the spiral groove section as the x-axis, as shown in Figure 3.

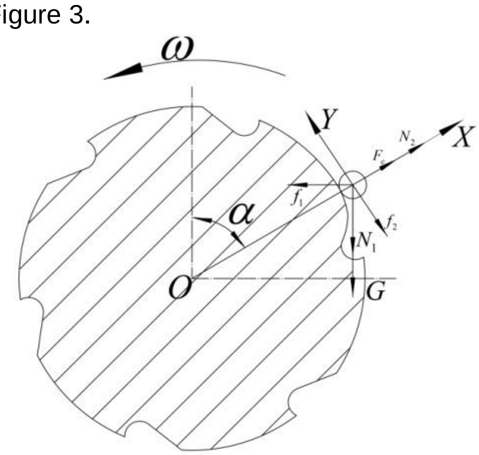

Fig. 3 - Stress sketch of spoon in the seed-filling process

To simplify the analysis, this article assumes that the rice buds are spherical and arranged regularly, the pressure on the buds is the sum of the gravity of all the above buds, and the lateral pressure is zero. According to the working conditions of the seed metering device, it can be known that the rice buds are filled into the spoon under the combined action of the gravity G, *the* centrifugal force F_e, the supporting force between the spiral grooved spoon and the buds N_1, the supporting force of the spiral grooved spoon on the buds, the friction force between the outer wall of the spiral grooved spoon and the buds f_2, as well as the internal friction f_1.

Decompose the force system to the normal and tangential directions of the cross section of the spiral grooved spoon, and establish a mechanical equilibrium equation:

$$\begin{cases} ma_x = (G+N_1)\cos\alpha + f_1 \sin\alpha - F_e - N_2 \\ ma_y = (G+N_1)\sin\alpha - f_1\cos\alpha + f_2 \\ f_1 = \mu_1 N_1 \\ f_2 = \mu_2 N_2 \\ F_e = mr\omega^2 \\ G = mg \end{cases} \tag{2}$$

where:

m—quality of rice buds, kg; a_x—the normal acceleration of rice buds, m/s²;

a_y—the tangential acceleration of buds, m/s²;

α—the angular displacement of buds, (°);

r—the distance from the centroid of the buds to the center of the spiral grooved spoon, mm;

ω—the angular velocity of buds, r/min;

μ_1— the friction factor between buds;

μ_2—the friction factor between the outer wall of the spiral grooved spoon and the buds.

It can be obtained by updating Eq.(2) that:

$$\begin{cases} a_x = \dfrac{(mg+N_1)\cos\alpha + \mu_1 N_1 \sin\alpha - N_2}{m} - r\omega^2 \\ a_y = \dfrac{(mg+N_1)\sin\alpha - \mu_1 N_1\cos\alpha + \mu_2 N_2}{m} \end{cases} \tag{3}$$

Analyzing the process of rice buds filling the spiral grooved spoon, it can be seen that the relationship between the displacement h of the centroid of the buds along the normal direction of the cross section of the spiral grooved spoon and the normal acceleration of the buds is as follows:

$$h = \frac{1}{2} a_x t^2 \tag{4}$$

where:

h— the depth of the spiral grooved spoon, mm;

t—the time that the centroid of the buds fills into the spiral grooved spoon, s.

Combine Eq.(3) and Eq.(4), it is obtained that:

$$t = \sqrt{\frac{2hm}{(mg+N_1)\cos\alpha + \mu_1 N_1 \sin\alpha - mr\omega^2 - N_2}} \tag{5}$$

In order to ensure that the rice buds are fully filled into the spiral grooved spoon, it is necessary to shorten the time for the buds to enter the spiral grooved spoon. According to Eq.(5), it can be seen that after determining the angle α of the filling area, the time t for the rice buds to fill the spiral grooved spoon is related to the budding parameters m and μ_1 , as well as the design parameters h, r and ω of the spiral grooved spoon.

Helix angle of the spiral groove

The movement of rice buds in the spiral groove can be divided into the axial movement and the radial rotation along the spiral grooved seed metering wheel. Decompose the speed of the bud M in the spiral grooved spoon at point A, when the lead angle θ of spiral groove is in the unfolded state, the spiral line is represented by an oblique straight line, as shown in Figure 4.

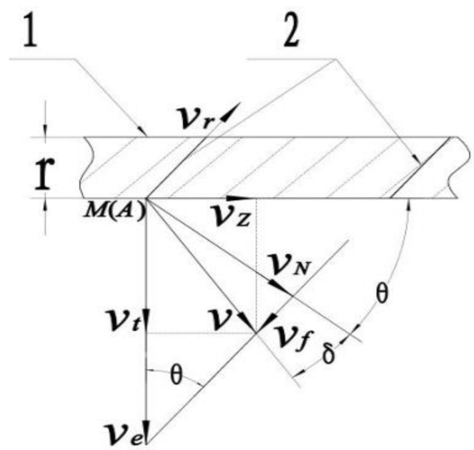

Fig. 4 - Particle velocity of buds
1. Axis; 2. Helix

The spiral grooved spoon rotates around the axis, and the direction of the linear velocity v_e of the bud M at point A is the tangential direction of this point, which is the implicated speed of the bud. v_r is the relative velocity, and its direction is parallel to the helix direction of point A. If the friction of the spiral groove is not taken into account, the bud will move along the normal direction of point A of the spiral line at the theoretical absolute velocity of v_N. However, due to the friction of the spiral groove, the actual absolute velocity v of the bud at point A will deflect an angle, which is approximately equal to the external friction equivalent angle δ of bud grains. The actual absolute velocity v is decomposed into the circumferential velocity v_t and the axial velocity v_Z of the bud, and it is obtained that:

$$\begin{cases} v_z = v\cos(\theta+\delta) \\ v_t = v\sin(\theta+\delta) \end{cases} \tag{6}$$

As shown in Figure 4, without considering the influence of friction, the theoretical absolute speed of buds has:

$$v_N = v_e + v_r \tag{7}$$

Due to the influence of the friction of the spiral groove, the relationship between the actual absolute velocity v and v_N as well as the deflection velocity v_f of the bud at point A is:

$$v = v_f + v_N \tag{8}$$

It can be obtained by velocity triangle that:

$$v = \frac{v_N}{\cos\delta} = \frac{v_e \sin\theta}{\cos\delta} \tag{9}$$

The transport velocity of rice bud at point A is:

$$v_e = \omega r = \frac{2\pi n r}{60} \tag{10}$$

Substituting Eq.(7),-Eq.(10) into Eq.(6), it can be obtained that:

$$\begin{cases} v_z = \dfrac{2\pi r n}{60}\dfrac{\sin\theta}{\cos\delta}\cos(\theta+\delta) \\ v_t = \dfrac{2\pi r n}{60}\dfrac{\sin\theta}{\cos\delta}\sin(\theta+\delta) \end{cases} \tag{11}$$

where:

n—rotation velocity of spiral grooved seed metering wheel, r/min.

From Eq. (11), when the rotation speed of the spiral grooved seeding wheel, the distance between the centroid of the rice bud and the center of the spiral groove, as well as the equivalent angle of external friction are determined, the trend of v_z and v_z as the helix angle of spiral groove increases is drawn using Matlab software. The curve is shown in Figure 5.

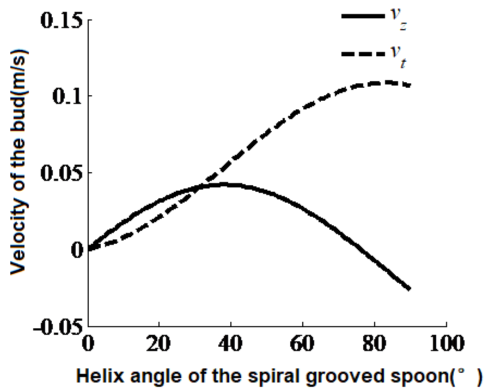

Fig. 5 - The curve of axial velocity and circumferential velocity

It can be seen from Figure 5 that with the increase of the helix angle, the axial velocity of rice buds first increases and then decreases. The circumferential velocity increases gradually. In a certain range of helix angle, the axial velocity V_Z and circumferential velocity V_T can be obtained, which makes the axial velocity small and reduces the variation coefficient of the hill diameter. The high circumferential velocity is beneficial to the smooth discharge of buds from the spiral grooved spoon. Therefore, according to the agricultural machinery design manual and the above analysis, when the seed metering performance test is carried out, the range of the spiral groove rise angle θ is 40°-86°.

Test

Test materials

In order to explore the influence of the velocity of seeding wheel, the spiral groove length and the helix angle of the spiral groove on the seeding performance, and to obtain the best working parameters, a bench test was carried out on the seed metering device, as shown in Figure 6.

Fig. 6 - The rack experiment of seed-metering device

1. seed-metering device; 2. mounting frame; 3. seed bed belt; 4. control motor

The experiment was conducted in the laboratory of seed metering performance of Northeast Agricultural University, and Longjing 36 was used in the experiment. The rice seeds need to be soaked to promote germination, so as to break the chest and expose white. The test device is the JPS-12 seed metering device detection test bench. The seed metering device is fixed on the mounting frame; the motor is controlled to drive the seed bed belt to rotate, and the seed bed belt is coated with a certain width of sticky seed oil. The rice buds are dropped from the seeding port to the sticky seed oil layer, and data can be collected in real time to achieve the purpose of measuring the performance indicators of various seeding.

Test factors and indicators

The working speed of metering wheel and spiral groove angle are the important factors that affect the axial and circumferential speed of bud. At the same time, the change of spiral groove length also has an important impact on the mass of seed metering. Therefore, the working speed of the seeding wheel, the length of the spiral groove and the helix angle of the spiral groove are selected as the test factors, combined with the GB/T6973-2005 " Testing methods of single seed drills (precision drills)", the percentage of the hills with 3-8 buds to the total number of hills is regarded as the qualified rate of hill grains. The percentage of hills with a diameter of less than 50mm and the total number of hills is regarded as the qualified rate of the hill diameter. The qualified rate of the hill grains, the qualified rate of hill diameter and the miss-seeding rate are regarded as the valuation indexes of seeding *(Liu et al., 2019)*.

RESULTS

Experiment design and result analysis

Firstly, a single-factor pre-test was carried out on the working speed of the seeding wheel, the length of the spiral groove and the lead angle of the spiral groove to determine the reasonable variation range of each factor. On this basis, the three-factor quadratic regression orthogonal rotation combination design is used for experimental analysis. The level codes of the experimental factors are shown in Table 2.

Table 2

Coding level of experimental factors

Code	Working speed x_1/(r/min)	Spiral length x_2/ (mm)	Spiral helix angle x_3/ (°)
1.682	30	12	86
1	27.6	10.8	76.7
0	24	9	63
-1	20.4	7.2	49.3
-1.682	18	6	40

23 sets of experiments were designed according to the quadratic regression-orthogonal rotation combination, and the experimental schemes and results are shown in Table 3. Among them, y_1 is the qualified rate of hill diameter, y_2 is the qualified rate of hill grains, and y_3 is the miss-seeding rate of hill grains.

Table 3

Schemes and results of experiment

No.	Test factors			Performance index		
	x_1 (r/min)	x_2 (mm)	x_3 (°)	y_1 (%)	y_2 (%)	y_3 (%)
1	20.40	7.20	49.30	89.16	87.13	6.28
2	27.60	7.20	49.30	88.95	85.09	7.86
3	20.40	10.80	49.30	90.87	87.24	8.2
4	27.60	10.80	49.30	90.25	84.56	9.2
5	20.40	7.20	76.70	89.74	87.45	8.22
6	27.60	7.20	76.70	87.97	87.55	7.38
7	20.40	10.80	76.70	91.31	91.97	4.36
8	27.60	10.80	76.70	89.76	89.71	7.18
9	18.00	9.00	63.00	90.33	76.74	7.48
10	30.00	9.00	63.00	88.54	72.41	5.18

Table 3
(Continuation)

Schemes and results of experiment

No.	Test factors			performance index		
	x_1 (r/min)	x_2 (mm)	x_3 (°)	y_1 (%)	y_2 (%)	y_3 (%)
11	24.00	6.00	63.00	88.08	94.1	2.32
12	24.00	12.00	63.00	91.04	94.07	4.8
13	24.00	9.00	40.00	89.41	88.1	9.06
14	24.00	9.00	86.00	90.28	93.32	6.3
15	24.00	9.00	63.00	91.05	93.41	3.2
16	24.00	9.00	63.00	90.40	90.13	2.74
17	24.00	9.00	63.00	90.71	88.31	3.32
18	24.00	9.00	63.00	90.54	91.2	3.72
19	24.00	9.00	63.00	90.76	90.38	3.96
20	24.00	9.00	63.00	91.11	90.82	3.04
21	24.00	9.00	63.00	90.59	94.04	5.46
22	24.00	9.00	63.00	90.64	89.72	3.2
23	24.00	9.00	63.00	90.70	93.63	5.5

Regression analysis was performed on the test data through Design-Expert 6.0.10 software, the significant influencing factors were screened out, and the corresponding regression equation was obtained.

$$y_1 = 46.97 + 1.78x_1 + 2.51x_2 + 0.34x_3 - 6.31x_1x_3 - 0.03x_1^2 - 0.11x_2^2 - 0.001x_3^2 \quad (12)$$

$$y_2 = -108.42 + 20.51x_1 - 9.14x_2 - 0.21x_3 + 0.04x_2x_3 - 0.43x_1^2 + 0.40x_2^2 \quad (13)$$

$$y_3 = 71.55 - 4.34x_1 + 2.47x_2 - 0.82x_3 - 0.04x_2x_3 + 0.09x_1^2 + 0.01x_3^2 \quad (14)$$

The response surface graph is shown in Figure 7 by Design-Expert 6.0.10 software.

Analysis of the above regression equation and response surface graph shows that the interaction between the spiral groove length and the helix angle of spiral groove has a significant impact on the number of hills and the miss-seeding rate. The interaction between the helix angle of spiral groove and the working speed of the metering wheel has a significant impact on the qualified rate of hill diameter.

It can be seen from Figure 7a that when the helix angle is constant, the qualification rate of hill diameters first increases and then decreases with the increase of working speed; when the working speed is constant, the qualified rate of hill diameters increases with the increase of helix angle. This result is consistent with the previous analysis of the influence of the helix angle of spiral groove on the axial velocity of rice buds.

It can be seen from Figure 7b that when the length of the spiral groove is constant, the qualified rate of hill grains first decreases and then increases with the increase of the spiral helix angle; when the spiral rise angle is constant, the qualified rate of hill grains decreases with the increase of the spiral groove length.

It can be seen from Fig. 7c that when the length of the spiral groove is constant, the miss-seeding rate first decreases and then increases with the increase of the helix angle; when the length changes, the miss-seeding rate varies widely, so the length of the spiral groove is the main factor affecting the leakage rate.

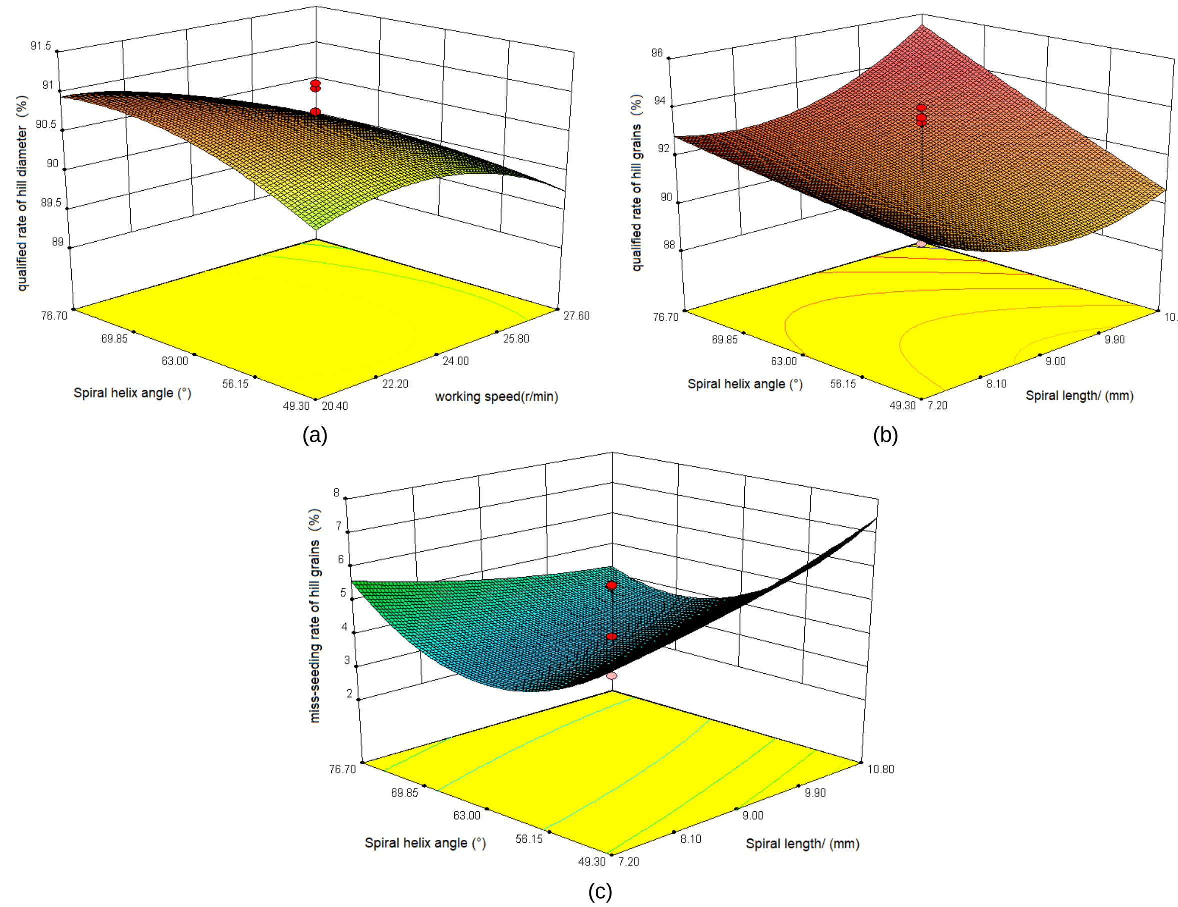

Fig. 7 - Response surface graph

Optimization and verification

In order to obtain the optimal combination of test factors, a mathematical model is established based on the boundary conditions of the factors, and the regression equations on the qualified rate of hill diameters, the qualified rate of hill grains, and the miss-seeding rate of hill grains are analyzed. The mathematical model is as follows:

$$\begin{cases} \max \ y_1 \\ \max \ y_2 \\ \min \ y_3 \\ s.t. \quad 18 \le x_1 \le 30 \\ \quad 6 \le x_2 \le 12 \\ \quad 40 \le x_3 \le 86 \\ \quad 0 \le y_1(x_1, \ x_2, \ x_3) \le 1 \\ \quad 0 \le y_2(x_1, \ x_2, \ x_3) \le 1 \\ \quad 0 \le y_3(x_1, \ x_2, \ x_3) \le 1 \end{cases} \tag{15}$$

When the working speed of the seed metering wheel is 23.2 r/min, the spiral groove length is 10.8mm and the helix angle of the spiral groove is 71.0°, the performance of the seed metering device is optimal. The qualified rate of hill diameter is 91.27%, the qualified rate of hill grains is 94.42% and the miss-seeding rate is 3.82% respectively.

According to the optimization results, the bench test is carried out, and the qualified rate of hill diameter is 91.06%, the qualified rate of hill grains is 94.64% and the miss-seeding rate is 3.64% respectively. The verification result is basically consistent with the optimization result, and the error is in an acceptable range.

CONCLUSIONS

A seed metering device that can realize direct seeding of rice hill is designed. The key components of the seed metering wheel and spiral grooved spoon are studied, and Matlab software is used to analyze the movement state of rice buds in the spiral groove during the seeding process. The analysis shows that with the increase of the helix angle of spiral groove during the seeding process, the axial velocity of the rice buds first increases and then decreases, and the circumferential velocity gradually increases.

The quadratic regression-orthogonal rotation combination design is used to establish the mathematical model of experimental factors and seeding performance index. The response surface graph is analyzed to obtain the relationship of factors on the influencing trend and interaction of factors, and then the bench test is carried out. The results show that the optimization results and the verification results are basically the same.

Design-Expert 6.0.10 software is used to analyze the test results, and the regression model is optimized and verified. When the working speed of the metering wheel is 23.2r/min, the spiral groove length is 10.8mm, and the helix angle of spiral groove is 71.0°, the best combination is that the qualified rate of hill diameter is 91.06%, the qualified rate of hill grains is 94.64%, and the miss-seeding rate is 3.64%.

ACKNOWLEDGEMENT

This work was supported by the National Natural Science Foundation of Zhejiang (No.LGN20E050005).

REFERENCES

[1] Arzu Y., Adnan D. (2014). Measurement of seed spacing uniformity performance of a precision metering unit as function of the number of holes on vacuum plate. *Measurement*, vol.56, pp. 128-135.

[2] Cao C.M., Qin K., Wang A.M, et al. (2015). Design and Experimental Research on Rice Hill Seeder with Air-blowing Special Hole & Scoop-wheel Type. *Transactions of the Chinese Society for Agricultural Machinery*, vol.46, no.1, pp. 66-72.

[3] Dudarev I., Kirchuk R. (2017). Simulation of bulk materials separation process in spiral separator. *INMATEH - Agricultural Engineering*, vol.53, no.3, pp.57-64.

[4] He L.N., Zhao M.M., Zhao T.C., Hao X.Z., Zhang X.Z., He R.Y. (2019). Design and experiment of the spiral trough seed metering for rice and wheat. *Journal of Hunan Agricultural University (Natural Sciences)*, vol.45, no. 6, pp. 657-663.

[5] Hevko R.B., Baranovsky V.M., Lyashuk O.L., et al. (2008). The influence of bulk material flow on technical and economic performance of a screw conveyor. INMATEH - Agricultural Engineering, vol.56, no.3, pp. 175-184.

[6] Huang M., Fang S.L., Cao F.B., et al. (2020). Early sowing increases grain yield of machine-transplanted late-season rice under single-seed sowing. *Field Crops Research*, no.253, pp.107832. https://doi.org/10.1016/j.fcr.2020.107832

[7] Liu C.L., Li Y.N., Song J.N., et al. (2017). Simulation design and experiment of a directional seed-feeding device. *International Agricultural Engineering Journal*, vol.26, pp.16-24.

[8] Liu C.L., Wang Y.L., Du X., et al. (2019). Filling performance analysis and verification of cell-belt rice precision seed-metering based on friction and repeated filling principle. *Transactions of the CSAE*, vol.35, no.4, pp.29-36.

[9] Lu F.Y., Ma X., Qi L., Xing X.P., Li H.W., Guo L.J. (2018). Theory and Experiment on Vibrating Small-amount Rice Sowing Device. *Transactions of the Chinese Society for Agricultural Machinery*, vol.49, no.6, pp. 119-128,124.

[10] Luo X.W., Liu T., Jiang E.C., et al. (2007). Design and experiment of hill sowing wheel of precision rice direct-seeder. *Transactions of the Chines eSociety of Agricultural Engineering*, vol.23, no.3, pp.108-112.

[11] Ren W.T., Lü X.R., Kong A.J., et al. (2009). Development of the taped type rice direct seeding machine. *Journal of Shenyang Agricultural University*, vol.40, no. 1, pp.62-66.

[12] Trokhaniak O.M., Hevko R.B., Lyashuk O.L. et al. (2020). Research of the of bulk material movement process in the inactive zone between screw sections. *INMATEH - Agricultural Engineering*, vol. 60, no.1, pp.261-268.

[13] Vasylkovska K.V., Vasylkovskyi O.M., Sc. Sviren M.O. et al. (2019). Determining the parameters of the device for inertial removal of excess seed. *INMATEH - Agricultural Engineering*, vol. 57, no.1, pp.135-140.

[14] Wang Y.L., Zhu D.F., Xing J, et al. (2020). Characteristics of seedling raising and mechanized transplanting of hybrid rice with a low seeding rate by precise seeding method. *Chinese Journal of rice Science*, vol.34, no.4, pp. 332-338. DOI: 10.16819/j.1001-7216.2020.9113

[15] Xing H., Wang Z.M., Luo X.W., et al. (2020). Design and experimental analysis of the stirring device for pneumatic precision rice seed metering device. *Transactions of the ASABE*, vol.64, no.4, pp. 799-808. Doi: 10.13031/trans.13096

[16] Xing H., Ying Z., Wang Z.M, et al. (2018). Design of an active seed throwing and cleaning unit for pneumatic rice seed metering device. *International Journal of Agricultural and Biological Engineering*, vol.11, no.2, pp. 62-69. DOI: 10.25165/j.ijabe.20181102.3844

[17] Yang Y. (2020). Rice cultivation status and high yield cultivation suggestions. *Modern Agricultural Science and Technology*, vol.10, pp. 50-51.

[18] Yin Z.K. (2020). Experimental study on fixed distance and precision sowing of rice. *Hybrid rice*, vol.50, no. 1, pp.38-40.

[19] Zhang M.H., Wang Z.M, Luo X.W, et al. (2018). Review of precision rice hill-drop drilling technology and machine for paddy. *International Journal of Agricultural and Biological Engineering*, vol.1, no.3, pp.1-11. DOI: 10.25165/j.ijabe.20181103.4249

[20] Zhang S., Li Y., Wang H.Y., Liao J., Li Z.D, Zhu D.Q. (2020). Design and Experiment of U-shaped Cavity Type Precision Hill-drop Seed-metering Device for rice. *Transactions of the Chinese Society for Agricultural Machinery*, vol.51, no.10, pp. 98-108.

[21] Zheng J.X., Gao Y.Y., Yuan H.F., et al. (2018). Design of shaped-hole Volume-variable Precision seeder. *INMATEH - Agricultural Engineering,* vol. 56, no.3, pp.129-136.

[22] Zhou H.B., Liang Q.Y., Wen T.L., et al. (2016). Design and test of the quantitative seed feeding device with external groove wheel of two-stage vibration precision seed metering device. *Transactions of the Chinese Society for Agricultural Machinery*, vol.47, no. Supp, pp. 57-61.

LOOSENING AND LEVELING DEVICE FOR PREPARING SOIL FOR MELON CROPS
/
РЫХЛИТЕЛЬНО-ВЫРАВНИВАЮЩЕЕ УСТРОЙСТВО ДЛЯ ПОДГОТОВКИ ПОЧВЫ ПОД БАХЧЕВЫЕ КУЛЬТУРЫ

Aldoshin N.V.[1)], Mamatov F.M.[2)], Kuznetsov Yu.A.*[3)], Kravchenko I.N.[1)], Kupreenko A.I.[4)], Ismailov I.I.[1)], Kalashnikova L.V.[5)] [1]
[1)]Russian State Agrarian University – Moscow Agricultural Academy named after K.A. Timiryazev / Russia;
[2)]Karshy Engeneering Economic Institute / Republic of Uzbekistan;
[3)]Orel State Agrarian University named after N.V. Parakhin / Russia;
[4)]Bryansk State Agrarian University / Russia;
[5)]Orel State University named after I.S. Turgenev / Russia
Tel: +79208289219; E-mail: kentury@yandex.ru
DOI: https://doi.org/10.35633/inmateh-64-26

Keywords: *strip tillage, soil, loosening and leveling device, slat roller*

ABSTRACT
The analysis of soil cultivation technologies for sowing melon crops was carried out. The design of a combined soil tillage tool capable of plowing, pre-sowing treatment and formation of irrigation furrows in one pass was substantiated. The main tillage is recommended to be done by front plow tools for smooth plowing. Plow bodies of two bottom plows should be mounted along the symmetry axis of the implement according to the lister scheme, which allows not to carry out a full rotation of soil layers and provides automatic formation of irrigation furrow. A loosening and leveling device for strip pre-sowing soil tillage in the sowing zone has been developed. The use of a combined soil tillage tool can reduce labor costs up to 25%, energy consumption for soil preparation up to 50%, reduce the duration of work, reduce soil compaction and retain moisture in the soil layer.

РЕЗЮМЕ
Проведен анализ технологий обработки почвы под посев бахчевых культур. Обоснована конструкция комбинированного почвообрабатывающего орудия, способного за один проход выполнять вспашку, предпосевную обработку и формирование поливных борозд. Основную обработку почвы рекомендовано проводить плужными рабочими органами фронтального плуга для гладкой вспашки. Плужные корпуса двухкорпусного плуга необходимо устанавливать по оси симметрии орудия по листерной схеме, что позволяет осуществлять не полный оборот пластов почвы и обеспечивает автоматическое формирование поливной борозды. Разработано рыхлительно-выравнивающее устройство для полосовой предпосевной обработки почвы в зоне посева. Использование комбинированного почвообрабатывающего агрегата позволяет снизить затраты труда до 25 %, энергопотребление на подготовку почвы до 50 %, сократить продолжительность проведения работ, уменьшить уплотнение почвы и сохранить влагу в почвенном слое.

INTRODUCTION
The most important link in the system of measures to ensure high quality agricultural crops and high yields of melon crops is soil cultivation. Success in cultivating melon crops largely depends on time and quality of soil cultivation, on how it is carried out and the perfection of machine design. In recent years, the capacity and potential of agricultural tractors have increased significantly, but the methods of tillage mostly remained the same, which in many cases is not justified agronomically *(Mamatov F.M. et al, 2018; Litvinov S.S. and Bykovskiy Yu.A., 2013; Mitev G., 2016; Moskvitchev A.Yu. et al, 2011; Reicosky D.C., 2015).*

Multiple passes of agricultural machinery through the cultivated field lead to soil compaction, which results in decrease in the yield of melon crops.

[1] *Aldoshin N.V., Prof. PhD. Eng. Sc.; Mamatov F.M., Prof. PhD. Eng. Sc.; Kuznetsov Yu.A., Prof. Dr. Eng. Sc.; Kravchenko I.N., Prof., Dr. Eng. Sc.; Kupreenko A.I., Assoc. Prof. Dr. Eng. Sc.; Ismailov I.I., Postgraduate; Phil.Sc. Kalashnikova L.V., Prof. PhD.*

Operations of the main and pre-sowing tillage are energy consuming *(Celik A. and Raper R.L., 2012; Mitkov V.B. et al, 2016; Sarauskis E. et al, 2012; Mirzaev B. et al, 2019)*. In this connection, there is a need to create new combined tools that allow the use of energy-saving methods of soil cultivation while reducing the number of passes of units across the field and reducing the duration of work *(Lal R. and Shukla M.K., 2004; Kudzaev A.B. et al, 2017; Elizarov V.P. et al, 2011; Mosyakov M.A. and Zvolinskiy V.N., 2015)*.

The main purpose of the research is to substantiate the layout scheme and design parameters of the loosening and leveling work tool of the combined tool for soil preparation for melon crops.

MATERIALS AND METHODS

When preparing the soil for sowing melon crops in a certain sequence, a number of technological operations are carried out: plowing, irrigation furrows formation, pre-sowing treatment. For their simultaneous performance, the authors offer a combined aggregate for strip tillage. It consists of two bodies of frontal plow, located on a lister scheme.

Such working bodies allow strip plowing of the area with the simultaneous formation of irrigation furrows, due to the incomplete turnover of layers. On both sides of the formed irrigation furrow, there are ridges of plowed soil layers, and in this area it is necessary to carry out pre-sowing tillage *(Romaneckas K. et al, 2016; Starovoytov V. et al, 2017; Izmailov A.Yu. et al, 2013)*.

For this purpose, a loosening and leveling device is designed, the parameters of which should be substantivized.

As a result of the combined tool usage, the following agrotechnical requirements for pre-sowing soil tillage must be fulfilled: the number of clods of up to 25 mm in the layer 0-10 cm must be no less than 80%.

In this case, the soil density in the horizon of 0-10 cm should be from 1.1 to 1.2 g/cm^3 *(Mamatov F.M. and Mirzaev B.S., 2018)*.

RESULTS

To realize the set goal various design variants of loosening and leveling devices for the combined soil tillage tool for melon crops were considered (fig.1-5).

Variant 1 (fig.1). The leveling device is a ski-shape leveler *1* and a slatted roller *2*. Levelers are installed symmetrically in the longitudinal axis of the unit over the ridges of arable beds at a certain attack angle. A slatted roller, which additionally destroys the soil clods and compacts the soil in the crops sowing area is located behind each of them. Studies have shown that this type of loosening and leveling device does not fully cope with its functions, not ensuring full compliance with agricultural requirements.

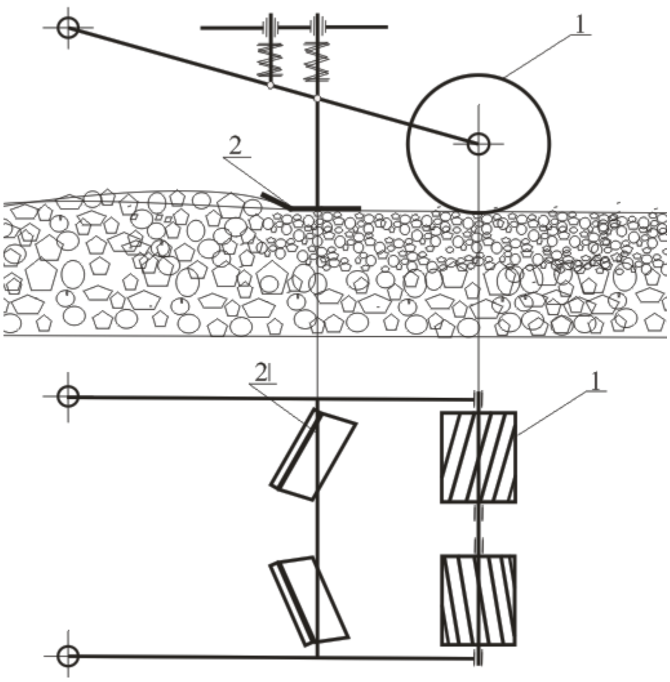

Fig. 1 - Loosening and leveling device (Variant 1)
1 - slatted roller; 2 – leveler

Variant 2 (fig.2). The device consists of ski-shape levelers *1* and flat discs with blade elements *2*. The levelers are mounted symmetrically on the longitudinal axis of the aggregate above the arable beds ridges. Blocks of the flat discs with the blade elements are mounted behind each of them. The leveled surface of the field is exposed to the discs, which additionally crush the soil clods.

In this case the leveling of the surface is partially violated. Such a working element does not fully meet agricultural requirements. Obviously, the presence of a special leveler in its design is not quite justified, as in the first variant.

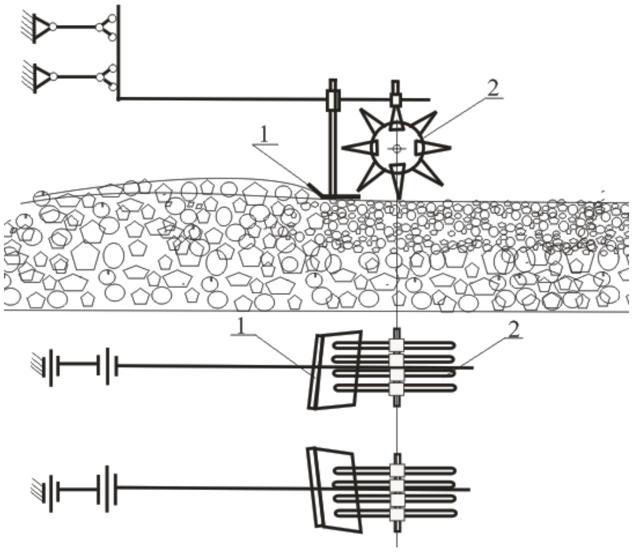

Fig. 2 - Loosening and leveling device (Variant 2)
1 - leveler; 2 - flat disc with blade elements

Variant 3 (fig.3). The device design is provided with rotary hoes *1* and slatted rollers *2*. Hoes blocks crush large soil clods on the ridges of the soil arable beds. The slatted rollers mounted behind them additionally crush them, compacting and leveling the soil selectively. The disadvantage of this design is incomplete performance of the rotary hoes.

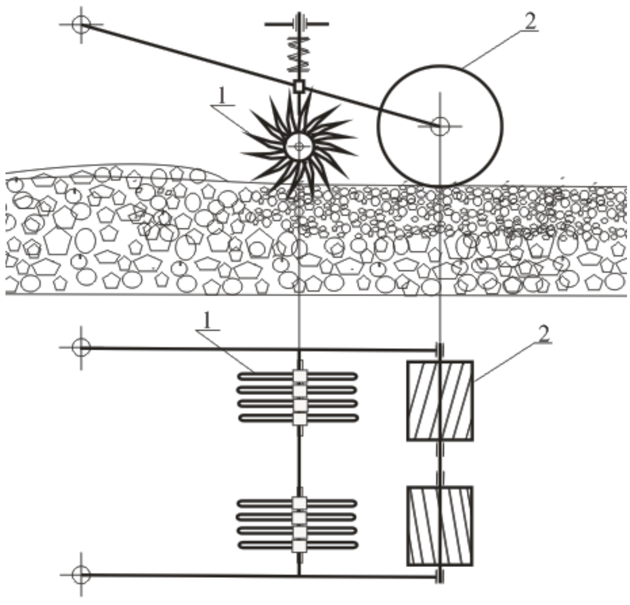

Fig. 3 - Loosening and leveling device (Variant 3)
1 - hoe wheel (rotary hoe); 2 - slatted roller

Variant 4 (fig.4). It includes flat discs with the blade elements *1* and slatted rollers *2*. Two blocks of flat discs with blade elements crush large soil clods on the ridges of the soil arable beds. The slatted rollers mounted behind them additionally crush, compacting and leveling the soil selectively. Such working bodies work better than the previous variants. Nevertheless, the discs blocks are subjected to clogging with soil and vegetation residues, and increasing distance between discs in the blocks leads to uneven tillage.

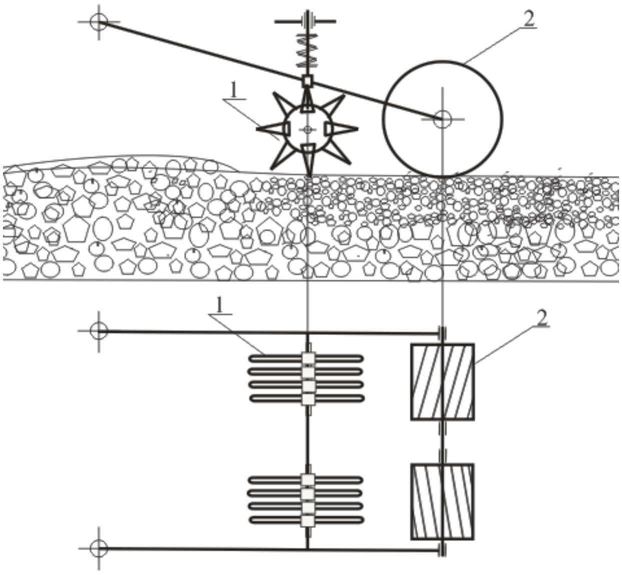

Fig. 4 - Loosening and leveling device (Variant 4)
1 - flat disc with blade elements; 2 - slatted roller

Variant 5 (fig.5). It consists of discs with multi-directional spherical blade elements *1* and slatted rollers *2*. The discs are combined into blocks located above the ridges of the arable beds. Having differently directed spherical blade elements, they crush soil clods. Behind them there are slatted rollers, which additionally crush compacted soil and level the soil in the sowing area selectively. This working body allows ensuring full implementation of agricultural requirements when using it *(Aldoshin N. et al, 2020)*. This option is the most effective in work, so it was chosen for further research.

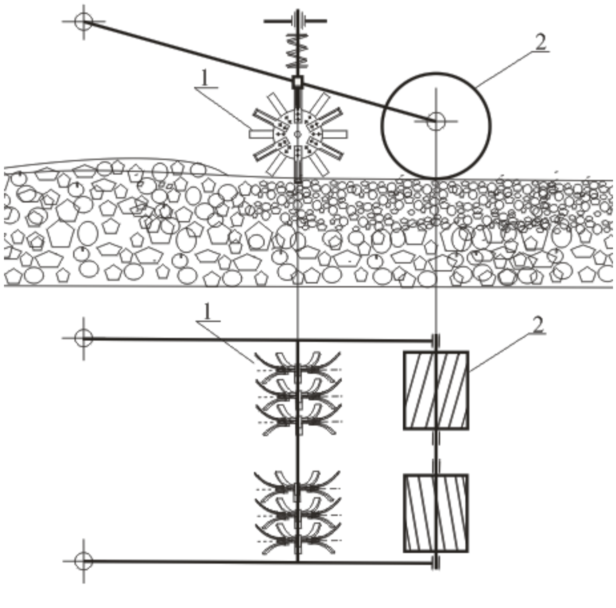

Fig. 5 - Loosening and leveling device (Variant 5)
1 - disc with multi-directional spherical blade elements; 2 - slatted roller

The efficiency of the loosening and leveling device (variant 5) is largely determined by the correct choice of its design parameters. Justification of soil-tilling discs with multi-directional spherical blade elements was done by us earlier. On this basis, the following parameters were accepted: diameter of the blade working body – 400 mm; radius of curvature of the blade element – 455 mm; thickness of the blade element – 4 mm, width – 40 mm *(Mamatov F.M. and Mirzaev B.S., 2018)*. The general view of the developed working body is shown in fig. 6.

Fig. 6 - General view of rotary soil-tilling working body with multi-directional spherical blade elements

Let's perform the calculation of the slatted roller. Its main parameters are: radius r_{KT}, slat height h_{SL}, the attack angle of slat γ_{SL}, the number of slats n_{SL}, the width of section B_S. Values of the most parameters of the roller are closely interrelated and they depend on its main parameter – the radius.

The radius value should be such that when meeting with a large clod, the roller is easily rolled over it.

If condition (1) is met, the soil clod between the field surface and the outer edge of the roller is pinched, soil compaction is excluded (fig. 7).

$$\delta \leq \varphi_1 + \varphi_2, \tag{1}$$

where:

δ – angle of pinching, [deg];

φ_1 – clod friction angle against the roller, [deg];

φ_2 – soil to soil friction angle, [deg].

When the roller slat is exposed to the side surface, the soil clod penetrates into the soil at a certain depth h_2.

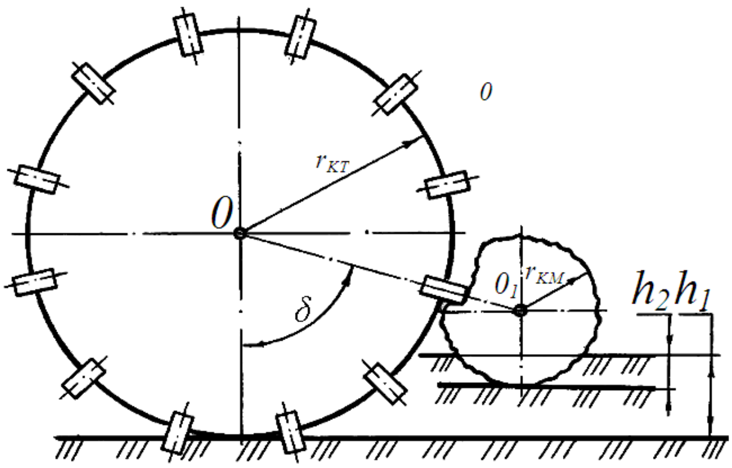

Fig. 7 - Scheme for determining the roller diameter

From figure 7, you can see that

$$r_{KT} \cdot (1-\cos\delta) - h_1 = r_{KM} \cdot (1+\cos\delta) - h_2, \tag{2}$$

where: r_{KM} – the soil clod radius, [m];

h_1 – the roller depth penetration, [m];

h_2 – the clod depth penetration, [m].

Thus, the radius of the roller r_{KT} will be determined:

$$r_{KT} = r_{KM} \cdot \frac{1+\cos\delta}{1-\cos\delta} + \frac{h_1}{1-\cos\delta} - \frac{h_2}{1-\cos\delta}, \tag{3}$$

Knowing that:

$$\frac{ctg^2\delta}{2} = \frac{1+\cos\delta}{1-\cos\delta}, \tag{4}$$

We obtain:

$$r_{KT} = r_{KM} \frac{ctg^2\delta}{2} + \frac{h_1 - h_2}{1-\cos\delta}, \tag{5}$$

The number of the roller slats is determined from the nature of its interaction with the soil. Rolling of the roller is accompanied by sliding. Sliding value varies along the path length. This leads to the fact that some parts of the soil are deformed in different ways. In addition, the slatted roller, in contrast to smooth rollers, affects the soil cyclically with its slats, which also leads to uneven soil deformation. The areas affected by the slats are more deformed, the areas between the slats - less. At a certain depth the deformed areas are connected by adjacent slats. Theoretically, the soil deformation should be equal at this depth, but because of roller sliding the difference in the deformation value exists.

The slat makes a rotational motion about the rotation axis of the roller at a rate ωr_{KT} (where: ω – angular rate, rad/s; r_{KT} – roller radius, m) and makes a translational motion together with the aggregate with rate v (fig. 8).

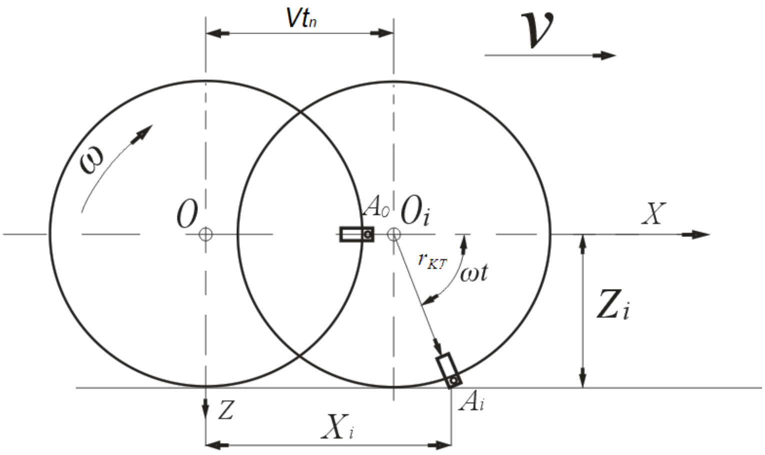

Fig. 8 - Scheme for determining the equation of the roller slat motion

Let's consider the movements of the extreme point A of the roller slat, which is at the initial moment in position A_0. After a certain period of time t the roller axis will move to the position O_i, passing the path $S_n=Vt_n$, and the roller disc will rotate by an angle ωt. As a result, point A will move from position A_0 to position A_i and its coordinates will be determined by the equations:

$$X_i = Vt_n + r_{KT} \cdot \cos\omega t, \tag{6}$$

$$Z_i = r_{KT} \cdot \sin\omega t, \tag{7}$$

The equations characterize the path of absolute motion of point A in parametric form. This path is a cycloid ("trochoid"). Any point of the roller slat describes the path of an extended cycloid in the process of work. Since several slats (8-12 pcs.) are fixed on one disc of the roller, the corresponding points of these slats describe the same cycloids, but shifted forward along the machine. So, if the previous roller slat with its furthest point from the rotation axis describes path 1 (fig. 9), the path 2 of the subsequent slat will be shifted horizontally by some distance S_n, called the feed on the slat. The feed on the slat $S_n=Vt_n$, where t_n – time, for which the subsequent slat in relative motion will take the position of the previous one, i.e. it will rotate by an angle equal to the central angle between them. The more slats on the roller disc, the less this time.

Therefore,

$$t_n = \frac{t_{do}}{n_{SL}}, \tag{8}$$

where: t_{do} – time, for which the roller disc turns by one revolution;

n_{SL} – slat number on the roller disc.

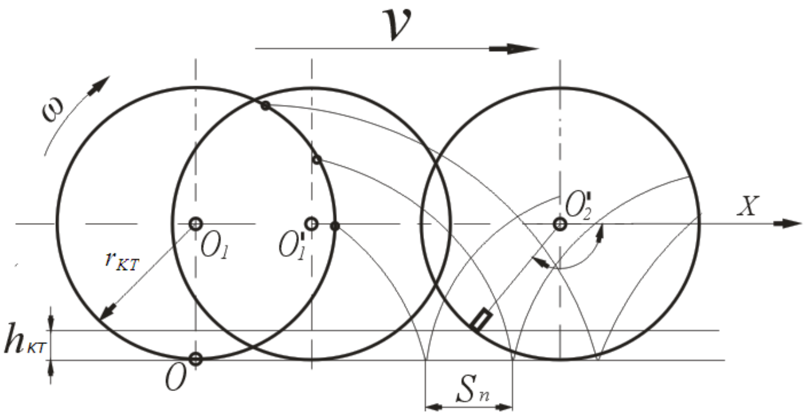

Fig. 9 - Kinematics of the roller motion

Revolution time is determined from the condition $\omega t_{do} = 2\pi$, where $t_{do} = \frac{2\pi}{\omega}$, and $t_n = \frac{2\pi}{\omega n_{SL}}$.

By substituting for t_n its value in the initial equation, we obtain:

$$S_n = \frac{\vartheta 2\pi}{\omega n_{SL}}, \tag{9}$$

where: ϑ – translation rate of aggregate.

The uniformity of compaction of the lower layers and loosening of the upper soil layer depends on the value S_n. The soil deformation area is determined by one slat.

The roller slat penetrates the soil at the rotation angle α_1, which corresponds to the time t_1, and comes out of the soil at the rotation angle α_2, which corresponds to the time t_2, (fig. 10). From the figure, we define the angles of input α_1 and output α_2.

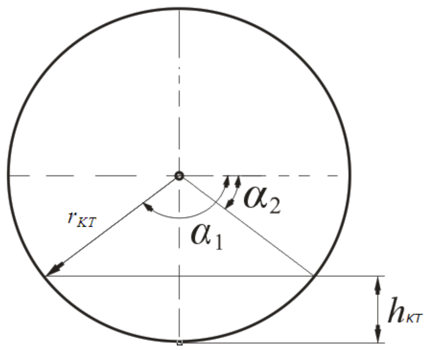

Fig. 10 - Scheme for determining angles α_1 and α_2

From the equation:

$$\frac{r_{KT}-h_{KT}}{r_{KT}}=\sin\alpha_1, \tag{10}$$

$$\alpha_1=\arcsin\frac{r_{KT}-h_{KT}}{r_{KT}}, \tag{11}$$

$$\alpha_1=\pi-\alpha_1, \tag{12}$$

Then the time value:

$$t_1=\frac{\alpha_1}{\omega}=\frac{\left(\arcsin\frac{r_{KT}-h_{KT}}{r_{KT}}\right)}{\omega}, \tag{13}$$

$$t_2=\frac{\alpha_2}{\omega}=\frac{\left(\pi-\arcsin\frac{r_{KT}-h_{KT}}{r_{KT}}\right)}{\omega} \tag{14}$$

The length of the deformed soil on the field surface can be determined as difference:

$$\Delta X=X_2-X_1=v\cdot(t_2-t_1)+r_{KT}(\cos\omega t_2-\cos\omega t_1) \tag{15}$$

Substituting values t_2 and t_1 from equation (13) in (14) we obtain:

$$\Delta X=\vartheta\left(\frac{\pi-\arcsin\frac{r_{KT}-h_{KT}}{r_{KT}}}{\omega}\right)-2(r_{KT}-h_{KT}) \tag{16}$$

Then the number of slats will be:

$$n_{SL}=\frac{2\pi r_{KT}}{\vartheta\left(\frac{\pi-\arcsin\frac{r_{KT}-h_{KT}}{r_{KT}}}{\omega}\right)-2(r_{KT}-h_{KT})} \tag{17}$$

The value of the attack angle of slat γ_{SL} should meet the following requirements: to contribute to the roller load balancing with the rotation angle; to contribute to the partial smoothing of the arable land by shifting the soil. Optimal attack angle γ_{SL} will be such, at which the greatest uniformity of drum rotation in providing the soil particles sliding on the slat surface is achieved. To provide the uniformity of the slats input and output from the soil, it is necessary that at full output of one end of the slat, the other end of the slat should be completely in the soil (fig. 11).

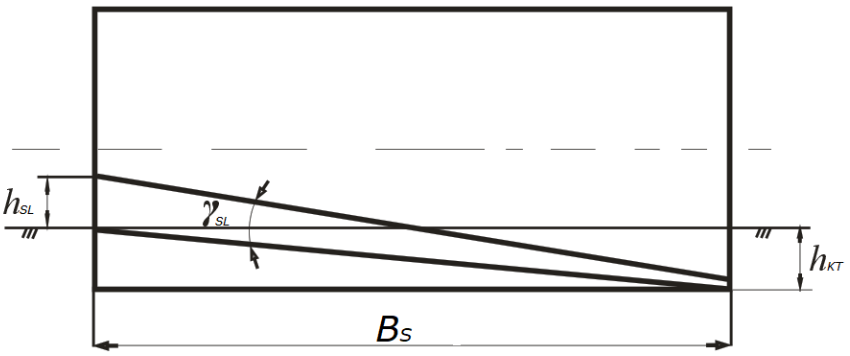

Fig. 11 - Scheme for determining the attack angle of the slat γ_{SL}

To fulfill this condition, it is necessary:

$$tg\gamma_{SL} = \frac{h_{KT} + h_{SL}}{B_S} \tag{18}$$

Where: h_{KT} – depth of the roller penetration into the soil;

h_{SL} – slat height;

B_S – width of the roller single section.

To obtain an angle γ_{SL}, the slats on the adjacent discs should be fixed with some offset by angle β_{OF}, which should be determined from equation:

$$\beta_{OF} = \arccos\frac{r_{KT} - h_{KT}}{r_{KT}} \tag{19}$$

On the other hand, to fulfil the condition of the soil displacement, the angle γ_{SL} must meet the condition:

$$\gamma_{SL} \langle \frac{\pi}{2} - \varphi_{fr} \tag{20}$$

Where: φ_{fr} – soil friction angle.

In our case γ_{SL} ≈12^0. This fully satisfies the condition of the equation (20).

Thus, on the basis of carried out researches the experimental sample of the loosening and leveling device included in the combined tool was designed and manufactured. It consists of a series of blocks of rotary tillage working bodies with multi-directional spherical blade elements and slatted rollers (fig. 12).

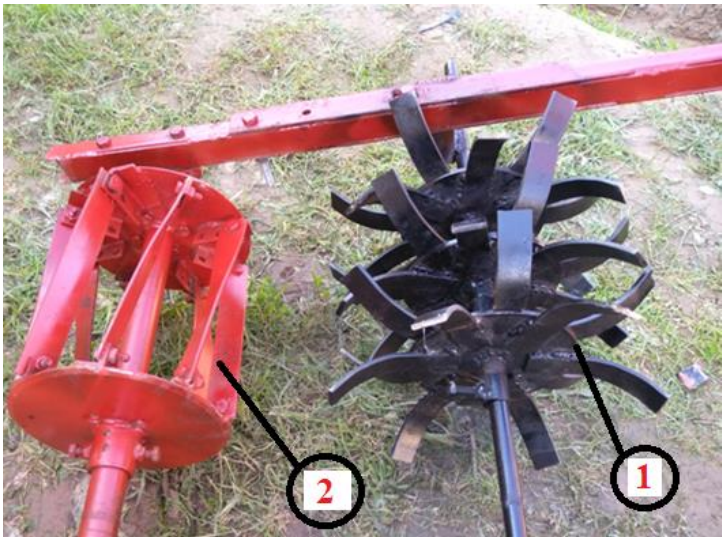

Fig. 12 - General view of the experimental loosening and leveling device for combined tillage tool
1 - rotary loosening working body with multi-directional spherical blade elements; 2 - slatted roller

CONCLUSIONS

The use of a combined tool for strip tillage for melon crops can reduce labor and energy costs by 25% and 50% respectively. This reduces the work duration, retains moisture in the soil, protects the field surface from compaction by reducing the number of passes of the aggregate and ensures high quality of technological operations.

REFERENCES

[1] Aldoshin N., Mamatov F., Ismailov I., Ergashov G., (2020), Development of combined tillage tool for melon cultivation, *19th International Scientific Conference Engineering for Rural Development*, pp. 767-772, Jelgava / Latvia;

[2] Celik A., Raper R.L., (2012), Design and evaluation of ground-driver rotary subsoilers, *Soil and Tillage Research*, Vol. 124, pp. 203-210, Elsevier BV / Netherlands;

[3] Elizarov V.P., Antyshev N.M., Beylis V.M., Shevtsov V.G., (2011), Initial requirements for technological operations in crop production (Исходные требования на технологические операции в растениеводстве), *Сельскохозяйственные машины и технологии (Сельскохозяйственные машины и технологии)*, Issue 1, pp.11-14, Moscow / Russia;

[4] Izmailov A.Yu., Lobachevsky Ya.P., Sizov O.A., (2013), Prospective ways of application of power and ecologically effective machine technologies and technical means (Перспективные пути применения энерго- и экологически эффективных машинных технологий и технических средств), *Agricultural machinery and technologies (Сельскохозяйственные машины и технологии)*, Issue 4, pp.8-11, Moscow / Russia;

[5] Kudzaev A.B., Urtaev T.A., Tsgoev A.E., Korobeynik I.A., Tsgoev D.V., (2017), Adaptive energy-saving cultivator equipped with the simultaneous adjuster of sections for working stony soils, *International Journal of Mechanical Engineering and Technology (IJMET)*, Vol.8, Issue 11, pp.714-720, Tamil Nadu / India;

[6] Lal R., Shukla M.K., (2004), *Principles of Soil Physics*, Marcel Dekker, 716 p., New York / USA;

[7] Litvinov S.S., Bykovskiy Yu.A., (2013), Melon growing: strategy and prospects of development (Бахчеводство: стратегия и перспективы развития), *Potatoes and vegetables (Картофель и овощи),* Issue 5, pp.2-6, Moscow / Russia;

[8] Mamatov F.M., Mirzaev B.S., (2018), New anti-erosion moisture-saving technologies and tools for soil tillage in Uzbekistan conditions (Новые противоэрозионные влагосберегающие технологии и орудия для обработки почвы в условиях Узбекистана), *Ecology and construction (Экология и строительство)*, Issue 4, pp.16-19, Moscow / Russia;

[9] Mamatov F.M., Shodmonov G.D.,Chujanov D.Sh., Ergashev G.X., (2018), New technology and combined machine for preparing soil for sowing gourds, *European science review,* Issue 1-2, pp.234-236, Vienna / Austria;

[10] Mitev G., (2016), Types of tillage as a prerequisite for retention or alteration of physical and mechanical properties of soil (Видове обработки на почвата като предпоставка за запазване или подобряване на физико-механичните и свойства), *Scientific proceedings in international scientific conference «Conserving soils and water»*, pp.79-84, Borovets / Bulgaria;

[11] Mitkov V.B., Kuvachov V., Ihnatiev Ye., Mitkov V.O., (2016), New approach to the choice of way of mechanical processing of soil in the south of Ukraine (Новый подход к выбору способа механической обработки грунта в условиях юга Украины), *International Scientific Journal «Mechanization in Agriculture»*, Issue 1, pp.29-31, Sofia / Bulgaria;

[12] Mirzaev B., Mamatov F., Aldoshin N., Amonov M., (2019), Anti-erosion two-stage tillage by ripper, *Proceeding of 7th International Conference on Trends in Agricultural Engineering – Czech University of Life Sciences Prague* – Faculty of Engineering, pp.391-395, Prague / Czech Republic;

[13] Moskvitchev A.Yu., Konotopskaya T.M., Nikulin M.S., Devyataev K.A., (2011), Improvement of the elements of watermelon cultivation technology in Volgograd area conditions (Совершенствование элементов технологии возделывания арбуза в условиях Волгоградской области), *Izvestia of the Lower Volga Agricultural University Complex (Известия нижневолжского агроуниверситетского комплекса)*, Issue 1(21), pp.1-6, Nizhnevolzhsk / Russia;

[14] Mosyakov M.A., Zvolinskiy V.N., (2015), Combined soil tillage unit for main and pre-sowing tillage (Комбинированный почвообрабатывающий агрегат для основной и предпосевной обработки почвы), *Agricultural machinery and technologies (Сельскохозяйственные машины и технологии)*, Issue 6, pp.30-35, Moscow / Russia;

[15] Reicosky D.C., (2015), Conservation tillage is not conservation agriculture, *Journal of Soil and Water Conservation*, Vol.70, Issue 5, pp.103-108, Ankeny / USA;

[16] Romaneckas K., Avižienytė D., Bogužas V., Šarauskis E., Jasinskas A., Marks M., (2016), Impact of tillage systems on chemical, biochemical and biological composition of the soil, *Journal of Elementology*, Issue 21(2), pp.513-526, Warsaw / Poland;

[17] Sarauskis E., Buragiene S., Romaneckas K.; Sakalauskas A., Jasinskas A., Vaiciukevicius E., Karayel D., (2012), Working time, fuel consumption and economic analysis of different tillage and sowing systems in Lithuania, *Engineering for Rural Development*, Issue 11, pp.52-59, Jelgava / Latvia;

[18] Starovoytov V., Starovoytova O., Aldoshin N., Alexandra Manohina A., (2017), Jerusalem artichoke as a means of fields conservation, *Acta Technologica Agriculturae*, Issue 1, pp.7-10, Slovaca Universitas Agriculturae Nitriae, Nitra / Slovakia.

REAL-TIME MISSED SEEDING MONITORING PLANTER BASED ON RING-TYPE CAPACITANCE DETECTION SENSOR

/

基于环形电容检测传感器的实时漏播监测播种机

Chen Kaikang[1,2], Zhao Bo[2], Zhou Liming[2], Wang Lili[2], Wang Yahui[3], Yuan Yanwei[2*)], Zheng Yongjun[1*)1]

[1)] College of Engineering, China Agricultural University, Beijing100083, China

[2)] Chinese Academy of Agricultural Mechanization Sciences, Beijing 100083, China

[3)]College of Agricultural Equipment Engineering, Henan University of Science and Technology, Luoyang 471003, China

E-mail: zyj@cau.edu.cn

DOI: https://doi.org/10.35633/inmateh-64-27

Keywords: *Corn, Seeding and fertilizing machine, Variables, Sensor.*

ABSTRACT

In order to improve the quality of corn sowing and fertilizer utilization, reduce labor costs, this paper aimed at the traditional tillage fertilizer machine to improve. The seeding and fertilizing machine with adjustable flow is designed by integrating particle fertilizer sensor and CAN bus transmission technology. It is mainly composed of seed and fertilizer discharging mechanism, ditch and soil covering mechanism, and leakage seeding and blockage monitoring system. Fertilizer drop signal can be obtained in real time by detecting the flow sensor outside the fertilizer discharge pipe. The speed of the stepper motor can be adjusted after signal processing, which can also realize the alarm of missing sowing and blocking light, and realize the precise variable sowing. The field experiment results show that the maximum relative error of seed leakage rate monitoring is 3.75%, and the alarm accuracy of fertilizer clogging is high. This machine can reduce the intensity of manual operation, and the quality of operation can be effectively monitored and controlled, can effectively reduce the production cost, has better practicability and economy.

摘要

为了提高玉米播种质量和肥料利用率，降低劳动成本，本文针对传统耕作施肥机进行改进。集成颗粒肥料传感器、CAN 总线传输等技术设计的流量可调的播种施肥机，主要由排种排肥机构、开沟覆土机构，漏播堵塞监测系统等组成。通过检测排肥管外的流量传感器可实时获取肥料下落信号。经信号处理后调节步进电机转速，还可实现漏播、堵塞灯光报警，实现精准变量播种。田间试验结果表明：该机种子漏播率监测相对误差最大为 3.75％，肥料堵塞报警准确率高。该作业机械能够减少人工作业强度，并对作业质量进行有效监测与控制，能有效降低生产成本，具有较好的实用性和经济性。

INTRODUCTION

As a big agricultural country, the development of agriculture occupies a pivotal position in China *(Jin et al., 2019)*. Sowing and fertilizing is one of the most important works in agricultural activities, which plays an important role in ensuring grain production and increasing agricultural output. However, the phenomenon of excessive and partial fertilizer application in agricultural production is widespread *(Jin et al., 2018)*. This causes a huge waste of resources and threatens the ecological environment. Sowing in most areas still depends on manpower. With the development of intelligent agriculture, variable seeding and fertilizer applicator also advances by leaps and leaps. Variable fertilization seeding technology is an important part of precision agriculture. It is based on the actual needs of crops, scientific fertilization methods and rational seed distribution *(Zhou et al., 2017)*. Computer is used to guide fertilization and seeding operations and to determine the variable input of crop growth requirements. Reasonable reduction of resource input can not only improve the natural ecological environment, but also achieve higher economic benefits *(Zhou et al., 2014)*.

---

[1]*Chen Kaikang, Ph.D. Stud.;Zhao Bo, Researcher. Ph.D.;Zhou Liming, Researcher. Ph.D.; Wang Yahui, Ph.D.; Yuan Yanwei, Researcher. Ph.D.;Zheng Yongjun, Prof. Ph.D.*

Foreign agricultural machinery and equipment have experienced more than 100 years of development, has been relatively mature at present, the main representative countries being Japan, Western Europe, the United States and other developed countries. At present, the foreign mainstream seeding machinery has been able to integrate land preparation, seeding, fertilization, watering, filling, suppression and other functions as one, reducing repeated labor, reducing the waste of human resources, to achieve the protection of the land *(Bai et al., 2020)*. A typical example is: German company AMA - ZONE developed a variable fertilizer application machine based on vision sensor. Through the sensor installed in the front end of the machine, the nutrient deficiency of the crop can be measured, and the amount of fertilizer top dressing can be calculated. After signal processing, the hydraulic motor is finally controlled to realize variable fertilization *(Xiong et al., 2020)*. The JD-1820 pneumatic variable fertilizing planter developed by John Deere is equipped with sowing quality monitors, star sensors, hydraulic motor drive controller monitors and other transmission and signal processing equipment. It can realize variable regulation of fertilizer application by controlling the opening of hydraulic proportional valve *(Jin et al., 2018)*. Case developed variable seeding and fertilizer applicator using digital image processing technology. During the operation, the high-speed camera was used to take the pictures of the seeding outlet at the natural frequency, and the seed out state parameters of the seeder were obtained by combining with the digital image processing technology. Then, the curve of seed motion trajectory was drawn according to the mathematical model. According to the curve, the scattered distribution state of seeds can be known, and the dynamic adjustment can be made to adjust the size of the sowing amount in real time.

In contrast, China's agricultural machinery started late and the industrial foundation is weak, so the technology is relatively backward *(Chen, 2017)*. The autonomous on-demand fertilization device, developed by Jilin University, uses IC cards, GPS and other devices only. The principle is to divide the field into grids of equal area, and the microcontroller identifies the cells to read the corresponding amount of work. The variable fertilization can be realized by adjusting the size of the opening degree of the chute wheel and changing the amount of work by adjusting the rotational speed of the chute wheel *(Jia, 2016)*. Shanghai Agricultural Machinery Research Institute and Shanghai Jiao Tong University jointly use the global positioning system GPS to design a multi-functional variable feeding machine, which is the first intelligent variable feeding machine based on GPS independently developed in China. The machine has two schemes of motor drive and hydraulic drive, as well as a variety of variable fertilization prescription generation mode, which can realize the touch screen display and modification of operation information *(Zhang, 2013)*.

On the basis of the existing research, the main seeding object of this paper is corn crop. It CAN deal with different demands for cultivation in different regions. It integrates technologies such as vehicle sensors, CAN bus transmission and PC terminal, aiming to realize seed fertilizer monitoring and variable fertilization under the condition of simultaneous sowing of corn seed fertilizer.

MATERIAL AND METHODS

OVERALL STRUCTURE DESIGN OF FERTILIZER APPLICATOR

2.1 Structural design, principle and main technical parameters

2.1.1 Structure design and working principle

The main structure of this machine includes the fertilizer box, fertilizer device, transmission bearing, controller, soil covering device, suppression wheel, rotating chain, suppression spring, seed discharging box, etc. The whole machine adopts the symmetrical structure design, in the advance process of the unit fertilizing first, and then sowing. The seed fertilizer box is installed on the upper part of the front end of the frame, and four internal groove wheel fertilizer drains are installed on the lower part. The fertilizer drains are connected to the front row furrow opener which can open deep trenches through the fertilizer drains pipe, and the furrow opener is fixed to the beam at the front end of the frame through the bolt connection. The seed box is arranged above the rear end of the frame, and the seed metering device at the bottom is connected to the frame through the L-shaped steel plate. The seed metering device is connected with the rear row-type trencher through the seed metering device pipe, and the seed trencher is also equipped with a parallelogram copying mechanism. The intermediate power transmission shaft is fixed to the rear of the frame by steel plates. The wheels are connected to the intermediate shaft through the H plate. One end of the compression spring is connected to the box frame by rotation, and the other side is connected to the H on the panel by rotation. In addition, there is a shaft in the middle of the spring to prevent the spring from moving in other directions.

Before the operation of the fertilizer applicator, the relevant parameters of the operation of the machine should be calibrated first, and then input into the database of the circuit control module. Then, the information of the fertilizer quantity of the section that needs fertilizer is also input into the circuit control module. The fertilizer applicator is driven by a diesel engine. There is a stepper motor at the outer end of the fertilizer spreader groove wheel to monitor the movement speed of the fertilizer spreader in real time. The speed information is transmitted to the circuit controller, and the circuit controller analyzes the data, calculates the rotation pulse frequency of the stepper motor and transmits it to the driver. The driver drives the stepper motor to rotate, so as to achieve the purpose of controlling the rotation speed of the transmission shaft. The fertilizer applicator applies a quantitative amount of chemical fertilizer deep into the fertilizer ditch directly below to complete quantitative and accurate fertilization.

2.1.2 Main technical parameters

The connection mode between the machine and the tractor is traction type, and its main technical parameters are shown in Table 1.

Table 1

Main technical parameters

Design content	Unit	Parameter
Auxiliary tractor	The bumper harvest - 180 type wheel tractor	18 (13.2 KW/ps)
Power disc diameter × rotation speed	(mm x r/min)	400 x 50
Spacing × number of rows	(cm x line)	60 x 4
Planting distance	(cm x strain)	20
Sowing depth	(cm)	2.5 ~ 5
Fertilization depth	(cm)	5 ~ 6
Operating speed	(km (h)	4 ~ 8
Machine weight	(kg)	**320**

2.2 Fertilization device design

2.2.1 Distribution

The existing fertilizer discharging methods of variable fertilizer applicator mainly include external centrifugal type, groove wheel type and spiral type *(Shi et al., 2017)*. Most of the domestic fertilizers discharging devices choose external groove wheel type. The outer groove wheel fertilizer discharge device is usually composed of a fertilizer discharge box, an outer groove wheel, a brush, a retaining ring etc., the seeding and fertilizing machine is mainly used for discharging granular urea, granular compound fertilizer and farm self-made granular fertilizer and other chemical fertilizers. The main technical characteristics of chemical fertilizers are shown in table 2.

Table 2

Main technical indexes of commonly used fertilizers

Type of fertilizer	Shape	Moisture content (%)	Mass per unit volume (g/L)	Natural angle of repose (°)
The urea	particles		720	35
Ammonium sulfate	granular	0.93	943	44
Ammonium nitrate	crystalline	2.13	1010	35
Ammonium bicarbonate	powder	2.87	920	37
Ammonium phosphate	crystals	2	840	
Calcium superphosphate	powder and granular	16	880	

Corn is seeded with chemical fertilizers such as compound or urea, which have similar physical properties and are granular and have a low water content. Therefore, in this design, the external groove wheel fertilizer discharge device is selected. As shown in Fig. 1, the advantages of the fertilizer discharge device are outstanding, with better stability and uniformity of fertilizer discharge, and there can be a more precise control of the displacement *(Zhang and Zhang, 2011)*.

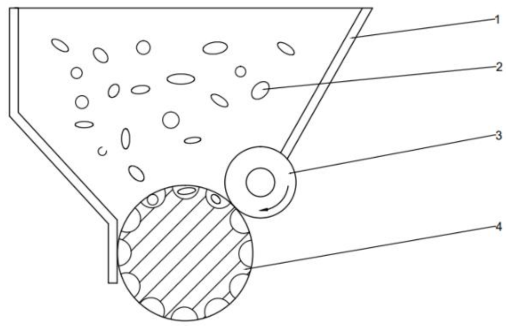

Fig. 1 - Structural schematic diagram of outer groove wheel seed platter

1. Seed box; 2. Seed; 3. Scraping wheel; 4. Placing wheel

When the fertilization device works, the chemical fertilizer in the fertilizer box enters the fertilizer discharge device from the fertilizer box under the action of gravity and fills the grooves of the groove wheel. The fertilizer discharging shaft drives the grooves to rotate, and the fertilizer in the grooves of the grooves is rotated by the grooves to force down, and finally is applied into the grooves opened by the trencher below.

The groove wheel is a key part of the process, accurately measuring the fertilizer and allowing it to flow into the manure ditch (Figure 2). The size of groove wheel determines the precision of fertilization and discharge effect, thus affecting the performance of the whole machine, so the size of groove is very important.

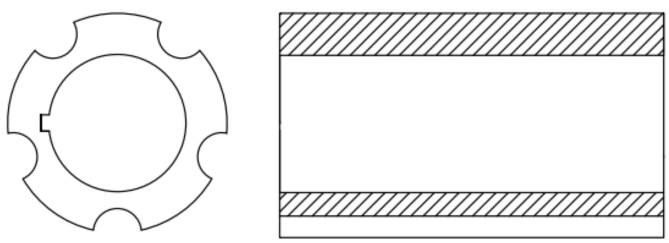

(a) Main view (b) Left view

Fig. 2 - Two-dimensional structure of groove wheel

The relationship between the displacement and the number of turns of the grooved wheel can be as follows:

$$Q_1 = 5bQ \tag{1}$$

Where$Q_1$is the displacement of a fertilizer discharge device within 50m length, g; b is for calculating line spacing, m; Q is the amount of fertilizer discharged, kg/hm²;

b= 0.6; Q=450 is substituted into Equation (1), and then: Q_1=1350 g

Number of turns of grooved wheel 50m forward:

$$N = \frac{Q_1}{q} \tag{2}$$

In the formula, $N$is the number of turns of the wheel shaft, integer; Q_1 is the displacement, g; q is the displacement of one turn of the fertilizer shaft, under the specified working length of the groove wheel.

Known: Q_1=1350 g

At that time a_0=0.8; L=1.5; λ=0.17;$q_1 = 49.0376\ g/r$ N=27

When a_0=0.17; L=3.0; λ=0.19;$q_1 = 100.63704\ g/r$ N=14

When a_0=0.19; L=6.0; λ=0.20;$q_1 = 202.8523\ g/r$ N=7

Grams/radius（g/r）is the mass of fertilizer discharged after one turn of the grooved wheel.

As can be seen from the above relation, when the external groove wheel fertilizer discharge device works, if the diameter is too large, the speed will decrease accordingly. If the diameter is too small, it will affect the discharge of fertilizer, or destroy fertilizer particles. According to the manual, determine the working length of the groove wheel of 40mm, the groove radius r=8 mm, and the groove number z=10.The length, size and position of the seed platter grooves and the speed of the distribution axis are the main influencing factors of the distribution working performance and a main evaluation index of stability. Through verification, it is concluded that the effective length of the outer grooved wheel is 60mm, the speed of the rotating shaft is 35-70 r/min, and the fertilizer discharge is relatively stable.

2.2.2 Metering plate

Seed platter is the key part of precision fertilization planter. The rationality of the structure designed according to the corresponding working principle directly determines the working performance of the whole machine. At present, the main mechanical seed planter is mainly under the action of gravity, relying on the structure to achieve seed filling and seed planter. The quality of the seed plate determines the quality of the seed.

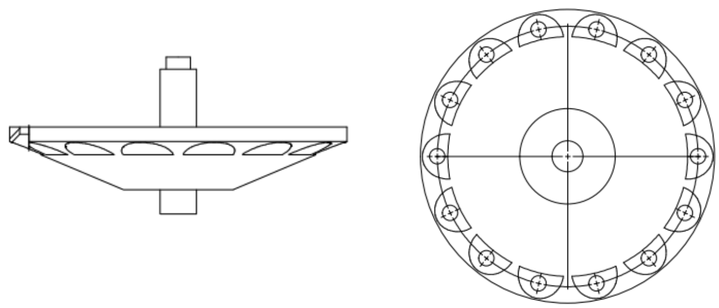

(a) Main view (b) Top view

Fig. 3 - Structure of inclined disc type row dial

The inclined disc seed platter requires that the seeds be treated before sowing, to pelletize the seeds, which enables different seeds to have similar physical properties. In the design of seed platter, the differences of seeds can be approximately ignored to obtain approximately stable seed flow, making the plant spacing more accurate. In this project, the inclined disc is used as the seeding mechanism as shown in Figure 3.The inclined disc design can make full use of the gravity of the seed itself to turn over the seeds to prevent too many seeds from entering a single mold control at the same time and causing the mold control to be blocked, and the inclined setting is also more conducive to cleaning out the seeds that have not been completely discharged from the seed platter.

2.2.3 Seeding opener

The function of the trencher in the design of the fertilizer seeder is to open the trenches before planting. The effect of trencher can indirectly determine the depth of seed row, so that the seeds can reach the predetermined depth, and then improve their survival rate.

The ditching parts shall meet the following requirements:

(1) After the furrow opener work, the shape of the ridge should be kept regular.

(2) Ditch opener should meet different agronomic requirements. For example, operation can be carried out under different row spacing.

(3) After opening the ditch, the bottom of the ditch is left with an appropriate amount of loose soil to facilitate the germination of seeds.

(4) The designed components should meet the characteristics of small working resistance and stable operation.

In the process of sowing in the field, the machine will affect the sowing effect due to the uneven field, so that the seeds cannot reach the predetermined depth. The copying mechanism can change with the change of terrain under the control of the limiting mechanism, and the seed ditch with a fixed depth can be changed within a certain range, so that the seed can have a fixed sowing depth in different operation requirements.

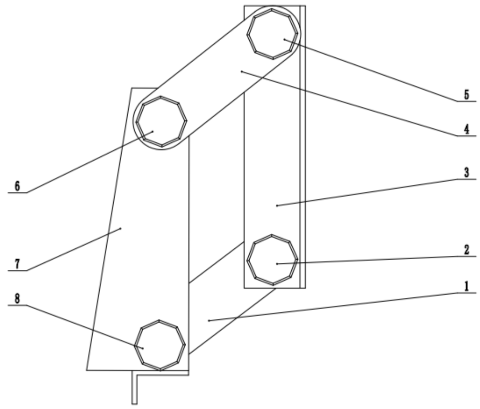

Fig. 4 - Profile mechanism

1, 4 pull rod; 2, 5, 6, 8 connecting pin; 3 mounting frame

Figure 4 shows the single profiling mechanism of the planter. This design adopts a single copying mechanism with slightly better copying effect. It can be known that the size of four connecting rods, traction angle, stiffness and strength of the mechanism will affect the effect of profiling *(Huang et al., 2014)*. The change of terrain will cause the change of support reaction force. In order to ensure the consistent sowing depth, pressure or tension spring should be added to make the copying mechanism always maintain the appropriate pressure on the ground.

Through comprehensive analysis of various data, it can be found that the average furrow depth obtained by using different forward speed and furrow opener is significantly different. Increasing the forward speed will affect the performance of the trencher and lead to an increase in the depth variation coefficient *(Tachibana et al., 2014)*. When the current feeding rate is 1.0 m/s, the actual average fertilization depth is approximated to the rated fertilization depth. The most uniform depth of the fertilizer can be obtained by using a hoe trencher at a forward speed of 1.2 m/s *(Tachibana et al., 2014)*. Therefore, we set the speed of the machine to be about 1.0-1.2 m/s.

2.3 Circuit control module

The online detection system of fertilizer application is mainly composed of capacitive fertilizer flow sensor, forward speed sensor and on-board terminal, as shown in Fig. 5.

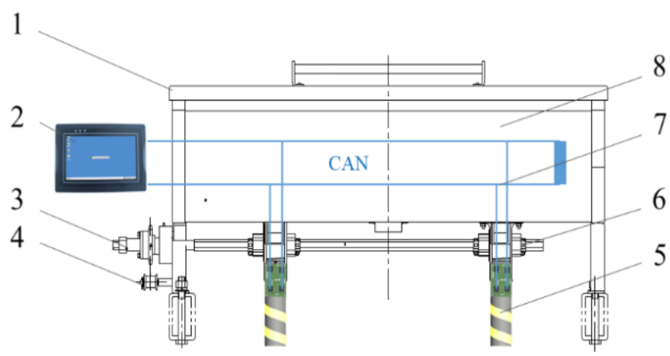

Fig.5- Schematic diagram of application rate detection system structure

1. Rack; 2. On-board display terminal; 3. Drive shaft; 4. Speed sensor; 5.Flow sensor; 6. Fertilizer discharge device; 7.CAN bus; 8. Fertilizer box

The system adopts CAN bus structure, which can realize distribution online detection of each fertilization pipeline and facilitate node expansion of fertilizer applicator with different width (*Marin et al., 2014*). The capacitive fertilizer flow sensor is installed on the fertilizer discharge pipe, which is mainly used to obtain the online mass flow of fertilizer. The forward speed sensor is located on the forward ground wheel, which is mainly used to obtain the forward speed of the machine and tools. The on-board terminal is located in the cab, which receives real-time information through the built-in CAN bus adaptation module, and displays the fertilizer application amount after processing the information (*Gângu et al., 2008*). In addition, the fertilizer flow sensor can judge the blocked state of the pipeline according to the state of fertilizer in the fertilizer pipe and display the alarm state through the alarm indicator light on the sensor.

2.3.1 Detection principle

When the fertilizer applicator operates normally, the fertilizer falls freely in the closed tube. The capacitive sensor is installed on the pipe wall. When fertilizer falls through the capacitor plate, the equivalent dielectric constant changes, causing the change of output capacitance parameters.

$$\Delta C = C - C_0 = \frac{s(\varepsilon_1 - \varepsilon_2)}{\rho_1 dV} m_1 \quad (3)$$

Where ΔC is the fertilizer through sensor capacitance variation, F; s is the plate area, m^2; ε_1 is the dielectric constant of fertilizer, F/m; ε_2 is the dielectric constant of air, F/m; ρ_1 is the density of fertilizer, kg/m^3; d is the plate spacing, m; V is the detection field volume between capacitance sensor plates, m^3; m_1 is the fertilizer quality in the sensor, kg.

It can be seen from Equation (3) that there is a linear relationship between the change of the output capacitance of the sensor and the quality of fertilizer in the testing site. Therefore, the on-line measurement of fertilizer mass flow rate can be realized by acquiring capacitance signal in real time. In addition, when the fertilizer pipe is blocked, the fertilizer in the sensor detection field will accumulate rapidly, the fertilizer quality will increase significantly, and the output capacitance of the sensor will increase sharply, so as to realize the monitoring and alarm of the obstruction fault of the fertilizer discharge pipeline.

2.3.2 Sensor detection circuit

Considering the influence of the detection accuracy, reliability and package size of the micro capacitor, the conditioning circuit of the fertilizer flow sensor was designed by using the capacitance digital conversion method. The capacitance digital conversion chip AD7746 and microcontroller STM32F103C8T6 were used to construct the micro capacitor signal measurement circuit (*Cay et al., 2018*).

MCU STM32F103C8T6, as the master control unit of the measuring node, is integrated with IIC and CAN transceiver module. It mainly completes the system configuration and initialization of the node, capacitance signal reading, preprocessing, alarm drive and data communication, etc. Among them, the microcontroller through the IIC interface and AD7746 data communication, in the completion of the AD7746 parameter setting, can read the converted capacitance information, and the signal pretreatment.

The AD7746 is a 24-bit capacitive digital converter with an operating voltage range of 2.7 to 5.25V.AD7746 internally mainly includes: modulator, voltage reference, excitation voltage source, digital/capacitor converter (CAPDAC), temperature sensor, digital filter, I2C bus interface. It includes two capacitive input channels that can be configured for single-ended input and differential input modes. Through the I2C interface, the configuration of AD7745 internal registers and the reading of internal conversion results can be realized. The AD7745 has a resolution of 4AF, an accuracy of 4FF, and a range of ±4pF.By setting the CAPDAC register with a range of 0~17pF, the range can be changed to CAPDAC±4pF with a sampling speed of 10~90Hz.The AD7745 can be directly connected to the capacitance sensor through a short wire to complete the capacitance measurement.

The sensor uses CAN bus for data interaction, and STM32F103C8T6 built-in CAN bus controller realizes the receiving and sending of CAN information through SN65HVD230 transceiver.SN65HVD230 is compatible with 3.3V voltage and its communication rate can reach 1M/s, which can meet the actual needs.

2.3.3 Signal acquisition and processing

The on-board terminal is the key part of the application amount detection system software operation. It receives the information of fertilizer flow rate and forward speed in real time, and calculates and processes the information. The terminal adopts the Atom motherboard based on X86 architecture as the core, integrates solid-state storage module, data communication module, liquid crystal display and input/output module, and obtains data on the bus in real time through the built-in USB-CAN communication adapter module.

Using Keil software development environment, the software of the lower microcontroller is written in C language. The software design adopts the modular programming method, and its functions mainly include system initialization, PCAP01 firmware writing CAN module initialization, capacitance data acquisition and preprocessing.

After the system is power-on, the SCM executes the initialization program to complete the configuration of each IO port, and then reads the firmware information of the internal EEPROM, and writes the SRAM area inside the PCAP01 through the SPI bus to enter the configuration state of PCAP01, where the sampling rate is configured at 10kHz and the blocking alarm threshold is 0.5pF.When the capacitance measurement is completed, the SCM reads the measurement result of PCAP01 and gets the capacitance information. On the one hand, the data is sent to the on-board terminal through CAN bus, and at the same time, the real-time capacitance is compared with the blocking threshold. Once the blocking threshold is exceeded, the SCM drives the corresponding IO port to make the alarm indicator light constantly on to realize the alarm.

RESULTS AND DISCUSSION

In order to test the accuracy of the fertilizer application rate detection system under the conditions of different fertilizer discharging speed, experiments were carried out in Shengfa Family Farm, Duanpolan Town, Qingdao City from September 18 to 20, 2020.Compound fertilizer, N-P_2O_5-K_2O, was used as experimental fertilizer ratio 24-14-9. Fertilizer particles are uniform without caking.

3.1 Experimental results of pipeline blocking alarm

A feeding box is placed at the fertilizer outlet of the measuring device, and the weighing method is adopted to calibrate the sensor. The rotation speed of fertilizer discharge shaft was set as 20r/min, and the rotation time of fertilizer discharge shaft was controlled by the upper computer respectively, and the difference of fertilizer discharge quality was realized according to the difference of running time. After each fertilizer discharge, an electronic balance (SL4001, Shanghai Minqiao Electronic Instrument Factory, 4000±0.1g) was used to measure the fertilizer quality in the receiving container, and at the same time, the cumulative capacitance value of the difference between the capacitance sensor and the reference capacitance sensor for each test was recorded. One calibration test was carried out for each fertilizer. Matlab software was used to process the calibration test data, and the response curve of fertilizer quality and capacitance value was obtained.

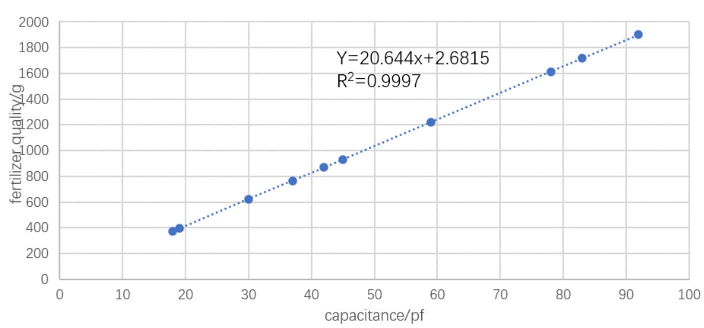

Fig. 6- Relation curve between capacitance sensor output and fertilizer quality

Figure 6 shows the signal response of the composite fertilizer after it passes through the improved sensor. As can be seen from the figure, when the fertilizer passes through the sensor, its capacitance value will change significantly, increasing from 8.75pF to 8.87pF.

The relationship model between capacitance and mass was obtained by linear fitting and normalization of the test data:

$$Q(t) = 20.644C(t) + 2.6815 \tag{4}$$

It can be seen that the capacitance output value of the granular fertilizer flow sensor has a linear relationship with the fertilizer quality. As the fertilizer quality increases, the capacitance output increases correspondingly. The determination coefficient of the model R^2=0.9997.

3.2 Analysis of fertilization effect results

During the experiment, the rotation speed of fertilizer discharge shaft was set between 25r/min and 35r/min, and fertilizers at the discharge hole were collected at the same time. The measured value of fertilizer application obtained by the detection system was compared with the actual weighing value of collected fertilizers, and the measured value was compared with the actual value. The results were shown in Table 3.

Table 3

Test results of fertilizer application rate detection system

Speed of fertilizer discharge shaft Rotation rate/ r/min	Measured value of fertilizer Measuringmass / g	Real quality Realmass /g	Error Relative error/ %
15	849.2919	864	1.70
	857.756	857	0.09
	345.5783	333	3.78
	643.2648	642	0.20
21	766.0966	776	1.28
	949.4153	961	1.21
	1424.021	1417	0.50
	1799.742	1786	0.77
27	1232.238	1231	0.10
	328.2374	327	0.38
	906.4758	913	0.71
	1919.064	1928	0.46
31	663.4959	650	2.08
	1223.774	1201	1.90
	2191.152	2157	1.58
	1901.723	1875	1.43

As can be seen from Table 3, the system can accurately measure the fertilizer application rate under the conditions of different fertilizer discharging speed, and the average measurement error is 1.13%, meeting the actual requirements.

CONCLUSIONS

1) The particle fertilizer detection technology for planters is proposed, which combines sensors and CAN bus. The planter is mainly composed of monitoring systems for seed metering, ditching and fertilizing, missed seeding, and leaking plugging by various institutions. It can realize four-row seeding operation at a speed of 8 km/h for continuous seeding and fertilization. It can complete the automatic monitoring of sowing and fertilization, and will send out an alarm to remind the staff when it is blocked.

2) This paper proposes a differential capacitive fertilizer flow sensor based on a ring pipe, and builds a micro-capacitance detection circuit composed of STM32F103C8T6 and PCAP01. The Fertilizer Application Rate Detection System based on Lab Windows/CVI was built to realize the on-line detection of fertilizer application.

3) According to the field test results, the maximum relative error of the missing seed rate is 3.75%. The accuracy of the fertilizer blockage alarm is reliable. Using this system can effectively monitor and control the quality of operations and reduce production costs.

ACKNOWLEDGEMENT

The work was sponsored by the National Key Research and Development Program of China Sub-project (2019YFB1312302) and Major Science and Technology Project (project number: 2018AA00404).

REFERENCES

[1] Bai H., Fang Z., Wang D., Yuan Y., Zhou L., Niu K. (2020). Design and test of comprehensive control system for corn planter sowing depth and compaction. *Journal of Agricultural Machinery*, 51(09): 61-72.

[2] Cay A., Kocabiyik H., May S., (2018), Development of an electro-mechanic control system for seed metering unit of single seed corn planters Part I: Design and laboratory simulation, *Computers and Electronics in Agriculture*，144, pp. 71-79;

[3] Chen Yan. (2017). Analysis on how to do a good job in the promotion of agricultural mechanization. *Friends of Farmers Getting Rich*. (6): 1.

[4] Gângu V., Cojocaru I., Marin E., Sorică C., Dobrin I., Prodan M., Jinga V., (2008), Innovative technologies for sowing and fertilizing weeding plants on ridges or directly in stubble field, *INMATEH -Agricultural Engineering*, Vol. 24, No. 1, pp. 13–22;
https://doi.org/10.1016/j.measurement.2019.05.059.

[5] Huang Xiang, Liu Haibin, Wang Ying, et al. (2014). Development of Fertilizer for Sugarcane Cultivation. *Agricultural Equipment & Vehicle Engineering*, 52(11):14-17.

[6] Jia Tiezhen. (2016). Research and design of variable fertilization operation control system. Hefei: University of Science and Technology of China. A dissertation for master's degree.1-49.

[7] Jin X., Chen K., Ji J., Pang J., Du X., Ma H. (2019). Intelligent vibration detection and control system of agricultural machinery engine. *Measurement*, 145:503-510.

[8] Jin X., Zhao K., Ji J., Du X., Ma H., Qiu Z. (2018). Design and implementation of Intelligent transplanting system based on photoelectric sensor and PLC. *Future Generation Computer Systems*, 88: p127-139.https://doi.org/10.1016/j.future.2018.05.034

[9] Marin E., Bolintineanu Gh., Sorică C., Manea D., Herak D., Croitoru Ş., Grigore I., (2014), Scientific researches on the qualitative working indexes of the sowing body of a modern technical equipment for sowing weeding plants, *INMATEH - Agricultural Engineering*, vol. 42 (1), pp. 19–26;

[10] Shi Yinyan, Chen Man, Wang Xiaochan, et al, (2017). Analysis and test of discharge performance of rice-wheat precise variable fertilizer application machine. *Transactions of the Chinese Society for Agricultural Machinery*, 48(7).97-103. DOI:10.6041/j.issn.1000-1298.2017.07.012

[11] Tachibana Yasuhiro, Kawaide Tetsuo, Shito Hirokatsu, Hirata Akira. (2014). Development of High-Speed Corn Planter Adaptable to No-tilled Fields. *Japanese Journal of Grassland Science*, 60(3). 200-205. DOI: 10.14941/grass.60.200

[12] Xiong S., Zhao B., Hu X., Li J., Zhou L., Fang X. (2020). Design and test of shrimp separation device. *Transactions of the Chinese Society of Agricultural Machinery*, 51(11): 357-365.DOI: 10.6041/j.issn.1000-1298.2020.11.039

[13] Zhang J C. (2013). Key technologies of variable fertilization system based on prescription chart. Harbin: Northeast Agricultural University.1-112

[14] Zhang Lan-zhen, Zhang Ling. (2011). 2cm-2 potato planter. *Mechanization of Rural Pastoral Areas*, (04):42-43.

[15] Zhang Xiaoli, Han Wei, Song Mingwei, et al. (2014). Design and experimental study of a new type weeding and fertilizing machine for middle row ploughing. *Journal of Gansu Agricultural University*, 49(03):162-164. DOI: 10.13432/j.cnki.jgsau.2014.03.029.

[16] Zhou L., Li S., Zhang X., Wang S., Yuan Y., Dong X. (2014). Cotton tube seed cotton mass flow detection based on capacitance method. *Transactions of the Chinese Society of Agricultural Machinery*, 45(06): 47-52. doi: 10.6041/ j.issn.1000-1298.2014.06.008

[17] Zhou L., Ma M., Yuan Y., Zhang J., Dong X., Wei C. (2017). Design and experiment of fertilizer quantity detection system based on capacitance method. *Transactions of the Chinese Society of Agricultural Engineering*, 2017, 33(24): 44-51. doi:10.11975/j.issn.1002-6819.2017.24.006

DIGITAL PUMPING UNIT WITH GEAR PUMPS USE TO PROVIDE THE FLOW REQUIRED FOR MOBILE EQUIPMENT WITH HIGH ENERGY EFFICIENCY
/
UNITATE DIGITALĂ DE POMPARE CU POMPE CU ROŢI DINŢATE UTILIZATĂ PENTRU FURNIZAREA DEBITULUI NECESAR ECHIPAMENTELOR MOBILE CU EFICIENŢĂ ENERGETICĂ MARE

Hristea Mihai Alexandru*[1]; Tudor Bogdan[1]; Radoi Radu[1]; Sefu Stefan Mihai [1]
Hydraulics and Pneumatics Research Institute INOE 2000-IHP / Romania
Tel: 021 3363991; E-mail: hristea.ihp@fluidas.ro
DOI: https://doi.org/10.35633/inmateh-64-28

Keywords: *Digital hydraulic, Gear pump, Digital pumping unit, Mobile equipment*

ABSTRACT
In this article, the authors want to present the benefits of digital hydraulics, by presenting a Digital Hydraulic Pumping System (DHPS), consisting of 4 fixed flow pumps, driven by a biaxial electric motor, 4 3/2 on/off electrohydraulic directional valve, 4/2 types electrohydraulic directional valve and a bidirectional hydraulic motor. With the help of a micro-controller, the 4 3/2 electrohydraulic directional valve, which independently control the output of each pump, are operated in a certain sequence, so that a regulation of the flow provided in the system in 15 discrete points is obtained. Due to the construction of the 3/2 electrohydraulic directional valve (electrohydraulic directional valve with port P to T), but also of the microcontroller, a variation of the flow supplied in the system with low energy losses is obtained. This system is designed within the digital hydraulics laboratory of the INOE 2000-IHP Research Institute, in order to obtain preliminary results, which will also lead to its physical realization. The article contains the results obtained by numerical simulation of using Digital fluid power technology in the field of hydraulic drives, systems which have advantages such as: the use of simple, robust components with a high degree of flexibility and programmability.

REZUMAT
În acest articol, autorii prezintă avantajele hidraulicii digitale, prin prezentarea unui sistem hidraulic de pompare, format din 4 pompe de capacitate fixa, antrenate de un motor electric biaxial cu turație constantă, 4 electrodistribuitoare 3/2 de tip on/off, un electrodistribuitoare de tip 4/2 și un motor hidraulic bidirecțional. Cu ajutorul unui micro-controler, cele 4 electrodistribuitoare 3/2, care controlează independent refularea fiecărei pompe, sunt acționate într-o anumită secvență, astfel încât se obține o reglare a debitului furnizat în sistem cu 15 valori discrete. Datorită construcției electrodistribuitoarelor 3/2 (distribuitoare cu portul P la T), dar și a microcontrolerului, se obține o modificare a debitului furnizat în sistem cu pierderi mici de energie. Acest sistem este proiectat în cadrul Laboratorului de hidraulică digitală al Institutului de cercetare INOE 2000-IHP, în vederea obținerii unor rezultate preliminarii, care vor conduce și la realizarea fizică a acestuia. Articolul cuprinde rezultatele obținute prin simulare numerică privind sistemele de pompare digitale în domeniul acționărilor hidraulice, sisteme care prezintă avantaje precum: utilizarea unor componente simple, robuste și cu un grad mare de flexibilitate și programabilitate.

INTRODUCTION
The development of electro-hydraulic servo-control components was based on a continuous improvement of their technical performances. The next stage of the hydraulics development process came with the introduction of microelectronics, making microprocessors and sensors integration in the hydraulic equipment, thus increasing the accuracy of dynamic control, feedback and reliability of the control unit *(Ioan et al. 2017).* At the beginning of the 21st century, increased production costs and the global context of reducing energy losses have forced industry and research teams to develop energy-efficient and reliable hydraulic components.

[1] *Hristea, Mihai Alexandru, Eng.; Tudor, Bogdan, Eng.; Radoi, Radu, PhD. Eng.; Sefu Stefan Mihai, Eng.*

In recent years, the main problem in the field of hydraulics has been how to reduce energy losses and reduce CO_2 emissions. Numerous studies conducted in recent years have shown that hydraulic systems are high energy consumers, resulting in almost 30% of its energy is dissipated in the form of heat *(Scheidl et al., 2013).* Generally, more than half of the output power of hydraulic pumps or motors is dissipated to spool valve or the pressure release valve.

With the introduction of "Industry 4.0" according to *Brandstetter et al., (2017),* the industrial system has put forward higher requirements for intelligent hydraulic systems and their applications. So, it can be said that if it is desired that the hydraulics survive after this market competition, the direction towards a high efficiency and low prices will be an inevitable direction to follow. Here digital hydraulics comes to provide a feasible way to achieve this goal (*Heitzig et al*, *2012).* An approach with a high potential for success has proven to use the concept of digital *hydraulics.*

The concept of digital hydraulics was theoretically presented many years in a row by renowned researchers such as Rudolf Scheidl, Matti Lindjama and others, but applied research could have begun a few years ago with the emergence of advances in electronics *(Qiwei et al., 2020, Viktor et al, 2020).*

According to *Scheidl et al*., (2012*)* the digital hydraulics it is superior over analog technology in areas as efficiency and standardization of components.

The concept of digital hydraulics is based on several principles *(Drumea et al, 2016):*

- Active control of system outputs;
- Use of on/off type directional valve;
- Smart control.

Digital hydraulics has a considerable advantage over the classic one in directions such as efficiency, redundancy, but also the standardization of components. Studies have shown that digital hydraulics can reduce energy loss compared to servo-control systems.

The authors simulated a drive diagram of a digital hydraulic pumping system for driving a rotary hydraulic motor. Having as possible applications: driving the drum of an elevator, a winch or a crane. The simulated scheme is composed of usual devices, unpretentious regarding the quality of the oil, these not needing a high degree of filtration unlike the proportional hydraulic devices. The system has a good energy efficiency due to the on / off valves that do not create hydraulic resistance when actuated. Reducing in this way the loss of energy transformed into heat (*Merill et al., 2011).*

The authors *Locateli et.al.*, *(2014)* approached a solution of this type for a hydraulic system with linear motor are presenting three operation methods (pump mode, motor mode and idle mode), which allows discrete valves to replace continuous or flow control valves in order to control the actuator. A variable displacement pump with large displacement is replaced by several small, fixed displacement units.

There are two independent methods for implementing DHPS, one of them is based on direct control of the pistons (in the case of radial hydraulic pumps or motors) or, as in our case, on a flow variation using the output control of fixed flow pumps *(Luke Wadsley, 2011).*

In this paper we approached the version with 4 pumps from which we can obtain 15 flow variations which was simulated with the help of the AMESim program, obtaining tables of flows, pressures and speeds of the hydraulic motor, showing in this way that the variable flow can be achieved with fixed pumps and low energy consumption.

MATERIALS AND METHODS

Parallel digital hydraulics involves the parallel connection of two or more hydraulic equipment and is based on a coding system, Pulse Code Modulation (PCM). PCM refers to the coding of equipment using either binary series, 2, 4, 8, 16… etc. practical 2^n, where "n" is the number of components that make up the system. *(Mantovani et al., 2020)*

Presentation of the system sketch

The hydraulic diagram of the DHPS (**D**igital **H**ydraulic **P**umping **S**ystem) is presented in figure 1, which is based of 4 pumps with fixed geometric displacement driven by an electric motor with constant speed of 1500 rpm. The pump geometric displacement is chosen in binary progression resulting as follows: P1 = 2 cm^3/rev, P2 = 4 cm^3/rev, P3 = 8 cm^3/rev, P4 = 16 cm^3/rev.

The total flow control can be performed for the version with 4 pumps in 15 stages, according to the binary progression. The total displacement of the pumps varies in multiples of 2 cm^3/rev and their capacity from 2 to 30 cm^3/rev. With the help of a controller, we can get 15 steps of flow values between 3 and 45 l/min with one step of 3 l/min. The flow in l/min results at a speed of the electric motor of 1500 rpm.

In the composition of the hydraulic diagram of DHPS we have: 4 pumps with fixed geometric displacement P1-P4, binary coded, DV1-DV4 on/off type electrohydraulic directional valves that control the output of each pump and which have the hydraulic scheme P to T on idle position, CV1-CV4 check valves, FM flow meter to be able to measure the flow resulting from DHPS, a PT pressure transducer, the HM hydraulic motor, a torque and speed transducer attached to the HM hydraulic motor shaft, the return filter F and the tank of hydraulic oil T. The command logic of the electrohydraulic directional valves for binary flow progression is performed by a controller. For such a pumping unit a PLC can be used or a dedicated controller can be developed with the help of a microcontroller.

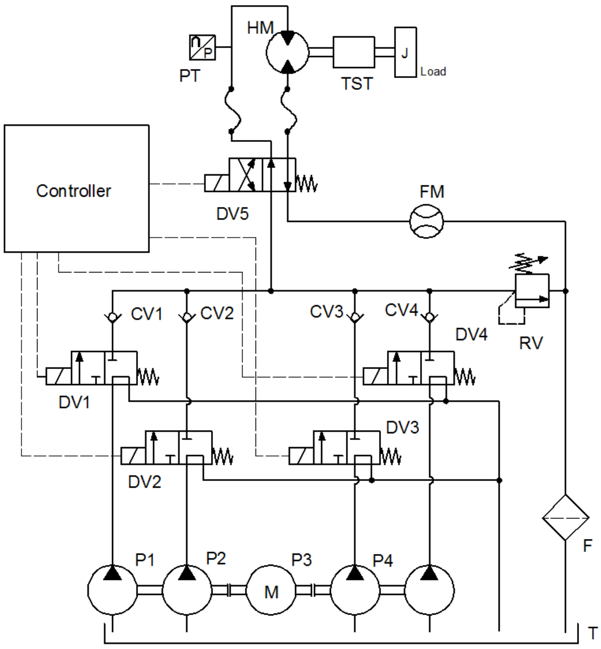

Fig. 1 - The hydraulic diagram of the pumping unit with 4 gear pumps

Modeling the drive system

The hydraulic circuit was modeled in AMESim. The hydraulic components have the sub-models in table 1 and the parameters value are shown in table 2.

Table 1

Component	Sub-model
Pump	PU001
Directional valve 3/2	HSV23_01
Directional valve 4/2	HSV24_01
Dynamic time table	SIGUDA01
Hydraulic motor	MO001
Pressure control	RV010

Table 2

Parametres		
Hydraulic Hose	**Directional valve (2/3)**	**Relief valve**
Pressure 1.013 bar	Flow rate 20 l/min	Cracking Pressure 250 bar
Diameter 10 mm	Pressure drop (ΔP) 5 bar	
Length 2,5 mm		
Hydraulic pipe	**Directional valve (2/4)**	**Hydraulic Motor**
Diameter 10 mm	Flow rate 50 l/min	Motor Displacement 30 cm^3/rev
Length 0.1 m	Pressure drop (ΔP) 5 bar	Coefficient of viscos friction 0.035 Nm/(rev/min)

The hydraulic pipes are modeled with the HL0000 sub-models, and the hoses are modeled with the HL0001R sub-model. The configured parameters for pipes and hoses are the nominal diameter and length. The system simulation sketch is presented in figure 2.

There are 4 directional valve 3/2 type that control the output of each pump and 4/2 types directional valve that controls the direction of rotation of the hydraulic motor. The electrohydraulic directional valves in the simulation have proportional valve sub-models, but in this case, they are controlled with maximum ON/OFF signal. Static models have been adopted for electrohydraulic directional valves. The system safety valve has been set to 250 bar.

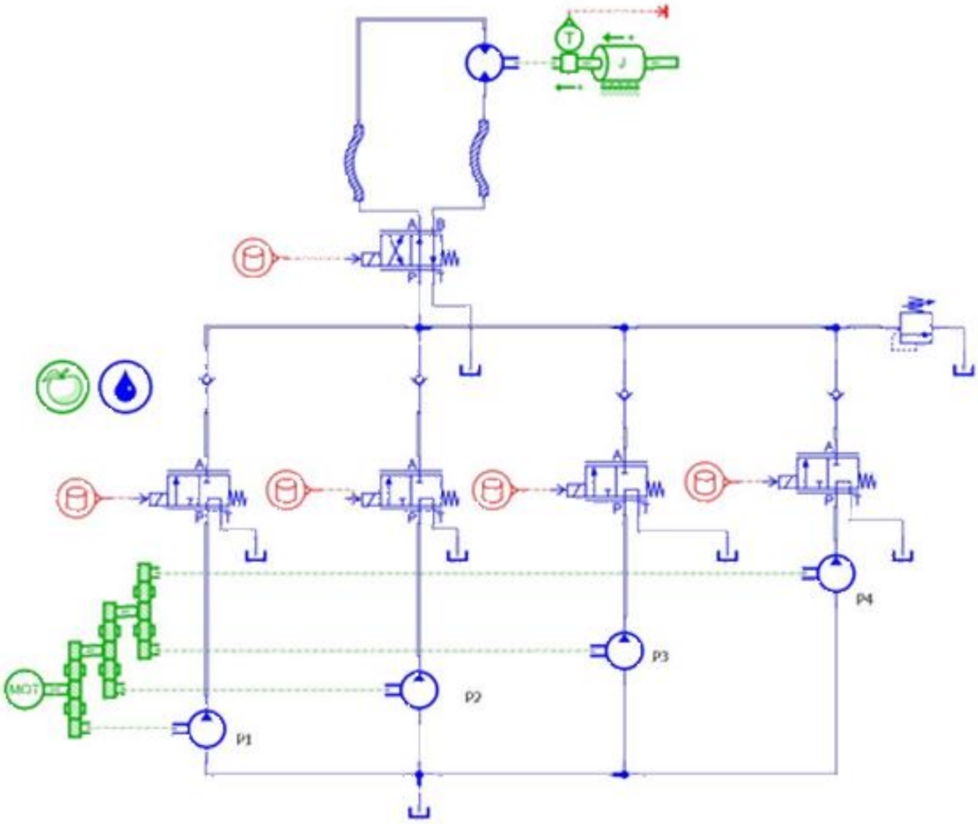

Fig. 2 - Simulation sketch

The bidirectional hydraulic motor with a geometric displacement of 30 cm^3/rev is connected with a friction centrifugal load. The sub-model for centrifugal friction load has as parameters the moment of inertia and a viscous friction coefficient.

Figure 3 shows the flows obtained and how they are obtained. The black hatched boxes represent the active pumps that send hydraulic fluid to the main line and the white boxes represent the pumps that send the hydraulic fluid to the tank with low energy losses. In the figure can be seen the status of the actuation signal for each directional valve connected one by one to the 4 pumps of the system.

Command step		OFF	1	2	3	4	5	6	7	8	9	10	11	12	13	14	15
P1	2 cc		■		■		■		■		■		■		■		■
P2	4 cc			■	■			■	■			■	■			■	■
P3	8 cc					■	■	■	■					■	■	■	■
P4	16 cc									■	■	■	■	■	■	■	■
Total Vg (cc)		0	2	4	6	8	10	12	14	16	18	20	22	24	26	28	30

Fig. 3 - Variation of the total capacity of the pumps (Vg) for the 15 stages

Table 3 contains the parameters for dynamic time table used to control the valves during the simulation.

Table 3

	Dynamic time table for P1 valve command		**Dynamic time table for P2 valve command**		**Dynamic time table for P3 valve command**		**Dynamic time table for P4 valve command**		**Dynamic time table for motor valve command**	
	X	**Y**	**X**	**Y**	**X**	**Y**	**X**	**Y**	**X**	**Y**
1	0	0	0	0	0	0	0	0	0	0
2	1	0	5	0	13	0	29	0	65	0
3	1.01	40	5.01	40	13.01	40	29.01	40	65.01	40
4	5	40	13	40	29	40	65	40	70	40
5	5.01	0	13.01	0	29.01	0	65.01	40		
6	9	0	21	0	45	0				
7	9.01	40	21.01	40	45.01	40				
8	13	40	29	40	65	40				
9	13.01	0	29.01	0						
10	17	0	37	0						
11	17.01	40	37.01	40						
12	21	40	45	40						
13	21.01	0	45.01	0						
14	25	0	53	0						
15	25.01	40	53.01	40						
16	29	40	65	40						
17	29.01	0								
18	33	0								
19	33.01	40								
20	37	40								
21	37.01	0								
22	41	0								
23	41.01	40								
24	45	40								
25	45.01	0								
26	49	0								
27	49.01	40								
28	53	40								
29	53.01	0								
30	57	0								
31	57.01	40								
32	61	40								
33	65	40								

Figure 4 shows the chart of time dynamics table for the control of the electrohydraulic directional valves that introduces in the circuit the P1 pump. The step of the control is at 4 s, and the total simulation time is 70 s. Each 3/2 directional valve is controlled by a dynamic time table sub-model according to the binary combination shown in figure 3.

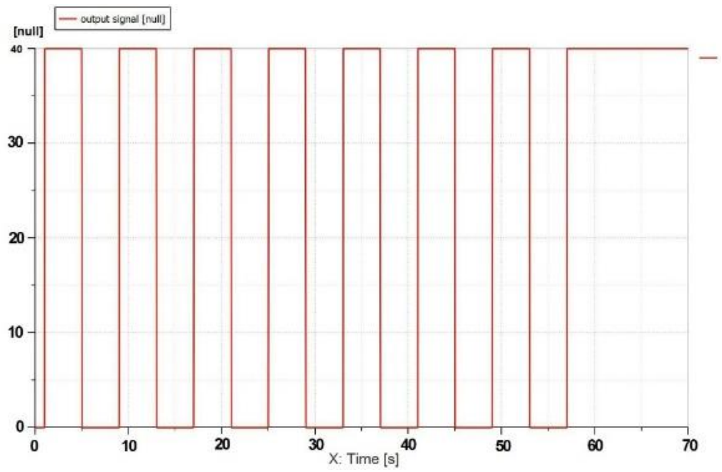

Fig. 4 - Command signal for directional valve of pump 1

In table 4 we can see the pumps that are operated, the resulting displacement, the flow provided in the system and the necessary power of the electric motor for each combination of pumps. For calculating the system flow and power in the table, the speed of the electric motor driving the pumps is 1500 rpm and the operating pressure is 315 bar.

Table 4

No.	Pump combination	Displacement [cm³/rev]				Total displacement [cm³/rev]	System flow [l/min]	Max power [kW]
		Vg4	Vg3	Vg2	Vg1			
1	Vg1				2	2	3	2
2	Vg2			4		4	6	4
3	Vg1+Vg2			4	2	6	9	6
4	Vg3		8			8	12	8
5	Vg3+Vg1		8		2	10	15	10
6	Vg3+Vg2		8	4		12	18	12
7	Vg3+Vg2+Vg1		8	4	2	14	21	14
8	Vg4	16				16	24	16
9	Vg4+Vg1	16			2	18	27	18
10	Vg4+Vg2	16		4		20	30	20
11	Vg4+Vg2+Vg1	16		4	2	22	33	22
12	Vg4+Vg3	16	8			24	36	24
13	Vg4+Vg3+Vg1	16	8		2	26	39	26
14	Vg4+Vg3+Vg2	16	8	4		28	42	28
15	Vg4+Vg3+Vg2+Vg1	16	8	4	2	30	45	30

RESULTS

The simulation results for the 4-pump digital system can be found in the following figures. The simulation consisted in obtaining the response for flow, pressure, motor speed and torque at the motor shaft by generating control signals so as to obtain the 15 combinations of pump displacement. The control steps occur at an interval of 4 sec. After reaching the maximum capacity, a reversal of the motor through the 4/2 electrohydraulic directional valve is also ordered.

Each command step is followed by pressure oscillations that are damped in ~ 2 sec, and the flow response oscillations are damped in about 1 sec. (fig. 5).

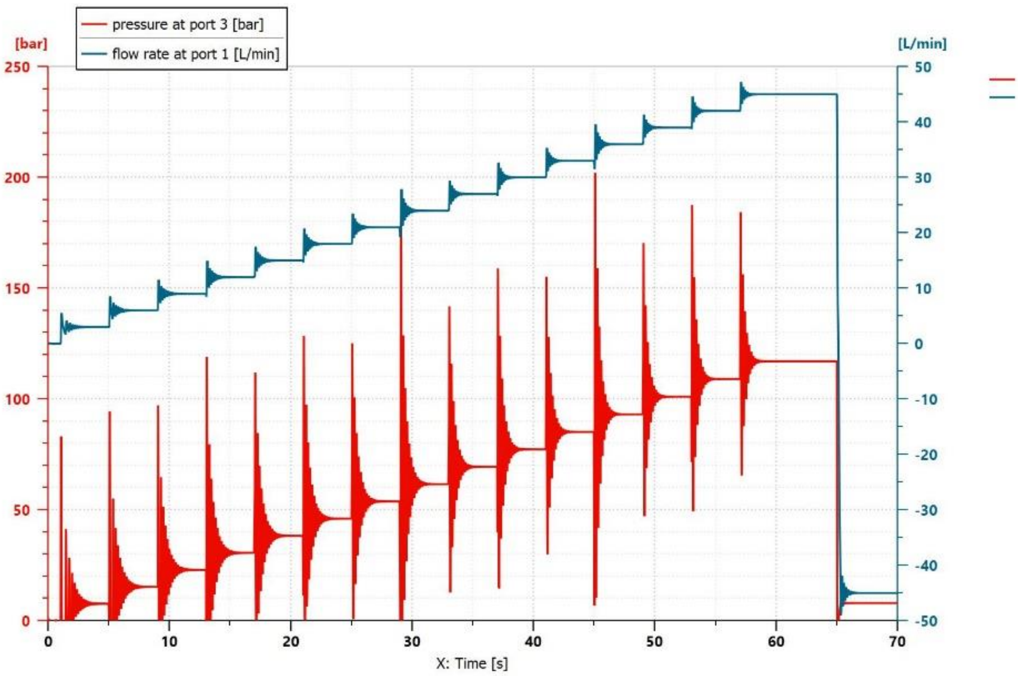

Fig. 5 - Pressure and flow rate at input port of the hydraulic motor

The speed and torque answers in fig. 6 follow the allure of the response diagrams for flow and pressure.

At the preliminary simulations the oscillations were even bigger, and for their reduction the length of the hoses to the hydraulic motor was increased from 1 m to 2.5 m.

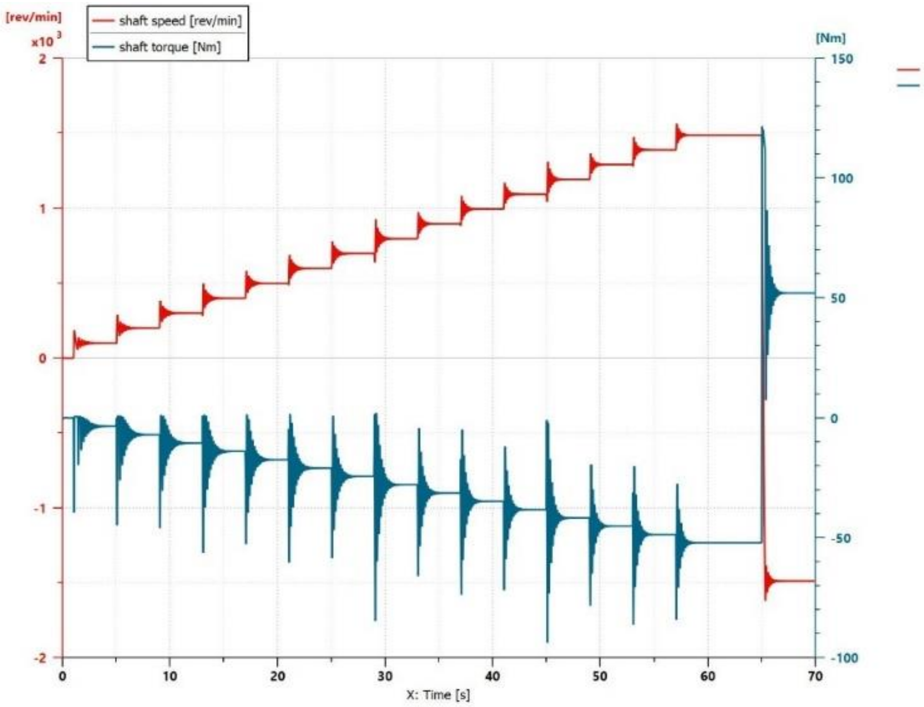

Fig. 6 - Hydraulic motor shaft speed and torque

CONCLUSIONS

- Following numerical simulations, a pressure variation could be observed at the moment of opening the electrohydraulic directional valve. In pressurized networks, static or dynamic events at a certain point affect all components of the system. Consequently, numerical simulation models must consider each pipe that is connected to a pressurized system.
- This pumping unit can be used to gradually adjust the speed of a linear or rotary hydraulic motor using a controller made with a microcontroller or an industrial PLC can be used.
- The DHPS cand be sucessfully used in aplications, where the flow control is needed.
- In a future work will be tried strategies to minimize or eliminate the amplitude and damping period of the pressure peaks, produced by switching the electrohydraulic directional valves.
- Based on the results obtained from these simulations, an experimental test stand for such equipment will be built.

ACKNOWLEDGEMENT

This paper has been funded by the Romanian Ministry of Research and Innovation under NUCLEU Programme, Financial Agreement no. 18N/2019, Ad 11/2020, Project code PN 19-18.01.01, Phase 17 "Comparative study of energy losses between current hydraulic systems, with classical and proportional equipment, and digital hydraulic systems". European funding has also been granted, under Competitiveness Operational Programme POC 2014-2020, call POC-A1-A.1.1.3-H-2016, Financial agreement no. 253/02.06.2020, signed between INOE 2000 and the Ministry of Education and Research for the project titled "Horizon 2020 Support Center for European project management and European promotion PREPARE", MYSMIS2014 code 107874.

REFERENCES

[1] Brandstetter R., Deubel T., Scheidl R., Winkler B., Zeman K. (2017). Digital hydraulics and "Industrie 4.0" https://doi.org/10.1177/0959651816636734.

[2] Drumea Petrin, Radu Rădoi, Bogdan Tudor and Ilare Bordeașu (2016). Digital Hydraulics Solutions. *Hervex International Conference on Hydraulics and Pneumatics,* Romania.

[3] Donkov V.H., Andersen Ole Torben, Linjama Matti, Ebbesen Morten Kjeld (2020) Digital Hydraulic Technology for Linear Actuation: A State of the Art Review. *International Journal of Fluid Power*, Vol. 21 Iss https://doi.org/10.13052/ijfp1439-9776.2125

[4] Heitzig S.; Sgro S.; Theissen H. (2012). Energy efficiency of hydraulic systems with shared digital pumps. *International Journal of Fluid Power*, Vol.13, pp.49-58.

[5] Locateli C.C., Teixeira P.L., Edson Roberto De Pieri et al. (2014). Digital Hydraulic System using pumps and on/off valves controlling the actuator. *Proceedings of the 8th FPNI PH. D Symposium on fluid power*, Article Number: V001T01A009, Published: 201 .

[6] Luke Wadsley, (2011). Optimal System Solutions Enabled by Digital Pumps *The 52nd National Conference on Fluid Power, Las Vegas*, pp.7-13.

[7] Mantovani I.J., Kagueiama H.A., Gama A.T.D.C., Dell' Amico A., Krus P., & De Negri V.J. (2020) "On/Off Valves Synchronization and Reliability Evaluation of a Digital Hydraulic Actuator." *Proceedings of the BATH/ASME 2020 Symposium on Fluid Power and Motion Control*. *BATH/ASME 2020 Symposium on Fluid Power and Motion Control*. Virtual, online. September 9–11. V001T01A041. ASME. https://doi.org/10.1115/FPMC2020-2778

[8] Merrill K.; Lumkes J.; Holland M. (2011). Analysis of Digital Pump/Motor Operation Strategies. *Proceedings of the 52nd National Conference on Fluid Power, Las Vegas, …………….*

[9] Pavel I., Rădoi R. I., Chiriță Al. P., Hristea M. Al., Tudor B. Al., (2017). Technical Solutions for Digital Hydraulic Cylinders and Test Methods (Solutii tehnice si metode de testare ca cilindrilor hidraulici digitali)*, HIDRAULICA, Magazine of Hydraulics, Pneumatics, Tribology, Ecology, Sensorics, Mechatronics*, No. 3, pp 41-49.

[10] Qiwei Zhang, Xiangdong Kong, Bin Yu, Kaixian Ba, Zhengguo Jin, Yan Kang (2020). Review and Development Trend of Digital Hydraulic Technology. *Novel Industry 4.0 Technologies and Applications*, Vol.10(2), p.579. https://doi.org/10.3390/app10020579

[11] Scheidl R., Linjama M., Schmidt S. (2012). Is the future of fluid power digital? *Proceedings of the Institution of Mechanical Engineers,* Part I: Journal of Systems and Control Engineering, Vol.226 (6), pp. 721-723.

[12] Scheidl R., Kogler H., Winkler B. (2013). Hydraulic switching control–objectives, concepts, challenges and potential applications. *HIDRAULICA Magazine of Hydraulics, Pneumatics, Tribology, Ecology, Sensorics, Mechatronics*, No.1, pp. 7-18.

RESEARCH ON OPTIMIZATION OF AGRICULTURAL MACHINERY FAULT MONITORING SYSTEM BASED ON ARTIFICIAL NEURAL NETWORK ALGORITHM
/
基于人工神经网络算法的农业机械视频监控体系优化研究

Jiaxin Zheng[1,2,3], Mei Li[1)], Shikang Hu[1,2)], Xuwen Xiao[1)], Hao Li[1)], Wenfeng Li * [1,2)]

[1)] Engineering Centre of Yunnan Colleges and Universities for Plateau Characteristic Modern Agricultural Equipment, Yunnan Agricultural University, Kunming / China

[2)] The Key Laboratory for Crop Production and Smart Agriculture of Yunnan Province, Yunnan Agricultural University, Kunming / China

[3)] Yunnan Plateau Characteristic Agricultural Industry Research Institute, Kunming, 650201 / China

*Corresponding authors: Dr. Wenfeng Li *E-mail: owml96699665fang@163.com*

DOI: https://doi.org/10.356.33/inmateh-64-29

Keywords: *agricultural machinery, video surveillance, neural network*

ABSTRACT

Aiming at the demand of mileage statistics, work area statistics, fault site return and related data automatic retention in the current agricultural machinery reliability appraisal process, the optimization of agricultural machinery video monitoring system based on artificial neural network algorithm was studied. Together with the new video monitoring technology, the agricultural machinery GPS, GSM and fuel consumption recorder technology are combined to realize the functions of real-time data transmission, monitoring, analysis and statistics. Aiming at intelligent fault analysis, a real-time online detection mechanism is proposed, and a cloud collaborative detection mechanism is proposed to solve the problem of inaccurate offline model detection. Use plane map or satellite map to browse. Thus, an online monitoring and visual testing platform for agricultural machinery faults without real-time monitoring records is established. Finally, the test platform is tested and applied. Test results show that the algorithm can greatly shorten the training time and improve the accuracy of training model detection. With the increase of online training iterations, it is helpful to improve the detection accuracy of the generated model. In a word, the system service platform can provide scientific and transparent data for agricultural machinery fault identification, ensure the scientific, open and fair principles of agricultural machinery fault identification, and greatly improve the efficiency of agricultural machinery management.

摘要

针对当前农机可靠性鉴定过程中里程统计、工区统计、故障点返回及相关数据自动保存的需求，研究了基于人工神经网络算法的农机视频监控系统的优化。结合新的视频监控技术，将农机 GPS、GSM 和油耗记录仪技术相结合，实现实时数据传输、监控、分析、统计等功能。针对智能故障分析，提出了实时在线检测机制，并针对离线模型检测不准确的问题，提出了云协同检测机制。使用平面地图或卫星地图浏览。建立了无实时监测记录的农机故障在线监测与可视化测试平台。最后，对测试平台进行了测试和应用。实验结果表明，该算法可以大大缩短训练时间，提高训练模型检测的准确性。随着在线训练迭代次数的增加，有助于提高生成模型的检测精度。总之，该系统服务平台可以为农机故障识别提供科学、透明的数据，保证农机故障识别的科学、公开、公平原则，大大提高农机管理效率。

INTRODUCTION

In recent years, our country has paid more attention to the research and development of new agricultural machinery technologies and tools. It is easy to identify whether the performance and economic indicators of newly designed agricultural machinery meet the design requirements, but it is difficult to evaluate whether its reliability meets the requirements *(Bajaj J. et al., 2020)*. With the dramatic increase of video data generated by camera equipment, how to deal with these data has become a thorny problem. In the process of agricultural machinery work, the traditional video surveillance needs supervisors to pay attention to the front surveillance picture all the time, but it is limited by human physiology. The supervisors cannot concentrate on the picture all the time. It is very easy to omit important monitoring information and cannot accurately obtain sensitive information *(Caixal G. et al., 2021)*.

The number of channels of monitoring equipment is proportional to the number of monitors needed. While the number of video channels increases, it needs to increase the huge human cost. In addition, in order to understand the occurrence process of the event after the monitor omitted some important real-time images, it is necessary to filter and interpret the massive video data manually. In this process, it also requires a lot of physical work and time *(Gandjbakhch E. et al., 2020)*. From this, we can see that the traditional video surveillance equipment only has the function of video playback and storage, and does not have the ability of video analysis and processing. In the process of using, it needs a lot of manpower and material resources, and pays a great cost. It has been difficult to meet the needs of modern society for security equipment. In this context, people pay more and more attention to the active security system equipment based on intelligent video surveillance *(Hassan M. M. et al., 2020)*.

Combining with the transcoding process of video stream, three schemes of capturing video frames from video stream are proposed, and the capturing time of three schemes is compared. The experimental results of three schemes are given under the multi-channel fast detection mechanism. Based on the artificial neural network algorithm, the process and principle of cloud cooperative detection mechanism are elaborated in detail. The pedestrian detection technology of HOG + SVM is analysed. The principle and process of off-line learning and on-line learning of agricultural machinery are introduced. Finally, the experiment verifies that the model learning efficiency is higher and the model detection effect is better by using the cooperative detection mechanism of agricultural machinery cloud.

The innovation of the research is to build an efficient video stream transponder for agricultural machinery and a platform for intelligent detection. It provides an application interface for other video surveillance processing algorithm models, facilitates the combination of machine learning model and video server, and improves the accuracy of the model through manual feedback and online incremental training. At the same time, while reducing the cost of manpower and material resources brought by agricultural machinery monitoring system, it also improves the monitoring efficiency of the monitoring system, and lays the foundation for the construction of an active monitoring mode which integrates pre-prevention, real-time response and assistant decision-making.

The optimization of agricultural machinery video surveillance system is studied based on artificial neural network algorithm. Based on the artificial neural network (ANN) algorithm, three schemes of capturing video frames from video streams are proposed. Then the proposed method is simulated on VS2010 IDE. The results of traditional SVM training model and incremental SVM training model are compared. The experimental results show the superiority of the design system.

Kariki O et al.'s research shows that during the actual use of agricultural machinery, if there is a certain deviation between the actual construction state and the original design state, a failure will occur, and the entire machine cannot continue to work or some functions cannot be realized. This will affect its actual production to a certain extent *(Kariki O. et al., 2020)*. However, in the process of actual work, it is inevitable that certain wear and circuit problems will occur between the machines. The long-term component friction will cause the gap and position between the different components to be misaligned, resulting in the fact that the machine cannot be used normally. *Kayraklioglu E et al.* pointed out that according to the current actual use of agricultural machinery, the most common failure causes in the current use of common agricultural machinery are: illegal work by operators, wear and tear of mechanical parts, corrosion and aging, and wear of parts, and electrical fault lights of agricultural machinery *(Kayraklioglu E et al., 2021)*. *Luz E et al.* introduced intelligent algorithm into equipment management of production workshop. Infrared monitoring system was installed to effectively supervise the use status and lease of equipment. Good results were achieved and work efficiency was greatly improved. *(Luz E. et al. 2021)*. *Mohibi S. et al.* pointed out that although video surveillance technology has made great progress, there are still many defects in traditional closed-circuit video surveillance system and digital surveillance system. The most notable one is that many incidents occur in video pictures, which require people to review videos afterwards, investigate and collect evidence, make detailed judgments, and fail to give full play to the initiative of video surveillance *(Mohibi S. et al., 2020)*. Pesut B. pointed out that intelligent video surveillance system, as a higher-end video surveillance application, can solve a series of problems such as management, forensics and so on. It combines machine vision algorithm with traditional video surveillance system by virtue of computer's powerful computing ability and data processing ability, thus improving the intelligent processing ability of surveillance system *(Pesut B et al., 2020)*. Pi J. et al. pointed out that in the development of agricultural remote monitoring; video technology plays a direct role in determining the quality of monitoring.

Applying Internet of Things technology to it can effectively improve the efficiency of video technology *(Pi J. et al., 2021)*. *Provvidenza C et al*. applied video surveillance coefficients to the supervision of factory robots. The application of far infrared technology can play a good supervisory role for robots within 100 meters from the camera, which is a breakthrough in the application of video surveillance in production *(Provvidenza C. et al., 2020)*. *Romney W et al*. pointed out that although the current video surveillance technology has made some progress, it is easy to be affected by the changes of the environment in the process of outdoor surveillance, applying wireless sensor technology to it, effectively reducing the impact of the surrounding environment on the quality of video surveillance *(Romney W. et al., 2020)*.

From this point of view, scholars have rich research on video surveillance, the development of video surveillance provides great convenience to people, and there is an urgent need for its development. However, the current research on video surveillance of agricultural machinery is still less, there is a certain theoretical blank, so based on the previous research, this paper studies it.

MATERIALS AND METHODS

Collaborative detection mechanism

Neural network is an operation model, which consists of a large number of nodes (or neurons) connected with each other. Each node represents a specific output function, called an excitation function. The connection between two nodes represents a weighted value for the signal passing through the connection, which is called the weight, which is equivalent to the memory of the artificial neural network. Based on the artificial neural network, the pedestrian detection algorithm is implemented in the system, which enables the camera to detect pedestrians or vehicles in the real-time video stream acquired in the deployment area. The accuracy and robustness of the detection algorithm are the bottlenecks restricting the overall performance of the system *(Shankar K. et al., 2020)*. To get rid of this bottleneck, cloud-based collaborative detection mechanism is adopted. As shown in Figure 1:

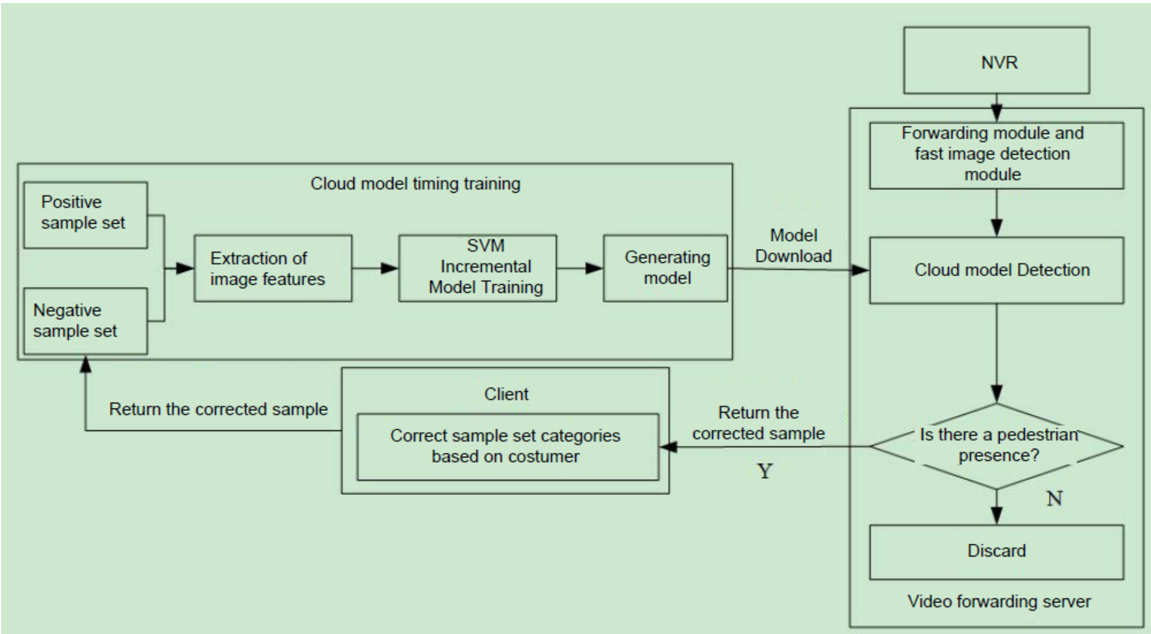

Fig. 1 - Flow chart of collaborative detection mechanism

When the video server starts to run, it will open the same number of video stream forwarding sub-threads according to the number of channels applied by the client. At the same time, the video server will also apply the corresponding sub-threads to capture the key frames in the buffer quickly by using the optimal scheme, and use the key frames as the effective pictures of the video to analyse whether there are any abnormalities. In this mechanism, the detection sub-threads and the completion of video stream forwarding sub-threads are independent of each other *(Warner E. et al., 2020)*. After the video server finishes capturing the video frames with potential abnormal behaviour, it extracts the features of the video frames by using the directional gradient histogram (HOG), extracts the video frames to be detected into vectors, and then detects them with the off-line training model, and sends the results to the client.

If the test result is abnormal, the client will remind and send the abnormal image to the customer, so that the customer can browse the abnormal conditions in the monitoring area. If the detection result is not abnormal, the detected image will be discarded. After the detection sub-thread completes these tasks, it will detect the image in the next detection time according to the response of the timer *(Zhao J. et al., 2020)*. The abnormal image sent to the client will be correctly labelled after the client has finished viewing, and then sent to the cloud server to update the sample set deployed on the server side. In this way, the sample set of the model will be continuously revised. After the change of the sample set, the mechanism will be applied to conceptual application of online learning. The server will train the existing model incrementally and regularly, and the completed model will be applied to the secondary detection of the video server. Through this model updating method, the accuracy and robustness of the system in specific scenarios can be improved.

The training process of the model is shown in the following figure: Firstly, the training sample is tailored to a suitable size, and the image is selected by directional gradient histogram (HOG). When feature selection is carried out, the detection sub-parameter file is generated according to the specific sample set, and the trained model is saved locally. According to the HOG feature extraction process, every picture in the sample set is extracted into one-dimensional vector. All the vectors generated by the image will participate in the training of SVM. Before the training of SVM, the corresponding parameters will be selected according to the actual needs. After setting the parameters, the training of SVM model will begin. The function flow chart of offline training module 2 shows:

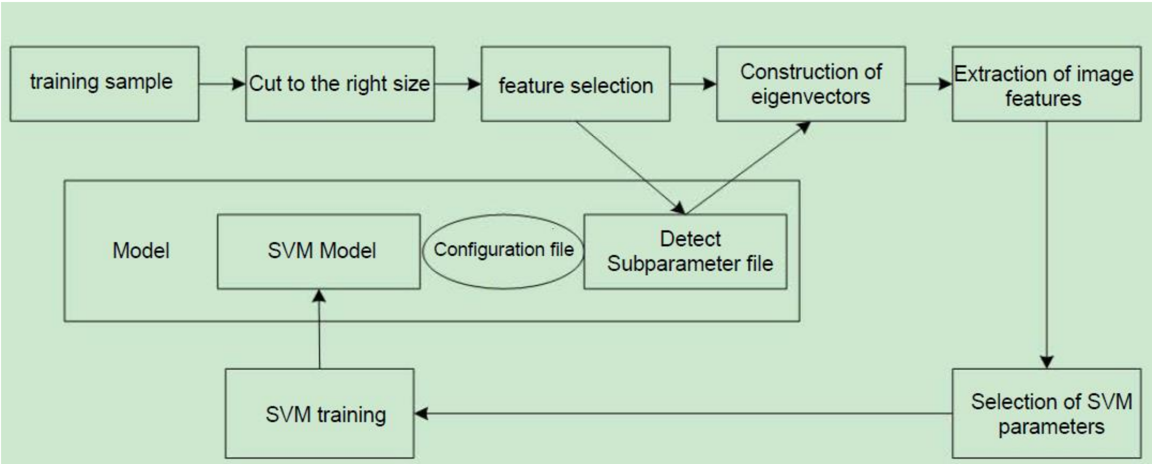

Fig. 2 - Flow chart of offline training module

The concept of online learning belongs to the category of incremental learning. The basic idea of online learning is to make the model perceive the environmental changes of the equipment deployment area by learning the image features of the new samples, to solve the disadvantage of the previous system algorithm model which is too single, and to improve the accuracy and robustness of the algorithm. Online learning is very suitable for the iterative updating of models in the case of continuous sample growth. Nowadays, most enterprises are applying off-line trained models and deploying them to predict or classify on-line. The model trains and learns the newly added data online. Only after collecting these new data in the background, the model integrates the new data with the original data before training. Compared with the incremental training method, this method not only wastes the storage space of the machine, but also wastes a lot of training time.

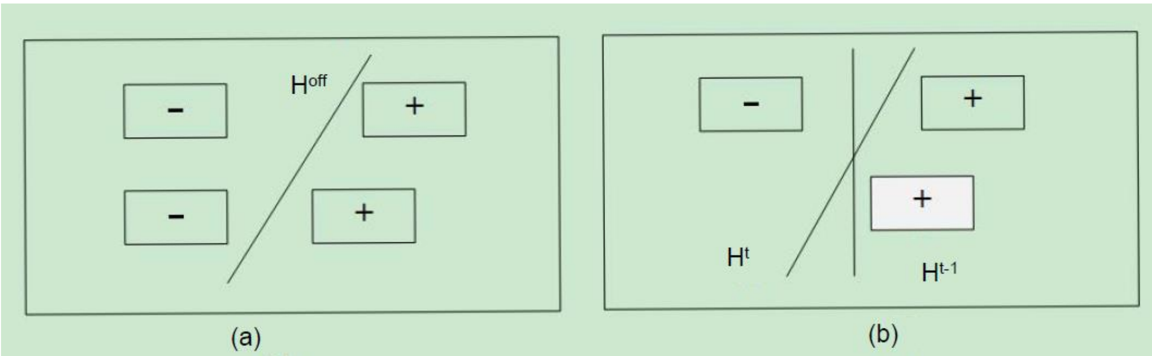

Fig. 3 - Principles of offline and online learning

The online learning process is shown in Figure 3. A chart shows the offline learning process and b chart shows the online learning process. The dotted line represents the initial classifier, in which the blue box represents the newly added samples for online learning. The newly added samples can be seen from the graph, and the classifier can be updated in real time. This process simulates the self-learning process of human beings and updates the decision-making power by constantly recognizing new things. In the online learning stage of the system, the video server sends the detected image to the client for alarm broadcasting. The client user determines the result. If the server judges the image without pedestrians as having pedestrians, then the client marks the image as a negative sample and sends it to the cloud server. When the cloud model is trained again, the information of the new sample set can be learned, and the pedestrian detection effect of the model under this background can be enhanced in continuous learning.

The online learning process is shown in Figure 4.

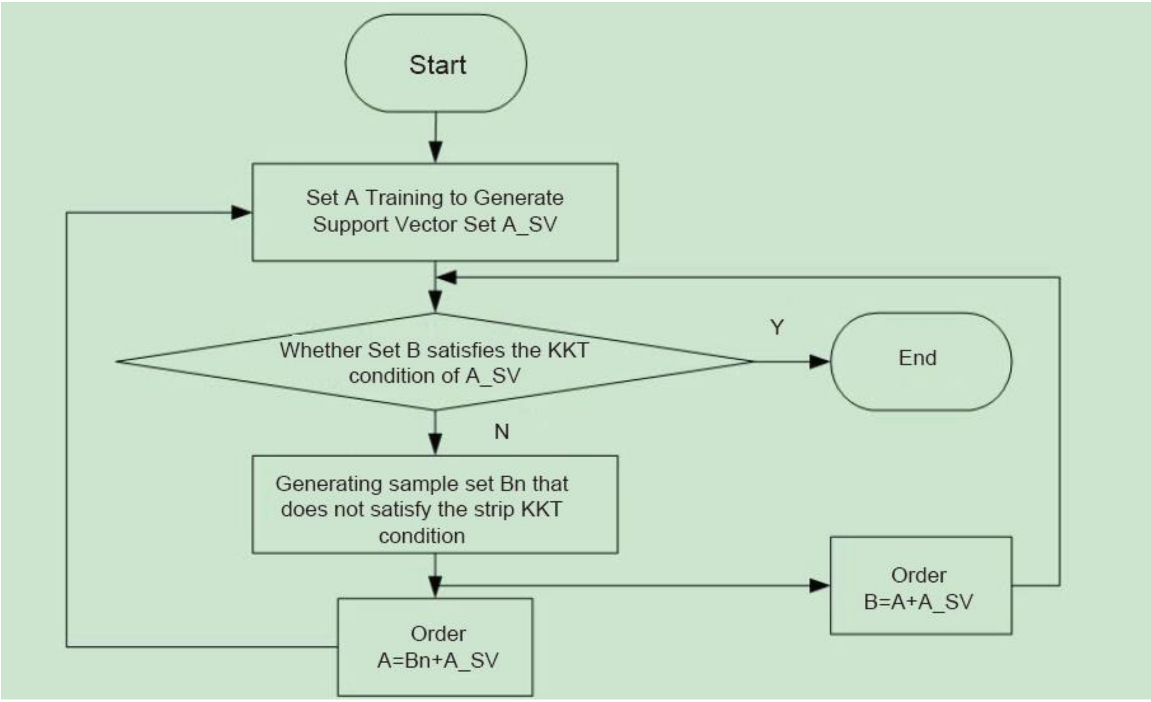

Fig. 4 - Incremental learning flow chart

The sample set of offline learning is A, the newly added sample set is B, the classifier trained by A is PA, and the support vector set of PA is SA_SV. The A_SV set satisfies the KKT condition. Sample B is validated according to the original KKT condition, and then the sample set B is divided into two categories according to satisfying KKT condition and not satisfying KKT condition, namely By and Bn; if Bn is empty, it ends. Otherwise, the union of A_SV and Bn is trained as a new training set, so that new model and new support vector set can be obtained; A_A_SV in A set is removed, and the remaining sample set in A is taken as a new sample set B1, so that B1 set is assigned to B, repeating the above steps; and the final result can be obtained by iterative training.

HOG Image feature extraction algorithms

Histogram of Oriented Gradients (HOG) is a feature composed of the gradient direction of the local area of a statistical image, which is often used in object detection in computer vision and image processing. Compared with other features, HOG has many advantages. Firstly, HOG operates on the local square of the image and keeps good invariance to the geometric and optical deformation of the image. Secondly, pedestrians are allowed to take some minor actions under the conditions of spatial and directional sampling and normalization, without affecting the detection effect. In an image, the shape of the local object can be described by the gradient statistical information, so each image is extracted by HOG, and the gradient statistical information is represented by the generated vector. The process of HOG feature extraction is shown in Fig. 5. Firstly, the image is regarded as a three-dimensional image of x, y and z, and then the contrast of the image is adjusted by standardizing the colour space of the image with Gamma correction method, so as to reduce the influence of local shadows and changes of the image, and also to suppress noise interference.

The normalization formula is as follows:

$$I(x,y) = I(x,y)^{Gamma}, Gamma take 1/2 \tag{1}$$

In order to capture the contour information of the image and further weaken the interference of care, the gradient of each pixel is calculated. Among them, the gradient has a direction, and the calculation formula is as follows:

$$\begin{aligned} G_x(x,y) &= H(x+1,y) - H(x-1,y) \\ G_y(x,y) &= H(x,y+1) - H(x,y-1) \end{aligned} \tag{2}$$

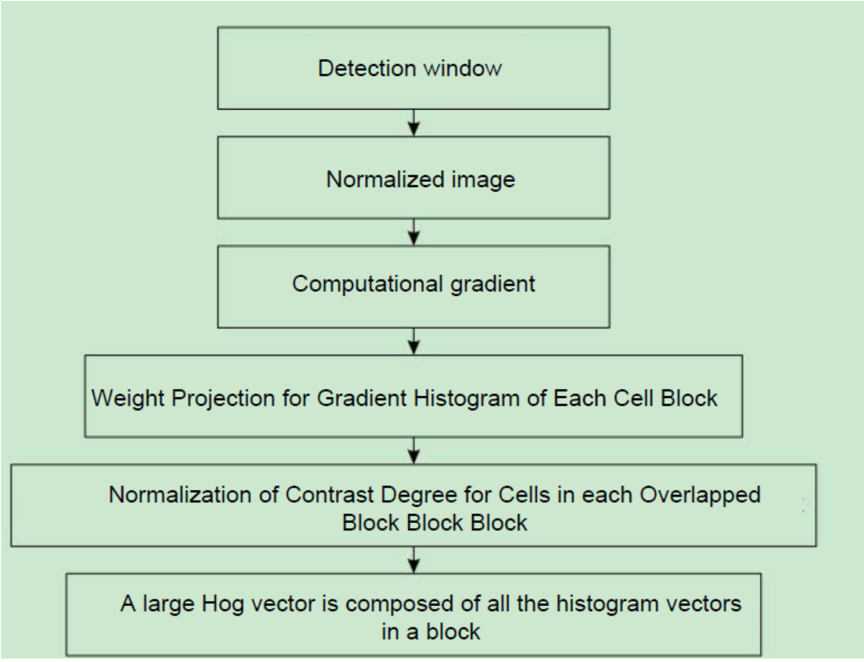

Fig. 5 - Flow chart of HOG feature extraction

Among them, $G_x(x,y)$ is the gradient of the pixels in the horizontal direction, $G_y(x,y)$ is the gradient of the pixels in the vertical direction. The formulas for calculating the gradient amplitude in the horizontal and vertical directions are as follows:

$$G(x,y) = \sqrt{G_x(x,y)^2 + G_y(x,y)^2} \tag{3}$$

$$\alpha(x,y) = \tan^{-1}\left(\frac{G_y(x,y)}{G_x(x,y)}\right) \tag{4}$$

Then the image is divided into small Cells (usually 6 x 6 pixels are a Cell); then the gradient histogram of each Cell under different gradient numbers is counted, i.e. the feature descriptor of each Cell is extracted; the fifth step is to make every three Cells into a block, and then connect the three Cell feature descriptors in series to get the block's feature descriptor. Then the HOG feature descriptors of all blocks in this graph can be connected in series to get the HOG feature of the target to be detected, which is the HOG feature vector to be extracted.

Neural network algorithms

For multi-layer artificial neural network, the interconnection mode formed by interconnection of many processing units in the neural network reflects the structure of the neural network, which determines the ability of the network. The stable structure of the nervous system stipulates and restricts the nature and information processing ability of the neural network, and limits the scope of the ability of the neural network system. At present, the structure of multi-layer neural network has been widely used because of its good performance, and the typical one is back propagation neural network (BP model).

In this kind of neural network model, the middle hidden neuron layer is introduced, so the standard BP model is composed of three neuron layers, the bottom layer is the input layer, the middle layer is the hidden layer, and the top layer is the output layer. There is a complete interconnection between neurons at all levels, and there is no connection between neurons at all levels, as shown in Figure 6.

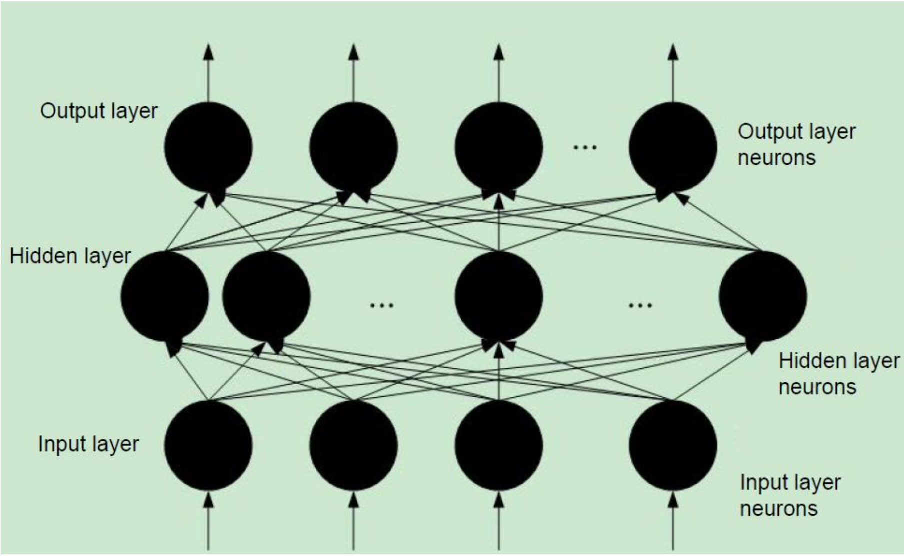

Fig. 6 - The structure of artificial neural network

The forward propagation of information and the reverse propagation of error constitute the core content of the learning process of BP model. The forward propagation here refers to the input data sample entering the network from the input layer, and then being processed by the weighted and hidden layer, the information is transmitted to the output layer for output. If the actual output information of the output layer does not match the desired output information, the learning and training process will turn to the back propagation stage of error information. In fact, the back propagation of errors is to transmit output errors in some form from hidden layer to input layer by layer, and distribute the error information to the neuron units of each layer network, and then obtain the feedback error information of each layer neuron, which can be used as the basic basis for correcting the weights of each unit. The process of information forward propagation and error back propagation as mentioned above and the process of adjusting the weights of each layer are carried out repeatedly in the learning and training stage. In summary, the continuous adjustment process of the weights between the layers has promoted the systematic training process, and finally the error of the network output falls within the allowable error range or meets other preset conditions, thus completing the training and learning process of network.

RESULS

Experimental environment

This experiment is simulated on VS2010 IDE. By comparing the effect of traditional SVM training model and incremental SVM training model, the performance of incremental SVM training results on pedestrian detection is verified, and it is suitable for use in the system. In this experiment, firstly, based on the off-line training model, its support vector set sets SA_SV, and then in the process of system operation, the image of the current person in the picture is captured, as a new sample B. For a 64*128 image, the practical process of extracting HOG features includes the following steps: after completing the above process, a 16*16-pixel block and an 8*8-pixel cell are set up in the 64*128 image window. Each block has four cells, and the number of gradient directions is bins=9. In each cell, the gradient directions of all pixels are histogram counted and a 9-dimensional feature vector is obtained. In this way, a 36-dimensional feature vector is obtained in each block, and then the sample image window is scanned by overlapping blocks. There are seven scanning areas in the horizontal direction and 15 scanning areas in the vertical direction. All the block features are connected. Finally, a 36*7*15=3780 dimension feature is obtained.

Analysis of experimental results

Off-line training module is a model generated by pre-training the sample set before the model goes online. The model generated by pre-training is not specific to specific detection scenarios. Before offline training of the algorithm, it is necessary to build an initial version of the sample library, including video frames (positive samples) containing pedestrians or other targets and video frames (negative samples) without people or other targets. In order to get a good classifier, a certain number and quality of samples are needed to represent the environmental characteristics of the monitoring equipment subordinate areas. These sample sets include as many states as possible. For example, negative samples use different illumination and angle images in the same area, while positive samples should collect pedestrian images of different ages, sexes and regions. In the off-line training module of cooperative detection mechanism, a more comprehensive INRIA pedestrian detection data set with illumination conditions and human posture in pictures is adopted, including 1218 negative sample pictures and 614 positive sample pictures. In this data set, each picture is calibrated for pedestrian area, and a rectangular frame is drawn to record the fixed point coordinates, rectangular length and width on the rectangular frame. In order to get better results when using INRIA data set, the original data is preprocessed, that is, 10 images of 64*128 size are randomly cut out from each original image, which not only increases the number of the original training set, but also increases the diversity of the original training set. The experimental results of sample distribution and iteration times are as follows:

Table 1

Comparison table of detection accuracy between traditional algorithms and online learning algorithms

Classification number	Training set	New Sample Set	Traditional algorithm		Online Learning Algorithms	
			Time /s	Accuracy rate	Time /s	Accuracy rate
2	Initial sample set	1832	976.5	83%		
	New Sample Set 1	100	1024.6	83.3%	18.3	83.3%
	New Sample Set 2	200	1119.1	84.2%	32.3	85.2%
	New Sample Set 3	200	1203.5	85.4%	31.2	85.9%
	New Sample Set 4	200	1312.3	85.6%	33.2	86.5%
	New Sample Set 5	200	1429.6	86.1%	34.3	86.7%

On-line training can adjust the number of iterations as needed. According to the experimental observation, the iteration times will affect the accuracy of the algorithm to a certain extent. The implementation of agricultural machinery fault monitoring is shown in Figure 7.

Fig. 7 - The implementation of agricultural machinery fault monitoring

The analysis of the above results is as follows: Online learning can greatly shorten the training time and effectively improve the accuracy of training model detection. With the increase of online training iterations, it is helpful to improve the detection accuracy of the generated model. The fault detection process of agricultural excavator is shown in Figure 8.

Fig. 8 - The fault detection process of agricultural excavator

The overall framework of cooperative detection mechanism, the process of cooperative detection, the process of feature extraction from HOG image and the problems needing attention in training are introduced. At the same time, the principle and overall process of cloud model off-line training and online incremental training are introduced. The simulation results show that online learning takes less time than traditional off-line training and has higher detection accuracy.

CONCLUSIONS

A video stream forwarding algorithm based on bidirectional ring buffer is proposed and implemented based on artificial neural network (ANN) algorithm and agricultural machinery video surveillance system. It realizes the efficient conversion of video frames compressed in H.264 encoding format to JPG format images captured by front-end cameras. After realizing the basic functions of traditional video surveillance, a cooperative detection algorithm based on artificial neural network is adopted. This algorithm takes the HOG+SVM pedestrian detection algorithm as the premise, applies the idea of online learning to the system, and then continuously updates the model on the iteration line, enhances the adaptability of the model to the environment and improves the accuracy of model detection. At the same time, the real-time on-line fast detection mechanism is adopted in this study. By shortening the program response time in two steps of acquiring video frames and detecting agricultural machinery video frames, the purpose of rapid detection is achieved, and valuable images are provided for subsequent detection, thereby improving the overall operational efficiency of the agricultural machinery system. Due to the limited time and laboratory conditions, some work needs to be further improved and expanded. Firstly, due to the limitation of the experimental equipment, there is no high-voltage test for the server under high concurrency. Secondly, in the online training of the model on the server, this part of the experimental process is carried out under the simulated experimental environment, because online training needs to continuously adjust the expert opinions of the test samples, and then return to the sample set on the remote server.

ACKNOWLEDGMENT

The work presented in this paper is financed by 2017 key projects of Hefei University Research Fund Project (17ZR02ZDB), Key projects of natural science research in universities and colleges in Anhui province in 2017 (KJ2017A531), and Anhui quality engineering project (No. 2018hfjyxm05, No. 2018hfmooc05).

REFERENCE

[1] Bajaj J., Hamilton M., Shima Y., (2020), An in vivo genome-wide CRISPR screen identifies the RNA-binding protein Staufen2 as a key regulator of myeloid leukemia. *Nature Cancer*, Vol.1, Issue 4, pp. 410-422. United States;

[2] Caixal G., Alarcón F., Althoff T. F., (2021), Accuracy of left atrial fibrosis detection with cardiac magnetic resonance: correlation of late gadolinium enhancement with endocardial voltage and conduction velocity. *EP Europace*, Vol. 23, Issue 3, pp. 380-388. England;

[3] Gandjbakhch E., Dacher J. N., Taieb J., (2020), Joint Position Paper of the Working Group of Pacing and Electrophysiology of the French Society of Cardiology and the French Society of Diagnostic and Interventional Cardiac and Vascular Imaging on magnetic resonance imaging in patients with cardiac electronic implantable devices. *Archives of cardiovascular diseases*, Vol. 113, Issue 6-7, pp. 473-484. France;

[4] Hassan M. M., Gumaei A., Alsanad A., (2020), A hybrid deep learning model for efficient intrusion detection in big data environment. *Information Sciences*, Issue 513, pp. 386-396. United States;

[5] Kariki O., Antoniou C. K., Mavrogeni S., (2020), Updating the Risk Stratification for Sudden Cardiac Death in Cardiomyopathies: The Evolving Role of Cardiac Magnetic Resonance Imaging. *An Approach for the Electrophysiologist. Diagnostics,* Vol. 10, Issue 8, pp. 541. Switzerland;

[6] Kayraklioglu E., Favry E., El-Ghazawi T., (2021), A Machine-Learning-Based Framework for Productive Locality Exploitation*. IEEE Transactions on Parallel and Distributed Systems,* Vol. 32, Issue 6, pp. 1409-1424. United States;

[7] Luz E., Silva P., Silva R., (2021), Towards an effective and efficient deep learning model for covid-19 patterns detection in x-ray images. *Research on Biomedical Engineering*, pp. 1-14. United States;

[8] Mohibi S., Zhang J., Chen X., (2020), PABPN1, a target of p63, modulates keratinocyte differentiation through regulation of p63α mRNA translation. *Journal of Investigative Dermatology,* Vol. 140, Issue 11, pp. 2166-2177. England;

[9] Pesut B., Duggleby W., Warner G., (2020), A mixed-method evaluation of a volunteer navigation intervention for older persons living with chronic illness (Nav-CARE, pp. findings from a knowledge translation study. *BMC palliative care*, Vol. 19, Issue 1, pp. 1-16. England;

[10] Pi J., Wang W., Ji M., (2021), YTHDF1 promotes gastric carcinogenesis by controlling translation of FZD7. *Cancer Research*, Vol. 81, Issue 10, pp. 2651-2665. United States;

[11] Provvidenza C., Townley A., Wincentak J., (2020), Building knowledge translation competency in a community-based hospital: a practice-informed curriculum for healthcare providers, researchers, and leadership. *Implementation Science*, Vol. 15, Issue 1, pp. 1-12. England;

[12] Romney W., Salbach N., Parrott J. S., (2020), A knowledge translation intervention designed and implemented by a knowledge broker improved documented use of gait speed: a mixed-methods study. *Journal of Geriatric Physical Therapy*, Vol. 43, Issue 3, pp. E1-E10. United States;

[13] Shankar K., Sait A. R. W., Gupta D., (2020), Automated detection and classification of fundus diabetic retinopathy images using synergic deep learning model. *Pattern Recognition Letters*, Issue 133, pp. 210-216. Netherlands;

[14] Warner E., Yee S., Seminsky M., (2020), Effect of a knowledge-translation intervention on breast surgeons' oncofertility attitudes and practices. *Annals of surgical oncology*, Vol. 27, Issue 5, pp. 1645-1652. United States;

[15] Zhao J., Di P., (2020), Optimizing the Memory Hierarchy by Compositing Automatic Transformations on Computations and Data. 2020 53rd Annual IEEE/ACM International Symposium on Microarchitecture (MICRO). *IEEE,* pp. 427-441.China.

EXPERIMENTAL INVESTIGATIONS ON THE SURFACE APPLICATION OF SUPERPHOSPHATE BY THE FERTILISER SPREADING TOOL WITH INCLINED AXIS
/
ЕКСПЕРИМЕНТАЛЬНІ ДОСЛІДЖЕННЯ ПОВЕРХНЕВОГО ВНЕСЕННЯ СУПЕРФОСФАТУ РОЗКИДАЧЕМ ДОБРИВ З ПОХИЛІЙ ВІССЮ ОБЕРТАННЯ

Bulgakov V.[1)], Adamchuk O.[2)], Ivanovs S.[3)], Olt J.[4)] [1]
[1)]National University of Life and Environmental Sciences of Ukraine, Ukraine;
[2)]National Scientific Centre, "Institute for Agricultural Engineering and Electrification, Ukraine;
[3)]Latvia University of Life Sciences and Technologies, Latvia,
[4)]Estonian University of Life Sciences, Institute of Technology, Estonia
DOI: https://doi.org/10.35633/inmateh-64-30

Keywords: *superphosphate, spreading, disc, inclination, distance.*

ABSTRACT
One of the possible ways to significantly increase the spreading distance of fertilisers (and, accordingly, efficiency) by the fertiliser spreading tools may be creation of a structure with an inclined axis of rotation. For experimental investigations an experimental setup was developed and a solid mineral superphosphate granular fertiliser was used as a material. Increasing the angle of inclination of the disc of the fertiliser sowing tool with an inclined axis in a horizontal plane from 0 to 30º at a disc rotation frequency of 1000 min^{-1} leads to an increase in the effective sieving distance of granulated superphosphate by 34.9. It has been established that the best indices of mineral fertilisation both in terms of the operating width and the irregularity of the fertiliser introduction are provided at the angles of inclination of the disc of the new fertiliser distributing tool in a horizontal plane within 25-30º.

АНОТАЦІЯ
Одним з можливих способів значного збільшення дальності розкидання мінеральних добрив знаряддями для розкидання добрив може бути створення конструкції розкидача з похилою віссю обертання. Для досліджень була розроблена експериментальна установка, а в якості матеріалу використано тверде мінеральне гранульоване добриво – суперфосфат. Збільшення кута нахилу диска розсівного апарату добрив з похилою віссю в горизонтальній площині від 0 до 30^{O} при частоті обертання диска 1000 min^{-1}. призводить до збільшення розкидання гранульованого суперфосфату на 34.9%. Встановлено, що найкращі показники внесення мінеральних добрив як по ширині захоплення, так і по рівномірності внесення добрив забезпечуються при кутах нахилу диска нового розподільника добрив в горизонтальній площині в межах 25-30^{O}.

INTRODUCTION

Despite the expansion of biological farming, the use of mineral fertilisers is still the most important means of increasing the soil fertility and reaching high yields of agricultural crops *(Antille et al., 2015; Adamchuk and Moiseenko, 2001; Vilde and Rucins, 2008).* Application of mineral fertilisers is carried out mainly using centrifugal spreaders *(Dintwa et al., 2004; Kobets et al, 2017; Przywara, 2015).* When creating new models of machines for surface application of solid mineral fertilisers, which are equipped with centrifugal disc fertiliser dispensing working tools, increasing the operating width is an urgent problem *(Abbou-ou-Cherif et al., 2019; Bulgakov et al., 2020).*

In the known centrifugal fertiliser dispensing tools with a vertical axis of rotation, an increase in the angle of descent of the fertilisers to the horizon is formed only due to the speed of the fertiliser particles moving along the blade of the disc (the transfer speed). At the same time the main share of the absolute spreading speed of fertilisers by the fertiliser spreading tools is the transfer speed but the relative speed does not exceed 15% of the indicated absolute speed (*Adamchuk, 2003; Bulgakov et al., 2016; Villette et al., 2007)*.

[1] *Bulgakov V., Prof. Ph.D. Eng.; Adamchuk O., Ph.D. Eng.; Ivanovs S., Ph.D. Eng.; Olt J., Prof.Ph.D. Eng.*

This gives grounds to formulate the following working hypothesis: the direction of the transfer speed at an angle to the horizon by setting the axis of the fertiliser spreading tool with an inclination to the vertical will provide an increase in the sowing distance of fertilisers, and, accordingly, an increase in the productivity of the machines.

An important quality criterion of the fertiliser spreaders is to ensure a sufficiently uniform application of the layer over the entire soil surface *(Grift and Kweon, 2006; Koko and Virin, 2009).* The distance from the disc increasing, the mass of the scattered fertilisers decreases; therefore, to ensure a uniform layer on the soil surface, the operating width should be less than the maximum spreading distance (i.e., total overlap of layers during the adjacent passes should be ensured). Due to the impact of many factors it is difficult to theoretically calculate the distribution of the fertiliser mass along the operating width *(Biocca et al., 2013; Bulgakov et al., 2019)* therefore it is necessary to conduct experimental investigations for a specific type of fertiliser.

The issues of increasing the efficiency of the technological process of applying mineral fertilisers to the soil have been relevant for scientists from many countries of the *world (Antille et al., 2015; Dintwa et al, 2004; Kobets et al., 2017; Adamchuk, 2003).* They have found out that the efficiency of the use of mineral fertilisers depends not only on the fertilisers themselves but also on the methods of their application. Many scientists were engaged in the improvement of the technological process of applying mineral fertilisers *(Przywara et al., 2020; Hofstee and Huisman, 1990).* It has been established by the conducted investigations that the main factor of the factors limiting the efficiency of fertiliser application is uneven distribution of the fertilisers over the field area. The latter significantly affects maturation of the plants, produces uneven yield and, in general, its lowering. However, their studies do not consider the installation scheme of the axis of the fertiliser spreading tool with an inclination to the vertical.

The aim of the work is an experimental investigation of the superphosphate introduction process by centrifugal disc fertiliser dispensing tools, the axes of which are installed obliquely.

MATERIALS AND METHODS

Experimental investigations were carried out using the developed methods and current state standards, regression analysis, statistical methods for processing the research results, standard and specially created experimental equipment. The calculations of the performed measurements were made using a PC in the Microsoft Office Excel 2007 software environment *(Adamovics et al., 2018; Dospehov, 2012; Moise et al., 2019; Ivanovs et al., 2014; Burdo et al., 2017).*

To carry out the experimental investigations on surface introduction of granular superphosphate, we developed and manufactured a special experimental setup (Fig. 1).

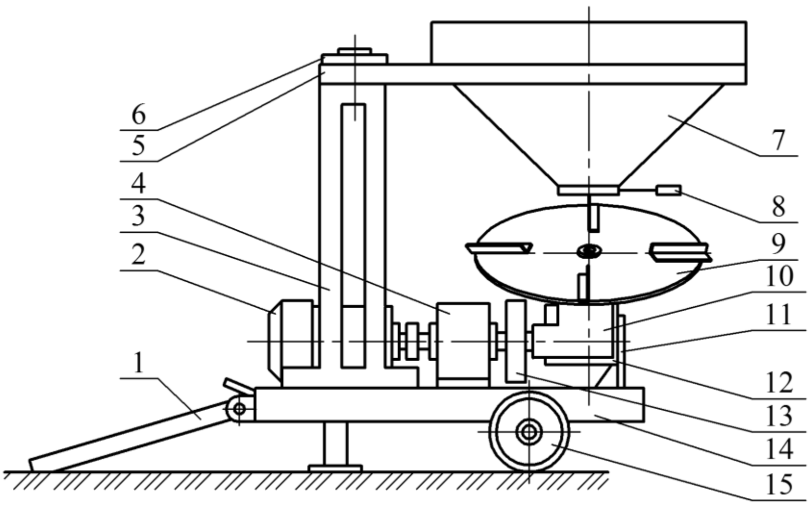

Fig. 1 - A structural diagram of the experimental setup for studying the surface application of superphosphate

1 – handle; 2 – electric motor 2; 3 – movable frame; 4 – chain variator; 5 – rotatable frame; 6 – joint for turning of the frame; 7 – hopper; 8 – shutter; 9 – spreading tool with an inclined axis; 10 – bevel gearbox; 11, 12 – brackets; 13 – overrunning clutch; 14 – the main frame; 15 – the supporting wheel

The design of the specially created experimental setup included a main frame *14* that was mounted on two wheels *15* and a support leg. A handle *1* was pivotally fixed on the main frame with the use of which, if necessary, the experimental setup on wheels *15* was moved to the place of experiments on a specially prepared site. On top of the main frame there were installed an electric motor *2*, a chain variator *4* and a bevel gearbox *10* which carry out a kinematic connection through the connecting and the overrunning *13* clutches. The bevel gearbox was fixed to the frame through brackets *11* and *12* having grooves for fastening, which make it possible to adjust the angle of inclination of the gearbox output shaft to the horizontal plane. On the output shaft of the bevel gearbox there was installed a fertiliser spreading tool with an inclined axis *9* which included a flat disc with four grooved blades radially fixed on its upper surface. The outer ends of the blades protruded beyond the disc. A movable frame *3* was installed on the main frame *14* with the possibility of longitudinally adjustable movement.

The design of the drive of the fertiliser spreading tool with an inclined axis provided for the possibility to change both the rotational frequency of its disk and the possibility to adjust the inclination angle of the disc to the horizontal plane.

In the process of experimental research we used the basic provisions of the standards *(European Standard EN 13739-2, Standard GOST 28714-2007).*

During the experimental investigations of the process of applying mineral fertilisers by means of this fertiliser spreading tool with an inclined axis, there were used granular superphosphate fertilisers, common in agriculture. Characteristics of the granular superphosphate used: - the average moisture content - 3.1%; -the average value of the bulk density - 1085 kg m^{-3}; - the coefficient of friction on steel - 0.51;- granulometric composition:< 1 mm - 4.9%;≥ 1 - < 2 mm - 20.6%; ≥ 2 - < 3 mm - 40.2%; ≥ 3 - < 4 mm - 24.7%; ≥ 4 mm - 9.6%.

Fig. 2 - A general view of the experimental setup with installed containers for studying the distribution of fertilisers in the direction of dispersion (for clarity, the rotatable frame and the hopper are removed)

RESULTS

A graphic interpretation of the research results is shown in Figs. 3 - 6.

According to the results of the research it was established that changing the angles of inclination of the disc to the horizontal plane within 0º - 30º, the increase in the frequency of rotation of the disc leads to an increase in both the efficient spreading distance of granulated superphosphate in the direction of its spreading and the distance from the fertiliser spreading tool with an inclined axis to the containers for collecting fertilisers with a maximum proportion of the sown fertiliser mass.

For example, at the disc rotation frequency of 600 min^{-1} and the horizontal position of the disc of the fertiliser spreading tool, the granular superphosphate is efficiently dispersed on an area by up to 35 containers (17.5 m) inclusive (Fig. 3 a), and the maximum proportion of the mass of the sown fertilisers (6.5%) falls into 12 containers (6 m).

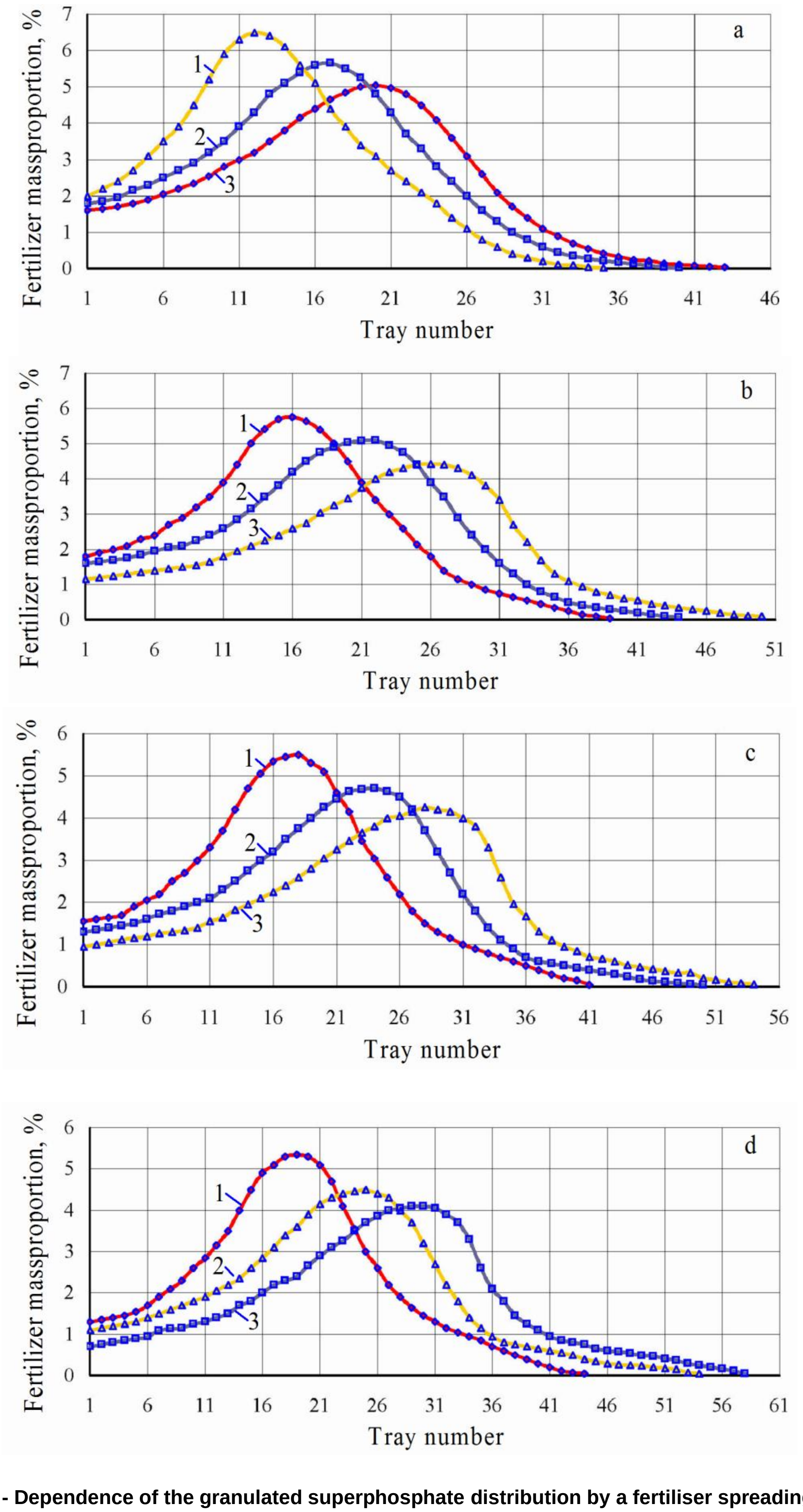

Fig. 3 - Dependence of the granulated superphosphate distribution by a fertiliser spreading tool with an inclined axis in the direction of distribution in containers on the rotation frequency of its disc and the angle of inclination

a, b, c, d – the angle of inclination of the disc to the horizontal plane, respectively, 0°, 10°, 20°, 30°;
1, 2, 3 – the rotation frequency of the disk, respectively, 600; 800; 1000 min^{-1}

Increasing the rotational frequency of the disc from 600 to 800 min^{-1} leads to an increase in the efficient spreading distance of the granulated superphosphate at the level of 40 containers (20 m). At the same time the maximum percentage of the sown fertiliser mass (5.65%) falls into 17 containers (8.5 m).

That is, there is an increase in the efficient sowing distance of the fertiliser by 14.3%, the distance from the fertiliser spreading tool with an inclined axis to the container with the maximum proportion of the fertiliser mass - by 41.7%, and a decrease in the specified proportion of the fertiliser mass by 1.15 times.

A similar phenomenon occurs when there is an increase in the rotational frequency of the disc of the fertiliser spreading tool with an inclined axis from 800 to 1000 min^{-1}; the efficient spreading distance of the granular superphosphate increases by 7.5%, the distance from the operating tool to the container with the maximum proportion of sown fertilisers is 17.6%, and the maximum proportion of the fertiliser mass that has fallen into the container has decreased by 1.12 times. Based on the results of the experimental research, it can be concluded: an increase in the disc rotation frequency leads to an increase in the efficient spreading distance of the granular superphosphate, which in turn leads to an increase in the distance from the fertiliser spreading tool with an inclined axis to containers with the maximum proportion of the sown fertiliser mass, as well as to a decrease the maximum proportion of the mass of the fertilisers distributed in containers. In addition, the increase in the rotational frequency of the disc from 600 to 1000 min^{-1} when the disc is horizontal, ensures an increase in the efficient spreading distance of the granular superphosphate by 22.9%, and an increase by 66.7% of the distance from the fertiliser spreading tool to the containers with the maximum proportion of the distributed fertiliser mass, which has decreased by 1.29 times.

The described regularities of the impact of the rotational frequency of the disc of the fertiliser spreading tool with an inclined axis upon the distribution of the granulated superphosphate in the direction of its spreading also take place under the condition of an increase in the angle of inclination of the disc to the horizontal plane (Fig. 3 b - 3 c). The results of investigations on the impact of the values of the angle of inclination of the disc of the fertiliser spreading tool with an inclined axis to the horizontal plane upon the granulated superphosphate spreading indices are shown in Fig. 4 - 6 as graphical dependencies.

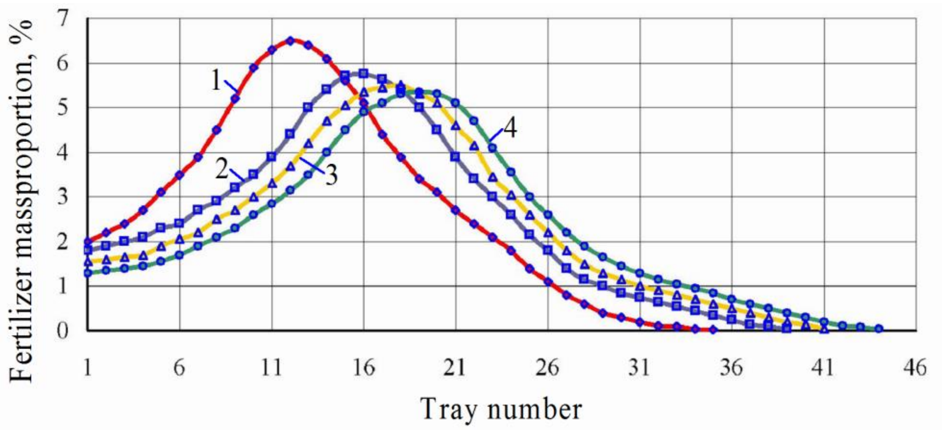

Fig. 4 - Dependence of the granular superphosphate distribution by the fertiliser spreading tool with an inclined axis in the direction of spreading at a disc rotation frequency of 600 min^{-1} on the angle of its inclination to the horizontal plane

1, 2, 3, 4 – the angle of inclination of the disc to the horizontal plane, respectively, equal to 0º, 10º, 20º, 30º

As the disc installation angle in the horizontal plane grows, a graphical dependence corresponds to a larger value of the disc inclination angle, in which the distribution of the entire mass of the granular superphosphate is characterised by a relative displacement to the right of its individual masses, sown into containers at a relatively greater distance from this fertiliser spreading working tool. For example, when the rotational frequency of the disc of fertiliser spreading tool is equal to 600 min^{-1} (Fig. 4) and the disc is installed horizontally, granular superphosphate is efficiently dispersed on the area of up to 35 containers (17.5 m) inclusive, the maximum percentage of the fertiliser mass (6.5%) falls into 12 containers (6.0 m). When the disc is installed at an angle of 10° to the horizontal plane, the granular superphosphate is efficiently dispersed on an area of up to 39 containers (19.5 m) inclusive; the maximum proportion of the mass of the sown fertilisers (5.75%) goes into 16 containers (8 m). An increase in the angle of installation of the disc of the fertiliser spreading tool with an inclined axis to the horizontal plane up to 20° causes an increase in the efficient spreading distance of the granulated superphosphate to 41 containers (21.5 m), an increase in the distance from the fertiliser spreading tool with an inclined axis to the container with a maximum proportion of the mass of sown fertilisers up to 9 m (18 containers) and a decrease in the maximum proportion of the mass of the sown granulated superphosphate in a container to 5.5%. When the indicated angle increases to 30°, the indicators characterising the distribution of fertiliser among the containers are, respectively: the efficient distribution distance - 22 m (44 containers), the distance from the fertiliser spreading tool having an inclined axis to the container with a maximum proportion of the sown fertiliser mass - 9.5 m (19 containers), the maximum proportion of the mass of the sown fertilizers in a container is 5.35%.

The results show that at a disc rotation frequency of the fertiliser spreading tool with an inclined axis of 600 min-1 changing the angle of its installation in the horizontal plane from 0º to:

– 10° leads to an increase in the efficient distribution distance of the granulated superphosphate by 11.4%, the distance from this fertiliser spreading tool to the container with a maximum proportion of the sown fertiliser mass - by 33.3%, and a decrease in the indicated fraction of the mass by 1.13 times;

– 20º leads to an increase in the efficient spreading distance of the granulated superphosphate by 17.1%, the distance from this fertiliser spreading tool to a container with the maximum proportion of the sown fertiliser mass - by 50%, and a decrease in the indicated fraction of the mass by 1.18 times;

– 30º leads to an increase in the efficient spreading distance of the granulated superphosphate by 30.3%, the distance from this fertiliser spreading tool to a container with a maximum proportion of the sown fertiliser mass - by 58.3%, and a decrease in this fraction of the mass by 1.21 times.

According to the results of the experimental investigations of the impact of the installation angle of the disc of the fertiliser spreading tool with an inclined axis to the horizontal plane at a frequency of its rotation of 800 min^{-1} upon the distribution of the granulated superphosphate in the direction of its spreading, it was found (Fig. 5) that an increase in its inclination angle to 10º leads to an increase in the efficient distribution distance of the granulated superphosphate up to the level of 44 containers (22 m) inclusive, an increase in the distance from this fertiliser spreading tool to the container with a maximum proportion of the sown fertiliser mass up to 11 m (22 containers), and the reduction of the maximum proportion of the sown fertiliser mass in the container up to 5.1%.

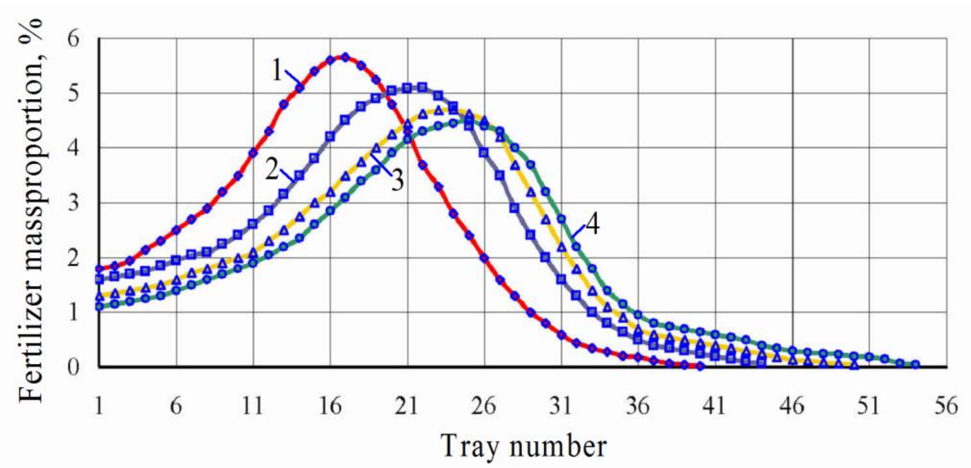

Fig. 5 - Dependence of the granulated superphosphate distribution by the fertiliser spreading tool with an inclined axis in the direction of distribution at a disc rotation frequency of 800 min^{-1} on the angle of its inclination to the horizontal plane

1, 2, 3, 4 – the angle of inclination of the disc to the horizontal plane, equal, respectively, to: 0º, 10º, 20º, 30º

The subsequent increase in the angle between the disc and the horizontal plane also causes an increase in the indicators characterising the spreading distance of the granular superphosphate. For example, an increase in the installation angle of the disc of the fertiliser spreading tool with an inclined axis to the horizontal plane up to 20° leads to an increase in the efficient spreading distance of the granulated superphosphate up to 50 containers (25 m) inclusive, an increase in the distance from this fertiliser spreading tool to the container with a maximum fraction of the sown fertilisers mass up to 12 m (24 containers), and reduction of the maximum proportion of the seeded granulated superphosphate mass in a container to 4.7%. When the indicated angle increases to 30°, the indicators characterising the distribution of fertiliser among the containers are, respectively: the efficient spreading distance - 27 m (54 containers), the distance from this fertiliser spreading tool to the container with a maximum proportion of the sown granulated superphosphate mass - 12.5 m (25 containers), the maximum proportion of the mass of sown fertilisers in the container is 4.5%.

When the rotational frequency of the disc of the fertiliser spreading tool with an inclined axis is equal to 800 min^{-1}, changing the angle of its installation in the horizontal plane from 0^o to:

– 10^o leads to an increase in the efficient distribution distance of the granulated superphosphate by 10%, the distance from this fertiliser spreading tool to the container with a maximum proportion of the sown fertiliser mass - by 29,4%, and a decrease in the indicated fraction of the mass by 1.11 times;

– 20^o leads to an increase in the efficient distribution distance of the granulated superphosphate by 25%, the distance from this fertiliser spreading tool to the container with a maximum proportion of the sown fertiliser mass - by 1.2 times;

– 30^o leads to an increase in the efficient distribution distance of the granulated superphosphate by 35%, the distance from this fertiliser spreading tool to the container with a maximum proportion of the sown fertiliser mass – by 47.1%, and a decrease in the indicated fraction of the mass by 1.23 times.

The results of investigations of the impact of the disc installation angle from the indicated fertiliser spreading tool to the horizontal plane at a rotation frequency of 1000 min^{-1} upon the distribution of the granulated superphosphate in the direction of its spreading are shown in the form of graphical dependences, presented in Fig. 6.

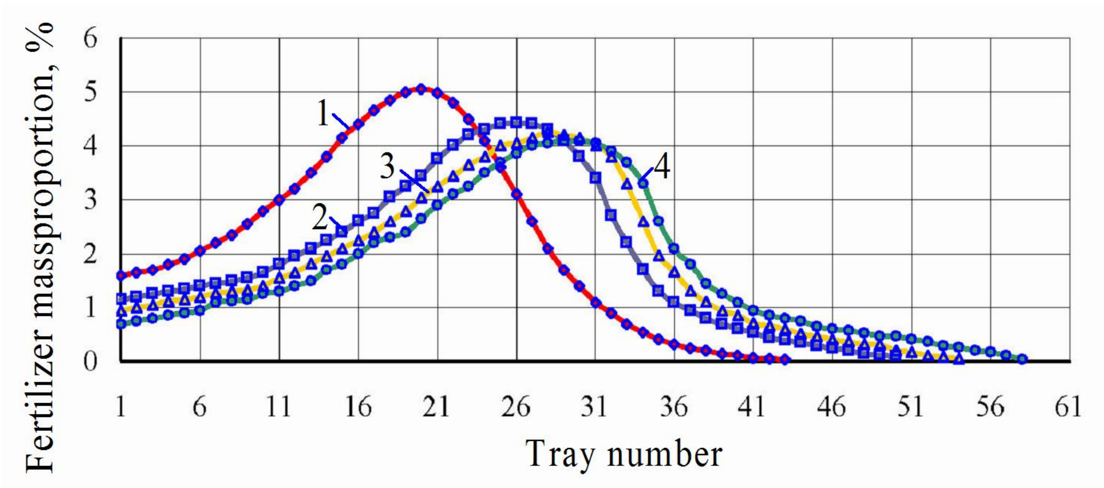

Fig. 6 - Dependence of the granulated superphosphate distribution by the fertiliser spreading tool with an inclined axis in the direction of spreading in containers at the disc rotation frequency of 1000 min^{-1} on the angle of its inclination to the horizontal plane:

1, 2, 3, 4 – the angle of inclination of the disc to the horizontal plane equal, respectively, to: 0^o, 10^o, 20^o, 30^o

It has been found that the increase in the angle of inclination of the disc of the fertiliser spreading tool with an inclined axis to 10° leads to an increase in the efficient spreading distance of the granulated superphosphate up to 50 containers (25 m) inclusive, an increase in the distance from the fertiliser spreading tool with an inclined axis to a container with a maximum proportion of the sown fertilisers mass up to 13 m (26 containers), and reduction of the indicated maximum fraction of the mass to 4.42%. With a subsequent increase in the angle between the disc and the horizontal plane, there is also an increase in the indicators characterising the distance of spreading of the granular superphosphate.

In particular, the increase in the disc angle of this fertiliser spreading tool with an inclined axis to the horizontal plane up to 20° causes an increase in efficient spreading distance of the granulated superphosphate up to 54 containers (27 m) inclusive, an increase in the distance from this fertiliser spreading tool having an inclined axis to the container with a maximum proportion of the mass of the sown fertilizers up to 14 m (28 containers), and a decrease in the maximum proportion of the sown granulated superphosphate mass in a container up to 4.25%.

The indicated tendency to change the studied parameters is also characteristic when the angle of inclination of the disc to the horizontal plane is increased up to 30°. Under these conditions the efficient spreading distance of the granular superphosphate increases to 29 m (58 containers), the distance from this fertiliser spreading tool to the container with a maximum proportion of the sown granular superphosphate mass increases to 14.5 m (29 containers), and the maximum proportion of the fertiliser mass in the containers decreases to 4.1% of its total sown mass.

Based on the obtained research results, it can be concluded that at a rotational frequency of the disc of the fertiliser spreading tool with an inclined axis equal to 1000 min^{-1}, changing the angle of its installation in a horizontal plane from 0º to:

– 10º leads to an increase in the efficient distribution distance of the granulated superphosphate by 16.3%, the distance from this fertiliser spreading tool to the container with a maximum proportion of the sown fertiliser mass - by 30%, and a decrease in the indicated fraction of the mass by 1.14 times;

– 20º leads to an increase in the efficient distribution distance of the granulated superphosphate by 25.6%, the distance from this fertiliser spreading tool to the container with a maximum proportion of the sown fertiliser mass - by 40%, and a decrease in the indicated fraction of the mass by 1.19 times;

– 30º leads to an increase in the efficient distribution distance of the granulated superphosphate by 34.9%, the distance from this fertiliser spreading tool to the container with a maximum proportion of the sown fertiliser mass – by 45%, and a decrease in the indicated fraction of the mass by 1.23 times.

The research results on the granulated superphosphate distribution by the fertiliser spreading tool with an inclined axis in the direction of its spreading in containers show that, with an increase in the rotational frequency of the disc from 600 to 1000 min^{-1} within all the studied installation values of the angle of the disc of this fertiliser spreading tool to the container, there is an increase in both the efficient spreading distance of the granular superphosphate and the distance from this fertiliser spreading tool to the container with a maximum proportion of the sown fertiliser mass. For example, an increase in the efficient spreading distance of the granular superphosphate is at the angles: 0º - 22.9%, 10º - 28.2%, 20º - 31.7%, 30º - 31.8%, and the increase in the distance from the fertiliser spreading tool to the container with a maximum proportion of the sown fertiliser mass will be at the angles: 0º - 66.7%, 10º - 62.5%, 20º - 55.5%, 30º - 52.6%.

At a constant rotational frequency of the fertiliser spreading disk in all the kinematic modes of its operation an increase in the installation angle of the investigated disc of the fertiliser distributing tool to the horizontal plane led to an increase in the indicators characterising the granulated superphosphate distribution in containers in the direction of its spreading. In particular, when the rotational frequency of the disc of this fertiliser spreading tool is equal to 1000 min^{-1} the increase in the efficient spreading distance of the granular superphosphate is, increasing the inclination angle of the disc from its horizontal position to 10º - 16.3%, 20º - 25.6%, 30º - 34.9%, and increasing the distance from the working tool to the container with a maximum proportion of the sown fertilisers mass: 10º - 30%, 20º - 40%, 30º - 45%. Increasing the inclination angle of the disc to the horizontal plane leads to an increase in the indicators characterising the spreading distance of the granular superphosphate and the working width of the machine for applying mineral fertilizers. Besides, the intensity of increasing these indicators is the highest when the inclination angle of the disc to the horizontal plane is increased from 0 to 10°, and there is a decrease in the indicated intensity as it continues increasing to 30°. Thus, the fertiliser spreading tool with an inclined axis of rotation ensures an increase in the indicators characterising the distribution of the granulated superphosphate in the direction of its distribution over a greater distance than that by the conventional fertiliser spreading tool with a vertical axis of rotation.

CONCLUSIONS

✓ The disc fertiliser spreading tool, the axes of which are installed obliquely, reliably ensures implementation of the technological process when the rotation frequency of its disc changes from 600 to 1000 min^{-1} and the installation angle of the disc changes to the horizon from 0 to 30°.

✓ The rational values of the rotational frequency of the disc of the new tool are 1000 min^{-1} for the introduction of the granular superphosphate

✓ An increase in both the rotational frequency of the disc of the new tool from 600 to 1000 min^{-1} and its inclination angle to the horizontal plane from 0 to 30º led to:

– significant displacement of the entire fertilizer mass from the tool in the direction of their spreading;

– increasing the efficient spreading distance of mineral fertilisers;

– increasing the distance from the tool to the containers into which the maximum proportion of the fertiliser mass was spread.

✓ Increasing the inclination angle of the disc of the fertiliser spreading tool with an inclined axis in the horizontal plane from 0 to 30º, at the disc rotation frequency of 1000 min^{-1} leads to an increase in: the efficient spreading distances of the granulated superphosphate by 34.9%, the distance from the tool to containers with a maximum proportion of the sown fertiliser mass by 45.0%, and a decrease in the indicated proportion of the fertilizer mass by 1.23 times.

✓ The best indicators of the fertiliser application both in terms of the working width of the operation and its unevenness are provided at the disc inclination angles of the new tool in the horizontal plane within 25-30º.

REFERENCES

[1] Abbou-Ou-Cherif, E.-M., Piron, E., Chateauneuf, A., Miclet, D., Villette, S. (2019). On-the-field simulation of fertilizer spreading: Part 3 – Control of disk inclination for uniform application on undulating fields. *Computers and Electronics in Agriculture*, 158, pp. 150-158.

[2] Adamchuk V.V., Moiseenko V.K. (2001). Farming of the future and technology for it. *Bulletin of Agrarian Science.* No. 11. pp.55-60.

[3] Adamchuk V.V. (2003). Investigation of the general case of dispersal of mineral fertilizers by a centrifugal dispersing body. *Bulletin of Agrarian Science.* No. 12. pp. 51-57.

[4] Adamovics A., Platace R., Gulbe I., Ivanovs S. (2018). The content of carbon and hydrogen in grass biomass and its influence on heating value. *Engineering for Rural Development,* 17, pp.1277-1281, Jelgava/Latvia

[5] Antille D.L., Gallar L., Miller, P.C.H., Godwin, R.J. (2015). An investigation into the fertilizer particle dynamics off the disc. *Applied Engineering in Agriculture,* Vol.31, Issue 1, pp.49-60

[6] Biocca M., Gallo P., Menesatti P. (2013). Aerodynamic properties of six organo-mineral fertiliser particles. *Journal of Agricultural Engineering,* Vol. 44, Art. e83, pp. 411-414

[7] Bulgakov V., Adamchuk O., Ivanovs S. (2016). Theoretical investigations of mineral fertiliser distribution by means of an inclined centrifugal tool. *Proceeding of 6th International Conference on Trends in Agricultural Engineering* - Part 1, pp.109-116. Prague/Czech Republic,

[8] Bulgakov V., Pascuzz, S., Beloev H., Ivanovs S. (2019). Theoretical investigations of the headland turning agility of a trailed asymmetric implement-and-tractor aggregate. *Agriculture* (Switzerland) Volume 9, Issue 10, Article number 224

[9] Bulgakov V., Adamchuk O., Ivanovs S., Nowak J. (2020). Research of descent of mineral fertiliser particle from disc inclined at angle to horizon. *Engineering for Rural Development,* Vol. 19, pp.390.-398, Jelgava/Latvia

[10] Burdo, O., Bandura, V., Kolianovska, L., Dukulis, I. (2017). Experimental research of oil extraction from canola by using microwave technology. *Engineering for Rural Development,* Volume 16, pp. 296-302, Jelgava/Latvia

[11] Dintwa, E., Tijskens, E., Olieslagers, R., De Baerdemaeker, J., Ramon, H. (2004). Calibration of a spinning disc spreader simulation model for accurate site-specific fertiliser application. *Biosystems Engineering*, 88 (1), pp. 49-62,

[12] Dospehov, B. (2012), *Methodology of field experiments.* Nauka, 352 p., Moscow/Russia,

[13] European Standard EN 13739-2:2011 (2011). *Agricultural Machinery—Solid Fertilizer Broadcasters and Full Width Distributors—Environmental Protection—Part 2: Test Methods* CEN: Brussels/Belgium

[14] Grift, T.E., Kweon, G. (2006). Development of a Uniformity Controlled Granular Fertilizer Spreader, *American Society of Agricultural and Biological Engineers,* pp. 1-14.

[15] Hofstee, J.W., Huisman, W. (1990). Handling and spreading of fertilizers: Part 1, Physical properties of fertilizer in relation to particle motion. *J. Agric. Eng. Res*, 62, pp. 9-24.

[16] Ivanovs, S., Adamovics, A., Rucins, A., Bulgakov, V. (2014). Investigations into losses of biological mass and quality during harvest of industrial hemp. *Engineering for Rural Development,* Vol. 13, pp.18-23, Jelgava/Latvia

[17] Kobets A.S., Naumenko M.M., Ponomarenko N.O., Kharytonov M.M., Velychko O.P., Yaropud V.M. (2017). Design substantiation of the three-tier centrifugal type mineral fertilizers spreader. *INMATEH - Agricultural Engineering,* Vol. 53, Issue 3, pp. 13-20, Bucharest/Romania;

[18] Koko, J., Virin, T. Optimization of a fertilizer spreading process (2009). *Mathematics and Computers in Simulation*, 79 (10), pp. 3099-3109.

[19] Przywara, A., Santoro, F., Kraszkiewicz, A., Pecyna, A., Pascuzzi, S. (2020). Experimental study of disc fertilizer spreader performance. *Agriculture* (Switzerland), Vol. 10, Issue 10, Article number 467, pp.1-11

[20] Przywara, A. (2015). The impact of structural and operational parameters of the centrifugal disc spreader on the spatial distribution of fertilizer. *Agric. Agric. Sci. Procedia*, 7, pp. 215-222.

[21] Koko, J., Virin, T. (2009). Optimization of a fertilizer spreading process *Mathematics and Computers in Simulation*, 79 (10), pp. 3099-3109.

[22] Moise V., Voicu G., Lazea M., Stoica D., Popa L., Tudor P., Ungureanu L. (2020). Kinetostatic analysis of the precompaction mechanism in municipal solid waste collecting equipment. *INMATEH - Agricultural Engineering*, Vol.60 (1), pp. 295-302, Bucharest/Romania;

[23] Standard GOST 28714-2007 (2007). Machines for applying solid mineral fertilisers. The test methods. Moscow/ Russia

[24] Vilde A., Rucins A. (2008). Simulation of the Impact of the Plough Body Parameters, Soil Properties and Working Modes on the Ploughing Resistance. *10th International Conference on Computer Modelling and Simulation.* Emmanuel College Cambridge, 1 – 3 April 2008, pp. 697–702.

[25] Villette, S., Cointault, F., Zwaenepoel, P., Chopinet, B., Paindavoine, M. (2007). Velocity measurement using motion blurred images to improve the quality of fertiliser spreading in agriculture. *Proceedings of SPIE-The International Society for Optical Engineering,* Vol.6356, Art. 63560I.

DESIGN AND OPERATION PARAMETERS OPTIMIZATION OF 4SGMS-220 PLOUGH LAYER RESIDUAL FILM RECOVERY MACHINE
/
4SGMS-220 型耕层残膜回收机的设计及参数优化

Xing Jianfei[1, 3)], Wang Xufeng*[1, 3)], Hu Can[1, 2, 3)], He Xiaowei[1, 2, 3)], Guo Wensong[1, 3)], Wang Long[1, 2, 3)] [1)]
[1)]College of Mechanical and Electronic Engineering, Tarim University, Alar Xinjiang, 843300 / China;
[2)] College of Engineering, China Agricultural University, Beijing, 100083 / China;
[3)] Key Laboratory of Colleges & Universities under the Department of Education of Xinjiang Uygur Autonomous Region, Alar Xinjiang 843300/ China
Tel: +86 13779803762; E-mail: wxfwyq@126.com
DOI: https://doi.org/10.35633/inmateh-64-31

Keywords: *residual film, plough layer, residual film recovery, working parameters optimization*

ABSTRACT
In view of the harm of residual film retention to soil environment in Xinjiang which even affected the germination of seeds and hindered the growth of crop roots in severe cases, in this paper, a 4SGMS-220 plough layer residual film recovery machine with a ground preparation device is designed. The main part of the machine is composed of a filming mechanism, a conveying mechanism, a soil crushing roller, and a film collecting box. The machine can achieve simultaneous film lifting, film stripping, collecting membrane and suppression operations. In this paper, primary focus is placed on the design of the filming mechanism, while the movement trajectory of the comb teeth and the filming condition are analysed in detail. In order to obtain the optimal combination of equipment and operating parameters, the equipment traveling speed, the filming device rotational speed, and the comb teeth depth are used as the influencing factors. Furthermore, the residual film recovery rate and impurity rates are employed as test indicators for three-factor three-level response surface experiment and optimization via Design-Expert software. The results indicate that optimal operation is achieved for the machine travel speed of 4.1 km/h, the filming device speed of 106 min^{-1}, and the comb tooth soil penetration depth of 139.2 mm. The residual film recovery rate is equal to 74.32%, while the residual film impurity rate is equal to 7.11%. The difference between the test results and the predicted values is relatively small. Thus, it can be concluded that the optimized model is reliable.

摘要
针对新疆残膜滞留对土壤环境产生了一定破坏、严重时会出现影响种子发芽和阻碍作物根系生长等问题，该文设计了一种带有整地装置的 4SGMS-220 型耕层残膜回收机,4SGMS-220 型耕层残膜回收机由起膜机构、输送机构、碎土辊、镇压辊和集膜箱等组成，可一次性完成起膜、脱膜、集膜、平土及镇压作业。机具重点设计了起膜机构和脱膜机构，并对梳齿的运动轨迹和脱膜条件进行了分析。为得到机具与作业参数的最佳组合，将机具行进速度、起膜辊转速、梳齿入土深度作为影响因素，以残膜回收率和残膜含杂率为试验指标进行三因素三水平响应面试验，利用 Design-Expert 软件进行优化。结果表明，机具行进速度 4.1km/h、起膜辊转速 106r/min、梳齿入土深度 139.2mm 时作业最佳，残膜回收率为 74.32%，残膜含杂率为 7.11%，试验结果与预测值相差较小，优化模型可靠。

INTRODUCTION
The crop growth soil environment affects the final crop yield. With the large-scale utilization of the film covering technology, environmental dependence of the crop growth can be effectively solved (*Zhao et al., 2017; Li et al., 2017*). Xinjiang is a large province of plastic film mulching cultivation, with cotton being the main planting crop, accounting for 74.3% of the country's total cotton planting area with the film input of more than 200,000 t per year (*Hu et al., 2019; Liu et al., 2018*). Owing to the incomplete film recovery, the remainder of the broken film requires ploughing the entire ground to the tillage layer. With time, a relatively large amount of residual film retention is accumulated. Hence, crop growth and development may be hindered (*Jiang et al., 2019; Ye et al., 2020*).

[1] *Xing Jianfei, Lec.; Wang Xufeng, Prof. Ph.D.; Hu Can, Ph.D. Stud.; He Xiaowei, Ph.D. Stud.; Wang Long, Ph.D. Stud.; Guo Wensong, A. Prof. Ph.D.*

In order to ensure a sustainable development of cotton fields and speed up the control of the residual film pollution, in June 2018 the State Council of the CPC Central Committee issued the Opinions on Comprehensively Strengthening ecological environment Protection and Resolutely Fighting pollution Prevention and Control. Furthermore, in 2020, the Ministry of Agriculture and Rural Affairs along with additional four departments jointly issued the Measures for the Administration of Agricultural Film, which is imperative for solving the problem of the residual film pollution in the tillage layer.

The residual film of all cotton field soil layers in Xinjiang is relatively scattered. According to *Yan et al., (2014)*, the tillage layer residual film is mainly concentrated at 0-300 mm depth (*Lin et al., 2019*). According to *Hu et al. (2019)* the average residual amount in Xinjiang region is 206.46 kg/hm^2, which exceeds the film limit of 75 kg/hm^2. The presence of the residual film in the tillage layer has seriously affected the development of the bed and root system of cotton species (*Liu et al., 2020*). Currently, there is a shortage of applicable tools for the tillage layer residual film recovery. (*Liu et al., 2019; Luo et al., 2018*). Thus, the mechanized recovery of the tillage layer residual film presents a problem that must be solved. Field experts and researchers in China have designed and analysed the film starting points of the tillage layer residual film. *Zhang et al. (2017)* proposed a chain-toothed tillage film recovery machine which can recover approximately 150 mm of residual film. However, the chain-tooth film consumption power is relatively large, while the maintenance of implements is quite complex. *Xie et al. (2019)* designed a curved tooth rolling layer residual film recovery machine. By employing the curved roller-tie film mechanism, the machine can complete the middle-till layer residual film recovery, with the corresponding depth of operation and width being 55 mm and 800 mm (*Han et al., 2021*), respectively. However, depth of operation does not meet the requirements. Furthermore, amongst other issues, the machine has low operating efficiency.

The key to the recovery of the tillage layer residual film is the starting film (*Sun et al., 2018*). In this paper, in order to solve the problem of the tillage layer residual film recovery, a 4SGMS-220 machine is designed and tested. The machine is designed according to the film recovery parts of the current tillage film recovery machine characteristics. The machine can simultaneously complete the membrane, film release, film collection, flat soil, and suppression operation. By analysing the function and structure of the combing film mechanism and the film stripper mechanism, parameters of each device are determined, field tests are performed, regression equations with the help of response surface analysis are established, optimal parameters selected, verification is carried out, and a test basis for design of the subsequent tillage residue recovery machine is provided.

MATERIALS AND METHODS

Overall structure

The configuration of the combing layer residue recovery machine is shown in Figure 1. The main components of the machine are: the traction frame, frame, transmission, depth limit wheel, film-lifting mechanism, film-stripping mechanism, syringe, conveyor chain, conveying chain active shaft, vibration wheel, crushed soil roller, film collection box, flat plate, suppression roller, and the walking wheel. The main parameters of the combing layer residue recovery machine are provided in Table 1.

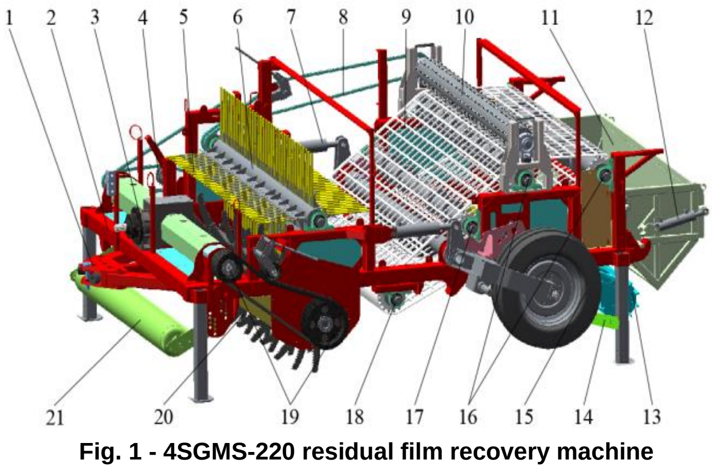

Fig. 1 - 4SGMS-220 residual film recovery machine

1) traction frame; 2) rack; 3) deceleration box; 4) tension pulley; 5) film belt; 6) film-stripping roller; 7) walking wheel hydraulic cylinder; 8) delivery chain; 9) delivery chain; 10) soil crushing roller; 11) film box; 12) film collection Box hydraulic cylinder; 13) suppression roller 14) flat plate; 15) walking wheel; 16) transmission chain; 17) vibration wheel; 18) transmission chain active shaft; 19) belt drive; 20) comb starting mechanism; 21) depth limit wheel.

Table 1

Main technical parameters

Items	Values
Overall dimension (mm×mm×mm)	4476×3264×1678
Matched power (kW)	100
Mode of traction	Traction type
Operation width (mm)	2200
Total weight of machine (kg)	3150

Working principle

As shown in Figure 1, when field work is performed, the implement tow frame is connected to the tractor suspension. The output shaft behind the tractor is connected to the implement gearbox. The output shaft provides the power output, and the chain drive transfers the power to the film starting mechanism, the film disfilming mechanism, the conveyor chain active shaft, and the crushing roller. The membrane knife rotates into the soil and grabs onto the residual film in the soil tillage layer. When the film disfilm belt and the combing membrane knife reverse their respective rotations, Under the action of the film belt, the film soil mixture on the film knife can be thrown onto the conveying chain. The film-lifting device rotates clockwise, while the disfilm device rotates counterclockwise. Thus, with the help of the disfilm belt, the film-and-soil mixture is thrown via combing epidural knife onto the conveyor chain. Vibration wheel and the crushed soil roller vibrate the membrane soil mixture and break the soil. This, in turn, causes the membrane-earth separation. The residual film in the transport chain is accumulated in the film collection box. Hence, the recovery of the residual film is completed.

Design of key components

The starting membrane mechanism

The combing film mechanism is one of the key machine components, as shown in Figure 2. In order to prevent combs from being subjected to excessive instantaneous force, production of Soil accumulation due to rotation, membrane leakage or other phenomena, the comb arrangement requirements between the portrait and the landscape have to be met (Zhang et al.,2017). The combs are placed in a double helix arrangement, with the starting points being 180° apart. The two adjacent combs are spaced 60 mm apart in the axial direction with a total of 72 teeth. The two adjacent teeth are angled at 20°, and the film roll diameter is equal to 180 mm.

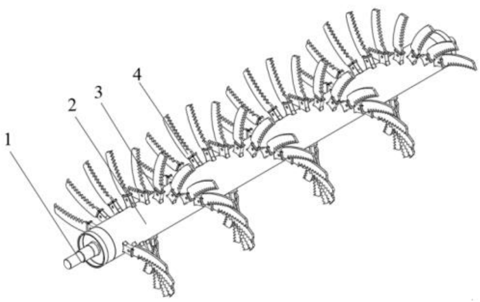

Fig. 2 - The filming mechanism

1) Filming axis; 2) Film roll; 3) Knife seat cover; 4) The membrane knife for combing

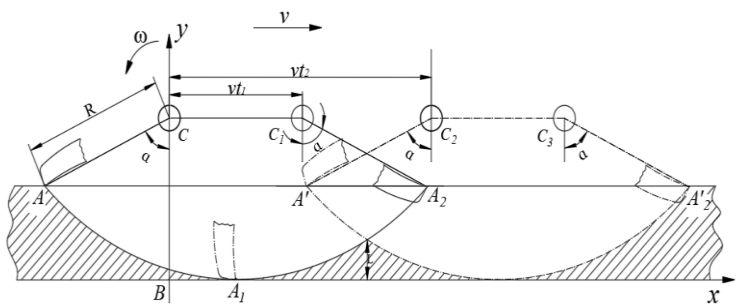

Fig. 3 - The motion trajectory of two adjacent combs

Leakage prevention conditions ensuring continuous operation

Film continuity during the implement operation should be ensured, while appearance of the tillage layer residual film leakage should be avoided. Thus, when a comb is unearthed, the adjacent combs simultaneously enter the soil film (*Wang et al., 2020*)**.** The motion trajectory of two adjacent combs is shown in Figure 3.

A to A_1 motion trajectory equation can be written as:

$$\begin{cases} x = vt + R\sin\omega t \\ y = R - R\cos\omega t \end{cases} \tag{1}$$

According to Eq. (1) and Figure 3:

$$\begin{cases} L = R(1-\cos(\alpha-\omega t)) \\ C_1C_2 = v(t_2-t_1) \end{cases} \tag{2}$$

Conversion to Eq. (2) is simplified as follows:

$$\begin{cases} t = \dfrac{t_1}{2} \\ C_1C_2 = v(t_2-t_1) \end{cases} \tag{3}$$

When A' and A_2 are simultaneously occurring, the membrane critical condition of the 3rd comb entering the soil is:

$$C_1C_2 = 2R\sin\alpha \tag{4}$$

The soil nature of the southern Xinjiang is mainly composed of sandy soil. According to the relevant data, the optimal seeding depth is equal to 30-40 mm. At this depth, both cotton seeding rate and quality are ideal. The root quality distributed at 0-100 mm depth accounts for more than 74.38%, the distribution depth of the seedling root system at 100-150 mm is beneficial to cotton production (Dong et al., 2013). In order to reduce the effect of residual film on development of the cotton root system, the film depth should meet the $R-L-R\cos\alpha>150$ criterion:

$$R-\left[R(1-\cos\frac{\omega t_1}{2})\right]-R\cos\alpha>150 \tag{5}$$

After meeting the requirements of cotton seeding and seedling development, conditions for residual film recovery and membrane leakage avoidance should be met:

$$\begin{cases} R(\cos\dfrac{\omega t_1}{2}+\cos\alpha)>150 \\ v(t_2-t_1)<2R\sin\alpha \end{cases} \tag{6}$$

where t_1 is time from the film knife entrance into the soil film until the unearthing point, s; Z represents the same circumferential membrane knife number; and $\theta=2\pi/z$ is the same circumferential membrane inter-tooth angle.

Then, for $t_3=2\pi/z\omega$ and $t_3=t_2-t_1$, Eq. (6) can be obtained:

$$\begin{cases} \cos\alpha>\dfrac{150}{2R} \\ \sin\alpha>\dfrac{\pi v}{z\omega R} \end{cases} \tag{7}$$

In Eqs. (2)-(7), C_1, C_2 is the centre of rotation of the comb teeth at different times; t_1 represents the time required for the membrane knife combing from A to A_2, s; t_2 represents the interval between the two adjacent combs entering the soil, s; and t_3 represents the time between the first and the last comb, s.

According to the prototype design structure, comb tooth film cutter gyration radius is equal to R = 375 mm. The residual film of the plough layer in the 0-200 mm cotton field is recovered. The comb tooth length is equal to 280 mm. Movement trajectory analysis of the combed film knife shows that the initial entry angle is α = 65.1°, and the number of the same circumferential film knife is Z = 2. According to the operating conditions of the residual film recovery tool, the operating speed of the set implement is 4-6 km/h (1.11-1.67 m/s). According to Eq. (7), ω>5.6 rad/s. In other words, the speed is greater than 54 r/min.

According to the aforementioned results, it can be seen that a decrease in the film roll speed results in a decrease of the film starting efficiency. If the film roll speed is relatively fast, film combing process will cause residual film destruction. According to the theoretical calculation and the actual film-starting effect in the field, it is determined that the starting film roller speed should be 100 r/min, which meets the film-starting requirements.

Stripping mechanism

Plough layer residual film geometric shapes and sizes are different. In order to ensure smooth removal of the film, the stripping mechanism is designed. It is mainly composed of the stripping roller, the stripping belt, and the reinforcing rib of the fixed plate. The film removal mechanism is shown in Figure 4.

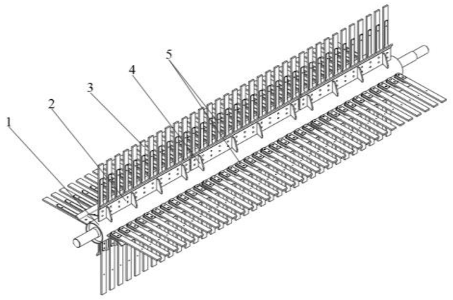

Fig. 4 - Demoulding mechanism
1) Stripping roller; 2) Strip fixed plate 3) Stripping belt; 4) Reinforcing rib of the fixed plate; 5) Belt pallet

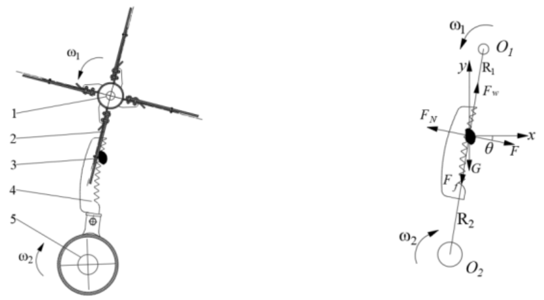

a b

Fig. 5 - Residual film instantaneous stress analysis diagram
1) Stripping roller; 2) Stripping belt; 3) Membrane soil mixture; 4) The membrane knife for combing; 5) Film lifting roller

Disfilming process analysis

In order to ensure the membrane disfilming effect, a step-by-step disfilming method is employed. This can reduce the residual membrane movement travel and damage. Thus, according to the disfilm condition analysis, for each turn of the film teeth, the film belt is guaranteed to hang with the film teeth at least 2 times (*Xie et al., 2019*). Residual membrane transient force analysis diagram is shown in Figure 5.

During operation, the stripping mechanism rotates counterclockwise. The influence of the electrostatic adsorption can be neglected during the stripping process. Thus, the residual film can be smoothly removed from the film lifting teeth if the centrifugal force provided by the stripping belt is greater than that of the film lifting teeth on the residual film (*Li et al., 2012*). Therefore, the condition of the film removal is as follows:

$$\begin{cases} F_w > F_f + G\cos\theta \\ F > F_N \end{cases} \tag{8}$$

$$F_w = \frac{mv^2}{R_1} \tag{9}$$

$$G = mg \tag{10}$$

By simplifying Eq. (8), Eq. (11) is obtained:

$$v_1 > \sqrt{\frac{(F_f + mg\cos\theta)R_1}{m}} \tag{11}$$

where F_f is the comb teeth force on the residual film, N; F is the residual film stripping belt force, N; F_N is the comb teeth supporting force on the residual film, N; m is the mass of the residual film on the comb teeth, Kg; g is the acceleration due to gravity, N; θ is the angle between the stripping force and the horizontal direction, °; and R_1 is the simplified radius of the release roller, m.

Since the F_f direction points towards the centre of the film roll, 1 mg is taken to test F_f. In order to increase the number of contact points between the stripping belt and the comb teeth, the $\omega_1 > k\ \omega_2$ requirement has to be met. In this paper, parameter k is taken as 2. Parameter ω_1 is the angular velocity of the stripping roller, while ω_2 is the angular velocity of the film lifting roller. According to the film roller speed, it can be seen that when ω_1 is 21 rad/s, the film release requirements are met.

Working performance test

Test conditions

In order to verify the operating performance of the 4SGMS-220 residual film recovery machine, the prototype was trial-produced and field tested in November of 2019. The test site was the 8th company of the 10th Regiment of the First Division of Xinjiang Production and Construction Corps. The test field was mainly composed of the sandy loam with continuous film coating. The cotton field area was approximately 3 hm^2, the film thickness was 0.01 mm, the soil moisture content of the cotton field was 17.6-21.4%, the soil firmness was 28 kg/cm^2, and the wind speed was 1.9 m/s. The test is shown in Figure 6, and the power was provided by Dongfanghong 1504.


Fig. 6 - Field trial

Determination of test indicators

The test indicators are based on the relevant requirements in the national standards GB/T 25412-2010 "Residual Plastic Film Recovery Machine" and GB/T 25413-2010 "Farmland Plastic Film Residue Limits and Determination".

The selected test response indicators are the residual film recovery rate p_1, and the residual film impurity rate p_2, which are used to express the efficiency of the machine tool:

$$p_1 = \frac{M_0 - M_1}{M_0} \times 100\% \quad (12)$$

$$p_2 = \frac{G_1 - M}{G_2} \times 100\% \quad (13)$$

where:

M_0 is the residual amount of the plastic film prior to the test, Kg; M_1 is the residual amount of the mulching film after the test, Kg; G_1 is the mass of the residual film and cotton stalk mixture after the test, Kg; M is the weight of the residual film in the mixture, Kg; and G_2 is the weight of all cotton stubble in the test area, Kg.

Experimental design

17 test areas were selected in the test field of 10 groups and 8 companies, with a single area equal to 2.4 m×50 m. The selected machine travel speed A, film take-up roller speed B, and the comb tooth penetration depth C are taken as the influencing factors. The residual film recovery rate p_1 and the residual film impurity rate p_2 are employed as the test indicators. The experimental design is conducted via Design-Expert software Box-Behnken. Three-factor three-level response surface analysis method is employed. A total of 17 sets of experiments were carried out, and the residual film recovery rate and impurity rate were obtained. The test factor level table is shown in Table 2, while the result is presented in Table 3.

Table 2

Test factor level table

Level	Factor		
	Machine travel speed A (km/h)	**Film take-up roller speed B (r/min)**	**Comb tooth penetration depth C (mm)**
1	3	90	120
0	4	100	150
-1	5	110	180

RESULTS AND DISCUSSION

Table 3 data is analysed via data analysis function in Design-Expert software. The variance analysis of the residual film recovery rate and the residual film impurity rate is shown in Table 4.

The results indicate that the model is extremely significant if p < 0.0001, whereas lack of fit is achieved if p > 0.0001. This indicates that the regression model of the residual film recovery rate and the impurity rate has a high degree of fit with experimental results.

Test results

Table 3

Test results

Serial number	Test factor level table: Machine travel speed A (km/h)	Film take-up roller speed B (r/min)	Comb tooth penetration depth C (mm)	Response index: Residual film recovery rate p1/%	Residual film impurity rate p2/%
1	-1	0	-1	68.6	6.3
2	0	1	1	75	9.6
3	0	0	0	75.3	7.3
4	0	0	0	75.6	7.2
5	-1	1	0	73.8	7.4
6	0	0	0	75.4	7.1
7	1	1	0	74.3	8.1
8	-1	-1	0	69.5	7
9	0	-1	-1	67.7	6.7
10	-1	0	1	72.6	9.2
11	0	-1	1	73.3	8.8
12	0	0	0	74.9	6.9
13	0	0	0	75.1	7
14	1	-1	0	72.1	7.8
15	1	0	1	73.5	9.8
16	0	1	-1	73.8	6.8
17	1	0	-1	72.1	6.5

According to the data sample in Table 4, three selected factors have an interactive effect. According to the software Design-Expert, multiple regression equation fitting is developed to establish the travel velocity of the machine, the rotational speed of the film roll, and the depth of the comb tooth which affects the residual film. The regression equations of the recovery rate p_1 and the residual film impurity rate p_2 are:

$$p_1 = 75.26 + 0.98A + 1.79B + 1.49C - 0.52AB - 0.73AC - 1.10BC - 1.76A^2 - 10.8B^2 - 1.73C^2 \quad (14)$$

$$p_2 = 7.10 + 0.29A + 0.20B + 1.39C - 0.025AB + 0.1AC + 0.17BC + 0.22A^2 + 0.25B^2 + 0.63C^2 \quad (15)$$

Table 4

Regression model analysis of variance table

Index	Source	Sum of Squares	df	Mean Square	F Value	P-value Prob >F	Significance
Residual film recovery rate	Model	92.77	9	10.31	60.92	< 0.0001	**
	A	7.61	1	7.61	44.94	0.0003	**
	B	25.56	1	25.56	151.06	< 0.0001	**
	C	17.7	1	17.7	104.61	< 0.0001	**
	AB	1.1	1	1.1	6.52	0.038	*
	AC	2.1	1	2.1	12.43	0.0097	**
	BC	4.84	1	4.84	28.6	0.0011	**
	A^2	12.97	1	12.97	76.64	< 0.0001	**
	B^2	4.91	1	4.91	29.02	0.001	**
	C^2	12.6	1	12.6	74.47	< 0.0001	**
	Residual	1.18	7	0.17			
	Lack of Fit	0.89	3	0.3	4.08	0.1041	
	Pure Error	0.29	4	0.073			
	Cor Total	93.96	16				
Residual film impurity rate	Model	18.85	9	2.09	38.83	< 0.0001	**
	A	0.66	1	0.66	12.26	0.01	**
	B	0.32	1	0.32	5.93	0.045	*
	C	15.4	1	15.4	285.59	< 0.0001	**
	AB	0.0025	1	0.0025	0.046	0.8357	
	AC	0.04	1	0.04	0.74	0.4176	
	BC	0.12	1	0.12	2.27	0.1755	
	A^2	0.21	1	0.21	3.95	0.0871	
	B^2	0.26	1	0.26	4.88	0.0629	
	C^2	1.64	1	1.64	30.5	0.0009	**
	Residual	0.38	7	0.054			
	Lack of Fit	0.28	3	0.093	3.7	0.1193	
	Pure Error	0.1	4	0.025			
	Cor Total	19.22	16				

Note: P<0.05(significant)/P<0.01(extremely significant**)*

Influence of various factors on recovery rate of the residual film

According to Figure 7a, when the comb tooth penetration depth of 150 mm is achieved, as the traveling speed of the machine and the rotational speed of the film roll increase, the residual film recovery rate first increases and then decreases. This can be observed from the contour plan. As a result, film pick-up roller velocity forms a non-linear relationship with the operating speed of the machine. When the travel speed of the machine is 4 km/h and the film pick-up roller speed is 100 r/min, optimal residual film recovery effect is achieved. When the machine travel velocity and the film take-up roller velocity continue to increase, the relationship between the linear velocity of the comb tooth tip on the film take-up device and the machine travel velocity cannot be satisfied. Hence, the residual film cannot be continuously applied when the film is captured, resulting in residual film pickup rate being reduced.

It can be seen from Figure 7b that when the comb tooth filming speed is determined, as the comb tooth depth increases from 120 mm to 180 mm and the machine travel speed increases from 3 km/h to 4 km/h. The recovery rate of residual film showed a slight change trend of first increase and then decrease. As the depth of the comb tooth penetration and machine travel speed increase simultaneously, the recovery rate of the residual film increases first and then decreases. This is due to the increase in the working depth, which increases the amount of residual film and improves the interaction between the comb teeth and the residual film. The force continues to increase, and as the traveling speed increases, the residual film is broken during the film formation process. This, in turn, increases the difficulty of recovering the residual film.

According to Figure 7c, when the filming device speed is less than 110 r/min and the comb tooth penetration depth increases from 120 mm to 180 mm, the residual film recovery rate shows an initial increasing trend which then decreases. Generally, as the film roll speed and comb tooth penetration depth increase simultaneously, the residual film recovery rate first increases and then decreases. This is due to the linear speed increase in the filming device and the filming depth. The amount of the residual film on the plough layer increases, and the film cannot be lifted to successfully throw the residual film onto the conveying device, resulting in a decrease in the recovery rate of the residual film.

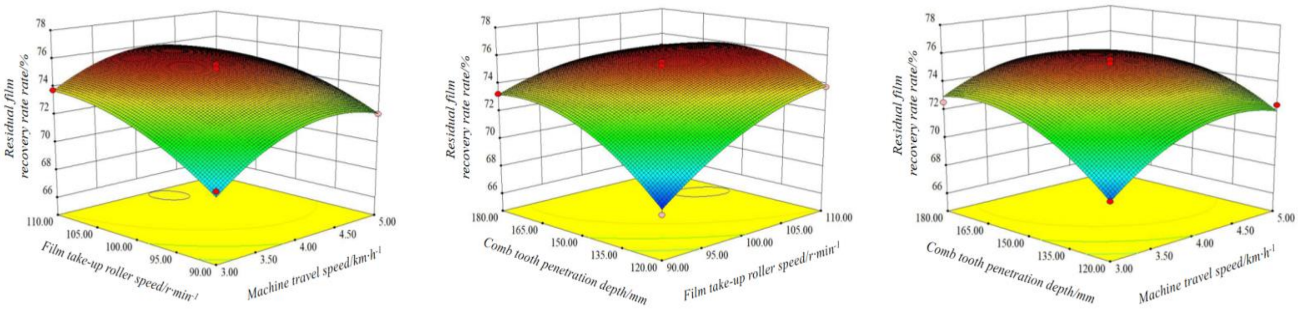

a) b) c)

Fig. 7 - Influence of various factors on recovery rate of the residual film

Influence of various factors on impurity rate of the residual film

According to Figure 8a, when the machine tool comb tooth penetration depth is determined, as the machine travel speed and the film roll speed increase, the residual film content first decreases and then slightly increases. When the machine travel speed is 4 km/h and the film-forming roller speed is 100 r/min, the residual film impurity rate is the lowest.

According to Figure 8b, when the rotational speed of the film roll is determined, the impurity content of the residual film first gradually increases with the increase of the soil penetration depth and the traveling speed of the machine. When the comb tooth penetration depth is greater than 144 mm, the impurity rate increase of the residual film is obvious. For the traveling speed of the machine equal to 3 km/h and the comb tooth depth of 120 mm, the residual film impurity rate is the lowest. In general, the residual film impurity rate increases with an increase in the comb tooth penetration depth and the machine travel speed. With the continuous increase in the soil depth and the machine traveling speed, the mixture of membrane impurities also increases. This results in a gradual increase in the impurity rate of the residual membrane.

According to Figure 8c, when the tool travel speed is determined, as the depth of the comb teeth increases, the impurity rate of the residual film also demonstrates a gradual increase trend. When the comb tooth penetration depth is less than 132 mm, with an increase in the rotational speed of the filming device, the residual film impurity rate will first slowly decrease and then slightly increase.

The rotational machine speed is 90 r/min in the filming device, and the comb tooth penetration depth is equal to 120 mm. Here, the residual film contains the smallest impurity rate. Generally speaking, the impurity rate of the residual film increases with an increase in the comb teeth depth and the rotational speed of the film roll. This is because an increase in the soil penetration depth causes an increase in the content of the impurity mixture. Furthermore, the rotational speed of the film forming roller increases, which consequently increases the contact frequency of the tooth and the impurity mixture. Lastly, this increases the impurity mixture from the farmland. Because of the inability of timely filtration, this leads to an increase in the impurity rate of the residual film.

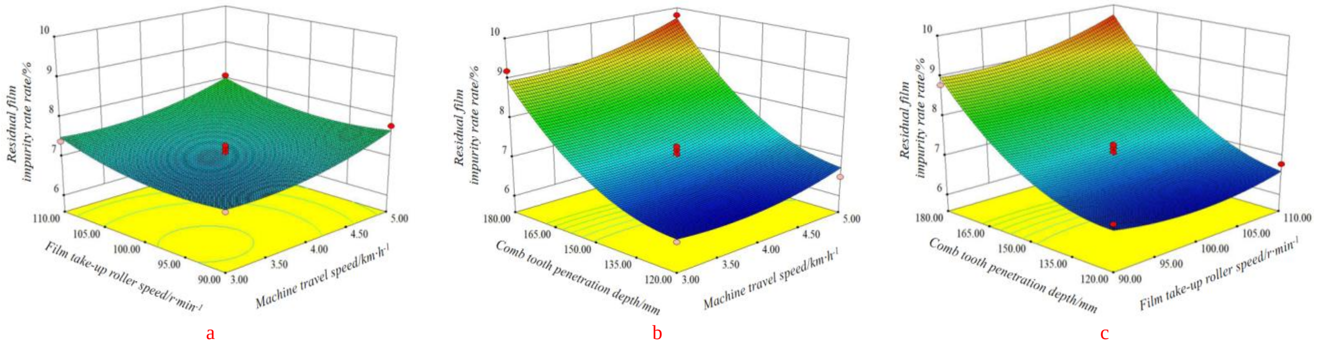

Fig. 8 - Influence of various factors on the impurity content of the residual film

Parameter optimization and experimental validation

In order to improve the recovery rate and reduce the impurity rate of the residual film, the Optimization function in Design-Expert is used to optimize the solution. The following optimal parameters are obtained: the machine traveling speed of 4.1 km/h, the film roll speed of 106 r/min, and the comb tooth penetration depth of 139.2 mm. For these parameters, the recovery rate of the residual film is 75.5%, and the impurity rate of the residual film is 6.88%.

In order to ensure the practicability of the optimized parameters, they are utilized for validation tests. The film roll rotational speed of 106 r/min, and the comb tooth penetration depth of 139.2 mm are employed. The recovery rate of the residual film is equal to 74.32%, which is 1.18% lower than the theoretically optimized value. The impurity content of residual film is 7.11%, which is lower than the theoretical optimization value of 2.3%. By comparing the field test results with the predicted results, it can be concluded that negligible difference between the results exists. Therefore, the optimization model is reliable. Optimization results can be used for the selection of optimal operating parameters of the comb-type plough layer residual film recovery machine.

CONCLUSIONS

Aiming at the difficulty of recovering the residual film of the cultivated layer in Xinjiang, a comb-type residual film recovery machine of the cultivated layer was developed, and the feasibility of the machine was verified through field experiments. Studies have shown that the main factor that affects the recovery rate of residual film is the rotation speed of the film pick-up roller, and the main factor that affects the film impurity rate is the depth of comb teeth into the soil. Use Design-Expert software Box-Behnken optimization module to optimize the parameters, and get the best operating parameters as follows: machine travel speed 4.1km/h, film roll speed 106r/min, comb tooth depth 139.2mm, field test verification, residual film recovery rate is 74.32%, and the residual film impurity rate is 7.11%. The optimized model is reliable and meets the operating requirements of the plough layer residual film recovery machine. This study provides a theoretical reference for the research and development of the residual film recovery machine in Xinjiang.

ACKNOWLEDGEMENT

The work was supported by the National Natural Science Foundation of China, under the Grant No.11562019, and the Major Scientific and Technological Projects of the Corps, under the Grant No.2018AA001/03, and the Corps Key R&D Projects, under the Grant No.2019AB007.

REFERENCES

[1] Dong, H., Liu, T., Li, G. et al, (2013), Effects of plastic film residue on cotton yield and soil physical and chemical properties in Xinjiang, *新疆棉田地膜残留对棉花产量及土壤理化性质的影响*, *Transactions of the Chinese Society of Agricultural Engineering*, vol. 29, no. 5, pp. 91-99. Beijing/China;

[2] Han, Y., Xie, J., Yang, Y. et al, (2021). Design and Test of Pick-up Mechanism of Nail Tooth Rolling Type Residual Film Recovery Machine, *Journal of Agricultural Mechanization Research*, vol. 43, no. 7, pp. 73-78, Heilongjiang/China;

[3] Hu, C., Wang, X., Chen, X. et al, (2019), Current situation and control strategies of residual film pollution in Xinjiang, *新疆农田残膜污染现状及防控策略*, *Transactions of the Chinese Society of Agricultural Engineering*, vol. 35, no. 24, pp. 223-234. Beijing/China;

[4] Jiang, D., Chen, X., Yan, L. et al, (2019), Design and Experiment on Spiral Impurity Cleaning Device for Profile Modeling Residual Plastic Film Collector, *随动式残膜回收螺旋清杂装置设计与试验*, *Transactions of the Chinese Society for Agricultural Machinery*, vol. 54, no. 4, pp. 137-145. Beijing/China;

[5] Li, B., Wang, J., Hu, K., & Jiang, B. (2012). Analysis and test of forward film removing mechanism for polythene film collector, *残膜回收机顺向脱膜机理分析与试验*, *Transactions of the Chinese Society of Agricultural Engineering*, vol. 28, no. 21, pp. 23-28. Beijing/China;

[6] Li, H., Li, S., Nan, L., et al, (2017), Meta-analysis of Effect of Plastic Film Mulching on Cotton Yield in China, *中国棉花地膜覆盖产量效应的Meta 分析*, *Transactions of the Chinese Society for Agricultural Machinery*, vol. 48, no. 7, pp. 228-235. Beijing/China;

[7] Lin, T., Tang, Q., Hao, W. et al, (2019), Effects of plastic film residue rate on root zone water environment and root distribution of cotton under drip irrigation condition, *地膜残留量对棉田土壤水分分布及棉花根系构型的影响*, *Transactions of the Chinese Society of Agricultural Engineering*, vol. 35, no. 19, pp. 117-125. Beijing/China;

[8] Liu, J., Zhang, X., Jin, W. et al, (2019), Design and Experimental Study on Membrane-earth Separation Device of Sprocket Residue Membrane Recovery Machine, *链齿式残膜回收机膜土分离装置的设计及试验研究*, *Journal of Agricultural Mechanization Research*, vol. 49, no. 9, pp. 110-114+141, Heilongjiang/ China;

[9] Liu, X., Yin, T., Li, Y. et al, (2020), Pollution of Plastic Film Residue in Xinjiang Under Different Agricultural Practice Systems, *新疆地区不同农田管理模式的残膜污染现状*, *Chinese Agricultural Science Bulletin*, vol. 36, no. 31, pp. 65-70 Beijing/China;

[10] Luo, K., Yuan, P., Jin, W., et al, (2018), Design of chain-sieve type residual film recovery machine in plough layer and optimization of its working parameters, *链筛式耕层残膜回收机设计与工作参数优化试验*, *Transactions of the Chinese Society of Agricultural Engineering*, vol. 34, no. 19, pp. 19-27. Beijing/China;

[11] Sun, Y., Jian, J., Tian, Y. et al, (2018), Analysis and Experiment of Filming Mechanism of Rotary Film-l ifting Device of Residual Film Recycling Machine, *残膜回收机旋转式起膜装置起膜机理分析与试验*, *Tra nsactions of the Chinese Society for Agricultural Machinery*, vol. 49, no. S1, pp. 304-310. China;

[12] Wang, Y., Zhao, W., Liu, X., et al, (2020), Improved Design and Experiment of Collector for Corn Whole Plastic Film Mulching on Double Ridges, *玉米全膜双垄沟残膜回收机优化设计与试验, Transactions of the Chinese Society for Agricultural Machinery*, vol. 52, no. 1, pp. 119-128. Beijing/China;

[13] Xie, J., Duan, W., Zhang, F., & Tang, W., (2019). Design and high-speed photography test of pole-tooth film-unloading Mechanism, *杆齿式卸膜机构的设计及高速摄像试验*, *Journal of Machine Design*, vol. 36, no. 5, pp. 60-64. Tianjin/China;

[14] Ye, Z., Bai, X., & Chen, B, (2020). Effects of different years of continuous cropping on cotton root morphology and yield, *Agricultural Research in the Arid Areas*, vol. 38 no.2, pp.135-141. Shanxi/China;

[15] Zhang, X., Bi, X., Wang, Z., et al, (2017), The Design and Research of Key-parts of Spiked Tooth Plastic Film Residue Recovery, Journal of Agricultural Mechanization Research, vol. 39, no. 10, pp. 72-76. Heilongjiang/China.

[16] Zhao, Y., Chen, X., Wen, H., et al, (2017), Research Status and Prospect of Control Technology for Residual Plastic Film Pollution in Farmland, *农田残膜污染治理技术研究现状与展望*, Transactions of the Chinese Society for Agricultural Machinery, vol. 48, no. 6, pp. 1-14. Beijing/China.

EXPERIMENTAL STUDIES ON A PLOW WITH A DISK DISINTEGRATOR
/
ЕКСПЕРИМЕНТАЛЬНІ ДОСЛІДЖЕННЯ ПЛУГА З ДИСКОВИМ ПОДРІБНЮВАЧЕМ

Golub G.A.[*1)], Marus O.A.[1)], Skorobogatov D.V.[2)], Yarosh, Y.D.[3)], Karpiuk N.A.[3)], Chuba V.V.[1)]
[1)] National University of Life and Environmental Sciences of Ukraine, Kyiv / Ukraine;
[2)] State Agrarian and Engineering University in Podilia, Kamianets-Podilskyi / Ukraine;
[3)] Polissia National University, Zhytomyr / Ukraine.
Tel: +380953115050; E-mail: gagolub@ukr.net
DOI: https://doi.org/10.35633/inmateh-64-32

Keywords: *plough, disk disintegration, disk approach angle, disk installation height, operating speed*

ABSTRACT
Studies were conducted on the operation of a plow with a disk disintegrator in a unit with an MTZ-82 tractor on black soil with a flat relief on soybean stubble with the amount of plant residues from 300 to 400 g/m^2. During the research, the following parameters were changed: the disk approach angle, the disk section installation height, and the tractor speed. As a result of the study, it was found that at the speed of a plow with a disk disintegrator from 4 to 5 km/h, the depth of plant residues embedding *is maximum and ranges from 15 to 19 cm, while fuel consumption becomes minimal in the range from 18 to 30 kg/ha.*

ABSTRACT
Були проведені дослідження роботи плуга з дисковим подрібнювачем в агрегаті з трактором МТЗ-82 на чорноземному ґрунті з рівним рельєфом по стерні сої при кількості рослинних решток від 300 до 400 г/м^2. При проведенні досліджень змінювали наступні параметри: кут атаки дисків, висоту установки дискової батареї та швидкість руху трактора. У результаті дослідження встановлено, що при швидкості руху плуга з дисковим подрібнювачем від 4 до 5 км/год глибина зароблянння рослинних решток є максимальною і знаходиться в межах від 15 до 19 см при цьому витрати палива набувають мінімального значення в межах від 18 до 30 кг/га.

INTRODUCTION
The use of green manure crops as green organic fertilizers is a widespread agrotechnical measure. Research by scientists has shown that the use of green manure crops leads to an increase in the amount of organic substances in the soil, an improvement in the physical, chemical and biological state of the soil, resulting in an increase in the yield of field crops *(Zhang et al, 2007; Saikia et al, 2019; Israr Khan et al, 2020)*. Studies are also known to determine the effect of green manure and rice straw on rice production *(Zhou et al, 2020)*. Five different types of combinations of their use were applied: no fertilizer; chemical fertilizer; chemical fertilizer plus green manure; chemical fertilizer plus rice straw; chemical fertilizer plus green manure and rice straw. The results of these studies showed that the use of chemical fertilizers and green manure increased rice yields by 4.1%, chemical fertilizers and rice straw by 4.7%, chemical fertilizers, green manure and rice straw by 9.6% when compared to chemical fertilizers. The results of studies (*Nazmus et al, 2013)* showed that the highest yield of corn was with deep embedding of green manure (20-25 cm) compared to the average depth of soil cultivation (10-12 cm) and the minimal one. The *authors (Astier et al, 2006)* conducted studies to determine the effect of using green manure crops (vetch) on the absorption of phosphorus and nitrogen by corn, which showed that the absorption of these substances was better when wrapping green manure in the soil compared to its surface mulching. Therefore, we can conclude that the depth of embedding of green manure crops affects their efficiency of use. The use of plowing when wrapping green manure crops will not allow this process to be carried out as efficiently as possible, depending on the crop and its overall parameters. Therefore, in order to perform a high-quality operation of embedding green manure crops in the soil, they must first be disintegrated (mulched), and then embedded. Step-by-step execution of disking and plowing operations requires high fuel consumption, so the combination of two operations when wrapping green manure crops is very relevant.

Without conducting experimental studies, it is impossible to objectively determine the parameters of working bodies for tillage. The study of the mutual influence of a disk disintegrator, ensuring the green manure stalks disintegration, and a plow on the quality of plant residues embedding and fuel consumption is one of the urgent tasks.

A significant number of publications have been devoted to substantiating the parameters of disks for surface tillage and plows for plowing *(Sineokov et al, 1977; Strelbitsky, 1978; Tsimmerman, 1978; Dubrovin et al, 2007; Kogut et al, 2016)*. A significant part of these works is devoted to the study of the influence of changes in the parameters of the working bodies of machines or the positional parameters of their installation on the quality of tillage, plant residues embedding, fuel consumption *(Zeng and Chen, 2018; Golub et al, 2019; Upadhyay and Raheman, 2018, 2020)*, as well as the dependence on the type of soil *(Gangwar et al, 2006)*. Of interest are combined units that make it possible to reduce the number of passes of equipment through the field by 1.5-2 times, preserve moisture, and reduce the time required to perform technological operations during periods of limited agrotechnical time *(Dubrovin et al, 2004)*. As for combined units for soil plowing, their share in the market of agricultural machinery in Ukraine is still insignificant. At the same time, they require research to determine the quality of plant residues embedding and fuel consumption, since the combination of a plow with a disk disintegrator significantly affects these indicators.

The purpose of the research is to experimentally determine the quality of plant residues embedding and fuel consumption when embedding plant residues of green manure and energy close-growing crops using a plow with a disk disintegrator.

Fig. 1 - Plow with disk disintegrator in operation

MATERIALS AND METHODS

Field studies of a plow with a disk disintegrator (conventional brand PLN-3-35D) in a unit with an MTZ-82 tractor (fig. 1) was carried out on black soil with a flat relief on soybean stubble with the amount of plant residues from 300 to 400 g/m^2 and the initial surface undulation – from 4 to 5 cm.

The layout parameters of the plow with a disk disintegrator had the following values: working width – 1,050 mm; working width of the body 350 mm; and in the longitudinal-vertical plane – 800 mm, the distance from the disk disintegrator to the point of the rear body – 1,300 mm.

The main design parameters of the working bodies of the disk disintegrator: working width 950 mm (with the disk approach angle of 32 deg.); limits for changing the disk approach angle from 24 to 41 deg., the diameter of the disks is 450 mm; the pitch between the disks is 140 mm.

The installation height of the disk section in relation to the plow point could vary from 20 to 80 cm. At the same time, the depth of tillage increased from 15 to 23 cm when the approach angle of the disk section changed from 24^0 to 32^0. This is due to the fact that the plow body was deepened until the depth force of the disks was balanced with the depth force of the plow bodies. The value intervals and levels of variation of factors are shown in table 1.

Table 1

Value intervals and levels of factors variation

Factor name	Factor levels			Variation intervals
	-1	0	+1	
Disk approach angle, deg.	24	28	32	4
Disk installation height, cm	20	50	80	30
Operating speed, km/h	2	4	6	2

Statistical processing of experimental results was carried out using well-known methods with an assessment of the uniformity of variances according to the Cochrane criterion, an assessment of the significance of regression coefficients according to the Student criterion, and an assessment of the adequacy of the regression equation according to the Fischer criterion (*Golub et al, 2018*).

When embedding green manure and plant residues of energy crops, disk-working bodies disintegrated the stems, loosened the soil, and mixed the disintegrated plant residues with the soil. The plow carried out their final embedding in the soil.

RESULTS

As a result of the implementation of the factor experiment according to the *D*-optimum Box-Behnken second-order design, data were obtained that characterize the depth of plant residues embedding and fuel consumption from the design and technological parameters of a plow with a disk disintegrator: the disk approach angle, the height of installation of disks and the speed of movement of a plow with a disk disintegrator. The average values of the studied ones obtained as a result of the experiment plan implementation, based on three repetitions, are shown in table 2.

Table 2

Results of experimental studies of the unit

Factors			Average values	
disk approach angle, deg.	disk installation height, cm	operating speed, km/h	depth of plant residues embedding, cm	fuel consumption, kg/ha
32	80	4	18	29.38
24	20	4	14	15.90
32	20	4	12	22.05
24	80	4	12	23.39
32	50	6	14	26.73
24	50	2	15	27.88
32	50	2	19	25.09
24	50	6	14	19.64
28	80	6	11	30.76
28	20	2	15	22.45
28	80	2	13	31.98
28	20	1	12	18.51
28	50	4	18	23.15
28	50	4	18	23.15
28	50	4	18	23.15

Processing of experimental data using standard machine software allowed obtaining the following second order mathematical models for each of the response functions:

$$h_P = -23.7917 + 2.1042\,\alpha - 0.1042\,h_D + 6.3542\,v - 0.0391\,\alpha^2 - 0.0038\,h_D^2 - 0.4688\,v^2 + 0.0167\,\alpha\,h_D - 0.125\,\alpha\,v + 0.0042\,h_D\,v; \quad (1)$$

$$q = 13.0999 + 2.016\,\alpha + 0.0817\,h_D - 14.8773\,v - 0.0486\,\alpha^2 + 0.0003\,h_D^2 + 0.6156\,v^2 - 0.0003\,\alpha\,h_D + 0.3089\,\alpha\,v + 0.0114\,h_D\,v; \quad (2)$$

where h_P – depth of plant residues embedding, [cm];

q – fuel consumption when operating a plow with a disk disintegrator, [kg/ha];
α – disk approach angle, [deg.];
h_D – disk installation height, [cm];
v – operating speed of the plow with a disk disintegrator, [km/h].

The study of the influence on the plant residues embedding depth of the disk approach angle and the height of disks installation and the speed of movement of a plow with a disk disintegrator is shown in Figs. 2, 3, 4. The quality of plant residues embedding depends on the dimensional parameters of their disintegration, as stated in some studies, which determined the dependence of wheat straw length (which varied from 130 to 230 mm in 20 mm increments) on the depth of its embedding in the soil of *(Fang et al, 2016)*. These studies have shown that as the length of plant residues decreases, the quality of embedding increases.

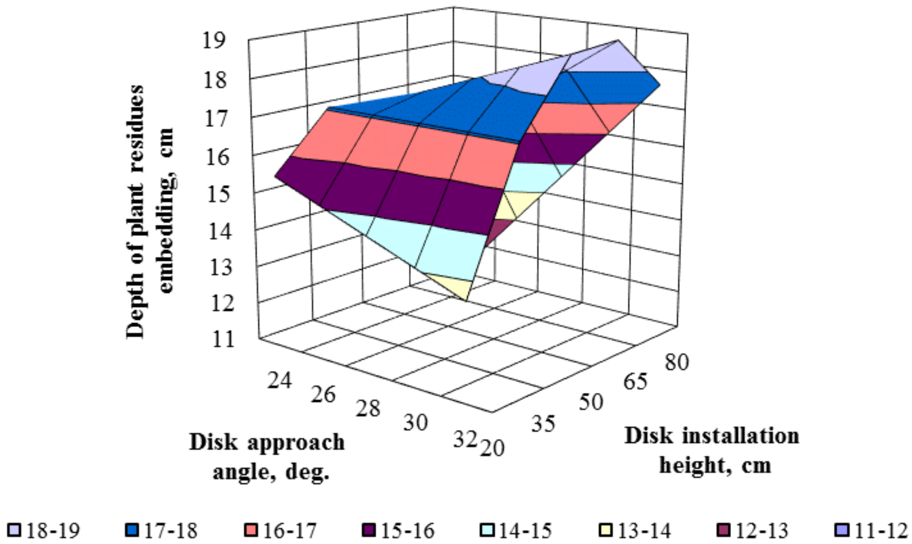

Fig. 2 - Influence of the disk approach angle and the height of disks installation on the depth of residues embedding using a plow with a disk disintegrator

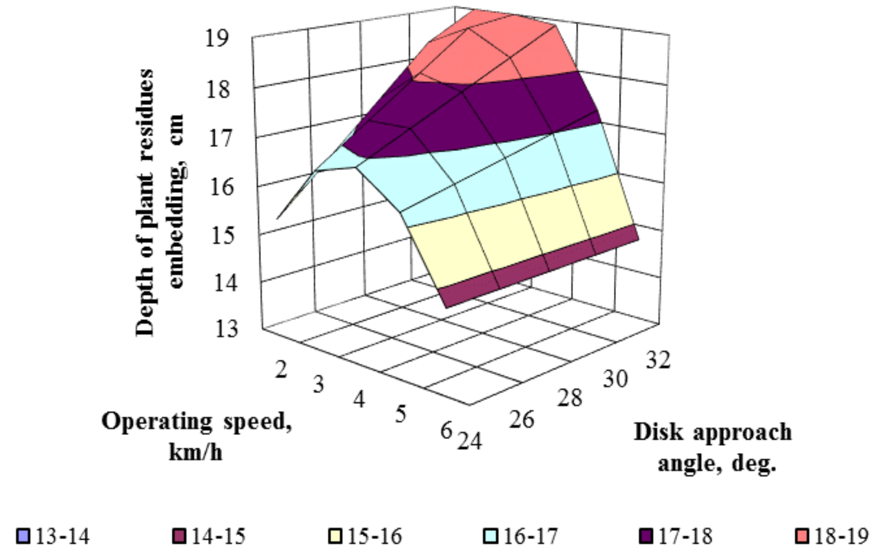

Fig. 3 - Influence of the disk approach angle and operating speed on the depth of residues embedding using a plow with a disk disintegrator

It is established that the depth of plant residues embedding is most affected by the height of the disk installation and the operating speed of the plow with a disk disintegrator. Some studies indicate that the quality of plant residues disintegration depended more on the operating speed and disk approach angle than on the depth of tillage, since the depth of tillage was relatively small – from 5 cm to 8 cm *(Damanauskas et al, 2019).*

Processing was carried out on loamy and clay-loamy soils. In our research, it was also found that at a low operating speed and a small disk approach angle, the level of quality of plant residues embedding was of poor quality – most of all plant residues were still on the surface, while when cultivating soil with a high operating speed and a large disk approach angle, plant residues disappeared from the soil surface.

With an increase in the installation height of the disk section in relation to the plow point, the depth of plant residues embedding increases. Thus, when the installation height of the disk section in relation to the plow point is from 40 to 60 cm, the depth of plant residues embedding is maximum and is from 17 to 19 cm. This is due to the fact that the plow body attracts a larger volume of soil when deepened. In the future, the trashboard comes into operation, which is equipped with a plow blade and the operation of which makes it possible to change the flight path of the upper soil layer where plant remains are concentrated.

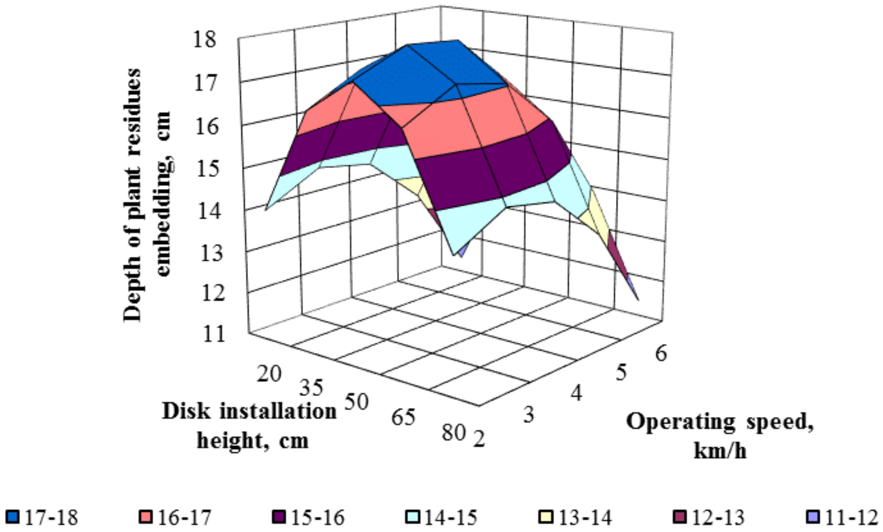

Fig. 4 - Influence of the operating speed and the height of disk installation on the depth of residues embedding using a plow with a disk disintegrator

Plant residues from the upper soil layer can be directed along three possible trajectories. The first is when the residues are placed on the slope of the previous furrow, the second is when the residues enter the bottom of the furrow, and the third is when the residues are placed on the slope of the newly formed furrow. The best option for the trajectory is the one when the residues lie on the bottom of the furrow.

The operating speed of a plow with a disk disintegrator ambiguously affects the depth of plant residues embedding, which is associated with the possible trajectories of their movement when descending from the trashboard. This is due to the influence of the operating speed of the plow with a disk disintegrator on the absolute speed of descent of plant residues from the trashboard, and, accordingly, their laying, either on the bottom of the furrow, or beyond it. The maximum depth of plant residues embedding is from 17 to 19 cm at the operating speed of the unit from 3 to 4 km/h.

Researchers *Liu et al (2010)* determined the effect of the tillage rate on the production of plant residues depending on their length, which varied from 60 to 250 mm. The obtained results showed that an increase in the length of plant residues leads to a decrease in the quality of their embedding, but with an increase in the speed of tillage, the quality of plant residues embedding increases too.

Studies of the influence of factors on fuel consumption during the operation of a plow with a disk disintegrator have shown (figs. 5, 6, 7) that it is partially affected by the disk approach angle. Thus, when the installation height of the disk section in relation to the plow point is 50 cm, fuel consumption ranges from 20 to 24 kg/ha while the disk approach angle changes from 24^0 to 32^0.

When the installation height of the disk section increases in relation to the plow point from 20 to 80 cm, fuel consumption increases from 16 to 29 kg/ha. The paper written by *Damanauskas et al. (2019)* also notes that hourly fuel consumption increases due to an increase in the disk approach angle, the depth of tillage, and the operating speed of the disk harrow. Similar studies have also been conducted which noted that fuel consumption increases due to an increase in disk approach angle, but decreases with operating speed increase *(Damanauskas, 2019)*. The operating speed of a plow with a disk disintegrator has an ambiguous effect on fuel consumption, which is associated with fuel overspending at low operating speeds and an increase in energy consumption when operating at high speeds.

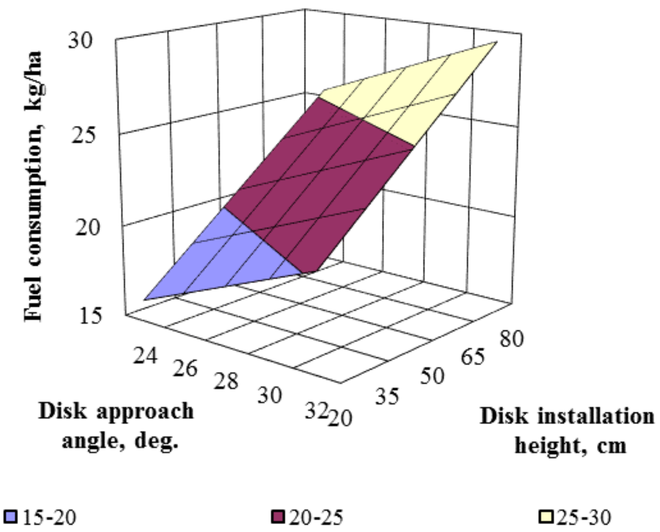

Fig. 5 - Influence of the disk approach angle and the height of the disk installation on fuel consumption when operating a plow with a disk disintegrator

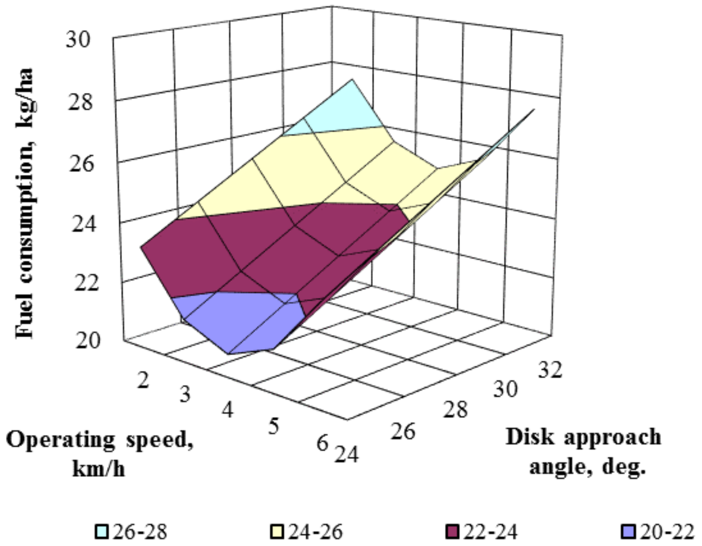

Fig. 6 - Influence of disk approach angle and the operating speed on fuel consumption when operating a plow with a disk disintegrator

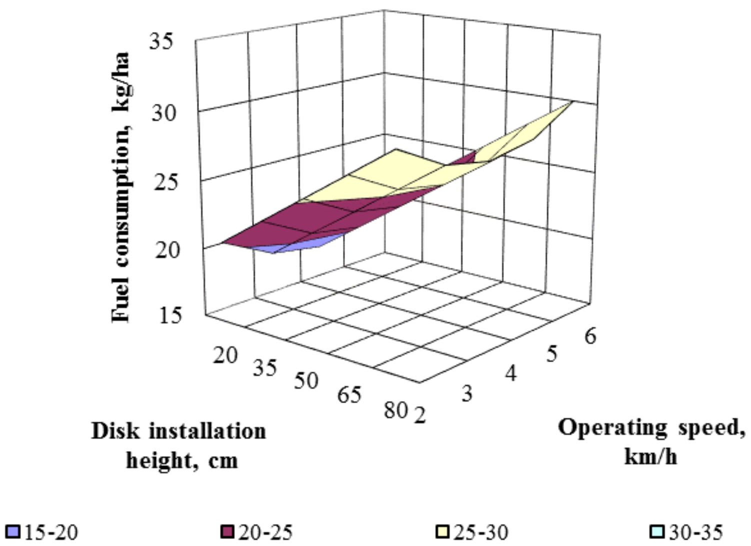

Fig. 7 - Influence of the height of the disk installation and the operating speed on fuel consumption when operating a plow with a disk disintegrator

When changing the operating speed of the plow with a disk disintegrator from 3 to 5 km/h, fuel consumption is minimal and ranges from 19 to 24 kg/ha. Within the same limits of changes in the operating speed of the plow with a disk disintegrator, the minimum fuel consumption is from 18 to 19 kg/ha with a disk section installation height relative to the plow point of 20 cm, from 23 to 24 kg/ha - with a disk section installation height relative to the plow point of 50 cm, and from 28 to 30 kg/ha - with a disk section installation height relative to the plow point of 80 cm.

CONCLUSIONS

- ✓ As a result of studying the influence of the disk approach angle, the depth of disks installation and the operating speed of a plow with a disk disintegrator on the depth of plant residues embedding, it was found that at the operating speed of a plow with a disk disintegrator from 4 to 5 km/h the depth of plant residues embedding is the maximum and is in the range from 15 to 19 cm, respectively.
- ✓ It is established that fuel consumption becomes minimal when the operating speed of a plow with a disk disintegrator is from 4 to 5 km/h and it is in the range from 18 to 30 kg/ha.

REFERENCES

[1] Astier, M., Maass, J. M., Etchevers-Barra, J. D. (2006). Short-term green manure and tillage management effects on maize yield and soil quality in an Andisol. *Soil & Tillage Research*, 88, 153–159. https://doi:10.1016/j.still.2005.05.003

[2] Damanauskas, V. (2019). Dependence of fuel consumption on winter rape stubble tillage quality in clay loam soil, *Proceedings of 18th International Scientific Conference “Engineering for rural development”*, Jelgava, Latvia, 221–226. https://doi: 10.22616/ERDev2019.18.N295

[3] Damanauskas, V., Velykis, A., Satkus, A. (2019) Efficiency of disk harrow adjustment for stubble tillage quality and fuel consumption. *Soil & Tillage Research*, 194, 1–10. https://doi.org/10.1016/j.still.2019.104311

[4] Dubrovin, V. O., Golub, G. A., Skorobogatov, D. V. (2007). Substantiation of diameter of disks of the shredder of stalks of sidereal cultures. *Scientific Bulletin of the National Agrarian University*, 117, 388–392.

[5] Dubrovin, V. O., Sushko, D. S., Skorobogatov, D. V., Roldugin, M. I., Volik, B. A. (2004). Features of the main tillage in the cultivation of corn. *Scientific Bulletin of the National Agrarian University.* 73(2), 55–60.

[6] Fang, H., Zhang, Q., Ali Chandio, F., Guo, J., Sattar, A., Arslan. C., Ji. C. (2016). Effect of straw length and rotavator kinematic parameter on soil and straw movement by a rotary blade. *Engineering in Agriculture, Environment and Food*, 3, 235–241. http://dx.doi.org/10.1016/j.eaef.2016.01.001

[7] Gangwar, K. S., Singh, K. K., Sharma, S. K., Tomar, O.K. (2006). Alternative tillage and crop residue management in wheat after rice in sandy loam soils of Indo-Gangetic plains. *Soil and Tillage Research*, 242-252. https://doi.org/10.1016/j.still.2005.06.015

[8] Golub, G. A., Chuba, V. V., Marus, O. A. (2019). Modeling of transition processes and fuel consumption by machine-tractor unit using biofuel. *INMATEH - Agricultural Engineering*, 58(2), 45–56. DOI:10.35633/INMATEH-58-05

[9] Golub, G. A., Kukharets, S. M., Tsyvenkova, N. M., Golubenko, A. A., Kalenichenko, P. S. (2018). Research on a boiler furnace module effectiveness working on small fracture wastes. *INMATEH-Agricultural Engineering*, 55(2), 9–18.

[10] Israr Khan, M., Suk Gwona, H., Ashraful Alama, M., Ji Songa, H., Dasb, S., Joo Kim, P. (2020). Short term effects of different green manure amendments on the composition of main microbial groups and microbial activity of a submerged rice cropping system. *Applied Soil Ecology*, 147, 1–9. https://doi.org/10.1016/j.apsoil.2019.103400

[11] Kogut, Z., Sergiel, L., Zurek, G. (2016). The effect of the disk setup angles and working depth on disk harrow working resistance. *Biosystems engineering*, 151, 328–337. http://dx.doi.org/10.1016/j.biosystemseng.2016.10.004

[12] Liu, J., Chen, Y., Kushwaha, R. L. (2010). Effect of tillage speed and straw length on soil and straw movement by a sweep. *Soil & Tillage Research*, 109, 9–17. https://doi:10.1016/j.still.2010.03.014

[13] Nazmus, S., Alam, Md. K., Islam, Md. M. Naher, L., Majid, N. (2013). Effects of green manure crops and tillage practice on maize and rice yields and soil properties. *Australian Journal of Crop Science*, 7(12), 1901–1911.

[14] Saikia, R., Sharma, S., Thind, H. S., Sidhu, H. S., Yadvinder-Singh (2019). Temporal changes in biochemical indicators of soil quality in response to tillage, crop residue and green manure management in a rice-wheat system. *Ecological Indicators*, 103, 383–394. https://doi.org/10.1016/j.ecolind.2019.04.035

[15] Sineokov, G. N., Panov, I. M. (1977). Theory and calculation of tillage machines. *Moscow: Mechanical engineering*, 311.

[16] Strelbitskiy, V. F. (1978). Disk tillage machines. *Moscow: Mechanical engineering*, 135.

[17] Tsimmerman, M. Z. (1978). Working bodies of tillage machines. *Moscow: Mechanical engineering*, 295.

[18] Upadhyay, G., Raheman, H. (2018). Performance of combined offset disk harrow (front active and rear passive set configuration) in soil bin. *Journal of Terramechanics*, 78, 27–37. https://doi.org/10.1016/j.jterra.2018.04.002

[19] Upadhyay, G., Raheman, H. (2020). Comparative assessment of energy requirement and tillage effectiveness of combined (active-passive) and conventional offset disk harrows. *Biosystems Engineering*, 198, 266-279. https://doi.org/10.1016/j.biosystemseng.2020.08.014

[20] Zeng, Z., Chen, Y. (2018). Performance evaluation of fluted coulters and rippled disks for vertical tillage. *Soil & Tillage Research*, 183, 93–99. https://doi.org/10.1016/j.still.2018.06.003

[21] Zhang, M., Fang, L. (2007). Effect of tillage, fertilizer and green manure cropping on soil quality at an abandoned brick making site. *Soil & Tillage Research*, 93, 87–93. https://doi:10.1016/j.still.2006.03.016

[22] Zhou, G., Gao, S., Lu, Y., Liao. Y., Nie, J., Cao, W. (2020). Co-incorporation of green manure and rice straw improves rice production, soil chemical, biochemical and microbiological properties in a typical paddy field in southern China. *Soil & Tillage Research*, 197, 1–9. https://doi.org/10.1016/j.still.2019.104499

EXTRACTION METHOD FOR CENTERLINES OF RICE SEEDLINGS BASED ON FAST-SCNN SEMANTIC SEGMENTATION

/

基于 Fast-SCNN 语义分割的秧苗列中心线提取方法

Yusong Chen, Changxing Geng*), Yong Wang, Guofeng Zhu, Renyuan Shen [1]

Robotics and Microsystems Centre, Soochow University, Suzhou/China;

Tel: +8618662299889; E-mail: chxgeng@suda.edu.cn

DOI: https://doi.org/10.35633/inmateh-64-33

Keywords: *rice seedlings; centerlines extraction; deep learning; contour extraction; visual navigation*

ABSTRACT

For the extraction of paddy rice seedling centerline, this study proposed a method based on Fast-SCNN (Fast Segmentation Convolutional Neural Network) semantic segmentation network. By training the FAST-SCNN network, the optimal model was selected to separate the seedling from the picture. Feature points were extracted using the FAST (Features from Accelerated Segment Test) corner detection algorithm after the pre-processing of original images. All the outer contours of the segmentation results were extracted, and feature point classification was carried out based on the extracted outer contour. For each class of points, Hough transformation based on known points was used to fit the seedling row centerline. It has been verified by experiments that this algorithm has high robustness in each period within three weeks after transplanting. In a 1280×1024-pixel PNG format color image, the accuracy of this algorithm is 95.9% and the average time of each frame is 158ms, which meets the real-time requirement of visual navigation in paddy field.

摘要

*为提取水田秧苗中心线，提出一种基于 Fast-SCNN (Fast Segmentation Convolutional Neural Network)语义分割网络的秧苗列中心线提取方法。通过训练 Fast-SCNN 网络，选取最优模型，将秧苗从图像中分割出来。将原始图像预处理后，采用 Fast(Features from Accelerated Segment Test)角点检测算法提取特征点。提取分割结果的所有外轮廓，基于提取到的外轮廓进行特征点分类，对于分类后的每类特征点，采用基于已知点的 Hough 变换拟合秧苗列中心线。经试验验证，本文算法在插秧后三周内各个时段，在杂草、缺株、反光等干扰时，均有较高的鲁棒性。处理每幅 1280*1024 像素的 PNG 格式彩色图像平均耗时 158ms，提取中心线的准确率为 95.9%，满足水田视觉导航的实时性要求。*

INTRODUCTION

Automatic navigation of agricultural machinery has been widely used in planting, cultivating, weeding, and harvesting. The navigation technology based on machine vision benefits from its low cost, good environmental adaptability, rich information, etc., which can effectively improve the operation quality and efficiency of agricultural machinery *(Meng et al., 2016)*. In the paddy field environment, the extraction of the centerline of rice seedlings is the core task of visual navigation. Since the working environment of agricultural robots is a typical unstructured environment and the working scene is complex, there are disturbances such as instability of natural light, lack of plants, weeds, etc. *(Yu et al., 2020)*. Therefore, designing a robust seedling centerline extraction algorithm for the specific environment of the paddy field is the focus and difficulty of visual navigation.

Many scholars have done research on the content of visual navigation line extraction in agricultural scenes. In view of the poor real-time performance and the difficulty of peak detection of the traditional Hough transform to extract the centerline, the researchers proposed a variety of improved Hough transform algorithms such as probabilistic Hough transform and Hough transform based on known points *(Chen et al., 2019; Mukhopadhyay et al., 2015; Zhang et al., 2017)*, which improve the efficiency to some extent. Least squares method is also a common method for crop row centerline detection *(Hou, 2020)*; in view of the shortcoming of this algorithm that is easily affected by noise points, some scholars have also improved it to improve its robustness *(Meng et al., 2013)*.

[1] *Yusong Chen, Ms. Stud. Eng.; Changxing Geng, As. Prof. PhD.Eng.; Yong Wang, Ms. Stud. Eng.; Guofeng Zhu, Ms. Stud. Eng.; Renyuan Shen, Ms. Stud. Eng.*

In addition, scholars have also proposed some other methods of extracting the centerline of crop rows creatively, which have achieved good results in some specific scenes. *Guerrero et al. (2017)* proposed a crop row positioning method based on geometric constraints to reduce the interference of weeds on the accuracy of visual navigation line extraction, aiming at the problem that the spectral characteristics of crops and weeds are close to each other in corn field. *Liao et al. (2019)* used sub-regional statistics of seedling pixel point distribution to extract the characteristic points of seedlings, and realizes the clustering of characteristic points with the clustering method based on neighbor relations. *García-Santillán et al. (2018)* segmented the green pixels based on the color feature, and under the condition of detecting the starting point, used the regression algorithm to extract the corn crop line or curve.

In recent years, with the rise of deep learning technology, scholars have designed a variety of semantic segmentation networks based on deep learning to extract information in unstructured environments, and achieved good results. Semantic segmentation network structure is mainly based on Fully Convolutional Network (FCN) *(Long et al., 2017)*. However, the amount of parameters of classical semantic segmentation models is too large, which leads to poor real-time performance and requires powerful GPU support. Mobile robots require semantic segmentation networks to have high real-time performance, and require low memory usage, which can be deployed in embedded devices. Therefore, several lightweight and lightweight real-time semantic segmentation models such as ICNet *(Zhao et al., 2018)* and BiseNet *(Yu et al., 2018)* were born, which achieved high-precision segmentation at a faster speed on public data sets.

In this study, a method based on semantic segmentation was proposed to extract the seedling row centerline. The Fast-SCNN model was used to segment the seedlings according to the row from the image *(Poudel et al., 2019)*. The segmentation results were combined with FAST corner detection algorithm to extract the centerline of seedling row *(Rosten et al., 2006)*.

MATERIALS AND METHODS

In the face of traditional image algorithms that are difficult to ensure robustness in unstructured environment, the study proposed a centerline extraction algorithm for rice seedlings based on semantic segmentation. The seedlings were segmented by column from the background through training the semantic segmentation network, then the outer contours were extracted based on the connected region in the segmentation result. FAST corner points were extracted as feature points in original images after graying and binarization. By judging whether the corner points are included a certain contour, the feature points were classified. Finally, for each class of feature points, Hough transform based on known points was used to fit the navigation line. The flow of the algorithm is shown in Figure 1.

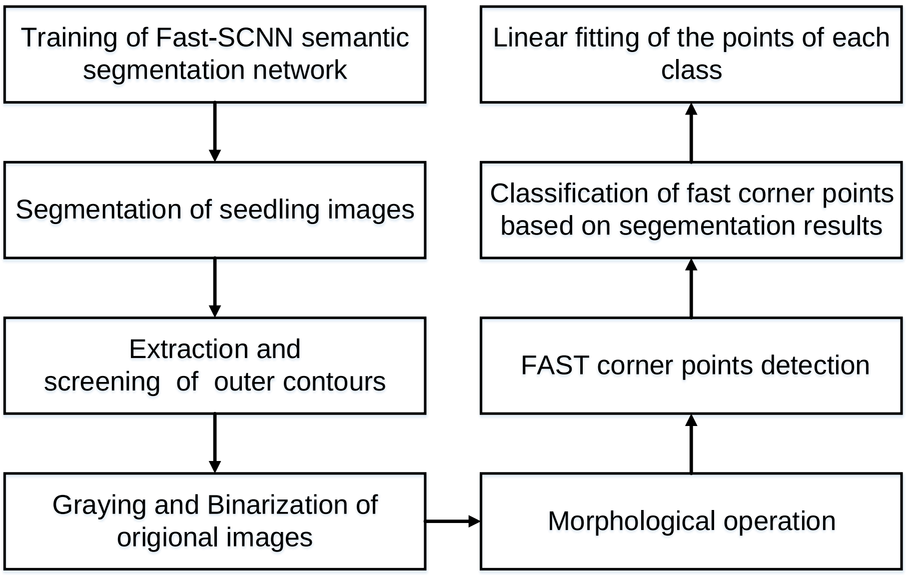

Fig. 1 - Flow chart of the algorithm proposed in this study

Production of paddy field image data set

The planting address of paddy field pictures selected for the experiment in this study is Taiping Street, Xiangcheng District, Suzhou City. 800 pictures of rice seedlings in two typical periods: one week after transplanting and three weeks after transplanting, were collected in different periods of a day.

All 800 images collected were divided into three categories, training set, test set and verification set, as shown in Table 1. The proportion of the three types of sample data was 8:1:1, all the pictures were randomly divided.

Table 1

Type and number of data sets

Object	Training set	Validation set	Test set	Total
Amount	640	80	80	800

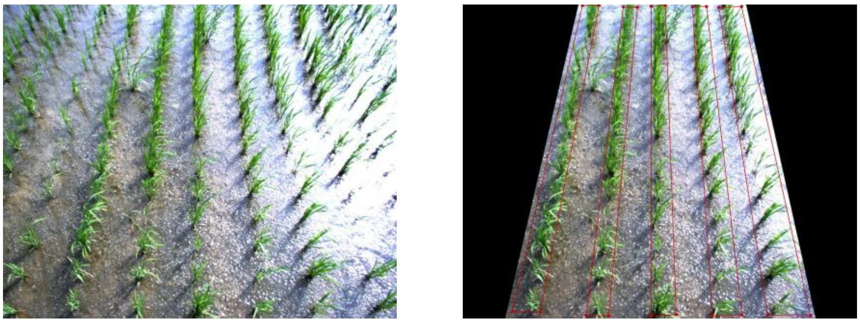

(a) (b)

Fig. 2 - Annotation of image

The semantic segmentation of images adopts the method of supervised learning, and a reasonable data annotation method is the premise of training convolutional neural network. In this study, 800 images collected were labeled with a software named Labelme. During the labeling of images, an irregular quadrilateral frame was used to frame the crop rows that appear completely in the images. In order to prevent the seedlings column in two sides of picture that were not labeled from causing ambiguity in training process, this study removed information that was outside the boundary lines and extended both sides to the outside by 15 pixels, filling with 0, as shown in Figure 2(b), and Figure 2(a) is the original color image. The boundary lines of every picture were determined by the left boundary of the leftmost crop row and the right boundary of the rightmost crop row, which were labeled and saved in a JSON format file. After annotation, labels were generated according to the four vertices of each quadrangle in the annotation information. The generated label was a single-channel image with the same size as the corresponding original image, the pixel value of background was set as 0 and the pixel value of the area of rice seedling was set as 1.

Segmentation of seedling images based on Fast-SCNN network

- Fast-SCNN network

On account of the relatively fixed distribution of rice seedlings in the field, this study used a semantic segmentation algorithm based on deep learning to segment the distribution area of seedlings from the background. The scene of the agricultural machinery's automatic operation in the paddy field is similar to the scene of autonomous driving, which requires real-time performance on embedded devices. Therefore, this study selected Fast-SCNN lightweight semantic segmentation network to segment crops from the background.

Fast-SCNN is a real-time semantic segmentation model, which is suitable for efficient computing on low-memory embedded devices. The Fast-SCNN network is characterized by a two-branch structure, using a shared shallow network to encode detailed information before branching. The network structure includes four parts: the learning down-sampling module, the global feature extraction module, the feature fusion module and the classifier module. It adopts cutting-edge convolutional neural network technologies such as Spatial Pyramid Pooling, Bottleneck, Distribution Shifting Convolution and Depthwise Separable Convolution. Fast-SCNN neural network achieves the balance between the quality and speed of segmentation.

- Model training and the selection of the optimal model

The images in training set were inputted into the network for training, and the parameters were iteratively updated through the backpropagation and gradient descent algorithm to meet the segmentation requirements. The original images were down-sampled to a size of 640*512 pixels before being inputted into the network, and BN (Batch Normalization) was used before the activation function of each layer to speed up the convergence and regularization. The study augmented the existing data before training to improve the generalization ability of the network. The data augmentation methods adopted in this study are showed as follows:

(1) Flip the original image horizontally with a probability of 0.5.

(2) Multiply each pixel in the original image by a random value between 0.8 and 1.3.
(3) Treat the original image with Gaussian disturbance whose variance is a random value between 0 and 3.

This study used an online augmentation method, which transformed the original pictures by the methods above before inputted into the network. During the training process, the model was saved every 10 rounds, the model effect is tested on the test set, and the effect is compared and the model with better generalization ability is selected. The training hyperparameters are shown in Table 2.

The value of the initial learning rate was set as 0.005, and the learning rate decay method was polynomial decay. The formula of the real-time learning rate when iterating to a certain round l_{rate} is shown as follows:

$$l_{rate} = base\_lr * (1 - n\_iteration/n\_max)^{pow} \tag{1}$$

where: $base\_lr$ -- initial learning rate
$n\_iteration$ -- the number of iteration rounds
n_max -- maximum number of iteration rounds
pow -- learning rate decay index

Table 2

Hyperparameter value of model training

Hyperparameter name	Value
Batch size	4
Gradient descent algorithm	SGD with momentum
Momentum	0.9
Weight decay coefficient	0.0005
Initial learning rate	0.005

In this study, the value of pow was set as 0.9, and the maximum number of iteration rounds was 6000. When the number of iteration rounds reached the maximum number, the learning rate dropped to 0 and the training stopped. After 6000 iterations of the weight parameters, the change of model loss is shown in Figure 3(a). It can be seen from the figure that the model was gradually stabilized after the 4000th iteration, and the loss value stabilized at about 0.04.

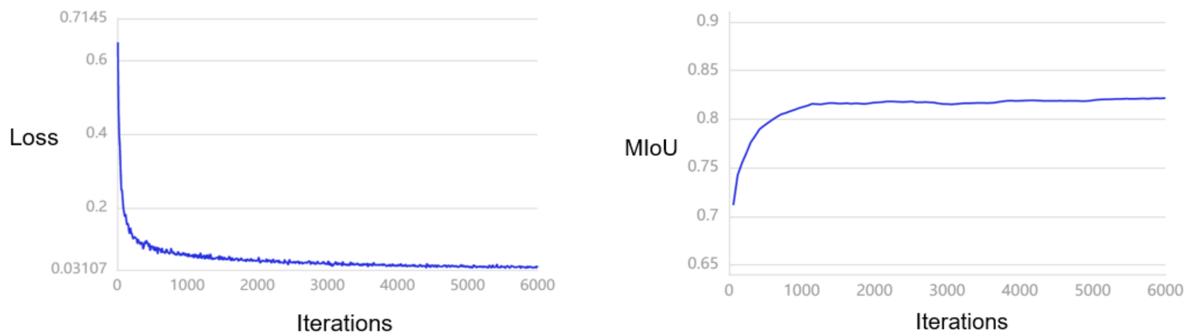

(a) (b)

Fig. 3 - The curve of loss and MIoU with the number of iteration

In this study, the optimal model among all the models saved during training was selected as the final model. The evaluation indicators of semantic segmentation result include Mean Intersection over Union (MIoU), accuracy and so on; this study used MIoU as the basis for selecting the optimal model. The change curve of the value of MIoU with the number of iterations in the validation set is shown in Figure 3(b). It can be seen from the figure that after the 4000th iteration, the value of MIoU tended to stabilize around 0.82. Therefore, the model saved at the 4000th iteration was selected as the optimal model, and the MIoU was 0.8206.

Extraction of centerlines of seedling columns based on segmentation result

- Detection and screening of counters

Due to perspective projection and shooting angle, the two ends of the segmentation result image will produce mutual adhesion between the columns, resulting in some irregular contours, which cause interference for subsequent contour detection, as shown in Figure 4(b), so these areas need to be eliminated. By analyzing the pictures of segmentation results, the study used the trapezoidal mask to process the segmentation results to remove the interference areas on both sides. After multiplying the original image and the mask image, the middle trapezoidal region of interest (ROI) would remain unchanged, while the values of the pixels outside ROI would be 0. The mask image is shown in Figure 4(c), the regions that are not part of ROI are right trapezoids in 2 sides of the image, whose topline is 300 pixels and the baseline is 100 pixels.

(a) (b) (c) (d)

Fig. 4 - Screening of counters

After extracting the segmentation result for the ROI, a row of seedlings in ROI will form a connected region. The study used an algorithm based on boundary tracking to extract all the outer contours of segmentation results *(Suzuki et al., 1985)*, which stores all the extracted outer contours as a point set. However, segmentation results showed that there were a few of invalid contours in the ROI area, which would cause interferences. In order to prevent the interference of invalid contours in the ROI area, this study screened the detected outer contours. Three indicators were used in the screening: area, perimeter, and area-perimeter ratio. As shown in Figure 4(d), the contours that comply with the indicators are filled with red, which will be preserved, or the contours are filled with blue, which will be ignored. After screening, the number of outer contours finally retained was n, which was the number of rows of rice seedlings detected, and each contour extracted was saved as a point set.

- Feature point extraction based on FAST corner detection algorithm

The first step of feature point extraction was graying of original color images. This study noticed that comparing with the other area of original images, the green feature of the color of seedlings is more prominent. So the super green operator based on the RGB color space was used for graying *(Søgaard et al., 2003)*. Experiments showed that this method can accurately distinguish the seedlings from the background. The calculation formula of the super green operator is shown as follows:

$$\mathrm{I(x,y)} = \begin{cases} 0, & 2g-r-b<0 \\ 2g-r-b, & 0 \le 2g-r-b \le 255 \\ 255, & 2g-r-b>255 \end{cases} \tag{2}$$

where: $\mathrm{I(x,y)}$ -- The grayscale value of a pixel in the grayed image with coordinates of (x,y)

r, g, b -- The values of channels R, G, and B in the original color image

After graying, the maximum variance between classes (OTSU) algorithm was used for binarization *(OTSU, 1979)*, and the morphological operation was used for denoising. The morphological method was using the open operation with a structure element of 5*5 square. In this way, a binary image with only two gray values of 0 and 255 was obtained. The pixels with gray value of 255 represent seedlings, and the pixels with gray value of 0 represent backgrounds.

After the binary image had been obtained, feature points were extracted based on the binary image. This study used the FAST corner detection to extract the corner points in the binary image as feature points. The algorithm of FAST corner detection uses a 37-pixel circular template to scan each pixel of the gray image to be detected, and counts the difference between the detected pixel and the 16-point pixels of the circular template, the center of the circle being the detected pixel. FAST corner detection algorithm can be expressed by the formula as follows:

$$N = \sum_{x \in circle(a)} |I(x) - I(a)| > K \tag{3}$$

where: $I(x)$ -- the value of a certain pixel on the periphery of the circular template

$I(a)$ -- the gray value of the detected point a

N -- the total corner response

K -- the threshold value of the corner response

When N is larger than a certain threshold N_0 and the pixels on N form a continuous arc, point a is considered a FAST corner point. In this study, the value of K is 100 and the value of N_0 is 9.

- Contour-based feature point classification

FAST corner detection extracted the feature point cloud of seedlings, but the feature point cloud includes all the feature points of seedlings, so these feature points need to be classified to distinguish different seeding columns. This paper adopted a contour-based method to classify feature points, whose specific steps are as follows:

(1) Store all the FAST feature points extracted in a same set.

(2) For the first outer contour, traverse all the feature points and judge whether the feature points are within the contour.

(3) If a feature point is in the contour, classify it as the crop row represented by the contour, delete the point from the feature point set, and return to step (2). If it is not in the contour, go directly to step (2). After traversing the feature points, enter step (4).

(4) For all other outer contours, repeat steps (2)-(3) in sequence until all contours are traversed.

For the method used to determine whether a point is within the contour, this study analyzed the shape of the extracted outer contour. As shown in Figure 5, all of the extracted contour were convex in the Y direction generally, and there is almost no depression in the Y direction. So the number of intersections between a horizontal line on the X axis and any contour can only be 0, 1, or 2. Based on this reasoning, this study adopted the following method to determine whether a point is within a contour.

For the feature point to be detected, search the point set of the contour for the points that with the same Y coordinate value as the detected point. If there are 0, 1, or more than 2 such points, it is considered that the point is outside the contour. If there are 2 such points, compare the X coordinates of the detected point with the X coordinates of these two points, as shown in Figure 5, assuming the detected point as point A(X_1, Y_1), draw a straight line through point A that is parallel to the X axis. The straight line and the contour intersect from left to right at point B(X_2,Y_2) and point C(X_3,Y_3). If the relationship among X1, X2, X3 satisfies any one of the following:

(1) X2>X1 and X3>X1

(2) X2<X1 and X3<X1

The detected point is outside the contour, otherwise the point is inside the contour.

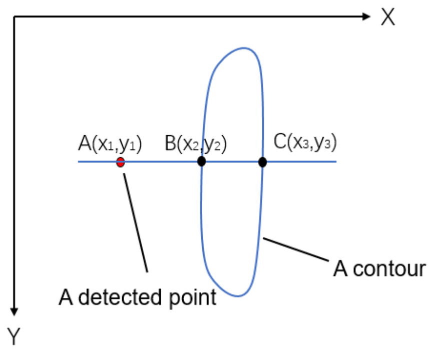

Fig. 5 - Determine of whether a point is within the contour

- Fitting of centerlines

After the feature point classification was completed, for the feature point set of each class, Hough transform based on known points was used to fit the centerline of seeding columns *(Zhang et al., 2012)*. This algorithm can avoid the disadvantages of traditional Hough transform with high time complexity and has high robustness. The fitting algorithm flow is as follows:

(1) For each feature point set, calculate the mean value of the abscissa and ordinate of all points to obtain the center point (X_{avg}, Y_{avg}) of the point set.

(2) Calculate the slope of the line determined by the point in each point set and the center point of the point set, calculate the maximum and minimum slopes, and take the minimum slope value and the maximum slope value as the upper and lower bounds of the interval, which is divided into 30 equal parts.

(3) Count the number of lines in each interval by means of regional voting, and find the interval with the most lines. Finally, take the average slope of all the lines in the interval as the slope of the seedling centerline represented by the point set, and the line goes through the class center point (X_{avg}, Y_{avg}).

RESULTS

Experiment platform

The experiment platform used in this study is configured with Intel Core i5 9400F CPU, whose basic frequency is 2.9GHz, 16GB memory, NVIDIA GTX1080Ti graphics card with 11GB video memory. The system of operating environment is Windows 10 (64-bit). The semantic segmentation model training environment is Python 3.6, Pytorch 1.2 framework, CUDA 10.0 parallel computing architecture and cuDNN7.6 deep neural network library. The development environment is Visual Studio 2017 and the development language is C++.

Determination of parameters

During the screening of contours, this study used three indicators to determine whether it is the contour of the seedling row: area, perimeter, and area-perimeter. The method for determining the three indicators is to count the area, perimeter, and area-perimeter ratio of all the contours of the seedling row from the segmentation results of 80 images in the test set. The area of contour is determined by the number of pixels inside the contour, and the perimeter of contour is determined by the number of pixels in the set of points that make up the contour. The extreme and average values of the indicators of valid contours are shown in Table 3.

From the data in the table, we can find the extreme values of the area, perimeter and area-perimeter ratio. This study took the highest and lowest values of the three indicators, with 1.1 margin coefficient as the criterion. The range of perimeter is 1964-3490, the range of area is 42307-111595 and the range of area-perimeter ratio is 19-46. The contour meeting all the three ranges is considered to be the contour of the seedling row, or it would be ignored.

Table 3

Statistics of area, perimeter and area-perimeter ratio

	Perimeter	Area	Area-perimeter ratio
Max value	3173	101450	41.74
Min value	2161	46538	21.28
Average value	2472	71667	31.11

The analysis of the semantic segmentation models' performance in the test set

The lightweight Fast-SCNN model used in semantic segmentation puts the pictures of the validation set into the trained model for verification. This study compared the effects of other two mainstream real-time semantic segmentation networks ICNet and BiSeNet. The experiment of other 2 algorithm used the same hardware and software conditions. The results on the test set are shown in Table 4.

Table 4

Test results of various semantic segmentation networks

Network name	Fast-SCNN	ICNet	BiseNet
MIoU (%)	82.06	84.48	79.40
Accuracy (%)	90.36	91.72	88.16
Time spent (ms)	24.04	53.25	31.82

From the comparison results, we can find that the MIoU value and accuracy of ICNet are a little higher than those of Fast-SCNN, however, the average time consuming of each frame is much higher. The segmentation quality and time consuming of BiseNet are both worse than Fast-SCNN. Therefore, in terms of segmentation quality and speed, Fast-SCNN performs better than the other two semantic segmentation networks in the application scenario of paddy field.

Results of centerline extraction

Through tracking and photographing the growth process of rice after transplanting, it can be found that there are three typical periods during rice growth. The first period is one week after transplanting, when the seedlings are very small and there is a large gap between the seedlings in each column. The second period is the third week after transplanting, when the seedlings in the same column are staggered and dense, and there is a wide gap between the columns. The third period is more than 5 weeks after transplanting, the seedlings grow densely, and the gaps between the columns are sealed by the seedlings. The weeding of rice seedlings mainly concentrated within 3 weeks after transplanting, weeding could not be carried out later than 3 weeks after transplanting because the seedlings seal the gaps. Therefore, this study researched the paddy field image within three weeks after transplanting, we used the paddy field images of one week after transplanting and three weeks after transplanting to test the extracted centerline of seedling columns.

In order to judge the accuracy of the extraction of seedling row centerlines with the algorithm in this paper, the method of comparing the extracted centerlines with the artificial fitting line was used as the basis of accuracy judgment. Draw the centerlines of the seedling manually, and calculate the angle deviation between them and the centerlines extracted with the algorithm proposed in this study. If the Angle deviation is greater than 5 degrees, the centerline is judged to be inaccurate.

- Extraction of centerlines one week after transplanting

At the period of one week after transplanting, the rice seedlings are very small, the distribution of seedlings is scattered, and there is no adhesion among seedlings. At this period, the main interference comes from reflection and bubbles on the water surface. This study selected 2 representative images from the images of this period for analysis, which were the strong light environment with serious reflection and the normal light environment, as shown in Figure 6(a) and Figure 6(f). They were processed with the following operations: the images were inputted into the trained Fast-SCNN network for segmentation, and the original image was grayed, binarized and morphologically denoised to extract fast corners, and then the fast corners were classified and fitted according to the screened contours of prediction results of segmentation.

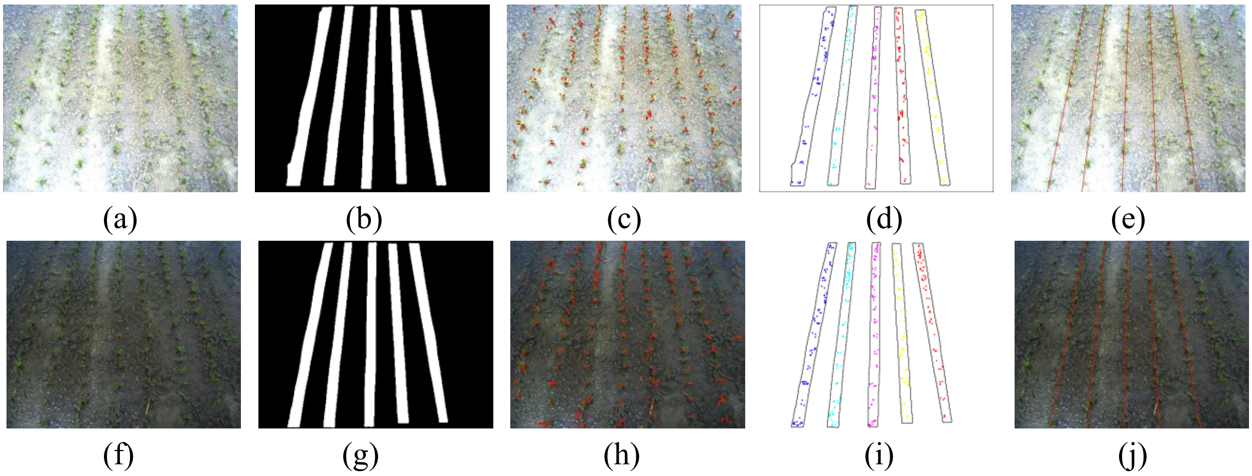

Fig. 6 - Extraction effect of centerlines 1 week after transplanting

Figure 6(b) and 6(g) are the results of counter extraction and screening; it can be seen from the figures that the Fast-SCNN semantic segmentation network can segment seedlings from the background by columns in both reflective and normal light conditions, and each column of seedlings can form a complete connected area. The feature points extracted by FAST corner detection are shown in Figure 6(c) and 6 (h). It can be seen that the feature points are concentrated in the seedlings' growth area, which represents the position of seedlings well. Feature points classification based on outer contours are shown in Figure 6(d) and 6(i). The results of classification show that the feature points that represent different column can be classified clearly, which can prevent the wrong clustering of a few of points caused by various clustering algorithms effectively. From the results of centerline extraction shown as Figure 6(e) and 6(j), we can find that the algorithm of this study can extract the centerlines of seeding columns in the middle section of picture accurately with high robustness. The average time spent per frame is 146ms, the accuracy is 96.4%, and the average angle error is 1.35 °.

- Extraction of centerlines three weeks after transplanting

At the period of 3 weeks after transplanting, the shape and distribution of seedlings are quite different from those at the period of one week after transplanting. The typical images shown in Figure7(a), 7(f) and 7(k) are three typical environments of weak light, normal light and strong light. It can be seen from the segmentation results in Figure 7(b), 7(g) and 7(l) that when the Fast-SCNN semantic segmentation network encounters the lack of plants and reflection, a row of seedlings can still form a complete connected area without being divided. No matter the size of weeds between seedling rows, they were predicted as the background by semantic segmentation network, thus effectively avoiding the influence of weeds on centerline extraction. It can be seen from the results of feature point extraction in Figure 7(c), 7(h) and 7(m) that the feature points extracted by FAST corner detection algorithm are all distributed in the seedling growth area, and feature points can be extracted in all the distribution areas of seedlings.

On account of the color characteristics of weeds between seedling columns are similar to those of seedlings, characteristic points can also be extracted in the area of weeds. However, the feature points generated by weeds are not within any contour detected in the result of semantic segmentation, so the feature points classification based on the outer contours of segmentation results can exclude the feature points generated by weeds, so as to avoid the influence of weeds on the centerline extraction. Feature points classification based on outer contours are shown in Figure 7(d), 7(i) and 7(n). From the fitting results of centerlines in Figure 7(e), 7(j) and 7(o), it can be seen that the algorithm proposed in this study can extract the seedling centerlines at the period of 3 weeks after transplanting in the middle section of picture accurately with high robustness. The average time spent per frame is 168ms, the accuracy is 95.5%, and the average angle error is 1.56°.

From the experimental results, it can be seen that the algorithm proposed in this study can extract the centerline of the middle 4-6 rows of seedlings with high accuracy in each stage of weeding operation, and the average time of each frame is 158ms, the accuracy is 95.9%. The speed meets the requirements of weeding robot navigation, which provides a reliable method for a visual navigation for agricultural robot.

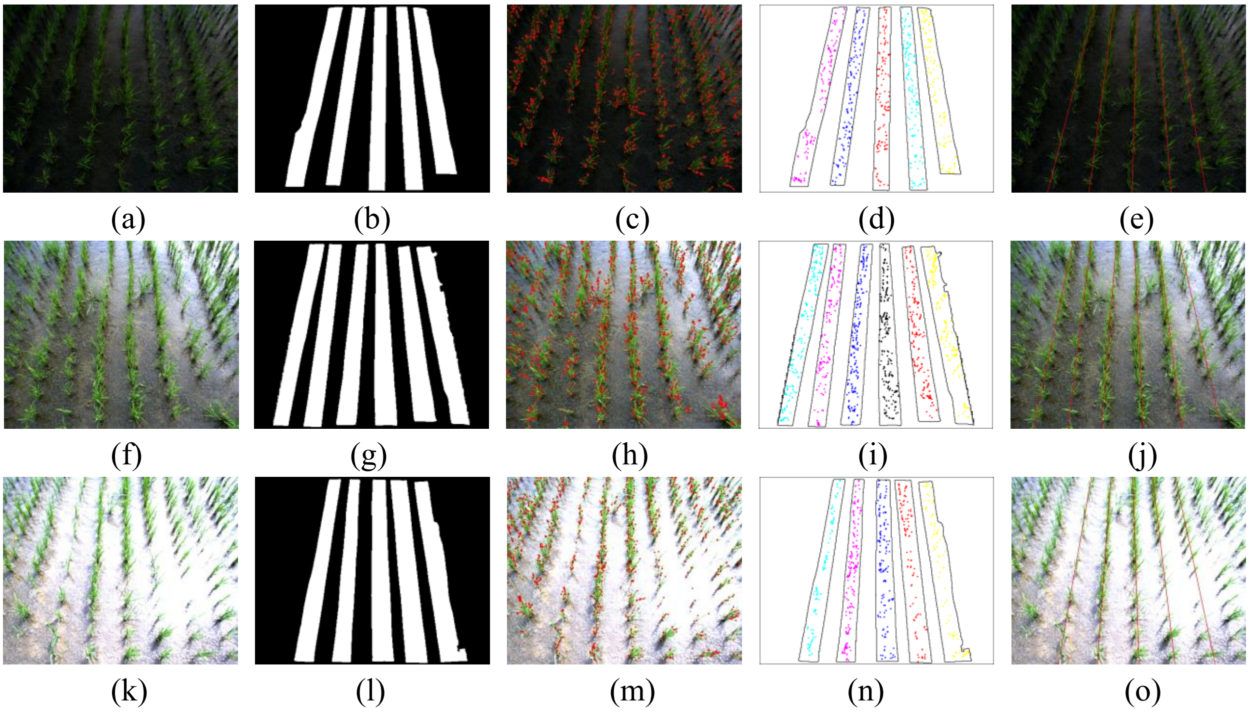

Fig. 7 - Extraction effect of centerlines 3 weeks after transplanting

CONCLUSIONS

(1) The images of rice seedlings with different brightness were collected at different period after transplanting, and the dataset was made by annotation of the images. Based on the dataset, the Fast-SCNN semantic segmentation network was trained, and the optimal model was selected to segment the seedlings from the background. Then contour detection was carried out based on the connected region in the segmentation results and the qualified outer contours were extracted as the contour of the seedling columns.

(2) The original image was grayed and segmented by super green operator based on RGB color space and Otsu algorithm. After the noise points were removed by morphological operation, the corner points in binary image were extracted as feature points of seedling image by FAST corner detection algorithm. The result of experiment showed that FAST corner points can respect the region of seedlings well.

(3) The extracted feature points were classified based on the contours, and each type of feature points were fitted by Hough transform based on known points. The results showed that the accuracy of the algorithm proposed in this study is 95.9%, and it takes 158ms to process a 1280*1024-pixel PNG format color image, which meets the real-time requirements of visual navigation.

ACKNOWLEDGEMENT

This study was supported by a National Key Research and Development Program of China (No. 2016YFD0700600).

REFERENCES

[1] Chen Z.W., Li W., Zhang W.Q., Li Y.W., Li M.S., Li H., (2019), Vegetable crop row extraction method based on accumulation threshold of Hough Transformation (基于自动 Hough 变换累加阈值的蔬菜作物行提取方法研究). *Transactions of the Chinese Society of Agricultural Engineering*, vol. 35, issue 10, pp.314-322;

[2] García-Santillán I., Guerrero J.M., Montalvo M., Pajares G., (2018), Curved and straight crop row detection by accumulation of green pixels from images in maize fields. *Precision Agriculture*, vol. 19, issue 1, pp.18-41;

[3] Guerrero J.M., Ruz J.J., Pajares G., (2017), Crop rows and weeds detection in maize fields applying a computer vision system based on geometry. *Computers and Electronics in Agriculture*, vol. 142, pp.461-472;

[4] Hou Z.K., (2020), Analysis of visual navigation extraction algorithm of farm robot based on dark primary color. *INMATEH Agricultural Engineering*, vol. 62, issue 3, pp.219-228;

[5] Liao J., Wang Y., Yin J.N., Zhang S., Liu L., Zhu D.Q., (2019), Detection of Seedling Row Centerlines Based on Sub-regional Feature Points Clustering (基于分区域特征点聚类的秧苗行中心线提取). *Transactions of the Chinese Society for Agricultural Machinery*, vol. 50, issue 11, pp.34-41;

[6] Long J., Shelhamer E., Darrell T., Berkeley UC, (2017), Fully Convolutional Networks for Semantic Segmentation. *IEEE Transactions on Pattern Analysis & Machine Intelligence*, vol. 39, issue 4, pp.640-651;

[7] Meng Q.K., Liu G., Zhang M., Si Y.S., Li M.X., (2013), Crop Rows Detection Based on Constraint of Liner Correlation Coefficient (基于线性相关系数约束的作物行中心线检测方法). *Transactions of the Chinese Society for Agricultural Machinery*, vol. 44, issue S1, pp.216-223;

[8] Meng Q. K., Zhang M., Yang G. H., Qiu R. C., Xiang M., (2016), Recognition of agricultural machinery navigation path based on particle swarm optimization algorithm under natural light (自然光照下基于粒子群算法的农业机械导航路径识别). *Transactions of the Chinese Society for Agricultural Machinery*, vol. 47, issue 6, pp.11－20;

[9] Mukhopadhyay P., Chaudhuri B.B., (2015), A survey of Hough Transform. *Pattern Recognition*, vol. 48, issue 3, pp.993-1010;

[10] Otsu N., (1979), A Threshold Selection Method from Gray-Level Histograms. *IEEE Transactions on Systems, Man and Cybernetics*, vol. 9, issue 1, pp.62-66;

[11] Poudel R.P.K., Liwicki S., Cipolla R., (2019), Fast-SCNN: Fast Semantic Segmentation Network. *30th British Machine Vision Conference, BMVC 2019*, arXiv:1902.04502v1 [cs.CV];

[12] Rosten E., Drummond T., (2006), Machine learning for high-speed corner detection. *Lecture Notes in Computer Science*, vol. 3951, pp.430-443;

[13] Søgaard H.T., Olsen H.J., (2003), Determination of crop rows by image analysis without segmentation. *Computers and Electronics in Agriculture*, vol. 38, issue 2, pp.141-158;

[14] Suzuki S., Abe K., (1985), Topological Structural Analysis of Digitized Binary Images by Border Following. *Computer Vision Graphics & Image Processing*, vol. 30, pp.32-46;

[15] Yu C.Q., Wang J.B., Peng C., Gao C.X., Yu G., Sang N., (2018), BiSeNet: Bilateral Segmentation Network for Real-time Semantic Segmentation. *Lecture Notes in Computer Science*, vol. 11217, pp.334-349;

[16] Yu N., Wang Q., Cao S.C., (2020), Road recognition technology of agricultural navigation robot based on road edge movement obstacle detection algorithm. *INMATEH Agricultural Engineering*, vol. 61, issue 2, pp.281-292;

[17] Zhang Q., Chen S.J., Li B., (2017), A visual navigation algorithm for paddy field weeding robot based on image understanding. *Computers and Electronics in Agriculture*, vol. 143, pp.66-78;

[18] Zhang Q., Huang X.G., Li B., (2012), Detection of rice seedlings rows' centerlines based on color model and nearest neighbor clustering algorithm (基于彩色模型和近邻法聚类的水田秧苗列中心线检测方法). *Transactions of the Chinese Society of Agricultural Engineering*, vol. 28, issue 17, pp.163-171;

[19] Zhao H.S., Qi X.J., Shen X.Y., Shi J.P., Jia J.Y., (2018), ICNet for Real-Time Semantic Segmentation on High-Resolution Images. *Lecture Notes in Computer Science*, vol. 11207 LNCS, pp.418-434.

DESIGN AND TEST OF AIR-SUCTION PEPPER SEED METERING DEVICE BASED ON AIR SUPPLY AND QUANTITATIVE SEED SUPPLY
/
基于气送定量供种的气吸式辣椒排种器设计与试验

Kaixing Zhang[1)], Lan Zhang[1)], Yang Ding[1)], Xianxi Liu[1,3)], Xiuyan Zhao[*2)] [1]
[1)] College of Mechanical and Electronic Engineering, Shandong Agricultural University, Shandong / China;
[2)] College of Information Science and Engineering, Shandong Agricultural University, Shandong / China;
[3)] Shandong Provincial Engineering Laboratory of Agricultural Equipment Intelligence, Shandong / China;
Tel: +86 13954895451; E-mail: zhaoxy@sdau.edu.cn
Corresponding author: Xiuyan Zhao
DOI: https://doi.org/10.35633/inmateh-64-34

Keywords: *agricultural mechanization engineering; pepper seeds; pneumatic; quantitative seed supply; seeder*

ABSTRACT
In order to solve the problem that the current precision seeder has difficulty in precision sowing pepper seeds, an air-suction pepper seed metering device based on air supply and quantitative seed supply was developed. Combined with its basic structure and working principle, the CFD-DEM coupling method was used for analysis, and the best combined hole parameters were obtained. A single factor experiment with the pass rate, replay rate, and missed rate as experimental indicators was designed. Regression model was established to obtain a reasonable range of each parameter. The results showed that when the speed of the drum barrel was 28.65r/min and the working negative pressure was 4.40kPa, the seeding pass rate of the seed meter was 91.32%, the replay rate was 4.51%, and the missed rate was 4.17%. The comprehensive performance index was better.

摘要
针对目前精密排种器难以对辣椒种子进行精密播种的问题，本文设计一种基于气送定量供种的气吸式辣椒排种器。结合其基本结构与工作原理运用 CFD-DEM 耦合方法进行分析，获得了最佳组合型孔结构。以合格率、重播率、漏播率为实验指标，设计单因素试验。通过正交试验建立回归模型，得到排种性能好时各参数的合理范围。实验结果表明：当滚筒转速为 28.65r/min，工作负压为 4.40kPa 时，排种器排种合格率为 91.32%，重播率为 4.51%，漏播率为 4.17%，排种性能好。

INTRODUCTION
Pepper is one of the most widely planted vegetables in China, and its annual output value ranks first among all kinds of vegetables (*Xia et al., 2017; Wang et al., 2016*). Pepper planting in China mainly relies on manual transplanting, which has low sowing efficiency and high cost, and it is only suitable for small-area planting. Therefore, the manufacture of precision pepper metering devices is of great significance to the further promotion of pepper planting (*Shu et al., 2018*).

According to the stricter planting requirements of pepper, the best method of direct seeding of pepper is precision seeding. *Cao et al., (2014),* used EDEM to simulate and analyse the seed trajectory, then, obtained the appropriate hole size, and designed a new type of centrifugal precision seed metering device to avoid the problem of clogging of the seed hole. *Chen and Li, (2002),* studied the law of seed motion in the process of supplying seeds under the action of vibration force through theory and test. *Karayel et al., (2004),* determined the vacuum negative pressure requirements when sowing different vegetable seeds by exploring a variety of vegetable seeds. The QRIETTA air-suction vegetable planter produced by MASCHIO adopts a high-precision metering device and reduces the planting point at the same time, which realizes the precision hole planting operation for smallest seed vegetables (*Guan et al., 2018; Qi and Xiang, 2020*).

Although the above research has made breakthroughs in different types of small particle metering devices, due to light texture and the short kidney flat structure of pepper, the above seeding device is not suitable for sowing pepper seeds (*Ding et al., 2018*).

---
[1] *Kaixing Zhang, Prof. Ph.D.; Lan Zhang, M.S. Stud.; Ying Ding, M.S. Stud.; Xianxi Liu, Prof. Ph.D.; Xiuyan Zhao, Prof. Ph.D.*

Based on this, this paper designed a new type of precision seed metering device with screw conveying and air conveying combined seed feeding and negative pressure suction, and determined the optimal combination parameters through simulation and bench test. The research in this paper can provide a theoretical basis for the design and improvement of pepper seeding device and optimization of motion parameters.

MATERIALS AND METHODS

The overall structure and working principle of the seed metering system

The whole frame

The structure diagram of the air-suction pepper metering device is shown in Fig. 1.

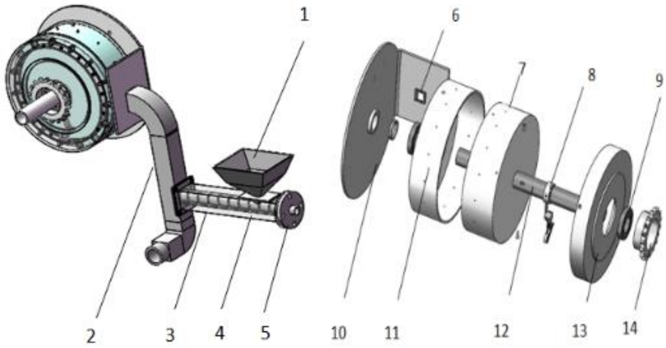

Fig. 1 - Overall structure of the seed metering system

1 - Feed hopper; 2 - Air flow seed tube; 3 - Spiral roller shell; 4 - Spiral roller blowing nozzle; 5 - End cap; 6 - Ferrule; 7 - Inner tube; 8 - Seeding wheel; 9 - Sealed bearing; 10 - Seed shell scraper; 11 - Seed shell; 12 - Seeding axis; 13 - Back shell; 14 – Sprocket

The air-suction pepper seed metering device is mainly composed of spiral rollers, inner and outer cylinders, rear shell, air flow seed tube, seed suction shell, seed metering wheel, seed metering shaft, feeding hopper and other components.

The working principle

During operation, the pepper seeds enter the spiral conveying mechanism through the seed box, and enter the air flow seed tube with the rotation of the spiral roller. Under the action of the air blowing force, the seeds are blown near the suction nozzle of the drum. Under the action of negative pressure, the seeds are absorbed by the seed suction holes on the drum machine and rotate with the drum. When the seeds turn to the position of the seeding wheel, the suction holes lose their adsorption force to the seeds. Under the action of gravity and centrifugal force, the seeds fall into the seed bed at a certain speed, and finally complete the seeding process.

Back shell structure design

The back shell structure is shown in Fig. 2, the blue part is the inner negative pressure cavity, and the yellow is the outer negative pressure chamber. Inside the disc, weld an annular welding plate with a diameter of 160mm concentric with the disc and a height of 13mm. A vent hole with a diameter of 4mm is opened on the annular welding plate to realize the connection of the internal and external negative pressure chambers. Part of the internal negative pressure chamber is welded with partition ribs of 4mm×10mm×10mm in length, width and height respectively. The internal negative pressure chamber is divided into separate isolated negative pressure chambers. The partition ribs are uniformly welded every 24°, and each isolated negative pressure chamber corresponds to a seed suction hole on the circumference of the inner and outer cylinders, and the pressure of each seed suction hole does not affect each other, which makes the air pressure at the seed suction nozzle more stable and avoids the negative pressure turbulence at the suction nozzle caused by unstable airflow.

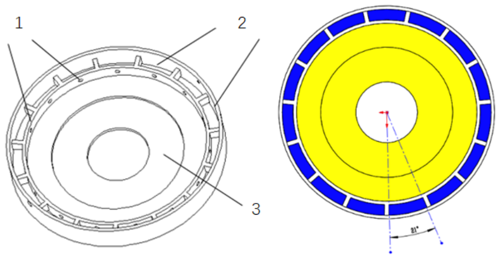

Fig. 2 - Design of the rear shell structure

1 – Vent hole; 2 - Isolated negative pressure chamber; 3 - Negative pressure chamber

Inner and outer cylinder structure design

The structure of the inner and outer cylinders of the seed metering device is shown in Fig. 3. The inner cylinder and the outer cylinder are nested with each other, and the vent holes on the inner and outer cylinders are aligned with each other. The inner cylinder is designed with uniformly distributed L-shaped negative pressure flow passages with a diameter of 1.5mm. Each L-shaped flow channel communicates with the internal negative pressure cavity on the rear shell to form a separate negative pressure flow channel. This single flow channel structure design makes the airflow of each seed suction hole affect the seed suction effect independently when the seed enters the seed metering device from the seed suction hole, ensuring the stability of the seed suction and seed carrying process.

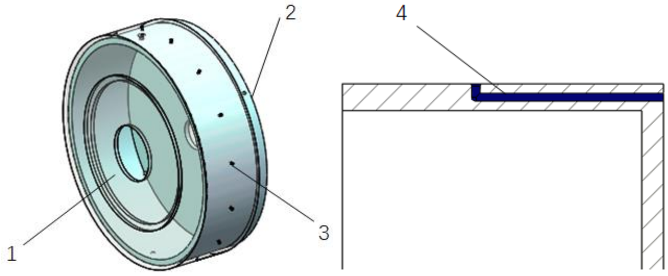

Fig. 3 - Structure of inner and outer cylinders

1 - Outer tube; 2 - Inner tube; 3 - Seed suction hole; 4 - Inner tube runner structure

Screw conveyor

The screw conveying mechanism is a mechanism that controls the amount of seed in the process of feeding. When the pitch is constant, the conveying capacity of the screw conveyor is mainly related to factors such as speed, screw diameter, and blade shape. The speed of screw conveying should be based on the conveying volume and screw. The diameter and the characteristics of the material are determined. The blade speed should not be too high when the conveying requirements are met, and it should not exceed the maximum allowable speed. The spiral speed is calculated using Eq.(1):

$$n \le n_{\max} = A \Big/ D^{1/2} \tag{1}$$

where:

A is material characteristic coefficient, A=20; D is spiral diameter, [m].

The size of the pitch s determines the lift angle of the spiral blade, so the pitch directly affects the slip surface of the seed material, and then affects the conveying capacity of the screw conveying mechanism. Two conditions should be met in the design and calculation of the pitch: one is to ensure the proper distribution relationship between the components of the speed; the other is to consider the frictional connection between the spiral body and the material, and the pitch is calculated using Eq. (2):

$$s = \left(0.8 \sim 1.2\right) D = \mathrm{kD} \tag{2}$$

Given the spiral diameter D=24mm, the maximum allowable speed nmax=130r/min and the pitch s=19~28.8mm can be calculated. In this paper, the thread pitch is selected as 20mm, and the distance for the spiral seeding is 157mm, as shown in Fig. 4.

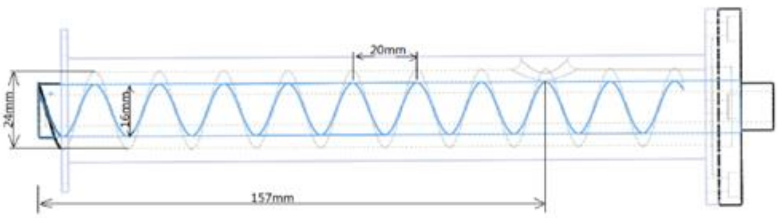

Fig. 4 - Structural design of spiral conveying

Optimization Simulation Analysis of Seed Metering Device

Based on the structural design of the seed metering system, CFD and DEM simulation are used to select the optimal seed blowing speed, and to verify the rationality of the structural parameters for seed feeding and seeding (Ji et al., 2018). The grid division of positive and negative pressure flow fields is shown in Fig. 5.

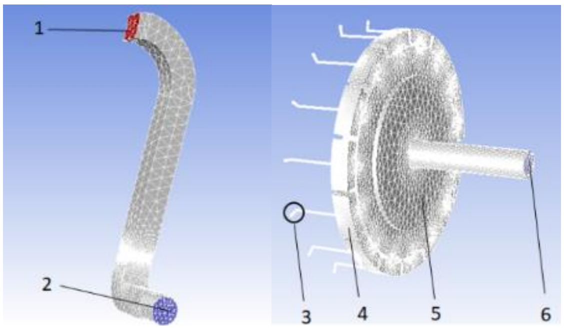

Fig. 5 - Meshing of positive pressure flow field and negative pressure flow field
1 - Positive pressure outlet; 2 - Positive pressure inlet; 3 - Suction nozzle; 4 - Internal negative pressure cavity; 5 - External negative pressure cavity; 6 - Negative pressure inlet

Optimal selection of suction hole structure

The roller of the seed metering device adopts a double-layer roller structure, combined with the special shape of pepper seeds, optimized on the basis of the single-layer roller suction hole structure, and designed stepped holes, tapered holes, straight one holes, and straight two holes. There are four types of holes. Use FLUENT fluid simulation to select a seed suction hole structure with uniform pressure and velocity distribution and appropriate values.

Define the flow velocity of the air inlet when the negative pressure is 4.5kPa, and the flow velocity of the inlet is 10m/s. The flow channels of different holes are simulated, and the pressure velocity distribution obtained is shown in Fig. 6. On the whole, the stepped hole produces a larger turbulent flow at the nozzle. The overall velocity and pressure distribution of the straight hole is relatively uniform, but the flow rate is small, and the power consumption is large. Obviously these two types of holes are not suitable for the seed suction holes of the seed metering device. The could diagram of pressure and velocity distribution of straight two holes and tapered holes are the same except for the nozzle. Taking into account the actual situation, although the tapered hole has a small part of turbulence at the nozzle, the tapered hole is more beneficial for the adsorption of pepper seeds. The shape of the suction hole is finally determined to be a tapered hole.

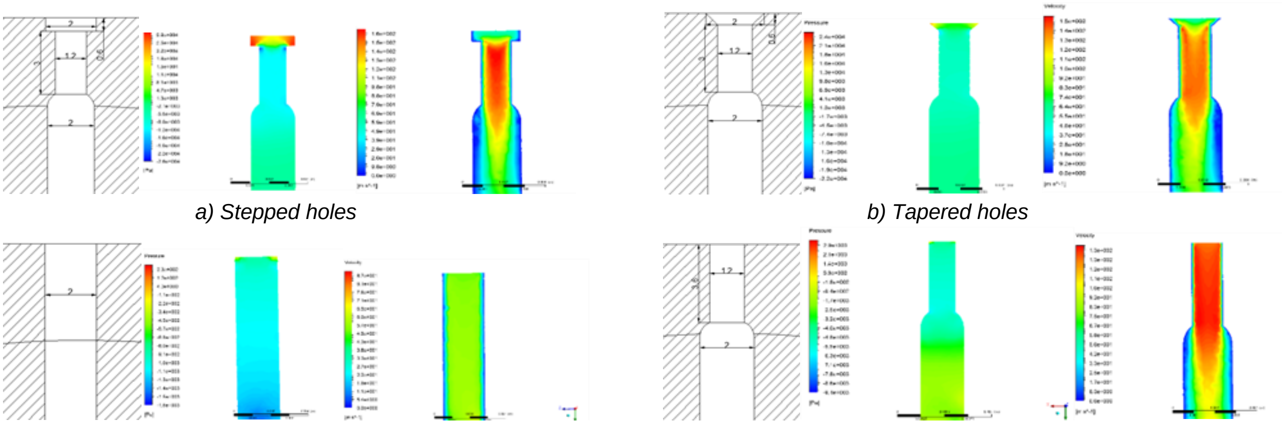

a) Stepped holes *b) Tapered holes* *c) Straight one holes* *d) Straight two holes*

Fig.6 - Cloud diagram of pressure velocity of different shaped holes

EDEM simulation analysis of seed supply process

This article uses EDEM 2018 and FLUENT17.0 for simulation, and couples EDEM and Fluent through journal files. The CFD-DEM simulation parameters are shown in Table 1.

Table 1

EDEM simulation parameter setting

material	Pepper seeds	steel
Poisson's ratio	0.3	0.3
Shear modulus	1.0e+06Pa	8.3e+10Pa
Density	461kg/m^3	7890kg/m^3
Collision recovery factor (with particles)	0.35	0.6
Static friction coefficient (with particles)	0.3	0.3
Dynamic friction coefficient (with particles)	0.01	0.12

In the spiral conveying stage, the force and trajectory of the particles are basically stable, which is mainly manifested in the interaction between the particles and the interaction between the blades and the particles. After many simulations, it was concluded that the speed of the spiral blade is relatively low, so the seeds in the seed feeding process were basically concentrated in the lower part of the blade, and the conveyed particles were divided into different parts by the blade, one rotation of the spiral blade could provide 80 seeds. Analysing the force of 4 particles at different positions during the spiral conveying process, the maximum force was 0.013N, 0.00034N, 0.0007N, 0.00045N, which would not damage the seeds; the speed of the particles when they finally collided with the drum was between 0.8m/s~1m/s; although the particles had a rebound effect after collision, they met the requirements of seeding, which were within the effective adsorption and seeding distance. Seed supply process and seed stress were shown in Fig. 7.

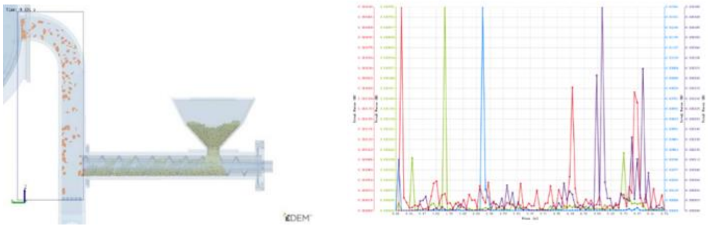

a) Particle fluidization effect *b) Particle force curve*

Fig. 7 - Particle velocity analysis

CFD simulation study of suction flow field

The air pressure inside the suction drum and the stability of the internal air flow affect the seed suction effect. Define the simulated negative pressure of the flow field as 4kPa, use the slipping grid command to define the rotation vector for the negative pressure boundary as (0, 0, 1), the speed is 4 rad/s, and analyse the distribution of velocity, turbulence velocity, dynamic pressure, and static pressure at different sections and times in the flow field, and output the distribution of the flow field z=2mm, z=5.5mm and z=45mm in the drum at 0.01s, 0.1s and 1s. The results are shown in Fig. 8.

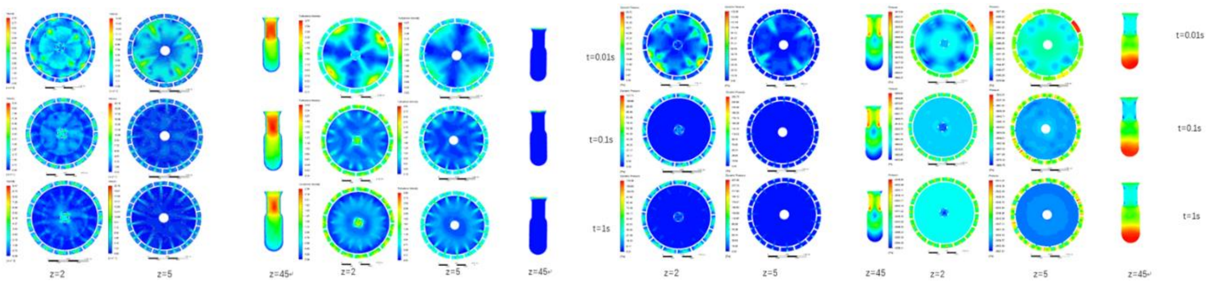

a) Total velocity distribution *b) Turbulence intensity distribution* *c) Dynamic pressure distribution* *d) Static pressure distribution*

Fig. 8 - Velocity and turbulent intensity distribution of the channel

It can be seen from Fig. 8 that the velocity, turbulence, dynamic pressure and static pressure distribution of the negative pressure chamber were significantly affected by the air inlet when the simulation was 0.01s, and there was also a phenomenon of negative pressure concentration. According to Fig.8a), the flow velocity of the negative pressure chamber was weakened by the influence of the air inlet at 0.1s, and the flow velocity and turbulence also tended to be stable; at 1s, the flow velocity of the internal negative pressure chamber had reached a relatively stable state, and the specific performance was that the flow velocity of the external negative pressure chamber was basically in the range of 0m/s~5m/s. According to Fig.8c), the dynamic pressure of the inner and outer negative pressure chambers had stabilized at 0Pa during the two stages of t=0.1s and t=1s. During the 0.01s~1s of the simulation, the values at the seed suction holes had been kept in a stable state, the flow velocity was maintained between 30m/s~40m/s, and the negative pressure could reach about 250Pa. According to force formula: force = pressure x force area (F=P·S), the suction was about 0.079N, which met the suction requirements of pepper seeds.

In general, the negative pressure flow channel of the flow field is small in size, the stable time is shortened, and the suction force at the seed suction nozzle better meets the requirements. After the flow field is stable, the pressure in the inner negative pressure chamber is higher than that in the outer negative pressure chamber, which can save pressure and reduce power consumption.

RESULTS AND DISCUSSION

Bench Test of Air-Suction Pepper Metering System

Test material

Two gold bars of pepper seeds were selected as the test object, and the seed metering test was conducted in the performance test of the JPS-12 seed metering device. The seed purity was >98%, the water content was <7%, and the plant spacing was 300mm/plant, the test was shown in Fig. 9.

Fig. 9 - Seed Meter Performance Tester

1 - High-speed camera; 2 - transmission shaft; 3 - Seed metering device; 4 - Negative pressure tube; 5 - Seed tube

Single factor test analysis

In order to explore the influence of the negative pressure and speed of the seed metering device on the seed metering performance, some researchers first conducted a single factor test on the seed metering device (*Yang et al., 2015*). This test researched working performance of the seed metering device under a forward speed of 7km/h, a drum speed of 25.9r/min, and negative pressure of 1.5~5.5kPa. It could be obtained from the test that during the process of working negative pressure from 1.5kPa to 3.5kPa, the pass rate showed a gradual upward trend, which was mainly manifested in the decrease of missed rate and increase of replay rate. The pass rate of negative pressure in the process of 3.5kPa to 5kPa tended to be stable. When the negative pressure was greater than 5kPa, the missed rate dropped rapidly, and the replay rate raised rapidly. Considering comprehensively, the seeding effect was good when the negative pressure range was 3.5~5kPa.

The rotation speed of the seed meter is determined by the seeding interval and the machine's forward speed, and the conversion relationship is shown using Eq. (3):

$$n_p = \frac{60 \times 10^3 v_m}{3.6 \cdot S \times Z} \tag{3}$$

where:

v_m is the forward speed of the planter, [km/h];

S is plant spacing;

Z is number of seeding disc holes, Z=15.

On the basis of the negative pressure single factor test, the negative pressure 4kPa with the highest pass rate is selected as the working pressure of the speed single factor test. Select the seed metering device speed and drum speed as shown in Table 3 and observe the seeding effect. The test results are shown in Table 3. Take the pass rate (coded value A), replay rate (coded value D), and missed rate (coded value M) as the test indicators. According to the test, during the process of increasing the working speed from 3 km/h to 5km/h, the pass rate showed a gradual downward trend, mainly manifested in the rapid increase of the missed rate and the slow decline of the replay rate. When the working speed increased from 5km/h to 9km/h, the pass rate tended to be stable; when the speed was greater than 9km/h, the replay rate remained unchanged, the missed rate gradually increased, and the pass rate showed a downward trend. Considering comprehensively, when the forward speed was 5-9km/h, the drum speed was 18.5-33.3 r/min, the seeding effect was good.

Table 2

Pressure single factor test results

Negative pressure (kPa)	-1.5	-2	-2.5	-3	-3.5	-4	-4.5	-5	-5.5
Missed rate (M %)	15.62	14.32	12.98	12.21	9.65	8.11	7.6	7.12	4.11
Replay rate (D %)	1.6	2.41	2.82	3.2	3.29	3.87	4.54	5.69	10.24
Pass rate (A%)	82.78	83.27	84.20	84.59	87.06	88.02	87.86	87.19	85.76

Table 3

Speed single factor test results

Speed of work (km/h)	3	4	5	6	7	8	9	10	11	12
Missed rate (M %)	2.34	4.77	7.82	7.16	8.11	7.2	8.6	9.86	10.12	13.11
Replay rate (D %)	6.37	5.78	4.15	3.41	3.87	3.34	3.76	2.64	3.54	3.72
Pass rate (A %)	91.29	89.45	88.03	89.43	88.02	89.46	87.64	87.5	86.34	83.17

Orthogonal test analysis

In order to further explore the interaction and influence law of negative pressure and rotation speed on the seed metering performance of the seed metering device (QI,2014), this paper carried out an orthogonal test. According to the single factor test results, the negative pressure range of the selected seed meter is 3.5~5kPa, and the forward speed range is 5-9km/h. The test factor codes are shown in Table 4 (*Cheng et al., 2020*).

Table 4

Factors and levels of orthogonal tests

Factor	Level				
	1	2	3	4	5
Work negative pressure (kPa)	3.5	4	4.5	5	5.5
Forward speed (km/h)	5	6	7	8	9

Analysis of test results

There are 16 groups of orthogonal tests. In order to comprehensively consider the interaction between factors, each group of tests is repeated 3 times, and the data is averaged. Each test handles no less than 200 seeds. The test results are shown in Table 5.

According to Table 6, the pass rate model of the seed metering device was $P<0.0001$, and the influence was extremely significant; the lack of fit item $P=0.7044$ ($P>0.05$), the influence was not significant. It showed that within the scope of the test data, the regression model of pass rate had a high degree of fit with the actual seeding situation. In this model, the regression terms A, AB, A2, and B2 had $P<0.0001$, which was extremely significant. Missed rate model $P<0.0001$, the impact was extremely significant; the lack of fit item $P=0.9648$ ($P>0.05$), the impact was not significant, indicating that there was no lack of fit factor in the test data interval the regression model of missed rate had a high degree of fit with the actual seeding situation (Wang et al., 2019). The replay rate model $P<0.0001$, the impact was extremely significant; the lack of fit item $P= 0.7880$ ($P>0.05$), the impact was not significant, indicating that there was no lack of fit factor in the test data interval, the regression model of replay rate had a high degree of fit to the actual seeding situation (*Zheng et al., 2019*).

Use Design-Expert 10.0 software to perform regression fitting on the test data. The response functions of the missed rate, replay rate and pass rate of the seed meter are Y1, Y2, and Y3 respectively, and establish a regression mathematical model with the coding of each influencing factor as the independent variables. The regression model of the influence of each factor level on the missed rate, replay rate and pass rate obtained by regression fitting is as follows:

$$\begin{cases} Y_1 = +14.09714 - 1.34467A - 4.27610B - 0.12019AB + 0.31166A^2 + 0.58847B^2 \\ Y_2 = +7.88255 - 1.14807A - 2.43898B - 0.093917AB + 0.22731A^2 + 0.67454B^2 \\ Y_3 = +78.05154 + 2.47395A + 6.69169B + 0.23097AB - 0.54362A^2 - 1.26431B^2 \end{cases} \tag{4}$$

After excluding the insignificant regression, the regression model of pass rate, missed rate and replay rate can be expressed as:

$$\begin{cases} Y_1 = +14.09714 - 1.34467A - 4.27610B - 0.12019AB + 0.31166A^2 + 0.58847B^2 \\ Y_2 = +7.88255 - 2.43898B - 0.093917AB + 0.22731A^2 + 0.67454B^2 \\ Y_3 = +78.05154 + 2.47395A + 0.23097AB - 0.54362A^2 - 1.26431B^2 \end{cases} \tag{5}$$

Table 5

Orthogonal test results

Test number	Test factors		Evaluation index			Test number	Test factors		Evaluation index		
	Forward speed A(km/h)	Work negative pressure B（kPa)	Missed rate Y_1 (%)	Replay rate Y_2 (%)	Pass rate Y_3 (%)		Forward speed A(km/h)	Work negative pressure B（kPa)	Missed rate Y_1 (%)	Replay rate Y_2 (%)	Pass rate Y_3 (%)
1	4	2	6.6	3.83	89.57	**9**	5	5	5.51	10.05	84.44
2	5	1	10.83	6.15	83.02	**10**	1	5	5.88	10.1	84.02
3	1	1	9.11	4.97	85.92	**11**	3	5	4.32	10.24	85.44
4	5	5	5.5	9.73	84.77	**12**	3	3	4.1	3.95	91.95
5	3	3	4.05	3.98	91.97	**13**	3	5	4.47	10.58	84.95
6	1	3	5.24	6.2	88.56	**14**	2	4	3.8	6.89	89.31
7	1	3	5.1	6.12	88.78	**15**	4	4	4.2	6.21	89.59
8	1	1	9.22	5.02	85.76	**16**	2	2	6.5	3.52	89.98

Note: A and B are the corresponding code values of Y1, Y2, and Y3, the same below.

Table 6

Analysis of variance of orthogonal test results

Source of Variance	Missing rate Y_1（%)				Replay rate Y_2（%)				Pass rate Y_3（%)			
	sum of square	Degree of freedom	*F*	*P*	sum of square	Degree of freedom	*F*	*P*	sum of square	Degree of freedom	*F*	*P*
A	0.76	1	63.89	0.003	0.23	1	4.34	0.0640	1.84	1	92.41	<0.0001
B	35.08	1	2935.73	<0.0001	38.01	1	729.24	<0.0001	0.055	1	2.76	0.1274
AB	1.04	1	87.16	0.0003	1.05	1	20.15	0.0012	4.18	1	209.62	<0.0001
A2	2.64	1	220.70	<0.0001	1.33	1	25.59	0.0005	7.62	1	382.46	<0.0001
B2	15.12	1	1265.57	<0.0001	12.60	1	241.77	<0.0001	55.62	1	2792.01	<0.0001
Model	63.79	5	1067.74	<0.0001	74.53	5	286.02	<0.0001	107.82	5	1082.40	<0.0001
Residual	0.12	10			0.52	10			0.20	10		
Lack of fit	0.017	5	0.17	0.9648	0.17	5	0.47	0.7880	0.075	5	0.60	0.7044
Error	0.10	5			0.36	5			0.12	5		
Sum	63.91	15			75.06	15			108.02	15		

Note: P<0.05 (significant impact), P<0.01 (very significant), P>0.25 is not significant.

Two-factor interaction analysis

In order to more intuitively analyse the relationship between the various influencing factors and performance of the seed metering device, and to seek the best combination of operating parameters, the test data is further processed through the Design-Expert 10.0 software to obtain the response surface diagram of the interactive factors (*Gao et al., 2019*). It could be found from Fig.10 that the interactive factors had a significant impact on the missed rate, replay rate and pass rate (*Ding et al., 2018; Liu et al., 2019*).

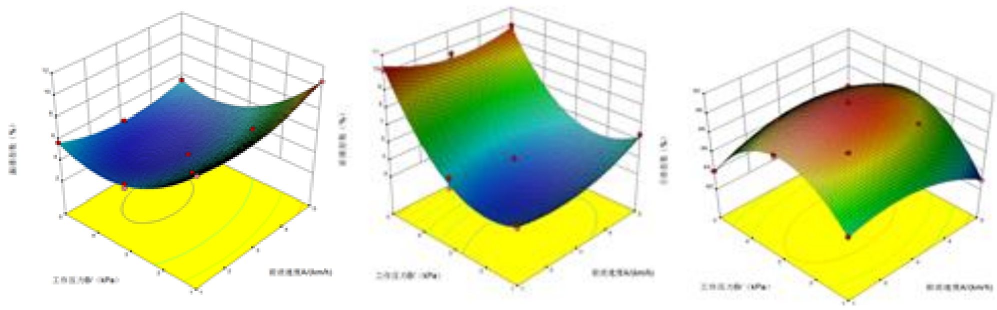

a) Missing rate *b) Replay rate* *c) Pass rate*

Fig. 10 - Interactive factor response diagram

It could be seen from Fig.10a) that the missed rate decreased first and then increased slightly with the increase of working negative pressure, while the missed rate first decreased and then increased during the change of forward speed, with a small change. It could be seen from Fig.10b) that the replay rate first increased slightly and then increased greatly with the increase of the working negative pressure, while the replay rate first decreased and then increased as the forward speed increased, with a small change.

It could be seen from Fig.10c) that the pass rate first increased and then decreased during the process of increasing working negative pressure and forward speed, and the changes were obvious. Among them, when the forward speed of the seed meter is 6~8km/h, that is, when the rotating speed is22-30 r/min and the working negative pressure is in the range of 4kPa~5kPa, the missed rate and replay rate of the seed metering device are at a low level, while the pass rate is at a high level. Based on comprehensive consideration, the best optimized parameters of the seed metering device are: forward speed 7.72km/h, that is, the drum speed is 28.56r/min, and the working negative pressure is 4.37kPa. At this time, the pass rate is 91.07% and the missed rate is 4.23. %, the replay rate is 4.70%.

The optimized theoretical results were tested and verified on the seed meter performance test bench. Here the optimized data is adjusted appropriately, the forward speed of the seed metering device is set to 7.72km/h (rotating speed is set to 28.56r/min), the working negative pressure is set to 4.40kPa and 4 repeated tests are performed. The average seeding pass rate is 91.32%, the average replay rate is 4.51%, and the average missed rate is 4.17%. The test result of the bench is basically consistent with the theoretical analysis result, which can be used as the final best working speed.

CONCLUSIONS

(1) The innovative design of the negative pressure chamber structure inside the seed meter makes the internal negative pressure of the seed metering device more stable.

(2) The tapered hole is selected as the suction hole structure, the CFD-DEM coupling method is used to simulate the seed supply process and the air flow field of the pepper precision metering device, which proves the rationality of the structure.

(3) The best optimized parameters of the seed metering system are: the rotation speed is 28.56r/min, the negative pressure is 4.40kPa, the average seed metering pass rate of the metering device is 91.32%, the average replay rate is 4.51%, and the average missed rate is 4.17%, which meets the demand for seeding.

ACKNOWLEDGEMENT

The study is supported by the Key Research and Development Programme (2019GNC106120) in Shandong province and "Double First-Class" Award and Supplementary Fund Project (SYL2017XTTD14) in Shandong province.

REFERENCES

[1] Chen J., Li Y.M., (2002). Study on the Law of Seed Movement in the Air Suction Vibration Seeding Test Bench (气吸振动式播种试验台内种子运动规律的研究). *Journal of Transactions of the Chinese Society of Agricultural Machinery*, Vol. I, issue 33, pp: 47-50;

[2] Cao X.Y., Liao Q.X., Cong J.L. et al., (2014). Structural design and test of centrifugal rapeseed seed metering device (离心式油菜精量排种器型孔结构设计与试验). *Journal of Transactions of the Chinese Society of Agricultural Machinery*, Vol. S1, issue 45, pp. 40-46;

[3] Cheng C., Fu J., Hao Fu P. et al., (2020) Effect of motion parameters of cleaning screen on corn cob blocking law (清选筛运动参数对玉米芯轴堵筛规律的影响). *Journal of Jilin University. (Engineering and Technology Edition)*, Vol. 01, issue 50, pp. 351-360;

[4] D. Karayel, Z.B. Barut, A. Özmerzi., (2004). Mathematical Modelling of Vacuum Pressure on a Precision Seeder. *Journal of Biosystems Engineering*, Vol. 4, issue 87;

[5] Ding L., Yang L., Wu D.H. et al., (2018). Simulation and experiment of corn air suction seed metering device based on DEM-CFD coupling (基于 DEM-CFD 耦合的玉米气吸式排种器仿真与试验). *Journal of Transactions of the Chinese Society of Agricultural Machinery*, Vol. 11, issue 49, pp. 48-57;

[6] Ding L., Yang L., Liu S.R. et al., (2018). Design of pneumatic maize seed-metering device with assistant seed filling plate (辅助充种种盘玉米气吸式高速精量排种器设计). *Journal of Transactions of the Chinese Society of Agricultural Machinery*, Vol. 22, issue 34, pp. 1-11.

[7] Guan C.S., Cui Z.C., Gao Q.S. et al., (2018). Research Status of Precision Vegetable Live Broadcasting Technology and Equipment (蔬菜精量直播技术及装备的研究现状). *Journal of China Vegetables*, Vol. 12, pp. 9-15;

[8] Gao X.J., Xu Y., He X.W. et al., (2019). Design and test of air-fed high-speed corn precision metering device guide turbine (气送式高速玉米精量排种器导流涡轮设计与试验). *Journal of Transactions of the Chinese Society of Agricultural Machinery*, Vol. 11, issue 50, pp. 42-52;

[9] Ji S.M., Ge J.Q., Gao T. et al., (2018). Processing characteristics of surface-constrained soft abrasive flow based on CFD-DEM coupling (基于 CFD-DEM 耦合的面约束软性磨粒流加工特性研究). *Journal of Mechanical Engineering*, Vol. 05, issue 54, pp. 129-141;

[10] Liu Y.Q., Zhao M.Q., Liu F. et al., (2016). Simulation and optimization of working parameters of air suction metering device based on discrete element (基于离散元的气吸式排种器工作参数仿真优化). *Journal of Transactions of the Chinese Society for Agricultural Machinery*, Vol. 7, issue 47, pp. 65－72;

[11] QI B., (2014). *Design and experimental research of central collection and exhaust precision seed metering device (中央集排气送式精量排种器设计与试验研究)*. China Agricultural University;

[12] Qi Y.Z., Xiang S.N., (2020). Research Status and Development Trend of Vegetable Planter at Home and Abroad (国内外蔬菜播种机的研究现状与发展趋势). *Journal of Chinese Journal of Agricultural Mechanization*, Vol. 01, issue 41, pp. 205-208;

[13] Shi S., (2015). *Design and experimental study of compressed corn precision seed metering device (气压组合孔式玉米精量排种器设计与试验研究)*. China Agricultural University;

[14] Shu S., Kang Y.Y., Wang Y. et al., (2018). Analysis of the development, characteristics and trends of the world protected horticulture (世界设施园艺发展概况、特点及趋势分析). *Journal of China Vegetables*, Vol. 07, pp. 1-13;

[15] Wang L.H., Fang Z.Y., Du Y.C., et al., (2016). Research on the development strategy of vegetable seed industry in China (我国蔬菜种业发展战略研究). *Journal of China Engineering Science*, Vol. 01, issue 18, pp. 123-136;

[16] Wang Q., Zhu L.T., Li M.W. et al., (2019). Vibration characteristics of finger-tipped corn no-till precision seeder and its effect on seeding performance (指夹式玉米免耕精密播种机振动特性及对排种性能的影响). *Journal of Agricultural Engineering*, Vol. 09, issue 35, pp. 9-18;

[17] Xia B.B., Li Y., Wang H.M., Li T., Xu X.W., Wu Z.M., (2017). Cluster Analysis of Morphological Traits of Hot Pepper Germplasm Introduced from Abroad (国外引进辣椒资源形态学性状的聚类分析). *Journal of Molecular Plant Breeding*, Vol. 08, Issue 15, pp. 3318-3330;

[18] Zheng W.X., Lu Z.Q., Zhang W.Z. et al., (2019). Design and test of single row sweet potato seedling recovery machine (单行甘薯秧蔓回收机设计与试验). *Journal of Agricultural Engineering*, Vol. 06, issue 35, pp. 1-9.

OPTIMIZATION OF SHEARING PARAMETERS OF CORN STALKS BASED ON DESIRABILITY FUNCTION APPROACH
/
基于满意度函数法的玉米秸秆剪切工艺参数优化

Huang Wanyuan, Qiu Shuo, Ren Dezhi, Gong Yuanjuan*, Bai Xuewei, Wang Wei [1]
College of Engineering, Shenyang Agricultural University, Shenyang/ China
Tel: +86-024-88487119; E-mail: gongyjSYND@126.com
Corresponding author: Gong Yuanjuan
DOI: https://doi.org/10.35633/inmateh-64-35

Keywords: *Corn stalk, Critical shearing strength, Shearing, Desirability function*

ABSTRACT
To determine the parameters of the whole corn stalks shearing, single factor and multi factor tests were carried out by using node and internode critical shearing strength as the evaluation indexes and the moisture content, sampling location and shearing speed as the influencing factors. The results showed that the moisture content, sampling location and shearing speed had significant effects on the critical shearing strength of internodes and nodes ($F > F_{0.05}$), the order of the influencing factors on the internode and node critical shearing strength were: moisture content >sampling location >shearing speed and sampling location >moisture content >shearing speed. By using Design-Expert and Desirability Function Approach, the optimization problem of three response values, including difference value of critical shearing strength between node and internode at the same segment (DV), the node and internode critical shearing strength, was transformed into a single response value optimization. The corn stalks with a moisture content of 15% had lower shearing strength and higher shearing stability at the shearing speed of 25 mm/min.

摘要
为确定玉米秸秆的整秆剪切工艺参数,本文以含水率、取样部位、剪切速度为试验因素，节间和节部临界剪切强度为试验指标进行单因素和多因素试验。试验结果表明：含水率、取样部位、剪切速度对节间和节部临界剪切强度均影响显著，节间临界剪切强度影响的因素主次顺序为含水率>取样部位>剪切速度，节部临界剪切强度影响因素主次顺序为取样部位>含水率>剪切速度。利用满意度函数法和 Design-Expert 数据分析软件，将节间、节部临界剪切强度及节部节间临剪切强度差值三个响应值优化转化成单一响应值优化。优化结果表明，使用 25mm/min 的速度剪切含水率为 15%的玉米秸秆，玉米秸秆的整秆剪切强度低，剪切平稳性高。

INTRODUCTION
Corn stalk is biomass resource that can be developed and utilized. Its comprehensive utilization can achieve ecological balance of agriculture and ease the pressure on energy and the environment (*Zhang et al., 2017*). Among the numerous and varied recycling modes of corn stalks, the three main approaches are as follows: using smashed corn stalks to make fodder, sprinkling crushed corn stalks back into the field, and directly harvesting entire corn stalks (*Han et al., 2002*). These approaches are inseparable from shearing components, which are the core components of the recycling machinery for corn stalks (*Wu, 2013*).

Chen Chaoke et al. studied the effects of test factors such as moisture content and sampling location on the shearing force of sugarcane stalks, and compared the shearing properties between its nodes and internodes (*Chen et al., 2016*). *Wang Yan* summarized the cutting force required for different harvest periods using the corn stalk harvest period as the influencing factor (*Wang, 2012*). Some researchers also carried out tensile and shearing characteristics tests on the rind of corn stalks, and discussed the effects of moisture content, sampling locations, and shearing speed on the tensile and shearing characteristics (*Chen, et al., 2012*). Numerous studies on the shearing characteristics of corn stalks had been investigated (*Igathinathane et al., 2010; Li et al., 2010; Zhang et al., 2018; Zhang et al., 2020*).

Huang Wanyuan, Ph.D. Stud. Eng.; Qiu Shuo, Lab.Techo. Ph.D. Eng.; Ren Dezhi, Lec.Ph.D. Eng.;
Gong Yuanjuan, Prof. ph.D. Eng.; Bai Xuewei, As. Prof. ph.D. Eng.; Wang Wei Ph.D. Stud. Eng.

However, the research about studying the effects of moisture content, sampling location and shearing speed on the shearing stability of corn stalks was not searched by author. Corn stalks having different moisture contents, sampling locations, and parts had different mechanical properties and required different shearing strength (*Zhang et al., 2016*). The difference may cause an imbalance in the workload of the corn stalk processing machine (*Chen et al., 2016*). Therefore, reducing the shearing strength of corn stalks and shearing strength difference of the whole stalk is an urgent problem to solve.

This study aimed to obtain the relatively stable parameters of the whole corn stalks shearing. Single-factor and multi-factor tests were carried out to study the significance of factors and establish regression models. Furthermore, by using the Design-Expert and Desirability Function Approach, the optimization problem of three response values was transformed into a single response value optimization to obtain the relatively stable shearing parameters. This study is of practical significance in prolonging the life-span of shearing tools and developing and designing shearing components.

MATERIALS AND METHODS

Test materials and equipment

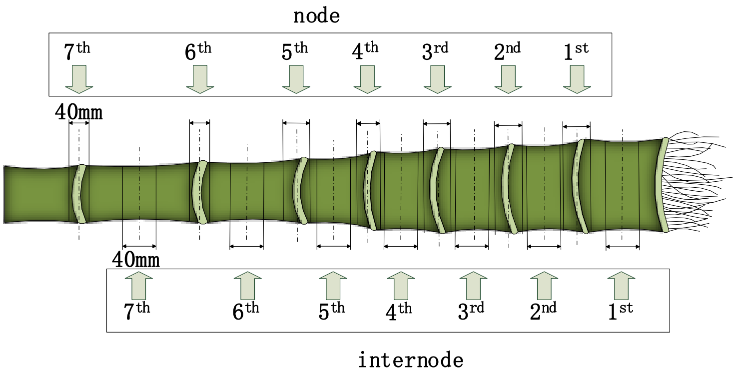

Fig. 1 - Sampling diagram

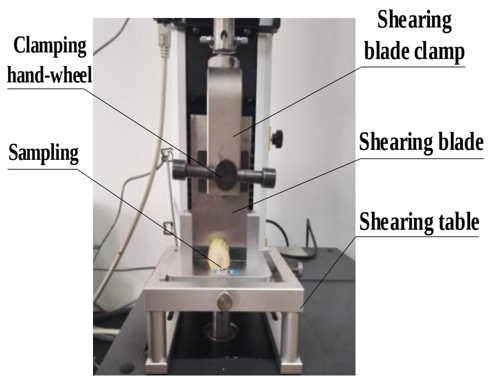

Fig. 2 - Measuring device for shearing strength

The test materials used in this study were corn stalks with a plant height range of 1.60-2.00m and a moisture content of 15%-75%. First, internode and node sections of the whole stalk from the prop root above the soil surface were marked with 1 to 7, as shown in Fig. **1**. Samples of 40 mm from each internode and node section were cut symmetrically taking the dotted line as the centre, as shown in Fig. 1.

Test equipment and instrument mainly include an universal testing machine (INSTRON-3344), as shown in Fig. **2**, a drying oven under forced convection (GuangMing 101), an electronic balance (JJ523BC, precision 1mg), and a Vernier calliper (precision 0.01 mm).

Test factors and indexes

In this study, the node and internode critical shearing strength, DV were selected as the evaluation indexes because the critical shearing strength is affected by the internal structure difference of the nodes and internodes of corn stalks. The moisture content of the corn stalks, sampling location, and shearing speed were selected as the influencing factors by reviewing the related literature and mechanical design requirements (*Zhang et al., 2016; Yu et al., 2012*).

The shearing strength–displacement curve was obtained from a corn stalk shearing test as shown in Fig. 3. It is clearly observed that the shearing strength linearly increased with the variation in the displacement during the initial stages; however, as the displacement increased further, the shearing strength increased faster after the turning point of the curve. The anti-shear ability became stronger and the shearing strength increased dramatically when the upper and bottom skin of the corn stalks was cut out and rind of corn stalks was compacted successively. The shearing strength immediately decreased, until the corn stalk was cut off. The peak value resulting from the shearing strength dramatically decreasing is called the critical shearing strength, which is considered as the test index in this study (*Xing, 2017*).

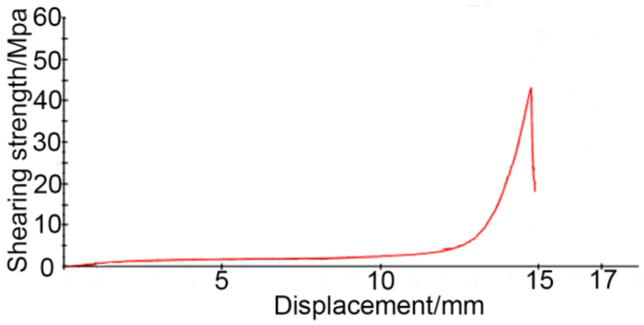

Fig. 3 - The curve of shearing strength-displacement for shearing test

Test design of single factor tests

The 4th nodes and internodes of the samples were selected, and the effect of the moisture content of samples on the critical shearing strength was examined at a shearing speed of 15 mm/min. Samples from different sections of the whole stalk were selected, and the moisture content of each sample was adjusted to 45%±2%, and the effect of the sampling location on the critical shearing strength was examined at a peeling speed of 15 mm/min. The moisture content of the sample in the 4th nodes and internodes were adjusted to 45%±2% to study the influence of the shearing speed on the critical shearing strength. The test was repeated 5 times at each test level, and the *F* value tests were performed at the level of P=0.05.

Test design of ternary quadratic regression orthogonal combination

Ternary quadratic orthogonal regression tests were carried out by using internode and node critical shearing strength ($Y_1$and Y_2) as the evaluation indexes and the moisture content (X_1), sampling location (X_2) and shearing speed (X_3) as the influencing factors. The test was repeated 5 times for each group and then the average values were calculated and recorded. The factor level coding table of the tests is shown in

Table **1**.

Table 1

Factor level coding table of the tests

Levels	**Moisture content** X_1 **[%]**	**Sampling location** X_2 **[node or internode]**	**Shearing speed** X_3 **[mm/min]**
+1.525	75	7	25
+1	65	6	59.67
0	45	4	15
-1	25	2	20.33
-1.525	15	1	5

Non-linear multi-objective optimization

The optimization of stable shearing parameters of corn stalks should be based on the following principles: the lower internode and node critical shearing strength, and DV. The DV Y_3 can be obtained from Equation (1):

$$Y_3 = Y_2 - Y_1 \tag{1}$$

By using Desirability Function Approach, the optimization problem of three response values, including DV, the node and internode critical shearing strength, was transformed into a single response value optimization, and then the whole corn stalk relatively stable shearing parameters were obtained. It could be known that the desirability degree would be high if the response values of node critical shearing strength, internode critical shearing strength and DV were low. The desirability function is calculated by Equation (2) (*Xu et al., 2020*).

$$d_i(Y_i) = \begin{cases} 1 & if \;\; Y_i < L_i \\ \dfrac{U_i - Y_i}{U_i - L_i} & if \;\; L_i \le Y_i \le U_i \\ 0 & if \;\; Y_i > U_i \end{cases} \tag{2}$$

where: d_i is the desirability function of the response surface; Y_i is the response value; L_i is the specification lower limit of the response value; U_i is the specification higher limit of the response value.

The overall desirability function D is shown in Equation (3) (*Xu et al., 2020*).

$$D = \left(\prod_{i=1}^{3} d_i^{r_i} \right)^{\frac{1}{\sum r^i}} \tag{3}$$

In the Equation (3), r_i is the weight coefficient, which depends on the importance of each response surface in the optimization design of stable shearing process parameters of corn stalks. In this paper, the importance of each response surface regression model was assumed to be the same, which is $r_1 = r_2 = r_3$. Putting $r_1 = r_2 = r_3$ into Equation (3) to get:

$$D = \sqrt[3]{d_1 \, d_2 \, d_3} \tag{4}$$

The overall desirability function D is the function of moisture content, sampling location and shearing speed, which can be used as the basis for the optimization of stable shearing parameters of corn stalks.

RESULTS

Results and analysis of single factor test

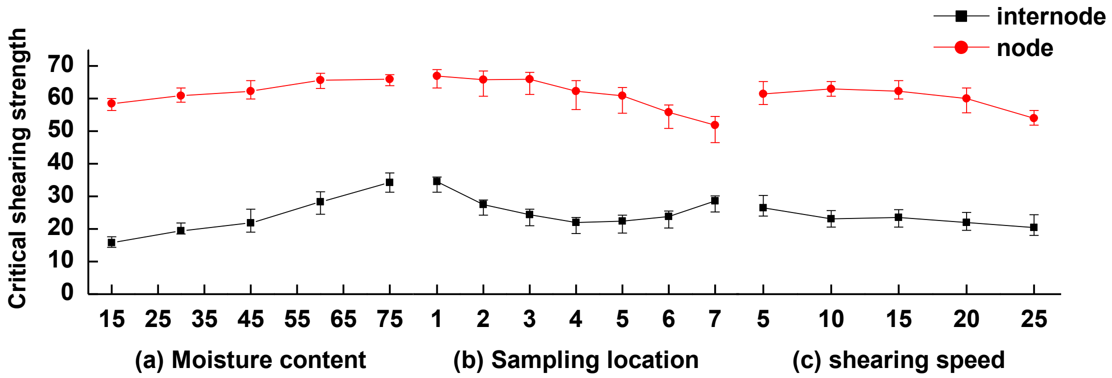

Fig. 4 - The critical shearing strength of internodes and nodes at different levels of factors

Table 2

F value test results

	Moisture content		Sampling location		Shearing speed	
	Internode	**Node**	**Internode**	**Node**	**Internode**	**Node**
***F* value**	36.71	15.21	46.57	38.33	4.40	10.48
$F_{0.05}$ crit	2.87	2.87	2.45	2.45	2.87	2.87

The internode and node critical shearing strength of corn stalks with different moisture contents are shown in Fig. 4, the *F* value test results at the level of P= 0.05 are shown in Table 2.

It can be observed from

Table **2**, $F_{internode}$ = 36.71> F_{node} = 15.21> $F_{0.05}$ (4, 20) = 2.87, indicating that moisture content has significant effects on internode and node critical shearing strength. At the shearing speed of 15 mm/min, the critical shearing strength values of the 4th nodes and internodes gradually increase and DV decreases with the increase of moisture content from 15% to 75%; moreover, the critical shearing strength of the nodes is about 2-3 times that of the internodes with the same moisture content (see Fig. 4(a)).

The higher the moisture content of corn stalks is, the denser the structure will be, the greater the critical shearing strength will be required and the moisture content may have effect on the DV which may be the reasons for the above results.

It can be observed from

Table 2, $F_{internode}$ = 46.57 > F_{node} =38.33 > $F_{0.05}$ (6, 28) = 2.45, indicating that sampling location has significant effects on internode and node critical shearing strength. At the shearing speed of 15 mm/min, for corn stalks with a moisture content of 45 ±2%, with the change of sampling location from 1st to 7th, the critical shearing strength values of nodes gradually decrease, that of internodes decreases overall, and DV first increases and then decreases; moreover, the critical shearing strength of the nodes is about 2-3 times that of the internodes on the same sampling location of the corn stalk (see Fig. 4(b)). The tissue structure at the bottom of corn stalks is denser than that at the top of corn stalks which may be the reason for the above results.

It can be observed from

Table 2, $F_{internode}$ = 4.4> F_{node}= 10.48> $F_{0.05}$ (4, 20) = 2.87, indicating that shearing speed has significant effects on internode and node critical shearing strength. For the 4th nodes and internodes of corn stalks with a moisture content of 45 ±2%, the node and internode shearing strength gradually decreases, with the increase of shearing speed from 5 mm/min to 25mm/min; moreover, the critical shearing strength of the nodes is about 3 times that of the internodes at the same shearing speed (see Fig. 4(c)). The greater the shearing speed is, the easier the corn stalks will be cut, the smaller the critical shearing strength will be required and the shearing speed has less effect on the DV which may be the reason for the above results.

Results and analysis of ternary quadratic regression orthogonal test

The results of the ternary quadratic regression orthogonal combined shearing tests are shown in Table 3. Design-Expert data analysis software was used to establish two regression models of coding values between influencing factors and the critical shearing strength of internodes and nodes of corn stalks, as shown in equations (5) and (6).

Table 3

Test results of shearing strength

Test No.	Factors and levels			Response indexes	
	Moisture content x_1 **[%]**	**Sampling location** x_2 **[node or internode]**	**shearing speed** x_3 **[mm·min^{-1}]**	**Internode critical shearing strength** Y_1 **[MPa]**	**node critical shearing strength** Y_2 **[MPa]**
1	-1	-1	-1	25.55	50.65
2	1	-1	-1	38.00	62.13
3	-1	1	-1	24.28	44.30
4	1	1	-1	30.08	45.95
5	-1	-1	1	17.70	47.10
6	1	-1	1	35.19	57.75
7	-1	1	1	20.82	42.93
8	1	1	1	27.58	42.10
9	-1.525	0	0	16.88	48.78
10	1.525	0	0	38.00	54.33
11	0	-1.525	0	34.52	53.88
12	0	1.525	0	30.41	41.08
13	0	0	-1.525	25.78	50.73
14	0	0	1.525	25.12	42.80
15	0	0	0	23.01	50.63
16	0	0	0	21.74	54.98
17	0	0	0	21.40	53.23
18	0	0	0	20.22	54.10
19	0	0	0	23.00	54.18
20	0	0	0	24.00	54.93

$$Y_1 = 22.56 + 5.91\ x_1 - 1.58\ x_2 - 1.39\ x_3 + 1.46\ x_1^2 + 3.62\ x_2^2 + 0.61\ x_3^2 - 2.17\ x_1x_2 + 0.75\ x_1x_3 + 0.59\ x_2x_3 \quad (5)$$

$$Y_2 = 53.44 + 2.48\ x_1 - 4.89\ x_2 - 1.99\ x_3 - 0.37\ x_1^2 - 2.12\ x_2^2 - 2.43\ x_3^2 - 2.66\ x_1x_2 - 0.41\ x_1x_3 + 0.34\ x_2x_3 \quad (6)$$

The results of the analysis of variance of regression models are shown in Table 4. It can be observed from Table 4 that the regression of the two regression models is extremely significant (p<0.01), the lack of fit is not significant (p>0.05) and R^2 of model 1 and model 2 are 0.9353 and 0.9489 respectively. The above results indicate that both of the regression models have a good and reasonable fit. It can be observed that the influencing factors order of critical shearing strength of the internode is moisture content (x_1) > sampling location (x_2) > shearing speed (x_3) and that of the node is sampling location (x_2) > moisture content (x_1) > shearing speed (x_3) through the comparison of F values. Moreover, the interaction term of x_1x_2 has significant effects on the internode and node critical shearing strength.

Table 4

Analysis of variance

Source	MS	*F* value	*P* value	Source	MS	*F* value	*P* value
Model 1	79.03	16.05	<0.0001**	**Model 2**	67.10	20.65	< 0.0001**
x_1	441.07	89.59	< 0.0001**	x_1	78.01	24.01	0.0006**
x_2	31.38	6.37	0.0301*	x_2	302.58	93.12	< 0.0001**
x_3	24.61	5.00	0.0494*	x_3	50.34	15.49	0.0028**
x_1x_2	37.81	7.68	0.0197*	x_1x_2	56.71	17.45	0.0019**
x_1x_3	4.51	0.92	0.3612	x_1x_3	1.36	0.42	0.5320
x_2x_3	2.77	0.56	0.4707	x_2x_3	0.91	0.28	0.6080
x_1^2	23.13	4.70	0.0554	x_1^2	1.48	0.46	0.5145
x_2^2	141.98	28.84	0.0003**	x_2^2	48.74	15.00	0.0031**
x_3^2	3.98	0.81	0.3897	x_3^2	63.82	19.64	0.0013**
Lake of Fit	7.99	4.31	0.0675	**Lake of Fit**	3.86	1.46	0.3430

*Note: P<0.01(extremely significant**), P<0.05(significant*); Model 1 is variance analysis of internode critical shearing strength. Model 2 is variance analysis of node critical shearing strength.*

Analysis of the effects of the interaction factors on node and internode critical shearing strength

When the shearing speed is set to the level of 0, the response surfaces of the moisture content and sampling location on the critical shearing strength of the internodes and the nodes are shown in Fig. 6.

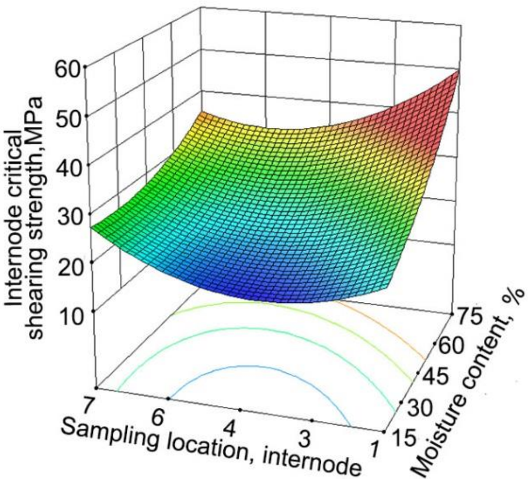

Fig. 5 - Interaction effects of moisture content and sampling location on internode critical shearing strength

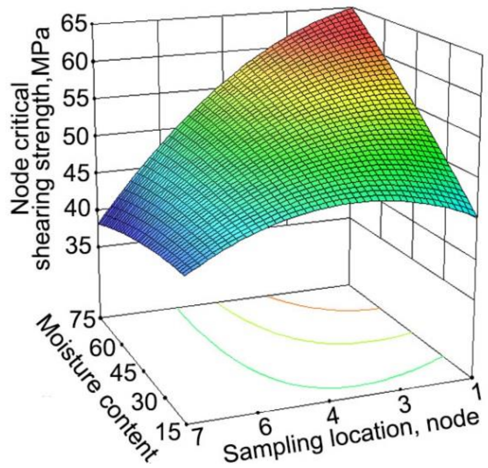

Fig. 6 - Interaction effects of moisture content and sampling location on node critical shearing strength

As shown in Fig. 5, with the decrease of moisture content, the critical shearing strength of the1st internodes decreased gradually, and that of the 7th internodes first decreased and then increased. The main reasons for these results are as follows: the internode samples near the solid surface have the characteristics of thicker fibre bundles and stronger supporting force. With the decrease of moisture content, the volume of internode samples shrank less and the tissues became sparse, so that the internode critical shearing strength decreased. The internode samples far from the solid surface have the characteristics of thinner fibre bundles and weaker supporting force. When the moisture content was high, with the decrease of moisture content, the supporting force of fibre bundles could restrain the volume shrink and the tissues became sparse, so that the internode critical shearing strength decreased; however, when the moisture content was low, with the decrease of moisture content, the supporting force of fibre bundles was insufficient, the volume of internode samples decreased sharply and the tissues became dense, so that the internode critical shearing strength increased.

As shown in Fig. 6, the higher the sampling location was, the lower the node critical shearing strength would be. The main reason for this result is as follows: The tissues of the node samples at different sampling locations were relatively dense. The higher the sampling location was, the thinner the fibre bundles and the lower the critical shearing strength of the node samples would be.

Non-linear multi-objective optimization

Design-expert software was used to optimize the parameters, in order to obtain the optimal parameter combination with small differenc in critical shearing strengths between nodes and internodes of corn stalks, and the weaker critical shearing strengths of the whole stalk. DV Y_3 (see Equation (7)) was derived from simultaneous equations (4), (5), and (6).

$$Y_3 = 30.88 - 3.42x_1 - 3.32x_2 - 0.6x_3 - 1.83x_1^2 - 5.75x_2^2 - 3.04x_3^2 - 0.49x_1x_2 - 1.16x_1x_3 + 0.25x_2x_3 \quad (7)$$

The optimization target ranges of response values were obtained by using Design-expert software, as shown in Table 5.

Table 5

Response optimization target range

Response	Internode critical shearing strength [MPa]	Node critical shearing strength [MPa]	DV [MPa]
Optimization target range	$14.14<Y_1<53.28$	$29.39<Y_2<65.88$	$0<Y_3<32.85$

When the sampling locations were different, the moisture content and shearing speed were optimized and analysed. Based on the Design-Expert software and equations 4, 5, 6, and 7, the response surfaces of the overall desirability function were obtained when the sampling location X_2=1, 2, 3, 4, 5, 6 and 7 as shown in Fig. 7.

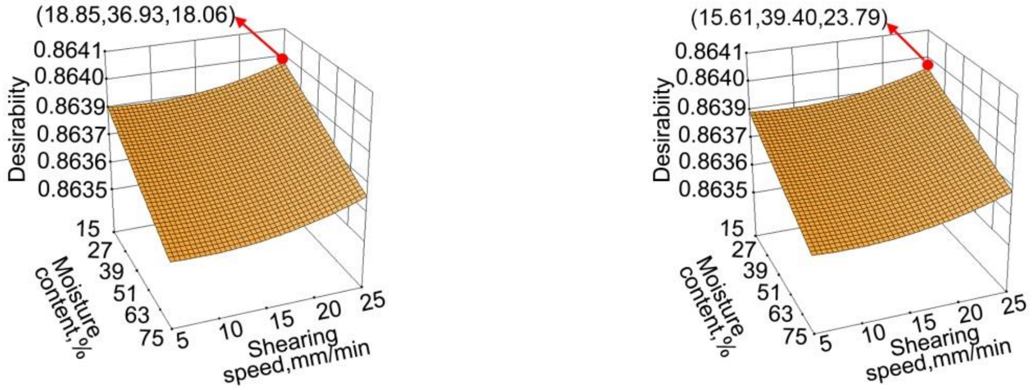

a (X_1,1,X_2) *b (X_1,2,X_2)*

a) *b)*

Fig. 7 a,b - Response surfaces of the desirability function of each sampling location

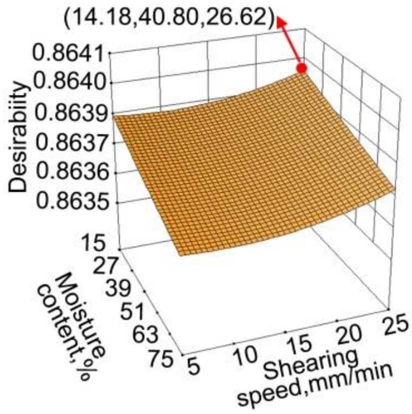

c (X1,3,X2)

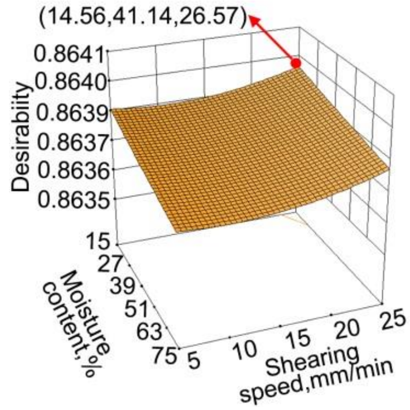

d (X1,4,X2)

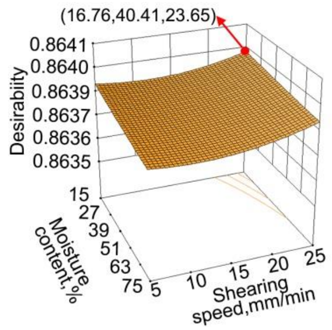

e (X1,5,X2)

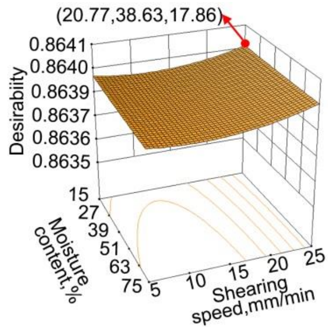

f (X1,6,X2)

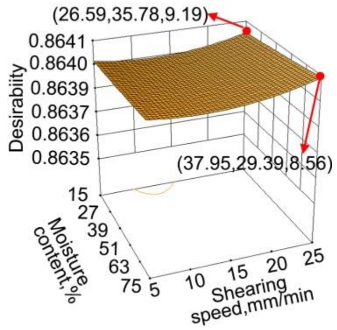

g (X1,7,X2)

Fig. 7 c,d,e,f,g - Response surfaces of the desirability function of each sampling location

The maximum values of the desirability function at different sampling locations are shown in Table 6. When the shearing speed was 25 mm/min, the desirability function of the 7th stalk section with a moisture content of 75% achieved the maximum value, which was similar to the 7th stalk section with a moisture content of 15%. Therefore, it is best relatively stable shearing technics to cut corn stalks with a moisture content of 15% at shearing speed of 25 mm/min. Using this shearing parameter to cut stalks has the characteristics of lower shearing strength of the whole stalk and higher shearing stability.

Table 6

Maximum values of the desirability function for each sampling location

Sampling location X_2 [node or internode]	Moisture content X_1 [%]	shearing speed X_3 [mm/min]	Internode critical shearing strength Y_1 [MPa]	Node critical shearing strength Y_2 [MPa]	DV Y_3 [MPa]	Maximum values of the desirability function D_{Max}
1	15	25	18.85	36.93	18.06	0.86397
2	15	25	15.61	39.40	23.79	0.86395
3	15	25	14.18	40.80	26.62	0.86396
4	15	25	14.56	41.14	26.57	0.86396
5	15	25	16.76	40.41	23.65	0.86397
6	15	25	20.77	38.63	17.86	0.86401
7	15	25	26.59	35.78	9.19	0.86406
	75	25	37.95	29.39	8.56	0.86409

CONCLUSIONS

(1) In this study, single factor test and analysis of variance were used to analyse the influencing factors of the critical shearing strength of nodes and internodes. The test results showed that the moisture content, sampling location and shearing speed had significant effects on the critical shearing strength of internodes and nodes.

(2) Regression models of internode and node critical shearing strength of corn stalks were established and analysed based on variance method and response surface method. The results showed that the order of the influencing factors on the internode critical shearing strength was moisture content >sampling location >shearing speed and that on the node critical shearing strength was sampling location >moisture content >shearing speed; the interaction factor of moisture content and sampling location had significant effects on the critical shear strength of nodes and internodes.

(3) Through the application of the Desirability Function Approach, the optimization problem of three response values, including DV, the node and internode critical shearing strength, was transformed into a single response value optimization, and then the relatively stable parameters of the whole corn stalks shearing were obtained. When using the shearing speed of 25 mm/min to cut corn stalks with a moisture content of 15%, the corn stalks had lower shearing strength and higher shearing stability.

ACKNOWLEDGEMENT

This research was funded by the Project supported by the National Natural Science Foundation of China (51405311) and Project Supported by Educational Commission of Liaoning Province (LSNZD201707).

REFERENCES

[1] Chen Zhengguang, Wang Defu, Li Liqiao, et al., (2012), Experiment on tensile and shearing characteristics of rind of corn stalk (玉米秸秆皮拉伸和剪切特性试验), *Transactions of the Chinese Society of Agricultural Engineering*, Vol.28, Issue 21, pp.59-65, Beijing/P.R.C;

[2] Chen Chaoke, Li Fade, Yan Yinfa, (2016), Analysis on the super capacitor vibration characteristic for hybrid electrical vehicle bus (高粱秸秆力学特性的试验), *Journal of Chinese Agricultural Mechanization*, Vol.37, Issue 5, pp.130-135, Nanjing/ P.R.C;

[3] Han Lujia, Yan Qiaojuan, Liu Xiangyang, et al., (2002), Straw resources and their utilization in China (中国农作物秸秆资源及其利用现状), *Transactions of the Chinese Society of Agricultural Engineering*, Vol.18, Issue 3, pp.87-91, Beijing/P.R.C;

[4] Igathinathane C., Womac A.R., Sokhansanj S., (2010), Corn stalk orientation effect on mechanical cutting, *Biosystems Engineering*, Vol.107, Issue 2, pp.97-106, Knoxville/USA;

[5] Li Qiang, Rouzi·Amuti, Li Shilong, (2015), Shear test of corn stalks(玉米秸秆剪切试验研究), *Journal of Chinese Agricultural Mechanization*, Vol.36, Issue 3, pp.63-66, Nanjing/ P.R.C;

[6] Wang Yan, (2012), *Research of mechanical properties and smash components of maize (玉米秸秆力学特性及饲草化部件研究)*, MSc dissertation, Jilin Agricultural University, Jilin/P.R.C;

[7] Wu Hongxin, (2013), *Research and simulated analysis for corn stalk harvesting technology and equipment (玉米秸秆收获关键技术与装备研究及数字化仿真分析)*, PhD dissertation, Chinese Academy of Agricultural Mechanization Sciences, Beijing/P.R.C;

[8] Wang Jinwu, Tang Han, Wang Jinfeng, (2017), Comprehensive utilization status and development analysis of crop straw resource in northeast China (东北地区作物秸秆资源综合利用现状与发展分析), *Transactions of the Chinese Society for Agricultural Machinery*, Vol.48, Issue 5, pp.1-21, Beijing/P.R.C;

[9] Xing Fang, (2017), *Experimental study on the physical and mechanical characteristics of corn stover (玉米秸秆物理机械特性试验研究)*, MSc dissertation, Shenyang Agricultural University, Shenyang/ P.R.C;

[10] Xu Zhengjie, Guo Xiaoyang, (2020), Optimization of bentonite parameters for shield tunnelling based on response surface method (基于响应面法的盾构施工膨润土改良参数优化), *Chinese Journal of Geotechnical Engineering*, pp.1-7, Nanjing/ P.R.C;

[11] Yu Yong, Lin Yi, Mao Ming, et al., (2012), Experimental study on tensile properties of corn straw (玉米秸秆拉伸特性的试验研究), *Transactions of the Chinese Society of Agricultural Engineering*, Vol.28, Issue 6, pp.70-76, Beijing/P.R.C;

[12] Zhang Kaifei, Li He, He Yujing, et al., (2016), Experimental Study on Mechanical Properties of Soybean Straw (大豆秸秆力学特性的试验研究), *Soybean Science*, Vol.35, Issue 2, pp.306-309, Haerbin/China;

[13] Zhang Yanqing, Cui Qingliang, Li Hongbo, et al., (2018), Effects of stem region, moisture content and blade oblique angle on mechanical cutting of millet stems, *INMATEH-Agricultural Engineering*, Vol.55, Issue 2, pp.105-112, Bucharest/Romania;

[14] Zhang Yanqing, Cui Qingliang, Li Hongbo, et al., (2020), Simulation and test of cutting mechanical characteristics of millet stalk based on ANSYS/LS-DYNA, *INMATEH-Agricultural Engineering*, Vol.61, Issue 2, pp.143-150, Bucharest/Romania.

DETERMINING THE EFFICIENCY OF A SMART SPRAYING ROBOT FOR CROP PROTECTION USING IMAGE PROCESSING TECHNOLOGY
/
تحديد كفاءة روبوت الرش الذكي لحماية المحاصيل باستعمال تقنية معالجة الصور

Mustafa Ahmed Jalal Al-Sammarraie*), Noor Ahmed Jasim [1]
College of Agricultural Engineering Sciences, University of Baghdad, Baghdad/Iraq
Tel: +964 7713489991; E-mail: mustafa.ahm@coagri.uobaghdad.edu.iq
Corresponding author: Mustafa Ahmed Jalal Al-Sammarraie
DOI: https://doi.org/10.35633/inmateh-64-36

Keywords: *machine learning, image processing, agricultural robot, forward speeds*

ABSTRACT
A system was used to detect injuries in plant leaves by combining machine learning and the principles of image processing. A small agricultural robot was implemented for fine spraying by identifying infected leaves using image processing technology with four different forward speeds (35, 46, 63 and 80 cm/s). The results revealed that increasing the speed of the agricultural robot led to a decrease in the mount of supplements spraying and a detection percentage of infected plants. They also revealed a decrease in the percentage of supplements spraying by 46.89, 52.94, 63.07 and 76% with different forward speeds compared to the traditional method.

الملخص
استخدم نظام لاكتشاف الإصابات في أوراق النبات من خلال الجمع بين التعلم الآلي ومبادئ معالجة الصور. تم تنفيذ روبوت زراعي صغير للرش الدقيق عن طريق تحديد الأوراق المصابة باستخدام تقنية معالجة الصور بأربع سرعات أمامية مختلفة (35 ، 46 ، 63 و 80 سم/ث). أظهرت النتائج أن زيادة سرعة الروبوت الزراعي أدى إلى انخفاض كمية رش المكملات ونسبة الكشف عن النباتات المصابة. كما انخفضت نسبة رش المكملات بنسبة 46.89 و 52.94 و 63.07 و 76٪ مع السرعات الأمامية المختلفة مقارنة بالطريقة التقليدية.

INTRODUCTION
One of the fundamental changes in human history is the "agricultural revolution", followed by the "industrial revolution", which contributed to the increase in the production of services and manufactured goods by greatly reducing the number of workers in the agricultural field (*Terzi et al., 2019*). Artificial intelligence technologies have also been developed. AI-based image processing applications are rapidly spreading in industrial agriculture. This technique has been used in various fields in the agricultural field, the most important of which is the fruit classification process using the image algorithm analysis technique. This technique proved successful with a high efficiency of 93.33% in the classification of pepper fruits using a Pixy2 camera *(Al-Sammarraie et al., 2021)*. Agricultural robots have also been used in modern technologies. Usually, these robots are electromechanical machines that are directed by a computer program or an electronic circuit. *(Dengyu et al. 2016)* developed a laboratory-type system controlled by image processing that could make various measurements on plants, extract types, growth rate, yield, and similar contents with great success. Artificial intelligence techniques have also been used in the diagnosis of plant diseases, as the application of pesticides in agriculture causes some negative aspects that affect human health and the environment. As a result of the intensive and unconscious use of agricultural pesticides, the pesticide itself or the by-products used may remain in the food, soil, water and air. Negative influences appear on other non-target organisms, humans and natural imbalances. Therefore, research is being conducted on ways to reduce pesticide spraying or control weeds or pests *(Malasli, 2010)*. The total production of pesticides in the world is approximately 3 million tons per year, and annual sales of pesticides range between 25-30 billion dollars *(Delen N, 2008)*. Herbicides and pesticides account for more than 70% of their use. The other pesticide groups had a 5% share. When evaluated in monetary terms, 31% of consumption consists of pesticides, 26% herbicides and 20% fungicides *(Tiryaki et al., 2010)*. The production of agricultural pesticides worldwide is increasing rapidly and new drugs are being developed daily. Therefore, the types of drugs used are increasing. Herbicides have the largest share of this increase, and it is estimated that the use of herbicides will become more widespread in the future. However, drugs used in chemical control have negative effects on human health, the environment, the natural balance and the increase in production costs; pesticides should be used sensitively and have minimal drug loss (*Çetin et al., 2018*). Therefore, the world today tends to use modern technologies that depend on image processing and automatic learning to spray pesticides accurately at different levels.

Mustafa Ahmed Jalal Al-Sammarraie, Assis. Lec. M.S.; Noor Ahmed Jasim, Assis. Lec. M.S. Eng.[1]

The development of weed control techniques has become a priority for the research community to increase crop yields and reduce costs, as well as the negative repercussions of herbicides *(Slaughter et al., 2008)*. *(Ali et al., 2017);* used a method to detect and classify major citrus diseases. The proposed technique applies a color difference algorithm to separate the affected area. Moreover, the pathology was classified using color graphs and compositional features. The authors claimed to have an accuracy of approximately 99.9%. *(Iqbal et al., 2018)* surveyed various methods used to detect and classify diseases in the leaves of citrus plants. They reported that only 22% of herbicides are required to reduce unwanted vegetation when applied in a precise manner. The authors identified the strengths and weaknesses of various image processing, segmentation, feature extraction, and classification methods. *(Søgaard et al., 2007);* introduced an automated system that uses a weed detection system to control the accurate dosing of herbicides. Weeds were detected using computer vision technology from data obtained through an independent vehicle resulting in a 50% reduction in herbicide use. *(Hossain et al., 2018)* used Support Vector Machine (SVM) to detect three different types of tea leaf diseases and achieved an accuracy of 90% using 150 training images and 50 test images. A similar process was used to detect anthracnose and canker disease and achieved 95% accuracy using 200 training images and 100 test images *(Gavhale et al., 2014)*. *(Sladojevic et al., 2016)* used a Convolutional Neural Network (CNN) classifier to identify 13 types of diseased leaves on 30,000 images. The system automatically detected diseases with an accuracy of 96.3%. *(Ferentinos, 2018),* has also improved the implementation of the CNN classification. Their proposed method can identify 58 diseases from 25 plants with 99.53% accuracy from 87,848 images. In addition, they used fine-tuning to significantly affect the overall resolution. *(Mohanty et al., 2016)* applied this approach to detect 26 out of 14 crop species with 99.35% accuracy using 54,306 images as a dataset.

Many disease detection algorithms require expensive and high-performance machines. In addition, it is difficult to obtain a high resolution. Moreover, a large number of human resources are needed to detect these diseases by naked eye. Therefore, it requires the use of smart agricultural sprinklers that can detect plant injuries or any other symptoms that appear on the leaf of the plant in real-time and can adjust the required amount of agrochemicals. This will lead to lower cost and improved spray quality by ensuring optimum application of spray materials, reducing farmer's exposure to toxic agricultural chemicals and reducing environmental impact. Robots have become a major part of our daily lifestyle and they have a wide scope in agricultural engineering. They play a vital role in the development of new technology. In this study, a model of a small agricultural robot was designed and implemented to spray pesticides or liquid fertilizers accurately at four different forward speeds (35, 46, 63 and 80 cm/s) based on the methodology of modern technology. This disease may cause several symptoms in the leaves. Therefore, the methodology used is to develop a system that detects plant diseases or any problem that appears in the leaf of the plant due to high heat, humidity, or a problem with the salinity of the soil effectively through the application of image processing and machine learning. This methodology can also detect healthy leaves. If any disease is detected, it determines the exact percentage of the pesticide or liquid fertilizer in the area affected by the disease.

MATERİALS AND METHODS

The methodology proposed in this research consists of five steps: image collection, image processing using Matlab software, image segmentation, Feature Extraction (color), data collection acquisition and description and finally programming the small agricultural robot to spray pesticides or liquid fertilizer at different levels and accurately. Figure 1 shows the proposed system.

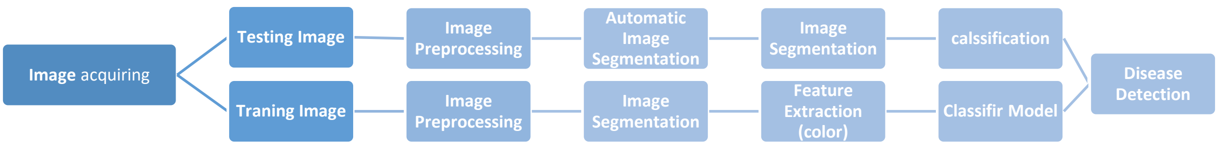

Fig. 1 - System methodology

As mentioned previously, the agricultural robot can detect leaves that show problems other than disease. Therefore, the term “infected plants or infected leaves” is adopted in the research. Images of the citrus Aurantium were taken from the College of Agricultural Engineering Sciences / University of Baghdad fields.

Reddish-yellow leaves are discovered due to heat and high humidity, or the cause may be due to the salinity of the soil. To treat soil salinity, improve its physical and chemical properties and activate beneficial microorganisms, a humic acid solution was added to an agricultural spraying robot. Some images were taken in the laboratory for laboratory calibration and the rest were taken from the field. The proposed model recognizes the following items:

1. Infected leaves.
2. Uninfected leaves.

Matlab software was used to process the plant images and the background of the image was removed leaving only the image of the Leaf. To detect the disease, it is necessary to remove the green parts of the image. After these operations, the only remaining part (Greenness elimination mask) showed symptoms significantly. Figure 2 shows the stages of the display of the affected part of the leaf.

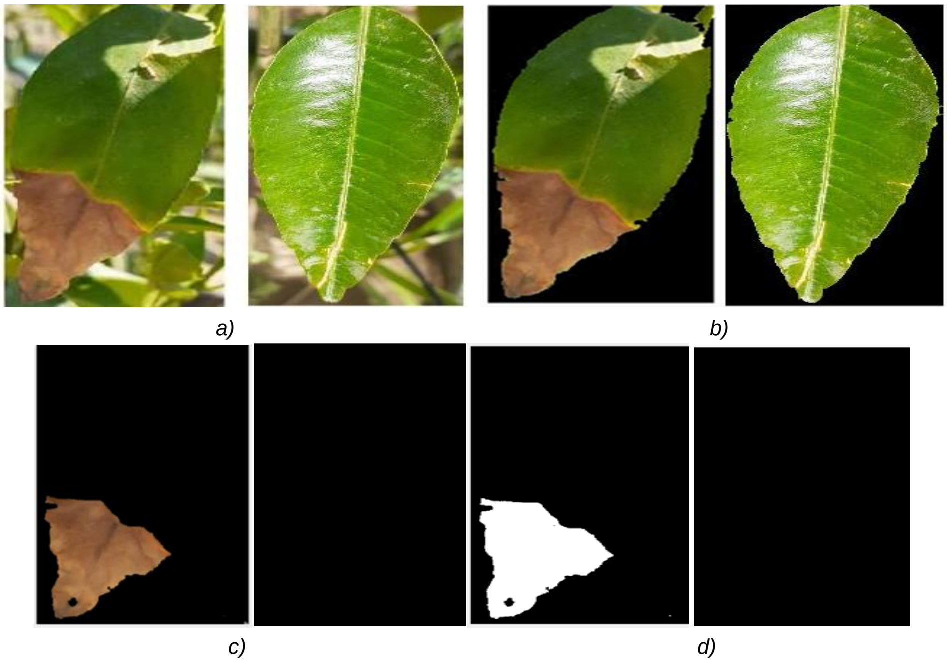

Fig. 2 - Image process

a) Original image; b) Primary image; c) Greenness elimination mask; d) Image thresholding

By observing the images of the affected and healthy areas, it can be seen that they have differences in color, edges and shapes. Therefore, all these features were used to classify the infected leaves. All these processes are shown in Figure 2. A green pixel was removed from the image because it represents the healthy area of the leaf. After removing it, only the affected part remains as we have already removed the background. Therefore, the perimeter of the diseased area can be easily detected now because of heat, humidity, or soil salinity.

As shown in Figure 3, the graph equation applied to the color tone of the affected leaf was applied. Using the Otsu thresholding algorithm, each image was converted into a binary image. This process separates each infected part away from the uninfected parts, the infected parts appear white and the rest black.

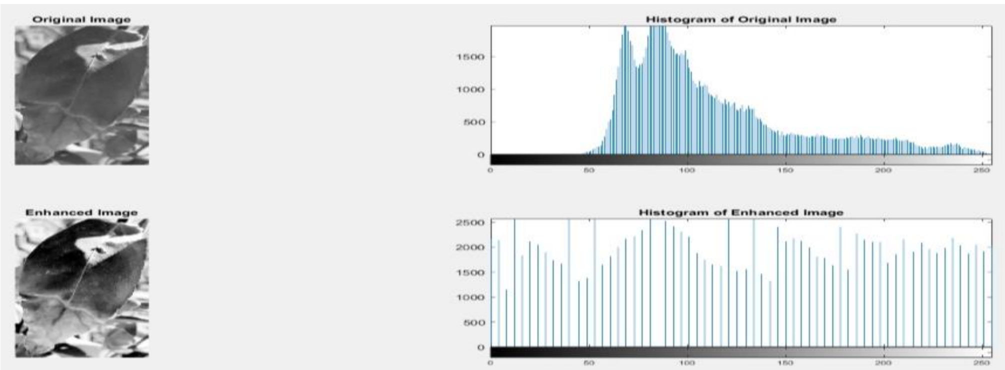

Fig. 3 - Histogram equalization on the hue of an image

RGB color space is designed to define colors in a cube unit using the added color mixing method. These three colors are mixed with a certain intensity to display any color on the digital screen. RGB color space can be considered as a three-dimensional space with format axes in red, green and blue (Figure 4). The colors to be created can be expressed in terms of the coordinates of these three primary colors *(Sabancı, 2014).*

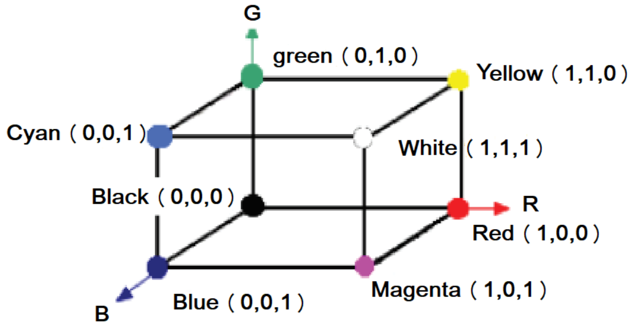

Fig. 4 - RGB color space coordinate axes

The image was classified into RGB channels to identify the plant leaf in the image, the image was taken by the digital camera on the micro-spray robot. Equation 1 was used to get the red value index, which will be targeted to select red-colored entities in image processing algorithms *(Ramaraju et al., 2014)*.

$$F = R - 0.5G - 0.5B \tag{1}$$

Where:

R is the red coefficient; G is the green coefficient; B is the blue coefficient of the image respectively. To distinguish red color information, the values of green (G) and blue (B) were multiplied by 0.5 and subtracted from the value of red (R). The purpose of this function is to determine how close color (F) is to red.

From the spatial point of view of infected and intact places, it was noted that both have different colors. Therefore, the features of the color chart can be used to classify infected plant leaf from uninfected. The image was converted to RGB scale (red, green, blue). When the image is converted to RGB the color chart is drawn. It can be observed in Figure 5 that the RGB scale is different for both images. The proportion of red in infected leaves is greater than in healthy leaves; in contrast, the proportion of green in healthy leaves is greater than in infected leaves.

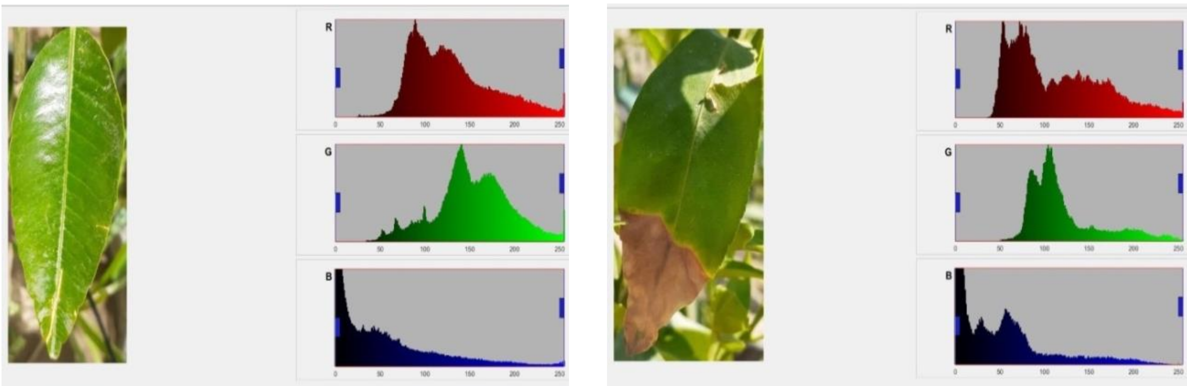

Fig. 5 - RGB scale for infected and healthy plant leaf

To demonstrate the previous conclusion, the proportion of the three colors in each region can be determined. Each pixel consists of three separate components, these ingredients weigh the primary colors red, green and blue that make up the color of the Pixel. Each component pixel of the image has red, green and blue values ranging from 0-255.

Figure 6 shows matrices for the three-color values of specific areas of healthy and infected leaves.

As discussed early, the healthy leaf image will show a higher percentage of green over red and blue, Figure 6.b. shows the lowest percentage of green color is 100, that the highest percentage of red color is 75, i.e. G< R and that indicates a healthy leaf, while Figure 6.a. shows that highest percentage of green color is 92 and the lowest percentage of red color is 138, i.e R<G which leads to conclude that this leaf was infected.

R: 73 G: 104 B: 10	R: 75 G: 106 B: 13	R: 74 G: 104 B: 14	R: 73 G: 103 B: 13	R: 72 G: 102 B: 12
R: 73 G: 104 B: 10	R: 75 G: 106 B: 13	R: 74 G: 104 B: 14	R: 73 G: 103 B: 13	R: 72 G: 102 B: 12
R: 70 G: 104 B: 9	R: 73 G: 104 B:11	R: 72 G: 103 B: 10	R: 71 G: 101 B: 11	R: 70 G: 100 B: 112
R: 70 G: 102 B: 5	R: 71 G: 103 B: 6	R: 71 G: 102 B: 8	R: 69 G: 100 B: 6	R: 68 G: 100 B: 6

R: 140 G: 90 B: 57	R: 140 G: 90 B: 57	R: 140 G: 90 B: 57	R: 140 G: 90 B: 57	R: 140 G: 90 B: 57
R: 140 G: 90 B: 57	R: 142 G: 92 B: 57	R: 142 G: 92 B: 59	R: 140 G: 90 B: 57	R: 138 G: 88 B: 55
R: 139 G: 89 B: 57	R: 141 G: 91 B: 58	R: 141 G: 91 B: 58	R: 140 G: 90 B: 57	R: 138 G: 88 B: 55
R: 139 G: 89 B: 56	R: 139 G: 89 B: 56	R: 139 G: 89 B: 56	R: 139 G: 89 B: 56	R: 138 G: 88 B: 55

a) *b)*

Fig. 6 - RGB value matrices

a) Infected; b) Healthy

Robot assembly

In traditional spraying methods, the nozzle is always open during spraying. Thus, spraying is carried out in places where there are no infected plants. In this study, a small high-performance robot with a mechanism for spraying liquid fertilizer based on image processing was designed. Precision spray robot was developed with a digital camera to acquire real-time leaf images, as the infected leaf image is captured by this camera, the spray will automatically start and nozzle spray will continue as long as the captured image is recognized as infected. For the robot to work successfully in the experimental environment, it is necessary to provide key kinetic abilities. First, infected leaves detection using an image that digital camera capture, second sprays the infected leaves that have been diagnosed by a designed spraying system (static discharge pump and nozzle). To successfully achieve these two processes, DC motors, wheel system and camera module are integrated for image analysis.

The microcontroller-based robot consists of a digital camera compatible with the Arduino Uno as well as a transceiver module. Industrial Pixy2 camera was used to capture real-time images of leaves. Due to its low cost and ease of use, it is commonly used in small projects related to robotics and artificial intelligence. The camera used has Omnivision OV9715 sensor, 1/4", 1280 × 800. It can receive 50 images per second (1 image per 20 milliseconds) and can be connected to a computer through USB. In addition, it is very lightweight at 27 g with a low power consumption of up to 140 mA *(Omosekeji, 2018)*. The camera with the Arduino Uno controller is connected using the serial communication protocol. L293d motor driver shield was also used to drive 4 DC motors and one DC pump with a discharge of 240 l/h that is driven by a DC motor by connecting to the required terminals. The Arduino Uno board represents an actual programming platform based on ATmega328 and is operated with an input voltage of 5.5 V and has a maximum operating frequency of 20 MHz *(Krishna et al., 2012)*. The power supply for Arduino Uno can be either via a USB connection, DC power supply or both. It is also a high-performance device with a low-power 8-bit AVR microcontroller with 32 KB in the system and advanced reduced instruction set computing *(Abdullah et al., 2012).* It also consists of an I/O port and software development environment. It has 13 digital I/O pins (6 of which can be used as PWM outputs), 6 analog inputs, a USB connection, a power socket, an ICSP head, and a reset button. It has everything needed to support the microcontroller. It can be simply plugged into a computer using a USB cable. The C programming language controller program is written in an editable format for processing sensor data. The work is also based on the Bluetooth Command Sending and receiving module. The remote control is a smart Android device with a Bluetooth app. Thus, the receiving area has an Arduino Uno board as a controller and an HC-05 Bluetooth module as a remote communication module for exchanging data over short distances (using short-wavelength UHF radio waves in the ISM range from 2.4 to 2.485 GHz). The range is about 5-30 meters, these units are based on the Cambridge BC417 wireless Bluetooth radio chip with a frequency of 2.4 GHz *(Jayantilal, 2014)*. When the Bluetooth application is launched and connects to the current system via Bluetooth, the robot will receive wireless commands using the functions programmed in the application. The robot moves in four directions: forward, backward, right and left. In forward movement, the four DC motors will move in the same direction and for the rear movement, the DC motors will reverse their direction. For left and right movements, the motors of one side will rotate depending on the direction of rotation. L293d motor driver shield was used as a two-way robot wheel controller.

This motor driver shield allows us to easily and independently control and drive the DC motors. It is ideal for robotic applications and perfectly suited to microcontrollers that only require control lines for each motor. Figure 7 shows the motor drive shield with Arduino and Bluetooth.

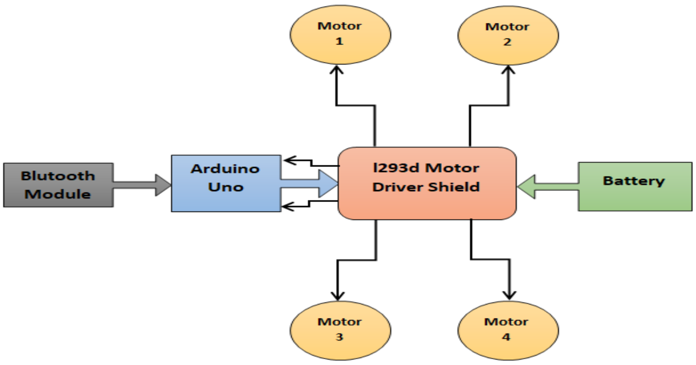

Fig. 7 - Arduino motor driver shield

The circuit consists of an Arduino UNO board, HC-05 Bluetooth Module, L293d motor driver shield, four 250 rpm geared DC motors (wheel rotation speed can be controlled by application) and an 11V rechargeable battery. The TX and RX pins of the Arduino are connected to the Rx and Tx pins of the Bluetooth module. The Bluetooth module is equipped with a voltage of 5V. The power supply was obtained by connecting the Lipo Battery as a power source for the first stage of the moving robot. This battery can save from mAh1800 of current and average voltage 11.1 V. These batteries are useful in terms of being rechargeable for many business robotic. Three solar cells were also used as battery charging sources with an average voltage of 15v and 660 mA, each cell gives 5V and 220 mA. Figure 8 shows the overall connection of the agricultural robot electrical circuit.

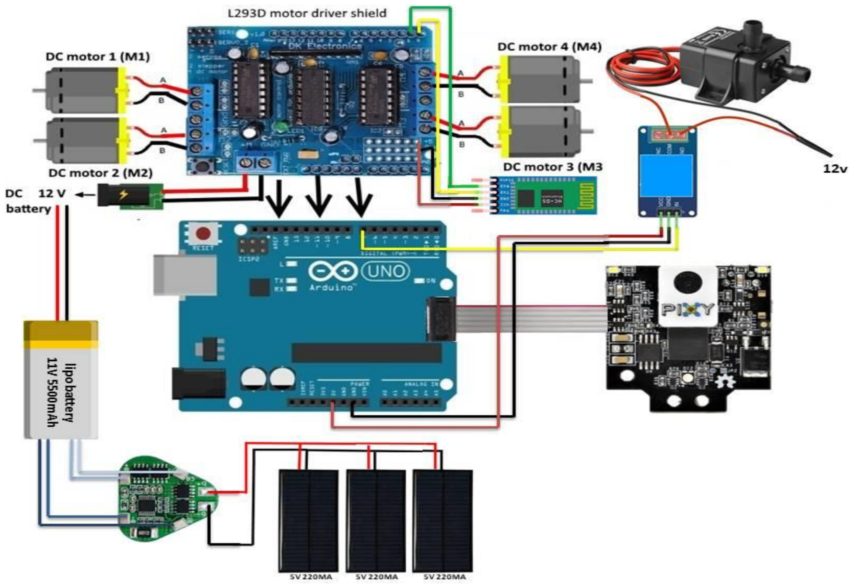

Fig. 8 - Agricultural robot diagram

Procedure

Images of infected citrus leaves were used in the experiment, these images were taken from the experiment field, image algorithms and analysis were performed to identify the infected leaves from healthy ones; as mentioned before, a threshold value of red color was chosen, the obtained images data were used as a reference to the microcontroller unit using Matlab and Arduino IDE software. The developed system works fast and stable. The proposed prototype robot was tested inside a greenhouse in the fields of the Agricultural Engineering Sciences College/ University of Baghdad. Four different speeds (35, 46, 63 and 80 cm/s) were used with a distance of 10 meters. Pixy2 camera was placed at a height of 50 cm from the ground to obtain real-time field images of plant leaves. As the proposed robot is a prototype and for the experimental test data was taken from the lower part of the plant, as the robot detects infected leaves (red color index exceeds a threshold value), control signal was given to the spray pump to spray liquid fertilizer using a spray arm, consisting of a nozzle with a screw valve, a specified amount of agricultural pesticides was applied depending on the operating time. The liquid fertilizer amount spraying was calculated for three levels of ground speed of the agricultural robot, comparing the amount of spraying with the manual method and studying the amount of discharge in the spraying of the starter. Figure 9 shows the experiment.

Fig. 9 - Robot prototype in the field

RESULTS

The experiment was conducted in a greenhouse for a distance of 10 meters. 20 planted pots were arranged along 10 meters, 12 of the plants being infected. By detecting 12 infected plants on the precise spray robot movement path, the amount of liquid spray fertilizer used in conventional spraying has been compared with the developed system. The robot applied approximately 1-7 ml of liquid spray in the micro-spray state of every single plant, the nozzle height was 50 cm and there were four different forward speeds (35, 46, 63 and 80 cm/s). The savings rates in the amount of liquid spray applied to infected plants were determined using a precision spray robot, according to ground speed. The results are shown in Figure 10.

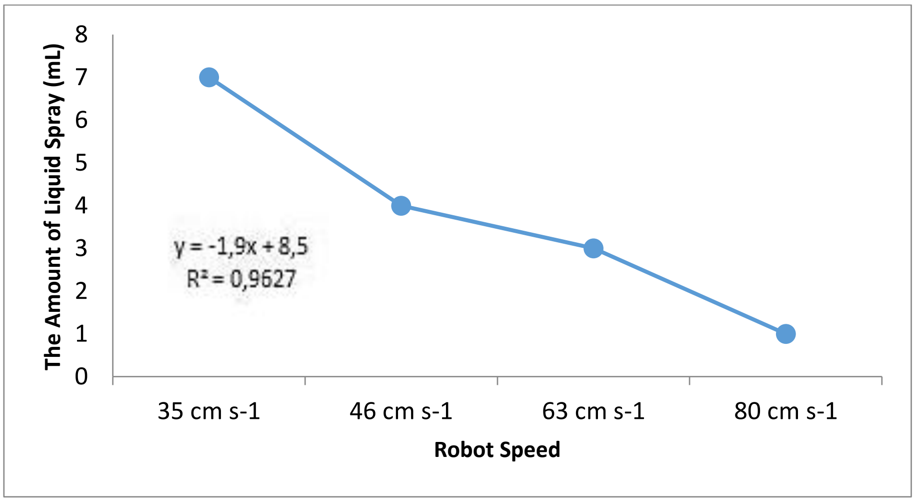

Fig. 10 - Robot speed vs liquid spray

As shown in Figure 10, the amount of fertilizer was reduced as the ground speed increased. The 80 cm/s speed shows the lowest spraying liquid fertilizer amount of about 1 ml while the 35 cm/s speed gives the highest spraying liquid fertilizer amount of 7 ml per infected plant. Increasing the speed of the spray robot leads to a decrease in the amount of liquid spray applied to the grass *(Sabancı, 2014)*. Regression equations and determination coefficients were calculated showing the relationship between ground velocity and the amount of liquid fertilizer spraying. It turns out that there is a polynomial relationship between ground velocity and the amount of liquid fertilizer spraying. The coefficient for determining regression equations is 96.27%. From this concept, it is clear that there is a clear inverse relationship between ground speed and the amount of liquid fertilizer spraying.

The amount of spray fluid changes according to the frequency of image capture as well as the percentage of detection of plant diseases. the spraying time increases with the decrease in ground speed because the value of the red color will take longer in the image frame as the agricultural robot moves forward. The rate of detection of infected leaves is also higher as the ground speed decreases. Therefore, the amount of pesticide applied was also higher.

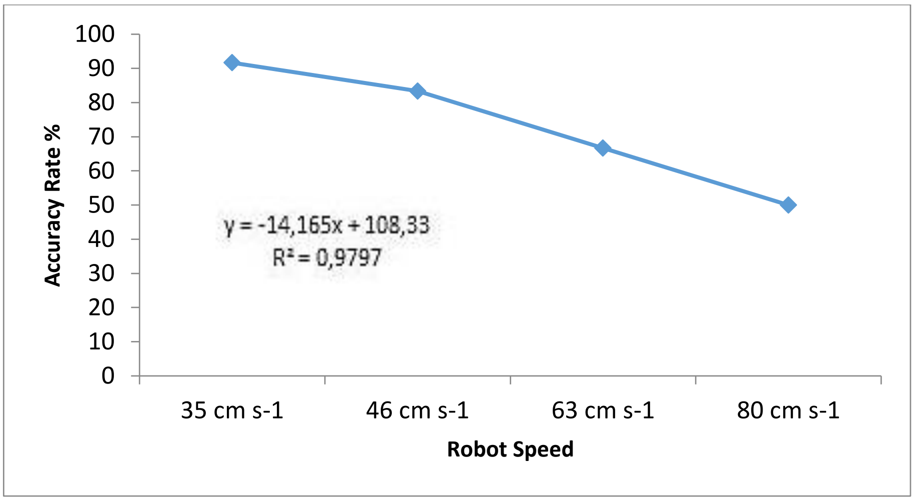

Fig. 11 - Robot speed vs. accuracy rate

As shown in Figure 11, the detection of plant diseases decreases as the ground speed increases. The 80 cm/s speed was recorded as the lowest rate of detection of plant diseases of 50%; the highest detection of plant diseases of 91.66% was measured for 35 cm/s speed. As the speed of the developed spray robot increases, the amount of spray liquid applied to the plant leaves decreases. As the speed of the micro-spray robot increases, the rate of images received by the webcam decreases *(Sabancı, 2014)*. Regression equations were calculated and coefficients showed that there was a distinguishing mark between the speed and the amount of liquid fertilizer spraying. The coefficient for determining the regression equations is 97.97%. This result shows that there is a clear inverse relationship between the ground speed of the precise spray robot and the amount of liquid fertilizer spraying.

In comparison with the traditional spraying method, for a distance of 1 meter approximately 6 - 77 ml liquid spray was applied using the robot system, while 25 - 145 ml of liquid spray was applied in the case of the traditional spraying. Figure 12 shows the relation between robot speed vs. spray amount for both techniques.

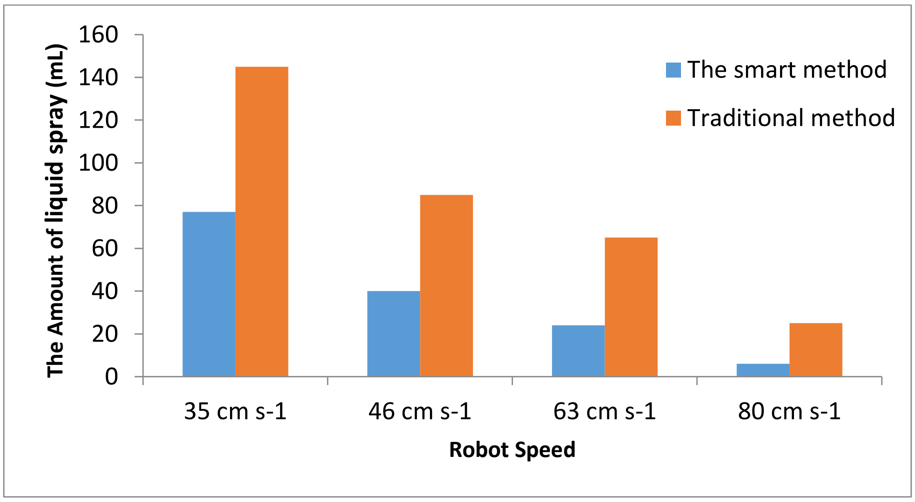

Fig. 12 - Robot speed vs. Spray amount for both techniques

Figure 12 shows that by increasing ground speed, the spraying rate decreases in both traditional and robotic ways. The spraying rates by using the traditional method are 145, 85, 65 and 25 ml while the rates of 77, 40, 24 and 6 ml are for robot spraying, respectively. When the speed of the precision spray robot increases from 35 cm/s to 46 cm/s, that is, the speed increase by 31.42% results in an 84.09% decrease in the amount of liquid spray applied by the smart method while the proportion of spraying by the traditional method decreased to 41.37%. The smart method gave a 46.89% (68 ml) reduction in the spraying rate compared to the traditional method at a first speed.

When the speed of the precision spray robot increases from 46 cm/s to 63 cm/s, the speed increases by 36.95%. This will reduce the amount of liquid spray by 40% using the smart method, while the traditional method gave a decrease of 23.52%. The smart spraying method gave a 52.94% (45 ml) reduction in the spray rate compared to the traditional method at the second speed. The third speed gave an average decrease of 63.07% (41 ml) compared to the smart and traditional method. Increasing the speed of the spray robot from 63 cm/s to 80 cm/s gave an increase in the ground speed of the agricultural robot by 26.98% resulting in a decrease in the spray rate by 75% in the smart method and 61.53% in the traditional method. The smart method gave a 76% reduction in the spray rate (19 ml) compared to the traditional method at the fourth speed.

Williams et al., (2000) states that the spray rate for weed control by developed sensors decreased by 11.5-98% compared to the amount of medicine applied compared to conventional methods. *Feyaerts et al., (1999)* found a 90% reduction in the amount of medication in image processing applications for herbicides. *Watchareeruetai et al., (2006)* showed that using image processing techniques, reported a 90-94% reduction in the use of chemical pesticides in spraying by detecting weeds in the grass.

CONCLUSIONS

The infected plants will be detected and the liquid will be sprayed only on the infected plants instead of the entire field using a precision agricultural robot. Human, environmental and animal health will be protected due to low pesticide or liquid fertilizer consumption. The precision spraying system developed in the experiment on 20 pots for a distance of 10 meters saved 46.89, 52.94, 63.07 and 76% of pesticide with different forward speeds respectively compared to the traditional method. The amount of liquid spray sprayed on infected plants has changed inversely with the speed of the precise spray robot. As the speed of the developed spray robot increased, the amount of liquid spray being sprayed on the infected plants decreased. When the speed of the precision spray robot increases from 35 cm/s to 46 cm/s, that is, the speed increase by 31.42% results in an 84.09% decrease in the amount of liquid spray applied by the smart method. The proportion of spraying by the traditional method decreased to 41.37%. When increasing the ground speed of the micro-spray robot from 46 cm/s to 63 cm/s, that is, increasing the speed by 36.95% reduced the amount of liquid spray by 40% using the smart method, while the traditional method gave a decrease of 23.52%. Increasing the speed of the spray robot from 63 cm/s to 80 cm/s gave an increase in the ground speed of the agricultural robot by 26.98% resulting in a decrease in the spray rate by 75% in the smart method and 61.53% in the traditional method. The excessive use of herbicides leads to significant contamination of both soil and Water Resources indirectly, or in the case of excessive spraying of liquid fertilizers, will lead to material losses. When the study was developed and applied in one of the greenhouses of the citrus Aurantium plant, liquid fertilizers applied only to the infected plants, in this case, there will be no drug fertilizers on the uninfected plants. The developed sensitive spraying system model can be developed and used in greenhouses to spray variable-level herbicides. The same system can be used to spray plants in vegetable fields and use liquid fertilizer, and input costs can be reduced.

ACKNOWLEDGEMENT

The project was not funded by any entity or institution. It was personally funded.

REFERENCES

[1] Abdullah, A., Sidek, O., Amran, N. A., Za'Bah, U. N., Nikmat, F., Jafar, H., & Hadi, M. A. (2012). Development of wireless sensor network for monitoring global warming. *2012 International Conference on Advanced Computer Science and Information Systems (ICACSIS)*, 107–111, Malaysia.

[2] Ali, H., Lali, M. I., Nawaz, M. Z., Sharif, M., & Saleem, B. A. (2017). Symptom based automated detection of citrus diseases using color histogram and textural descriptors. *Computers and Electronics in Agriculture*, 138, 92–104, Pakistan.

[3] Al-Sammarraie, M. A. J., & Özbek, O. (2021). Comparison of the Effect Using Color Sensor and Pixy2 Camera on the Classification of Pepper Crop. *Journal of Mechanical Engineering Research and Developments*, 44(1), 396–403, Baghdad/Iraq.

[4] Çetin, N., Sağlam, C., & Demir, B. (2018). Pülverizatör Memelerinde Püskürtme Açısı Değişimlerinin Görüntü İşleme Yöntemiyle Belirlenmesi. *3rd International Mediterranean Science and Engineering Congress*, 1592–1596.

[5] Delen N. (2008). *Fungisitler*. Nobel Yayın Dağıtım. Nobel Yayın No: 1360, Ankara/Turkey.

[6] Dengyu, X., Liang, G., Chengliang, L., & Yixiang, H. (2016). Phenotype-based robotic screening platform for leafy plant breeding. *IFAC-PapersOnLine*, 49(16), 237–241, China.

[7] Ferentinos, K. P. (2018). Deep learning models for plant disease detection and diagnosis. *Computers and Electronics in Agriculture*, 145, 311–318, Greece.

[8] Feyaerts, F., Pollet, P., Van Gool, L., & Wambacq, P. (1999). Sensor for weed detection based on spectral measurements. *Proceedings of the Fourth International Conference on Precision Agriculture*, 1537–1548, Belgium.

[9] Gavhale, K. R., Gawande, U., & Hajari, K. O. (2014). Unhealthy region of citrus leaf detection using image processing techniques. *International Conference for Convergence for Technology-2014*, 1–6, India.

[10] Hossain, S., Mou, R. M., Hasan, M. M., Chakraborty, S., & Razzak, M. A. (2018). Recognition and detection of tea leaf's diseases using support vector machine. 2018 *IEEE 14th International Colloquium on Signal Processing & Its Applications (CSPA)*, 150–154, Bangladesh.

[11] Iqbal, Z., Khan, M. A., Sharif, M., Shah, J. H., ur Rehman, M. H., & Javed, K. (2018). An automated detection and classification of citrus plant diseases using image processing techniques: A review. *Computers and Electronics in Agriculture*, 153, 12–32, Pakistan.

[12] Jayantilal, S. H. (2014). Interfacing of AT Command based HC-05 Serial Bluetooth Module with Minicom in Linux. *International Journal for Scientific Research & Development*, 2(3), 329–332, India.

[13] Krishna, R., Bala, G. S., ASC, S. S., Sarma, B. B. P., & Alla, G. S. (2012). Design and implementation of a robotic arm based on haptic technology. *Int. J. of Eng. Research and Applications*, 2(34), India.

[14] Malasli, M. Z. (2010). *Şeker pancarı üretim alanlarında yabancı otla mücadele yöntemleri ve uygulama etkinliklerinin belirlenmesi / Weed control methods in sugarbeet production fields and determination of application efficiency*. MSc Thesis, Turkey.

[15] Mohanty, S. P., Hughes, D. P., & Salathé, M. (2016). Using deep learning for image-based plant disease detection. *Frontiers in Plant Science*, 7, 1419, Switzerland.

[16] Omosekeji, G. M. (2018). Industrial Vision Robot with Raspberry Pi using Pixy Camera: *Stereo Vision System*, Finland.

[17] Ramaraju, S., & Kumar, N. U. (2014). Saliency detection algorithm for locating perceptible objects. *Int. J. Electron. Commun. Technol*, 5(3), 97–100, India.

[18] Sabancı, K. (2014). Image Processing Based Precision Spraying Robot. *Journal of Agricultural Sciences*, 20(4), 406, Turkey.

[19] Slaughter, D. C., Giles, D. K., & Downey, D. (2008). Autonomous robotic weed control systems: A review. *Computers and Electronics in Agriculture*, 61(1), 63–78, United States.

[20] Søgaard, H. T., & Lund, I. (2007). Application accuracy of a machine vision-controlled robotic micro-dosing system. *Biosystems Engineering*, 96(3), 315–322, Denmark.

[21] Sladojevic, S., Arsenovic, M., Anderla, A., Culibrk, D., & Stefanovic, D. (2016). Deep neural networks based recognition of plant diseases by leaf image classification. *Computational Intelligence and Neuroscience*, 2016, Serbia.

[22] Terzi, İ., Özgüven, M. M., Altaş, Z., & Uygun, T. (2019). Tarimda Yapay Zeka Kullanimi. International Erciyes Agriculture, *Animal & Food Sciences Conference*, 245–255.

[23] Tiryaki, O., Canhilal, R., & Horuz, S. (2010). The use of pesticides and their risks. Erciyes University *Journal of the Institute of Science and Technology*, 26(2), 154–169, Turkey.

[24] Watchareeruetai, U., Takeuchi, Y., Matsumoto, T., Kudo, H., & Ohnishi, N. (2006). Computer vision based methods for detecting weeds in lawns. *Machine Vision and Applications*, 17(5), 287–296, Japan.

[25] Williams, M. M., Gerhards, R., & Mortensen, D. A. (2000). Two-year weed seedling population responses to a post-emergent method of site-specific weed management. *Precision Agriculture*, 2(3), 247–263, Germany.

DESIGN AND EXPERIMENT OF TRANSPLANTING MACHINE FOR CABBAGE SUBSTRATE BLOCK SEEDLINGS
/
甘蓝基质块苗移栽机设计与试验

Zhichao Cui[1)], Chunsong Guan[1)], Tao Xu[2)], Jingjing Fu[1)], Yongsheng Chen[1)], Yating Yang[1)], Qingsheng Gao[1)] [1]

[1)] Nanjing Institute for Agricultural Mechanization, Ministry of Agriculture and Rural Affairs, Nanjing 210014, China

[2)] Institute of Agricultural Facilities and Equipment, Jiangsu Academy of Agricultural Science, Nanjing 210014, China

TEL：+86 02584346254；E-mail: cs.guan@163.com

Corresponding author: Chunsong Guan

DOI: https://doi.org/10.35633/inmateh-64-37

Keywords: *transplanter, substrate block seedlings, automatic seedling separating, planting device, cabbage, lodging rate, missing rate*

ABSTRACT
Aiming at the problems of high specificity and low efficiency of vegetable transplanting machine, a substrate block seedling transplanter was designed. Through theoretical calculation and force analysis, the structural parameters of two key components of automatic seedling separation device and planting device are determined. Taking cabbage seedlings with 40 × 40 × 40mm substrate block size as the experimental object, the effects of forward speed, planting frequency, front conveyor belt speed on lodging rate, missing rate and qualified rate were studied by single factor test and three factor three-level orthogonal test. Based on the analysis of the significance and interaction of the experimental data, the best combination of the forward speed of 1.1km/h, the planting frequency of 55 plants / min and the front conveyor belt speed of 0.5km/h was obtained. The verification test of the best combination showed that the average qualified rate of planting was 93.31%, which met the relevant industry standards.

摘要
针对现有蔬菜移栽机专用性强，低效费工等问题，设计了一种基质块苗移栽机。通过理论计算、受力分析确定了自动分苗装置和栽植装置两大关键部件的结构参数。以基质块尺寸为40×40×40mm的甘蓝苗为试验对象，通过单因素试验和三因素三水平正交试验，研究了前进速度、栽植频率、前输送带速度等因素对倒伏率、漏栽率和合格率的影响，并进行了显著性和交互作用影响分析，获得了前进速度为1.1km/h、栽植频率为55株/min、前输送带速度为0.5km/h的最佳参数组合，对最佳组合进行了验证试验表明，平均栽植合格率为93.31%，满足相关行业标准。

INTRODUCTION
Cabbage is one of the most widely planted vegetable varieties in China. The annual planting area is maintained at 900,000 hm^2 and the annual output is 2.2 million tons. It has a prominent position in vegetable production and supply (*Yang et al., 2016*). The planting of cabbage mostly adopts the technology of seedling raising and transplanting, which is hard to guarantee the quality of operation due to the high labor intensity and low operation efficiency of manual transplanting. The development of cabbage transplanting machine is of great significance for improving transplanting efficiency, reducing manual labor intensity and improving operation quality (*Chen, 2017; Cui et al., 2020; Prasanna, G., 2008*). The existing vegetables transplanter has strong specificity and poor adaptability to substrate block seedlings. At present, there is still a lack of transplanter suitable for substrate block seedlings of cabbage in China.

European countries started to study the technology and equipment of substrate block seedling transplanting earlier (*RYU K H et al., 1998; Pramod, C. et al., 2017; Yu et al., 2014; Feng et al., 2015; Jin et al., 2015; Zhou et al., 2015; He et al., 2018; Cui et al., 2019*). For example, FPC developed by Italy's Ferrari and Tre Matic transplanting machine developed by Hortech have realized automatic transplanting of vegetable substrate block seedlings on film.

[1] *ZC Cui, Assis. Rese.M.S. Eng; CS Guan, Assis. Rese. Ph. D. Eng; T Xu, Assis. Rese.M.S. Eng; JJ Fu, Assis. Rese.. Ph. D. Eng; YS Chen, Rese. B.C. Eng; YT Yang, Assoc. Rese. Eng; QS Gao, Assis. Rese.M.S. Eng.*

Based on the principle of pneumatic control, French company CM&Regero developed the R2010 substrate block seedling transplanter, which realized the high speed and efficient transplanting of vegetables., a greenhouse fixed channel substrate block seedling transplanter was developed by Chrysant Arcadia, a Dutch company, which can realize the periodic and continuous automatic planting of chrysanthemum substrate block seedlings. The substrate block seedling transplanter developed by European and American countries is mainly developed for the domestic crop planting mode and agronomic requirements. The whole machine tends to be large and functional, and requires higher land conditions, so it is not suitable for the substrate block seedling transplanter of cabbage under the complex terrain environment in China. At present, the research focus of Chinese scholars on the vegetable transplanter is mainly on the hole dish seedling and blanket seedling. For example, Hu Jianping's team based on the pneumatic and PLC control principle developed a vegetable hole plate seedling self-propelled transplanter, which realized the function of multi-row seedling synchronous selection and seedling casting (*Hu et al., 2016; Yang et al., 2018)*. Wu Chongyou's team developed an automatic transplanting machine for rapeseed blanket seedlings, which realized continuous supply and high-speed transplanting of rapeseed seedlings *(Wu et al., 2016; Wu, et al., 2020)*. Mechanized transplanting has been realized in the above two seedling raising methods, but there are also problems of missing transplanting and lodging in the process of taking and throwing seedlings, and there are few reports on the substrate block seedling transplanting machine of cabbage.

In view of the problems of missing and lodging of the existing transplanter affecting the planting quality, a pneumatic substrate block seedling transplanter was developed with the cabbage substrate block seedling as the research object. The whole row of substrate block seedlings were separated by individual plants by the pneumatic stopper structure, and the single plant substrate block seedlings were transplanted into the soil by the directional clamping function of the planter. This transplanter solves the problem that the existing transplanter cannot adapt to the operation of substrate block seedling. Besides, it provides reference for the development of mechanized transplanting technology of Chinese cabbage.

MATERIALS AND METHODS

Design of the test prototype

Overall structure and Working principle

The transplanter is mainly composed of row-based seedling intermittent conveying devices, automatic seedling separating devices, planting devices, transmission systems, trenching and soil covering devices, and racks. Among these, the row-based seedling intermittent conveying devices, automatic seedling separating devices, and planting devices are longitudinally connected sequentially, and are arranged in a modular manner inside the rack. The seedling separating devices and the conveying device, respectively, connect the front conveying belt and the rear conveying belt in the substrate block seedling transportation, and the front conveyor belt extends from the side into the upper circumferential planter of the planting device. The planting device is equipped with a roller in front of the planting device, with a trenching and soil covering device directly below it. The air compressor and hydraulic pump are placed at the forefront of the frame and are connected to the tractor’s power output shaft. Ground wheels are positioned at the four corners of the frame. One pass of the transplanter can realize ridge surface smoothing, ditching, transplanting, and soil suppression. The structure of the transplanter is shown in Fig. 1.

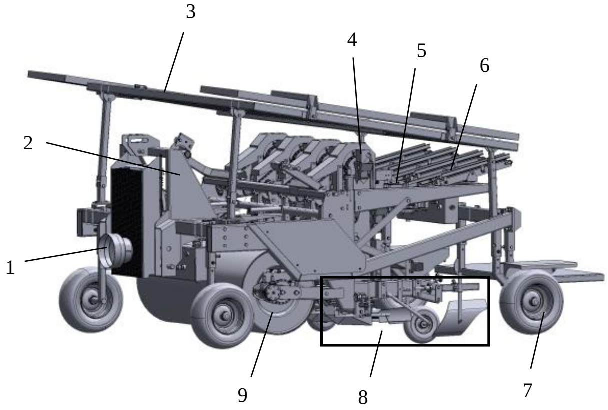

Fig. 1 – Overall structural of the transplanter

1- Power input shaft; 2- Rack; 3- Seedling tray support; 4- Planting device; 5- Automatic seedling separating device; 6- Intermittent conveying device; 7- Ground wheel; 8; Trench covering device; 9- Roller

The entire machine is pulled by a tractor, and the power of the tractor is simultaneously transmitted to the hydraulic pump and the air compressor via the output shaft. The hydraulic motor sequentially transmits power to the drum, row-based seedling intermittent conveying device, automatic seedling separating device, and planting device through a transmission chain to achieve ground leveling, and the operation of the seedling block conveyor belt and transplanting device. Moreover, the air compressor performs work, temporarily stores compressed gas in the gas storage tank, and is connected to the cylinders of the row-based seedling intermittent conveying device and the automatic seedling separating device through the reversing valve to realize the conveyance of substrate block seedlings and automatic seedlings. During operation, rows of substrate block seedlings are removed and fed to the intermittent conveyor. After being distributed by the automatic seedling separating device, there is always a substrate block seedling at the top of the front conveyor belt. Under the action of the parallel four-bar mechanism, the planter on the planting device remains perpendicular to the ground and rotates with the chain. When it crosses the front end of the front conveyor belt, it clamps onto the substrate block seedlings to be removed, and then the planter moves toward the ground. At this time, the planter is forced to open by the opener, and the substrate block seedlings fall into a rectangular trench dug by the opener. Then, the soil-covering device buries the substrate block seedlings to complete the planting.

The technical parameters of the whole machine are shown in Table 1.

Table 1

Technical parameters of the transplanter

Parameters	Value
Overall dimensions (Length×Width×Height) [mm]	3100×3000×1600
Working rows	4
Row spacing [mm]	270~810
Plant spacing [mm]	200~2600
Substrate block size [mm]	40×40×40
Frequency [plants/min•row]	50~60

Automatic seedling separating device

The automatic seedling separating device distributes the row-based substrate block seedlings one by one at a given speed. The execution part of the device uses a pneumatic transmission for direct power, and it works with the multi-link mechanism to realize compound movement. As shown in Fig. 2, when planter Q_2 reaches point *c*, the arched rod is lifted to the I state, the reversing valve mechanical arm is constrained by the arched rod, the left circuit is connected, the cylinder *B* piston rod extends, and the stop pin swings out and releases seedlings. When planter Q_1 leaves point *d*, and planter Q_2 has not yet reached point *c*, the arched rod falls back to the II state and releases the restriction on the mechanical arm of the reversing valve, the right circuit is connected, the piston rod of cylinder *B* returns, and the stop pin swings in and does not release the seedlings. Planter Q_2 then fetches the seedlings. This action cycles in sequence.

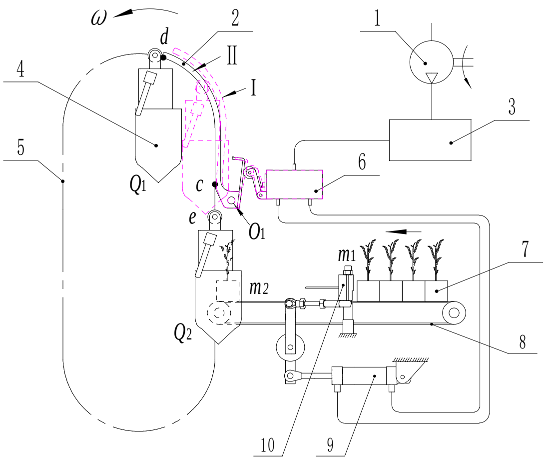

Fig. 2 – Automatic seedling separation process

1- Air compressor; 2- Bow lever; 3- Air storage tank; 4- Planter; 5- Chain; 6- Directional valve; 7- Substrate block seedling; 8. Front conveyor belt; 9- Cylinder B; 10- Stop pin where:

Q_1 is the front planter; Q_2 is the rear planter; I is the arched rod raised state; II is the arched rod reset state; point *c* is the starting point of contact between the rear planter and the arch rod; point *d* is the front planter and arch rod breakaway point; O_1 is the center of rotation of the bow.

The planting rate of this machine is 1 plant/s (60 plants/min), and the time *t* required for point *e* of planter Q_2 to reach point c of the bow is 1 s. The following conditions should be met for automatic seedling distribution:

$$0.5 < t_1 \leq t_2 < 1 \tag{1}$$

$$L_{m1m2} = L_{cd} = 210 \tag{2}$$

where:

t_1 is the seedling release time [s], t_2 is the seedling blocking time [s], L_{m1m2} is the distance moved by the substrate block seedling [mm], *and* L_{cd} is the distance the planter slides through the bow bar [mm].

In order to prevent the sudden stoppage of the substrate block seedlings during transportation, which affects the seedling distribution and planting quality, it is necessary to analyze the force of the blocking pin when it contacts the substrate block to determine the position of the blocking pin. When the substrate block seedling is blocked by the stop pin, it is subject to the thrust of the stop pin, the inertial force of its own motion, the friction of the conveyor belt, its own gravity, and the conveyor belt support force. Under ideal conditions, the substrate block seedling does not stop suddenly. When dumping occurs, it is necessary to ensure that the thrust of the blocking pin against the substrate seedling and the inertial force of its own motion are equal in magnitude, opposite in direction, and act along a straight line, so that the optimal position of the stop pin is equivalent to the position of the center of gravity of the substrate block seedlings.

However, in actual operation, it is difficult to ensure that the size of the substrate block remains the same. Therefore, it is unlikely that the stop pin is aligned with the center of gravity of all the substrate block seedlings. As shown in Fig. 3 (a), when the stop pin is above the center of gravity of the substrate block, the substrate block is momentarily stopped owing to the inertial force. It will turn backward around point *f*. At this point in time, the thrust force F_t generated by the stop pin on the substrate block is below the horizontal line of the substrate block center of gravity, thereby generating a moment to prevent the substrate block from turning downward, balancing the turning moment, and prompting the substrate block to stop and balance. As shown in Fig. 3 (b), when the stop pin is below the substrate block center of gravity, the substrate block turns forward around point *b* at the moment it is stopped due to the inertial force. The stop pin exerts an upward thrust on the substrate block, and there is no support above the substrate block to keep it from flipping. Therefore, the substrate block may be overturned.

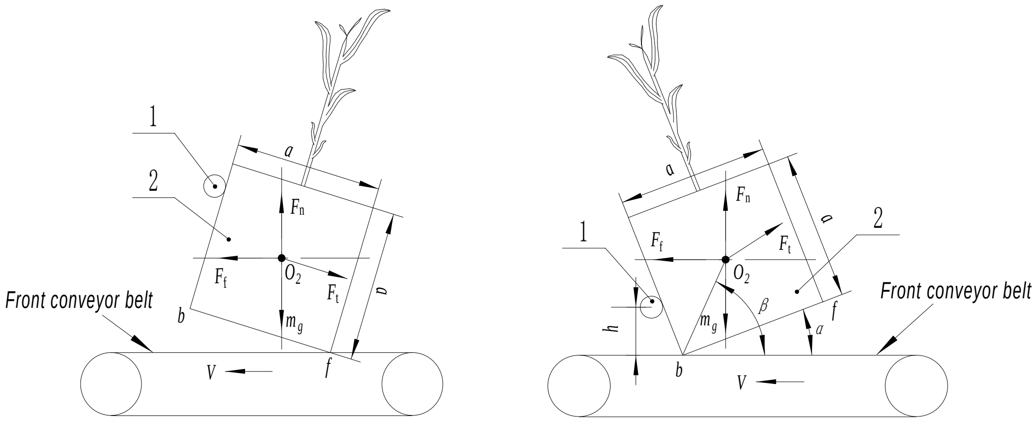

(a) (b)

Fig. 3 – The force of the stop pin when it contacts the substrate block

1- Stop pin; 2- Substrate block

2-

where: (a) the stop pin is located above the substrate block center of gravity; (b) the stop pin is located below the substrate block center of gravity; F_n is the supporting force; F_t is the thrust of the stop pin; F_f is the frictional force; *G* is the gravity; O_2 is the center of gravity of the substrate block seedling; *a* is the edge length of the substrate block; and *h* is the vertical distance between the stop pin and the front conveyor belt.

The angle *β* between the line connecting point *b* and the center of gravity O_2 with respect to the ground when the substrate block flips is:

$$\beta = arccos\frac{\sqrt{2}}{2} + \alpha \tag{3}$$

When the substrate block is overturned, the limit height of the stop pin from the front conveyor belt is *h*, as follows:

$$\frac{m_g\sqrt{2}}{2}a\cos\beta + F_t h\cos\alpha \geq \frac{F_f\sqrt{2}}{2}a\sin\beta + \frac{F_n\sqrt{2}}{2}a\cos\beta \tag{4}$$

$$h \geq \frac{\frac{\sqrt{2}}{2}a\left[F_f\sin\beta+\left(F_n-m_g\right)\cos\beta\right]}{F_t\cos\alpha} \tag{5}$$

According to the law of conservation of energy, the speed V of the front conveyor belt is as follows:

$$\Delta E_1 = -\Delta E_2 \tag{6}$$

$$\Delta E_1 = m_g\left[\frac{\sqrt{2}a}{2}\cos\beta - \frac{a}{2}\right] \tag{7}$$

$$\Delta E_2 = -\frac{mV^2}{2} \tag{8}$$

$$V = \sqrt{m_g[2a^2\cos\beta - \alpha]} \tag{9}$$

According to formulas (3)~(9), the probability of the substrate block overturning is directly related to the installation height h of the stop pin and the front conveyor belt speed V. The installation height restricts the speed of the belt; conversely, the speed of the belt determines the maximum installation height.

Planting device

As shown in Fig. 4, the planter is installed on the Z-shaped rod through a fixed sleeve, and the Z-shaped rod is connected to the active chain and the driven chain. The planter keeps the tip vertical to the ground under the action of the Z-shaped bar while it moves with the chain. When the planter rotates to position *C*, it crosses the front conveyor belt, and the inner plate clamps onto the substrate block to remove it. When the planter moves with the chain to transplanting position *E*, the planter lever is affected by the opener. The planter overcomes the pretension of the tension spring under the interaction between the convex plate and the concave plate, so that the inner plate and the outer plate open symmetrically around their respective rotation axes, and the substrate block seedlings fall into the planting trench under their own weight. When the planter moves to position *D*, the roller releases the constraint of the opener. The inner and outer plates of the planter close around the rotating shaft under the force of the tension spring, and a certain pretension is maintained to process the next round of seedlings.

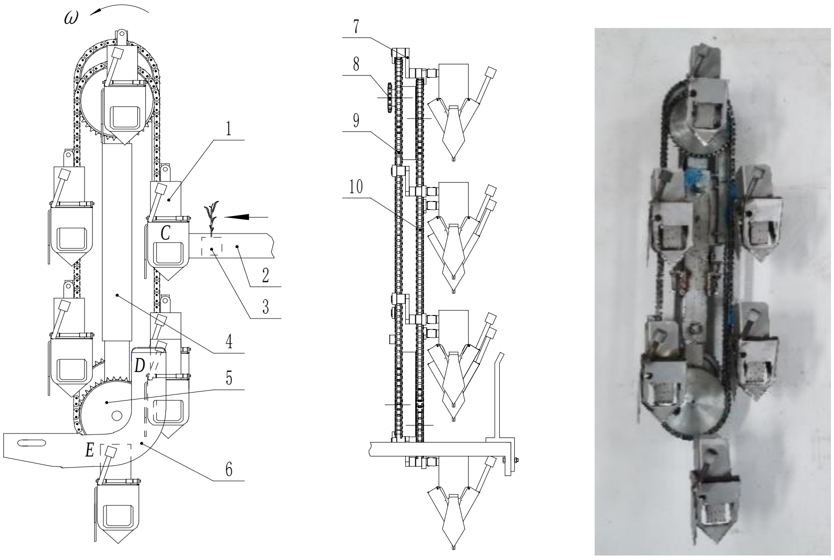

(a) *(b)*

Fig. 4 – Planting device

(a) Structure diagram; （*b*）*Real diagram*

1- Transplanter; 2- Front conveyor belt; 3- Substrate-block seedling; 4- Support frame; 5- Sprocket; 6- Opener; 7- Z-shaped rod; 8- Transmission sprocket; 9- Active chain; 10- Follower chain

The structure of the planter is designed in pairs, as shown in Fig. 5. It is composed of an external beak, a pair of inner tongues, mutually meshing concave-convex plates, fixing frame, tension spring, dial rod, guide plate, etc. The outer beak is used for breaking the membrane into the soil, and the inner tongue is used for clamping the seedlings. The dial rod and the outer beak are fixedly connected. the planter can be opened and closed under the joint action of the concave and convex plate and the tension spring. In order to ensure that the opening of the planter does not affect the free fall of the substrate block seedlings, the opening size of the substrate block should be ≥40 mm according to the design requirements. In the design of the inner tongue, it is necessary to increase the success rate of clamping and greatly reduce the clamping force applied on the substrate block to reduce the rate of breakage. The test on the failure resistance of 30 days old cabbage substrate block seedlings showed that the reliable clamping force of tongue in the planter should be between 89.95 and 119.29 N, which should be less than 89.95 N for safety (*Guan et al., 2020*).

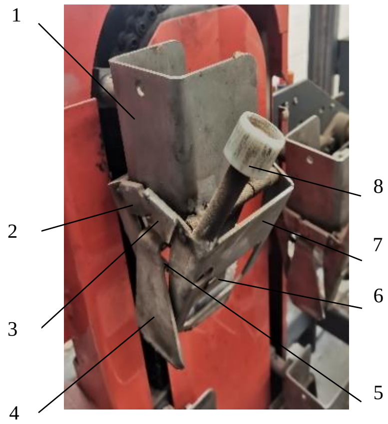

Fig. 5 – Structure of the planter

1- Fixing frame; 2- Convex plate; 3- Concave plate; 4- Guide plate; 5- Tension spring; 6- Inner tongue; 7- Outer beak; 8- Lever

Test conditions

As shown in Fig. 6, field performance tests were conducted at the Changshu Hengtang Vegetable Professional Cooperative in December 2019. Before the test, a double-type ridger was used to rotate and ridge the test field to ensure that the soil on the ridge surface was fine and smooth, and the soil moisture content was 15%~25%. The soil type was loam. The test object was a 40 × 40 × 40 mm cubic cabbage seedling substrate block with seedlings aged 30 days. The average seedling height was 82.74 mm, and there was no adhesion or rooting between the substrate blocks. During transplanting, the moment generated by the seedling tilt on the substrate block did not affect the planting state.

The matching power was John Deere 1204 wheeled tractor. The test instruments mainly included the DM6235P tachometer produced by Shenzhen Shengli High Electronic Technology Co., Ltd, ECA-SW1 soil moisture rapid tester produced by Beijing Yikangnong Technology Development Co., Ltd, and 05 series fiber tape measure produced by Ningbo Baofeng Tools Co., Ltd.

Fig. 6 – Field test

Test factors and indexes

According to the preliminary research on the cabbage substrate seedling transplanter, the main factors affecting the planting quality were the forward speed of the transplanter, the planting frequency and the speed of the conveyor belt. Therefore, the forward speed, planting frequency and conveyor speed of the vegetable substrate block seedling transplanter were used as the test factors, and the lodging rate and the missing rate were used as the test indicators to conduct single factor test and three-factor three-level orthogonal test.

In the test, the speed of the transplanter was changed by changing the tractor gear position, and the frequency of the transplanter and the speed of the front conveyor belt were adjusted by simultaneous interpreting the number of sprocket teeth with different transmission ratios. After the transplanting operation under each group of parameters was completed, three transplanting areas were randomly selected. One line was taken from each transplanting area, and 120 planting points were continuously measured. The number of lodged and missing seedlings was counted, and the lodging rate, missing planting rate, and planting qualified rate were calculated. Referring to the industry standard of Ministry of Agriculture (NY/T 3486-2019) and the dry land planting machinery industry standard (JB/T 1029-2013), the lodging rate *T*, missing planting rate *E,* and planting qualified rate *Q* are calculated by formulas (10)~(12).

$$T = \frac{N_{DF}}{N} \times 100\% \tag{10}$$

$$E = \frac{N_{LM}}{N} \times 100\% \tag{11}$$

$$Q = (1 - T - E) \times 100\% \tag{12}$$

where: T is the lodging rate, [%]; N_{DF} is the number of lodged plants; N is the number of plants measured in the test section; E is the missing planting rate, [%]; N_{LM} is the number of missed planting plants; Q is the planting qualified rate, [%].

RESULTS AND ANALYSIS

Test result of single factor

Fig. 7 shows that the forward speed and conveyor belt speed have little influence on the lodging rate fluctuation, which was basically stable between 3.5% and 5.5%. With the increase of advance speed, planting frequency and front conveyor belt speed, the rate of missing rate decreased first and then increased.

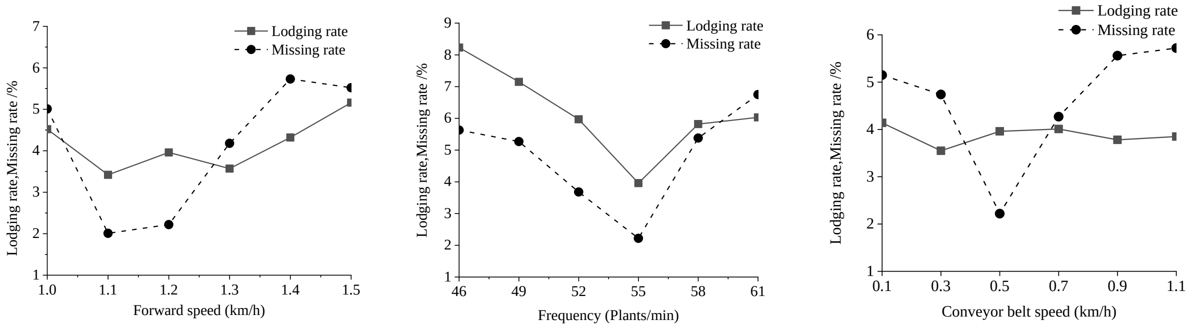

(a) (b) (c)

Fig. 7 – Single factor test results

Results of orthogonal test

Based on the single factor test results, the actual working conditions of the prototype, and the operational requirements of the transplanter, the forward speed *A* range was 1.1~1.3 km/h, the frequency *B* range of the planter was 52~58 plants/min, and the speed of the front conveyor belt *C* was 0.3~0.7 km/h. The test factors and level codes are listed in Table 2.

Table 2

Factors and levels

Code	Factors		
	A [km/h]	*B* [Plants/min]	*C* [km/h]
1	1.1	52	0.3
2	1.2	55	0.5
3	1.3	58	0.7

Significance analysis

A three-factor three-level orthogonal test is used for experimental research and taking the average value of three measurements for each test as the test data, the total number of tests was 9，each experiment was repeated three times. The test results and analysis are shown in Table 3. The results of the variance analysis for lodging rate and missing planting rate are shown in Table 4.

Table 3

Test results

Test number	*A*	*B*	*C*	Lodging rate *T* [%]	Missing rate *E* [%]
1	1	1	1	4.26	4.81
2	1	2	2	3.42	2.01
3	1	3	3	7.16	8.37
4	2	1	2	5.97	3.68
5	2	2	3	4.01	4.27
6	2	3	1	8.33	12.74

Table 3
(continuation)

Test number	*A*	*B*	*C*	Lodging rate *T* [%]	Missing rate *E* [%]
7	3	1	3	8.71	10.46
8	3	2	1	5.06	7.04
9	3	3	2	9.74	6.45
Lodging rate / *T*	K_1	17.84		21.94	18.65
	K_2	18.31		10.49	19.13
	K_3	21.51		25.23	19.88
	R	3.67		14.74	1.23
Better scheme		$A_1B_2C_1$			
Missing rate / *E*	K_1	15.19		18.95	24.59
	K_2	20.69		13.32	12.14
	K_3	23.95		27.56	23.1
	R	8.76		14.24	12.45
Better scheme		$A_1B_2C_2$			

Table 4

Analysis of variance results

Source	*T* [%]						*E* [%]					
	Sum of squares	*d*	Mean square	F-value	P-value	Significance	Sum of squares	*d*	Mean square	F-value	P-value	Significance
A	6.126	2	3.063	5.095	0.028	*	0.580	2	0.290	0.192	0.828	
B	12.113	2	6.057	31.824	0.000	**	7.044	2	3.522	7.044	0.032	*
C	1.190	2	0.595	3.125	0.081		3.2014	2	1.6007	6.6859	0.0226	*
AB	4.478	4	1.119	11.764	0.001	**	0.201	4	0.050	0.066	0.936	
AC	0.084	4	0.021	3.50	0.062		7.208	4	1.802	3.25	0.093	
BC	0.303	4	0.076	0.796	0.474		11.190	4	5.595	20.125	0.000	**
Pure Error	2.284	17	0.190				18.137	17	1.511			
Correlation total	26.578	35					47.561	35				

According to the analysis of variance for the orthogonal test in Table 4, for a given significance level $\alpha = 0.05$, factor *A* had a significant influence on the lodging rate, and factor *B* and the interaction $A \times B$ had a high significant influence on lodging rate. Factors *B* and *C* had significant effects on the rate of missing planting, and the interaction $B \times C$ had a high significant effect on the rate of missing planting. As the test indexes were the lodging rate and the missing planting rate, the smaller the better. Considering the range analysis in Table 2 without considering the interaction, the combination with the lowest lodging rate was $A_1B_2C_1$, and the combination with the lowest missing planting rate was $A_1B_2C_2$.

Analysis of interaction factors

Because the interaction $A \times B$ had a high significant effect on the lodging rate, and the interaction of $B \times C$ had a high significant impact on the rate of missing planting, the selection of the three factor levels cannot be considered alone. In order to further analyze the influence of the interaction between forward speed and planting frequency on the lodging rate, and the interaction between planting frequency and front conveyor belt speed on the missing planting rate, the contour map was drawn by using origin 9.0 software according to the results of Orthogonal test, as shown in Fig. 8.

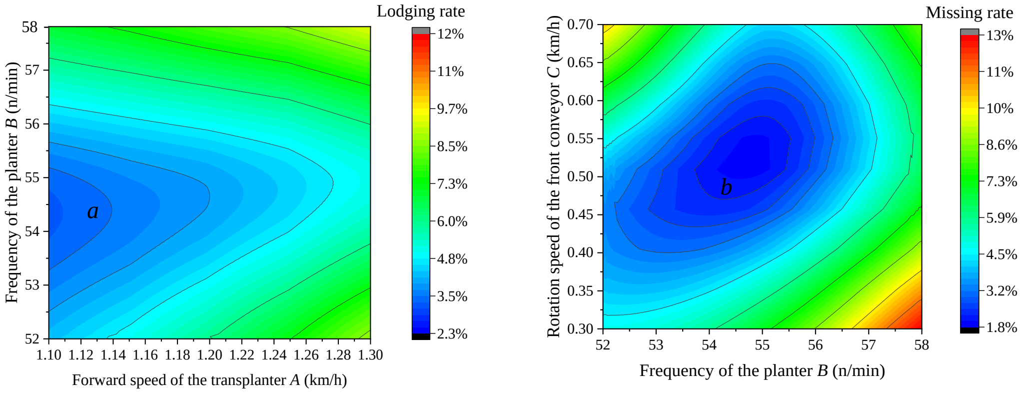

(a) Lodging rate (b) Missing rate

Fig. 8 – Contour map of the influence of multiple factors on the planting effect

It can be seen from Fig. 8 (a) that under the interaction of forward speed and planting frequency, the lowest lodging rate appeared in the curve *a* area when the forward speed was 1.1 km/h and the planting frequency was 53.3~55.7 plants/min. In Fig. 8 (b), the area in curve *b* had a low rate of missing planting, that was, when the planting frequency was 53.7~55.5 plants/ min and the conveyor belt speed was 0.475~0.575 km/h. According to the analysis of orthogonal test results, the combination of the factors with the lowest lodging rate and the lowest missing rate and the highest qualified rate can choose the forward speed of 1.1km/h, the planting frequency of 55 plants/min, the speed of conveyor belt being 0.5 km/h, namely $A_1B_2C_2$, the lodging rate was 3.42%, the missing rate was 2.01%, and the qualified rate of planting calculated by formula (14) was 94.57%.

Verification test result

In order to verify the accuracy of orthogonal test results, the optimal combination $A_1B_2C_2$ was validated. The forward speed was set to be 1.1km /h, the planting frequency was 55 plants/min, and the conveyor belt speed was 0.5 km /h. Three repeated tests were conducted to take the mean value, and 120 substrate block seedlings were selected for testing in each group. The test verification results are shown in Table 5. The average qualified rate of the substrate block seedlings was 93.31%. The test results meet the industry standard of vegetable transplanting machine operation quality (NY / T3486-2019) and the industry standard of dryland planting machinery (JB / T 1029-2013) (Lodging rate≤7%, Missing rate≤5%, Pass rate≥90%).

Table 5

Verification test result

Project	Lodging rate [%]	Missing rate [%]	Pass rate [%]
1	3.58	4.25	92.17
2	2.37	2.91	94.72
3	2.83	4.15	93.02
Average	2.92	3.77	93.31

CONCLUSIONS

In this paper, a transplanting machine of cabbage substrate block seedling was designed, which adopted pneumatic control technology. According to the characteristics of independent seedling raising and high standing stability of substrate block, a transplanting scheme of whole row seedling collection — intermittent transportation — pneumatic seedling separation — clip transplanting was created, which realized the rapid transplanting of cabbage substrate block seedlings and broke the situation of inorganic availability of mechanized transplanting of substrate block seedlings.

Through theoretical calculation and stress analysis, the structural parameters of the key components affecting the planting quality were determined. Taking cabbage seedlings with 40 × 40 × 40mm substrate block size as the experimental object, the effects of forward speed *A*, planting frequency *B*, front conveyor belt speed *C* on lodging rate *T* and missing rate *E* were studied by single factor experiment and three factor three level orthogonal experiment. By means of range significance analysis, the parameter combinations $A_1B_2C_1$ and $A_1B_2C_2$ with the lowest lodging rate *T* and missing planting rate *E* were obtained respectively. On this basis, the effects of the interaction between forward speed *A* and planting frequency *B* on lodging rate *T*, the interaction between planting frequency *B* and front conveyor belt speed *C* on missing rate *E* were further analyzed. The parameter combination of the lowest lodging rate *T*, missing rate *E* and the highest pass rate *Q* was as follows: the forward speed *A* was 1.1km/h, the planting frequency *B* was 55 plants /min, and the front conveyor belt speed *C* was 0.5km/h. The verification test showed that the average planting qualified rate *Q* was 93.31%, and the test results met the relevant indexes of "industry standard for operation quality of vegetable transplanter" (NY / T 3486-2019) and "industry standard for dryland planting machinery" (JB / T 1029-2013).

ACKNOWLEDGEMENTS

The study was supported by Demonstration and Promotion of Modern Agricultural Machinery Equipment and Technology in Jiangsu Province, China (No. NJ2019-05); Jiangsu Agricultural Science and Technology Innovation Fund, China (No. CX [18] 3050).

REFERENCES

[1] Chen, Y., (2017), *Mechanization technology and model of vegetable production* (蔬菜生产机械化技术与模式), vol.1, "Jiangsu University" Publishing House, ISSN 978-7-5684-0535-5, Zhenjiang/China.

[2] Cui, Z., Chen, Y., Guan, C., Yang, Y., Gao, Q., & Zhao, G., (2019), Experimental study on substrate transplanter for vegetable seedlings (蔬菜基质块苗移栽机的试验研究), *Journal of Agricultural Mechanization Research*, vol.41, issue 10, pp.158-161, Heilongjiang/China.

[3] Cui, Z., Guan, C., Yang, Y., Gao, Q., Chen, Y., & Xiao, T., (2020), Research status of vegetable mechanical transplanting technology and equipment(蔬菜机械化移栽技术与装备的研究现状), J*ournal of Chinese Agricultural Mechanization*, vol.41, issue 3, pp.85-92, Nanjing/China.

[4] Feng, Q., Zhao, C., Jiang, K., Fan, P., & Wang, X., (2015), Design and test of tray-seedling sorting transplanter, *International Journal of Agricultural and Biological Engineering*, vol.8, issue 2, pp.14-20, Beijing/China.

[5] Guan, C., Xu, T., Cui, Z., Yang, Y., Chen, Y., & Gao, Q., (2020), Optimized parameters for compression molding of vegetable seedling substrate block for mechanical transplanting, *International Agricultural Engineering Journal*, vol.3, issue 29, pp.77-89, Beijing/China.

[6] He, Y., Yan, H., Cui, W., Chen, K., Han, Z. & Bao, C., (2018), Research status and analysis of automatic vegetable transplanting technology (蔬菜自动移栽技术研究现状与分析), *Agricultural Engineering*, vol.8, issue 3, pp.1-7, Beijing/China.

[7] Hu, J., Zhang, C., Wang, L., & Han, L., (2016), Design and experiment on automatic greenhouse seedling transplanting machine (温室自动移栽机的设计与试验), *Transactions of the Chinese Society for Agricultural Machinery*, vol.47, issue S1, pp.149-154, Beijing/China.

[8] Jin, X., Du, X., Ji, J., Wang, S., Dong, X. & Du M., (2015), Physical characteristics of plug seedling transplanted by the return-blank type transplanter, *International Agricultural Engineering Journal*, vol.24, issue 4, pp.1-10, Beijing/China.

[9] Pramod, C., Prasanna Kumar, G., Pallab, K. & Prasanta, N., (2017), Production of soil block seedlings in plug trays for mechanical transplanting, *International Journal of vegetable science*, issue 4, pp. 1-15, India.

[10] Prasanna, G., & Kumar, H., (2008), Vegetable transplanters for use in developing countries - a review, International J*ournal of Vegetable Science*, vol.14, issue 3, pp.232-255, India.

[11] Ryu, K, H., & Kim, G, Y., (1998), Development of a gripper for robotic transplanter and evaluation of its transplanting performance, *Korean Society for Agricultural Machinery*, vol.23, issue 3, pp.271-276, Korea.

[12] Wu, C., Wu J., Zhang, M., & Tang,Q., (2016), Research on machine transplanting techniques of blanket rapeseed (油菜毯壮苗机械移栽技术研究), *Journal of Chinese Agricultural Mechanization*, vol.37, issue 12, pp.6-10, Nanjing/China.

[13] Wu, J., Yu, W., Zhang, M., & Wu, C., (2020), Design and experiment of 2ZY-6 rapeseed blanket seedling transplanting machine (2YZ-6型油菜毯壮苗移栽机设计与试验), *Transactions of the Chinese Society for Agricultural Machinery*, vol.51, issue 12, pp.95-102+275, Beijing/China.

[14] Yang, L., Fang, Z., Zhuang, M., Zhang, Y., Lv, H., Liu, Y., & Li, Z., (2016), Advances of research on cabbage genetics and breeding during 'The Twelfth Five-year Plan'in China ("十二五"期间我国大白菜遗传育种研究进展), *China Vegetables*, issue 11, pp.1-6, Beijing/China.

[15] Yang, Q., Li, X., Shi, X., Ahamd, I., Mao, H., Hu, J., & Han, L., (2018), Design of seedlings separation device with reciprocating movement seedling cups and its controlling system of the full-automatic plug seedling transplanter, *Computers and Electronics in Agriculture*, issue147, pp 131-145, Netherlands.

[16] Yu, X., Zhao, Y., Chen, B., Zhou, M., Zhang, H., & Zhang, Z., (2014), Current status and prospect of transplanterry development (移栽机械发展现状与展望), Transactions of the Chinese Society for Agricultural Machinery, vol.45, issue 8, pp.44-53, Beijing/China.

[17] Zhou, H., Yang, B., Yan, H., &Yang, X., (2015), Current status and prospects of dry farming transplanterry industry (旱地移栽机械产业发展现状及展望), Agricultural Engineering, vol.5, issue 1, pp.12-13, Beijing/China.

ASPECTS REGARDING THE REPRESENTATION OF FARINOGRAPHIC CURVE TO ASSESS WHEAT FLOUR DOUGH BY MATHEMATICAL EQUATIONS
/
ASPECTE PRIVIND REPREZENTAREA CURBEI FARINOGRAFICE DE APRECIERE A ALUATURILOR PE BAZĂ DE FĂINĂ DE GRÂU PRIN ECUAȚII MATEMATICE

Tudor Paula [1)], Voicu Gheorghe [1)], Constantin Gabriel-Alexandru [1*)], Stefan Elena-Madalina [1*)], Munteanu Mariana-Gabriela [1)], Stefan Vasilica [2)]

[1)] University Polytechnic of Bucharest, Romania; [2)] INMA Bucharest

Tel: +40723.850975; +40726043472; E-mail: madalina.stefan@upb.ro; gabriel_alex99@gmail.com

DOI: https://doi.org/10.35633/inmateh-64-38

Keywords: *bread dough, farinographic curve, mathematical equation, regression coefficient*

ABSTRACT

The Brabender farinograph is a device with which important indications for baking are obtained, namely: dough development time (DDT), water absorption (WA), dough stability time (DST), softening degree (SD), Farinograph Quality Number (FQN), important parameters for determining flour mixtures. These parameters are represented on the farinographic curve drawn during the farinograph test. Dough development or formation (formation of gluten) is represented by the ascending branch of the farinographic curve, which has a steep ascending slope, because time (expressed in minutes), fixed on the abscissa of the diagram, has relatively low values (about 1.2–3 min for regular flours), while consistency, fixed on the ordinate of the diagram, reaches the maximum value (peak time) of the dough. In comparison, the descending branch of the farinogram, which starts from the maximum value of the dough consistency (peak time), has a slow descending slope, because the kneading time is extended up to 20 minutes, and the consistency decreases relatively little. The paper presents the appreciation of this branch of the farinogram by mathematical equations for several types of doughs from wheat flour mixed with different percentages of salt.

REZUMAT

Farinograful Brabender este un aparat cu ajutorul căruia se obțin indicații importante pentru panificație și anume: timpul de dezvoltare a aluatului (DDT), capacitate de absorbție a apei (WA), timpul de stabilitate a aluatului (DST), gradul de înmuiere (SD), Indicele de calitate farinografic (FQN), parametri importanți pentru stabilirea amestecurilor de făină. Acești parametri sunt reprezentați pe curbă farinografică trasată în timpul testului cu farinograful. Dezvoltarea sau formarea aluatului este reprezentată de ramura ascendentă a curbei farinografice, care prezintă o pantă crescătoare abruptă, deoarece timpul (exprimat în minute), fixat pe abscisa diagramei, are valori relativ mici (circa 1.2–3 min pentru făinuri obișnuite), în timp ce consistența, fixată pe ordonata diagramei, atinge valoarea maximă a aluatului. Comparativ, ramura descendentă a farinogramei, care pornește de la valoarea maximă a consistenței aluatului, prezintă o pantă descrescătoare lentă, deoarece timpul de frământare se prelungește până la 20 minute, iar consistența scade relativ puțin. Lucrarea prezintă aprecierea acestei ramuri a farinogramei prin ecuații matematice pentru câteva tipuri de aluaturi din făină de grâu în amestec cu diferite procente de sare.

INTRODUCTION

Farinographic parameters (dough development time, absorption capacity, softening degree, farinograph quality number, dough stability) are widely used to predict the functionality of flour and dough. They can be easily identified by reading the farinographic curve drawn in farinograph experiments (figure 1).

According to the water absorption characteristic, the flour is classified as having a good and very good capacity when the absorbed water is between 57 and 62% and the dough development time is between 1.5-3 minutes. By the methodology of the response surface, the authors *Temea (Moroi) et al., (2016*), established that the optimal conditions for the maturation process of wheat flour type FA-650 (0.65% medium ash content) should be: storage temperature 28°C, storage time 21 days, environmental humidity 68-70%.

For these conditions, farinographic records showed that water absorption increased by about 0.5% compared to the initial flour (immediately after grinding), the stability time of the dough increases by ~20%, and the degree of softening of the dough is reduced by 27-30%.

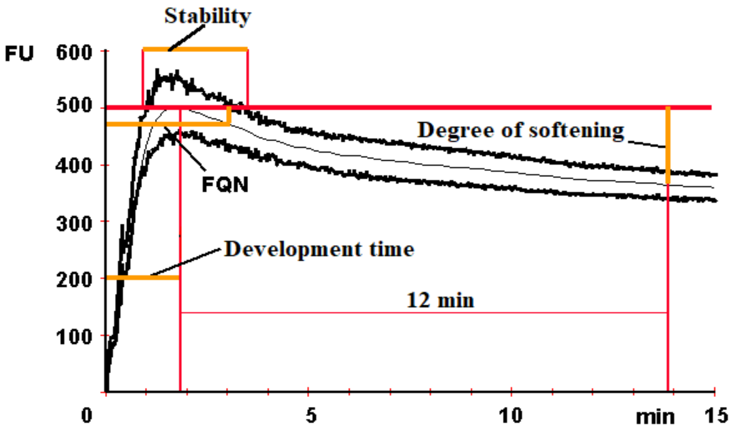

Fig. 1 - Example of a farinographic curve and how to interpret it

It is known that there is a significant correlation between the volume of bread and the characteristics of the flours used in its preparation (protein content, Zeleny sedimentation index, dough development time, absorption capacity, softening degree, farinograph quality number, dough stability, the last five parameters being indicated in farinograph tests). Dough development time (peak time) shows the quality of wheat proteins. *Aydogan, et al., (2015*) found values of this parameter within the limits 1.35-12.17 min, with an average value of 4.22 min for 111 Turkish grains. The absorption capacity of flour, determined by the authors, was within the limits of 54.8-68.4% (average value 61.76%). Positive and significant correlations were found between the volume of bread, on the one hand, and dough development time, farinograph quality number, dough stability, flour absorption capacity, on the other hand, respectively a significant negative correlation between the volume of the bread and the degree of dough softening at 12 minutes of kneading.

Dough development time, its stability to kneading and farinograph quality number, are indicators of flour resistance, higher values suggesting stronger doughs. A high water absorption capacity, combined with a low degree of softening indicates a good quality flour, while a high water absorption combined with a high degree of softening indicates a poor quality flour.

The salt added to the dough has the main role of flavouring the bread, but beyond that it also contributes to the improvement of the gluten network. Naturally, the proteins that make up gluten (gliadin and glutenin) reject each other, but salt helps them get over this trend, practically forcing them to join in gluten strings faster and better. However, salt in food should be reduced for better human health, so as to achieve a maximum salt intake of 5 g per day in adults. A high dietary intake of sodium leads to increased blood pressure and the occurrence of chronic cardiovascular disease. Bread is thus a major source of sodium in the daily intake of the population and, therefore, various strategies are undertaken to reduce the consumption of salt in bakery products. Research has been done on the characterization of bread dough prepared with low-sodium sea salt or dry wheat flour dough, *Voinea et al. (2020*), as substitutes for sodium chloride on the basis of rheological properties obtained with different apparatus, including the farinograph. Thus, the optimal quantities found by the authors were 1.396 g of sea salt and 2.683 g of dry dough, both per 100 g of wheat flour. For these values, the absorption capacity was 60.01%, the development time 1.59 min, the stability of the dough 1.33 min, the softening degree 88.0 UB. It has been found, however, that during mixing and spreading, sea salt strengthens the wheat flour dough, while the dry dough weakens it.

Supplementing wheat flour with other types of flour changes, in general, the rheological characteristics of the obtained doughs but also of the finished products. Usually the final recipes, which give the best properties to both the dough and the finished product, are obtained through several tests and research in the laboratory and on the production flow. Such research has been done in the past and does not stop being done today. In this respect, supplementation with Chinese yam for the preparation of noodles has led to changes in their chemical attributes, texture, cooking, rheology and microstructure. Moreover, the addition of Chinese yam also affects the structure of starch granules, as well as the sensory characteristics of noodles, and it is not recommended to substitute wheat flour with more than 30% yam in industrial applications (*Sun, et al., 2019; Li, et al., 2020*).

It is known that wheat bread with bran is obtained by adding them to the kneading of the dough, after its development in the kneader, and not by using flour mixed from the beginning with bran. Eating bran bread significantly suppresses appetite, causing a feeling of fullness, also having a beneficial effect on the microflora of the digestive tract. Brans have the ability to absorb toxins and harmful substances, helping to remove them from the body, increasing immunity and iron content in the blood, but also bring benefits to the human body.

Cardone, et al., (2020) discussed the addition of sprouted wheat bran to wheat flour doughs. It has been shown that the sprouting process reduces phytic acid by about 20%, insoluble dietary fibre by about 11% and water retention by about 8%, but leads to increased simple sugars and enzymatic activities in dough processing. Changes in the interactions between fibre and gluten have also been observed, with sprouted wheat bran leading to a worsening of the mixing properties (on the farinogram the stability is much shorter and the degree of softening is much more pronounced) and fermentation, but does not significantly affect the extensibility of the dough. The volume of bread, on the other hand, increases by about 10% compared to the use of un-sprouted wheat bran, and their use could be useful to produce fibre-rich bread with improved characteristics.

It should be noted that the use of potato starch in the preparation of wheat flour doughs leads to changes in the water absorption characteristics of the flour mixture, decreasing significantly with increasing potato starch content, while the stability of the dough, determined by farinograph, increases significantly with the increase of this content. At the same time, it was found that additions of up to 5% potato starch do not significantly affect the flour drop rate, the results being applicable to certain wheat-based foods, such as noodles, bread, and biscuits (*Sarker et al., 2008*).

Slukova et al., (2017), studied the characteristics of wheat flour (with gluten) and buckwheat (gluten free) doughs in order to evaluate changes in protein structure during dough formation. It has been shown that the mixing time significantly affects the structures of the three-dimensional gluten networks in wheat and buckwheat doughs, which can ultimately influence the quality of the dough baking. At the same time, there were pronounced differences between undeveloped, optimally developed and overmixed wheat dough, but no significant differences were observed between the structures of undeveloped, optimally developed and overmixed buckwheat doughs.

The characteristics of mixtures of wheat flour and buckwheat were also studied by *Stefan et al., (2018*). The addition of whole buckwheat flour to wheat flour influenced the technological and rheological parameters of the flour mixtures. Thus, the increase in the amount of whole buckwheat flour (from 10% to 40%) leads to a decrease in the fall time (from 411 s to 234 s) and the sedimentation index (from 28 ml of wheat flour to 18 ml). Also, the increase of the buckwheat flour content, leads to the increase of the amount of water absorbed at mixing from 58.6% to 79.9%, as well as the development time of the dough from 2.2 min. at 8.7 min., but the stability of the dough decreases significantly. Farinograph quality number also had significant changes.

Based on the farinographic curves obtained for eight wheat flours of different varieties, a mathematical model was developed to simulate the middle curve of the farinograms. The model consisted of five common first- and second-order differential equations that describe the dynamic behaviour of state variables using four kinetic parameters to estimate the mean curve of the farinogram (*Hermannseder et al., 2016*).

The expression of the farinographic curve by mathematical functions is generally cumbersome because it has at least two variations along it, namely a steep increase on its first portion, followed by a portion of the curve decreasing slowly, possibly with sinusoidal variations, depending on the type of flour and the additions to change its quality. An attempt at mathematical expression of the farinographic curve is presented in the paper (*Mis et al., 2017*), the authors presenting the differences obtained between farinographic curves for plain flour and supplemented flour with eight types of botanical fibres from the market.

The results presented by the authors showed differences between farinograms, their shape being strongly influenced by the supplements introduced, in the sense that two peaks appeared along it. The presence of these peaks allowed the distinction of two types of rheological activity of each fibre supplement, namely the weakening or strengthening of the consistency of the bread dough during its development. If the carrot, oat, cranberry and cocoa fibres predominantly showed an action of strengthening the consistency of the dough, the fibres of chokeberry, carob, apple and flax had mainly an action of weakening its consistency. The mathematical equation proposed in the mentioned paper has two terms, one for each visible portion of the farinographic curve.

The paper presents the variation of the farinographic curves after reaching the point of maximum consistency and the equations that represent the respective curves, for the farinograms obtained in experiments with wheat flour in which different percentages of salt were added (between 0-2%), as well as the differences obtained between them. The curves were obtained by regression analysis using the experimental data obtained in the MS Office Excel program for plotting consistency farinographic curves using the Brabender electronic farinograph.

MATERIALS AND METHODS

The authors of this paper have previously performed farinographic determinations on a series of different flours, with different percentages of added salt (*Voicu et al., 2016*), different percentages of other types of flours (*Voicu et al., 2012; Stefan et al., 2018; Munteanu et al., 2015*) or different amounts of water added (*Voicu et al., 2017*).

Research in the field continued to find a method for estimating the farinographic curve by mathematical relations, including how to change the parameters of the equations used in regression analysis depending on the type of flour used to prepare the dough.

The farinographic curve, together with its parameters, shows the evolution of the structure and consistency of the dough during kneading and some basic rheological characteristics of it. The two branches of the farinographic curve can be expressed relatively easily by mathematical equations, although not much is known in this regard.

Voicu et al., (2016) have tried to identify the main Eulerian mathematical functions that can assess the development and formation of the dough (the ascending part of the farinogram) until reaching maximum consistency, for wheat flour dough with different percentages of added salt. Weibull function, lognormal function, hyperbolic function, exponential function and gamma function were tested, the most appropriate degree of correlation being given by the gamma function. ($R^2 \geq 0.967$), and the present paper represents a continuation of the investigations carried out in the above-mentioned paper.

Moreover, *Mis et al., (2017)*, tested a composite sigmoid function (with two basic components) to describe how the dough consistency of wheat flour dough mixed with eight types of dietary fibre.

The E-Brabender farinograph used for making the determinations has the vat capacity of 300 g of flour (450-500 g of dough), and the possibility of maintaining a constant temperature (30+1ºC). The farinograph software records the measurement data, evaluates them according to standard methods (AACC, ICC) and prints the farinographic curve together with some data related to the properties of flour and dough.

For the experimental research were used samples of flour type FA-650 with an average moisture content of 11%, mixed with salt in percent from 0.4% to 2%, compared to flour. The flour used was procured from the S.C. Spicul S.A. Roșiorii de Vede, from the wheat production in the southern part of Romania in 2008. The methodology of the experiments complies with the AACC 54–21 method, for farinographic experiments and with the AACC 54–50 method for determining the flour absorption capacity and with the instructions in the technical book of the apparatus.

The determinations were performed in June 2009, in the specialized laboratory of the Department of Biotechnical Systems of the Polytechnic University of Bucharest.

The absorption capacity of the flour was determined according to the moisture content of the flour, previously determined with a MAC-110 thermobalance, with heating with halogen lamps, at a drying temperature of 105°C and the type of flour. It had values between 60.2 - 63.7%.

Based on the experimental data obtained in the farinographic experiments, the correlation of the values of the experimental points on the descending branch of the curve with two known mathematical functions was tested:

[a]. exponential type: $$y = a\, e^{-bx} \tag{1}$$

[b]. power type: $$y = a\, x^{b} \tag{2}$$

The aim of the paper is not to present the characteristics of wheat flour dough with different percentages of salt, but rather to present the possibility of identifying the farinographic curve with an exponential or power mathematical function, as well as how it varies the coefficients of the equation with the parameters of the dough.

RESULTS

Table 1 shows the values of the parameters of the farinograms obtained in experiments with FA-650 flour, by adding salt in different percentages.

Table 1

Parameters of flour dough farinograms with different salt contents, recorded in experiments

Salt (%)	WA (%)	DT (min)	S (min)	DS (f.u.)	C_{max} (f.u.)	FQN
0%	63.7	2.0	5.8	49	528	43
0.4%	61.4	2.8	13.5	18	477	148
0.8%	61.8	2.5	15.6	9	470	165
1.2%	61.2	2.3	16.1	19	508	150
1.6%	60.6	2.5	18.7	16	484	185
2.0%	60.2	2.3	18.7	11	490	200

WA – water absorption, DT – development time, S – stability, DS – degree of softening, Cmax – maximum consistency, FQN – farinographic index; f.u. – farinographic units

The results of the regression analysis regarding the variation of the descending part of the farinographic curves for the maximum curve, the average curve, respectively the minimum curve, of the farinogram are presented in fig.2 and Table 2.

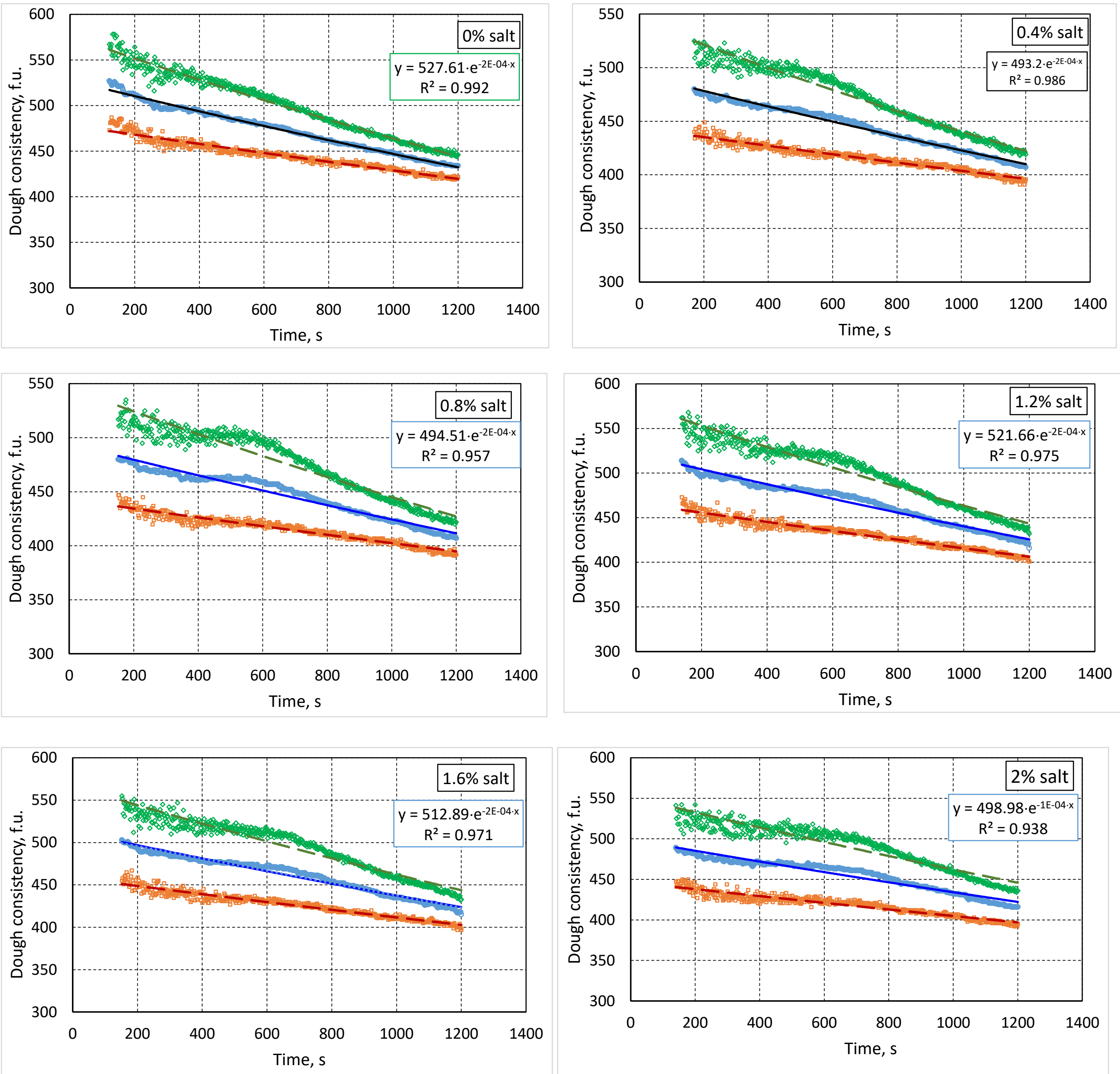

Fig. 2 – Curves obtained by regression analysis for the stability and softening phase of the dough

Note: the regression function is presented only for the median curve of the farinogram

The analysis of the data presented in Table 1 shows that the increase of the salt content in the dough leads to the hardening of the dough, a phenomenon observable by the values of the degree of softening, which decreases in principle with the added salt content, but especially by the values of the farinographic index FQN which gives an appreciation of the power of the flour when mixing (the values of FQN increase constantly with the increase of the salt content).

The analysis also shows that, for values of the amount of salt greater than or equal to 0.4%, the amount of water absorbed by the flour shows values of approx. 61.04 ±0.5% for a 95% confidence interval, while the degree of softening of the dough obtained has average values of 14.6 ±3.4 f.u., for the same confidence interval, and the maximum consistency of the dough does not reach the threshold of 500 f.u. which means less water added to the kneading (consistency had average values of 485.8 ±11.3 f.u. at a confidence interval of 95%).

Table 2

The values of the coefficients of the regression equations and of the correlation coefficient R^2, for regression analysis of flour dough farinograms with different salt contents

	$C = a \cdot \exp(-b \cdot x)$			$C = a \cdot x^b$		
Salt (%)	a	b	R^2	a	b	R^2
0%	527.61	$2 \cdot 10^{-4}$	0.992	813.90	-0.086	0.933
0.4%	493.20	$2 \cdot 10^{-4}$	0.986	762.95	-0.084	0.891
0.8%	494.51	$2 \cdot 10^{-4}$	0.957	742.89	-0.080	0.831
1.2%	521.66	$2 \cdot 10^{-4}$	0.975	813.80	-0.088	0.863
1.6%	512.89	$2 \cdot 10^{-4}$	0.971	787.44	-0.084	0.860
2.0%	498.98	$1 \cdot 10^{-4}$	0.938	711.94	-0.070	0.796

From the analysis of the drawn regression curves, in relation to the experimental points, as well as from the analysis of the values of the correlation coefficient R^2 presented in Table 2, the concordance of the proposed mathematical laws with the experimental data is ascertained. However, the values of the correlation coefficient R^2 shows a better correspondence of the experimental data with the exponential law, which has values in the range 0.938-0.992 for this function, while for the power type function its values R^2 were in the range 0.796-0.933.

We must also note that the salt added to the dough gives the farinographic curves visible undulatory variations especially on the maximum curves, where they are further away from the regression curve, but also on the minimum curves, respectively on the median curve of the farinogram. The farinographic curve for salt-free dough (compared to which we refer) is smoother and has fewer ripples, which makes the regression function have a higher value of the regression coefficient.

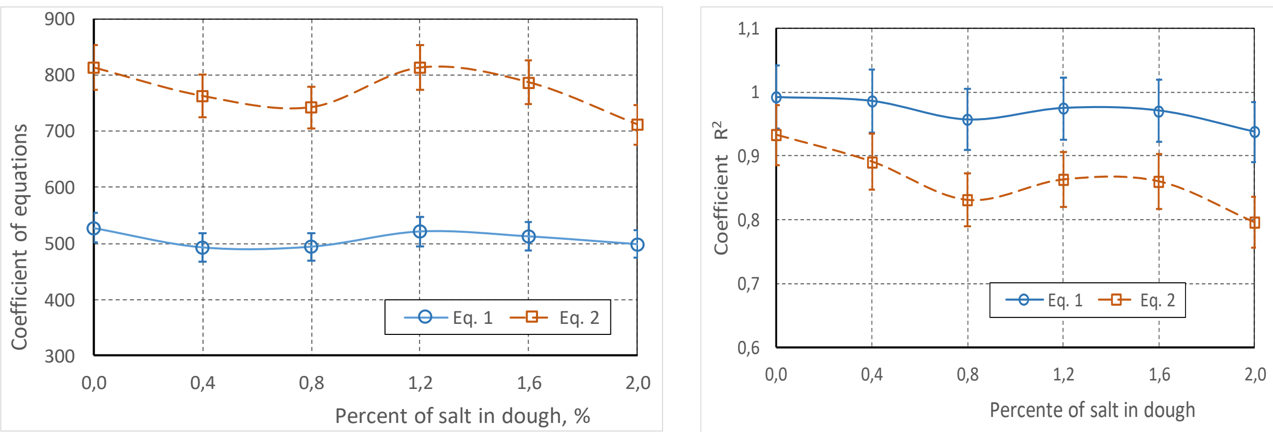

Fig. 3 – Variation of the values of the coefficients of the exponential and power regression equations
left – coefficient of equations (1) and (2); right – correlation coefficient R^2 for eq.(1) and eq.(2)

We find that, both for the exponential function and for the power function, the coefficients and exponents of the mathematical relations have relatively close values, with small variations depending on the percentage of salt added to the kneading. Thus, for the exponential law, the coefficient of the mathematical relationship shows a sudden decrease in value with the addition of salt to the dough, but increases as the percentage of salt increases, but does not reach the value it has for dough without salt. However, for salt percentages above 1.6% the values of this coefficient show a decreasing trend (figure 3).

The values of this coefficient fall within the limits 508.14 ±10.72, for a 95% confidence interval, and the correlation coefficient obtained in the regression analysis is R^2 = 0.970 with an average of deviations ±0.014.

The same mode of variation, relatively identical, is presented by the power function coefficient. Here, its values are on average 772.15 ±29.72 within the 95% confidence interval, but the correlation coefficient has much lower values, i.e. R^2 = 0.862 ±0.035 in the same confidence interval, with a standard deviation ±0.042.

Regarding the values of the exponents of the mathematical relations used in the regression analysis, they are very close, regardless of the percentage of salt added to the dough.

If we compare the values of the coefficient of the exponential relationship with those of the maximum consistency of the dough obtained at kneading, we find that these values are relatively close, which may lead to the conclusion that this coefficient could be set at the average maximum consistency values (with deviations previously), but in this case the values of the exponent of the relationship could be different from those obtained previously.

In the case of the power type relationship, the values of the relationship coefficient are very different from those of the maximum consistency of the dough, and the comparative analysis between the two categories of values does not have a physical significance in the kneading process.

CONCLUSIONS

Farinographic curves are used for the rheological assessment of doughs obtained mainly from wheat flour to which various quantities of other cereal flours may be added. This curve can provide important information for workers in the bakery technology flow, both in terms of flour and dough parameters and in terms of material balance (with reference to the amount of water added, the percentage of salt or the quantities of other food flours).

Being a curve with two slopes, one steep ascending and one descending with a smooth slope, the farinographic curve could be represented by mathematical functions that express as confidently as possible the curve obtained with the help of the Brabender electronic farinograph.

Both the ascending part of the farinographic curve and its descending part can be appreciated by exponential or power type mathematical functions (but also by other types of functions), with a greater or lesser degree of correlation.

It is necessary to identify that mathematical relationship that is as close as possible to the curve obtained experimentally, so that through other mathematical artifices can obtain additional information about the physical and rheological characteristics of the dough and flours used.

The authors of this paper discussed the use of exponential and power mathematical functions to describe the farinographic curve of an FA-650 flour with different percentages of added salt. In addition to the information that the farinographic curve initially transmits, the parameters of the mathematical relations (coefficients and exponents) and the R^2 correlation coefficient were identified. Correlation coefficient shows the degree of proximity or distance of the mathematical functions of the real farinographic curve. For the second part of the curve (the downward slope with a smooth slope), it was found that this coefficient has values R^2 = 0.970 ±0.014 for the exponential mathematical function (for a 95% confidence interval), which shows a relatively high degree of correlation.

ACKNOWLEDGEMENT

The paper was funded both from the project "Improving the base of practical applications in solariums, gardens, orchards and vineyards (IMPRASGLIV)", CNFIS-FDI-2021-0021, from the Ministry of Education through the Executive Agency for Financing Higher Education, Research, Development and Innovation.

REFERENCES

[1] Aydogan, S., Sahin, M., Gocmen Akcacik, A., Hamzaoglu, S., Taner, S. (2015). Relationships between farinograph parameters and bread volume physicochemical traits in bread wheat flours, *Journal of Bahri Dagdas Crop Research*, 3(1), 14-18;

[2] Cardone, G., D'Incecco, P., Casiraghi, M.C., Marti, A. (2020). Exploiting milling by-products in bread-making: the case of sprouted wheat, *Foods*, 9(3), 260, https://doi.org/10.3390/foods9030260;
[3] Hassoon, W.H., Dziki, D., Mis, A., Biernacka, B. (2021). Wheat grinding process with low moisture content: a new approach for wholemeal flour production, *Processes*, 9(1), 32, https://doi.org/10.3390/pr9010032;
[4] Hermannseder, B., Ahmad, M.H., Kugler, P., Hitzmann, B., (2016). Development of a model for the simulation of Farinograph measurements, *19th Int. ESAFORM Conference on Material Forming*, 1769, 180006, https://doi.org/10.1063/1.4963609;
[5] Li, Q.-M., Li, Y., Zou, J.-H., Guo, S.-Y., Wang, F., Yu, P., Su, X.-J., (2020). Influence of adding Chinese yam (*dioscorea opposita thunb*.) flour on dough rheology, gluten structure, baking performance, and antioxidant properties of bread, *Foods*, 9(3), 256, https://doi.org/10.3390/foods9030256;
[6] Mekuria, B., Emire, S.A. (2015). Effects of vital gluten enrichment on qualities of value added products, *Journal Food Processing and Technology*, vol. 6, 11, https://doi.org/10.4172/2157-7110.1000508;
[7] Mis, A., Nawrocka, A., Dziki, D. (2017). Behaviour of dietary fibre supplements during bread dough development evaluated using novel farinograph curve analysis, *Food and Bioprocess Technology*, 10(6), 1031–1041, https://doi.org/10.1007/s11947-017-1881-8;
[8] Reisner, A.-M., Beer, A., Struck, S., Rohm, H. (2020). Pre-hydrated berry pomace in wheat bread: an approach considering requisite water in fiber enrichment, *Foods*, 9(11), 1600, https://doi.org/10.3390/foods9111600;
[9] Sarker, Z.I., Yamauchi, H., Kim, S.-J., Matsuura-Endo, C., Takigawa, S., Hashimoto, N., Noda, T. (2008). A Farinograph study on dough characteristics of mixtures of wheat flour and potato starches from different cultivars, *Food Sci. Technol. Res*., 14(2), 211–216, https://doi.org/10.3136/fstr.14.211;
[10] Slukova, M., Levkova, J., Michalcova, A., Horackova, S., Skrivan, P. (2017). Effect of the dough mixing process on the quality of wheat and buckwheat proteins, *Czech Journal of Food Sciences*, 35(6), 522–531, https://doi.org/10.17221/220/2017-CJFS;
[11] Sroan, B.S., Kaur, A. (2004). Effect of antioxidants on farinograph and amylograph characteristics of wheat flour, *International Journal of Food Properties*, 7(3), 379–391, https://doi.org/10.1081/JFP-200032921;
[12] Stefan, E.-M., Voicu, Gh., Constantin, G.-A., Ipate, G., Munteanu, M. (2018). Effect of whole buckwheat flour on technological properties of wheat flour and dough, *Engineering for Rural Development*, vol.17, 1533, https://doi.org/10.22616/ERDev2018.17.N393;
[13] Sun, K.-N., Liao, A-M., Zhang, F., Thakur, K., Zhang, J.-G., Huang, J.-H., Wei, Z.-J. (2019). Microstructural, textural, sensory properties and quality of wheat–yam composite flour noodles, *Foods*, 8, 519;
[14] Szafranska, A. (2015), Predicting the farinograph and alveograph properties of flour based on the results of Mixolab parameters, *Acta Agrophysica*, 22(4), 457-469;
[15] Temea (Moroi), A.M., Pircu (Vartolomei), N., Simion, A.I., Grigoras, C.G., Ungureanu (Carbune), R.E., Alexe, P. (2016). Improvement of flour and dough rheological properties by maturation process, *Romanian Biotechnological Letters*, 21(2), 11381-11392, https://e-repository.org/rbl/vol.21/iss.2/15.pdf;
[16] Voinea, A., Stroe, S.-G., Codina, G.G. (2020). The efect of sodium reduction by sea salt and dry sourdough addition on the wheat flour dough rheological properties, *Foods*, 9(5), 610, https://doi.org/10.3390/foods9050610;
[17] Voicu, Gh., Stefan, E.-M. Constantin, G.A., Tudor, P., Constantin Gh. (2016). The relationship between dough consistency and its development time, farinographic curves analysis, *Actual Tasks on Agricultural Engineering*, vol.44, 371-379,
[18] Voicu, Gh., Constantin, Gh., Stefan, E.M., Ipate, G. (2012). Variation of farinographic parameters of doughs obtained from wheat and rye flour mixtures during kneading, *Scientific Bulletin of UPB*, Series D: Mechanical Engineering, 74(2), 2012, 307-320
[19] Munteanu, M., Voicu, Gh., Ştefan, E.M., Constantin, G.A., Popa, L., Mihailov, N. (2015). Farinograph characteristics of wheat flour dough and rye flour dough, *Proceedings of ISB-INMA-TEH Agricultural and Mechanical Engineering Symposium*, p.645;
[20] Voicu, Gh., Constantin, Gh., Ipate, G., Tudor, P. (2017). Farinographic parameter variation of doughs from wheat flour with amount of water added, *16th International Scientific Conference Engineering for Rural Development*, Jelgava, Latvia, p.976-981.

RESEARCH ON COLOR CORRECTION METHOD OF GREENHOUSE TOMATO PLANT IMAGE BASED ON HIGH DYNAMIC RANGE IMAGING

/

基于高动态范围成像的温室番茄植株图像色彩矫正方法

Min Li

Department of electronic information, Xinxiang Vocational and Technical College, Xinxiang, Henan, 453006, China

** E-mail: cii67757@163.com*

DOI: https:// doi.org/10.35633/inmateh-64-39

Keywords: *greenhouse tomato, images, visual information, color*

ABSTRACT

In this paper, aiming at the need of stable access to visual information of intelligent management of greenhouse tomatoes, the color correction method of tomato plant image based on high dynamic range imaging technology was studied, in order to overcome the objective limitation of complex natural lighting conditions on the stable color presentation of working objects. In view of the color distortion caused by the temporal and spatial fluctuation of illumination in greenhouse and sudden change of radiation intensity in complex background, a calibration method of camera radiation response model based on multi-exposure intensity images is proposed. The fusion effect of multi band image is evaluated by field test. The results show that after multi band image fusion processing, the brightness difference between the recognized target and other near color background is significantly enhanced, and the brightness fluctuation of the background is suppressed. The color correction method was verified by field experiments, and the gray information, discrete degree and clarity of tomato plant images in different scenes and periods were improved.

摘要

本文针对温室番茄智能管理对视觉信息稳定存取的需要，研究了基于高动态范围成像技术的番茄植株图像颜色校正方法，为了克服复杂自然光照条件对工作物体稳定色彩呈现的客观限制。针对温室内光照的时空波动和复杂背景下辐射强度的突变引起的颜色畸变，提出了一种基于多曝光强度图像的摄像机辐射响应模型标定方法。通过现场测试，评价了多波段图像的融合效果。结果表明，经过多波段图像融合处理后，识别出的目标与其它近彩色背景的亮度差异显著增强，背景亮度波动得到抑制。通过田间试验验证了该方法的有效性，提高了不同场景、不同时期番茄植株图像的灰度信息、离散度和清晰度。

INTRODUCTION

With the reduction of agricultural labor force and the rise of labor cost, the labor cost of tomato planting management has increased year by year, which has reached more than 30% of the total production cost *(Albino V.S. et al., 2018)*. In recent years, with the increase of labor cost, the labor cost of tomato planting management has increased to about 45% of the total production cost. The high labor cost has become an objective factor limiting the growth of tomato planting efficiency. In view of the unique advantages of robot in intelligent detection and complex operation, the research and development of agricultural robot which can replace manual operation is an effective way to deal with the current situation from the perspective of engineering technology, aiming at labor-intensive and complex planting management links such as greenhouse tomato picking, pruning, pollination and spraying *(Alvarado K.A. et al., 2020)*. Plant information is an important decision-making basis for intelligent facility gardening control system to achieve accurate control, and it is also a key element of plant phenotypic omics research. Because plant growth information is not only controlled by genetic factors, but also influenced by growth environment, the external three-dimensional geometry and internal physiological information of plants are complex and varied. Tomato plants are clustered and staggered, the working objects grow randomly along the main stem, overlap and block each other, and the space between rows of plants is narrow. There are many problems in collecting and processing images with large field of view, such as small imaging object distance and redundant interference.

Using manual operation for reference, tracking and collecting discrete small-field images in different areas and searching different working objects along the main stem of plants are effective ways to improve the efficiency of working object recognition and location.

With the development and wide application of modern technology, agriculture has entered a new stage of development, and the modernization of agriculture has been paid more and more attention. At the same time, due to the rapid urbanization process and the increasing demand for agricultural products, China attaches great importance to the modern mechanized planting technology of agriculture *(Aznar-Sánchez J. A. et al., 2020)*. Accurately acquiring the visual characteristics of working objects is a necessary prerequisite for intelligent operation of robots. For different management links, the stems, leaves and fruits of tomato plants may be working objects or background interference. However, plants in greenhouse are densely clustered and disorderly, and tomato stems, leaves and green fruits are similar color organs, so it is difficult to realize accurate recognition of plant specific objects based on broad visible light image information *(Bielza P. et al., 2020)*. Visual information is the sensory embodiment of the comprehensive action of the illumination conditions in the working area and the reflection characteristics of the working objects. However, in the agricultural environment, natural illumination fluctuation and complex background interference are the key factors affecting the stable imaging of visual information, which are manifested by the dynamic changes of illumination in time and space and the different radiation characteristics of multiple targets in the field of view. In this paper, aiming at the need of stable access to visual information of intelligent management of tomato in greenhouse, the color correction method of tomato plant image based on high dynamic range imaging technology is studied to overcome the objective limitation of complex natural lighting conditions on the stable color presentation of working objects *(Zhou J. et al., 2018)*. In view of the image color distortion caused by spatiotemporal fluctuation of illumination and mutation of complex background radiation intensity in greenhouse, a calibration method of camera radiation response model based on multi exposure image fusion was proposed.

Visual information acquisition is one of the core technologies to support intelligent production. The plants in greenhouse are dense and disordered, and the stems, leaves and green fruits of tomato are similar color organs. Based on the extensive visible light image information, it is difficult to realize the accurate recognition of plant specific objects. With the continuous growth of the plant, the relative height of the working area to the ground remains unchanged by releasing the hanging line wrapped around the main stem. In the aspect of plant physiological diagnosis, the physiological diagnosis model is mainly built based on multi band two-dimensional spectral image features. Because the two-dimensional image is only a single perspective imaging feature, it cannot reflect all plant features, and cannot reflect the distribution and spatial position of specific physiological features *(Sun G. et al., 2019)*. Traditional manual measurement, loss measurement and low-throughput measurement methods have been unable to meet the needs of intelligent management of modern precision agriculture and the development of plant Phenomics. It is urgent to study highly integrated, high-throughput and high-precision plant phenotypic measurement system. In this paper, high dynamic range imaging technology is used to recover the relative radiation intensity of different objects in the field of view by fusing the image information of different exposures, so as to compensate and correct the color distortion of the image, and then realize the constant presentation of the color of complex background objects. This study can provide a reference for the research on the acquisition of color information of the operation object image under complex lighting conditions.

The plant disease recognition classifier based on probabilistic neural network (PNN) can classify tomato late blight, septal spot, bacterial spot, bacterial ulcer, tomato leaf curl image and tomato healthy plant image by extracting the color, shape and texture features of tomato plant images, then using decision trees sort *(Chaitanya D. N. V. et al., 2018; Chatterjee N. et al., 2019)*. Using machine learning technology, a plant disease severity recognition system can be designed. Combined with support vector machine network and spectral vegetation index, sugar beet disease type diagnosis was realized. An Android application platform was developed to monitor greenhouse vegetables and realize remote observation of vegetable disease degree *(Park G. et al., 2020; Redström J., 2020; Smith H. A. et al., 2019)*. Now the LabVIEW interface for monitoring greenhouse fruits and vegetables has been developed, but these detection applications can only see video. If we want to save historical images for analysis, the storage capacity will be very large, and resources will be wasted. Therefore, it is very important to realize the automatic acquisition system of disease image. By dynamically adjusting the camera exposure gain and white balance parameters, the color of petal image can be presented stably *(Siddique M.A.A. et al., 2020).*

Combining depth vision technology with multispectral imaging technology, tomato plants in greenhouse were studied *(Tan G. et al., 2017).* The RGB-D images and multispectral images of each plant were collected in the same imaging room at the same time, and the multispectral reflectance of each plant was recorded in the depth coordinate system by using the principle of phase correlation *(Lee P. U. et al., 2018).*

The problem of kiwifruit night vision recognition is solved by setting foreground led complementary light source, highlighting the boundary of overlapping targets and reducing background interference. By analyzing the color quality of the target image in real time and dynamically adjusting the control parameters of the filling light source, the low energy consumption and high efficiency exposure compensation is realized. The litchi image preprocessing method based on Retinex image enhancement algorithm overcomes the problem of uneven brightness of camera field of view under natural light. By using Caffe framework and deep convolution network, 14 kinds of diseases are recognized, and good results are achieved. Support vector machine (SVM) was used to classify healthy and ill conditioned images of soybean leaves. The main steps of the experiment are: image acquisition, leaf extraction under complex background, statistical analysis and classification, and finally good results were achieved. The performance of several machine learning techniques in pattern recognition and classification of leafy plant diseases is compared. Finally, the conclusion that support vector machine has more advantages is drawn.

MATERIALS AND METHODS

Temporal and spatial fluctuation of light parameters

As tomato is a kind of fruit and vegetable with high sales value and high yield demand, this paper takes tomato plant diseases as the research object, and processes 300 images of tomato leaf gray mold, late blight, powdery mildew and normal leaves. GMM (Gaussian Mixture Model) is used to segment the image background, HSI (Hue Saturation Intensity) algorithm is used to segment the diseased spots, and then three kinds of change model algorithms are used to extract color features. At present, the target recognition and classification methods based on spectral characteristic images mainly take the strongest reflection band of the target as the imaging band, only emphasize the brightness of the target area image, and lack the fusion of the background weak reflection band image, which cannot fully achieve the purpose of highlighting the strong reflection target and diluting the weak reflection background interference. Registration and mosaic of discrete field images is a necessary way to obtain the overall morphological characteristics of tomato stem. Camera pose matching obtains the spatial pose parameters of camera in real time, and analyzes the transformation relationship of target shape from different perspectives based on perspective imaging principle. Influenced by the change of direction and intensity of solar illumination during the day, the illumination parameters in semi-open greenhouse show temporal and spatial dynamic changes. According to the internal parameters of Kinect sensor, the sensor converts RGB-D images from different angles into three-dimensional point clouds.

The change of illumination intensity in greenhouse is the main factor that leads to the color variation of the target image. Accurate analysis of dynamic radiation intensity information in different areas of the camera field of view is the premise of compensating and correcting the fluctuation of ambient illumination. Figure 1 is a three-dimensional schematic diagram of color.

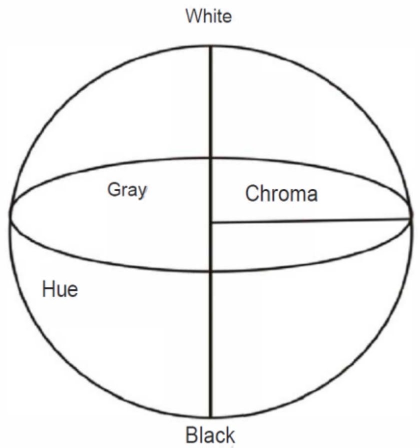

Fig. 1 - Color stereo schematic

Figure 2 shows two images collected under different exposure intensities. In Figure 2a, the ceiling sky and wall colors are normal, and the tomato plant area is underexposed. In Figure 2b, the color of tomato plants is normal, and the ceiling and wall areas are overexposed.

(a) Underexposure (b) Overexposure

Fig. 2 - Image color distortion caused by the difference in target radiation characteristics

Because each spatial coordinate point contains RGB value and reflectivity value of each band, the multi-modal 3D point cloud model reconstruction is realized when realizing 3D point cloud model reconstruction. Single spectral feature data lacks target spatial information, so it is difficult to be used as the basis of visual servo control, and is mostly used for the classification of biological tissue components and physiological characteristics such as pests and diseases, weed species and leaf density. The spectral image data obtained by imaging technology is the comprehensive embodiment of the spectral reflection characteristics of the target and its spatial position information, which can be used as the basis for the robot to recognize the target and accurately target the operation. Kinect sensors collect RGB images and depth images.

To realize multi-modal 3D reconstruction of tomato plants, it is necessary to align the multispectral reflectance of the plants to the depth coordinates, that is, each 3D spatial coordinate contains RGB values and multispectral reflectance. There are mainly displacement, rotation angle and scaling transformation problems between SOC710 image and Kinect image. Collect RGB-D images of the electric turntable surface from two perspectives, identify the yellow and red calibration point cloud coordinates of the turntable surface from each perspective according to the color threshold, calculate the calibration point center, and calculate the center coordinate and normal vector of the turntable rotating shaft according to the center of gravity. In view of the differences in the components of different organs, such as stems, leaves and fruits, classification and recognition according to their specific spectral characteristics is an effective way to solve the problem of visual recognition of plant objects with similar colors.

Mutation of radiation intensity in complex background

In view of the non-uniform structure of the object to be measured, and its surface morphology, composition and texture are irregular, spectral data are collected for each sample for 5 times, and the average value is the spectral measurement data of a single sample. The spectral characteristic curves of stems, leaves and green fruits of tomato plants were obtained by filtering, denoising and averaging the spectral data of various samples. The radiation characteristics of different targets are different under the complex background of greenhouse, among which the radiant brightness of the near tomato plant is greatly different from that of the far greenhouse ceiling and wall. In addition, there is a sudden change in brightness between the shadow area projected by the steel structure at the top of the greenhouse and the direct sunlight area.

However, the range of radiation fluctuation in the field of view presented by the camera imaging chip is limited, which will lead to overexposure and underexposure in the image area under specific exposure intensity, resulting in distortion of target color information. By rotating the wheel, the filter in front of the camera lens can be switched to collect images in different bands. 180W halogen lamp is selected as the light source, and 5000lx radiation intensity is formed in the field of view of the camera to overcome the influence of illumination fluctuation in the experimental environment.

Under the radiation environment of the same light source, the illumination intensity of different bands is different, and the sensitivity of the camera imaging chip to different bands is also different. In order to make the image brightness correspond to the target spectral reflection intensity, it is necessary to collect images of different bands for brightness correction. Figure 3 shows the system structure of plant digital image analysis based on high dynamic range.

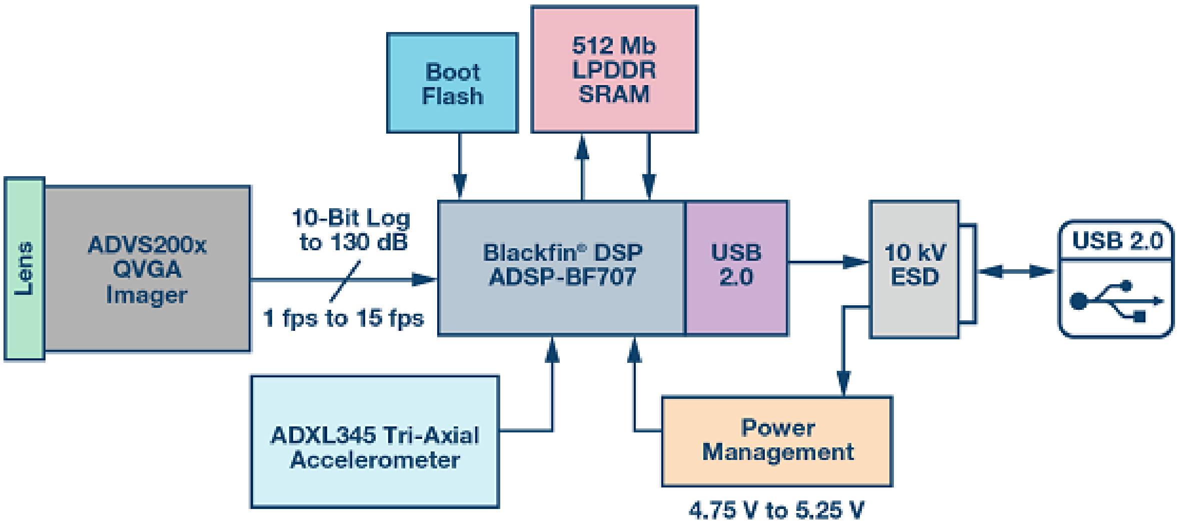

Fig. 3 - The structure of the plant digital image processing and analysis system

The Gaussian kernel is the only kernel that can generate multi-scale space. The scale space of an image, $L(x,y,\sigma)$ is defined as the original image $I(x,y)$ and a variable-scale two-dimensional Gaussian function $G(x, y, \sigma)$ convolution operation, as shown in formula (1)(2):

$$G(x_i, y_i, \sigma) = \frac{1}{2\pi\sigma^2} \exp\left(-\frac{(x-x_i)^2 + (y-y_i)^2}{2\sigma^2} \right) \tag{1}$$

$$L(x, y, \sigma) = G(x, y, \sigma) * I(x, y) \tag{2}$$

The Gaussian difference function $D(x, y, \sigma)$ can be calculated by the difference between two adjacent scale images with a constant multiplication factor k, as shown in equation (3):

$$D(x, y, \sigma) = [G(x, y, k\sigma) - G(x, y, \sigma)] * I(x, y) = L(x, y, k\sigma) - L(x, y, \sigma) \tag{3}$$

Single global exposure control can easily lead to color distortion of foreground and background objects, which is an objective limitation for cameras to obtain images of greenhouse tomato plants. In view of this, it is an effective way to correct exposure distortion in image areas by fusing multi-exposure image information to restore radiation intensity in different areas of the field of view.

The flow chart of the image processing system is shown in Figure 4.

The standard color plate can be pushed into a specific position of the camera field of view near the tomato plant by a mechanical device. By triggering the acquisition mode, the camera collects one image of tomato plant and standard color plate in the same wave band, and the camera exposure parameters remain unchanged during the acquisition process. Under the same light source radiation environment, the illumination intensity in different bands is different, and the sensitivity of camera imaging chips to different bands is also different. In order to make the image brightness correspond to the target spectral reflection intensity, it is necessary to collect images in different bands for brightness correction. The standard color plate can be pushed into a specific position of the camera field of view near the tomato plant by a mechanical device. By triggering the acquisition mode, the camera collects one image of tomato plant and standard color plate in the same wave band, and the camera exposure parameters remain unchanged during the acquisition process. The purpose of multi-band image data fusion is to make the target pixel area stand out from diverse backgrounds and keep the brightness of non-target background areas balanced, so as to reduce the difficulty of target area segmentation.

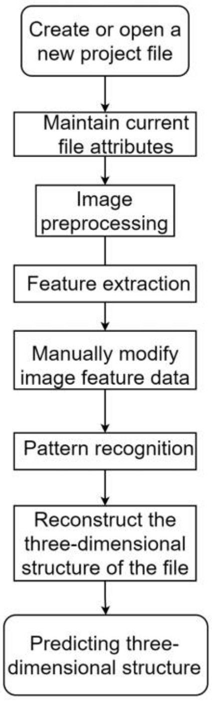

Fig. 4 - Image processing system flow

RESULTS

The purpose of contour extraction and contour tracking is to obtain the external contour features of the image. On this basis, a certain method is applied to express the characteristics of the contour to prepare for the shape analysis of the image. After multi-band image fusion processing is performed on specific targets of tomato stems, leaves, and green fruits, the pixel brightness of the targets with similar color backgrounds all show obvious differences. In the original optimal imaging band and the fusion result image, 500 pixels were selected for the stem, leaf and green fruit area respectively. After multi-band image fusion processing is performed on specific targets of tomato stems, leaves, and green fruits, the pixel brightness of the targets with similar color backgrounds all show obvious differences. In the original optimal imaging band and the fusion result image, 500 pixels were selected for the stalk, leaf and green fruit area respectively, and the grayscale difference between green fruit-leaf, stem-green fruit and stem-leaf was calculated. Since the height of the visual field of the vision system is about 400 mm, in order to cover the height of the main stem of the work area, the camera pan/tilt is set to automatically adjust twice from the horizontal initial posture, and 3 images are tracked and collected for each tomato, and in this sequence of images the morphology of the main stem is spliced and measured. The tomato plant stem and leaf features are completely segmented, but some background and reference template edges are also segmented and retained. Therefore, the segmented binary image needs to be further filtered to remove information other than tomato plants.

In view of the fact that the greenhouse light fluctuation is mainly reflected in the change of light intensity, this article focuses on the correction of the image color brightness in order to achieve the purpose of reconstructing the target true color. The CIE XYZ color model is a three-primary color system designed based on the human eye's perception of the color of visible light sources. All visible colors can be represented by three-color values (X, Y, Z). The color description of digital image acquisition and display is based on the ITU709 standard.

The conversion formula of image RGB color information and CIE XYZ color model is:

$$\begin{bmatrix} X \\ Y \\ Z \end{bmatrix} = \begin{bmatrix} 0.4086 & 0.3581 & 0.1802 \\ 0.2099 & 0.7204 & 0.0731 \\ 0.0217 & 0.1189 & 0.9534 \end{bmatrix} \begin{bmatrix} R \\ G \\ B \end{bmatrix} \tag{4}$$

in which X and Z are CIE XYZ image chroma components, Y is CIE XYZ image brightness components, and R, G and B are digital image color components.

The sequence exposure images of different scenes in specific periods are shown in Figure 5.

Fig. 5 - Sequence exposure images of different scenes at specific times

In order to make up for the deficiency of the existing contraction function, a new curve contraction function is constructed to make the estimated value continuous at the threshold. With the increase of radial component, it can reach and exceed the true value.

The contraction trend of adaptive nonlinear curve is shown in Figure 6.

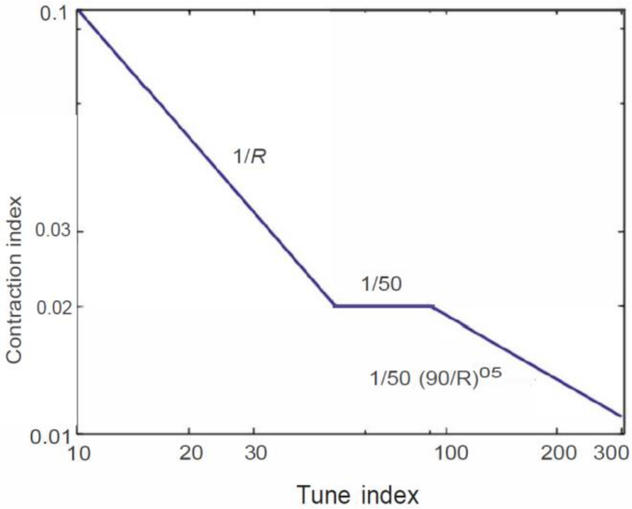

Fig. 6 - The shrinking trend of adaptive nonlinear curve

The S-curve function is used to map the high dynamic image data to the gray scale range of 0-255. The brightness of the compressed image is:

$$Y_i^d = \frac{255 \log_5 \left(E_i / \overline{E} + 1\right)}{\lg\left(E_{\max} / \overline{E} + 1\right)\left(1 + \exp\left(-\log_2 E_i\right)\right)} \tag{5}$$

In which:

$$\overline{E} = \exp\left(\frac{1}{N}\sum_{i=1}^{N} \ln E_i\right) \tag{6}$$

Where E_{max} is the maximum brightness of the high dynamic image, Y_i^d is the image brightness after compression, and $\overline{E}$ is the average brightness of the high dynamic image. Based on the radiation characteristics of the scene in Figure 7, the calibrated camera radiation response curve is shown in Figure 7.

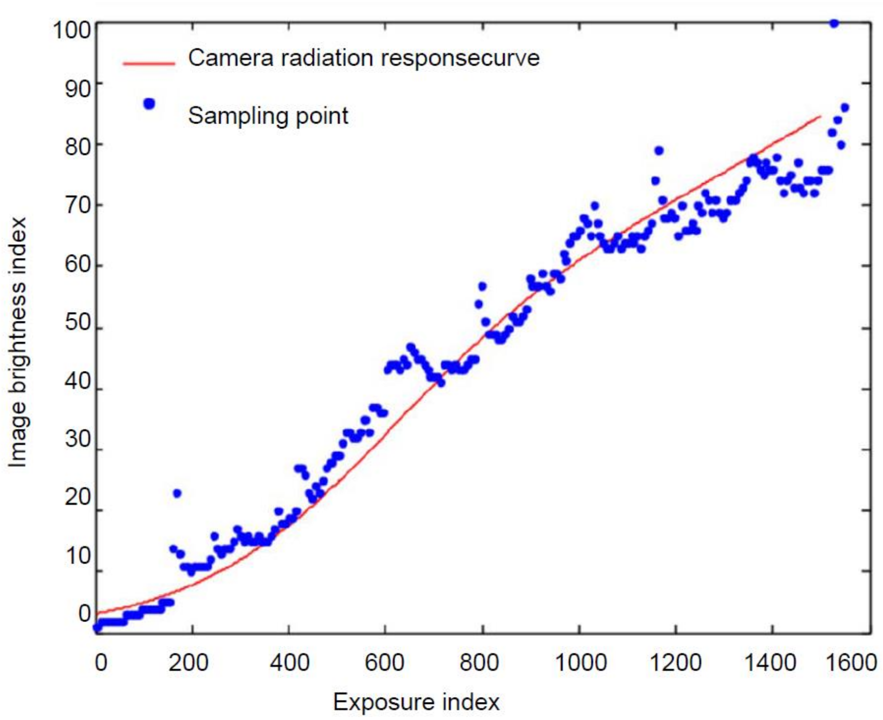

Fig. 7 - Camera radiation response curve

In order to quantitatively evaluate the effect of image correction, information entropy and average gradient are used as evaluation indexes to evaluate the gray information content, dispersion degree and clarity of the image before and after color correction.

Statistics of evaluation parameters of original and corrected images of tomato plants in different scenes and periods are shown in Table 1 and Table 2 respectively.

Table 1

Image information entropy statistics

t/ms	Scene 1: Sunlight scene				Scene 2: Cloudy scene			
	8:00	10:00	12:00	14:00	8:00	10:00	12:00	14:00
0.02	4.78	4.76	4.60	4.61	3.85	3.45	3.36	3.46
0.04	5.23	5.01	4.89	4.89	3.73	3.55	3.32	3.36
0.06	4.77	4.82	4.69	4.70	3.55	3.47	3.17	3.42
0.08	4.73	4.84	4.18	4.33	3.55	3.46	3.23	3.33

Table 2

Image average gradient statistics

t/ms	Scene 1: Sunlight scene				Scene 2: Cloudy scene			
	8: 00	10: 00	12: 00	14: 00	8: 00	10: 00	12: 00	14: 00
0.02	0.031	0.039	0.039	0.039	0.021	0.025	0.026	0.030
0.04	0.036	0.041	0.041	0.042	0.025	0.031	0.035	0.035
0.06	0.029	0.033	0.033	0.033	0.024	0.029	0.030	0.031
0.08	0.035	0.039	0.038	0.038	0.028	0.033	0.033	0.032

From the statistical results, the brightness of the image area of tomato stems, leaves and fruits increases with the increase of imaging wavelength, that is, the intensity of plant reflection is greater in the long-wave area. The transmitted sunlight forms an obvious spot area in the short-wave image, but the brightness is not obvious in the long-wave image area. Since the boundary is continuous, each boundary point can be represented by the angle formed by this boundary point to the previous boundary point.

Therefore, the following tracking criteria can be used, that is, starting from the first boundary point, define the initial search direction to be along the upper left, if the upper left is a black point, it is the boundary point, otherwise the search direction is rotated clockwise by 45°.

Since the main stem is suspended in space and flexibly bent, and the contact and collision during manual measurement may change its natural shape, manual measurement results still cannot accurately reflect the true natural shape of the main stem. After multi-band image fusion, the main areas of similar color targets can be segmented from the background through conventional automatic segmentation algorithms. Nevertheless, the segmentation results for stems and fruits show that the specular reflection area on the fruit surface becomes the main error segmentation area. Therefore, to overcome the smooth surface specular reflection of the tomato fruit surface to improve the target imaging effect is the focus of further research.

CONCLUSIONS

Plant information is an important decision-making basis for intelligent facility gardening control system to achieve accurate control, and it is also a key element of plant phenotypic omics research. In this paper, aiming at the problem of fluctuation of light intensity in greenhouse environment and sudden change of brightness in complex background, an image color correction method based on high dynamic range imaging is proposed, which effectively overcomes the problem of color distortion of tomato plant image under global exposure.

The method of tracking and measuring the main stem of a plant based on a binocular pan/tilt camera can realize the collection and splicing of images in discrete areas, and measure the three-dimensional morphological parameters such as the length, height and growth angle of the visible area. There is a linear correlation between the manual measurement results of living plants and the automatic measurement results of images. In gray-scale transformation enhancement, histogram specification purposefully enhances some gray levels and improves the visual effect of disease images, but this enhancement method does not play a role in suppressing various noises.

The relative relationship of brightness of similar color target image obtained by multi-band image online acquisition system is consistent with its spectral reflection intensity. In this paper, high dynamic range imaging technology is used to restore the relative radiation intensity of different targets in the field of view by fusing the image information with different exposures, so as to compensate and correct the image color distortion, and then realize the constant presentation of complex background target color.

REFERENCES

[1] Albino V. S., Peixoto J. R., Junior V. C., (2018), Rootstock performance for cherry tomato production under organic, greenhouse production system. *Horticultura Brasileira*, Vol. 36, Issue 1, pp. 130-135. Brazil;

[2] Alvarado K. A., Mill A., Pearce J. M., (2020), Scaling of greenhouse crop production in low sunlight scenarios. *Science of The Total Environment*, Issue 707, p. 136012. Netherlands;

[3] Aznar-Sánchez J. A., Velasco-Muñoz J. F., García-Arca D., (2020), Identification of opportunities for applying the circular economy to intensive agriculture in Almería (south-east Spain). *Agronomy*, Vol. 10, Issue 10, p. 1499. United States;

[4] Bielza P., Balanza V., Cifuentes D., (2020), Challenges facing arthropod biological control: identifying traits for genetic improvement of predators in protected crops. *Pest management science*, Vol. 76, Issue 11, pp. 3517-3526. England;

[5] Chaitanya D. N. V., Arunkumar S., Akhilesh G. B., (2018), Design of Rice Transplanter. *Iop Conference,* p. 377, United Kingdom;

[6] Chatterjee N., Gupta S., (2019), Efficient Phrase Table pruning for Hindi to English machine translation through syntactic and marker-based filtering and hybrid similarity measurement. *Natural Language Engineering*, Vol. 25, Issue PT.1, pp. 171-210. England;

[7] Lee P. U., So J. H., Nam Y. S., (2018), Power analysis of electric transplanter by planting distances. *Korean Journal of Agricultural Science*, p. 45. Korea;

[8] Park G., Hong J., Yoo S., (2020), Design of a 3-DOF Parallel Manipulator to Compensate for Disturbances in Facade Cleaning. *IEEE Access,* Vol. 99, pp. 1-1. United States;

[9] Redström J., (2020), Certain uncertainties and the design of design education. *She Ji: The Journal of Design, Economics, and Innovation*, Vol. 6, Issue 1, pp. 83-100. Netherlands;

[10] Sharkawy A. N., Koustoumpardis P N, Aspragathos N., (2020), Neural Network Design for Manipulator Collision Detection Based Only on the Joint Position Sensors. *Robotica*, Vol. 38, Issue 10, pp. 1737-1755. England;

[11] Siddique M. A. A., Kim W. S., Kim Y. S., (2020). Effects of Temperatures and Viscosity of the Hydraulic Oils on the Proportional Valve for a Rice Transplanter Based on PID Control Algorithm. *Agriculture*, pp. 10. Switzerland;

[12] Smith H. A., Krey K. L., (2019), Three release rates of Dicyphus hesperus (Hemiptera: Miridae) for management of Bemisia tabaci (Hemiptera: Aleyrodidae) on greenhouse tomato. *Insects*, Vol. 10, Issue 7, p. 213. Switzerland;

[13] Sun G., Ding Y., Wang X., (2019), Nondestructive determination of nitrogen, phosphorus and potassium contents in greenhouse tomato plants based on multispectral three-dimensional imaging. *Sensors*, Vol. 19, Issue 23, p. 5295. Switzerland;

[14] Tan G., Lei Z., Tan X., (2017), Neuron Pruning-Based Discriminative Extreme Learning Machine for Pattern Classification. *Cognitive Computation,* Vol. 9, Issue 1, pp. 581-595. Germany;

[15] Zhou J., Chen H., Zhou J., (2018), Development of an automated phenotyping platform for quantifying soybean dynamic responses to salinity stress in greenhouse environment. *Computers and Electronics in Agriculture*, Issue 151, pp. 319-330. England.

DESIGN AND KINEMATICS ANALYSIS OF MECHANICAL ARM OF TRIMMER
/
枣树修剪机机械臂的设计与运动学分析

Qiang Liang[1)]*, Hao Wang[1)]
[1)] Xinxiang Vocational and Technical College, Xinxiang, Henan, 453006, China
*E-mail: gipws4349@163.com
DOI: https://doi.org/10.35633/inmateh-64-40

Keywords: *trimmer, mechanical arm, kinematics analysis*

ABSTRACT
The development of mechanization has greatly liberated the labour force, promoted socialized mass production, and created infinite social wealth. Its influence is significant and far-reaching, and agricultural production has undergone revolutionary changes. Aiming at the problems of poor working environment, high labour intensity and low working efficiency of manual pruning, a mechanical arm of branch pruning machine was designed, which realized the three-dimensional layered cylindrical pruning of individual tree. In this paper, a five-degree-of-freedom trimmer manipulator is designed, which is mainly composed of base, big arm, small arm, wrist and finger blade. The motion equation of the mechanism is established by using the Denavit–Hartenberg parameter (D-H parameter) method, and the corresponding motion curve is fitted by using MATLAB software. The components of the trimmer arm are designed virtually by using 3D modeling software, and assembled into a complete trimmer arm. The assembly drawing is imported into the simulation analysis software ADAMS for kinematics simulation. The results show that the speed-time pattern has obvious positive and negative changes at 3s, which proves that this stage is the hand cutting stage of jujube pruning; The acceleration time graph is gentle in the whole movement, and the curve approaches to a straight line, which proves that the movement of the mechanical arm of the jujube pruning machine is stable in the pruning process. Through the analysis of the simulation curve, it provides a theoretical basis for the research of the mechanical arm of the trimmer.

摘要
机械化的发展极大地解放了劳动力，促进了社会化大生产，创造了无限的社会财富。其影响重大而深远，农业生产发生了革命性的变化。针对人工修剪存在的工作环境差、劳动强度大、工作效率低等问题，设计了一种树枝修剪机机械臂，实现了单株树木的三维分层圆柱形修剪。本文设计了一种五自由度切边机械手，主要由底座、大臂、小臂、手腕和指叶组成。采用 D-H 参数法建立了机构的运动方程，并用 MATLAB 软件拟合了相应的运动曲线。利用三维建模软件对切刀臂的各部件进行虚拟设计，组装成一个完整的切刀臂。将装配图导入仿真分析软件 ADAMS 进行运动学仿真。结果显示速度时间图形在 3s 处有较为明显的正负值变化，证明了该阶段为枣树修剪手切割阶段；加速度时间图形在全程运动中较为平缓，并且曲线基本趋近于一条直线，证明了在修剪过程中枣树修剪机机械臂的运动较为稳定。通过对仿真曲线的分析，为切边机机械臂的研究提供了理论依据。

INTRODUCTION
There are many kinds of unmanned mechanical systems in the field of agricultural production, such as unmanned tractors, combine harvesters, transplanters and automatic thrusters, etc. They walk in the field by themselves through the combined sensing system *(Chaitanya D.N.V. et al., 2018)*. These different mechanical systems, with or without operators, can sense the environment through sensing systems and realize autonomous operation through algorithms, which is a control mode with functions similar to human perception and intelligence. These robots refer to robots in a broad sense, including most intelligent mechanical systems *(Zhang J. et al., 2020)*

There are two main types of existing branch pruning equipment, one is short twig pruning, the handle is short and unsuitable for pruning, and second, pruning of tall branches: aiming at pruning of tall and thick branches, the handle is long, the weight is heavy, the alignment is low during pruning, and it is not easy to operate *(He W. et al., 2018)*. Manual pruning tools, i.e. electric, pneumatic and hydraulic scissors, are commonly used for manual pruning of single branches. Among them, manual pruning tools are used for large-scale pruning operations, which have high labour intensity, low work efficiency and are easy to cause occupational diseases. Electric, pneumatic and hydraulic scissors need to be equipped with power sources, and the scissors are heavy, so manpower is not suitable for long-term operation *(Tian H. et al., 2020)*. The experiment shows that the above two new pruning pieces of equipment are not suitable for pruning operation of low and dense planting. Therefore, the mechanical arm of trimmer with simple and practical design mechanism will have a good market prospect in the field of agricultural equipment with its lower manufacturing cost and higher economic benefit *(Li X. et al., 2020).*

This paper has studied the mechanical arm of branch trimmer, which is an agricultural mechanical arm. The performance of the mechanical arm is directly related to the overall performance of the mechanical arm control system. In this paper, based on the motion space analysis of the selected manipulator configuration, a 5-DOF manipulator is designed by using 3D software, and the hardware platform of the manipulator motion control system is realized. Finally, kinematics simulation and verification are carried out.

Nowadays, robots are not only limited to factories, but also special robots have appeared in many specific occasions, such as: explosive robots, surgical robots, service robots, line patrol robots, forestry robots, picking robots, etc. The best development of robots used in pruning is automatic lawn mowers, which have the ability of path planning and have been applied to lawns in family communities. There are no robots with automation ability in trimmers. Although there are trimmers imitating robots, there are still many problems to be solved in performance *(Chatterjee N. and Gupta S., 2019)*.

At present, trimmers can be divided into three categories:

- Manual trimming equipment, namely hedge shears and hand saws;
- Backpack small portable trimmer;
- Large-scale airborne trimmers, namely, vehicle-mounted, vehicle-mounted suspension and boom suspension.

Different types of trimmers have been continuously upgraded and have gradually worked in corresponding workplaces.

It has been more than 40 years since the development of trimmer equipment in foreign countries, from the most primitive manual scissors to mobile equipment. The United States and Japan take the lead in promoting the use of vehicle-mounted hanging trimmer, which combines the cutting and conveying device of reciprocating trimmer, and adopts hydraulic drive to adjust the position and posture of cutting device to trim hedges with different heights and different inclination angles. It is suitable for trimming the central isolation belt and green belts on both sides of expressways, and can meet the requirements in similar places with heavy workload and height according to the growth characteristics of branches of grape, apple, pear and other fruit trees, curtain trimmer is introduced to trim upright branches, which improves the pruning efficiency *(Gonzalez D.J. and Asada H.H., 2017; Hong J. et al., 2020)*. Some researchers designed and developed a double reciprocating grape trimmer, which can trim by adjusting the angle of trimming cutter *(Kang J.L. et al, 2019).* Literature developed a front hanging red jujube trimmer. The trimmer is composed of top and side parts. The disc cutters are alternately arranged on the tool holder, driven by hydraulic system, and the "door" copying trimming operation is realized. The cutting missing rate is less than 10%, but the three-dimensional layered copying cylindrical trimming cannot be realized *(Bamdad M. and Bahri M.M., 2019)*.

The development of domestic pruning machinery started late. In the late 1970s, landscaping maintenance machinery began to appear. Domestic enterprises mainly relied on the introduction of foreign mature technologies or products in the early stage in combination with China's national conditions. In order to adapt to domestic characteristics, imitation or improved equipment began to appear. In order to solve the problems of narrow domestic roads and small scale of road greening, hanD-Held semi-automatic agricultural and forestry machinery was designed. The development of intelligent trimmer in China is still in its initial stage, without perfect technical system, unified standard, various control methods, and it often fails to achieve the desired results when working. The flexibility and reliability of trimming equipment are far behind those of foreign countries, so it is urgent to develop a small vehicle-mounted trimmer equipment.

The researcher studied and designed the double-sided high-efficiency trimming machine. The key technologies of loquat pruning robot are studied, the application of image recognition technology in loquat pruning robot is studied, and the loquat pruning end effector is designed *(Minakov I.A. and Nikitin A.V., 2019)*. Although these prototypes can realize automatic pruning to a certain extent, they are far from being fully automatic or even intelligent *(Roshanianfard A.R. and Noguchi N., 2018)*.

To sum up, domestic agricultural and forestry machinery and equipment are still in the primary stage, and there is a big gap with developed countries in terms of performance, quality and automation level. In the next stage, we should proceed from reality develop various types of equipment that can adapt to the planting characteristics of domestic green belts, develop stable and reliable operation platforms, gradually master core technologies, and produce key core components, so as to build intelligent modern trimmers *(Sharkawy A.N. et al., 2020; Freire-Tellado M.J. et al., 2020).*

MATERIALS AND METHODS

Mechanical arm design of trimmer

Its design idea is the working principle of linkage mechanism in mechanical principle (see Figure 1). The mechanical arm of trimmer is mainly composed of hydraulic motor, coupling, cutter shaft, cutter head, cutter head fixing sleeve, supporting device, copying wheel, bearing seat and frame. The cutter shaft is vertically installed on the frame through a bearing seat, and a plurality of groups of cutter heads are horizontally fixed on the cutter shaft to realize the three-dimensional layered sawing function; The cutter group assembly moves from side to side with the random frame, and moves back and forth with the whole machine at the same time, thus realizing the cylindrical trimming function.

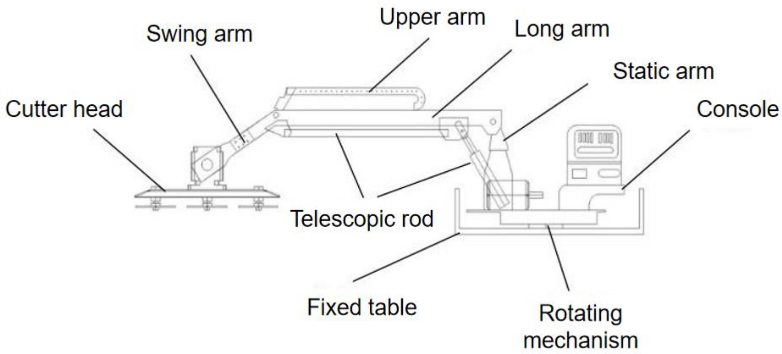

Fig. 1 - Overall plan view of mechanical arm of jujube trimmer

When working, the hydraulic system of the whole machine provides driving force for the trimming device. The hydraulic motor generates torque through the hydraulic system, drives the cutter shaft to rotate at high speed, and drives a plurality of groups of cutter heads horizontally fixed on the cutter shaft to rotate. The high-speed rotation of the cutter head produces inertial force, and the cutting edge of the cutter head performs sawing and trimming operation under the action of inertial force. The trimming device moves along with the whole machine, and two groups of cutter head assemblies of the trimming device are driven to move left and right respectively through the interaction between the follow-up copying wheel and the trunk. Three-dimensional layered trimming can be realized when multiple sets of horizontally installed and vertically spaced cutterheads are sawed and trimmed. During the advancing process of the trimming device, the two groups of cutter head assemblies fit the circular arc movement by moving left and right, which can realize the individual tree-like cylindrical trimming function.

The folding mechanism is the main component of this design. In order to meet the requirements of different shapes at present, the design goal is to realize the change from three-side trimming posture to one-side trimming on the premise of first meeting the simultaneous trimming on three sides. Moreover, because the industrial platform of this design selects the front tractor, which is equipped with hydraulic device and does not need to set up another power source (as the vertical and horizontal position control of trimming machinery operation), we choose the hydraulic cylinder as the expansion control component of the folding mechanism here. When the trimming mechanism is required to trim three sides, the hydraulic cylinder contracts, so that the cutters on both sides are folded to the vertical position, and the side of the green belt can be trimmed. When the trimming mechanism needs to complete the single-side trimming task, the hydraulic cylinder extends again, so that the three-side cutters are in a horizontal plane, which can complete the trimming work of a large area on one side. Not only the horizontal trimming task can be realized, but also the large-area trimming can be realized.

By using the hydraulic system, the control of each hydraulic cylinder can be realized through the joystick in the cab, and the semi-intelligent design is realized. Selecting hydraulic cylinder as the component for adjusting and controlling the working mode of the trimmer can meet the design requirements with only a small size, which is beneficial to the light weight of the whole tool holder and is more economical and practical.

Compared with other control devices, the hydraulic cylinder works more stably and the technology is more mature *(Redström J., 2020).*

The structure of the folding mechanism is shown in Figure 2.

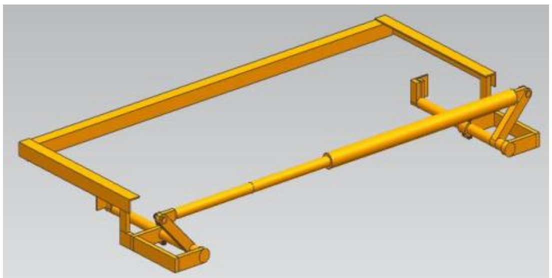

Fig. 2 - Basic mechanism diagram of folding mechanism

Fig.2 includes hydraulic cylinder, fixing bracket and cutter link plate. The cutters on both sides are linked with cutter link plates to form a rigid integrated structure, and the other side of the link plates is a transverse rotating shaft. The end points and middle points on the upper side of the rotating shaft are respectively in contact with the outer bracket, and under the constraint of the bracket, the shaft cannot move but can only rotate along the axis. The support bears the load of other components in the whole structure, and plays a certain role in restraining the rotating shaft. The hydraulic cylinder drives the rotation of the rotating shaft through its own expansion and contraction, thus realizing the vertical and horizontal transformation of the cutters on both sides.

The transmission system design of the mechanical arm of jujube trimmer adopts high-speed gear hydraulic motor to drive the triangle belt wheel. Among the classic chain drive and belt drive modes of long-distance transmission, belt drive is simple and safe, so belt drive mode is chosen. The high-speed hydraulic motor is used as the driving element, and the high-speed rotation operation of the auxiliary tip trimming scissors is realized by means of V-belt transmission.

Choose high-speed gear motor, in order to save space and reduce mass, choose O-shaped V-belt. Tractors with 50 HP (36.8 kW) are commonly used, and their hydraulic output is generally 40 L/min. The trimmer needs three hydraulic motors to drive. Considering the efficiency, the actual supply flow of each motor should be 10 L/min, and the motor speed should be 2 000 r/min. The transmission ratio should be i=1.4 if the speed of the auxiliary tip trimming scissors is n=3 000 r/min, and it is calculated that the minimum pulley diameter of the triangular pulley is d_1=100 mm when the quasi-0 = 38, so the pulley assembled by the motor is: d_2= d_1 × i = 100×1.4=140 mm.

According to the hydraulic flow and v, the linear speed of V-belt, should be less than 25 m/s. Considering the interference problem, set the pulley size d_2=140mm between trimming knives, and according to formula (1),

$$v = \pi d_2 n \tag{1}$$

Available:

$$n = \frac{v}{\pi d_2} = \frac{25}{3.14 \times 140} \times 1000 \times 60 = 3412\ r/min \tag{2}$$

Too high speed of trimmer can easily cause vibration, noise and resonance, etc. Finally, the pulley diameter d_2=140mm between trimmers is selected, and the moving speed range of trimmer is 3 000 ~ 4 000 r/min.

The wrist of the mechanical arm determines the attitude of the end effector. According to the characteristics of pruning operation, in order to ensure the closed inverse kinematics solution, the three-degree-of-freedom common intersection RBR wrist structure is selected, which has the advantages of compact and flexible structure. Wrist can be divided into single degree of freedom, two degrees of freedom and three degrees of freedom, among which wrist with three degrees of freedom is called "universal" wrist because of its high flexibility. In this paper, the orthogonal spherical wrist structure of the mechanical arm RBR of jujube trimmer is designed, that is, the wrist can realize two coaxial rotary motions (R) and one pin rotary motion (B). RBR orthogonal spherical wrist structure, with wrist rotation, wrist swing and hand rotation.

The transmission chain is divided into two parts: one part is at the rear end of the forearm, which is transmitted from the distal end of the forearm to the proximal end of the forearm in the way of parallel shaft output, and finally transmitted to the coaxial transmission mandrel and sleeve. The other part of the transmission chain is wrist, which realizes wrist rotation, wrist swing and hand rotation.

X-axis, Y-axis and Z-axis of wrist mechanism meet at one point. When the rotation angle is not limited, it can theoretically achieve any posture, and the position and posture can solve the problem, which is beneficial to inverse kinematics analysis. In the specific pruning process, the control strategy can be simplified by controlling the position and posture in sequence, that is, the wrist is delivered to the vicinity of the fruit through the base, arm and forearm, and then trimmed by adjusting the wrist posture.

Kinematics parameters between joints are determined by the connecting rod between them, and the connecting rod module is another important module to determine the configuration. The connecting rod modules with vertical axis and parallel axis are designed for the connection between joint modules. In addition, for the convenience of configuration, the threaded quick connection structure is adopted between the modules.

Each joint module and connecting rod module have the same mechanical interface and electrical interface, which can be quickly assembled into mechanical arms with different configurations to meet the needs of users, and the ends can be connected with different clamping or operating mechanisms.

Kinematics analysis

Manipulator dynamics studies the relationship between the motion of manipulator and the force and moment that makes it move. The dynamics of manipulator belongs to the category of mechanism dynamics, and the dynamics of manipulator involves two problems. One is the inverse dynamics problem, which is known as the trajectory point of manipulator and the velocity and acceleration at the end to solve the joint force, and the inverse dynamics problem is used to solve the control and structural design problems. The other is the forward dynamics problem, in which the position, velocity, acceleration and other parameters of the operating arm are solved by knowing the shutdown force, which is mainly used for the simulation of the operating arm.

Up to now, this method has become the basic method to study the establishment of robot kinematic coordinate system. By using this method, the mathematical modeling of robot motion analysis can be carried out, and the homogeneous transformation matrix of the whole mechanism can be established by the homogeneous matrix of each mechanism obtained after modeling. The three-dimensional coordinate system of trimmer manipulator established by Cartesian coordinate system is an orthogonal coordinate system, and its three coordinate axes X, Y, Z are established perpendicular to each other. Because the mechanical arm of the trimmer is composed of five joints, it is very important to set the motion parameters if we want to calculate the motion equation of the end position of the trimmer hand which changes with the size and length of each joint and the joint angle. Setting motion parameters in Cartesian coordinate system not only makes the set parameters clear, but also improves the accuracy of data.

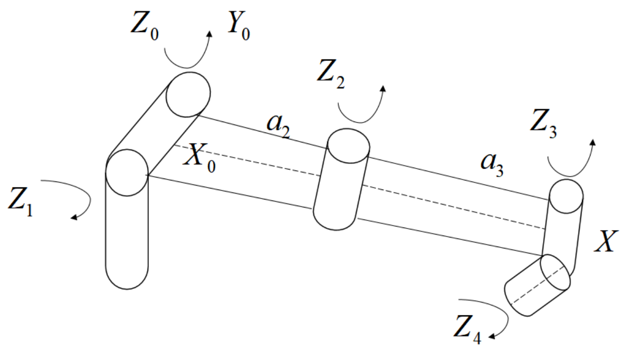

Fig. 3 - Mechanism coordinate system

According to the D-H parameter representation, a coordinate system is established for each mechanism of the trimmer manipulator, and then the transformation process from the current joint to the next joint is determined. As shown in Figure 3, the Z -axis direction is expressed as the joint axis direction of each rotating joint, so the Z -axis set from the base, the joint between base and big arm, the joint between big arm and small arm, the joint between wrist and small arm, and the joint between hand and wrist are Z_0-Z_4 respectively. The direction of X axis is expressed as the extension line direction of the current joint axis along the next joint axis. Y-axis direction can be determined by right-hand rule.

In the process of setting parameters, the variable θ_1-θ_5 is used to express the angle between the common vertical lines of the two connecting rods. d_1-d_5 is used to represent the common vertical distance of two connecting rods.

a_1-a_5 is respectively expressed as the distance of the common perpendicular of the two shafts of the two connecting rods. Because the trimming hand and the upper part of the base are on the same horizontal line in the initial position of the mechanism, the distance a_1 between the base and the axis of the big arm is 0.

Because the axis perpendicular direction of wrist and the axis perpendicular direction of forearm are also on the same line, the distance a_4 between wrist and forearm is 0.

Since the direction of the axis perpendicular of the hand and the direction of the axis perpendicular of the wrist are also on the same line, the distance a_5 between the axis perpendicular of the hand and the wrist is 0.

The known motion parameters include the distance a_2 between the axis of the big arm and the base and the distance a_3 between the small arm and the axis of the big arm. The axial included angle of the two connected rotating joints is expressed by a_1-a_5, and the degrees expressed by a_1-a_5 of the mechanical arm of the trimmer are 90°, -90°, 0°, 90°, 0° respectively according to the initial position.

According to the motion parameters analysed above, the D-H parameters of the mechanical arm of the trimmer are shown in the following Table 1.

Table 1

Parameter table of D-H of trimmer mechanical arm

Variable/joint	1	2	3	4	5
θ_i	θ_1	θ_2	θ_3	θ_4	θ_5
d_i	0	0	0	0	0
a_i	0	a_2	a_3	0	0
a_i	90°	-90°	0°	90°	0°

By setting the D-H parameter table accurately, it can provide a data source for the position kinematics of the mechanical arm of the trimmer, and provide a powerful basis for the establishment of the homogeneous coordinate matrix of each rotating mechanism.

Static analysis and kinematics equation theory analysis

Static equation

On the basis of the previous analysis, in the following analysis, it is necessary to assign the velocity and acceleration to 0, and then get the following formula (1) (called statics equation) after finishing.

$$\begin{bmatrix} \frac{\partial F}{\partial q}\left(\frac{\partial \Phi}{\partial q}\right)^T \\ \frac{\partial \Phi}{\partial q} \end{bmatrix}_j \begin{Bmatrix} \Delta q \\ \mathrm{H}\lambda \end{Bmatrix}_j = \begin{Bmatrix} -F \\ -\Phi \end{Bmatrix}_j \tag{3}$$

where: $\frac{\partial F}{\partial q}$ is the stiffness matrix of the system; $\frac{\partial \Phi}{\partial q}$ - Damping matrix of the system; Δq -Stiffness;

$\mathrm{H}\lambda$ - speed; F - acceleration; Φ - resistance.

Kinematics equation is mainly obtained after simplifying the analysis process. After processing, the main content is to theoretically analyse the displacement, velocity, acceleration and resistance of the constrained parts in the whole system, so solving the constraint equation of the system becomes formula (2).

$$\Phi(q, t_n) = 0 \tag{4}$$

where: q - constrained parts; t_n - displacement.

Newton-Raphson iterative method in the equation can be used to solve the change of the specific position of the main components, such as formula (3).

$$\frac{\partial \Phi}{\partial q}\Big|_j \Delta q_j = -\Phi(q_n, t_n) \tag{5}$$

in which:

$$\Delta q_j = q_{j+1} - q_j \tag{6}$$

where: q_{j+1} is the part of the $j+1$-th constraint; j-the j th iteration.

The calculation of speed and acceleration at t_n time can be realized by first-order or second-order derivation of formula (3), such as formulas (5) and (6).

$$\left(\frac{\partial \Phi}{\partial q}\right)\dot{q} = -\frac{\partial \Phi}{\partial t} \tag{7}$$

$$\left(\frac{\partial \Phi}{\partial q}\right)\ddot{q} = \left\{\frac{\partial^2 \Phi}{\partial t^2} + \sum_{k=1}^{n}\sum_{l=1}^{n}\frac{\partial^{2\Phi}}{\partial q_k \partial q_t}\dot{q}_k q_l + \frac{\partial}{\partial t}\left(\frac{\partial \Phi}{\partial q}\right)\dot{q} + \frac{\partial}{\partial q}\left(\frac{\partial \Phi}{\partial t}\right)\dot{q}\right\} \tag{8}$$

where: $\frac{\partial \Phi}{\partial q}$ - damping matrix of the system; $\frac{\partial \Phi}{\partial t}$ - speed.

The following formula (7) can be obtained by bringing the force at t_n time into Lagrange equation.

$$\left(\frac{\partial \Phi}{\partial q}\right)^T \lambda = \left\{-\frac{d}{dt}\left(\frac{\partial T}{\partial \dot{q}}\right)^T + \left(\frac{\partial T}{\partial q}\right)^T + Q\right\} \tag{9}$$

where: $\frac{\partial T}{\partial q}$ -the quality matrix of the system; λ-coefficient of friction; Q-mechanical arm length.

According to the Jacobian of the manipulator, the kinematic model of the manipulator can be established, and the linear velocity v and angular velocity w of the end-effector can be expressed as linear functions of the joint velocity.

RESULTS

Motion simulation and analysis

Kinematics simulation analysis is mainly to verify the correctness of the kinematics model of trimmer manipulator and the correctness of the algorithms of forward and inverse pose solutions. The results of kinematics analysis lay a foundation for dynamic modeling and analysis. Kinematics simulation, dynamics simulation and optimization simulation are all programmed by MATLAB software. The shape of the trimmer arm is shown in Figure 4, and its working process is shown in Figure 5.

Fig. 4 - Modeling of mechanical arm of trimmer

Fig. 5 - Working process of mechanical arm of trimmer

In order not to drive the big joints as much as possible, the waist joints of the mechanical arm can be locked when trimming a certain area, and the position and posture of the end effector can meet the trimming requirements by relying on other joints. After the operation in this area is completed, the waist joints and the mobile platform are adjusted again, so that the trimming operation can be regarded as plane motion locally, thus simplifying kinematic analysis. However, in order to check the performance of the designed mechanical arm, in the forward kinematics simulation, only the length of the arm is locked equal to that of the arm, so that the basic kinematics performance of the trimmer mechanical arm can be checked.

Establishment of physical model

The steps of modeling and simulation are shown in Figure 6.

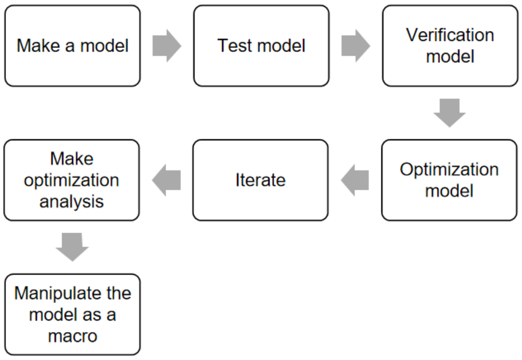

Fig. 6 - Flow chart of modeling and simulation steps

Main contents: (1) select the desired coordinate system; (2) Setting the material properties of parts; (3) Add corresponding constraints to each component. Analyse the constraints of each component in the working process of the designed trimming mechanism, and input and output various data on the pulley, and the cutting tool outputs corresponding data. The constraints of each component are shown in Table 1.

Table 1

Constraint summary table of each component of trimming mechanism

Constrained object	Types of constraints
Pulley-spindle	Fixed pair
Base-spindle	Rotating pair
Base-earth	Fixed pair
Pendulum ring-spindle	Rotating pair
Pendulum fork-pendulum ring	Rotating pair
Pendulum fork-base	Fixed pair
Swing fork-swing arm	Fixed pair
Swing arm-connecting rod	Rotating pair
Connecting rod-moving tool	Fixed pair

Motion simulation and measurement results

The motion simulation of the end position and posture of the trimmer manipulator is carried out by using the simulation in ADAMS to study the motion performance of the end position and posture of the trimmer manipulator. After the simulation is finished, save the simulation results, and enter the post-processing module in ADAMS to analyse the simulation results of the mechanism. The position, velocity and acceleration images of the end pose of the trimmer arm in X, Y, Z axis obtained by simulation are shown in Figure 7 and Figure 8.

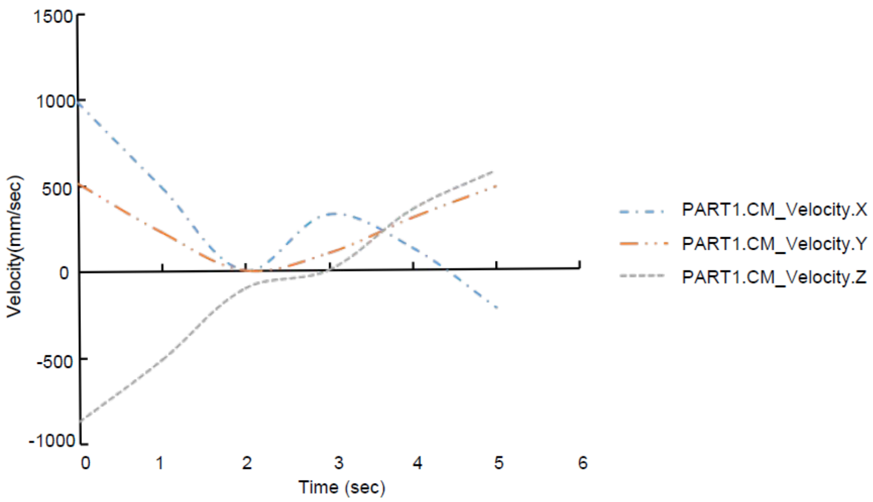

Fig. 7 - Velocity-time graph at the end

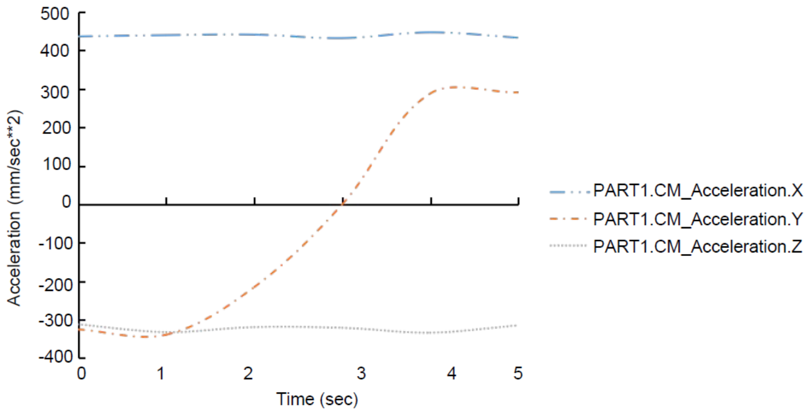

Fig. 8 - End pose acceleration-time graph

From the simulation characteristic curves in Figure 7 and Figure 8, it can be seen that the position and time graph of the end position of the trimmer manipulator is relatively flat in the whole movement process, and there is no drastic transformation stage, which verifies the rationality of the designed motion equation. The velocity-time pattern has obvious positive and negative changes at 3s, which proves that this stage is the cutting stage of pruning hand. The acceleration time graph is gentle in the whole movement, and the curve approaches to a straight line, which proves that the motion of the trimmer arm is stable in the trimming process, which is convenient for the trimmer arm to realize the trimming.

Introduction of the force changes of the cutter and swing arm under the condition that the input speed is 300r/min, the simulated resistance is 1000N, and the relative friction of each rotating pair is not considered (ideal condition). The tool force is shown in Figure 9. The force on the swing arm is shown in Figure 10.

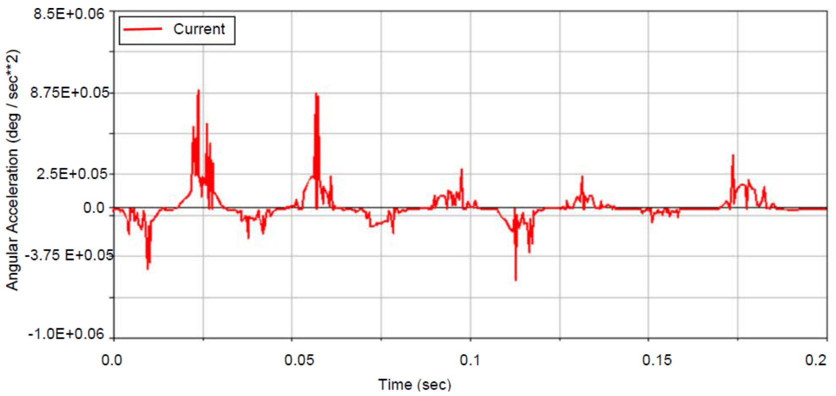

Fig. 9 - Force situation of cutting tools

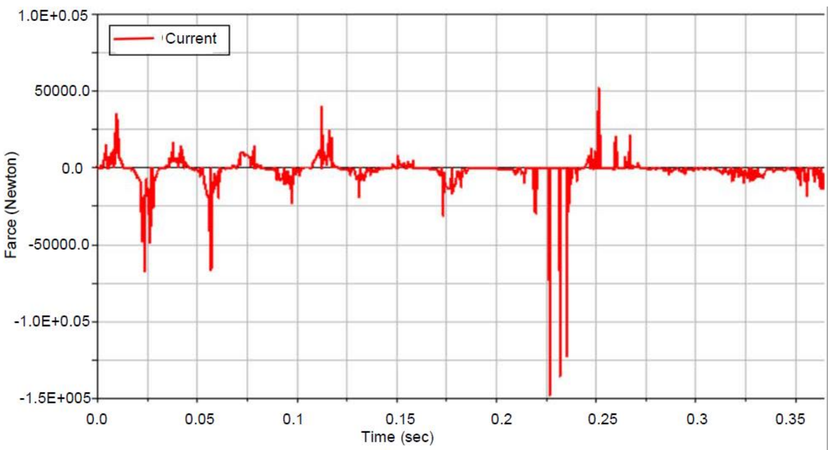

Fig. 10 - Force situation of swing arm

CONCLUSIONS

In this paper, a robot arm of jujube pruning machine is designed. According to the simplified model of the robot arm of jujube pruning machine, D-H parameters are listed, and the linkage coordinate system is established. Then the coordinate transformation matrix and Jacobian matrix of the robot arm are established by D-H method. On this basis, the kinematic model of the robot arm of jujube pruning machine is established. Finally, the ADAMS program is compiled to simulate the forward kinematics of the mechanical arm of jujube trimmer. Through ADAMS motion simulation, it is concluded that under the condition that the input speed is 300r/min, the simulated resistance is 1000N, and the relative friction of each rotating pair is not considered (ideal condition), the force changes of the cutter and swing arm, the movement speed and acceleration curve of the mechanism change smoothly, and the mechanism has good movement performance.

REFERENCES

[1] Bamdad M., Bahri M. M., (2019), Kinematics and manipulability analysis of a highly articulated soft robotic manipulator. *Robotica*, Vol. 37, Issue 5, pp. 868-882. United Kingdom;

[2] Chaitanya D. N. V., Arunkumar S., Akhilesh G. B., (2018), Design of Rice Transplanter. *IOP Conference Series: Materials Science and Engineering. IOP Publishing*, Vol. 377, Issue 1, pp. 012037. United Kingdom;

[3] Chatterjee N., Gupta S., (2019). Efficient Phrase Table pruning for Hindi to English machine translation through syntactic and marker-based filtering and hybrid similarity measurement. *Natural Language Engineering*, Vol. 25, Issue PT.1, pp. 171-210. England;

[4] Freire-Tellado M. J., Muñoz-Vidal M., Pérez-Valcárcel J., (2020), Scissor-Hinged Deployable Structures Supported Perimetrally on Rectangular Bases. *Journal of the International Association for Shell and Spatial Structures*, Vol. 61, Issue 2, pp. 158-172. Spain;

[5] Gonzalez D. J., Asada H. H., (2017), Design and analysis of 6-dof triple scissor extender robots with applications in aircraft assembly. *IEEE Robotics and Automation Letters*, Vol. 2, Issue 3, pp. 1420-1427. United States;

[6] He W., He X., Zou M., (2018), PDE model-based boundary control design for a flexible robotic manipulator with input backlash. *IEEE Transactions on Control Systems Technology*, Vol. 27, Issue 2, pp. 790-797. United States;

[7] Hong J., Kim T., Chae H., (2020), Design of window-cleaning robotic manipulator with compliant adaptation capability. *IEEE/ASME Transactions on Mechatronics*, Vol. 25, Issue 4, pp. 1878-1885. United States;

[8] Kang J. L., Hou W. P., Li C. Y., (2019), Design and characteristic analysis of multifunctional gardening pruning robot arm. *Forest Engineering,* Vol. 35, Issue 04, pp. 86-92. Croatia;

[9] Li X., Quan Z., Liu D., (2020), Design of Control System for 6-DOF Manipulator. *OP Conference Series: Materials Science and Engineering. IOP Publishing*, Vol. 772, Issue 1, pp. 012041. United Kingdom;

[10] Minakov I. A., Nikitin A. V., (2019), Agricultural market development: trends and prospects. *International journal of innovative technology and exploring engineering*, Vol. 9, Issue 1, pp. 3842-3847. India;

[11] Redström J., (2020), Certain uncertainties and the design of design education. *She Ji: The Journal of Design, Economics, and Innovation*, Vol. 6, Issue 1, pp. 83-100. Netherlands;

[12] Roshanianfard A. R., Noguchi N., (2018), Kinematics analysis and simulation of a 5DOF articulated robotic arm applied to heavy products harvesting. *Journal of Agricultural Sciences*, Vol. 24, Issue 1, pp. 90-104. Serbia;

[13] Sharkawy A. N., Koustoumpardis P N, Aspragathos N., (2020), Neural Network Design for Manipulator Collision Detection Based Only on the Joint Position Sensors. *Robotica*, Vol. 38, Issue 10, pp. 1737-1755. England;

[14] Tian H., Wang T., Liu Y., (2020), Computer vision technology in agricultural automation—A review. *Information Processing in Agriculture*, Vol. 7, Issue 1, pp. 1-19. China;

[15] Zhang J., Yang X., Li Y., (2020), Path Planning Simulation of 6-DOF Manipulator. *Journal of Physics: Conference Series*, Vol. 1574, Issue 1, pp. 012156. United Kingdom;

STUDY ON REMOTE SENSING MONITORING MODEL OF AGRICULTURAL DROUGHT BASED ON RANDOM FOREST DEVIATION CORRECTION
/
基于随机森林偏差校正的农业干旱遥感监测模型研究

Shao Li[1)]*, Xia Xu[1)]
[1)] The School of Mathematics and Computer Science, Xinyang Vocational and Technical College, Xinyang, Henan, 464000 / China
E-mail: wenpang9838yunsh8@163.com
DOI: https://doi.org/10.35633/inmateh-64-41

Keywords: *remote sensing data, drought monitoring, random forest*

ABSTRACT
Using remote sensing data to monitor large area drought is one of the important methods of drought monitoring at present. However, the traditional remote sensing drought monitoring methods mainly focus on monitoring single drought response factors such as soil moisture or vegetation status, and the research on comprehensive multi-factor drought monitoring is limited. In order to improve the ability to resist drought events, this paper takes Henan Province of China as an example, takes multi-source remote sensing data as data sources, considers various disaster-causing factors, adopts random forest method to model, and explores the method of regional remote sensing comprehensive drought monitoring using various remote sensing data sources. Compared with neural network, classification regression tree and linear regression, the performance of random forest is more stable and tolerant to noise and outliers. In order to provide a new method for comprehensive assessment of regional drought, a comprehensive drought monitoring model was established based on multi-source remote sensing data, which comprehensively considered the drought factors such as soil water stress, vegetation growth status and meteorological precipitation profit and loss in the process of drought occurrence and development.

摘要
利用遥感数据进行大面积干旱监测是目前干旱监测的重要方法之一。然而，传统的遥感干旱监测方法主要侧重于监测土壤水分或植被状况等单一干旱响应因子，而对多因子干旱综合监测的研究却十分有限。为了提高抗旱能力，本文以河南省为例，以多源遥感数据为数据源，考虑各种致灾因素，采用随机森林法进行建模，探讨了利用各种遥感数据源进行区域遥感综合干旱监测的方法。与神经网络、分类回归树和线性回归相比，随机森林的性能更稳定，对噪声和离群点的容忍度更高。为了为区域干旱综合评价提供一种新的方法，综合考虑土壤水分胁迫等干旱因素，建立了基于多源遥感数据的干旱综合监测模型，干旱发生发展过程中植被生长状况与气象降水盈亏。

INTRODUCTION
Agricultural drought refers to the imbalance of water supply and demand in the process of crop growth due to insufficient water supply, which hinders the normal growth of crops *(Bao Q. L. et al., 2019)*. Agricultural drought is mainly related to soil temperature, effective precipitation and crop water demand. The frequent occurrence of drought has a serious impact on the ecological environment, agricultural production and socio-economic situation. Since ancient times, mankind has suffered from drought disasters. Drought has become the most serious natural disaster affecting agricultural production due to its high frequency, long duration, wide range of impact and great delayed impact. As a common and frequent disaster, drought has always posed a serious threat to agricultural production, food security, ecological environment and economic and social development *(Carolyn Q. et al., 2019)*. The direct cause of agricultural drought is water deficit. When drought develops to a certain extent, vegetation will show the characteristics of increasing canopy temperature and decreasing vegetation index. Meteorological monitoring and remote sensing monitoring are the main drought monitoring methods at present, although the meteorological drought monitoring methods are relatively mature. However, due to the limited number of stations, uneven spatial distribution, and the lack of consideration on the response of surface and vegetation to drought in monitoring mechanism, drought monitoring has limitations *(Elena G. et al., 2021)*.

Conventional soil moisture monitoring methods have few measuring points and poor representativeness, so it is difficult to achieve large-scale, real-time and dynamic drought monitoring. Remote sensing has the advantages of macro, large area, real-time dynamic monitoring, and is widely used in agricultural drought monitoring.

Drought is one of the most serious meteorological disasters in the world, which is characterized by high frequency, large influence range and long duration *(Dietz K. J. et al., 2019)*. Its frequent occurrence has brought huge economic losses to the national economy, especially agricultural production. Drought refers to the situation that during the growth period of crops, the soil water in the farming layer is not supplied by precipitation, groundwater and irrigation water, the soil water supply is constantly consumed, the water absorbed by crops from the soil cannot meet the normal physiological needs, and the growth of crops is restricted by water conditions *(Hassan M. A. et al., 2019).* Remote sensing drought monitoring has the advantages of macroscopical, fast and continuous data in time and space, but it mainly monitors the vegetation growth or soil moisture and other single factors, which cannot fully reflect the drought information. Traditional agricultural drought monitoring methods are not only time-consuming and labour-intensive, but also have certain limitations in terms of spatial representation and sampling period. Remote sensing has the advantages of macroscopic, large-area, and real-time dynamic monitoring, and is currently widely used in agricultural drought monitoring. Random forest is a relatively new machine learning algorithm with fast learning process, fast calculation speed, good stability, high efficiency in processing large data sets, high prediction accuracy, and not easy to produce over-fitting *(Hirayama H. et al., 2019)*. This paper takes multi-source remote sensing data as the data source, considers multiple hazards, uses random forest method to model, and explores the use of multiple remote sensing data sources for regional remote sensing comprehensive drought monitoring methods. The research comprehensively considers the drought-causing factors such as soil water stress, vegetation growth status and meteorological precipitation surplus and loss during the occurrence and development of drought, and establishes a comprehensive drought monitoring model based on multi-source remote sensing data in order to provide a new method for comprehensive regional drought assessment *(Wu M. Y. et al., 2018).*

Drought is a hot scientific issue in global climate change research. As a major meteorological disaster, drought has a great impact on China's economic and social development and agricultural production. Therefore, research on drought monitoring technologies and assessment methods will improve the government's ability to respond to natural disasters. It has important practical significance *(Kumar K. C. A. et al., 2021)*. Constructing an accurate drought monitoring model can not only reflect the occurrence of drought events in a timely manner, but also provide scientific support and guarantee for local governments to formulate disaster reduction and production measures *(Shah D. et al., 2021)*. Abnormal precipitation change, vegetation growth, abnormal evaporation and soil moisture are important indicators reflecting drought degree from different levels, which have been widely used in drought monitoring *(Tirivarombo S. et al., 2018)*. However, drought is a slow process involving many aspects such as precipitation, and the drought evaluation results relying on a single index are different from the actual situation. As a major meteorological disaster affecting China, drought seriously threatens China's economic and social development and food security. Therefore, in order to enhance the ability to resist drought events, it is of practical significance to study drought monitoring technology and evaluation methods. Compared with neural network, classification regression tree and linear regression, the performance of random forest is more stable and tolerant to noise and outliers.

Drought refers to a disaster in which crops suffer from drought during the growth period. Agricultural drought monitoring includes agricultural drought monitoring, early warning and post-disaster assessment *(Javed T. et al., 2021)*. The direct inducement of agricultural drought is water shortage. When drought develops to a certain extent, vegetation will show the characteristics of canopy temperature rising and vegetation index falling *(Chaitanya D. N. V. et al., 2018)*. Literature *(Haekyung P. et al., 2019)* uses RF, Cubist and Bagging methods to build a comprehensive drought index, and the results show that RF algorithm has better fitting ability. Literature shows that RF algorithm is more accurate in drought prediction than enhanced regression tree and Cubist method. The RF algorithm is based on the average results of several decision trees, and its results are relatively accurate and credible, but at the same time it will lead to certain deviations, especially its ability to predict extreme values is weak.

For drought disasters, extreme conditions often bring greater losses, which should be paid more attention to. *(Javed T. et al., 2021)* comprehensively considered the drought factors of soil moisture and meteorological precipitation, weighted the vegetation water supply index and the precipitation anomaly drought index to add linearly, the agricultural drought index is put forward, and the monitoring effect of agricultural drought index is good in practical application, which will avoid greater losses due to extreme conditions.

Based on the above principles, remote sensing drought monitoring generally considers the extraction of drought information from the temporal and spatial characteristics of soil moisture, canopy temperature, vegetation index and other elements. Literature proposed a comprehensive drought monitoring index (DMI) based on the combination of temperature vegetation index (TVDI) and precipitation anomaly index (PPAI). It was applied to drought monitoring in the main winter wheat producing areas in China *(Khalili K. et al., 2019)*.

Other authors combines traditional meteorological drought monitoring indicators, remote sensing monitoring indicators, and other biophysical information to develop a vegetation drought response index VegDRI, which takes into account vegetation growth conditions, precipitation surplus, and ecological environment parameters, including surface cover types and topography *(Lee S. J. et al., 2021)* and other factors *(Sadri S. et al., 2018).*

Remote sensing drought monitoring methods are widely used because of their high temporal and spatial resolution and the ability to obtain regional continuous spatial drought conditions. However, the previous remote sensing drought monitoring methods mostly focused on considering single factors such as soil and vegetation, especially most remote sensing drought monitoring methods, which cannot reflect the precipitation profit and loss information in the drought-causing factors. Literature established a comprehensive drought monitoring model based on the idea of classification regression tree, and put forward a comprehensive drought index SDI, which was applied to drought monitoring in Henan Province, and could quantitatively monitor the spatial-temporal evolution and development characteristics of regional actual drought and historical drought. Literature proposes to combine remote sensing monitoring with traditional meteorological monitoring, and obtain agricultural drought index by using the linear weighting of crop water supply index and precipitation anomaly index *(Yan L. et al., 2021)*

MATERIALS AND METHODS

Research area survey

Henan Province is located in the middle east of China, between 110°22′E-116°37′E, 31°24′N-36°23′N. The terrain gradually decreases from west to east, and plains account for about 53.2% of the province's total area. Henan Province belongs to the transitional climate of northern subtropical humid climate and warm temperate semi-humid monsoon climate. The annual average temperature from south to north is 10.5-16.50ºC, the average annual precipitation is 406.5-1290.5 mm, and the seasonal distribution of precipitation is uneven, 50% of the annual precipitation is concentrated in summer, with an average annual sunshine of 128.6-2290.8 hours and a frost-free period of 200 to 280 days throughout the year, which is suitable for the growth of a variety of crops. The terrain is high in the west and low in the east, with mountains in the north, west and south, plains in the east and basins in the southwest, spanning the Yellow River, Haihe River, Huaihe River and Yangtze River.

The planting structure in Henan Province is relatively simple, mainly including summer harvest crops and autumn harvest crops. Winter wheat is the main summer harvest crop, and autumn harvest crops include corn, cotton and so on. Considering the different responses of different crops to drought under the same conditions such as meteorological conditions and topography. The topography of Henan is high in the west and low in the east, and the northern, western and southern sides are distributed in a semi-circular shape along the provincial boundary by Taihang Mountain, Funiu Mountain, Tongbai Mountain and Dabie Mountain. The central and eastern parts are Huang-Huai-Hai alluvial plain. Nanyang Basin is located in the southwest. Plains and basins, mountains and hills account for 55.7%, 26.6% and 17.7% of the total area respectively. According to topography, Henan is mainly divided into five areas: western mountainous and hilly area, southern border area mountainous and hilly area, loess area, southwest Nanyang Basin, and eastern and northern Henan Plain.

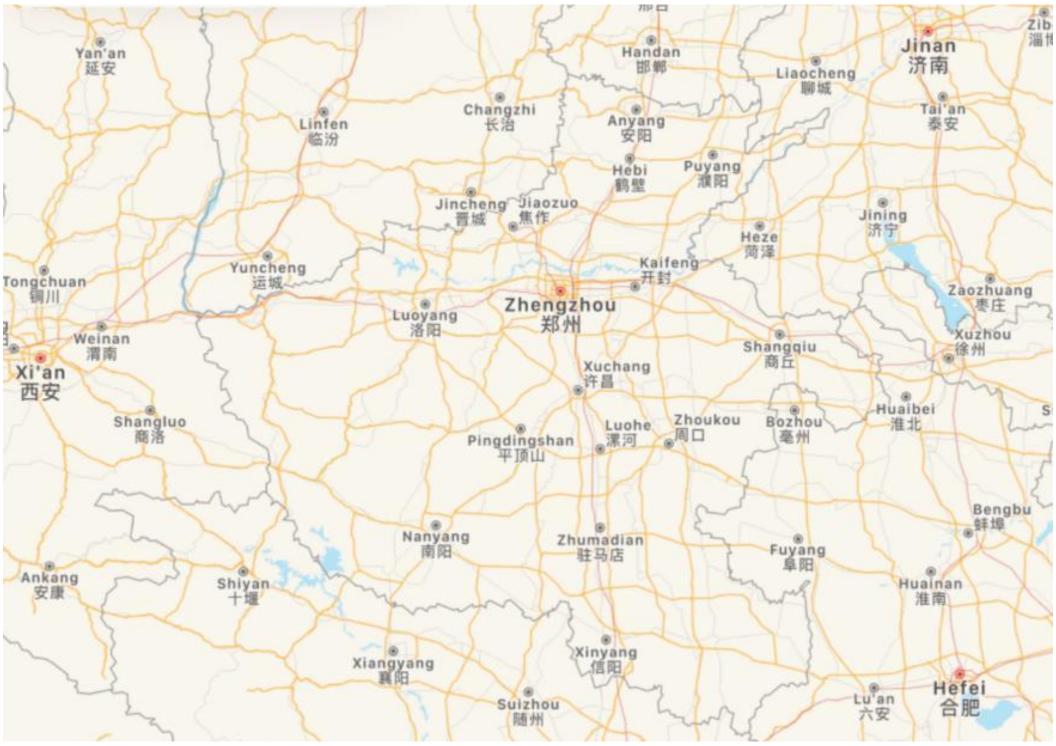

Fig. 1 - Administrative area map of the study area

As a major agricultural province in China, Henan Province is the largest commodity grain base in China, so it is of great significance to prevent drought for food security in Henan Province. The unique geographical location and climatic characteristics of Henan Province have made the meteorological disasters in Henan Province frequent, such as drought, flood, wind, hail, earthquake, thunder, snow, etc., which are characterized by many kinds of natural disasters, high frequency of occurrence, wide influence range and serious harm. The main agrometeorological disasters in Henan Province are drought, waterlogging, hail and freezing. Among them, drought is the most frequent disaster in the province and has a serious impact on agricultural production, and there is a saying of "nine droughts in ten years" in history. Drought basically occurs in every season. Because Henan is located in the temperate monsoon climate zone, there is less precipitation in spring, coupled with the rapid rise of temperature, the increase of gale days and evaporation, spring drought occurs most frequently. In recent years, the drought situation in Henan Province has gradually intensified, which has seriously threatened human daily life and agricultural production. Therefore, it is of great significance to build a suitable drought monitoring index for the development of agriculture and the protection of people's life in Henan Province.

Data sources and processing

At present, Palmer drought index PDSI and standardized precipitation index SPI are widely used and mature in monitoring and analysing regional drought, both of which can be used to characterize the probability of regional drought and flood disasters under different climate and soil characteristics. The water supply of crops mainly comes from soil moisture, and the growing season of crops is the key period of water demand of crops. The essence of drought monitoring is to monitor soil water content. The distribution range and degree of drought can be reflected by the amount and distribution of soil water content. Soil water evaporation is large, soil water loss is serious, and drought will develop rapidly. PDSI is a meteorological drought index based on the balance equation of water supply and demand. Its calculation begins with estimating the difference between actual precipitation and climate suitable precipitation (CAFC-P) to determine the deviation degree between drought and flood in the study area and the average monthly level for many years. Then, the monthly water anomaly is transformed into a water anomaly index by adding and multiplying weight factors. Finally, the severity of drought and flood can be inferred from the monthly water anomaly index and PDSI value of the previous month and the study month. Standardized precipitation index only needs precipitation data, which is simple in calculation and comparable in different time and space scales. It is widely used in meteorological drought monitoring at home and abroad.

Assuming that precipitation at a certain time scale is a random variable x, the probability density function of its Gamma distribution is:

$$g(x)=\frac{1}{\beta^{\alpha}\Gamma(\alpha)}x^{a-1}e^{-x/\beta} \quad (x>0) \tag{1}$$

$$\Gamma(\alpha)=\int_{0}^{\infty}x^{a-1}e^{-x}dx \tag{2}$$

Where: α is the shape parameter of the Γ distribution function; β is the scale parameter, and $\Gamma(\alpha)$ is the gamma function. α and β can be estimated by the maximum likelihood method, see equations (3) and (4).

$$\hat{s}=\frac{1+\sqrt{1+4A/3}}{4A} \tag{3}$$

$$\hat{\beta}=\frac{\bar{x}}{\hat{a}} \tag{4}$$

$$A=\ln(\bar{x})-\frac{\sum \ln x}{n} \tag{5}$$

In the formula: $\bar{x}$ is the average value of precipitation for many years, and n is the length of the sample sequence. Because x>0 in the Gamma function, and precipitation can be 0 in actual conditions, $\bar{x}$ is the average value of non-zero items in the multi-year precipitation series. Assuming that there are n zero items in the precipitation sequence and the total length is m, the cumulative probability of a certain time scale is calculated by equation (6):

$$SPI=S\left(1-\frac{c_2k^2+c_1k+c_0}{d_3k^3+d_2k^2+d_1k+1}\right) \tag{6}$$

Where: $k=\sqrt{\ln\frac{1}{F(x)^2}}$. When $F(x)>0.5$, S=1, when $F(x)\le 0.5$, S=-1.

In this paper, MODIS vegetation index products (MOD13A3), surface temperature products (MOD11A2), land cover type products (MCD12Q1), TRMM 3B43 products and SRTM-DEM data from 2011 to 2021 are taken as the main remote sensing data sources. MOD13A3 is a monthly land vegetation index product, MOD11A2 is a land temperature product synthesized every 8 days, the spatial resolution of MODIS products is 1km, and MCD12Q1 is an annual land cover type product with a spatial resolution of 500m. This paper adopts the meteorological data of 20 main meteorological stations and 10 agrometeorological stations in Henan Province from 2001 to 2021, such as monthly average temperature, precipitation data, and relative soil humidity. The data has passed quality control. In addition, in order to calculate the effective soil water content (AWC), the Chinese soil particle size distribution data set released by Beijing Normal University was adopted with a spatial resolution of 1km. The TRMM3B43 data is converted from hourly precipitation to monthly precipitation, and projected with MODIS data and SRTM-DEM data into WGS84/Geographic system, resampled to 0.0059°×0.0059°. For mod13a3 and mod11a2 data, the normalized vegetation index (NDVI) and land surface temperature (LST) were extracted, and the invalid values in the images were removed by using the quality control file, and the data of other years in the same month were used for filling.

Construction of comprehensive drought model

Agricultural drought is due to the abnormal shortage of precipitation for a long time, and the soil moisture cannot meet the water demand for crop growth, which leads to the stress of crop growth. It can be seen that the agricultural drought is essentially caused by the imbalance between the environmental water supply and the normal growth of vegetation. In order to extract the vegetation index with reliable quality, the study uses the quality information file of the data set, writes an algorithm to control the quality of MOD13A3 data after projection transformation and cutting in the study area, eliminates low-quality pixels, and fills with the average values of vegetation index of the same month in other years. On the one hand, the environmental water supply comes from atmospheric precipitation, on the other hand, it comes from the water content of soil itself. Therefore, when insufficient atmospheric precipitation causes meteorological drought, if the soil water can meet the water demand of crops, it will not cause agricultural drought. The random forest method randomly selects n sample sets in the original data set by bootstrap self-help method. The data of 2 / 3 sample capacity are taken as the data in the bag each time, n decision trees are built to construct the random forest, and the average value of regression results of N decision trees is used to predict.

Drought is a natural disaster caused by precipitation. Traditional agricultural drought is only a single vegetation information obtained from remote sensing to obtain and monitor drought. Because of the lag of vegetation response to drought, this leads to a certain lag in the traditional agricultural drought monitoring. Although the 8-D surface temperature data can eliminate some invalid values in the process of synthesizing monthly surface temperature data, there are still some invalid value areas in the synthetic data. Therefore, the average algorithm is used to repair the invalid value of monthly surface temperature data. The integrated drought monitoring process is shown in Figure 2.

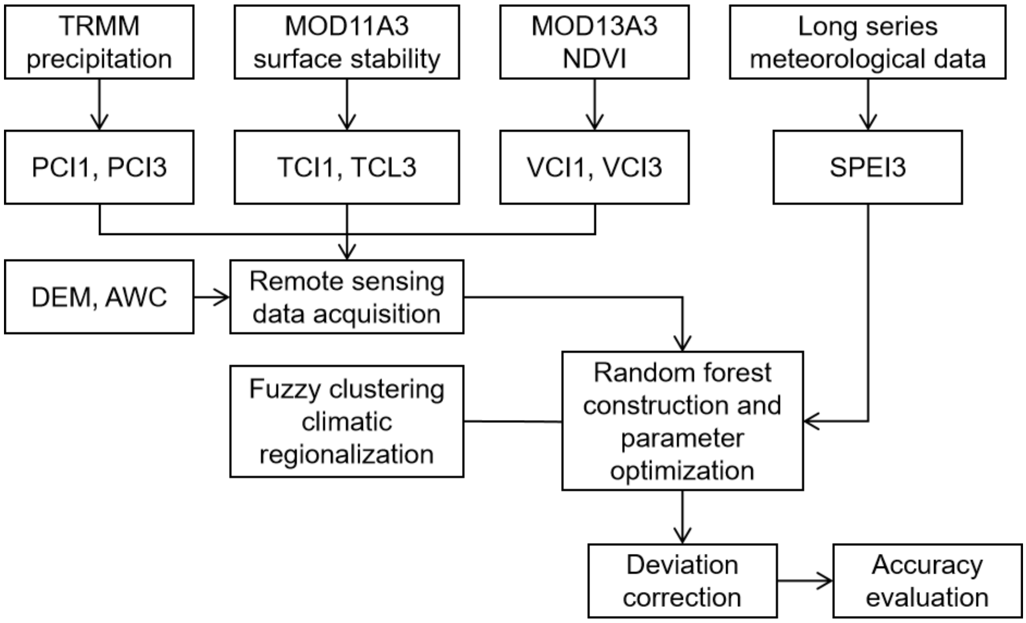

Fig. 2 - Integrated drought monitoring process

The linear relationship between the predicted value of the data in the bag and the actual value is established, and the linear relationship is used to correct the predicted value of the sample data outside the bag to achieve the effect of deviation correction. The calculation formula is:

$$y_{obs} = a + b\hat{y}_{pre} \tag{7}$$

In the formula: y_{obs} is the actual value, y_{pre} is the predicted value, and a and b are coefficients.

Dry early is a complex and changeable process, and many droughts may occur within one month. Although short-term dry early disasters cannot be monitored by the dry early index based on the monthly scale, short-term drought will directly lead to the reduction of grain production during the flowering and growth period of crops. The MOD11A2 surface temperature data also uses the quality control algorithm to eliminate some filling values and low-quality pixels in the synthesis process and fill them with invalid values. Since MODIS does not have monthly synthetic LST products with 1km resolution, this study synthesized monthly LST products with 8D LST products. In order to build the agricultural drought monitoring model with multiple drought factors, the standardized precipitation evapotranspiration index (spei), vegetation state index (VCI), temperature state index (TCI) and Temperature Vegetation Drought Index (TVDI) from 2011 to 2021 were input into the model as eigenvalues based on decision tree classification.

RESULTS

In the process of modeling, firstly, vegetation state index VCI, temperature state index TCI and temperature vegetation drought index TVDI are extracted in ENVI software according to each index calculation formula. Then, according to the longitude and latitude information of the ground meteorological stations in Henan Province, the values of the coordinate positions of the above-mentioned spatial data in each meteorological station are extracted.

The agricultural drought process is determined by a variety of disaster-causing factors, which are not only related to atmospheric precipitation, vegetation growth status and soil water stress, but also related to evaporation, soil effective water holding capacity and other factors. A single index has insufficient reflection on drought, and the coupling relationship between hazards is complicated. Due to the limitation of data and the complexity of drought causes, it cannot fully reflect the relationship between agricultural drought and meteorological drought, soil drought, and evaporation. To make up for the deficiencies of the data itself and improve the drought monitoring mechanism, drought monitoring research tends to be a comprehensive method of multi-source information. Figure 3 shows the remote sensing detection of agricultural drought in Henan Province.

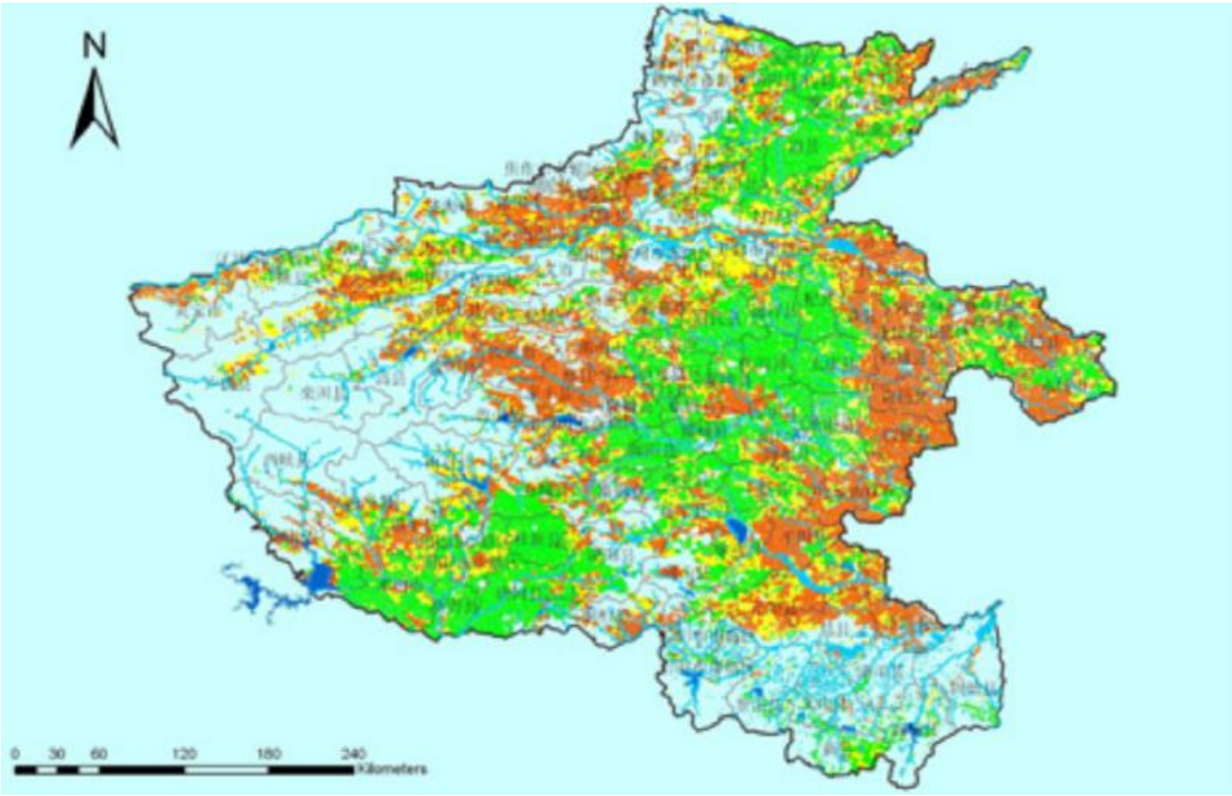

Fig. 3 - Remote sensing detection of agricultural drought in Henan Province

In this study, the data from the training set and the test set are input into the model respectively, and the predicted values of the model are obtained. The mean relative error absolute value (MRE), root mean square error (RMSE) and correlation coefficient R between the predicted values of the model and the actual comprehensive meteorological drought index (CI) are calculated.

- As shown in Table 1 and Table 2, the correlation coefficient of training sets in each season is above 0.975. The correlation coefficient of the test set is slightly lower than that of the training set, but it also reaches more than 0.75, and both have a significant correlation. However, the root mean square error (RMSE) of training set and test set is small, and the simulation accuracy of the model is high. The mean absolute relative error (MRE) of the test set does not exceed that of the training set, which shows that the model has good generalization performance and strong applicability to new data.

Table 1

Accuracy analysis of training set model

	Absolute value of average relative error %	Root-mean-square error	Correlation coefficient
Spring	0.581	0.345	0.975**
Summer	0.501	0.328	0.980**
Autumn	0.478	0.310	0.990**
Winter	0.521	0.325	0.975**

Table 2
(continuation)

Accuracy analysis of test set model

	Absolute value of average relative error %	Root-mean-square error	Correlation coefficient
Spring	1.436	0.751	0.765**
Summer	1.613	0.748	0.753**
Autumn	1.248	0.698	0.886**
Winter	1.376	0.732	0.769**

In order to verify the applicability of the drought classification of the model, the classification results of the training set and the test set were compared with the actual drought. The calculation method is as follows:

$$\text{Overall coincidenc e rate} = \frac{\text{Number of sites with the same rank}}{\text{Research Year} \times \text{Number of Sites}} \tag{8}$$

$$\text{Empty evaluation rate} = \frac{\text{The number of stations with drought monitoring results but no actual drought}}{\text{The actual number of stations with drought above light drought}} \tag{9}$$

$$\text{Leakage evaluation rate} = \frac{\text{The monitoring result is the number of stations without drought but with actual drought}}{\text{The actual number of stations with drought above light drought}} \tag{10}$$

The status of crops under drought stress can be measured by the change of the vegetation index at this time relative to the vegetation index under normal conditions. Such remote sensing monitoring indexes include Anomaly Vegetation Index (AVI) and Conditional Vegetation Index (VCI). The algorithm is as follows:

$$AVI = NDVI - \overline{NDVI} \tag{11}$$

$$VCI = \frac{NDVI - NDVI_{\min}}{NDVI_{\max} - NDVI_{\min}} \tag{12}$$

Agricultural drought is defined as crop water shortage caused by the failure of soil water supply to meet crop water demand. It usually first shows the lack of soil moisture caused by the decrease of precipitation. At the same time, with the continuous loss of water from crop transpiration, the water in the crop cannot meet the normal physiological activities, which is manifested by inhibiting crop growth, resulting in crop yield reduction or crop failure, and the effects of drought on different growth periods of crops are significantly different. The correlation between the drought affected area calculated by the integrated remote sensing drought monitoring model and the disaster affected area in the statistical yearbook is higher than that of the disaster affected area, which indicates that the drought monitoring situation of the integrated remote sensing drought monitoring model can well monitor the area caused by drought in the Huaihe River Basin [21]. The correlation between the comprehensive remote sensing drought monitoring model and the agricultural drought disaster area is higher than that of the disaster area, which also shows that the comprehensive remote sensing drought monitoring model can better monitor the drought disaster area and accurately evaluate the drought situation of Huaihe River Basin.

CONCLUSIONS

The correlation between drought-affected areas and disaster-affected areas calculated by the remote sensing integrated drought monitoring model in Statistical Yearbook is higher than that in disaster areas, which indicates that the drought monitoring situation of the remote sensing integrated drought monitoring model can monitor the arid areas of Huaihe River Basin well. The correlation between the integrated remote sensing drought monitoring model and agricultural drought-stricken areas is higher than that in the disaster areas, which also shows that the integrated remote sensing drought monitoring model can better monitor the drought-stricken areas and accurately evaluate the drought situation in Huaihe River Basin. Remote sensing and geographic information system (GIS), as effective means to obtain information on a large scale and effective tools to manage spatial data, have been widely used in drought monitoring and forecasting research.

Agricultural drought involves precipitation, vegetation, temperature and environmental factors, and its drought process is very complex. Monitoring with multi-source remote sensing data can effectively explain the complexity of agricultural drought. In this paper, a remote sensing drought monitoring model based on random forest algorithm is established by using MODIS, TRMM and other multi-source remote sensing data, and the model is verified. The drought index improved in this paper can only detect and monitor the drought accurately and timely, but cannot predict the drought. Therefore, drought forecasting is an urgent problem to be solved in future work. The agricultural drought process is determined by various disaster factors, which are not only related to atmospheric precipitation, vegetation growth and soil water stress, but also related to evaporation, soil effective water retention capacity and other factors.

The reflection of drought by a single index is insufficient, and the coupling relationship between disasters is complicated. Because of the limitation of data and the complexity of drought causes, it cannot fully reflect the relationship between agricultural drought and meteorological drought, soil drought and evaporation. From the perspective of energy balance, the occurrence and development of agricultural drought are discussed by making full use of the underlying surface information obtained by remote sensing, combined with atmospheric model and hydrological model, and the occurrence and development of agricultural drought are monitored and predicted to achieve the goal of disaster reduction and prevention. This is the development direction and goal of agricultural drought monitoring by remote sensing in the future.

REFERENCES

[1] Bao Q. L., Ding J. L., Wang J. Z., (2019), Hyperspectral detection of soil organic matter content based on random forest algorithm. *Arid Zone Geography*, Vol. 188, Issue 06, pp. 178-188. United States;

[2] Carolyn Q., Hao X. J., John J. Q., (2019), "Monitoring extreme agricultural drought over the Horn of Africa (HOA) using remote sensing measurements." *Remote Sensing*, Vol. 11, Issue. 8, pp. 902. Switzerland;

[3] Chan Y. S., Seo Y., (2019), Remote Sensing-based Agricultural Drought Monitoring using Hydrometeorological Variables. *KSCE Journal of Civil Engineering*, Vol. 23, Issue 12, pp. 5244-5256. Germany;

[4] Dietz K. J., Laxa M., Liebthal M., Telman W., Chibani K., (2019). The role of the plant antioxidant system in drought tolerance. *Antioxidants*, Vol. 8, Issue 4, pp. 94. Switzerland;

[5] Elena G., Ekaterina S., Philipp G., (2021), Leaf Rust Resistance Genes in Wheat Cultivars Registered in Russia and Their Influence on Adaptation Processes in Pathogen Populations. *Agriculture*. Vol. 11, Issue 4, pp. 319. Switzerland;

[6] Haekyung P, Kim K. (2019), "Prediction of severe drought area based on random forest: using satellite image and topography data." *Water*, Vol. 11, Issue 4, pp. 705. Switzerland;

[7] Hirayama H., Sharma R. C., Tomita M., (2019), Evaluating multiple classifier system for the reduction of salt-and-pepper noise in the classification of very-high-resolution satellite images. *International journal of remote sensing,* Vol. 40, Issue 7-8, pp. 2542-2557. England;

[8] Hassan M. A., Yang M., Rasheed A., (2019), A rapid monitoring of NDVI across the wheat growth cycle for grain yield prediction using a multi-spectral UAV platform. *Plant science*, Issue 282, pp. 95-103. Netherlands.

[9] Javed T., Zhang J., Bhattarai N., (2021), Drought characterization across agricultural regions of China using standardized precipitation and vegetation water supply indices. *Journal of Cleaner Production*, Issue 12, pp. 78-106. United States;

[10] Javed T., Li Y., Rashid S., (2021), Performance and relationship of four different agricultural drought indices for drought monitoring in China's mainland using remote sensing data. *Science of The Total Environment,* Vol. 759, Issue 143530. Netherlands;

[11] Kumar K. C. A., Reddy G. P. O., Masilamani P., (2021), Integrated drought monitoring index: A tool to monitor agricultural drought by using time-series datasets of space-based earth observation satellites. *Advances in Space Research*,vol. 67, Issue 1, pp. 298-315. England;

[12] Khalili K., Abbasi A., Behmanesh J., (2019), Drought monitoring and prediction using SPEI index and gene expression programming model in the west of Urmia Lake. *Theoretical and Applied Climatology*, Vol. 138, Issue 1, pp. 553-567. Germany;

[13] Lee S. J., Kim N., Lee Y., (2021), Development of Integrated Crop Drought Index by Combining Rainfall, Land Surface Temperature, Evapotranspiration, Soil Moisture, and Vegetation Index for Agricultural Drought Monitoring. *Remote Sensing*, Vol. 13, Issue 9, pp. 1778. Switzerland;

[14] Shah D, Mishra V., (2021), Integrated Drought Index (IDI) for drought monitoring and assessment in India. *Water Resources Research,* Vol. 56, Issue 2, pp. e2019WR026284. United States;

[15] Sadri S., Wood E. F., Pan M., (2018), Developing a drought-monitoring index for the contiguous US using SMAP. *Hydrology and Earth System Sciences*, Vol. 22, Issue 12, pp. 6611-6626. Germany;

[16] Tirivarombo S., Osupile D., Eliasson P., (2018), Drought monitoring and analysis: standardised precipitation evapotranspiration index (SPEI) and standardised precipitation index (SPI). *Physics and Chemistry of the Earth, Parts A/B/C*, Issue 106, pp. 1-10. England;

[17] Wu M. Y., Lin Y. H., Ke C. K., (2018), WSN-based Automatic Monitoring Management Platform for Plant Factory. *International Journal of Digital Content Technology & Its Applications,* Vol. 8, Issue 6, pp. 303-311. South Korea;

[18] Yan L., Xiao D. S., Jin W., Qiang D., Chao Y. W., Chun B. D., Tian L., (2021). Effects of nitrogen application rate on protein components and yield of low-gluten rice. *Agriculture,* Vol.11, Issue 4, pp.302. Switzerland.

DESIGN AND EXPERIMENTAL STUDY OF EQUAL-AREA VARIABLE-PITCH SCREW STRUCTURE FOR WHEAT FLOUR

/

小麦粉变距螺旋结构优化设计与试验研究

Xuemeng Xu, Changpu Shen, Feixiang Li, Long Wang, Yongxiang Li* [1]

School of Mechanical and Electrical Engineering, Henan University of Technology, Zhengzhou 450001, China

E-mail: qdx0406@126.com

Corresponding author: Yongxiang Li

DOI: https://doi.org/10.35633/inmateh-64-42

***Keywords:** Screw feeding, variable-pitch design, discrete element method, experimental design*

ABSTRACT

The parameters of a wheat flour equal-pitch screw feeder are mainly based on empirical design. A method comparing the effect of the number of blocked zones on the feeding sections is proposed to complete the screw parameter of four feeding sections. According to the designed screw structure, Solid Works was used to build the three-dimensional model, and EDEM software was imported for discrete element analysis. It is found that the optimal solution is the screw design with two blocked zones, in which the cutting stock of the feeding sections is very uniform with high feeding accuracy on the premise of satisfying the screw feeding. In order to verify the rationality of the design of the screw structure, the screw was processed based on the optimal parameters, and the screw feeding device of the transparent outer cylinder was built with acrylic plate, and then the feeding stability of wheat flour was observed. The flow fluctuation of the designed screw is relatively small, and the feeding is more uniform, so the accuracy of the screw feed is higher. The experiment verifies the rationality of the variable pitch design and provides a reference for the design and development of wheat flour screw feeding device.

摘要

为提高小麦粉螺旋定量给料精度，针对等径变距螺旋主要以经验设计为主、缺乏系统设计方法的问题，提出基于进料段不同死区个数对称性分析设计的方法,并完成四种进料段螺旋结构参数设计。根据所设计的螺旋结构，利用 Soliworks 软件建立三维模型，导入 EDEM 软件进行离散元分析，存在两个死区的设计方案为最优的螺旋结构设计，此螺杆进料段下料均匀，在满足螺旋给料流量的前提下，给料精度高。为验证变距螺旋结构设计方法的合理性，根据最优参数加工螺杆，利用亚克力板搭建透明料筒的螺旋给料试验装置，分析小麦粉进料段下料稳定性。由检测结果可知，本文设计螺杆的流量波动相对较小，下料较为均匀，螺旋给料的精度较高，验证了变距螺旋结构设计的合理性，为小麦粉螺旋给料装置的设计研发提供参考。

INTRODUCTION

Screw feeders are widely used in the short-distance and high-precision feeding of bulk materials in food, chemical, agricultural and mineral processing industries. The main structure of the screw feeder includes three parts: bin, trough and screw. When the screw rotates, the material is drawn out from the hopper, and transported along the chute, and finally flows out from the discharge port. The screw feeder not only has good feeding accuracy control, but also can avoid environmental pollution caused by the material conveying process. However, when the powder is delivered through the screw feeder, it will fall in the hopper unevenly due to poor fluidity of powder, which results in mass flow fluctuation of screw feeding, uneven screw force and other problems. Most researchers use theoretical and experimental methods to study the flow law of materials in the screw feeder and the pressure drop of materials in the hopper. However, there are few researches on the design of screw feeder aimed at the stability of blanking in the hopper in the literature.

[1] *Xuemeng Xu, Associate Prof. Eng.; Changpu Shen, Ph.D. Stud. Eng.; Feixiang Li, M.S. Stud. Eng.; Long Wang, M.S. Stud. Eng.; Yongxiang Li, Prof. Eng.*

Bates used different screws and materials to conduct matching experiments to study the flow laws (*Bates, 1969*). *Haaker et al*. also discussed theories for volumetric efficiency of screw feeders (*Haaker et al., 1993*). The theories were proposed based on deformation of bulk solid and on plug flow of bulk material. Experiments were conducted on a test rig and results were compared with prediction from the theories. Based on the theoretical model, *Yu* proposed a uniform flow pattern based on the characteristics of the screw pitch (*Yu, 1996*). *Roberts* use the pressure drop of the hopper material to predict the flow pattern generated in the hopper under a given screw (*Roberts et al., 1993a*). *Roberts and Manjunath* used these methods to analyze the volume reduction characteristics of the screw feeder in the hopper (*Roberts et al., 1993b*). Scholars have done a lot of research on the feeding uniformity of the hopper segment, but systematic research of its optimization is lacking (*Bates, 1969; Fernandez, 2011; Peng, 2017; Qiu et al., 2008; Zhang, 2006; Zhao and Yu, 2018*).

In order to improve the feeding stability of the screw feeder and the falling stability of the material in the hopper, a design method based on the symmetry analysis of the number of different dead zones in the hopper section is proposed, and four kinds of equal-diameter variable-pitch screw structures are designed. The 3D models are established by Solid Works software, and then introduced into EDEM software for discrete element analysis. It is found that the optimal design of the screw structure is the design of two dead zones, the feeding of the hopper section of the screw is uniform, and the feeding accuracy is high on the premise of satisfying the feeding flow of the screw. In order to further verify the rationality of the screw structure design and the reliability of the simulation, a wheat flour screw feeding experiment platform was built to carry out the experiment. The results show that the design of the variable pitch screw is reasonable, which provides a reference for the development and design of the wheat flour screw feeding device.

MATERIALS AND METHODS

Theoretical method

Each pitch of the equal-pitch screw feeder has the same conveyor capacity. In the hopper section, the front powder is pushed by the screw to fill the back space, so the back part cannot receive the powder in the hopper, resulting in the phenomenon of compaction (dead zone) (*Song, 1996; Su and Zhao, 1989; Yu, 1982; Gong, 1984*) of the powder in the hopper, thus affecting the precision of the screw feeding, as shown in Fig. 1.

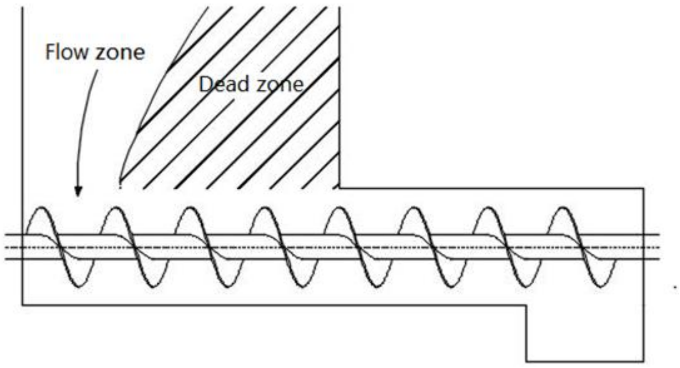

Fig. 1 - Equal pitch screw conveying

The length and structure of the screw in the hopper section are two main factors affecting the uniformity of feeding. This paper analyzes the structure of the screw in the hopper section with the uniform distribution of the dead zone and the flowing zone. As shown in Fig. 2, assume that the screw of the hopper section has a total of n pitch, denoted as S_1, S_2, S_3 and S_n. The number of turns corresponding to each pitch is k_1, k_2, k_3 and k_n. The dead zone is represented by A_1, A_2, A_3 and A_n. The first pitch for each pitch will always be the flowing area, while the last pitch will always be pushed forward to make a dead area above it.

So, we can know that:

$$A_1 = k_1 S_1,\ \ A_2 = k_2 S_2,\ \ A_3 = k_3 S_3 \cdots A_n = k_n S_n \tag{1}$$

S_1, S_2, S_3 ...... S_n are the pitch values of the screw feeding section, [mm];

k_1, k_2, k_3 ...... k_n are the number of turns corresponding to each pitch value;

A_1, A_2, A_3 ...... A_n are lengths of dead sections, [mm].

In order to ensure uniform feeding, the flowing zone and dead zone are symmetrically discussed, that is to guarantee:

$$A_1 = A_n\,,\ \ A_2 = A_{n-1}\,,\ \ A_3 = A_{n-2}\cdots\cdots \tag{2}$$

For the feeding area, in order to ensure the uniform transition of the pitch, the arithmetic series principle is adopted between the pitch, so it can be known that:

$$S_2\text{-}S_1 = S_3\text{-}S_2 = S_4\text{-}S_3 = \cdots = S_n\text{-}S_{n-1} \tag{3}$$

The symmetry of the feeding area should be taken into account, so it can be known that $S_1 = S_n\text{-}S_{n-1}$. From this, the relationship between each pitch and the first pitch can be obtained:

$$S_2 = 2S_1\,,\ \ S_3 = S_1 + S_2 = 3S_1\,,\ \ S_4 = S_1 + S_3 = 4S_1 \cdots S_n = S_1 + S_{n\text{-}1} = nS_1 \tag{4}$$

If the total length of the feed section is L, the relationship between each pitch and the total length can be known as:

$$k_1S_1 + k_2S_2 + k_3S_3 + \ldots k_nS_n = L \tag{5}$$

L is the total length of the feed section, [mm].

According to the above assumptions and conclusions, the different situations of the number of dead zones A are discussed and analyzed in the following, so as to design and analyze the variable pitch structure of the feed section.

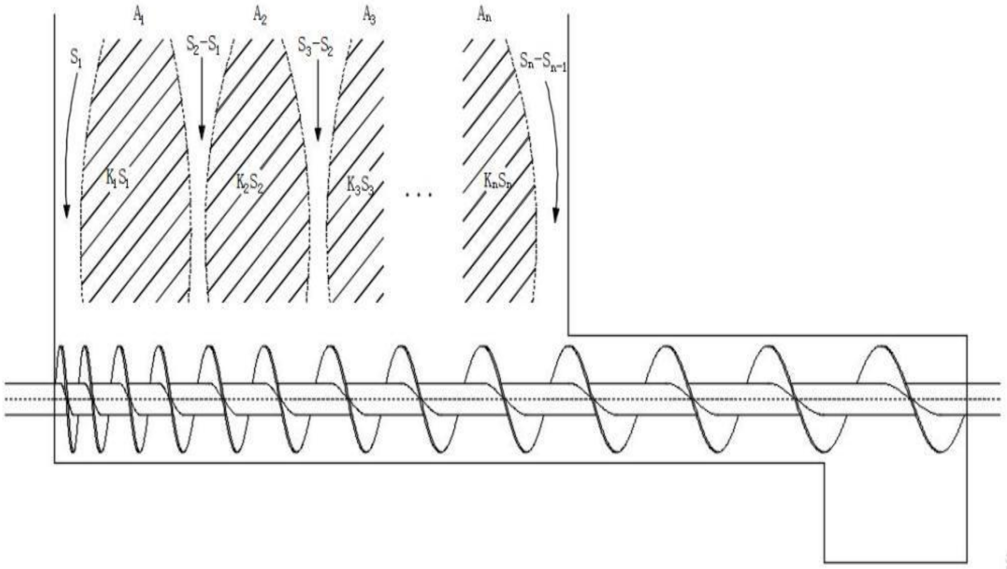

Fig. 2 - Equal diameter variable pitch screw

Single dead zone

When the dead zone $A=1$, two pitch are adopted for the design of the feeding section. In order to ensure uniform feeding, then:

$$k_1S_1 + S_2 = L$$

If $k_1 = 1$, then $L = 3S_1 \Rightarrow S_1 = \frac{L}{3}; S_2 = \frac{2L}{3}$.

If $k_1 = 2$, then $L = 4S_1 \Rightarrow S_1 = \frac{L}{4}; S_2 = \frac{1L}{2}$.

If $k_1 = 3$, then $L = 5S_1 \Rightarrow S_1 = \frac{L}{5}; S_2 = \frac{2L}{5}$.

$$\text{If } k_1 = n\text{, then } L = (n+1)S_1 \Rightarrow S_1 = \frac{L}{(n+1)}; S_2 = \frac{2L}{(n+1)} \tag{6}$$

The dead zone should be minimized to ensure uniform feeding. Therefore, $K_1 \leq 3$ is better for a dead zone.

Double dead zones

When the dead zone *A=2*, three pitches are adopted for the design of the feeding section. In order to ensure uniform feeding, then:

$$A_1 = A_2 \Rightarrow k_1S_1 = k_2S_2 \Rightarrow k_1 = 2k_2 \tag{7}$$
$$k_1S_1 + k_2S_2 + S_3 = L$$

If $k_2 = 1$, $k_1 = 2$; then $L = 2k_1S_1 + S_3 \Rightarrow S_1 = \frac{L}{7}; S_2 = \frac{2L}{7}; S_3 = \frac{3L}{7}$.

If $k_2 = 2$, $k_1 = 4$; then $L = 2k_1S_1 + S_3 \Rightarrow S_1 = \frac{L}{11}; S_2 = \frac{2L}{11}; S_3 = \frac{3L}{11}$.

If $k_2 = 3$, $k_1 = 6$; then $L = 2k_1S_1 + S_3 \Rightarrow S_1 = \frac{L}{15}; S_2 = \frac{2L}{15}; S_3 = \frac{3L}{15}$.

The dead zone should be minimized to ensure uniform feeding. Therefore, it is better to take $K_1 \le 4$ for the two dead zones.

Three dead zones

When the dead zone *A=3*, four pitches are adopted for the design of the feeding section. In order to ensure uniform feeding, then:

$$A_1 = A_2 \Rightarrow k_1S_1 = k_3S_3 \Rightarrow k_1 = 3k_3 \tag{8}$$
$$k_1S_1 + k_2S_2 + k_3S_3 + S_4 = L$$

In order to ensure uniform feeding, the powder of the second dead zone should be as much as possible less than the first and third dead zones. Then:

$$k_1S_1 \ge k_2S_2 \Rightarrow k_1 \ge 2k_2 \tag{9}$$

If $k_3 = 1$, $k_1 = 3$; then $L = 2k_1S_1 + k_2S_2 + S_4$.

The dead zone should be minimized to ensure uniform feeding, then $K_3 \ge 2$ and $K_1 \ge 6$ are not considered for the three dead zones.

From $K_1S_1 \ge K_2S_2 \Rightarrow K_1S_1 \ge 2K_2$, then $K_1S_1 \ge K_2S_2 \Rightarrow 3 \ge 2K_2 \Rightarrow K_2 \le 1.5 \Rightarrow K_2 = 1$. So:

$$L = 2k_1S_1 + k_2S_2 + S_4 \Rightarrow S_1 = \frac{L}{12}; S_2 = \frac{L}{6}; S_3 = \frac{L}{4}; S_4 = \frac{L}{3} \tag{10}$$

Four dead zones

When the dead zone *A=4*, five pitches are adopted for the design of the feeding section. In order to ensure uniform feeding, then:

$$A_1 = A_4 \Rightarrow k_1S_1 = k_4S_4 \Rightarrow k_1 = 4k_4,\ A_2 = A_3 \Rightarrow k_2S_2 = k_3S_3 \Rightarrow 2k_2 = 3k_3$$
$$k_1S_1 + k_2S_2 + k_3S_3 + k_4S_4 + S_5 = L \tag{11}$$

If $K_4=1$, $K_1=4$; then $L=2K_1S_1+2K_2S_2+S_5$. The dead zone should be minimized to ensure uniform feeding, then $K_4 \ge 2$ and $K_2 \ge 6$ are not considered for the four dead zones.

From $K_2S_2=K_3S_3 \Rightarrow 2K_2=K_3$, then $K_3 \ge 4$ and $K_2 \ge 6$ are not considered, so:

$$L = 2k_1S_1 + 2k_2S_2 + S_5 \Rightarrow S_1 = \frac{L}{25}; S_2 = \frac{2L}{25}; S_3 = \frac{3L}{25}; S_4 = \frac{4L}{25}; S_5 = \frac{L}{5} \tag{12}$$

When the dead zone *A=5*, the feeding section is designed with 6 pitches. In order to ensure uniform feeding, then $A_1=A_5 \Rightarrow K_1S_1=K_5S_5 \Rightarrow K_1=5K_5$. The pitch of the first turn S_1 should be at least five, but the dead zone is large, so the situation of the dead zone $A \ge 5$ is not considered.

Simulation experiment of screw feeding of wheat flour

The discrete element method can be used to conduct a comprehensive systematic study of the interaction between the powder and screw mechanism and the movement state of powder flow, but also can provide real-time monitoring of flow rate of screw feeder, material particle velocity distribution and stress distribution, which is convenient to make real-time contribution in accordance with the status of screw feeder. On this basis, screw parameters can be optimized to improve the speed and precision of wheat flour packaging, increase research and development efficiency and reduce the cost. In this paper, the feeding process of the screw feeder is simulated by using the EDEM software of the Altair (Shanghai) company.

Simulation model and parameters

Combined with related references, a three-dimensional model of screw conveyor is established by SolidWorks software of Dassault Systemes Company in France (*Rozbroj et al., 2015; Pezo et al., 2018; Orefice and Khinast, 2017*). The hopper height is 350 mm from the center line of the barrel; the caliber on the hopper is 300 mm long and 200 mm wide; the angle between the edge line of the lower mouth of the hopper and the end line of the barrel is 30 degrees, as shown in Fig. 3.

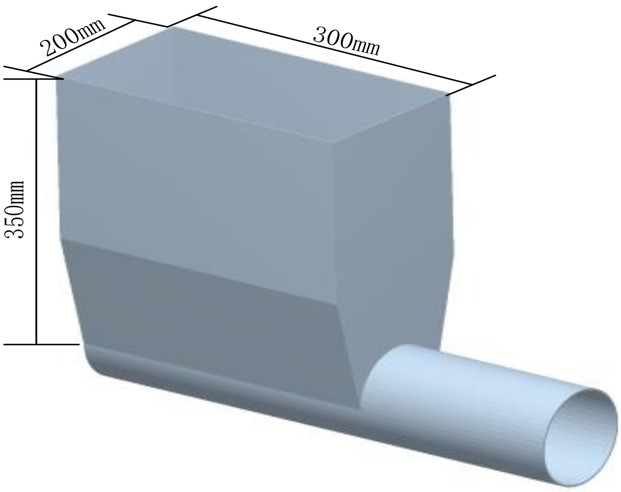

Fig. 3 - Three-dimensional model of the barrel

The outer diameter of the simulation screw blade is 100 mm. According to the size of the hopper, the length of the feeding section is 300mm. The screw is designed according to the method of considering the number of dead zones proposed. The three-dimensional models of the four types of screws below are constructed by Solid Works software. Their core size, blade diameter and the gap between the barrel wall and the blade are the same, except the structural parameters of the feed section of the screws. The three-dimensional model of the screw is shown in Fig. 4, and the structural parameters of the feeding section are shown in Table 1.

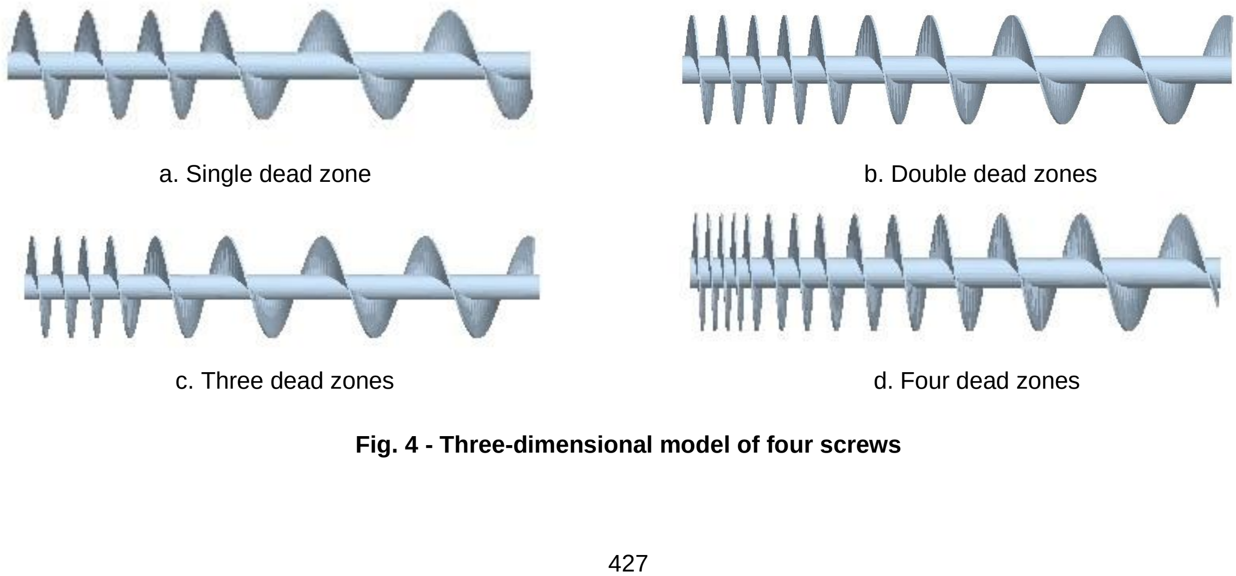

a. Single dead zone

b. Double dead zones

c. Three dead zones

d. Four dead zones

Fig. 4 - Three-dimensional model of four screws

In order to reduce simulation time, wheat flour particles were amplified to a radius of 1mm for simulation. Parameter calibration was completed based on the method of wheat flour parameter calibration in references *(Li et al., 2019)*. The error between the simulation angle of repose and the actual value was less than 0.5%, and the wheat flour simulation parameters were obtained as shown in Table 2.

Table 1

Structural parameters of the four screw feed sections

The number of dead zones	Screw feeding section parameters (pitch × number of sections)
1	S1=60 mm x 3，S2=120 mm x 1
2	S1=27 mm x 4，S2=55mm x 2，S3=82 mmx1
3	S1=25 mm x 3，S2=50 mm x 1，S3=75 mm x 1，S4=100 mm x 1
4	S1=12 mm x 4，S2=24 mm x 3，S3=36 mm x 2，S4=48 mm x 1，S5=60 mm x 1

Table 2

Discrete element simulation parameter table of wheat flour enlarged particles

Simulation parameters	Value
Density of wheat flour/($kg \cdot m^{-3}$)	1960
Poisson's ratio of wheat flour	0.2
Shear modulus of wheat flour/Pa	6×107
Density of Stainless steel/($kg \cdot m^{-3}$)	7800
Poisson's ratio of Stainless steel	0.3
Shear modulus of Stainless steel/Pa	7×1010
Wheat flour-wheat flour restitution coefficient	0.2
Wheat flour-wheat flour static friction coefficient	0.65
Wheat flour-wheat flour rolling friction coefficient	0.23
Wheat flour-stainless steel restitution coefficient	0.2
Wheat flour-stainless steel static friction coefficient	0.72
Wheat flour-stainless steel rolling friction coefficient	0.25
JKR	0.145

Simulation process and post-processing

The isometric screw is a conventional screw structure, so the simulation process is illustrated by taking the isometric screw structure as an example. Then pitch value of isometric screw structure is 100 mm. Particle simulation adopts soft ball model, and particle generation method is Dynamic (*Wang et al., 2019; Wen et al., 2020; Luo et al., 2018*). The top of the powder in the hopper is in a horizontal state, and the distance from the center line of the barrel is 400 mm. The screw speed was set as 80 r/min, the simulation step size was set as 0.05s, and the simulation time was set as 10 s.

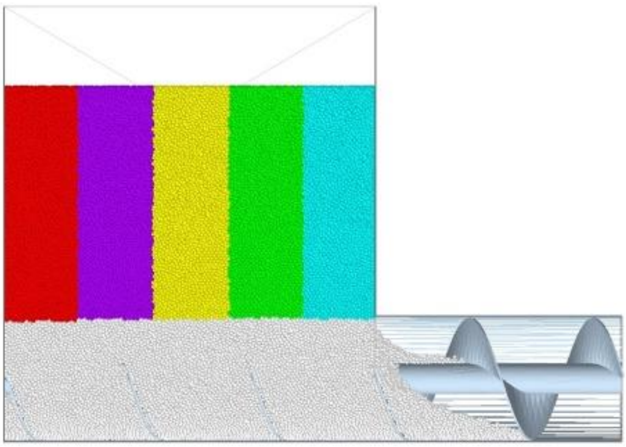

Fig. 5 - Setting of different color ribbons of wheat flour in different areas in the barrel

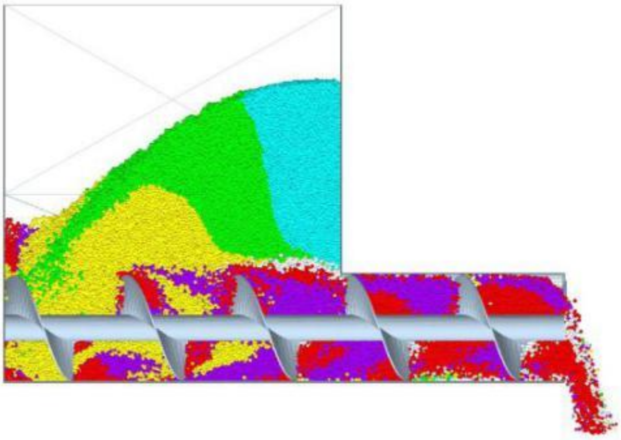

Fig. 6 - Isometric screw feeding state of wheat flour

After the end of the simulation, the feeding uniformity of the screw feeding section was analyzed by the method of references (*Fernandez et al., 2011; Gan et al., 2016; Li et al., 2019*). Manual Selections tool in post-processing is used to establish ribbon areas, and wheat flour was colored before conveying, as shown in Fig. 5. The simulation time was set at 10 s.

As shown in Fig. 6, there is little red and purple in the hopper, and the powder forms obvious funnel-shape. White powder in the screw cylinder has been completely conveyed; the yellow powder in the hopper has been entered the feeding section. Isometric screw structure of the dead zone phenomenon can be clearly observed.

Real experiment of wheat flour screw feeder

In order to verify the feasibility of the design method of variable pitch screw structure, a wheat flour screw feeding experimental platform was built. In the experiment, the feeding uniformity of wheat flour, the flow rate and precision of the screw feed were mainly considered, and the design of the variable pitch screw was evaluated based on the experimental results.

Experimental materials and equipment

Raw materials: wheat flour, Zhengzhou Haijia Food Co., Ltd., water content 13.5%, ash 0.51%, loose density 0.52 t/m^3.

Acrylic cylinder: In order to facilitate the observation of the feeding performance of the screw feeder, the screw feeder cylinder is made of transparent acrylic plate, which is made by Shanghai Baoyou Technology Products Co., Ltd. The size of the acrylic cylinder is designed according to the size of the screw feeder produced by Henan Jingu Industrial Co., Ltd.

Fig. 7 - Screw feeding experimental platform

Variable pitch screw: the three kinds of experimental screw was processed by Henan Jingu Industrial Co., Ltd.. One is the conventional equal-diameter and equal-pitch screw structure, the second is the existing design of equal diameter variable pitch screw structure, and the third is the equal-diameter and equal-distance variable pitch screw structure optimized in this paper. The material is 304 stainless steel.

RS485 plane weighing sensor: Hengyuan Sensor Technology Co., Ltd.，weighing range 0-50 kg, sampling frequency 10Hz-30Hz, measurement error ±0.003 kg.

The acrylic cylinder, screw, motor and other devices are assembled, the installed wheat flour screw feeding equipment is fixed on the table top and placed horizontally, and the experiment platform is set up as shown in Fig. 7.

Wheat flour screw feeding experiment procedures

1) In screw feeding, more wheat flour is needed. Prepare 100 kg of wheat flour before the experiment.

2) Three different speeds were used in the experiment. Before pouring wheat flour into the hopper, the laser velocimetry was used to measure the frequency of the frequency converter corresponding to three different speeds.

3) Adjust the frequency of the frequency converter to meet the speed requirements, pour the wheat flour into the hopper and let the screw feeder operate. After the wheat flour is completely filled into the packing barrel, scrape the top of the wheat flour in the hopper, as shown in Fig. 8.

4) At this time, the camera is fixed and the feeding state is photographed every 5 seconds. When the powder in the hopper reaches the screw blade, the operation is stopped, and the time is about 20 seconds.

5) When the powder in the hopper is basically delivered, the sensor and the feeding device are suspended, and the quality-time data are derived for processing and analysis. The data are measured five times at each speed.

Fig. 8 - Wheat flour state before feeding

RESULTS AND DISCUSSIONS

Simulation results and discussion

Feed flow rate

The feed flow rate is an important index for evaluating the performance of the screw feeder. After the end of the simulation, the fast-filling period of the material is removed, and the feed flow rate is collected during the feed stable time period. The post-processing flow sensor is used to set the position as the discharge port at the end of the barrel to detect the feed flow in the stable period of time in real time (*Dai and Grace, 2008; Evstratov et al., 2015; Jia et al., 2017; Moysey and Thompson, 2015; Nachenius et al., 2015; Orefice and Khinast et al., 2017; Pezo et al., 2018; Rozbroj et al., 2015; Ruiz-Carcel et al., 2018*). The results are shown in Fig. 9.

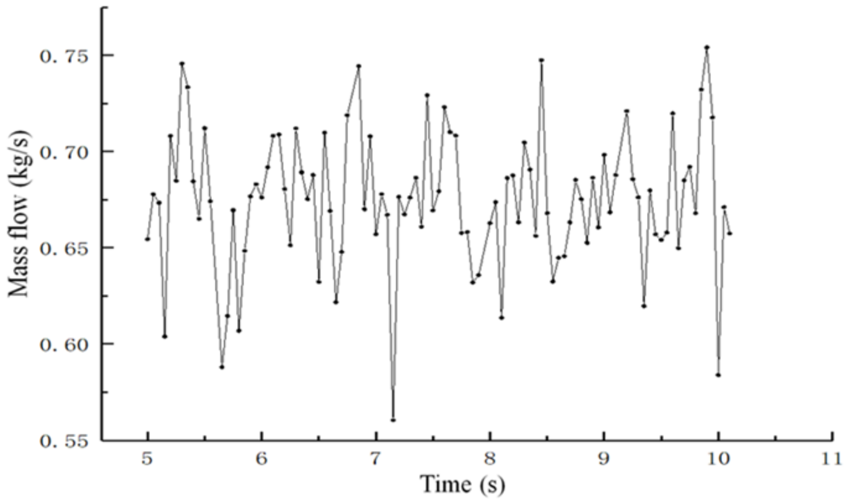

Fig. 9 - The mass flow curve of wheat flour at the outlet of the isometric screw feeder

It can be seen from Fig. 9 that the material flow presents a wave shape in a period of time. This is mainly due to the influence of the termination end face of the screw blade in the feeding of unit screw pitch. When the screw blade rotates to different positions, the blade and the feed cylinder form different storage spaces. In the time of a screw rotation, the unit turn angle presents different feeding amount. It can be seen from the Fig. 9 that the average flow of isometric screw feeding is 0.67 kg/s, and the flow fluctuates within the range of 0.56 kg/s-0.75 kg/s. The flow fluctuates greatly within the range of 11.94%-16.42%, and the precision of screw feeding is small.

Analysis of feeding uniformity of four kinds of screw feeding segments

As shown in Fig. 10, the materials in the hoppers in Fig. 10a and Fig. 10c have formed an obvious inclined funnel shape at this time, showing an obvious large dead zone phenomenon. The blanking of b and d is relatively uniform. The simulation results of the four screw types are shown in Table 3.

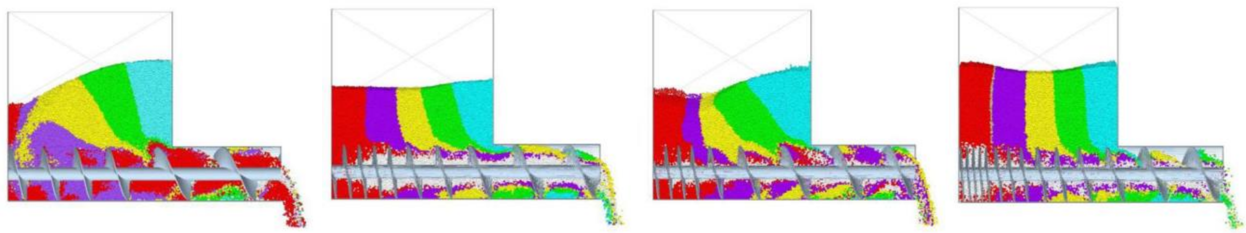

a. Single dead zone b. Double dead zones c. Three dead zones d. Four dead zones

Fig. 10 - State diagram of screw feeder with different number of dead zones (t=10 s)

Table 3

Simulation results of four screws at 10 s

The number of dead zones	Analysis of simulation result
1	The red and purple ribbons have basically completely entered the cylinder, and the area above the first turn of the pitch forms a blanking state, and the obvious blanking dead zone is formed above the other pitches except the first turn of the pitch in the feeding section. At this time, the yellow, green and cyan ribbons all have a tendency to move towards the first screw pitch. (Fig. 10a)
2	The five ribbons in the hopper are basically in a vertical state, and the top edge surface of the five ribbons in the hopper is relatively horizontal, indicating that the feeding is more uniform. (Fig. 10b)
3	The pitch value of the first turn of the structure in Fig. c is small, and the width of the purple and red ribbons is thinner than that of other color ribbons, indicating that there is more blanking here. The top edges of the red, purple and yellow ribbons are horizontal, and the dead zone is mainly in the green and green areas. Compared with Fig. a, the distribution of the dead zone is slightly reduced. (Fig. 10c)
4	Each ribbon in the hopper is basically vertical, and the edges of the five ribbons form an obvious symmetrical concave shape. A large number of white materials are left in the cylinder. There are more white materials in the first pitch value, and the dead zone is mainly distributed at both ends of the feeding section. (Fig. 10d)

Screw feed flow analysis

After the end of the simulation, the post-processing flow sensor is used to detect the feed flow and collect the mass flow of 6 s-8 s to the discharge port of the cylinder during the stable feeding period, the results being shown in Fig. 11.

As can be seen from Fig. 11, the average feed flow distribution of each screw is greatly different, for screw a and screw c, the flow size and fluctuation are basically the same. Considering the four dead zones, the feed flow of d screw is relatively reduced, while the feed flow of b screw with more uniform feeding is significantly smaller.

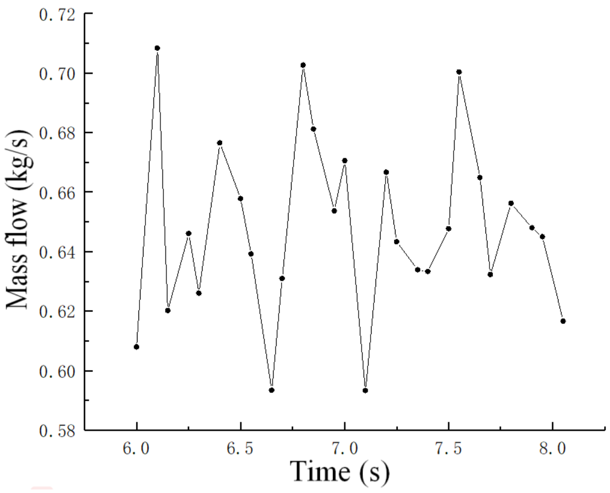

a. Single dead zone

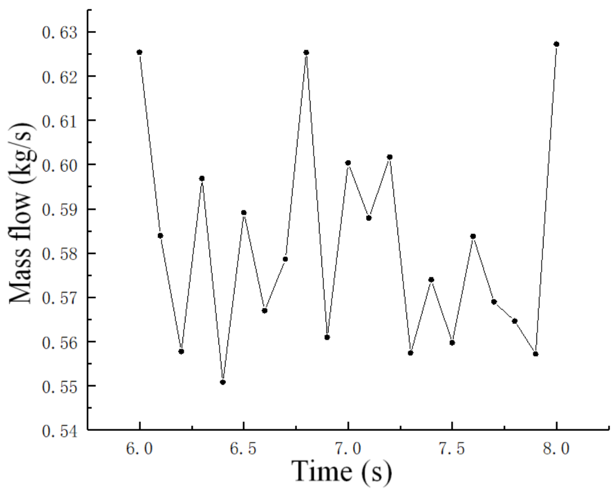

b. Double dead zones

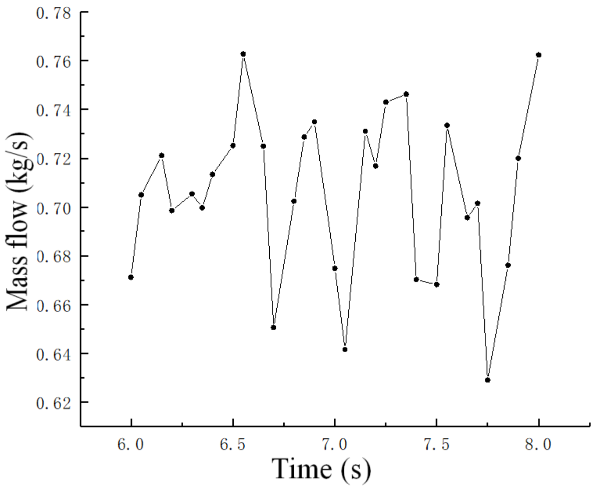

c. Three dead zones

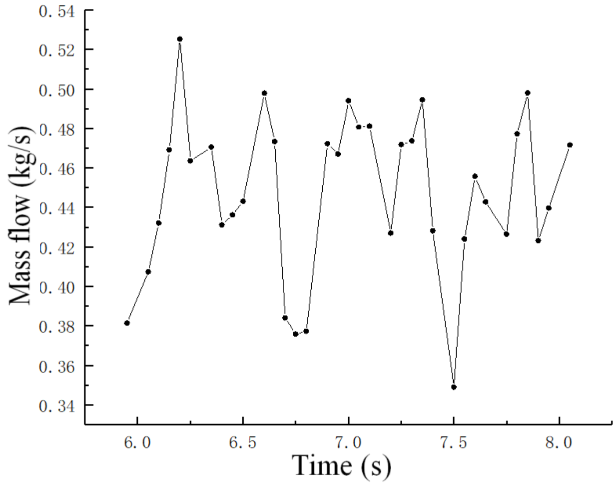

d. Four dead zones

Fig. 11 - Mass flow rate of screw feeder with different number of dead zones (t=6…8 s)

Table 4

Analysis of flow stability of screw feeders with different numbers of dead zones

screw	Average feed flow (kg/s)	Flow fluctuation range (kg/s)	Percentage flow fluctuation (%)
a. Single dead zone	0.648	0.593kg/s-0.708kg/s	±9.26
b. Double dead zones	0.593	0.558kg/s-0.627kg/s	±5.91
c. Three dead zone	0.705	0.629kg/s-0.763kg/s	±8.23
d. Four dead zone	0.447	0.349kg/s-0.525kg/s	±17.45

Optimal design of screw feeder

Based on the simulation comparison and analysis of the above four screws, the optimal screw structure was selected, according to the simulation results of the feeding uniformity, the blanking conditions of b and d screw structures were relatively uniform, in which the blanking end face of b screw basically presented a vertical state, while the blanking end face of d screw presented a slight concave type. It can be seen from the mass flow that the flow fluctuation of the b screw is smaller than that of the d-screw, indicating that it has a higher feeding accuracy. Therefore, the structure design of the screw feeder adopts b screw structure (considering two dead zones). Although the average feeding flow rate of a and c screw is large, the fluctuation range of its flow value is large, which affects the weighing speed and accuracy when weighing and quantifying, especially in the fine feeding process.

Contrast and analysis with existing design

According to the relevant reference (Du and Zhao, 2014), the screw pitch design of the feeding section of the screw used to convey wheat flour is generally 0.3D, 0.5D, 0.7D and 1D (D is the diameter of screw blade). The following is a simulation comparison and analysis based on the optimal designed screw structure and the design structure in the reference. For the convenience of comparison and analysis, the screw design in the reference also adopts the same outer diameter, and the same speed. It can be concluded that the screw pitch values of the feeding section designed in the reference are 30 mm, 50 mm, 70 mm and 100 mm, and the screw pitch value of the conveying section is 100 mm.

Comparison of blanking uniformity

As can be seen in Fig. 12 a, the ends of the five color ribbons in the hopper are basically in a horizontal state, and the powder at the outlet of the screw feed are in a mixed state of five colors. As can be seen in Fig. 12 b, the phenomenon of dead zone of materials is more obvious. The red and purple ribbon in the hopper have basically all entered the cylinder, and the Yellow-green-cyan ribbon have formed obvious slip surfaces, all of which have a tendency to slide towards the pitch of the first turn. Compared with Fig. 12 b, the feeding in Fig. 12 a is obviously more uniform.

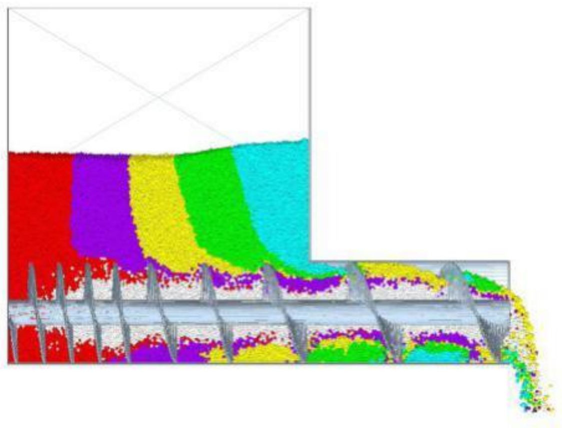

a. Double dead zones *b. Reference design*

Fig. 12 - Comparison of the feeding status of the two dead zones and the reference design screw feeder (t=10 s)

Comparison of feeding flow comparison

As can be seen from Fig. 13, the feed flow distribution of the two helical structures is greatly different, and the feed flow of the two dead zone helical structures is obviously smaller than that of the design in the reference. According to the calculation and analysis of the derived image data, it can be concluded that the average feed flow of the screw with two dead zone is 0.593 kg/s, and the flow fluctuation range is 0.558 - 0.627 kg/s, and the fluctuation percentage is within ±5.91%. The average feed flow of the screw designed in the reference is 0.642 kg/s, the flow fluctuation range is 0.559 - 0.718 kg/s, and the fluctuation percentage is within ±11.83%. According to the experimental data, the flow fluctuation of the screw with more uniform feeding (two dead zones) is relatively small.

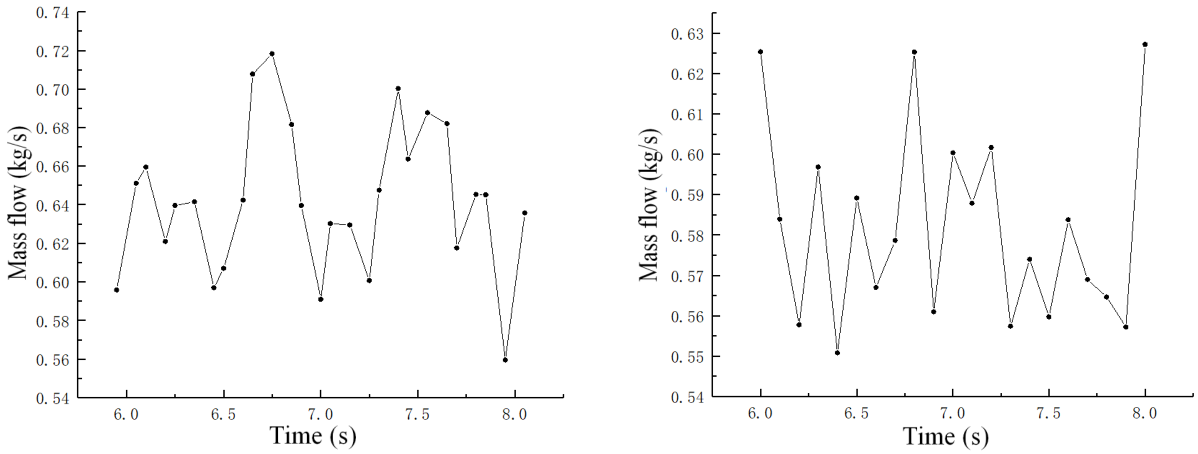

a. Double dead zones *b. Reference design*

Fig. 13 - Comparison of mass flow between two dead zones and the reference design screw feeders (t=6…8 s)

Results and discussion of real experiments

Comparative analysis of feeding uniformity

As can be seen from Fig. 14, the material states of the simulation experiment and the real experiment are very similar at 10 seconds, indicating that the simulation experiment is relatively accurate. The surface of the material is relatively flat, indicating that the screw design is reasonable.

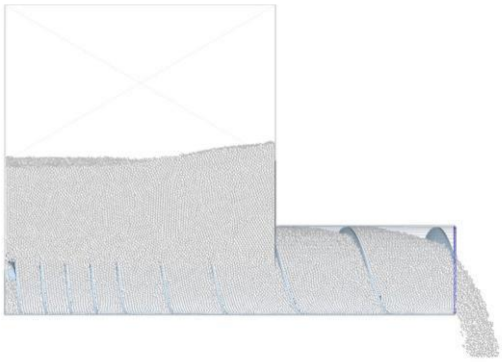

a. Simulation state

b. Experiment status

Fig. 14 - Comparison of simulation experiment and real experiment of two dead zone screw feeders (t=10 s)

Comparative analysis of the mass flow

In view of the screw feeding flow of wheat flour, the weighing sensor was used to detect the mass flow rate in real time, and the mass-time curve was derived to acquire the average mass flow rate for evaluation. The real-time detection data were processed (Fig. 15), and the stability and feeding accuracy of the screw structure were analyzed according to the quality-time curve after processing.

It can be seen from Fig. 15 that the experimental results are similar to the simulation results. According to the experimental data, when r=80r/min, the average mass flow rate of wheat flour conveyed by conventional equidistance screw is 0.573 kg/s, and the flow fluctuation range is 0.502 kg/s-0.673 kg/s, and the fluctuation percentage is within ±17.5%. The average feed flow of wheat flour conveyed by the variable pitch screw designed in this paper is 0.535 kg/s, and the flow fluctuation range is between 0.493 kg/s-0.572 kg/s, and the fluctuation percentage is within ±7.85%. Then, the flow fluctuation of the screw designed in this paper is relatively small when the feeding is more uniform.

It can be seen from the comparison of experimental results that the screw structure designed and optimized for this paper has significantly smaller flow fluctuations, stable feeding and higher feeding accuracy.

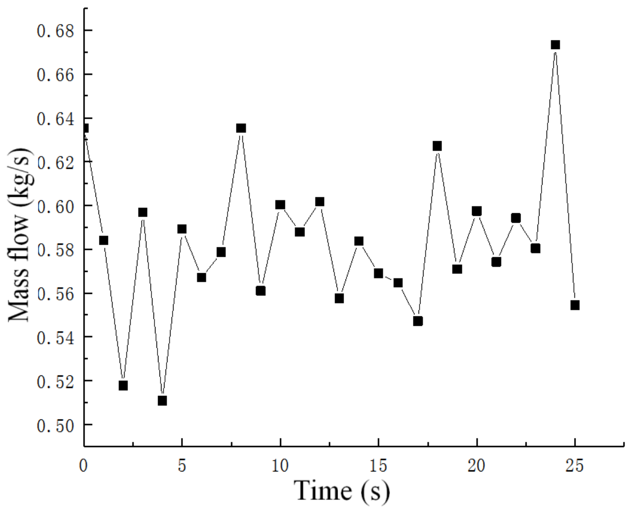

a. Conventional equidistant

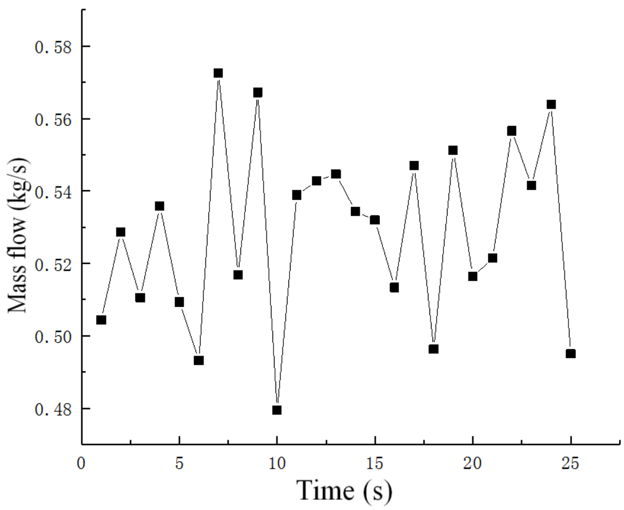

b. Design in this paper

Fig. 15 - The mass flow curve of wheat flour at the speed of 80r/min for the isometric and the screw feeder designed in this paper

CONCLUSIONS

1) In view of the problem that the equal-diameter variable pitch screw of wheat flour conveying is mainly designed by experience and there is a lack of systematic design method, in this paper, a method of analysis and design considering the symmetry of the number of different dead zones in the feeding section is presented, and four kinds of equal-diameter variable-pitch screw structures are designed. Solid works was used to build the three-dimensional model. EDEM software was imported to analyze the stability and feed flow of wheat flour under screw feeding. Compared with the isometric screw structure and the variable-pitch screw structure designed by the existing experience, the screw structure designed in this paper has the advantages of uniform feeding and small fluctuation of mass flow.

2) In order to further verify the rationality of the variable pitch screw structure design, the screw is processed according to the optimized parameters, and the screw feeding device of the transparent barrel is built using acrylic to observe the stability of the feeding section of the wheat flour. The mass flow rate of wheat flour was measured by plane weighing sensor. When r=80 r/min, the average mass flow rate of wheat flour conveyed by conventional equidistance screw is 0.573 kg/s, and the flow fluctuation range is 0.502-0.673 kg/s, and the fluctuation percentage is within ±17.5%. The average feed flow of wheat flour conveyed by the variable pitch screw designed in this paper is 0.535 kg/s, and the flow fluctuation range is between 0.493-0.572 kg/s, while the fluctuation percentage is within ±7.85%. Simulation and experiment results show that the flow fluctuation of the screw designed in this paper is relatively small, and the feeding is more uniform, which can improve the precision of screw quantitative feeding of wheat flour.

ACKNOWLEDGEMENT

Project supported by: National Key R&D Program of China (2018YFD0400704).

REFERENCES

[1] Bates, L. (1969). Entrainment patterns of screw hopper dischargers. J*ournal of Manufacturing Science & Engineering*, 91(2), pp. 295-302.

[2] Dai, J., & Grace, J. R. (2008). A model for biomass screw feeding. *Powder Technology*, 186(1), pp. 40-55.

[3] Du, H.Y., & Zhao, J. (2014). Design and Fabrication of Circular Tube Spiral Feeder. *Modern Flour Industry*, 28(02), pp. 16-19.

[4] Evstratov, V. A., Rud, A. V., & Belousov, K. Y. (2015). Process modelling vertical screw transport of bulk material flow. *Procedia engineering*, 129, pp. 397-402.

[5] Fernandez, J.W., Cleary, P.W., & McBride, W. (2011). Effect of screw design on hopper drawdown of spherical particles in a horizontal screw feeder. *Chemical engineering science*, 66(22), pp. 5585-5601.

[6] Gan, J. Q., Zhou, Z. Y., & Yu, A. B. (2016). A GPU-based DEM approach for modelling of particulate systems. *Powder Technology*, 301, pp. 1172-1182.

[7] Gong, Z.M. (1984). Preliminary study on the screw structure parameters of the screw batcher. *Grain and Oil Processing and Food Machinery*, 5(7), pp. 22-28.

[8] Haaker, G., van Poppelen, M.P., Jongejan, M.P., & Bekhuis, J.H. (1993). Improvement of screw feeder geometry for better draw-down performance 2nd international symposium. *Reliable Flow of Particulate Solids II*, pp. 568–581.

[9] Jia, H.Y., Wu, B.X., & Sun, W.B. (2017). Research on the influence of the conveying law and friction coefficient of horizontal screw conveyor. *Mechanical Design and Manufacturing*, (9), pp. 236-239.

[10] Li, F.X., Li, Y.X., & Xu, X.M. (2019). Pitch design and simulation analysis of variable pitch screw structure. *Packaging Engineering*, 40(13), pp. 214-221.

[11] Li, Y.X., Li, F.X., & Xu, X.M. (2019). Calibration of discrete element parameters of wheat flour based on particle scaling. *Transactions of the Chinese Society of Agricultural Engineering*, 35(16), pp. 320-327.

[12] Luo, S., Yuan, Q.X., & Gouda, S.B. (2018). Discrete element method parameter calibration of earthworm feces based on JKR bonding model. *Journal of Agricultural Machinery*, 49(04), pp. 343-350.

[13] Moysey, P.A., & Thompson, M.R. (2005). Modelling the solids inflow and solids conveying of single-screw extruders using the discrete element method. *Powder Technology*, 153(2), pp. 95-107.

[14] Nachenius, R. W., van de Wardt, T. A., & Ronsse, F. (2015). Torrefaction of pine in a bench-scale screw conveyor reactor. *Biomass and Bioenergy*, 79, pp. 96-104.

[15] Orefice, L., & Khinast, J.G. (2017). DEM study of granular transport in partially filled horizontal screw conveyors. *Powder Technology*, 305, pp. 347-356.

[16] Peng, B. (2017). Design and analysis of powder packaging precision measurement system. *Hubei University of Technology*.

[17] Pezo, M., Pezo, L., & Jovanović, A. P. (2018). Discrete element model of particle transport and premixing action in modified screw conveyors. *Powder Technology*, 336, pp. 255-264.

[18] Qiu, A.H., Gong, S.G., & Xie, G.L. (2008). Parametric model and performance simulation of variable-diameter and variable-pitch screw shaft. *Journal of Mechanical Engineering*, 44(5), pp. 131-136.

[19] Roberts, A. W. (1993a). *Basic principles of bulk solids storage, flow and handling.* Institute for Bulk Materials Handling Research.

[20] Roberts, W., Manjunath, K.S., & McBride, W. (1993b). Mechanics of screw feeder performance for bulk solids flow control.

[21] Rozbroj, J., Zegzulka, J., & Nečas, J. (2015). Use of DEM in the determination of friction parameters on a physical comparative model of a vertical screw conveyor. *Chemical and biochemical engineering quarterly*, 29(1), pp. 25-34.

[22] Ruiz-Carcel, C., Starr, A., & Nsugbe, E. (2018). Estimation of powder mass flow rate in a screw feeder using acoustic emissions. *Powder Technology*, 336, pp. 122-130.

[23] Song, Y.Y. (1996). Theoretical study on structural parameters of variable pitch helix. *Journal of Soochow University (Natural Science Edition)*, (04), pp. 96-100.

[24] Su, Y.L., & Zhao, S.Y. (1989). Determination of main parameters of screw auger with variable pitch and diameter. *Mechanical Engineer*, (2), pp. 28-30.

[25] Wang, S., Li, H., & Tian, R. (2019). Numerical simulation of particle flow behavior in a screw conveyor using the discrete element method. *Particuology*, 43, pp. 137-148.

[26] Wen, X.Y., Jia, H.L., & Zhang, S.W. (2020). Experiment on determination of suspension speed of granular fertilizer based on EDEM-Fluent coupling. *Journal of Agricultural Machinery*, 51 (03), pp. 69-77.

[27] Yu, W.J. (1982). Design and calculation of equi-variable variable-diameter variable-pitch screw conveyor. *Modern Agriculture,* 14(2), pp. 21-22.

[28] Yu, Y., & Arnold, P.C. (1996). The influence of screw feeders on bin flow patterns. *Powder Technol,* 88, pp. 81-87.

[29] Zhang, D.H. (2006). Optimization Research of Screw Conveyor. *Yalian: Dalian University of Technology*.

[30] Zhao, D.M., & Yu, S.H. (2018). Pitch design and performance analysis of variable-pitch screw conveyor. *Mechanical Design and Manufacturing*, 14(6), pp. 55-55.

RESEARCH ON PLC SYSTEM DESIGN OF A NEW TYPE OF ROTARY TILLER CONTROL PARAMETERS (Programmable Logic Controller)
/
一种新型旋耕机调控参数的 PLC 系统设计研究

Xiuli Zhai[1)]*, Xibao Sun[2)]
[1)] Department of Electronic Information，Xinxiang Vocational and Technical College，Xinxiang, Henan, 453006 / China
[2)] College of Intelligent Manufacturing，Xinxiang Vocational and Technical College，Xinxiang, Henan, 453006 / China
E-mail: teje53242@163.com
DOI: https://doi.org/10.35633/inmateh-64-43

Keywords: *PLC fuzzy control, tillage depth control, rotary tiller.*

ABSTRACT

The purpose of this paper is to design a rotary tiller control system based on programmable controller technology, and verify the application of this control system. In this paper, the traction and depth control of rotary tiller are transformed into the control of piston rod displacement of hydraulic cylinder, and the intelligent fuzzy control of axial extension displacement of rotary tiller and output torque of piston rod is realized. According to the characteristics of the mathematical model, the objective function is determined and the motion parameters are optimized by the steepest descent method, which provides a reliable calculation model for the optimization design of the overall parameters of the rotary tiller. The rotary tiller control system based on PLC (Programmable Logic Controller) can realize the effective control of rotary tillage depth and speed, and the error of rotary tillage depth can be guaranteed within 4.5%. When the soil resistance of the rotary tiller suddenly increases, the fuzzy control of the comprehensive tillage depth value of the stressed position can effectively improve the rotational speed stability of the hydraulic motor for tillage depth control. PLC technology puts the digital control of rotary tiller on a higher technical platform, thus reducing the labour required for agricultural planting, providing a good growth environment for crops and realizing the intelligence of rotary tiller.

摘要

本文设计了一种基于可编程控制器技术的旋耕机控制系统，并验证该控制系统的应用。将旋耕机的牵引力和深度控制转化为液压缸活塞杆位移控制，实现了旋耕机轴向伸出位移和活塞杆输出扭矩的智能模糊控制。根据数学模型的特点确定目标函数和用最速下降法优化运动参数，为旋耕机总体参数的优化设计提供了可靠的计算模型。基于 PLC 的旋耕机控制系统实现了旋耕深度和速度的有效控制，旋耕深度误差保证在 4.5%以内。当旋耕机土壤阻力突然增大时，应力位置综合耕深值的模糊控制可以有效地提高液压马达的转速稳定性。PLC 技术将旋耕机的数字化控制置于更高的技术平台上，减少了农业种植所需的劳动力，为农作物提供了良好的生长环境，实现了旋耕机的智能化。

INTRODUCTION

Solving the food problem of national population is the top priority of agricultural development, and maintaining national food security is the top priority of agricultural production *(Chen Y. L. et al., 2018)*. Farming is the first link of agricultural production. The purpose of tillage and soil preparation is to increase the deep plough layer and promote the development of crop roots, which is the basic condition for high yield of crops. Through tillage and soil preparation, the subsoiling layer can be obtained, which is conducive to the smooth extension and transplanting of crop roots. At the same time, the soil aggregate structure can be restored and the soil maturity can be promoted *(Pretty J. et al., 2018)*. The improved subsoil was transferred to the upper layer to keep the permeability and ventilation of the soil. Field preparation can also reduce the occurrence of plant diseases and insect pests.

In agricultural production, the most important and basic link is cultivated land operation, and its cultivation quality directly affects the growth of crops *(Storm H. et al., 2020)*. The literature adopts the parameter index of roller-skating rate of operating units to control the cultivation depth *(Minakov I. A. and Nikitin A. V. 2019)*. The monitoring module group including radar, magnetic and other hardware sensors is used to feed back the actual farming depth of farming machinery in real time.

Ahmed I. et al., (2017) developed the tractor electro-hydraulic suspension system, which can adjust the resistance value of the tillage parts of the tillage machinery, the position of the parts, the working pressure of the hydraulic system actuator and the slip rate in real time to a great extent. *Kerr W. C. et al., (2019),* innovatively proposed to introduce the time domain analysis method into the research of dynamic performance. At the same time, based on this, the mathematical model of some components of hydraulic system with resistance adjustment was constructed, and the research work focused on the effects of two parameters, namely resistance coefficient and natural frequency, on the system. *Mariotte P. et al., (2018)* made a detailed inquiry into the motion and mechanical characteristics encountered in the field of tillage depth adjustment of hydraulic system of tillage machinery. By introducing the dynamic balance relationship into the establishment of the mathematical model of the system, the balance equation was successfully written, and on this basis, the transfer mathematical relationship between the natural frequency value and the loaded hydraulic system was obtained.

Ji J. T. et al., (2019) studies the arrangement of blades. The experimental results show that the spiral arrangement is simple and the parameters are single, but the lateral offset torque produced in the operation process is large, which is easy to cause the soil or straw to move laterally. *Zhou Z. et al., (2017),* conducted field experiments on micro rotary tillers with different blade arrangement forms and numbers. Before the experiment, the soil firmness was determined to be 245-1442kPa, and the soil moisture content was 34.6%. The test results showed that the micro rotary tiller with double four rotary tillers arranged opposite to each other had the best operation performance and less power consumption during operation. *Ma L. et al., (2019)*, when studying the structural parameters and arrangement of blades, it also devotes itself to studying the wear resistance of rotary tillage blades. By processing rotary tillage blades, the corresponding operation performance can be improved. *Aliev E. B. et al., (2018),* studied the rotary tillage blades, and carried out laboratory soil trough experiments by optimizing the existing three types of rotary tillage blades, namely C-shaped, L-shaped and RC-shaped. The rotation angles of the three blades are different, and the cutting distances during working are also different. *Rasmussen L. V. et al., (2018),* studied the deep ploughing rotary tiller and the reverse rotary tiller respectively, with the aim of improving the operation quality and increasing the tillage depth of the rotary tiller under the premise of low power consumption. *Du X. et al., (2020),* applied smooth fluid dynamics theory to simulate the soil cutting process of rotary tiller, and analysed the soil cutting process of rotary tiller. The simulation results provided theoretical basis for the optimization design of the whole machine or its parts.

Rotary tiller is mainly powered by tractor, which is composed of control system, frame, transmission mechanism, cutter roller, soil retaining cover and levelling pallet *(Huang Y. et al., 2018)*. Different control systems use different control methods to exchange information between the controller and the executive parts of the rotary tiller, which cannot achieve mutual compatibility between different systems. Programmable Logic Controller (PLC), as a logic control operating system, can edit and store programs, and realize the input/output, operation and control of control programs *(Taheripour F. and Tyner W. E., 2018)*. Therefore, a control system of rotary tiller is designed based on PLC technology, and the application of the control system is verified.

MATERIALS AND METHODS

Working principle of control system

The electric control hydraulic system of rotary tiller mainly includes three parts: hydraulic, electric control and mechanical. Among them, the hydraulic system mainly includes hydraulic components such as hydraulic pump, hydraulic cylinder and control valve. The electronic control system mainly includes ploughing depth, resistance sensor and controller in its hardware composition. Mechanical system mainly includes three-point suspension mechanism, cutter shaft and cutter. The theory of realizing digital control of rotary tiller is to use PLC technology to control the rotary tillage depth and the walking speed of rotary tiller, and to combine computer with sensors. The field information is collected by sensors, and the information is fed back to the control centre for analysis. The output results control the lifting of the horizontal adjusting rod, so as to achieve the purposes of uniform rotary tillage depth, stable walking speed and guarantee the rotary tillage quality.

The working principle of the system is as follows: by transmitting the displacement signals of traction resistance and tillage depth of rotary tiller detected by the resistance and tillage depth sensors in the electronic control system to the controller, the actual resistance and tillage depth values are calculated. At the same time, the controller takes the tillage depth value set on the control panel as the target signal, compares it with the actual value, adjusts the function control valve in the system, and completes the control of the rotary tillage depth of the rotary tiller.

The comprehensive control of force and position firstly synthesizes the traction resistance and tillage depth control of rotary tiller into the control of telescopic displacement of hydraulic cylinder (rotary tillage depth control), then uses the deviation between target and actual value as the input signal of the system control centre, outputs the control signal after processing, and adjusts the control valve in the hydraulic system, thus completing the control of the tillage depth of rotary tiller.

The comprehensive coefficient α is expressed as the proportion of rotary tiller tillage depth control in the comprehensive control formula of rotary tiller traction resistance and tillage depth. The actual tillage depth measured by the tillage depth sensor is h_1, and the traction resistance F of the rotary tiller is measured in real time by the resistance sensor. Use the following formula to transform F into the depth value h_2.

$$h_2 = \frac{F}{\beta \cdot b} \tag{1}$$

In the formula 1, β is soil specific resistance, (N/mm^2); b is ploughing width, (mm).

$$h = \alpha h_1 + (1-\alpha) h_2 \tag{2}$$

In the formula 2, h is the comprehensive actual ploughing depth.

The control system takes the rotary tillage depth detection signal, $x(t)$, collected by the sensor as negative feedback, and forms an annular control analysis system with the setting signal $y(t)$, when the rotary tiller works. The setting signal $y(t)$ in the single chip microcomputer is compared with the signal $x(t)$ detected by the sensor installed on the rotary tiller.

When the set signal is greater than the detection signal, that is, the actual rotary tillage depth is less than the set rotary tillage depth, the control system will send a signal, reduce the output power, reduce the walking speed of the rotary tiller or stop, control the horizontal rod to descend, adjust the rotary tillage depth of the blade to reach the set value, and then continue to work.

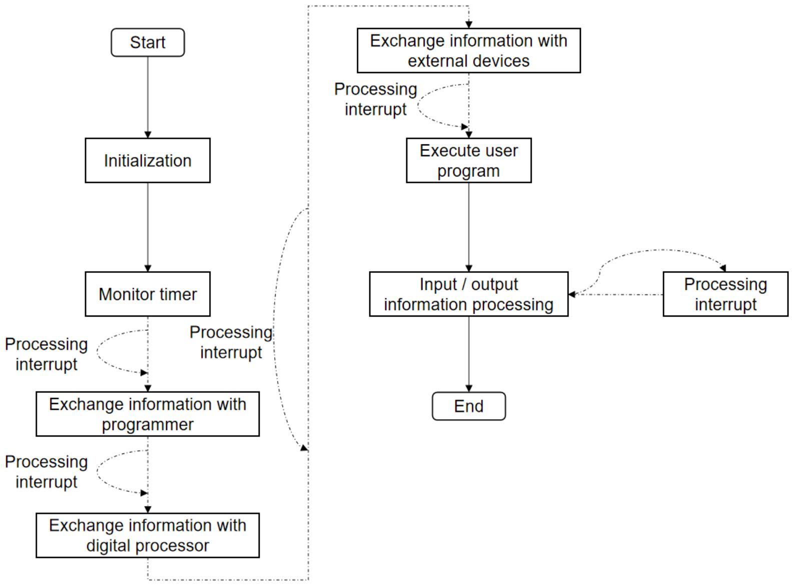

Fig. 1 - Working procedure of PLC technology control system

When the set signal is less than the detection signal, that is, the actual rotary tillage depth meets or even exceeds the set rotary tillage depth, then the control system outputs a signal to order the rotary tiller to continue to move forward and carry out the next rotary tillage of soil. The working procedure of the control system is shown in Figure 1.

The control system converts and compares the collected signals, analyses the comparison results, generates signals and outputs judgment signals, and adjusts the machines and tools to meet the requirements. The control of rotary tillage depth and walking speed is mainly by changing the output power of the engine, which is mainly accomplished by frequency converter. Changing the frequency can control the rotation speed of the engine, thus controlling the walking speed and rotary tillage depth. The main task of MCU is to digitize, pre-emphasize, filter and window the signal, and output the analysis results.

Fuzzy controller design

Fuzzy control has great similarities with people's thinking mode. By transforming the empirical knowledge of engineers and technicians in this field into language rules that the controller can handle, the decision is completed. Therefore, compared with the traditional control mode, fuzzy control does not need an accurate mathematical model of the controlled object, and makes the control mechanism and strategy easy to be understood by engineers and technicians. Therefore, the design of the control system is simple and the application is convenient. This control method has five core components: fuzzy controller, actuator, input/output interface, controlled object and detection device. As shown in figure 2.

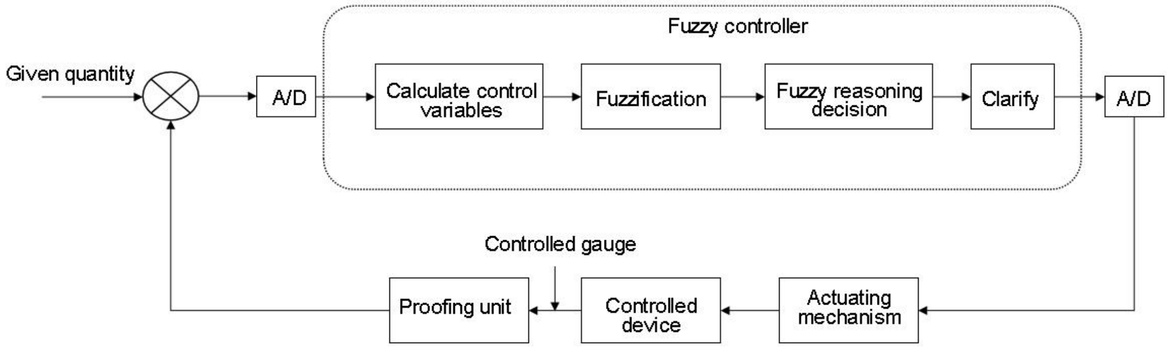

Fig. 2 - Schematic diagram of fuzzy control system

To a great extent, this kind of controller fully absorbs the knowledge and experience of engineers and technicians in this field, and transforms human experience into language rules. The working principle of the controller is that the digital quantity x_1 input by the system is firstly converted into fuzzy quantity by fuzzification (D/F), and then the converted fuzzy quantity is processed by the inference module containing fuzzy rules to obtain fuzzy output signals, and finally converted into clear quantity u by the defuzzification module (F/D), which is output to the controlled object, finally realizing fuzzy control.

The inputs of fuzzy controller are displacement deviation e and deviation change rate de/dt of hydraulic cylinder piston, and their fuzzy definitions are shown in Table 1.

Table 1

Input parameters of fuzzy controller

Input parameter	Definition
Displacement of piston rod of hydraulic cylinder (mm)	0-280
Basic universe of piston rod displacement deviation e	[-280-280]
Deviation e discrete universe	{-5,-4,-3,-2,-1,0,1,2,3,4,5}
Fuzzy subset of deviation e	NB, NM, NS, Z, PS, PM, PB
Basic universe of deviation e, change rate de/dt	[-80, 80]
de/dt discrete universe	{-5,-4,-3,-2,-1,0,1,2,3,4,5}
de/dt fuzzy subset	NB, NM, NS, Z, PS, PM, PB

The output of the fuzzy controller is the control current I, and the fuzzy definition is shown in Table 2.

Table 2

Output parameters of fuzzy controller

Output parameters	Definition
Control current I	[-1300, 1300]
Discrete universe of control current I	{-6,-5,-4,-3,-2,-1,0,1,2,3,4,5,6}
Fuzzy subset of control current I	

The quantization and scaling factors obtained from Table 1 and Table 2 are as follows: K_e=5/280=0.018; K_{de}=5/80=0.063; K_I=1300/6=217.

The fuzzy controller used in this paper is double input-single output, in which the control language rules are the most common form.

See Table 3 for the control rules of the comprehensive fuzzy control system of rotary tiller force and position.

Table 3

Fuzzy control rule table

		Displacement deviation e						
		NB	NM	MS	Z	PS	PM	PB
Deviation rate of change de/dt	NB	PB	PB	PM	PS	Z	PS	PB
	NM	PB	PM	PS	PS	Z	PS	PB
	NS	PM	PS	PS	Z	MS	PM	PB
	NS	PS	PS	PS	PM	MS	PM	Z
	Z	Z	PS	Z	PM	MS	PM	Z
	Z	Z	Z	Z	PS	PB	NM	NB
	PB	PS	PS	Z	PS	PB	NB	NB

PLC programming

PLC is a controller developed in recent years, which has played a great role in industry. The design and installation of PLC are convenient. In PLC, the complex wiring in relay control system can be replaced by soft relay system to realize the internal logic system, which is convenient for debugging and modification. PLC also has the functions of self-diagnosis, fault alarm, fault alarm type display and network communication, which is convenient for operators and maintenance personnel to check.

Siemens S7-200 series PLC system is simple and easy to program, and can work normally under different environments, such as high temperature, high humidity, strong vibration and impact interference. It has good adaptability and good economy, and can be used for automatic steering design of rotary tiller blade hot rolling. Its control system is stable and reliable, which improves the generation efficiency and meets the application requirements.

According to the requirements of automatic steering control, in which each sensor signal detection original occupies an input point, each power execution original occupies an output point, and the display of each indicator lamp also occupies an output point, so the device has four input signals and five output signals. The input and output points corresponding to each signal are shown in Table 4.

Table 4

I/O allocation table

Input signal	I point	Output signal	O point
Sensor signal K_1	X_{001}	Actuation of cylinder 4	Y_{001}
Sensor signal K_2	X_{002}	Actuation of cylinder 12	Y_{002}
Sensor signal K_3	X_{003}	Indicator lamp HL1	Y_{003}
Sensor signal K_4	X_{004}	Indicator lamp HL2	Y_{004}
		Indicator lamp HL3	Y_{001}

Note: The cylinder 4 realizes that before the blade slides down to the cylinder, the sensor senses and the cylinder executes the push-out action; The air cylinder 12 is used to push the incoming blades to the production line and realize automatic steering. Sensor K_1 is the signal before sensing blade sliding down, sensor K_2 is the signal of blade before cylinder 4, sensor K_3 is the signal of blade before cylinder 12, and sensor K_4 is the demand signal of production line, in which status indicator HL1 before blade sliding down, indicator HL2 before blade sliding down cylinder 4 and indicator HL3 before blade sliding down cylinder 12 are on.

According to the I/O port allocation table of PLC, I/O electrical wiring diagram can be designed from the input points and output points, as shown in fig. 3.

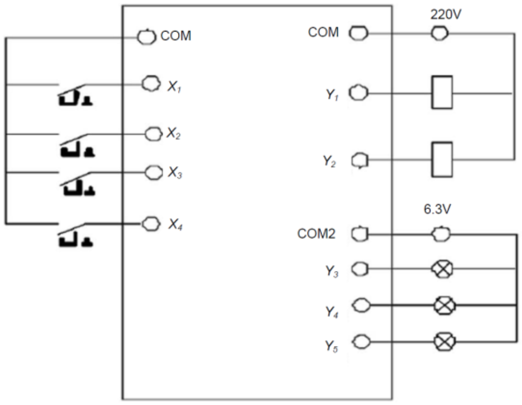

Fig. 3 - I/O wiring diagram

In the design process, the designed program should be able to complete the automatic steering function of rotary tiller blade hot rolling. Try to use simple programs to achieve the required functions and the programs should be easy to read. The ladder diagram of program design is shown in Figure 4.

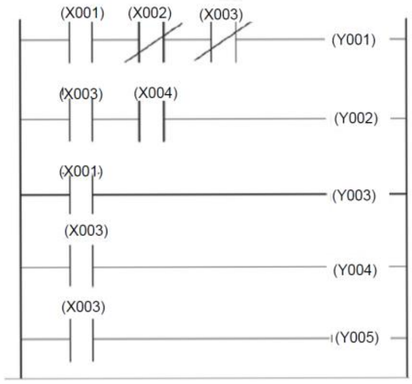

Fig. 4 - Ladder diagram

Ploughing width design module

The theoretical value of the bulge height is equal to the distance c between the intersection of two adjacent cycloids and the bottom of the ditch, and the bulge height of the bottom of the ditch is generally less than 20% of the cultivated depth. Therefore, the bulge height conditions of the bottom of the ditch are as follows:

$$c < 0.2h$$
$$R\sqrt{1-\frac{(R-c)^2}{R}}+\frac{v_m}{\omega}\arcsin\frac{(R-c)}{R}=\frac{v_m}{\omega}\left(\frac{\pi}{z}+\frac{\pi}{z}\right) \tag{3}$$

For rotary tillage blades cutting soil in the same longitudinal plane, the advancing distance of the unit is called the cutting pitch in the time interval of cutting soil one after another. According to the test, the S (soil cutting distance) is about 100-110mm for dry ploughing of cultivated land (water content 20%-30%); Farming light and medium viscosity soil (water content is more than 35%), S is 70-90mm; S should be 50-60mm for heavy soil and grassland. Therefore, the cutting pitch conditions are as follows:

$$\frac{S_{\min}}{2\pi}z<\frac{v_m}{\omega}<\frac{S_{\max}}{2\pi}z \tag{4}$$

Efficiency

When the rotary cultivator works, the forward speed directly affects the tillage quality of the rotary cultivator. Therefore, in order to ensure better soil tillage quality, the forward speed of the unit can neither be too fast nor too slow, and if the forward speed is too fast, the tillage quality is not good, and if it is too slow, it leads to the decrease of production efficiency and the increase of power.

The power consumption of rotary tiller is one of the important factors affecting the cultivation width. The formula of total power consumption of rotary tiller is as follows:

$$N = N_P + N_Q + N_T + N_F + N_K \tag{5}$$

Where N is the total power consumed by the rotary tiller; N_p is throwing power; N_Q is cutting power; N_T is the forward power; N_F is transmission friction power; N_K is the blocking power of soil. The energy consumption ratio of rotary tillage is also one of the important factors affecting the tillage width. The commonly used energy consumption ratio of rotary tillage is the energy consumed by rotary tillage per unit volume of soil, and the formula is:

$$K_R = \frac{N}{BHV_M} \tag{6}$$

Where N is the total power consumed by the rotary tiller; B is the width of rotary tillage; H is the depth of rotary tillage; V_M is the forward speed.

RESULTS

Accuracy analysis of rotary tillage depth and rate control of rotary tiller

In order to test the precision of rotary tillage depth and speed control of rotary tiller in actual situation, a 200m × 200m dry land was selected as the experimental site, and the sensors were installed on the rotary tiller and the initial parameters of the control system were set for the experiment. Figure 5 shows the working process of the rotary tiller based on the PLC control system.

Fig. 5 - Working process of rotary tiller based on PLC control system

The performance test of digital control system of agricultural rotary tiller based on PLC technology, the initial rotary tillage depth is set as 5 rotary tillage depth tests of 8, 9, 10, 11 and 12 cm, the rotary tiller runs freely in the ground, each rotary tillage depth is tested for 3 times, and the rotary tillage depth is detected manually, and the walking speed of the rotary tiller is detected by a speed measuring instrument. Test data are shown in Table 5.

Table 5

Rotary tillage depth detection data

Depth setting	1 times/cm	2 times/cm	3 times/cm	Average error/%
8cm	8.2	8.1	8.4	4.3
9cm	9.3	9.6	9.1	3.6
10cm	10.2	10.6	10.5	4.5
11cm	11.3	11.7	13.6	3.7
12cm	14.7	13.9	14.8	3.9

The detection results of the above data show that the maximum average error of rotary tillage depth is 4.5%, which can meet the requirements of cultivated land. It can be seen from the data in table 5 that the rotary tillage speed of the three groups of tests is not much different, that is, the numerical control system of agricultural rotary tiller based on PLC technology works stably. In the simulation test, the accuracy of the test data from multiple test points is controlled within an acceptable range, which meets the requirements of field levelling.

Simulation and result analysis

The experiment simulates that rotary tillage parts move from off-the-ground state to specific tillage depth position (working condition 1) and the tillage depth needs to be adjusted according to the change of soil conditions (working condition 2). It is necessary to consider not only the working condition that the rotary tillage knife reaches the designated tillage depth from zero position when just started, but also the working condition that the soil structure changes and changes the tillage depth during the rotary tillage operation. At the same time, when the rotary tillage operation is considered, the rotary tiller encounters the sudden increase of soil resistance. During the simulation process, the soil load was 0.1 under normal conditions and kept for 2.5s seconds, and then the soil load suddenly changed to 0.25(KN). The changes of soil load change signal and tillage depth target set value signal are shown in Figure 6 and Figure 7 respectively.

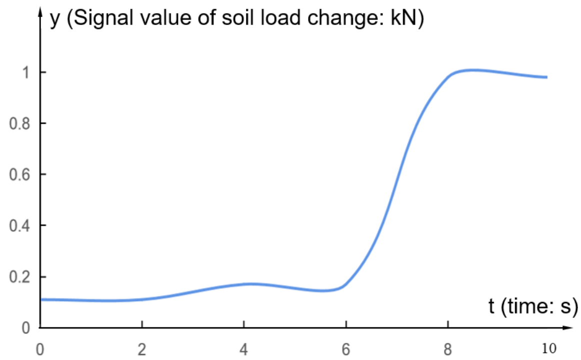

Fig. 6 - Soil load change signal

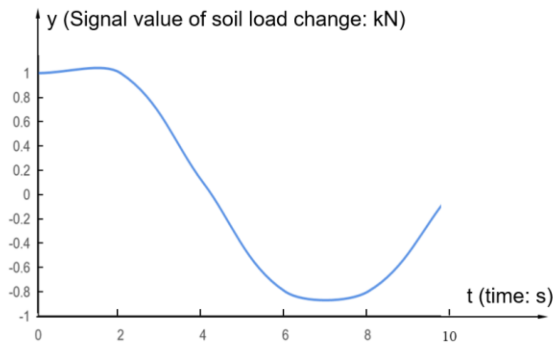

Fig. 7 - Ploughing target set value signal

The simulation results of overflow flow of rotary tiller hydraulic actuator system are shown in Figure 8.

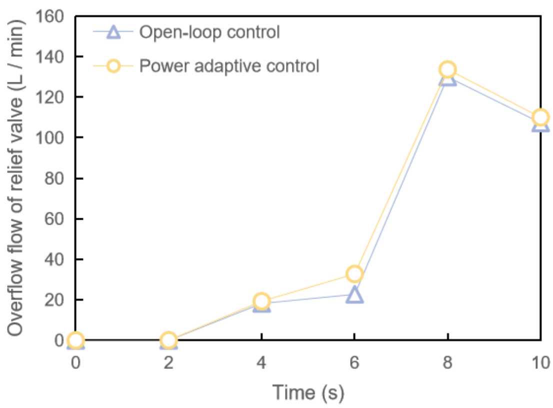

Fig. 8 - The simulation results of overflow flow of rotary tiller hydraulic actuator system

The analysis shows that when the rotary tiller blade reaches the designated tillage depth, the electro-hydraulic reversing valve loses power, and the system stops supplying high-pressure oil to the hydraulic cylinder (tillage depth control actuator), and all of it flows into the hydraulic motor that drives the rotary tiller blade shaft to rotate, thus causing a large overflow loss.

When the system working condition changes, the fuzzy control mode with comprehensive tillage depth value of force position can effectively improve the volumetric efficiency and power utilization rate of the hydraulic system of the rotary tiller, reduce oil consumption and improve operation efficiency.

The simulation results of hydraulic motor output speed are shown in Figure 9.

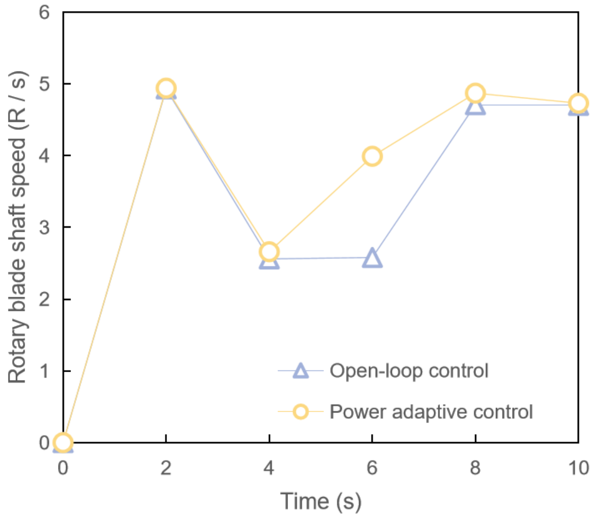

Fig. 9 - Simulation results of output speed of hydraulic motor

The analysis shows tht, when the soil resistance of the rotary tillage knife suddenly increases during the rotary tillage operation, the fuzzy control of force and position comprehensive tillage depth value can effectively improve the speed stability of the hydraulic motor for tillage depth control, reduce the speed fluctuation of the rotary tillage knife shaft and improve the system stability and the efficiency of rotary tillage operation under the condition of self-adaptive system power.

Comparative simulation analysis of hydraulic cylinders under working conditions 1 and 2 is carried out. Figure 10 below shows the comparison of simulation results of hydraulic cylinders under working conditions 1 and 2.

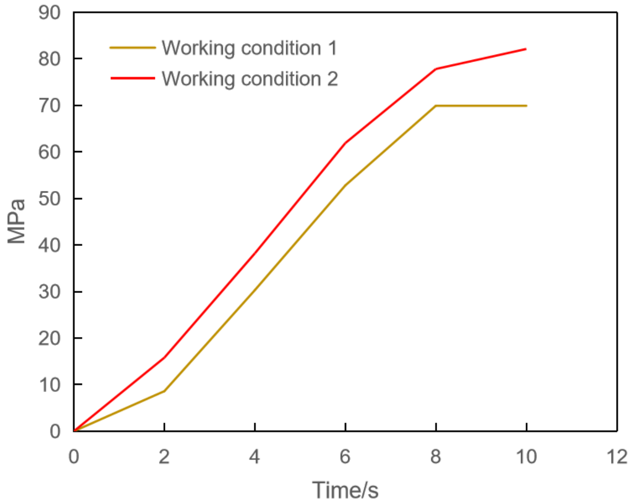

Fig. 10 - Comparison of hydraulic cylinder simulation results between working condition 1 and working condition 2

According to the simulation results of two working conditions, in the process of rotary tillage, after the rotary tiller blade reaches the designated tillage depth, the electro-hydraulic reversing valve loses power, the system stops supplying high-pressure oil to the hydraulic cylinder, and all of it flows into the hydraulic motor that drives the rotary tiller blade shaft to rotate, which will undoubtedly produce a large overflow loss and reduce the efficiency of the rotary tiller engine. In view of the low efficiency and low energy saving effect of the system, it is necessary to improve the parameters of the control system, optimize the control effect, improve the output efficiency of the rotary tiller engine, and reduce the oil consumption, so that the tillage depth control system can achieve better control effect.

CONCLUSIONS

In view of the present situation of agricultural land preparation technology, this paper takes the level automatic control system of tractor rotary tiller as the research object, and puts forward a new PLC system design for adjusting and controlling parameters of rotary tiller based on the application research of related technologies and agricultural machinery horizontal automatic control system. Experiments show that the rotary tiller control system based on PLC can effectively control the rotary tillage depth and speed, and the error of rotary tillage depth can be guaranteed within 4.5%. In the process of rotary tillage, when the soil resistance of rotary tillage knife suddenly increases, the fuzzy control of comprehensive tillage depth value of force position can effectively improve the rotational speed stability of hydraulic motor for tillage depth control, reduce the speed fluctuation of rotary tillage knife shaft and improve the system stability and efficiency of rotary tillage operation under the condition of self-adaptive system power. PLC technology puts the digital control of rotary tiller on a higher technical platform, reduces the labour required in agricultural planting, provides a good growth environment for crops, is beneficial to the improvement of crop yield, realizes the intelligence of rotary tillage operation, and provides a reference for modern agricultural mechanization production.

REFERENCES

[1] Ahmed I., Obermeier S., Sudhakaran S., (2017), Programmable logic controller forensics. *IEEE Security & Privacy*, Vol. 15, Issue 6, pp. 18-24. United States;

[2] Aliev E. B., Bandura V. M., Pryshliak V. M., (2018), Modeling of mechanical and technological processes of the agricultural industry. *INMATEH-Agricultural Engineering*, Vol. 54, Issue 1, pp. 95-104. Romania;

[3] Chen Y. L., Sun C. Y., Lu Z. S., (2018), Design of control system for spray chilling operation of pig carcass based on PLC. *Journal of agricultural engineering,* Vol. 034, Issue 003, pp. 273-278. USA;

[4] Du X., Yang X., Pang J., (2020), Design and test of automatic detection platform for soil fragmentation rate in rotary tillage. *International Journal of Agricultural and Biological Engineering*, Vol. 13, Issue 5, pp. 40-49. China;

[5] Huang Y., Chen Z., Tao Y. U., (2018), Agricultural remote sensing big data: Management and applications. *Journal of Integrative Agriculture*, Vol. 17, Issue 9, pp. 1915-1931. Netherlands;

[6] Ji J. T., Yang L. H., Jin X., (2019), Design of intelligent transplanting system for vegetable pot seedling based on PLC control. *Journal of Intelligent & Fuzzy Systems*, Vol. 37, Issue 4, pp. 4847-4857. Netherlands;

[7] Kerr W. C., Ye Y., Greenfield T. K., (2019), Changes in spirits purchasing behaviours after privatisation of government-controlled sales in Washington, *USA. Drug & Alcohol Review*, Vol. 38, Issue 3, pp. 294-301. United States;

[8] Ma L., Long H., Zhang Y., (2019), Agricultural labour changes and agricultural economic development in China and their implications for rural vitalization. *Journal of Geographical Sciences*, Vol. 29, Issue 2, pp. 163-179. China;

[9] Mariotte P., Mehrabi Z., Bezemer T. M., (2018), Plant–soil feedback: bridging natural and agricultural sciences. *Trends in Ecology & Evolution*, Vol. 33, Issue 2, pp. 129-142. United Kingdom;

[10] Minakov I. A., Nikitin A. V., (2019), Agricultural market development: trends and prospects. *International journal of innovative technology and exploring engineering*, Vol. 9, Issue 1, pp. 3842-3847. India;

[11] Pretty J., Benton T. G., Bharucha Z. P., (2018), Global assessment of agricultural system redesign for sustainable intensification. *Nature Sustainability*, Vol. 1, Issue 8, pp. 441-446. United Kingdom;

[12] Rasmussen L. V., Coolsaet B., Martin A., (2018), Social-ecological outcomes of agricultural intensification. *Nature Sustainability*, Vol. 1, Issue 6, pp. 275-282. United Kingdom;

[13] Storm H., Baylis K., Heckelei T., (2020), Machine learning in agricultural and applied economics. *European Review of Agricultural Economics*, Vol. 47, Issue 3, pp. 849-892. United Kingdom;

[14] Taheripour F., Tyner W. E., (2018), Impacts of possible Chinese 25% tariff on US soybeans and other agricultural commodities. *Choices,* Vol. 33, Issue 2, pp. 1-7. United States;

[15] Zhou Z., Ming R., Zang Y., (2017), Development status and countermeasures of agricultural aviation in China. *Transactions of the Chinese Society of Agricultural Engineering*, Vol. 33, Issue 20, pp. 1-13. China;

RESEARCH ON REMOTE OPERATING SYSTEM OF PICKING ROBOT BASED ON BIG DATA AND WIFI
/
基于大数据和 WIFI 的采摘机器人远程操作系统研究

Beibei Sun
Zibo Vocational Institute, Zibo, Shandong, 255314, China
**E-mail: rmw6625009@163.com*
DOI: https://doi.org/10.35633/inmateh-64-44

Keywords: *big data, WIFI, picking robot, remote operating system*

ABSTRACT
Agricultural mechanization has become the main mode of agricultural production and represents the development direction of modern agriculture. The amount of data generated in the agricultural production process is extremely huge, so it is necessary to introduce the concept and analysis method of big data. Combining agricultural robots with big data can improve the performance and application effect of robots. This paper combines big data, WLAN technology and robot technology to realize man-machine remote cooperation platform. This gives full play to the advantages that people are good at object recognition and robots are good at execution, and improves the fruit picking efficiency. The target fruit positioning and recognition system aided by machine vision is adopted to realize the accurate positioning of the fruit to be picked. Design of LFM control signal fitting based on big data clustering. In order to verify the feasibility of the scheme, taking the tomato picking robot as an example, the communication error and control accuracy using big data and WIFI (Wireless Fidelity) technology were tested, and the positioning and navigation efficiency with and without remote monitoring system was compared. Test results show that using big data and WIFI remote monitoring technology can effectively improve the efficiency and accuracy of positioning and navigation of remote operating system, which is of great significance for the design of automatic control system of picking robot.

摘要
农业机械化已成为农业生产的主要方式，代表了现代农业的发展方向。农业生产过程中产生的数据量巨大，有必要引入大数据的概念和分析方法。将农业机器人与大数据相结合，可以提高机器人的性能和应用效果。本文结合大数据、无线局域网技术和机器人技术，实现了人机远程协作平台。这充分发挥了人善于识别物体、机器人善于执行的优势，提高了采摘效率。采用机器视觉辅助的目标水果定位识别系统，实现对被采摘水果的精确定位。基于大数据聚类的 LFM 控制信号拟合设计。为了验证该方案的可行性，以番茄采摘机器人为例，利用大数据和 WIFI 技术对其通信误差和控制精度进行了测试，并对有无远程监控系统的定位导航效率进行了比较。试验结果表明，采用大数据和 WIFI 远程监控技术可以有效提高远程操作系统的定位导航效率和精度，对采摘机器人自动控制系统的设计具有重要意义。

INTRODUCTION
The 21st century is an era of information development. Computer technology, information collection and processing technology have made great progress, and have automatically entered the field of agricultural production. Under the new situation, the production mode and technology have greatly promoted the renewal and development of agricultural production, and further promoted the intelligentization of agricultural production *(Boesch A. et al., 2020)*. In this form, the field fruit picking robot has attracted the attention of agricultural production, and has become an important development direction of theoretical intelligent control of agricultural production. Therefore, in this form, it is of practical significance to explore the influence of field fruit picking robots on agricultural production.

There are many labor-intensive operations in agricultural mechanization production, among which fruit and vegetable picking is the most time-consuming and laborious link in the agricultural production chain with strong seasonality, complex working environment and high labor intensity.

As a large agricultural country, China needs to spend a lot of manpower and material resources every year, and with the aging of the population, China's agricultural labor force is gradually decreasing, resulting in a corresponding increase in agricultural production costs, which greatly reduces the market competitiveness of products *(Francois J. M. et al., 2020)*. Remote control technology enables people to completely control the controlled machine at the other end of the network through a simple terminal, thus realizing the information acquisition and powerful control function of the controlled machine at the other end *(Jin Z et al., 2020)*. Because of the complexity of the working environment of the picking robot, it is unrealistic to rely on the wired network to control the robot remotely. However, due to the limitation of transmission speed and distance, the application of traditional WIFI mobile network in remote control of picking robot is also limited *(Joppa M. et al., 2018)*.

The announced fruit harvesting robot has the characteristics of automation and intelligence, and achieved good research results, but the cost performance of the fully autonomous fruit harvesting robot is far from people's expectations. Robot experts deeply reflect on the research direction of autonomous robots, and think that due to the limitation of robot-related technologies, it is difficult to achieve the goal of developing robots that can work autonomously in complex environments for a long time in the future *(Krawczyk A. I. et al., 2020)*. More and more science and technology try to cross-integrate with network technology to realize the self-evolution of technology to meet the requirements of the new era. Distance education, teleconferencing and remote monitoring have gradually become an important part of life. Therefore, how to combine robots with big data Internet technology and develop commercially valuable robots by using existing or future technologies in the network has become an important subject in robotics. At present, in the classification of robot technology, teleoperation semi-autonomous robot is the closest technical direction to this form. Telerobot has been used in space, deep sea and dangerous operations, but there are few cases of its application in agriculture.

With the development of new generation information technologies such as cloud computing and Internet of Things, big data and WIFI technologies have been applied to various fields. Cloud platform adopts distributed storage mode and parallel computing, which can effectively improve the utilization rate of computing resources and reduce the cost of computing and storage resources through resource sharing. The advantage of WIFI transmission is that it is easy to regroup and maintain without connecting communication lines, but there are many difficulties in WIFI communication, such as unreliable WIFI channel, dynamic random attenuation characteristics of WIFI channel, weak anti-interference ability and so on *(Ma X et al., 2021)*. Therefore, a set of picking robot remote operating system based on big data and WIFI is designed, which can realize the navigation and remote control of picking robot.

The research of fruit picking robot is mainly divided into four directions: the visual system of picking robot, the design of picking execution terminal, the obstacle avoidance and motion planning of manipulator, and the navigation of robot in natural environment. The fruit picking robot works in unstructured environment, which requires the system to have high intelligence and intelligent behavior similar to human. At present, the visual system based on visible light is generally regarded as the most important environmental sensing component of fruit picking robot, which has the following functions: fruit target segmentation, recognition and positioning, recognition and positioning of obstacles such as vines, robot navigation, motion servo control based on visual feedback, etc.

In the control theory, the man-machine cooperation model can be understood as a closed-loop system with man as a feedback link, which is one of the earliest and most studied theoretical branches in teleoperation related technologies *(Mrozik D. et al., 2020)*. Man-machine interaction is the main research object of this research direction. How to provide efficient interactive interface and humanized input mode on the premise of as little data transmission as possible is a hot research issue.

Oktarina Y. et al., (2021) applied the feedback technologies such as prediction technology, augmented reality and virtual reality, and the input technologies such as advanced instruction and voice recognition realized the online control of two educational robots, and the interface had the characteristics of flexible control *(Olesen A. S. et al., 2020).* The design shared seven cameras, which put forward strict requirements for network quality. *Rahul T et al., (2019),* developed a remote teaching robot system by studying the remote control mode of robot. Due to the problem of network bandwidth, the visual field feedback is not ideal. The network-controlled robot in reference *(Wang Z. W. et al., 2019)* can be controlled to complete picking, placing and transporting operations.

Geng L. et al., (2020) developed a strawberry picking robot with a three-degree-of-freedom orthogonal coordinate system, which can be used for strawberry harvesting in ridge cultivation.

The eggplant harvesting robot developed by *Yi D., (2019),* picks eggplant in laboratory environment at an average speed of 64.1 seconds, with a success rate of 62.5%. The low picking success rate of the robot is mainly due to the long time consumption of data processing and the accuracy of visual positioning. *Krishnamurthy S. L. et al., (2020),* simplifies the working environment of the robot by adopting the principle of agricultural mechatronics, and designs a cucumber picking robot, which collects at an average rate of 45 seconds, with a success rate of about 80% and a visual inspection success rate as high as 95%. The software and hardware performance of the platform affects the picking rate. *Li Y. B. et al., (2020),* developed a field strawberry picking robot with Cartesian structure. Two sets of cameras were used for rough positioning and target detail detection. Under normal circumstances, the correct rate of strawberry recognition is 93.6%, but in complex environments such as blocked light, the recognition rate is 70.8%, and picking a single strawberry takes 16.6 seconds, which is still subject to visual problems.

To sum up, the technology of fruit and vegetable picking robot is one of the most dynamic research hots pots in the world, but most of them are still in the laboratory research stage, and there are no products available for practical production. At home, the research in this field has just started, and compared with the international advanced level, there is still a big gap. It is urgent to intensify efforts to speed up the research work in this field, catch up with and surpass the research pace of international counterparts, and meet the actual needs of China's agricultural modernization development.

MATERIALS AND METHODS

Big data processing process

Big data is a collection of data collected by machine vision, GPS positioning and sensors, which contains information related to robot operation and can be obtained through a series of analysis and processing processes. The analysis process of big data involves the entry and reading of PB-level data, so large-scale modeling and calculation are needed. The big data analysis hardware carried by the robot is a PC Server type server with x86 architecture, and the configuration includes Ruilong AMDRYZEN 7 type 2-way 8-core CPU, DDR4 type 128GB memory and Intell350T2 type Gigabit network card, which can meet the actual requirements in terms of computing speed and storage space. This technology can run a simple parallel computing model, has strong fault tolerance and scalability, and has a good analysis and processing effect on large-scale data.

The data collected by various devices carried by the robot enter the switch through the network and transmission interface, and the switch is connected with the data collector to perform the functions of data exchange and convergence, and finally transmit to the big data processor. The above transmission process implements IEEE1588 time synchronization protocol, which can reduce the exchange delay and improve the real-time and accuracy of data. On this basis, carry out follow-up analysis and processing. The analysis process of big data includes preprocessing, content analysis, information mining and result display in turn, realizing the data-centered analysis mode.

In view of the diverse features of big data structure, parallel processing is adopted to improve the analysis speed. The processing of big data is shown in Figure 1.

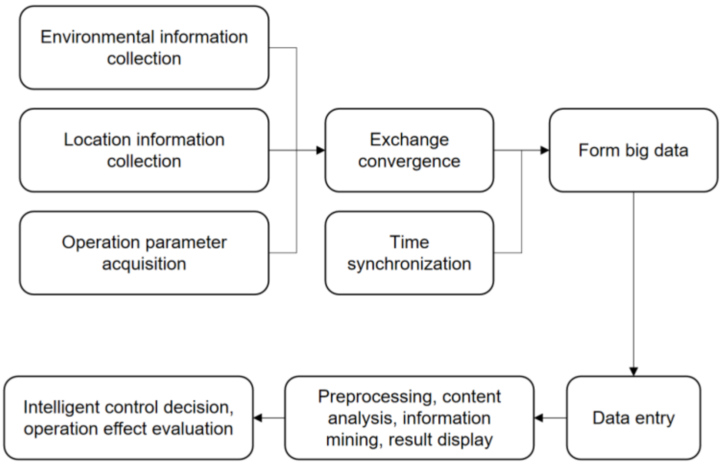

Fig. 1 - Big data processing process

Parallel processing is to comprehensively monitor and classify big data in real time while recording data, and distribute data to corresponding application systems according to types; Then, run the decision-making aided by professional knowledge base to provide the basis for information mining; Finally, the results of comprehensive monitoring, analysis and processing are gathered into the storage and management module to form an application function database, form the intelligent control decision of the robot, and evaluate the operation effect.

Linear frequency modulation control signal fitting based on big data clustering

Firstly, the distributed structure model of big data in control system is established. According to the concept of fuzzy control, the fuzzy control of big data in control system is studied, and the limited data set of massive control data in control system is established as:

$$Y = \{y_1, y_2, \cdots, y_n\} \subset R \tag{1}$$

In which Y represents a finite data set; n represents the number of samples included in the big data distributed structure model in the control system; R represents the vector space of big data clustering under arbitrary norm. When the clustering channel fitting factor of the finite data set Y is 0, the formula (2) is satisfied at this time:

$$\rho(y) = \frac{2}{1 + \exp\left|-h \cdot \mathrm{sgn}(y)\right|} \tag{2}$$

In the formula, ρ represents the clustering channel fitting factor; h represents the iteration times of big data clustering; sgn stands for symbolic function. In the distributed structure of big data in control system, there is an iterative function of fuzzy control, and the function can converge the clustering center of data. When the control system is in a state where the initial value of the cluster center is unknown, the distributed structure of big data in the control system will simulate the control data with nonlinear and time-varying LFM control signals, thus providing help for basic feature extraction and realizing the optimal clustering of data.

Then, using the fitting idea of fuzzy control and industrial robot control system, the LFM signal of big data information flow in the control system is fitted and processed, and the big data information characteristic points of the control system are calculated by combining the big data clustering algorithm. The formula is:

$$X(a,b) = \sum\left[(a_i, b_i) - (a_i + \Delta a b_i + \Delta b)\right]^2 \tag{3}$$

In the formula, $X(a,b)$ represents the feature point function; $\triangle a$ and $\triangle b$ represent the two-dimensional characteristic displacement of big data information flow of control system; (a_i,b_i) denotes chirp characteristics. According to formula (3), the fitting of LFM control signal in the control system is completed.

WLAN topology

As shown in fig. 2, there are three topologies of WLAN, which are basic service set, independent basic service set and extended service set:

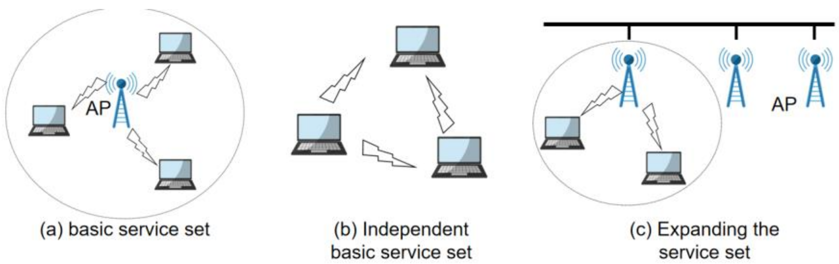

Fig. 2 - WLAN topology

The central station of BSS (Basic Service Set) is a WIFI access point. All network devices connected to the access point are controlled by it, and its network structure is shown in Figure 2(a). Due to the power limitation, the coverage of each WIFI access point is very limited, so this structure is suitable for the network demand with little service space. The disadvantage of this structure is poor reliability, and the failure of WIFI access point will lead to the collapse of the whole network.

IBSS (Independent Basic Service Set) network has no central node, and its basic network structure is shown in Figure 2(b). IBSS network, also known as P2P network or Ad-Hoc network, is a dynamically built WIFI network. All nodes in the network are equal, interconnected by the same identification number and password, and all nodes communicate through CSMA/CA MAC protocol on a common channel to realize point-to-point and point-to-multipoint communication.

ESS (Extended Service Set) is a WIFI communication structure established for the small coverage of BSS, which meets the network requirements of large space coverage. The structure is shown in Figure 2(c). In fact, this structure is to connect multiple BSS networks to realize the expansion of BSS networks.

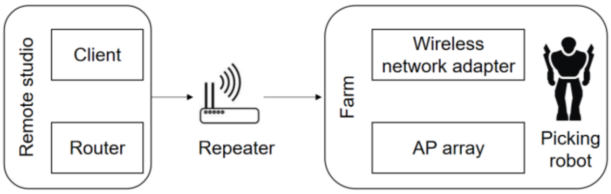

Fig. 3 - WLAN deployment scheme

The robot platform developed in this paper will be applied in the field. Because the field occupies a large area, it is difficult to achieve full coverage of signals by BSS structure, so ESS structure is adopted to deploy the network. As shown in the WLAN deployment scheme in fig. 3, the solid line is wired connection and the lightning symbol is WIFI connection. WIFI relay can greatly extend the coverage of WLAN, and information transmission between buildings with a distance of more than 500 meters can be realized through a pair of relays, which provides support for monitoring fruit picking robots in the office.

Positioning algorithm of picking robot

When the picking robot is positioned, in order to make the robot respond quickly, it can use machine vision and adopt the multi-hop self-organizing WIFI network node positioning model algorithm, and can get the information of picking targets or fruits to be picked in advance, and these positions' information can be marked with sensor nodes in advance. It is assumed that the picking operation area is a two-dimensional spatial area plane, and there is a sensor network in the area plane, which can be expressed as $S=\{S_1,S_2,\cdots,S_{m+n}\}$. Where m represents the marked position node; n represents an unmarked location node. Positioning coordinates can be expressed as:

$$pos(S_a)=(x_a,y_a)T, P=1,\cdots,m+n \tag{4}$$

Among them, the position of $S_i \in B$ has been marked, and the positions of other nodes $S_j \in U$ are unknown; $B=\{S_{i|i=1,2,\cdots,m}, S_{i|i=m+1,2,\cdots,m+n}\}$, the minimum hop count and distance collected at the marked position are respectively stored in two sets of data sets. The hop count from node S_i to S_j is:

$$h(S_i,S_j)=H=\{0,1\cdots\} \tag{5}$$

The euclidean distance from node S_i to S_j is:

$$d(s_i,s_j)=\sqrt{(x_i-x_j)^2+(y_i-y_j)^2} \tag{6}$$

The positioning nodes of the picking robot are distributed in the multi-hop self-organizing network to form a dynamically distributed real-time positioning virtual environment, which can lock the position of the fruit to be picked. This design adopts tree network structure, the self-organizing network is equivalent to trunk, and the positioning node is equivalent to branch. Among them, the main part of multimedia information is equivalent to leaves, while the redundant part of data is dynamically allocated to the leaf structure. The tree structure function is expressed by F, and the following structural tree formula is generally adopted as:

$$H(e,f,k)=\begin{cases} F(f_c)(e=f) \\ F\left(\left(H\left(e,\frac{e+f-1}{2}\right),F,\left(H\left(\frac{e+f+1}{2}\right),j,F\right)\right)(e<f)\right) \end{cases} \tag{7}$$

Among them, e,f represents the signal strength with or without interference, and when $e=f$, the communication ability is the best; When $e<f$ is used, the signal needs to be denoised.

Assuming that the virtual storage space of the multi-hop network positioning node is represented by $S=[S_1,S_2,\cdots,S_i]^T$, the expression of the branch structure is:

$$Q(S)=\prod_{i=1}^{n}Q(S_i) \tag{8}$$

The multi-hop self-organizing network of picking robot will consume a lot of energy in the positioning process, and the maximum allowable distance of power loss is:

$$y=\frac{Y_m-Y_n-Y_c-2K_p-L_p}{\lambda_a-\lambda_b} \tag{9}$$

In which Y_m represents completely lost power; Y_n represents the receiving sensitivity in case of interference; Y_c represents WIFI rate; λ_a, λ_b respectively represents WIFI consumption coefficient; K_p represents the loss at the interface; L_p indicates the maximum communication rate of multi-hop ad hoc network.

Among them, the communication limit distance of ad hoc network is:

$$S=\frac{P}{k} \tag{10}$$

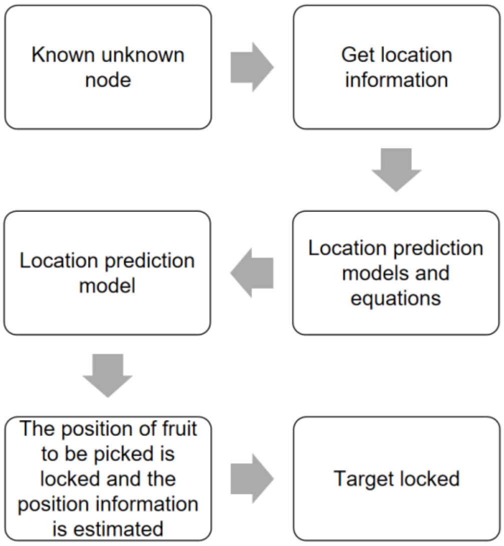

Fig. 4 - The flow of determining the location node of picking robot

The prediction model is obtained from the obtained estimation items. When positioning, not only the known positioning nodes can be directly positioned, but also the coordinates of unknown nodes can be calculated. The process is shown in Figure 4. By substituting known positioning nodes into the ranging model, the corresponding distance information can be obtained, and by combining the position coordinates and distance information of known nodes, the location area of unknown nodes can be estimated, and finally the area to be picked can be locked.

Design of WIFI data transmission program for picking robot

In the WIFI data transmission part of picking robot, the master-slave WIFI receiving programs all adopt interrupt response mode, which saves system overhead and has good real-time performance. The sending program is written in the form of function module and can be called directly. After receiving the data, the communication host WIFI repackages the USB and outputs it to the robot control computer, so that it can make a judgment and issue a control command. The flow chart of picking robot WIFI transceiver program is shown in fig. 5.

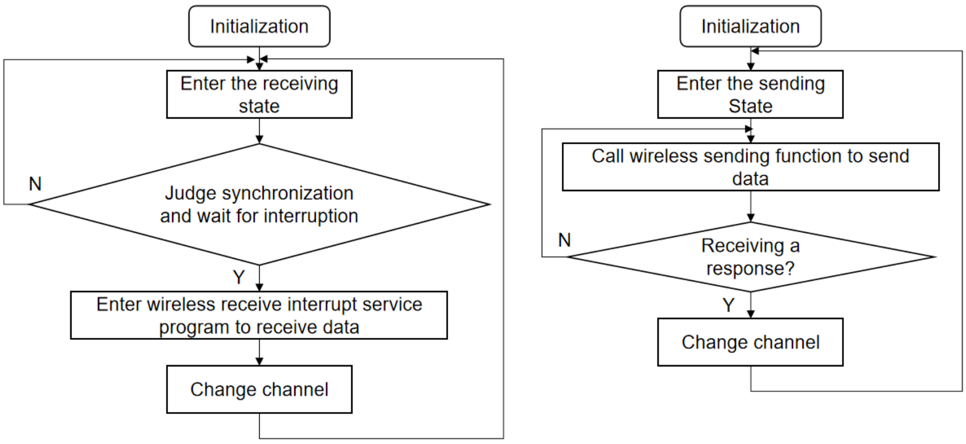

Fig. 5 - WIFI transceiver program flow chart of picking robot

Interactive interface based on depth image

At present, the interactive flow of the control interface of the picking robot system is mainly process-oriented. Process-oriented interaction process is that after analyzing the goal of the task, people interact with the robot step by step according to the process of achieving the goal, and control the robot to complete the task according to the process [26]. The disadvantage of the operation mode based on this idea is that users are forced to disassemble the task objectives into the combination of small tasks, and pay attention to the details of task execution in the process of task execution, so they cannot divert their attention to other places before a task is completed. This operation mode is extremely dependent on people's familiarity with the system, relevant operation experience and people's attention.

How to clearly point out the operation object to the robot is a problem that human-computer interaction tries to solve. For autonomous control robots, the object model description method is generally adopted, which requires the invariant features that can fully describe the object and can be understood by the machine. If we take direct control, we can avoid the description of the operation object, but it is too cumbersome to directly control the movement of every joint of the robot.

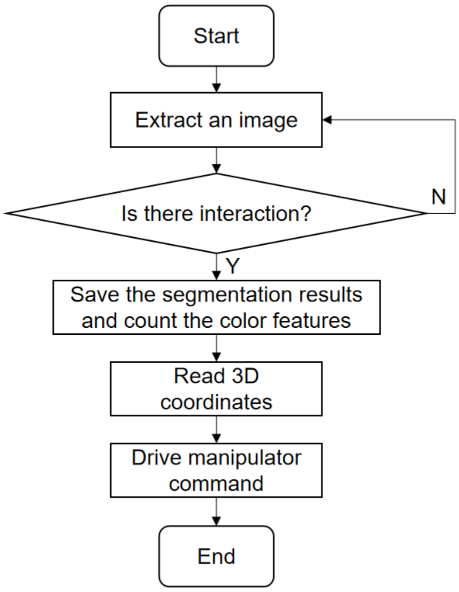

Fig. 6 - Interface interaction flow based on depth image

Fig. 6 is an interactive flow chart, in which the interface continuously displays the latest robot visual field image in the cache, and when the user's interactive action is sensed, it is fixed in the frame to wait for the interaction to end. The user selects the target on the image with the mouse circle, and the system uses the interactive results to segment the image by flooding in the background, and performs the following actions.

Save the segmentation results and provide picking object samples for subsequent research

The color features of segmentation results are counted to provide support for image segmentation algorithms. After reading the three-dimensional coordinates of the object corresponding to the segmentation result from the server, and confirming that it does not exceed the motion range and whether it will cause the interference of the mechanical body, the command to drive the mechanical arm is issued, so that the motion control module of the robot on-site server can pick the fruit.

RESULTS

The contradiction between the rapid development of fruit and vegetable production and the shortage of agricultural labor force and excessive labor intensity has become increasingly apparent, and the complex human labor of replacing selective harvesting can only be realized through the in-depth study of picking robot technology. The research and development of fruit and vegetable picking robot is of great significance for reducing the labor intensity of agricultural practitioners, liberating agricultural labor and improving the intensive production level of fruits and vegetables.

Tomato is the favorite of people from all over the world, and it is also the most demanding fruit and vegetable in the world. However, the non-human harvest of fresh fruit is one of the most difficult operations. At the same time, tomato is also one of the most difficult fruit and vegetable varieties picked by robots. At present, facing the demand of fresh food, common tomatoes are usually picked with single fruit, while cherry tomatoes are picked in clusters. For most common tomato varieties and cultivation methods at present, compared with fruits and vegetables such as cucumber, eggplant and apple, there are 3~5 tomato fruits per ear, which grow densely and touch each other, and the difference of fruit growth orientation is more significant, thus posing a greater challenge to the intelligent picking of robots.

The close and overlapping occlusion between fruits is more serious. For the vision system of the picking robot, although the mature tomato fruits can be easily identified by color difference, it is difficult to segment or even completely block the images of multiple fruits, which makes it difficult to identify and locate the target fruits. Tomatoes grow into ears and touch each other, which causes the clamping space of the picking robot to the target fruit to be limited, the clamping action fails or the adjacent fruit is bruised; The growth orientation of tomato fruit varies greatly, and the relationship between posture and force changes every time; The fruit stalks are short and different in length, which makes it difficult for the mechanical cutter to cut the fruit stalks smoothly. However, the mechanical action law of twisting and breaking the fruit stalks changes greatly, and the success rate is limited, which further increases the difficulty of picking.

In this section, the remote operating system of picking robot based on big data and WIFI designed in this paper is applied to tomato picking robot and analyzed. The tomato picking robot is shown in Figure 7.

Fig. 7 -Tomato picking robot

In order to realize the autonomous walking of the automatic guided vehicle of the picking robot, the most important thing is that the front-end acquisition equipment identifies the picking environment to plan the autonomous walking route and access the video information in the server, which can be divided into data flow and information flow according to different functions, as shown in Figure 8.

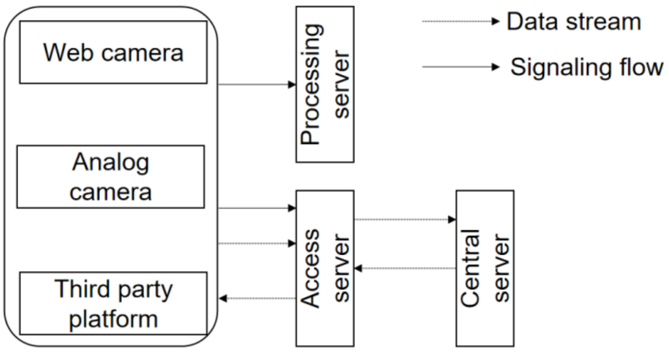

Fig. 8 - Frame diagram of video acquisition system

In order to reduce the burden of the front-end camera, the video stream is not directly sent to the streaming media server, but accessed to the platform first, so as to facilitate different customers to access the same stream. By collecting the picking environment and identifying the route of the cloud platform server, the picking robot can automatically guide the AGV system to carry out route planning, so as to realize autonomous walking. The walking route can also be displayed on the GIS map in real time, and the remote monitoring system can make reasonable scheduling according to the operation situation of the picking robot.

The tomato picking robot has a guide car as its carrier, which can navigate autonomously during formation and scheduling, and the remote system can make reasonable scheduling and planning according to the real-time position of the guide car equipment. In order to verify the influence of remote monitoring system and WIFI control system on the operation effect of picking robot, and to test the reliability of monitoring and control system, the communication error and control accuracy of monitoring and control system were measured respectively, and the operation situations of using and not applying monitoring and control system were compared. Test results of communication error and control accuracy are shown in Table 1.

Table 1

Statistical results of communication error and control accuracy

Statistical serial number	Communication error packet loss rate %	Navigation accuracy/ %
1	0.25	98.3
2	0.27	99.1
3	0.33	97.5
4	0.28	98.5

Through the statistical results of many tests, it can be seen that the communication error of the remote monitoring and control system is low, the maximum error is not more than 0.5% according to the packet loss rate, and the navigation accuracy of the automatic guided vehicle of the picking robot is over 90%, which meets the design requirements of the automatic guided equipment of the picking robot.

Table 2

Comparison of positioning and navigation efficiency

Statistical serial number	Use remote monitoring and control system to locate time /s	Positioning time without remote monitoring and control system/s
1	3.36	5.67
2	3.25	5.82
3	3.29	5.90
4	3.55	5.64

Table 2 shows the comparison results of positioning and navigation efficiency of picking robot with and without remote monitoring and WIFI control system. It can be seen from Table 2 that the navigation efficiency of picking robot using remote monitoring and control system is high, which verifies the feasibility of the scheme.

CONCLUSIONS

In view of the dilemma that the autonomous fruit and vegetable picking robot still can't meet the market requirements after a lot of research, a fruit picking robot system based on big data and WIFI is designed by combining WLAN and fruit picking robot platform. WLAN is one of the most widely used WIFI communication means at present, and it is the best choice for civil teleoperation system in terms of technology, maturity of framework and economy. Communication between PC and picking robot is realized. When working, the picking robot sends its own position and motion information to the background PC, which uses big data technology to analyze the running status of the picking robot and provide reference information for the remote control of the picking robot. The communication error and control accuracy of the system are tested. The results show that the communication error of the system is small and the control accuracy is high, which can meet the design requirements of the remote system of the picking robot. Finally, the positioning and navigation efficiency is tested, and the results show that the WIFI control system based on big data technology has high positioning and navigation efficiency, which plays an important role in the design of automatic control system of picking robot.

REFERENCES

[1] Boesch A., de Montmollin A., (2020), Indicators for assessing the sustainability of cities. *Sustainability Assessments of Urban Systems*, pp. 311. Poland;

[2] Francois J. M., Alkim C., Morin N., (2020), Engineering Microbial Pathways for Production of Bio-Based Chemicals from Lignocellulosic Sugars: Current Status and Perspectives. *Biotechnology for Biofuels,* Vol. 13, Issue 1, pp. 1-23. England;

[3] Geng L., Wang Y., Wang J., (2020), Numerical simulation of the influence of fuel temperature and injection parameters on biodiesel spray characteristics. *Energy Science & Engineering,* Vol.8, Issue 2, pp.312-326, USA;

[4] Jin Z., Sun W., Zhang J., (2020), Intelligent Tomato Picking Robot System Based on Multimodal Depth Feature Analysis Method. *IOP Conference Series Earth and Environmental Science*, Issue 440, pp. 042074. United States;

[5] Joppa M., Köhler H., Kricke S., (2018), Simulation of jet cleaning diffusion model for swellable soils. *Food and Bioproducts Processing*, Vol.113, pp. 168-176, Netherland;

[6] Krawczyk A. I., Van Duijvendijk G. L. A., Swart A., (2020), Effect of rodent density on tick and tick-borne pathogen populations: Consequences for infectious disease risk. *Parasites & Vectors*, Vol. 13, Issue 1, pp. 1-17. England;

[7] Krishnamurthy S. L., Pundir P., Warraich A. S., (2020), Introgressed saltol QTL lines improves the salinity tolerance in rice at seedling stage. *Frontiers in plant science*, Issue 11, pp. 833. Switzerland;

[8] Li Y. B., Li H., Guo X., (2020). Online Parameter Identification of Rice Transplanter Model Based on Ipso-Ekf Algorithm. *INMATEH Agricultural Engineering*, Vol.61, Issue 2, pp.25-34, Romania;

[9] Ma X., Zhou J., Zhang X., (2021), Design of a New Catheter Operating System for the Surgical Robot. *Applied Bionics and Biomechanics*, Vol. 2021, Issue 1, pp. 1-9. Netherlands;

[10] Mrozik D, Mikolajczyk T, Moldovan L., (2020), Unconventional Drive System of a 3D Printed Wheeled Mobile Robot. *Procedia Manufacturing,* Issue 46, pp. 509-516. United States;

[11] Oktarina Y., Dewi T., Risma P., (2021), BLOB analysis of an automatic vision guided system for a fruit picking and placing robot. *International Journal of Computational Vision and Robotics*, Vol. 11, Issue 3, pp. 315. United States;

[12] Olesen A. S., Gergaly B. B., Ryberg E. A., (2020), A Collaborative Robot Cell for Random Bin-picking based on Deep Learning Policies and a Multi-gripper Switching Strategy. *Procedia Manufacturing*, Issue 51, pp. 3-10. United States;

[13] Rahul T., Reddy K. T., Mary A., (2019), Cost Effective Robotic System Using Arduino. *Journal of Computational and Theoretical Nanoscience,* Vol. 16, Issue 8, pp. 3222-3227. United States;

[14] Wang Z. W., (2019), Research and Analysis of Obstacle Avoidance System of Picking Robot Based on Fuzzy Control System. *Agricultural mechanization research*, Vol. 041, Issue 001, pp. 230-233. Japan;

[15] Yi D., (2019), Research State and Trend of Fruit Picking Robot Manipulator Structure. *International Equipment Engineering and Management: English Version*, Issue 1, pp. 36-50. United States.

DETECTION OF BEHAVIOUR AND POSTURE OF SHEEP BASED ON YOLOv3
/
基于YOLOv3的绵羊行为姿态检测

Xuefeng Deng*[1)], Xiaoli Yan[2)], Yiming Hou[1)], Hui Wu[1)], Chenru Feng[1)], Lingyu Chen[1)], Maoxing Bi[1)], Yi Shao[1)] [1]

[1)] College of Information Science and Engineering, Shanxi Agricultural University, Taigu / China

[2)] Taiyuan Jinshan Middle School, Taiyuan / China

Tel: 13546632115; E-mail: dxf@sxau.edu.cn

DOI: https://doi.org/10.35633/inmateh-64-45

***Keywords:** YOLOv3, Posture recognition, Object detection, Sheep posture*

ABSTRACT

The behaviour and posture of animals are closely related to their physiological conditions. To some extent, we can judge their physiological activity by their behaviour and posture. Sheep's behaviour change significantly during illness or parturition, these behaviours are composed of simple postures, such as standing, eating, lying down. This paper takes the YOLOv3 algorithm as the core technology. It extracts features of sheep's behaviour and posture through constructing the deep network structure, and uses the pyramid feature fusion and multi-scale prediction to detect the behaviour and posture of sheep. The experimental results show that the training model can effectively detect the three behaviours and postures of sheep: standing, eating, and lying down. The mean average precision is 92.47%. This experiment can be used as a basic technology to judge the physiological activities of sheep. It can be applied to the intelligence of animal husbandry, and has a broad application prospect.

摘要

动物的行为姿态与其生理状况息息相关，通过动物的行为姿态可以在一定程度上判断其生理活动。绵羊在出现疾病或分娩时其行为会有显著的变化，这些行为由站立、进食和躺卧等简单姿态的组合而成，本文以YOLOv3算法作为核心技术，通过构建深层网络结构，提取绵羊行为姿态特征，采用金字塔特征融合和多尺度的预测对绵羊行为姿态进行检测。经实验表明，训练的模型可以有效检测出绵羊的站立、进食、躺卧三种行为姿态，平均精度均值达到了92.47%。本实验可以作为判断绵羊生理活动的一种基础技术，可以应用到畜牧业智能化中，具有广阔的应用前景。

INTRODUCTION

The behaviour of animals is closely related to their physiological conditions. The behaviour detection of animals can judge their physiological activities to a certain extent *(He et al., 2016).* It is the core content of accurate animal husbandry. For example, feeding, excretion and drinking behaviour of animals are an important basis for judging animal health. When animals excrete, feed and drink too frequently, this means that they may have diseases such as viral diarrhoea and infectious gastroenteritis *(Zhu et al., 2010)*. When the animal often appears chewing without food, lying down, walking back and forth, constantly looking back at the abdomen and other behaviours, it means that the animal is during pregnancy. Accurate detection and analysis of animal postures is a basic process of animal behaviour detection. Animal behaviours show different combinations of postures. Sheep is a common breeding animal. In the process of feeding, posture recognition of sheep can make a relatively objective evaluation of its growth, health and pregnancy state, and can timely take effective measures such as prevention and treatment, human intervention and other effective measures, so as to reduce the loss to the minimum.

With the development of artificial intelligence technology, intelligent methods can be used to detect and classify animal postures. Because traditional animal husbandry relies on the continuous observation of the breeders and their own experience to judge illness or parturition time of animals and so on, this will cause heavy labour burden, low work efficiency, and also increase the transmission rate of zoonosis, so it is very necessary to use intelligent means to conduct behaviour detection.

[1] *Xuefeng Deng*, assoc.prof, PhD; Xiaoli Yan, Lec, M.Eng.; Yiming Hou, undergraduate; Hui Wu, undergraduate; Chenru Feng, undergraduate; Lingyu Chen, undergraduate; Maoxing Bi, undergraduate; Yi Shao, undergraduate.*

At present, there is a variety of algorithms widely used in animal posture detection.

Xue et al., (2018), solved the difficulties in posture recognition of suckling sows caused by the changes of light and thermal light lines in the environment with day and night alternation and the attachment between sows and piglets in the free pen scene. Taking the deep video image as the data source, they proposed an improved Faster R-CNN posture recognition algorithm for suckling sows. That is, through end-to-end training network, at the same time, the detection of lactating sows and the classification of five postures, such as standing, sitting, prone lying down, abdominal lying down, side lying down and so on, are realized. Although the speed of the algorithm is fast, the accuracy is not high.

To solve the problem of the low degree of automatic detection of pig crossing behaviour at present, *Li et al., (2019),* proposed a crawling behaviour of pigs recognition algorithm based on Mask R-CNN. By obtaining the top view image of the pig, using LabelImg to make the data set label, and introducing the transfer learning method to train the ResNet-FPN network, the pig segmentation results were obtained and the mask pixel area of each sample is extracted, but the algorithm is slow in image processing and takes a long time.

Ye et al., (2019), proposed a test method based on Faster-RCNN. When broilers are in stun state, make use of Convolution neural network to extract broilers' features. The speed of this algorithm can meet production needs, but its training speed is low and its occupancy space is big.

Zhuang et al., (2020), proposed a convolutional neural network algorithm for recognizing the oestrus behaviour of large white sows in view of the characteristics such as the erect ears of large white sows during the oestrus test. By collecting the ear images of large white sows in oestrus test and non-oestrus test, the training set samples (80%) and validation set samples (20%) were divided for later training. The algorithm has a high recognition rate, but its speed is still low and has the disadvantages of spending too long time. In recent years, intelligent methods have been introduced in feeding sheep to analysis and research sheep's behaviour, so it can promote production process intelligentization. For example, *Fogarty et al. (2020)* proposed a sheep behaviour classification method based on machine learning. It can identify sheep's behaviour such as grazing, lying down, standing, walking and so on by machine learning. The combination of these postures can identify sheep's many behaviours.

Sun et al. (2019) research sheep parturition behaviour and get Faster-RCNN model based on Soft-NMS algorithm and VGG16 feature extraction network which can detect sheep's parturition behaviour well. *Salama et al. (2019)* proposed a sheep identification method based on deep learning and Bayes optimization. It uses Bayes optimization algorithm to set convolutional neural network parameter automatically, so it can identify sheep's face in order to achieve the goal of identifying sheep.

Ma et al. (2020) researched sheep identification location and proposed a Faster-FCNN neural network model based on Soft-NMS algorithm, which can real time monitor and locate sheep in complex raise conditions.

In sheep research above artificial intelligence algorithms there are problems such as computational efficiency and running space, during animal identification and monitoring.

This paper adopts YOLOv3 to identify sheep's postures. It uses Labellmg tool to annotate sheep's postures such as standing, feeding, lying down. Through training, it generates YOLOv3 network which can identify relevant postures. This algorithm has the characteristics of fast detection speed and high accuracy. It is close to real-time detection and provides a technical solution of artificial intelligence method applied to sheep feeding.

MATERIALS AND METHODS

Image acquisition of behaviour and posture of sheep

Collection of experimental data on a sheep farm in Lianbai Village, Hejin City, Shanxi Province, which covers an area of about 40m*25m and raises a variety of sheep such as Australian white sheep, Suffolk sheep, Dorper sheep, Small-tailed Han sheep and Hybrid sheep. Considering the influence of different illumination on the establishment of the model, we take photos in the morning and afternoon respectively to ensure that the number of pictures under different lighting conditions is the same.

Since April 3, 2021, three hours of pictures have been taken in the morning and afternoon, for five consecutive days, and 1500 images have been collected as data sets. The images collected include three behaviours and postures of sheep: eating, standing and lying down, as shown in Figure 1.

Fig. 1 - Three Behaviours and Postures of Sheep

<u>Sheep postures image data preprocessing</u>

Data preprocessing mainly includes the following processes: data filtering, data enhancement and data annotation. The data preprocessing process is shown in Figure 2.

Data filtering mainly refers to the uniform selection of pictures of sheep with different behaviours and postures in different time periods, different illumination intensity and different shooting directions. 1000 pictures were selected in this experiment. Data enhancement mainly involves random flipping, random rotation, random clipping, and random scaling of the image. In this experiment, some pictures are randomly symmetrically flipped so as to enhance the state information of sheep in different positions. Data annotation is to classify and label the original image. The corresponding labels of different postures such as eating, standing and lying down are marked respectively, preparing for further data processing.

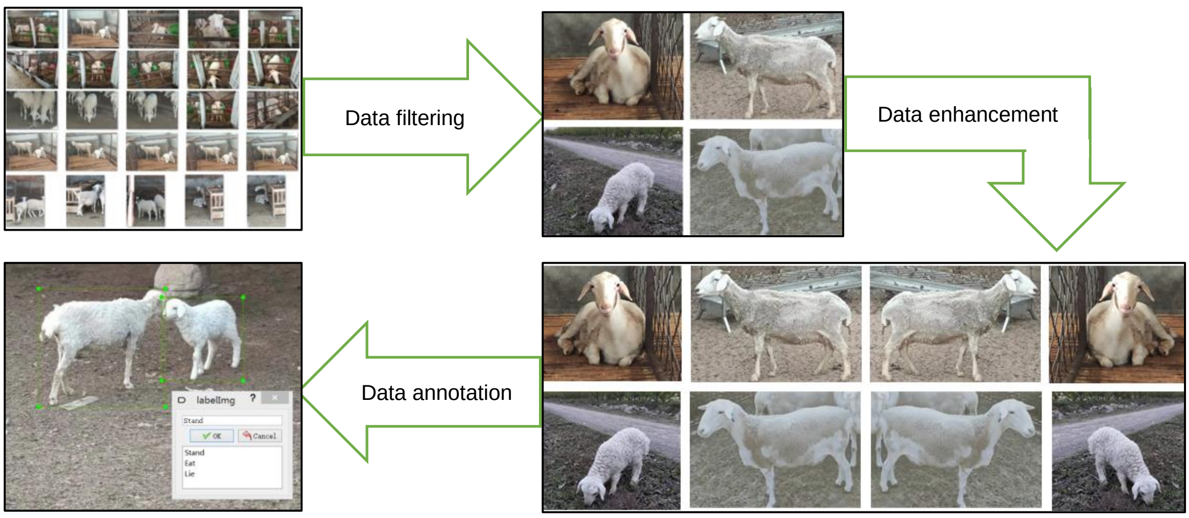

Fig. 2 - Data Preprocessing Process of Sheep Posture Images

<u>Introduction of behaviour and posture recognition methods for sheep</u>

This paper uses the YOLOv3 algorithm and Darknet-53 network model to detect behaviour and posture of sheep. The flow of sheep behaviour and posture detection method is shown in Figure 3.

In the data input part, the pre marked data is used as input. The Labellmg image annotation tool was mainly used to label the standing, eating and lying behaviour and posture of sheep. Then save the label information marked on the picture to an XML file accordingly. In the part of constructing feature extraction network, a reasonable feature extraction network is selected to meet the needs of detection. In this paper, D is used as the network structure for posture feature extraction. Feature fusion and posture prediction mainly use YOLOv3 algorithm to build the relevant network structure and complete the later processing. Finally, after selecting the optimal prediction result, input the posture detection result of sheep.

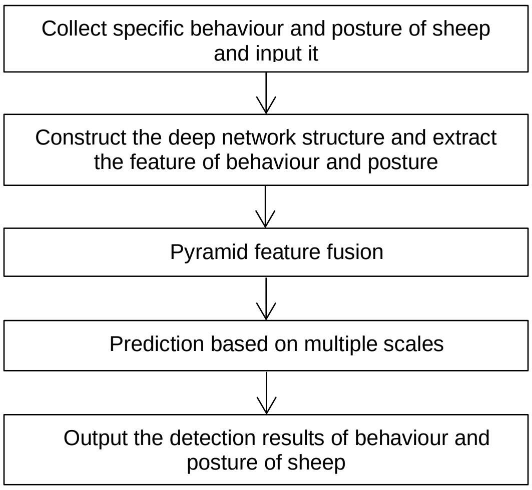

Fig. 3 - Detection Process of Behaviour and Posture of Sheep

RESEARCH METHOD OF SHEEP POSTURE DETECTION

Introduction of YOLOv3 algorithm

As we all know, a more accurate and faster object detection algorithm is the primary principle of our algorithm selection. YOLO series algorithm is a popular algorithm in the field of object detection, YOLOv3 is a masterpiece of integrated SSD (multi-scale prediction), FCN (full volume machine), FPN (feature pyramid), DenseNet network (feature channel concat). It is a typical representative of a single-stage object detection algorithm. Compared with two-stage algorithms such as Fast RCNN, the YOLO series algorithm abandons the step of candidate region extraction, and only uses a one-level network to complete object detection and location, which can complete the object detection task at near real-time speed*(Sun et al., 2021)*.

YOLOv3 is an object detection model based on Darknet-53 proposed by Joseph Redmon et al. The essence of object detection is recognition and regression. YOLOv3 combines the Darknet-53 network model with the feature pyramid model as the backbone network. At the same time, it also introduces the more advanced Resnet residual network, which is helpful to solve the problem of gradient disappearance and the explosion of a deep network *(Pan et al., 2021).* The method of feature pyramid is used in the object detection of theYOLOv3 algorithm. The feature maps of different depths are detected respectively, so that the feature maps of the current layer will sample and use the feature maps of the future layer. The small-size feature map can detect large-size objects, and the large-size feature map can detect the role of small-size objects. Compared with YOLOv1 and YOLOv2, YOLOv3 improves the accuracy and speed of object detection, completes the adjustment of network structure, uses multi-scale features for object detection, and replaces softmax with logistic in object classification *(Tan et al., 2021)*.

Principle of posture discrimination of sheep base on YOLOv3

The basic structure of object detection by YOLOv3 is shown in Figure 4. The basic structure includes input layer, convolution layer, feature fusion layer and output layer, with 107 layers in total, of which 0-74 layers are convolution layer; 75-105 layers are responsible for object detection, classification and regression. In the input layer, we choose to input the image of 416×416×3. YOLOv3 network is with Darknet-53 network model as convolutional layers to sample under 32 times, so input layers should be three-channel RGB image of n × n, and n should be a multiple of 32. The Convolutional layer is from 0 to 74th layer, and it consists of residual modules and convolutional modules sampling between residual modules. The convolution modules sample under 32 times, 16 times and 8 times use steps of two, which effectively reduces the loss of low-level features. Adding a residual module can ensure that the network structure can continue to converge in a very deep situation to a certain extent. At the same time, the amount of calculation is reduced. The feature fusion layer is 75-105, and 416×416×3 images as input, object detection, mosaic feature information, fusion 13 ×13, 26 × 26, 52 ×52. Each scale interacts with local features through a convolution kernel to complete pyramid feature fusion. The output layer is mainly responsible for the classification and position regression of the three scale feature maps output by the feature fusion layer. These three feature maps will be transferred into the logistic layer respectively.

The reason why the softmax layer is not used is that the softmax layer can only generate one classification for each frame, but in our object detection task, there may be multiple target objects overlapping. In this way, there will be multiple classifications, so logistics is used in YOLOv3 to generate the output of the model. There are 13 ×13 ×3 + 26 ×26 ×3 + 52 ×52 ×3 predictions in YOLOv3 *(Zhang et al., 2021)*.

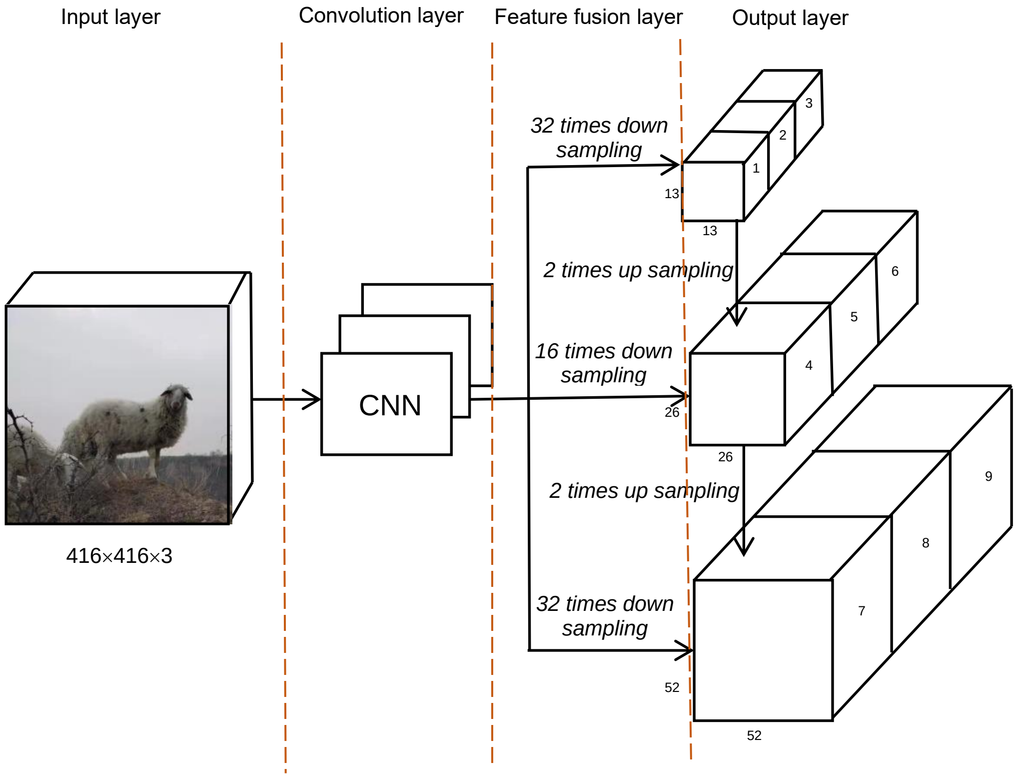

Fig. 4 - Basic Structure of Detection by YOLOv3

Darknet-53 network structure

Based on the idea of Resnet, compared with Darknet-19 network, the accuracy and speed of Darknet-53 network processing a large number of picture data have been greatly improved. Because the network structure contains 53 convolution layers, it is named Darknet-53, which is integrated from the convolution layers with better performance selected from various mainstream network structures. In ImageNet image classification, the processing speed of Darknet-53 is 78 images per second, which is much faster than Resnet with the same precision, twice the efficiency of Resnet-152, and the effect is better than Darknet-19. Darknet-53 adds a residual module into the network, which has a convolution core of 32 filters and 5 groups of residual units. Each unit of these 5 groups of residual units is composed of a separate convolution layer and a group of repeated convolution layers. The repeated convolution layers are repeated once, twice, eight times, eight times, four times respectively, then perform a series of convolution layers of 3 × 3 and 1 × 1. The reason why the residual module is added is that it can solve the gradient problem of deep network. Because the deeper the network is, the phenomenon of gradient disappearing will become more and more obvious, and the training effect of the network will not be very good. The residual neural network is to solve the problem of gradient disappearance under the condition of deepening the network. The residual structure does not pass convolution, mapping directly from the previous feature layer to the following feature layer (jump connection) is helpful for training and feature extraction, which is easy to optimize *(Sun et al., 2021)*.

FORMATION PROCESS OF CLASSIFICATION OF SHEEP BEHAVIOUR AND POSTURE

Feature extraction of sheep image

The purpose of this paper is to detect the object of three kinds of designated behaviour and posture of sheep. In order to recognize accurately and quickly, we adopt the YOLOv3 algorithm as the core technology. The core idea of YOLOv3 object detection is to output the detected object information at one time, including category and location.

It only needs to find out which grid the centre of the object is in, and it does not need many ASK like Fast-RCNN. It can be summarized as the following steps: First, input sheep image, YOLOv3 will set it to 416 × 416 images, and add a blackness bar to prevent distortion; second, the image will be divided into three kinds of grid images, which are 13 × 13, 26 × 26 and 52 × 52. Among them, 13 × 13 is mainly used for large object detection, 26 × 26 is used for medium object detection, 52 × 52 is used for small object detection, and 13 × 13 grids are selected for sheep image recognition; third, if the centre of the bounding box corresponding to ground truth in the training set just falls into a grid cell of the input image, then the grid cell is used to predict the object; fourth, because each grid cell will predict a fixed number of bounding boxes, the largest bounding box is used to predict the object. The steps of YOLOv3 object detection are shown in Figure 5 *(Cai et al., 2020)*.

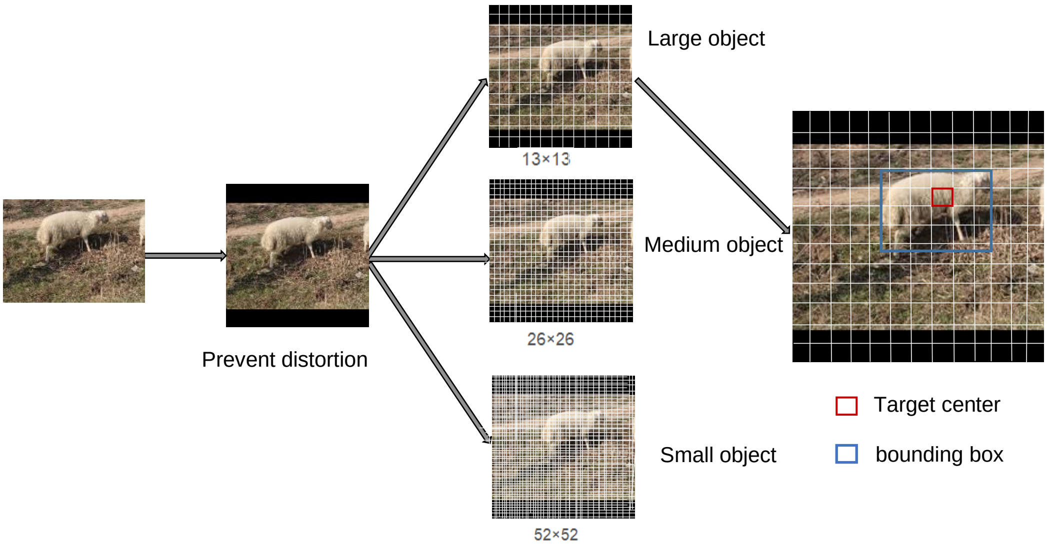

Fig.5 - Detection Steps of Sheep Based on YOLOv3

Network recognition of sheep posture features and calculation method

YOLOv3 algorithm is based on intersection and union ratio as one of the important indexes of the evaluation model, the union ratio refers to the union ratio between the generated candidate box and the original marked box. It can be used to evaluate the object detection algorithm and judge whether it works well. It is the standard performance measure of object class segmentation problem, and its expression is

$$R_{IOU} = \frac{I\ (X)}{U\ (X)} \tag{1}$$

Where $I(x)=\Sigma_{v\in V}XvYv$, $U(X)=\Sigma_{v\in V}(Xv+Yv\text{-}XvYv)$

$V=\{1, 2, \ldots, N\}$ is the pixel set of all the images of behaviour and posture of sheep in the training set; X is a network output for the pixel probability on the set V; Y is the actual pixel probability situation on the set V.

The main idea of calculating the bounding box in YOLOv3 is to divide the input picture of behaviour and posture of sheep into uniform equivalent cells, and then calculate the coordinate position of the cell where the centre is located, so as to realize the prediction of the bounding box. YOLOv3 predicts four coordinate values for each bounding box (t_x, t_y, t_w, t_h). For the predicted grid cell, according to the offset of the upper left corner of the image (c_x, c_y) and the width and height of the bounding box (P_x, P_y) to predict the bounding box in the following way, the calculation formula is as follows:

$$b_x = \delta(t_x) + c_x \tag{2}$$

$$b_y = \delta(t_y) + c_y \tag{3}$$

$$b_w = P_w\ e^{t_w} \tag{4}$$

$$b_h = P_h\ e^{t_h} \tag{5}$$

Among them, t_x, t_y, t_w, t_h is the predicted four coordinate values; t_x, t_y represents the offset of the predicted coordinates; t_w, t_h represents the scaling of the dimensions respectively;

P_x, P_y represents the width and height of the prediction bounding box;

c_x, c_y is the upper left corner coordinate of a grid cell, which represents the width and height of the cell, that is, the coordinate offset;

$\delta(t_x)$, $\delta(t_y)$ represents the cell coordinates of the centre point in the cell in which it is located; b_x, b_y, b_w, b_h represents the coordinate position and size of the bounding box relative to the input image, that is, the predicted output coordinates *(Qu et al., 2021).*

YOLOv3 algorithm uses K-means clustering to determine the size of the annotation box, and continues the method of YOLOv2. Three kinds of prior boxes are set for each down sampling scale, and a total of 9 kinds of size prior boxes are clustered. When calculating the dimension box, the coordinates x and y of the centre point of all the dimension boxes are set to 0, so that all the dimension boxes are placed in the same position, to a certain extent, it can be more effective to calculate the similarity between the annotation boxes, the clustering distance measurement function is as follows:

$$\mathrm{D} = 1 - R_{IOU} \tag{6}$$

The last level of convolution of the YOLOv3 algorithm is 1 × 1, so the calculation formula of convolution kernel size is:

$$l = [\mathrm{B}\times(5+\mathrm{C})\times 1\times 1] \tag{7}$$

Where B is predicting the number of bounding boxes for the network; C is the number of categories; 5 is the four coordinate values and one confidence level, for this experiment to detect behaviour and posture of sheep, C will be set to 3, B will be set to 3.

The confidence level of the YOLOv3 algorithm can be used to evaluate the reliability of the test image. The intersection and union ratio of the probability of an object contained in a grid cell and the object detection is the confidence level of the YOLOv3 algorithm. The calculation formula is as follows:

$$F_{con} = Pr(Obj)R_{IOU} \tag{8}$$

Where the value of the $Pr(Obj)$ is determined by the probability of whether the prediction box contains the object to be detected. When the sheep is detected as one of the three postures of eating, standing and lying down, it will be set to 1, otherwise it will be set to 0; R_{IOU} represents the union ratio, as can be seen above.

Realization process of behaviour and posture of sheep

The process of detection model of behaviour and posture of sheep based on YOLOv3 is as follows, as shown in Figure 6:

I. Construction of sheep behaviour and posture data set.

The data set of behaviour and posture of sheep was obtained by human shooting. From the 1500 pictures taken, 1000 pictures with good shooting effect were selected as the input data set of this experiment, including three postures of sheep standing, eating and lying down, and the number of pictures of these three behaviours and postures was equal. Then the images will be resized and normalized. Because there are 5 downsampling steps of 2 in the Darknet-53, the feature map will be reduced by 32 times. So we need to resize the image to a multiple of 32. In this experiment, we resize the image of sheep data set to 416×416. In order to speed up the convergence of the training network, the image is normalized from 0-255 pixels to 0-1 pixels without changing the image information. Then LabelImg is used to label the image to accurately mark the specific position of the corresponding category of objects in the image *(Zhao et al., 2021)*.

II. Model construction and training detection model

(1) The datasets are divided, dividing the training set and test set at 9:1. 900 pictures are randomly extracted as the training set and 100 images as the test set.

(2) The YOLOv3 network is configured, and the main YOLOv3 network parameters adjusted in this experiment include: after each iteration, the number of images sent to the network is batch=16. Each batch is divided into the number of subdivision corresponding numbers, the number of calculations set to subdivisions = 16. The width of the input image is width=416, and the height of the input image is height=416. The number of objects identified by the network is set to classes=3. The filters in the last convolutional layer before each layer is set to filters=24.

(3) Download the pre-trained weight darknet53.conv.74 before starting the training. The training process includes: higher resolution training for backbone networks, backbone and detection networks combined, reading training data and preprocessing, defining loss functions, model training.

After training the backbone network, we add the corresponding convolutional layer based on this network, realize the architecture of image feature pyramid (FPN), and then output three different eigenvalues of different image resolutions, and finally build a network detection system that can subsample the pictures by 8 times, 16 times and 32 times.

This model takes the three outputs route1, route2 and route3 of the backbone network darknet-53 as input, and the final output predict is the prediction result of three different dimensions.

III. To verify the accuracy of the model.

This experiment uses loss curves and Region Avg IOU curve to evaluate model training effects. At last, mean average precision (mAP) is calculated from the test set data to verify the availability of the model.

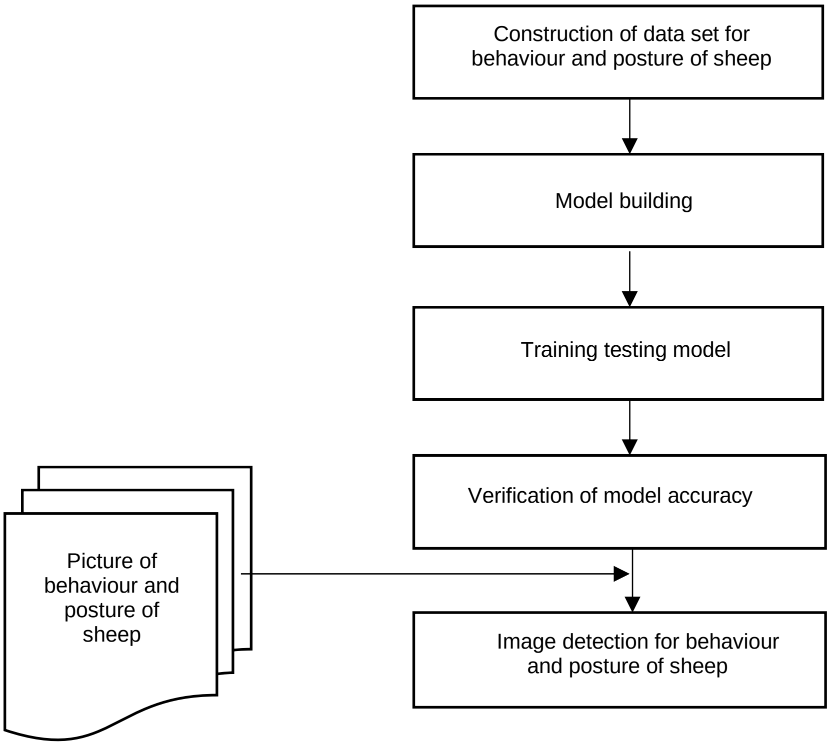

Fig. 6 - Flow Chart of Detection Model of Behaviour and Posture of Sheep

CLASSIFICATION OF SHEEP BEHAVIOUR AND POSTURE

The verification effect of this experiment is shown in Figure 7. The following images in Figure 7 are selected in the test set by random. When we put these pictures in our training model of sheep's behaviour and posture, it can accurately identify sheep's three postures such as eating, standing and lying down, according to the characteristics of the input images. It can be seen from the effect in the figure that this method can distinguish the relevant posture of a single sheep. If there are multiple target objects in a scene, it can also achieve good results.

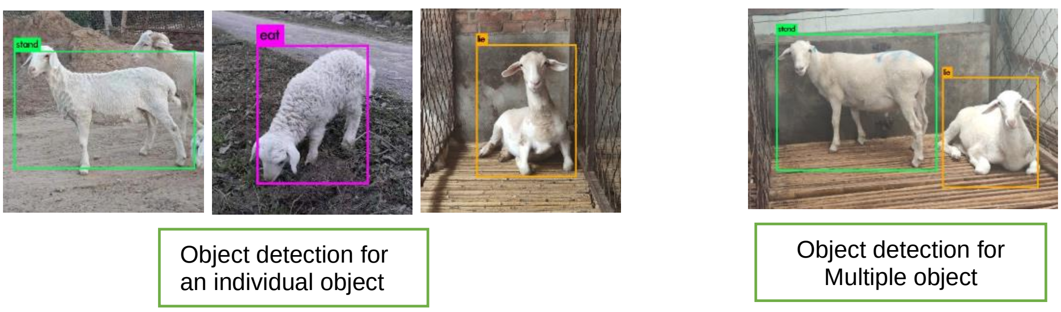

Fig. 7 – Classification of Sheep Behaviour and Posture

By analysing the output data in the training process, the loss curves and Region Avg IOU curves can be drawn. The Loss curves is shown in Figure 8. In this experiment, when the training times exceed 800 times, the loss value has been lower than the set threshold, which proves that the training can be stopped and the results can be tested. The region AVG IOU curve is shown in Figure 9. It can be seen from the curve that when the training times reach 600, the IOU value has approached 1, indicating that the coincidence degree between the predicted rectangular box and the target in the training model detection results has met the requirements.

By analysing the test set and using the detector valid command of darknet network, the test results of three categories to be detected in this experiment can be obtained in the darknet/results directory. Through the comparison between the test results and the annotation in the test set, the average precision of various postures is calculated respectively (standing posture is 84.38%, eating posture is 95.74%, lying posture is 97.29%). So the Mean Average Precision (mAP) is 92.47%. It can meet the detection requirements in accuracy.

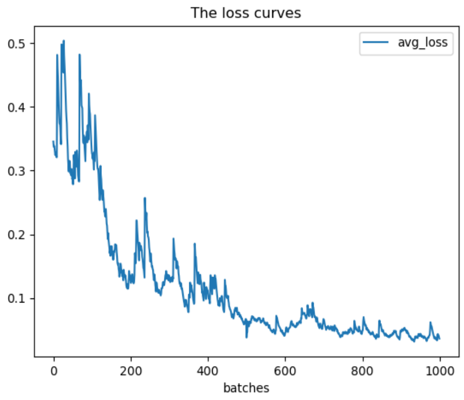

Fig. 8 – The Loss Curves

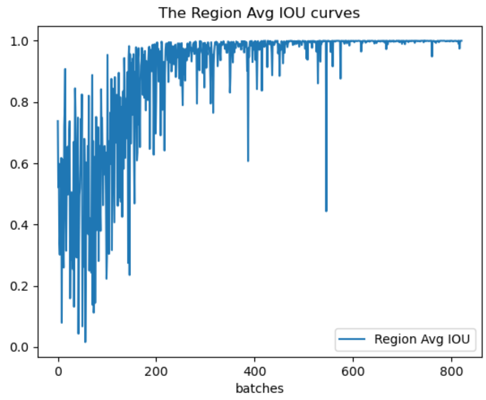

Fig. 9 – The Region Avg IOU Curves

CONCLUSIONS AND PROSPECTS

In view of the situation that behaviour and posture of sheep will change significantly when they suffer from illness or parturition, this paper uses the YOLOv3 algorithm as the core to realize the detection of behaviour and posture of sheep, which can effectively and accurately identify their three behaviours: standing, eating and lying down. By predicting the behaviour and posture of animals in advance, we can effectively judge the physiological activities of animals, which is helpful for breeders to stop the abnormal behaviour of sheep in advance. It also saves human resources and enhances the production and economic benefits of agriculture.

The detection results in this paper have achieved good results for individual posture detection. However, when multiple individuals are mixed, if there is no mutual occlusion, the algorithm can accurately detect posture of multiple target individuals. However, when different individuals block each other or some sheep are blocked by other obstacles, the detection results of blocked individuals are not accurate. This is also a problem to be studied in the future. Yolov3 is a real-time target detection tool. After verification, the method in this paper can be added to the real-time video processing system for the application of real-time monitoring scene, which provides a practical and feasible scheme for the application in related fields.

ACKNOWLEDGEMENT

This research, titled ‘DETECTION OF BEHAVIOUR AND POSTURE OF SHEEP BASED ON YOLOv3’, was funded by the research project of Shanxi Province excellent doctor work Award Fund (Research on model detection technology of Agricultural Internet of things, No: SXYBKY201721), Scientific Research Start of Doctor of Shanxi Agricultural University (Research on Detection Technology of Agricultural Internet of Things Model, 2017YJ30). The authors are grateful and honoured to receive this support.

REFERENCES

[1] Cai F.H., Zhang Y.X., Huang J., (2020), Detection Algorithm of Bridge Surface Crack Based on YOLOv3 and Attention Mechanism. *Pattern Recognition and Artificial Intelligence*, 10, 33, 926-933.

[2] Fogarty E.S., Swain D.L., Cronin G.M., Moraes L.E., Trotter M., (2020), Behaviour classification of extensively grazed sheep using machine learning. *Computers and Electronics in Agriculture*, 169: 105175.
[3] He D.J., Liu D., Zhao K.X., (2016), Review of Perceiving Animal Information and Behaviour in Precision Livestock Farming. *Journal of Agricultural Machinery*, 05, 47, 231-244.
[4] Li D., Zhang K.F., Li X.J., Chen Y.F., Li Z.B., Pu D., (2019), Mounting Behaviour Recognition for Pigs Based on Mask R-CNN. *Journal of Agricultural Machinery*, S1, 50, 261-266+275.
[5] Ma C., Sun X., Yao C., et al. (2020), Research on Sheep Recognition Algorithm Based on Deep Learning in Animal Husbandry. *Journal of Physics: Conference Series.* IOP Publishing, 1651(1): 012129.
[6] Pan Y.H., Wei J.S., Zeng L.P., (2021), Farmland bird detection algorithm based on YOLOv3. *Progress in Laser and Optoelectronics*, 1-16.
[7] Qu J.S., Zhu Z.Q., Wan Q.B., (2021), Face Key Point Detection Based on YOLOv3. *Yangtze River Information Communication*, 01, 34, 55-58.
[8] Salama A., Hassanien A.E., Fahmy A., (2019), Sheep identification using a hybrid deep learning and Bayesian optimization approach. *IEEE Access*, 7: 31681-31687.
[9] Sun Q.Y., Zhang Z.D., (2021), Crowd Density Estimation Based on YOLOv3 Enhanced Model Fusion. *Application of Computer Systems*, 04, 30, 271-276.
[10] Sun S., Qin J., Xue H., (2019), Sheep delivery scene detection based on faster-RCNN. *The Second International Conference on Image, Video Processing and Artificial Intelligence.*
[11] Tan F., Mu P.A., Ma Z.X., (2021), Multi-object Tracking Algorithm Based on YOLOv3 Detection and Feature Point Matching. *Journal of Computing*, 02, 42, 157-162.
[12] Xue Y.J., Zhu X.M., Zheng C., Mao L., Yang A.Q., Tu S.Q., Huang N., Yang X.F., Chen P.F., Zhang N.F., (2018), Lactating Sow Postures Recognition From Depth Image of Videos Based on Improved Faster R-CNN. *Transactions of the Chinese Society of Agricultural Engineering*, 09, 34, 189-196.
[13] Ye C.W., Kang R., Qi C., Liu C., Zhao Y., Chen K.J., (2019), Detection method of broiler strike based on Faster-RCNN. *Journal of Agricultural Machinery*, 12, 50, 255-259.
[14] Zhang X.C.，Zhao J.S., Wang S.Z., Zhang M, Cheng C., (2021), Binocular Vision Detection and Positioning Method for Ships Based on YOLOv3 Algorithm. *Journal of Shanghai Maritime University*, 01, 42, 26-32.
[15] Zhao Y.Y., Zhu J., Xie Y.K., Li W.L., Guo Y.K., (2021), Improved Yolo-v3 Video Image Flame Real-time Detection Algorithm. *Geomatics and Information Science of Wuhan University*, 03, 46, 326-334.
[16] Zhuang Y.R., Yu J.H., Teng G.H., Cao M.B., (2020), Study on the Detection of Estrus Behaviour in Big White Pig Based on Convolutional Neural Network. *Journal of Agricultural Machinery*, S1, 51, 364-370.
[17] Zhu W.X., Pu X.F., Li X.C., Lu C.F., (2010), Automatic identification system of suspected sick pigs based on behavioural monitoring. *Journal of Agricultural Engineering*, 01, 26, 188-192.

ANALYSIS AND CALIBRATION OF PARAMETERS OF BUCKWHEAT GRAIN BASED ON THE STACKING EXPERIMENT
/
基于堆积试验的荞麦籽粒离散元参数分析及标定

Rong Fan, Qingliang Cui *), Yanqing Zhang, Qi Lu [1]
College of Agricultural Engineering, Shanxi Agricultural University, Taiyuan, 030801/China;
Tel: +8618404981210; E-mail: sxau_fr@126.com
Corresponding author: Cui Qingliang
DOI: https://doi.org/10.356.33/inmateh-64-46

Keywords: *buckwheat grain, simulation parameters, repose angle, calibration*

ABSTRACT
The stacking test based on response surface method (RSM) was carried out to calibrate the simulation parameters of buckwheat grain by discrete element method (DEM). The static friction coefficient of buckwheat-buckwheat and that of buckwheat-steel are significant factors affecting the repose angle. A quadratic polynomial model for the repose angle and the 2 significant parameters was established and optimized. The optimal combination was obtained: buckwheat-buckwheat static friction coefficient of 0.482, buckwheat-steel static friction coefficient of 0.446. It was found that there was no significant difference between the results of the simulation test and physical test (P>0.05), indicating that the parameter calibration method based on RSM is feasible. The calibrated parameters can provide reference to the simulation of buckwheat production process and machineries design.

ABSTRACT
为了确定离散元模拟所需的荞麦籽粒参数，本文基于堆积试验进行了荞麦籽粒休止角的测量与模拟试验。以得到的休止为响应值，采用响应面法对仿真参数进行了标定。在 Plackett-Berman 试验中，荞麦-荞麦和荞麦-钢板的静摩擦系数是影响休止角的重要因素。根据最陡爬坡试验和中心组合设计的结果，建立了休止角和 2 个显著参数的二次多项式模型，并进行了优化。通过求解优化后的回归方程，得到最佳参数组合：荞麦-荞麦静摩擦系数为 0.482，荞麦-钢静摩擦系数为 0.446。在最佳组合下进行了验证实验。结果表明，验证试验结果与测量试验结果无显著性差异（P>0.05），说明基于响应面法的参数标定方法是可行的。标定参数的优化组合可为荞麦生产过程的离散元模拟仿真及机具设计提供参考。

INTRODUCTION
Coarse cereals having rich nutrition and high economic benefits are grains of an important variety which improve dietary structure and promote nutritional health, as well as important cash crops for improving the income of farmers in old and rural areas. Buckwheat plays an important role in the kingdom as one of the main varieties of coarse cereals. However, buckwheat is a kind of crop with Infinite inflorescence. Its maturity is extremely inconsistent, and the moisture content of the stem in the harvest period is very high, which makes it easily breakable. Therefore, mechanical harvesting faces some difficulties, such as high impurity content, high loss rate and high damage rate, which seriously restrict the development of buckwheat industry.

With the development of computer technology, the discrete element method (DEM) is being used increasingly in agricultural equipment research *(Li Z. et al., 2011; Qiu B. et al., 2012; Li H. et al., 2011; Ma Z. et al., 2017; Zhang T. et al., 2016; Boac J. et al., 2014; Sarnavi H. et al., 2013)*. A comprehensive and systematic simulation study on buckwheat would be helpful to the application of the DEM in the research and development of agricultural equipment for buckwheat production.

It is well known that many parameters are required in DEM simulation, of which the static friction coefficient, rolling friction coefficient and collision recovery coefficient are the basic contact parameters. At present, there are two methods to obtain the parameters: direct measurement and indirect calibration. When the direct measurement method is adopted, the measured values vary widely due to the influence of humidity, material and shape, which create some difficulties in the research and application.

[1] *Rong Fan, M.S. Stud. Eng.; Qingliang Cui, Prof. Ph.D. Eng.; Yanqing Zhang, Lecturer M.S. Eng.; Qi Lu, Lecturer M.S. Eng.*

Therefore, many scholars use computation based "virtual calibration" method to study the parameters. *Yuan C. et al., (2020),* calibrated the simulation parameters of the fermented sheep manure by the skateboard test, and obtained optimal parameters of three kinds of fermented sheep organic manure with different moisture contents. In the collapse experiment, *Liu Y. et al., (2019),* calibrated the static friction coefficient and rolling friction coefficient of rice grains. *Grima A. et al., (2011),* calibrated and verified the rolling friction coefficients required by dry and wet particles in the DEM simulation. Based on the response surface method (RSM), *Santos K. et al., (2015),* measured the dynamic repose angle of dried cherry fruits using a rotary drum device, and calibrated some parameters required in the DEM simulation. *Yu Q. et al., (2020),* determined the optimal contact parameters between Panax notoginseng seeds, and verified the seed metering test.

The stacking test is favored by some scholars because of its convenient and simple operation, and many measurable parameters *(Jia F. et al., 2014; Grima A. et al., 2011)*. However, such studies either adopt a trial and error method or lack a standardized parameter calibration method. So, some scholars have proposed standardized methods for parameter calibration by the DEM based on the RSM *(Liu F. et al., 2016; Wang Y. et al., 2016)*. In this study, taking buckwheat grain as the research object and the repose angle obtained by cylinder lifting as the response value, the simulation parameters were calibrated by the Plackett-Burman (PB) test, steepest climb test and central composite test, and the simulation and real test values were compared and verified. The calibrated parameters of buckwheat grain can provide a reference to the analysis and research on the DEM simulation of production process for buckwheat, such as sowing, threshing and cleaning. It can also help in developing equipment for buckwheat production and realizing production mechanization.

MATERIALS AND METHODS

The buckwheat variety used in the experiment was Heifeng No.1, which was collected from the experimental field. The moisture content of the grain was 13.68% and its density was 698kg/m^3. The real repose angle of buckwheat grains was first measured by the cylinder lifting device, and then the simulation of cylinder lifting was carried out by EDEM 2.7. Taking the obtained repose angle of buckwheat grains as the response value, the simulated parameters of buckwheat grain were calibrated by the PB test, the steepest climb test and center combination test. All tests were designed by Design Expert 10.0. After that, the calibrated optimal parameters were used in simulating the verification test, and drawing conclusions.

Entity measurement test of repose angle

A cylinder lifting test device was used in this research. The three-dimensional design drawing of the device was shown in Fig.1.

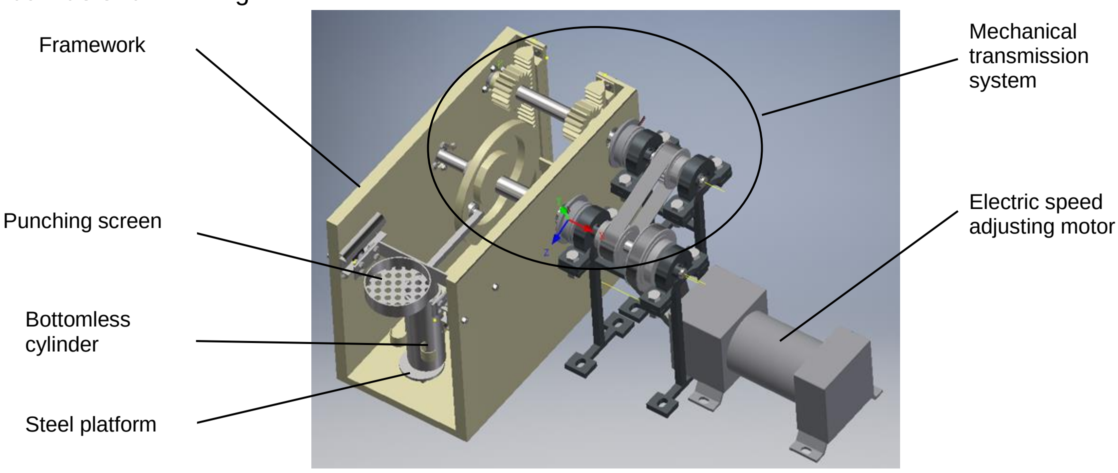

Fig. 1 - The three-dimensional design drawing of test device

A bottomless Q235 steel cylinder was used in the test. The surface roughness of the inner wall of the cylinder was made close to that of the cleaning screen of buckwheat combine harvester, which is about 50μm. The size of the cylinder was determined according to the particle size of buckwheat. The shape of the buckwheat grain is tri-pyramid with a maximum grain size of 7.60mm. Hence, the inner diameter of the cylinder was determined to be 35mm and its height to be 110mm, which conformed to the requirements proposed by *Jia F. et al., (2014)*, that the diameter should be about 4-5 times of the maximum grain size, and the ratio of height to diameter is about 3:1.

At the time of taking measurement, the cylinder was attached to a fixed horizontal circular steel platform, and filled with buckwheat grains by particle accumulating method *(Sun Q. et al., 2009)*. Then the cylinder was lifted by a driving mechanism at a constant speed of 0.05 m/s, and then a pile with pyramidal grains was formed on the circular platform as shown in Fig.2 *(Li Q. et al., 2010)*. When the artesian surface of the heap became relatively static, the angle between the artesian surface and the horizontal plane was measured, which was the repose angle. The test was repeated for 5 times.

Fig. 2 - Experiment of buckwheat grain cylinder lifting

In order to improve the measurement accuracy and to avoid human error as far as possible, Image J and MATLAB software were used in this paper to process the images collected under the above experimental conditions. The procedure is shown in Fig. 3. The slope of the fitted line was determined by counting pixels in both horizontal and vertical directions, and the repose angle was obtained by calculating the inverse tangent of the slope of the line as shown in Formula (1).

$$\theta = \frac{tan^{-1}|k|\times 180^{\circ}}{\pi} \tag{1}$$

where: θ is the repose angle and k is the slope of the fitted line.

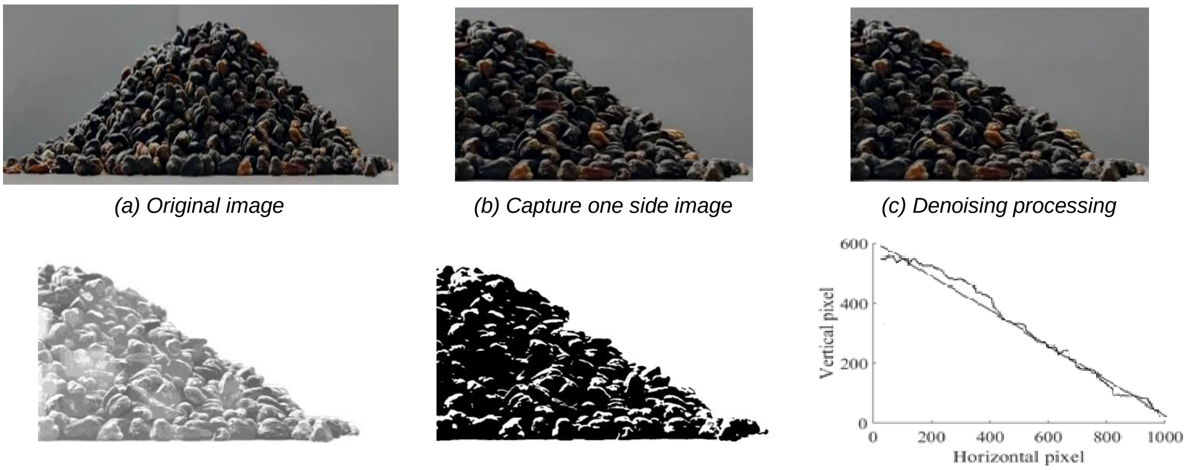

(a) Original image *(b) Capture one side image* *(c) Denoising processing*

(d) Gray processing *(e) Threshold segmentation* *(f) Linear fitting*

Fig. 3 - Image processing procedure of repose angle of buckwheat grain

After the cylinder lifting test, image process and data analysis, the results of 5 entity tests were obtained. The mean repose angle and standard deviation of buckwheat granules are 30.148° and 0.518°, respectively.

Contact model and parameters

In the simulation, the Hertz-Mindlin (no slip) contact model was adopted. The normal force (N) and tangential force (T) of buckwheat-buckwheat particles and buckwheat particles-geometric bodies are determined by formulas (2) and (5), respectively, *(Sun Q. et al., 2009)*.

The normal force (N) between particles:

$$N = \frac{4}{3}E^{*}(R^{*})^{1/2}\delta_n^{3/2} \tag{2}$$

where:

δ_n represents the normal overlapping of particle 1 and particle 2; E^* is equivalent elastic modulus; and R^* is the equivalent particle radius. R^*, E^* are calculated by formulas (3) and (4), respectively.

$$\frac{1}{R^*} = \frac{1}{R_1} + \frac{1}{R_2} \tag{3}$$

$$\frac{1}{E^*} = \frac{1-\nu_1^2}{E_1} + \frac{1-\nu_2^2}{E_2} \tag{4}$$

where: R_1, E_1, ν_1; R_2, E_2, ν_2 are the radius, elastic modulus and Poisson's ratio of particle 1 and particle 2, respectively.

The tangential force (T) between particles:

$$T = -S_t \delta_t \; ; \; S_t = 8G^* \sqrt{R^* \delta_n} \tag{5}$$

where: δ_t is the tangential overlap; and S_t is the tangential stiffness. G^* is the equivalent shear modulus, which is calculated by formula (6).

$$G^* = \frac{2-\nu_1}{G_1} + \frac{2-\nu_2}{G_2} \tag{6}$$

where: G_1 and G_2 are the shear modulus of the two particles, which are determined from the relations of the corresponding elastic modulus and Poisson's ratios as expressed by formula (7).

$$G_1 = \frac{E_1}{2(1+\nu_1)}; \; G_2 = \frac{E_2}{2(1+\nu_2)} \tag{7}$$

Buckwheat grains are complex and diverse, and some parameters are dispersed. According to the reported results of agricultural material and DEM simulation, Table 1 describes the parameters and range *(Hou H., 2019; Sun J., 2019; Keppler I. et al., 2012)*.

Table 1

Parameters and value required in DEM simulation

Parameters	Value
Poisson's ratio of buckwheat	0.16~0.42
Buckwheat shear modulus /MPa	6.81~61.84
Buckwheat density /(kg/m^3)	698
Poisson's ratio of steel plate	0.30
Steel plate shear modulus / MPa	70000
Steel plate density /(kg/m^3)	7800
Buckwheat-buckwheat restitution coefficient	0.10~0.26
Buckwheat- steel plate restitution coefficient	0.20~0.80
Buckwheat-buckwheat coefficient of static friction	0.32~0.60
Buckwheat- steel plate coefficient of static friction	0.18~0.58
Buckwheat-buckwheat coefficient of rolling friction	0.03~0.08
Buckwheat-steel plate coefficient of rolling friction	0.02~0.09

Development of discrete element model

The buckwheat grain used in this test is almost of a tri-pyramid shape. Its structure is shown in Fig. 4 (a). According to the measured tri-axial dimensions (the average height of 5.90mm, and the three bottom edges of 3.94mm, 3.92mm and 3.93mm respectively), the contour of buckwheat grain was established in AutoCAD, which was imported into EDEM 2.7 during the setting of the parameters of simulated materials. Nine overlapping spherical particles were manually filled in the CAD contour to get buckwheat particles. While filling, the radius and spherical coordinate of each spherical particle need to be specified to clarify the position relationship between spherical particles. The model of buckwheat grain is shown in Fig. 4 (b).

(a) *(b)*

Fig. 4 - Buckwheat grain and DEM model

The model of a bottomless steel cylinder and a horizontal steel plane of the same size as the solid test was imported into the EDEM 2.7, and the size of buckwheat grain was dynamically generated according to the standard normal state, whose mean value was 1, and standard deviation was 0.05. The generating rate was 3000 per second, and which poured into the cylinder at a vertical velocity of 0.5 m/s. When the cylinder was filled with buckwheat grains, the calculation area was reset. The cylinder was set to move vertically upward at a speed of 0.05 m/s. In this experiment, 25% of the Rayleigh time was used. The simulation time was 5.5s. The simulation process is shown in Fig. 5. After the completion of the simulation, the size of the simulation interface was made the same, and the image of repose angle was obtained by the screenshot processing. The measuring method for repose angle is the same as that of entity measurement test.

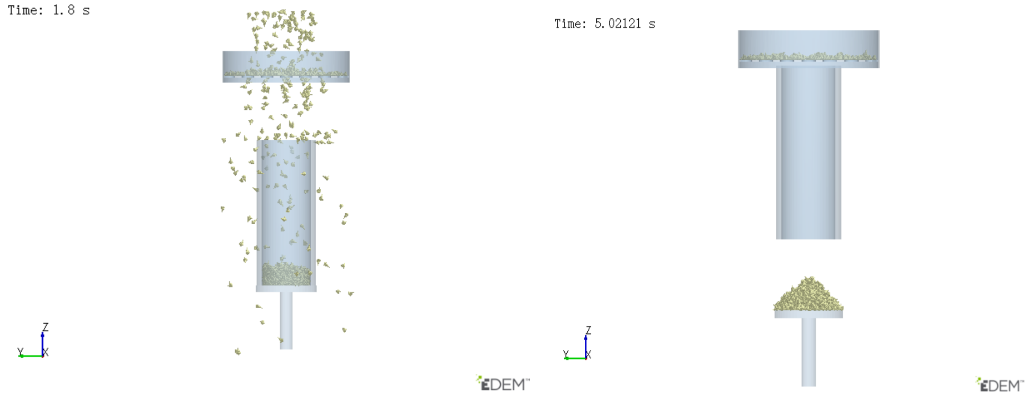

(a) (b)

Fig. 5 - The simulation process

Plackett - Burman test

Many parameters will be used in the DEM simulation. If all of them are calibrated, it is difficult to achieve. Therefore, the PB test was performed to screen out the parameters having significant influence on the repose angle. Out of the parameters related to the buckwheat grains used in the DEM simulation, 8 were selected as parametric variables and 3 were kept in reserve as dummy variables for error analysis. In this paper, a PB table with N=12 was used. The repose angle was taken as the response value, and 2 levels of each variable were taken as high (+1) and low (-1). Table 2 shows the factors and levels for simulation.

Table 2

Factors and levels of Plackett-Burman experiment

Factors		Levels	
Symbol	Parameters	Low level (-1)	High level (+1)
A	Poisson's ratio of buckwheat	0.16	0.42
B	Buckwheat shear modulus / MPa	6.81	61.84
C	Buckwheat-buckwheat restitution coefficient	0.10	0.26
D	Buckwheat-steel plate restitution coefficient	0.20	0.80
E	Buckwheat-buckwheat coefficient of static friction	0.32	0.60
F	Buckwheat-steel plate coefficient of static friction	0.18	0.58
G	Buckwheat-buckwheat coefficient of rolling friction	0.03	0.08
H	Buckwheat-steel plate coefficient of rolling friction	0.02	0.09
I_1,I_2,I_3	Virtual parameters	—	—

The steepest climb test

According to the results of the PB test, it is difficult to establish an effective response surface fitting equation. The best region of each significant factor can be approached quickly and economically by the steepest climb test. In this test, the direction of the climb path was determined according to the positive and negative effects of the significant factors in the PB test. The step size was determined by the t-value of effect.

The central combination test

After approximating the optimal response area by the steepest climb test, the response surface analysis was carried out by the central combination test. Five levels of significant factors and the average level of the non-significant factors were selected. Meanwhile, 5 central points were used in the design. According to the test results, the regression equation was obtained by fitting the response surface model, and the best combination of simulation parameters of buckwheat grain closest to the actual angle of repose was predicted.

RESULTS

Results of Plackett - Burman test

The design and results are shown in Table 3, and Table 4 shows the results of ANOVA. The static friction coefficient of buckwheat-steel plate and that of buckwheat-buckwheat had significant influence on the repose angle (P<0.1), while the influence of other factors was not significant (P>0.1). Therefore, only the two significant factors were selected for the steepest climb test.

Table 3

Design and results of Plackett-Burman test

No.	Factors											Repose angle θl (deg)
	A	B	I_1	C	D	I_2	E	F	I_3	G	H	
1	1	-1	1	1	1	-1	-1	-1	1	-1	1	9.265
2	-1	1	1	-1	1	1	1	-1	-1	-1	1	15.329
3	-1	-1	-1	-1	-1	-1	-1	-1	-1	-1	-1	9.110
4	1	1	-1	-1	-1	1	-1	1	1	-1	1	22.968
5	1	-1	1	1	-1	1	1	1	-1	-1	-1	24.444
6	-1	1	1	1	-1	-1	-1	1	-1	1	1	27.597
7	-1	-1	1	-1	1	1	-1	1	1	1	-1	21.647
8	1	1	1	-1	-1	-1	1	-1	1	1	-1	9.902
9	-1	-1	-1	1	-1	1	1	-1	1	1	1	14.425
10	1	1	-1	1	1	1	-1	-1	-1	1	-1	12.150
11	1	-1	-1	-1	1	-1	1	1	-1	1	1	29.954
12	-1	1	-1	1	1	-1	1	1	1	-1	-1	30.784

Table 4

Analysis of significance of parameters in Plackett-Burman test

Parameters	Sum of squares	*F* value	*P* value	Significance
A	8.69	1.25	0.3445	5
B	8.14	1.17	0.3578	6
C	7.93	1.14	0.3632	7
D	9.51	1.37	0.3260	4
E	40.70	5.87	0.0939*	2
F	633.84	91.44	0.0024**	1
G	1.19	0.17	0.7067	8
H	11.02	1.59	0.2964	3

Note: "" and "**" represent significant levels of 0.1 and 0.01, respectively.*

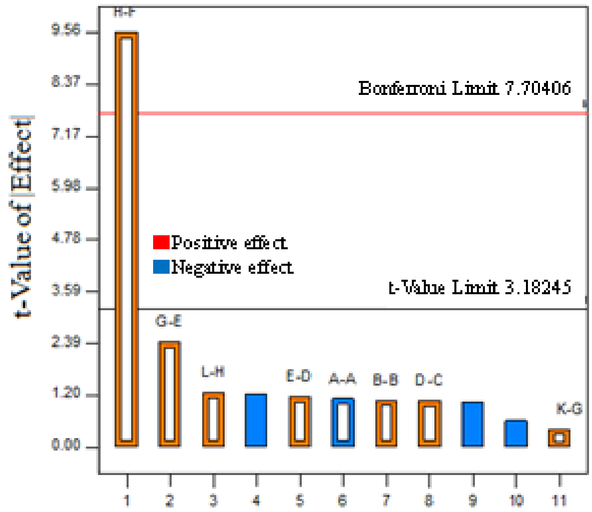

Fig .6 - Pareto chart of Plackett-Burman experiment

The Pareto chart (Fig. 6) shows that the static friction coefficient of buckwheat-steel and that of buckwheat-buckwheat had positive effects on the repose angle. Hence, the two factors became the rising path in the steepest climb test.

Results of the steepest climb test

Table 5 shows the design and results of the steepest climb test. With increasing static friction coefficient of buckwheat-steel plate and that of buckwheat-buckwheat, the relative error of the repose angles between the simulation and solid tests first decreased and then increased. The No.4 had the smallest error, indicating that the optimal area of each factor was near test 4. Therefore, the static friction coefficient of buckwheat-buckwheat and that of buckwheat-steel plate were taken as 0.48 and 0.45, respectively, which were selected as the center points for subsequent response surface tests.

Table 5

Design and results of steepest ascent test

No.	Buckwheat-buckwheat static friction coefficient (*E*)	Buckwheat- steel static friction coefficient (*F*)	Repose angle *θ*/ (deg)	Relative error /%
1	0.30	0.15	9.348	68.99
2	0.36	0.25	19.389	35.69
3	0.42	0.35	28.097	6.80
4	0.48	0.45	29.766	1.26
5	0.54	0.55	31.601	4.82
6	0.60	0.65	33.085	9.74

Results of the central composite design

According to the result above, the center combination test of 2 factors with 5 levels was designed. Table 6 shows the design and results. A quadratic polynomial fitting was performed, and the regression model between the repose angle and significant parameters was developed as follows:

$$\theta = 59.714 - 107.570E - 43.457F + 121.167EF + 70.678E^2 - 3.890F^2 \tag{8}$$

Table 6

Results of the central composite design

No.	Buckwheat-buckwheat static friction coefficient (*E*)	Buckwheat- steel static friction coefficient (*F*)	Repose angle *θ*/ (deg)
1	1 (0.54)	-1 (0.35)	29.176
2	0 (0.48)	0 (0.45)	30.913
3	-1 (0.42)	-1	28.643
4	0	0	30.481
5	0	0	30.271
6	0	1.414 (0.591421)	31.554
7	0	0	29.619
8	-1.414 (0.395147)	0	29.757
9	0	-1.414 (0.308579)	29.002
10	1.414 (0.564853)	0	31.972
11	0	0	29.685
12	-1	1 (0.55)	29.865
13	1	1	33.306

Table 7

ANOVA of the steepest ascent test

Source of variation	Freedom	Mean square	*F* value	*P* value
Model	5	3.79	14.17	0.0015*
E	1	6.31	23.06	0.0018*
F	1	10.04	37.52	0.0005*
EF	1	2.11	7.90	0.0261*
E^2	1	0.45	1.68	0.2357
F^2	1	0.011	0.039	0.8484
Residual	7	0.27		
Lack of fit	3	0.23	0.76	0.5740
Pure error	4	0.30		
Sum	12			
R^2=0.9101, R^2_{Agj}=0.8459; C.V.=1.71%; Adeq precision=13.128				

*Note: * shows the term is significant(P<0.05).*

The Analysis of variance (ANOVA) of this model is shown in Table 7. The *P*-value of the model was 0.0015 (P<0.01), which indicated that the independent and dependent variables in this model were highly correlated. The fitting degree of the model equation was good. The static friction coefficient of buckwheat-buckwheat, and that of buckwheat-steel plate, and the interaction between them had a significant influence on the repose angle of buckwheat grain. While the loss fitting term, which was 0.5740 (P>0.05), had no significant effect. The precision of the regression equation was 13.128, the correlation coefficient was 0.9101, and the correlation coefficient of calibration was 0.8459, which indicated that the model was highly reliable and the predicted value was correlated with the measured value.

In order to further optimize the model equation, on the premise of ensuring good significance and high correlation coefficient of the model, non-significant factors were eliminated, and then the optimized regression equation was obtained as follows:

$$\theta = 60.799 - 108.921E - 46.958F + 121.167EF + 72.086E^2 \tag{9}$$

The ANOVA was performed for the optimized model (Table 8), and the fitting model (P=0.0003) was significantly improved after the optimization. The coefficient of variance was reduced to 1.60%, and the test reliability was further increased. The correlation coefficient was 0.9096, and the correction adjustment coefficient was 0.8644, both were close to 1, which indicated that the model had a high degree of fitting. The precision was increased to 15.219, about 16% higher than that before optimization.

Table 8

ANOVA of the modified model of central composite design experiment

Source of variation	Freedom	Mean square	*F* value	*P* value
Model	4	6.13	36.10	0.0003*
E	1	6.31	37.17	0.0008*
F	1	6.06	35.66	0.0002*
EF	1	6.02	35.46	0.0172*
E^2	1	0.48	2.02	0.1926
Residual	8	0.24		
Lack of fit	4	0.17	0.58	0.6970
Pure error	4	0.30		
Sum	12			
R^2=0.9096, R^2_{Agj}=0.8644; C.V.=1.60%; Adeq precision=15.219				

Note: shows the term is significant (P<0.05).*

Interactive effect of regression model

Table 8 shows the Interactive term (EF) between the static friction coefficient of buckwheat-buckwheat and that of buckwheat-steel had a significant influence on the repose angle (P<0.05).

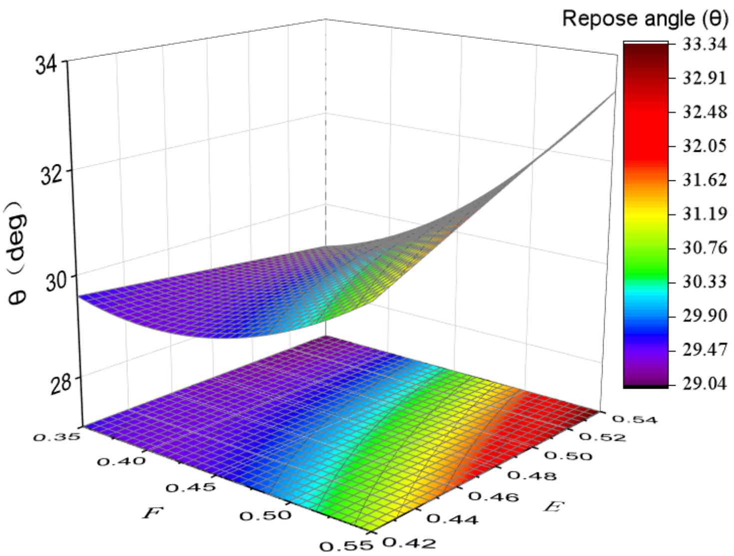

Fig. 7 - Response surface of interaction

As seen in the Fig.7, the repose angle increased with the static friction coefficient of buckwheat-steel and buckwheat-buckwheat. And the increasing rate with the static friction coefficient of buckwheat-steel was larger than that with the static friction coefficient of buckwheat-buckwheat. When either of the two parameters was taken as the larger value, the increasing trend of the repose angle with the increase of the other parameter is greater than that with the former parameter being smaller.

Determination of optimal parameter combination and test verification

Making the measured repose angle of buckwheat grain as the starting point of the optimized regression model, the optimal parameter combination close to the target value was obtained: the static friction coefficients of buckwheat-buckwheat and buckwheat-steel plate are 0.482 and 0.446, respectively.

Fig. 8- Verification of the repose angle by DEM simulation

In order to verify the accuracy and effectiveness of the optimal parameters obtained by the RSM, the calibrated simulation parameters were used in verification test (Fig.8). In the test, the Poisson's ratio was 0.29, and the elastic modulus was 34.325 MPa. The static friction coefficient of buckwheat-buckwheat was 0.482, and that of buckwheat- steel was 0.446. The rolling friction coefficient of buckwheat-buckwheat was 0.055, and that of buckwheat- steel was 0.055. The recovery coefficient of buckwheat-buckwheat was 0.180, and that of buckwheat-steel was 0.500. The experiment was repeated for 3 times, in which the repose angles were 30.121°, 31.574° and 29.283°, respectively, with an average value of 30.321°. The T test was carried out on the results, where *P* value is 0.7685 (P>0.05), indicating that there was no significant difference between the simulation value and the measured value, indicating that the agreement was good.

CONCLUSIONS

(1) The static friction coefficient of buckwheat-buckwheat and that of buckwheat-steel had significant influences on the repose angle of buckwheat grain. And the Poisson's ratio, shear modulus, recovery coefficient and rolling friction coefficient had no significant influence on the repose angle.

(2) A quadratic polynomial model for the repose angle and the 2 significant parameters was established and optimized. Furthermore, the 2 significant parameters and their interaction had significant effects on the repose angle of buckwheat grain.

(3) The optimal combination of the parameters of buckwheat grain obtained by calibration were as follows: the Poisson's ratio of 0.29, elastic modulus of 34.325MPa. The buckwheat-buckwheat static friction coefficient of 0.482, rolling friction coefficient of 0.055, and recovery coefficient of 0.180. The recovery coefficient was 0.500, static friction coefficient was 0.446, and rolling friction coefficient was 0.055 between buckwheat grain and steel plate. There was no significant difference between the repose angle of buckwheat grain obtained from the verification test and solid test (P>0.05), indicating that the model can be used to predict the repose angle of buckwheat grain. The response surface method was feasible to calibrate the discrete element parameters of buckwheat grain based on the stacking test, which could improve the accuracy of the DEM simulation.

ACKNOWLEDGEMENT

This research was funded by the National Key Research and Development Program of China (2016YFD0701801). We would like to express our gratitude to EditSprings (https://www.editsprings.com/) for the expert linguistic services provided.

REFERENCES

[1] Boac J.M., Ambrose K., Casada M.E. et al., (2014), Applications of Discrete Element Method in Modeling of Grain Postharvest Operations. *Food Engineering Reviews*, Vol. 6, Issue 4, pp.128-149, United States.

[2] Grima A.P., Wypych P.W., (2011), Development and validation of calibration methods for discrete element modeling. *Granul Matter*, Vol.13, Issue 2, pp.127-132, Berlin/Germany.

[3] Hou H.M., (2019), Experimental study on cleaning dynamic characteristics of coarse cereals crops harvested by machinery, *杂粮作物机械收获清选动力学特性研究*. PhD dissertation, Shanxi Agricultural University, Taiyuan/China.

[4] Jia F.G., Han Y.L., Liu Y. et al., (2014), Simulation prediction method of repose angle for rice particle materials. *Transactions of the Chinese Society of Agricultural Engineering*, Vol.30, Issue11, pp.254－260, Beijing/China.

[5] Keppler I., Kocsis L., Oldal I. et al., (2012), Grain velocity distribution in a mixed flow dryer. *Advanced Powder Technology*, Vol.23, Issue 6, pp.824-832, Amsterdam/Netherlands.

[6] Li H.C., Li Y.M., Tang Z., et al., (2011), Numerical simulation and analysis of vibration screening based on EDEM. *Transactions of the Chinese Society of Agricultural Engineering*, Vol.27, Issue5, pp.117－121, Beijing/China.

[7] Li Q.L., (2010), The Research of Granular Piling and Bulk Material Transfer Process Using DEM, *颗粒堆积性质和散状物料转载过程 DEM 仿真研究*. PhD dissertation, Northeastern University, Shenyang/China.

[8] Li Z.Q., Yu J.Q., Zhang W.L. et al., (2011), Simulation analysis of working process and performance of inside-filling seed metering device by discrete element method. *Transactions of the Chinese Society of Agricultural Engineering*, Vol.27, Issue 11, pp.32-36, Beijing/China.

[9] Liu F.Y., Zhang J. Li B. et al., (2016), Calibration of parameters of wheat required in discrete element method simulation based on repose angle of particle heap. *Transactions of the Chinese Society of Agricultural Engineering*, Vol.32, Issue 12, pp.247-253, Beijing/China.

[10] Liu Y.P., Zhang T., Liu Y., (2019), Calibration and experiment of discrete element contact parameters of rice grain based on discrete element method. *Journal of Agricultural Science and Technology*, Vol.21, Issue 11, pp.70-76, New York/America.

[11] Ma Z., Li Y.M., Xu L.Z. et al., (2017), Dispersion and migration of agricultural particles in a variable-amplitude screen box based on the discrete element method. *Computers and Electronics in Agriculture*, Vol.142, Part A, pp.173-180, Amsterdam/Netherlands.

[12] Qiu B.J., Jiang G.W., Yang N. et al., (2012), Discrete element method analysis of impact action between rice particles and impact-board. *Transactions of the Chinese Society of Agricultural Engineering*, Vol.28, Issue 3, pp.44-49, Beijing/China.

[13] Santos K. G., Campos A. V. P., Oliveira O. S. et al., (2015), DEM simulations of dynamic angle of repose of acerola residue: a parametric study using a response surface technique. *Blucher Chemical Engineering Proceedings*, Vol.1, Issue 2, pp.11326-11333, Sao Paulo/Brazil.

[14] Sarnavi H. J., Mohammadi A. N., Motlagh A. M. et al., (2013), DEM Model of Wheat Grains in Storage Considering the Effect of Moisture Content in Direct Shear Test. *Research Journal of Applied sciences Engineering & Technology*, Vol.5, Issue 3, pp.829-841, Sao Paulo/Brazil.

[15] Sun J.X., (2019), Study on biomechanical characteristics and damage mechanism of coarse grain, *杂粮籽粒生物力学特性及损伤机理研究*. PhD dissertation, Shanxi Agricultural University, Taiyuan/China.

[16] Sun Q.C., Wang G.Q., (2009), *Introduction to mechanics of granular matter,* China Science Press, pp.198-234, Beijing/China.

[17] Wang Y.X., Liang Z.J., Zhang D.X. et al., (2016), Calibration method of contact characteristic parameters for corn seeds based on EDEM. *Transactions of the Chinese Society of Agricultural Engineering*, Vol.32, Issue 22, pp.36-42, Beijing/China.

[18] Yu Q.X., Liu Y., Chen X.B., et al., (2020), Calibration and Experiment of Simulation Parameters for Panax notoginseng Seeds Based on DEM. *Transactions of the Chinese Society for Agricultural Machinery*, Vol.51, Issue 2, pp.123-132, Beijing/China.

[19] Yuan C.Q., Xu L.M., Ma S. et al., (2020), Calibration of simulation parameters of fermented sheep manure organic fertilizer based on skateboard test. *International Agricultural Engineering Journal,* Vol.29, Issue 2, pp.1-7, Beijing/China.

[20] Zhang T., Li Y. M., Xu L.Z. et al., (2016), Effect of fan's parameters on adhesion mechanism of threshold rape mixture to cleaning sieve. *INMATEH - Agricultural Engineering*, Vol.62, No. 3, pp.211-218, Bucharest/ Romania.

EFFECT OF DITCHING'S PARAMETERS ON OPERATION QUALITY OF ORCHARD DITCHING-FERTILIZER MACHINE

/

开沟参数对果园开沟施肥机作业质量的影响

ChunBao Xu[1)], HongJian Zhang[1)], ShuangXi Liu[1,2)], Chengfu Zhang[4)], Junlin Mu[1)], JinXing Wang[*1,3)]

[1)] College of Mechanical and Electronic Engineering, Shandong Agricultural University, Taian 271018, China;

[2)] Shandong Provincial Key Laboratory of Horticultural Machinery and Equipment, Taian 271018, China;

[3)] Shandong Provincial Engineering Laboratory of Agricultural Equipment Intelligence, Taian 271018, China;

[4)] Gaomi City Yifeng Machinery Co., Ltd., Gaomi 261500, China;

Tel: +86 05388246826; E-mail: jinxingw@163.com

DOI: https://doi.org/10.35633/inmateh-64-47

***Keywords:** orchard, ditching-fertilizer machine, ditching device, working parameters, optimization test*

ABSTRACT

This study aims to evaluate the effects of different parameter settings on the ditching performance using a ditching-fertilizer. We aimed to improve the performance of ditching-fertilizer machine performance in sustainable agriculture. With Box-Behnken experimental design method, taking forward speed, the rotation speed of the ditching cutter, and the deflection angle of ditching cutter as experimental factors, taking ditching depth stability and soil coverage rate as test indexes, the operation parameters of orchard ditching-fertilizer machine are studied. The regression model between test indexes and experimental factors is established, and the influence of each factor on the experimental indexes is analyzed. The test factors are comprehensively optimized. The results show that when the forward speed is 0.8km/h, the rotation speed of the ditching cutter is 348r/min, and the deflection angle of the ditching cutter is 32°, the ditching effect is the best. At this time, the stability coefficient of the ditching depth is 98.33%, and the soil coverage rate is 81.53%. As for the field test, which measured the stability coefficient of ditching depth, and the average soil cover rate is 96.24%, and 79.14%, respectively, and the relative errors from the optimized value are 2.17%, and 3.02%, respectively.

摘要

针对果园开沟作业存在开沟深度稳定性差、覆土率低等问题，基于离散元仿真开展果园开沟施肥机开沟作业参数优化试验，以探究整机作业工况下开沟装置作业参数对开沟深度稳定性、覆土率的影响规律。应用 Box-Behnken 试验设计方法，以前进速度、开沟刀转速、开沟刀偏转角为试验因素，以开沟深度稳定性、覆土率为试验指标，对果园开沟施肥机作业的参数进行试验研究，建立了试验指标与试验因素之间的回归模型，分析了各因素对试验指标的影响，并对试验因素进行了综合优化。结果表明，当前进速度为 0.8km/h、开沟刀转速为 348r/min、开沟刀偏转角为 32°时，开沟深度稳定性达到 98.33%、覆土率达到 81.53%。田间试验实测开沟深度稳定性、覆土率平均值分别为96.24%和79.14%，与优化值相对误差分别为2.17%和3.02%。研究结果可为果园开沟装置的结构改进和开沟作业参数控制提供参考。

INTRODUCTION

China is a big country of fruit production and consumption, which the cultivated area and output of fruit trees rank first in the world *(Huairui Shu et al, 2018; Xiuxin Deng et al, 2018)*. According to the National Bureau of Statistics, the planting area and fruit output of orchards are 11.87493 million hectares and 256.88 million tons respectively. In recent years, the level of orchard production and management mechanization in China is gradually improving. Among them, orchard ditching-fertilizing technology and equipment had made great progress, and gradually became the industry research hotspot *(Xiwen Luo et al, 2016;Zhi Chen, 2001)*. Orchard ditching-fertilizer machines can complete ditching, fertilization, soil covering, and other operational processes at one time *(Yichuan He et al, 2018)*. Comparing with traditional manual ditching fertilization, it has higher efficiency, low cost, and good fertilization effect. However, the complex structure of the orchard ditching-fertilizer machine, the harsh working environment, the different material composition, the large attribute difference, the diversified movement characteristics, and other factors have caused the ditching operation to have poor stability of the ditching depth and low soil cover rate. This directly affects the quality of orchard ditching operations and the yield of fruit trees *(Yao Fan et al, 2013; Yuexiang Lin et al, 2020)*.

As the main working part for the ditching-fertilizer machine, the performance of the ditching device directly affects the quality of the ditching operation. At present, domestic and foreign scholars have carried out relevant research on the structural design and optimization of orchard ditching devices, analysis of soil movement characteristics, influence law of ditching power consumption, etc. *(Dawei Liu et al, 2019; Aili Hasimu et al, 2014; Honglei Jia et al, 2020)*. *Wang Shaowei et al., (2019),* designed the ditching components of the Mountain Orchard ditching machine, optimized the structure parameters of the ditching blade by simulation test, and analyzed the influence of operation parameters on ditching power consumption. *Zhang Yongliang et al., (2012),* applied the theory of throwing soil to analyze the process of throwing soil, finding the trajectory equation of the thrown soil particles, establishing a mechanics model of soil discrete element contact, and studying its throwing performance with the method of experimental verification. *Kang Jianming et al., (2016),* established the finite element model of soil ditching cutter head by using the smoothed particle hydrodynamics method and obtained the variation law of power consumption of the slotting cutter head in the soil cutting process through simulation analysis. *Barr et al., (2016),* studied the effects of different openers on soil disturbance and soil pressure at different speeds through the orthogonal test and reduced soil disturbance by increasing the ditching operation speed. *Abdul et al., (1999),* analyzed the influence law of subsoiling shovel on the sandy soil cutting process and established a regression equation between traction force and soil moisture content and cutting depth.

Based on the above researches, the parameters of orchard ditching operation mainly affect the ditching power consumption, soil throwing performance, soil cutting speed, and then affect the stability of the ditching operation and the soil coverage rate. This paper takes the optimal ditching depth stability and soil cover rate as the research objectives, and uses the ditching device of self-developed orchard ditching-fertilizing to complete the ditching operation parameter optimization test based on the discrete element simulation method. This article explores the influence law of ditching operation parameters on the stability of ditching depth and soil coverage rate.

MATERIALS AND METHODS

Ditching operation parameters analysis

The ditching device is mainly composed of a ditching transmission box, ditching cutter head, and ditching cutter. The operation process is shown in Figure. 1. When working, the power output from the tractor is transmitted to the ditching transmission box, which drives the ditching cutter head and ditching cutter to rotate, to realize the ditching operation. According to the structure and working parameters of the ditching device of the orchard ditching-fertilizer machine, combined with the preliminary test, three key parameters affecting the operation quality were selected in this experiment: forward speed v, rotation speed of ditching cutter n, deflection angle of ditching cutter α.

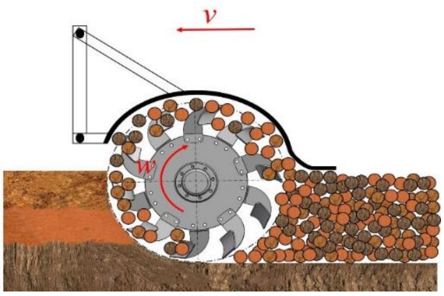

Fig. 1 - Schematic diagram of ditching operation

The forward speed directly affects the performance of the orchard ditching-fertilizer machine *(Xiaopeng Liu et al, 2019)*. According to the actual operation requirements and NY/T740—2003, the forward speed range of orchard ditching-fertilizer machinery is set as 0.8~1.2m/s. The motion parameters of the ditching parts in the ditching device affect the operation performance, especially the rotation speed of the ditching cutter determines the throwing distance, and its size directly affects the power consumption *(Jiqiang Peng et al, 2018)*. According to the previous field test, the best rotation speed range of a ditching cutter is set at 320~450 r/min.

In ditching operation, the ditching cutter should meet the requirements of cutting and throwing soil *(Guangwei Wu et al, 2014)*. According to the actual needs of ditching operation, the concave cutter with good cutting and throwing capacity is selected *(Xu Ma et al, 2001)*.

The concave cutter is mainly composed of a handle and a blade, and the included angle is the deflection angle of the ditching cutter, as shown in Figure. 2. The value of the ditching cutter deflection angle directly affects the operation contour of the ditching device. According to the actual operation requirements, combined with the previous field test, the optimal range of ditching cutter deflection angle is set at 25° to 45°.

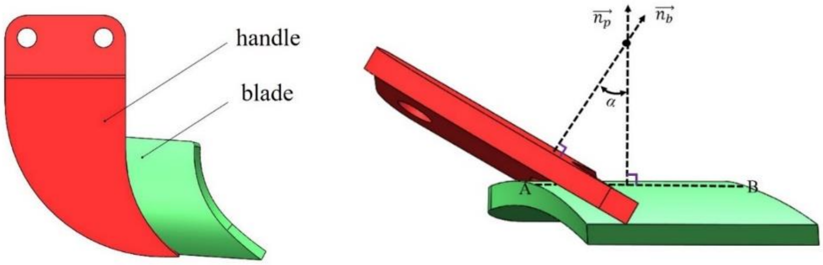

(a) (b)

Fig. 2 - Structure and deflection angle of ditching cutter

(a) Structure of the ditching cutter; (b) deflection angle of the ditching cutter

Note: the straight line AB is the intersection line between the blade surface and its tangent plane. $\overrightarrow{n_p}$ is the normal vector perpendicular to the tangent plane; $\overrightarrow{n_b}$ is the normal vector perpendicular to the plane of the handle.

Stability coefficient of ditching depth y_1

The stability degree of the ditching depth of the ditching-fertilizer machine is expressed by the stability coefficient y_1 of the ditching depth under the given working conditions. The calculation formula is as follows.

Through the analysis of the movement of fertilizer particles, we know that three factors affect the fertilizer discharge effect of the orchard double row ditching-fertilizing machine: one is the mechanical structure parameters of the machine; the other is the characteristics of the fertilizer itself; the third is the environmental factors. Under the influence of irresistible environmental factors and the characteristics of fertilizer itself, this study mainly studies the influence of the structural parameters of the machine on the law of fertilizer discharge to solve the problems in practical work.

$$h=\sum_{i=1}^{N} h_i \Big/ N \tag{1}$$

$$S=\sqrt{\frac{\sum_{i=1}^{N}(h_i-h)^2}{N-1}} \tag{2}$$

$$V=\frac{S}{h}\times 100\% \tag{3}$$

$$y_1=1-V \tag{4}$$

where h is average ditching depth, cm; h_i is ditching depth of the ith measuring point, cm; N is selected measuring points in the operation area; S is the standard deviation of ditching depth, cm; V is variation coefficient of ditching depth, %; y_1 is stability coefficient of ditching depth, %.

Coverage rate y_2

During the ditching operation, the soil is cut by the cutter and scattered. Under the action of the covering device, most of the soil is rebounded back into the ditching, and some residual splash soil is distributed in a triangle shape outside the ditching. The soil coverage rate is the proportion of soil volume in trapezoidal ditching to the total volume of soil scattered by the ditching cutter.

$$y_2=\frac{\sum_{i=1}^{n}\frac{Q_{1i}}{Q_{0i}}}{n}=\frac{\sum_{i=1}^{n}\frac{S_{1i}L}{(S_{1i}+S_{2i})L}}{n}=\frac{\sum_{i=1}^{n}\frac{S_{1i}}{S_{1i}+S_{2i}}}{n}=\frac{\sum_{i=1}^{n}\frac{N_{1i}}{N_{0i}}}{n} \tag{5}$$

where Q_{1i} is soil volume in the trapezoidal ditch after operation; Q_{0i} refers to the total volume of soil scattered during trenching; S_{1i} refers to the projected area of soil in the trapezoidal ditch after operation; S_{2i} is the projected area of the soil thrown out when ditching; L is forward distance; N_{1i} is the number of soil particles in the trapezoidal ditch after ditching; N_{0i} is the number of soil particles in the trapezoidal ditch before ditching.

Establishment of geometric model of ditching device

To shorten the simulation time, reduce the amount of simulation calculation, and improve the simulation efficiency, the three-dimensional model of the ditching device is reasonably simplified *(Shuai Ma et al, 2018)*. Among them, to ensure the simulation accuracy, the ditching device model is treated with 1:1, and the ditching transmission gear, bearing, support shaft, and other parts that do not directly contact the orchard soil are simplified. Import the processed 3D model into EDEM simulation software, as shown in Figure 3.

Establishment of the ditching soil model

An accurate soil particle model is the basis to ensure the validity of simulation results. Existing studies have shown that the "Hertz Mindlin with JKR" contact model can well simulate the interaction between particles by introducing surface energy *(Xuezhen Wang et al, 2018)*. Therefore, the "Hertz Mindlin with JKR" contact model considering the adhesion force between particles is selected for discrete element simulation.

According to the overall size and operation parameters of the ditching device, a virtual soil bin with a size of 3000mm × 800mm × 400mm was established in EDEM software. To accurately simulate the interaction process between the ditching device and soil, the radius of the soil particle unit is determined to be 8 mm in combination with reference *(Kan Zheng et al, 2016)*. According to the simulation parameters in Table 2, the soil particle model of each layer is generated. Its thickness and section shape is similar to the actual situation in the field, as shown in Figure. 3.

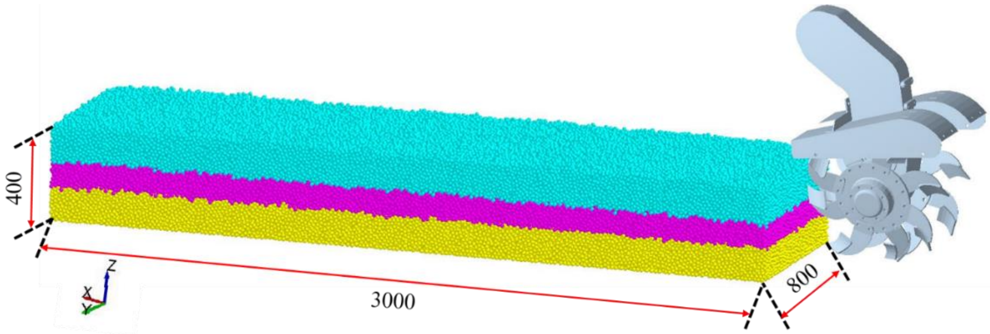

Fig. 3 - Simulation soil bin and geometric model of ditching device.

Determination and setting of soil particle contact parameters

The parameters of DEM simulation mainly include intrinsic parameters and contact parameters *(Kan Zheng et al, 2016)*. Among them, intrinsic parameters include shear modulus, density, and Poisson's ratio of orchard soil and ditching device; contact parameters include static friction coefficient, dynamic friction coefficient, and recovery coefficient between soil-soil and soil-steel. Simulation parameters directly affect the accuracy of the results. To accurately grasp the parameters of the test and simulation, the value of each parameter is determined based on the method of combining the test with the reference. Among them, the soil density is obtained by actual measurement with the ring knife method. The static friction coefficient and dynamic friction coefficient of 65Mn-soil and soil-soil were measured by inclined test-bed. Soil-soil surface can determine the corresponding values in EDEM according to the previous parameters, stacking angle test, and particle radius; other parameters refer to the data in reference *(Xuezhen Wang et al, 2018; Kan Zheng et al, 2016)*, and simulation parameters, as shown in Table 1.

Table 1

EDEM simulation parameters of ditching operation

Material	parameter	value	source
soil	Density/kg·m^{-3}	1669	determination
	Poisson's ratio	0.40	Reference [23]
	Shear modulus/MPa	1.0	Reference [23]
65Mn	Density /kg·m^{-3}	7.82×10^3	Reference [23]
	Poisson's ratio	0.29	
	Shear modulus/MPa	8.19×10^4	

65Mn-soil	Coefficient of restitution	0.6	Reference [24]
	Static friction coefficient	0.5	determination
	Dynamic friction coefficient	0.11	determination
soil-soil	Coefficient of restitution	0.6	literature [24]
	Static friction coefficient	0.4	determination
	Dynamic friction coefficient	0.15	determination
	JKR/J·m^2	2.3	Test calibration

Simulation process

To better characterize the influence of working parameters on the working state, the ditching depth was fixed at 350mm. Taking a certain working condition as an example, the pre-test is carried out. Set the parameters of the machine in EDEM: the forward speed v is 1.1m/s, and the direction is along the direction of the machine; the rotation speed of ditching cutter n is 385 r/min, and it rotates clockwise around the positive direction of the y-axis; the angle of the ditching cutter α is 35°. The parameters of the simulator module in EDEM software are set as follows: time step 20% (i.e. 2.06×10^{-4} s), action time 3.5 s, the interval time of data storage 0.05 s, and grid cell size 2 times the average particle radius. In EDEM, the operation status of the orchard ditching-fertilizer machine is shown in Figure. 4.

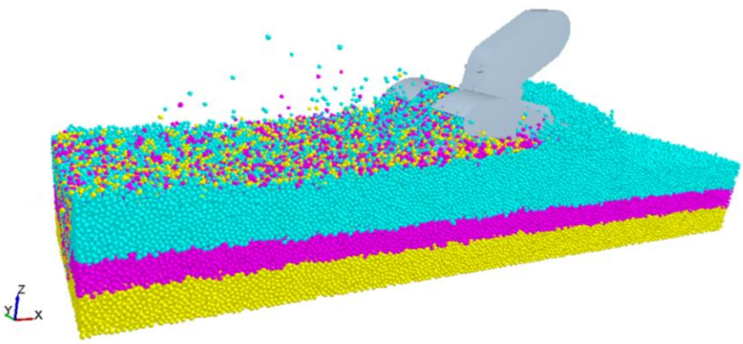

Fig. 4 - Status of orchard ditching

Analysis of simulation results

According to the working parameters and simulation parameters set in Table 1, the simulation test is carried out in EDEM. After the test, the depth of ditching and the number of particles covered with soil were measured and counted in EDEM post-processing. Among them, the ditching line of ditching is the fitting straight line of the transverse position of the deepest ditching. The ditching depth h is the distance from the ditching bottom line to the horizon, the sideline of the ditching contour is the line fitted by the side part of the ditching contour. According to the calculation formula of ditching depth stability coefficient y_1 and soil coverage rate y_2, the corresponding values are calculated, which are used as indicators to evaluate the effect of the ditching device, as shown in Figure 5. In the pretest, the stability coefficient of ditching depth y_1 and the coverage rate y_2 is 97.44%, 72.78% respectively.

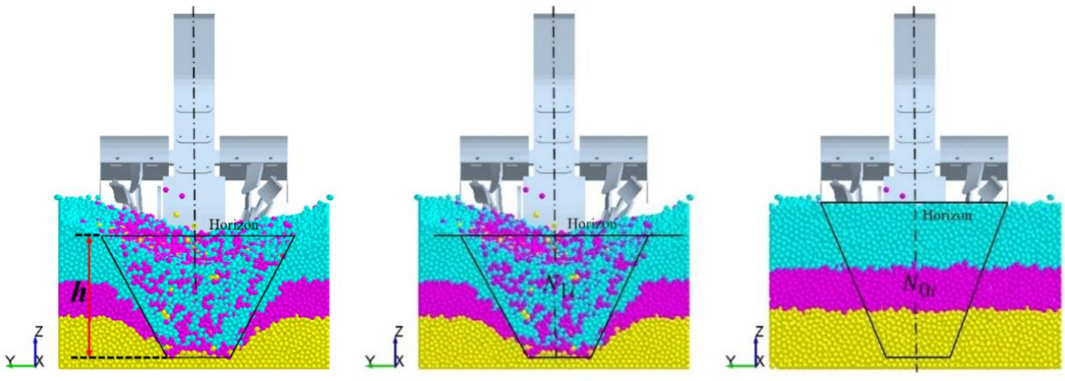

Fig. 5 - Measurement of various indexes in ditching operation

Experimental design

To explore the interaction and influence law of the three parameters, including forwarding speed, the rotation speed of the ditching cutter, and the deflection angle of the ditching cutter, on the stability of ditching depth and soil coverage rate.

Box-Behnken test design was used to carry out experimental research on operating parameters of the orchard ditching-fertilizer machine, and to seek the optimal working conditions for ditching operation parameters of orchard ditching-fertilizing machine method *(Jinqing Lu et al, 2016)*. According to the results of the orthogonal test, forward speed v, the rotation speed of the ditching cutter n, and the deflection angle of the ditching cutter α are set as independent variables x_1, x_2, and x_3 respectively. The stability coefficient of ditching depth and the coverage rate are set as y_1, y_2 respectively.

The experimental factors and coding levels of three factors and two levels are formulated, as shown in Table 2, and the results of the orthogonal test are shown in Table 3.

Table 2

Table of factor sand levels

levels	forward speed x_1/(m·s^{-1})	speed of the ditching cutter x_2/(r·min^{-1})	deflection angle of the ditching cutter x_3/(°)
low-level	0.8	320	25
mid-level	1.0	385	35
high-level	1.2	450	45

Table 3

Experimental design and results of ditching operation

Test number	x_1/(m·s^{-1})	x_2/(r·min^{-1})	x_3/(°)	y_1/(%)	y_2/(%)
1	1.0	450	45	93.99	74.49
2	1.0	450	25	96.44	75.54
3	1.2	450	35	97.61	70.77
4	1.2	385	25	95.42	73.26
5	1.0	385	35	96.99	74.31
6	0.8	385	45	96.10	82.76
7	1.0	320	45	94.87	77.92
8	1.0	385	35	97.54	74.03
9	1.0	320	25	95.41	79.17
10	1.2	385	45	97.98	71.89
11	0.8	450	35	94.77	77.64
12	0.8	385	25	97.12	81.51
13	0.8	320	35	98.34	82.60
14	1.0	385	35	96.91	73.81
15	1.0	385	35	97.61	74.99
16	1.2	320	35	94.11	74.65
17	1.0	385	35	96.51	75.40

RESULTS AND ANALYSIS

Establishment of the regression model and variance analysis

Design-Expert 8.0 software is used to establish a response surface regression model of forwarding speed, rotation speed of the ditching cutter, and deflection angle of the ditching cutter on the ditching depth stability coefficient and soil coverage rate. Variance analysis of the regression model is conducted, and the results are shown in Table 4.

It can be seen from Table 4 that the model significance P values of ditching depth stability coefficient and soil coverage rate are all less than 0.05, indicating that the regression model is significant. The P values of the mismatching items were all greater than 0.05, indicating that there was no mismatch factor, indicating that the regression equation had a high fitting degree, and the regression model could be used to replace the real test results for analysis. The order of significance of each factor on ditching depth stability is the deflection angle of the ditching cutter, forward speed, and rotating speed of the ditching cutter from large to small. The order of significance of influencing soil coverage rate is forward speed, the deflection angle of the ditching cutter, and the rotating speed of the ditching cutter. The R^2 of the model for the stability coefficient of the trench depth and the coverage rate are 0.8736, 0.9751, respectively, which indicates that 12.64% and 2.49% of the variation cannot be explained by the model. They indicated that the model has a good fitting degree and can be used for test prediction.

For the stability of ditching depth, the regression terms x_1x_2 had a significant impact ($P < 0.01$), and x_1x_3 and x_2^2 had a significant impact ($P < 0.05$). For the coverage rate, the regression terms x_1, x_2, x_3^2 had a significant impact ($P < 0.01$), and x_1^2 had a significant impact ($P < 0.05$).

Using Design-Expert 8.0 software to conduct multiple regression analysis on the test results in Table 4, the code value quadratic regression model of ditching depth stability and soil coverage rate affected by various factors is obtained, as shown in equations (6)~(7).

$$y_1=97.11-0.15x_1+0.01x_2-0.18x_3+1.77x_1x_2+0.89x_1x_3-0.48x_2x_3+0.29x_1^2-1.19x_2^2-0.74x_3^2 \tag{6}$$

$$y_2=74.51-4.24x_1-1.99x_2-0.30x_3+0.27x_1x_2-0.66x_1x_3+0.053x_2x_3+1.24x_1^2+0.67x_2^2+1.61x_3^2 \tag{7}$$

Variance analysis of regression model **Table 4**

evaluating indicator	Source of variance	Sum of squares	freedom	mean square	P	Significance
Stability coefficient of ditching depth y_1/(%)	model	25.85	9	5.38	0.0187	*
	x_1	0.18	1	0.34	0.5778	
	x_2	0.00	1	0.00	0.9682	
	x_3	0.26	1	0.49	0.5046	
	x_1x_2	12.47	1	23.34	0.0019	**
	x_1x_3	3.19	1	5.97	0.0446	*
	x_2x_3	0.92	1	1.71	0.2320	
	x_1^2	0.35	1	0.65	0.4476	
	x_2^2	5.96	1	11.16	0.0124	*
	x_3^2	2.32	1	4.34	0.0757	
	residual	3.74	7			
	Mismatch term	2.88	3	4.49	0.0903	
	Pure error	0.86	4			
	sum	29.59	16			
Coverage rate y_2/(%)	model	199.44	9	30.41	< 0.0001	**
	x_1	143.95	1	197.51	< 0.0001	**
	x_2	31.62	1	43.38	0.0003	**
	x_3	0.72	1	0.99	0.3519	
	x_1x_2	0.29	1	0.40	0.5491	
	x_1x_3	1.72	1	2.37	0.1679	
	x_2x_3	0.01	1	0.02	0.9053	
	x_1^2	6.47	1	8.88	0.0205	*
	x_2^2	1.87	1	2.56	0.1534	
	x_3^2	10.85	1	14.88	0.0062	**
	residual	5.10	7			
	Mismatch term	3.32	3	2.49	0.1999	
	Pure error	1.78	4			
	sum	204.55	16			

*Note: * indicates significant effect, P < 0.05; * * indicates extremely significant effect, P < 0.01.*

The model y_1 and y_2 are optimized by eliminating the insignificant items in the model, as shown in equation (7) ~ (8).

$$y_1=97.11+1.77x_1x_2+0.89x_1x_3-1.19x_2^2 \tag{7}$$

$$y_2=74.51-4.24x_1-1.99x_2+1.24x_1^2+1.61x_3^2 \tag{8}$$

Analysis of the interaction effect of two factors

In the regression Equation (6) ~ (7), taking any factor level as the medium level, and the influence of the other two factors on the stability coefficient of ditching depth, the soil coverage rate is studied. The response surface of interaction factors is analyzed by Design-Expert 8.0 software, as shown in Figure 7~8.

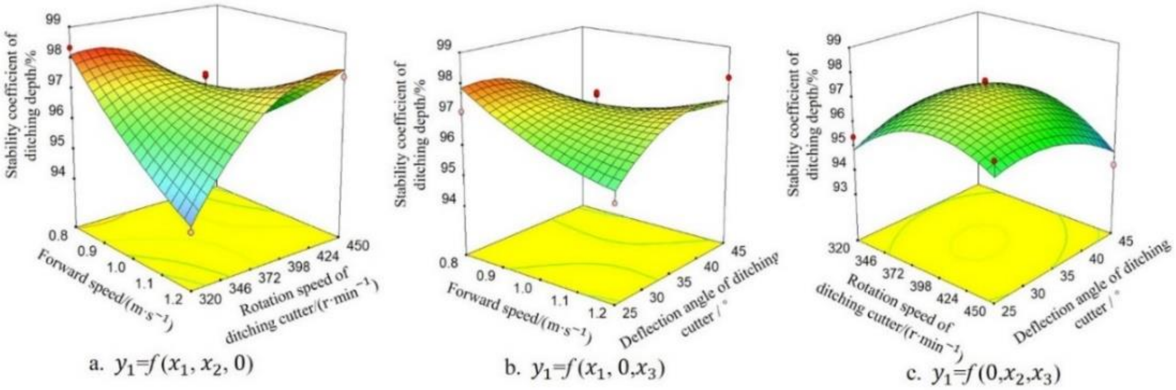

Fig. 7 - Response surfaces of test factors influence on ditching depth stability

Figure 7a shows the interactive influence of the forward speed and the rotation speed of the ditching cutter on the stability coefficient of the ditching depth. When the forward speed is at a low level, the impact of the rotation speed of the ditching cutter on the stability coefficient of the ditching depth is obvious, which is shown in the figure that the stability curve of the ditching depth is steep. When the forward speed is in the range of 0.8 ~ 1.0m/s, the stability of the ditching depth can be significantly improved by properly reducing the rotation speed of the ditching cutter. It can also be seen that when the rotation speed of the ditching cutter is the same, the stability of the ditching depth gradually decreases with the increase of the machine's forward speed. The stability of the ditching depth increases first and then decreases with the increase of the speed of the machine. Figure. 7b shows the interactive influence of the forward speed and the deflection angle of the ditching cutter on the stability of the ditching depth. The stability of the ditching depth decreases with the increase of the forward speed of the machine under the same deflection angle of the ditching cutter. The stability of the ditching depth increases at first and then decreases with the increase of the deflection angle of the ditching cutter at the same forward speed of the machine. Figure. 7c shows the interactive influence of the ditching cutter speed and the ditching cutter deflection angle on the ditching depth stability. Under the same ditching knife deflection angle, the ditching depth stability increases with the increase of the whole machine speed At the same speed of the cutter, the stability of the ditching depth increases first and then decreases with the increase of the forward speed of the whole machine.

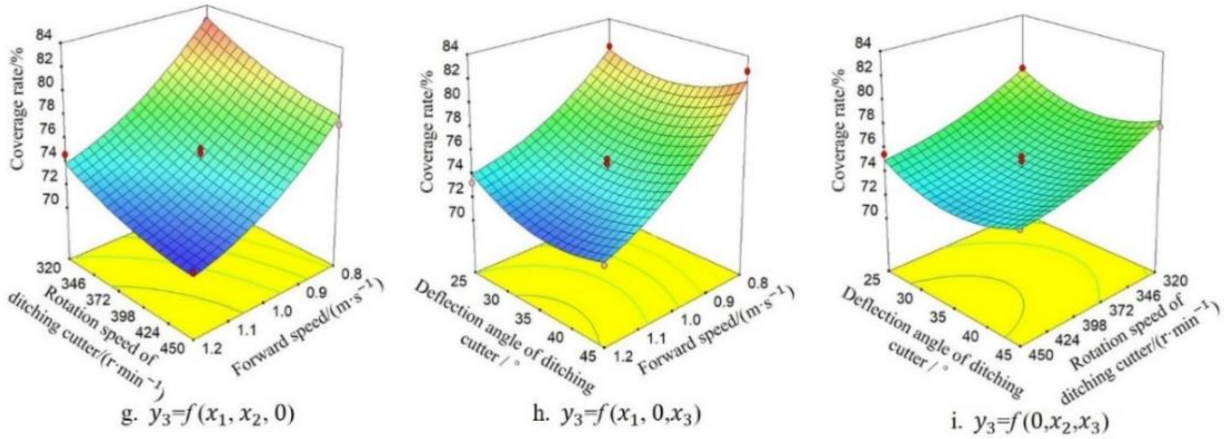

Fig. 8 - Response surfaces of test factors influence on coverage rate

Figure 8g shows the interaction between the forward speed and rotation speed of the ditching cutter on the soil coverage rate. When the rotation speed of the ditching cutter is at a low water level, the influence of the forward speed on the coverage rate is obvious, which is shown in the figure that the curve of the covering rate is steep. When the rotation speed of the ditching cutter is in the range of 320-372r/min, the covering rate can be significantly increased by a proper small forward speed. However, when the rotation speed of the cutter and the forward speed is reduced, the cover rate will increase obviously. Figure 8h shows the interaction between the forward speed and the deflection angle of the ditching cutter on the covering rate. Under the same forward speed, the covering rate decreases first and then increases with the increase of the deflection angle of the ditching cutter. At the same deflection angle of the ditching cutter, the covering rate decreases with the increase of the forward speed. Figure 8i shows the interaction between the rotation speed of the ditching cutter and the deflection angle of the ditching cutter on the covering rate. Under the same rotation speed of the cutter, with the increase of the deflection angle of the ditching cutter, the soil coverage rate first decreases slowly and then increases slowly. Under the same deflection angle of the ditching cutter, the rate of covering soil decreases with the increase of the rotation speed of the ditching cutter.

Parameter optimization

According to the agronomic requirements of orchard ditching operation, combined with the actual situation of orchard ditching-fertilizer machine ditching operation, it is required that ditching depth stability and soil coverage rate reach the optimal level. Due to the inconsistent influence of various factors on the target value, global multi-objective optimization is needed *(Chao Cheng et al, 2016; Wenxiu Zheng et al, 2019)*. Taking the stability of ditching depth and soil coverage rate as objective functions, the forward speed, the rotation speed of the ditching cutter, and the deflection angle of the ditching cutter are optimized. The optimized mathematical model is as follows

$$\begin{cases} \max y_1 = (x_1, x_2, x_3) \\ \max y_2 = (x_1, x_2, x_3) \\ st. \begin{cases} 0.8 \le x_1 \le 1.2 \text{ m/s} \\ 320 \le x_2 \le 450 \text{ r/min} \\ 25 \le x_3 \le 45 \text{ °} \end{cases} \end{cases} \tag{9}$$

To find the best combination of parameters, the influence of three factors on the stability of ditching depth and the coverage rate is comprehensively considered. The optimal working parameters were obtained as follows: the forward speed was 0.8 km/h, the rotation speed of the ditching cutter was 348.03 r/min, and the deflection angle of the ditching cutter was 32.23° under these conditions, the stability of the ditching depth was 98.33%, and the covering rate was 81.53%.

Verification test

According to the optimization results of the ditching operation parameters of the orchard ditching-fertilizer machine, a field verification test was carried out to test the reliability of the regression model and optimal combination. 2FQG-2 orchard ditching-fertilizer machine developed by Shandong Agricultural University was used in the experiment. The structure of the machine is the same as the test prototype used in this paper. The test site is the test base of Gaomi Yifeng Machinery Co., Ltd. The soil is loam soil, the absolute moisture content is 16.7%, the ground is relatively flat, and the area is about 650m^2, as shown in Figure 9.

Fig. 9 - Validation test in the field

To facilitate the practical application, the optimized parameters are rounded properly. The forward speed is set as 0.8km/h, the rotation speed of the ditching cutter is 348r/min, and the deflection angle of the ditching cutter is 32°. The test methods and indicators refer to GB/T5262-2008 general provisions for determination of test conditions of agricultural machinery and the operation quality evaluation test method of ditching machinery specified in NY/T740-2003 *(2006, 2008)*. After three repeated tests, the average value is obtained. The stability of the ditching depth is 96.24%, and the coverage rate is 79.14%. The comparison between the predicted value and the measured test result is shown in Table 5.

Table 5

Comparison of predicted values of test indexes with measured results

index	stability of ditching depth y_1/%	coverage rate y_2/%
Optimization value	98.33	81.53
Test value	96.24	79.14
Relative error	2.17	3.02

The experimental results show that the relative errors between the measured values and the predicted values are less than 5%, and the measured values are in good agreement with the predicted values, indicating that the regression model is reliable.

CONCLUSIONS

(1) To obtain the optimal parameters of the orchard ditching-fertilizer machine, Box-Behnken experimental design was adopted. The forward speed, the rotation speed of the ditching cutter, and the deflection angle of the ditching cutter were set as independent variables. The stability of the ditching depth and the soil coverage rate were set as the response values. Through the analysis of the model interaction and response surface, the influence of the forward speed, the rotation speed of the ditching cutter, and the deflection angle of the ditching cutter on the response index are obtained.

(2) The optimization model of operation parameters of the orchard ditching-fertilizer machine was established. The optimal parameters of ditching depth stability and soil coverage rate were obtained: the forward speed was 0.8 km/h, the rotation speed of the ditching cutter was 348 r/min, and the deflection angle of the ditching cutter was 32°. At this time, the stability of the ditching depth is 98.33% and the coverage rate is 81.53%. The results show that the relative errors between the measured values and the predicted values are less than 5%, which indicates that the regression model is reliable.

ACKNOWLEDGEMENT

This research was funded by National Key Research and Development Plan of China, grant number 2016YFD0201104, National Apple Industry Technology System Project of China, grant number CARS-27.

REFERENCES

[1] Abdul M.M., Miklos N., Helmut S., Martin R., (1999), Tillage tool design by the finite element method: Part 2. Experimental validation of the finite element results with bin test. *Journal of Agricultural Engineering Research,* vol.72, issue 1, pp.53–58.

[2] Barr J.B., Desbiolles-Jack M.A., Fielke J.M., (2016), Minimizing soil disturbance and reaction forces for high speed sowing using bentleg furrow openers. Biosystems Engineering, vol.151, pp.53–64.

[3] Cheng C., Fu J., Chen Z., Hao F., Cui F., Ren L., (2019), Optimization experiment on cleaning device parameters of corn kernel harvester. *Transactions of the Chinese Society for Agricultural Machinery* vol.50, issue 7, pp.151–158.

[4] Chen Z., (2001), A sustainable development of agriculture and agricultural mechanization in China. *Transactions of the Chinese Society for Agricultural Machinery*, vol.32, issue 1, pp.1–4, 15.

[5] Deng X., Shu H., Hao Y., Xu Q., Han M., Zhang S., Duan C., Jiang Q., Yi G., Chen H., (2018), Review on the centennial development of pomology in China. *Journal of Agriculture*, vol.8, issue 1, pp.24–34.

[6] Fan Y., Liu J., Li J., (2013), Design of high clearance orchard dynamic chassis. *Journal of Agricultural Mechanization,* vol.35, issue 4, pp.92–95.

[7] GB/T5262—2008 *Measuring methods for agricultural machinery testing conditions—General rules*. 2008.

[8] Hasimu A., Chen, Y., (2014), Soil disturbance and draft force of selected seed openers. *Soil &Tillage Research,* vol.140, pp.48–54.

[9] He Y., Tang Z., Meng X., Qin T., (2015), Design and experiment of 2FK-40 orchard ditching fertilizer combined machine. *Journal of Agricultural Mechanization Research,* vol.37, issue 12, pp.201–204.

[10] Jia H., Meng F., Liu L., Shi S., Zhao J., Zhuang J., (2020), Biomimetic design and experiment of core-share furrow opener. *Transactions of the Chinese Society for Agricultural Machinery*, vol.51, issue 4, pp.44－49, 77.

[11] Kang J., Li S., Yang X., Liu L., Li C., (2016), Experimental verification and simulation analysis on power consumption of disc type ditcher. *Transactions of the CSAE,* vol.32, issue 13, pp.8–15.

[12] Lin Y., Shang S., Wang D., Yu H., Zhang C., (2020), Design and test of the multi-functional field management machine for orchard. *Journal of Agricultural Mechanization Research,* vol.42, issue 4, pp.40–46.

[13] Liu D., Xie F., Ye Q., Ren S., Li X., Liu Mi., (2019), Analysis and experiment on influencing factors on power of ditching parts for 1K-50 orchard ditching. *Transactions of the CSAE,* vol.35, issue 18, pp.19–28.

[14] Liu X., Zhang Q., Liu L., Wei G., Xiao L., Liao Q., (2019), Surface optimization of ship type ditching system based on differential geometry and EDEM simulation. *Transactions of the Chinese Society for Agricultural Machinery,* vol.50, issue 8, pp.59–69.

[15] Lü J., Shang Q., Yang Y., Li Z., Li J., Liu Z., (2016), Design optimization and experiment on potato haulm cutter. *Transactions of the Chinese Society for Agricultural Machinery* vol.47, issue 5, pp.106–114.

[16] Luo X., Liao J., Hu L., Zang Y., Zhou Z., (2016), Improving agricultural mechanization level to promote agricultural sustainable development. *Transactions of the CSAE*, vol.32, issue 1, pp.1–11.

[17] Ma X., Zhao Y., Wang J., Ma C., (2001), Fuzzy prediction study on lifting and throwing soil capacity of reverse-rotational rotor with concave surface blade. *Transactions of the CSAE,* vol.32, issue 4, pp.61–66.

[18] Ma S., Xu L., Xing J., Yuan Q., Yu C., Duan Z., Chen C., Zeng J., (2018), Development of unilateral cleaning machine for grapevine buried by soil with rotary impeller. *Transactions of the CSAE,* vol.34, issue 23, pp.1–10.

[19] [19] National Bureau of Statistics of China. Chinese statistics yearbook. Beijing: China statistics Press, 2018.

[20] NY/T740—2003 Field operation quality of ditchers. 2006.

[21] Peng J., Kang J., Jian S., Yang X., Liu L., (2018), Parameter optimization and power consumption and kinematics analyses of clockwise and counterclockwise ditching. *Journal of China Agricultural University,* vol.23, issue 8, pp.151–159.

[22] Shu H., Chen X., (2018), The current task of the development of fruits industry in China. *China Fruits*, issue 2, pp.1–3.

[23] Wang S., Li S., Zhang Y., Zhang C., Chen H., Meng L., (2018), Design and optimization of inclined helical ditching component for mountain orchard ditcher. *Transactions of the CSAE,* vol.34, issue 23, pp.11－22.

[24] Wu G., Fu W., Dong J., Cong Y., Meng Z., (2014), Design and experiment of 1KY-40 hydraulic drive ditcher for farmland conduit. *Transactions of the Chinese Society for Agricultural Machinery,* vol.45, issue supp.1, pp.302–308.

[25] Wang X., Yue B., Gao X., Zheng Z., Zhu R., Huang Y., (2018), Discrete element simulations and experiments of disturbance behavior as affected by mounting height of subsoil's wing. *Transactions of the Chinese Society for Agricultural Machinery,* vol.49, issue 10, pp.124–136.

[26] Zhang Y., (2012), Simulation and experimental study on soil throwing performance of reverse rotary tillage fertilizing seeder based on discrete element method. Zhenjiang: Jiangsu University.

[27] Zheng K., He J., Li H., Diao P., Wang Q., Zhao H., (2016), Research on polyline soil-breaking blade subsoiler based on subsoiling soil model using discrete element method. *Transactions of the Chinese Society for Agricultural Machinery* vol.47, issue 9, pp.62–72.

[28] Zheng W., Lu Z., Zhang W., Liu Z., Lu Y., Li Y., (2019), Design and test of single row sweet potato vine recycling machine. *Transactions of the CSAE,* vol.35, issue 6, pp.1–9.

RESEARCH OF SEED GROUP STRUCTURE CHARACTERISTICS OF VERTICAL DISC METERING DEVICE BASED ON DISCRETE ELEMENT METHOD
/
基于离散元法的垂直圆盘侧充排种器种群结构特性研究

Yulong Chen, Zeqi Liu, Meng Zhang, Yubin Lan, Lili Yi, Xiang Yin* [1]

[1)] School of Agricultural Engineering and Food Science, Shandong University of Technology, Zibo 255000, China;
[2)] Shandong Provincial Collaborative Innovation Center of Dry-farming Intelligent Agricultural Equipment, Zibo 255000, China;
[3)] Research of Institute of Ecological Unmanned Farm, Shandong University of Technology, Zibo 255000, China;
[4)] Shandong provincial key laboratory of dry-farming machinery and informatization, Zibo 255000, China;
Tel: +86 18369916558; E-mail: 666513@163.com
DOI: https://doi.org/10.35633/inmateh-64-48

Keywords: *vertical disc metering device, seed group, discrete element method, seed chamber structure, seed filling performance*

ABSTRACT
The vertical disc seed metering device was selected to study the influence of the structural characteristics of seed group on the filling performance of seed metering device. The working process of seed metering device was simulated by discrete element software to study the influence of seed quantity and structure characteristics of seed chamber on seed movement and filling results. The seed group was divided into four zones: ascending zone, relative static zone, collapse zone and recirculation zone. The number of seeds and the rotation speed of disk have no effect on the inclination angle of the recirculation zone upper surface, which was always about 35°. But they had a significant effect on the filling performance. When the number of seeds was 500-1500, QFI (quality of feed index) decreased, MIS (miss index) increased and MUL (multiple index) did not change significantly. However, when the number of seeds was 2000, the change trend of filling performance was completely opposite. Inner surface inclination angle and axial width of the seed chamber have significant effects on the filling performance. QFI first increased and then decreased with the increase of inclination angle, reaching the maximum at 20° and MIS showed the opposite trend. QFI increases with the increase of thickness and tends to be stable at 40mm. Similarly, MIS has the opposite trend.

摘要
为了了解种子群的结构特性对排种器充种性能的影响规律，选取垂直圆盘侧充排种器为研究对象，利用离散元软件 EDEM 对排种器的工作过程进行仿真试验，研究种群数量及种室的结构特征对种群运动和充种效果的影响规律。离散元仿真显示种群分为上升区、相对静止区、塌落区、回流区。回流区上表面的倾角与种子数量及排种盘的转速无关，始终保持在 35° 左右。种群数量和排种盘转速对充种结果具有显著影响，种子数为 500-1500 时，QFI 随转速增加而降低，而 MIS 逐渐增大，同时 MUL 变化不显著;当种子数为 2000 时，充种性能的变化与 500-1500 时刚好相反。种室的底面倾角和厚度对充种性能具有显著影响，QFI 随倾角的增大先增大后降低，在 20° 时达到最大，MIS 变化与 QFI 相反；合格率随厚度增加而逐渐增大并在 40mm 时趋向稳定，同样 MIS 的变化趋势与 QFI 完全相反。

INTRODUCTION
Sowing is the key link of agricultural production, and the seed metering device is one of the important parts that affect the sowing effect *(Yang et al., 2016)*. Pneumatic seed metering device is the main type of seed metering device in the world *(Correia et al., 2016; Singh., 2007; Jack., 2013; Yu et al., 2014).* Pneumatic metering device is the main metering device in the world, and it is widely used in developed countries. However, due to its high production cost and complex use and maintenance, mechanical metering device is still used in many countries (*Wang et al., 2017; Yi et al., 2014*).

[1] *Yulong Chen, Lecture Ph.D. Eng.; Zeqi Liu, M.S. Stud. Eng.; Meng Zhang, M.S. Stud. Eng.; Yubin Lan, Prof. Ph.D. Eng.; Lili Yi, As. Ph.D. Eng.; Xiang Yin, As. Ph.D. Eng.*

Vertical disc seed metering device is a common mechanical seed metering device, which is mainly used for sowing round seeds such as soybean and pea *(Liu et al., 2015; Vianna., 2014)*. The author has carried out the research on the vertical disc metering device, optimized the structure of seed stirring on the disk, and obtained the concave type agitator with better seed stirring effect *(Chen et al., 2021)*. The optimal value of depth and angle of concave type agitator were 3.1mm and 60.5°, respectively.

The discrete element method is often used in the research of seed metering device, because the seed is a typical discrete material *(Khatchatourian, Binelo, & Lima, 2014; Li et al., 2013)*. The movement law of particles can be deeply studied and analyzed by using discrete element software, and EDEM is the most widely used discrete element software *(Wang et al., 2015)*.

At present, the research of seed metering device focuses on the influence of disk on seed movement and seed metering performance *(Kocher et al., 2011; Mao et al., 2015)*. Researchers innovate the structure of seed picking mechanism, optimize the design of seed stirring and seed cleaning mechanism, and improve the detection method of seed metering performance *(Jiang., 2021; Li., 2021; Zhang et al., 2015)*. However, there were few studies on the structure and movement characteristics of seed group in the process of seeding. Therefore, in this paper, the discrete element method was used to research the structure and movement characteristics of the population.

MATERIALS AND METHODS

Vertical disc metering device

The vertical disc seed metering device is mainly composed of shell, flexible seed cleaning part, disk, flange, bearing, base and shaft (Fig. 1). The disk is fixedly connected to the shaft through the flange and rotates with the shaft. The shaft is connected to the shell through the rolling bearing. Seed taking groove and seed agitator are evenly distributed on the outside of the disk, and there are suction holes at the bottom of the seed taking groove.

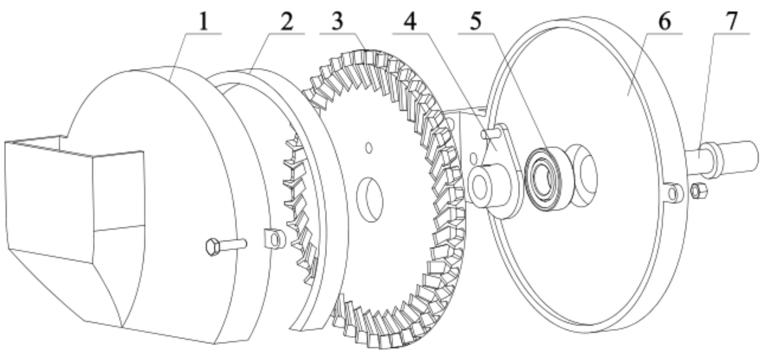

Fig. 1 - Structure diagram of seed metering device

1. Shell; 2. Flexible seed cleaning part; 3. Disk; 4. Flange; 5. Bearing; 6. Base; 7. Shaft; 8. Hole; 9. Seed agitator

The relationship between the rotation speed of disk and the forward speed of planter was shown as follows:

$$n = \frac{v}{60 \cdot k \cdot s} \tag{1}$$

where:

n is the speed of disk, [r/min];

v is the forward speed of planter, [m/s];

k is the number of seed holes on the disk, it is designed as 40;

s is the sowing distance, it is designed as 0.05m.

EDEM is a mature commercial discrete element simulation software (*Wang et al., 2015*) and version 11.0 of EDEM was used for virtual simulation test in this paper.

In the simulation, the vertical disk seed metering device was simplified by removing the shaft, bearing, flexible seed cleaning part and other components, leaving only the shell and disk (Fig. 2). The disk and shell were made of PMMA (polymethyl methacrylate), a transparent material.

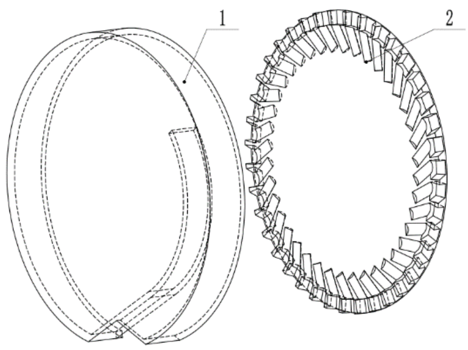

1. Shell; 2. Disk

Fig. 2 - Simulation model of seed metering device

Soybean seed used here was Jiyu202 (Table 1), which was widely planted in Northeast, the major soybean production region of China.

Table 1

Physical properties of soybean

Physical property	Mean	Standard error
L [mm]	7.21	0.32
W [mm]	6.11	0.31
T [mm]	6.32	0.44
D [mm]	6.52	
Φ [%]	91.88	
Thousand seed mass [g]	180.55	0.21

Note: *L* average length; *W* average width; *T* average Thickness; *D* means of geometrical diameter and calculated as $D=(LWT)^{1/3}$ respectively. ϕ means of sphericity and calculated as $\phi=\frac{(LWT)^{1/3}}{L}\times 100$.

Hertz-Mindlin non-sliding contact model was adopted in simulation. The global parameters used in the simulation were obtained by reference (*Li et al., 2013; Zhang et al., 2017*) (Table 2).

Table 2

Parameters used in simulation

Property	Soybean	PMMA	Property	Soybean-Soybean	Soybean-PMMA
Poisson's ratio	0.4	0.33	Collision recovery coefficient	0.6	0.5
Shear modulus [Pa]	1.1×10^7	8×10^7	Static friction coefficient	0.5	0.3
Density [kg/m^3]	1053	1190	Rolling friction coefficient	0.01	0.09

Test plan

There are two factors affecting the structure of seed group. One is the number of seeds entering the chamber from the entrance, which is determined by the size and location of the entrance. Another factor is the structure of seed chamber, which is determined by inner surface inclination angle and axial width. Single factor simulation tests were carried out with seed number n, inner surface inclination angle α, axial width b as factors (Fig. 3).

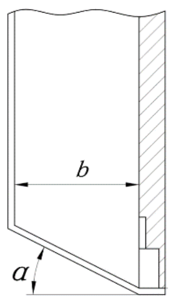

Fig. 3- Schematic diagram of seed chamber structure

The number of seeds was set as 500, 1000, 1500 and 2000 respectively. Inner surface inclination angle was set as 0°, 10°, 20° and 30°, respectively. Axial width was set as 20, 30, 40 and 50 mm, respectively (Table 3).

Table 3

Factors and levels of seed chamber structure

Level	Factors		
	n	*α* [°]	*b* [mm]
1	500	0	20
2	1000	10	30
3	1500	20	40
4	2000	30	50

Measurement and computing method

According to GB/T 6973-2005 test methods for single seed (precision) planter, 250 seeds were collected for statistics in each group of experiments, and the test was repeated 3 times, and the seed metering performance evaluation indexes were *MUL*, *MIS* and *QFI* (*Mao et al, 2015; Zhang et al, 2015*).

$$MUL = N_1 / N \times 100\% \tag{2}$$

$$MIS = N_2 / N \times 100\% \tag{3}$$

$$QFI = (1 - MIS - MUL) \times 100\% \tag{4}$$

where:

N_1 is the number of seed holes containing multiple seeds in the simulation test.

N_2 is the number of seed taking holes that are not filled in the simulation test.

N is the total number of seed holes recorded in the simulation test.

RESULTS AND ANALYSIS

Structural characteristics of seeds

EDEM was used to get the velocity vector of seeds in the working process of vertical disc seeder. According to the velocity size and direction of seed particles, the seed group can be divided into four zones (Fig. 4), ascending zone, relative static zone, collapse zone and recirculation zone。

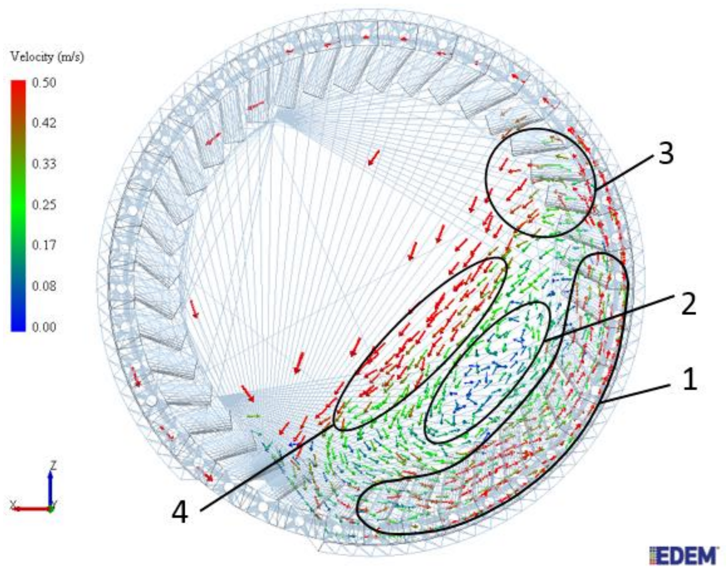

Fig. 4- Simulation diagram of seed movement

1. Ascending zone; 2. Relative static zone; 3. Collapse zone; 4. Recirculation zone

In the lower part of the seed group, seeds near the seed agitator have the highest speed, and the seed move upward from the bottom, so this area was the ascending area. The speed in this area was higher because the seed agitator passes through and drives the seed to move upward from the bottom.

Above the ascending area, seeds carried by the seed hole fall down under the action of gravity and enter into the seed group. This zone was called collapse zone. Seed movement in this area was violent, and the speed direction changes from up to down. The size of the collapse area was related to the rotation speed of the disk.

Seeds in the middle of the seed group only rotate around themselves, and the relative position with the metering device remains basically unchanged. This region was called relative static zone.

Seeds on the surface of the seed group move from the top to the bottom. This area was called recirculation zone. The area was mainly composed of seeds falling back to the group in the collapse zone. Seeds move to the bottom under the action of gravity, and then return to the bottom of the population.

Influence of seed quantity

In the pre-processing of discrete element simulation, the number of particles generated by particle factory was set as 500, 1000, 1500 and 2000 respectively. The forward speed of the planter was set as 2, 4, 6, 8 and 10km/h respectively. The rotation speed of disk was calculated by formula (1), and the corresponding rotation speed is 16.7, 33.3, 50.0, 66.7 and 83.3rpm respectively. The discrete element simulation was carried out (Fig. 5).

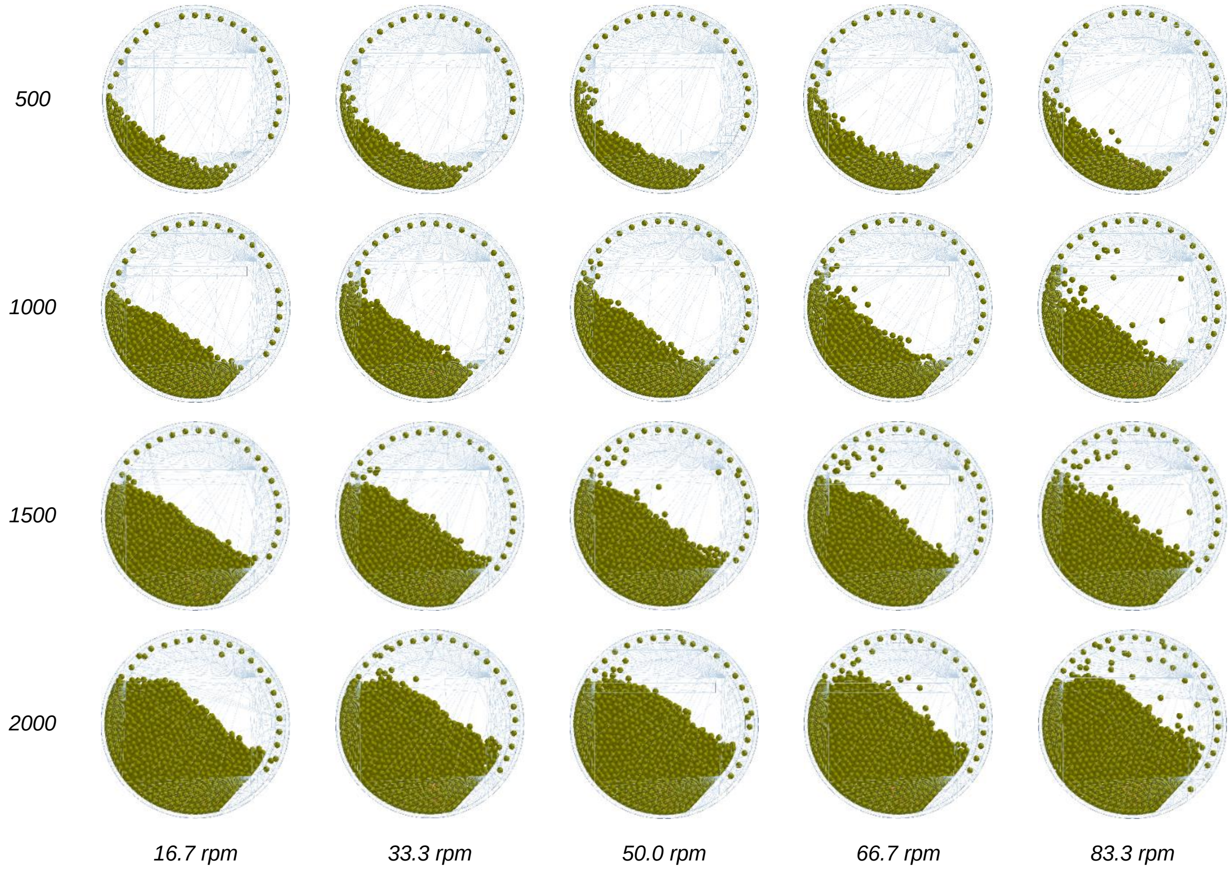

Fig. 5- Effect of seed number on movement

With the increase of the rotation speed, the movement of the seeds became more and more intense. But the simulation results show that the number of seeds has no significant effect on the inclination angle of the upper surface of the recirculation zone. When the number changes from 500 to 2000, the inclination angle was maintained at about 35°.

Similarly, the rotation speed has no significant effect on the inclination angle of the recirculation zone when the rotation speed changes from 16.7rpm to 83.3rpm, and the inclination angle was always maintained at about 35°.

Therefore, the inclination angle of the seed group was only related to its inherent characteristics and the structure of the metering device, but not to the seed number and the rotation speed of the disk.

Although the seed number and rotation speed had no significant effect on the seed group inclination, the range of collapse zone increased. Observing the simulation process, it was found that the time required for the seed to leave the hole in the axial direction was increased. The movement time of seeds following the metering tray became longer. More seeds were driven out of the group by seed holes. When the number of seeds reaches 2000 and the rotation speed reaches 83.3 rpm, the seeds separate from the highest part of the upper surface of the seed group and impact on the inner surface of the shell. The scope of the collapse area reached the seed outlet.

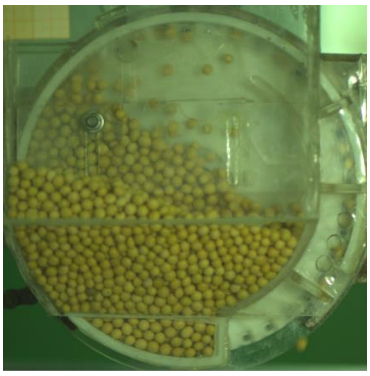

Fig. 6 - High speed photography of seed movement

The movement state of the physical prototype of the seed metering device was recorded by high-speed camera (Fig. 6), and the inclination angle of the seed group was 34.5°, which was consistent with the simulation results. This verifies the reliability of the discrete element simulation test.

The results of seed filling performance under different seed numbers were statistically analyzed (Fig. 7). Results showed that the seed number had a significant effect on the filling performance.

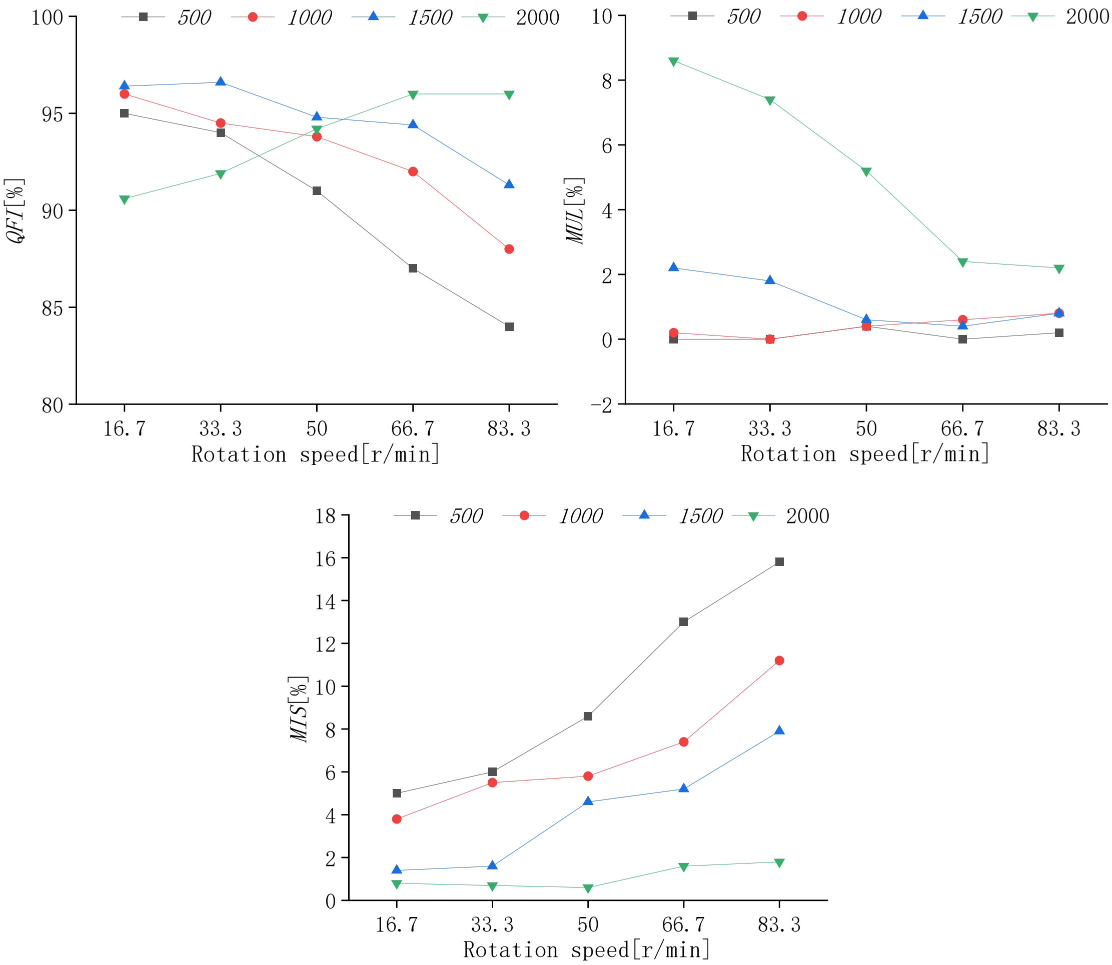

Fig. 7- Effect of seed number on seed filling

When the number of seeds was from 500 to 1500, the change of filling results was similar. With the increase of speed, QFI decreased significantly, MUL did not change significantly, and it was always low. However, MIS and QFI showed the opposite trend, which increased significantly. At 16.7 rpm, QFI of 500 to 1500 was 95.2%, 96.0%, 96.4% respectively. At 83.3 rpm, QFI of 500 to1500 was 84.3%, 88.5%, 91.3% respectively. QFI decreased by 11.4%, 7.8% and 5.3%, respectively. The smaller the number of seeds, the greater the reduction of QFI. The MIS was 4.8%, 3.8% and 1.4% at 16.7 rpm, and increased to 15.5%, 10.7% and 7.9% at 83.3 rpm.

When the number of seeds was 2000, the change of QFI was opposite to that of 500-1500, which increased gradually with the increase of speed. It was 90.6% at 16.7 rpm and tended to be stable at 96.1% after reaching 66.7 rpm. The change of MUL was contrary to that of QFI, which was 8.6% at 16.7rpm and stabilized at 2.4% after reaching 66.7rpm. MIS was 0.8% at 16.7 rpm and 1.8% at 88.3 rpm, with little change.

Influence of seed chamber structure

When the number of seeds was 1500 and the rotation speed was 50.0rpm, the inner surface inclination angle and the axial width of the seed chamber were changed to carry out the simulation experiment. The experiment was divided into two parts. Firstly, the axial width was set to 40mm, the inner surface inclination angle was changed from 0 to 30°, the simulation experiment was carried out, and the statistical results were obtained (Fig. 8.a).

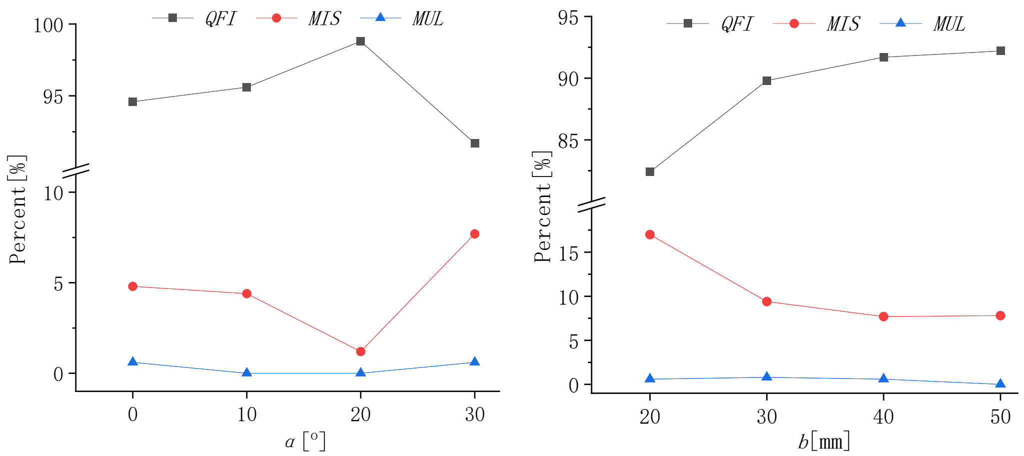

a. Inner surface inclination angle *b. Axial width*

Fig. 8 - Effects of seed chamber structure on seed filling

When the inclination angle changed, the MUL did not change significantly and remained at a low level. The change of QFI and MIS was completely opposite, QFI first increased and then decreased, MIS first decreased and then increased. At 20°, the maximum QFI was 98.8%, and the minimum MIS was 1.2%. According to the simulation analysis, with the increase of inclination angle, seeds attached to the bottom face were subjected to lateral force, which helps the seeds move laterally into the seed hole, resulting in the increase of QFI. When the inclination angle was more than 20 degrees, despite the further increase of lateral force, the smaller angle between the bottom surface and the seed hole resulted in the smaller effective filling area. It was more difficult for the seed to enter the hole, which resulted in the increase of MIS.

The value of axial width was changed when the inner surface inclination angle was the best value of 20° and the simulation test was carried out (Fig. 8.b).

Results showed that the change of axial width also have no significant effect on MUL, and it always kept a low level. The change of QFI and MIS was completely opposite. QFI increased at first and tended to be stable gradually. MIS decreased at first and tended to be stable gradually. The minimum QFI was 82.4% and the maximum MIS was 17.0% when the thickness was 20mm. When the thickness was 40mm, QFI was stable at 91.7% and MIS was stable at 7.7%. Observing the simulation process, it was found that when the thickness was small, there were fewer seeds on the front of the seed hole, fewer chances of filling and higher MIS. With the increase of axial width, the more seeds on the front of the hole, the more chance of filling and the higher QFI. However, when the thickness reached 40mm, the effective driving layer of the seed group reached its maximum. Even if the axial width continues to increase, the effective driving layer would not continue to increase, so QFI and MIS tend to stabilize.

CONCLUSIONS

(1) When the vertical disc seed metering device works, the seed group was divided into four zones: ascending zone, relative static zone, collapse zone and recirculation zone. The inclination angle of the top surface of the recirculation zone was not related to the number of seeds and the rotation speed, but it was always kept at about 35 degrees.

(2) The number of seeds had a significant effect on seed filling performance. When it was between 500 and 1500, the variation of filling performance with speed was similar, QFI decreased gradually, MUL did not change significantly, but MIS increased gradually. When it was 2000, QFI was just opposite to the previous trend, gradually increased and stabilized, MUL gradually decreased and stabilized, while MIS was not significant.

(3) The inner surface inclination angle and axial width of seed chamber have significant effects on seed filling performance. With the increase of inclination angle, QFI first increases and then decreases, reaching the maximum value of 98.8% at 20°. The change of MIS and QFI was just opposite, first decreases and then increases, and the minimum value was 1.2% at 20°, while MUL remains stable at a low level. With the increase of thickness, QFI gradually increases and tends to be stable at 40mm, and the change of MIS and QFI was opposite, while MUL also remains stable at a low level.

ACKNOWLEDGEMENT

This work was supported by the National Natural Science Foundation of China (Grant No. 51905318), Shandong Provincial Colleges and Universities Youth Innovation Talent Induction Program (Smart Agriculture Research and Innovation Team), Top Talents Program for One Case One Discussion of Shandong Province ([2018]27), and Zibo School City Integration Project Academy of Ecological Unmanned Farm (Grant No. 2019ZBXC200).

REFERENCES

[1] Chen, Y., Zhang, M., Liu, Z., Lan Y., Yi, L., Peng, Q. & Yin, X. (2021), Design and experiment of seed agitator for vertical disk seed metering device, *INMATEH - Agricultural Engineering*, vol. 63, issue 1, p 179-188;

[2] Correia, T., Sousa, S., Silva, P. & Patricia, P. (2016), Sowing performance by a metering mechanism of continuous flow in different slope conditions, *Engenharia Agrícola*, vol.36, issue 5, pp.839-845; 10.1590/1809-4430-Eng.Agric.v36n5p839-845/2016

[3] Ding, Y., Wang, K., Liu, X., Liu, W., Chen, L., Liu, B. & Du, C. (2021), Research progress of seeding detection technology for medium and small size seeds, *Transactions of the CSAE*. vol.37, issue 8, pp.30-41;

[4] Jiang, M., Liu, Cai., Du, X., Dai, L., Huang, R. & Yuan, H. (2021), Development of seeding rate detection system for precision and small amount sowing of wheat, *Transactions of the CSAE*. vol.37, issue 5, pp.50-58;

[5] Khatchatourian, O., Binelo, M., & Lima, R. (2014), Simulation of soya bean flow in mixed-flow dryers using DEM, *Biosystems Engineering*, vol.123, pp.68-76; https://doi.org/10.1016/j.biosystemseng.2014.05.003

[6] Kocher, M., Coleman, J., Smith, J. & Kachman, S. (2011), Corn seed spacing uniformity as affected by seed tube condition, *Applied Engineering in Agriculture*, vol.27, issue 2, pp.177-183; 10.13031/2013.36484;

[7] Li, Z., Yu, J., Feng, Z., Fu, H., Zhang, L. & Fei, X. (2013), Simulation and performance analysis of a soybean seed metering device using discrete element method, *Sensor Letters*, vol.11, issue 6-7, pp.1217-1222; https://doi.org/10.1166/sl.2013.2897

[8] Liu, H., Guo, L., Fu, L., & Tang, S. (2015), Study on multi-size seed-metering device for vertical plate soybean precision planter, *International Journal of Agricultural and Biological Engineering*, vol.8, issue 1, pp.1-8; https://doi.org/10.3965/j.ijabe.20150801.001;

[9] Mao, X., Yi, S., Tao, G., Yang, L., Liu, H., & Ma, Y. (2015), Experimental study on seed-filling performance of maize bowl-tray precision seeder, *International Journal of Agricultural and Biological Engineering*, vol.8, issue 2, pp.31-38; https://doi.org/10.3965/j.ijabe.20150802.1809

[10] Singh, R., Singh, G., & Saraswat, D. (2007), Design and operational parameters of a pneumatic seed metering device for planting of groundnut (Arachis hypogaea) seeds, *Indian Journal of Agricultural Sciences*, vol.77, issue 1, pp.40-42;

[11] St Jack, D., Hesterman, D. & Guzzomi, A. (2013) Precision metering of Santalum spicatum (Australian Sandalwood) seeds, *Biosystems Engineering*, vol.115, issue 2, pp. 171-183; 10.1016/j.biosystemseng.2013.03.004

[12] Vianna, L., Reis, A., & Machado, A. (2014), Development of a horizontal plate meter with double seed outlets, *Revista Brasileira de Engenharia Agricola e Ambiental-Agriambi*, vol.18, issue 10, pp.1086-1091; https://doi.org/10.1590/1807-1929/agriambi.v18n10p1086-1091

[13] Wang, J., Tang, H., Wang, J., Li, X., & Huang, H. (2017), Optimization design and experiment on ripple surface type pickup finger of precision maize seed metering device, *International Journal of Agricultural and Biological Engineering*, vol.10, issue 1, pp. 61-71; https://doi.org/10.3965/j.ijabe.20171001.2050

[14] Yang, L., Yan, B., Yu, Y., He, X., Liu, Q., Liang, Zh., Yin, X., Cui, T., & Zhang, D. (2016), Global overview of research progress and development of precision maize planters, *International Journal of Agricultural and Biological Engineering*, vol.9, issue 1, pp. 9-26;

[15] Yi, S., Liu, Y., Wang, C., Tao, G., Liu, H., & Wang, R. H. (2014), Experimental study on the performance of bowl-tray rice precision seeder, *International Journal of Agricultural and Biological Engineering*, vol.7, issue 1, pp. 17-25; https://doi.org/10.3965/j.ijabe.20140701.002

[16] Yu, J., Liao, Y., Cong, J., Yang, S., & Liao, Q. (2014), Simulation analysis and match experiment on negative and positive pressures of pneumatic precision metering device for rapeseed, *International Journal of Agricultural and Biological Engineering*, vol.7, issue 3, pp. 1-12;

[17] Zhan, Z., Yafang, W., Jianjun, Y., & Zhong, T. (2015). Monitoring method of rice seeds mass in vibrating tray for vacuum-panel precision seeder, *Computers and Electronics in Agriculture*, vol.114, pp.25-31; 10.1016/j.compag.2015.03.007

[18] Zhang, G., Zang, Y., Luo, X., Wang, Z., Zhang, Q. & Zhang, S. (2015), Design and indoor simulated experiment of pneumatic rice seed metering device, *International Journal of Agricultural and Biological Engineering*, vol.8, issue 4, pp.10-18; 10.3965/j.ijabe.20150804.1626

[19] Zhang, T., Liu, F., Zhao, M., Liu, Y., Li, F., Ma, Q., Zhang, Y., & Zhou, P. (2017), Measurement of physical parameters of contact between soybean seed and seed metering device and discrete element simulation calibration, *Journal of China Agricultural University*, vol.22, issue 9, pp. 86-92.

DESIGN OF RICE REGIONAL TEST INFORMATION COLLECTION SYSTEM BASED ON CLOUD COMPUTING
/
基于云计算的水稻区域试验信息采集系统设计

Xin Zha
ZiBo Vocational Institute, Shandong ZiBo, 255000 / China
E-mail: vwfdbel926085@163.com
DOI: https://doi.org/10.35633/inmateh-64-49

Keywords: *cloud computing, rice regional test, information collection system*

ABSTRACT
This paper combines the image processing and analysis technology of artificial intelligence to realize the function of farmland data acquisition and analysis. The data acquisition function is completed by different types of sensors. The collected information can be divided into two categories: meteorological information and image and GPS information. Based on cloud computing technology, an information collection system for rice regional experiment was established. The information collected by the sensor was analysed by cloud computing technology, which provided a basis for agronomic operation and result evaluation of regional experiment. The test results show that there is no significant difference between the rice data collected by cloud computing and the manually collected rice data. It can replace the manually collected rice information, reduce labour costs and improve experimental quality. Regional test of crop varieties is an intermediate link in the breeding and popularization of new varieties, and the results of regional test are the main basis for the approval of crop varieties. With the popularization and application of network, it brings opportunities for the networking of regional test management, statistics and variety evaluation. At the same time, with the help of network function, it can realize the online transmission of data, solve the delay problem of regional test results, and query the statistical analysis and evaluation results of regional test at any time.

摘要
本文结合人工智能的图像处理与分析技术，实现了农田数据采集与分析的功能。数据采集功能由不同类型的传感器完成，采集的信息可分为两类，一类是气象信息，另一类是图像和 GPS 信息。基于云计算技术，建立了水稻区域试验信息采集系统，利用云计算技术对传感器采集到的信息进行分析，为区域试验的农艺操作和结果评价提供依据。测试结果表明，云计算采集的大米数据与人工采集的大米数据没有明显差异，可以替代人工采集的大米信息，降低人工成本，提高实验质量。农作物品种区域试验是新品种选育和推广的中间环节，区域试验结果是农作物品种审定的主要依据。随着网络的普及和应用，给区域试验管理、统计和品种评价网络化带来了机遇。同时，借助网络功能，可以实现数据的在线传输，解决区域测试结果的延时问题，随时查询区域测试的统计分析和评价结果。

INTRODUCTION
The crop regional test is to plant the tested varieties in different locations for many years, investigate agronomic characteristics and measure the yield to evaluate their adaptability and high yield under large-scale planting conditions *(Wakhare P B. et al., 2020)*. Crop regional trials provide important scientific basis for variety approval and are an important link between crop breeding and variety promotion and application. It has always been highly valued by breeding companies, scientific research units and agricultural management departments *(Elena G. et al., 2021)*. Intelligent agriculture provides a reliable way for the future development of agriculture. Smart agriculture adopts cutting-edge science and technology, realizes accurate agricultural sowing, reasonable irrigation and spraying of water, fertilizer and pesticides, and makes agricultural production with low consumption and high efficiency, high quality and high yield of agricultural products. According to the provisions of the Seed Law, before new varieties are approved and applied to production, they must go through regional tests *(Hua X. et al., 2021)*. The regional test of crop varieties is a multi-site joint test organized by the administrative department of agriculture and carried out within a certain ecological area. It includes two parts: multi-site test and production test. The regional test of rice is a new variety of rice from selection to promotion.

The indispensable intermediate test, through the identification of the high yield, adaptability, stress resistance and quality of the new variety, provides a scientific basis for the variety certification and promotion *(Wen Y. et al., 2020)*. Rice regional test is an experimental process to correctly identify the production traits and adaptation range of new rice varieties (combinations) and provide the basis for the popularization and application of varieties. The test must be carried out in multiple years and places *(Huang S. et al., 2020)*.

It is difficult for general varieties to adapt to all test sites, and some excellent varieties will be eliminated due to poor performance at individual test sites. At present, affected by some subjective and objective factors, there are also some problems in the process of regional trials of crops, which will affect the quality and effect of the trials *(Raskin P. D., et al., 2010)*. Precision agriculture systems generally consist of different systems such as global positioning systems, information collection systems, remote sensing monitoring systems, geographic information systems, expert systems, intelligent agricultural machinery systems, environmental monitoring systems, and network management systems *(Liu F. et al., 2020)*. Therefore, we use ASP as the technical support of the foreground service and the technology provided by the database system Access as the background data management to establish a network management information system suitable for regional trials of rice varieties *(Wu Q. L. et al., 2018)*. The main characteristic of precision planting is to fully consider the spatial differences of farmland characteristics and implement different management measures for crops according to the spatial differences of farmland properties, such as variable fertilization, variable irrigation, etc., in order to obtain maximum economic benefits and produce minimum environmental pollution *(Siahaan P. et al., 2020)*. Because the selection and application of fine varieties play a huge role in the world's agricultural production, governments and seed companies all over the world attach great importance to the regional testing and approval of crop varieties, and many countries have already implemented the approval system of crop varieties *(Yu L. et al., 2020)*. Regional experiment, according to the characteristics of the variety, develop appropriate cultivation techniques to promote the popularization and application of the variety *(Na Q et al., 2020)*. Based on cloud computing technology, this paper established an information collection system of rice regional experiment, and analysed the information collected by sensors by using cloud computing, which provided basis for agronomic operation and result evaluation of regional experiment *(Zhu H. et al., 2020)*.

The application of new technology methods is the development trend of modern intelligent agriculture, and it is also an inevitable choice to solve the problems faced by crop regional experiments *(Lee P. U. et al., 2018)*. Driven by artificial intelligence technology and combined with automatic collection, analysis and processing technology of artificial intelligence machine, researchers realize the real-time collection, analysis and processing of farmland information. At the same time, according to the analysis results, the operation of the corresponding intelligent equipment is controlled to improve the growth environment of crops, save manpower and material resources while increasing the yield of crops, and realize the intelligent, efficient and sustainable development of agriculture *(Uga Y. et al., 2021)*. The main tasks of regional trials of crop varieties can be summarized as follows: scientifically evaluate the high-yield, stable-yield, stress-resistance and other major economic characters of the tested varieties, and clarify the popularization value, adaptation range and supporting high-quality and high-yield cultivation techniques of new varieties, so as to provide the main basis for variety approval and regional layout of improved varieties *(Zhao L. et al., 2020)*. Therefore, it is very important to do a good job in regional trials of varieties. In the process of implementing precision agriculture, firstly, the parameters related to crop growth must be obtained through automated agricultural machinery, and then the variable operation diagram can be obtained through computer system analysis according to crop demand, and then the intelligent agricultural machinery can operate to realize variable management of agricultural production. There is no obvious difference between the rice data collected by cloud computing and the manual survey results, which can replace the manual collection of rice information, reduce labour costs and improve the quality of experiments. With the popularization and application of the network, opportunities are brought to the network of regional test management, statistics and variety evaluation. At the same time, with the help of network functions, it can realize online data transmission, solve the problem of delay in regional test results, and can query the statistical analysis and evaluation results of regional test at any time.

Literature points out that the combination of Internet and agriculture is an innovative way of agricultural production, sales and management, which has a great impact on various links of different industrial chains, such as agricultural production, operation, management and service, through real-time, internet of things and intelligent means, and also provides a brand-new power source for the development process of traditional agriculture transforming to modernization.

With the continuous improvement of national requirements for regional test, more and more regional test stations with perfect facilities have established regional test stations, which not only meet the planting and normal growth of crops, but also need to carry out growth period investigation, fertilization and irrigation, pest and bird control and harvest yield measurement, etc. The content of the experimental research in the literature can fully reflect the characteristics of local natural conditions and economic conditions, can solve the key problems in production practice, and can meet the requirements of short-term or long-term production technology development. Literature shows that when setting up pilots, it is necessary to consider not only the economic effectiveness of the number of pilots, but also the representativeness of their ecological conditions. The test site must be representative, and the soil conditions and climate environment of the test site must be typical of the pilot site to facilitate the correct evaluation and utilization of the test results. Literature shows that due to the limitation of test conditions or the influence of human factors, observation and measurement are uncertain, the true value is usually difficult to obtain, and the test error is inevitable in general. In the same pilot, the principle of taking the variety as the only difference should be strictly implemented, and the field operation and cultivation management should be absolutely consistent. Literature shows that adopting appropriate and scientific experimental design can effectively control the experimental error caused by the difference of soil fertility among different regions, but it cannot control the experimental error caused by the difference of soil fertility within different regions. Therefore, fields with uniform soil fertility should be selected as far as possible, which is the most effective means to control the test error caused by the difference of soil fertility.

MATERIALS AND METHODS

Operation of the system

The operation process of the system includes two stages: the initialization stage and the operation stage. The operation stage includes three system modules: data editing, data processing, and data query. In order to improve the accuracy of the experiment, a scientific and reasonable experiment design must be carried out. The rice area experiment generally adopts a random block design. In actual operation, the following work should be done in earnest. Set up duplicates.

The number of repetitions varies with the number of tested varieties. If the number of tested varieties is small, 4 repetitions are better, and if there are more varieties, 3 repetitions. The area of the repeated plots is suitable for the tested varieties to form a normal population, which is generally 13.33m^2. Rectangular shape is preferred, but the aspect ratio should be controlled within 3:1 to reduce marginal effect. Set the zone group. According to the principle of local control, the same repeated plot of all tested varieties is controlled in a certain section to form a block, and the number of test blocks is the same as the number of repetitions. In order to obtain unbiased test error estimation, 7 points must be scored for each tested variety in the block, with 1 point added for every 3 days, 5 points at most, 1 point deducted from 7 points for every 3 days, and no score for less than 3 days. The experimental field is the carrier and platform of rice variety test. Choosing the appropriate experimental field is of great significance to ensure the safety, representativeness and effectiveness of the test and improve the accuracy, precision and efficiency of the test. Therefore, the ability to scientifically and objectively evaluate and compare the quality of the tested varieties depends to a large extent on the accuracy of the test.

The error variation coefficient is used to express the test accuracy, that is, the percentage of the standard error of the error term to the test mean:

$$CEV\% = \left(S_e / \bar{X}\right) \times 100 \tag{1}$$

In the formula, S_e is the standard error of the test error, X is the test mean, and CEV is the test accuracy.

Under a certain probability a, the percentage of the smallest significant difference of the variety mean that can be identified by the regional test to the test mean:

$$RLSD\alpha(\%) = \left(LSD\alpha / \bar{X}\right) \times 100 \tag{2}$$

In the formula, $LSDa$ is the least significant difference of the mean value of the variety, and $\bar{X}$ is the mean value of the experiment. $RLSD$ is also a relative number, and its size is the same as CEV.

$$GCV = \left(\sqrt{MS_V}\,/\,\overline{Y}\right)\times 100 \tag{3}$$

In the formula, MS_V is the genetic variance of the tested varieties, and $\overline{Y}$ is the test mean. GCV is the genetic variation coefficient of yield among various experimental varieties.

System composition and working principle

The information needed to implement precision planting mainly includes GPS positioning information, farmland geographic information, field sampling information, agrometeorological information, crop growth and yield information, and expert knowledge related to crop planting, etc.

Image recognition is an important branch of artificial intelligence. Its meaning is to imitate the activities of human image recognition and transform this recognition process into computer programs, so that the machine can imitate the human brain to perform image recognition and classification activities. As the application of image recognition technology becomes more and more widespread, some people also use it for agricultural product quality inspection and agricultural disease identification. In order to ensure the accuracy of classification, machine learning gradually can no longer meet the requirements. At this time, deep learning, which is a neural network with multiple hidden layers, appears. Generally, there are three kinds of networks: convolutional neural networks, cyclic neural networks and time-dependent recurrent neural networks. Among them, convolutional neural networks are mostly used to deal with the problem of image data classification. Rice information collection system consists of three parts: information perception layer, network transport layer and information management layer. The information perception layer includes three modules: meteorological information, environmental information and crop information, as shown in Figure 1.

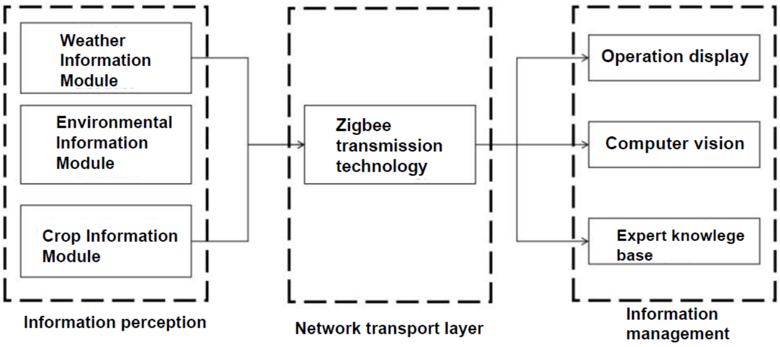

Fig. 1 - The components of the system

The rice information collection system includes four parts: an information collection module, a wireless communication module, an information processing module, and a control execution module. The process is shown in Figure 2. The information collection module is a variety of sensors and cameras, which can collect meteorological information, environmental information and crop information in the test station.

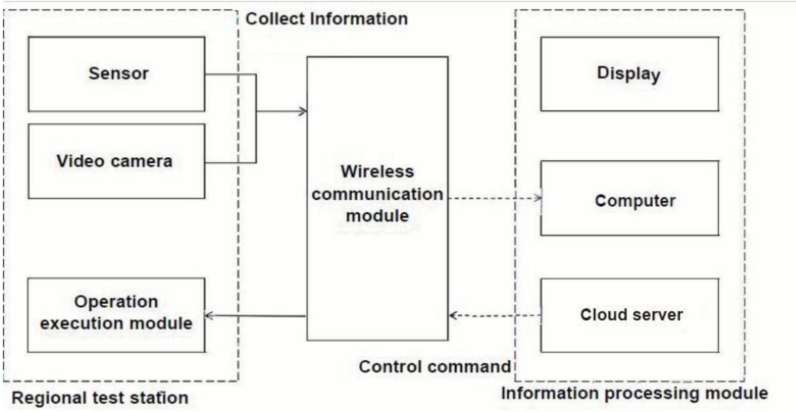

Fig. 2 - System workflow

Figure 3 is the structure diagram of the whole system. The farmland environmental information such as soil temperature, humidity, wind direction and wind speed, illumination intensity sensor, atmospheric pressure sensor, rainfall sensor and CO_2 gas concentration sensor are sensed, and remote real-time monitoring of farmland is realized through remote data transmission.

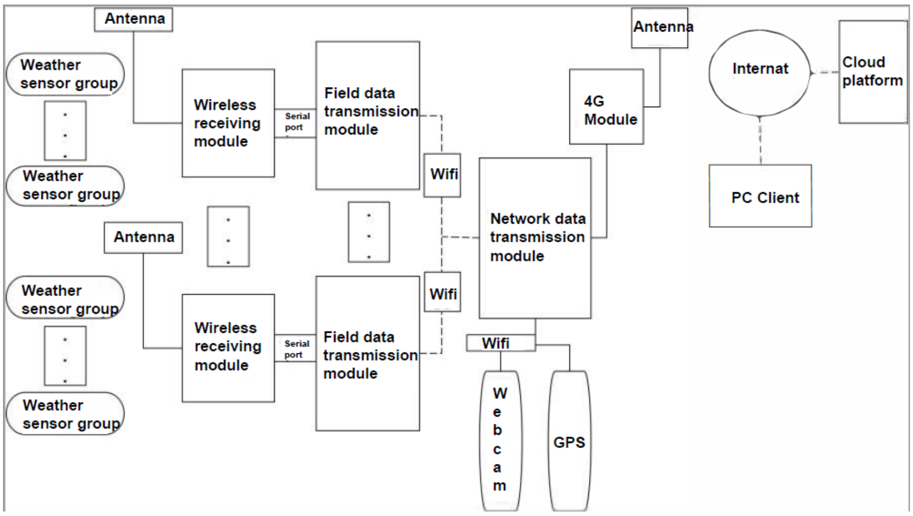

Fig. 3 - Four-layer IoT system structure diagram

The equipment of the information perception layer mainly collects meteorological information, environmental information and crop information. The network transmission layer transmits the information collected by the information perception layer to the information management layer, which is the link between the two. The information management layer is located in the office area of the test station. The computer of the information processing module is a Lenovo Yangtian 4000 desktop computer with an Intel i7 processor, 8G memory and 1T hard disk, and Windows 10 operating system is installed. The display is LS2223WC, which can be used for parameter setting and data display. The work map should be a raster data structure, but at the same time it should include vector coordinates and field boundary information, so that it is convenient for agricultural machinery automation and manual work when there is no machinery. Similarly, compared with rice leaves, insect bodies are quite different in shape and colour.

Table 1 and Table 2 show the colour and shape characteristics of diseases and insect pests.

Table 1

Disease colour and shape characteristics

Disease name	Colour characteristics	Shape feature
Chronic leaf rice blast	Yellowish brown	Fusiform
White leaf blight	Yellow-brown, gray-white	Yellow-brown, gray-white
Slice disease	Wilting and yellowing	Thin strip
Sheath blight	Greyish green or greyish brown	Moire or oval
Helminthosporium oryzae	Dark brown	Ellipse
Rice Sheath Rot	Brown, light in the middle	Irregular type with indistinct margin
Rice leaf smut	Dark brown to black	Along the vein of the leaf, it is intermittent and linear
Aphelenchoides besseyi	Yellowish white or yellowish brown	Twisted paper

Table 2

Pest body colour characteristics

Pest name	Body colour characteristics
Striped rice borer	Head greyish brown, forehead white to smoky, round, apex pointed.
Chilo suppressalis	The head, chest and front wings of the male moth are greyish brown, and the lower lip must be very long and protruding forward. The abdomen is gray on both sides. The female moth has yellow forewings and a black spot in the lower corner of the middle chamber.
Cnaphalocrocis medinalis	The body and wings are yellowish brown. When resting, the wings spread obliquely on both sides of the back. Compound eye black, antennae filiform, yellow white.
Rice planthopper	It can be divided into two types: long winged and short winged. All brown, shiny. There are three distinct convex lines in the front of the sternum. There are small spines outside the first tarsal of hind foot.

Decision-making system should have the function of model management, which can not only add new decision-making models into the system, but also modify and improve existing decision-making models. In the operation stage, the experimental data are mainly processed, including data input, modification, statistics, analysis, summary, query and data exchange with other software and sites. The error of rice regional test refers to the difference between the observed and measured values and their true values in yield, growth period and various economic characters of the tested varieties. In order to improve the accuracy of the test, the error must be controlled by the following ways. First, the use of scientific experimental design can effectively reduce and estimate errors. Second, choose a good test site to minimize soil differences. Third, strict field operations and cultivation management to make them standardized and standardized. The rice precision planting information system should include several parts such as attribute data management subsystem, farmland spatial data management subsystem, remote sensing data processing subsystem, rice planting expert system and decision-making subsystem. The system structure and function are shown in Figure 4.

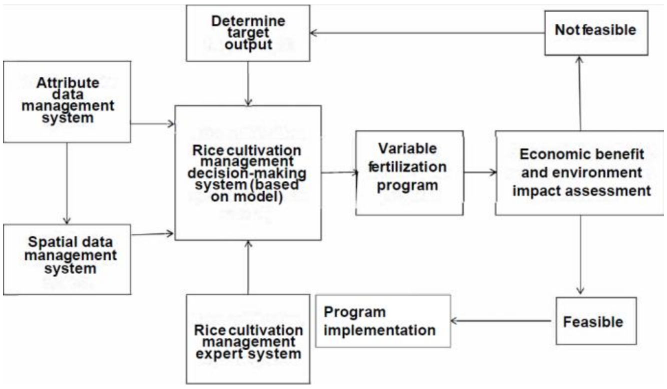

Fig. 4 - Structure and function of rice precision planting information system

RESULTS

In 2018, the function of the information collection system was tested in the early rice regional test of a unit. Based on cloud computing technology, an information collection system for rice regional experiment was established, which includes four parts: information collection module, wireless communication module, information processing module and control execution module. Five varieties were randomly selected from the early rice planted in the current season, and the heading date, effective panicles per unit, grains per panicle and yield of each variety were collected by manual investigation and cloud computing, and the difference of information collected by the two methods was compared. The heading period is the number of days the rice is harvested from sowing to 50% tiller. The effective number of ears per unit is the total number of rice ears per 667m^2 field. The yield is calculated after the yield of the test plot. The difference of the information collected by the two methods is shown in Table 3. Among the five sets of data, cloud computing has the most accurate assessment of the heading date, which is only 1 to 2 days behind the actual results. Therefore, cloud computing can replace manual collection of rice growth and yield information, which can greatly reduce the labour cost of regional trials and improve the test quality.

Table 3

Differences in information collected by the two methods

Varieties tested	Collection method	Heading date [d]	Effective ears per unit area [10,000 ears·/ 667m^2]	Number of grains per panicle	Output [t·hm^{-2}]
1	Manual survey	84.3	22.4	99.3	7.45
	Cloud computing	85.0	23.2	96.3	7.74
2	Manual survey	76.3	18.7	106.5	7.33
	Cloud computing	81.5	19.6	110.1	6.36

Table 3
(continuous)

Varieties tested	Collection method	Heading date [d]	Effective ears per unit area [10,000 ears·/ 667m^2]	Number of grains per panicle	Output [t·hm^{-2}]
3	Manual survey	87.3	25.9	96.7	7.56
	Cloud computing	87.8	23.5	94.5	8.20
4	Manual survey	88.6	20.0	105.6	7.62
	Cloud computing	84.1	19.5	106.3	7.62
5	Manual survey	86.3	19.5	107.3	7.15
	Cloud computing	85.7	21.2	104.8	7.56

The camera of the data acquisition equipment continuously collects field images and sends them to the network data transmission module. The network data transmission module conducts preliminary identification of the image to identify whether the picture is a diseased picture. The error coefficient of variation is analysed by formula (1). If there is a suspected diseased part on the image, it will be calibrated and retaken. The Internet of Things technology is used to build parameters including soil temperature and humidity, air temperature and humidity, wind direction and speed, rainfall, radiation, etc., and wireless communication technology is integrated to form a farmland environment monitoring and sensing system with wireless interface, and to build a mobile terminal platform such as crop growth, field management information collection, decision consultation and information inquiry. Fig. 5 shows the installation equipment of rice regional test information collection system.

Fig. 5 - The installation equipment of rice regional test information collection system

In order to highlight the disease part, the image data is segmented before classification, and the disease location is proposed. Refer to Table 1 and Table 2 for segmentation of colour and shape characteristics of diseases and pests. Before segmentation, the image is smoothed and realized with the cvSmooth function to reduce the influence of noise. The role of the application layer is to process and analyse the collected image data and integrate all farmland information and display it on the client software interface. Build the client application program interface, and classify and display the image data classification results together with meteorological information and geographical location information on the client interface. The application layer workflow is shown in Figure 6.

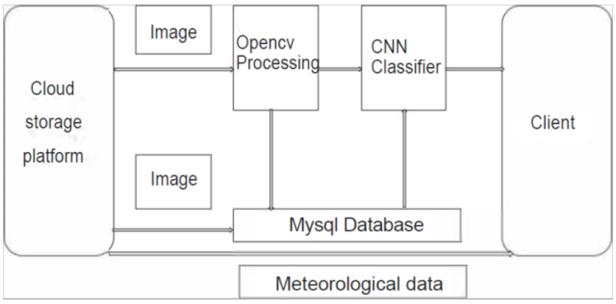

Fig. 6 - Application layer work flow chart

The main sources of test errors are as follows: First, the differences of external conditions and pests during the test. Second, the inconsistency between experiment management and farming operation. Third, the heterogeneity of the test material itself. Selecting suitable test sites, adopting appropriate plot technology, applying good test design and selecting corresponding statistical models can effectively reduce test errors and improve test accuracy. This system establishes database files in the district pilot unit, calls the data in the library through the module program, summarizes and analyses them, so that each point must establish its own data file in a unified format to facilitate the standardized management of the files. This system uses the multi-point repeated linear model that is currently widely used in regional tests for many years:

$$Y = \mu + V_{\mathrm{i}} + S_j + W_k + (VS)_{ij} + (VW)_{ik} + (SW)_{jk} + (VSW)_{\mathrm{ijk}} + R_{jkl} + Ei_{jkl} \tag{4}$$

Where $\mu = \sum Y_{ijkl} / WLVR$ is the total average of traits, Vi is variety effect, Sj is place effect, W_{k} is year effect, $(VS)_{ij}$ is variety and place interaction effect, $(VW)_{ik}$ is variety and year interaction effect, $(SW)_{jk}$ is variety, place and year interaction effect, $(VSW)_{iik}$ is variety, place and year interaction effect, R_{jk} is year and place block effect, Ei_{jkl} is random error. The model evaluates the high yield according to the main effect of varieties, and the varieties with large main effect have better high yield.

For the analysis of variety stability, this system is realized by the following three mathematical models, namely:

Linear regression model：

$$Y = \mathrm{a} + \mathrm{b}X; \quad \mathrm{b} = \frac{\sum(\mathrm{x} - \bar{\mathrm{x}})(\mathrm{y} - \bar{\mathrm{y}})}{\sum(\mathrm{x} - \bar{\mathrm{x}})^2} \tag{5}$$

Y is observed value, $\bar{\mathrm{y}}$ is average value, X is environmental value, $\bar{\mathrm{x}}$ is average value, b is regression coefficient and a is regression intercept.

Model of Eberhart stability parameters:

$$Y_{\mathrm{ij}} = \mathrm{m} + B_i I_{\mathrm{j}} + \sigma_{\mathrm{ij}} \tag{6}$$

where $\mathrm{Y_{ij}}$ represents the average value of the i-th variety in the j-th environment (i=1, 2...v) (j=1, 2...s), and m is the average value of the i-th variety in all environments, σ_1 is the separation regression of i varieties in j environments, B_i is the regression coefficient, used to measure the response of the i-th variety to different environments, I_{j} is the environmental index, which is the average of all varieties in the i-th environment calculated by subtracting the total average number from the number.

Mathematical model of Tai stability parameters:

$$X_{\mathrm{ijk}} = U + \mathrm{g_i} + \mathrm{l_j} + (\mathrm{gl})_{\mathrm{ij}} + \mathrm{b_{jk}} + \theta_{\mathrm{ijk}} \tag{7}$$

In which X_{ijk} is the observed value of the i-th variety in the k-th repeated in the j-th environment, U is the total average of all varieties in all environments, $\mathrm{g_i}$ is the i-th variety effect, $\mathrm{l_j}$ is the j-th environmental effect, $(\mathrm{gl})_{\mathrm{ij}}$ is the interaction effect between the i-th variety and the j-th environment, $\mathrm{b_{jk}}$ is the k-th repeated effect in the j-th environment, and θ_{ijk} is the random error of dispersion of the i-th variety in the k-th repeated in the j-th environment. In ANOVA model, the yield (Y_{ijk}) of the ith variety in the kth repetition at the jth site can be expressed as:

$$Y_{ijk} = \mu + g_i + e_j + ge_{ig} + \rho_{\mathrm{jk}} + \varepsilon_{ijk} \tag{8}$$

As for the model of variance analysis, one view is that the pilot in regional trials is fixed, not randomly selected, so the pilot effect should be regarded as fixed. Some studies are based on the least square principle, and all the sources of variation are regarded as fixed effects. Another point of view is that the pilot is only a group of samples in an ecological region, and the test results should be extended to other environments outside the pilot, so it is more appropriate for the pilot effect to be random. Generally speaking, when the pilot effect is fixed, the standard of significant difference among varieties is lower, and when the pilot effect is random, the standard of significant difference among varieties is higher. Therefore, compared with the ANOVA model and the LR model, this model has a wider range of applications. Wide, and the evaluation of the tested varieties is also relatively accurate. The model is tested by testing sample data. Table 4 shows the classification accuracy rates of different classification models obtained by statistics.

Table 4

Statistical results of model classification accuracy

Edition	**Correct number Accuracy**	**Accuracy**	**Edition**	**Correct number Accuracy**	**Accuracy**
Colour V1	469	89.45%	Ordinary V1	432	82.47%
Colour V2	449	85.68%	Ordinary V2	451	86.15%
Colour V3	478	91.25%	Ordinary V3	469	89.5%
Shape V4	490	93.41%	Ordinary V4	463	88.27%
Shape V5	502	95.8%	Ordinary V5	473	90.18%
Shape V6	459	87.65%	Ordinary V6	480	91.56%
Shape V7	442	84.35%	Ordinary V7	443	84.58%
Texture V8	434	82.74%	Ordinary V8	464	88.59%
Texture V9	490	92.47%	Ordinary V9	422	80.58%
Texture V10	474	89.33%	Ordinary V1	450	85.45%

By selecting different sample data from different data sets to train models, different classification models can be obtained, and the model with the highest accuracy rate is selected as the final classification model.

CONCLUSIONS

Assumption of perfecting regional trials of rice varieties: establishing standardized technical operation rules of regional trials, building an independent regional trial network system, implementing the scrapping system of regional trials, and determining the verification results of regional tests. In this paper, the idea of cloud computing and artificial intelligence is combined to design a rice farmland information real-time viewing system, which can realize the collection and transmission of farmland meteorological data and image data as well as the processing and classification of image data. In practical application, the system still needs to be improved, and further research and improvement are needed in the future. The test results showed that the early rice heading date, effective panicle number per panicle, grain number per panicle, and yield obtained by cloud computing are not significantly different from the results of manual investigation, and the estimation of the heading date is the most accurate. Therefore, cloud computing can replace manual collection of rice information, reduce labour costs for regional trials, and improve trial quality. Generally speaking, when the pilot effect is fixed, the standard for significant differences between varieties is lower, and the pilot effect is random, and the standard for significant differences between varieties is higher. Because of the interaction between genotype and environment during the growth of rice, different locations, different cultivation methods and different management may affect the performance and evaluation of varieties. The formulation of scientific and reasonable rice cultivation and management scheme requires not only a large amount of data and advanced technology, but also a long time to adjust, modify and perfect the process, method and mode of formulating the scheme.

REFERENCES

[1] Elena G., Ekaterina S., Philipp G., (2021), Leaf Rust Resistance Genes in Wheat Cultivars Registered in Russia and Their Influence on Adaptation Processes in Pathogen Populations. *Agriculture*. Vol. 11, Issue 4, pp. 319. Switzerland;

[2] Hua X, Han X, Sun H. Design of Environment Monitoring System for Greenhouse Based on OneNET. 2021 IEEE Asia-Pacific Conference on Image Processing, Electronics and Computers (IPEC). *IEEE*, pp. 307-310. United States;

[3] Huang S., Wu S., Sun C., (2020), Deep localization model for intra-row crop detection in paddy field. *Computers and Electronics in Agriculture*, Issue 169, pp. 105203. England;

[4] Lee P. U., So J. H., Nam Y. S., (2018), Power analysis of electric transplanter by planting distances. *Korean Journal of Agricultural Science*, pp. 45. Korean;

[5] Liu F., Dong L., Zhou J., (2020), Investigation Regarding Optimization and Improvements of Natural Education in Urban Parks in Post-epidemic Era. *Design Engineering*, pp. 246-269.

[6] Na Q., Wen Y., (2020), Design of Multi-point Intelligent Temperature Monitoring System for Transformer Equipment. Journal of Physics: Conference Series. *IOP Publishing*, Vol. 1550, Issue 6, pp. 062007.China;

[7] Raskin P. D., Electris C., Rosen R. A., (2010), The century ahead: searching for sustainability. Sustainability, Vol. 2, Issue 8, pp. 2626-2651. Switzerland;

[8] Siahaan P., Dewi E., Suhendi E., (2020), Introduction, connection, application, reflection, and extension (ICARE) learning model: The impact on students' collaboration and communication skills. *Jurnal Ilmiah Pendidikan Fisika Al-BiRuNi*, Vol. 9, Issue 1, pp. 109-119. Indonesia;

[9] Uga Y., (2021), Challenges to design-oriented breeding of root system architecture adapted to climate change. *Breeding science*, Vol. 71, Issue 1, pp. 3-12. Japan;

[10] Wakhare P. B., Neduncheliyan S., Sonawane G. S., (2020), Automatic Irrigation System Based on Internet of Things for Crop Yield Prediction. 2020 International Conference on Emerging Smart Computing and Informatics (ESCI). *IEEE*, pp. 129-132. United States;

[11] Wen Y., Li W., Yang Z., (2020), Evaluation of various approaches to predict cadmium bioavailability to rice grown in soils with high geochemical background in the karst region, Southwestern China. *Environmental Pollution*, Issue 258, pp. 113645. England;

[12] Wu Q. L., Westbrook J. K., Hu G., (2018), Multiscale analyses on a massive immigration process of Sogatella furcifera (Horváth) in south-central China: influences of synoptic-scale meteorological conditions and topography. *International Journal of Biometeorology*, Vol. 62, Issue 8, pp. 1389-1406. Netherlands;

[13] Yu L., Yan X., Kuang Z., (2020), Driverless bus path tracking based on fuzzy pure pursuit control with a front axle reference. *Applied Sciences*, Vol. 10, Issue 1, pp. 230. Switzerland;

[14] Zhao L., Xie L., Zhang Q., (2020), Integrative analysis of reference epigenomes in 20 rice varieties. *Nature communications*, Vol. 11, Issue 1, pp. 1-16. England;

[15] Zhu H., Li C., Gao C., (2020), Applications of CRISPR–Cas in agriculture and plant biotechnology. *Nature Reviews Molecular Cell Biology*, Vol. 21, Issue 11, pp. 661-677. England.

EXPLORING THE ROLE OF CORPORATE SOCIAL RESPONSIBILITY IN CONSUMER PURCHASE INTENTION. A STUDY FROM THE AGRICULTURE SECTOR

企业社会责任对消费者购买意愿的影响：一项来自农业部门的研究

Lucian-Ionel Cioca [1], Muhammad Ibrahim Abdullah *[2], Larisa Ivascu [3,4], Muddassar Sarfraz *[4,5], Ilknur Ozturk [6]

[1] Department of Industrial Engineering and Management, Faculty of Engineering, Lucian Blaga University of Sibiu, Sibiu/ Romania

[*2] Department of Management Sciences, COMSATS University Islamabad, Lahore/Pakistan

[3] Faculty of Management in Production and Transportation, Politehnica University of Timisoara, Timisoara / Romania

[4] Research Center in Engineering and Management, Politehnica University of Timisoara, Timisoara/ Romania

[*4,5] Binjiang College, Nanjing University of Information Science and Technology, Wuxi/ China

[6] Faculty of Economics and Administrative Sciences, Cag University, Mersin/ Turkey

Tel : +92-3224133025 ; +86-18751861057 ; E-mail : miabdullah@cuilahore.edu.pk; muddassar.sarfraz@gmail.com

Corresponding authors: Muhammad Ibrahim Abdullah, Muddassar Sarfraz

DOI: https://doi.org/10.35633/inmateh-64-50

Keywords: *CSR; Environmental Management; Theory of Planned Behavior; Purchase Intention; Buying Behavior*

ABSTRACT

Corporate Social Responsibility (CSR) significantly transforms the global agricultural sector, thereby boosting the foreign economy. Primarily, the study focuses on the social practices of Agro-companies operating in Pakistan, thus influencing consumer buying intention. The study presents the extended theoretical contribution to the theory of planned behavior. However, it provides a fundamental framework for integrating CSR orientation with consumer buying behavior. The data of 587 respondents has been collected through questionnaires by adopting a quantitative research approach and simple random sampling technique. Results reveal that consumers prefer brands and are unwilling to pay the higher price for products involved in CSR activities. Both emotional and purchasing factors affect purchasing intentions. Consumers are willing to support CSR cause and intend to buy their products without compromising on elements of purchase intentions.

摘要

企业社会责任极大地改变了全球农业部门，从而推动了对外经济的发展。本研究主要关注在巴基斯坦运营的农业公司的社会实践，从而研究影响消费者购买意愿。这项研究在理论上拓展了计划行为理论。进一步地，它为整合企业社会责任与消费者购买行为研究提供了一个基本框架。本研究采用定量研究方法和简单随机抽样技术，通过问卷调查收集了587名受访者的数据。结果表明，消费者更喜欢品牌，不愿意为参与企业社会责任活动的产品支付更高的价格。此外，情感因素和购买因素都会影响购买意愿。消费者愿意支持企业社会责任事业，并会在不损害购买意愿因素的情况下购买他们的产品。

INTRODUCTION

CSR is a practice that aims at the social responsibility of sustainable development. Sustainable development has become a concern for most industries in the recent business world. Agriculture is a sector that applies many sustainable principles and aims at several sustainable development goals. With the modernization of agriculture in the Asian region, the concept of CSR has gained considerable importance. The CSR initiatives seek to connect socially responsible activities to human buying behavior. However, despite the current advancement in technology, countries are still experiencing economic vulnerabilities (i.e., poverty). CSR studies are based on organizations initiative, which concerns everyone, but in the actual individual who mainly gets influence by the implementation and execution of CSR policies (*Aguinis, 2011*). The concept of CSR initially started between the 1930s and 1940s, thus splitting the term into four distinct dimensions: environment, social, economic, and stakeholders *(Carroll, 1991)*. The founder of CSR has suggested that businesses should adopt policies that benefit the global environment in his book.

On the other hand, *Brown (1953)* suggests organizational practice should contribute to the development of an individual community. Indeed, this broad term emphasizes CSR performance and outcome, thereby developing a three-dimensional conceptual model *(Wood, 1991)*. CSR has four different types, economical, ethical, legal, and philanthropic. Managerial discretion played the leading role and as the governing body with an emphasis on CSR. Public responsibility means business is responsible for society's goodwill and must consider the community when making profits.

Agriculture activities play a fundamental role in the development of a country's economy. The worldwide agricultural industry has evolved from traditional manufacturing to industrial framing, producing premium commercialized Agro-products *(Kimuyu, 2018)*. A recent study reveals that Indonesian Agro companies are fundamentally performing better than others, thereby radically launching novel CSR policies *(Syamni, Wahyuddin, Damanhur, & Ichsan, 2018)*. Similarly, another study suggests that CSR programs have significantly increased the universal production of agriculture industries across different regions *(Ika, Akbar, Puspitasari, Sumbodo, & Widagdo, 2021)*. Perhaps, CSR holds mounting attention in the global agricultural sector. Indeed, the CSR prism has drastically revolutionized the agriculture businesses, thereby boosting total agriculture consumption.

CSR's role cannot be neglected in the development of societies. There is a need for such CSR activities that can be beneficial to social progress. In Pakistan, several organizations are implementing CSR policies effectively and efficiently. Multinational companies are more involved in CSR, and domestic firms are less interested in these activities due to the CSR perception. Most managers think that CSR activities are unnecessary for society, and they do not feel any pressure from civil society. Multinational organizations are bringing their culture because CSR activities are embedding in their culture. Developing countries are facing severe challenges in the sustainable development policies implementation. One of the critical problems is high inflation and more rations for low-income families. It is also due to the unequal distribution of wealth. In developed countries, wealth is equally distributed among people, so CSR activities are less needed. CSR holds strategic importance in formulating business strategies. Finding reveals a significant relationship of CSR practices with stakeholder orientation *(Amankwah-Amoah et al., 2018)*. Corporate social activities allow the stakeholder to design effective business strategies. It helps in improving the organization's performance, thus achieving a superior competitive advantage. From the business perspective, organizations should work towards translating their legal and economic responsibilities into ethical considerations. There are different ways to involve in social activities. Firms have chosen different ways to conduct CSR activities. Companies are cooperating with a non-profit organization.

Organizations spread CSR activities through various channels, which include media, Word of mouth, and advertisement. Consumers actively respond to social events organized by the companies. Consumers are ready to buy CSR companies products, and companies will be rewarded due to their social behavior *(Becker-Olsen et al., 2006; Creyer & Ross, 1997; Lichtenstein et al., 2004)*. Previous studies show that consumers' behavior changed through CSR activities *(Becker-Olsen et al., 2006; Gupta & Pirsch, 2006; Lee & Shin, 2010; Madrigal & Boush, 2008; Mohr & Webb, 2005).* CSR activities also provide opportunities for companies to differentiate their brand name in the global business.

Consumer purchasing decision-making is divided into two categories. One is from the market size, and the second one is from the organization side. The initialization of CSR in corporate activities has significantly influenced customer buying behavior. *Beckmann (2007)* reveals a positive relationship between firm CSR activities and customers' intention to respond. In explaining this notion, different international researches highlight the association between CSR and consumer purchasing decisions in developing countries (*Creyer & Ross, 1997; Maignan, 2001; Uusitalo & Oksanen, 2004)*. Furthermore, the literature suggests that poor implementation of CSR practices affects the company's reputation. Perhaps, CSR is a solution to environmental, social, and economic problems in developing countries *(Muthuri et al., 2012)*. The presence of CSR cannot be denied. There is a debate going on whether companies should keep caring for corporate social activities or not. The study shows that consumers care about CSR. Companies are using different CSR strategies to attract more and more customers. Notably, the growing significance of CSR practices has allowed companies to add value to the global capitalist economy. With sustainable economic development, CSR appears to be a prime factor in achieving superior financial outcomes. It helps businesses in making optimal decisions by reducing challenges such as environmental hazards and poverty. Pakistan's economy is heavily dependent on its agriculture production. That implies that incorporating CSR practices in agricultural production will help Pakistan to boost its agricultural capacity. The findings suggest that improved CSR activities encourage the participation of consumers in buying agricultural products.

CSR is a newly developing concept in Pakistan, and only a few organizations are following it. Multinational companies are more concerned about CSR policies. Still, the local industry became aware of CSR in 1996 by breaking the local carpet industry and the Sialkot support industry threat. Though taking the reactive measures, the joint efforts of the industrialists and financial institutes saved the most significant damage, but there are no proactive measures to implement these policies. In Pakistan, a limited number of laws and regulations related to CSR have no role in customer retention. The customer gives preference to price and other factors *(Sarfraz, 2014)*. There are a variety of laws that lead to CSR. These include environmental laws, labor laws, corporate laws, and consumer protection laws. Research has analyzed the relationship between CSR and profitability in Pakistan through the data of 100 companies. In Pakistan, the oil and gas sector mainly contributes to CSR. The financial sector is the second-largest contributing sector, whereas the textile is less involved in social development activities. Organizational justice has a partial mediating role in CSR and Employees performance *(Sarfraz et al., 2018a)*. Organizations are neglecting environmental factors *(Sarfraz et al., 2018b).*
Companies are trying to focus on their CSR policies and their implementation. Most of the managers believe that they can satisfy their customers by showing responsible society organization. They expect every company to implement and participate in CSR *(Sarfraz et al., 2020)*. Implementation of CSR does not depend on how large an organization is in terms of size and profitability. Managers are still expecting it to be an integral part of their performance. Arguably, despite its increasing significance, societies are still experiencing multiple environmental vulnerabilities worldwide. Societies expect companies to play a vital role in solving their problems and using their resources effectively and efficiently. Previous studies have limited focus on CSR. *Sen & Bhattacharya (2001)* stated organizations had focused more on CSR in the business market but no significant research was made on CSR effects. Investors and policymakers are getting help from adopting renewable energy projects *(Liang et al., 2021)*. Pollution through toxic industrial activities is a serious issue in developing countries, polluting the natural resources likewise groundwater, resulting in soil salinity and low crop yield *(Aleem et al., 2016, 2017)*.

Remarkably, Pakistan is the fast-growing agricultural market, generating maximum profitability through its agriculture activities (i.e., 22% GDP) *(Nazam, Usman, & Ayub, 2018)*. However, despite having a large agro-economy, CSR is still a new concept for Pakistan's agricultural sector. However, the finding indicates that with a steady increase in CSR awareness in Pakistan's agriculture sector, companies are altering consumer’s buying behavior through their green practices *(Javaid & Nawaz, 2018)*. Indeed, CSR is a new initiative adopted by businesses for achieving economic sustainability and growth in multiple areas of agriculture. The increasing CSR modifications have made the agricultural sector a prime recipient of CSR implications. Therefore, companies are now exploring new opportunities in agriculture for promoting sustainable investments through the implementation of advanced environmental and social practices (i.e., CSR). Consequently, the finding suggests that agro-companies should embrace socially responsible practices for achieving positive ethical performance.

Significantly, this research explores the impact of cooperative social responsibility factors affecting consumer buying intentions. Primarily, the growing importance of CSR has influenced consumer buying behavior in developing countries such as Pakistan. The strong initialization of CSR practices has made people compromise on various other elements, thus increasing the purchase of CSR commodities. With this given statement, this study aims to examine the companies' CSR initiatives, altering consumer purchasing behavior. Additionally, by incorporating the elements of the planned behavior model, this study investigates the crucial factors predicting consumer purchasing choices. The study aims to focus on understanding the dominant effect of CSR practices on agricultural consumption. Moreover, the paper investigates to answer the emerging research questions. For example, whether CSR practices are the prime concern of consumers while buying a commodity. Are the consumers willing to compromise on CSR practices? Does a company's poor social practice affect the consumers' buying choices? Do the social practices alter consumers' attitudes towards the product? However, the answers to these findings have satisfied the gap by identifying the integral factors determining consumers' intention in developing countries. Subsequently, the study highlights the significance of CSR practices by suggesting a need for extensive research work concerning the environmental incentives of CSR practices. Pakistan being among the fast-growing agricultural countries' is experiencing an immense economic boost concerning agriculture consumption. Hence, this study suggests that the growing knowledge about CSR activities has made Pakistan realize the CSR implications, influencing an individual purchasing intention.

MATERIALS AND METHODS

Purposely, this study incorporates the fundamental components of human behavioral theory in understanding the relationship between CSR activities and individuals' buying intention. The theory of planned behavior explains the unusual aspects of human behavior named Behavioral Intention. Behavioral Intentions depicts the combination of three different components; Attitude towards Behavior (AB), Subjective Norms (SN), and Perceived Behavioral Control (PBC). However, the human planned behavior model *(Ajzens, 1985)* assists in predicting the consumer purchasing intention concerning the purchase of CSR products. Nonetheless, this theory forms a crucial component of this research by providing an opportunity for understanding the behavioral aspect of a consumer's buying pattern.

The present study focuses on agriculture consumer behavior for CSR firm's products in Pakistan. The theoretical framework is developed, and purchase intention is the dependent variable. Study participants are using different Agri products related to crops and livestock production. Data is collected from the agricultural products consumers by using the simple random sampling method. We distributed 650 questionnaires among consumers, and 587 questions were found to be valid for data analysis. Respondents belong to different age groups, religions, and ethnicity.

Pakistan's agriculture sector is considered the backbone of the economy, and it has made significant developments in the last few decades. The analytical plan defines a rigorous interpretation process, using the proposed quantitative research model SPSS (Statistical Package for the Social Science). Purposely, the data evaluation process records the use of a linear regression analysis. Significantly, the use of statistical software (i.e., SPSS) had made it easy to elaborate the findings by producing systematic results. Empirically, for analysis, the data has been collected from the customers of the agriculture sector. A significant population participated, providing first-hand information regarding their purchase experiences. Consequently, to achieve data authenticity, reliability and validity were being ensured during the analysis procedure. Reliability refers to the consistency of the methodological process *(Miles, Huberman, & Saldana, 2014)*, while validity defines the data accuracy.

The quantitative approach is chosen due to the study nature, and this method is appropriate for the generalization and testing of hypotheses. The quantitative method would also facilitate the generalization of the study findings. For data analysis, a pilot study for examining the feasibility of different variables had adopted. A pilot study supports the main study by testing the appropriateness of the data collection method *(Cooper, Schindler, & Sun, 2006)*. However, this trial method ensures that accurate and reliable data is being gathered, thus checking the appropriateness of chosen research tool (i.e., questionnaire).

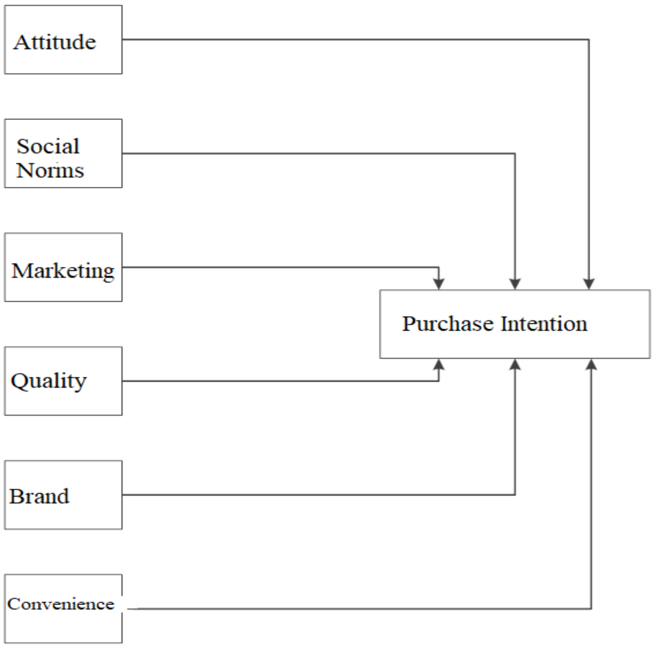

Fig. 1 - Theoretical Framework

Good questionnaire design and layout are essential, influencing and impacting the response rate *(Thomas & Loft, 2005)*. The development of the questionnaire design in this study is elicited the relevant data related to CSR. Moreover, collecting a significant amount of data from a questionnaire method would provide a wide range of results. The survey questionnaire was designed, administered, and analyzed to replicate a quantitative approach *(May 1993)*. Data collection is the most crucial part of any research. In this study, the data are collected through the questionnaire survey. Primary data is called self-generating data, and it is received through the questionnaire. The questionnaire survey is used to obtain the respondents' perceptions regarding different factors' effect on purchase intention.

H1: Attitude has a positive relationship with CSR purchase intention.

H2: Social Norms have a positive relationship with CSR purchase intentions.

H3: Price has a negative relationship with CSR purchase intentions.

H4: Marketing has a positive influence on CSR purchase intention

H5: Brand has a positive influence on CSR purchase intention

H6: Convenience has a positive relationship with CSR purchase intention.

RESULTS

Table 1 shows the individual variable reliability analysis. Bartlett's test of sphericity and Kaiser-Meyer-Olkin is performed to check the validity of the variables. KMO value less than 0.05 indicates the appropriateness of the factor analysis. The value of KMO analysis should be higher than 0.05. Convenience has the highest .956 value, and attitude has the lowest value of .811. Cronbach's alpha values are higher than 0.7 in table 1. Table 2 presents KMO and Bartlett's Test.

Table 1

Reliability Analysis

Variables	Cronbach's Alpha	N of Items
Attitude	0.811	7
Social Norms	0.934	7
Price	0.919	7
Marketing	0.921	7
Brand	0.941	7
Convenience	0.956	7
Purchase Intention	0.849	6

Table 2

KMO and Bartlett's Test

Kaiser-Meyer-Olkin Measure of Sampling Adequacy.		0.753
Bartlett's Test of Sphericity	Approx. Chi-Square	37280.878
	df	1485
	Sig.	0.000

The correlation represents the relationship between two or more than two variables. Pearson's correlation method represents a linear relationship among variables, and its range is from -1 to +1. A value closer to +1 shows the positive linear relationship *(Udo, 2007)*, while a value closer to -1 shows a negative relationship. Pearson's correlation method is adopted to test the relationship between the dependent and independent variables in this research.

Table 3

Correlation Analysis

		Attitude	Social norms	Price	Marketing	Brand	Convenience	Purchase Intention
Attitude	Correlation	1	.711**	-.144**	.525**	.579**	.473**	.721**
	Sig. (1-tailed)	0	0	0.001	0	0	0	0
Social Norms	Correlation	.711**	1	-.249**	.553**	.619**	.483**	.720**
	Sig. (1-tailed)	0		0	0	0	0	0
Price	Correlation	-.144**	-.249**	1	-.194**	-.194**	-.138**	-.249**
	Sig. (1-tailed)	0.001	0		0	0	0	0
Marketing	Correlation	.525**	.553**	-.194**	1	.777**	.546**	.709**
	Sig. (1-tailed)	0	0	0		0	0	0

Table 3
(continuation)

		Attitude	Social norms	Price	Marketing	Brand	Convenience	Purchase Intention
Brand	Correlation	.579**	.619**	-.194**	.777**	1	.606**	.747**
	Sig. (1-tailed)	0	0	0	0		0	0
Convenience	Correlation	.473**	.483**	-.138**	.546**	.606**	1	.579**
	Sig. (1-tailed)	0	0	0	0	0		0
Purchase Intention	Correlation	.721**	.720**	-.231**	.709**	.747**	.579**	1
	Sig. (1-tailed)	0	0	0	0	0	0	
	N	587	587	587	587	587	587	587

Table 3 has shown the correlation between different items used in this research. It shows how different variables defined in this study correlate with each other. It is evident from the table that all variables have a good correlation with each other and have less error values. Study variables are positively correlated with each other except that of the price, which is negatively associated with all other variables, reflecting that it has a negative impact on purchase intention and negatively affects other factors. It means all variables except price have a positive correlation, but the price has a negative relation, proving our hypothesis.

Hypothesis Testing

Multiple variable linear regression was used in the SPSS 19.0 software to test the results of the hypothesis. Table 4 shows the model summary, and R has a value of 0.754 while the value of the R^2 was 0.516, and the adjusted R^2 was 0.509. The model is accepted according to the results, and table 5 presents ANOVA analysis.

Table 4

Model Summary

Model	R	R^2	Adjusted R^2	Std. the error of the Estimate
1	0.754[a]	0.516	0.509	0.58912

a. Predictors : (Constant), Convenience, Price, attitude, quality, brand, social norms

Table 5

ANOVA Analysis

Model		Sum of Squares	df	Mean Square	F	Sig.
1	**Regression**	212.576	6	34.596	98.599	0.000[a]
	Residual	215.509	490	0.351		
	Total	428.085	496			

a. Predictors: (Constant), Convenience, Price, attitude, Marketing, brand, social norms
b. Dependent Variable: Price intension

Table 6

Coefficients Analysis

Model		Unstandardized Coefficients		Standardized Coefficients	t	Sig.
		B	Std. Error	Beta		
1	(Constant)	0.401	0.314		1.524	0.119
	Att	0.390	0.050	0.245	8.211	0.000
	Sn	0.160	0.029	0.121	7.089	0.001
	Pr	-0.180	0.009	-0.172	-3.119	0.031
	Ma	0.081	0.018	0.111	4.178	0.001
	Br	.0.322	0.030	0.383	9.990	0.000
	Cn	0.157	0.019	0.080	4.213	0.041

In this study, a Multivariable linear regression analysis is performed to test the six hypotheses. The hypothesis (H1) is developed to test the consumer attitude impact on purchase intention. Results show attitude has a positive relationship with the dependent variable (ß = .390, t= 8.211) and p-value is less than $p<0.01$. There is a positive relationship between attitude and consumer intention, and study results are consistent with theory and previous studies *(Armitage & Conner, 2001; Dean et al., 2006, Raats & Shepherd, 2008; Mahon et al., 2006)*. This study has shown that the consumer's attitude towards the purchase of CSR products is highly positive, and they feel that it is good to buy the products of the companies involved in CSR.

The eight items scale was used to measure social norms and their effect on purchase intentions towards companies' products are involved in CSR. Hypothesis H2 tests social norms' impact on the purchase intention and shows a positive relationship between social norms and purchase intention (ß = .160, t= 7.089). Pakistanis live in large houses with several family members, and they have strong relations and meetings with neighbors and other people. So, they influence buying behavior when they meet each daily routine. So, social norms are an essential factor that affects the Pakistani people's intention. The result has shown an adverse effect of price and cost on purchase intention. Consumers are unwilling to pay more for CSR products which show higher intention towards price and lower preference towards CSR products, while study results for the price are (ß =-.180, t =. -3.119 at significant level $p > .05$). Consumers are aware of CSR's importance. However, their private interests influence the purchase intention. The consumer buying decision is affected by personal interests. Consumers are not neglecting the importance of CSR. Still, they prioritize less expensive products, and some customers avoid choosing CSR companies' products *(Trapero, De Lozada, & García, 2010)*.

Most of the consumer's products selection is based on the price. It is evident from the results that the purchase intention of CSR is positively affected by the marketing of the product, and consumers do not want to compromise product marketing. They prefer marketing more instead of buying CSR products (ß = .0811, t =. 4.178 at significant level $p > .05$). Consumer judgment is limited in Pakistan. Consumer decisions are based on products, services, and company brand. Agriculture firms are doing CSR activities, but they are not receiving appreciation from customers. Brand plays a vital role in product or service decision-making. Our study has shown that consumers in Pakistan also consider the brand and are willing to buy branded products from agriculture firms. Companies involved in CSR activities face severe challenges, but consumers have less interest in CSR firms' products. So, brand effects CSR purchase intention, brand reputation, and brand trust influence intentions and consumers. The results for products marketing are (ß =0.322, t=9.990) at a significant level $p > .05$), which indicates that customers have more trust in a brand rather than CSR products purchase. Consumers give more importance and weight to the branded products rather than CSR activities by the companies.

The study results have shown that convenience is positively related to CSR purchase intentions, and the consumer is less willing to compromise on convenience for CSR purchase. The results show that (ß = 0.157, t = 4.213 at significant level $p < .05$) but this relation is weak.

CONCLUSIONS

The agricultural sector plays a vital role in Pakistan's economic growth, and domestic and multinational firms are engaged in agriculture. The study examines factors affecting consumer purchase intention of agriculture products. The current research examines whether consumers are willing to pay the extra price for those companies' products involved in CSR activities and what factors affect consumer purchase intention in the agriculture sector. CSR has a profound effect on consumer behavior in developed countries, and people are willing to compromise on various elements to purchase CSR products in the agriculture sector. In Pakistan, consumers are less aware of CSR activities. Not surprisingly, attitude, social norms, price, marketing, availability, convenience, and brand familiarity are still critical criteria when making purchase decisions. The study provides an empirical implication of the theory of the planned behavior model. Extended attitude model, social norms, and emotions are good towards CSR purchase, but there are few hurdles in practice such as price, marketing, brand, and convenience. Consumers are unwilling to pay the high price but won't compromise on quality. Consumers appreciate the company's CSR activities, and they want to purchase their products due to involvement in CSR. The agriculture sector consumers face several hurdles, including economic conditions, poverty, and lack of resources. Consumers are unwilling to pay higher/ more prices, and they do not want to compromise on essential issues, including brand and convenience. According to consumers, companies must do CSR activities for society, and their attitude towards buying CSR products is positive. Still, they do not buy at the cost of paying more or compromising quality, convenience, and brand. It has shown that customers do not pay attention to CSR for purchase, but they care about the product, brand, comfort, and price more than CSR.

REFERENCES

[1] Aleem, M., Rashid, H., & Awan, A. N. (2016). Characterization and removal of dyeing effluents by adsorption and coagulation methods. *J Agric Res*, *54*(1), 97-106.

[2] Amankwah-Amoah, J., Danso, A., & Adomako, S. (2018). Entrepreneurial orientation, environmental sustainability and new venture performance: Does stakeholder integration matter? *Business Strategy and the Environment*, *28*(1), 79–87. https://doi.org/10.1002/bse.2191

[3] Aleem, M., Shun, C. J., Rashid, H. R., Aslam, A. M., Javed, M. F. J., & Sarwar, M. W. (2017). Impact assessment of Dijkot branch drain effluent on groundwater quality using GIS technique. *J. Glob. Innov. Agric. Soc. Sci*, *5*, 20-27.

[4] Ajzen, I. (1985). From intentions to actions: A theory of planned behavior. In *Action control* (pp. 11-39). Springer, Berlin, Heidelberg.

[5] Armitage, C. J., & Conner, M. (2001). Efficacy of the theory of planned behaviour: A meta‐analytic review. *British journal of social psychology*, *40*(4), 471-499. https://doi.org/10.1348/014466601164939

[6] Arredondo Trapero, F. G., Maldonado de Lozada, V. D. C., & de la Garza García, J. (2010). Consumers and their buying decision making based on price and information about corporate social responsibility (csr).: Case study: Undergraduate students from a private university in Mexico. *Estudios Gerenciales*, *26*(117), 103-118. https://doi.org/10.1016/S0123-5923(10)70136-4

[7] Aguinis, H. (2011). Organizational responsibility: Doing good and doing well. In S. Zedeck (Ed.), A*PA handbook of industrial and organizational psychology*, Vol. 3. Maintaining, expanding, and contracting the organization (pp. 855–879). American Psychological Association. https://doi.org/10.1037/12171-024

[8] Becker-Olsen, K. L., Cudmore, B. A., & Hill, R. P. (2006). The impact of perceived corporate social responsibility on consumer behavior. *Journal of business research*, *59*(1), 46-53. https://doi.org/10.1016/j.jbusres.2005.01.001

[9] Beckmann, S. C. (2007). Consumers and corporate social responsibility: Matching the unmatchable? *Australasian Marketing Journal*, *15*(1), 27-36. https://doi.org/10.1016%2FS1441-3582%2807%2970026-5

[10] Bowen, H. R. (2013). *Social responsibilities of the businessman*. University of Iowa Press.

[11] Carroll, A. B. (1991). The pyramid of corporate social responsibility: Toward the moral management of organizational stakeholders. *Business horizons*, *34*(4), 39-48.

[12] Donald, R., & Cooper, P. S. (2007). Business research methods. Vol. 9 New York: McGraw-Hill Irwin

[13] Creyer, E. H. (1997). The influence of firm behavior on purchase intention: do consumers really care about business ethics? *Journal of Consumer Marketing,14*(6), 421-432. https://doi.org/10.1108/07363769710185999

[14] Dean, M., Raats, M. M., & Shepherd, R. (2008). Moral concerns and consumer choice of fresh and processed organic foods 1. *Journal of Applied Social Psychology*, *38*(8), 2088-2107. https://doi.org/10.1111/j.1559-1816.2008.00382.x

[15] Gupta, S., & Pirsch, J. (2006). The company‐cause‐customer fit decision in cause‐related marketing. *Journal of consumer marketing, 23*(6), 314-326.

[16] Ika, S. R., Akbar, F., Puspitasari, D., Sumbodo, B. T., & Widagdo, A. K. (2021). Corporate social responsibility reporting of agriculture companies: evidence from Indonesia. *IOP Conference Series: Earth and Environmental Science*, *800*(1), 012037. https://doi.org/10.1088/1755-1315/800/1/012037

[17] Javaid, A., & Nawaz, S. (2018). Review analysis on Agricultural Sector in Pakistan. *International Journal of Research and Innovation in Social Sciences*, 2(10), 93-94. http://dx.doi.org/10.29322/IJSRP.8.8.2018.p8095

[18] Kimuyu, P. (2018). *The Impact of Industrial Farming on the Environment*. GRIN Verlag.

[19] Lee, K. H., & Shin, D. (2010). Consumers' responses to CSR activities: The linkage between increased awareness and purchase intention. *Public Relations Review*, *36*(2), 193-195. https://doi.org/10.1016/j.pubrev.2009.10.014

[20] Liang, Y., Ju, Y., Qin, J., & Pedrycz, W. (2021). Multi-granular linguistic distribution evidential reasoning method for renewable energy project risk assessment. *Information Fusion*, *65*, 147-164. https://doi.org/10.1016/j.inffus.2020.08.010

[21] Lichtenstein, D. R., Drumwright, M. E., & Braig, B. M. (2004). The effect of corporate social responsibility on customer donations to corporate-supported nonprofits. *Journal of marketing*, *68*(4), 16-32. https://doi.org/10.1509%2Fjmkg.68.4.16.42726

[22] Madrigal, R., & Boush, D. M. (2008). Social responsibility as a unique dimension of brand personality and consumers' willingness to reward. *Psychology & Marketing*, *25*(6), 538-564. https://doi.org/10.1002/mar.20224

[23] Mahon, D., Cowan, C., & McCarthy, M. (2006). The role of attitudes, subjective norm, perceived control and habit in the consumption of ready meals and takeaways in Great Britain. *Food Quality and Preference*, 17(6), 474-481. https://doi.org/10.1016/j.foodqual.2005.06.001

[24] Maignan, I. (2001). Consumers' perceptions of corporate social responsibilities: A cross-cultural comparison. *Journal of business ethics*, *30*(1), 57-72. https://doi.org/10.1023/A:1006433928640

[25] May, T. (2011). *Social research: Issues, methods and research*. McGraw-Hill Education (UK).

[26] Miles, M. B., Huberman, A. M., & Saldana, J. (2014). Qualitative data analysis a Methods Sourcebook. Retrieved June 5, 2021, from https://www.scirp.org/(S(351jmbntvnsjt1aadkposzje))/reference/ReferencesPapers.aspx?ReferenceID=1977773

[27] Mohr, L. A., & Webb, D. J. (2005). The effects of corporate social responsibility and price on consumer responses. *Journal of consumer affairs*, *39*(1), 121-147. https://doi.org/10.1111/j.1745-6606.2005.00006.x

[28] Muthuri, J. N., Moon, J., & Idemudia, U. (2012). Corporate Innovation and Sustainable Community Development in Developing Countries. *Business & Society*, *51*(3), 355–381. https://doi.org/10.1177/0007650312446441

[29] Nazam, M., Usman, M., & Ayub, M. (2018). Analyzing Relationship Between Corporate Social Responsibility and Customer Loyalty for Beverage Consumers: A Case Study. *Journal of Marketing and Consumer Research*, 44(1), 1-7.

[30] Sarfraz, M. (2014). Do consumers consider CSR, a case of cellular companies in Pakistan? Global Journal of Management and Business Research, *14*(6), 2249-4588.

[31] Sarfraz, M., Qun, W., Abdullah, M. I., & Alvi, A. T. (2018a). Employees' perception of corporate social responsibility impact on employee outcomes: mediating role of organizational justice for small and medium enterprises (SMEs). *Sustainability*, *10*(7), 2429. https://doi.org/10.3390/su10072429

[32] Sarfraz, M., Qun, W., Hui, L., & Abdullah, M. I. (2018b). Environmental risk management strategies and the moderating role of corporate social responsibility in project financing decisions. *Sustainability*, *10*(8), 2771. https://doi.org/10.3390/su10082771

[33] Sarfraz, M., Shah, S. G., Fareed, Z., & Shahzad, F. (2020). Demonstrating the interconnection of hierarchical order disturbances in CEO succession with corporate social responsibility and environmental sustainability. *Corporate Social Responsibility and Environmental Management*, *27*(6), 2956-2971. https://doi.org/10.1002/csr.2014

[34] Syamni, G., Wahyuddin, Damanhur, and Ichsan, (2018), "CSR and Profitability in IDX Agricultural Subsectors", Proceedings of MICoMS 2017 (Emerald Reach Proceedings Series, Vol. 1), Emerald Publishing Limited, Bingley, pp. 511-517. https://doi.org/10.1108/978-1-78756-793-1-00034

[35] Sen, S., & Bhattacharya, C. B. (2001). Does doing good always lead to doing better? Consumer reactions to corporate social responsibility. *Journal of Marketing Research*, *38*(2), 225-243. https://doi.org/10.1509%2Fjmkr.38.2.225.18838

[36] Thomas, S. J., & Loft, R. D. (2005). The NCAR spectral element climate dynamical core: Semi-implicit Eulerian formulation. *Journal of Scientific Computing*, *25*(1), 307-322. https://doi.org/10.1007/s10915-004-4646-2

[37] Udo, M. (2007). Consumer Purchase Behavior toward Environmentally Friendly Products in Japan. *Unpublished master's thesis, The University of Nottingham, Nottingham, UK*.

[38] Uusitalo, O., & Oksanen, R. (2004). Ethical consumerism: a view from Finland. *International journal of consumer studies*, *28*(3), 214-221. https://doi.org/10.1111/j.1470-6431.2003.00339.x

[39] Uduji, J. I., & Okolo-Obasi, E. N. (2016). Multinational Oil Firms' CSR Initiatives in Nigeria: The Need of Rural Farmers in Host Communities. *Journal of International Development*, *29*(3), 308–329. https://doi.org/10.1002/jid.3243

[40] Wood, D. J. (1991). Corporate social performance revisited. *Academy of management review*, *16*(4), 691-718. https://doi.org/10.5465/amr.1991.4279616

WRITING INSTRUCTIONS

Article Types

Three types of manuscripts may be submitted:

1. **Regular articles:** These should describe new and carefully confirmed findings, and experimental procedures should be given in sufficient detail for others to verify the work. The length of a full paper should be the minimum required to describe and interpret the work clearly (max.10 pages, even number);
2. **Reviews:** Submissions of reviews and perspectives covering topics of current interest are welcome and encouraged (max.12 pages, even number).

Manuscripts should be written in English (American or British usage is accepted, but not a mixture of these) and submitted **electronically** at the following e-mail addresses: ***inmatehjournal@gmail.com***

Please be sure to include your full affiliation and e-mail address (see Sample manuscript)

The authors are responsible for the accuracy of the whole paper and references.

There are allowed 2 papers by each first author.

The text layout should be in single-column format. To avoid unnecessary errors it is strongly advised to use the "spell-check" and "grammar check" functions of your word processor.

Review Process

All manuscripts are reviewed by 2 members of the Scientifically Review Office. Decisions will be made as rapidly as possible and the journal strives to return reviewers' comments to authors in approx.3 weeks.

The editorial board will re-review manuscripts that are accepted pending revision.

NOTE:

Submission of a manuscript implies: that the work described has not been published before (excepting as an abstract or as part of a published lecture or thesis) that it is not under consideration for publication elsewhere.

1. REGULAR ARTICLES

- Manuscripts should be concise, in ***1.15 line spacing***, and should have 2 cm all over margins. The font should be ***Arial 10 pt.*** Ensure that each new paragraph is clearly indicated, using **TAB at 1 cm**.
- Title will be ***Arial 12 pt***. and explicit figures will be ***Arial 9 pt***.
- Text will be written in English.
- Chapters' titles are written by ***Arial 10 pt, Bold, Uppercase*** (e.g. **INTRODUCTION, MATERIALS AND METHODS**), between chapters is left a space for 10 pt. At the beginning of each paragraph, TAB of 1 cm.
- The paper body will be written in ***Arial 10 pt., Justify alignment***.

TITLE ***Arial 12 pt., Uppercase, Bold, Center*** *(in English language)* and ***Bold Italic*** *(in native language)*.
Should be a brief phrase describing the contents of the paper. Avoid long titles; a running title of no more than 100 characters is encouraged (without spaces).

AUTHORS ***ARIAL 9, Bold, Centre alignment***
Under the paper's title, after a space (enter) 9 pt., write ***authors' names*** and ***affiliations (Arial 8 pt.-Regular)***
When the paper has more than one author, their name will be followed by a mark (Arabic numeral) as superscript if their affiliation is different. Less than 6 authors.
Corresponding author's name (next row), ***(Arial 8 pt.)***. Should be added also: phone, fax and e-mail information, for the paper corresponding author (***font: 8 pt., Italic***).

KEYWORDS ***(In English)*** about 4 to 7 words that will provide indexing references should be listed (title: ***Arial 10pt, bold italic,*** text ***Arial 10 pt., italic***).

A list of non-standard *Abbreviations* should be added. In general, non-standard abbreviations should be used only when the full term is very long and used often. Each abbreviation should be spelled out and introduced in parentheses the first time it is used in the text. Standard abbreviations (such as ATP and DNA) need not to be defined.
ABSTRACT ***(in English and Native language, Arial 10 pt.)***, the title *bold*; the text of abstract: *italic*) should be informative and completely self-explanatory, briefly present the topic, state the scope of the experiments, indicate significant data, and point out major findings and conclusions. The Abstract should be max.250 words. Complete sentences, active verbs, and the third person should be used, and the abstract should be written in the past tense. Standard nomenclature should be used and abbreviations should be avoided. No literature should be cited.
INTRODUCTION (***Arial 10 pt.***) should provide a clear statement of the problem, the relevant literature on the subject, and the proposed approach or solution. It should be understandable to colleagues from a broad range of scientific subjects. We should refer to the current stage of researches performed in the field of the paper to be published, by quoting up-to-date specialty studies, preferably published after 2006, excepting certain referential specialty

books/studies, especially papers issued in magazines/journals/conferences/ISI quoted symposia or in other international data bases, which are well known and available.

MATERIALS AND METHODS (***Arial 10 pt.***) should be complete enough to allow experiments to be reproduced. However, only truly new procedures should be described in detail; previously published procedures should be cited, and important modifications of published procedures should be mentioned briefly. Methods in general use need not be described in detail.

RESULTS (***Arial 10 pt.***) should be clarity presented. The results should be written in the past tense when describing findings in the authors' experiments. Results should be explained, but largely, without referring to the literature. Discussion, speculation and detailed interpretation of data should not be included in the Results, but should be put into the Conclusions section.

CONCLUSIONS (***Arial 10 pt.***) The main conclusions drawn from results should be presented in a short Conclusions section. Do not include citations in this section.

Formulae, symbols and abbreviations: Formulae will be typeset in Italics (preferable with the Equation Editor of Microsoft Office 2003) and should be written or marked as such in the manuscript, unless they require a different styling. They should be referred to in the text as Equation (4) or e.g. (4). The formulae should be numbered on the right side, between brackets ***(Arial 10 pt.)***:

$$P = F \cdot v \tag{1}$$

Terms of the equation and the unit measure should be explained, e.g.

P is the power, [W];
F – force, [N];
v – speed, [m/s]

SI units must be used throughout.

Tables should be self-explanatory without reference to the text. The details of the methods used in the experiments should preferably be described in the legend instead of in the text. The same data should not be presented both in table and graph form or repeated in the text.

Table's title will be typed ***Arial 9 pt, Bold, Centered***

In the table, each row will be written Arial 9 pt, single-spaced throughout, including headings and footnotes.

The table should be numbered on the right side, ***Arial 10 pt.***

Figures ***(Arial 9 pt., Bold, Center)***should be typed in numerical order (Arabic numerals). Graphics should be high resolution (e.g.JPEG).Figure number is followed by what represent the figure or graph e.g.:

Fig.1 – Test stand

Legend: ***Arial 8 pt, Italic, Center,*** e.g.:

1 - plansifter compartments; 2- break rolls; 3 – semolina machines; 4 – reduction rolls; 5 – flour

ACKNOWLEDGMENTS (***Arial 10 pt.***) of people, grants, funds etc should be brief (*if necessarily*).

REFERENCES (***Arial 10 pt.***)

(In alphabetical order, in English and in the original publication language).
Minimum 10 references, last 10 years, minimum 3 references from the last 2 years

It can be used "*References*" tool from the *Word Editor*. **APA Style (American Psychological Association)**
https://apastyle.apa.org/style-grammar-guidelines/references/examples

All references must be provided in English
Authors are fully responsible for the accuracy of the references.

References should be **alphabetically**, with complete details, as follows:

Examples:

Books: https://apastyle.apa.org/style-grammar-guidelines/references/examples/book-references

Jackson, L. M. (2019). *The psychology of prejudice: From attitudes to social action* (2nd ed.). American Psychological Association. https://doi.org/10.1037/0000168-000

Kesharwani, P. (2020). *Nanotechnology based approaches for tuberculosis treatment*. Academic Press.

Sapolsky, R. M. (2017). *Behave: The biology of humans at our best and worst*. Penguin Books.

Torino, G. C., Rivera, D. P., Capodilupo, C. M., Nadal, K. L., & Sue, D. W. (2019). *Microaggression theory: Influence and implications*. John Wiley & Sons. https://doi.org/10.1002/9781119466642

In text:

- ***Parenthetical citations***: (Jackson, 2019; Sapolsky, 2017)
- ***Narrative citations***: Jackson (2019) and Sapolsky (2017)

Journal Article:

https://apastyle.apa.org/style-grammar-guidelines/references/examples/journal-article-references

Grady, J. S., Her, M., Moreno, G., Perez, C., & Yelinek, J. (2019). Emotions in storybooks: A comparison of storybooks that represent ethnic and racial groups in the United States. *Psychology of Popular Media Culture*, *8*(3), 207–217. https://doi.org/10.1037/ppm0000185

In text:

- ***Parenthetical citation***: (Grady et al., 2019)
- ***Narrative citation***: Grady et al. (2019)

Conference or Symposium:

https://apastyle.apa.org/style-grammar-guidelines/references/examples/conference-proceeding-references

Duckworth, A. L., Quirk, A., Gallop, R., Hoyle, R. H., Kelly, D. R., & Matthews, M. D. (2019). Cognitive and noncognitive predictors of success. *Proceedings of the National Academy of Sciences*, *USA*, *116*(47), 23499–23504. https://doi.org/10.1073/pnas.1910510116

In text:

- ***Parenthetical citation***: (Duckworth et al., 2019)
- ***Narrative citation***: Duckworth et al. (2019)

Dissertation / Thesis:

https://apastyle.apa.org/style-grammar-guidelines/references/examples/published-dissertation-references

Zambrano-Vazquez, L. (2016). *The interaction of state and trait worry on response monitoring in those with worry and obsessive-compulsive symptoms* [Doctoral dissertation, University of Arizona]. UA Campus Repository. https://repository.arizona.edu/handle/10150/620615

In text:

- ***Parenthetical citations***: (Kabir, 2016; Miranda, 2019; Zambrano-Vazquez, 2016)
- ***Narrative citations***: Kabir (2016), Miranda (2019), and Zambrano-Vazquez (2016)

https://apastyle.apa.org/style-grammar-guidelines/references/examples/unpublished-dissertation-references

Harris, L. (2014). *Instructional leadership perceptions and practices of elementary school leaders* [Unpublished doctoral dissertation]. University of Virginia.

In text:

- ***Parenthetical citation***: (Harris, 2014)
- ***Narrative citation***: Harris (2014)

Patents: Names and initials of authors, year (between brackets), patent title (Italic), patent number,country:
Grant, P. (1989). *Device for Elementary Analyses*. Patent. No.123456. USA.

Legal regulations and laws, organizations:

https://apastyle.apa.org/style-grammar-guidelines/references/examples/iso-standard-references

International Organization for Standardization. (2018). *Occupational health and safety management systems—Requirements with guidance for use* (ISO Standard No. 45001:2018). https://www.iso.org/standard/63787.html

Occupational Safety and Health Administration. (1970). *Occupational safety and health standards: Occupational health and environmental control: Occupational noise exposure* (OSHA Standard No. 1910.95). United States Department of Labor. https://www.osha.gov/laws-regs/regulations/standardnumber/1910/1910.95

In text:

- ***Parenthetical citations***: (International Organization for Standardization, 2018; Occupational Safety and Health Administration, 1970)
- ***Narrative citations***: International Organization for Standardization (2018) and Occupational Safety and Health Administration (1970)

Web references: The full URL should be given in text as a citation, if no other data are known. If the authors, year, and title of the documents are known and the reference is taken from a website, the URL address has to be mentioned after these data.

Citation in text

Please ensure that every reference cited in the text is also present in the reference list (and vice versa).

Do not cite references in the Abstract and Conclusions !.

Unpublished results, personal communications as well as URL addresses are not recommended in the references list.

Making personal quotations (one, at most) should not be allowed, unless the paper proposed to be published is a sequel of the cited paper. Articles in preparation or articles submitted for publication, unpublished, personal communications etc. should not be included in the references list.

Citations style

***Text**:* All citations in the text may be made directly (or parenthetically) as bellow.

- ***single author**:* the author's name (without initials, unless there is ambiguity) and the year of publication:
  "as previously demonstrated *(Brown, 2010)*".
- ***two authors**:* both authors' names and the year of publication: *(Adam and Brown, 2008; Smith and Hansel, 2006; Stern and Lars, 2009)*
- ***three or more authors**:* first author's name followed by "et al." and the year of publication: "As has recently been shown *(Werner et al., 2005; Kramer et al., 2000)* have recently shown ...."

Citations of groups of references should be listed first alphabetically, then chronologically.

Units, Abbreviations, Acronyms

- Units should be metric, generally SI, and expressed in standard abbreviated form.
- Acronyms may be acceptable, but must be defined at first usage.

2. REVIEWS

Summaries, reviews and perspectives covering topics of current interest in the field, are encouraged and accepted for publication. Reviews do not have the requirements for regular articles. However, should include: (*) an introductory chapter, (**) a careful and critical presentation of the relevant aspects of the topic approached and (***) emphasis of the aspects that aren't known and require further research to progress. Reviews should be concise (max. 12 pages).

Edited by: INMA Bucharest
6, Ion Ionescu de la Brad Blvd., sect. 1, Bucharest, ROMANIA
Tel: +4021.269.32.60; Fax: +4021.269.32.73
https:// inmateh.eu
e-mail: ***inmatehjournal@gmail.com***